XIII REUNIÓN CIENTÍFICA DE LA SOCIEDAD ESPAÑOLA DE ASTRONOMÍA

SEA

SALAMANCA, 16–20 DE JULIO DE 2018

HOSPEDERÍA FONSECA

COMITÉ CIENTÍFICO:
Andrés Asensio (IAC)
Fernando Atrio (USAL)
Paula Benavidez (UA)
Fernando Buitrago (IA, Lisboa)
Benjamín Montesinos (CAB) (Coordinador)
Rainer Shoedel (IAA)
Alicia Sintes (UIB)
Licia Verde (ICCUB)
Eva Villaver (UAM)

COMITÉ LOCAL:
Fernando Buitrago (IA, Lisboa) (Coordinador)
José Antonio Caballero (CAB)
Juan Manuel Corchado (USAL)
Fernando de la Prieta (USAL)
Belén Pérez (USAL)
María Ángeles Pérez (USAL)
Inés Rodríguez (Museo de la Ciencia, Valladolid)

ESA/Hubble

#SEASalamanca2018

Highlights on Spanish Astrophysics X, Proceedings of the XIII Scientific Meeting of the Spanish Astronomical Society held on July 16 – 20, 2018, in Salamanca, Spain. B. Montesinos, A. Asensio Ramos, F. Buitrago, R. Schödel, E. Villaver, S. Pérez-Hoyos, I. Ordóñez-Etxeberria (eds.), 2019

Content

Highlights on Spanish Astrophysics X, Proceedings of the XIII Scientific Meeting of the Spanish Astronomical Society held on July 16 – 20, 2018, in Salamanca, Spain. B. Montesinos, A. Asensio Ramos, F. Buitrago, R. Schödel, E. Villaver, S. Pérez-Hoyos, I. Ordóñez-Etxeberria (eds.), 2019

Athena: Mission and Spanish participation.

Francisco J. Carrera

Instituto de Física de Cantabria (CSIC-U. Cantabria), Santander, Spain

Abstract

Athena (Advanced Telescope for High ENergy Astrophysics) is the X-ray observatory mission selected by ESA to address the Hot and Energetic Universe theme, due for launch in the early 2030s. *Athena* addresses three key scientific objectives: 1) Determine how and when large-scale hot gas structures formed in the Universe and track their evolution from the formation epoch to the present day. 2) Perform a complete census of black hole growth in the Universe, determine the physical processes responsible for that growth and its influence on larger scales, and trace these and other energetic and transient phenomena to the earliest cosmic epochs. 3) Provide a unique contribution to astrophysics in the 2030s by exploring high energy phenomena in all astrophysical contexts, including those yet to be discovered.

From the unique perspective endowed to *Athena* by its unprecedented spectroscopic and imaging capabilities in the 0.5-12 keV range, this mission will lead the quest into solving these questions from its launch.

The *Athena* mission concept is that of a single large-aperture grazing-incidence X-ray telescope, utilising a novel technology (Si pore optics) developed in Europe, with 12 m focal length and 5 arcsec HEW angular resolution. The focal plane contains two instruments. One is the Wide Field Imager (WFI) providing sensitive wide field of view imaging and low resolution spectroscopy, as well as bright source observation capability. The other one is the X-ray Integral Field Unit (X-IFU) delivering spatially resolved high-resolution X-ray spectroscopy over a limited field of view. Synergies with other facilities (ESO, SKA, CTA, LISA, etc.) are being identified and developed.

Spain has an important role in *Athena*, with a significant contribution to the X-IFU instrument, including the dewar for the detector cooling system, the algorithms for the on-board pulse detection software, and a leading scientific contribution. Spain also leads the *Athena* Community Office, set up to help optimising the participation of the more than 800 scientists which are helping to shape up the mission through its working groups.

1 Introduction

Thanks to its unprecedented spectroscopic and imaging capabilities in the 0.5-12 keV range, *Athena*[1] [18] will lead the quest to solve several key questions of modern astrophysics, relevant to the Hot and Energetic Universe science theme.

Our current understanding is that most of the ordinary (baryons) matter in the Universe is today locked in Mpc-scale filamentary structures of gas at million degree temperatures, both inside the potential wells of groups and clusters of galaxies [21, 9] and in the so-called Warm Hot Intergalactic Medium (WHIM) [15]. Investigating how such hot gas structures formed and evolved, and how and when the material trapped in them was energised and chemically enriched, is possible only through observations in the X-ray band, combining wide-field imaging with high resolution spectroscopy, both of high sensitivity. Such capabilities will also reveal the physical properties of the WHIM, both via its emission, and in absorption against bright background targets.

Performing a complete census of black hole growth in the Universe has become a most pressing issue since the realisation that all nearby massive galaxies harbour a Super-Massive Black Hole (SMBH), with a mass intriguingly proportional to that of the galaxy bulge. Furthermore, the cosmic evolution of galaxy growth through star formation and SMBH growth via accretion (shining as Active Galactic Nuclei or AGN) follow parallel tracks, increasing back in time from the present time to its heyday at redshifts $z \sim 1 - 3$. Do these fascinating clues imply that AGN actually shape their host galaxies? How does this happen? How far back does this start? Wide field X-ray observations have the ability to pinpoint AGN among the myriad sources in the sky, even if they are heavily obscured. This capability will enable the detection of even the most elusive specimens of this population, such as the most heavily obscured [13] or those at higher redshift [1]. X-ray spectroscopy and time variability will reveal the workings of the inner parts of the AGN engine [12] (and those of other stellar-mass accreting engines in our Galaxy) as well as the outflows of ionised gas that may carry sufficient momentum and kinetic energy to regulate star formation in the host galaxy[8, 5]. Finally, the fast Target of Opportunity capabilities of *Athena* will enable studies of Gamma Ray Bursts and other transient phenomena to the earliest cosmic epochs [14].

Aside from these topics, the singular and outstanding capabilities of *Athena* as an observatory are expected to make a profound impact in essentially all fields of Astrophysics. For instance they will allow understanding the structure and energetics of stellar winds and their interplay with atmospheres and magnetospheres of planets [4, 24]. They will also permit exploring the behaviour of matter under extreme conditions of density and magnetic fields in stellar binaries and neutron stars [17]. As a final example *Athena* will probe the physics of the enrichment and heating of our Galaxy's Interstellar Medium by supernova explosions [10].

This will not happen in isolation, but taking full advantage of *Athena*'s synergies with the set of multi-wavelength and multi-messenger astronomical facilities in operation in the early 2030s (e.g. LOFAR, SKA [6], ALMA, ELT[19], LSST, CTA, LISA, to name but a few),

[1] https://www.the-athena-x-ray-observatory.eu/

see also contributions by M. Díaz-Trigo [11], M. Ribó [23] and M.A. Pérez-Torres [20] in this volume.

2 An observatory for the whole astronomical community

Athena will be a large X-ray observatory offering spatially resolved X-ray spectroscopy and deep wide-field X-ray spectral imaging with performance greatly exceeding that offered by current X-ray observatories like *XMM-Newton* and *Chandra*, or by missions to be launched shortly like *XRISM* and *SRG*/eROSITA.

Athena will be launched by an Ariane 6 vehicle, with equivalent or larger lift capability and fairing size to that of the Ariane 5. It will operate at the second Sun-Earth Lagrangian point (L2) in a large halo orbit, although the possibility of an L1 halo orbit is also being assessed. Such orbits offer a very stable thermal environment as well as good instantaneous sky visibility and high observing efficiency.

Athena has a baseline mission lifetime of 4 years, although it will be designed and have consumables for a longer time. Operations will be performed as in standard ESA science missions, with the Mission Operations Centre (MOC) at ESOC (Darmstadt, Germany) and the Science Operations Centre (SOC) at ESAC (Villafranca del Castillo, Spain). Two Instrument Science Centres (one each for the X-IFU and WFI) will complement the SOC in performing scientific ground segment activities.

Athena will be operated as an observatory, in a similar fashion to prior missions such as *XMM-Newton* and *Herschel*. Users will access the observatory via open proposal calls.

3 A state of the art payload

The *Athena* observatory consists of a single X-ray telescope [25] with a fixed 12 m focal length, with an effective area of 1.4 m^2 (at 1 keV) and a spatial resolution of $5''$ on axis. The mirror is based on ESA's Silicon Pore Optics (SPO) technology. SPO provides an excellent ratio of collecting area to mass, while still offering good angular resolution. It also benefits from a high Technology Readiness Level and a modular design highly amenable to mass production, necessary to achieve the unprecedented telescope collecting area. A movable mirror assembly can focus X-rays onto either one of *Athena*'s two instruments at any given time.

The Wide Field Imager (WFI[2]) [22, 16], is a Silicon-based detector using DEPFET Active Pixel Sensor technology with a field of view of $40' \times 40'$, offering 150 eV spectral resolution, with a pixel size of $2.2''$. The large field of view of the instrument is provided by a Large Detector Array (LDA) consisting of four DEPFET chips. A further, smaller DEPFET detector is optimised for fast readout to accommodate measurement of the brightest X-ray sources in the sky, at a time resolution of 80 μs.

The X-ray Integral Field Unit (X-IFU[3]) [2, 3], provides spatially-resolved high resolu-

[2]http://www.mpe.mpg.de/ATHENA-WFI/
[3]http://x-ifu.irap.omp.eu/

tion spectroscopy. The instrument is a cryogenic X-ray micro-calorimeter, based on a large array of Transition Edge Sensors, offering 2.5 eV spectral resolution, with $< 5''$ pixels, over a field of view of $5'$ in equivalent diameter and a timing resolution of 10 μs. An active anti-coincidence detector placed underneath the main TES array aims at reducing the non X-ray background. The focal plane assembly holding the detectors is cooled at 50 mK by a series of mechanical coolers.

4 The *Athena* Community and the *Athena* Community Office

The remit of the *Athena* Science Study Team (ASST) involves multiple tasks, which include acting as a focus for the involvement of the broad scientific community. With the agreement of ESA, the ASST has established a Working Group structure populated by members of the community[4]. These Working Groups and Topical Panels are intended to bring the expertise and effort of that community to bear in support of *Athena*. The mission is currently supported by about 800 researchers.

At the moment there are 5 Working Groups (SGW1 The Hot Universe, SWG2 The Energetic Universe, SWG3 Observatory Science, TWG4 Telescope and MWG5 Mission Performance). Most of them are organised in Topical Panels (TP e.g. SWG1.3, MPG5.2, etc).

The ASST appointed the *Athena* Community Office (ACO)[5] to obtain assistance in organisational aspects and optimisation of community efforts, keeping the *Athena* Community informed and developing communication and outreach activities around *Athena*. The ACO is led by IFCA (CSIC-UC) in Spain, with contributions from IRAP (France), MPE (Germany) and the Université de Genève (Switzerland). For more details see contribution by M.T. Ceballos [7] in this volume.

5 Spanish participation in *Athena*

At mission level a total of 48 researchers from Spanish institutions serve in the TP, including 2 TP chairs (G. Miniutti and F.J. Carrera) and 2 members in SWG1, 30 in SWG2, 20 in SWG3, 2 in TWG4 and 7 in MWG5.

As mentioned just above, the *Athena* Community Office is led by IFCA (CSIC-UC).

At instrument level there is some small-scale involvement in the scientific definition of the WFI through the survey and TP 2.1 (Understanding the build-up of SMBH and their host galaxies, led by F.J. Carrera, S. Mateos and A. Corral).

However, the main participation is focussed on X-IFU in whose consortium board M. Mas Hesse represents Spain. M. Mas and M.T. Ceballos are Instrument co-Investigators. The Detector Cooling System cryostat (dewar) is being developed by INTA and CAB (Phase A) under the leadership of J. Gómez, with A. Balado as Project Manager, with the participation of: M.A. Alcacera, J. Azcue, A. Balado, L. Bastide, F. Cabrerizo, J.M. Encinas, M.

[4]https://www.the-athena-x-ray-observatory.eu/community.html

[5]See the ACO leaflet under https://www.the-athena-x-ray-observatory.eu/resources/athena-brand.html

Fernández, A. García, C. Moravec, M. Pajas, J.M. Pintado, M. Reina, J. Sanmillan and I. Vera. Additionally, IFCA is developing the Event Processor algorithms, led by M.T. Ceballos and with the participation of B. Cobo.

Spain is also participating in the science support for X-IFU J.M. Torrejón being a member of the X-IFU Science Team and X. Barcons being science co-I of that instrument.

Finally, IFCA and the U. de Alicante are members of the X-IFU Instrument Science Centre.

Acknowledgments

F.J.C. gratefully acknowledges the contribution of the ACO, the ASST and SWG chairs to the *Athena* leaflet[6] in which this contribution is heavily based. F.J.C. thanks M.T. Ceballos and J. Gómez for useful discussion. F.J.C. acknowledges financial support through grant AYA2015- 64346-C2-1-P (MINECO/FEDER).

References

[1] Aird J., et al., 2013, arXiv:1306.2325

[2] Barret D., et al., 2013, arXiv:1308.6784

[3] Barret D., et al., 2018, to appear in Proc. SPIE Astronomical Telescopes and Instrumentation, arXiv:1807.06092

[4] Branduardi-Raymont G., et al., 2013, arXiv:1306.2332

[5] Cappi M., et al., 2013, arXiv:1306.2330

[6] Cassano R., et al., 2018, arXiv: 1807.09080

[7] Ceballos M.T., et al. 2019, in "Highlights on Spanish Astrophysics X, Proceedings of the XIII Scientific Meeting of the Spanish Astronomical Society (Salamanca 2018), B. Montesinos, A. Asensio Ramos, F. Buitrago, R. Schödel, E. Villaver, S. Pérez-Hoyos (eds.)

[8] Croston J., et al., 2013, arXiv:1306.2323

[9] Ettori S., et al., 2013, arXiv:1306.2322

[10] Decourchelle A., et al., 2013, arXiv:1306.2335

[11] Díaz-Trigo M., et al. 2019, in "Highlights on Spanish Astrophysics X, Proceedings of the XIII Scientific Meeting of the Spanish Astronomical Society (Salamanca 2018), B. Montesinos, A. Asensio Ramos, F. Buitrago, R. Schödel, E. Villaver, S. Pérez-Hoyos (eds.)

[12] Dovciak M., et al., 2013, arXiv:1306.2331

[13] Georgakakis A., et al., 2013, arXiv:1306.2328

[14] Jonker P., et al., 2013, arXiv:1306.2336

[15] Kaastra J., et al., 2013, arXiv:1306.2324

[6] Available here https://www.the-athena-x-ray-observatory.eu/resources/athena-brand.html

[16] Meidinger N., et al., 2018, to appear in Proc. SPIE Astronomical Telescopes and Instrumentation

[17] Motch C., et al., 2013, arXiv:1306.2334

[18] Nandra K., Barret D., Barcons X., et al., 2013, arXiv:1306.2307

[19] Padovani P., et al., 2017, arXiv: 1705.06064

[20] Pérez-Torres M.A., et al. 2019, in "Highlights on Spanish Astrophysics X, Proceedings of the XIII Scientific Meeting of the Spanish Astronomical Society (Salamanca 2018), B. Montesinos, A. Asensio Ramos, F. Buitrago, R. Schödel, E. Villaver, S. Pérez-Hoyos (eds.)

[21] Pointecouteau E., et al., 2013, arXiv:1306.2319

[22] Rau A., et al., 2013, arXiv:1308.6785

[23] Ribó M., et al. 2019, in "Highlights on Spanish Astrophysics X, Proceedings of the XIII Scientific Meeting of the Spanish Astronomical Society (Salamanca 2018), B. Montesinos, A. Asensio Ramos, F. Buitrago, R. Schödel, E. Villaver, S. Pérez-Hoyos (eds.)

[24] Sciortino S., et al., 2013, arXiv:1306.2333

[25] Willingale R., et al., 2013, arXiv:1308.6785

Highlights on Spanish Astrophysics X, Proceedings of the XIII Scientific Meeting of the Spanish Astronomical Society held on July 16 – 20, 2018, in Salamanca, Spain. B. Montesinos, A. Asensio Ramos, F. Buitrago, R. Schödel, E. Villaver, S. Pérez-Hoyos, I. Ordóñez-Etxeberria (eds.), 2019

ALMA: Science with exceptional submillimeter capabilities.

Itziar de Gregorio-Monsalvo[1,2]

[1] Joint ALMA Observatory, Alonso de Córdova 3107, Vitacura 763-0355, Santiago, Chile
[2] European Southern Observatory, Avenida Alonso de Córdova 3107, Vitacura 763-0355, Santiago, Chile

Abstract

The Atacama Large Millimeter/submillimeter Array (ALMA) is an outstanding facility for millimeter and submillimeter-wave Astronomy with transformational capabilities to study the origin of galaxies, stars, and planets. ALMA consists of sixty six antennas located on the Chajnantor plateau at five thousand meters altitude in northern Chile, and equipped with receivers covering atmospheric windows between 30 and 950 GHz. ALMA is an international partnership of Europe, North America and East Asia in cooperation with the Republic of Chile. Since its third Call for Proposals ALMA received more submissions than any other telescope in history, surpassing 1800 proposal in the latest Call for Cycle 6.

1 Introduction

The Atacama Large Millimeter/submillimeter Array consists of sixty-six high precision antennas working in interferometric mode at millimeter/submillimeter wavelengths at 5000 m height close to San Pedro de Atacama, in the north of Chile.

It is composed by a big array of fifty antennas with twelve meter diameter (called 12-m array), and a smaller one (called Morita Array) with twelve antennas of seven meter plus four antennas of twelve meters diameter to recover extended emission from astronomical sources. The 12-m array is movable from compact to very extended configurations (baselines from $\simeq 150$ m up to $\simeq 16$ km) to achive different spatial resolutions, ranging from $\simeq 5''$ to $\simeq 0.04''$ at 110 GHz and to $\simeq 0.5''$ to $\simeq 0.0044''$ at 950 GHz. Thanks to the interferometry technique we can see detailed images in field of views of $\simeq 70''$ at 3.5 mm to $\simeq 7''$ at 315 μm. ALMA operates in eight different bands (band 3 to band 10) from frequencies between 84 to 950 GHz respectively.

Signals from different antennas are combined in a very powerful supercomputer, the

ALMA correlator, characterized for being a very flexible machine that allows simultaneous high and low spectral resolution observations (Fig. 1). ALMA has a bandwidth of 8 GHz and up to 7680 frequency channels, providing a very high sensitivity in the continuum and very high velocity resolution.

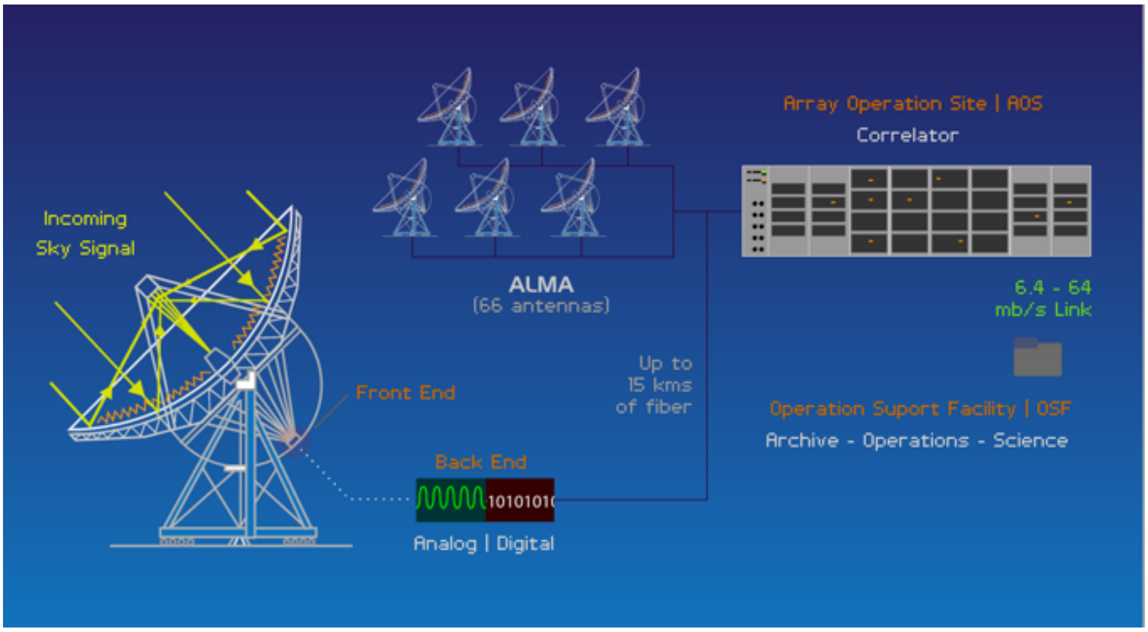

Figure 1: ALMA signal combination. Courtesy: ALMA(ESO/NAOJ/NRAO)

1.1 Submillimeter Astronomy

ALMA is capable to study the part of the electromagnetic spectrum in between the far infrared and the radio waves, observing the light comming from very cold objects. At submillimeter wavelengths we mainly see thermal continuum emission from cold dust, and spectral lines from molecular gas that yield information on the physical conditions, chemistry and kinematics.

Many objects produce emission in the millimeter/submillimeter regime: from Solar System objects, molecular clouds, star forming regions, protoplanetary disks, and evolved stars, to nearby and very distant galaxies. ALMA allows us for the first time to study at high angular resolution and high sensitivity the properties of dust and gas in a wide range of sources from the local to the very distant Universe.

1.2 The ALMA site: 5000 m height in the Atacama Desert

The Atacama Large Millimeter Array is located at five thousand meters height in Llano Chajnanator, a plain in the middle of the Atacama desert very close to San Pedro de Atacama, in Northern Chile (see Fig. 2). This place was selected to host the ALMA antennas because

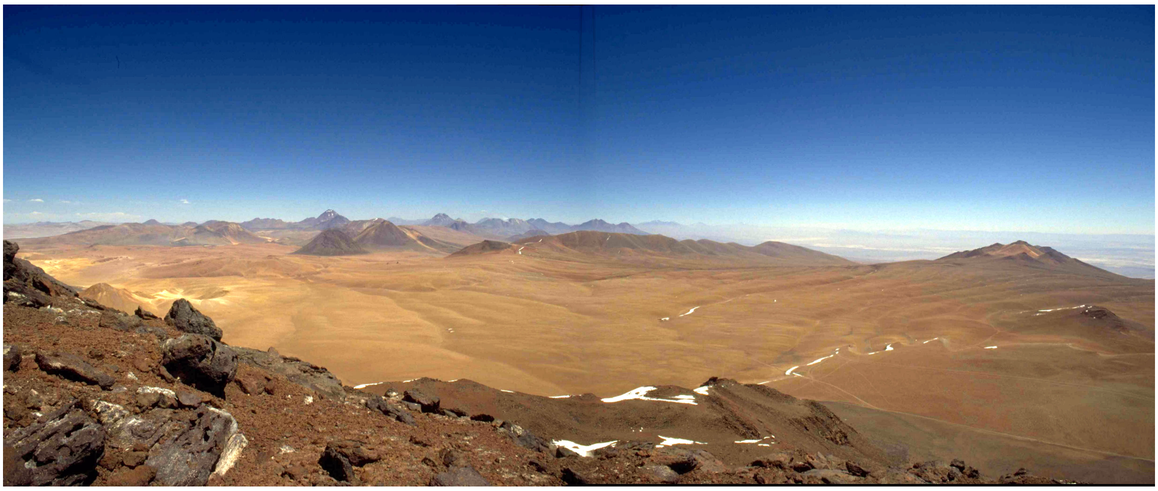

Figure 2: ALMA site in 1994. Courtesy: S. Radford

it possesses very good conditions to carry out sucessfully interferometric observations in the submillimeter/millimeter regime in terms of atmospheric transparency and stability.

Inhomogeneities in the distribution of the water vapor in the atmosphere cause variations in the electrical path length of the incoming signal, which induces larger phase errors degrading the sensitivity and the spatial resolution of interferometric images. The high altitude of Llano Chajnantor reduces the thickness of the atmosphere above the observatory, and the very dry air of the desert helps to decrease the absorption of the incoming radiation by the trophosferic water molecules.

2 ALMA science operations

ALMA is an international partnership of Europe, North America and East Asia in cooperation with the Republic of Chile. There are more than twenty countries contributing to ALMA. Chile is the host country and Chilean astronomers can access to the 10% of total observing time to carry out their own research.

ALMA science operations is led by the Joint ALMA Observatory in Chile, and the ALMA Regional Centers (ARCs) from Europe (led by the European Southern Observatory), North America (led by the National Radioastronomy Observatory), and from East Asia (led by the National Astronomical Observatory of Japan), see Fig. 3.

The Joint ALMA Observatory provides array operations, scheduling of projects, execution of observations, data quality assurance and trend analysis, calibration plan maintenance, delivery of data to the archives, archive operations, pipeline operations, and software subsystem scientists. The ARCs are the interfaces to the user community and as core tasks they provide user support (via helpdesk and face to face), delivery of data to the principal investigators of scientific projects, mirror archive operations, astronomers on duty, subsystem scientists, and data quality assurance.

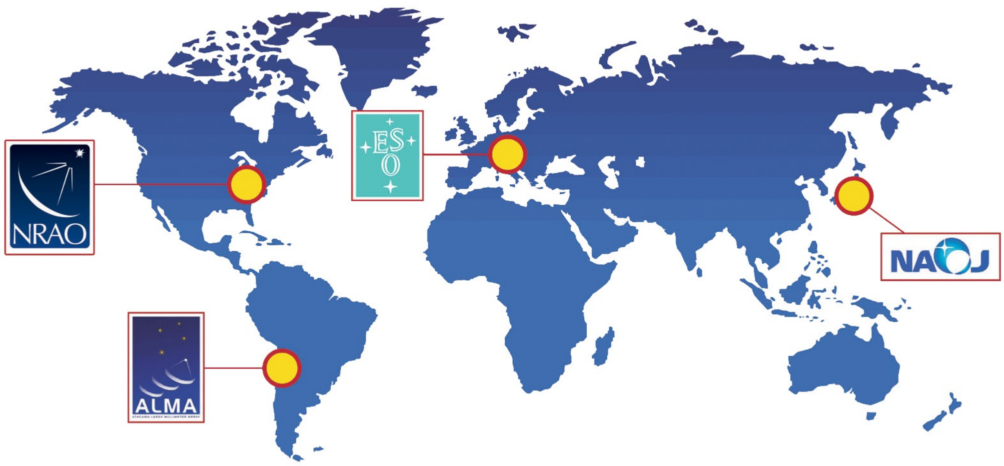

Figure 3: ALMA Science Operations Centers. Courtesy: ALMA(ESO/NAOJ/NRAO)

The Joint ALMA Observatory is composed by three different places: The Operations Support Facility (OSF; where the technical building and the Residencia are located), the Array Operations Site (AOS; with the antennas, correlator, local oscilator and fiber optics network), and the Santiago central Offices (SCO; where the main archive, data transmission to the ARCs, and the offices for Science, Computing, Administration and Management are located).

2.1 From the Call for Proposals to the observations

ALMA Call for proposals is announced once per year through the ALMA Regional Centers. All information and documentation is presented at the ALMA Science Portal. Every year Europe and North America access to 33.75% of the total observing time each, East Asia to 22.5%, and Chile as host country receives 10% of the available time. Users can send their proposals through the ALMA Observing Tool (Phase 1).

Afterwards all proposals go through the ALMA Proposals Review Process, where several ALMA Review Panels of different scientific areas provide the science assessment. The technical feasibility of projects are checked by scientific personnel at the Joint ALMA Observatory. Proposals are ranked and graded in the review panels meeting. A merge of all panels outputs is made by a committee composed by the panels chairs, where the final rank is produced.

In a second step the Joint ALMA Observatory evaluates the scheduling feasibility of the proposals, fine tune the configurations periods, and adjusts grades of proposals to have an homogenous distribution of proposals pressure per LST and per configuration. The approved proposals will be admitted to produce observing files (Phase 2).

2.2 High-level concepts for ALMA Science Operations

Observations at ALMA are done in service mode at the Operations Support Facily. Scientific ALMA staff from the JAO and from the ARCs carry out those observations using a dynamic scheduling. All science observations are executed in the form of scheduling blocks, each of which contains all information necessary to schedule and execute the observations. The Scheduling Blocks are repeated until the rms requested by the Principal Inverstigator of a proposal is reached. All science and calibration raw data are captured and archived and, by default, calibrations are done with a dynamic query. The default output to the astronomers are processed images, calibrated by the ALMA pipeline in the case of standard observing modes or by ALMA staff in the case of non standard observing modes.

The JAO in Chile is responsible for the data product quality and the Users Support is done at Regional Centers level, face to face or through the ALMA helpdesk system.

2.3 ALMA capabilities offered in Cycle 6

Along the six years that ALMA has been operating, commissioning activities and science observations of accepted projects ran in parallel. In Cycle 6 ALMA offered at least fourty three antennas in the 12-m Array movable into ten different configurations with maximum baselines from 160 m to 16 km. In the Morita Array ten seven meter antennas are ready for recovering extended emission, and three twelve meter antennas for making single-dish maps. Eight different receivers are offered from band 3 to band 10. Bands 8, 9 and 10 can be used with maximum baselines up to 3.6 km, band 7 up to 8.5 km , and bands 3, 4, & 6 up to 16 km.

Spectral line and continuum observations with the 12-m Array and the Morita Array are possible in all bands, as well as single field interferometry. Mosaics can be done in Bands 3 to 9 with the 12-m Array and the Morita Array. Single dish spectral line observations can be done in Bands 3 to 8.

In Cycle 6 on-axis and single-pointing polarization capabilities are offered. Full (linear and circular) polarization observations for continuum are possible with full spectral resolution observations in Band 3 to 7 on the 12-m Array. In this Cycle Solar observations and VLBI proposals are offered in continuum mode for Bands 3 and 6.

In relation to the proposals types, principal investigators can submit regular proposals, Large programs, Target of Opportunity (ToO), and time constrains projects.

3 Science with ALMA

The Fundamental Science Drivers that inspired the construction of ALMA, as detailed here, are:

- The ability to detect spectral line emission from CO or C^+ in a normal galaxy like the Milky Way at a redshift of z = 3, in less than 24 hours of observation.

- The ability to image the gas kinematics in a solar-mass protoplanetary disk at a distance of 150 pc, enabling one to study the physical, chemical, and magnetic field structure of the disk and to detect the tidal gaps created by planets undergoing formation.

- The ability to provide precise images at an angular resolution of $0.1''$.

Given the current status of the array we can say that all the scientific goals that provoked the construction of ALMA have been now achieved.

Since the very first observations ALMA has contributed to the advance of knowledge in many different fields, providing high impact publications and excellent data for doing transformational science (see Fig. 4).

Figure 4: The first ALMA press releases. Courtesy: ALMA(ESO/NAOJ/NRAO)

In the field of Extragalactic Astronomy (see Fig. 5) ALMA was able to measure the mass of a black hole with extreme precision in NGC 1332 using the CO(J=2-1) spectral line transition [3], as well as to yield the sharpest view ever of star formation in the distant Universe through the high spatial resolution image of the gravitationally lensed galaxy SDP.81 [8].

In the evolved stars framework ALMA showed spectacular images of a Gaseous spiral-shell pattern characteristic of elliptical binaries in LL Pegasi [5] (see Fig. 6), and it shed light into the formation of multiple systems by caughting in act of forming close multiple young stellar objects via disk fragmentation in L1448 IRS3B [12].

ALMA, for the first time is providing high spatial resolution and sentivity to observe Solar System objects in millimeter/submillimeter wavelegths confirming the complex chemistry in Titan's atmosphere by detecting vinyl cyanide molecule [7].

One of the science topics where ALMA has provided transformational science is in the field of protoplanetary disks and planet formation, where studies of the dust temperature distribution and nature of dust particles, as well as high angular resolution observations of

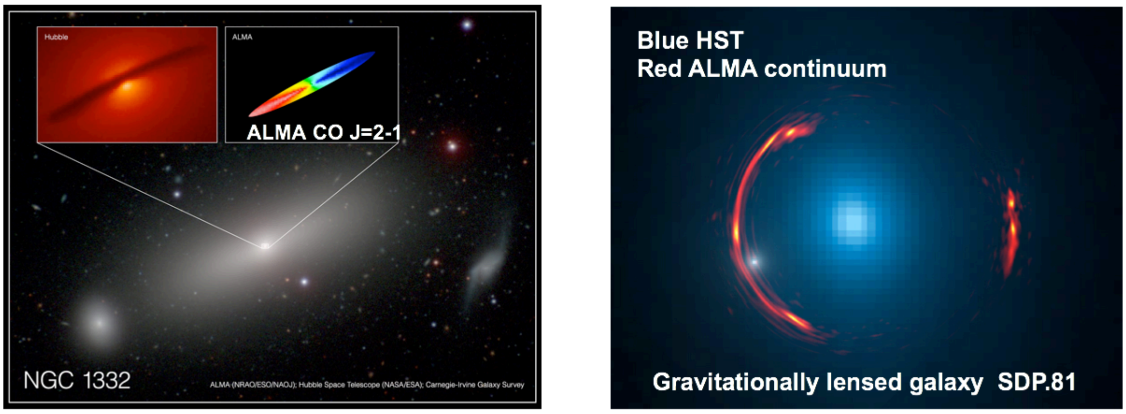

Figure 5: Left: Kinematics surrounding a black hole in NGC 1332 [3]. Right: continuum emission from the gravitationally lensed galaxy SDP.81 [8] . Courtesy: ALMA(ESO/NAOJ/NRAO)

the gas dynamics are now possible with unprecedented detail. As a few examples, ALMA was capable to show planet formation in Earth-like Orbit around the young Sun-like star TW Hydrae [1], cavities and spiral arms in MWC 758 [4] (see Fig. 6), and the discovery of a trio of infant planets around newborn stars [9], [11].

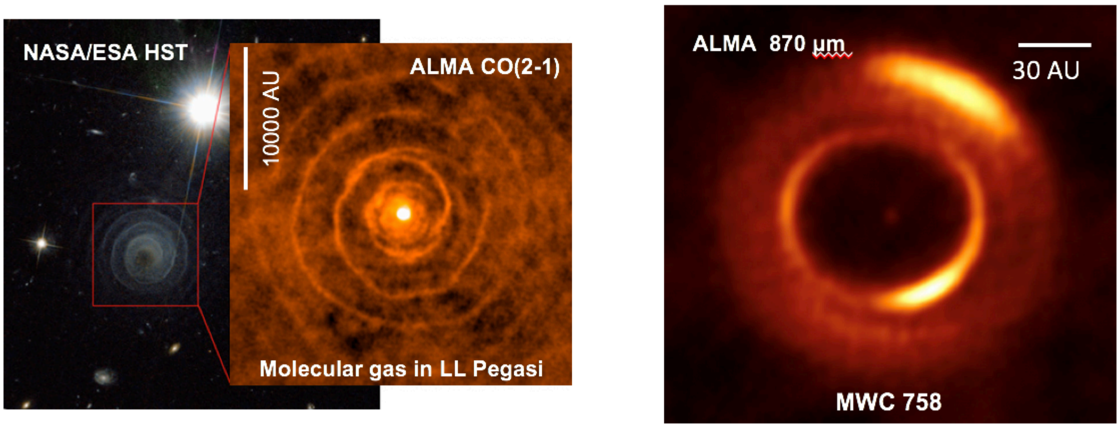

Figure 6: Left: Spiral shell pattern seen in molecular in LL Pegasi. Right: detailed dust structures in the disk surrounding MWC 758 [5]. Courtesy: ALMA(ESO/NAOJ/NRAO)

Recently ALMA discovered cold dust around the nearest star Proxima Centauri [2]. And in the Astrochemistry and Astrobiology fields ALMA is also giving new insights, like the detection of the first extragalactic hot molecular core in the Large Magellanic Cloud [10], or the first detection of the prebiotic complex organic molecule Methyl Isocyanate, involved in the synthesis of peptide and amino acids, in a solar-type Protostar [6].

Observations of the Sun are now possible with ALMA and since Cycle 4 ALMA has become part of the global VLBI networks operating in the millimeter and submillimeter, working at 3 mm in conjunction with the Global Millimeter VLBI Array (GMVA), and at 1.3 mm in conjunction with the Event Horizon Telescope (EHT) network (to observe nearby supermassive black holes).

4 Future of ALMA

While ALMA is achieving its Full Operations state, the commissioning of some observing modes still needs some work to be finished, like:

- High frequencies observations for long baselines, Solar, single-dish, Compact Array standalone, and polarization.
- Phased Array (VLBI) mode to support observations in spectral lines and pulsars.
- Single-dish observations in continuum and at high frequencies.
- Wide field polarization mode.
- Improved observing efficiency.

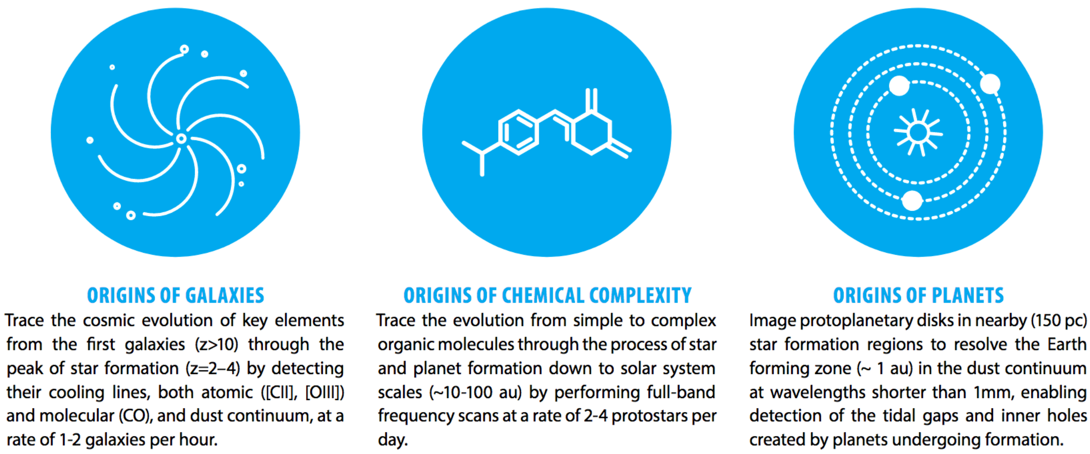

Figure 7: Fundamental science drivers for ALMA developments over the next decade. Courtesy: ALMA(ESO/NAOJ/NRAO)

There is a development plan to improve ALMA future capabilities, which is a three-years cycle of studies that can be software or hardware oriented. First calls went out in 2010, 2013, and 2016. Thanks to these programs the Band 5 was offered in Cycle 5 and ALMA VLBI observations could be offered from Cycle 4. Development programs will also provide improved receivers: a Band 2 + Band 3 prototype is on-going, a Band 7/Band 9 upgrade will come soon, and the Band 1 is expected to be ready for Cycle 8.

Very recently the ALMA development working group set new science drivers that will lead new development of ALMA until 2030 for the next decade (Fig. 7) The main drivers will focus into the study of the origins of galaxies, origin of chemical complexity, and the origin of planets. For that the receivers, the digital systems, and the correlator must be upgraded. The ALMA archive will be further developed using data mining tools to exploit it.

References

[1] Andrews, S. M., Wilner, D. J., Zhu, Z., et al. 2016, ApJL, 820, L40

[2] Anglada, G., Amado, P. J., Ortiz, J. L., et al. 2017, ApJL, 850, L6

[3] Barth, A. J., Boizelle, B. D., Darling, J., et al. 2016, ApJL, 822, L28

[4] Dong, R., Liu, S.-y., Eisner, J., et al. 2018, ApJL, 860, 124

[5] Kim, H., Trejo, A., Liu, S.-Y., et al. 2017, Nature Astronomy, 1, 0060

[6] Martín-Doménech, R., Rivilla, V. M., Jiménez-Serra, I., et al. 2017, MNRAS, 469, 2230

[7] Palmer, M. Y., Cordiner, M. A., Nixon, C. A., et al. 2017, Science Advances, 3, e1700022

[8] ALMA Partnership, Vlahakis, C., Hunter, T. R., et al. 2015, ApJL, 808, L4

[9] Pinte, C., Price, D. J., Ménard, F., et al. 2018, ApJL, 860, L13

[10] Shimonishi, T., Onaka, T., Kawamura, A., & Aikawa, Y. 2016, ApJ, 827, 72

[11] Teague, R., Bae, J., Bergin, E. A., Birnstiel, T., & Foreman-Mackey, D. 2018, ApJL, 860, L12

[12] Tobin, J. J., Kratter, K. M., Persson, M. V., et al. 2016, Nat, 538, 483

Highlights on Spanish Astrophysics X, Proceedings of the XIII Scientific Meeting of the Spanish Astronomical Society held on July 16 – 20, 2018, in Salamanca, Spain. B. Montesinos, A. Asensio Ramos, F. Buitrago, R. Schödel, E. Villaver, S. Pérez-Hoyos, I. Ordóñez-Etxeberria (eds.), 2019

Gaia DR2: contents and properties of the second Gaia data release.

Xavier Luri[1], on behalf of Gaia DPAC

[1] Dept. Fisica Quantica i Astrofisica, Institut de Ciències del Cosmos (ICCUB), Universitat de Barcelona (IEEC-UB), Martí Franquès 1, E08028 Barcelona, Spain

Abstract

The second data release of ESA's Gaia mission (Gaia DR2) was published in April 2018. It is just another step in the Gaia release scenario, to be followed by other more complete and precise releases in the coming years, but already represents a huge step ahead. Gaia DR2 contains data positions and G magnitudes for more than 1.7 billion objects, and provides five-parameter astrometry for more than 1.3 billion of them, the biggest astrometric catalogue ever by several orders of magnitude. The release contains also additional photometric, radial velocity and physical parameters data for different subsets and specialized datasets for variability and solar system objects.
In this paper we review the properties of Gaia DR2 and discuss some of the shortcomings and limitations that have to be taken into account to properly use its data. We also review the archive systems where the data can be accessed and the expected contents of future Gaia data releases.

1 Introduction: the Gaia mission

The European Space Agency's (ESA) astrometric mission Gaia was launched in September 2013. Its main aim was to generate an astrometric catalogue with highly accurate positions, parallaxes and proper motions for more than 1 billion sources brighter than magnitude 20. A description of the mission, its principles and scientific case can be found in [7], while a more extensive scientific motivation for the mission is presented in [6].

The data processing required to transform the spacecraft's telemetry into a scientifically useful dataset was entrusted by ESA to an european-wide consortium, the Gaia Data Processing and Analysis Consortium (DPAC, also described in [7]). This consortium is currently formed by more than 450 scientists and engineers from all around Europe, with a significant presence of Spanish teams. At the time of its creation, and as part of its agreements with ESA, a plan for a staged publication of the mission results was defined. This so-called "data release scenario" includes several intermediate data releases based on preliminary calibrations and the subset the measurements available at a given time, and a final release with the complete satellite telemetry. The current details of this data release scenario (which is periodically revised) can be found in ESA's Gaia web site.

As part of this release scenario ESA and DPAC have published in April 2018 the Gaia Second Data Release (Gaia DR2). The properties of this release are reviewed in the coming sections, and we encourage the reader to consult two key sources of information for it: the Astronomy & Astrophysics special edition devoted to Gaia DR2 and the Gaia DR2 on-line documentation at the Gaia archive.

The Gaia data can be accessed through the main Gaia archive or through one of the Gaia partner data centers. There are also replicas of the archive in other sites around the world and in addition the Gaia data can be downloaded for local use through the Gaia download site.

2 Gaia DR2 contents

A full review of the Gaia DR2 contents can be found in [2]. Here we present a brief summary of its characteristics.

First of all, the Gaia DR2 main content is the overall catalogue. This table, named GaiaSource in the main archive, contains 1,692,919,135 sources for which *at least* a sky position and a G magnitude (see [8] for a review of the Gaia photometry) are available. Besides this basic information, additional data is available for subsets of this main dataset as described in Table 1.

Subset	number of objects
Full catalogue	1,692,919,135
Objects with 5-parameter astrometry	1,331,909,727
Objects with 2-parameter astrometry	361,009,408
Objects with G_{BP} magnitude	1,381,964,755
Objects with G_{RP} magnitude	1,383,551,713
Objects with radial velocity	7,224,631
Objects with estimated T_{eff}	161,497,595
Objects with estimated A_G and $E(G_{BP} - G_{RP})$	87,733,672
Objects with estimated radius and luminosity	76,956,778

Table 1: Number of sources for which a given data product is available in Gaia DR2. Extracted from Table 1 in [2]

In addition to this main dataset, DR2 contains other specialised datasets:

- A dataset for 550,737 identified variable stars, including light curves and classification into variability type for most of them

- A dataset for 14,099 Solar System Objects, including epoch photometry and astrometry
- Pre-computed cross-match catalogues against DR2 for a dozen of external catalogues (2mass, HIP, AllWise, and others)
- Cross-Id table for AllWiseAgn and ICRF sources (QSOs) used to define the celestial reference frame of Gaia DR2 (Gaia-CRF2)

3 Gaia DR2 properties

The sky distribution of the global DR2 dataset is presented in Figure 1. Notice that one can still faintly appreciate the distribution of the different sets and subsets as a function of the G magnitude is presented in Figure 2. Notice that the main dataset contains sources well beyond the nominal limit of Gaia observations of $G = 20.7$, but as discussed in the next section it is complete only around magnitude $G \simeq 19$.

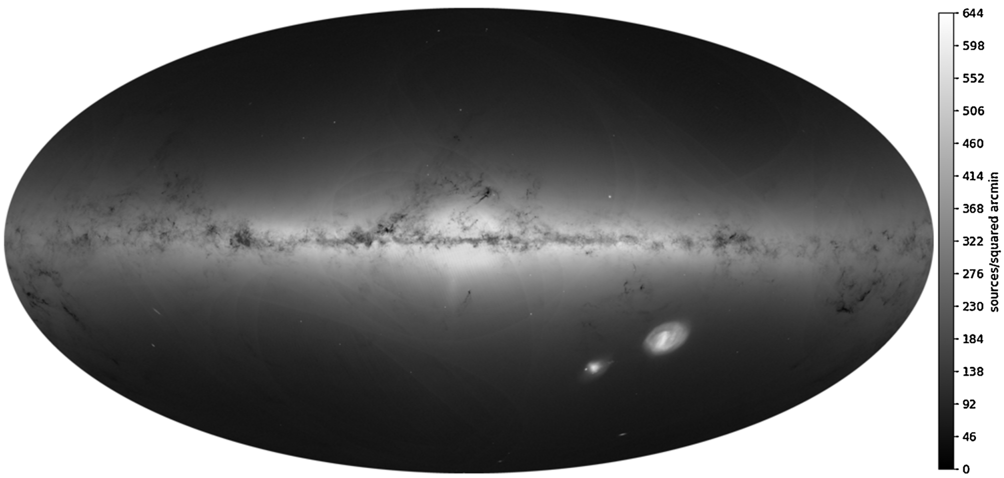

Figure 1: Sky distribution of all Gaia DR2 sources in Galactic coordinates. The figure has been extracted from [2].

3.1 Astrometric data

The astrometric processing and the properties of the Gaia DR2 astrometry are described in detail in [5]. The formal uncertainties for the Gaia astronomy are individually provided for each object in the catalogue but in general vary with the G magnitude, being more precise for bright objects and progressively less precise for fainter ones, as illustrated in Figure 3. A summary of these formal uncertainties is presented in Table 2 and a detailed list of values as a function of the magnitude can be found in Table B.1 of [5].

As seen in the figures these uncertainties are dominated by photon noise above $G \simeq 15$, but show a plateau at brighter magnitudes, where the limitation is the present knowledge

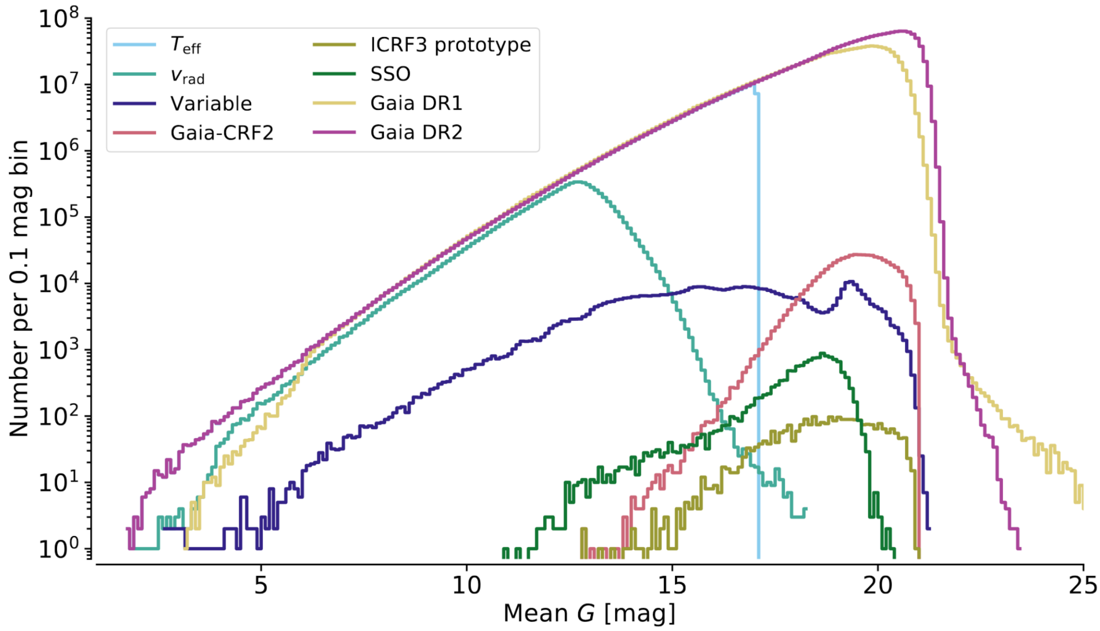

Figure 2: Distribution of the mean values of G magnitude for the different sets and subsets of Gaia DR2 sources shown as histograms with 0.1 mag wide bins. It also includes the distribution for Gaia DR1 sources. The figure has been extracted from [2].

of the instrument calibrations. We expect to improve these limitations in the instrument calibrations and, together with an increase in precision due to the accumulation of additional data, reach precisions in the bright end around $10 - 20\mu as$.

When using the astrometric data it is important to take into account that, due to the characteristics of the processing, the uncertainties of the five astrometric parameters are correlated. A correlation matrix is included as part of the Gaia data to allow a proper treatment of the joint uncertainity distribution.

The astrometric data processing has been designed to minimize as much as possible any systematic error present in the data. However, at this stage of the mission, still working with just a part of the total expected observations and with a partial knowledge of the instrument calibrations, there are still uncontrolled effects that can creep into the astrometry. Some of these are already known (and its magnitude estimated) after the validation process carried out by DPAC on the astrometric solution, including a global zero point on the parallaxes ($-30\mu as$ in the sense Gaia minus external data), a residual rotation on the proper motions and some regional effects. Also, unlike for Gaia DR1, the parallax uncertainties have not been calibrated externally, i.e., they are known, as an ensemble, to be underestimated by 8–12 percent for faint sources ($G > 16$ mag) outside the Galactic plane and by up to 30 percent for bright stars ($G < 12$ mag).

G	position (mas)	parallax (mas)	proper motion (mas yr^{-1})
15	0.03	0.04	0.06
17	0.08	0.09	0.15
20	0.5	0.7	1.1
21	1.5	2.1	3.2

Table 2: Astrometric formal uncertainities as a function of the G magnitude. Extracted from Table B.1 in [5]

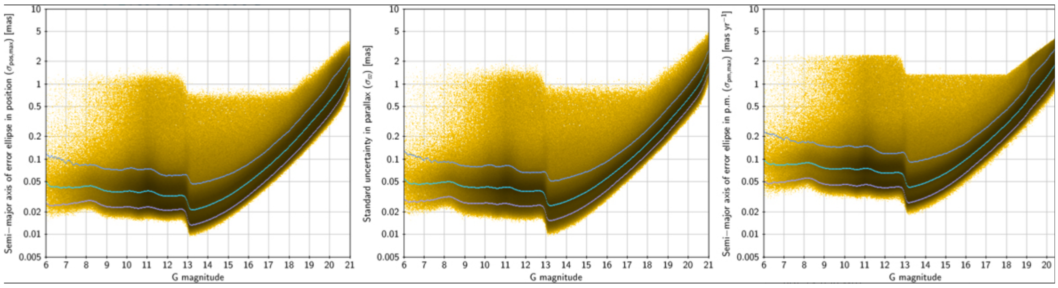

Figure 3: Formal uncertainties for parallax (left), proper motion in right ascension (middle) and declination (right) of the objects in Gaia DR2 as a function of the G magnitude. The cyan curve is the median uncertainty and the blue curves are the 10th and 90th percentiles. The yellow points correspond to a representative subset added as background. The figure has been extracted from [5].

A review of these and other known issues in the data are collected in Gaia's know issues page, and specifically for astrometry a document from Lennart Lindegren linked in this same page provides a useful summary of the known systematics. See also Section 6.3.1 in [2].

3.2 Photometric data

The photometric processing Gaia DR2 is described in detail in [8] and the properties of the DR2 photometry are discussed in [4]. As discussed in the previous section all the 1.7 billion published objects have at least a G magnitude, and about 1.3 billion of them also have a G_{BP} (blue) and/or G_{RP} (red) magnitude. Thus, in many cases the Gaia objects have three-band photometry; from these values a figure of the average color in each sky region has been composed (Figure 4).

The passbands definining the G, G_{BP} and G_{RP} filters are published as a numerical table in the Gaia archive. However, these passbands have been revised after the publication of DR2 using a larger library of standard stars, providing updated estimations. We recommend to use the passbands published in [1].

The photometric data processing considered three types of sources, "Gold", "Silver", and "Bronze", which represent decreasing quality levels of the photometric calibration achieved;

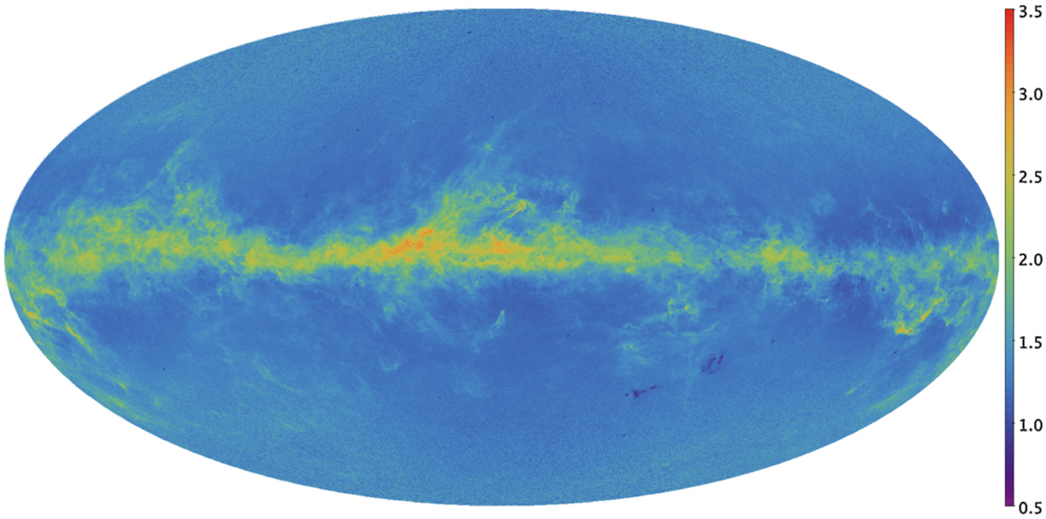

Figure 4: Colour distribution as a function of sky position in Galactic coordinates. Each pixel represents the median colour ($G_{BP} - G_{RP}$) of all sourceswith $G < 19$ in that pixel. The figure has been extracted from [4].

in particular, in the case of the Bronze sources no colour information is available. This is indicated in the released catalogue by a numeric field (`phot_proc_mode`) assuming values 0, 1 and 2 for gold, silver, and bronze sources respectively. Similarly to the astrometric data the uncertainties are strongly dependent on the G magnitude; at the bright end the photometric uncertainties are dominated by calibration effects and flatten around a few millimagnitudes, except for the very bright stars where they are substantially higher due to saturation effects. At the faint end the uncertainties are dominated by the photon noise and reach 0.1 mag around $G = 20$. The distribution of uncertainties as a function of G magnitude is depicted in Figure 5.

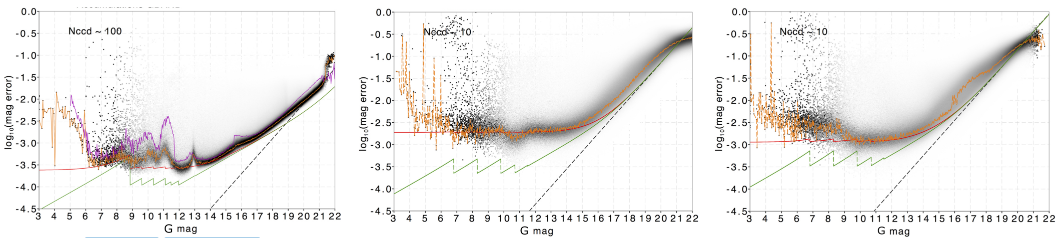

Figure 5: Distribution of uncertainty on the weighted mean magnitude for the three Gaia bands as a function of the G magnitude. The figures have been extracted from [4].

Please refer to section 6.3.2 of [2] for a discussion of the limitations of the photometric Gaia data at this stage of the mission, including a discussion about the so-called “flux excess”, the photometric zero points and the calibrations. See also [1] for a discussion of a magnitude trend in G for objects brigther than $G \simeq 16$.

3.3 Radial velocities

As described in previous sections, besides the astrometric and photometric data Gaia DR2 also provides radial velocity data for a subset of the objects. These data are acquired using the Radial Velocity Spectrometer (RVS) instrument described in [3]. The processing of the RVS data is described in detail in [9]. The processing pipeline delivered median radial velocities for Gaia stars with narrow-band near-IR magnitude $G_{RVS} \leq 12$ (approximately brighter than $V \simeq 13$). Stars identified as double-lined spectroscopic binaries were removed from the pipeline, while variable stars, single-lined, and non-detected double-lined spectroscopic binaries were treated as single stars. Furthermore, for the hottest ($T_{eff} \geq 7000$ K) and coolest ($T_{eff} \leq 3500$ K) starts the accuracy and precision of the stellar parameter estimates were not sufficient to allow selection of appropriate templates and the radial velocities obtained for these stars are not published in DR2. The overall accuracy of radial velocity measurements is around 200-300 m s^{-1}, and the overall precision is 1 km s^{-1}, reaching 200 m s^{-1} for the brightest stars. The overall distribution of uncertainties of radial velocities as a function of the G magnitude is depicted in Figure 6.

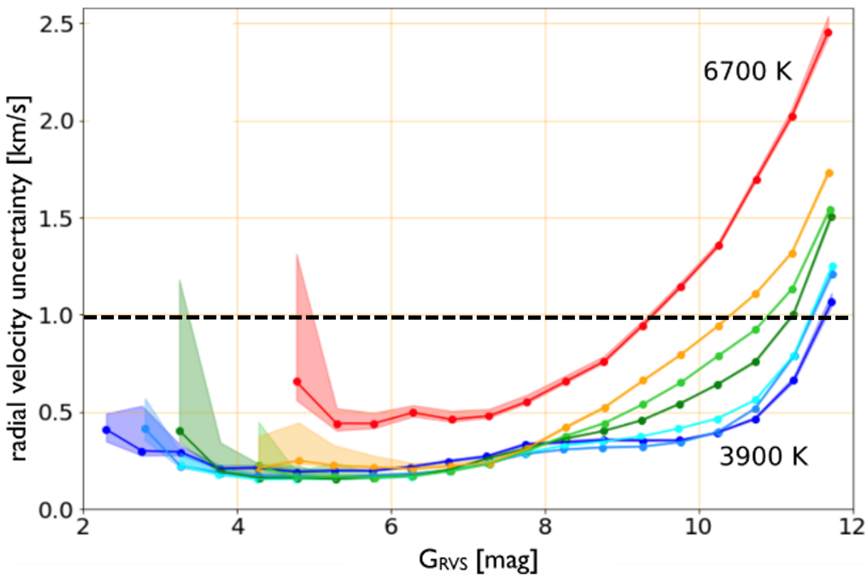

Figure 6: Distribution of uncertainty on the mean radial velocity as a function of the G magnitude.

Please refer to section 6.3.3 of [2] for a discussion of the limitations of the Gaia radial velocities at this stage of the mission, including a discussion about the treatment of spectroscopic binaries.

4 Conclusions

The publication of the Gaia DR2 has been an outstanding success. After a huge peak in publication of papers in the months immediately after the release (about 120 papers from non-DPAC authors in two months, about 17% of them including Spanish authors) we are now seeing about 2 papers per day based on Gaia data. The science with Gaia is becoming a reality and in many areas the Gaia data is allowing significant breakthroughs. We also direct the reader to the Astronomy & Astrophysics special issue on Gaia DR2 where a collection of science demonstration papers by DPAC can be found along the release papers.

Furthermore, in the not too far future, around mid-2021, the next Gaia data release (DR3) will arrive, with even more precise and more varied data. The expected contents of this new release include:

- Covering 34 months of data (22 months in DR2)
- Better precision and accuracy in astrometry and photometry
- Accelerated/orbital solutions in astrometry: binary systems
- More RVs: fainter magnitude, wider surface temperature range, more precise
- Mean spectra in the BP/RP and RVS bands
- Stellar parameters from spectra (BP/RP, RVS): more precise, fainter magnitude, surface gravity (log g), age, [Fe/H] and various element abundances
- Source classifications (e.g. quasars, binaries, galaxies)
- More solar system objects, reflectance spectra, colours
- More light curves, new variable source classifications

And more to come with other future releases. Updated information about the upcoming publications of Gaia data can be found in the Gaia data release scenario web page.

Acknowledgments

This work has made use of results from the European Space Agency (ESA) space mission *Gaia*, the data from which were processed by the *Gaia Data Processing and Analysis Consortium* (DPAC). Funding for the DPAC has been provided by national institutions, in particular the institutions participating in the *Gaia* Multilateral Agreement. The *Gaia* mission website is `http://www.cosmos.esa.int/gaia`. The authors are current or past members of the ESA *Gaia* mission team and of the *Gaia* DPAC.

This work was supported by: the MINECO (Spanish Ministry of Economy) through grant ESP2016-80079-C2-1-R (MINECO/FEDER, UE) and ESP2014-55996-C2-1-R (MINECO/FEDER, UE) and MDM-2014-0369 of ICCUB (Unidad de Excelencia 'María de Maeztu'); the DLR (German space agency) via grant 50 QG 1403.

References

[1] Apellaniz, J. & Weiler, M., accepted, http://cdsads.u-strasbg.fr/abs/2018arXiv180802820M

[2] Gaia Collaboration, Brown, A. et al., 2018, A&A , 616, A1

[3] Gaia Collaboration, Cropper, M. et al., 2018, A&A , 616, A5

[4] Gaia Collaboration, Evans, D. et al., 2018, A&A , 616, A4

[5] Gaia Collaboration, Lindegren, L. et al., 2018, A&A , 616, A2

[6] Perryman, M. A. C. et al., 2001, A&A , 369, 339

[7] Gaia Collaboration, Prusti, T. et al., 2016, A&A , 595, A1

[8] Gaia Collaboration, Riello, M. et al., 2018, A&A , 616, A3

[9] Gaia Collaboration, Sartoretti, P. et al., 2018, A&A , 616, A6

Highlights on Spanish Astrophysics X, Proceedings of the XIII Scientific Meeting of the Spanish Astronomical Society held on July 16 – 20, 2018, in Salamanca, Spain. B. Montesinos, A. Asensio Ramos, F. Buitrago, R. Schödel, E. Villaver, S. Pérez-Hoyos, I. Ordóñez-Etxeberria (eds.), 2019

Making galaxies passive: Insights from resolved studies of nearby galaxies.

Miguel Querejeta[1,2]

[1] European Southern Observatory, Karl-Schwarzschild-Str. 2, D-85748 Garching, Germany
[2] Observatorio Astronómico Nacional (IGN), C/Alfonso XII 3, E-28014 Madrid, Spain

Abstract

The rapid suppression of star formation is thought to be an important process in the evolution of the most massive galaxies, but the mechanisms involved are still subject to debate. In this PhD thesis, we consider two agents that can control star formation: AGN feedback and galaxy mergers. First, we focus on the interplay between stellar structures, nuclear activity, and molecular gas. We start presenting our public catalogue of stellar mass maps for more than 1500 nearby galaxies. Based on the baryonic mass distribution of the spiral galaxy M51, we show that there is sufficient molecular gas inflow to feed the AGN, as well as feedback effects which include a molecular outflow and a radio plasma jet interacting with the surrounding ISM. In a second part, we address the role of galaxy mergers in the buildup of a passive population of lenticular galaxies (or S0s), the most common early-type galaxies in the local Universe. Using numerical simulations, we show that major mergers of spiral galaxies can result in lenticulars, with a bulge-disc coupling and specific angular momentum in agreement with observations. Globally, our results show that both internal processes (transport of gas and AGN feedback) and external mechanisms (mergers) have the ability to regulate and eventually suppress star formation in galaxies.

1 Foreword

This is a summary of the PhD thesis that I conducted at the Max Planck Institute for Astronomy in Heidelberg, Germany, under the supervision of Eva Schinnerer. The thesis was developed in the framework of the European project DAGAL (Marie Curie ITN, PI: Johan Knapen), including extended stays at the Instituto de Astrofísica de Canarias, Universidad Complutense de Madrid, and the University of Groningen.

2 Introduction

It is remarkable how much our understanding of galaxies and the structure of the Universe has evolved in the last century; after all, it was less than 100 years ago that galaxies were proven to be external to our own Milky Way. At fixed stellar mass, galaxies are known to show a bimodality in terms of colour [1, 2]; in a colour-magnitude diagram, the relative scarcity of galaxies between the so-called *blue cloud* and *red sequence* has been recognised as evidence of the short timescales over which star formation is suppressed [5]. At the same time, a strong correlation exists between colour and morphology, suggesting an evolutionary link: ellipticals and lenticulars tend to be passive and red, implying low degrees of star formation, as opposed to actively star-forming blue spirals and irregulars.

One of the most fundamental challenges of modern astrophysics is indeed understanding the process by which gas transforms into stars, and how this process is orchestrated in the context of galaxies and as a function of environment. Star formation regulates the interchange of energy between stars, gas, and dust, explains the chemical enrichment of the interstellar medium (ISM), and, overall, it can determine the structure and ultimate fate of a given galaxy. In this thesis, we consider two specific mechanisms that have the ability to control and suppress star formation in galaxies: feedback from an active galactic nucleus (AGN) and galaxy mergers. However, rather than trying to learn about them by studying large samples of distant sources, our goal is to exploit the power of the high spatial resolution available for the nearest galaxies, establishing synergies between observations and simulations.

3 An important observational tool: Stellar mass maps

While light is the most direct observable in astrophysics, the evolution of galaxies is largely constrained by their *mass* distribution. However, measuring stellar mass distributions in practice is challenging: at optical wavelengths, light is biased by luminous young stars and can suffer from intense dust extinction; additionally, the large uncertainties associated with late evolutionary phases in stellar population synthesis models make it difficult to unambiguously connect light and mass. Near-infrared observations constitute a promising alternative to circumvent these problems: the stellar mass-to-light ratio is much more uniform than at optical wavelengths and extinction problems are minimised.

In this thesis, we use near-infrared imaging, together with an algorithm to correct those images for dust emission (3.3 μm PAH feature and dust continuum) to calculate stellar masses with high accuracy. Specifically, we rely on uniform imaging at 3.6 and 4.5 μm for more than 2000 galaxies from the *Spitzer* Survey of Stellar Structure in Galaxies (S^4G), and exploit the fact that the spectral energy distribution of old stars and dust at these wavelengths have an intrinsically different shape. We have implemented a pipeline based on Independent Component Analysis (ICA) to separate both components, allowing to identify the true stellar mass distribution. This has resulted in an increase by an order of magnitude in the amount of resolved stellar mass maps available so far, which we have made publicly available. In conjunction with dynamical masses, these stellar mass maps can help constraining the distribution of baryonic to nonbaryonic matter in galaxies; the stellar mass distribution is also

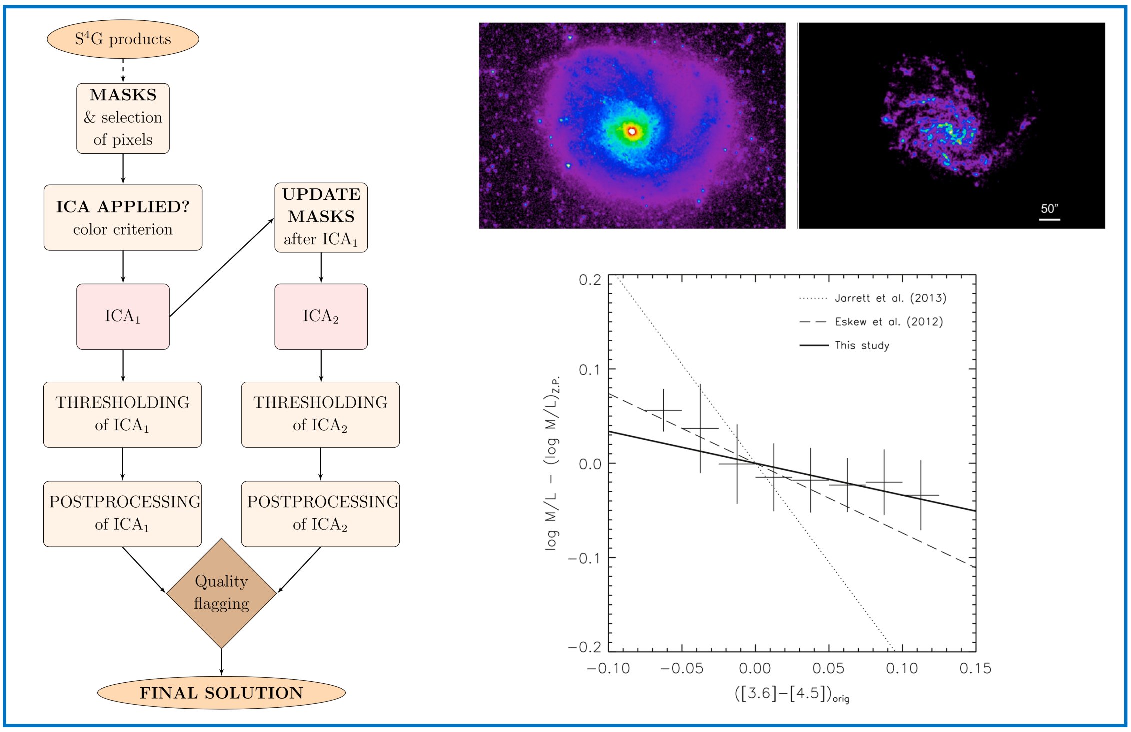

Figure 1: *Left:* Flow chart summarising the steps of the Pipeline. *Right top:* ICA separation of the 3.6 μm image of NGC 4254 into stars (left) and dust (right). *Right bottom:* New calibration for effective M/L as a function of [3.6]-[4.5] colour, based on more than 1500 galaxies, and comparison to previous calibrations.

instrumental to any calculations of specific star formation rates (SFR/$M_\odot$), and it is critical when it comes to calculating gravitational torques, which can trigger flows of gas towards an active nucleus. We will examine this last possibility in the next section.

4 AGN and their relation to quenching: Feeding and feedback in M51

Active galactic nuclei are recognised as some of the most energetic sources of the Universe, with the potential to dramatically influence the evolution of their host galaxy: their bolometric luminosities of $10^5 - 10^{13}\,L_\odot$ can sometimes outshine their host [12]. Active nuclei also play a pivotal role in reconciling cosmological simulations with observations; indeed, AGN feedback is invoked to explain the lower stellar-to-total mass ratio in the halo of the most

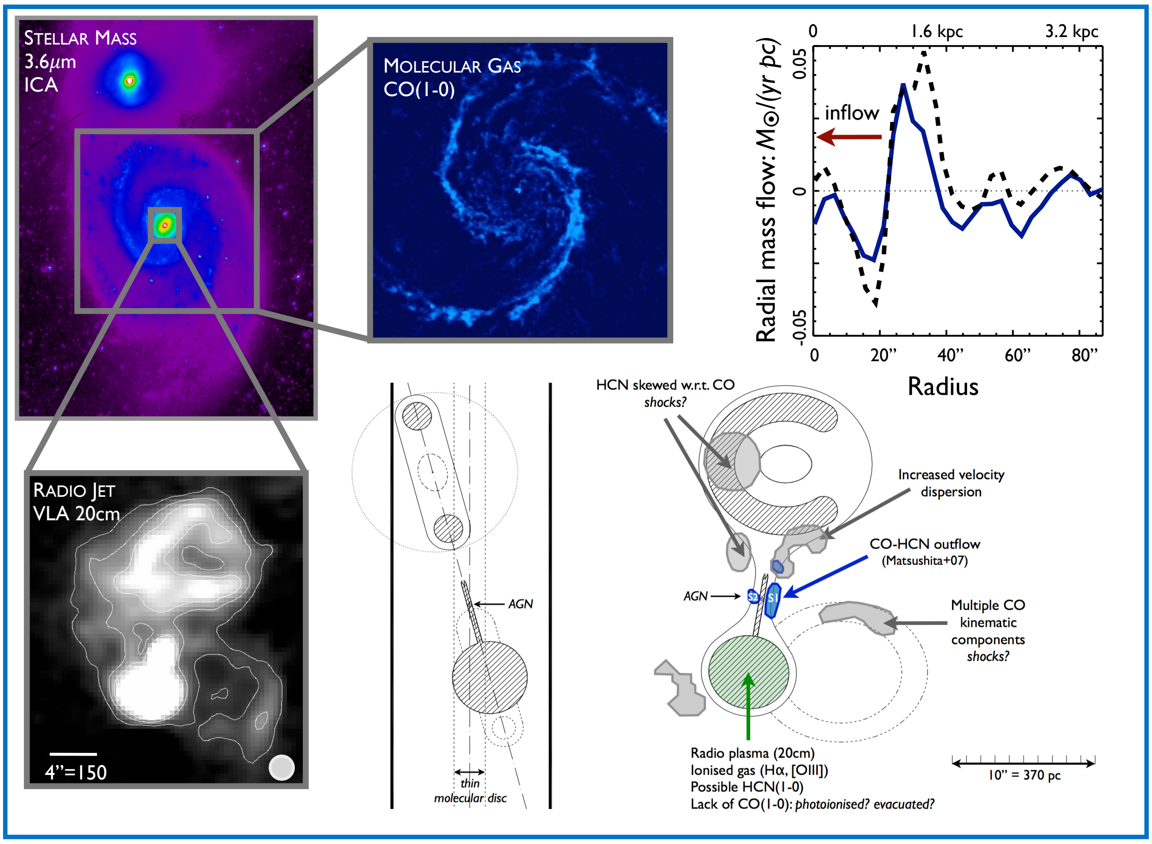

Figure 2: *Top left:* stellar mass map of M51. *Top right:* plot demonstrating that gravitational torques imply gas inflow for the central kiloparsec of the galaxy (*dashed*: uncorrected 3.6 μm). *Bottom left:* VLA 20 cm continuum map revealing the radio plasma jet through synchrotron emission. *Bottom right:* summary of AGN feedback effects found in M51, with the proposed geometry.

massive galaxies [11], but it remains to be confirmed whether the strong feedback effects introduced *ad hoc* by simulators are realistic.

Here, we quantify the transport of gas to the nucleus as the result of gravitational torques in the spiral galaxy M51. We derive the torques from the stellar mass map obtained as part of the previous project, and assess their effect on the molecular gas distribution mapped by the PAWS survey [13]. We show that there is evidence for molecular gas inflow in the central ~kpc due to the asymmetry introduced by a nuclear bar, and we carefully analyse the uncertainties and limitations involved in such calculations.

Another critical piece in the puzzle of AGN and their potential relation to the regulation of star formation is the so-called AGN feedback process. The ability of gas to flow towards the nucleus can indirectly control any feedback effects, which could in turn contribute to explaining the tight scaling relations observed between the properties of the nuclear black hole and the surrounding stellar bulge [9, 7]. We have also revisited this important topic in the context of new observations for M51, one of the few galaxies that affords the possibility to study the distribution and kinematics of the circumnuclear gas at high spatial resolution as a consequence of its proximity. We analysed both the bulk molecular gas traced by PAWS (through the CO line) and new NOEMA observations of dense gas tracers (e.g. HCN); these show an intimate connection with the kpc-scale radio plasma jet detected in radio continuum (clearly visible in archival VLA imaging). We find evidence for a massive molecular outflow (traced both by CO and HCN), as well as shocks and increased turbulence which are probably the result of the interaction of the expanding radio plasma structures and the surrounding molecular gas. We also find a large region where CO emission is significantly under-abundant, and which coincides with the position and extent of a radio plasma bubble (connected to the end of the collimated radio jet). We also find that the HCN line profiles have higher velocity dispersions and are more skewed than the CO line for positions in the vicinity of the radio plasma structures, which is suggestive of shocks. Overall, we interpret these features as the result of the radio jet propagating across the disc plane and pushing the molecular gas as it expands. Such effects could alter the phase balance of the interstellar medium and eventually affect the fraction of gas which can be converted into stars. Thus, AGN feedback can be regarded as a mechanism which is capable of indirectly regulating star formation.

5 Passive discs: Creating lenticular galaxies with mergers

Disc-dominated lenticular galaxies represent the majority of early-type galaxies in the local Universe [4]; therefore, far from being exceptional examples, they constitute one of the most important end-products of galaxy evolution. They have some transversal properties, in the sense that they share with elliptical galaxies low levels of star formation (relative to their stellar mass), while they contain large-scale galactic discs, in analogy to spiral galaxies. However, in spite of their cosmological relevance, the evolutionary tracks that lead to lenticular galaxies are still poorly characterised. Arguably, the most popular process to explain the emergence of lenticular galaxies is *ram-pressure stripping*, the expulsion of gas from a spiral galaxy by the pressure exerted by the intergalactic medium, which is expected to be especially relevant in clusters [8]; deprived of fuel to form new stars, the stellar populations will gradually age. However, this and similar mechanisms (e.g. harassment, strangulation), which operate preferentially in high-density environments, are not expected to significantly modify the stellar kinematics of the progenitor galaxy.

We explore whether mergers of spiral galaxies can explain the origin of lenticular galaxies in groups rather than clusters, where they are at least as common [14]. Comparing N-body numerical simulation from the GalMer project [3] with observations, we show how, after initially destroying the pre-existing discs, the debris from major mergers of spirals can settle down into a new stellar disc under favourable orbital conditions. The remnant would be visually classified as an S0, and the disc and bulge of the resulting galaxy obey the tight photometric scaling relations observed in real lenticulars, and even the presence of pseudo-bulges [10]. In addition, we have also analysed the kinematics of the resulting lenticular systems in these simulations, and found that they can explain the recent finding from the CALIFA

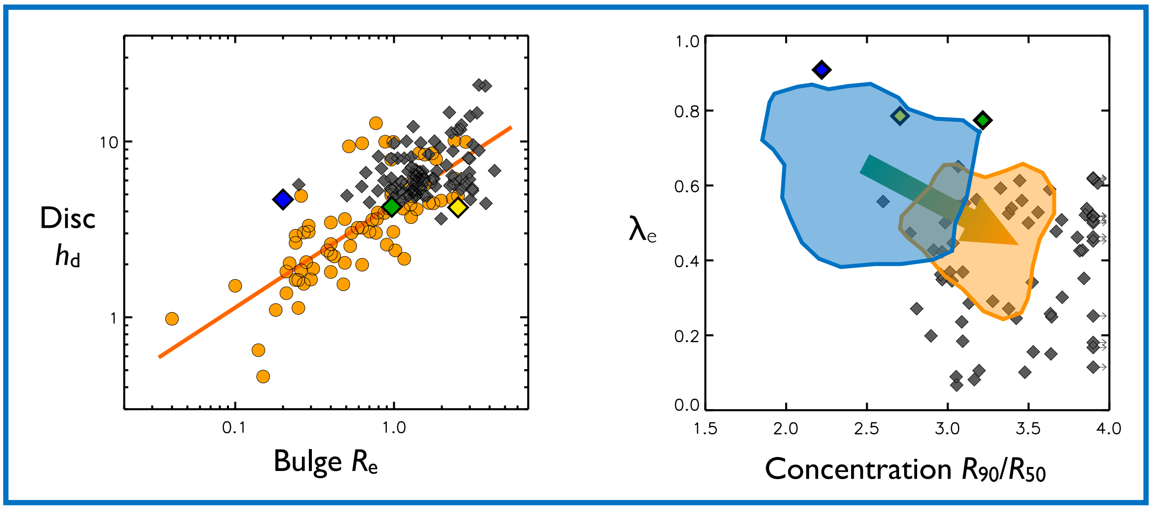

Figure 3: *Left:* the S0-like remnants (black diamonds) of major mergers of spirals simulated by GalMer (progenitors: colour diamonds). They have scaling relations compatible with observational S0s (orange circles); here, disc scale-length vs bulge effective radius. *Right*: the simultaneous change in angular momentum and concentration triggered by those major mergers explains the discrepancy in $\lambda_{\rm Re} - R_{90}/R_{50}$ between spirals (blue cloud) and S0s (orange cloud) found by CALIFA.

survey pointing to a systematic offset between spirals and S0s when the specific angular momentum ($\lambda_{\rm Re}$) and light concentration (R_{90}/R_{50}) are simultaneously taken into account [6]. Since simple fading is not expected to substantially change the angular momentum of the galaxy, this constitutes an important challenge to that paradigm, and suggests that mergers could play a relevant role in quenching spiral galaxies into lenticular systems.

6 Towards an integral picture of star formation suppression in galaxies

The main conclusion from our work is that both *internal* processes (gas transport and AGN feedback) and *external* mechanisms (mergers) have the potential to control star formation in galaxies. Many of these processes are interdependent: our results suggest an intimate connection between gas inflow and AGN feedback; nuclear activity is indirectly controlled by the transport of gas to the centre of the galaxy, and, at the same time, the feedback from the nucleus regulates the amount of gas that can reach the AGN. On the other hand, the main lesson learned from this thesis could well be that it is important to be aware of the uncertainties and limitations intrinsic to a certain method, and that it can be extremely fruitful to explore synergies between observations and numerical simulations. We live in exciting times for the study of galaxy evolution, with ALMA and NOEMA eventually reaching their full power; in that sense, this thesis has presented some results which can be easily built upon in the near future, and which could be useful in guiding the exploitation of the datasets that these new instruments are just starting to deliver.

Acknowledgments

I would like to warmly thank Eva Schinnerer and Sharon Meidt for their constant support supervising my thesis, and Carmen Eliche-Moral for introducing me to the fascinating realm of lenticular galaxies. I acknowledge financial support to the DAGAL network from the People Programme (Marie Curie Actions) of the European Union's Seventh Framework Programme FP7/2007- 2013/ under REA grant agreement number PITN-GA-2011-289313. I would also like to acknowledge the International Max Planck Research School for Astronomy and Cosmic Physics at the University of Heidelberg (IMPRS).

References

[1] Baldry, I. K., Glazebrook, K., Brinkmann, J., et al. 2004, ApJ, 600, 681

[2] Brinchmann, J., Charlot, S., White, S. D. M., et al. 2004, MNRAS, 351, 1151

[3] Chilingarian, I. V., Di Matteo, P., Combes, F., Melchior, A.-L., & Semelin, B. 2010, A&A, 518, A61

[4] de Vaucouleurs, G., de Vaucouleurs, A., Corwin, Jr., H. G., et al. 1991, Third Reference Catalogue of Bright Galaxies, Vol. Volume 1-3, XII, 2069 (Springer-Verlag Berlin Heidelberg New York), 7

[5] Faber, S. M., Willmer, C. N. A., Wolf, C., et al. 2007, ApJ, 665, 265

[6] Falcón-Barroso, J., Lyubenova, M., & van de Ven, G. 2015, in IAU Symposium, Vol. 311, IAU Symposium, ed. M. Cappellari & S. Courteau, 78–81

[7] Ferrarese, L. & Merritt, D. 2000, ApJL, 539, L9

[8] Gunn, J. E. & Gott, III, J. R. 1972, ApJ, 176, 1

[9] Häring, N. & Rix, H.-W. 2004, ApJL, 604, L89

[10] Laurikainen, E., Salo, H., Buta, R., Knapen, J. H., & Comerón, S. 2010, MNRAS, 405, 1089

[11] Moster, B. P., Somerville, R. S., Maulbetsch, C., et al. 2010, ApJ, 710, 903

[12] Robson, I. 1996, Active galactic nuclei

[13] Schinnerer, E., Meidt, S. E., Pety, J., et al. 2013, ApJ, 779, 42

[14] Wilman, D. J., Oemler, Jr., A., Mulchaey, J. S., et al. 2009, ApJ, 692, 298

Highlights on Spanish Astrophysics X, Proceedings of the XIII Scientific Meeting of the Spanish Astronomical Society held on July 16 – 20, 2018, in Salamanca, Spain. B. Montesinos, A. Asensio Ramos, F. Buitrago, R. Schödel, E. Villaver, S. Pérez-Hoyos, I. Ordóñez-Etxeberria (eds.), 2019

Cosmology with the Cosmic Microwave Background: Latest Results from the PLANCK satellite and the QUIJOTE experiment.

José Alberto Rubiño-Martín[1,2] on behalf of the Planck Collaboration and the QUIJOTE Collaboration

[1] Instituto de Astrofísica de Canarias, E-38200 La Laguna, Tenerife, Spain
[2] Dpto. de Astrofísica, Universidad de La Laguna, E-38205 La Laguna, Tenerife, Spain

Abstract

This talk presents an overview of the recent results derived from the observations of the ESA's Planck mission and the QUIJOTE experiment. The Planck 2018 cosmological results correspond to the third (and final) data release from the Planck collaboration. Several improvements in the calibration, the treatment of the polarization data and systematic effects lead to more robust constraints on many parameters. As in previous releases, the base six-parameter ΛCDM model provides an excellent description to the data. I briefly discuss some parameter extensions and the remaining tensions in the data. I also review the current status and first results of the QUIJOTE (Q-U-I JOint TEnerife) experiment, a project with the aim of characterizing the CMB polarization and other Galactic or extra-galactic physical processes that emit in microwaves in the frequency range 10–42 GHz, and at large angular scales (around one degree resolution).

1 Introduction

The study of the anisotropies of the Cosmic Microwave Background (CMB) is one of the most powerful tools in modern cosmology, and has played a crucial role in building our current understanding of the Universe. Here I will review the latest results of two experiments in which the Spanish CMB community has been involved: the ESA's *Planck*[1] satellite and the QUIJOTE experiment[2].

---

[1] *Planck* is a project of the European Space Agency (ESA) with instruments provided by two scientific consortia funded by ESA member states (in particular the lead countries France and Italy), with contributions from NASA (USA), and telescope reflectors provided by a collaboration between ESA and a scientific consortium led and funded by Denmark.

[2] QUIJOTE web page: http://www.iac.es/proyecto/cmb/quijote

Planck [31, 12] was a third generation space mission dedicated to measure the CMB temperature and polarization anisotropies over the whole sky with a sensitivity limited by cosmic variance and the ability to remove the astrophysical foregrounds. The satellite was launched in May 2009, and operated without interruptions over three times the initially planned mission duration until October 2013, with a performance exceeding expectations. It observed the microwave sky in 9 frequency bands from 30 to 857 GHz, and with angular resolutions from 5' to 30'. Sect. 2 summarizes the main results of the *Planck* 2018 data release.

The *QUIJOTE* (Q-U-I JOint TEnerife) Experiment is a collaboration between the Instituto de Astrofísica de Canarias, the Instituto de Física de Cantabria, the universities of Cantabria, Manchester and Cambridge (UK), and the IDOM company (Spain). It started operations in November 2012, and consists of two telescopes and three instruments [29, 30] dedicated to measure the polarization of the microwave sky in the frequency range 10–40 GHz, and with angular resolutions from 55' to 16'. Sect. 3 reviews the project status, including the low-frequency maps (10–20 GHz) that will be released in the coming months.

2 Overview of *Planck* 2018 cosmology results

The *Planck* mission had two instruments, with technological performances never achieved in space before. The *Low Frequency Instrument* (LFI) [10, 1, 11] covered three bands at 30, 44 and 70 GHz using low-noise heterodyne amplifiers cooled down to 20 K. The *High Frequency Instrument* (HFI) [8, 13] covered six bands at 100, 143, 217, 353, 545 and 857 GHz with bolometers cooled to 0.1 K. Polarization measurements were obtained in all but the highest two frequency bands [9, 28]. Two data processing centers (DPCs) analyzed and calibrated the data, and made the nine frequency maps of the sky [32, 14].

The scientific results of the mission were presented in various sets of papers and three data releases. The nominal mission data release (PR1) took place in 2013, and the associated results were part of the A&A special issue Vol. 517 [15]. The extended mission data release (PR2) occurred in 2015, and the associated set of papers are part of the A&A special issue Vol. 594 [18]. The third legacy data release (PR3) took place in July 17th, 2018. It contained the series of papers corresponding to the final analysis of the full mission done by the Planck collaboration. Here, I summarize the main results presented in those papers [20, 21, 22, 23, 24, 25, 26, 27]. All the Planck Collaboration papers can be downloaded from here. All the *Planck* data can be downloaded via the Planck Legacy Archive.

An overview of the main 2018 results, as well as the cosmological legacy of *Planck* is given in [20]. The data processing pipelines and calibration procedures used for both instruments LFI and HFI are described in [21] and [22], respectively. For the LFI, several improvements have been made with respect to previous releases, especially in the calibration process and in the correction of instrumental features such as the effects of nonlinearities in the response of the analogue-to-digital converters. For the HFI, major improvements in the map-making, the calibration process and in the treatment of the polarization data and systematic effects have been achieved since the previous 2015 release. An extensive series of

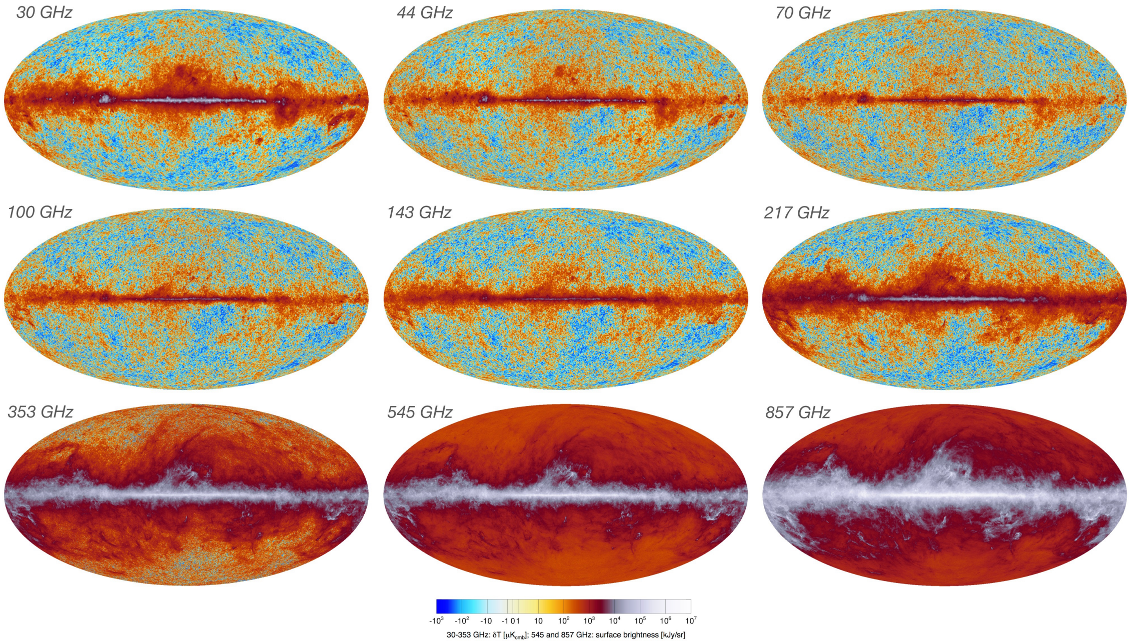

Figure 1: Total intensity emission in each of the nine *Planck* 2018 frequency bands, after removal of a common dipole component. The first seven maps are expressed in equivalent CMB temperature units, while the two highest frequencies, monitoring the dust emission, are expressed in brightness units. Courtesy of ESA and the Planck Collaboration, taken from [20].

null tests dedicated to check the consistency of the maps is also provided [21, 22].

Fig. 1 and 2 show the sky as seen by *Planck* in intensity and polarization, respectively. Each panel in Fig. 1 represents one of the nine Planck's frequency channels, displayed in Galactic coordinates. Similarly, Fig. 2 shows the linear polarization maps (Stokes Q and U parameters) measured by Planck at its lowest seven frequency channels.

2.1 CMB maps and power spectra

As in previous *Planck* data releases, four different component separation methods were used and optimized to produce CMB maps based on *Planck* data alone (Commander, NILC, SEVEM, and SMICA). Those CMB maps and accompanying simulations are the basic input for all analyses of homogeneity, stationarity, and Gaussianity of the CMB fields [25]. Figure 3 shows the intensity map obtained with the SMICA method (left panel), and also the polarization field smoothed on scales of 5°. In addition to the CMB component separation, three methods (Commander, GNILC, and SMICA) were used to extract astrophysical components, i.e. foregrounds. The component separation methodology is described in detail in [23].

The foreground-subtracted, frequency-averaged, cross-half-mission intensity (TT) and

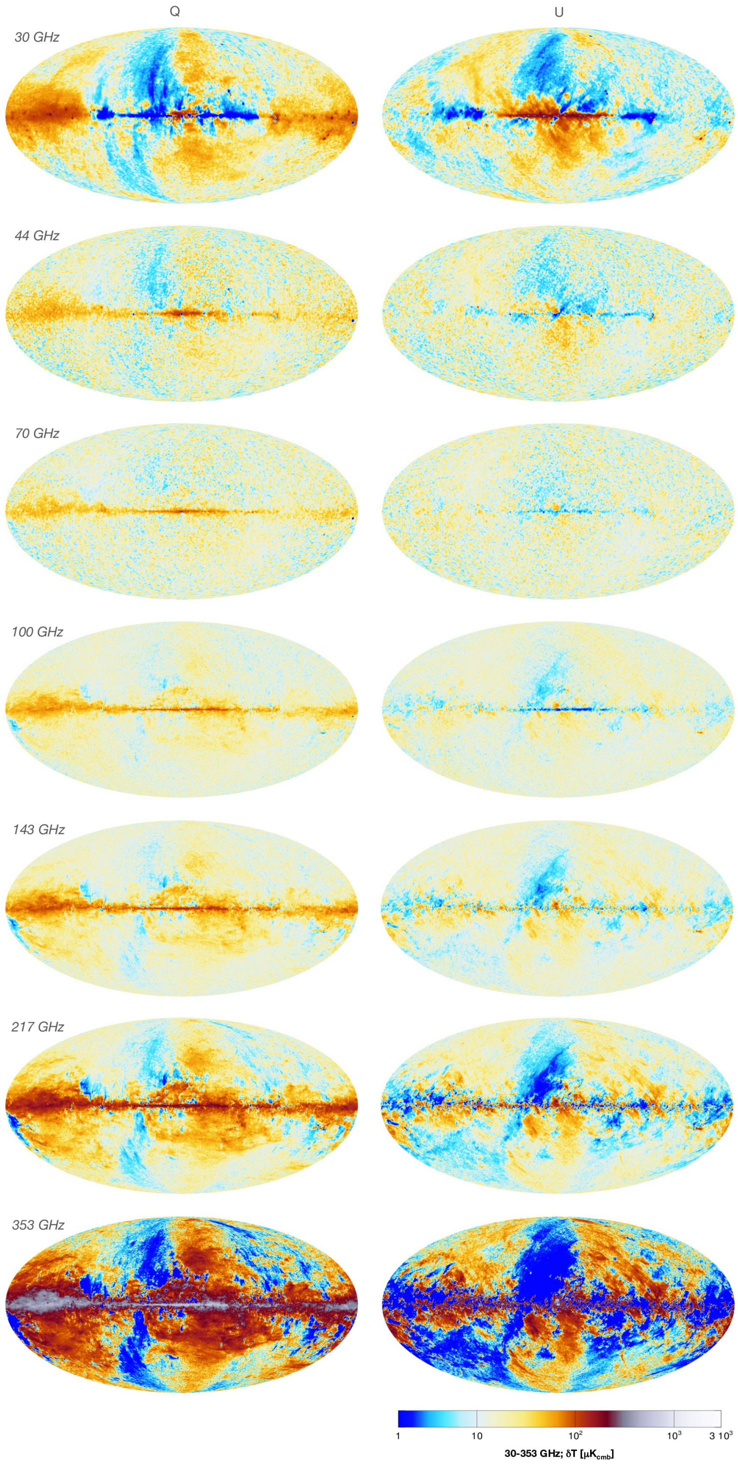

Figure 2: The seven sky polarization maps of Planck 2018. The first two columns show the Q and U Stokes parameters measuring linear polarization, and the last column presents the polarized intensity, $P = \sqrt{Q^2 + U^2}$. Courtesy of ESA and the Planck Collaboration, taken from [20].

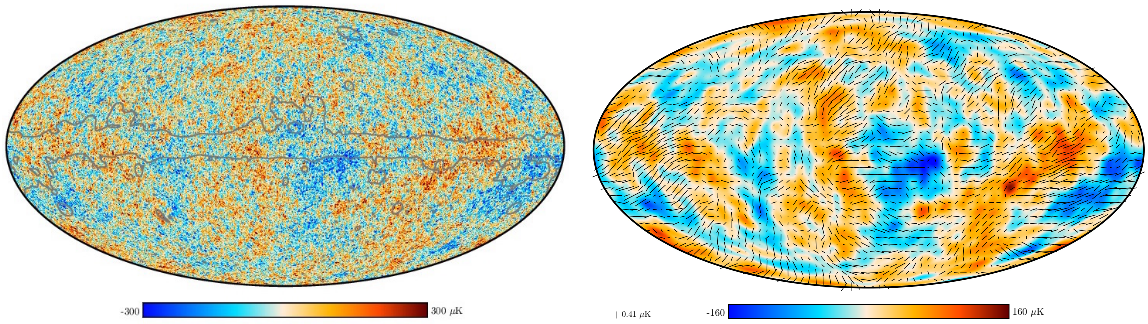

Figure 3: CMB maps obtained with the *Planck* 2018 data release. Left panel: reconstructed SMICA temperature map. Right panel: linear polarization field represented as rods of varying length, superimposed on the temperature map, when both are smoothed at 5° scales. Both CMB maps have been masked and inpainted in regions where residuals from foreground emission are significant. That mask is delineated by a grey line in the left figure, and covers mostly the Galactic plane. Courtesy of ESA and the Planck Collaboration, taken from [20].

polarization (TE and EE) spectra are plotted in Fig. 4, together with the Commander power spectrum at multipoles $\ell < 30$. The blue-line in the figure shows the best-fit base-ΛCDM theoretical spectrum fitted to the combination of temperature, polarization and lensing data. The intensity TT spectrum (top panel) constitutes an extremely precise measurement over three decades in multipole range, allowing to characterize seven acoustic peaks in detail. The uncertainties of that plot are dominated by sampling variance, rather than by instrumental noise or foreground residuals, at all scales below multipole $\ell = 1800$. The polarization power spectra (TE and EE) have improved significantly with respect to previous releases at low multipoles, thanks to the inclusion of the HFI low-ℓ data. The measured TE spectrum has about the same constraining power (in terms of final error bars on the cosmological parameters) as the TT one, while the EE spectrum still has a sizeable contribution from noise. Moreover, the excellent agreement of the TE and EE polarization spectra with the prediction of the ΛCDM theoretical spectrum fitted to the temperature data only constitutes one of the most important consistency tests for the cosmological model.

The bottom-right panel in Fig. 4 shows the power spectrum of the lensing potential. On small angular scales, the primordial CMB anisotropies are distorted by gravitational lensing, primarily sourced by the large-scale structure of the Universe at relatively high redshifts (peaking at $z \sim 2$). The 2018 result represents the highest signal-to-noise ratio detection of CMB lensing to date, exceeding 40σ [25] using intensity and polarization, and with a polarization lensing detection at 9σ. The inclusion of this information in the cosmological analyses breaks some parameter degeneracies inherent to the CMB anisotropies alone.

2.2 *Planck* 2018 Cosmological Parameters

As in the two previous data releases, the *Planck* 2018 measurements of the CMB anisotropies and lensing-potential power spectra are very well described by a standard spatially-flat six

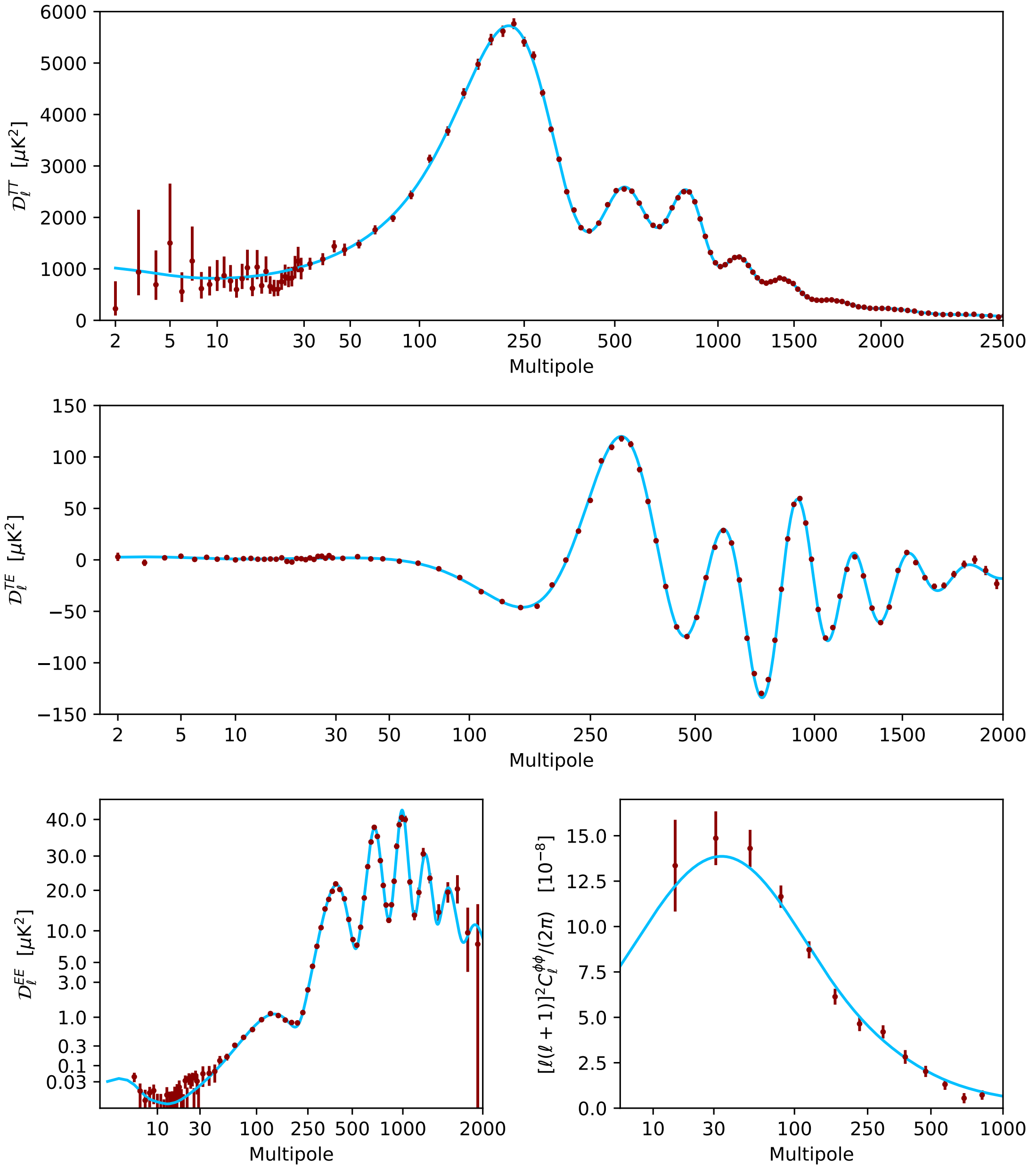

Figure 4: Planck 2018 CMB power spectra. These are foreground-subtracted, frequency-averaged, cross-half-mission angular power spectra for temperature (top), the temperature-polarization cross-spectrum (middle), the E mode of polarization (bottom left) and the lensing potential (bottom right). The blue lines show the best-fitting ΛCDM model. Courtesy of ESA and the Planck Collaboration, taken from [20].

Table 1: Parameter confidence limits derived from the *Planck* CMB temperature, polarization and lensing power spectra, and with the inclusion of BAO data. Error bars in all cases correspond to 68 % confidence limits. The first set of values corresponds to the six base ΛCDM parameters. The remaining parameters shown below the line are derived from those six. More details can be found in [24].

Parameter	*Planck* alone	*Planck* + BAO
$\Omega_b h^2$	0.02237 ± 0.00015	0.02242 ± 0.00014
$\Omega_c h^2$	0.1200 ± 0.0012	0.11933 ± 0.00091
$100\theta_{MC}$	1.04092 ± 0.00031	1.04101 ± 0.00029
τ	0.0544 ± 0.0073	0.0561 ± 0.0071
$\ln(10^{10} A_S)$	3.044 ± 0.014	3.047 ± 0.014
n_S	0.9649 ± 0.0042	0.9665 ± 0.0038
H_0 (km s^{-1} Mpc^{-1})	67.36 ± 0.54	67.66 ± 0.42
Ω_Λ	0.6847 ± 0.0073	0.6889 ± 0.0056
Ω_M	0.3153 ± 0.0073	0.3111 ± 0.0056
σ_8	0.8111 ± 0.0060	0.8102 ± 0.0060

parameter ΛCDM model with adiabatic scalar perturbations [24]. This consistency helds either fitting all the power spectra separately or in combination. The derived values for the six parameters of this base model, together with some derived parameters, are summarized in Table 1. Except for the reionization optical depth, the other five base parameters are measured with sub-percent accuracy. In particular, the CDM component is measured at 100σ, the angular acoustic scale to 0.03 % precision, and n_S is found to be 8σ away from scale invariance ($n_S = 1$).

All parameters remained quite consistent across the different analyses (2013, 2015, 2018) [16, 19, 24]. Compared to the 2015 results [19], the improved measurements of the large-scale polarization allow the reionization optical depth to be measured with higher precision, which in turn leads to a better precision for other correlated parameters. Moreover, the improved modeling of the small-scale polarization also leads to more robust constraints on many parameters, with residual modeling uncertainties estimated to affect them only at the 0.5σ level.

2.3 Cosmological parameters: beyond the base model

As in previous releases, several one-parameter extensions to the base (six-parameter) model have been explored [24]. However, the main conclusion of those analyses is that we do not find any compelling evidence for any of the considered extensions. For example, when considering spatial curvature, the joint constraints with baryon acoustic oscillation (BAO) measurements provides consistency with a flat universe, finding $\Omega_K = 0.0007 \pm 0.0019$. There is no evidence for additional relativistic degrees of freedom, beyond the Standard Model prediction ($N_{\rm eff} = 3.046$). When combining *Planck* 2018 with BAO, we find $N_{\rm eff} = 2.99 \pm 0.17$.

In the neutrino sector, we find that sum of the neutrino masses is tightly constrained to $\Sigma m_\nu < 0.12\,\mathrm{eV}$, again in combination with BAO measurements. In addition, we find no evidence for dynamical dark energy; combining with Type Ia supernovae (SNe), the dark-energy equation of state parameter is measured to be $w_0 = -1.03 \pm 0.03$, consistent with a cosmological constant. Finally, we find no evidence for deviations from a purely power-law primordial spectrum, and combining with data from BAO, BICEP2, and Keck Array data, we place a limit on the tensor-to-scalar ratio of $r_{0.002} < 0.07$.

2.4 Tensions

The *Planck* base-ΛCDM parameters shown in Table 1 are in good agreement with BAO, SNe, standard big-bang nucleosynthesis predictions for the helium and deuterium abundances, and with some galaxy lensing observations. However, they are in slight tension with the Dark Energy Survey's combined-probe results including galaxy clustering (which prefers lower fluctuation amplitudes or matter density parameters), with the cluster number counts and the Sunyaev-Zeldovich Comptonization maps (although the lower value of τ slightly alleviates the tension) [17], and in significant tension with local measurements of the Hubble constant (which prefer a higher value) [24]. Simple model extensions that could in principle partially resolve those tensions are not favored by the data. As in previous releases, the CMB spectra continue to prefer higher lensing amplitudes than predicted in base ΛCDM at over 2σ. However, this is not supported by the lensing reconstruction or the BAO data.

2.5 The legacy of *Planck*

Planck has measured the properties of our Universe to percent-level fidelity, and has been used to test our understanding of the cosmological model to high precision. Here there is a list of topics in which the mission has provided an important legacy: it gave the most precise picture of the universe (6-parameter ΛCDM model); the best characterization of the isotropy and statistics of the CMB anisotropies; the most stringent constraints on inflation physics and primordial non-Gaussianity; constraints on fundamental physics (including neutrino physics, dark energy, modified gravity and primordial magnetic fields); a map of the lensing potential; very rich SZ science (including two catalogs of galaxy clusters with 1653 detections, a full sky SZ map, and the detection of peculiar velocities); a measurement of the ISW effect; maps of the CIB; important studies of extra-galactic sources, both in radio (quasars and radio galaxies) and infrared (dusty star-forming galaxies); a detailed information on the space-frequency distribution of the diffuse Galactic components (synchrotron, free-free, thermal dust, spinning dust emission, magnetic field,...); galactic sources (cold cores, HII regions and young star-forming regions); and the best determination of the Solar Dipole.

3 The *QUIJOTE* experiment

The theoretical framework where we can accommodate all these cosmological results is the ΛCDM cosmology together with inflation, a period of accelerated expansion at the early in-

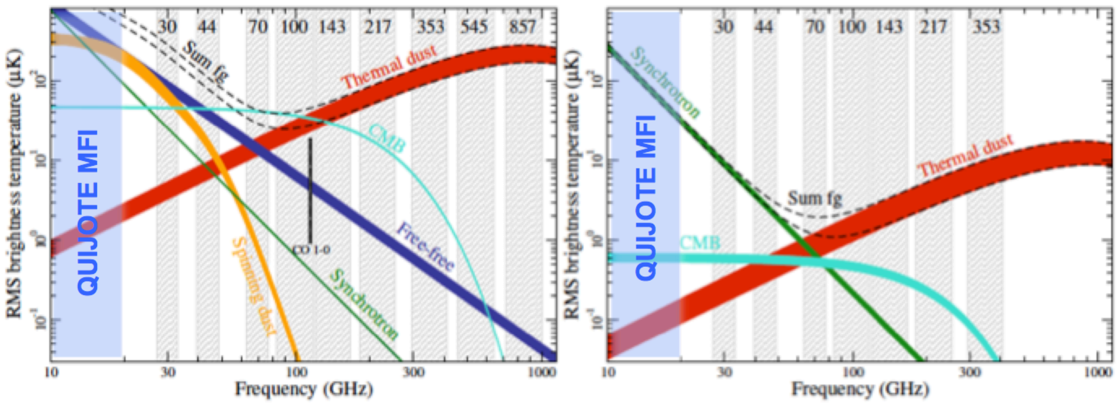

Figure 5: Estimated frequency dependence of the different astrophysical foregrounds in the microwave domain, both in intensity (left) and polarization (right panel). The figure on the right assumes no polarization for the AME. The locations of the *Planck* and *QUIJOTE-MFI* frequency bands are indicated using grey and blue bands, respectively. Adapted from [18].

stants after the Big-Bang. All basic inflationary predictions have been confirmed by *Planck* (i.e. a spatially flat Universe, with nearly scale-invariant spectrum of density perturbations, which is almost a power-law, dominated by adiabatic Gaussian scalar perturbations). However, there is still an inflationary prediction not yet verified. According to the inflationary paradigm, quantum fluctuations in the space-time metric created a background of gravitational waves that imprinted a unique signature on the polarization maps of the CMB: B-modes at large angular scales.

The main scientific driver of *QUIJOTE* is to carry out observations of the CMB polarization, to constrain the primordial B-mode signal down to the level of $r = 0.05$. In addition, another important goal is to characterize the low-frequency polarized foregrounds. One of the main legacy results of *Planck* is the demonstration that foreground signals, and in particular, the polarized emission from our galaxy, will be a major limiting factor of the possible constraints on the existence of B-modes. In this context, the *QUIJOTE* maps in the 10–20 GHz band provide a complementary window to the *Planck* data, bringing valuable information in an almost unexplored frequency domain (see Fig. 5), and providing the essential information to properly correct for the Galactic synchrotron and the anomalous microwave emissions (AME). This legacy information from *QUIJOTE* will be essential for future sub-orbital or satellite experiments.

The *QUIJOTE* project has two phases. In the first phase, we installed the first QUIJOTE telescope unit (QT1) together with the multi-frequency instrument (MFI) [6] at the Teide Observatory. The MFI covers four frequency bands at 11, 13, 17 and 19 GHz, and started operations in November 2012. The second phase includes a second QUIJOTE telescope (QT2) installed in July 2014, and two additional instruments. The thirty-gigahertz instrument (TGI) consists of 31 receivers at 30 GHz [7], while the forty-gigahertz instrument (FGI) has also 31 receivers at 42 GHz. At this moment, we are in the commissioning phase of a hybrid-instrument covering 30 and 42 GHz simultaneously, with half TGI receivers and the other half with FGI ones, but sharing the same cryostat. More information on the *QUIJOTE* instruments and telescopes can be found in [30] and references therein.

3.1 *QUIJOTE-MFI* preliminary results: the wide survey

The *QUIJOTE-MFI* instrument has been operating for almost six years. After this period, we have accumulated $\sim 24,000$ h of data, corresponding to approximately 50 % observing efficiency. As described in [30], the observations carried out with the MFI are of two types: either deep integrations using a raster scan mode at constant elevation in selected sky areas (e.g. Galactic regions, calibrators or cosmological fields), or a wide survey mode using continuous 360° azimuth scans at constant elevation.

Scientific results have been presented for some of the deep observations in a few Galactic regions, as the Perseus molecular complex [4], the W43, W44 and W47 area [5], or the Taurus molecular complex. Here, I discuss the status of the MFI wide Galactic survey, that will be published soon. This wide survey covers around 20,000 $\deg^2$ every day, aiming for a final aggregated sensitivity of $\sim 30\,\mu$K/deg in polarization (Stokes Q and U maps) in the four MFI bands. To date, we have accumulated around 10,000 h of data in this so-called “nominal mode”. The preliminary maps have sensitivities around 40–55 μK/deg.

Figure 6 shows the status of the maps for the two lowest MFI frequency bands (11 and 13 GHz). The polarization maps have sensitivities of around 50–55 μK/deg, and provide a high signal-to-noise detection of the polarized synchrotron emission at these frequencies, including the diffuse emission in North-Polar Spur or the Fan regions. The *QUIJOTE* maps are now being used to constrain the spectral behavior of the polarized synchrotron emission, in combination with the WMAP and *Planck* frequency bands. Our preliminary results provide a synchrotron spectral index with an average value of $\beta_{\rm s} = -3.00 \pm 0.05$, and with an average synchrotron-dust correlation of $\sim 20\,\%$ at large scales, but with significant spatial variations in those properties. Other studies based on these *QUIJOTE* maps, as component separation analyses, the study of multiple AME regions, the characterization of radio-sources in the maps, or the diffuse emission in the north polar spur and the Fan region are in preparation, and will be presented in the coming months.

These analyses are partially funded by the RADIOFOREGROUNDS[3] project (2016-2018), a H2020-COMPET-2015 program aiming to provide the best possible description of the synchrotron emission and AME in our Galaxy in the Northern sky, by adding the information contained in the *QUIJOTE-MFI* frequencies to the *Planck* maps. The associated data products will be made publicly available at the end of the project.

3.2 Future plans

The commissioning phase of the combined TGI/FGI instruments is now taking place. The observing plan is to conduct a cosmological survey during 3 effective years, and to combine

[3]RADIOFOREGROUNDS web: http://www.radioforegrounds.eu.

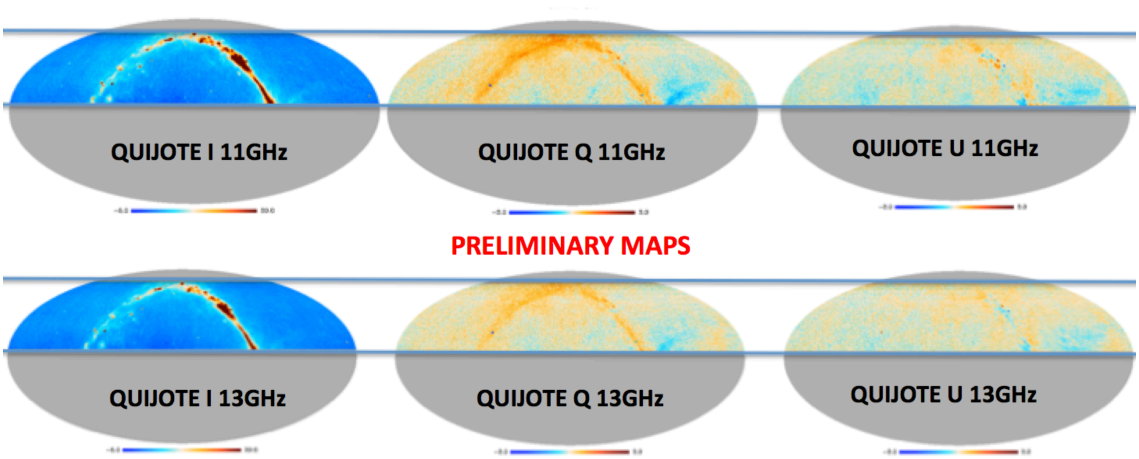

Figure 6: Preliminary maps of the *QUIJOTE-MFI* wide survey, displayed in equatorial coordinates. We show the 11 GHz (first row) and 13 GHz (second row) maps for Stokes I (left), Q (center) and U (right) parameters. The horizontal lines define the declination band between $\delta = 5^\circ$ and $\delta = 80^\circ$. We note that the Stokes Q and U parameters are referred to the Galactic coordinate system, although they are displayed in equatorial coordinates.

these data with the MFI maps. In addition to *QUIJOTE*, two new CMB polarization experiments will be installed soon at the Teide Observatory (Tenerife): Groundbird and STRIP. GroundBird [2] is a MKIDs array to study the CMB polarization in two bands centered at 145 and 220 GHz. It is a collaboration formed by RIKEN, KEK, NAOJ, and Saitama, Kyoto and Tohoku universities in Japan, the Korea University and the IAC. The installation is planned for early 2019. STRIP [3] is part of LSPE, a combined program of ground-based and balloon-borne polarization observations. STRIP will operate in the 42 and 90 GHz bands, and will be installed at the Teide Observatory in mid 2019. Altogether, *QUIJOTE*, STRIP and Groundbird will constitute an unique microwave polarization observatory in the Northern hemisphere, with ten frequency bands covering from 10 to 240 GHz.

Acknowledgments

The development of *Planck* has been supported by: ESA; CNES and CNRS/INSU-IN2P3-INP (France); ASI, CNR, and INAF (Italy); NASA and DoE (USA); STFC and UKSA (UK); CSIC, MICINN, JA and RES (Spain); Tekes, AoF and CSC (Finland); DLR and MPG (Germany); CSA (Canada); DTU Space (Denmark); SER/SSO (Switzerland); RCN (Norway); SFI (Ireland); FCT/MCTES (Portugal); and PRACE (EU). A description of the Planck Collaboration and a list of its members, including the technical or scientific activities in which they have been involved, can be found here. The *QUIJOTE* experiment is being developed by the IAC, IFCA and the Universities of Cantabria, Manchester and Cambridge. Partial financial support is provided by the Spanish Ministry of Science, Innovation and Universities under the projects AYA2007-68058-C03-01, AYA2010-21766-C03-02, AYA2014-60438-P, AYA2017-84185-P and also by the Consolider-Ingenio project CSD2010-00064 (EPI: Exploring the Physics of Inflation). JAR-M is grateful to the organizers of the SEA2018 conference for the invitation to present these results. This project has received funding from the European Union's Horizon 2020 research and innovation program under grant agreement 687312 (RADIOFOREGROUNDS).

References

[1] Bersanelli, M., Mandolesi, N., Butler, R. C., et al. 2010, A&A, 520, A4

[2] Choi et al. 2018, European Physical Journal Web of Conferences, 168, 01014

[3] Franceschet et al. 2018, Proceedings of the SPIE, 10708, id. 107081G 17 pp.

[4] Génova-Santos, R., Rubiño-Martín, J. A., Rebolo, R., et al. 2015, MNRAS, 452, 4169.

[5] Génova-Santos, R., Rubiño-Martín, J. A., Peláez-Santos et al. 2017, MNRAS, 464, 4107.

[6] Hoyland, R. J., et al. 2012, SPIE Conference Series, 8452, 845233

[7] Hoyland, R., et al. 2014, SPIE Conference Series, 9153, 915332

[8] Lamarre, J., Puget, J., Ade, P. A. R., et al. 2010, A&A, 520, A9

[9] Leahy, J. P., Bersanelli, M., D'Arcangelo, O., et al. 2010, A&A, 520, A8

[10] Mandolesi, N., Bersanelli, M., Butler, R. C., et al. 2010, A&A, 520, A3

[11] Mennella et al. 2011, A&A, 536, A3

[12] Planck Collaboration I. 2011, A&A, 536, A1

[13] Planck HFI Core Team. 2011a, A&A, 536, A4

[14] Planck HFI Core Team. 2011b, A&A, 536, A6

[15] Planck Collaboration I, 2014, A&A, 517, A1.

[16] Planck Collaboration XVI, 2014, A&A, 517, A16.

[17] Planck Collaboration XX, 2014, A&A, 517, A20.

[18] Planck Collaboration I, 2016, A&A, 594, A1.

[19] Planck Collaboration XIII, 2016, A&A, 594, A13.

[20] Planck Collaboration I, 2018, A&A submitted, arXiv:1807.06205.

[21] Planck Collaboration II, 2018, A&A submitted, arXiv:1807.06206.

[22] Planck Collaboration III, 2018, A&A accepted, arXiv:1807.06207.

[23] Planck Collaboration IV, 2018, A&A submitted, arXiv:1807.06208.

[24] Planck Collaboration VI, 2018, A&A submitted, arXiv:1807.06209.

[25] Planck Collaboration VIII, 2018, A&A submitted, arXiv:1807.06210.

[26] Planck Collaboration X, 2018, A&A submitted, arXiv:1807.06211.

[27] Planck Collaboration XII, 2018, A&A submitted, arXiv:1807.06212.

[28] Rosset, C., Tristram, M., Ponthieu, N., et al. 2010, A&A, 520, A13

[29] Rubiño-Martín, Rebolo, Aguiar et al. 2012, SPIE Conference Series, 8444, 84442Y

[30] Rubiño-Martín, J. A. et al. 2017, Highlights on Spanish Astrophysics IX, 99

[31] Tauber, J. A., Mandolesi, N., Puget, J., et al. 2010, A&A, 520, A1

[32] Zacchei et al. 2011, A&A, 536, A5

Highlights on Spanish Astrophysics X, Proceedings of the XIII Scientific Meeting of the Spanish Astronomical Society held on July 16 – 20, 2018, in Salamanca, Spain. B. Montesinos, A. Asensio Ramos, F. Buitrago, R. Schödel, E. Villaver, S. Peréz-Hoyos (eds.), 2019

The shape of the ionised gas abundance distribution in spiral galaxies.

Laura Sánchez-Menguiano[1,2], Sebastián F. Sánchez[3], and Isabel Pérez[4]

[1] Instituto de Astrofísica de Canarias, La Laguna, Tenerife, Spain
[2] Departamento de Astrofísica, Universidad de La Laguna, La Laguna, Tenerife, Spain
[3] Instituto de Astronomía, Universidad Nacional Autónoma de México, México
[4] Dpto. de Física Teórica y del Cosmos, Universidad de Granada, Granada, Spain

Abstract

In this contribution we review some of the most relevant results of the PhD thesis awarded with the XIV SEA PhD prize in 2018. The thesis is aimed at characterising the ionised gas abundance distribution in spiral galaxies by using two sets of high-quality integral field spectroscopic data from the CALIFA and AMUSING surveys. We observe that, together with the well-known radial negative gradient, a significant number of galaxies also display a drop in the abundances towards the inner parts of the discs and a flattening in the outermost regions. This suggests that the widely accepted scenario in which the oxygen abundance distribution of spiral galaxies is well described by a single radial negative gradient might be incomplete and deviations from it are needed for a proper characterisation of the distribution. In addition, in the particular case of the galaxy NGC 6754, we perform an analysis of its azimuthal abundance and velocity-residual distributions. This galaxy shows, for the first time, clear signatures of ongoing gas radial migration affecting the abundance distribution. The results obtained in this thesis provide strong constraints to chemical evolution models aimed at explaining the formation and evolution of spiral galaxies, trying to do our bit in the comprehension of the Universe around us.

1 Introduction

The thesis, entitled "The shape of the ionised gas abundance distribution in spiral galaxies", was conducted by Laura Sánchez Menguiano in the Instituto de Astrofísica de Andalucía (IAA-CSIC) under the supervision of Sebastián Sánchez and Isabel Pérez. In the context of the formation and evolution of spiral galaxies, the study of their gas-phase chemical composition has proven to be a powerful tool to improve our knowledge on the evolution of these complex systems. In particular, the analysis of H II regions (regions of ionised gas associated with star formation) is of great importance, as it is through the birth and death of stars that the galaxies chemically evolve.

In this thesis we use two sets of high-quality integral field spectroscopic (IFS) data from two different surveys, CALIFA [28] and AMUSING [9], to characterise the oxygen abundance distribution of the ionised gas in star-forming (SF) regions of spiral galaxies. The first survey provides a sample of 122 disc galaxies extracted from a well-defined, statistically significant mother sample, representative of galaxies in the Local Universe. The latter provides a sample of 102 galaxies that allows us to complement the study based on CALIFA data using a higher spatial resolution dataset.

The abundance distribution of the analysed galaxies is determined based on the calibration proposed by [16] for the O3N2 strong-line indicator (although others are also tested showing that all the qualitative results derived from this study are not contingent upon the choice of the used calibrator). To measure the emission lines involved we apply FIT3D-Pipe3D [30], an extensively tested code designed to deal with spatially resolved IFS data (see [32, 33]).

The study of the 2-dimensional (2D) ionised gas abundance distribution is addressed by analysing separately the radial and azimuthal trends. The large number of SF regions provided by both analysed samples, together with the good coverage of the galaxy discs with high spatial resolution, allow us to undertake this study as never done before. In the following sections we will present the main results of each of these analyses and the conclusions resulting from our work.

2 Radial oxygen abundance distribution

The radial distribution of the chemical abundances in disc galaxies has been studied for decades, being nowadays unquestionable that spiral galaxies exhibit in general a negative trend in metallicity. This was firstly proposed in the 1970s [38, 39, 40, 25], and since then, an extensive body of literature has been amassed on the subject of abundance gradients in nearby galaxies supporting these negative trends [42, 41, 24, 31, 29, 12, 2].

However, gas metallicity studies have also presented some hints of the existence of some behaviours in the oxygen abundance profiles that deviate from the pure radial decline: A decrease or a nearly flat distribution of the abundance in the innermost region of discs (e.g. [3, 27, 29]); and a flattening in the gradient in the outer regions measured in several works ([18, 43, 41, 27, 31, 46], among others). Despite the wide variety of mechanisms proposed to explain the presence of these features (such as radial migration, [21, 22]; or satellite accretion, [26, 4]), its origin is still unclear.

However, most of the previously mentioned studies were limited by statistics, either in the number of observed H II regions, their coverage across the galaxy surface or the size of the analysed sample of galaxies. The study of the radial oxygen abundance distribution carried out in this thesis is first performed in a spaxel-by-spaxel basis using the CALIFA sample (122 galaxies), taking advantage of the full 2D information to properly map the abundance distribution. This type of analysis is feasible because the spaxel size of CALIFA

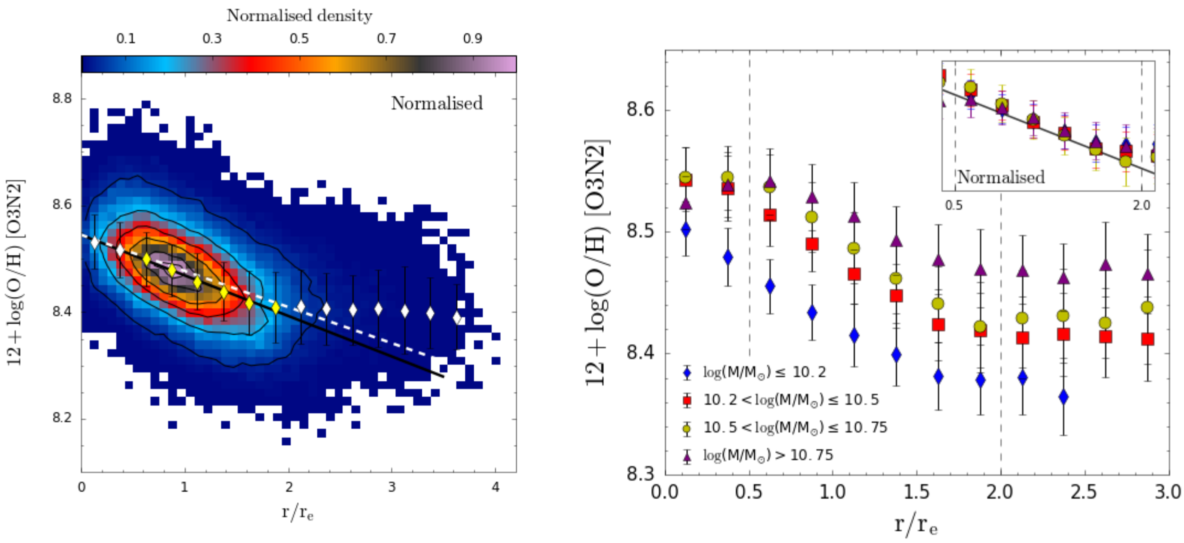

Figure 1: *Left*: Normalised radial density distribution of the oxygen abundance in the CALIFA sample, where the presence of a common gradient between 0.5 and 2.0 r$_e$ and an outer flattening beyond 2.0 r$_e$ are observed. *Right:* Average oxygen abundance radial profiles for galaxies divided in four different mass bins, where it is visible the existence of an inner abundance drop and its dependency with the galaxy mass.

datacubes is of the order of the size of an H II region and prevents us to resolve its ionised structure. With this premise, we also analyse the oxygen abundances derived for individual H II regions for comparison purposes, obtaining equivalent results with both procedures. In addition to the general negative gradient displayed by the galaxies, an inner drop and/or outer flattening are observed in the oxygen abundance radial profile (see Fig. 1). Concerning the negative trend, we find that there is a common abundance gradient between 0.5 and 2.0 r$_e$ of $\alpha_{O/H} = -0.075 \pm 0.016\,\mathrm{dex/r_e}$ when normalising the distances to the disc effective radius. By performing a set of KS tests, we determined that this slope is independent of other galaxy properties, such as morphology, absolute magnitude, and the presence or absence of bars. In particular, barred galaxies do not seem to display shallower gradients, as predicted by numerical simulations and reported by early studies (e.g. [45]). Interestingly, we find that a high number of galaxies with reliable oxygen abundance values beyond two effective radii (57) present a flattening of the abundance gradient in these outer regions. This flattening is not associated with any morphological feature, which suggests that it is a common property of disc galaxies. Finally, we detect a drop or truncation of the abundance in the inner regions of 27 galaxies in the sample; this is only visible for the most massive galaxies. For more details of this analysis performed with CALIFA data we refer the reader to [35].

The high spatial resolution provided by AMUSING data allows us to improve the study on the radial oxygen abundance distribution. This dataset helps us to increase the number of H II regions detected in individual galaxies with respect to previous studies. In addition, we can avoid the dilution effects and reduce the contamination of the diffuse emission in the

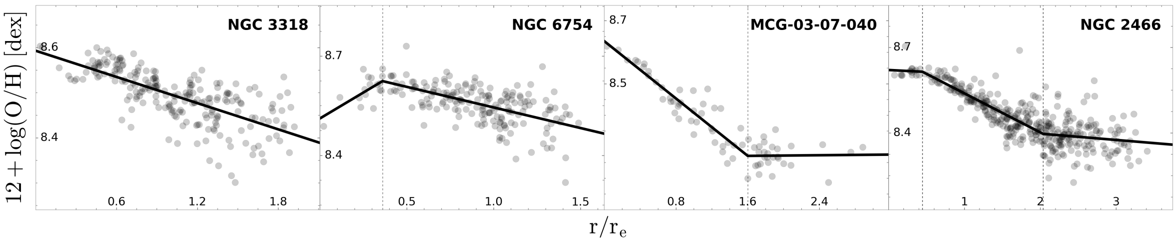

Figure 2: Examples of the different shapes found in the oxygen abundance radial distribution of the H II regions. The solid black line represents the fit to the distribution and the dashed vertical lines correspond to the radial position of the inner drop and/or outer flattening.

detected regions, effects that affected the spaxel-by-spaxel analysis with CALIFA. In this analysis we develop a new methodology to automatically fit the abundance radial profiles (see Fig. 2), finding that 55 galaxies of the sample exhibit a single negative gradient. The remaining 47 galaxies also display, as well as this negative trend, either an inner drop in the abundances (21), an outer flattening (10), or both (16), which suggests that these features are a common property of disc galaxies. We confirm the results found with CALIFA: the presence and depth of the inner drop depends on the stellar mass of the galaxies with the most massive systems presenting the deepest abundance drops, while there is no such dependence in the case of the outer flattening (see Fig. 3). As opposite to the previous study, where the radial position of these features was deduced based on visual inspections of the general shape of the gradient, in this analysis the developed methodology allowed us to determine automatically their actual location. We find that the inner drop appears always around $0.5\,\mathrm{r_e}$, while the position of the outer flattening varies over a wide range of galactocentric distances. Regarding the main negative gradient, we find a characteristic slope in the sample of $\alpha_{O/H} = -0.10 \pm 0.03\,\mathrm{dex/r_e}$ (compatible with the value recovered from the CALIFA data, see Fig. 3). This slope is independent of the presence of bars and the density of the environment. However, when inner drops or outer flattenings are detected, slightly steeper gradients are observed. This suggests that radial motions might play an important role in shaping the abundance profiles. Besides, we define a new normalisation scale ('the abundance scalelength', $r_{O/H}$) for the radial profiles based on the characteristic abundance gradient, with which all the galaxies show a similar position for the inner drop ($\sim 0.5\,r_{O/H}$) and the outer flattening ($\sim 1.5\,r_{O/H}$). Finally, an analysis of the dispersion around the negative gradient arises no significant dependence with any property of the galaxies, with values compatible with the uncertainties associated with the derivation of the abundances. A more detailed explanation of this analysis with AMUSING data can be found in [37].

3 Arm and interarm abundance gradients

Spiral arms are one of the most distinctive features in disc galaxies. These structures can exhibit different patterns, namely grand design and flocculent arms, with easily distinguishable

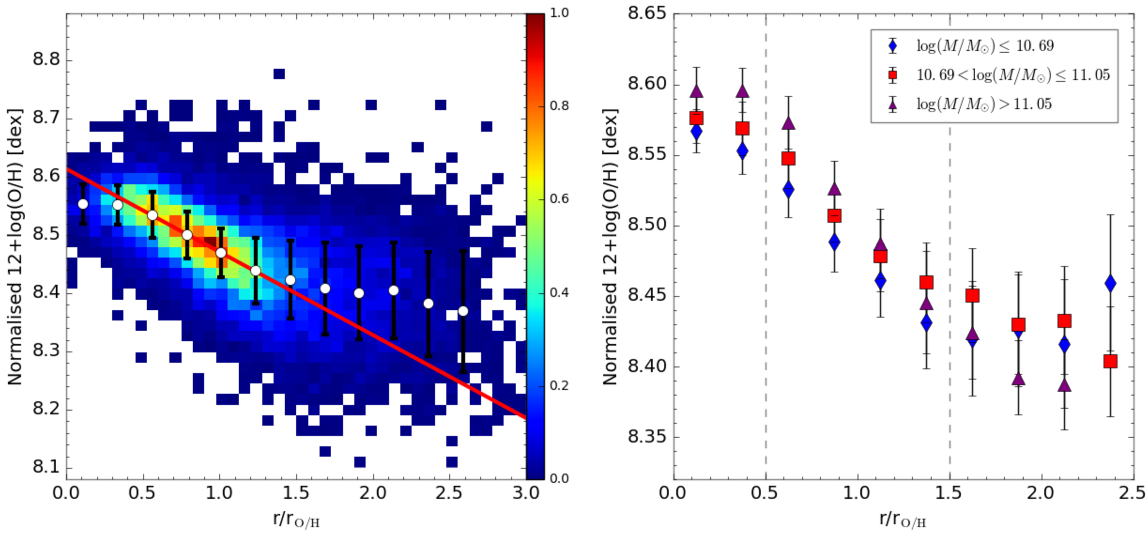

Figure 3: Same as Fig. 1 but for the AMUSING sample and normalising the galactocentric distances to the new defined normalisation scale $r_{O/H}$ ('the abundance scalelength'). See text for more details.

characteristics (long, symmetric, and continuous arms in the former case, small and patchy in the latter). However, their origin and the mechanisms shaping them are unclear. The overall role of spirals in the chemical evolution of disc galaxies is another unsolved question. In particular, it has not been fully explored if the H II regions of spiral arms present different properties from those located in the interarm regions. Very few works have focused on this study, all of them based on small sample of galaxies and not finding evidences of chemical differences between arm and interarm regions [19, 7].

In this thesis we also study the radial oxygen abundance gradient of the arm and interarm SF regions of a subsample of 63 galaxies using CALIFA data. We focus the analysis on three characteristic parameters of the profile: slope, zero-point, and scatter. The sample was morphologically separated into flocculent versus grand design spirals and barred versus unbarred galaxies. We find subtle but statistically significant differences between the arm and interarm distributions for flocculent galaxies, while no significant differences are found for grand design systems. In addition, we find an increase in the scatter when moving away from the spiral arms for flocculent galaxies, whereas grand designs present a similar scatter within the interarm region (see Fig. 4). All this suggests that the mechanisms generating the spiral structure in both type of galaxies may be different. Grand design arms would be linked to quasi-stationary density waves, which move across the disc affecting the gas content of the entire galaxy and diluting possible differences between the arm and interarm regions. On the other hand, flocculent arms would be associated with transient local density instabilities, that affect always the same material (SF regions in the arms), increasing the differences between the arm and the interarm regions. Another possibility is that these differences may be due to a higher star formation *outside* the spiral arms for the flocculent galaxies and a

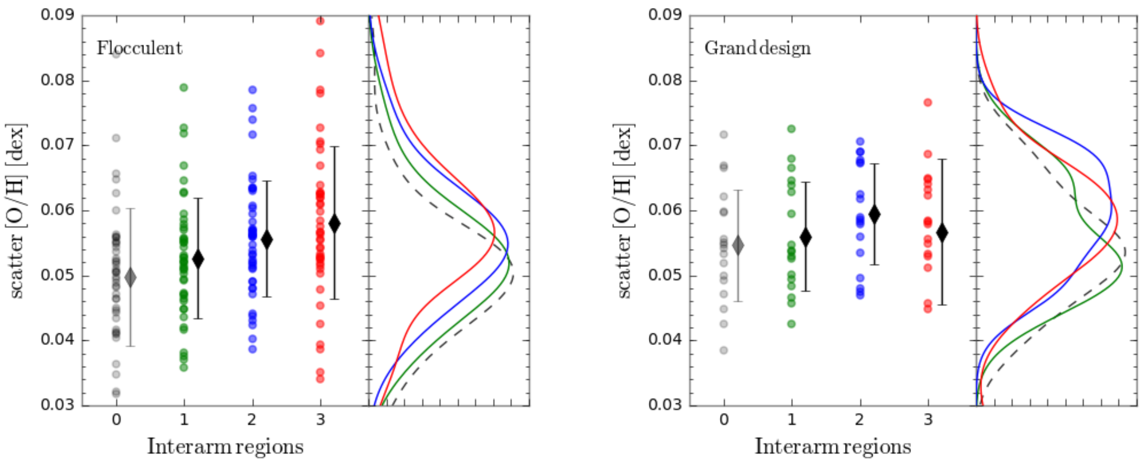

Figure 4: Distribution of the scatter of the oxygen abundances in the interarm regions according to the angular distance to the spiral arms (labeled as region 0) for flocculent (*left panel*) and grand design (*right panel*) galaxies. Each point represents the scatter of the SF spaxels within the corresponding interarm region for a particular galaxy. The black diamonds represent the mean values within each region; the error bars indicate the standard deviations. The distribution of values for each region are also shown in the right auxiliary panels.

more concentrated star formation in the arms for the grand design ones. We also find small differences in barred galaxies, not observed in unbarred systems, hinting that bars may affect the chemical distribution of these galaxies but not strongly enough as to be reflected in the overall abundance distribution. This entire analysis of arm and interarm abundance gradients performed with CALIFA data is described in [36].

4 Azimuthal abundance variations

Recently, with the advent of instruments that provide data covering large FoVs with high spatial resolution, systematic azimuthal variations of the gas oxygen abundance distribution have started to be measured, always focused on the study of individual galaxies [13, 44].

From a theoretical point of view, the presence of azimuthal variations induced by radial migration was recently proposed in simulations of spiral galaxies [8, 11]. Although these predictions were focused on the stellar component, it is known that both gas and stars are affected by these movements (e.g. [23, 10]). Indeed, streaming motions of gas along the spiral arms have been proposed [10, 1], which could produce azimuthal variations of the gas abundance.

In this thesis we take advantage again of the high spatial resolution of AMUSING data to analyse the presence of possible azimuthal abundance variations in one galaxy of the sample, NGC 6754, in order to better investigate the subtle differences found in the arm/interarm analysis performed with CALIFA data. This way, in order to measure azimuthal variations

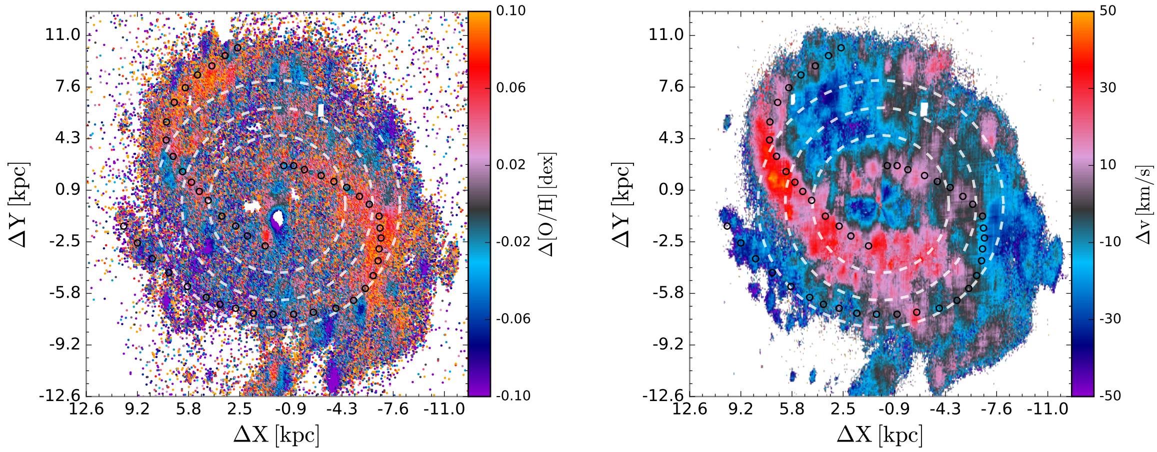

Figure 5: 2D deprojected distributions of the gas abundance (*left*), and Hα LOS velocity (*right*) residuals. Dashed white circles indicate the three radial positions R = 4.5, 6.3 and 8.1 kpc of the azimuthal profiles shown in Fig. 6.

in the abundance distribution of NGC 6754 we need to derive the abundance residuals (see left panel of Fig. 5) by removing the characteristic radial profile displayed by this galaxy to the observed 2D distribution. In addition to the abundance distribution, we also analyse for this galaxy the line-of-sight (LOS) Hα velocity distribution to find some possible links between kinematics and the observed pattern in the azimuthal abundance variations (as suggested by theoretical works). Similarly, the residual velocities (see right panel of Fig. 5) are obtained after subtracting the LOS projection of the derived rotation model to the observed distribution.

Analysing the azimuthal profiles of both residuals at three different galactocentric distances represented as dashed white circles in Fig. 5 (see Fig. 6), we find that the velocity profiles show a peak located just after the peak in the light distribution (leading side of the arm[1]), with an amplitude between $\sim 28-38$ km/s, and a minimum just before the light peak (trailing side). Remarkably, these maxima (minima) in the velocity profile appear together with a decrement (increment) in the abundance profile at all the radii, with a total amplitude (peak-to-peak) up to ~ 0.1 dex.

Considering the galaxy orientation and assuming trailing spiral arms [14], positive (negative) residual velocities indicate radially inward (outward) motions of the gas and tangentially faster (slower) motions of the gas for the eastern spiral arm. Thus, the positive velocity residuals displayed by NGC 6754 in a wide extension of the leading part of the eastern arm can be interpreted either as gas moving radially inward, gas moving tangentially faster, or a combination of both. Following a similar reasoning, the negative velocity residuals in the trailing part can be the result of gas moving radially outward, gas moving tangentially

[1]The leading side of a spiral arm is the edge of the arm that points towards the direction of disc rotation, that is, the front of the arm. The trailing side is, on the other hand, the edge of the arm that points towards the opposite direction of disc rotation, that is, the back of the arm.

slower, or both. The asymmetries found in the metallicity residuals are in agreement with a transport of metal-rich gas from the inner disc toward the outer regions at the trailing side of the spiral arm and more metal-poor gas from the outer disc toward the inner ones at the leading side, which is strikingly consistent with the velocity asymmetries mentioned above. These trends are observed at all three radii, which indicates strong evidence of the radial migration happening in a large radial range.

In other to interpret these results we also analyse the gas content of a simulated galaxy (N-body+SPH), which allows us to analyse separately the radial and tangential components of the LOS velocity. In light of the comparison between the observations and the simulations we conclude that the trailing (leading) edge of the NGC 6754 spiral arms show signatures of tangentially slower, radially outward (tangentially faster, radially inward) streaming motions of metal-rich (poor) gas over a large range of radii. These results show direct evidence of gas radial migration for the first time. In addition, the simulated galaxy displays spiral morphological features rotating with a similar speed as the gas at every radius. Although it is not guaranteed that the nature of the spiral arms in the observed galaxy is the same as in the simulations, the consistency found indicates that the spiral arm features in NGC 6754 may be transient, with a pattern speed decreasing with radius. A more detailed explanation of this analysis of NGC 6754 with AMUSING data can be found in [34].

5 Conclusions

The existence of a radial decrease in the gas chemical abundances of spiral galaxies was well established by observations decades ago (e.g. [38, 25, 17, 15, 27, 6]), supporting the inside-out scenario for disc evolution [20, 5]. With the advent of IFS surveys like CALIFA, abundance studies using larger samples of H II regions have become feasible [31, 29], with the same results as in previous studies.

In this thesis we go a step further and analyse for the first time the oxygen abundance distribution for a large sample of galaxies taking advantage of the full 2D information provided by the CALIFA and AMUSING surveys, improving the statistics over previous studies in the field. This way, it comprises the most complete 2D characterisation of the oxygen abundance distribution of the ionised gas in a large and statistically significant sample of spiral galaxies up to date. We show that, besides the negative gradient, this distribution displays a wide range of features such as inner drops, outer flattenings, and azimuthal variations, as opposed to the simplistic view of a single radial decline. These features display clear trends with galaxy properties such as spiral structure, mass, or bar presence. All these results provide strong constraints to chemical evolution models aimed at explaining the formation and evolution of spiral galaxies, contributing to improve our understanding of the Universe around us.

Acknowledgments

The funding for the PhD thesis reviewed here came from the Spanish Ministerio de Economía y Competitividad (MINECO) via grant BES-2013-062927 (AYA2012-31935 and AYA2016-79724-C4-4-

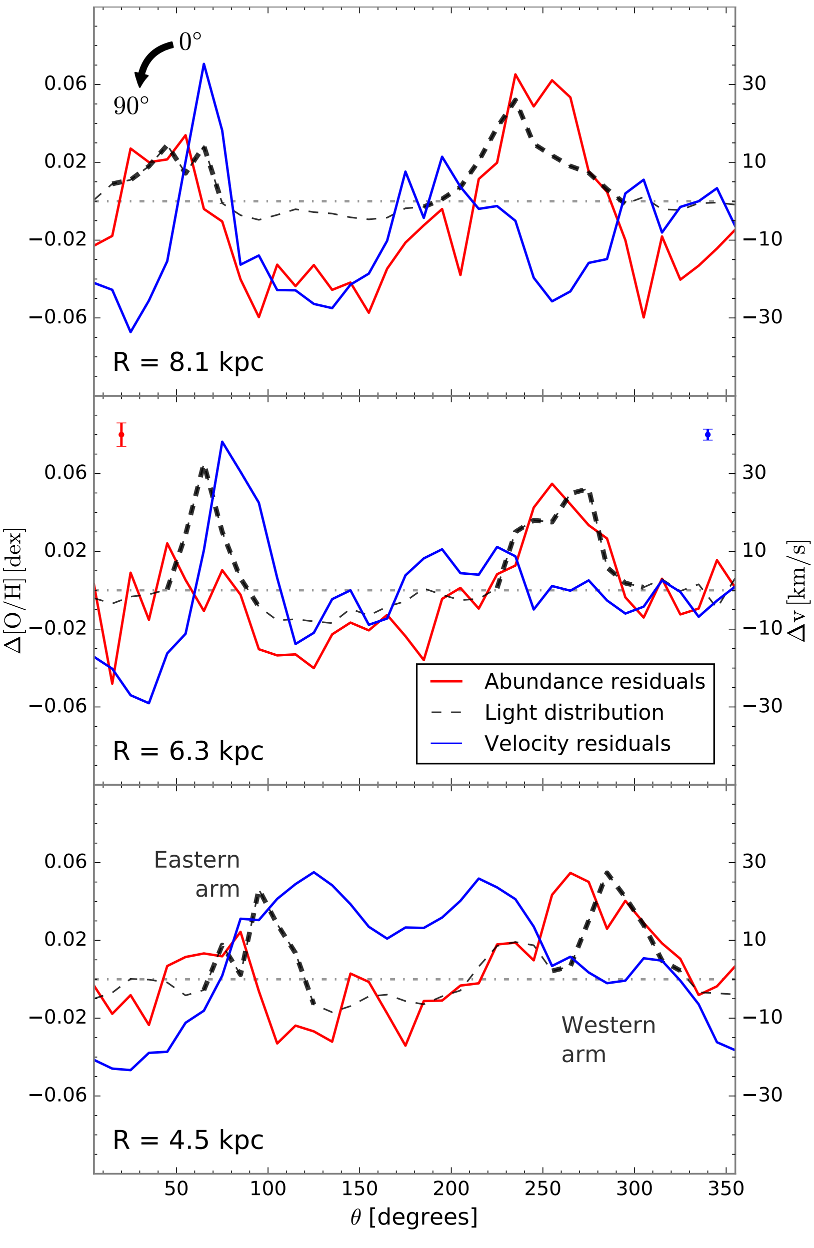

Figure 6: Azimuthal profiles of the light (black dashed), oxygen abundance residuals (blue, left-hand y-axis) and Hα LOS velocity residuals (red, right-hand y-axis) at three different radii (shown in Fig. 5). The position of the spiral arms is marked with the bold dashed line. Mean errors in the azimuthal profiles are denoted by the vertical lines in the middle panel. The angles are measured counter-clockwise from the positive Y-axis in Fig. 5.

P projects). We also acknowledge support from the "Junta de Andalucía" local government through the FQM-108 project and from the ConaCyt funding programme 180125 and DGAPA IA100815. Finally, LSM would like to personally thank to her PhD supervisors for their support and wise advice.

References

[1] Baba, J., Morokuma-Matsui, K., Miyamoto, Y., Egusa, F., & Kuno, N. 2016, MNRAS, 460, 2472

[2] Belfiore, F., Maiolino, R., Tremonti, C., et al. 2017, MNRAS, 469, 151

[3] Belley, J. & Roy, J.-R. 1992, ApJS, 78, 61

[4] Bird, J. C., Kazantzidis, S., & Weinberg, D. H. 2012, MNRAS, 420, 913

[5] Boissier, S. & Prantzos, N. 1999, MNRAS, 307, 857

[6] Bresolin, F., Kennicutt, R. C., & Ryan-Weber, E. 2012, ApJ, 750, 122

[7] Cedrés, B. & Cepa, J. 2002, A&A, 391, 809

[8] Di Matteo, P., Haywood, M., Combes, F., Semelin, B., & Snaith, O. N. 2013, A&A, 553, A102

[9] Galbany, L., Anderson, J. P., Rosales-Ortega, F. F., et al. 2016, MNRAS, 455, 4087

[10] Grand, R. J. J., Kawata, D., & Cropper, M. 2015, MNRAS, 447, 4018

[11] Grand, R. J. J., Springel, V., Kawata, D., et al. 2016, MNRAS, 460, L94

[12] Ho, I.-T., Kudritzki, R.-P., Kewley, L. J., et al. 2015, MNRAS, 448, 2030

[13] Ho, I.-T., Seibert, M., Meidt, S. E., et al. 2017, ApJ, 846, 39

[14] Hubble, E. 1943, ApJ, 97, 112

[15] Kennicutt, Jr., R. C., Bresolin, F., & Garnett, D. R. 2003, ApJ, 591, 801

[16] Marino, R. A., Rosales-Ortega, F. F., Sánchez, S. F., et al. 2013, A&A, 559, A114

[17] Martin, P. & Roy, J.-R. 1992, ApJ, 397, 463

[18] Martin, P. & Roy, J.-R. 1995, ApJ, 445, 161

[19] Martin, P. & Belley, J. 1996, ApJ, 468, 598

[20] Matteucci, F. & Francois, P. 1989, MNRAS, 239, 885

[21] Minchev, I., Famaey, B., Combes, F., et al. 2011, A&A, 527, A147

[22] Minchev, I., Famaey, B., Quillen, A. C., et al. 2012, A&A, 548, A126

[23] Minchev, I., Chiappini, C., & Martig, M. 2014, A&A, 572, A92

[24] Patterson, M. T., Walterbos, R. A. M., Kennicutt, R. C., Chiappini, C., & Thilker, D. A. 2012, MNRAS, 422, 401

[25] Peimbert, M. 1979, in IAU Symposium, Vol. 84, ed. W. B. Burton, 307–315

[26] Qu, Y., Di Matteo, P., Lehnert, M. D., van Driel, W., & Jog, C. J. 2011, A&A, 535, A5

[27] Rosales-Ortega, F. F., Díaz, A. I., Kennicutt, R. C., & Sánchez, S. F. 2011, MNRAS, 415, 2439

[28] Sánchez, S. F., Kennicutt, R. C., Gil de Paz, A., et al. 2012, A&A, 538, A8

[29] Sánchez, S. F., Rosales-Ortega, F. F., Iglesias-Páramo, J., et al. 2014, A&A, 563, A49

[30] Sánchez, S. F., Rosales-Ortega, F. F., Kennicutt, R. C., et al. 2011, MNRAS, 410, 313

[31] Sánchez, S. F., Rosales-Ortega, F. F., Marino, R. A., et al. 2012b, A&A, 546, A2

[32] Sańchez, S. F., Pérez, E., Sánchez-Blázquez, P., et al. 2016a, Rev. Mexicana Astron. Astrofis., 52, 21

[33] Sánchez, S. F., Pérez, E., Sánchez-Blázquez, P., et al. 2016b, Rev. Mexicana Astron. Astrofis., 52, 171

[34] Sánchez-Menguiano, L., Sánchez, S. F., Kawata, D., et al. 2016a, ApJ, 830, L40

[35] Sánchez-Menguiano, L., Sánchez, S. F., Pérez, I., et al. 2016b, A&A, 587, A70

[36] Sánchez-Menguiano, L., Sánchez, S. F., Pérez, I., et al. 2017, A&A, 603, A113

[37] Sánchez-Menguiano, L., Sánchez, S. F., Pérez, I., et al. 2018, A&A, 609, A119

[38] Searle, L. 1971, ApJ, 168, 327

[39] Shields, G. A. 1974, ApJ, 193, 335

[40] Smith, H. E. 1975, ApJ, 199, 591

[41] van Zee, L., Salzer, J. J., Haynes, M. P., O'Donoghue, A. A., & Balonek, T. J. 1998, AJ, 116, 2805

[42] Vila-Costas, M. B. & Edmunds, M. G. 1992, MNRAS, 259, 121

[43] Vilchez, J. M. & Esteban, C. 1996, MNRAS, 280, 720

[44] Vogt, F. P. A., Pérez, E., Dopita, M. A.,Verdes-Montenegro, L., & Borthakur, S. 2017, A&A, 601, A61

[45] Zaritsky, D., Kennicutt, Jr., R. C., & Huchra, J. P. 1994, ApJ, 420, 87

[46] Zinchenko, I. A., Pilyugin, L. S., Grebel, E. K., Sánchez, S. F., & Vílchez, J. M. 2016, MNRAS, 462, 2715

Highlights on Spanish Astrophysics X, Proceedings of the XIII Scientific Meeting of the Spanish Astronomical Society held on July 16 – 20, 2018, in Salamanca, Spain. B. Montesinos, A. Asensio Ramos, F. Buitrago, R. Schödel, E. Villaver, S. Pérez-Hoyos, I. Ordóñez-Etxeberria (eds.), 2019

Spain joins the SKA.

Lourdes Verdes-Montenegro[1], Julián Garrido[1], and Marina Fernández-Peña Mollá[1]

[1] IAA-CSIC

Abstract

The Square Kilometre Array (SKA) is an international project, qualified as ESFRI (European Strategy Forum on Research Infrastructures) Landmark, to build the largest and most sensitive radio telescope ever conceived, with the potential to achieve fundamental advances in Astrophysics, Fundamental Physics and Astrobiology. Since 2011, the IAA-CSIC coordinates the Spanish participation in the SKA. **On last 1st June 2018 Spain became the eleventh member of the SKA Organisation**. In the following sections, we summarize the process that has been followed in Spain to achieve it.

1 Introduction

SKA is being built in order to address open key questions in several areas, such as Astrophysics, Astrobiology and Fundamental Physics. Some examples of them are: the formation of the 1st galaxies in a dark Universe dominated by atomic gas, the evolution of the atomic gas and the star formation till the current epoch, strong field tests of gravity using pulsars and black holes, understanding the acceleration in the expansion of the Universe, or the study of extrasolar planets and their formation through proto-planetary disks, or the presence of biomarkers.

All of these questions have several aspects in common, which may be translated, from an instrumental point of view, on requirements such as the capability of detecting ultrafaint radio signals in a large bandwidth (MHz to GHz, e.g. 21cm HI line), high angular resolution and high survey speed.

All these requirements led to the development of an instrument like the Square Kilometre Array, an interferometer with a total collecting area equivalent to 1 square kilometre. This is achieved by combining thousands of antennas with different technologies that cover a wide frequency range. The antennas are separated by thousands of kilometres, located in up to 9 countries in Africa (starting in South Africa) and Australia (starting in the West of the country). Technically, it may be considered as a sensors network at a continental scale.

The SKA Observatory will be a single observatory organised in three sites i.e. the headquarters (located in United Kingdom) and two telescopes in different continents.

1.1 SKA1

SKA is an interferometer, hence it allows for a phased development. The first phase of SKA (SKA1) is currently at the end of its design phase. SKA-low will consist of 131.000 dipoles in Australia covering ranges from 50 to 350 MHz (low frequencies), reaching baselines of 65 km. SKA1-mid will consist of almost 200 dishes in South Africa (including 64 MeerKAT dishes), covering ranges from 350 MHz to 14GHz and with baselines of 150 km.

The cost cap for the deployment baseline of SKA1 is €674 M (financial value of 2016) and it will enter into the procurement phase in 2020-2021, with construction expected in the period 2021-2027. Early Science is planned to start by 2026.

1.2 SKA2

SKA2 (to be developed in the period 2024-2030) will increase the number of dipoles and dishes (approximately 500.000 dipoles + 2500 dishes) of SKA1, that will extend to baselines of up to 3500 kms, as well as improve other capacities based on what is called an *Advanced instrumentation program*. It will include achieving lower frequencies (200 - 500 MHz) and larger fields of view with approx. 250 dense aperture array stations, as well as by adding Phased Array Feeds (PAF) to the dishes, and aiming to reach extremely wide bandwidths.

1.3 International (and European) Context and Organization

The SKA Organisation (SKAO) is currently composed of 12 member countries: Australia, Canada, China, France, India, Italy, New Zealand, South-Africa, Spain, Sweden, the Netherlands and UK, being Spain and France the last 2 to join the project, in June and July respectively. But this project goes much further, counting with the involvement of many other countries: Brazil, Japan, Malta, South Korea, Poland, Portugal, Russia, USA, Germany, Switzerland, Mexico, Ireland, Russia. In short, it involves more than 1000 scientists and engineers from more than 270 institutions and 20 countries.

2 SKA in Spain

The Spanish participation in the SKA started with the participation of the U. Alcalá-IGN and U. Valencia in the FP6 Project SKADS (SKA Design Studies, 2005-2009). In 2010, the MICINN qualified the project as *high-priority* in its roadmap. After that, in 2011, the RIA meeting *Science and technical opportunities in the SKA era* showed a broad and strong scientific interest of Spanish researchers in the SKA. This interest kept growing making possible that the MICINN applied for Spain to become an SKA Observer country in September 2011. Since then, other SKA-related projects/scientific networks have been carried out: from 2011 to 2014, the *Spanish Scientific Network of SKA* (FIS2011-14593-E, PI. J. C. Guirado, U. Valencia) funded by the MICINN, counted with 6 research institutions and 5 universities.

In December 2011, the project *VIA-SKA: Feasibility study of the Spanish participation in the SKA* started, led by IAA-CSIC, and gathering 7 research institutions plus 8 Universities that worked together in the elaboration of a feasibility study and promoted the participation of Spanish companies and academic centres in the SKA design.

Several activities beyond the original scope of the VIA-SKA project have been performed during these years, such as: a) Diffusion and organisation of SKA activities in coordination with the SKA Communication and Outreach Network (SKACON), including the support to the organization of meetings and conferences, conferences in research centres, outreach talks, maintenance of the SKA Spanish website, called minisite, or diffusion in media; b) Support to academic groups, industry and the Ministry, including interaction with design consortia, the SKA Office, support to apply at funding calls and coordination of proposals, or support to the incorporation to SKA committees/Science Working Groups/Key Science Projects/design Working Packages; c) Creation of the capacity map of Spanish industry, preparation for the procurement phase (in collaboration with CDTI), and d) Joint discussions with international SKA related stakeholders.

2.1 SKA Science in Spain

In terms of Science, we highlight the effort made in the preparation of the **Spanish SKA White Book** [1] in 2015, where 120 researchers from 40 centres participated in 29 chapters, covering most of the areas mentioned in the SKA Science Book [2]). This last book counted with the participation of Spanish researchers in more than 14 chapters, representing approximately a 10% of the book.

2.2 Preparatory work: precursors and pathfinders

Spanish researchers also participate in preparatory works with SKA precursors and pathfinders. Precursors are those radio telescopes that are located in the sites where SKA will be established, while pathfinders are those that are testing some of the technologies that will be used in SKA. This will allow our community to get prepared for the scientific data analysis when SKA will be fully operational. Since SKA will not be only an instrument for radioastronomers, it is of relevance to consider the synergies with instruments working at different wavelengths, like those performing optical 3D spectroscopy.

2.3 Workshops, Conferences and Meetings

In the last years, several workshops, conferences and SKA related meetings have been organized. In 2012, the SKAO visited Abengoa facilities, and in 2016, the Plataforma Solar de Almería (PSA-CIEMAT) with the aim of making the SKAO aware of the Spanish expertise in renewable energies. In November 2012, the workshop *SKA: Strategic Position & Future Opportunities for Spanish Industry* took place, with more than 50 companies and academic centres involved. **In October 2014, a Spanish SKA Day was held at the IAA-CSIC**, with 18 institutions and 17 companies participating. **In February 2016, an SKA Industry Day was organised by CDTI, the SKAO and IAA-CSIC**. It counted with 80 participants, including the attendance of the SKA Director General and SKA design consortia leaders. In November 2017, the meeting *Physics opportunities with a new universes view: the SKA radio telescope* was held in Valencia and, last May, the *VI Meeting on Fundamental Cosmology* counted with 4 talks related to SKA.

2.4 Membership in SKA Committees

Spanish researchers participate in several SKA committees and in positions and representation in boards of the SKA Organisation or SKA Consortia, such as the following:

- SKA Power Supply Option Working Group
- Spanish Liaison Industry Officer (ILO)
- Boards of SKA design consortia (Dish, SaDT, SDP)
- Dish consortia
- SKA Regional Centre Coordination Group (SRCCG)
- SKA Communications Steering Committee (SKACOSC) and SKACON
- SKA Office (SKAO)
- Science Working Groups (SWGs). currently 28 researchers from 11 Spanish institutions participate in 9 out of the 11 SKA SWGs, with 2 of them acting as co-chairs

2.5 Technological developments for SKA Design

In March-June 2013 a Request for Proposals was issued by the SKA Office corresponding to the work packages to be established for the design of SKA. As a result, 12 Spanish research centres and 12 companies participate in 8 SKA international Preconstruction Consortia (contribution estimated at approximately €2M in Feb 2014). More recently, Spanish research centres have been invited to join the PAF consortium whose activities will continue during the SKA1 Construction.

2.6 Industry capacity map

In the context of the VIA-SKA project, the IAA-CSIC elaborated in 2013 the capacity map of Spanish industry for the SKA design and construction. This was the beginning of several activities related to industry:

- In April 2013, a report called *VIA-SKA: Feasibility study of the Spanish technological participation in the SKA* was presented to MINECO and the RIA, based on the above mentioned capacity map.

- From January to October 2017 a revision of potential contracts for the Spanish Industry was done in collaboration with CDTI, when the SKA ILO from CDTI made a survey to the Spanish industry for construction contribution.

- In May 2018, a **response to an SKA Construction Request for Information** was prepared by CDTI in collaboration with IAA-CSIC.

2.7 Milestones

We can summarize the performed activities in the last years with the following milestones:

- In January 2012, 9 VIA-SKA members entered in the Work Breakdown Structure Working Groups.

- Since October 2013, a MINECO representative has been regularly invited to the SKA Board meetings.

- In January 2014, the RIA Board endorsed the recommendation issued by the G1 RIA committee in November 2013 on the interest of joining the SKA before SKA construction

- In February 2014, the Spanish participation in SKA design was valued in 2M€ by SKA.

- **In December 2015, a letter from the Secretary of State to SKA DG started a dialog to explore scenarios for Spain to join the SKA**.

- In 2016, SKA was included in the Spanish National budget.

- In June-July 2016, a report was produced for **the Evaluation of the participation of Spain in the SKA** and submitted to the Secretary of State; **the outcome was positive**. This action was followed by on-going negotiations with the SKA DG and Board.

- July 2017 - June 2019. RED-SKA: Excellence network for the scientific and technological participation of Spain in the SKA -AYA2016-82017-REDT. Coordination: IAA-CSIC. Participants: CAB-CSIC, ICE-CSIC, IFCA/DICOM, Universidad de Valencia, BSC, UPM, UGR, IAC, CIEMAT-PSA.

- From July 2017 to June 2019, the RED-SKA project is being developed: Excellence network for the scientific and technological participation of Spain in the SKA -AYA2016-82017-REDT. Coordinated by IAA-CSIC, it counts with the participation of CAB-CSIC, ICE- CSIC, IFCA/DICOM, Universidad de Valencia, BSC, UPM, UGR, IAC and CIEMAT-PSA.

- In May 2018, the Secretary of State sent to the SKA Organisation the official request for Spain to become Member of the SKA Organization.
- **Since 1st June 2018, Spain is the 11th Member country of the SKA Organization.**

3 Conclusions

Spain has developed a solid scientific community, strategically positioned within the SKA project, working in close collaboration with engineers and industry, ready to play a major role in SKA1 Key Science Projects, and also performing key contributions to the SKA design phase and construction, with an impact in society. As a consequence of these efforts, Spain has become a Member of the SKA Organization. This is of special relevance since SKA is an ESFRI Landmark project with the potential for transformational science that will lead to a scientific revolution beyond radio astronomy. This will imply I+D+i in cutting edge technologies, and will attract the best scientists, engineers and managers.

Acknowledgments

The authors of this paper acknowledge support from grants AYA2016-82017-REDT, AYA2015-65973-C3-1-R, AYA2015-71939-REDI, AYA2014-52013-C2-1-R from Ministerio de Economía y Competitividad, AIC-A-2011-065 and AYA2008-06181-C02 from Ministerio de Ciencia e Innovación.We would also like to thank all the Spanish scientists and engineers involved in the SKA project because nothing would have been possible without them.

References

[1] The Spanish Square Kilometer Array White Book. Editors: M. Pérez-Torres, L. Verdes-Montenegro, J.C. Guirado, A. Alberdi, J. Martín-Pintado, R. Bachiller, D. Herranz, J. M. Girart, S. Migliari, J. M. Rodríguez-Espinosa. 2015. http://spain.skatelescope.org/ska-science/libro-blanco-ska/

[2] Advancing Astrophisics with the Square Kilometre Array. PoS 2015 New official SKA science book, 2000 pages. https://www.skatelescope.org/books/

Highlights on Spanish Astrophysics X, Proceedings of the XIII Scientific Meeting of the Spanish Astronomical Society held on July 16 – 20, 2018, in Salamanca, Spain. B. Montesinos, A. Asensio Ramos, F. Buitrago, R. Schödel, E. Villaver, S. Pérez-Hoyos, I. Ordóñez-Etxeberria (eds.), 2019

J-PLUS Data Release 1.

C. López-Sanjuan[1], A. J. Cenarro[1], C. Hernández-Monteagudo[1], M. Moles[1], D. Cristóbal-Hornillos[1], A. Marín-Franch[1], A. Ederocrite[1,2], J. Varela[1], R. E. Angulo[1,3], H. Vázquez Ramió[1], K. Viironen[1], S. Bonoli[1,3], A. A. Orsi[1], and the J-PLUS collaboration.

[1] Centro de Estudios de Física del Cosmos de Aragón, Unidad Asociada al IAA-CSIC, Plaza San Juan 1, 44001 Teruel, Spain
[2] Instituto de Astronomia, Geofísica e Ciências Atmosféricas, Universidade de São Paulo, R. do Matão 1226, 05508-090 São Paulo, Brazil
[3] Donostia International Physics Center, Paseo Manuel de Lardizabal 4, 20018 Donostia-San Sebastián, Spain

Abstract

We present the first data release of the Javalambre Local Universe Photometric Survey (J-PLUS), an ongoing photometric survey with 12 optical bands observing thousands of square degrees of the sky from the JAST/T80 telescope at the Observatorio Astrofísico de Javalambre (OAJ). T80Cam is a 2 deg^2 field-of-view (FoV) camera mounted on JAST/T80, and is equipped with a unique system of filters spanning the entire optical range ($3500 - 10000$ Å), optimally designed to extract the rest-frame spectral features that are key to both characterize stellar types and to deliver a low-resolution photo-spectrum for each observed object. With a typical depth (5σ in 3 arcsec aperture) of AB ~ 20.7 mag per band, we release the first 1022 deg^2 of J-PLUS data, containing about 4.3 million stars and 3.0 million galaxies at $r < 21$ mag.

1 Introduction

J-PLUS [5] is being conducted from the OAJ, using a unique set of 12 broad, medium and narrow-band filters (Fig. 1 and Table 1; [15]). This filter set has been particularly defined to be sensitive to key stellar spectral features in the rest frame, thus being optimal for Milky Way science and studies of galaxies in the local Universe. In addition, the survey strategy has been fine-tuned to optimize the scientific return in a wide range of applications in many other areas of Astrophysics.

The OAJ is an astronomical facility located at the Pico del Buitre (1957 m) of the Sierra de Javalambre, in Teruel, Spain. The site has excellent astronomical characteristics in terms of median seeing (0.71 arcsec in V band), fraction of clear nights (53 % totally clear, 74% with at least a 30% of the night clear) and darkness, with a typical sky surface brightness of V $\sim$ 22 mag arcsec^{-1} at zenith during dark nights [18].

The OAJ was defined, designed and constructed to carry out large sky surveys with dedicated telescopes. The two main telescopes at the OAJ are the Javalambre Survey Telescope (JST/T250), a 2.55 m telescope with 3 deg diameter FoV, and the Javalambre Auxiliary Survey Telescope (JAST/T80), a 83 cm telescope with a FoV diameter of 2 deg. JAST/T80 is the telescope dedicated to the development of J-PLUS, whereas J-PAS (Javalambre Physics of the accelerating universe Astrophysical Survey, [2]) will be carried out at the JST/T250.

JAST/T80 is mounted with T80Cam, a sigle CCD 9.2k x 9.2k pixel camera with an effective FoV of 2 deg^2, and equipped with the twelve J-PLUS filters. Full technical details on T80Cam can be found in [14] and [16].

The management, reduction, validation, calibration, and public dissemination of the J-PLUS images have been done by the *Unidad de Procesado y Archivo de Datos* (UPAD) at CEFCA [6].

The J-PLUS, including extra technical details, survey strategy and science cases, is fully detailed on its presentation paper [5], so there is significant overlap between the present contribution and the content in that publication.

Table 1: The J-PLUS filter system and the goal limiting magnitudes of J-PLUS (5σ in 3 arcsec aperture), presented together with the averaged limiting magnitudes obtained for the DR1. The zero point calibrations and their uncertainties are also indicated. Comments: (a) In common with J-PAS; (b) SDSS.

Filter	Central Wavelength [Å]	FWHM [Å]	Comments	$m_{\mathrm{lim}}^{\mathrm{J-PLUS}}$	$m_{\mathrm{lim}}^{\mathrm{DR1}}$	$\langle\mathrm{ZP}\rangle$	$\sigma_{\mathrm{ZP}}^{\mathrm{DR1}}$
u	3485	508	(a)	20.5	20.8	21.13	0.02
$J0378$	3785	168	[OII]	20.5	20.7	20.54	0.03
$J0395$	3950	100	Ca H+K	20.5	20.7	20.32	0.02
$J0410$	4100	200	H_δ	20.7	20.9	21.30	0.02
$J0430$	4300	200	G-band	20.7	20.9	21.37	0.02
g	4803	1409	(b)	21.5	21.7	23.58	0.02
$J0515$	5150	200	Mgb Triplet	20.7	20.9	21.52	0.01
r	6254	1388	(b)	21.5	21.6	23.52	0.01
$J0660$	6600	138	Hα; (a)	20.7	20.9	21.04	0.01
i	7668	1535	(b)	21.2	21.1	23.25	0.01
$J0861$	8610	400	Ca Triplet	20.0	20.2	21.54	0.02
z	9114	1409	(b)	20.2	20.3	22.63	0.02

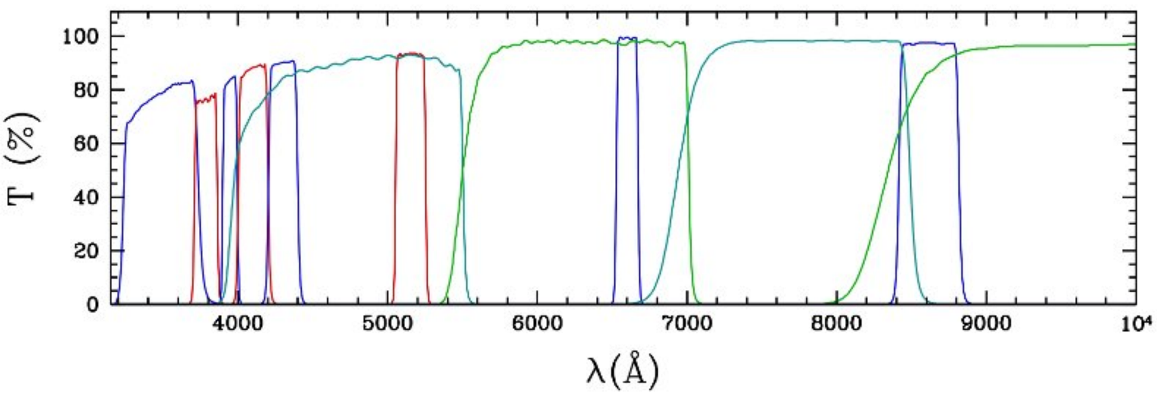

Figure 1: Transmission curves for the set of 12 J-PLUS filters.

2 J-PLUS DR1

J-PLUS DR1 comprises the J-PLUS tiles observed from the start of the survey up to the beginning of 2018, that is, 511 tiles amounting to 1022 deg^2 ($\sim$900 deg^2 after masking, Fig. 2), with more than 13 million objects in the catalogue and $\sim$8.3 million sources at $r < 21$. The DR1 is available at the J-PLUS web portal since this contribution, on July 2018.

The FWHM and ellipticity distributions of the J-PLUS DR1 $r-$band reference images are shown in Fig. 3. We note that DR1 includes all J-PLUS tiles irrespective of their final image qualities, explaining the tails with > 1.5 arcsec and < 0.98 in the FWHM and ellipticity distributions, respectively. These however have little impact on the average quality of the DR1 data.

The DR1 limiting magnitude (5σ in 3 arcsec aperture) distributions in the 12 J-PLUS bands are presented in Table 1 and in Fig. 4, where the expected J-PLUS limits are indicated by vertical dotted lines. The limiting magnitudes fulfil, on average, the targeted depths. The DR1 includes all tiles of the survey acquired so far, incorporating a few ones that were observed deeper in some bands at the beginning of the survey, when testing the system performance. They appear as a secondary, fainter peak in the depth distribution.The typical scatter in the survey depths is $\sim 0.2 - 0.3$ mag, depending on the band. This scatter reflects the variations in observing conditions from night to night, mainly in transparency and seeing.

The photometric calibration of J-PLUS faces two main challenges: the variety of observational conditions in which J-PLUS images are taken and the use of a unique set of filters. However, the difficulty of these tasks is alleviated by the large amount of reference external data from projects like SDSS [25], PanSTARRS [11], and *Gaia* [8]. We explored different calibration procedures, i.e. spectro-photometric standard stars, synthetic photometry of SDSS spectra, and direct comparison with SDSS and PanSTARRS photometry. Currently, the default calibration method is based on the *stellar locus* technique. This procedure profits from the way stars with different stellar parameters populate colour-colour diagrams, defining a well limited region (stellar locus). A specific stellar locus approach for the calibration of J-

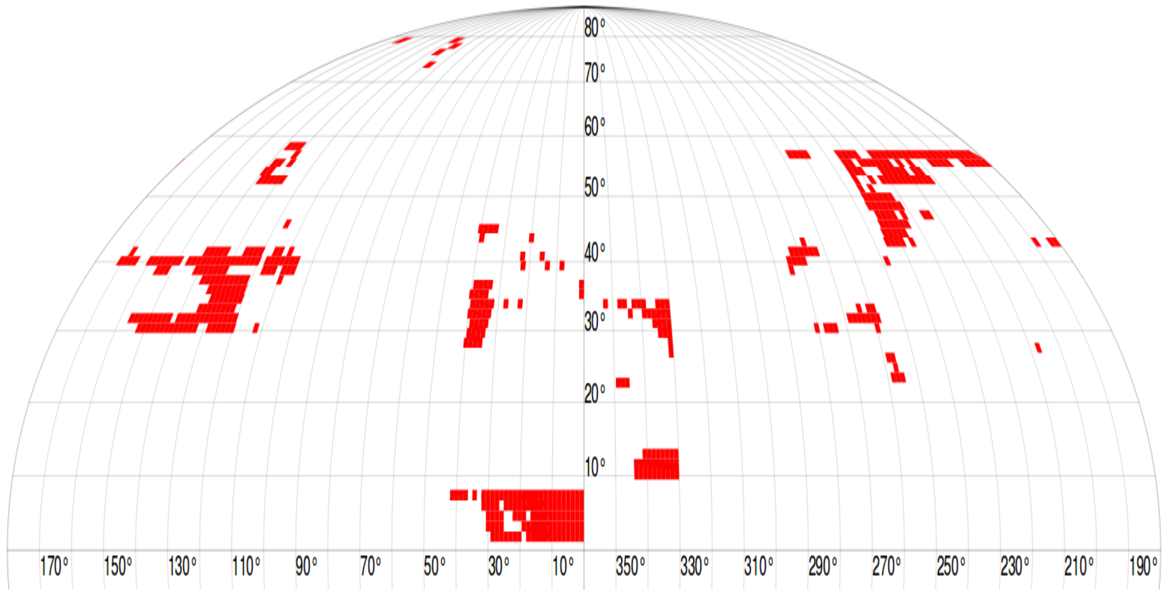

Figure 2: Footprint of the J-PLUS DR1. Red squares represent the 511 pointings of 2 deg^2 provided by T80Cam at JAST/T80. The DR1 amounts effectively to $\sim 900\,\text{deg}^2$ after masking low exposure regions, the surroundings of bright stars, observational reflections or artefacts, and overlapping areas. Figure from [5].

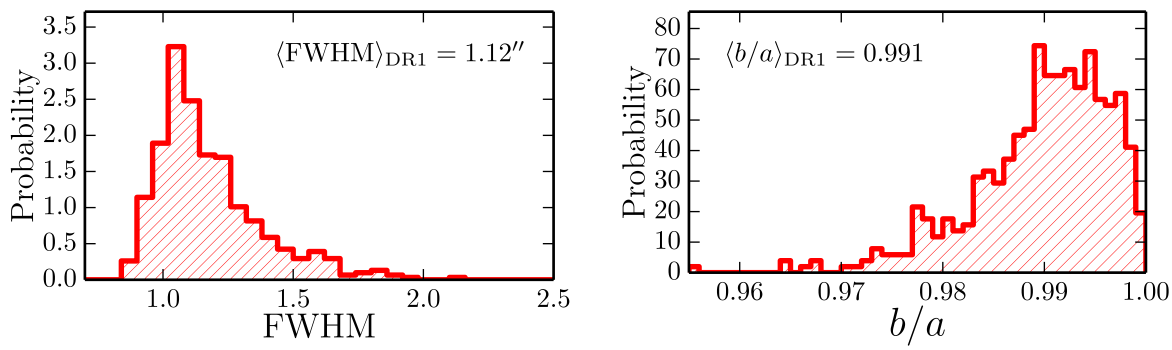

Figure 3: FWHM and ellipticity (b/a ratio) statistics of the J-PLUS DR1 (red hatched histograms) as measured in the reference r band on objects classified as point-like sources.

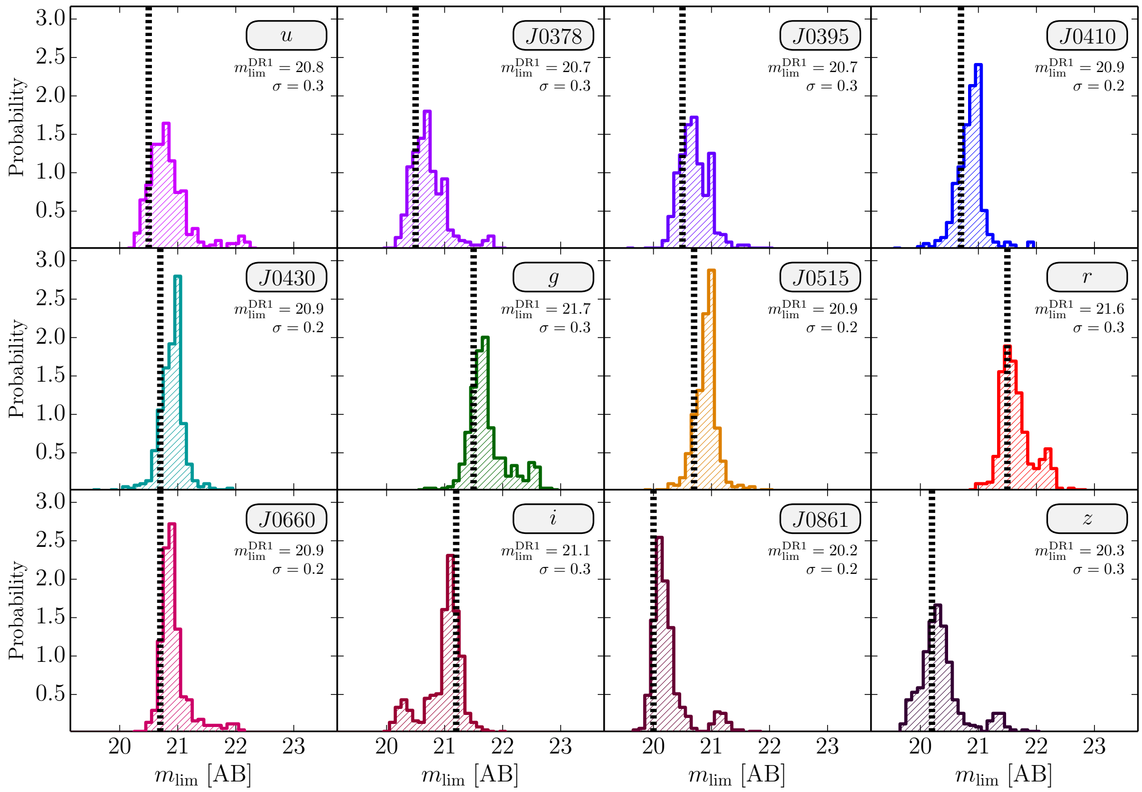

Figure 4: Normalised distribution of the limiting magnitudes (5σ, $3''$ aperture) of the J-PLUS DR1 (511 tiles). The black dashed vertical lines mark the targeted J-PLUS limiting magnitudes as reported in Table 1.

PLUS has been developed, obtaining consistent zero point calibrations over the full J-PLUS area and spectral range with $\sigma_{\mathrm{ZP}} \sim 0.02$ (Table 1).

In addition to several calibrated magnitudes for each source, the J-PLUS DR1 also comprises a set of value-added properties: a Bayesian star/galaxy classification, with a prior based on *Gaia* data for those sources having a parallax measured with SNR> 3 classified as stars [13], effective temperatures estimates for Milky Way stars, and photometric redshift for galaxies.

The J-PLUS star and galaxy number counts are studied in [13], providing results in agreement with the literature up to $r = 21$. We report 4.3 million stars and 3 million galaxies in DR1. We present a representative example of a J-PLUS pointing in Fig. 5, with the J-PLUS SEDs of several astrophysical objects (stars, galaxies, and QSOs) in Figs. 6, 7, and 8, respectively.

Photometric redshifts for J-PLUS DR1 galaxies have been computed using BPZ2 [1, 19], *LePhare* [9], and TPZ [4] . These three estimations are providedin the DR1 catalogues. A quantitative comparison between J-PLUS DR1 photometric redshifts from BPZ2 and SDSS spectroscopic values is provided in Fig. 9. We find that the spectroscopic values are retrieved with no significant bias ($|\Delta z| \equiv |z_{\mathrm{phot}} - z_{\mathrm{spec}}| < 0.005$ for $r-$band magnitude < 20), and a typical error $\delta_z/(1+z)$ in the range $0.005 - 0.03$ for $r \in [16, 20]$. In particular, we find $\delta_z/(1+z) < 0.02$, 0.03 and 0.05 precision for z < 0.1, 0.3 and 0.5 galaxies, respectively.

The access to J-PLUS DR1 data can be done in several ways, from a sky navigator (Fig. 10) to an ADQL query service, including cone and list search. The data is also accessible with Virtual Observatory tools.

3 J-PLUS science

The J-PLUS data have already provided a set of scientific papers, some of them in press at Astronomy & Astrophysics, including among others:

- **Multiple stellar population in the M15 globular cluster** [3]. This cluster has been observed well beyond the tidal radius with uniform photometry thanks to the large Fov of T80Cam. We show that the colour-magnitude diagram (CMD) $J0378$ versus $(J0378 - J0861)$ yields the detection of a clear split into two distinct sequences, suggesting a link to light elements abundances, because the $J0378$ and $J0861$ filters are sensitive to N and Ca.

- **Study of the nearby galaxy clusters A2589 (z**$= 0.0414$**) and A2593 (z**$= 0.044$**)** [20]. The indiscriminate photo-z estimation for galaxies in these clusters opens the way to statistical study cluster membership, while providing valuable data for optimal target selection in spectroscopic follow-ups. In particular, photo-zs produced by J-PLUS are going to be used by the WEAVE cluster surveys in the process of target selection. It is expected that this will increase the spectroscopic success rate by a factor 2–3. Also the intracluster light of nearby surveys can be studied, providing clues about their origin [10].

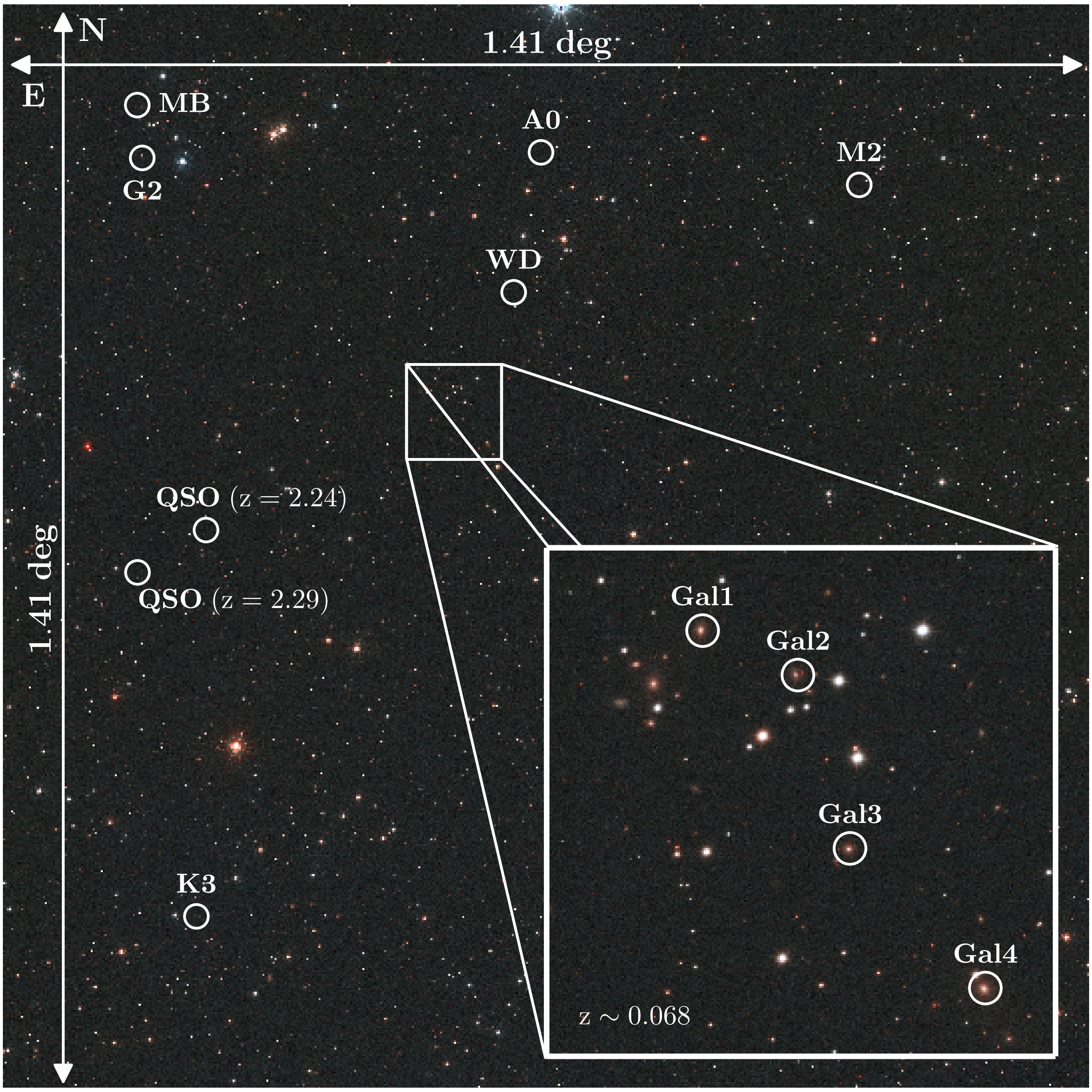

Figure 5: Colour composite of the J-PLUS pointing 1488. Several astrophysical objects are labelled in the figure: four MW stars of different spectral types (A0, G2, K3, M2, see Fig. 6); one white dwarf (WD), a minor body (MB) of the Solar System, four galaxies belonging to a $z = 0.068$ nearby cluster (Gal1, Gal2, Gal3, Gal4, see Fig. 7), and two high-z quasars (QSOs, see Fig. 8). Figure from [5].

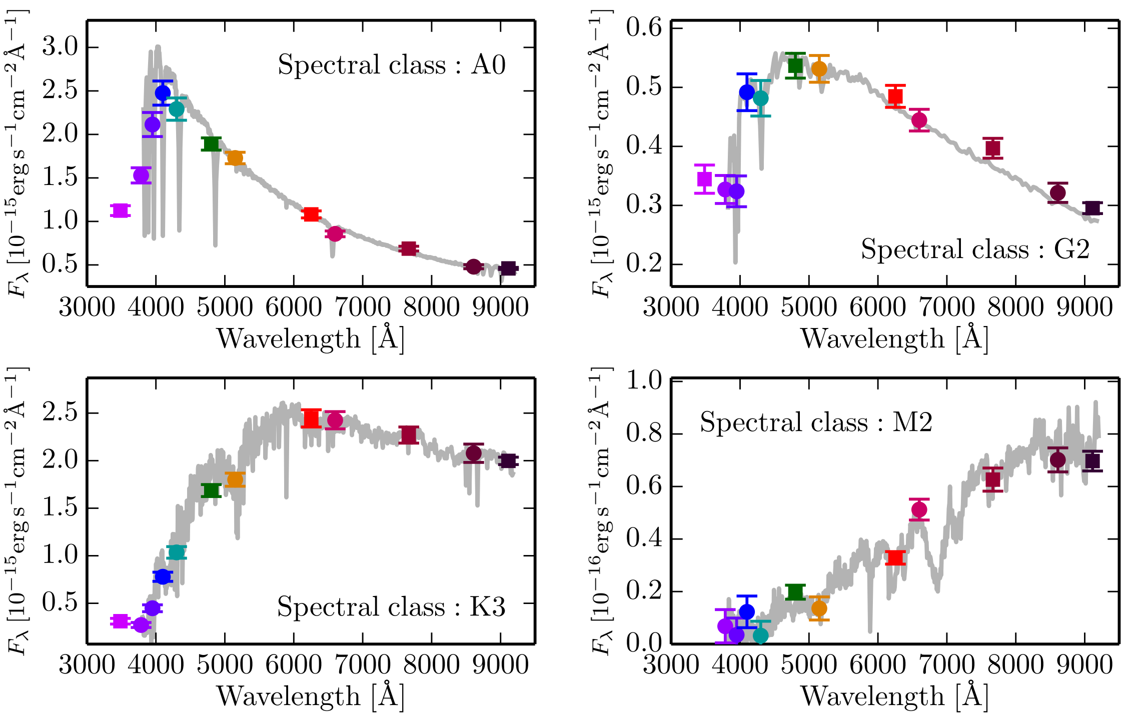

Figure 6: J-PLUS photo-spectra of the four Milky Way stars marked in Fig. 5. The grey lines show the SDSS spectra of these stars. Figure from [5].

- **Estimation of the Hα flux in nearby galaxies** [12]. We trace the Hα emission at $z < 0.017$ thanks to the $J0660$ filter and the continuum with the other eleven J-PLUS filters. The comparison with spectroscopically derived fluxes in common HII regions with SDSS and CALIFA [21] provides a ratio $R = 1.05 \pm 0.25$, confirming the expectations from [24]. The local star formation rate density derived from J-PLUS DR1 is presented in these proceedings by Vilella-Rojo et al.

- **2D Stellar Populations in the nearby galaxies NGC 5473 and NGC 5485** [23]. A technique for studying 2D stellar populations in multi-narrow band photometric surveys has been presented in [22], where resolved galaxies in the ALHAMBRA [17] survey are analysed via a Centroid Voronoi Tessellation and characterized by multi-color photometry SED fitting with MUFFIT [7]. This technique has been applied to the galaxies NGC 5473 and NGC 5485, observed by J-PLUS and CALIFA.

- **Lyα emitters ar z$\sim$**2.2. The J-PLUS filter configuration allows to select samples of emission-line galaxies and QSOs at z$\sim$2.2, when the Lyα emission can be isolated and characterized with the $J0395$ filter (Fig. 8). We have more than 600 candidates selected in J-PLUS DR1, some of them already followed up with OSIRIS/GTC spectroscopy. That confirmed 85% of the candidates at high-z QSOs. More details are presented in these proceedings by Spinoso et al.

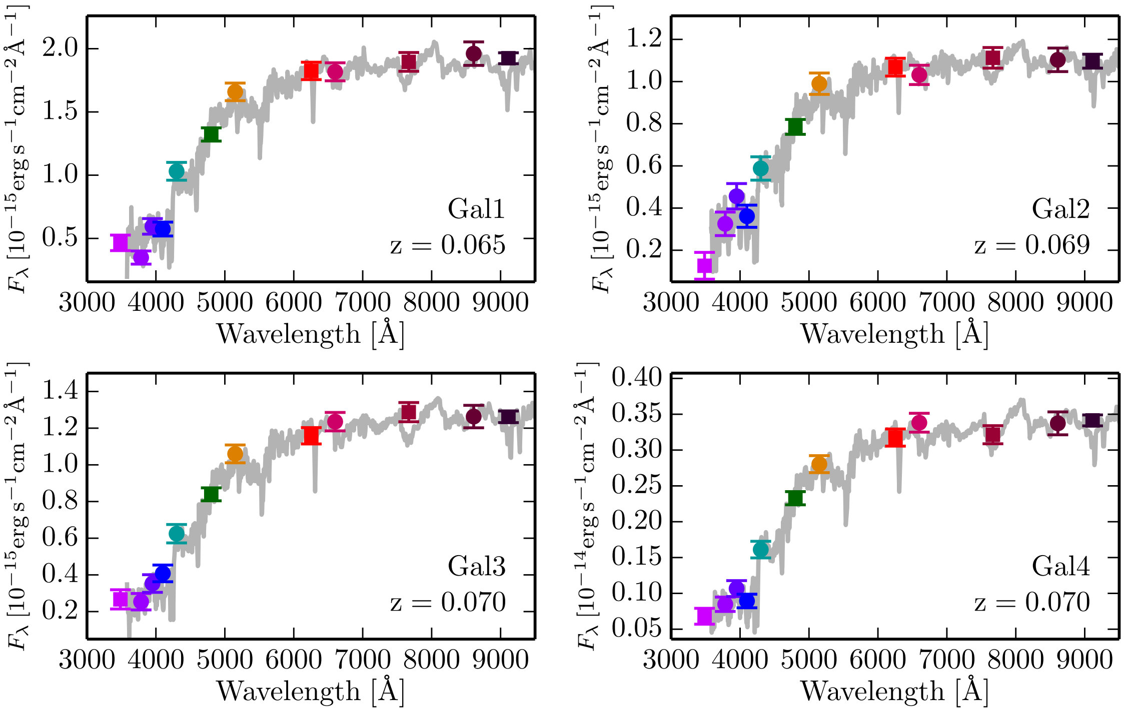

Figure 7: J-PLUS photo-spectra of the four galaxies marked in Fig. 5. The grey lines show the SDSS spectra of these galaxies and their spectroscopic redshift. Figure from [5].

4 Summary and Conclusions

This contribution aims to release the first 1022 deg^2 of J-PLUS data, amounting to 4.3 million stars and 3 million galaxies at $r < 21$ mag observed in 12 broad, intermediate and narrow optical bands. This dataset is used to illustrate some of the science cases that will be addressed by J-PLUS. At the time of writing this manuscript, J-PLUS has already mapped more than 1400 deg^2, providing unprecedented information of the SED for millions of stars and galaxies.

To conclude, J-PLUS may thus be opening an exciting and interesting new phase in optical, large scale, astrophysical surveys. Ultimately, J-PLUS will become a powerful multicolour view of the nearby Universe that will observe and characterize tens of millions of galaxies and stars of the Milky Way halo, with a wide range of astrophysical applications and a striking potential for bringing unexpected discoveries to our knowledge of the Universe. The J-PLUS data will be made public progressively in subsequent data releases, an expression of its commitment to become a major legacy project for the astronomy and astrophysics of the next decades.

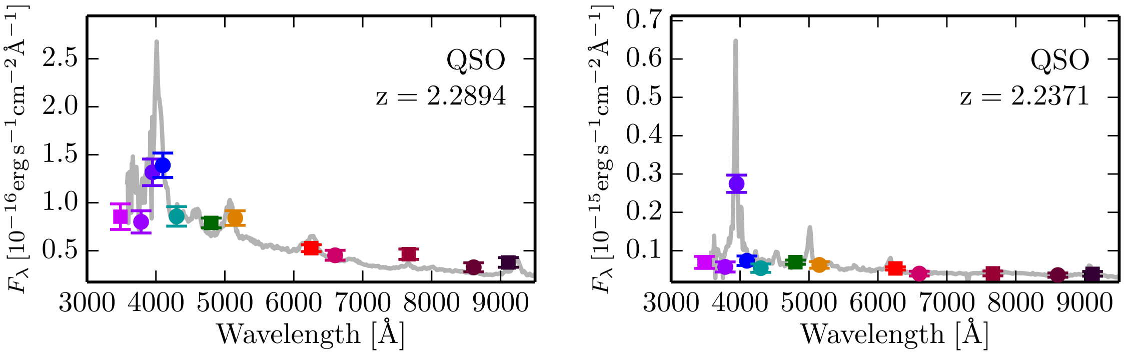

Figure 8: J-PLUS photo-spectrum of two QSOs with SDSS spectra (marked in Fig. 5). The Lyα broad-line emission is clear in both sources and is captured by the $J0395$ filter. Figure from [5].

Acknowledgments

Funding for the J-PLUS Project has been provided by the Governments of Spain and Aragón through the Fondo de Inversiones de Teruel, the Spanish Ministry of Economy and Competitiveness (MINECO; under grants AYA2017-86274-P, AYA2016-77846-P, AYA2016-77237-C3-1-P, AYA2015-66211-C2-1-P, AYA2015-66211-C2-2, AYA2012-30789, AGAUR grant SGR-661/2017, and ICTS-2009-14), European FEDER funding (FCDD10-4E-867, FCDD13-4E-2685), and the Reseach Groups E96, E103, and E16_17R of the Aragón Government.

References

[1] Benítez, N. 2000, ApJ, 536, 571

[2] Benítez, N., Dupke, R., Moles, M., et al. 2014 [arXiv:1403.5237]

[3] Bonatto, C., Chies-Santos, A. L., Coelho, P. R. T., & J-PLUS collaboration 2018, A&A, in press [arXiv:1804.03966]

[4] Carrasco Kind, M, & Brunner, R. J. 2013, MNRAS, 432, 1483

[5] Cenarro, A. J., Moles, M., Cristóbal-Hornillos, D., et al. 2018, A&A, submitted [arXiv:1804.02667]

[6] Cristóbal-Hornillos, D., Varela, J., Ederoclite, A., et al. 2014, in Proc. SPIE, Vol. 9152, Software and Cyberinfrastructure for Astronomy III, 91520O

[7] Díaz-García, L. A., Cenarro, A. J., López-Sanjuan, C., et al. 2015, A&A, 582, A14

[8] Gaia Collaboration, Prusti, T., de Bruijne, J. H. J., et al. 2016, A&A, 595, A1

[9] Ilbert, O., Arnouts, S., McCracken, H. J., Bolzonella, M.; Bertin, E et al. 2006, A&A, 457, 841

[10] Jiménez-Teja, Y., Dupke, R. A., Lopes de Oliveira, R., & J-PLUS collaboration 2018, A&A, in press [arXiv:1810.01424]

[11] Kaiser, N., Aussel, H., Burke, B. E., et al. 2002, in Proc. SPIE, Vol. 4836, Survey and Other Telescope Technologies and Discoveries, ed. J. A. Tyson & S. Wolff, 154–164

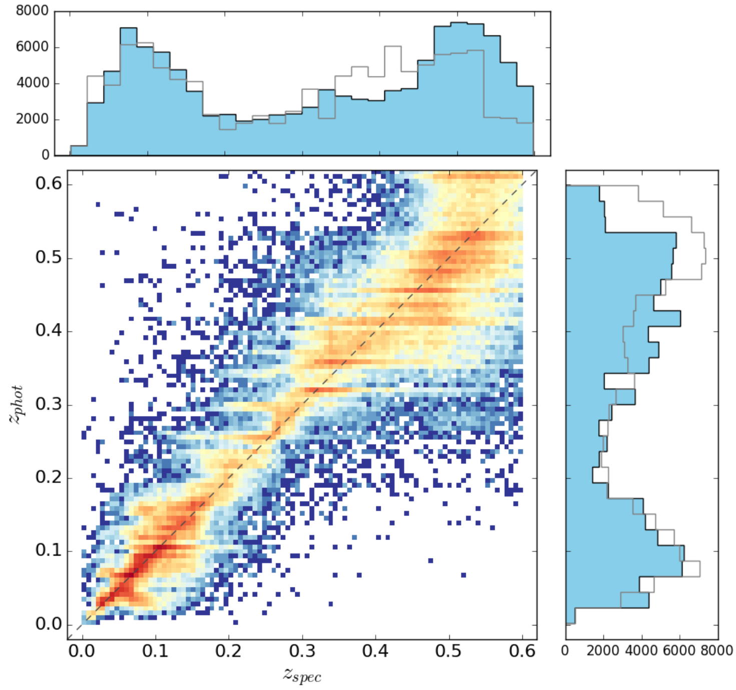

Figure 9: J-PLUS photometric redshifts from BPZ2 vs SDSS spectroscopic redshifts for the common sources in the DR1. The side panels show the projection in redshift space of the photometric (right) and spectroscopic (top) values. Figure from [5].

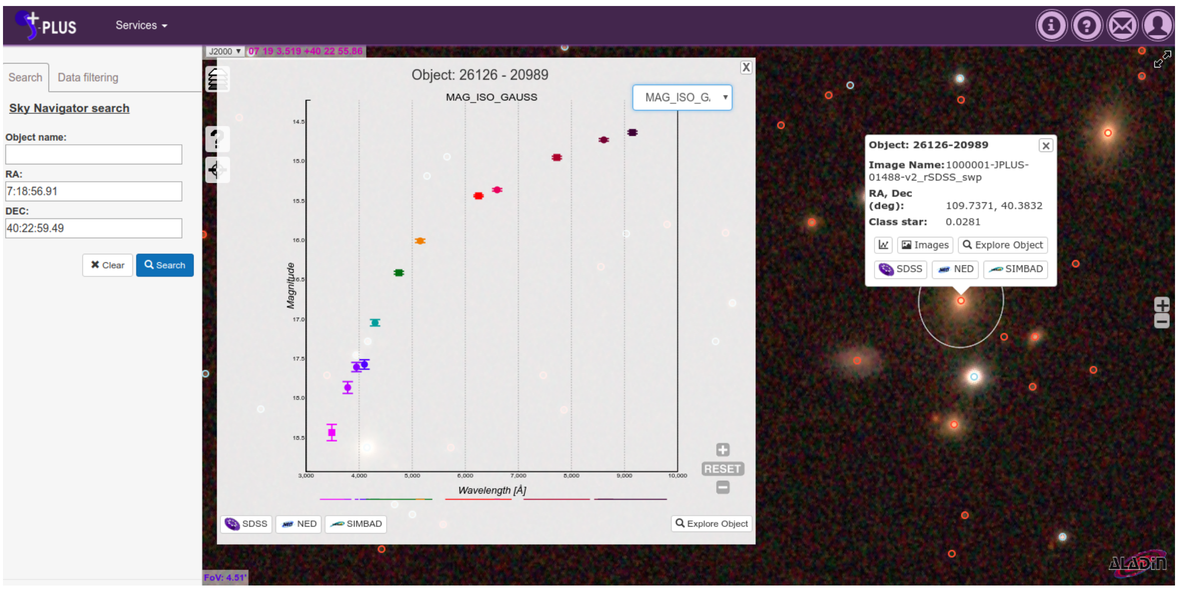

Figure 10: J-PLUS sky navigator.

[12] Logroño-García, R., Vilella-Rojo, G., López-Sanjuan, C., & J-PLUS collaboration. 2018, A&A, in press [arXiv:1804.04039]

[13] López-Sanjuan, C., Vázquez Ramió, H., Varela, J., et al. 2018, A&A, in press [arXiv:1804.02673]

[14] Marín-Franch, A., Taylor, K., Cepa, J., et al. 2012, in Society of Photo-Optical Instrumentation Engineers (SPIE) Conference Series, Vol. 8446, Society of Photo-Optical Instrumentation Engineers (SPIE) Conference Series

[15] Marín-Franch, A., Chueca, S., Moles, M., et al. 2012, in Society of Photo-Optical Instrumentation Engineers (SPIE) Conference Series, Vol. 8450, Society of Photo-Optical Instrumentation Engineers (SPIE) Conference Series

[16] Marín-Franch, A., Taylor, K., Cenarro, J., Cristóbal-Hornillos, D., & Moles, M. 2015, IAU General Assembly, 22, 2257381

[17] Moles, M., Benítez, N., Aguerri, J. A. L., et al. 2008, AJ, 136, 1325

[18] Moles, M., Sánchez, S. F., Lamadrid, J. L., et al. 2010, PASP, 122, 363

[19] Molino, A., Bennítez, N., Moles, M., et al. 2014, MNRAS, 441, 2891

[20] Molino, A., Costa-Duarte, M. V., Mendes de Oliveira, C., & J-PLUS collaboration 2018, A&A, in press [arXiv:1804.03640]

[21] Sánchez, S. F., Kennicutt, R. C., Gil de Paz, A., et al. 2012, A&A, 538, A8

[22] San Roman, I., Cenarro, A. J., Díaz-García, L. A., et al. 2018a, A&A, 609, A20

[23] San Roman, I., Sánchez-Blázquez, P., Cenarro, A. J., & J-PLUS collaboration 2018b, A&A, submitted [arXiv:1804.03727]

[24] Vilella-Rojo, G., Viironen, K., Lṕez-Sanjuan, C., et al. 2015, A&A, 580, A47

[25] York, D. G., Adelman, J., Anderson, Jr., J. E., et al. 2000, AJ, 120, 1579

Highlights on Spanish Astrophysics X, Proceedings of the XIII Scientific Meeting of the Spanish Astronomical Society held on July 16 – 20, 2018, in Salamanca, Spain. B. Montesinos, A. Asensio Ramos, F. Buitrago, R. Schödel, E. Villaver, S. Pérez-Hoyos, I. Ordóñez-Etxeberria (eds.), 2019

The OTELO survey.

Ángel Bongiovanni[1,2,3], on behalf of the OTELO Team

[1] Instituto de Astrofísica de Canarias (IAC), E-38200 La Laguna, Tenerife, Spain
[2] Departamento de Astrofísica, Universidad de La Laguna (ULL), E-38205 La Laguna, Tenerife, Spain
[3] Asociación Astrofísica para la Promoción de la Investigación, Instrumentación y su Desarrollo, ASPID, E-38205 La Laguna, Tenerife, Spain

Abstract

The evolution of galaxies across the cosmic time are observationally studied by means of extragalactic surveys that cover significant volumes of Universe, with a wealth of multi-wavelength ancillary data. OTELO survey provides the deepest narrow band survey to date, in terms of minimum detectable flux, and emission line equivalent width, that has allowed detecting the faintest extragalactic emission line systems. In this way, OTELO data complements other broad band, narrow band, and spectroscopic surveys. The data has been obtained using the red Tunable Filter of the OSIRIS instrument at the 10.4 m telescope GTC, pointing at the most deeply explored EGS region. This catalogue is complemented with public data ranging from deep X-ray to FIR, including high resolution HST images, that allowed deriving precise photometric redshifts, and obtaining the morphological classification of the extragalactic objects detected. In the present contribution the final catalogue and other value-added products, that will be publicly available by mid 2019, are presented. The improved reduction techniques, the high astrometric and photometric quality achieved, and the main survey demographics are also presented. A total of 11 237 raw sources have been detected in a sky area of 56 sq.-arcmin. Within them, about 1 800 are fair candidates to the strongest emission lines in the UV-optical domain, 81 are candidates to stars, while other 483 are candidates to be absorption line systems. The 50% completeness of OTELO catalogue is obtained at an AB magnitude of 26.38. Photometric redshifts have been derived with an accuracy better than $|\Delta z|/(1+z) \leq 0.2$ for 6 600 sources.

1 Introduction

Tracing the star formation rate (SFR) in the Universe along the cosmic eras, as well as the detailed study of the large diversity of activity modes in galaxies, are fundamental science drivers of the modern extragalactic astronomy. For these purposes, the systematic discovering of emission-line sources (ELS) with increasingly fainter luminosities becomes an essential task. Modern narrow-band and spectroscopic surveys with large aperture telescopes provide large collections of these sources, which facilitate both the follow-up of individual ones as the statistical study of their fundamental properties. In particular, they allow the construction of accurate SFR-line indicator functions, which contribute to a better knowledge of the star formation history of the Universe, and provide valuable constraints to the current models of galaxy evolution.

OTELO (OSIRIS Tunable filter Emission-line Object[1]) is a very deep, 2D spectroscopic survey designed primarily for the search of galaxies with emission lines and the measurement of their fluxes and equivalent widths (EW), through the exploitation of the red tunable filter (TF) of the OSIRIS instrument [7]. OTELO obtains spectra of all sources in the field only limited by flux and spectral range, searching for emission lines at different cosmological volumes between redshifts 0.4 and 6, and thereby providing valuable data for tackling a wide variety of science projects, which include the evolution of star formation density up to redshift $\sim$1.5, an approach to the demographics of low-luminosity emission-line galaxies and detailed studies of emission-line ellipticals in the field, high-z QSO, Lyman-α emitters, and Galactic emission-line stars [8].

OTELO shares characteristics of those surveys for the search of emission-line sources, based on spectral scans that use narrow band filters of fixed cavity, such as COMBO-17 [34], ALHAMBRA [22], SHARDS [25], or J-PAS [1], or those that use filters with variable cavity such as TTF [2], CADIS [19] and more recently GLACE [31], or the slit-less spectroscopic surveys limited by the PSF of the system as KISS [33], UCM [15], CUYS [3], and PEARS [32]. However, the data products of OTELO also can be used for a classical narrow-band ELS selection approach [6] from color-magnitude diagrams, such as the described in [24], HiZELS [16], or the surveys compiled in the framework of the HSC-SSP [18]. This possibilities makes OTELO a versatile ELS-finding machine. As most of the mentioned explorations for the search of faint ELS, OTELO will also provide useful predictions for the planning of future surveys (e.g.) DESI [13], PFS [30] or 4MOST-WAVES [12], and space missions like Euclid[2] or WFIRST-ATLAS [10] that will use these sources as tracers of the large-scale structure.

2 Survey description

OTELO targets a region of the Extended Groth Strip (EGS) embedded in the Deep field 3 of the Canada–France–Hawaii Telescope Legacy Survey[3] (CFHTLS) and the deepest pointing of GALEX in imaging and spectroscopy, among other ancillary data which include public images from WIRDS[4], source catalogues from Chandra [26], *Spitzer*-IRAC and MIPS 24 μm, *Herschel*-PACS 100, 160 μm and -SPIRE 250, 300, 500 μm, as well as spectroscopic redshifts up to $r_{\rm AB}$=24.1 from DEEP2 [23]. The relative position of the OTELO field in the framework

[1]`http://www.iac.es/proyecto/otelo`
[2]`http://sci.esa.int/euclid/`
[3]`http://www.cfht.hawaii.edu/Science/CFHTLS`
[4]`http://terapix.iap.fr/rubrique.php?id_rubrique=261`

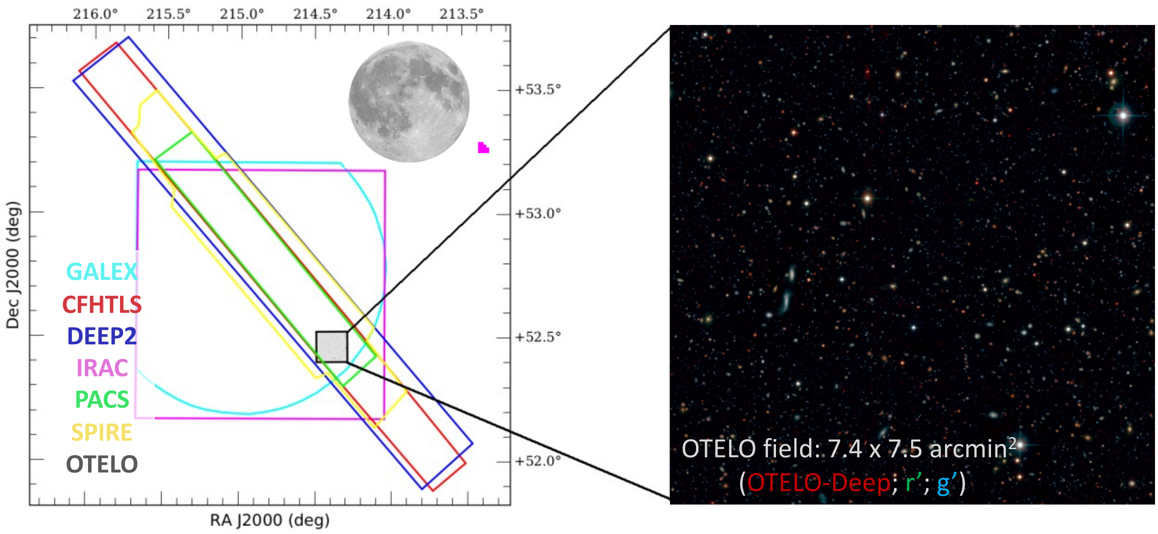

Figure 1: Relative position of the OTELO field together with the UV, optical, IR, and spectroscopic data imprints in the Extended Groth Strip region (left). The RBG composition at right expands the surveyed area represented (7.5×7.4 arcmin^2) and it is a coadding of the OTELO TF scans (i.e. OTELO-Deep image) combined with the resampled CFHTLS r'- and g'-band images.

of complementary surveys in the EGS is shown in Figure 1.

OTELO was conceived as a narrow band spectral scan (resolution $R \simeq 700$), defined in a window of 230 Å, centred at 9 175 Å, between two airglow Meinel bands. Hence, the scan is embedded in the SDSS z-band response. The main part of the survey consisted of a tomography of 36 slices evenly distributed in the the wavelength range defined above. A TF width (FWHM) of 12 Å was adopted, scanning every 6 Å. This sampling is close to the best equilibrium between a reasonable observing time and the deblending of the Hα from the [NII]6548,6584 emission lines ([20]). A total of 108 dark hours (net integration time: 6 600 s/slice), under a guaranteed gime (GT) agreement[5], distributed over four campaigns between 2010 and 2014, were used for gathering the TF raw data.

The physics behind the TF is the same as the interference filters that are commonly used in astronomy, but with the versatility given by the possibility to control the width of the resonant cavity and, therefore, the wavelength of filter response for a given interference order. The particular characteristics and calibration details of the OSIRIS TF are well studied and can be looked up in [17] and additional references given in the GTC URL[6].

The TF data was properly reduced using both standard and ad-hoc procedures designed for removing sky rings and image fringing. After flux and wavelength calibrations of TF data, two products emerged: (i) a raw catalogue of 11 237 sources detected in the synthesis of the TF individual images (i.e. the OTELO-Deep image), and (ii) an equal number of *pseudo-*

[5] Defined between the OSIRIS Instrument Team and the Instituto de Astrofísica de Canarias.
[6] `http://www.gtc.iac.es/instruments/osiris/osiris.php`

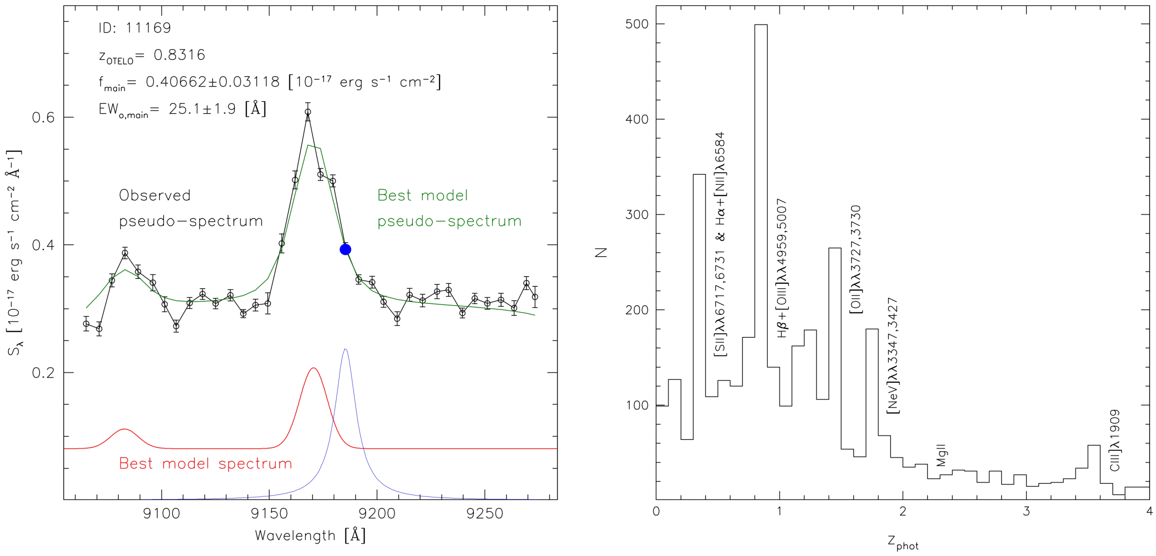

Figure 2: Left: example of a pseudo-spectrum corresponding to a [OIII] ELS at z=0.8316 (black dots). The convolution of the best model spectrum is the best fit of the observed data. The blue curve is the TF transmission of the slice corresponding to the blue dot. Right: photometric redshift distribution of the OTELO sources up to z=4.

spectra. Unlike the spectra obtained by diffraction devices, in a pseudo-spectrum the SED of a given source is convolved in the wavelegth space by the TF instrumental response. An example of a real pseudo-spectrum from OTELO data is given in Figure 2 (left panel). Sources that show two or more consecutive slices with a flux excess $\geq 2\sigma$ above the measured background in the OTELO pseudo-spectra are defined as preliminary ELS candidate. Under this criterium, and taking into account the basic parameter space (i.e. line flux, line profile width, flux density at the continuum) of the survey, as well as the measurements of real noise in the TF scan images, we carried out educated simulations ([27, 5]) for modeling the ELS detection probability function. The results of these simulations are useful to predict (e.g.) the emission-line limiting flux and the completeness profiles for specific ELS subsamples.

3 The OTELO database

In order to obtain reliable photometric redshifts for labelling the spectral feature(s) in pseudo-spectra, the availability of the observed SED distributions of the OTELO sources is mandatory. This is also true for the spectral classification of these sources and the estimation of the stellar mass and gas metallicity, among other parameters. The OTELO-Deep image was used not only for obtaining an integrated flux (limiting magnitude AB=26.4 at 50% completeness), but also as a detection image to measure broad-band fluxes of the sources (via PSF-matched photometry) in the registered/resampled optical and near-infrared (NIR) ancillary images from the CFHTLS and WIRDS. The base catalogue obtained in this way was carefully cross-correlated with complementary data mentioned above, giving rise to the OTELO *multi-wavelength catalogue.*

The OTELO photometric redshifts were determined using libraries for Hubble-sequence and starburst galaxies, Seyferts, QSOs, and star templates, including M, L and T dwarfs. The accuracy of the photometric compared to high quality spectroscopic redshifts from DEEP2 is better than $|\Delta z|/(1+z) \leq 0.2$. Hence, the OTELO catalogue has 9 709 sources with non-null photo-z solutions, and 6 600 of them have an uncertainty $\delta z < 0.2\,(1+z)$. From the latter subset, the right panel of Fig. 2 shows the photo-z distribution of all preliminary ELG candidates up to z=4. As expected, most prominent features in this histogram correspond to the strongest emission lines in the optical, summing up about 1 500 candidates. On the other hand, the high-redshift raw subsample is composed by more than 300 candidates. The detailed analysis of these sources is a part of the on-going and forthcoming works.

The OTELO multi-wavelength catalogue, including the best photometric redshifts, the pseudo-spectra, and the cross-references with other catalogs, constitute the database of the survey. Further details about the survey planning, the TF data reduction and calibration, as well as the construction of the OTELO database, can be found in the survey description article [4]. The essential OTELO products and a Web-based tool for data visualization will be publicly released on mid 2019.

4 First results

Apart from the survey presentation, several contributions account for the first scientific exploitation of the OTELO survey. Some of these works start from the general census of the ELS candidates. For instance, the first analysis of the [OIII]4959,5007 ELS at z$\sim$0.9 [5] yields that OTELO reaches line flux limits $\approx 10^{-19}$ erg s^{-1} cm^{-2}, and observed EW in the order of the TF scan sampling (Fig. 3, left panel). We have adopted these values as the characteristic ones of the whole survey and they are consistent with the predictions obtained from the simulations described above. This sensitivity translates to the faint-end of the LF[OIII] (Fig. 3, right panel). Even though OTELO have nothing to say about the bright side, mainly because the effects of the cosmic variance (which force to adopt a mean L^* value), the faint-end can be sampled up to a luminosity of log $L_{[\mathrm{OIII}]}$ [erg s^{-1}] $\sim$ 38, in a region of the diagram about 10 to 100 times fainter than the lowest luminosity observed through the most recent narrow-band surveys, at the same redshift [21, 11, 18]. Accordingly, OTELO is sampling a population of star-forming galaxies with stellar masses between 10^7 and $\sim 10^{11}$ M$_\odot$, most of them compact and disk-like sources.

The results described above are qualitatively consistent with those obtained by [28] from the analysis of the Hα+[NII] ELS subset at redshift z$\sim$0.4. In this case, the SFR function obtained extends the faint-end in $\sim$1 dex the ensemble of the most recent data given in literature. This work also includes a prescription about the increasing AGN-host contribution with the Hα luminosity at this redshift. About the latter sources, a first inventory of AGN hosts identified in OTELO at redshift z<3, through different diagnostics, is given in [29].

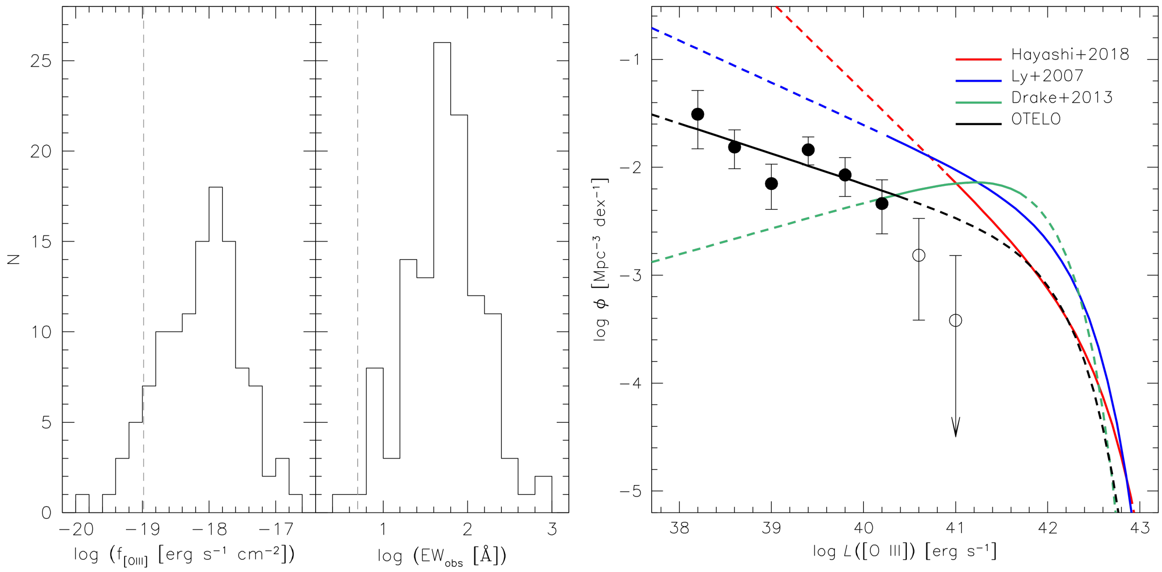

Figure 3: Left: line flux and equivalent width distribution of the OTELO [OIII] ELS sample. Dashed lines are the corresponding limits obtained from ad-hoc simulations of detection probability. Right: luminosity function (LF) of the OTELO [OIII] ELS as given in [5]. Dashed segments are Schechter LF extrapolations from fitted data.

On the other hand, the morphological analysis of the galaxy population in OTELO up to redshift ∼2 is being currently developed. This analysis is providing clues for additional interpretations of the stellar mass-gas metallicity relation (MZR) for the Hα+[NII] ELS subsample, using the EWαn2 optical diagnostic diagram given in [9] (see the contribution of J. Nadolny in these Proceedings).

Finally, it is worth pointing out that the OTELO survey is also a very deep probe of the Milky Way halo. The analysis of its stellar component is being carried out. In particular, a cross-correlation with GAIA-DR1 [14] and CFHTLS data has yielded 16 possible emission line stars from a collection of 81 low-mass star candidates (see the contribution of E. Alfaro in these Proceedings).

5 Summary

The OSIRIS tunable filter emission-line survey (OTELO) was designed for the search of ELS by pushing the Gran Telescopio Canarias and this instrument at the limit of their technical capabilities. In this sense, OTELO is detecting ELS with line fluxes as low as $\approx 10^{-19}$ erg s^{-1} cm^{-2} and observed EW > 5 Å. Therefore, OTELO goes one step beyond the conventional spectroscopic surveys and without their selection biases, despite the small sky area (50 arcmin2) and spectral range (230 Å) explored. These facts confirm the initial expectations of the project, demonstrating the success of the TF tomography technique for this kind of surveys.

First science exploitation of OTELO was focused on the analysis of the Hα+[NII]6584 and [OIII]4959,5007 ELS at z$\sim$0.4 and 0.9, respectively, as well as the first inventory of AGN hosts. Ongoing efforts are being devoted to the analysis of other ELS subsets, as well as in the morphology classification of all sources detected at z$<$2, and the analysis of Galactic halo stars in the field explored.

The OTELO survey is the first large program of GTC whose products will be publicly released on mid 2019.

Acknowledgments

This work was supported by the Spanish Ministry of Economy and Competitiveness (MINECO) under the grants AYA2013-46724-P, AYA2014-58861-C3-1-P, AYA2014-58861-C3-2-P, AYA2014-58861-C3-3-P, AYA2016-75808-R, AYA2016-75931-C2-2-P, AYA2017-88007-C3-1-P and AYA2017-88007-C3-2-P. Based on observations made with the Gran Telescopio Canarias (GTC), installed in the Spanish Observatorio del Roque de los Muchachos of the Instituto de Astrofísica de Canarias, on the island of La Palma. This study makes use of data from AEGIS, a multi-wavelength sky survey conducted with the Chandra, GALEX, Hubble, Keck, CFHT, MMT, Subaru, Palomar, Spitzer, VLA, and other telescopes and supported in part by the NSF, NASA, and the STFC. Based on observations obtained with MegaPrime/MegaCam, a joint project of CFHT and CEA/IRFU, at the Canada-France-Hawaii Telescope (CFHT), which is operated by the National Research Council (NRC) of Canada, the Institut National des Science de l'Univers of the Centre National de la Recherche Scientifique (CNRS) of France, and the University of Hawaii. This work is based in part on data products produced at Terapix available at the Canadian Astronomy Data Centre as part of the Canada-France-Hawaii Telescope Legacy Survey, a collaborative project of the NRC and CNRS. Based on observations obtained with WIRCam, a joint project of the CFHT, Taiwan, Korea, Canada, France, at the Canada-France-Hawaii Telescope (CFHT) which is operated by the National Research Council (NRC) of Canada, the Institute National des Sciences de l'Univers of the Centre National de la Recherche Scientifique of France, and the University of Hawaii. This work is based in part on data products produced at TERAPIX, the WIRDS (WIRcam Deep Survey) consortium, and the Canadian Astronomy Data Centre.

References

[1] Benítez, N., Dupke, R., Moles, M., et al., 2014, arXiv 1403.5237B

[2] Bland-Hawthorn, J., & Jones, D. H. 1998, PASA, 15, 44

[3] Bongiovanni, A., Bruzual, G., Magris, G., et al. 2005, MNRAS, 359, 930

[4] Bongiovanni, A., et al. 2018a, A&A, forthcoming

[5] Bongiovanni, A., et al. 2018b, A&A, submitted (under 2nd. revision)

[6] Bunker, A. J., Warren, S. J., Hewett, P. C., & Clements, D. L. 1995, MNRAS, 273, 513

[7] Cepa, J., et al. 2003, SPIE, 4841, 1739

[8] Cepa, J., Bongiovanni, A., Pérez García, A. M., et al. 2013, RMxAC, 42, 70

[9] Cid Fernandes, R., Stasińska, G., Schlickmann, M. S., et al. 2010, MNRAS, 403, 1036

[10] Content, R., Wang, Y., Roberto, M., et al. 2018, Space Telescopes and Instrumentation 2018: Optical, Infrared, and Millimeter Wave, 10698, 106980I

[11] Drake, A. B., Simpson, C., Collins, C. A., et al. 2013, MNRAS, 433, 796

[12] Driver, S. P., Davies, L. J., Meyer, M., et al. 2016, The Universe of Digital Sky Surveys, 42, 205

[13] Eisenstein, D., & DESI Collaboration 2015, American Astronomical Society Meeting Abstracts #225, 225, 336.05

[14] Gaia Collaboration, Brown, A. G. A., Vallenari, A., et al. 2016, A&A, 595, A2

[15] Gallego, J., Zamorano, J., Rego, M., et al., 1993, Astronomische Gesellschaft Abstract Series, No. 8, p. 39

[16] Geach, J. E., Smail, I., Best, P. N., et al. 2008, MNRAS, 388, 1473

[17] González, J. J., Cepa, J., González-Serrano, J. I., Sánchez,-Portal, M. 2014, MNRAS, 443, 3289

[18] Hayashi, M., Tanaka, M., Shimakawa, R., et al. 2018, PASJ, 70, S17

[19] Hippelein, H., Maier, C., Meisenheimer, K., et al. 2003, A&A, 402, 65

[20] Lara-López, M. A., Cepa, J., Castañeda, H., et al. 2010, PASP, 122, 1495

[21] Ly, C., Malkan, M. A., Kashikawa, N., et al. 2007, ApJ, 657, 738

[22] Moles, M., Benítez, N., Aguerri, J. A. L., et al., 2008, AJ, 136, 1325

[23] Newman, J. A., Cooper, M. C., Davis, M., et al. 2013, ApJS, 208, 5

[24] Pascual, S., Gallego, J., & Zamorano, J. 2007, PASP, 119, 30

[25] Pérez-González, P.G., Cava, A., Barro, G., et al., 2013, ApJ 762, 46

[26] Pović, M., Sánchez-Portal, M., Pérez García, A. M., et al. 2009, ApJ, 706, 810

[27] Ramón-Pérez, M. 2017, Study of Active Galactic Nuclei in the OTELO survey. Universidad de La Laguna. PhD thesis

[28] Ramón-Pérez, M., et al. 2018a, A&A, accepted

[29] Ramón-Pérez, M., et al. 2018b, A&A, submitted (under 2nd. revision)

[30] Takada, M., Ellis, R. S., Chiba, M., et al. 2014, PASJ, 66, R1

[31] Sánchez-Portal, M., Pintos-Castro, I., Pérez-Martínez, R., et al. 2015, A&A, 578, A30

[32] Straughn, A.N., Pirzkal, N., Meurer, G.R., et al. 2009, AJ, 138, 1022

[33] Wegner, G., Salzer, J.J., Jangren, A., et al. 2003, AJ, 125, 2373

[34] Wolf, C., Meisenheimer, K., Rix, H.-W., et al. 2003, A&A, 401, 73

Highlights on Spanish Astrophysics X, Proceedings of the XIII Scientific Meeting of the Spanish Astronomical Society held on July 16 – 20, 2018, in Salamanca, Spain. B. Montesinos, A. Asensio Ramos, F. Buitrago, R. Schödel, E. Villaver, S. Pérez-Hoyos, I. Ordóñez-Etxeberria (eds.), 2019

Are we missing massive red galaxies at z>3?

Belén Alcalde Pampliega[1], Pablo G. Pérez-González[1,2], Guillermo Barro[3] Helena Domínguez Sánchez[4] and M. Carmen Eliche-Moral[5]

[1] Departamento de Física de la Tierra y Astrofísica, Faultad de CC Físicas, Universidad Complutense de Madrid E-2840 Madrid, Spain
[2] Centro de Astrobiología (CAB, INTA-CSIC), Carretera de Ajalvir km 4, E-28850 Torrejón de Ardoz, Madrid, Spain
[3] Astronomy Department,Department of Physics, University of the Pacific, Stockton, CA 95211, USA.
[4] Department of Physics and Astronomy, University of Pennsylvania, Philadelphia, PA 19104, USA.
[5] Instituto de Astrofísica de Canarias, Calle Vía Láctea, s/n, E-38205, La Laguna, Tenerife, Spain.

Abstract

We present the detection of a sample of galaxies which are extremely faint in the optical and near-infrared but bright at mid-infrared wavelengths. This population of galaxies, missed by the deepest HST surveys such as CANDELS or Hubble Frontier Fields, are considerably bright in IRAC. The bulk of the sample (65%) is located in a 2σ region around the main sequence. Approximately 20% of the Balmer Break Galaxies (BBGs) are very dusty starbursts with strong mid-to-far infrared detections and extreme star formation rates. The remaining, 15%, are located more than 2σ below the main sequence and might be either regular star-forming galaxies or quiescent systems. Nearly one third of them are MIPS emitters, most probably revealing the presence of an obscured AGN co-existing with the intense star formation, as measured by Herchel. Only 2 sources are detected in X-rays and 3 at sub-millimiter or radio wavelengths. Our results point out that BBGs significantly contribute (35%) to the general population of massive red galaxies at z$= 4-6$ and that one of every ten massive $\log(M/M_{\odot}) > 11$ galaxies in the local Universe was assembled in the first 1.5 Gyr after the Big Bang.

1 Introduction

Understanding when the first massive galaxies appeared in the Universe is essential for models of galaxy evolution. While the ΛCDM paradigm predicts that most massive halos assembled at lower redhshifts, observational studies suggest that the most massive local galaxies

($\log(M/M_\odot) > 11$) formed early in the universe [6, 5, 2]. Recently, many surveys have identified a substantial population of massive galaxies at redshifts up to $z \sim 4$, when the universe was only 1.5 Gyr old [10, 1] some of them showing evidences of evolved stellar populations [8]. Characterizing the star formation activity and the number density of massive high redshift is particularly important to improve our picture of galaxy evolution and to constrain galaxy formation models. A major complication to address these questions is gathering a complete, robust and un-biased census of massive galaxies up to the highest redshifts possible. Most studies up to date are based in UV-selected samples, which are particularly sensitive to detect young and/or blue system but are strongly biased against red, dusty or evolved galaxies. Thus, rest-frame UV-selected samples at high-redshift are likely incomplete, missing massive red galaxies which could potentially be identified with observations at longer wavelengths.

2 Selection process

Our selection technique is based on two conditions. BBG candidates are required to be bright in the first two channels of IRAC, [3.6] and [4.5] ≤ 24.5 mag, and undetected (dropouts) in the HST/F160W (H$\gtrsim$27) publicly available catalogues published by the CANDELS and 3D-HST teams —[3], [7], Barro et al. 2018, in prep.—). We have used TFIT residual frames to search for potential H-band dropouts with bright IRAC magnitudes. Briefly, TFIT is used to generate a model of the IRAC image by convolving the high spatial resolution HST/F160W mosaic with the appropriate PSF transformation kernel. Then, the fluxes on the resulting "template" image are scaled to those of the galaxies in the IRAC frame on a galaxy-by-galaxy basis. Lastly, TFIT subtracts the scaled "template" image from the original IRAC mosaic creating a residual frame which is used to verify the quality of the source extraction and flux measurements. Before searching for BBG candidates in the residual IRAC image, we applied three different cleaning masks for the bright H-band sources, brightest stars and artifacts. We also applied a mathematical morphology method to the regions around H-band bright sources to avoid extra flux arising from their wings.

3 Observed IR colors, photometric redshifts and masses of BBGs

In this Section we analyze the distribution of observed colors, photometric redshifts and stellar mass of the 33 BBGs using the results from the UV-to-FIR SED fitting techniques. We also compare BBGs with two samples constructed with the CANDELS GOODS H-band selected catalogs. The mass-selected sample is composed by massive ($M > 10^{10}\,M_\odot$) galaxies at $z > 3$. The color-selected sample, aimed to reproduce our BBG selection, is composed by red ($H - [3.6] > 2.5$) faint ($H > 25$) galaxies.

The $H - [3.6]$ red colors of most of our sources are compatible with evolved populations or heavily extincted starbursts. However, our sample includes a distinct population of blue (both in their observed $H - [3.6]$ and their UVJ rest-frame colors) galaxies. This population have similar SEDs to galaxies from the mass-selected sample. They indeed present uncommon

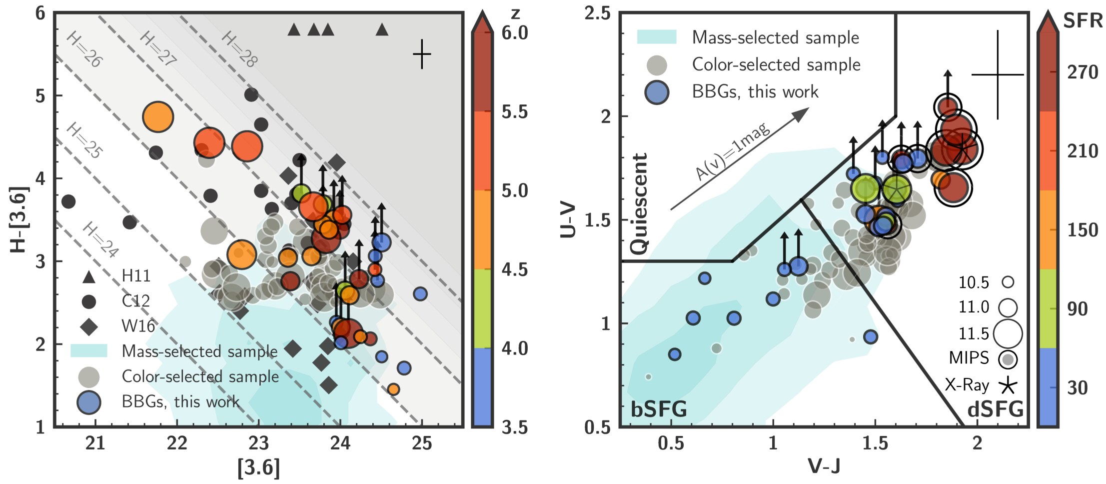

Figure 1: *Left panel:* Observed-frame $H-[3.6]$ color plotted versus the observed [3.6] magnitude for our sample of BBGs, color-coded by their photometric redshift and scaled in size as a function of their stellar mass (legend shown in right panel). *Right panel:* Rest-frame $U-V$ vs. $V-J$ color-color plot, where BBGs are color-coded by SFR and scaled by stellar mass.

blue [3.6]-[4.5] colors that might be caused by the presence of an emission line in the [3.6] band (converting them in red sources in our selection color $H-[3.6]$). We also note that they correspond to some of the less massive (M $< 10^{10.5}$M$_\odot$) BBGs in our sample. Therefore, their detection might be a consequence of our improved photometric technique to recover faint sources and reliable upper limits. In addition, we compare our sample of BBGs with the samples of galaxies of similar nature presented in [4, 1], and [9] (see. left panel legend in Fig. 1).

Subdividing BBGs by their rest-frame UVJ colors (see right panel in Fig. 1), we find a mix of blue SFGs and dusty SFGs. Although no clearly quiescent galaxies are found, 3 of our BBGs (located close to the quiescent boundary) have mass-weighted ages that are large enough ($t_m \geqslant 0.9$ Gyr) to be consistent with evolved or quiescent galaxies.

We have also proved that a $H-[3.6]$ color and IRAC magnitude cuts imply a redshift selection as shown in the the left panel of Fig. 2. The redshift distributions, of both the BBGs and the color-selected sample peak at $z = 4-5$, while the mass-selected sample presents an exponentially decreasing redshift distribution (typical of flux limited samples). Our selection criterion is also adequate to probe the high mass end of the stellar mass function (M $\gtrsim 10^{10}$M$_\odot$). The BBG stellar mass distribution peaks at M $\sim 10^{10.5}$M$_\odot$. The color-selected sample presents a comparable histogram with a longer tail at higher masses due to their brighter IRAC magnitudes. The mass-selected sample, in contrast, presents a distribution that decreases with increasing masses.

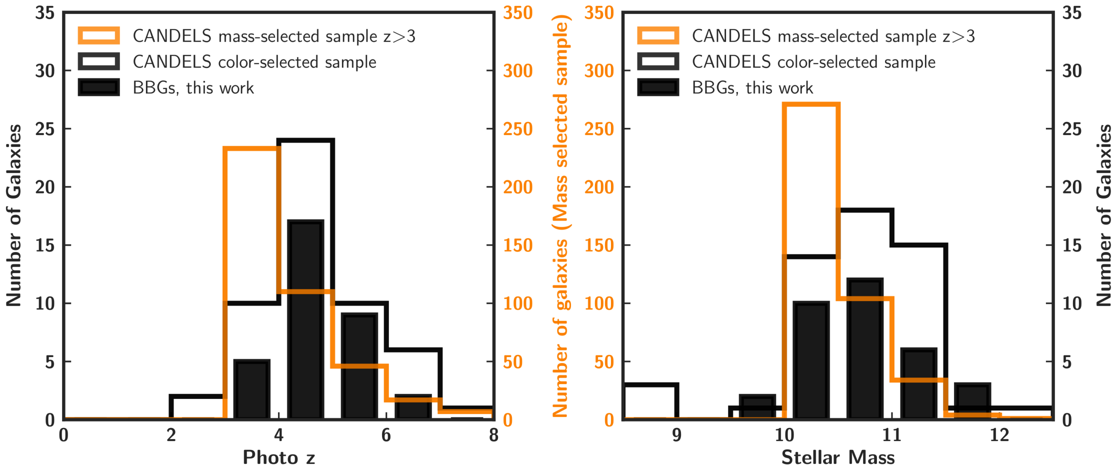

Figure 2: Photometric redshift (*left panel*) and stellar mass (*right panel*) distributions of our sample of BBGs compared to those of the color-selected and mass-selected CANDELS samples. Given the substantially higher number of galaxies among the mass-selected sample, a different axis has been used for it, as indicated by the orange labels.

4 BBGs and the star formation main sequence

From the SED modelling, we find a strong evidence that massive red galaxies at $z = 3 - 6$ span a diverse range in stellar population properties. In order to understand the nature of the heterogeneous sample of BBGs, we have divided the sources in three star formation regimes according their position with respect to the main sequence (MS) from GOODS: starbursts, MS and sub-MS galaxies (Fig. 3). Analyzing the average SEDs of BBGs, we confirm that, in general, mass-selected galaxies present bluer SEDs than those from the BBG and the color-selected samples. However we identify a subsample of BBGs in the MS which are blue and harder to separate from the general population probed by a mass-selected sample. In addition, we find a small number of sub-MS galaxies (16%), most of them with M $< 10^{10.5}$M$_\odot$, characterized by low extinctions and larger mass-weighted ages (t_m). On the other hand, starbursts are found in the most massive (M $> 10^{10.5}$M$_\odot$) galaxies from the BBGs (20% of the total number of BBGs are starburst) and color-selected (15%) sources. Starbursts are characterized by very high extinctions and young t_m. It is remarkable that 5 BBGs out of the 6 starbursts have FIR emission, all are at least detected at 24μm, 3 emit at submillimeter wavelengths and one is an X-Ray source as well. This suggests that a significant fraction of the BBGs (∼25 and up to ∼75%) might host an obscured AGN. MS galaxies represent a constant proportion of BBGs (∼65%) and color-selected (∼60%) up to the highest masses M $\sim 10^{11.5}$M$_\odot$. However, an important fraction (25%) of the MS galaxies have been assigned with a SFR lower limit (given their detection by MIPS, but their high redshift (z> 5) prevents from obtaining a robust SFR estimation) and may correspond to starburst galaxies. BBGs in the MS present a larger scatter in their extinctions, mass-weighted ages and and UVJ colors.

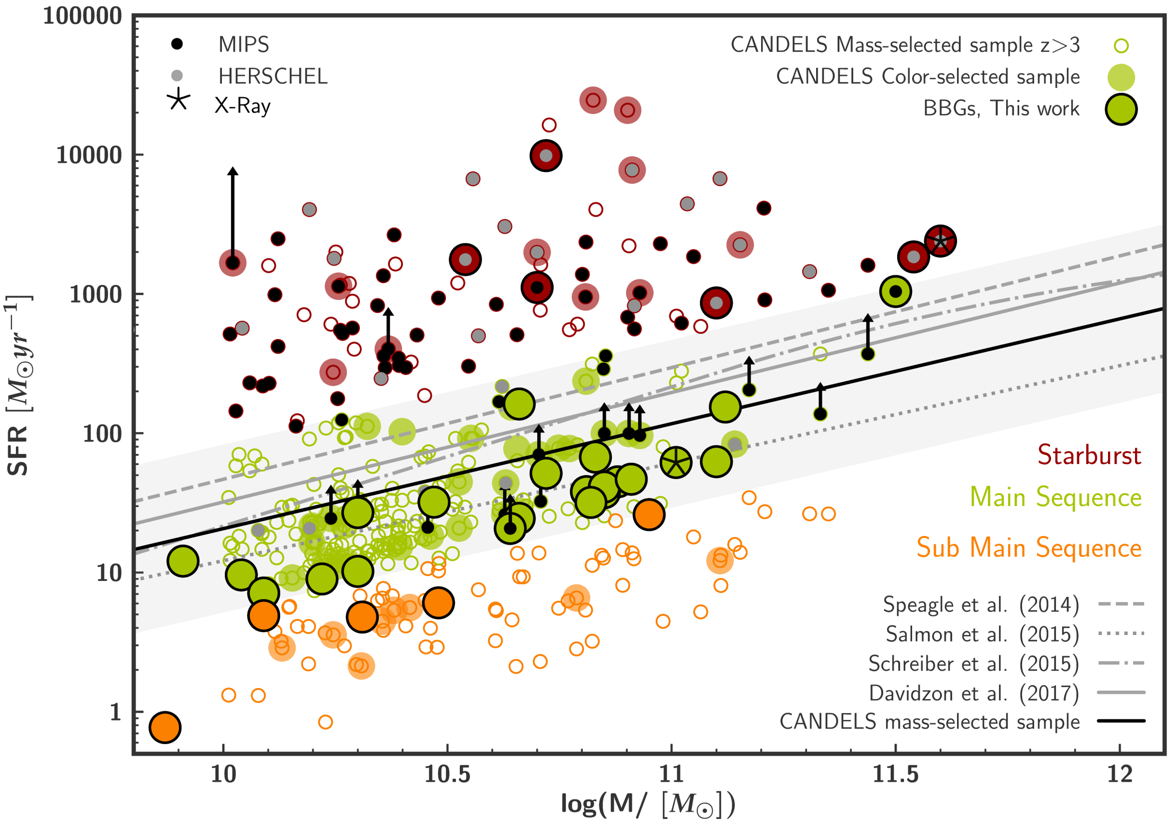

Figure 3: SFR vs stellar mass plane for the CANDELS comparison samples (color-selected —filled symbols— and mass-selected —open symbols—) and the BBGs (filled symbols enclosed by a black circle) reported in this work, color coded according to their position with respect to the main sequence: starburst, MS and sub-MS galaxies are shown in deep-red, green, and orange respectively. The MS from the literature at $z = 4$ are shown with different grey lines (see the legend in the panel). The MS inferred for the CANDELS mass-selected sample is shown with a black solid line. The grey-shaded region delimits the 2σ area around the MS. MIR/FIR emitters are marked with an enclosed black/grey circle. The galaxies with MIPS detections but no IR-derived SFRs are shown as lower limits. X-rays emitters are also highlighted with a star symbol.

5 The role of BBGs in galaxy evolution

We have found that the red BBGs presented in this work account for 7% of the total number density of $\log(\mathrm{M}/\mathrm{M}_{\odot}) > 10$ galaxies at $z > 3$ found by public catalogues such as CANDELS' or 3D-HST's. Our BBGs are, however, a major contributor (30%) to the general (adding catalogue galaxies and our BBGs) population of $\log(\mathrm{M}/\mathrm{M}_{\odot}) > 11$ galaxies at $4 < z < 6$ and, more remarkably, to the population of red massive galaxies (i.e., evolved or dusty systems) in the same redshift interval, accounting for 35% of this population. Adding the BBGs presented in this work to the known population of $4 < z < 6$ and $\mathrm{M} > 10^{11}\,\mathrm{M}_{\odot}$ we have found a total number density of $1.1{\times}10^{-5}$galaxies/Mpc^3. This represents 8% of the the number density of local M> $10^{11}\,\mathrm{M}_{\odot}$ meaning that nearly 1 in 10 massive galaxies in the local Universe must have assembled more than $10^{11}\,\mathrm{M}_{\odot}$ in the first 1.5 Gyr of the Universe.

6 Summary and conclusions

Combining ultra-deep data taken in the WFC3 $F160W$ and IRAC 3.6 and 4.5 μm bands, we have identified a sample of 33 IRAC bright/optically faint Balmer Break Galaxies (BBGs) at high redshift within the two GOODS fields. We have also proved the effectiveness of a $H - [3.6]$ color and IRAC magnitude cuts in selecting red massive galaxies at $z > 3$.

Most of our sources are compatible with heavily extincted starbursts and 30% of them being compatible with evolved populations. This population of BBGs is major contributor (30%) to the general (adding catalogued galaxies and our BBGs) population of $\log(\mathrm{M}/\mathrm{M}_{\odot}) > 11$ galaxies at $4 < z < 6$ and, more remarkably (35%), to the population of red massive galaxies in the same redshift interval.

Accounting for this kind of objects is key to understand the population of massive galaxies at high redshift and their number density is specially important among red massive galaxies at $z = 4 - 6$. Moreover, BBGs represents 8% of the the number density of local M> $10^{11}\,\mathrm{M}_{\odot}$ meaning that nearly 1 in 10 massive galaxies in the local Universe must have assembled more than $10^{11}\,\mathrm{M}_{\odot}$ in the first 1.5 Gyr of the Universe.

Acknowledgments

We acknowledge support from the Spanish Programa Nacional de Astronomía y Astrofísica under grants AYA2015-63650-Pand BES-2013-065772. We also acknowledge SEA support for young astronomers.

References

[1] Caputi,K., Dunlop, J.S., McLure, R.J., 2011, ApJ, 750(1):L20x

[2] Grazian,A., Fontana, A, Santini, P. 2015 575:A96

[3] Guo, Y., Ferguson, H. C, Giavalisco, M. 2013, apjs, 207:24

[4] Huang,J-S, XZ Zheng, Rigopoulou,D. 2011, Apjs, 742(1):L13

[5] Mancini, C., Matute, I., Cimatti, A., 2009, A&A, 500(2):705–723

[6] Pérez-González, P. G., Rieke, G. H., Villar,V.,2008, ApJ, 675(1):234

[7] Skelton,R. E., Whitaker,K. E., Momcheva,I. G. 2014, apjs, 214:24

[8] Straatman,C. M. S., Spitler,L. R., Quadri,R. F. 2016, apj, 830:51

[9] Wang,T., Elbaz,D. , Schreiber,C. 2016, apj, 816:84

[10] Wiklind,T., Dickinson,M., Ferguson,H. C., 2008, apj, 676:781–806

Highlights on Spanish Astrophysics X, Proceedings of the XIII Scientific Meeting of the Spanish Astronomical Society held on July 16 – 20, 2018, in Salamanca, Spain. B. Montesinos, A. Asensio Ramos, F. Buitrago, R. Schödel, E. Villaver, S. Pérez-Hoyos, I. Ordóñez-Etxeberria (eds.), 2019

The origin of progenitors in merging black hole binaries.

Nicola Bellomo[1,2], Giulio Scelfo[1,3,4], Alvise Raccanelli[1,5], Sabino Matarrese[3,6,7,8] and Licia Verde[1,9]

[1] ICC, University of Barcelona, IEEC-UB, Martí i Franquès, 1, E-08028 Barcelona, Spain.
[2] Dept. de Física Quàntica i Astrofísica, Universitat de Barcelona, Martí i Franquès 1, E-08028 Barcelona, Spain.
[3] Dipartimento di Fisica e Astronomia G. Galilei, Università degli Studi di Padova, via Marzolo 8, I-35131 Padova, Italy.
[4] SISSA, Via Bonomea 265, I-34136 Trieste, Italy.
[5] Theoretical Physics Department, CERN, 1 Esplanade des Particules, CH-1211 Geneva 23, Switzerland.
[6] INFN - Sezione di Padova, via F. Marzolo 8, I-35131 Padova, Italy.
[7] INAF - Osservatorio Astronomico di Padova, vicolo dell'Osservatorio 5, I-35122 Padova, Italy.
[8] Gran Sasso Science Institute, viale F. Crispi 7, I-67100 L'Aquila, Italy.
[9] ICREA, Pg. Lluis Companys 23, Barcelona, E-08010, Spain.

Abstract

Are the stellar-mass merging binary black holes, recently detected by their gravitational wave signal, of stellar or primordial origin? Answering this question will have profound implications for our understanding of the Universe, including the nature of dark matter, the early Universe and stellar evolution. We develop the idea that the clustering properties of merging binary black holes can provide information about binary formation mechanisms and origin, in particular the cross-correlation of galaxy with gravitational wave catalogues carries information about whether black hole mergers trace more closely the distribution of dark matter – indicative of primordial origin – or that of stars harboured in luminous and massive galaxies – indicative of a stellar origin. We forecast the detectability of such signal for several forthcoming and future gravitational wave interferometers and galaxy surveys. Our results show that forthcoming experiments could allow us to test most of the parameter space of the still viable models investigated, and shed more light on the issue of binary black hole origin and evolution.

1 Introduction

The first detection of gravitational waves (GWs) emitted by the coalescence of two black holes (BHs) of approximately 30 $M_\odot$ [2] opened the era of gravitational waves astronomy, not only by confirming General Relativity predictions, but also establishing a new way to observe and analyse the cosmos. Even if some authors expected such massive progenitors to be the first sources to be detected [6], this fact was hailed by part of the community as unexpected and led some researchers to suggest that such events may not be uncommon. Indeed other GWs events followed and confirmed that apparently a significant fraction of the detected progenitors has masses between 20 and 40 $M_\odot$. Such large masses of the progenitors are not incompatible with classical stellar/binary evolution [5]. Nevertheless the possibility that BHs with an origin different from the standard end-point of stellar evolution and constituting a significant fraction of the dark matter regained interest [9].

Primordial Black Holes (PBHs) formed during radiation-dominated era because of the collapse of large density fluctuations in the primordial cosmic fluid that overcame pressure forces [15]. These results were later confirmed by the authors of Ref. [20], who were the first to provide general relativistic numerical computations of PBHs formation during the radiation-dominated era.

Given the high interest in PBHs as dark matter candidates, a remarkable amount of different observational constraints have been obtained, including constraints coming from gravitational lensing effects, dynamical effects and accretion effects (see e.g., Ref. [26] for a recent review). Even if these constraints cover the whole mass range and seem to disfavour PBHs as a significant fraction of the dark matter, these results are far from being conclusive due to the variety of assumptions involved, see e.g., Ref. [7]. Some mass "windows" still exist, for instance one around 10^{-12} $M_\odot$ and another 10 $M_\odot$, where the latter one can be probed by future GWs observatories as Advanced LIGO (aLIGO) [1], KAGRA [29], LIGO-India [31] or Einstein Telescope (ET) [27].

Despite the fact PBHs may not constitute the totality of the dark matter, it is valuable to explore different ways to determine if mergers progenitors' origin is stellar or primordial. In this work we focus on developing further the cross-correlation approach suggested by the authors of Ref. [24], who show that the statistical properties of the type of galaxy (or halo) hosting a GWs event can provide information about the system origin (stellar or primordial). In fact, in more massive halos the typical velocities are higher than those in the less massive ones. As a consequence, it is much more probable that two PBHs form a gravitationally bound binary through GWs emission in low-mass halos, since the cross section of such process is inversely proportional to some power of the relative velocity of the progenitors. The higher velocity dispersion of high-mass halos make this process for PBHs less likely to happen. In addition, low-mass halos tend to be less luminous than high-mass ones and trace more closely the dark matter distribution than high-mass halos. On the other hand the merger probability for stellar black holes is more likely to correlate with galaxies' (or halos') stellar mass, hence stellar black holes mergers tend to happen in more luminous and massive halos. Recall that star formation efficiency increases with halo mass for halo of masses below $10^{12} M_\odot$. It decrease for higher mass-halos but these are very rare and more closely associated to galaxy clusters rather than galaxies [14]. The clustering properties of these two halos populations are different, in particular low-mass halos are less strongly clustered than high (stellar) mass galaxies: they have different *bias* parameters. The bias parameter governs the ratio of clustering amplitude of the selected tracer to that of the dark matter.

At the moment too few GWs events have been detected to measure the auto and cross correlation of maps of GWs events and galaxies, but during next LIGO's runs, thousands of events are likely to be detected due to the improved sensitivity. On the other hand, during the next decade a large volume of the Universe at high redshift will be surveyed thanks to several surveys, as EMU [22], DESI [4] or SKA [18], which we consider in the rest of the paper.

In this brief communication we report just a small fraction of the framework we have developed and analysed. The interested reader can find more details and a broader discussion in the complete work in Ref. [28].

2 Methodology

Since BH-BH mergers do not have an electromagnetic counterpart, the identification of their host object is impossible even if the event is measured by more than three detectors. Because of the poor localisation in the sky of the GWs events, the GWs maps are typically very "low resolution". For this reason we approach the problem in a statistical way, by using measurements and statistical properties of their number counts. In particular, we work in harmonic space and we consider the number counts angular power spectrum, C_ℓ, where only low multipoles ℓ are considered because of the maps' low angular resolution. The maximum multipole $\ell_{\max}$ is determined by the angular resolution θ that can be achieved: $\ell_{\max} \sim 180^o/\theta$. For the aLIGO+Virgo network $\ell_{\max} = 20$, once also LIGO-India and KAGRA are included, we improve the spatial resolution up to $\ell_{\max} = 50$ and finally with the futuristic Einstein Telescope, $\ell_{\max} = 100$ will be reached [21].

In the following we assume to have (tomographic) maps of GWs events and of galaxies (i.e., the *tracers*). The observed harmonic coefficients used to compute the angular power spectra are given by $a^X_{\ell m}(z_i) = s^X_{\ell m}(z_i) + n^X_{\ell m}(z_i)$, where $s^X_{\ell m}$ and $n^X_{\ell m}$ are the partial wave coefficients of the signal and of the noise for tracer X. We consider the noise angular power spectrum to be given only by a shot noise term $\mathcal{N}^X_\ell(z_i)$ and we assume that the noise terms from different experiments and different redshift bins are uncorrelated. The expectation value of the signal gives the $C^{XY}_\ell(z_i, z_j)$ [23], while the signal-cross-noise expectation value is zero since we assume signal and noise to be statistically independent. In general the observed number count fluctuation receives contributions from density, velocity, lensing and gravity effects [12]. Even if the bias parameter b_X of the tracer X enters only in the density contribution, we cannot overlook the effect of the other terms on the signal-to-noise, as sometimes done in the literature. The reader interested in a more in general discussion on the importance of a correct modelling of an observable can check Ref. [8]. We extend the public code `CLASS` [10, 13] to include the possibility to have different tracers ($X \neq Y$). We present this new version of `CLASS`, called `Multi_CLASS`, in Ref. [8].

We estimate the capability of future GWs observatories and large scale structure surveys to determine BHs mergers progenitors' origin in a way close to an actual data analysis. We assume that we can model well enough some properties of the tracers that are currently still uncertain and that cosmological parameters are known. We perform what can be seen as a null hypothesis testing, comparing two models, one in which progenitors origin is stellar, the other in which is primordial. We assume one model as fiducial and we check if the alternative model can be differentiated from the fiducial one by computing a Signal-to-Noise ratio S/N. The null hypothesis is that the model is indistinguishable from the fiducial, which happens for low values of the Signal-to-Noise ratio ($S/N \lesssim 1$). We quantify the distance of an alternative model from the fiducial using a $\Delta\chi^2$ statistics. In our case the $\Delta\chi^2$ is given by the logarithm of a likelihood, in particular we assume a likelihood quadratic in the angular power spectra. The resulting $\Delta\chi^2$ statistics reads as

$$\left(\frac{S}{N}\right)^2_{\sqrt{\Delta\chi^2}} \sim \Delta\chi^2 := f_{\rm sky} \sum_{2}^{\ell_{\max}} (2\ell+1)(\mathbf{C}_\ell^{\rm Alternative} - \mathbf{C}_\ell^{\rm Fiducial})^T \mathrm{Cov}_\ell^{-1} (\mathbf{C}_\ell^{\rm Alternative} - \mathbf{C}_\ell^{\rm Fiducial}), \tag{1}$$

where $\mathbf{C}_\ell^T = \left(C_\ell^{\rm gg}(z_1, z_1), \cdots, C_\ell^{\rm gGW}(z_1, z_1), \cdots, C_\ell^{\rm GWGW}(z_1, z_1), \cdots\right)$, $f_{\rm sky}$ is the observed fraction of the sky and Cov_ℓ is a covariance matrix, computed from angular power spectra of the fiducial model as explained in Ref. [8]. Notice that the ability to distinguish between two scenarios can differ according to which model is the alternative model and which one is the fiducial, since the covariance matrix and thus the errors depend (sometimes strongly) on the fiducial model adopted.

3 Tracers

In this section we describe the two tracers we consider in this work, galaxies and GWs. For cosmological purposes, each of these tracers is characterised by a source number density per redshift bin and square degree $d^2N_X/dzd\Omega$, bias $b_X(z)$ and magnification bias $s_X(z)$ parameters. Even if some of these quantities are uncertain at the moment, we exploit their evolution in redshift to maximize the differences between the two models.

3.1 Galaxies

Depending on the experimental set up under consideration, we choose as luminous tracers emission-line galaxies in the redshift range $[0.6 - 1.7]$, targeted by DESI, or star-forming galaxies, targeted by EMU and SKA in the redshift range $[0.0 - 5.0]$. For DESI galaxies we use data in Ref. [4], while for EMU and SKA we use the Tiered Radio Extragalactic Continuum Simulation (T-RECS) [11] catalogue with different detection threshold (100 μJy for EMU and 5 μJy for SKA). We report in the top left panel of figure 1 the three normalized number densities $d^2N_{\rm g}/dzd\Omega$.

The bias $b_{\rm g}(z)$ for emission-line galaxies is taken from Ref. [4], while the bias for EMU and SKA star-forming galaxies is modelled as in Ref. [25]. We show the bias redshift dependence in the bottom left panel of figure 1.

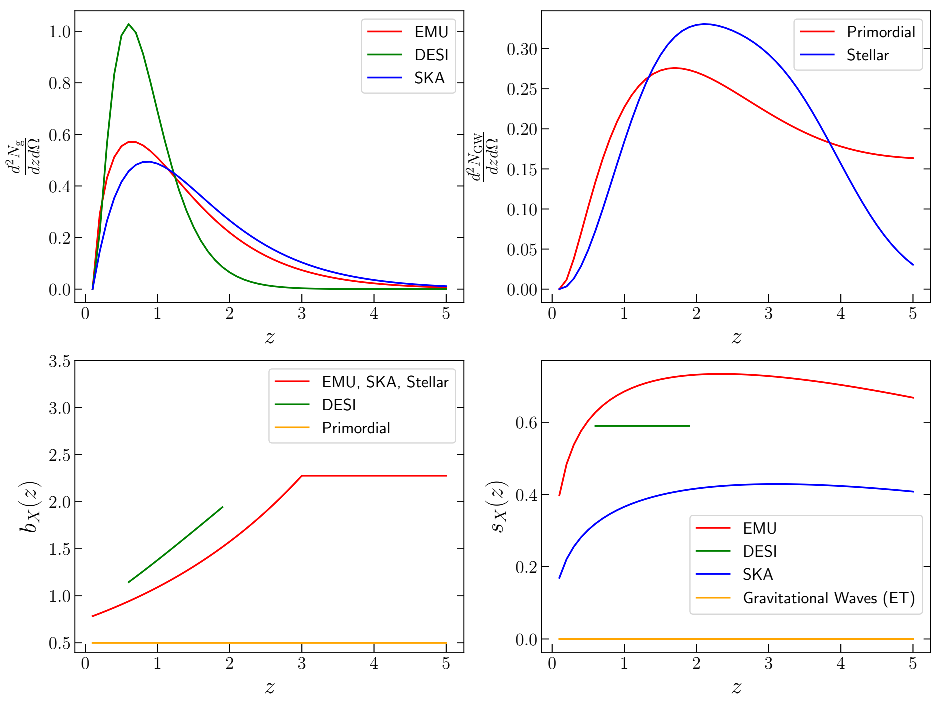

Figure 1: *Top panels*: normalized number density distribution per redshift bin per square degree $d^2N_X/dzd\Omega$ for galaxies (*top left*) and GWs (*top right*). *Bottom panels*: bias $b_X(z)$ (*bottom left*) and magnification bias parameter $s_X(z)$ (*bottom right*) for galaxies and GWs. We report the GWs magnification bias parameter associated to a BHs population with monochromatic mass distribution detected by an interferometer with characteristics similar to those of ET.

Gravitational lensing changes the sources surface density on the sky in two competing ways [30], by increasing the area, which in turn decreases the projected number density, but also by magnifying individual sources and promoting faint objects above the magnitude limit. The change in the number of observed sources depends on the magnification bias $s_g(z)$, the value of the slope of the faint-end of the luminosity function [16]. For DESI we use the magnification bias reported in Ref. [4], while for EMU and SKA we use the T-RECS catalogue [11] to compute it. We report the magnification bias parameter $s_g(z)$ in the bottom right panel of figure 1.

3.2 Gravitational Waves

The number density of detected GWs events per redshift bin per square degree $d^2N_{\rm GW}/dzd\Omega$ is proportional to the total comoving merger rate $\mathcal{R}_{\rm tot}(z)$, which in turn depends on the progenitors origin. The uncertainty in the total merger rate is of orders of magnitude, however what enters in the calculation of the angular power spectra C_ℓ^{XY} (i.e., the signal) is the shape of $d^2N_{\rm GW}/dzd\Omega$, not the global amplitude. On the other hand, the merger rate (and its normalisation) affects the signal-to-noise ratio (i.e., the error-bars): a larger number density will decrease the shot noise, improving the constraints on the cosmological parameters of interest. We report in the top right panel of figure 1 the normalized number densities corresponding to the stellar and primordial scenarios.

If the progenitors have primordial origin and merge according to the scenario proposed in Ref. [9], then the merger events trace low-velocity dispersion low-mass halos ($M_{\rm halo} < 10^6 M_\odot$). The bias of these halos is given by $b_{\rm lmh}(z) \simeq 0.5$ [19], independently on redshift. On the other hand, when progenitors of a merging event have stellar origin, they are more likely correlated with higher-mass halos that had a higher star-formation rate, therefore their bias will be the same of the galaxies under consideration, i.e. $b_{\rm GW}(z) = b_{\rm g}(z)$. We show the bias redshift dependence in the bottom left panel of figure 1.

We calculate for the first time the magnification bias for GWs [28], finding that for common BHs mass distribution and for future GWs observatories it stays close to zero at every redshift considered. We show the magnification bias for GWs in the bottom right panel of figure 1.

4 Results

In this section we provide forecasts for specific combinations of GWs observatories and large scale structure surveys.

Merger rates are poorly known, both on the observational and theoretical side, spanning several orders of magnitude and affecting the overall expected number of GWs events. After the first run of LIGO, the observational merger rate today is estimated to be $\mathcal{R}^{\rm LIGO}_{\rm today} \simeq 9 - 240~{\rm Gpc}^{-3}{\rm yr}^{-1}$ [3], while the theoretically predicted merger rates for the stellar and primordial scenario are $\mathcal{R}^{\rm Stellar}_{\rm today} \simeq 150~{\rm Gpc}^{-3}{\rm yr}^{-1}$ [17] and $\mathcal{R}^{\rm Primordial}_{\rm today} \simeq 4~{\rm Gpc}^{-3}{\rm yr}^{-1}$ [9]. We parametrize the uncertainty on the number of GWs events by introducing a new parameter r constant in redshift, in which we include every uncertainty in the modelling. The values $r^{\rm Stellar,\,Primordial} = 1$ correspond to the merger rates reported above. To account for several theoretical uncertainties that can influence the merger rates, we provide results for a range $r^{\rm Stellar,\,Primordial} \in [10^{-1}, 10]$.

We report the Signal-to-Noise forecasts in figure 2 (stellar as fiducial model) and figure 3 (primordial as fiducial model). In each of these figures we show two panels: in the left panels we show bar charts obtained for different values of the parameter r at fixed maximum multipole $\ell_{\rm max}$ (50 for aLIGO and 100 for ET), while in the right panels we report the scaling of the Signal-to-Noise for different values of the maximum angular resolution when $r^{\rm Stellar,\,Primordial} = 1$.

We explicitly show that surveys covering a bigger volume (or redshift range) can discriminate better between different models, i.e. have higher Signal-to-Noise ratios, as expected from surveys with smaller shot noise. Notice that in the cases of stellar as fiducial, we have better Signal-to-Noise ratio than in the primordial scenario, due to higher merger rates, thus higher number of detected sources and lower shot noise. Achieving high angular resolutions is fundamental to discriminate between the two models. In general we can conclude that future

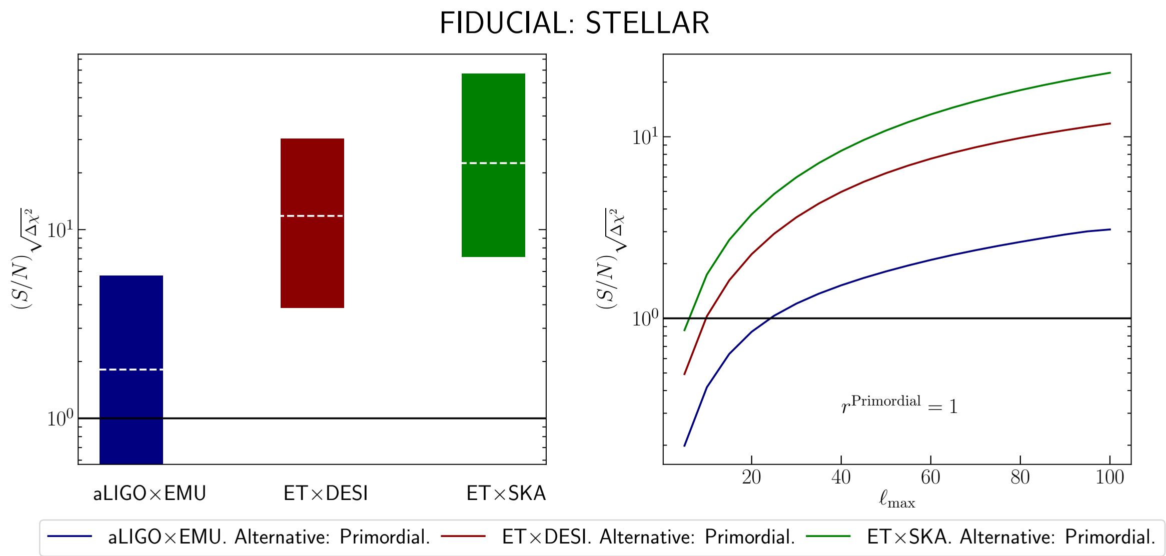

Figure 2: Signal-to-Noise S/N estimates for specific surveys combinations. *Left panel:* Signal-to-Noise S/N estimates as a function of r, assuming a fixed $\ell_{\max}$. The horizontal dashed white lines refer to the $r = 1$ case. *Right panel:* Signal-to-Noise S/N estimates as a function of $\ell_{\max}$ for the fiducial merger rate case $r = 1$.

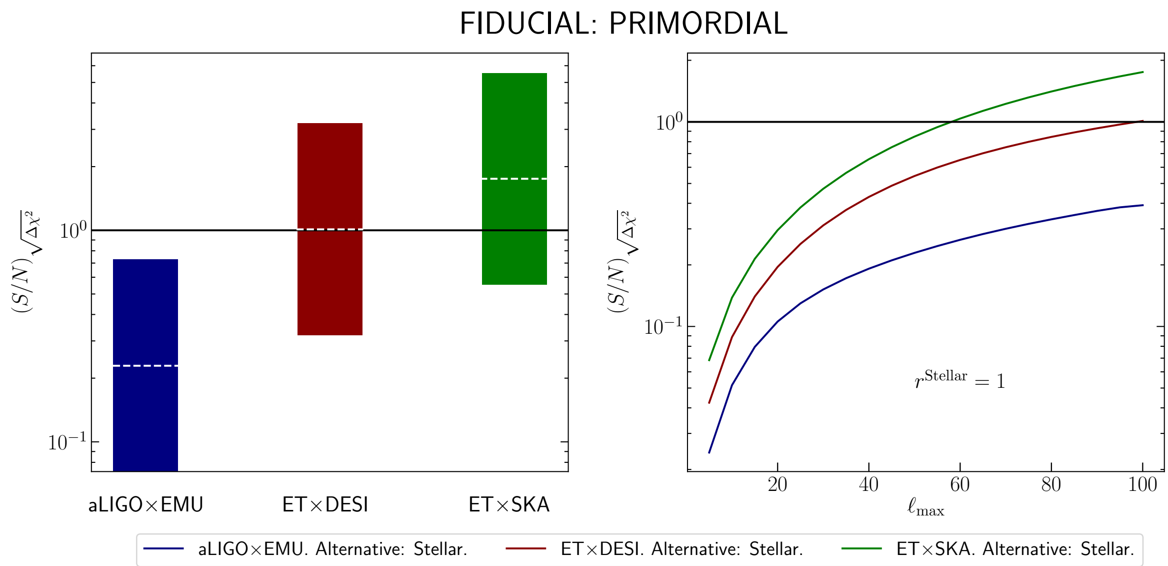

Figure 3: Signal-to-Noise S/N estimates for specific surveys combinations. *Left panel:* Signal-to-Noise S/N estimates as a function of r, assuming a fixed $\ell_{\max}$. The horizontal dashed white lines refer to the $r = 1$ case. *Right panel:* Signal-to-Noise S/N estimates as a function of $\ell_{\max}$ for the fiducial merger rate case $r = 1$. The horizontal dashed white lines refer to $r = 1$.

surveys will enable us to address questions about binary BHs mergers given enough observation time (here assumed to be 10 years) and angular resolution. One caveat is that this does not always happen for the aLIGO×EMU combination, which will have a Signal-to-Noise lower or very close to unity in some cases (especially if mergers come from the primordial formation mechanism). This is due to the fact that this combination of GWs observatory and large scale structure survey can only cover a low redshift range, where the biases are very similar (see e.g., the bottom left panel of Figure 1) and we have an higher shot noise due to the scarce number of detected objects.

5 Conclusions

The renewed interest in primordial black holes has highlighted their importance not only as a possible constituent of the dark matter but also because their existence (if confirmed) would have profound implications about the physics of the early Universe. It is therefore essential to explore new ways to discriminate between primordial or stellar origin of the black holes which mergers have been observed with laser interferometers. Beyond the standard ways to constrain the existence of stellar mass primordial black holes through lensing or the effect on cosmic backgrounds, a complementary approach is to assess whether the GWs signal from merging binary BHs we detect are produced by objects of primordial origin or not.

Here we build on the idea that the cross-correlation of galaxy catalogues with GWs (from the merger of binary BHs) maps is a powerful tool to statistically study the origin of the progenitors of BHs mergers [24]. This will be possible once the next generation of GWs detectors will provide localization of enough events to make low resolution maps. Galaxy catalogues covering a significant fraction of the sky and an overlapping redshift range are also under construction or at an advanced planning stage. Then, by measuring the bias of the halos hosting the binary BHs mergers we can infer the clustering properties of the progenitors of the binary BHs. Clustering properties matching those of luminous, high velocity-dispersion, high stellar-mass galaxies, would indicate a stellar origin, while clustering properties more similar to those of low-mass galaxies preferentially populating the filamentary structure of large-scale structures indicate a primordial origin.

In complete work in Ref. [28] we have also considered different models for the binary BHs formation, accretion mechanism, merger rate, mass distribution and clustering properties, both for the stellar and primordial nature of the BHs. We generalized similar studies on the cross-correlation between galaxy and gravitational wave maps by performing a full multi-tracer analysis that accounts for different redshift distributions, galaxy bias evolution, magnification bias of luminous sources as well as GWs, and relativistic projection effects. Even including all these uncertainties we found quite general results that can be still used once some of such quantities will be better understood. Our results show that forthcoming experiments could allow us to test most of the parameter space of the still viable models investigated, and shed more light on the issue of binary black hole origin and evolution. We firmly believe that the present work can contribute to further develop the new avenue of GW-LSS synergies, and that the vast range of parameters and models explored here make our results general enough to provide a realistic forecast of what this can teach us on the nature of binary BHs progenitors in the next decade.

Acknowledgments

We thank Sathyaprakash Bangalore, Enrico Barausse, José Luis Bernal, Anna Bonaldi, Yacine Ali-Haïmoud, Ely Kovetz, Julien Lesgourgues, Antonio Riotto and Matteo Viel for comments on the draft. We also thank Stefano Camera, Neal Dalal, Vincent Desjacques, Raul Jimenez and Sergey Sibiryakov for discussion. Funding for this work was partially provided by the Spanish MINECO under projects AYA2014-58747-P AEI/FEDER, UE, and MDM-2014-0369 of ICCUB (Unidad de Excelencia María de Maeztu). NB is supported by the Spanish MINECO under grant BES-2015-073372. GS was supported by the Erasmus+ for Trainership grant during the early stages of this work, subsequently by grant from the "Maria de Maeztu de Ciències del Cosmos" project mentioned above. AR has received funding from the People Programme (Marie Curie Actions) of the European Union H2020 Programme under REA grant agreement number 706896 (COSMOFLAGS). SM acknowledges partial financial support by ASI Grant No. 2016-24-H.0. LV acknowledges support by European Union's Horizon 2020 research and innovation programme ERC (BePreSySe, grant agreement 725327). LV acknowledges the Radcliffe Institute for Advanced Study of Harvard University for hospitality during the latest stages of this work.

References

[1] Aasi, J., Abbott, B.P., Abbott, R., et al. 2015, CQG, 32, 074001

[2] Abbott, B. P., Abbott, R., Abbott, T. D., et al. 2016, PRL, 116, 241103

[3] Abbott, B. P., Abbott, R., Abbott, T. D., et al. 2016, PRX, 6, 041015

[4] Aghamousa, A., Aguilar, J., Ahlen, S., et al. 2016

[5] Belczynski, K., Bulik, T., Fryer, L., et al. 2010, ApJ, 714, 1217

[6] Belczynski, K., Dominik, M., Bulik, T., et al. 2010, ApJ, 715, L138

[7] Bellomo, N., Bernal, J. L., Raccanelli, A. et al. 2018, JCAP, 01, 004

[8] Bellomo, N., Bernal, J. L., Scelfo, G., et al. 2018, in prep.

[9] Bird, S., Cholis, I., and Muñoz, J. B., et al. 2016, PRL, 116, 201301

[10] Blas, D., Lesgourgues, J., Tram, T. 2011, JCAP, 07, 034

[11] Bonaldi, A., Bonato, M., Galluzzi, V., et al. 2019, MNRAS, 482, 2

[12] Bonvin, C., Durrer, R. 2011, PRD, 84, 063505

[13] Di Dio, E., Montanari F., Lesgourgues, J., et al. 2013, JCAP, 11, 044

[14] Erb, D. K. 2015, Nature, 523, 169

[15] Hawking, S. 1971, MNRAS, 152, 75

[16] Hui, L., Gaztañaga, E., LoVerde, M. 2007, PRD, 76, 103502

[17] Mapelli, M., Giacobbo, N., Ripamonti, E., et al. 2017, MNRAS, 472, 2422

[18] Maartens, R., Abdalla, F. B., Jarvis, M., et al. 2015

[19] Mo, H. J., White, S. D. M. 1996, MNRAS, 282, 347

[20] Musco, I., Miller, J. C., Rezzolla, L. 2005, CQG, 22, 1405

[21] Namikawa, T., Nishizawa, A., Taruya, A. 2016, PRL, 116, 121302

[22] Norris, R. P., Hopkins, A. M., Afonso, J., et al. 2011, PASA, 28, 215

[23] Raccanelli, A., Bonaldi, A., Negrello, M., et al. 2008, MNRAS, 386, 2161

[24] Raccanelli, A., Kovetz, E. D., Bird, S., et al. 2016, PRD, 94, 023516

[25] Raccanelli, A., Zhao, G.-B., Bacon, D. J., et al. 2012, 424, 801

[26] Sasaki, M., Suyama, T., Tanaka, T. et al. CQG, 35, 063001

[27] Sathyaprakash, B., Abernathy, M., Acernese, F., et al. 2012, CQG, 29, 124013

[28] Scelfo, G., Bellomo, N., Raccanelli, A., et al. 2018, JCAP, 09, 039

[29] Somiya, K. 2012, CQG, 29, 124007

[30] Turner, E. L., Ostriker, J. P., Gott III, J. R. 1984, ApJ, 284, 1

[31] Unnikrishnan, C. S. 2013, IJMPD, 22, 1341010

Highlights on Spanish Astrophysics X, Proceedings of the XIII Scientific Meeting of the Spanish Astronomical Society held on July 16 – 20, 2018, in Salamanca, Spain. B. Montesinos, A. Asensio Ramos, F. Buitrago, R. Schödel, E. Villaver, S. Pérez-Hoyos, I. Ordóñez-Etxeberria (eds.), 2019

Signatures of primordial black holes as seeds of supermassive black holes.

José Luis Bernal[1,2], Alvise Raccanelli[1,3], Licia Verde[1,4] and Joseph Silk[5,6,7]

[1] Institut de Ciències del Cosmos (ICCUB), Universitat de Barcelona (IEEC-UB), Martí Franquès 1, E08028 Barcelona, Spain
[2] Dept. de Física Quàntica i Astrofísica, Universitat de Barcelona, Martí i Franquès 1, E08028 Barcelona, Spain
[3] Theoretical Physics Department, CERN, 1 Esplanade des Particules, CH-1211 Geneva 23, Switzerland
[4] ICREA, Pg. Lluís Companys 23, 08010 Barcelona, Spain
[5] Department of Physics and Astronomy, Johns Hopkins University, 3400 N. Charles St., Baltimore, MD 21218
[6] Institut d'Astrophysique de Paris, UMR 7095, CNRS, UPMC Univ. Paris VI, 98 bis Boulevard Arago, 75014 Paris, France
[7] BIPAC, Department of Physics, University of Oxford, Keble Road, Oxford OX1 3RH, UK

Abstract

It is broadly accepted that Supermassive Black Holes (SMBHs) are located in the centers of most massive galaxies, although there is still no convincing scenario for the origin of their massive seeds. It has been suggested that primordial black holes (PBHs) of masses $\gtrsim 10^2\ M_\odot$ may provide such seeds, which would grow to become SMBHs. We suggest an observational test to constrain this hypothesis: gas accretion around PBHs during the cosmic dark ages powers the emission of high energy photons which would modify the spin temperature as measured by 21cm Intensity Mapping (IM) observations. We model and compute their contribution to the standard sky-averaged signal and power spectrum of 21cm IM, accounting for its substructure and angular dependence for the first time. While SKA could provide a detection, only a more ambitious experiment would provide accurate measurements.

1 Introduction

We know that Supermassive Black Holes (SMBHs) inhabit the centers of most galaxies: observations of quasars at $z \sim 6-7$ indicate that, even at these early times, there were SMBHs with masses of several $10^9 M_\odot$ (e.g., [2]). The existence of a population of intermediate mass black holes of masses around $10^2 - 10^6 M_\odot$ at $z \sim 20-15$ would suffice to seed them. However, the origin and formation mechanism of the massive seeds are still uncertain. There are two main scenarios proposed to explain their origin.

According to the first hypothesis, the seeds of SMBHs are remnants of Population III stars, formed with masses of tens of solar masses at $z \gtrsim 20$, which grow due to gas accretion and mergers. However, in order to reach masses such as those observed at $z \sim 6-7$, supercritical accretion over extended periods of time is needed [7]. However, cosmic X-ray background observations impose constraints on the growth of SMBHs, constraining the abundance of quasars with supercritical accretion and miniquasars at high redshift [9].

On the other hand, SMBH seeds might also be formed due to the collapse of gas clouds which do not fragment or form ordinary stars, but directly form a massive black hole ($M \sim 10^5 - 10^6 M_\odot$) at lower redshifts ($z \lesssim 15$) [6]. This kind of seed is called a Direct Collapse Black Hole (DCBH). Moreover, DCBHs are a good candidate for explaining the large-scale power spectrum of the Near Infrared Background and its cross correlation with the cosmic X-ray background [10], and there are candidates of possible detections. Nonetheless, the exact conditions and the probability of obtaining DCBHs are still uncertain; recent theoretical studies suggest that this mechanism might explain the abundance of the most luminous quasars at $z \sim 6-7$, but not the general population of SMBHs.

In summary, neither of these two scenarios individually provide an entirely convincing explanation for the origin of the seeds of SMBHs. However, Primordial Black Holes (PBHs) might be the seeds which will grow to become SMBHs. The mass range required for PBHs to be the seeds of SMBHs without requiring supercritical accretion is $\gtrsim 10^2 M_\odot$. In this mass range, the PBH abundance, $f_{\rm PBH} = \Omega_{\rm PBH}/\Omega_{\rm CDM}$, is strongly constrained by e.g., CMB observations [1, 4]. However, if PBHs of these masses are only required to be the seeds of SMBHs and not a substantial part of the dark matter, $f_{\rm PBH} \sim 10^{-8} - 10^{-6}$ (which satisfies all observational constraints) is enough.

In this work, we focus on the imprints of PBHs as seeds of SMBHs on 21 cm Intensity Mapping (IM). Observations of spin temperature maps in the dark ages provide a direct window into the matter density fluctuations free of complications such as galaxy bias and most astrophysical processes. Therefore, in order to avoid astrophysical uncertainties, we concentrate on the dark ages ($z \gtrsim 30$). Besides, if massive seeds are to be found in these redshifts, they must be primordial. We model the signature of massive PBHs, with abundances required to explain the current SMBH population in the 21 cm IM signal. We compute 2-point statistics of the fluctuations accounting explicitly for the brightness temperature (T_{21}) profiles around the PBHs in a comprehensive way, for the first time. The work and results reported on this Proceeding are collected more complete and with further discussion in [5].

2 Effects of PBHs on the 21cm IM signal

The presence of PBHs affects the gas spin temperature: the PBH accretion triggers the emission of high-energy photons which heat and ionize the gas around. We assume that all processes are in equilibrium, given that their timescales are much smaller than the Hubble

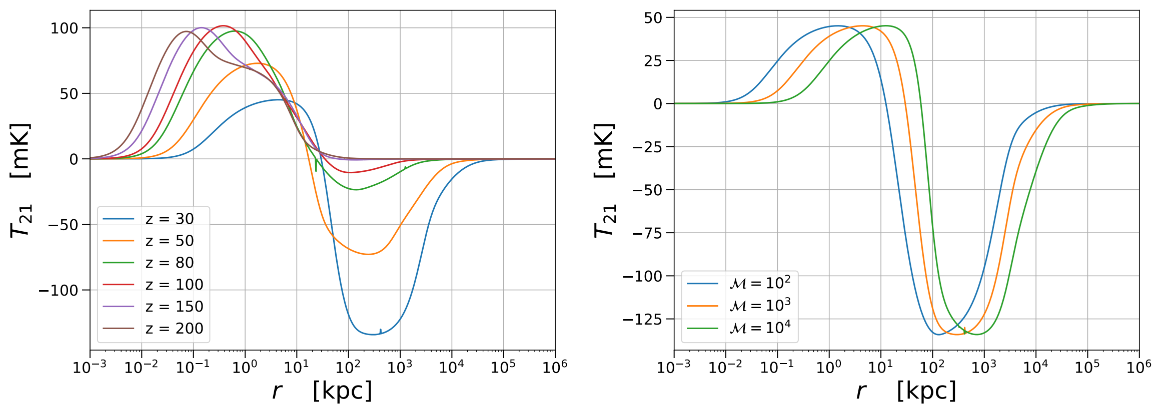

Figure 1: Differential brightness temperature profile for a PBH with $\mathcal{M} = 100$ at various redshifts (left) and for a PBH with various values of $\mathcal{M}$ at $z = 30$ (right).

timescale. The steady-state approximation is very precise for masses $M \lesssim 3 \times 10^4 M_\odot$ [8], so we limit our exploration to $M \leq 10^4 M_\odot$. Given the slow growth of the PBHs at $z \gtrsim 30$, we assume that the PBH mass at different redshifts is the same. Finally, we consider for simplicity that all PBHs have the same mass. This is an unrealistic scenario, but constraints for monochromatic mass distributions can be translated to any extended mass distribution using e.g., the methods proposed in [3].

We assume that gas accretion around the PBH powers a spherically symmetric X-ray emission, $F(E) = \mathcal{A}(M\lambda)\, E^{-1}\mathrm{s}^{-1}$, where $\mathcal{A}$ is a normalization factor chosen to have a luminosity $L = \lambda L_{\mathrm{Edd}}$, where λ is the Eddington ratio and L_{Edd} is the Eddington luminosity. Relevant quantities, as the neutral fraction, x_H, or T_{21}, only depend on the redshift and the intensity of the emission. Therefore, in order to illustrate how these quantities depend on both λ and M, we will show them in terms of $\mathcal{M} = M\lambda$.

The ionized and heated region around the PBH changes with redshift and $\mathcal{M}$. With increasing redshift, the hydrogen density increases; in a given volume at fixed photon flux, there are more atoms to ionize, hence the size of the ionized region decreases. On the other hand, for larger $\mathcal{M}$, as the PBH emission is more intense, the ionized region becomes larger. In the inner regions, the heating due to the emission of the PBH is coupled only to the neutral hydrogen, but, as the number of photons decays exponentially with the distance, this heating is more efficient close to the PBH. At intermediate distances, PBH heating loses efficiency and T_k drops even below the CMB temperature.

Due to the modified neutral fraction and kinetic temperature of the gas, a bubble with spin temperature, hence T_{21}, different from the background value is formed around the PBH. The $T_{21}(r)$ profile shown in 1 can be explained as follows. In the inner part, $T_{21} = 0$ because all of the gas is ionized. The region with $T_{21} > 0$ corresponds to the region where $T_k > T_{\mathrm{CMB}}$ and x_H starts to grow; then, where T_k drops because the PBH heating is less efficient, T_{21} drops to negative values. Finally, T_{21} rises again due to the collisional and Lyman-α coupling of the photons to the source with the gas becomes totally inefficient. Given that we consider the isolated PBH signal, at these distances, $T_{21} = 0$.

3 PBH contribution to the power spectrum

We use the halo model to characterize the total T_{21} angular power spectrum during the dark ages in the presence of PBHs: $C_\ell^{\rm PBH} = C_\ell^{\rm PBH(1h)} + C_\ell^{\rm PBH(2h)}$. We compute the observed fluctuations on T_{21} produced by a population of PBHs with number density $n_{\rm PBH}$. As the standard contribution in the linear regime without the PBHs comes from a continuum where there are no haloes, we consider that the one-halo term of the standard contribution vanishes. Therefore, the total angular power spectrum is the sum of:

$$C_\ell^{\rm PBH(1h)} = \frac{2}{\pi} n_{\rm PBH} \int_0^\infty dk k^2 \, \left(\mathcal{T}_\ell^{\rm PBH}\right)^2; \; C_\ell^{\rm PBH(2h)} = \frac{2}{\pi} \int_0^\infty dk k^2 \, \left(\mathcal{T}_\ell + n_{\rm PBH} b \mathcal{T}_\ell^{\rm PBH}\right)^2 P_m(k), \tag{1}$$

where $\mathcal{T}_\ell$ and $\mathcal{T}_\ell^{\rm PBH}$ are the transfer function for the 21 cm IM fluctuations due to the standard contribution and the PBHs, respectively, $P_m(k)$ is the matter power spectrum, b is a scale-independent bias, and we assume that PBHs are completely correlated with the dark matter distribution. Given that the formation of a PBH is a rare event and PBHs spatial distribution is discrete, there is a Poissonian fluctuation in the number density of PBHs. Therefore, in addition to the standard matter power spectrum, there is an extra contribution, $P_{\rm Poisson}(z) = \frac{9}{4}(1+z_{\rm eq})^2 D^2(z) \frac{f_{\rm PBH}^2}{n_{\rm PBH}}$, where $D(z)$ is the growth factor.

It is easy to notice that the PBH contribution depends only on two quantities besides the redshift: $n_{\rm PBH}$ and $\mathcal{T}_\ell^{\rm PBH}$. Therefore, although we do consider three parameters regarding PBHs (M, λ and $\Omega_{\rm PBH}$), the relevant quantities are combinations of them: $\mathcal{M} = M\lambda$ and $n_{\rm PBH} \propto \Omega_{\rm PBH}/M$. Essentially, varying $\mathcal{M}$ shifts the features related with PBHs to different multipole ranges (via $\mathcal{T}_\ell^{\rm PBH}$). The latter is a rescaling of the amplitude of such contributions. These two effects are relevant to determine at which scale the PBH contribution starts to dominate. We show how the total angular power spectrum changes with respect to the PBH parameters and the redshift in Figure 2. As can be seen, the PBH-induced deviation from the standard signal decreases with redshift because the size of the bubble also does it (see Figure 1), so the scale at which the deviation is appreciable increases.

4 Conclusions

The origin and formation mechanism of SMBHs remains largely unknown. There are three candidates to be the seeds of SMBHs: remnants of Population III stars, DCBHs or PBHs. In this work, we address the observational signatures that intermediate mass PBHs would have on 21 cm IM during the dark ages. We model this signal starting from the characterization of the radial profiles of T_{21} around a single PBH to compute the contribution to the angular power spectrum, using the halo model. This is the first time that the signature of PBHs

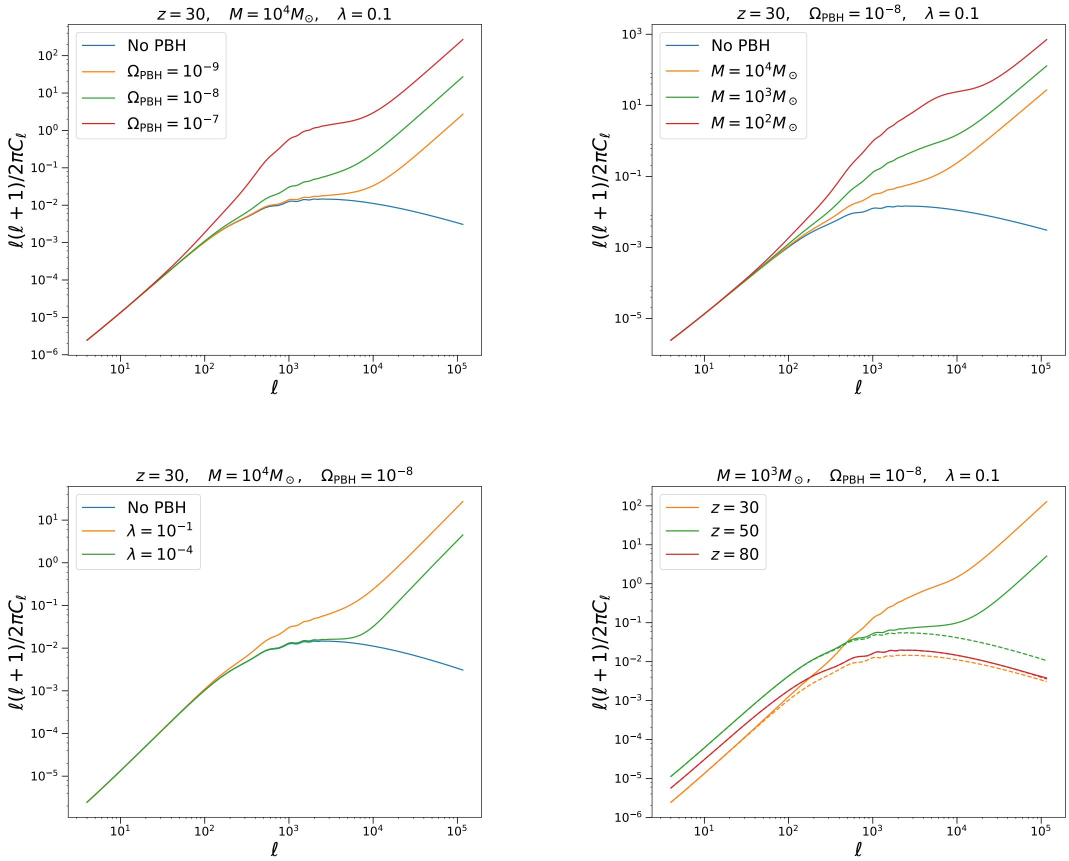

Figure 2: Angular power spectrum of the total signal in 21 cm IM at $z = 30$ varying the the density parameter of PBH (top left), the mass (top right) and the Eddington ratio (bottom left), and varying redshift for $M = 10^3 M_\odot$, $\Omega_{\rm PBH} = 10^{-8}$, $\lambda = 0.1$ (bottom right).

accounting for its full scale dependence is modeled in the 21 cm IM power spectrum. We consider several configurations of the PBH parameters, since they are largely unconstrained.

The presence of PBHs increases the amplitude of the 21 cm IM angular power spectrum for $\ell \gtrsim 10^2 - 10^3$, which decays with redshift. We forecast the detectability of the PBH contribution and the potential to measure the PBH parameters by future experiments, ranging from SKA to more ambitious futuristic ground experiment, as well as radio array in the far side of the Moon. Given that the atmosphere is opaque for frequencies $\lesssim 45$ MHz, a ground experiment will not be able to observe much further than $z \approx 30$; however, with the lunar radio arrays, tomography for $30 \lesssim z \lesssim 200$ is possible. The PBH signal will be barely detected by SKA, since only for extreme cases in which $n_{\rm PBH}$ is very large, the signal-to-noise ratio, S/N, for $\Omega_{\rm PBH}$ and λ is larger than unity. As the amplitude of the power spectrum increases greatly at small scales, being able to resolve very small scales (i.e., large interferometer baseline, which implies large $\ell_{\rm cover}$) will be key to detect the PBH signal and constrain the parameters. On the other hand, the contribution of PBHs to the power spectrum decays with redshift (see Figure 2), hence the S/N between the case with PBHs and the standard one decreases fast with redshift. As tomography does not add much information, $\ell_{\rm cover}$ has more impact in the final S/N

To summarize, although a detection of the PBH contribution in the dark ages might be achieved by SKA, in order to measure $\Omega_{\rm PBH}$ and λ accurately, a more ambitious experiment with a larger baseline is needed. Such measurements will be more precise if tomography is possible, for which experiments such as a lunar radio array are needed.

The advent of new experiments and corresponding observations will shed light on how SMBHs reached such huge masses and on the nature of the massive seeds needed to explain their existence. It is also possible that the three kinds of seeds discussed above coexist and give different signatures. We eagerly await observations that will open the window toward higher redshifts and will give us the opportunity to improve our understanding of some of the most extreme structures in the Universe.

Acknowledgments

Funding for this work was partially provided by the Spanish MINECO under projects AYA2014-58747-P AEI/FEDER UE and MDM-2014-0369 of ICCUB (Unidad de Excelencia Maria de Maeztu). JLB is supported by the Spanish MINECO under grant BES-2015-071307, co-funded by the ESF and thanks the Royal Observatory of Edinburgh for hospitality. AR has received funding from the People Programme (Marie Curie Actions) of the European Union H2020 Programme under REA grant agreement number 706896 (COSMOFLAGS). LV acknowledges support of European Union's Horizon 2020 research and innovation programme ERC (BePreSySe, grant agreement 725327).

References

[1] Ali-Haimoud, Y. & Kamionkowski, M., 2017, PRD, 95, 043534

[2] Bañados, E. et al. 2018, Nature, 553, 473

[3] Bellomo, N., Bernal, J. L., Raccanelli, A., Verde, L., 2018, JCAP01(2018)004

[4] Bernal, J. L., Bellomo, N., Raccanelli, A., Verde, L., 2017, JCAP10(2017)052

[5] Bernal, J. L., Raccanelli, A., Verde, L., Silk, J., 2018, JCAP05(2018)017

[6] Bromm, V. & Loeb, A., 2003, ApJ 596, 34

[7] Inayoshi, K., Haiman, Z., Ostriker, J. P., 2016, MNRAS, 459, 3738

[8] Ricotti, M., 2007, ApJ, 662, 53

[9] Salvaterra, R., Haardt, F., Volonteri, M., Moretti, A., 2012, A&A, 545, L6

[10] Yue, B., Ferrara, A., Salvaterra, R., Xu, Y., Chen, X., 2013, MNRAS 433, 1556

Highlights on Spanish Astrophysics X, Proceedings of the XIII Scientific Meeting of the Spanish Astronomical Society held on July 16 – 20, 2018, in Salamanca, Spain. B. Montesinos, A. Asensio Ramos, F. Buitrago, R. Schödel, E. Villaver, S. Pérez-Hoyos, I. Ordóñez-Etxeberria (eds.), 2019

Thick discs in galaxies were most likely not accreted.

Sébastien Comerón[1], Heikki Salo[1], Johan H. Knapen[2,3,4] and Reynier F. Peletier[5]

[1] University of Oulu, Astronomy Research Unit, P.O. Box 3000, FI-90014 Oulu, Finland
[2] Instituto de Astrofísica de Canarias E-38205, La Laguna, Tenerife, Spain
[3] Departamento de Astrofísica, Universidad de La Laguna, E-38205, La Laguna, Tenerife, Spain
[4] Astrophysics Research Institute, Liverpool John Moores University, IC2, Liverpool Science Park, 146 Brownlow Hill, Liverpool, L3 5RF, UK
[5] Kapteyn Astronomical Institute, University of Groningen, P.O. Box 800, NL-9700 AV Groningen, the Netherlands

Abstract

The origin of thick discs in galaxies remains shrouded in mystery. A variety of formation scenarios has been proposed. Here we aim to test one such scenario where the thick disc stars are proposed to be accreted from satellite galaxies. In this scenario, in at least some galaxies a fraction of thick disc stars would rotate in a retrograde way, which would cause a large thick disc velocity lag. Here, we compare the rotation curves of the thin and the thick discs of eight edge-on galaxies observed with MUSE at the VLT. We find that the velocity lags of the thick discs are compatible with those expected from asymmetric drift. If we consider the galaxies with thick disc rotation curves in the literature, only one in about fifteen shows clear signs of an accreted thick disc. Based on simulations in the literature we estimate that if thick discs were accreted, at least one in six would show clear signs of retrograde material. Thus, there is a growing tension between the observations and the hypothesis that thick discs are made of accreted stars.

1 Introduction

The formation and early evolution epoch of galaxies is hard to study due to observational issues such as cosmological dimming and the lack of means to properly resolve objects at large angular diametre distance. An alternative approach to unveil how galaxies evolved is to study with an exquisite level of detail the oldest stars in local objects and deduce their origin (this approach is called galactic archæology). The oldest stars of a galaxy are typically found in the halo and in the thick disc. In this paper we will focus on the thick discs to advance in our understanding of galaxy evolution.

In edge-on galaxies thick discs are seen as roughly exponential excesses of light that become apparent a few thin disc scale-heights above the mid-plane. They contain a significant fraction of the baryons in a galaxy and, in low-mass galaxies, can be as massive as the thin discs[30, 6, 7, 10].

The origin of thick discs has been a source of debate. Some authors have argued for an internal origin of the thick disc stars. Either a pre-existing thin disc would have been thickened by dynamical heating[28, 23, 24, 19], or the thick disc would have been born thick in an early phase of the galaxy evolution when the interstellar medium was very turbulent and the specific star formation rate was much larger than it is nowadays[12, 2, 8]. Alternatively, the thick discs could have been accreted through minor mergers[1].

The stars of the Milky Way thick disc are now known to be mostly of internal origin[22, 18, 15]. However, it is known that at least one external thick disc – that in FGC 227 – has stellar rotation velocities close to zero[29], which implies that about half of the light is emitted by retrograde stars. This strongly suggests an external origin for a large fraction of its thick disc stars. Unfortunately, the number of thick disc rotation curves in the literature is small – about ten[29, 30, 9, 11, 14, 16] –, so it is not possible to say whether the case of FGC 227 is unique or not.

Here we aim to obtain additional thick disc rotation curves to determine whether accretion is a plausible origin for the majority of stars in thick discs.

2 Sample, observations, and data processing

We observed eight nearby edge-on galaxies with MUSE at the VLT. MUSE is an integral field unit with a $1' \times 1'$ field of view and a simultaneous wavelength coverage between 4750 Å and 9300 Å. All the observed galaxies had previously been observed within the *Spitzer* Survey of Stellar Structure in Galaxies (S^4G)[25] and have photometric decompositions available in 3.6μm[10]. The selected galaxies are relatively small with circular velocities below $180\,\mathrm{km\,s^{-1}}$. All but one are bulgeless.

The galaxies were exposed for almost three hours. They were reduced using the standard ESO pipelines. We used `ZAP`[26] to remove the sky residuals. The datacubes where Voronoi-binned[3] to a signal-to-noise ratio of $S/N \sim 25$ in the wavelength range between 5490 Å and 5510 Å. Then `PPXF`[4] was applied to the spectra obtained for each Voronoi bin. `PPXF` fits the spectra with a linear combination of spectral energy distribution templates and obtains the line of sight velocity distribution. We used the templates from the MIUSCAT library[27]. The templates and the spectra where Gauss-convolved to match their spectral full width at half maximum at every wavelength.

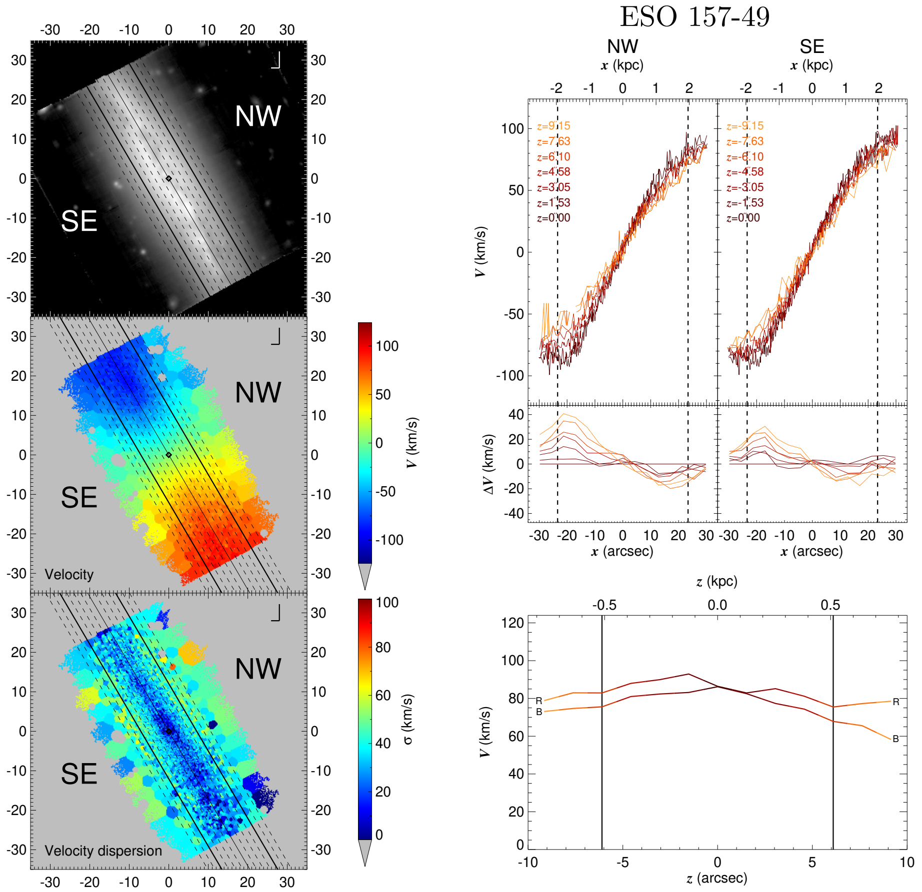

Figure 1: *Top-left:* Image of ESO 157-49. *Middle-left:* Velocity map of ESO 157-49. *Bottom-left:* Velocity dispersion map of ESO 157-49. The values in the axes are in arcseconds. North is up and East is left (shown by the reverse-L symbol). The lines parallel to the mid-plane denote the heights for which the rotation curves (*top-right* panels) were computed. The thin continuous line indicates the mid-plane and the thick continuous lines indicate the height where the thick disc starts to dominate the surface brightness[10]. The *middle-right* panels show the difference between the velocity at a given height and that at the mid-plane. The dashed vertical lines indicate where the rotation curve becomes flat. The *bottom-right* panel shows the velocity as a function of height for the flat part of the rotation curve for the blue-shifted and red-shifted sides of the galaxy (indicated by "B" and "R", respectively). The vertical lines indicate the height above which the thick disc dominates the surface brightness.

3 Results

We produced velocity and velocity dispersion maps for the eight galaxies in our sample. We used the velocity maps to compute rotation curves at different heights above and below the mid-planes. In Fig. 1 we show the maps and the rotation curves extracted for ESO 157-49.

In Fig. 2 we show, for the eight galaxies in our sample, the circular velocity as a function of height for the regions where the rotation curve of the galaxies is flat. We find

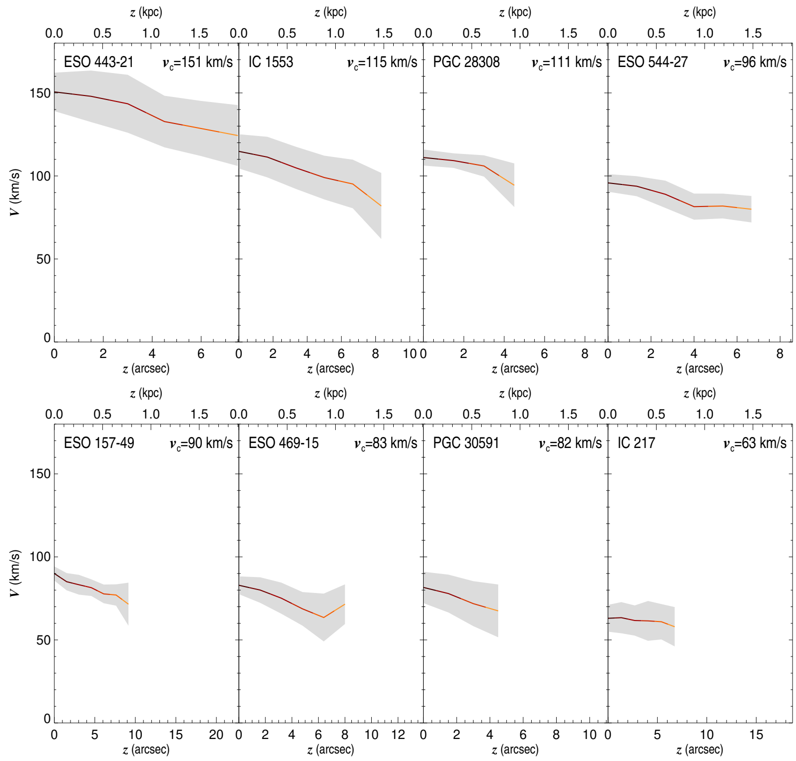

Figure 2: Velocity as a function of height for the flat part of the rotation curve for the galaxies in our sample. The horizontal axes are scaled so all the plots cover the same height range. The grey bands indicate the dispersion in the velocity for the Voronoi bins used to compute each data point. The maximum velocity at the mid-plane is denoted by v_c.

that the maximum velocity is lower at increasing distances from the mid-plane, with a lag at large heights of a few tens of kilometres per second for all the galaxies in the sample. This is compatible with the combined effects of asymmetric drift and a not perfectly edge-on orientation. Indeed, in the past we have shown that retrograde thick disc fractions larger than $10-20\%$ would result in lags larger than those that we detect[9]. Also, large retrograde material fractions would result in a velocity dispersion comparable to the circular velocity of the galaxy, v_c. Therefore, our data indicate a very small fraction – compatible with zero – of retrograde stars in the thick discs. We shall however note that only five out of our eight galaxies have massive thick discs that dominate the luminosity at some of the observed height range[10].

4 Discussion and conclusions

Our observations increase the number of available thick disc rotation curves to about fifteen. Only one of them (FGC 227[29]) shows clear evidence for retrograde stars. One may thus naively conclude that accreted thick discs are rare. This is, however, not necessarily true because accretion is more efficient for prograde encounters than it is for retrograde ones. The reason for that is how dynamical friction works. Dynamical friction in its linear regime acts over an infalling satellite as described by the Chandrasekhar formula[5]

$$F \propto \mathcal{M}^2 \rho / V^2, \tag{1}$$

where $\mathcal{M}$ is the mass of the satellite, ρ the density of the main galaxy, and V the relative velocity between the satellite and the particles of the main galaxy. When the satellite is far away from the disc of the main galaxy, V does not depend on whether the merger is prograde or retrograde because the dark matter halo is pressure-supported and, hence, has a mean velocity of zero. However, as the satellite falls and becomes influenced by the disc, prograde objects feel a larger force than retrograde ones. The detailed calculation on the decay times of satellites requires numerical simulations, and it can be estimated that a retrograde satellite takes at most two times longer than a prograde one to be accreted[20]. Given a halo merger rate proportional to $\propto (1+z)^2$[13], isotropic accretion, and a galaxy age of 10 Gyr, we obtain that about a third of the satellites accreted by now had retrograde orbits.

Another effect to be taken into account is in-plane dragging. Prograde satellites with orbital inclinations smaller than $i = 20^{\rm o}$ are dragged into the plane of the main galaxy by dynamical friction and dissolve into the thick disc[21]. Satellites with larger incoming inclinations dissolve into the inner halo. The effect of in-plane dragging is diminished for retrograde satellites and we estimate that only those with inclinations smaller than $i = 10^{\rm o}$ are accreted into the thick disc. Hence, an accreted retrograde satellite is two times less likely to end in a thick disc than a prograde satellite.

In summary: 1) one third of the satellites accreted by now by disc galaxies were retrograde and 2) a retrograde merger is two times less likely to contribute to a thick disc than a prograde one. This implies that in the limit where all thick discs have been created in single merger events, we expect $\sim 1/6$ of the thick discs to be retrograde. However, the observed figure is $\sim 1/15$. Hence, our results point to a tension between the observations and the hypothesis of accreted thick discs. If thick discs were created in a small number of mergers (two or three), the tension would worsen. We can therefore conclude that an accretion origin for thick discs is not favoured by the observations.

Acknowledgments

SC and HS acknowledge support from the Academy of Finland. HS, JHK, and RFP acknowledge financial support from the European Union's Horizon 2020 research and innovation programme under Marie Skłodowska-Curie grant agreement No. 721463 to the SUNDIAL ITN network. JHK acknowledges additional support from the Spanish Ministry of Economy and Competitiveness (MINECO) under grant number AYA2016-76219-P, as well as from the Fundación BBVA under its 2017 programme of assistance to scientific research groups, for the project "Using machine-learning techniques to drag galaxies from the noise in deep imaging", and from the Leverhulme Trust through the award of a Visiting Professorship at LJMU.

References

[1] Abadi, M. G., Navarro, J. F., Steinmetz, M., et al. 2003, ApJ, 597, 21

[2] Bournaud, F., Elmegreen, B. G., & Martig, M. 2009, ApJ, 707L, 1

[3] Cappellari, M., & Copin, Y. 2003, MNRAS, 342, 354

[4] Cappellari, M., & Emsellem, E. 2004, PASP, 116, 1

[5] Chandrasekhar, S. 1943, ApJ, 97, 255

[6] Comerón, S., Elemgreen, B. G., Knapen, J. H., et al. 2011, ApJ, 741, 28

[7] Comerón, S., Elemgreen, B. G., Salo, H., et al. 2012, ApJ, 759, 98

[8] Comerón, S., Elemgreen, B. G., Salo, H., et al. 2014, A&A, 571, 58

[9] Comerón, S., Salo, H., Janz, J., et al. 2015, A&A, 584, 34

[10] Comerón, S., Salo, H., Knapen, J. H. 2018, A&A, 610, 5

[11] Comerón, S., Salo, H., Peletier, R. F., et al. 2015, A&A, 593L, 6

[12] Elmegreen, B. G., & Elmegreen, D. M. 2006, ApJ, 650, 644

[13] Fakhouri, O. & Ma, C.-P. 2008, MNRAS, 386, 577

[14] Guérou, A., Emsellem, E., Krajnović, D. 2016, A&A, 591, 143

[15] Haywood, M., Di Matteo, P., Snaith, O., et al. 2015, A&A, 579, 5

[16] Kasparova, A. V., Katkov, I. Y., Chilingarian, I. 2016, 460L, 89

[17] Kazantzidis, S., Bullock, J. S., Zentner, A. R., et al. 2008, ApJ, 688, 254

[18] Lehnert, M. D., Di Matteo, P., Haywood, M., et al. 2014, ApJ, 789L, 30

[19] Loebman, S. R., Roŝkar, R., Debattista, V. P, et al. 2011, ApJ, 737, 8L

[20] Peñarrubia, J., Kroupa, P., & Boily, C. M. 2002, MNRAS, 333, 779

[21] Read, J. I., Lake, G., Agertz, O., et al. 2008, MNRAS 389, 1041

[22] Ruchti, G. R., Read, J. I., Feltzing, S., et al. 2014, MNRAS, 444, 515

[23] Scönrich, R., & Binney, J. 2009, MNRAS, 396, 203

[24] Scönrich, R., & Binney, J. 2009, MNRAS, 399, 1145

[25] Sheth, K., Regan, M., Hinz, J. L. 2010, PASP, 122, 1397

[26] Soto, K., Lilly, S. J., Bacon, R., et al. 2016, MNRAS, 458, 3210

[27] Vazdekis, A., Ricciardelli, E., Cenarro, A. J., et al. 2012, MNRAS, 424, 157

[28] Villumsen, J. V. 1985, ApJ, 290, 75

[29] Yoachim, P., & Dalcanton, J. J. 2005, ApJ, 624, 701

[30] Yoachim, P., & Dalcanton, J. J. 2006, AJ, 131, 226

Highlights on Spanish Astrophysics X, Proceedings of the XIII Scientific Meeting of the Spanish Astronomical Society held on July 16 – 20, 2018, in Salamanca, Spain. B. Montesinos, A. Asensio Ramos, F. Buitrago, R. Schödel, E. Villaver, S. Pérez-Hoyos, I. Ordóñez-Etxeberria (eds.), 2019

Correlations between the size and the stellar population properties of quiescent galaxies.

L. A. Díaz-García[1,2], A. J. Cenarro[1], and C. López-Sanjuan[1]

[1] Centro de Estudios de Física del Cosmos de Aragón (CEFCA), Plaza San Juan 1, Floor 2, E–44001, Teruel, Spain. E-mail: ladiaz@asiaa.sinica.edu.tw

[2] Academia Sinica Institute of Astronomy & Astrophysics (ASIAA), 11F of Astronomy-Mathematics Building, AS/NTU, No. 1, Section 4, Roosevelt Road, Taipei 10617, Taiwan

Abstract

We aim to state new constraints on the mechanisms that can drive the growth in size of massive galaxies through the stellar population properties of quiescent galaxies within the stellar mass–size plane. Our sample is composed of ~ 830 quiescent galaxies down to $I \leq 23$ from the ALHAMBRA survey with reliable size measurements up to redshift $z \sim 1$. The stellar content (age, metallicity, and extinction) of galaxies is retrieved via SED-fitting and composite stellar population models using the multi-band photometry of ALHAMBRA and the code MUFFIT. At fixed stellar mass, our results point out that more compact quiescent galaxies are older, more rich in metals, and slightly less reddened by dust than their more extended counterparts since $z \sim 1$. We state that the regions of constant stellar population parameters in the stellar mass–size plane are well reproduced by lines of the form $M_\star \propto r_{\mathrm{c}}^{0.5-0.6}$, which are also compatible with constant values of velocity dispersion using spectroscopic quiescent galaxies from SDSS. This result points out that the driver of stellar populations would be partly related to dynamical properties of galaxies, as well as to stellar mass. Scenarios including mergers or the "progenitor" bias also agree with these results to explain the growth in size of quiescent galaxies.

1 Introduction

As revelead in previous studies, there are tight correlations between the stellar mass of galaxies and their stellar population properties (see e. g. [15, 25, 8] and references in these works). In general, more massive galaxies exhibit older stellar populations (usually referred as the "downsizing" scenario, e. g. [7]), that are also more rich in metals (stellar mass metallicity correlation or MZR, e. g. [15]) than their less massive counterparts. Nevertheless, other parameters such as the stellar surface density or velocity dispersions also present remarkable correlations with the stellar content of galaxies (e. g. [26, 18, 14, 4]). Consequently, it is still matter of debate which is the driver of the stellar content of galaxies.

Recently, many studies have revealed that massive spheroids/quiescent galaxies has grown in size a factor of 4 since redshift $z \sim 2$, whereas since $z \sim 1$ has doubled in size (e. g. [27, 31, 29]). Although this fact has been widely studied, there is no consensus about which is the mechanism responsible for this strong growth in size. Among the mechanisms proposed in the literature, the more promising ones are: i) Mergers (e. g. [21]), the accretion of less massive galaxies at lower redshifts via mergers would produce an increase in size. ii) The "puffing-up" scenario (e. g. [12]) or a redistribution of the stellar content of galaxies via AGN or quasar feedbacks. iii) The "progenitor" bias (e. g. [30, 28]) or the arrival of new and larger members to the red population.

A detailed study of the distribution of stellar population parameters of quiescent within the stellar mass–size plane (MSP) at different redshifts may constrain the mechanism responsible for the growth in size, as well as to shed light on the mechanisms driving the evolution and assembly of galaxies. For this reason, we explore the stellar content of the quiescent galaxies from the ALHAMBRA survey[1] ([19]) as a function of their sizes. Throughtout the present study, we assume a ΛCDM cosmology with $H_0 = 71$ km s^{-1} , $\Omega_{\rm M} = 0.27$, and $\Omega_\Lambda = 0.73$. Stellar masses are given in solar mass units [$\rm M_\odot$] and magnitudes in AB-system [22].

2 Sample of quiescent galaxies from the ALHAMBRA survey

Our reference catalogue is the sample of quiescent galaxies published by [9], which was obtained by an optimized rest-frame colour-mass diagram corrected for extinction. This catalogue is complete in stellar mass and provides mass-weighted formation epochs, ages, metallicities, extinctions, stellar masses, and redshifts for $\sim 8\,500$ quiescent galaxies at $0.1 \leq z \leq 1.1$ from the ALHAMBRA survey. This survey was acquired at the 3.5 m telescope of the Calar Alto Observatory[2] (CAHA) and comprises 20 top-hat medium bands in the optical range ($\lambda\lambda$3500–9700 Å, $FWHM \sim 300$ Å) and 3 in the NIR (J, H, and $K_{\rm s}$). The effective area of this surveys is ~ 2.8 deg^2 along the northen hemisphere. The stellar population properties were obtained via SED-fitting techniques using the code MUFFIT ([10]) including the removal of strong emission lines and the photometry and photo-z constraints of the ALHAMBRA Gold catalogue[3] ([20], $I \leq 23$). For the analysis, the sets of single stellar population (SSP) models of [2] and [32] (hereafter BC03 and EMILES, respectively) were used to build two independent sets of composite stellar population models (mixtures of two SSPs, more details in [10, 9]). Extinctions were added as a foreground screen to the composite stellar population models with values in the range $A_V = 0.0$–3.1 using the extinction law of [13].

As the ALHAMBRA survey partly overlaps with some *Hubble* fields, we build a subsample of shared quiescent galaxies with reliable size measurements, circularized radius $r_{\rm c}$, from the Advanced Camera for Surveys (ACS) general catalogue of structural parameters [16]. Finally, there are 830 quiescent galaxies in common at $0.1 \leq z \leq 0.9$ with reliable size measurements to study the distribution of stellar population parameters within the MSP.

[1] http://www.alhambrasurvey.com
[2] http://www.caha.es
[3] http://cosmo.iaa.es/content/alhambra-gold-catalog

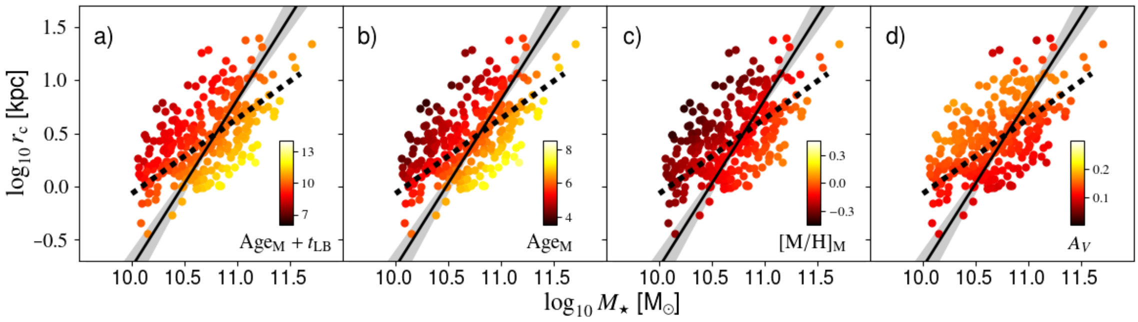

Figure 1: *From left to right* distribution of mass-weighted formation epochs, ages, metallicities, and extinctions of quiescent galaxies (*panels a, b, c*, and *d*, respectively) in the stellar mass–size plane at $0.3 \leq z < 0.5$ using EMILES models. Solid black line show the curve of constant formation epoch, whereas the grey area is the 1 σ uncertainty. Dashed black line illustrates the stellar mass–size relation of quiescent galaxies at this redshift.

3 Stellar population parameters in the stellar mass–size plane

Before studying the mass-weighted formation epochs, ages, metallicities, and extinctions as a function of size, we carried out a bidimensional and locally weighted regression method or LOESS ([6, 5]) in the MSP. This allows us to average the values in the MSP without assuming any predefined function or model. As a result, we obtain clear correlations between the stellar populations of quiescent galaxies and their sizes at $0.1 \leq z \leq 0.9$ (see Fig. 1). At fixed stellar mass, more compact quiescent galaxies are older and more rich in metals. These differences can amount to $\Delta\mathrm{Age}_\mathrm{M} = 2$–$3$ Gyr and $\Delta[\mathrm{M/H}]_\mathrm{M} \sim 0.2$ dex (see panels a, b, and c in Fig. 1). There are also hints pointing out that more compact quiescent galaxies show lower extinctions with differences of $\Delta A_V \lesssim 0.1$ (panel d in Fig. 1).

These correlations with the size strongly reflect that the stellar mass is not the only parameter driving the evolution of the stellar population of galaxies. To constrain the real driver, we empirically determine the regions of constant stellar population parameters within the MSP. At $0.1 \leq z \leq 0.9$ and for $\log_{10} M_\star \geq 9.6$, we find that the values of mass-weighted formation epoch, $\mathrm{Age}_\mathrm{M}+t_\mathrm{LB}$, are properly fitted by a plane of the form: $\mathrm{Age}_\mathrm{M}+t_\mathrm{LB}(z)/\mathrm{Gyr} = a \cdot \log_{10} M_\star/\mathrm{M}_\odot + b \cdot \log_{10} r_\mathrm{c}/\mathrm{kpc} + c(z)$. The regions of constant formation epoch are those that $M_\star \propto r_\mathrm{c}^\alpha$, where $\alpha = -b/a$. As a result, we retrieve that $\alpha = 0.5$–0.6 ± 0.1 (see black line in Fig. 1). Note that α slightly depends on the models. We repeat this process for the rest of stellar population parameters (ages, metallicities, and extinctions) getting also a compatible result with $\alpha = 0.5$–0.6. In addition, we checked whether the slope of the stellar mass–size relation matches the empirical α obtained above for stellar population parameters. After fitting our distribution of quiescent galaxies to a function of the form $r_\mathrm{c}/\mathrm{kpc} = A(z) \cdot (M_\star/5 \cdot 10^{10}\mathrm{M}_\odot)^{1/\beta}$, we obtain a slope of $\beta = 1.39 \pm 0.04$, i. e. incompatible with the empirical value obtained for stellar population parameters (see dashed line in Fig. 1).

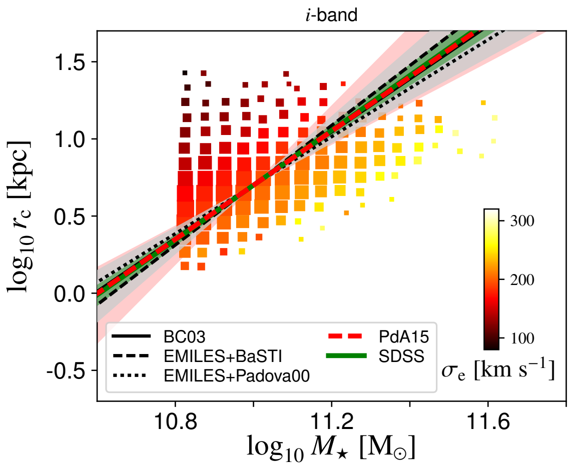

Figure 2: Velocity dispersions of SDSS quiescent galaxies in the stellar mass–size plane at $0.02 \leq z \leq 0.08$ for the i-band. Colours illustrate the average velocity dispersion in each bin, while the marker size illustrates the number of galaxies. Black lines exhibit the empirical curves of constant formation epoch for BC03 and EMILES. Green line shows the curve of constant velocity dispersion from SDSS data. Red dashed line shows the relation obtained by [23] at $z \sim 1$. Shaded areas delimit the 1 σ uncertainties for each case.

Furthermore, the average growth in size of our sample of quiescent galaxies is around 2.3 ± 0.1 since $z \sim 1$ in good agreement with previous results such as [27, 29].

Motivated by previous studies as [26, 18, 14, 4], we explored the distribution of surface densities and velocity dispersions within the MSP. By definition, constant curves of mass surface density imply that $M_\star \propto r_{\rm c}^2$, which largely differs to the value of α obtained before. As ALHAMBRA is a photometric survey, we explore the distribution of velocity dispersions of quiescent galaxies making use of the he NYU Value Added Galaxy Catalogue DR7 of the Sloan Digital Sky Survey (SDSS, [1]). We selected all the quiescent galaxies using a ugJ colour-colour diagram ([24]) at $0.02 \leq z \leq 0.08$ and $\log_{10} M_\star \geq 10.8$. A set of quality criteria is applied to remove unreliable velocity dispersions and sizes using the SDSS i-band as in [23] ($70 \leq \sigma \leq 320$ km s^{-1} , $0.3 \leq r_{\rm c} \leq 30$ kpc, and $r_{\rm c} \geq 1''$). To avoid aperture effects, all the velocity dispersions were corrected to one effective radius, $\sigma_{\rm e}$, following [3]. Values of $\sigma_{\rm e}$ are averaged in equally-sized bins of stellar mass and circularized effective radius (see Fig. 2). Our results strongly agree with a correlation between average values of $\sigma_{\rm e}$ and $r_{\rm c}$ at fixed stellar mass. The more compact the quiescent galaxy, the larger the velocity dispersion at fixed stellar mass. As above, to determine the curves of constant $\sigma_{\rm e}$, the distribution of average $\sigma_{\rm e}$ values are fitted to a plane. As a result, the curves of constant $\sigma_{\rm e}$ for the quiescent galaxies from SDSS are properly expressed as $M_\star \propto r_{\rm c}^{0.56\pm0.05}$ (see green solid line in Fig. 2). In a similar way, [23] retrieved that $M_\star \propto r_{\rm c}^{0.57\pm0.18}$ for massive spheroid-like galaxies at $z \sim 1$ (see red solid line in Fig. 2). Both results being compatible with our empirical relation for stellar population parameters since $z \sim 1$ (see black lines in Fig. 2).

4 Implications on the evolution and formation of galaxies

As revealed in Section 3, there are tight correlations between the stellar population parameters and its position in the MSP, meaning, the stellar mass is not the only parameter driving the stellar content of galaxies. This allows to empirically constrain its driver as $M_\star \propto r_c^\alpha$ with $\alpha \sim 0.5$–0.6 ± 0.1. Moreover, constant values of σ_e are also compatible with this value ($\alpha \sim 0.56$). This suggests that the driver of stellar populations would be partly related to dynamical properties of galaxies, as well as to stellar mass.

The distributions of mass-weighted formation epochs, ages, metallicities, and extinctions within the MSP may constrain the mechanisms responsible of the growth in size of galaxies. Under the "puffing-up" scenario assumption, AGN and quasar feedbacks would produce a redistribution of the stellar content in the inner parts of galaxies yielding an increase in size of a galaxy. Therefore, the most extended galaxies would show older ages than their more compact counterparts at fixed stellar, that is, the opposite distribution than the one revealed here (see Section 3). In view of these results, the "puffing-up" scenario can be discarded as a responsible mechanism of the growth in size of galaxies.

Regarding the "progenitor" bias, an arrival of recently quenched galaxies to the population of quiescent galaxies with larger effective radius would show that more extended quiescent galaxies exhibit younger stellar populations. Previous works such as [27, 17, 29, 8] reveal that star-forming galaxies are typically larger than quiescent ones, as well as there is an increasing number of quiescent galaxies at lower redshifts. Both results support that part of the growth in size of galaxies may be due to the "progenitor" bias. On the other hand, mergers acting on the MSP can also yield a growth in size of the relation (e. g. [21]). When the merger history of galaxies is independent of the size, as showed by [11], this would not alter the distribution of stellar populations in the MSP, but increasing the average size. Consequently, mergers and the "progenitor" bias acting in parallel would explain in part the evolution in size of quiescent galaxies.

Acknowledgments

The authors are grateful to the "Programa Nacional de Astronomía y Astrofísica" of the Spanish Ministry of Economy and Competitiveness (MINECO, grants AYA2012-30789 and AYA2015-66211-C2-1-P), the Government of Aragón (Research Group E103) and "Caja Rural de Teruel" for the financial support to perform this research. L. A. D. G. acknowledges support from the Ministry of Science and Technology of Taiwan (grant MOST 106-2628-M-001-003-MY3) and by Academia Sinica (grant AS-IA-107-M01).

References

[1] Blanton, M. R., Schlegel, D. J., Strauss, M. A., et al. 2005, AJ, 129, 2562

[2] Bruzual, G. & Charlot, S. 2003, MNRAS, 344, 1000

[3] Cappellari, M., Bacon, R., Bureau, M., et al. 2006, MNRAS, 366, 1126

[4] Cappellari, M., McDermid, R. M., Alatalo, K., et al. 2013a, MNRAS, 432, 1862

[5] Cappellari, M., Scott, N., Alatalo, K., et al. 2013b, MNRAS, 432, 1709

[6] Cleveland, W. & Devlin, S. 1979, Journal of the American Statistical Association, 83, 596

[7] Cowie, L. L., Songaila, A., Hu, E. M., & Cohen, J. G. 1996, AJ, 112, 839

[8] Díaz-García, L. A., Cenarro, A. J., López-Sanjuan, C., et al. 2018, ArXiv e-prints[arXiv:1802.06813]

[9] Díaz-García, L. A., Cenarro, A. J., López-Sanjuan, C., et al. 2017, ArXiv e-prints[arXiv:1711.10590]

[10] Díaz-García, L. A., Cenarro, A. J., López-Sanjuan, C., et al. 2015, A&A, 582, A14

[11] Díaz-García, L. A., Mármol-Queraltó, E., Trujillo, I., et al. 2013, MNRAS, 433, 60

[12] Fan, L., Lapi, A., De Zotti, G., & Danese, L. 2008, ApJ, 689, L101

[13] Fitzpatrick, E. L. 1999, PASP, 111, 63

[14] Franx, M., van Dokkum, P. G., Förster Schreiber, N. M., et al. 2008, ApJ, 688, 770

[15] Gallazzi, A., Charlot, S., Brinchmann, J., White, S. D. M., & Tremonti, C. A. 2005, MNRAS, 362, 41

[16] Griffith, R. L., Cooper, M. C., Newman, J. A., et al. 2012, ApJS, 200, 9

[17] Ilbert, O., McCracken, H. J., Le Fèvre, O., et al. 2013, A&A, 556, A55

[18] Kauffmann, G., Heckman, T. M., White, S. D. M., et al. 2003, MNRAS, 341, 54

[19] Moles, M., Benítez, N., Aguerri, J. A. L., et al. 2008, AJ, 136, 1325

[20] Molino, A., Benítez, N., Moles, M., et al. 2014, MNRAS, 441, 2891

[21] Naab, T., Johansson, P. H., & Ostriker, J. P. 2009, ApJ, 699, L178

[22] Oke, J. B. & Gunn, J. E. 1983, ApJ, 266, 713

[23] Peralta de Arriba, L., Balcells, M., Trujillo, I., et al. 2015, MNRAS, 453, 704

[24] Schawinski, K., Urry, C. M., Simmons, B. D., et al. 2014, MNRAS, 440, 889

[25] Thomas, D., Maraston, C., Bender, R., & Mendes de Oliveira, C. 2005, ApJ, 621, 673

[26] Trager, S. C., Faber, S. M., Worthey, G., & González, J. J. 2000, AJ, 120, 165

[27] Trujillo, I., Conselice, C. J., Bundy, K., et al. 2007, MNRAS, 382, 109

[28] Valentinuzzi, T., Poggianti, B. M., Saglia, R. P., et al. 2010, ApJ, 721, L19

[29] van der Wel, A., Franx, M., van Dokkum, P. G., et al. 2014, ApJ, 788, 28

[30] van Dokkum, P. G. & Franx, M. 2001, ApJ, 553, 90

[31] van Dokkum, P. G., Franx, M., Kriek, M., et al. 2008, ApJ, 677, L5

[32] Vazdekis, A., Koleva, M., Ricciardelli, E., Röck, B., & Falcón-Barroso, J. 2016, MNRAS, 463, 3409

Highlights on Spanish Astrophysics X, Proceedings of the XIII Scientific Meeting of the Spanish Astronomical Society held on July 16 – 20, 2018, in Salamanca, Spain. B. Montesinos, A. Asensio Ramos, F. Buitrago, R. Schödel, E. Villaver, S. Pérez-Hoyos, I. Ordóñez-Etxeberria (eds.), 2019

Ultra-Diffuse Galaxies: a formation scenario.

Arianna Di Cintio[1,2], Christopher B. A. Brook[1,2], Aaron A. Dutton[3], Andrea V. Macciò[3], Aura Obreja[3] & Avishai Dekel[4]

[1]Instituto de Astrofísica de Canarias, Calle Via Láctea s/n, E-38206 La Laguna, Spain
[2]Universidad de La Laguna. Avda. Astrofísico Fco. Sánchez, La Laguna, Spain
[3]New York University Abu Dhabi, PO Box 129188, Abu Dhabi, UAE
[4]Racah Institute of Physics, The Hebrew University, Jerusalem 91904, Israel

Abstract

A large number of Ultra-Diffuse Galaxies (UDGs) has been detected over the past few years, both in clusters and in isolation. UDGs have stellar masses typical of dwarf galaxies but effective radii of Milky Way-sized objects, and their origin remains puzzling. Using hydrodynamical zoom-in simulations from the NIHAO project we show that UDGs form naturally in dwarf-mass haloes, as a result of episodic gas outflows associated with star formation. The simulated UDGs live in isolated haloes of masses $10^{10-11}\mathrm{M}_\odot$, have stellar masses of $10^{7-8.5}\mathrm{M}_\odot$, effective radii larger than 1 kpc and dark matter cores. Remarkably, they have a non-negligible HI gas mass of $10^{7-9}\mathrm{M}_\odot$, which correlates with the extent of the galaxy. Gas availability is crucial to the internal processes that form UDGs: feedback driven gas outflows, and subsequent dark matter and stellar expansion, are the key to reproduce faint, yet unusually extended, galaxies. This scenario implies that UDGs represent a dwarf population of low surface brightness galaxies and that they should exist in the field. Several predictions and comparisons with stat-of-the-art observational data will be presented. Amongst other, we will show that the largest isolated UDGs sistematically contain more HI gas than less extended dwarfs of similar $\mathrm{M}^\star$, corroborating our proposed formation scenario.

1 Introduction

Recently, a substantial number of faint - yet extended - galaxies have been discovered in deep imaging surveys of several clusters of galaxies, including Coma [20, 9], Virgo [11], Fornax and eight low redshift clusters [19], as well as in the field and groups [18, 10]. These objects have the stellar mass and magnitudes typical of dwarf galaxies ($\mathrm{M}^\star\sim10^{7-8.5}\mathrm{M}_\odot$) but the extent of Milky Way-like spirals. A small number of stars and a large effective radius of r_e>1 kpc implies that these objects have a very low surface brightness, between 24 and

28 mag/arcsec^2: they have been named Ultra-Diffuse Galaxies (UDGs). UDGs differ from regular low surface brightness galaxies (LSBs) mostly in color, being redder than LSBs, and in the stellar content which is typical of dwarf galaxies, unlike LSBs that also include large spiral galaxies. More recently, however, it appeared clear that blue UDGs exist in the field. UDGs could either be giant Milky Way galaxies that stopped forming stars ('failed L*' galaxies) or genuine dwarf galaxies with an unusually extended size. Understanding the properties and formation of UDGs is challenging: a key question is whether such diffuse galaxies can arise within the current ΛCDM model of galaxy formation. An appealing possibility is that the formation of UDGs is not connected to the cluster environment, but rather to internal processes. Simulation work extensively showed that feedback driven gas outflows are able to cause expansion not only of the central DM distribution in galaxies, but also of the stellar one [8, 7]: the mass range where we expect maximum efficiency in core formation overlaps nicely with that of UDGs, i.e. galaxies with $M^\star \sim 10^{7-9} M_\odot$ should form large DM and stellar cores, while at higher and lower masses energy from stellar feedback alone becomes less efficient at creating cores [5, 17]. We explore feedback driven expansion as viable mechanism for the formation of UDGs, by using numerical simulations from the NIHAO project. We refer the interested reader to the main manuscript in which a detail analysis is presented [6].

2 Hydrodynamical simulations

The simulated galaxies are taken from the Numerical Investigation of a Hundred Astrophysical Objects (NIHAO) project [22], evolved using the SPH code Gasoline [21]. Star formation and feedback follows the model used in the MaGICC simulations, that for the first time reproduced several galaxy scaling relations over a wide mass range, adopting a threshold for star formation of $n_{\rm th}$>10.3cm^{-3} [3]. Stars feed energy back into the ISM via blast-wave supernova feedback and early stellar feedback from massive stars [16]. Particle masses and force softenings are chosen to resolve the mass profile to below 1% of the virial radius at all masses, ensuring that galaxy half-light radii are well resolved. The NIHAO galaxies cover a broad mass range, from dwarfs to Milky Way mass. The galaxies are all centrals and isolated, and lie on abundance matching predictions, having the expected $M^\star$ for each $M_{\rm halo}$. Within the NIHAO simulations, we identified those galaxies that match the UDG definition, by following the criteria: i) their 2D effective radius, r_e, is larger than 1 kpc, ii) their absolute magnitude in R band is $-16.5 \lesssim M_{\rm R} \lesssim -12$, corresponding to a stellar mass of $10^7 \lesssim M^\star/M_\odot \lesssim 10^{8.5}$, iii) their effective surface brightness is low, with μ_e>23.5 mag/arcsec^2. We found a total of 21 simulated galaxies that meet these requirements. We then explore how these UDG-like objects arise in our simulations.

3 UDG formation scenario

In the left panel of Fig. 1 we summarize the properties of simulated UDGs: from top to bottom we specify stellar mass, halo mass, HI gas mass ($M_{\rm HI}$), 2D effective radius, effective surface brightness, R-band absolute magnitude, B-R color, Sérsic index, DM halo inner slope, spin parameter and concentration. Specifically, the Sérsic index $n_{\rm Sersic}$ is computed by fitting the 2D surface brightness profile in R-band out to $2\times r_e$ with a Sérsic profile, the inner slope γ of the DM halo is found by fitting its density profile with a power law between 1 and 2% of the virial radius, in a region where all our galaxies are well resolved. All the currently observed structural properties of UDGs ($M_{\rm HI}$, $M^\star$, $n_{\rm Sersic}$, color, $M_{\rm R}$, r_e and μ_e) are in excellent agreement with the ones of the simulated sample. The mean value of the spin parameter is close to the peak of the distribution of spin parameters for DM haloes (log($\lambda \sim$-1.45), indicating that our simulated UDGs do not live in particularly high-spin objects as suggested by [1]. The range of DM inner slopes, -0.78<γ<-0.01, shows that UDGs live in expanded DM haloes, whose logarithmic inner slope is shallower than the universal NFW value of γ=-1. This is closely linked to the formation of UDGs. Indeed, the formation of DM density cores is related to rapid oscillations of the central potential driven by gas outflows following bursty star formation [12]: this purely gravitational mechanism affects as well the stellar distribution [7, 4]. In the right panel of Fig. 1 we show the evolution of the 3D stellar density as a function of redshift for all stars (solid lines) and old stars (tform<5 Gyrs, dashed lines). As the DM halo expands and forms a central core due to episodic and powerful gas outflows driven by star formation, the stellar distribution expands as well: r_e increases and μ_e decreases bringing the dwarf onto the UDG regime. We confirm that r_e increases due to expansion of the stellar distribution, by separating the contribution of all stars and old stars: we observe that even the oldest stellar population expands as a response to core creation.

X	$\overline{X} \pm \sigma$	$X_{min,max}$
log($M^\star$[$M_\odot$])	7.66±0.42	6.83 , 8.40
log($M_{\rm halo}$[$M_\odot$])	10.53±0.18	10.22 , 10.85
r_e[kpc]	1.87±0.53	1.07 , 3.06
μ_e[mag/arcsec^2]	25.23±0.94	23.69 , 26.84
M_R	-14.61±1.07	-16.25 , -12.57
B-R	0.77±0.12	0.54 , 0.97
$n_{\rm Sersic}$	0.83±0.27	0.31 , 1.46
γ(1-2%R_{vir})	0.37±0.18	0.01 , 0.78
log(λ)	-1.48±0.25	-2.04 , -1.17

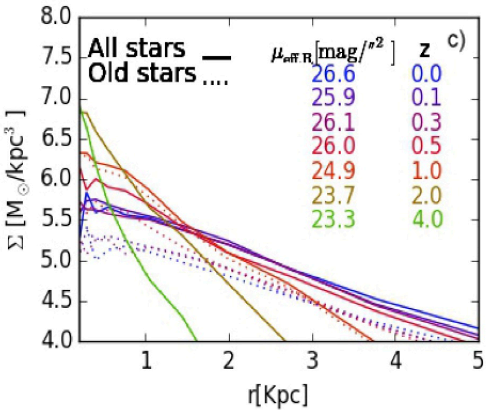

Figure 1: Left panel: Average properties of simulated UDG sample. Concentrations and spin parameters were computed in the original DM-only run. Right panel: formation of UDGs, the contribution of all stars and old stars formed within the first 5 Gyrs of the galaxy's life is indicated as solid and dashed line, respectively, with the μ_e evolution also shown.

4 Observational prediction

In Fig. 2 we show the SFH of galaxies whose effective radii are the largest (right column) and smallest (left column) in their respective mass bin. From top to bottom, we pair galaxies with

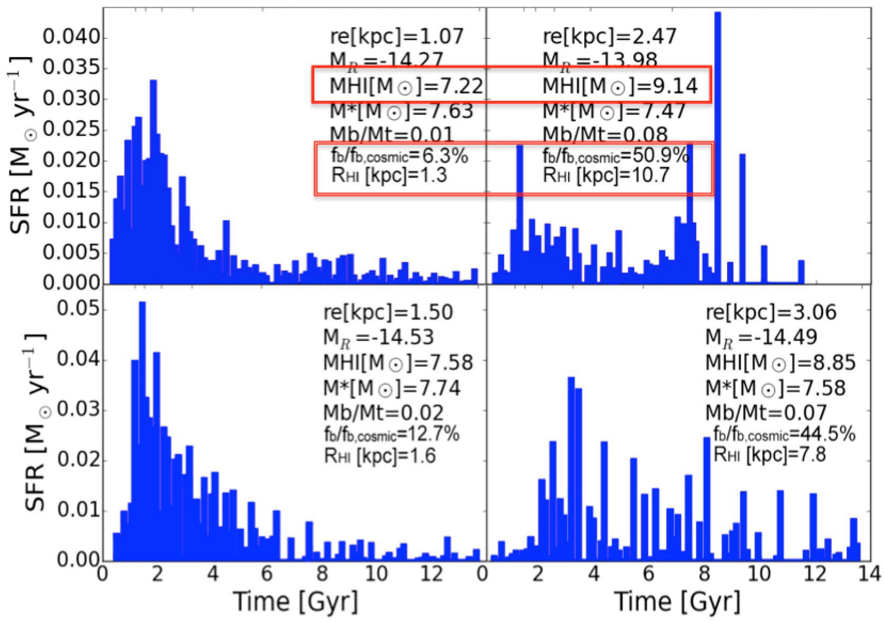

Figure 2: SFHs of galaxies with the largest (right column) and smallest (left column) effective radius in their mass bin. From top to bottom, each row shows galaxies with similar halo mass and magnitude, $\log_{10}(\mathrm{M_{halo}}/\mathrm{M_\odot})\sim$10.45,10.50 and $M_\mathrm{R}\sim$-14.0,-14.5. In each panel r_e, M_R, $\mathrm{M_{HI}}$, $\mathrm{M}^\star$, f_b and HI radius are indicated. The largest isolated UDGs contain more HI gas, have a larger baryon fraction and a more extended and bursty SFH than less extended dwarfs of similar $\mathrm{M}^\star$.

similar halo and stellar masses, quoting in each panel the r_e, M_R, $\mathrm{M_{HI}}$, $\mathrm{M}^\star$, HI radius (the radius at which the HI surface density reaches 1 $\mathrm{M/pc^2}$) and baryon fraction relative to the cosmic one, f_b . The difference in properties between the most extreme UDGs (right panels) and the less extreme, more compact dwarfs (left panels) are striking: galaxies with large r_e also have a larger $\mathrm{M_{HI}}$, baryon fraction and HI radius, and more prolonged and persistently bursty SFH, including a larger fraction of young stellar population, compared to galaxies with a smaller r_e. This is because when most of star formation happens in the first 3-4 Gyrs, feedback can eject significant amounts of gas from relatively shallow potential wells at early times, resulting in low baryon fractions by z=0. Since gas is expelled at early stages, there is less gas for ongoing star formation and crucially there is less gas to be expelled from the inner regions when star formation occurs, being this the key aspect of the mechanism for core creation. Conversely, galaxies with star bursts occurring after the rapid halo growth phase has finished are the ones that can keep their gas, which can not escape the deeper potential well: they have enough gas available at all time to drive DM cores and a spatially extended stellar distribution, retaining about 50%f_b and up to $10^9\mathrm{M_\odot}$ in HI gas by z=0. This prediction has been recently confirmed. Using the ALFALFA survey, $\sim$ 115 isolated HI sources bearing UDGs have been identified: they are bluer than in clusters, supporting the scenario in which UDGs form in isolation and then accrete into clusters, and, most importantly, they all have large HI radii and are HI-rich relative to their stellar masses [10].

5 Conclusions

State-of-the-art cosmological simulations of isolated galaxies from the NIHAO project, which include feedback from SNe and massive stars, reproduce a population of Ultra-Diffuse Galaxies (UDGs): feedback driven gas outflows give rise to a spatially extended stellar component, while simultaneously expanding the dark matter halo, leading to the emergence of low surface brightness dwarf galaxies, or UDGs. Our findings imply that UDGs: i) are dwarf galaxies, with $M_{\rm halo}{\sim}10^{10-11}M_{\odot}$, in agreement with recent estimates in clusters and field [2, 15], ii) are expected to be found in the field, where they should be extremely gas rich, with HI gas mass $\sim 10^{7-9}M_{\odot}$, as later on demonstrated using the HI ALFALFA survey [10] iii) have typical distributions of halo spin and concentration, an average Sérsic index of less than one and dark-matter cores, and iv) the largest UDGs should retain the highest baryon fraction, largest amount and extent of HI gas, and, interestingly, they should have an high fraction of young stars. The latter point has recently been demonstrated to be valid for Local Group dwarfs [13], such that galaxies that stopped forming stars over 6 Gyrs ago favour high central densities (and small, <1kpc, r_e), while those with more extended star formation favour dark matter cores and larger, >1 kpc, r_e. Nevertheless, the field of deriving reliable SFHs for UDGs is still in its initial stage. Significant progress has been recently made, using deep optical spectroscopic data from the OSIRIS instrument, in characterising the stellar component of a sample of UDGs [14]: the recovered SFHs are compatible with both bursty star forming episodes declining with time as well as with a more gradual decrease in the SFH, making impossible, at the present stage, to further validate our prediction. In the future, better data and sophisticated analysis will be necessary to verify the correlation between sizes and extent of HI gas, SFHs and retained baryon fraction, further supporting our proposed formation scenario.

Acknowledgments

ADC acknowledges financial support from a Marie-Skłodowska-Curie Individual Fellowship grant, H2020-MSCA-IF-2016, Grant agreement 748213 DIGESTIVO. Computational resources were provided by the High Performance Computing at NYUAD, the THEO cluster at MPIA and the HYDRA clusters at Rechenzentrum in Garching.

References

[1] Amorisco N. C., Loeb A., 2016, MNRAS, 459, L51

[2] Beasley M. A., Trujillo I., 2016, ApJ, 830, 23

[3] Brook C. B., Stinson G., Gibson B. K., Wadsley J., Quinn T., 2012, MNRAS,424, 1275

[4] Chan T. K., Kere D., Wetzel A., Hopkins P. F., Faucher-Giguere C.-A., El-Badry K., Garrison-Kimmel S., Boylan-Kolchin M., 2018, MNRAS,478, 906

[5] Di Cintio A., Brook C. B., Macciò A. V., Stinson G. S., Knebe A., Dutton A. A., Wadsley J., 2014a, MNRAS, 437, 415

[6] Di Cintio A., Brook C. B., Dutton A., Macciò A. V., Obreja A., Dekel A., 2017, MNRAS, 466, L1

[7] El-Badry K., Wetzel A., Geha M., Hopkins P., Keres D., Chan T. K.,Faucher-Giguere C.-A., 2016, ApJ, 820, 131

[8] Governato F., et al., 2010, Nature, 463, 203

[9] Koda J., Yagi M., Yamanoi H., Komiyama Y., 2015, ApJ, 807, L2

[10] Leisman L., et al., 2017, ApJ, 842, 133

[11] Mihos J. C., et al., 2015, ApJ, 809, L21

[12] Pontzen A., Governato F., 2012, MNRAS, 421, 3464

[13] Read J. I., Walker M. G., Steger P., 2018, preprint, arXiv:1808.06634

[14] Ruiz-Lara T., et al., 2018, MNRAS, 478, 2034

[15] Sifòn C., van der Burg R. F. J., Hoekstra H., Muzzin A., Herbonnet R., 2018, MNRAS, 473, 3747

[16] Stinson G. S., Brook C., Macci'o A. V., Wadsley J., Quinn T. R., Couchman H. M. P., 2013, MNRAS, 428, 129

[17] Tollet E., et al., 2016, MNRAS, 456, 3542

[18] Trujillo I., Roman J., Filho M., Sanchez Almeida J., 2017, ApJ, 836, 191

[19] van der Burg R. F. J., Muzzin A., Hoekstra H., 2016, A&A, 590, A20

[20] van Dokkum P., Abraham R., Merritt A., Zhang J., Geha M., Conroy C., 2015a, ApJ, 798, L45

[21] Wadsley J. W., Stadel J., Quinn T., 2004, NewA, 9, 137

[22] Wang L., Dutton A. A., Stinson G. S., Macciò A. V., Penzo C., Kang X.,Keller B. W., Wadsley J., 2015, MNRAS, 454, 83

Highlights on Spanish Astrophysics X, Proceedings of the XIII Scientific Meeting of the Spanish Astronomical Society held on July 16 – 20, 2018, in Salamanca, Spain. B. Montesinos, A. Asensio Ramos, F. Buitrago, R. Schödel, E. Villaver, S. Pérez-Hoyos, I. Ordóñez-Etxeberria (eds.), 2019

Self-consistent spatially-resolved star formation histories of $2 < z < 3$ galaxies from CANDELS.

Ángela García Argumánez[1], Pablo G. Pérez-González[1,2], Armando Gil de Paz[1], and Javier Gorgas[1]

[1] Departamento de Física de la Tierra y Astrofísica, Universidad Complutense de Madrid, Plaza Ciencias, 1, E-28040 Madrid, Spain
[2] Centro de Astrobiología (CAB, INTA-CSIC), Carretera de Ajalvir km 4, E-28850 Torrejón de Ardoz, Madrid, Spain

Abstract

In order to shed new light on how Milky Way-like galaxies are formed, we analyze the star formation histories (SFHs) and mass surface density profiles of massive galaxies ($\log(M_*/M_\odot) > 10$) at $2 < z < 3$ in the GOODS-N and GOODS-S fields observed by the Cosmic Assembly Near-infrared Deep Extragalactic Legacy Survey (CANDELS). Stellar population parameters are obtained in two-dimensions (2D) by first performing multi-wavelength photometry using optical and near-infrared broad-band data from HST. Subsequently, the observed SEDs are fit to stellar population models attenuated by dust. The galaxy sample has been divided according to its activity (star-forming vs. quiescent) and compactness (compact vs. extended). We will discuss the differences in SFH and mass distribution for each subsample and propose an evolutionary connection among them.

1 Introduction

In general, galaxies increase their mass by gas accretion, travelling within the Main Sequence [10] until stellar formation ceases because of some feedback mechanism or by gas depletion. At that moment, they reach a quiescent state, in which their mass might continue increasing by dry mergers. Nevertheless, we know there is a significant number of massive quiescent galaxies already in place at high redshift, without any stellar formation [5], [6], and whose number densities are a challenge to galaxy formation models [11], [9]. Understanding the evolution between star-forming and quiescent galaxies is essential to improve our comprehension of feedback processes in massive star-forming galaxies and the evolution of galaxies in general.

In this contribution we will introduce the first preliminary results of our study, intended to establish an evolutionary connection between massive star-forming and quiescent galaxies at high redshift. To do so, we will analyse the stellar populations in 2D of massive galaxies at $2 < z < 3$ using multi-wavelength photometry. We will also briefly introduce our on-going work focused on improving our analysis by taking into account photometric data with different spatial resolution.

1.1 Massive galaxy formation and analysis plan

Massive quiescent galaxies are supposed to be formed by two different mechanisms: a fast track, through which massive Star-Forming (SF) Galaxies at $z \gtrsim 2$ first evolve to a compact starbursting remnant (or blue nugget) by usually very fast, violent, dissipative processes. Then, the subsequent star-formation quenching in these compact star-forming galaxies transforms them into compact quiescent galaxies (or red nuggets), which increase their size afterwards by dry mergers and abandon the compact region by $z \sim 1$. Alternatively, there is also a slow track at $z \lesssim 2$, through which normal-sized SF galaxies populate the red sequence by secular evolution. Fig. 1 shows an schematic view of these two mechanisms [1].

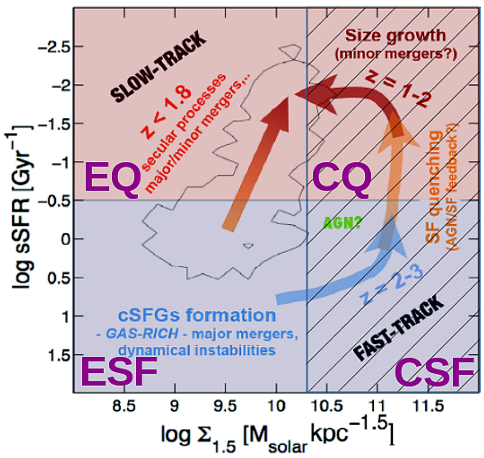

Figure 1: Figure adapted from Barro et al. [1] that shows an schematic view of the two different ways through which massive quiescent galaxies are formed: early and fast tracks. The black contour shows the galaxy distribution at low redshift. The four quadrants in the figure correspond to the galaxy types in our classification: ESF (extended star-forming), CSF (compact star-forming), EQ (extended quiescent) and CQ (compact quiescent) galaxies.

Our work focuses on studying whether there is a link among galaxy types in the fast track by analysing their stellar population and morphological properties. In particular, we will do that by analysing stellar masses and densities to understand the assembly of structures and the recent star formation locally on star-forming galaxies. Our approach to the problem includes the study of the global Star Formation Histories (SFHs) of different types of galaxies (according to their morphology and star formation activity), the analysis of their averaged surface stellar density profiles and the study of the spatially resolved stellar populations properties. Directly related to this goal, we will also try to understand the intrinsic and typical degeneracies of stellar populations synthesis studies.

2 2D stellar population analysis

The initial galaxy sample was built using the CANDELS/F160W catalog in the GOODS-S field only considering massive galaxies ($M > 10^{10}\ M_\odot$) at $2 < z < 3$. These galaxies were classified into the three subsamples of interest according to their activity (star-forming vs. quiescent) and compactness (compact vs. extended): ESF (extended star-forming), CSF (compact star-forming) and CQ (compact quiescent) galaxies. Quiescent and star-forming galaxies are differentiated by a cut in specific SFR (sSFR) in $10^{-0.5}$ Gyr^{-1}. Compact galaxies are defined like [1] as those with $\Sigma_{1.5} \equiv M/{r_{\rm eff}}^{1.5} > 10^{10.3}\ M_\odot\ \mathrm{kpc}^{-1.5}$. Fig. 2 shows this classification.

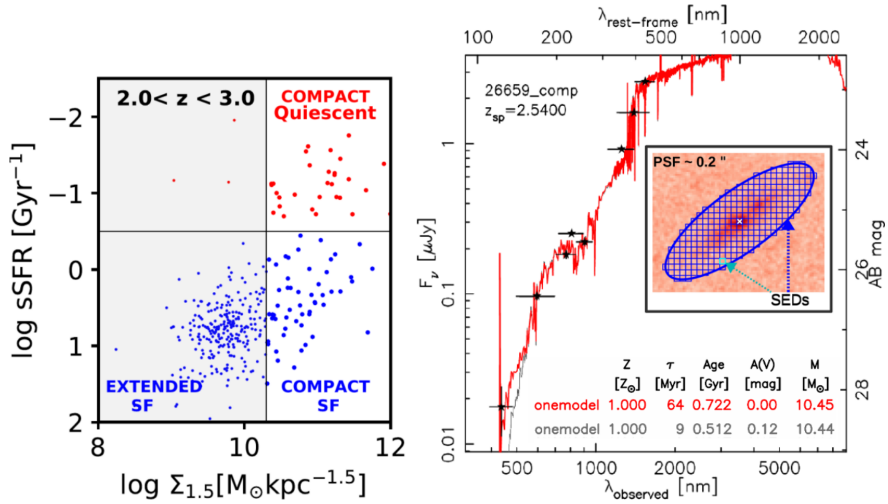

Figure 2: *Left:* selection of our sample and classification. The black lines define the selection criteria for star-forming (blue) and quiescent (red) galaxies, and for compact and extended (shaded area). *Right:* example of a Spectral Energy Distribution (SED) that has two possible clusters of solutions in the age-τ plane. The red fit corresponds to the median values of the most significant cluster of the elliptical aperture in the inset (92% of the simulated solutions belong to this cluster).

Photometry was measured using nine broad-band visible and near-infrared HST filters: F435W, F606W, F775W, F814W and F850LP in the ACS/WFC [8], and F105W, F120W, F140W and F160W in the WFC3 [7]. Photometry was measured on each galaxy inside an aperture defined by its Kron radius and using a grid with size equal to 0.2″.

The SEDs were compared with the stellar population models of Bruzual & Charlot (2003) [2], assuming a Chabrier (2003) IMF [4] and a Calzetti (2000) attenuation law [3]. For the SFH, we assumed a time-delayed exponential with a τ star formation timescale, $SFR(t) \propto t \cdot e^{-t/\tau}$. Our modelling assumed solar metallicity. We set as free parameters the masses, ages, τ and $A(V)$. To study degeneracies, Montecarlo simulations were performed for each galaxy by allowing the photometric data to randomly vary within their photometric error and then refitting. The clustering of the solutions in the age-τ plane provided us with information about what degeneracies we had and about the uncertainty of our solutions. Fig. 2 *right* shows an example of a SED-fit with two different clusters in this plane.

3 Surface stellar density profiles of CQ, CSF and ESF galaxies

Once stellar masses were calculated for different regions in each galaxy, azimutally averaged surface stellar density profiles were built. Then, we produced average profiles for the different types of galaxy. Fig. 3 shows the median profiles for the three subsamples. The shaded areas include 68% of the values. Median surface density values as a function of radius for each galaxy are also depicted. At the bottom, we show the median profiles normalized by their maximum value and fit to a Sérsic law [12]. CQ and CSF galaxies show very similar profiles and are more concentrated than those of ESF galaxies. Additionally, the mass density profiles for compact galaxies (either quiescent or star-forming) are well described by only one Sérsic law. This can be interpreted as both types of galaxies having only one mass component, probably a bulge.

Concerning ESF galaxies, only one Sérsic component is not enough to describe the mass profile. It can be noticed that while the outer part of the curve could be explained by an exponential disc, the inner part is better described by the combination of this exponential component and a second Sérsic component. A possible explanation for that is the presence of a bulge which is being formed.

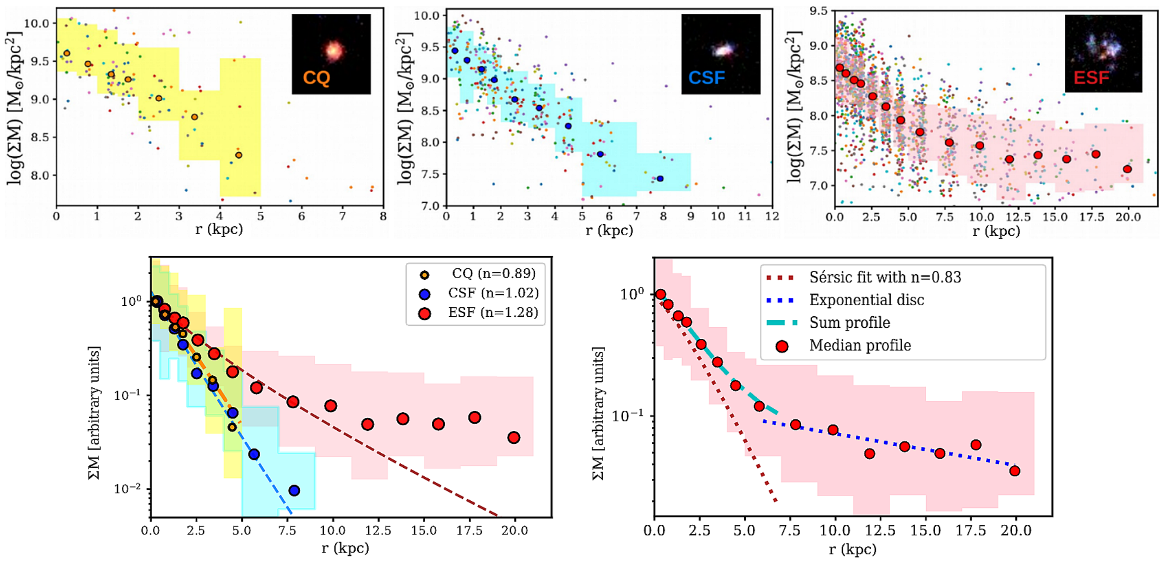

Figure 3: *Top:* surface stellar density profiles for CQ (left), CSF (middle) and ESF (right) galaxies. Shaded areas include 68% of the values. Median profiles for each galaxy are shown as coloured circles. *Bottom left:* median profiles normalized by their maximum value and fit to a Sérsic law. *Bottom right:* Median profile for ESF galaxies fit with two Sérsic components.

4 Star Formation Histories of CQ, CSF and ESF galaxies

For each galaxy, the SFH within the global elliptical aperture was built from the age, τ and mass values corresponding to the best cluster of solutions (Fig. 4 *left*). The median SFH of each galaxy type (Fig. 4 *right*) was calculated from the SFHs of the galaxies in each subsample.

According to this, CQ galaxies were the first to start their star formation ($\sim$ 1 Gyr ago). They would have had a very fast and violent star formation peak $\sim$ 0.7 Gyr ago with a SFR of $\sim$ 300 $M_\odot$/yr, being practically dead at present. CSF galaxies would have begun their SFH $\sim$ 0.7 Gyr ago and their SFR would have been decreasing since then, except for some minor star formation burst in the last 200 Myr. In contrast, the ESF galaxies would have formed their stars more recently (in the last $\sim$ 500 Myr) and their SFR would be approximately constant ($\sim$ 100 $M_\odot$/yr) since 200 Myr ago (or slightly decreasing at the moment).

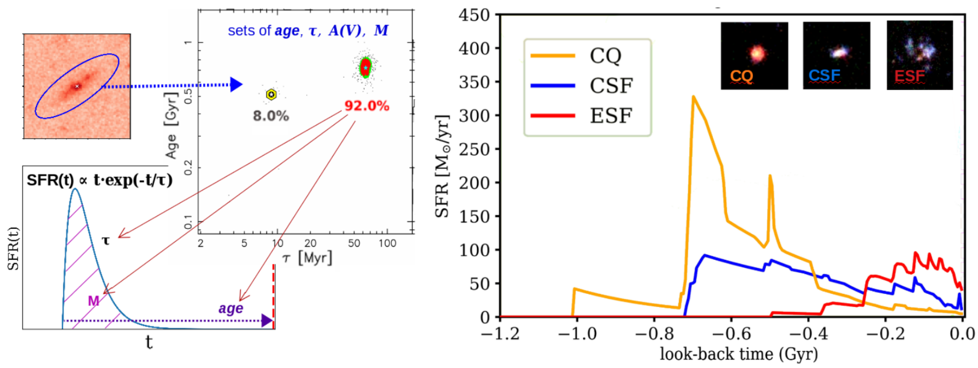

Figure 4: *Left:* Methodology: SFHs were built from the age, τ and mass values corresponding to the best cluster of solutions in the age$-\tau$ plane for the elliptical aperture of each galaxy. *Right:* Median SFH for each galaxy type: CSF (blue), CQ (orange) and ESF (red) galaxies.

5 Discussion: linking blue and red nuggets

Taking into account both the azimutally averaged surface stellar density profiles and the SFHs of each galaxy type, we could establish a possible evolutionary link among the three galaxy types. In the first place, the fact that CQ and CSF galaxies show very similar mass profiles could be explained assuming that CSF galaxies slowly die (or are already dying) keeping their structure until they become CQ galaxies. This would explain why CQ galaxies show the oldest mass-weighted ages.

Secondly, ESF galaxies, with a younger stellar population, could be the progenitors of CSF and CQ galaxies. In order to become a CSF galaxy, ESF systems must have lost their outer discs and become compact spheroids with intense star formation: CSF galaxies. These latter systems would reach a quiescent state with an old stellar population: CQ galaxies.

6 Self-consistent spatially resolved stellar populations

We are currently improving our 2D stellar population analysis by using data at lower spatial resolution, but better spectral resolution, such as photometric data from the SHARDS survey (OSIRIS@GTC) or spectrocopic data from HST grism. The left panel of Fig. 5 shows a zoom in the SHARDS zone for the sum of the spectra of each box in the photometric grid (cyan), aperture-corrected using the integrated photometry values for our HST bands (blue circles). The stars are photometric data we have measured for that galaxy in the SHARDS bands.

Our current work is focused on making this sum of the spectra of the boxes in the grid consistent, not only with the photometric values of SHARDS, but also with the spectrum measured for the whole galaxy using the HST grism shown in the right panel of Fig. 5, or, in the future, with ALMA data. Therefore, we would have access to, for example, both absorption and emission lines to constrain our SED-fits.

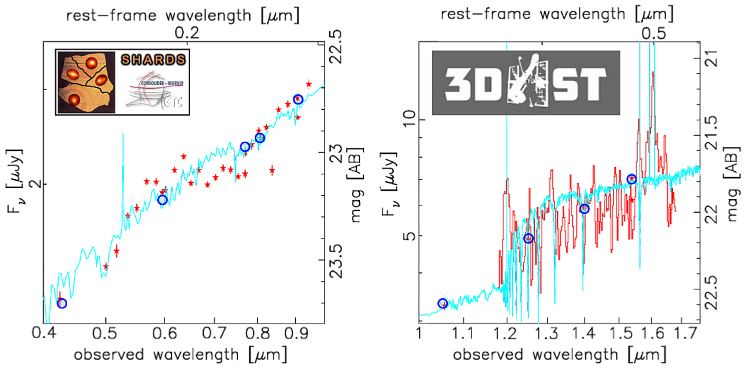

Figure 5: *Left:* zoom in the SHARDS filters spectral range. Sum of the spectra of the boxes in the grid (cyan) for galaxy GDN-25066, aperture-corrected with integrated photometry values of HST bands (blue circles). Red stars are photometric data in the SHARDS bands. *Right:* spectrum of the whole galaxy from the HST grism. Emission-lines are clearly detected. These lines could be used to constrain the properties of the most recent star formation in our SFHs.

References

[1] Barro, G., Faber, S. M., Pérez-González, P. G., et al. 2013, ApJ, 765, 104

[2] Bruzual G., Charlot S., 2003, MNRAS, 344, 1000

[3] Calzetti, D., Armus, L., Bohlin, R. C., et al. 2000, ApJ, 533, 682

[4] Chabrier, G. 2003, ApJ, 586, L133

[5] Cimatti A., et al., 2004, Nature, 430, 184

[6] Domínguez Sánchez H., Pozzi F., Gruppioni C. e. a., 2011, MNRAS, 417, 900

[7] Dressel, L., 2010. "Wide Field Camera 3 Instrument Handbook, Version 3.0" (Baltimore: STScI)

[8] Maybhate, A., et al. 2010, "ACS Instrument Handbook", Version 10.0 (Baltimore: STScI)

[9] Muzzin A., et al., 2013, ApJ, 777, 18

[10] Noeske K. G., Weiner B. J., Faber S. M. e. a., 2007, ApJ, 660, L43

[11] Pozzetti L., et al., 2010, A&A, 523, A13

[12] Sérsic, J. L. 1968, *Atlas de galaxias australes*, Universidad de Córdoba

Highlights on Spanish Astrophysics X, Proceedings of the XIII Scientific Meeting of the Spanish Astronomical Society held on July 16 – 20, 2018, in Salamanca, Spain. B. Montesinos, A. Asensio Ramos, F. Buitrago, R. Schödel, E. Villaver, S. Pérez-Hoyos, I. Ordóñez-Etxeberria (eds.), 2019

Spatially-resolved color–mass-to-light ratio relations in the CALIFA survey.

R. García-Benito[1], R. M. González Delgado[1], E. Pérez[1], R. Cid Fernandes[2], S. F. Sánchez[3], and A. L. de Amorim[2],

[1] Instituto de Astrofísica de Andalucía (CSIC), P.O. Box 3004, 18080 Granada, Spain
[2] Departamento de Física, Universidade Federal de Santa Catarina, P.O. Box 476, 88040-900, Florianópolis, SC, Brazil
[3] Instituto de Astronomía, Universidad Nacional Autónoma de México, Circuito Exterior, Ciudad Universitaria, Ciudad de México 04510, México

Abstract

We calculate the mass-to-light versus color relations (MLCRs) derived from the spatially-resolved star formation history (SFH) of a sample of galaxies from the integral field spectroscopy CALIFA survey. Using full spectral fitting methods we derive the stellar mass ($M_\star$) and combine these results with observed and synthetic colors in optical broad bands. We obtain the radial structure of the mass-to-light ratio (M/L) at several bands and study the MLCRs. Our sample covers a wide range of Hubble types, with stellar masses ranging from $M_\star \sim 10^{8.4}$ to 10^{12} M$_\odot$.

1 Introduction

Large surveys have shown that stellar mass ($M_\star$) is a useful parameter to classify galaxies [22, 9], which in turn is correlated with other global galaxy properties like the stellar mass surface density ($\Sigma_\star$) [15]. Spatially resolved data has shown that $\Sigma_\star$ is a fundamental parameter that drives the star formation history (SFH) of galaxies [2], while integral field spectroscopic surveys have found local relations between $\Sigma_\star$ and other local parameters such as gas and stellar metallicity, age or star formation rate [20, 12, 13].

$M_\star$ and $\Sigma_\star$ are key properties of galaxies that cannot be measured directly. Deriving these quantities from observed data involves stellar populations synthesis (SPS) models. The most common methods to obtain the relation between light and mass involve: a) modeling the galaxy spectrum via full spectral fitting [17, 11] or using spectral indices with a library of parametric star formation histories [16], b) model the spectral energy distribution from optical-NIR broadband photometry [23], or c) obtaining the relation between colors and the mass-to-light ratio at some wavelength:

$$\log M/L_{\lambda_i} = a_{\lambda_i} + b_{\lambda_i} \times (m_{\lambda_j} - m_{\lambda_k}), \tag{1}$$

where the bands λ_i, λ_j, and λ_k may be independent, or $\lambda_i = \lambda_j$ or $\lambda_i = \lambda_k$.

Certainly, the M/L_λ-color relation (MLCR) is the simplest method to derive $M_\star$, as it relies on photometry in only two bands.

Most previous works obtain MLCRs based on the integrated M/L_λ [3, 10, 14, 18]. However, galaxies have M/L_λ and color gradients, and the MLCRs can be affected by the spatial variations. In this work, we use the full spectral synthesis technique, fitting the spatially resolved optical spectroscopy provided by the CALIFA survey, to obtain the spatially resolved M/L. Optical colors are measured on observed and on synthetic spectra to explore the effect from the emission lines on the colors in the MLCR. Because the CALIFA sample covers all Hubble types, we are able to explore the radial profiles of M/L_λ and their gradient with galaxy morphology, and their effect on the MLCR.

The sample is selected from the final CALIFA data release [21], with a total of 446 galaxies with the COMB setup, the one used in this work. We group the galaxies into seven morphology bins: E (65 galaxies), S0 (54, including S0 and S0a), Sa (70, including Sa and Sab), Sb (75), Sbc (76), Sc (77, including Sc and Scd), and Sd (35, including Sd, Sm, and Irr).

2 Methodology

We obtain the spatially-resolved SFH of each galaxy to derive the stellar mass surface density ($\Sigma_\star$) and $M_\star$. We follow the same methodology as in previous works (e.g. [12, 13, 11]). In short, we use STARLIGHT [7] to fit the spectrum of each individual spaxel (pixelwise) within the isophote level where the average signal-to-noise ratio (S/N) ≥ 3, decomposing the spectra in terms of stellar populations with different ages and metallicities.

We used base CBe, a set of 246 SSPs from [4] models (Charlot & Bruzual 2007; private communication). The metallicity $\log Z_\star/Z_\odot$ covers from -2.3 to $+0.4$, while ages run from 1 Myr to 14 Gyr. The IMF is that of [6]. Dust effects are modeled as a foreground screen with a [5] reddening law with $R_V = 3.1$. The results are then processed through PyCASSO (the Python CALIFA STARLIGHT Synthesis Organizer; [8, 1]) to produce a multi-dimensional dataset of spatially resolved stellar population properties. From them, 2D maps of $M_\star$, stellar extinction (A_V), and luminosity, are obtained to derive 2D maps and radial profiles of M/L.

Colors are computed in two alternative ways: a) convolving the CALIFA data cubes with the SDSS g and r and the Johnson B and V filter responses, and b) convolving the synthetic data cubes obtained from the (pixelwise) full spectral fitting with filters SDSS u, g, r, i, z bands and the B, V, R Johnson bands (*Syn* label).

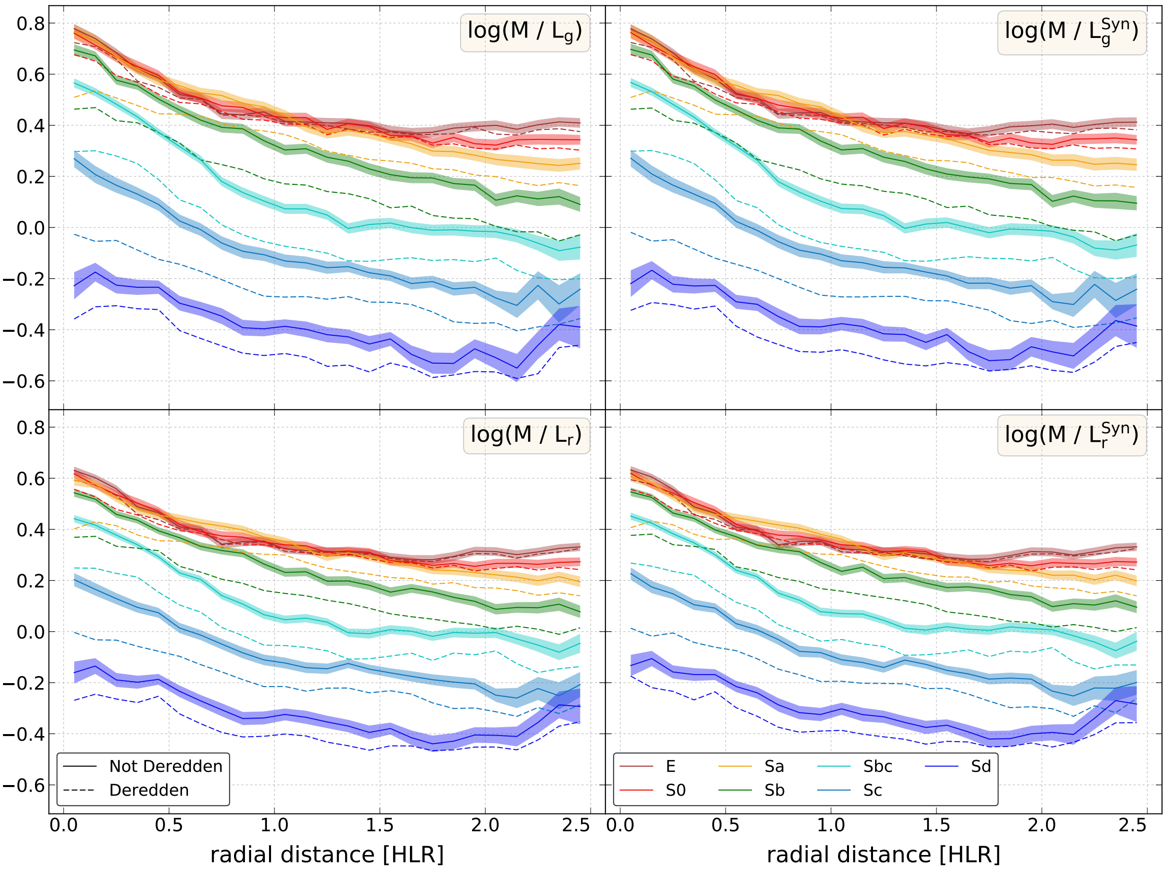

Figure 1: Radial profile of M/L for g band (upper panels) and r band (lower panels) stacked by Hubble type for the observed (left panels) and synthetic restframe spectra (right panels), with intrinsic (continuous lines) and dereddened luminosities (dashed lines).

3 M/L radial profiles

For each galaxy the radial variation of M/L_λ is obtained by compressing each individual 2D map in azimuthally averaged radial profiles. The radial distance is expressed in units of the galaxy's half-light-radius, a convenient metric.

Figure 1 displays azimuthally averaged radial profiles of M/L_g and M/L_r. They have been stacked by Hubble type in seven morphological classes. On the left panels, the profiles are obtained from the observed spectrum, both *not* dereddened (continuous lines) and dereddened (dashed lines). On the right panels we use the M/L images obtained from the synthetic spectra.

All profiles decrease outwards, with inner regions having larger M/L. The profiles scale with the Hubble type. At any given distance, M/L is larger for early type galaxies than for late type spirals. The effect of the extinction is more significant in the central regions of

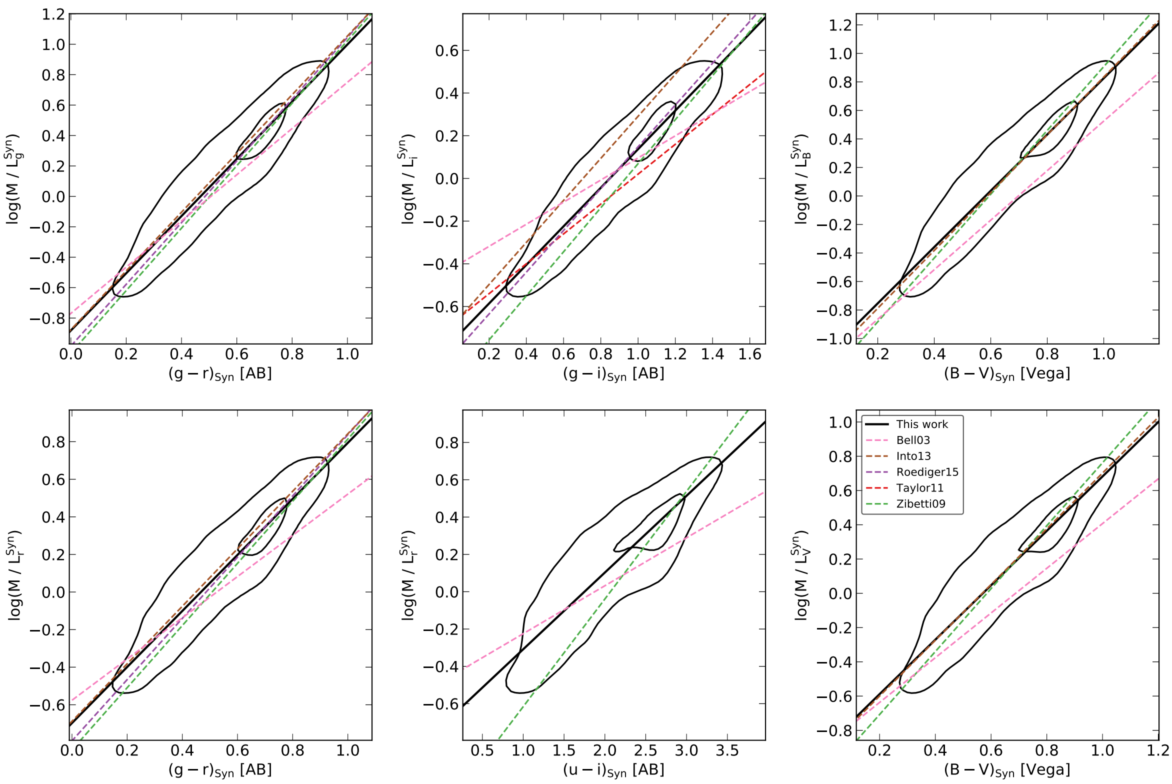

Figure 2: Comparison of the relation between restframe color and M/L for different bands for all galaxies to relations from the literature. The contours represent the density distribution encompassing 90% and 20% of the points.

intermediate type spirals, in particular in Sb/Sbc.

The effect of emission lines is very small, as can be seen from the comparison between observed (left) and synthetic profiles (right). For M/L_g (M/L_r) the maximum difference is around 0.01 dex (0.02 dex) for late type spirals.

4 Spatially-resolved MLCRs

Figure 2 compares a few examples of our empirically calibrated color-log(M/L) relation for different representative bands to other works found in the literature. The (black) contours represent the density distribution of the whole sample encompassing the 90% and 20% of the points. Our spatially resolved MLCRs fits are plotted in solid black lines. All relations have been scaled to our Chabrier IMF.

One of the first linear color-log(M/L) methods was developed by [3], based on on [4] SPS models using dust-free single exponential SFH libraries. As already noticed by later works, the [3] relations present large discrepancies. They strongly deviate towards lower values of M/L, with differences of a few dex in some filters (e.g. $g-i$).

Later works have compiled new MLCRs using different ingredients and methods. For example, [14] disc galaxy models runs very close to ours, except for $g-i$, which overestimates M/L by ~ 0.15 dex as compared to our results.

Relations by [18] and [24] also run close to our values, although the later has some discrepancies in the $\mathrm{M/L_i} - (g-i)$, particularly in the $\mathrm{M/L_i} - (g-i)$ combination for low M/L ratios.

Finally, the [23] relation, calibrated using SDSS *ugriz* multi-band photometry of a large sample of galaxies, diverges from our relation in the $\mathrm{M/L_i} - (g-i)$ plane for medium to large M/L values, i.e. intermediate and early type galaxies.

5 Conclusions

Our results are in agreement with previous results based on integrated M/L and colors of galaxies, with $\mathrm{M/L_g}$ and $\mathrm{M/L_r}$ being remarkably similar to the results from [24], [14], and [18]. In the plane $\mathrm{M/L_i} - (g-i)$ there is more dispersion, but our results are similar to [18] and they are in between [24] and [14] for (g-i) < 1, and [23] and [14] for redder colors. In the plane $\mathrm{M/L_r} - (u-i)$ our relation is in between [3] and [24]. In the $\mathrm{M/L_V} - (B-V)$ plane, our results are in perfect agreement with [18], and very close to [24]. The relation $\mathrm{M/L_B} - (B-V)$ is very tight and all the results, ours included, agree very well, with the exception of [3].

The values of the slope and intercept of the MLCRs for all bands, for the whole sample and with different morphological bins, can be found in our webpage `http://pycasso.iaa.es/ML`.

Acknowledgments

CALIFA is the first legacy survey carried out at Calar Alto. The CALIFA collaboration would like to thank the IAA-CSIC and MPIA-MPG as major partners of the observatory, and CAHA itself, for the unique access to telescope time and support in manpower and infrastructures. We also thank the CAHA staff for the dedication to this project. We thank the support of the IAA Computing group. Support from the Spanish Ministerio de Economía y Competitividad, through projects AYA2016-77846-P, AYA2014-57490-P, AYA2010-15081, and Junta de Andalucía P12-FQM-2828. SFS is grateful for the support of a CONACYT (Mexico) grant CB-285080, and funding from the PAPIIT-DGAPA-IA101217 (UNAM).

References

[1] de Amorim, A. L., García-Benito, R., Cid Fernandes, R., et al. 2017, MNRAS, 471, 3727

[2] Bell, E. F., & de Jong, R. S. 2000, MNRAS, 312, 497

[3] Bell, E. F., McIntosh, D. H., Katz, N., & Weinberg, M. D. 2003, ApJS, 149, 289

[4] Bruzual, G., & Charlot, S. 2003, MNRAS, 344, 1000

[5] Cardelli, J. A., Clayton, G. C., & Mathis, J. S. 1989, ApJ, 345, 245

[6] Chabrier, G. 2003, PASP, 115, 763

[7] Cid Fernandes, R., Mateus, A., Sodré, L., Stasińska, G., & Gomes, J. M. 2005, MNRAS, 358, 363

[8] Cid Fernandes, R., Pérez, E., García Benito, R., et al. 2013, A&A, 557, A86

[9] Driver, S. P., Hill, D. T., Kelvin, L. S., et al. 2011, MNRAS, 413, 971

[10] Gallazzi, A., & Bell, E. F. 2009, ApJS, 185, 253

[11] García-Benito, R., González Delgado, R. M., Pérez, E., et al. 2017, A&A, 608, A27

[12] González Delgado, R. M., Pérez, E., Cid Fernandes, R., et al. 2014, A&A, 562, A47

[13] González Delgado, R. M., Cid Fernandes, R., Pérez, E., et al. 2016, A&A, 590, A44

[14] Into, T., & Portinari, L. 2013, MNRAS, 430, 2715

[15] Kauffmann, G., Heckman, T. M., White, S. D. M., et al. 2003, MNRAS, 341, 54

[16] López Fernández, R., González Delgado, R. M., Pérez, E., et al. 2018, A&A, 615, A27

[17] Panter, B., Heavens, A. F., & Jimenez, R. 2003, MNRAS, 343, 1145

[18] Roediger, J. C., & Courteau, S. 2015, MNRAS, 452, 3209

[19] Sánchez, S. F., Kennicutt, R. C., Gil de Paz, A., et al. 2012, A&A, 538, A8

[20] Sánchez, S. F., Rosales-Ortega, F. F., Jungwiert, B., et al. 2013, A&A, 554, A58

[21] Sánchez, S. F., García-Benito, R., Zibetti, S., et al. 2016, A&A, 594, A36

[22] Stoughton, C., Lupton, R. H., Bernardi, M., et al. 2002, AJ, 123, 485

[23] Taylor, E. N., Hopkins, A. M., Baldry, I. K., et al. 2011, MNRAS, 418, 1587

[24] Zibetti, S., Charlot, S., & Rix, H.-W. 2009, MNRAS, 400, 1181

Highlights on Spanish Astrophysics X, Proceedings of the XIII Scientific Meeting of the Spanish Astronomical Society held on July 16 – 20, 2018, in Salamanca, Spain. B. Montesinos, A. Asensio Ramos, F. Buitrago, R. Schödel, E. Villaver, S. Pérez-Hoyos, I. Ordóñez-Etxeberria (eds.), 2019

Angular Redshift Fluctuations. A New Cosmological Observable.

Carlos Hernández-Monteagudo[1]

[1] Centro de Estudios de Física del Cosmos de Aragón (CEFCA)
Plaza San Juan, 1, E-44001, Teruel, Spain

Abstract

We study the angular statistical properties of maps of galaxy redshifts as computed as the average weighted redshift of all galaxies falling in the same sky pixel. The choice for this weights is a Gaussian centered upon some input redshift $z_{\rm obs}$ and with a typical width σ_z in the range 10^{-2}–10^{-1}. At each position of the sky $\hat{n}$, this defines an angular map of redshifts given by $z(\hat{n}) = \bar{z} + \delta z(\hat{n})$. We predict the angular power spectrum of such angular redshift fluctuations (ARF), for every generic choice of $z_{\rm obs}$ and σ_z, under cosmological linear perturbation theory. We find that ARF are sensitive to the underlying cosmological density and radial peculiar velocity fields, providing a *tomographic* description of those fields which does not rely upon any fiducial cosmological model converting redshifts into distances. The ARF are also found to provide *additional* cosmological information on top of that provided by angular galaxy density fluctuations (ADF), while behaving much more robustly in the presence of systematics biasing the observed number of galaxies. These theoretical predictions are confirmed when comparing to the outcome of 100 COLA numerical simulations, which also quantify the impact of non-linear evolution at different angular scales and cosmological epochs. When applying our formalism on the BOSS DR12 spectroscopic galaxy sample, we obtain unprecedented tomographic and very competitive measurements on the galaxy bias and growth rate for the LOWZ and CMASS galaxy samples.

1 Introduction

For the last twenty years different efforts have been scanning the universe wider and deeper, attempting to gain insight on the processes of the expansion of the universe and the growth of structure therein [2, 11, 1, 5]. These processes encode precious information of the (arguably) largest enigmas in current fundamental physics: the nature of dark matter and dark energy. According to the standard cosmological model, the former is the dominant form of matter in the universe (about 5 times more abundance than standard, baryonic matter), while the latter constitutes a repulsive form of energy amounting to roughly 70 % of the total energy budget in the universe [9].

These two problems are, at the same time, coupled to other open questions in physics: is Einstein's theory of gravity correct on the largest cosmological scales? How much room is there left for alternative theories of gravity? What is the weight and hierarchy of the neutrinos? Are there other light particle species in the universe? Can we test extensions of the particle physics standard model with astrophysical and/or cosmological observations?

In this very exciting context, it becomes essential to develop techniques that assure an unbiased and quasi-optimal extraction of cosmological information out of the data. Currently, standard techniques compute the 2- and 3-point statistics of the spatial and/or angular density of galaxies, which are seen as biased samplers of the underlying matter density field. Since the only proxy for the distance to those galaxies is the observed redshift, it is customary to map the galaxies' angular and redshift coordinates into the tridimensional space. This process, however, requires the assumption of an underlying cosmological (fiducial) model that enables the mapping between the (observed) redshift and the corresponding distance to the galaxies. In this mapping, the contribution of the galaxies' radial peculiar motion becomes visible through the so-called *redshift space distortions* (RSD). These peculiar velocities are triggered by gravity, and thus provide information on the growth of structure at each cosmological epoch. Measuring these velocities accurately has implications not only for gravity, but also for dark energy studies and investigations towards the presence of additional light particle species in the universe.

Here we introduce a novel method to probe the cosmological density and radial peculiar velocity fields that (i) works in a tomographic way, providing a measurement for each choice of cosmological redshift, (ii) does not rely upon the assumption of any fiducial cosmological model, and (iii) is particularly robust with respect to systematics biasing the observed number density of matter tracers (galaxies, QSOs, etc).

2 The Angular Redshift Fluctuations (ARF)

The ARF are based upon the estimation of the average redshift, within a given sky pixel, of all galaxies falling in that pixel after assigning them a Gaussian weight. Such Gaussian weights are adopted to be of the form $W_j \equiv \exp -(z_j - z_{\rm obs})^2/(2\sigma_z^2)$, where z_j is the observed redshift of the j-th galaxy, and $z_{\rm obs}$ and σ_z are the observer's choices for the central redshift and redshift width with which conducting the analyses. In this way, for a given sky position/sky pixel $\hat{n}$, the ARF would be computed as

$$\delta z(\hat{n}) = \frac{\sum_{j\in\hat{n}} W_j (z_j - \bar{z})}{\langle \sum_{j\in\hat{n}} W_j \rangle_{\hat{n}}}. \tag{1}$$

The sum in the numerator goes through all galaxies falling within a pixel centred upon $\hat{n}$, and $\bar{z}$ stands for the average redshift of the sample under the same Gaussian width in the entire footprint of the survey, $\bar{z} = (\sum_j W_j z_j)/(\sum_j W_j)$. Finally, the brackets $\langle ... \rangle_{\hat{n}}$ denote angular averages over the same footprint of the galaxy survey.

As shown in [6], it is easy to show that, at first order, the ARF field is sensitive to both the matter density and the radial peculiar velocity fields under the Gaussian redshift windows:

$$\bar{z}+\delta z(\hat{\mathrm{n}}) = \mathcal{F}[z_H]+\mathcal{F}[b_g\delta_{\mathrm{m}}\,(z_H-\mathcal{F}[z_H])]+\mathcal{F}\left[\frac{\mathbf{v}\cdot\hat{\mathrm{n}}}{c}(1+z_H)\left(1-\frac{d\log W}{dz}(z_H-\mathcal{F}[z_H])\right)\right]+\,\mathcal{O}(2^{\mathrm{nd}}), \tag{2}$$

where $\mathcal{F}[g]$ denotes the (normalized) integral of function g under the Gaussian redshift window, b_g refers to the galaxy bias, z_H is the Hubble flow redshift, and $\mathbf{v}$ is the proper peculiar velocity vector.

The kernels are such if either the matter density δ_m or the line-of-sight velocity are constant under the Gaussian window, then they do not contribute to the ARF: for δ_m, the kernel is very close to a line-of-sight dipole/gradient, while for the line-of-sight velocity the kernel is sensitive to smaller scale radial variations. Interestingly, for small values of σ_z (σ_z 10^{-2}), these kernels are practically orthogonal to the corresponding kernels of the galaxy number angular density fluctuations (hereafter ADF), that are given by

$$\delta_g(\hat{n}) = \mathcal{F}[b_g\delta_{\mathrm{m}}\,] + \mathcal{F}\left[\frac{\mathbf{v}\cdot\hat{\mathrm{n}}}{c}(1+z_H)\frac{d\log W}{dz}\right] +\ \mathcal{O}(2^{\mathrm{nd}}). \tag{3}$$

This means that the ARF provide *complementary* information to that provided by ADF. Furthermore, it is also worth mentioning that, due to the peculiar gradient-like form of the kernel for the δ_m term, the ARF are highly correlated to the line-of-sight projected peculiar velocities under the Gaussian redshift shell, making the ARF an ideal proxy for radial peculiar velocities at any redshift. This permits cross-correlating ARF maps with other maps containing information about radial peculiar velocities, like CMB maps containing contribution from the kinetic Sunyaev-Zeldovich effect (see [4] for first application of this methodology on CMB data from the *Planck* experiment).

Finally, if at the time of conducting any given galaxy survey the observed number of galaxies in a given region of the sky is biased due to either multiplicative (γ) or additive (ϵ) systematics, $n_{g,\mathrm{obs}} = \gamma(n_g + \epsilon)$, then it is easy to prove that the resulting ARF will be biased only by the additive systematics if these change significantly under the (usually narrow) redshift Gaussian window shell, $\delta z_{\mathrm{obs}} = \delta z + \mathcal{F}[\epsilon(z-\bar{z})]$. Otherwise, the impact of systematics biasing the ADF cancels at leading order for the ARF.

3 Comparison to numerical simulations

In order to asses the correctness of the equations outlined in the previous section, we compare those equations with the output of 100 *quick* numerical simulations computed with the `COLA` algorithm [8]. These simulations were run on a 3 Gpc box, with 1024^3 particles under a set of cosmological parameters compatible to *Planck* observations [9], see [3] for further details. For each of these simulations, a lightcone providing the position and peculiar velocity for each particle was computed, and the resulting comparison is shown in Fig. 1. In the left set of panels in Fig. 1 we provide the raw comparison of the average of the angular power spectra (C_ls) from the COLA simulations (solid lines in top panels) with the linear theory expectations (dashed lines). This comparison is conducted at $z_{\mathrm{obs}} = 0.5$ and $\sigma_z = 0.01$.

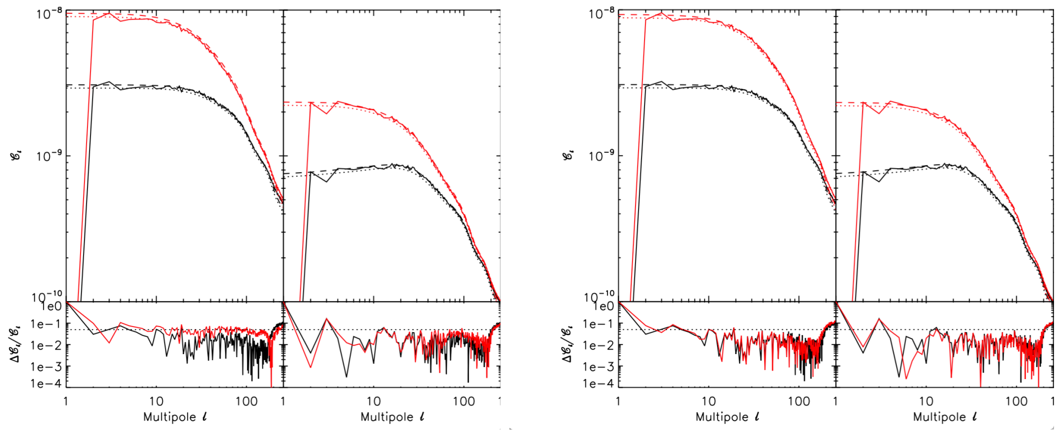

Figure 1: *Left set of panels:* Comparison of measured angular power spectra C_ls from theory and COLA simulations. The left panels refer to ARF, while the right panels to ADF. Bottom panels display relative errors. Black and red colors refer to real and redshift space, respectively. This comparison is conducted for a Gaussian redshift shell centered upon $z_{\rm obs} = 0.5$ and width $\sigma_z = 0.01$. *Right set of panels:* Comparison of measured angular power spectra C_ls as in the left set of panels, but after introducing a correction for non-linear velocities as a thermal, Gaussian PDF of $\sigma_{th} = 1\,500\,{\rm km\,s^{-1}}$.

The dotted lines display the linear theory expectations suppressed by 5 %. Red color denote results obtained in redshift space (i.e., the selection of the particles under the Gaussian redshift window takes into account the particles' peculiar velocities), while the black lines are obtained in real space, after nulling the particles' peculiar velocities. In both plots, the left panels refer to ARF angular power spectra, while the right panels to the angular power spectra of ADF. We can see that, in the left two panels of Fig. 1, the comparison of the angular power spectra in real space (black color) is very good: the bottom panels (providing the relative error) show that differences between the theory and the average output of the simulations is at the level of a few percent, as expected from the number of COLA simulations. In redshift space, however, the situation is different: the velocities seem to drive the C_ls for ARF systematically below the linear theory expectation by $\sim 5\,\%$. This low bias is not so evident for ADF, and is absent for wider choices of σ_z, $\sigma_z > 0.02$, and higher values of $z_{\rm obs}$.

It turns out that this low bias is due to non-linear, thermal peculiar velocities of the particles in the simulations, caused by non-linear gravitational growth of structures, affecting preferentially small spatial scales and later epochs/lower redshifts. This can be easily modeled by a Gaussian distribution function of the type $\mathcal{P} \propto \exp -v_{los}^2/(2\sigma_{th}^2)$, with the value of the thermal broadening in the radial velocity distribution function being a fit from numerical simulations. In the right set of panels in Fig. 1 we show that adopting $\sigma_{th} = 1\,500\,{\rm km\,s^{-1}}$ provides a satisfactory fit in all multipoles up to $l \sim 150$, where the impact of other non-linearities become dominant. The value of $\sigma_{th} = 1\,500\,{\rm km\,s^{-1}}$ is indeed higher than expected for typical thermal motions of particles at $z_{\rm obs} = 0.5$. This effective value of thermal broadening also includes the smearing of anisotropy due to the fact that galaxies/particles are

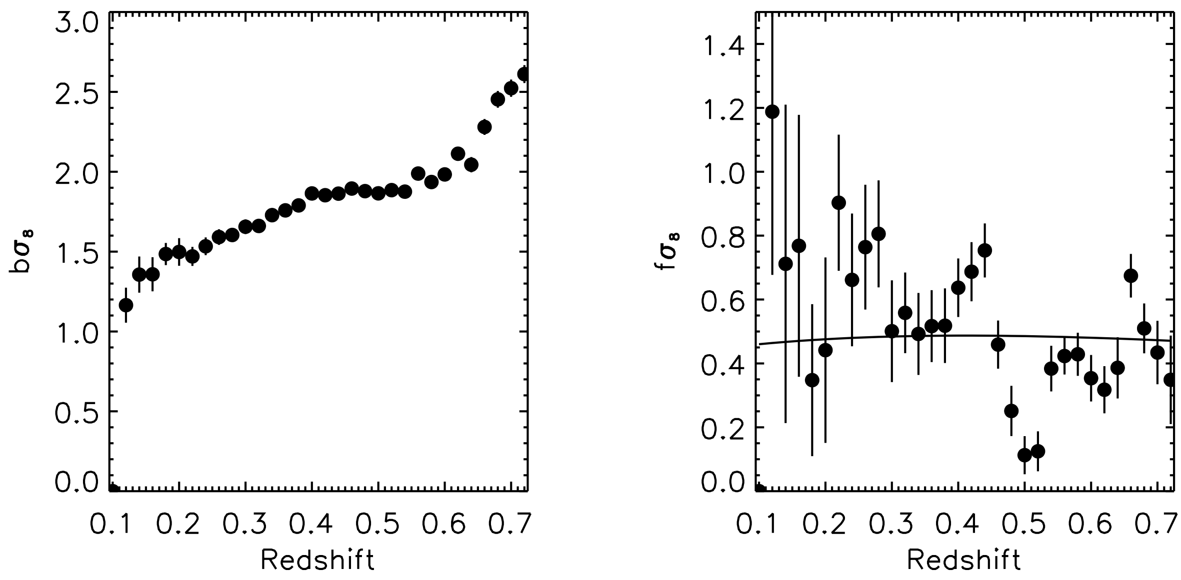

Figure 2: Preliminary measurements of the bias and growth rate for the LOWZ and CMASS galaxy samples of Data Release 12.

selected in redshift space: for a finite particle number density, the selection of particles under the Gaussian redshift modifies the anisotropy pattern, and this (un-modeled) effect is more important for narrow redshift shells.

4 First application to real data and conclusions

We use the Data Release 12 of the BOSS collaboration for testing the proposed methodology. In particular, we focus on both the LOWZ and CMASS galaxy samples, which contain more than 1.2 million galaxies in a footprint covering almost a quarter of the sky ($f_{sky} \approx 0.23$). We compute both the ADF and the ARF, but find that the former, on the large angular scales, are dominated by spurious power that is known to be caused predominantly by the blinding induced by stars at the moment of target definition (see, e.g., [10], for one of the first works addressing systematics in BOSS data). We see that the ARF are, instead, pretty immune to these systematics, and find no clear evidence for excess power. These confirms our expectations that ARF are more robust against systematics, as outlined above.

We conduct ARF tomography throughout the redshift range sampled by the LOWZ and CMASS samples, providing measurements of the galaxy bias $b_g\sigma_8$ and the velocity growth factor $f\sigma_8$ after combining our measurements with those of the *Planck* experiment. We display our results in Fig. 2, which is obtained after combining the information for ARF measurements with $\sigma_z = 0.01$ and 0.05. Our bias and velocity measurements are compatible with previous estimates of the BOSS collaboration, although ours constitute the first tomographic estimations with unprecedented redshift resolution. We are currently polishing these measurements, and exploring the possibility of constraining dark energy and the nature of gravity with these data (see [7] for further details).

The ARF constitute a new cosmological observable which is sensitive to both the density and radial velocity fields. It works in a tomographic way, its phases are correlated to those of the projected radial velocities, and is particularly robust against systematics biasing the observed number density of galaxies. Its application on real data is currently providing competitive measurements of the growth rate of the universe. Future prospects for this observable include (but are not limited to) measurements of f_{NL}, the parameter accounting for local-type non-Gaussianity during inflation, the presence of light particle species, relativistic corrections (including gravitational potential shifts), or its application in Lyman-α or in HI 21 cm surveys.

Acknowledgments

I thank the SEA SOC for giving me the opsportunity of presenting this work during the SEA Scientific Meeting at the University of Salamanca, my *Alma mater*.

References

[1] Alam, S., Ata, M., Bailey, S., et al. 2017, MNRAS, 470, 2617

[2] Colless, M., Dalton, G., Maddox, S., et al. 2001, MNRAS, 328, 1039

[3] Chaves-Montero, J., Angulo, R. E., & Hernández-Monteagudo, C. 2018, MNRAS, 477, 3892

[4] Chaves-Montero, J., Hernández-Monteagudo, C., Hurier, G., & Angulo, R. E., 2018, MNRAS (in preparation)

[5] Dawson, K. S., Kneib, J.-P., Percival, W. J., et al. 2016, AJ, 151, 44

[6] Hernández-Monteagudo, C., Hurier, G., Chaves-Montero, J., Angulo, R., & Bonoli, S., 2017, Physical Review Letters, (submitted).

[7] Hernández-Monteagudo, C., Hurier, G., Chaves-Montero, J., Angulo, R., Aricò, G., & Bonoli, S., 2018, Physical Review Letters, (in preparation).

[8] Koda, J., Blake, C., Beutler, F., Kazin, E., & Marin, F. 2016, MNRAS, 459, 2118

[9] Planck Collaboration, Ade, P. A. R., Aghanim, N., et al. 2016, A&A, 594, A13

[10] Ross, A. J., Ho, S., Cuesta, A. J., et al. 2011, MNRAS, 417, 1350

[11] Wakamatsu, K., Colless, M., Jarrett, T., et al. 2003, The Proceedings of the IAU 8th Asian-Pacific Regional Meeting, Volume 1, 289, 97

Highlights on Spanish Astrophysics X, Proceedings of the XIII Scientific Meeting of the Spanish Astronomical Society held on July 16 – 20, 2018, in Salamanca, Spain. B. Montesinos, A. Asensio Ramos, F. Buitrago, R. Schödel, E. Villaver, S. Pérez-Hoyos, I. Ordóñez-Etxeberria (eds.), 2019

Lightening up Dark Galaxy candidates beyond redshift 3 with MUSE.

Raffaella Anna Marino[1], Sebastiano Cantalupo[1], Simon Lilly[1] and the MUSE collaboration.

[1]Department of Physics, ETH Zürich,Wolfgang−Pauli−Strasse 27, 8093 Zürich, Switzerland

Abstract

Theoretical models suggest that each galaxy pass through a 'dark galaxy' phase of formation that involves an epoch when galaxies are gas-rich but inefficient at forming stars. Here, I present the new results published in Marino et al. 2018 on the search for dark galaxies at high redshift ($z > 3$) from the analysis of six MUSE (Multi Unit Spectroscopic Explorer) deep fields. In particular, we take advantage of the quasar-induced fluorescent Lyman α emission to detect and study these otherwise invisible objects to our optical telescopes. In addition, contrary to previous studies based on deep narrow-band (NB) imaging, our integral field survey has several advantages including a nearly uniform sensitivity coverage over a large volume in redshift space as well as full spectral information at each location. Specifically, in Marino et al. 2018, we study the rest-frame equivalent width (EW_0) distributions of the Lyα sources detected in proximity to the quasars and in control samples. We find a clear correlation between the locations of high EW_0 objects and the quasars. This correlation is not seen in other properties such as Lyα luminosities or volume overdensities, suggesting their possible fluorescent nature. Our main result is the discovery of 8 Lyα sources without continuum counterparts and EW_0 limits larger than 240 Å that, so far, are the best and only candidates for dark galaxies at $z > 3$.

1 Introduction

A substantial effort, both observationally and theoretically, has been done in the past decade with the aim to characterize the fuel for the formation of the first stars, i.e. the cold gas ($T \sim 10^4$ K) surrounding the galaxies. However, due to small sample sizes and technical limitations of the current facilities [9], our knowledge about the nature of the Intergalactic Medium (IGM) and Circumgalactic Medium (CGM) at high redshift ($z > 3$) is still limited.

Theoretical models have suggested the existence of a primordial phase (which is almost optically dark) in galaxy formation where gas-rich galaxies reside in low-mass halos (e. g.,

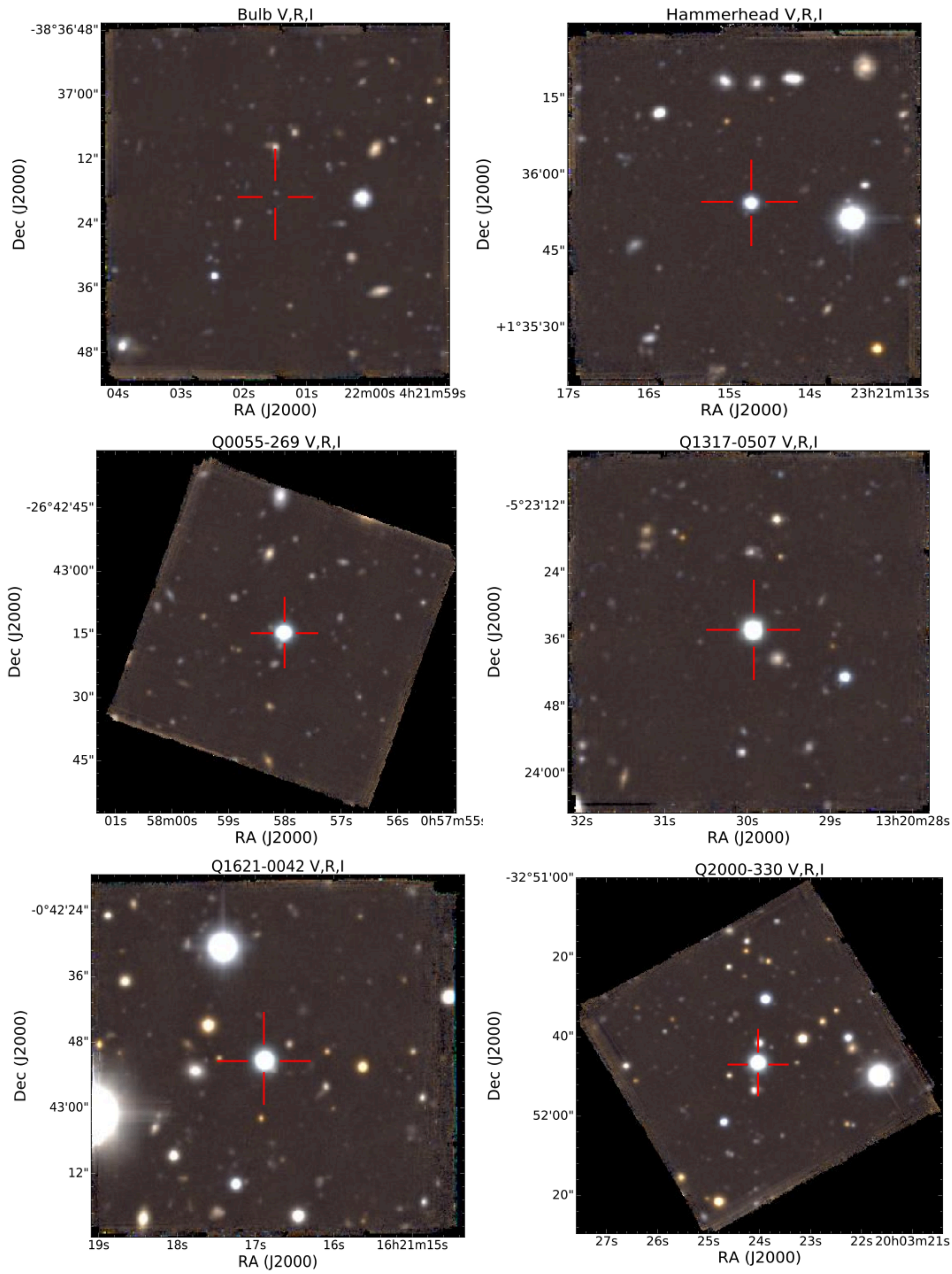

Figure 1: Composite pseudo−color images of the MUSE fields. The RGB colors correspond to the V-, R-, and I-band images obtained from the MUSE datacubes. Each image is 60" ×60" and the red cross indicates the AGN/QSO location. North is up and East is left.

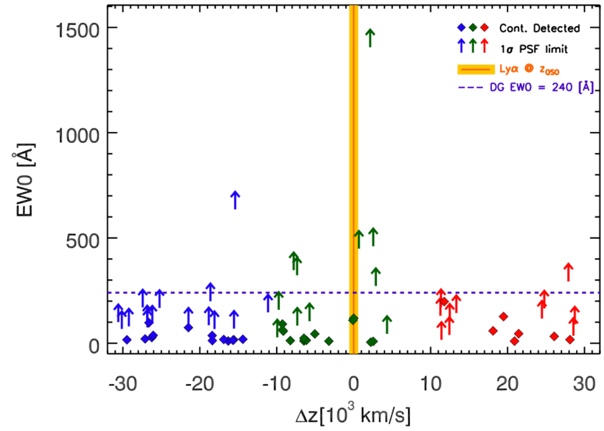

Figure 2: MUSE high$-z$ $EW_0(Ly\alpha)$ distribution versus the spectral distance (velocity) from the QSO. Blue and red symbols represent those LAEs detected in the control samples, while green symbols indicate the LAEs closer to the QSO. Diamonds symbolize those LAEs with continuum counterparts, and with the arrows the lower limit (at 1σ) EW_0 values for continuum undetected LAEs are plotted. The QSO velocity position (plus the 1σ error) is shown with the shaded yellow area. The horizontal dashed line denotes the EW_0 threshold (240 Å) for the Dark Galaxy candidates.

[8, 12, 13]) with very low star formation efficiencies ($\mathrm{SFEs}=\mathrm{SFR}/\mathrm{M_{gas}} < 10^{-11}\,\mathrm{yr}^{-1}$). This less efficient star formation phase of the IGM gas at high redshift could depend on several factors, including the metal-free gas present in the environment at that epoch, the H_2 self-regulation effect or the reduced CGM cooling rate [5].

Different approaches have been taken to further investigate this dark phase of galaxy formation in the literature, but in most of the studies conducted so far, the proto-galactic phase preceding the first spark of star formation (SF) has been poorly constrained. The different methods that have been used in the past to try to detect the "starless" IGM gas, are summarized in [15]. In our case, we make use of the QSO-induced fluorescent Lyα emission that can locally boost the signal from dense and otherwise optically-dark gas clouds by orders of magnitude [10, 3, 6, 11, 16] acting as a flashlight on its surroundings. Moreover, we use an alternative approach to narrow band imaging to search for the fluorescent Lyα emission, by using the MUSE instrument [1]. MUSE has several advantages over previous instrumental techniques: (1) homogeneous data quality, (2) large wavelength range (which means a large cosmological volume) and (3) provides 2D information for robust analysis, enabling us to investigate how the IGM gas is converted into stars. More importantly, the use of Integral Field Spectroscopy (IFS) provides the ability to build control samples under the same instrumental and observational conditions, as well as data reduction and analysis techniques, with respect to the main dataset.

2 Data and Analisis

In Marino et al. 2018, we study six QSO medium-deep (~ 10 hr each) fields at $z > 3$ part of MUSE Guaranteed Time Observation (GTO) program. The observations comprise 270 exposures ($\approx$ 65 hours) in total. Each MUSE datacube is made of 321×328 spaxels with a sampling grid of 0.2" $\times$ 0.2" $\times$ 1.25 Å yielding $\sim$90,000 spectra per frame. The composite pseudo-color images computed from the MUSE datacube combining the broad V-, R- and I-band images are shown in Figure 1.

The reduction of all 65 hrs of the MUSE data was performed using both the latest version of the ESO MUSE Data Reduction Software (DRS, pipeline version 1.6, [18]), complemented with the `CubExtractor` package (`CubEx` hereafter; Cantalupo, in prep.). We use the DRS routine *MUSE scibasic* for the master-bias, the master-flat, the twilight and illumination corrections, and wavelength calibration. The individual datacubes are created with the *MUSE scipost* routine after performing the flux calibration, together with the geometry and astrometry corrections. Next, we performed the post-processing using several routines of the `CubEx` package in order to improve the automatic flat-fielding correction, the pipeline sky subtraction and to combine the different exposures into the final datacubes (see [15] for further details). The analysis of the six fields comprises the Point Spread Function (PSF) subtraction, to ensure minimum contamination from the QSO PSF in our LAEs detection as well as the subtraction of the brightest foreground continuum sources, again using the `CubEx` tools. Subsequentaly, we build three different sub-cubes from each datacube with the same spectral width 200 Å (or 160 spectral pixels). The on-source datacube is centered on the QSO Lyα wavelength. Two control sample adjacent to the on-source datacube were extracted on the blue and red sides. We blindly implemented 3D source detection on the 18 reduced and post-processed datacubes using `CubEx` with the same threshold parameters ((I) a minimum of 40 connected voxels above a (II) signal-to-noise ratio (SNR) threshold of 3.5 and (III) a SNR measured on the Lyα emission line from the 1D extracted spectrum above 4.5). Finally, we obtained a full catalog of $\sim$ 200 line emitters automatically detected in the on-source and control sample datacubes over the six MUSE fields. Specifically, in a total volume of $\sim$90 physical Mpc^3, we found 186 LAEs, 25 [O II], 13 [O III] emitters and 8 AGN candidates.

3 Lyα equivalent width distribution

Here we only present the equivalent width (EW) results because of space limitation and the reader is referred to the original paper for a complete overview of the dark galaxies results [15]. In order to compute the rest-frame equivalent width, EW$_0$(Lyα), of our targets, we decide to follow two different approaches depending on the detection (or not) of our LAE in the continuum image. A LAE is defined as continuum detected (CD) if its continuum flux measured within the PSF size aperture is higher than 3 times the standard deviation, i.e. the local noise *std*, of the continuum image otherwise the LAE is considered continuum undetected (CU). Of the 186 LAEs selected in our sample, 54% were undetected in the continuum. In the case of the continuum detected LAEs, we used the matched-aperture approach as in [6] while for those LAEs undetected in the continuum image, we used the PSF$-$aperture approach (see [15] for a detailed description of the EW$_0$(Lyα) measurements).

In Figure 2, we present the measured EW$_0$(Lyα) values and limits as a function of the distance (velocity) from the QSO of the high redshift sample (i. e. Q1317, Q0055, Q1621, Q2000 fields at $z > 3.2$). The vertical yellow shaded area marks the position of the QSO.

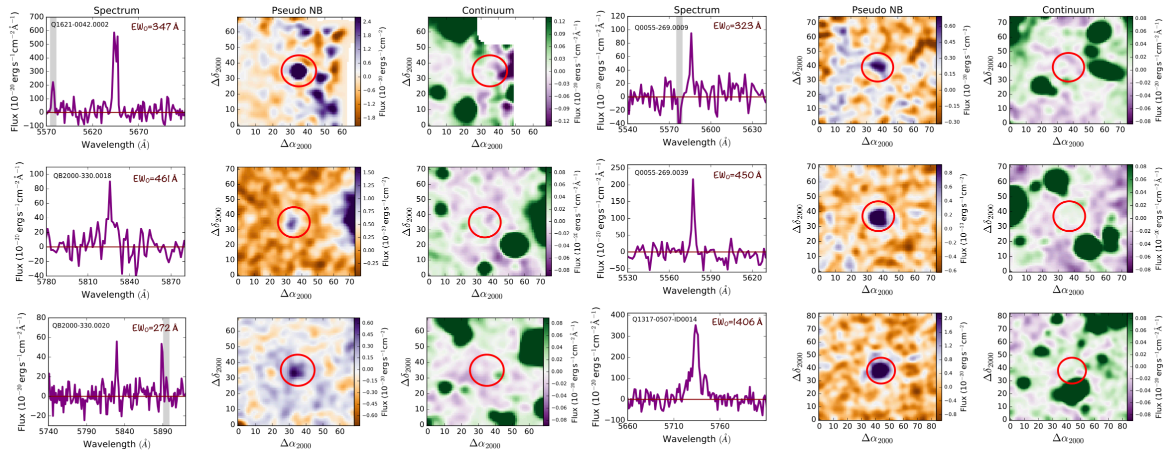

Figure 3: Dark Galaxy candidates detected in the MUSE high$-z$ fields. For each DG, a zoom in of the MUSE spectrum around the observed Lyα emission wavelength, the MUSE Lyα pseudo narrow$-$band images and the continuum broad$-$band image obtained from the MUSE datacube are shown. The position of the candidate is marked by the red circle. In each panel North is up and East is left. Plate scale is 0.2"/pix.

The CD LAEs are shown with diamond symbols while the arrows represent the lower limit EW_0(Lyα) estimations for the CU LAEs. Green colors indicate the LAEs detected in the on-source (QSO) samples, while the blue and the red ones represent the control samples. The horizontal dashed line at 240 Å denotes the EW_0(Lyα) limit expected for galaxies with PopII stellar population ([7, 14]). In all MUSE high$-z$ fields we clearly see a higher occurrence of objects with EW_0(Lyα)$>$ 240Å closer to the QSOs rather than in the control samples.

In particular, for the MUSE high$-z$ fields we found that 8 LAEs present a lower limit on their EW_0(Lyα) larger than 240 Å, and 6 of them are observed in proximity of the quasars. In Figure 3, we show the spectra and postage stamps of these 6 high EW_0 objects, a.k.a Dark Galaxies, detected in the high redshift samples.

4 Conclusions

Making use of medium-deep ($\sim$10 hr) MUSE GTO observations around five bright QSOs and one Type-II AGN, we have searched for fluorescently illuminated Dark Galaxies at $z >$ 3.2 among Lyα emitters in proximity of the quasars. Within a volume of 90 physical Mpc^3, we have detected $\sim$ 200 line emitters. We estimated their EW_0(Lyα) in a homogenous way among the main and the control samples using two different approaches depending on the detection in the continuum of each source. In particular, we found 11 objects with EW_0(Lyα) lower limits larger than 240 Å. The analysis of the EW_0(Lyα) distribution revealed that these high EW_0 LAEs tend to preferentially reside within $\sim$ 10^4 km/s from the quasar systemic redshift. This excess of high EW_0 sources correlated with distance from the quasar is completely consistent with the expectations of quasar fluorescent illumination (e.g., [2, 6, 4, 17]). Therefore, the 8 LAEs with $EW_0(Ly\alpha) > 240$ Å and without the continuum counterpart located in close proximity of the QSOs represent the best and only candidates up to date for Dark Galaxies at $z > 3$ (see Marino et al. 2018 for more details).

Acknowledgments

This work is based on observations taken at ESO/VLT in Paranal and we would like to thank the ESO staff for their assistance and support during the MUSE GTO campaigns.

References

[1] Bacon, R., Accardo, M., Adjali, L., et al. 2010, Proc. SPIE, Vol. 7735, 773508

[2] Borisova, E., Lilly, S. J., Cantalupo, S., et al. 2016b, ApJ, 830, 120

[3] Cantalupo, S., Porciani, C., Lilly, S. J., & Miniati, F. 2005, ApJ, 628, 61

[4] Cantalupo, S., Lilly, S. J., & Porciani, C. 2007, ApJ, 657, 135

[5] Cantalupo, S. 2010, MNRAS, 403, L16

[6] Cantalupo S., Lilly S. J., Haehnelt M. G., 2012, MNRAS, 425, 1992

[7] Charlot, S., & Fall, S. M. 1993, ApJ, 415, 580

[8] Dekel, A., Birnboim, Y., Engel, G., et al. 2009, Nature, 457,451

[9] Fumagalli, M., Hennawi, J. F., Prochaska, J. X., et al. 2014, ApJ, 780, 74

[10] Haiman, Z., & Rees, M. J. 2001, ApJ, 556, 87

[11] Kollmeier, J. A., Zheng, Z., Davé, R., et al. 2010, ApJ, 708, 1048

[12] Krumholz, M. R., & Dekel, A. 2012, ApJ, 753, 16

[13] Kuhlen, M., Madau, P., & Krumholz, M. R. 2012, ApJ, 776, 34

[14] Malhotra, S., & Rhoads, J. E. 2002, ApJL, 565, L71

[15] Marino, R. A., Cantalupo, S., Lilly, S. J., et al. 2018, ApJ, 859, 53

[16] Martin, N. F., Ibata, R. A., Rich, R. M., et al. 2014, ApJ, 786, 106

[17] Trainor, R. F., & Steidel, C. C. 2012, ApJ, 752, 39

[18] Weilbacher, P. M. 2015, Science Operations 2015: Science Data Management, Zenodo, doi:10.5281/zenodo.3465

Highlights on Spanish Astrophysics X, Proceedings of the XIII Scientific Meeting of the Spanish Astronomical Society held on July 16 – 20, 2018, in Salamanca, Spain. B. Montesinos, A. Asensio Ramos, F. Buitrago, R. Schödel, E. Villaver, S. Pérez-Hoyos, I. Ordóñez-Etxeberria (eds.), 2019

The Stellar Tidal Stream Survey.

David Martínez-Delgado[1]

[1]Astronomisches Rechen-Institut, Zentrum für Astronomie der Universität Heidelberg, Heidelberg, Germany

Abstract

Mergers and tidal interactions between massive galaxies and their dwarf satellites are a fundamental prediction of the Lambda-Cold Dark Matter cosmology. These events are thought to influence galaxy evolution throughout cosmic history and to provide important observational diagnostics of structure formation. Stellar streams in the Local Group are spectacular evidence for satellite disruption at the present day. However, constructing a significant sample of tidal streams beyond our immediate cosmic neighborhood has proven a daunting observational challenge and their potential for deepening our understanding of galaxy formation has yet to be realized. Over the last decade, the Stellar Tidal Stream Survey has obtained deep, wide-field images of nearby Milky-Way analog galaxies with a network of robotic amateur telescopes, revealing for the first time an assortment of large-scale tidal structures in their halos. I discuss the main results of this project and future plans for performing dynamical studies of the discovered streams.

1 Stellar Tidal Streams as Galaxy Formation Diagnostic

Within the hierarchical framework for galaxy formation, the stellar bodies of massive galaxies are expected to form and evolve not only through the inflow of cold gas, but also the infall and successive mergers of low-mass, initially bound systems. Commonly referred to as satellites, they span a wide mass range and consist of dark matter, gas, and, in most cases, stars. While the interaction rate is expected to drop to the present-day epoch, numerical cosmological models, built within the Λ-Cold Dark Matter (LCDM) paradigm (e.g. [3]; [4]), predict that such satellite disruption still occurs around all massive galaxies. As a consequence, the stellar halos of these galaxies should contain a wide variety of diffuse structural features, such as **stellar streams** or shells, that result from interactions and mergers with dwarf satellites. The most spectacular cases of tidal debris are long, dynamically cold stellar streams, formed from a disrupted dwarf satellite, that wrap around the host galaxy's disk and roughly trace the orbit of the progenitor satellite. Although these fossil records disperse into amorphous

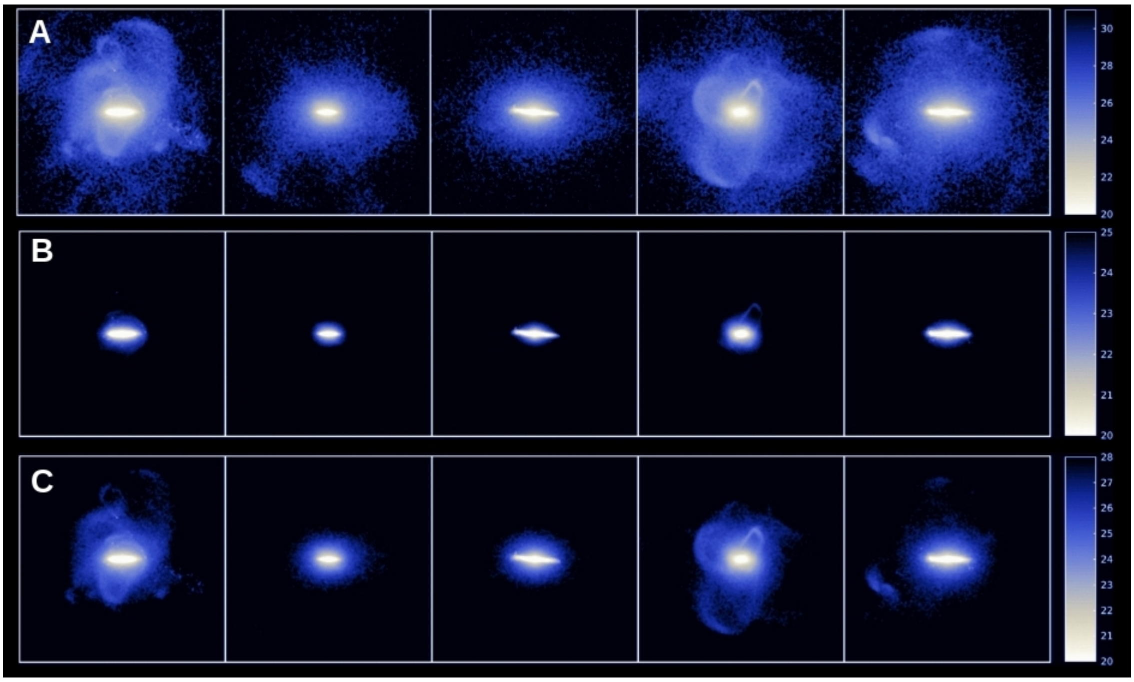

Figure 1: Expected 'halo streams' around a Milky Way - like galaxy from the Auriga cosmological simulations ([9]). The panels show an external perspective of several realizations of a simulated galaxy within the hierarchical framework, with streams resulting from tidally disrupted satellites. They illustrate a variety of typical accretion histories for Milky Way-type galaxies. Each panel is 300 kpc on a side. The different rows show theoretical predictions for detectable tidal features in each halo model, assuming three different surface brightness (SB) limit detection limits (A: $\mu_{\rm lim} = 31$, B:$\mu_{\rm lim} = 25$ and C: $\mu_{\rm lim} = 28$ mag/arcsec^2). This suggests that the number of tidal features visible in the outskirts of spirals varies dramatically with the SB limit of the data, with no discernible sub-structure expected for surveys with SB limits brighter than ~ 25 mag/arcsec^2 (e.g. POSS-II and SDSS).

clouds of debris (through phase-mixing) in a few Giga-years, LCDM simulations predict that stellar streams may be detected nowadays, with sufficiently deep observations, in the outskirts of almost all nearby galaxies.

The detection of these faint tidal remnants is a ubiquitous aspect of galaxy formation that has not yet been fully exploited, mainly because they are challenging to observe. Although the most luminous examples of diffuse stellar streams and shells around massive elliptical galaxies have been known for many decades, recent studies have showed that fainter analogues of these structures are common around spiral galaxies in the local universe, including the Milky Way and Andromeda ([2]; [10]). These observations provide sound empirical support for the ΛCDM prediction that tidally disrupted dwarf galaxies could be important contributors to the stellar halo formation in the Local Group spirals.

While stellar streams in the Milky Way and Andromeda can be studied in detail,

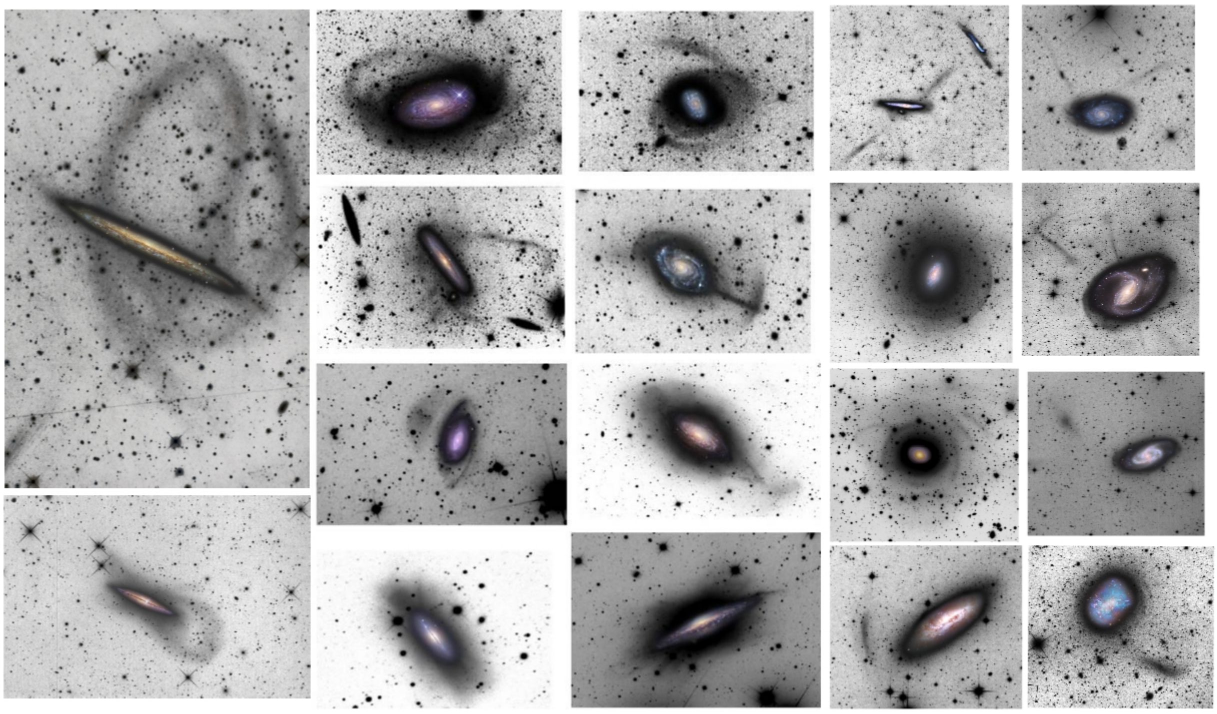

Figure 2: Luminance filter images of nearby galaxies from the Stellar Tidal Stream Survey showing large, diffuse light structures in their outskirts. A color inset of the disk of each galaxy has been overplotted for reference. An illustrative comparison of some of these features to the surviving structures visible in cosmological simulations is given in [14] (their Fig. 2). The typical surface brightness (r-band) of these streams is as faint as 26 mag/arcsec^2. All these images were taken with robotic amateur telescopes with an aperture range of 0.1–0.5-meter.

comparison with cosmological models is limited by 'cosmic variance', the differences in the individual dynamical pre-histories of overall similar galaxies. A search for analogues to these galactic fossils in a larger sample of nearby galaxies is required to understand if the recent merging histories of the Local Group spirals are 'typical', an issue that remains unclear. However, in contrast to detailed predictions from simulations, the observational portrait of minor accretion events is far from complete, owing primarily to the inherent difficulty of detecting low surface brightness features. The current LCMD numerical simulations can guide this quest for star-stream observational signatures (e.g. [12]; [4]). Recent simulations have demonstrated that the characteristics of sub-structure currently visible in the stellar halos are sensitive to recent (0-8 Gyr ago) merger histories of galaxies, over a timescale that corresponds to between the last few tens of percent of mass accretion for a spiral galaxy like the Milky Way. These models predict that a survey of $\sim$100 parent galaxies reaching a surface brightness of $\sim$29 mag/arcsec^2 would reveal many tens of tidal features, perhaps nearly one detectable stream per galaxy. However, a direct comparison of these simulations with actual observations is not yet possible because no suitably deep data sets exist.

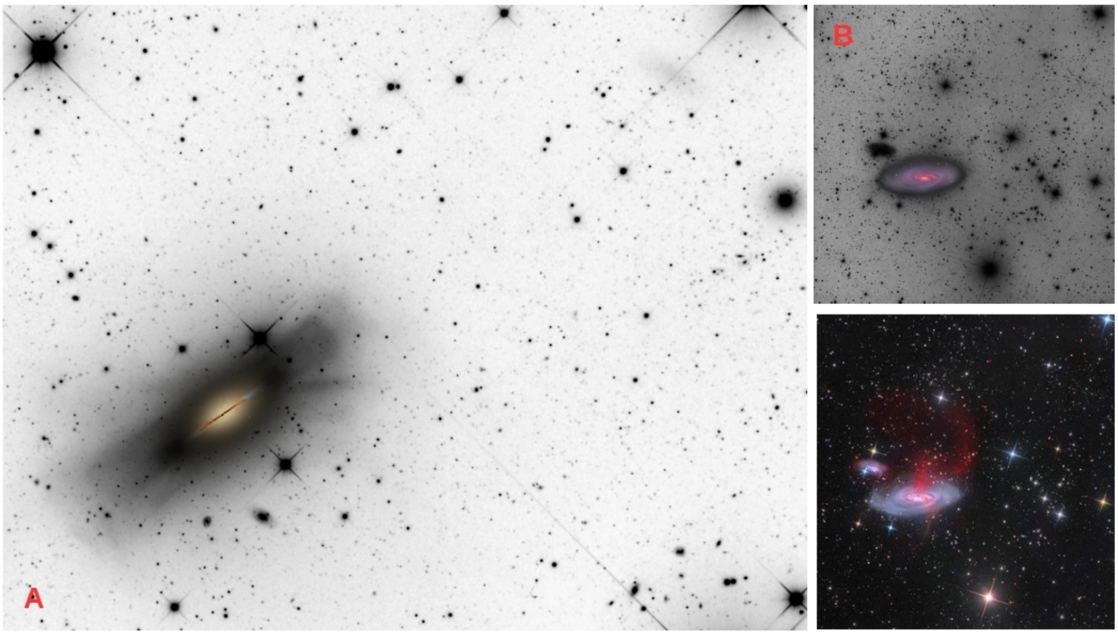

Figure 3: (*Panel A*): The complex tidal structures of the halo of NGC 5866 (together with a tidal disrupted satellite), detected for the first time in our pilot survey in 2010, revisited with a modern commercial CCD camera in 2018. Image taken by Adam Block with the Mount Lemmon 0.8-m telescope. (*Panel B*): An example of very faint diffuse light detected around NGC 4569 (top panel) associated to the presence of ionized gas emission in its halo, as revealed in our follow-up deep H_α imaging (red color in the image displayed in the bottom panel). Both images were taken with a 0.5-m telescope by Mark Hanson.

2 The Stellar Stream Survey: the first decade

Stellar tidal streams around nearby galaxies cannot be resolved into stars with our modest telescopes and thus appear as elongated diffuse light regions that extend over several arc minutes as projected on the sky. Our survey has established a search strategy that can successfully map such tidal streams to extremely faint surface brightness limits. Their typical surface brightness is 26 mag/arcsec^2 or fainter, depending on the luminosity of the progenitor and the time they were accreted ([11]). Detecting these faint features requires very dark sky conditions and wide-field, deep images taken with exquisite flat-field quality over a wide region ($>$ 30 arcmin) around the targets.

The observations of the Stellar Tidal Stream Survey (STSS) are conducted with ten privately owned observatories equipped with modest-sized telescopes (0.1-0.8-meter) equipped with a latest generation astronomical commercial CCD camera and located in Europe, the United States and Chile. Each observing location features spectacularly dark, clear skies with seeing below 1.5”. The survey strategy strives for multiple deep exposures of each target using high throughput clear filters with near-IR cut-off, known as luminance (L) filters (4000 Å$<\lambda<$7000 Å) and a typical exposure times of 7-8 hours. Our typical 3-σ SB detection limit (measured in random 2" diameter apertures) is $\sim$ 28 and 27.5 mag/arcsec^2 in g and r respectively, which is approximately two magnitudes deeper than the Sloan Digital Sky Survey (SDSS) DR8 images.

We have devised a set of straightforward sample selection criteria similar to that used in the SAGA survey ([7]): isolated Milky Way analog galaxies within 40 Mpc that have an K-band absolute magnitude $M_K <$ -19.6 and lying more than 20 degrees above the Galactic plane (avoiding cirrus dust and high stellar density fields). The luminosity range was selected to ensure that our sample included a significant number of Milky-Way analogue systems. Several targets that satisfied this criteria were not included, such as galaxies lying less than 20 degrees from the Galactic plane or galaxies with clear signatures of current major mergers.

Our observational effort has also revealed previously undetected stellar streams thus making it the largest sample of tidal structures outside the Local Group. The most conspicuous examples are displayed in Figure 2. Our collection of galaxies presents an assortment of tidal phenomena exhibiting striking morphological characteristics consistent with those predicted by cosmological models. For example, in addition to identifying *great-circles* features that resemble the Sagittarius stream surrounding our Galaxy (e.g NGC 5907, [13]), our observations uncovered enormous structures resembling an open umbrella that extends tens of kilo-parsecs into the halos of the spiral. These structures are often located on both sides of the host galaxy, and display long narrow shafts that terminate in a giant shell of debris (e.g. NGC 4651; [6]). We have also found isolated shells, giant clouds of debris floating within galactic halos, jet-like features emerging from galactic disks and large-scale diffuse structures that are possibly related to the remnants of ancient, already thoroughly disrupted satellites. Together with these remains of possibly long-defunct companions, our data also captured surviving satellites caught in the act of tidal disruption, displaying long tails departing from the progenitor satellite. We also detected a stellar tidal stream in the halo of NGC 4449, an isolated dwarf irregular galaxy analogue to the Large Magellanic Cloud ([15]). This appears to be the lowest-mass primary galaxy with a verified stellar stream so far. This discovery suggests that satellite accretion can play a significant role in building up the stellar halos of low-mass galaxies, and possibly triggering their starburst.

Our current sample so far comprises $\sim$ 50 confirmed stellar streams with a large variety of morphological types.[1] The promising results of this foray advocate a comprehensive study of tidal streams in the nearby universe and a more insistent attention to this brand new way of understanding galaxy formation.

3 Future Plans

The Stellar Tidal Stream Survey has yielded so far an unprecedented sample of bright stellar streams in nearby spiral galaxies, including the discovery of observational analogues to the canonical morphologies found in cosmological simulations of stellar halos. This offers a unique

[1]Only three external tidal streams were known when the pilot survey started in 2007. We also found a large number of negative detections, in agreement with the estimated low frequency of streams at this low surface brightness regime ([16]).

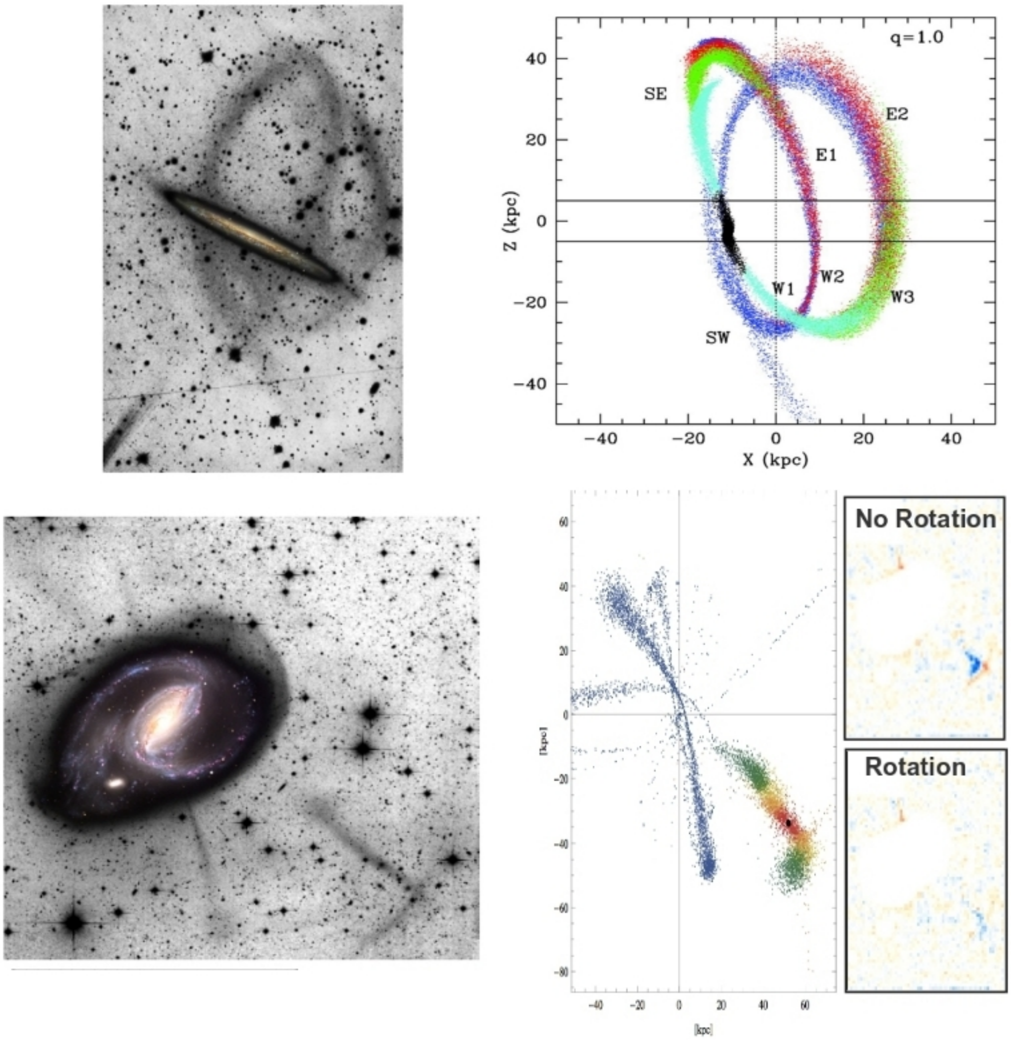

Figure 4: (*Top panel*): N-body simulations of the multiple wraps of the NGC 5907 tidal stream ([13]). Different colors correspond to the escape time of the particles. All the visible structure is explained by the destruction of a single satellite accreted ~ 3.5 Gyr ago. (*Bottom panel*): A spray-particle model fitting to our luminance-filter image of the NGC 1097 tidal stream [1]. The stellar material shedded by the progenitor is modelled using a purposely tailored modification of the *particle-spray* method ([8]). This technique faithfully reproduces the debris of an N-body disruption by ejecting particles from the Lagrange points of the progenitor, allowing to model the disruption in a few CPU-seconds.The best-fitting model quantitatively reproduces the remnant location and the X-shape of the four 'plumes'. The normalized residuals of that model to the surface brightness data shows that the peculiar perpendicular ('dog-leg') stream morphology can only be reproduced if rotation of the dwarf progenitor is included.

opportunity to study in detail the apparently still dramatic last stages of galaxy assembly in the local Universe and to probe the anticipated estimates of frequency of tidal stellar features from the LCDM paradigm for MW-sized galaxies.

These discoveries have also enabled first qualitative tests with predictions from N-body models of galaxy disruption/accretion (see Figure 4) based only on the fitting of the sky-projected features available from the imaging. Dynamical analysis of these tidal structures can provide unique views of the dark matter halos (and asymmetries) of their host galaxies. The main degeneracy of modelling streams with imaging data alone is between the orbit and the inclination. Even just a handful of individual kinematic line-of-sight velocities in different parts of the streams can break that degeneracy, especially if the streams has more than a single wrap and if the velocities are on opposite sides of the host galaxy. In fact, the properties of the host galaxy that we can constrain depend on the morphology of the streams. Assuming some kinematics is available, radial streams ('umbrellas') are useful to probe the dark matter density profile and slope on very extended radial intervals, from the centre to almost the virial radius of the host galaxy. This is shown in the analysis of the NGC 1097 tidal stream ([1]; see Figure 4 upper panel), whose stream is sufficiently unique that one kinematic point alone (the progenitor) was enough. Great circle streams (like NGC 5907; see Figure 4 top panel) with kinematics can probe the shape of the dark matter halo. Dark matter halos are expected to be triaxial and a large stream sample will allow to test this with a statistical measurement of the shapes of the dark matter halos in the local Universe.

To obtain radial velocities of individual tidal debris stars around nearby galaxies is not yet feasible with the current ground-based facilities. The current state-of-the-art for spectroscopic follow-up of these features is given by the recent study of the NGC 4449 stream (situated at 4 Mpc) by [17]. These authors used the Keck-DEIMOS spectrograph to do a first kinematic study of a stellar stream outside the Local Group based on blends of red giant branch stars, including a first spectroscopic metallicity estimate of this stream. However, more robust results using velocities of hundreds of streams stars with better signal-to-noise (S/N $\geq$20) demands observations with the European Extremely Large Telescope (ELT) and the future MOSAIC instrument ([5]) early in the next decade. The GLAO[2] High Multiplex mode will allow Calcium-Triple line observations of up to 200 objects, providing an exciting new dataset to probe the dark matter halos of at least 10 galaxies of interest beyond the Local Group.

During the upcoming years, the main objective of the STSS will be to identify those stellar streams in our cosmic neighborhood that, based on their properties (surface brightness, morphology, orbital orientation, etc), are the most promising targets to undertake a dynamical study with the MOSAIC instrument. Besides this primary objective, the results of this survey have the potential to tackle a significant number of other topics that are the focus of current astrophysical research (e.g. stellar populations of halos, the resilience of the disks involved in minor mergers, accretion of globular clusters, intra-halo light, induced star formation in streams, near-field cosmology, satellite dynamics, dark matter halo shapes, etc). This research will also provide an essential framework for exploring whether the Milky Way is a template for the archetypal spiral galaxy. In this regard, our survey will be complementary

[2]Ground Layer Adaptive Optics

in interpreting the local Galactic archaeological data from the next generation of Galactic surveys (e.g. LSST) and the astrometry mission Gaia in the context of galaxy formation and evolution, providing unique data in order to quantify how typical the Milky Way is with respect to other nearby galaxies of its type.

Acknowledgments

I thank to the Sociedad Española de Astronomía for the *I Premio Javier Gorosabel de Colaboración ProAm en Astrofísica* and the astrophotographers of the STSS who have contributed to this project during the last 10 years: R. Jay Gabany, Ken Crawford, Mark Hanson, Karel Teuwen, Johannes Schedler and Adam Block. I also thank Nicola Amorisco, Andrew Cooper, Denis Erkal, Seppo Laine, Giuseppe Donatiello, Emilio Gálvez and Chris Evans for useful comments. I thank Facundo A. Gómez for the snapshots from the Auriga cosmological simulations showed in Figure 1. I acknowledge support by Sonderforschungsbereich (SFB) 881 "The Milky Way System" sub-project A2 of the German Research Foundation (DFG) and the Spanish MINECO grant AYA2016-81065-C2-2.

References

[1] Amorisco, N., Martínez-Delgado, D., Schedler, J. 2015, arXiv:1504.03697

[2] Belokurov, V. et al. 2006, ApJ, 642, L137

[3] Bullock, J. S., Johnston, K. V. 2005, ApJ, 635, 931

[4] Cooper, A. P. et al. 2010, MNRAS, 406, 744

[5] Evans, C. J. et al. 2018 in *Early Science with ELTs*, Proceeding IAU Symposium No. 247 (arXiv: 1810.01738)

[6] Foster, C. et al. 2014, MNRAS, 442, 3544

[7] Geha, M. et al. 2017, ApJ, 847, 4

[8] Gibbons, S. L. J., Belokurov, V., Evans, N. W. 2014, MNRAS, 445, 3788

[9] Grand, R. J. J. et al. 2017, MNRAS, 467, 179

[10] Ibata, R., Martin, N. F., Irwin, M. et al. 2007, ApJ, 671, 1591

[11] Johnston, K. V., Sackett, P. D., Bullock, J. S. 2001, ApJ, 557, 137

[12] Johnston, K. V., Bullock, J. S., Sharma, S., et al. 2008, ApJ, 689, 936

[13] Martínez-Delgado, D., Peñarrubia, J., Gabany, R. J. et al. 2008, ApJ, 689, 184

[14] Martínez-Delgado, D. et al. 2010, ApJ, 140, 962

[15] Martínez-Delgado, D. et al. 2012, ApJ, 748, 24

[16] Morales, G., Martínez-Delgado, D., Grebel, E. K. et al. 2018, A&A, 614, 143

[17] Toloba et al. 2016, ApJ, 824, 35

Highlights on Spanish Astrophysics X, Proceedings of the XIII Scientific Meeting of the Spanish Astronomical Society held on July 16 – 20, 2018, in Salamanca, Spain. B. Montesinos, A. Asensio Ramos, F. Buitrago, R. Schödel, E. Villaver, S. Pérez-Hoyos, I. Ordóñez-Etxeberria (eds.), 2019

The OTELO survey as morphological probe of galaxy evolution in the last 10 Gyr.

Jakub Nadolny[1,2] on behalf of the OTELO team

[1] Instituto de Astrofísica de Canarias, E-38205 La Laguna, Tenerife, Spain
[2] Universidad de La Laguna, Dept. Astrofísica, E-38206 La Laguna, Tenerife, Spain

Abstract

OTELO (OSIRIS Tunable filter Emission Line Objects) is an emission-line object survey covering a spectral range between 9070 and 9280Å in a window of reduced airglow emission. The first pointing of OTELO, in the Extented Groth Strip, consists of 36 tomographic slices sampled at 6Å, obtained with the red tunable filter of OSIRIS at the Gran Telescopio de Canarias. The limiting flux detecte of $\sim 5\times10^{-20}$ erg s^{-1} cm^{2} makes it the deepest survey in its category to date. Taking advantage of OTELO survey characteristics in selection of Emission Line Systems (ELS) we aim to present qualitative and quantitative morphological analysis of ELS and non-ELS in a specific redshift ranges (given by specific emission line, e.g Hα at z$\sim$0.4 or [OIII] at z$\sim$0.8) up to z=2 using *HST*-ACS high resolution images. The source selection process, Sérsic profile fitting, the visual morphology classification and a preliminary results are presented.

1 Introduction

OTELO is a blind low-resolution ($\sim$700) 2D-spectroscopic survey defined in the spectral window centered at 9175Å and with width of 210Å. Using tomographic spectra scans of red tunable filter images we construct Pseudo-Spectra (PS). PS are then browsed in order to find sources which shows emission lines (Emission Line System or ELS) at specific redshift for given chemical spices. For details on the survey design, data reduction, etc. we refer to the OTELO presentation article [3], hereafter OTELO-I.

In this work we aim to provide morphological classification of all the OTELO sources up to z=2 regardless if these show emission or not in PS. Possibility to distinguish between ELS and non-ELS give us an opportunity to compare both samples down to low-end luminosity/mass regime (e.g. Hα sample at z$\sim$0.4 have stellar masses in the range of 10^7 and 10^{11} M$_\odot$, for details see Nadolny et al., in prep.).

2 Data

This work make a use of the OTELO data-products: OTELO catalogue, OTELO-deep image and Pseudo-spectra (PS). Shortly, OTELO catalogue contain multi-wavelength PSF-matched photometric data from X-rays to far-infrared recompiled by OTELO team. OTELO photometric redshift (`z_BEST_deepQ`, where `Q` is `Y` or `N`, see following sections) is estimated using `LePhare` code ([1], [6]) employing three different object libraries: galaxy, QSO and star. For details on OTELO data-products we refer to the OTELO-I where OTELO photometry, photometric redshifts, PS as well as auxiliary PSF-matched photometry, spectroscopic redshifts together with methods used are described. See also Bongiovanni Á. et al. contribution in this Proceedings.

The high-resolution *HST*-ACS F606W and F814W (hereafter V- and I-band, respectively) publicly available images were used to provide quantitative and visual morphological analysis. Images were retrieved from All-sky Extended Groth Strip International Survey (AEGIS) data base[1]. Both sets of images in V- and I-band (4 tiles per filter) were aligned to the same reference catalogue (i.e. the Canada-France-Hawaii Telescope Legacy Survey D3-25 i-band sources catalogue[2]) and in the same manner (using `ccxymatch` and `ccmap` IRAF tasks) as the OTELO data (see OTELO-I sec. 3.3).

3 Methods

In the morphological classification we decided to use solely aligned high-resolution images with average resolution of $\sim$0.15 arcsec (and native pixel scale of 0.03 arcsec/px). The OTELO-deep image is used only to get the OTELO detection radius in order to discriminate the contamination by unresolved in OTELO-deep image nearby sources which are detected in the *HST*-ACS data.

3.1 Sample selection

The sample selection process is based on the OTELO photometric redshift solutions. As described in OTELO-I, there are two sets of redshifts: with (`z_BEST_deepY`) and without (`z_BEST_deepN`) OTELO-deep photometry with estimated error σ(`z_BEST_deepQ`) defined as given in OTELO-I, sec. 5.6, equation 16. We decided to select sources with best redshift solution firstly with OTELO-deep photometry for sources with σ(`z_BEST_deepY`) $< 0.2 \times$ (1+`z_BEST_deepY`) and lower than σ(`z_BEST_deepN`). If these requirements are not met we select `z_BEST_deepN` solution, always if σ(`z_BEST_deepN`) $<0.2 \times$ (1+`z_BEST_deepN`). If neither solution is selected (due to σ(`z_BEST_deepQ`)), and the sources have redshift solution using QSO templates, we select firstly `z_QSO_deepY` and secondly `z_QSO_deepN`. In total we selected $\sim$6900 sources up to z=2 for the morphological analysis.

[1] `http://aegis.ucolick.org/mosaic_page.htm`

[2] See "T0007 : The Final CFHTLS Release" documentation at `http://terapix.calet.org/cplt/T0007/doc/T0007-doc.pdf`

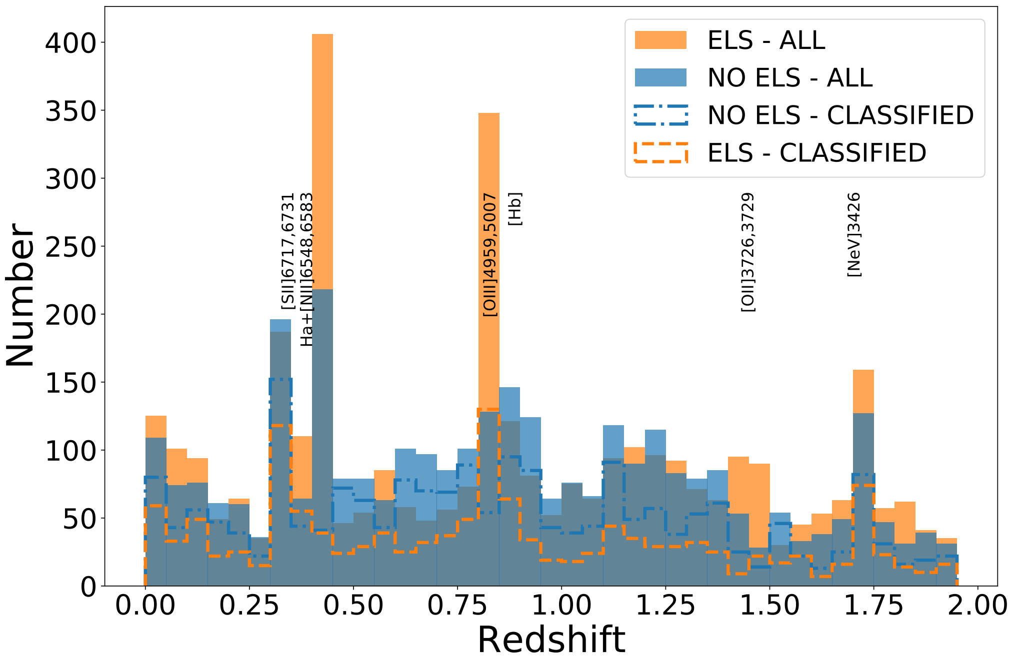

Figure 1: Redshift distribution of selected ELS (orange) and non-ELS (blue) up to z=2. The peak distributions at discrete redshifts (at ∼0.3, 0.4, 0.8, 1.4 and 1.75) shows sources with emission lines of specific chemical species which are redshifted to the spectral window of OTELO which is 210Å width and centered at 9175Å.

3.1.1 Emission Line Systems selection

ELS selection is done in a basis of automatic and visual inspection of PS and colour excess in the colour-magnitude diagram. Both methods are complementary and they are described in OTELO-I, sec 6.2 and Fig. 23. In total we have ∼3600 ELS and 3200 non-ELS. Resulting difference between sum of ELS and non-ELS and with the total selected described in previous section is due to star candidates in the field. Figure 1 shows redshift distribution of selected sources up z=2. Orange histogram shows objects selected as ELS, while blue shows non-ELS (orange and blue dashed lines show visually classified ELS and non-ELS, respectively).

3.2 Parametric classification

In order to provide parametric classification we use `IDL`-based `GALAPAGOS-2` software developed by MegaMorph group[3] [5]. We perform simultaneous fit (in V- and I-band) of single-Sérsic [9] profile of objects detected in I-band images. Together with Sérsic index we obtain other morphological parameters of the fitted model from `GALAPAGOS-2` (magnitude, effective radius, ellipticity, etc.). We perform also source extraction using `SExtractor` [2] software in dual, high-dynamical range mode with the same input parameters as given in GALAPAGOS-

[3]`https://www.nottingham.ac.uk/astronomy/megamorph/`

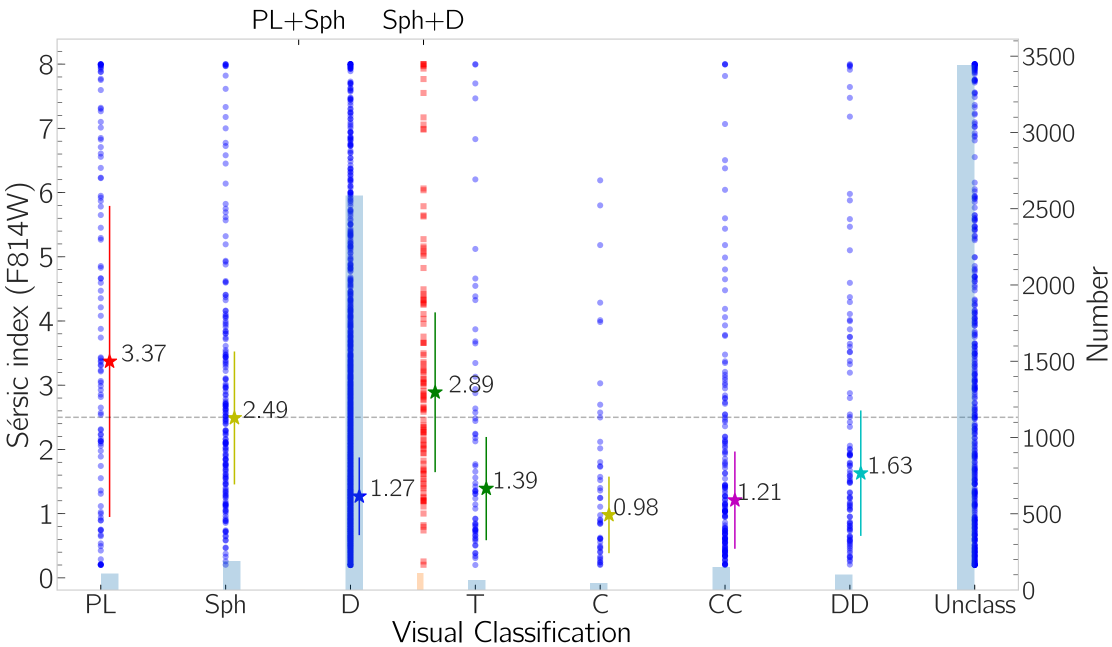

Figure 2: Visual classification correlation with Sérsic index. Blue points represent sources classified in one class, red squares show sources classified in mixed class. Star markers represent median Sérsic index per class with error bars calculated as median absolute deviation.

2 in order to get further information about detected sources (eg. flux radius at 20, 30, 50, 70 and 90% of the flux, magnitudes, etc.).

3.3 Visual classification

Visual classification is performed using MorphGUI [7], software developed originally for CANDELS. We modified the interface by extending basic morphological classes (Point-like, Spheroid and Disk) with Tadpole, Chain, Clumpy Cluster and Double following [4]. We decided to use this classification in order to take into account object diversity which is seen at higher redshifts.

4 Preliminary results

Figure 2 we resume both classifications: parametric and visual. We can notice that median Sérsic index n for early-type classes (Point-Like, Spheroid and mixed class Spheroid+Disk) is around and above $n = 2.5$. Sources classified as late-type objects (Disk, Tadpole, Chain, Clumpy Cluster, Double) are described with median n in range of $\sim$1 up to $\sim$1.6. This is expected behavior and observed in previous works (see e.g. [10]). In Figure 3 we show redshift distribution of sources in each morphological class. As we can notice the median

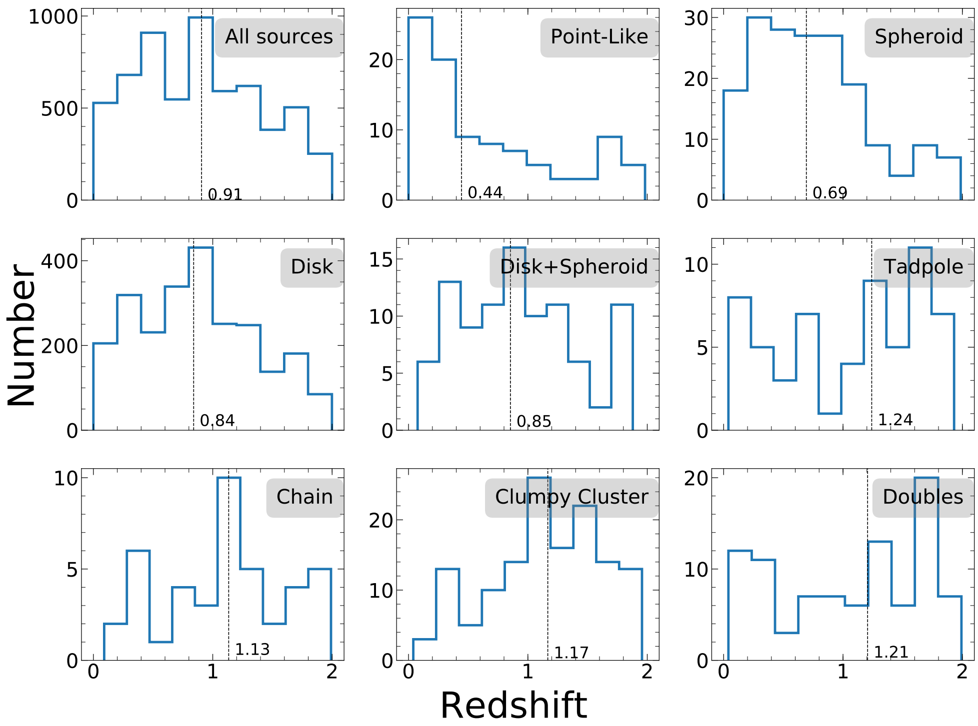

Figure 3: Redshift distribution per morphological class. Vertical dashed line shows median redshift per class.

redshift (vertical dashed line) for peculiar morphological classes (T, C, CC and DD) are higher than z=1. This behavior was observed also by [4] (see their Fig. 2).

5 Summary

In this work we provide qualitative and quantitative morphological classification for ~ 7000 sources from OTELO catalogue up to z=2, regardless if these show or not emission line in PS. Automatic classification is done using `GALAPAGOS-2` software providing morphological parameters of analiytic model fitted to the sample sources. The dual, high-dynamical range model of `SExtractor` provide us with morphological parameters measured directly on the scientific image. Visual classification is carried out in order to disentangle the true nature of the sources (if possible due to the source size and brightness) taking advantage of high-resolution *HST*-ASC images. We decided to follow morphological classes given by [4] due to the fact that classical Hubble classification began to be not sufficient at higher redshifts where we can find sources which do not fit non of the Hubble sequence classes.

The main focus of the work – the comparison of ELS and non-ELS morphologies at specific redshifts where OTELO sees emission lines of different chemical spices – is in progress and we refer to Nadolny et al. (in prep.) for further analysis.

References

[1] Arnouts, S., Cristiani, S., Moscardini, L., et al. 1999, MNRAS, 310, 540

[2] Bertin, E., et al., 2002, ASPC, 281, 228B

[3] Bongiovanni, Á, et al. 2018, A&A, accepted 19/09/2018, `https://doi.org/10.1051/0004-6361/201833294`; OTELO-I

[4] Elmegreen, D. M., et al. 2007, ApJ, 658, 763E

[5] Häußler, B., et al. 2013, MNRAS, 430, 330

[6] Ilbert, O., Arnouts, S., McCracken, H. J., et al. 2006, A&A, 457, 841

[7] Kartaltepe, J. S., et al., ApJS, 221, 11K

[8] Newman, J. A., Cooper, M. C., Davis, M., et al. 2013, ApJS, 208, 5

[9] Sérsic, J. L., 1968

[10] Vika, M., et al. 2015, A&A, 577, A97

Highlights on Spanish Astrophysics X, Proceedings of the XIII Scientific Meeting of the Spanish Astronomical Society held on July 16 – 20, 2018, in Salamanca, Spain. B. Montesinos, A. Asensio Ramos, F. Buitrago, R. Schödel, E. Villaver, S. Pérez-Hoyos, I. Ordóñez-Etxeberria (eds.), 2019

Deep imaging of the most massive galaxies of the nearby Universe.

S. N. dos Reis[1,2], F. Buitrago[1,2], and P. Papaderos[3]

[1] Instituto de Astrofísica e Ciências do Espaço, Universidade de Lisboa, OAL, Tapada da Ajuda, PT1349-018 Lisboa, Portugal
[2] Departamento de Física, Faculdade de Ciências da Universidade de Lisboa, Edifício C8, Campo Grande, PT1749-016 Lisboa, Portugal
[3] Instituto de Astrofísica e Ciências do Espaço, Universidade do Porto, CAUP, Rua das Estrelas, PT4150-762 Porto, Portugal

Abstract

Taking advantage of deep photometric data from HST, we analyze the $z < 0.5$ massive galaxies obtained in the H- and I-bands, in order to disentangle the several components that might constitute most massive galaxies in our Universe. We perform single and double-Sérsic analysis for our sample of 17 galaxies. From our photometric analysis, we notice that Sérsic index values are not a good representation of a galaxy' morphological type and find no trend between B/T and redshift. We detect within our sample two late-type galaxies with sizes smaller than expected. Additionally, our set of simulations shows that the apparent magnitudes and Sérsic index are the key parameters to a good recovery of the structural parameters.

1 Introduction

The most massive ($M_{\rm stellar} \geq 10^{11} M_\odot$) galaxies in the Universe undergo a dramatic transformation in their observational properties across cosmic time, from compact star-forming disks to huge red and dead spheroidal galaxies [3]. However, how galaxies acquire their mass and how they evolve morphologically are still open questions. One important finding from the work by [3] is that late-type galaxies (LTGs) and irregular objects are the dominant morphologies among massive galaxies at $z \sim 2.5$, whereas since $z \sim 1$ they are dominated generally by early-type galaxies (ETGs).

The current most favored galaxy formation model for massive galaxies is a two-phase formation scenario that predicts a rapid formation phase at $2 < z < 6$ dominated by in-situ star formation [12], and a second phase in which they are predicted to suffer intense minor mergers [8, 9, 11, 2, 10, 5, 4] that may transform them into the spheroids that we see today.

The availability of deep photometric data from the Hubble Space Telescope (HST) with combination of 3D-spectroscopy surveys allows a detailed analysis of these massive systems to investigate their structure and evolution. The part dedicated to the deep photometric data is presented here, and it is by means of multi-band surface photometry and bulge-disk profile decompositions of 17 nearby ($z < 0.5$) massive galaxies from the Cosmic Assembly Near-infrared Deep Extragalactic Legacy Survey (CANDELS)[1] [6, 7].

2 Analysis

For our analysis we used two filters: F160W (WFC3 H-band) which is the reddest HST filter, and F814W (ACS I-band) corresponding to the closest to the optical rest-frame.

We used SExtractor [1] to identify the neighboring objects to be masked or chosen to be fit simultaneously with the galaxy target. The values of apparent magnitude, size, axis ratio and position angle retrieved from SExtractor were then used as initial guesses in fitting the galaxies' structural parameters with GALFIT [13]. We performed single Sérsic fits and bulge-disk decompositions with the aim to describe each galaxy's surface brightness profile as accurately as possible, and to disentangle between a bulge and a disk in the case of a LTG, or to check if an ETG is purely elliptical or contains other components (e.g., a disk or bar).

After a detailed analysis trying to retrieve the best possible fit to our galaxy sample, we derived their sizes. Following the definition of effective radius (r_e), we computed curves of growth for the best-fitting two-component GALFIT models by integrating the flux within concentric elliptical apertures until we reach half of the galaxy total flux. These multi-component r_e are expected to yield a more accurate measure of size since the two-component fits generally provide a better match to the 2D surface brightness distribution of our sample galaxies than a single Sérsic model.

We further derived the surface brightness profiles for each galaxy and construct a mass-size relation for the sake of comparison with standard references in the literature.

Additionally, we conducted a set of simulations to test the robustness of our measured structural parameters, both for the H- and I-bands. This was achieved by creating $\sim$2500 mock galaxies uniformly distributed along the entire parameter space value ranges of the structural parameters from our analysis, placing each galaxy randomly on the correspondent band image and convolving with the respective PSF. We analyzed each artificial galaxy with the same methodology used in our real sample for the single Sérsic fits.

3 Results

Figure 1 shows the histograms obtained for the two bands' single Sérsic fits. Following [14] who use $n = 2.5$ as a division line between ETGs and LTGs, our sample would result in two

[1] http://candels.ucolick.org/data_access/Latest_Release.html

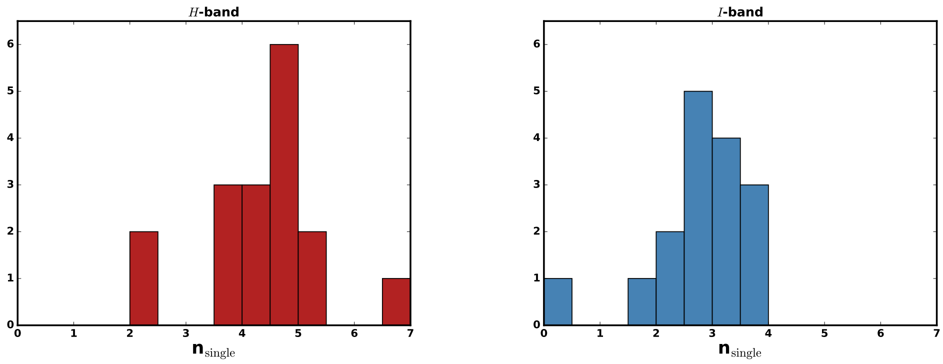

Figure 1: Sérsic index histograms for single-Sérsic fits values, both for the H-band (left) and the I-band (right). It is remarkable that in the H-band our sample contains nine visually classified LTGs, yet accordingly with Sérsic index fits only two would be classified as disk-like objects ($n < 2.5$).

galaxies classified as disk-like ($n < 2.5$) in the H-band, and four in the I-band, but by visual inspection in the H-band we classified nine galaxies as being LTGs. Our results imply that the Sérsic index provides a poor means for the quantification of the visual morphology of our galaxy population.

We construct the mass-size relation for our H-band data in Fig. 2 and compare with the results from [14] and from [16] for the lowest redshift bin centered at $z = 0.25$. ETGs are represented with red dotted points and the LTGs with spiral points (blue or purple in the case of a galaxy with a bar). We show in the y-axis the computed multi-component effective radii. The results from [16] for each galaxy in our sample, which were inferred from fitting single Sérsic functions, are represented by a triangle and connected with a line to our data. The colored dashed lines correspond to [16] at $z = 0.25$ (red for ETGs and blue for LTGs), while the red and blue shaded regions correspond to [14] local relation. Our results are consistent with those found by [14], having almost the entire sample falling inside their scatter. There are however two LTGs with sizes $\sim 2\sigma$ under the relation, being then much smaller than expected. These objects are worth a further investigation in the future.

In Fig. 3 we present surface brightness profiles for two representative galaxies from our sample that were visually classified as being ETG (top panels) and LTG with a bar (bottom panels). The left panels show the profiles in the H-band whereas the right panels in the I-band. Inside each profile we display the corresponding galaxy stamp in units of surface brightness (mag arcsec^{-2}) with shadowed areas matching the masks used to recover the observed light profile. All galaxies in our sample are more luminous in the H-band. For most of the objects in our sample we obtain an over-prediction of the light in the outskirts when performing a single-Sérsic fit (solid purple line). By using more Sérsic functions we recover a better description of the total light distribution, thus having a better match between the observed profile (black points) and the multi-component fit (solid green line). Nevertheless, for most of the cases, the light is under-estimated in the outskirts of our multi-component

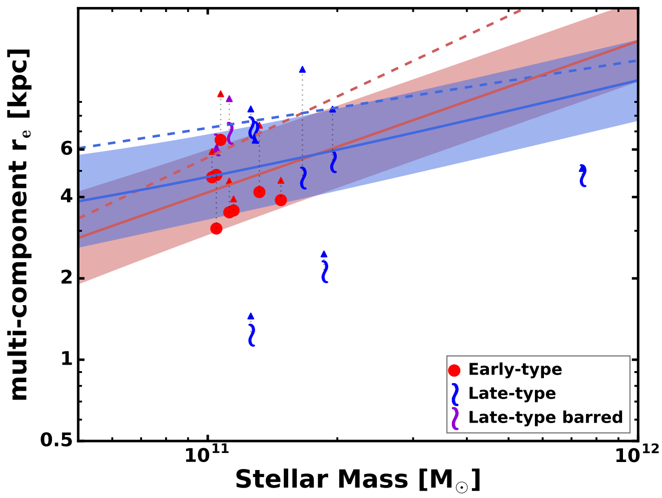

Figure 2: Size-stellar mass distribution of our H-band data, linked to [16] results represented by a triangle. The colored dashed lines correspond to [16] at $z = 0.25$. [14] local relation for ETGs and LTGs is represented by the solid red and blue lines, respectively, with the corresponded scatter being the shaded red and blue regions. Our results are in agreement with [14], having most of our sample matching the local relation. However, there are two LTGs smaller than expected (by $\sim 2\sigma$), thus being interesting to further investigate.

Sérsic fits.

Our set of simulations on mock galaxy images demonstrates that, on the statistical average, GALFIT can retrieve Sérsic model parameters with a satisfactory accuracy. However individual fits can yield substantial systematic deviations from observed profiles, in particular in their low-surface brightness periphery. Uncertainties in non-linear fitting and also the mathematical nature of the Sérsic law itself can be the ones to blame for such deviations.

The strong dependence of the fit on the central data points urges for a precise correction for PSF convolution effects and offers an explanation for systematic deviations between the best-fitting Sérsic model and the observed SBP in the low-surface brightness periphery of galaxies. From several GALFIT models from our sample, both single and multi-component fits, such deviations are apparent at the level of $\sim$1, requesting for a careful judgment of solutions from GALFIT and parametric image decomposition tools in general. A conclusive investigation of the buildup history of the extended stellar envelope of massive galaxies appeals for a test in whether the color profiles implied by subtraction of GALFIT models in two different bands are replicatable by evolutionary synthesis models and consistent with a two-phase galaxy formation scenario.

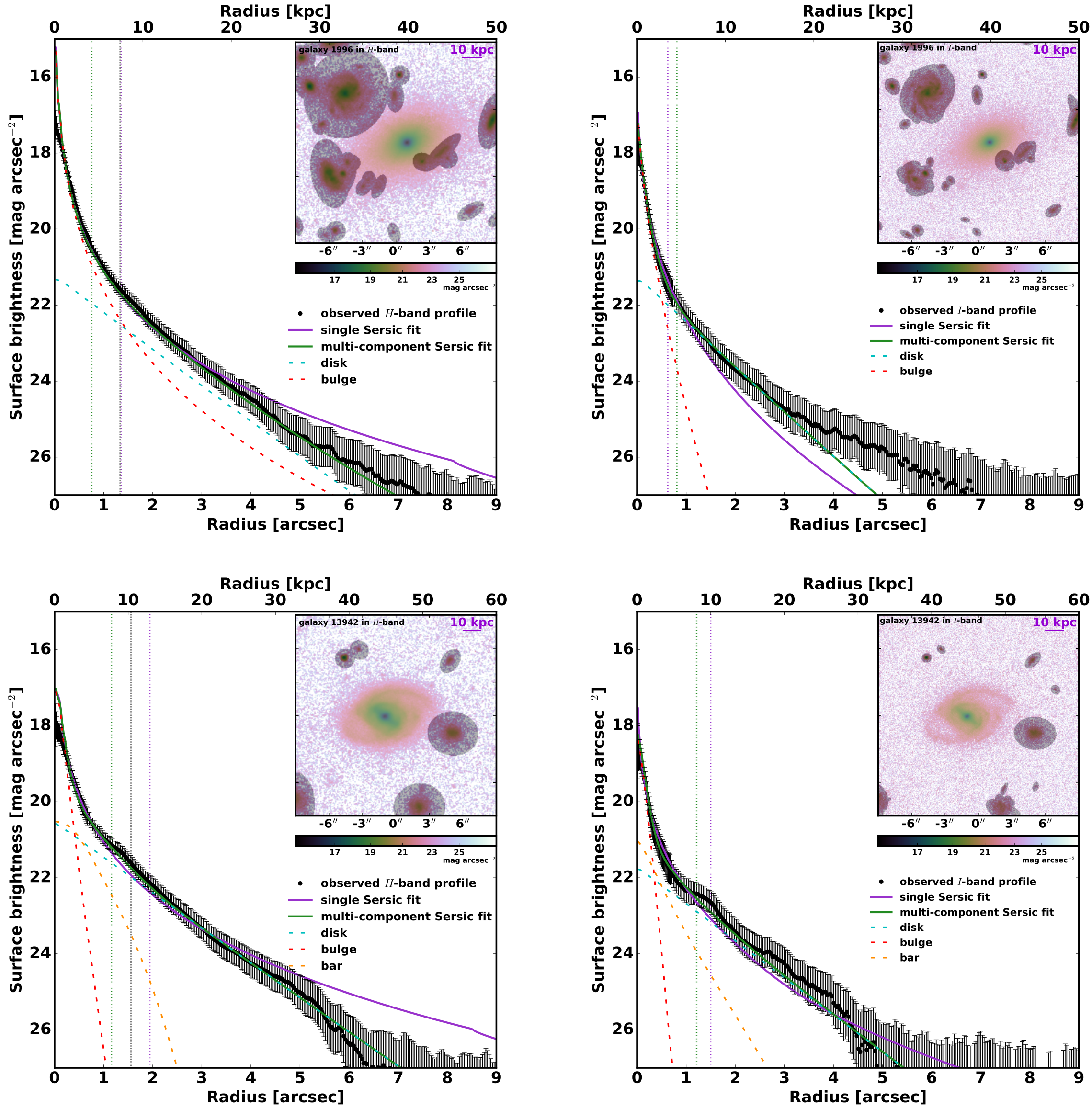

Figure 3: Surface brightness profiles in the H-band (left panels) and in the I-band (right panels) for two different morphological galaxies in our sample: ETG (top panels) and barred LTG (bottom panels). The violet and green colors correspond, respectively, to the results from single Sérsic fit and multi-component Sérsic fit. Black points represent the observed luminosity profile, solid lines show the models convolved with the PSF, dashed lines stand for the decomposition of the multi-component model into bulge (red), disk (blue) and bar (orange), dotted vertical lines represent the effective radius and the dotted grey vertical line is the [15] effective radius. We display the galaxy stamp in units of surface brightness (mag arcsec^{-2}) with shadowed areas matching the masks used to obtain the observed light profile, the galaxy ID on top left and a scale bar on top right corresponding to 10 kpc. The respective color bar is shown below the stamp.

Acknowledgments

This work was supported by FCT through national funds and by FEDER through COMPETE by the grants UID/FIS/04434/2013 & POCI-01-0145-FEDER-007672 and PTDC/FIS-AST/3214/2012 & FCOMP-01-0124-FEDER-029170. FB acknowledges the support by FCT via the postdoctoral fellowship SFRH/BPD/103958/2014. PP acknowledges support by FCT through Investigador FCT contract IF/01220/2013/CP1191/CT0002. This project has benefited from support by European Community Programme ([FP7/2007-2013]) under grant agreement No. PIRSES-GA-2013-612701 (SELGIFS). This work is based on observations taken by the CANDELS Multi-Cycle Treasury Program with the NASA/ESA HST, which is operated by the Association of Universities for Research in Astronomy, Inc., under NASA contract NAS5-26555.

References

[1] Bertin, E. & Arnouts, S. 1996, A&AS, 117, 393

[2] Bluck, A. F. L., Conselice, C. J., Buitrago, F., et al. 2012, ApJ, 747, 34

[3] Buitrago, F., Trujillo, I., Conselice, C. J., & Häußler, B. 2013, MNRAS, 428, 1460

[4] Ferreras, I., Hopkins, A. M., Gunawardhana, M. L. P., et al. 2017, MNRAS, 468, 607

[5] Ferreras, I., Trujillo, I., Mármol-Queraltó, E., et al. 2014, MNRAS, 444, 906

[6] Grogin, N. A., Kocevski, D. D., Faber, S. M., et al. 2011, ApJS, 197, 35

[7] Koekemoer, A. M., Faber, S. M., Ferguson, H. C., et al. 2011, ApJS, 197, 36

[8] López-Sanjuan, C., Balcells, M., Pérez-González, P. G., et al. 2010, ApJ, 710, 1170

[9] López-Sanjuan, C., Le Fèvre, O., de Ravel, L., et al. 2011, A&A, 530, A20

[10] López-Sanjuan, C., Le Fèvre, O., Ilbert, O., et al. 2012, A&A, 548, A7

[11] Mármol-Queraltó, E., Trujillo, I., Pérez-González, P. G., Varela, J., & Barro, G. 2012, MNRAS, 422, 2187

[12] Oser, L., Ostriker, J. P., Naab, T., Johansson, P. H., & Burkert, A. 2010, ApJ, 725, 2312

[13] Peng, C. Y., Ho, L. C., Impey, C. D., & Rix, H.-W. 2002, AJ, 124, 266

[14] Shen, S., Mo, H. J., White, S. D. M., et al. 2003, MNRAS, 343, 978

[15] van der Wel, A., Bell, E. F., Häußler, B., et al. 2012, ApJS, 203, 24

[16] van der Wel, A., Franx, M., van Dokkum, P. G., et al. 2014, ApJ, 788, 28

Highlights on Spanish Astrophysics X, Proceedings of the XIII Scientific Meeting of the Spanish Astronomical Society held on July 16 – 20, 2018, in Salamanca, Spain. B. Montesinos, A. Asensio Ramos, F. Buitrago, R. Schödel, E. Villaver, S. Pérez-Hoyos, I. Ordóñez-Etxeberria (eds.), 2019

Multi-wavelength mock observations (of the WHIM) in a simulated galaxy cluster.

Susana Planelles[1], Petar Mimica[1], Vicent Quilis[1,2] and Carlos Cuesta-Martínez[1]

[1] Departament d'Astronomia i Astrofísica, Universitat de València, c/ Dr. Moliner, 50, 46100 - Burjassot (València), Spain
[2] Observatori Astronòmic, Universitat de València, E-46980 Paterna (València), Spain

Abstract

In this contribution we introduce a novel numerical approach, based on a full-radiative transfer code, which is able to generate multi-wavelength synthetic observations of the gas component in cosmological simulations by integrating the transfer equation along the null-geodesic of photons. In order to test the capabilities of this numerical tool, we have applied the code on a large galaxy cluster developed in a full cosmological simulation and we have compared the emission associated to the whole inter-galactic medium (IGM) and to the warm-hot intergalactic medium (WHIM) gas components in three different energy bands: in soft X-rays, through the thermal Sunyaev-Zel'dovich (SZ) effect and in radio.

1 Introduction

As suggested by hydrodynamical simulations [10], most of the "missing" baryons are supposed to be located in a mildly overdense, warm-hot intergalactic medium (WHIM). The WHIM, which is thought to contain ∼50% of the local cosmic baryons, is expected to be mainly in filaments but also around large clusters and between pairs of interacting systems. Therefore, the WHIM plays a central role in the solution of the "missing baryons problem". Moreover, despite its relatively low densities (from $\sim 4\times10^{-6}$ to $\sim 10^{-4}$ cm^{-3}) and temperatures ($10^7 - 10^8$ K), the WHIM also represents a perfect scenario for multi-wavelength observations. In this sense, the forthcoming generation of telescopes will certainly improve our understanding of the WHIM in several wavelength bands.

Within this context, our goal is to use a well-resolved simulated galaxy cluster to generate multi-wavelength synthetic images (of the IGM and of the WHIM) directly comparable with observations. In order to compute the emission, we introduce a novel numerical approach, based on a relativistic full-radiative transfer code, to post-process the simulation data. To compute the change in the intensity along each line of sight, the code integrates the null-geodesic of photons. Although in our case the absorption is negligible, the code is also able to compute the self-absorption. Therefore, in this contribution we briefly compare the emission associated to the IGM and to the WHIM gas components in soft X-rays, through the thermal SZ (tSZ) effect, and in radio at a frequency of 1.4 GHz. We wish to emphasize that all bands are treated consistently, without tuning of parameters, by the same code.

While this is just a short contribution, we refer the interested readers to [11], where an extended and more detailed description of the employed numerical approach and of the obtained results is presented.

2 Numerical details

Below we only provide a brief description of the present study, while we refer the reader to [11] for further details.

2.1 The cosmological simulation

We analyse a simulation performed with the cosmological code MASCLET [12]. The simulation, which accounts for a flat ΛCDM universe, consists in a computational box with a comoving side length of 40 Mpc, with a peak physical spatial resolution of $\sim$ 610 pc at $z = 0$ (see [13] for further details). The best mass resolution for the dark matter particles is $\sim 2 \times 10^6\, M_\odot$. The simulation is set up to develop a big galaxy cluster at the centre of the computational domain.

Besides gravity and hydrodynamics, the simulation includes inverse Compton and free-free cooling, UV heating, atomic and molecular cooling for a primordial gas, cooling rates dependent on metallicity, star formation and feedback from SN-II. However, feedback from SN-Ia, stellar winds, or AGN are not included.

Using the halo finder ASOHF ([8, 4]) we have identified the central and largest halo ($M_{vir} \sim 3.2 \times 10^{14} M_\odot$ and $R_{vir} \sim 1.7$ Mpc) in the simulation at $z = 0.33$. In the following, we will analyse the X-ray, SZ or radio signals coming from inside and from an extended region of $5 \times R_{vir}$ around this main central halo. Within this region we will consider two gas components: the IGM (formed by all the gas elements) and the WHIM (formed by those gas elements with a temperature within $10^5 K < T < 10^7 K$).

2.2 Computing the emission

To compute the thermal and non-thermal emission in different observational bands we employ the full-radiative transfer code SPEV [6, 7, 1]. SPEV can produce consistent multi-band and multi-epoch synthetic observations by following the emission along the null-geodesics. Therefore, in order compute the emission from MASCLET outputs, we apply SPEV in post-processing (see [11] for further details on the code). In particular, we have implemented in SPEV the computation of three different signals:

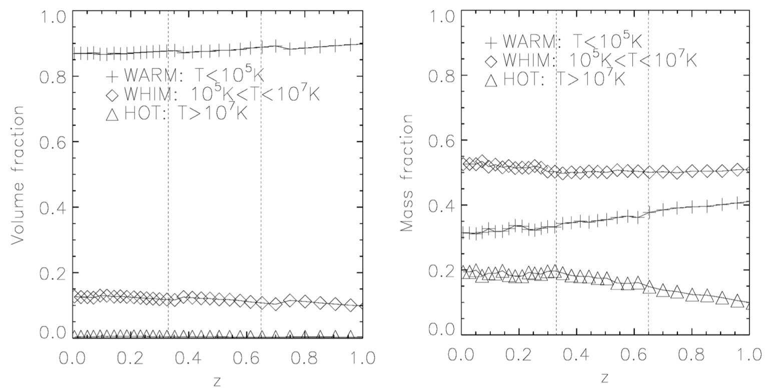

Figure 1: Evolution with redshift of the fraction in volume (left) and in mass (right) occupied by different gas components within the whole simulated domain. Figure from [11].

- Thermal emission. In order to account for the contribution from both free-free thermal Bremsstrahlung and metal line emission, we built a large interpolation table of the X-ray emission in different energy bands using the publicly available code CLOUDY [3].
- Non-thermal emission. To compute the synchrotron emission at different frequencies, we accounted for several simplifications: we assumed that the magnetic field satisfies flux conservation, we did not include any transport scheme for the non-thermal (NT) electrons, and we used a simplified formalism to estimate the NT electron distribution.
- The SZ effect. We took advantage of the way in which SPEV sorts the data along different lines of sight to compute the thermal (tSZ) and kinematic (kSZ) SZ effects in the non-relativistic approximation.

3 Results

As a consistency check, Fig. 1 shows the redshift evolution of the fractions in mass and in volume occupied by the warm ($T < 10^5 K$), the WHIM ($10^5 K < T < 10^7 K$), and the hot ($T > 10^7 K$) gas components within the whole simulated box. As expected, most of the volume is occupied by the warm and the WHIM gas components. In agreement with previous studies, the WHIM represents up to $\sim 55\%$ of the mass content at $z = 0$.

Figure 2 shows the density maps, projected along the line of sight, of the IGM and of the WHIM gas phases within our volume of interest. As expected, while the central cluster dominates the IGM map, in the case of the WHIM the map is mainly connected to the smallest objects and shows a much more filamentary and volume-filling distribution.

In Fig. 3 we show a sample of some of the mock images we presented in [11]. In particular, we show, for IGM and WHIM (top and bottom rows, respectively), the soft X-ray emission (left column), the signal associated to the tSZ effect at $\nu = 128$ GHz (middle

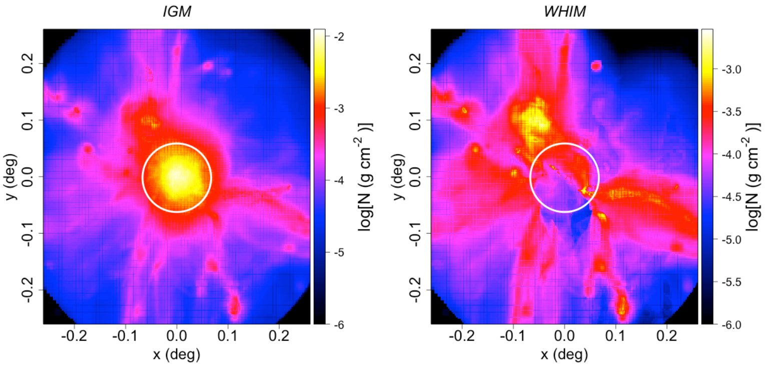

Figure 2: Surface density maps of the IGM and the WHIM gas components within a region of $\sim 0.6° \times 0.6°$ around the main cluster in the simulation. The cluster virial radius is represented by the white circle. Figure from [11].

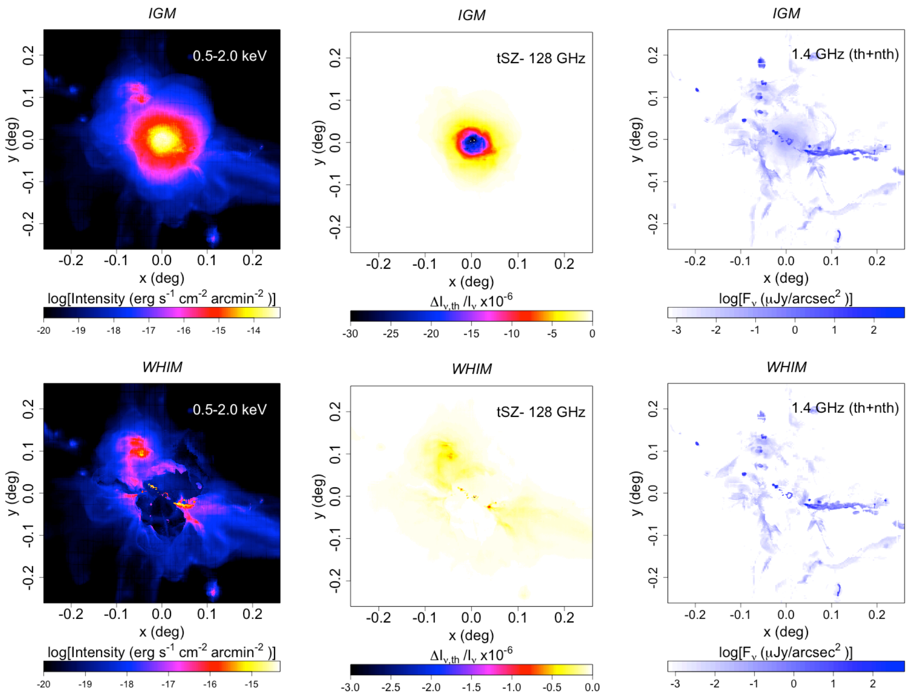

Figure 3: *Left column:* X-ray thermal emission maps associated to the IGM and to the WHIM gas components (top and bottom rows, respectively) at the soft $(0.5 - 2$ keV) energy band. *Middle column:* Intensity maps, $\Delta I/I_\nu$, of the thermal SZ effect at $\nu = 128$ GHz for the IGM and the WHIM. *Right column:* Mock radio observations of the IGM and the WHIM gas components at 1.4 GHz for a beam size of 1×1 arcsec^2. Composited image from [11].

column), and the radio emission at 1.4 GHz (right column).

The synthetic X-ray emission maps shown in the left column of Fig. 3 have a pixel size of $\sim 0.68''$. Although this resolution is in line with that of *XMM-Newton* and *Chandra*, we did not account for the response function of any specific observational instrument. Qualitatively, as already shown in previous studies, most of the IGM thermal emission is detected in the soft regime, where the emission from small structures is highlighted. Instead, the WHIM emission is mainly found in outer cluster regions around the main cluster with a more filamentary and extended distribution. Quantitatively, we obtain a broad agreement between the IGM soft X-ray emission associated to our simulated cluster and recent observations of massive galaxy clusters (e.g. [2]).

As shown in the middle column of Fig. 3, the tSZ signal at $\nu = 128$ GHz shows always negative values and is dominated by the main galaxy cluster, which can reach central intensities as high as $|\Delta I_{\nu,th}/I_\nu| \sim 3 \times 10^{-5}$. Regarding the WHIM, most part of the central tSZ signal is removed, leaving a much fainter and outer distribution around the cluster. On average, most part of the tSZ signal is contributed by hot and/or massive structures. Despite the weakness of the WHIM tSZ effect, its observational detection, especially at high redshift, represents a valuable complementary approach to X-ray observations.

Analyzing the radio maps shown in the right column of Fig. 3, we can draw several general conclusions: (i) only a small fraction of the cluster volume emits in radio, (ii) the IGM radio emission is correlated with dense and hot IGM regions and, (iii) there is a minor radio signal at the very outer cluster regions ($r \geq 4 \times R_{vir}$). Overall, IGM and WHIM have a maximum radio signal of around half mJy arcmin^{-2} at 1.4 GHz. In our case, the comparison of these radio maps with the distribution of shock waves (see [9, 5] for details on the detection of shocks) suggests that most of the cluster radio emission is connected to weak internal shocks within the cluster, whereas there is only a tiny contribution from strong external accretion shocks.

4 Summary and conclusions

In view of the next generation of improved observational facilities (e.g. *ATHENA+*, *SKA* or *CCAT-prime*), it is important to produce and analyse proper multi-band synthetic observations derived from full cosmological simulations. The combination of observational and synthetic images of the cosmic web in different bands is crucial to deepen our knowledge of the IGM physics in a number of aspects.

In this short contribution (an extended analysis is presented in [11]), we analyse a massive galaxy cluster, formed in a full cosmological simulation, through the comparison of the spatial distributions and the emissions associated to the IGM and to the WHIM gas components in different wavebands. In order to generate proper synthetic observations of the IGM and of the WHIM gas components, we present a novel numerical approach, based on the full-radiative transfer code SPEV [6], that integrates the transfer equation along the null-geodesic of photons in order to compute the intensity along each line of sight. We have modified SPEV in order to estimate, using exactly the same numerical scheme, the emission in X-rays, through the thermal SZ effect, and in radio at different frequencies. In general, as discussed in [11], we obtain at all three bands a broad agreement with previous numerical and observational estimates.

We would like to emphasize that this analysis represents our first attempt in the design of a complex numerical approach able to treat, consistently, the IGM emission at any observational frequency. Despite the optimistic results we have obtained, the employed simulation and the presented numerical procedure show some limitations that we will certainly improve in the near future. In this regard, now that the method has been tested, we are working on a new set of larger and improved simulations (in terms of physics and statistics) that will produce a larger sample of clusters. Moreover, we are already improving the estimation of the different observational signals in SPEV in order to produce improved and more realistic mock observations.

Acknowledgments

We acknowledge support by the *Spanish Ministerio de Economía y Competitividad* (MINECO, grant AYA2016-77237-C3-3-P). SP is "Juan de la Cierva" fellow (ref. IJCI-2015-26656) of the Spanish MINECO. PM acknowledges the support from the European Research Council (grant CAMAP-259276). CC-M acknowledges the support of ACIF/2013/278 fellowship.

References

[1] Cuesta-Martínez, C., Aloy, M. A. & Mimica, P. 2015, MNRAS, 446, 1716

[2] Eckert, D. et al. 2015, Nature, 528, 105

[3] Ferland, G. J. et al. 2017, MNRAS, 53, 385

[4] Knebe, A. et al. 2011, MNRAS, 415, 2293

[5] Martin-Alvarez, S., Planelles, S. & Quilis, V. 2017, ApSS, 362, 91

[6] Mimica, P. et al. 2009, ApJ, 696, 1142

[7] Mimica, P. et al. 2016, Journal of Physics Conference Series, 719, 012008

[8] Planelles, S. & Quilis, V. 2010, A&A, 519, A94

[9] Planelles, S., Quilis, V., 2013, MNRAS, 428, 1643

[10] Planelles, S., Schleicher, D. R. G. & Bykov, A. M. 2015, SSR, 188, 93

[11] Planelles, S., Mimica, P., Quilis, V. & Cuesta-Martínez, C. 2018, MNRAS, 476, 4629

[12] Quilis, V. 2004, MNRAS, 352, 1426

[13] Quilis, V., Planelles, S. & Ricciardelli, E. 2017, MNRAS, 369, 80

Highlights on Spanish Astrophysics X, Proceedings of the XIII Scientific Meeting of the Spanish Astronomical Society held on July 16 – 20, 2018, in Salamanca, Spain. B. Montesinos, A. Asensio Ramos, F. Buitrago, R. Schödel, E. Villaver, S. Pérez-Hoyos, I. Ordóñez-Etxeberria (eds.), 2019

Understanding planes of satellites.

I. Santos-Santos[1], R. Domínguez-Tenreiro[1], H. Artal[1,2], A. Serna[3], M.A. Gómez-Flechoso[4], C. Brook[5], P. Tissera[6], S. Pedrosa[1,7] and L. Bignone[6].

[1] Dpto. Física Teórica & CIAFF, Univ. Autónoma de Madrid, Cantoblanco, Madrid, Spain
[2] Next-Limit Technologies S.L., Madrid, Spain
[3] Dpto. de Física y A.C., Univ. Miguel Hernández, Elche, Alicante, Spain
[4] Dpto. Física de la Tierra y Astrofísica, Univ. Complutense de Madrid, Madrid, Spain
[5] Instituto Astrofísico de Canarias y Univ. de La Laguna, Tenerife, Spain
[6] Grupo de Astrofísica, Univ. Andrés Bello, Santiago, Chile
[7] Instituto de Astronomía y Física del Espacio, CONICET-UBA, Buenos Aires, Argentina

Abstract

Planes of satellites are observed in the Milky Way and Andromeda, and recent observations claim their presence as well in other nearby galactic systems. Moreover, recent proper motion data of MW satellites allege an important fraction of satellites are co-orbiting within the plane they define.

However, the quality and degree of co-orbitation of the planes of satellites reported so far from simulations within a ΛCDM context have been insufficient to explain the observational data.

In order to further understand the origin of planes of satellites we have carried out a detailed study of planes of satellites in zoom-in cosmological hydro-simulations of disc galaxies, focusing on plane-finding methods and plane quality analyses. We report on a method to identify kinematically-coherent satellites based on their orbital angular momentum vectors. We find a group of co-orbiting satellites in the PDEVA-5004 simulation that forms a persistent planar structure across cosmic time, with characteristics compatible with those of the observed planes in the MW and M31.

1 Introduction

The satellite galaxies of the Milky Way (MW) show a very anisotropical distribution. Their positions trace a plane that is approximately perpendicular to the Galactic disc [14, "VPOS"], and in addition, a high fraction of satellites present a common orbitation within the plane [4]. Planar configurations of satellites have also been found in Andromeda (M31) [7], and recently claimed for in other nearby galactic systems like Centaurus A, though still with high uncertainties [13]. Theoretical studies within the ΛCDM cosmological context have tried to link these observations with the large scale structure in which the system is embedded. In particular, dark matter-only simulations have shown that an anisotropical spatial distribution of satellites is indeed expected: satellite accretion occurs along preferential directions given by the velocity field shear tensor, following the filamentary structure of the cosmic web [8]. Hydrodynamical simulations have recently also studied this issue showing the important influence of baryons on the final number and distribution of the satellite sample [1, 10]. Despite these findings, the quality of the planes and the degree of co-orbitation found in previously reported simulations has been insufficient to explain observational data. Therefore this topic has been considered as one of the most challenging small-scale problems in ΛCDM.

The ultimate motivation of this study is to further understand the origin of planes of satellites within a ΛCDM context with baryons, addressing whether the observed planes of satellites in the MW and M31 are a unique occurrence in nature or if there are certain fundamental physical and evolutionary conditions that may favour their emergence. To this end, first a detailed analysis of planes in simulations and their evolution is needed. Here we report on one such detailed study, focusing on plane-finding methods and plane-quality analyses.

2 The simulation

We have analyzed a set of zoom-in cosmological hydrodynamical simulation of disc galaxies. We present here the results for PDEVA-5004 [17]. This simulation has been run with an entropy conserving AP3M-SPH code whose primary concern is that conservation laws (like angular momentum) hold accurately. It includes an inefficient star formation scheme working at sub-grid scales to mimick the regulation effects of stellar feedback, as well as detailed chemical enrichment and feedback methods implemented by [11]. As a result, the simulation gives a defined stellar and gaseous disc at all redshifts, with properties that match observational constraints (see [3] and references therein). The mass resolution of baryonic and dark matter particles is $m_{\rm bar} = 3.94 \times 10^5\,{\rm M}_\odot$, and $m_{\rm dm} = 1.98 \times 10^6\,{\rm M}_\odot$, respectively.

Satellite galaxies have been selected at redshifts $z = 0$ and also $z = 0.5$ to include objects that may end up accreted by the central disc galaxy later on. All selected objects are above a resolution limit of at least ~ 50 baryonic particles and have been checked to be bound to the host galaxy by following the orbit during the analysis period ($z = 1.4 - 0$, $\equiv$ $\mathrm{T_{uni}} = 4.7 - 13.7\,\mathrm{Gyr}$). The tool used for the selection of satellites has been `IRHYS` (by H. Artal). In order to accurately compare our results to the observational data of the MW, in the analysis that follows we have taken into account the effects of Galactic obscuration (which prevents us from observing satellites orbiting in the plane of the Galactic disc). We apply a bias that hinders objects at latitudes $|b| < 12^\circ$ when projected on the sphere [16]. A total number of 35 satellites have been identified, 30 surviving until $z = 0$. When the obscuration bias is applied the numbers range from 32-20.

The satellites of the sample present very different evolutionary histories that reflect in a variety of orbits. Some lose angular momentum and are eventually accreted by the

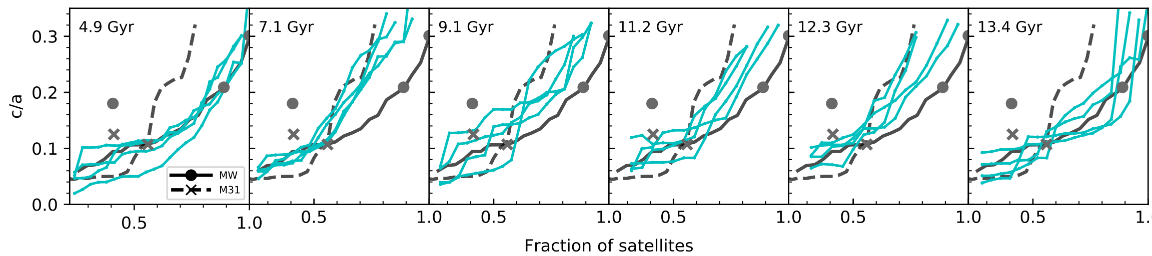

Figure 1: Quality analysis of the planar structures found in PDEVA-5004 with the *4-galaxy-normal* density plot method at certain timesteps: Variation of the short-to-long axis ratio (c/a) with the fraction of satellites included in the plane. Gray solid and dashed lines show the result for the MW and M31 at $z = 0$. Points show the specific values for observed planes of satellites mentioned in the literature [15].

disc, some follow regular orbits, and some have just been captured by the halo and orbit at long distances, sometimes even outside the virial radius. The distribution of satellite radial distances at different timesteps reveals that the system contracts and expands as it evolves. In fact, when the orbits of all satellites are plotted together, it is clear that there are certain moments where many satellite pericenters coincide (i.e., resonances). Interestingly, PDEVA-5004's satellite radial distribution is very similar to that of the MW at $z = 0$.

3 Finding planes of satellites from a positional analysis

We have started searching for planes of satellites by following the *4-galaxy-normal* density plot method [15]. In short, this method consists in fitting a plane (through the Tensor of Inertia, ToI, technique [12]) to every combination of 4 satellites and drawing a density map with the projection of the resultant normal vectors on the sphere. An over-density signals the normal direction to a predominant planar arrangement of satellites. When applied to PDEVA-5004 at each timestep, we obtain different density plots that reflect an anisotropic distribution. We have developed an extension to this method that consists in an iterative plane-fitting process, starting with the 7 satellites that contribute most to each over-density (at each timestep) and then continuously adding one more satellite at a time by contribution order. This allows for a study of the quality of the prominent planar arrangements found, through, for example, the variation of the c/a parameter (short-to-long axis ratio of the ToI) with the number of satellites included in the plane. Results for PDEVA-5004 at representative timesteps are shown in Fig. 1. Note the gray solid and dashed lines, which show the same analysis for the MW and M31 galaxies, respectively. The two galaxies have very different satellite distributions: while the MW satellites form a regular structure that remains a fairly thin plane ($c/a < 0.3$) even when including all of them, only approximately half of M31's satellites form a thin plane, the structure breaking down when including more objects in the plane. PDEVA-5004 presents at every timestep planes of satellites that are both thin and populated, compatible with the observed structures.

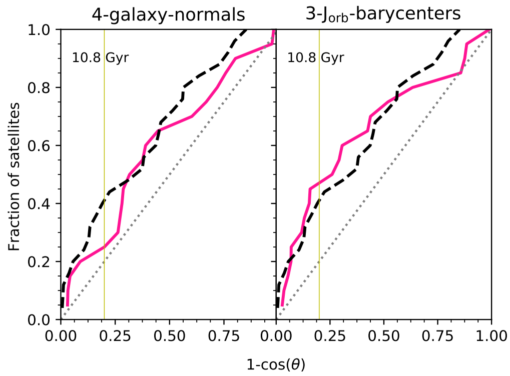

Figure 2: Fraction of co-orbiting satellites in the best planar structure with 70% of satellites found at $T_{uni} = 10.8$ Gyr in PDEVA-5004 using the *4-galaxy-normals* and *3-Jorb-barycenters* methods. The dashed line shows the result for the MW and the dotted line an isotropic distribution. A yellow vertical line marks an angle of 36.78° which represents 10% the area of the sphere [4].

We now study if the very thin and populated planes of satellites found with the 4-galay-normal method are kinematically-coherent structures that contain a relevant fraction of co-orbiting satellites. To this aim we compute the orbital angular momentum vectors $\vec{J}_{\rm orb}$ of satellites and check the fraction of them that are aligned with the normal vector to the plane they define[1]. In [4] the MW satellites with $\vec{J}_{\rm orb}$ vectors within 36.78° (area of 10% of the sphere) around the VPOS are defined as co-orbiting. We therefore compute the angle $\theta(\vec{J}_{\rm orb}, \vec{n}_{\rm plane})$ between each satellite's $\vec{J}_{\rm orb}$ and the normal $\vec{n}_{\rm plane}$ to the best plane found at that timestep including 70% of satellites. This is shown in the left panel of Fig. 2 at a given timestep as an example, where only $\sim 23\%$ of the total number of satellites co-orbit. We find that in general the very high quality planes found at all timesteps with the *4-galaxy-normal* method do not contain a high fraction of co-orbiting satellites. This is indicating that satellites align by chance and the planes they form are therefore *transient* (see also [5, 2]).

4 Finding kinematically-coherent structures

In view of the previous results we have developed a new method that makes use of the full 6D-space-phase information of satellites: the *3-$\vec{J}_{\rm orb}$-barycenter method*. It consists in calculating the barycenter of the minimal spherical triangle formed by the projections of every combination of 3 $\vec{J}_{\rm orb}$ vectors. As before, we project the resultant barycenters on the sphere and draw density maps. In this case, over-densities or accumulation areas indicate the presence of a kinematically-coherent group of satellites. When measuring now the angular distance between the center of the main over-density at a given timestep and each satellite's $\vec{J}_{\rm orb}$ vector, we find at all timesteps that at least 40% of satellites are co-orbiting about the direction given by the 3-$\vec{J}_{\rm orb}$-barycenter over-density, matching the MW value at $z = 0$ [4,

[1]Note that we do not differentiate between co-rotation and counter-rotation with the disc of the central galaxy.

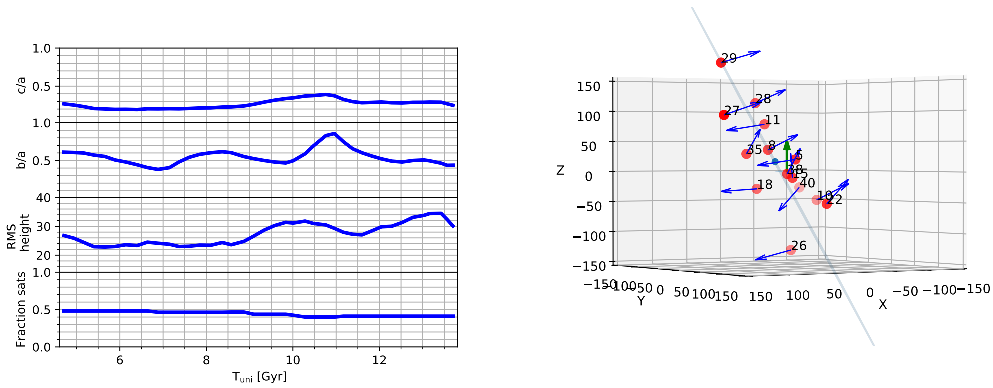

Figure 3: Left: Evolution with time of the properties (i.e., short-to-long axis ratio c/a, intermediate-to-long axis ratio b/a, root-mean-square thickness RMS-height, and fraction of satellites involved) of the plane of kinematically-coherent satellites. Right: Edge-on view of the plane of kinematically-coherent satellites at T_{uni}=12.5 Gyr. Blue arrows represent the orbital angular momentum vectors of satellites.

∼40%]. An example is shown in the right panel of Fig. 2. Note it is at the same timestep as the results on the left panel obtained with the *4-galaxy-normal* method.

A group of co-orbiting satellites across time In order to identify a group of satellites with aligned $\vec{J}_{\rm orb}$ during a long period of time, at each timestep we iteratively fit planes to groups of satellites as ordered by smaller angular distance between their $\vec{J}_{\rm orb}$ and the peak of each over-density. Specifically, to delimit such a persistent group of kinematically-coherent satellites, we have followed a criteria of choosing those that contribute most to the best planes with 40% of the satellites at each timestep. A group of 14 satellites has been singled out in PDEVA-5004.

We fit a plane to the positions of these satellites at each timestep, finding that they form a persistent planar structure that remains fairly thin across cosmic time (see Fig. 3 for the evolution of some plane properties). Moreover, these satellites represent the 48% of the total number of satellites at $z = 0$, proving this as the best plane+kinematics structure found with hydro-simulations so far (see Fig. 3 for an edge-on view of the plane at a given moment). Finally, the projection of the normal vectors on the sphere are shown in Fig. 4, color-coded by redshift. The reference frame is such that the central disc galaxy lies at latitud=0°. They appear very much clustered at latitud $\sim 0°$, which indicates that the plane of kinematically-coherent satellites is approximately perpendicular to the galactic disk, as occurs with the VPOS in the MW.

Possible origin? Previous studies have suggested a common large scale structure origin for persistent planes of co-orbiting satellites. We therefore trace the baryonic particles of the kinematically-coherent satellites back in time until redshift $z \sim 2.80$. We observe that co-orbiting satellites originate at different locations of the local cosmic web at high redshift

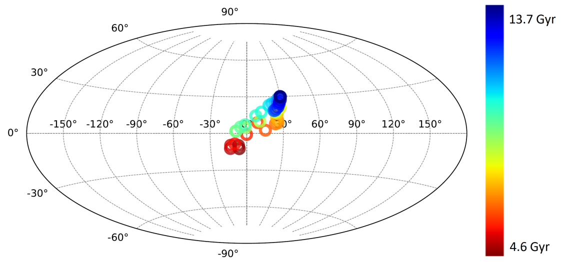

Figure 4: Projection on the sphere of the normal vectors to the plane of kinematically-coherent satellites. The colorbar indicates the corresponding age of the Universe.

but are accreted onto the central main halo through common entrace channels. Although more statistics and a proper numerical quantification of these effects is needed, results seem to support that found in [9] obtained by measuring the velocity field shear tensor: the bulk of the mass (i.e, a higher fraction of satellites) will follow the main direction of local collapse at high redshift (as expected from the Adhesion Model [6]). After, substructure will be accreted to virialized halos following the direction of weakest collapse depending on the given local cosmic web structure in which it is embedded, gaining in the process a common dynamics. In addition, an overall quiet merger history at late times prevents the destabilization of the system and allows angular momentum conservation, what possibly favors these kinematically-coherent groups to persist in time (Santos-Santos et al. in prep.).

Acknowledgments
This work has received support from MINECO/FEDER (Spain) grant AYA2015-63810-P, and the European Union's Horizon2020 research and innovation program under grant agreement No. 734374 (LACEGAL-RISE).

References

[1] Ahmed, S. H., Brooks, A. M., & Christensen, C. R. 2017, MNRAS, 466, 3119.

[2] Buck, T., Dutton, A. A., & Macciò, A. V. 2016, MNRAS, 460, 4348.

[3] Domínguez-Tenreiro, R., Obreja, A., Brook, C. B., et al. 2017, ApJ, 846, 72.

[4] Fritz, T. K., Battaglia, G., Pawlowski, M. S., et al. 2018, A&A, 619, A103.

[5] Gillet, N., Ocvirk, P., Aubert, D., et al. 2015, ApJ, 800, 34.

[6] Gurbatov, S. N., Saichev, A. I., & Shandarin, S. F. 2012, Physics Uspekhi, 55, 223.

[7] Ibata, R. A., Lewis, G. F., Conn, A. R., et al. 2013, Nature, 493, 62.

[8] Libeskind, N. I., Hoffman, Y., Knebe, A., et al. 2012, MNRAS, 421, L137.

[9] Libeskind, N. I., Knebe, A., Hoffman, Y., et al. 2014, MNRAS, 443, 1274.

[10] Maji, M., Zhu, Q., Marinacci, F., et al. 2017, ArXiv e-prints , arXiv:1702.00497.

[11] Martínez-Serrano, F. J., Serna, A., Domínguez-Tenreiro, R., et al. 2008, MNRAS, 388, 39.

[12] Metz, M., Kroupa, P., & Jerjen, H. 2007, MNRAS, 374, 1125.

[13] Müller, O., Pawlowski, M. S., Jerjen, H., et al. 2018, Science, 359, 534.

[14] Pawlowski, M. S., Pflamm-Altenburg, J., & Kroupa, P. 2012, MNRAS, 423, 1109

[15] Pawlowski, M. S., Kroupa, P., & Jerjen, H. 2013, MNRAS, 435, 1928.

[16] Pawlowski, M. S. 2016, MNRAS, 456, 448.

[17] Serna, A., Domínguez-Tenreiro, R., & Sáiz, A. 2003, ApJ, 597, 878.

Highlights on Spanish Astrophysics X, Proceedings of the XIII Scientific Meeting of the Spanish Astronomical Society held on July 16 – 20, 2018, in Salamanca, Spain. B. Montesinos, A. Asensio Ramos, F. Buitrago, R. Schödel, E. Villaver, S. Pérez-Hoyos, I. Ordóñez-Etxeberria (eds.), 2019

The Dark Energy Survey and Data Release 1.

I. Sevilla-Noarbe[1] on behalf of the DES Collaboration

[1] Centro de Investigaciones Energéticas, Medioambientales y Tecnológicas (CIEMAT), Av. Complutense 40, 28040, Madrid, Spain

Abstract

The Dark Energy Survey is a major international effort to pin down the nature of dark energy by performing a photometric survey of the southern sky, covering 5000 square degrees up to magnitude i = 23.7 and doing a repeat, deep scan of 27 square degrees to identify and accumulate type Ia supernovae. In this contribution, we summarize the most relevant cosmological results to date from this project. The first data release of the project DR1, encompassing the first three years of the project, is also presented for the community to explore and exploit.

1 The Dark Energy Survey project

The Dark Energy Survey (DES, [5]) is a photometric survey using the $grizY$ filters of the DECam camera ([11]). Its main goal is to create a deep and wide map of galaxies to probe the nature of cosmic acceleration, using the observational channels proposed by the Dark Energy Task Force ([4]) within a single project and using the same instrument. It has been operating since 2013 and is scheduled to finish operations in early 2019. By the end of it, the camera will have surveyed approximately 5000 square degrees, reaching depths in flux of $i = 23.7$ and redshifts of $z \sim 1.2$.

In addition to providing tight constraints to cosmological parameters, including those related to the dark energy equation of state, the richness of this dataset allows for a very varied array of research lines both for astrophysics and fundamental cosmology, including the measurement of the optical counterparts of gravitational wave events ([17]), the discovery of new Milky Way companions ([1]), accurate measurements of tidal streams around our own Galaxy ([16]), or the discovery of new Solar System objects ([2]).

In this contribution, we briefly summarize the main cosmological results obtained from the detailed analysis of the first year dataset and present the first Data Release, which includes three years of observations and is available publicly.

2 Year 1 cosmology results

2.1 Constraints from galaxy clustering and weak lensing

One of the most constraining sources of information from this type of dataset comes from the information provided by the statistical correlations of shapes and positions of galaxies at different redshifts, specially for the Ω_m, S_8 parameters. With DES data, we obtained a constraining power comparable to Cosmic Microwave Background experiments, and jointly with them, it is possible to obtain the most precise ones to date (Figure 1) in the context of the ΛCDM model [7]: $S_8 = 0.802 \pm 0.012$ and $\Omega_m = 0.298 \pm 0.007$.

The galaxy samples used are of two types: the lens sample, which is characterized by Luminous Red Galaxies defined with a uniform comoving space density (`redMaGiC`,[15]); and the source sample, on which we will infer the weak lensing shears produced by foreground matter density. The correlation function of the positions of galaxies in the former category is estimated within a redshift bin and between bins (five redshift bins in total, spanning the range $z = 0.15 - 0.9$, [10]) whereas the correlation of shapes with respect to positions in the sky using the source samples is measured in four redshift bins as well (in the range $z = 0.2 - 1.3$), that is, the shear-shear correlation function ([18]). The combination of both types of measurements is also included (galaxy-galaxy lensing) ([14]).

Each of them provides a data vector which is combined in a Markov Chain MonteCarlo estimation of the most probable contours for the cosmological parameters, using as nuisance parameters different astrophysical and methodological biases. Besides the precise constraints on the current cosmological standard model, galaxy biases have been determined with a precision of 10% and intrinsic alignments have been determined as a necessary feature to include in any current or future modeling of shear measurements.

The data and MCMC chains are available at http://des.ncsa.illinois.edu/y1a1 for fellow scientists to use and check our results as well as to combine with different datasets.

2.2 Constraints from supernovae

Using the spectroscopically confirmed supernovae from the first three years of the project, plus a collection of supernovae from low redshift surveys (totalling 329 type Ia supernovae), we are able to provide constraints on the equation of state value for dark energy under the wCDM model, which is compatible with -1 as predicted by the cosmological constant hypothesis, when combining with CMB information, reaching a 6% error. See Figure 2. These results are summarized in [8].

In addition, using a distance calibration method based on the baryon acoustic oscillation (BAO) scale from the BOSS 'consensus' measurement from DR12 instead of the commonly used direct approach building up from Cepheid variables, it was possible to measure the Hubble constant as 67.77 ± 1.30 km s^{-1} Mpc^{-1} therefore providing additional insight into the current discrepancies for measuring this parameter using different methodologies ([12]).

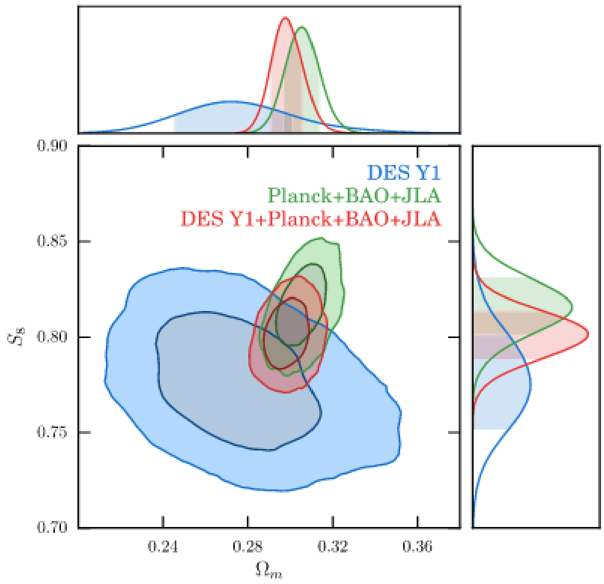

Figure 1: DES clustering constraints combined with external datasets (from [7]).

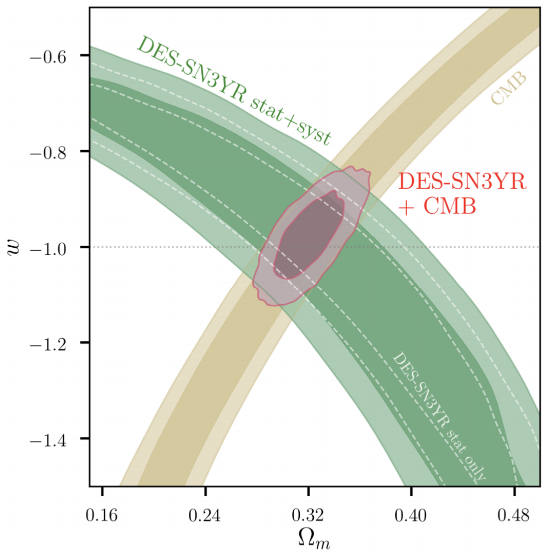

Figure 2: DES SN constraints on $\Omega_m - w$ for a flat wCDM model (from [8]).

2.3 Combined constraints from several probes

Finally for the first time we are able to make multiple probe constraints combining clustering, weak lensing shear, baryon acoustic oscillation scale and the Hubble-Lemaître diagram from type Ia supernova using DES data exclusively ([9]). These measurements rule out a Universe with no dark energy with 4σ significance, without requiring a flat Universe in our model. It also provides, with a probe independent of the CMB, a constraint on Ω_b being different than Ω_m at a very high significance. See Figure 3.

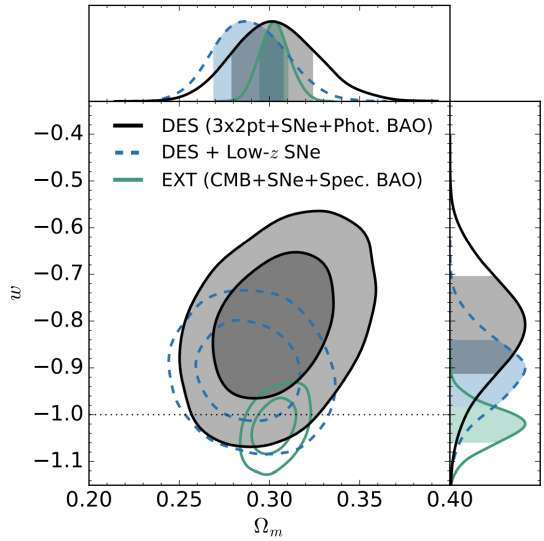

Figure 3: Multiple probe constraints on the equation of state for dark energy w and the density of matter parameter using DES data only, compared to the constraints of the combination from Planck's CMB measurements, BOSS BAO and the Pantheon supernova compilation (from [9]).

3 Data Release 1

The DES Data Release 1 (DR1, [6]) includes nearly 400 million objects detected over the complete DES footprint, using coadd detections from combinations of $\sim 39,000$ distinct single-epoch exposures. These have been collected over 345 nights of observations corresponding to DES operations from August 2013 to February 2016. See Figure 4 for a diagram of the footprint in celestial coordinates. Some of the characteristics of this dataset are listed below:

- The median PSF Full-Width-Half-Maximum is below 1 arcsecond in most bands except for g.
- The depth for signal-to-noise 10 objects is 24.33, 24.08, 23.44, 22.69, 21.44 for $grizY$.

- The astrometric precision is ~ 150 milliarcseconds vs Gaia's DR1 measurements.
- The photometric precision is $\sim 0.5\%$ (the statistical precision of the zero points).

The release itself is available at http://des.ncsa.illinois.edu/dr1 and is composed of both calibrated single-epoch images and coadd images, and a coadd catalog including morphological and photometric information obtained from the DESDM ([13]) pipelines based on SExtractor ([3]). The data can be accessed through different toolsets provided by NOAO, LineA and NCSA, including an SQL web client, cutout servers, sky/image viewers, Python and command-line query clients, and a Jupyter notebook server.

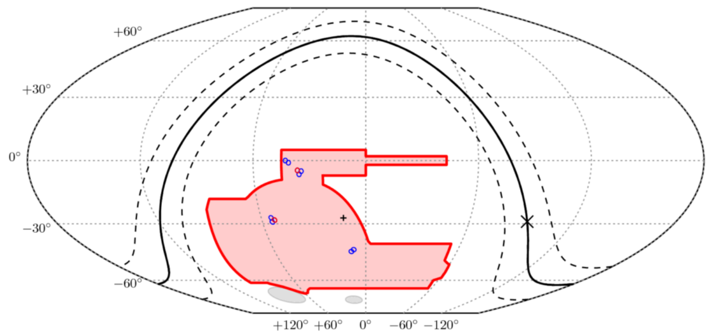

Figure 4: The DES survey area in celestial coordinates. The 5000 square degree DR1 footprint is shown in red. The 8 shallow supernova fields are shown as blue circles, and the 2 deep supernova fields are shown as red circles. The Milky Way plane is shown as a solid line, with dashed lines in a band 20 degrees wide in galactic latitude. The Galactic center ('x') and south Galactic Pole ('+') are also marked. The Large and Small Magellanic Clouds are indicated in gray (from [6]).

Acknowledgments

Funding for the DES Projects has been provided by the U.S. Department of Energy, the U.S. National Science Foundation, the Ministry of Science and Education of Spain, the Science and Technology Facilities Council of the United Kingdom, the Higher Education Funding Council for England, the National Center for Supercomputing Applications at the University of Illinois at Urbana-Champaign, the Kavli Institute of Cosmological Physics at the University of Chicago, the Center for Cosmology and Astro-Particle Physics at the Ohio State University, the Mitchell Institute for Fundamental Physics and Astronomy at Texas A&M University, Financiadora de Estudos e Projetos, Fundação Carlos Chagas Filho de Amparo à Pesquisa do Estado do Rio de Janeiro, Conselho Nacional de Desenvolvimento Científico e Tecnológico and the Ministério da Ciência, Tecnologia e Inovação, the Deutsche Forschungsgemeinschaft and the Collaborating Institutions in the Dark Energy Survey.

The Collaborating Institutions are Argonne National Laboratory, the University of California at Santa Cruz, the University of Cambridge, Centro de Investigaciones Energéticas, Medioambientales y Tecnológicas-Madrid, the University of Chicago, University College London, the DES-Brazil Consortium, the University of Edinburgh, the Eidgenössische Technische Hochschule (ETH) Zürich, Fermi National Accelerator Laboratory, the University of Illinois at Urbana-Champaign, the Institut de Ciències de l'Espai (IEEC/CSIC), the Institut de Física d'Altes Energies, Lawrence Berkeley National Laboratory, the Ludwig-Maximilians Universität München and the associated Excellence Cluster Universe, the University of Michigan, the National Optical Astronomy Observatory, the University of Nottingham, The Ohio State University, the University of Pennsylvania, the University of Portsmouth, SLAC National Accelerator Laboratory, Stanford University, the University of Sussex, Texas A&M University, and the OzDES Membership Consortium.

Based in part on observations at Cerro Tololo Inter-American Observatory, National Optical Astronomy Observatory, which is operated by the Association of Universities for Research in Astronomy (AURA) under a cooperative agreement with the National Science Foundation.

The DES data management system is supported by the National Science Foundation under Grant Numbers AST-1138766 and AST-1536171. The DES participants from Spanish institutions are partially supported by MINECO under grants AYA2015-71825, ESP2015-66861, FPA2015-68048, SEV-2016-0588, SEV-2016-0597, and MDM-2015-0509, some of which include ERDF funds from the European Union. IFAE is partially funded by the CERCA program of the Generalitat de Catalunya. Research leading to these results has received funding from the European Research Council under the European Union's Seventh Framework Program (FP7/2007-2013) including ERC grant agreements 240672, 291329, and 306478. We acknowledge support from the Australian Research Council Centre of Excellence for All-sky Astrophysics (CAASTRO), through project number CE110001020, and the Brazilian Instituto Nacional de Ciência e Tecnologia (INCT) e-Universe (CNPq grant 465376/2014-2).

References

[1] Bechtol, K., Drlica-Wagner, A., Balbinot, E. et al. 2015, ApJ, 807, 1

[2] Becker, J.C., Khain, T., Hamilton, J., et al. 2018, AJ, 156, 2

[3] Bertin, E. & Arnouts, S. 1996, A&AS, 117, 393

[4] The Dark Energy Task Force, ArXiv e-prints, astro-ph/0609591

[5] The DES Collaboration 2005, ArXiv e-prints, astro-ph/0510346

[6] The DES Collaboration 2018, ArXiv e-prints, arXiv:1801.03181

[7] The DES Collaboration 2018, Phys.Rev.D, 98, 043526

[8] The DES Collaboration 2018, ArXiv e-prints, arXiv:1811.02374

[9] The DES Collaboration 2018, ArXiv e-prints, arXiv:1811.02375

[10] Elvin-Poole, J., Crocce, M., Ross, A.J. et al. 2018, Phys.Rev.D, 98, 042006

[11] Flaugher, B., Diehl, H.T., Honscheid, K. et al. 2015, AJ, 150, 5

[12] Macaulay, E., Nichol, R.C., Bacon, D. et al. 2018, ArXiv e-prints, arXiv:1811.02376

[13] Morganson, E., Gruendl, R.A., Menanteau, F. et al. 2018, PASP, 130, 989

[14] Prat,J., Sánchez, C., Fang. Y. et al. 2018, Phys.Rev.D, 98, 042005

[15] Rozo, E., Rykoff, E.S., Abate, A. et al. 2016, MNRAS, 461, 2

[16] Shipp, N., Drlica-Wagner, A., Balbinot, E. et al. 2018, ApJ, 862, 2

[17] Soares-Santos, M., Holz, D.E., Annis, J. et al. 2017, ApJL, 848, 2

[18] Troxel, M.A., MacRann, N., Zuntz, J. et al. 2018, Phys.Rev.D, 98, 043528

Highlights on Spanish Astrophysics X, Proceedings of the XIII Scientific Meeting of the Spanish Astronomical Society held on July 16 – 20, 2018, in Salamanca, Spain. B. Montesinos, A. Asensio Ramos, F. Buitrago, R. Schödel, E. Villaver, S. Pérez-Hoyos, I. Ordóñez-Etxeberria (eds.), 2019

The Hubble constant from SN Refsdal.

J. Vega-Ferrero[1,2], J. M. Diego[2], V. Miranda[1], and G. M. Bernstein[1]

[1] Department of Physics and Astronomy, University of Pennsylvania, 209 S. 33rd St, Philadelphia, PA 19104, USA
[2] IFCA, Instituto de Física de Cantabria (UC-CSIC), Av. de Los Castros s/n, 39005 Santander, Spain

Abstract

On December 2015, Hubble Space Telescope (HST) observations detected the expected fifth counter image of SN Refsdal at $z = 1.49$. In [33], we compare the time delay predictions from numerous models with the measured value derived by [16] from very early data in the light curve of the SN Refsdal, and find a best value for $H_0 = 64^{+9}_{-11}$ km s^{-1} Mpc^{-1} (68% CL), in excellent agreement with predictions from CMB and recent weak lensing data + BAO + BBN (from the DES Collaboration). This is the first constraint on H_0 derived from time delays between multiple lensed SN images, and the first with a galaxy cluster lens, so subject to systematic effects different from other time delay H_0 estimates. Additional time delay measurements from new multiply-imaged SNe will allow derivation of competitive constraints on H_0.

1 Introduction

Galaxy clusters bend the path of photons emitted by distant objects, creating multiple images of the same background source, each with different magnification and arrival times. Time delays between multiple images of the same source depend on the cosmological model, and most notably on the Hubble constant, H_0. The potential to constrain H_0 with multiple supernova (SN) images was first suggested by [26] more than half a century ago. However, no multiply imaged (and resolved) SN has ever been observed until just recently. In 2014 four counter-images of the same supernova, SN Refsdal [15, 28, 16, 17], located at redshift $z = 1.49$, were found around a member galaxy in the cluster MACSJ1149.5+2223 (hereafter MACS1149, [7]) at redshift $z = 0.544$. The predicted time delay between these four images is relatively small (a few days) making them impractical to derive useful constraints on H_0. Approximately a year after the initial detection of the four supernova images, a fifth counter-image appeared, this one having a considerably longer time delay (see Figure 1). The

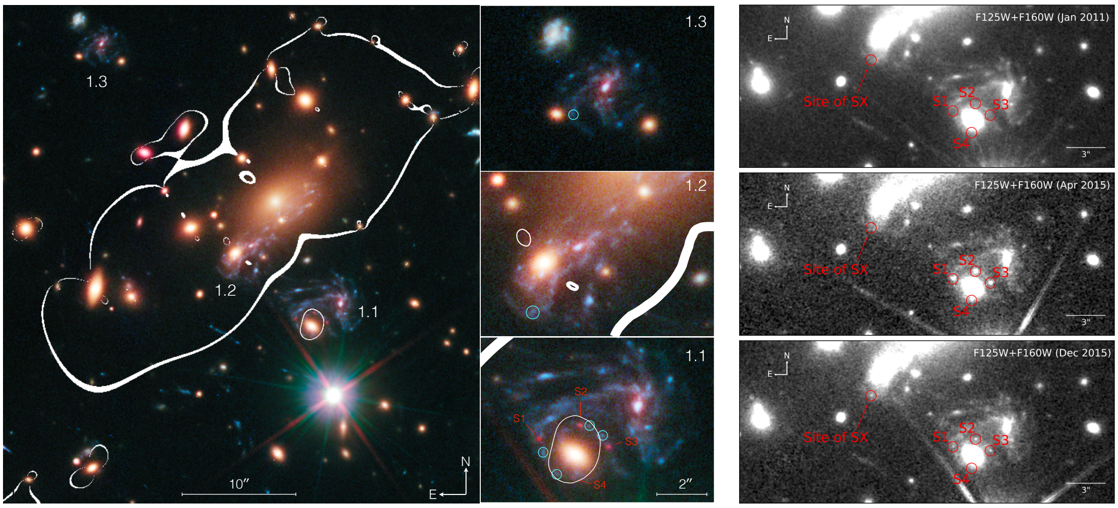

Figure 1: Left-hand panel extracted from [15]: Color-composite image of the galaxy cluster MACSJ1149. The white contours correspond to the critical curves for sources at the $z = 1.49$ (i.e., the redshift of the SN Refsdal's host galaxy). Three images of the host galaxy formed by the cluster are marked with white labels (1.1, 1.2, and 1.3) in the left panel and enlarged in the right panel. The four current images of SN Refsdal that we detected (labeled S1 to S4 in red) appear as red point sources in image 1.1. Right-hand panel extracted from [16]: images of the MACS J1149 galaxy cluster field taken with HST WFC3-IR. The top panel shows images acquired in 2011 before the SN appeared in S1–S4 or SX. The middle panel displays images taken on 2015 April 20 when the four images forming the Einstein cross are close to maximum brightness, but no flux is evident at the position of SX. The bottom panel shows images taken on 2015 December 11 which reveal the new image SX of SN Refsdal.

position and the time of reappearance were predicted by different lens models with remarkable precision [24, 30, 6, 32, 12]. This accuracy is possible since MACS1149 has been observed with unprecedented detail as part of the *Hubble Frontier Fields* program (hereafter, HFF, [21]).

The predictions for the SN time delay were based on a set of assumptions, including the value $H_0 = 70$ km s^{-1} Mpc^{-1}, which was adopted by all teams in their model predictions. Since time delays are inversely proportional to H_0, it is possible to constrain the value of H_0 directly, as originally suggested by Refsdal in 1964.

In [33], we derived an estimate of H_0 based on the observed time delay for the SN Refsdal system and an ensemble of lens models derived by different teams that use independent reconstruction methods. Our results provide a separate geometrical inference for H_0 at intermediate redshift [18, 29, 34, 3]. Hereafter, we adopt a fiducial cosmological model with $\Omega_m = 0.3$ and $\Omega_\Lambda = 0.7$, which is the cosmology used to infer the lens models. When rescaling the value of the predicted time delay, the only cosmological parameter being changed is H_0 (see section 2 for details).

2 Hubble constant estimate from SN Refsdal time delays

The time delay Δt with respect to an unperturbed null geodesic depends on the angular separation between the image and the source, on the lensing potential at the position of the image, and on the cosmological model through the angular diameter distances. Distances, in turn, depends on the cosmic expansion history of the universe, which is proportional to the Hubble rate,

$$\Delta t(\bar{\theta}) = \frac{1+z_d}{c}\frac{D_d D_s}{D_{ds}}\left[\frac{1}{2}(\bar{\theta}-\bar{\beta})^2 - \psi(\bar{\theta})\right], \quad (1)$$

where $\bar{\beta}$ is the unlensed source position and $\psi(\bar{\theta})$ is the lens potential at the position of the observed counter-image $\bar{\theta}$. The quantities D_d, D_s and D_{ds} are the angular diameter distance to the lens, to the source and between the lens and the source, respectively. These three distances are inversely proportional to H_0, and therefore the time delay is also inversely proportional to H_0. The factor $D_d D_s/D_{ds}$ encodes the cosmological dependency that, as shown by [3], is mostly sensitive to H_0 and depends weakly on other cosmological parameters. For instance, a change of 10% in the cosmological parameter Ω_m translates into a change of only $\approx 0.1\%$ in Δt. Because of this weak dependence on other cosmological parameters, we consider the cosmological model fixed and vary only H_0. The difference in the predicted time delay between two positions in the lens plane depends on a delicate balance between the lensing potential and the relative separations. Nevertheless, the uncertainties in the lensing potential are the primary source of systematic errors in the prediction of the time delays, followed by the unknown value of H_0.

Luckily, lensing models for clusters like MACS1149 are constrained by tens of multiply-imaged lensed background galaxies with a wide range of known redshifts [9, 10, 11, 19, 35, 4, 5, 6, 14, 20, 22], reducing the uncertainties in the lens models [13, 1]. Model predictions for time delays are less prone to errors in regions where the number of lensing constraints are more abundant. In the case of MACS1149, the highest density of lensing constraints is found in the vicinity of the multiple supernova images. One should then expect systematics to be relatively small in the case of the SN Refsdal.

2.1 The case of SN Refsdal

The SN Refsdal [15, 28, 16, 17] was the first example of a resolved multiply imaged lensed SN. The first estimation of the relative time delay and magnification ratio of S1 (position of knot 1 in the original quadruplet image) and SX (the position at which SN Refsdal reappeared) based on the early light curve of SX was presented by [16] . The lensing constraints from the HFF program allowed for a variety of predictions of the time delay and relative magnification of a fifth image. These predictions where made assuming a fiducial cosmological model, needed for computing the distances in equation 1. If the fiducial model assumed the wrong H_0 this would translate into a predicted time delay that is biased with respect to the measured one. Table 1 in [33] summarizes the predicted time delays Δt_{X1} between SX and S1, and the magnification ratios, $\mu_{X1} \equiv \mu(X)/\mu(1)$, as derived by the different models presented in [32] and by the model presented in [6]. The predictions ranged from ≈ 8 months [30] to ≈ 1 year

[6]. Similar predictions extending from ≈ 7.2 months to ≈ 12.3 months were later published in [32] by different teams. SN Refsdal reappeared promptly approximately one year after its first appearance. Overall, the lens models predict reasonably well the time of reappearance of SN Refsdal [16].

Although the uncertainties in the lens models are difficult to quantify, they are generally small in regions on the lens plane where lensing constraints are abundant, as shown by [23]. In this work, as proposed by [31], we adopt a conservative level of 6% for systematic errors in the time delay predictions (see also [8] for a similar discussion). We refer the reader to section 2.1 in [33] for a detailed discussion on the model uncertainties.

The lens models assumed a fiducial Hubble constant of $H_0^{\rm fid} = 70$ km s^{-1} Mpc^{-1}, and using the lens geometry data G each modeler m derived a probability $p_m(\Delta t_{X1}, \mu_{X1}|H_0^{\rm fid}, \mathrm{G})$. Since the time delay is inversely proportional to H_0 as given by equation 1, we can rescale this to any alternative value of H_0 via

$$p_m(\Delta t_{X1}, \mu_{X1}|H_0, \mathrm{G}) = p_m\left(\frac{H_0^{\rm fid}}{H_0}\Delta t_{X1}, \mu_{X1}|H_0^{\rm fid}, \mathrm{G}\right). \tag{2}$$

3 Bayesian analysis

The time delays Δt_{X1} and magnifications μ_{X1} predicted by the different lens models can be compared with those inferred by [16] from the observed light curve data (LC) of both SN images. The probability $p_d(\Delta t_{X1}, \mu_{X1}|\mathrm{LC})$ derived by [16] shows substantial correlation between Δt_{X1} and μ_{X1} as a consequence of the incompleteness in the light curve data they analyze. By re-scaling the predictions as described in equation 2, we can infer the most likely value of H_0 that best matches the model predictions with the observations. For this purpose, we adopt a standard Bayesian approach, but keeping in mind that our observational data D are the union of lens geometry (G) and SN light curve data (LS), and both are interpreted in terms of time delay and magnification ratio. The probability of H_0 given the data D is expressed as

$$\begin{aligned}
\mathrm{P}(H_0|\mathrm{D}) &\propto \mathrm{P}(H_0)\ \mathrm{P}(\mathrm{D}|H_0) \\
&= \mathrm{P}(H_0)\int d\Delta t_{X1}\, d\mu_{X1}\, \mathrm{P}(\Delta t_{X1}, \mu_{X1}|\mathrm{D}, H_0)\mathrm{P}(\mathrm{D}) \\
&\propto \mathrm{P}(H_0)\int d\Delta t_{X1}\, d\mu_{X1}\ p_m(\Delta t_{X1}, \mu_{X1}|H_0, \mathrm{G}) \times\ p_d(\Delta t_{X1}, \mu_{X1}|\mathrm{LC}),
\end{aligned} \tag{3}$$

where the prior, $\mathrm{P}(H_0)$, is the credibility of the H_0 values without the data D, and the likelihood, $\mathrm{P}(\mathrm{D}|H_0)$, is the probability that the data could be generated by the models with parameter value H_0. Equation 3 is basically the product of the observed probability distribution of the observed time delay and magnification (p_d) times the probability distribution from the individual models (p_m). For a particular model, the maximum of the probability is obtained for a value of H_0 that maximizes the overlap of the SN light curve data and model probabilities.

For each individual lens model, we assume a bivariate but separable normal distribution for $p_{m,i}(\mu_{X1}, \Delta t_{X1}|H_0)$. The mean values of μ_{X1} and Δt_{X1} for each model are given in table 1 in [33] along with their statistical uncertainties. In the computation of $p_{m,i}(\mu_{X1}, \Delta t_{X1}|H_0)$, we also take into account that the statistical uncertainties are non-symmetric for three of the listed lens models. For the observational data, we associate a bivariate normal distribution to $p_d(\mu_{X1}, \Delta t_{X1})$ based on the best-fit ellipse to the 68% CL in Figure 3 of [16] (for brevity, we drop the dependences on G and LC from our notation). Both $p_{m,i}(\mu_{X1}, \Delta t_{X1}|H_0)$ and $p_d(\mu_{X1}, \Delta t_{X1})$ are normalized to unity. Note that $p_m(\mu_{X1}, \Delta t_{X1}|H_0)$ depends on H_0 as defined in equation 2. On the contrary, the probability distribution of the observational data, $p_d(\mu_{X1}, \Delta t_{X1})$, does not depend on H_0.

We adopt two strategies for combining the probabilities p_m derived by different lens models, which we can label by $i = 1 \ldots M$. A very optimistic view is that each model has errors that are independent and are drawn from an ensemble with zero mean. In this case, we can set

$$p_m(\Delta t_{X1}, \mu_{X1}|H_0) \propto \prod_{i=1}^{M} p_i(\Delta t_{X1}, \mu_{X1}|H_0), \tag{4}$$

and we will label the resultant posterior derived from equation 3 as $\mathrm{P}_\times(H_0|\mathrm{D})$. A more conservative (and more realistic) assumption is that only one of the models is correct, with prior probability q_i that model i is the one. In this case, we have

$$p_m(\Delta t_{X1}, \mu_{X1}|H_0) = \sum_{i=1}^{M} q_i p_i(\Delta t_{X1}, \mu_{X1}|H_0). \tag{5}$$

We will assign equal priors $q_i = 1/M$ to each model, such that we effectively average the probabilities of the models, and denote the resultant posterior distribution as $\mathrm{P}_+(H_0|\mathrm{D})$. Note that the models do not contribute equally to the posterior: those whose predictions of μ_{X1} disagree with the measurements of [16] will be downweighted in the integral of equation 3.

4 Results and conclusions

In the left-hand panel in figure 2, we show the contribution from each model to the total posterior $\mathrm{P}_+(H_0|\mathrm{D})$ using a flat prior for H_0 between $H_0 = 30$ and 100 km s^{-1} Mpc^{-1}. The right-hand panel in figure 2 summarizes our main result for the posterior $\mathrm{P}_\times(H_0|\mathrm{D})$ and $\mathrm{P}_+(H_0|\mathrm{D})$. We have assumed that all model predictions are equal prior validity (but see [23] for a comparison of the performance of the different lensing reconstruction techniques). The median value and 68% CL for H_0 are: $H_0 = 62^{+4}_{-4}$ km s^{-1} Mpc^{-1} for the $\mathrm{P}_\times(H_0|\mathrm{D})$ posterior; and $H_0 = 64^{+9}_{-11}$ km s^{-1} Mpc^{-1} for the $\mathrm{P}_+(H_0|\mathrm{D})$ posterior. These values of H_0 already include a systematic uncertainty at the 6% level which has been added at the end in quadrature to the statistical uncertainty.

We constrain, for the first time, the Hubble constant following Refsdal's original idea to use a multiple-lensed SN with measured time delays and precise lens model predictions. By combining the results of multiple lens models, we account for statistical and some systematic

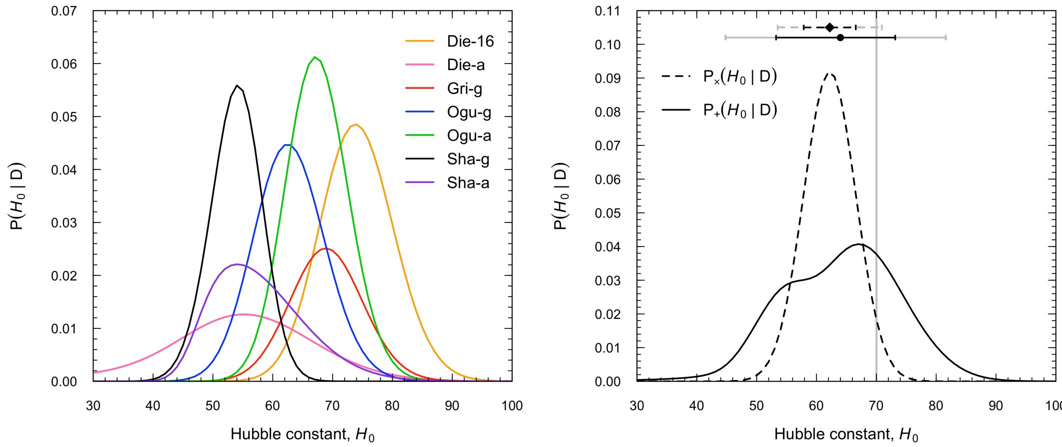

Figure 2: Left-hand panel extracted from [33]: Contribution of each lens model prediction (in different colors) to the posterior $P_{+}(H_0|D)$ obtained by equation 3. Right-hand panel extracted from [33]: Total posterior $P_{\times}(H_0|D)$ (dashed line) and $P_{+}(H_0|D)$ (solid line). Both curves include a systematic uncertainty at the 6% level added at the end in quadrature to the statistical uncertainty. We explicitly show the median, 68% CL (black error bars) and 95% CL (grey error bars) on the top of the figure for both posteriors. The vertical line corresponds to the fiducial $H_0^{\rm fid} = 70$ km s^{-1} Mpc^{-1} assumed in all the lens models.

errors due to assumptions made during the lens reconstruction. These results are in good agreement with recent constraints from CMB, LSS, and local distance ladders [25, 27, 2]. We use a very weak prior to better show the sensitivity of the Refsdal data to the parameter H_0. Future improved constraints on the observed time delay and magnification will reduce the uncertainty in the Hubble parameter using this technique, and additional estimates derived from different clusters will provide a competitive test for H_0.

Acknowledgments

We thank P.L. Kelly and D. Scolnic for feedback helpful discussions. J.V-F and G.M.B. acknowledge support from the Space Telescope Science Institute (contract number 49726). J.M.D. acknowledges the support of projects AYA2015-64508-P (MINECO/FEDER, UE), AYA2012-39475-C02-01, and the consolider project CSD2010-00064 funded by the Ministerio de Economía y Competitividad. J.V-F and J.M.D. acknowledge the hospitality of the University of Pennsylvania. V.M. was supported in part by the Charles E. Kaufman Foundation.

References

[1] Acebron, A., Jullo, E., Limousin, M., et al. 2017, MNRAS, 470, 1809

[2] Abbott, T. M. C., Abdalla, F. B., Annis, J., et al. 2018, MNRAS, 480, 3879

[3] Bonvin, V., Courbin, F., Suyu, S. H., et al. 2017, MNRAS, 465, 4914

[4] Diego, J. M., Broadhurst, T., Molnar, S. M., Lam, D., & Lim, J. 2015a, MNRAS, 447, 3130

[5] Diego, J. M., Broadhurst, T., Zitrin, A., et al. 2015b, MNRAS, 451, 3920

[6] Diego, J. M., Broadhurst, T., Chen, C., et al. 2016, MNRAS, 456, 356

[7] Ebeling, H., Edge, A. C., & Henry, J. P. 2001, ApJ, 553, 668

[8] Greene, Z. S., Suyu, S. H., Treu, T., et al. 2013, ApJ, 768, 39

[9] Jauzac, M., Jullo, E., Eckert, D., et al. 2015a, MNRAS, 446, 4132

[10] Jauzac, M., Jullo, E., Eckert, D., et al. 2015b, MNRAS, 446, 4132

[11] Jauzac, M., Richard, J., Jullo, E., et al. 2015c, MNRAS, 452, 1437

[12] Jauzac, M., Richard, J., Limousin, M., et al. 2016, MNRAS, 457, 2029

[13] Johnson, T. L., & Sharon, K. 2016, ApJ, 832, 82

[14] Kawamata, R., Oguri, M., Ishigaki, M., Shimasaku, K., & Ouchi, M. 2016, ApJ, 819, 114

[15] Kelly, P. L., Rodney, S. A., Treu, T., et al. 2015, Science, 347, 1123

[16] Kelly, P. L., Rodney, S. A., Treu, T., et al. 2016a, ApJ Letters, 819, L8

[17] Kelly, P. L., Brammer, G., Selsing, J., et al. 2016b, ApJ, 831, 205

[18] Kundić, T., Turner, E. L., Colley, W. N., et al. 1997, ApJ, 482, 75

[19] Lam, D., Broadhurst, T., Diego, J. M., et al. 2014, ApJ, 797, 98

[20] Limousin, M., Richard, J., Jullo, E., et al. 2016, A&A, 588, A99

[21] Lotz, J. M., Koekemoer, A., Coe, D., et al. 2017, ApJ, 837, 97

[22] Mahler, G., Richard, J., Clément, B., et al. 2018, MNRAS, 473, 663

[23] Meneghetti, M., Natarajan, P., Coe, D., et al. 2017, MNRAS, 472, 3177

[24] Oguri, M. 2015, MNRAS, 449, L86

[25] Planck Collaboration, Ade, P. A. R., Aghanim, N., et al. 2016, A&A, 594, A13

[26] Refsdal, S. 1964, MNRAS, 128, 307

[27] Riess, A. G., Macri, L. M., Hoffmann, S. L., et al. 2016, ApJ, 826, 56

[28] Rodney, S. A., Strolger, L.-G., Kelly, P. L., et al. 2016, ApJ, 820, 50

[29] Sereno, M., & Paraficz, D. 2014, MNRAS, 437, 600

[30] Sharon, K., & Johnson, T. L. 2015, ApJ Letters, 800, L26

[31] Suyu, S. H., Auger, M. W., Hilbert, S., et al. 2013, ApJ, 766, 70

[32] Treu, T., Brammer, G., Diego, J. M., et al. 2016, ApJ, 817, 60

[33] Vega-Ferrero, J., Diego, J. M., Miranda, V., & Bernstein, G. M. 2018, ApJ Letters, 853, L31

[34] Wong, K. C., Suyu, S. H., Auger, M. W., et al. 2017, MNRAS, 465, 4895

[35] Zitrin, A., Zheng, W., Broadhurst, T., et al. 2014, ApJ Letters, 793, L12

Highlights on Spanish Astrophysics X, Proceedings of the XIII Scientific Meeting of the Spanish Astronomical Society held on July 16 – 20, 2018, in Salamanca, Spain. B. Montesinos, A. Asensio Ramos, F. Buitrago, R. Schödel, E. Villaver, S. Pérez-Hoyos, I. Ordóñez-Etxeberria (eds.), 2019

The Hα Luminosity Function and the Star Formation Rate Density of the local Universe with J-PLUS DR1 data.

Gonzalo Vilella-Rojo[1], Rafael Logroño-García[1], Carlos López-Sanjuan[1], Jesús Varela[1], Kerttu Viironen[1], and The J-PLUS team

[1] Centro de Estudio de Física del Cosmos de Aragón, Unidad Asociada al CSIC, Plaza San Juan 1, 44001 Teruel, Spain

Abstract

The First Data release of the J-PLUS photometric survey is already public and available for the scientific community. It includes millions of sources in a usable area of 897 deg^2. With it, we analyse nearby star-forming galaxies ($z < 0.017$) to obtain the Hα Luminosity Function of the Local Universe, the Star Formation Main Sequence, and the Star Formation Rate Density of the Local Universe. Our results are the most local values for these properties, using a large and homogeneous sample of sources with no target pre-selection.

1 Introduction

The Javalambre Photometric Local Universe Survey (J-PLUS, hereafter) is a photometric survey conducted from the Observatorio Astrofísico de Javalambre, in Teruel, Spain. It is carried out using an 83 cm diameter telescope (JAST/T80) and a large camera (T80Cam) that provide an effective Field of View of 2 square degrees. The filter system includes a set of 5 broadband filters (almost identical to the SDSS photometric system), and 7 medium and narrow bands, placed in key stellar features. All the details of the J-PLUS survey can be found in [2].

In this contribution we present the first determination of the Hα Luminosity Function at $z = 0$ with the homogeneous sample of sources present in the first J-PLUS Data Release. In Section 1, we present the properties of the data sample. In Section 2, we describe the process to select sources with an emission line inside the J0660 filter. Section 3 summarizes the criteria to discern objects at low redshift from contaminants at higher redshift. The Luminosity Function, Star Formation Main Sequence, and Star Formation Rate Density are presented in Section 4. Finally, we discuss the results and summarize the main points of this contribution in Section 5.

2 Data

In this Section we present the main characteristics of the J-PLUS first Data Release (DR1 hereafter). J-PLUS DR1 includes high-quality multiband information of 897 deg^2 (1022 deg^2 before masking), around 8.4 million objects with $r < 21$ detected in dual mode, including stars, galaxies, or QSO. Aside from the photometry, value-added catalogs are provided with extra information, that includes photometric redshifts, object classification, or cross-matches with pre-existing catalogs, among others. It is publicly accessible via ADQL queries in the J-PLUS website[1]. Custom queries can be performed to retrieve data according to different criteria. J-PLUS DR1 is described in these proceedings by López-Sanjuan *et al.*

For this study, we select all objects with $r \leq 18$. We apply this cut to ensure that we are complete in detection. We do not expect this to significantly bias our selection due to the nature of our sources. Star-forming galaxies in the nearby Universe should not be much fainter than this cut, and it helps to filter contaminants at higher redshift, which will be mainly [OIII] emitters at $z \sim 0.3$.

3 Emitter Selection

In this Section we explain the method that we use to select sources with an emission inside the J0660 filter, and how we discern between low-z and high-z emitters. We recall here that the [OIII] emission is within the J0660 wavelength range at $z \sim 0.3$.

To select emitters at low-z, we retrieve all $J0660$, r, and i fluxes from the database. We infer a linear continuum that spans from the central wavelength of r, to the central wavelength of i, thus inferring a local continuum for $J0660$ at the wavelength range of Hα. All the equations and details about this method can be found in Vilella-Rojo *et al.*, 2015 [12].

We do this in a Monte-Carlo approach. We perform many iterations of this routine, varying each time the value of the flux inside each filter within its error bar, assigning each time a component of noise that is drawn from a Gaussian distribution with σ that is the photometric error of each flux. Each time we do this, we store the obtained value. In the end, each source has a N values of excess inside $J0660$, where N is the number of iterations that we repeated this process. In the end we consider as emitters all sources that fulfill the condition

$$\frac{\langle F \rangle}{\mathrm{NMAD}\,(F)} \geq 3 \tag{1}$$

where $\langle F \rangle$ is the median of all the N excess measurements for each source, and $\mathrm{NMAD}\,(F)$ is the normalized median absolute deviation, as given by $1.48 \times \mathrm{median}\,(\,|\,F_i - \langle F \rangle\,|\,)$.

[1] http://www.j-plus.es/

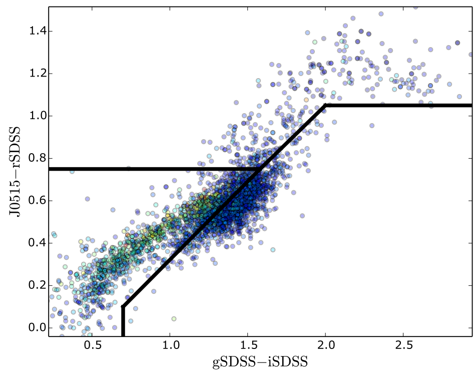

Figure 1: Color-color plot used to separate sources. Dots are color-coded according to the area of the `SExtractor` ellipse that encloses the source. Three regions are drawn according to the nature of the sources. The upper region is a stellar locus. Lower right region contains galaxies at a redshift higher than our redshift of interest. Low redshift galaxies are clustered in the lower left region.

All the emitting sources are then plotted in a $J0515 - r$ *vs* $g - i$ color-color diagram. In Figure 1 we plot this diagram. Dots are color coded according to the area of the ellipse of the detection in `SExtractor` MAG_AUTO mode using the r filter as the detection band.

We cross-match all the sources with preexisting catalogs that include spectroscopic redshifts. We find that low-z objects are populating a sequence in the lower left corner. Sources with a redshift higher than our redshift of interest are clustered around $g - i \sim 1.5$. We select all the sources that are candidates to be low redshift, and we check them by eye to classify them as low redshift emitters. The numbers that describe this sample are summarised in Table 1

Table 1: Summary of redshift distribution of the candidates that lie within the region of low-z candidates inside the color-color diagram.

With spec-z		Without spec-z		
Low z	High z	Low z candidates	High z candidates	Total
466	485	166	431	1548

The final sample of low z galaxies contains 632 galaxies. The purity of this sample should be around 100%; we might not be complete, but given the cuts that we apply in the color-color diagram, and the visual inspection, we do not expect completeness to significantly bias our results.

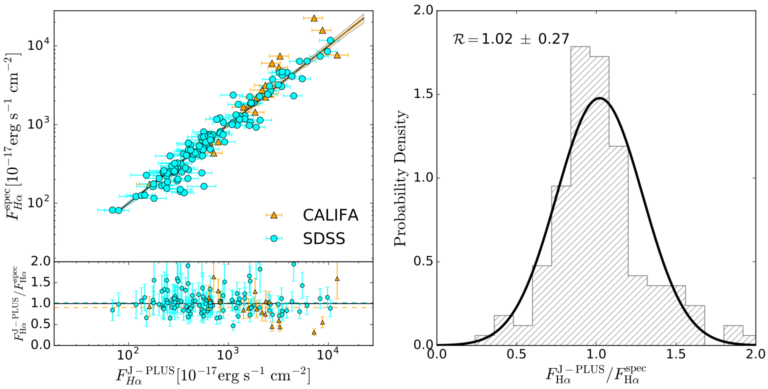

Figure 2: **Left panel:** Comparison between the clean Hα flux as measured with J-PLUS, and SDSS or CALIFA, for a sample of galaxies that are observed in the three surveys. **Right panel:** Histogram of the Ratio R between the Hα flux measured with J-PLUS and the spectroscopic values.

3.1 Performing the photometry

Once we identify our sources of interest, we repeat the photometry using only the emitting regions of each galaxy. This routine is described in detail in the work by Logroño-García *et al.* [6]. With it, we retrieve the photometry in the 12 J-PLUS filters, and with these we measure the Hα+[NII] excess. The Hα flux is then obtained using the SED-fitting method and corrections described in Vilella-Rojo *et al.*, 2015 [12]. The reliability of this method is tested against spectroscopic data, using galaxies in common with the SDSS and CALIFA surveys. Results can be found in [6] and in Figure 2 in this contribution.

4 Results

In this Section we present the main results of this study. These include the Hα Luminosity Function (Hα LF), the Galaxy Star Formation Main Sequence, and the Star Formation Rate Density ρ_* in the local volume.

4.1 The Hα Luminosity Function

To compute the distance to our galaxies, we use the spectroscopic redshift when these are available. Sources without spectroscopic redshift are assigned a random distance according to a volume prior. We do this with all the sources 5000 times. Each round we assign a different distance, hence a different luminosity. In each iteration, we stack the resulting luminosities, and in the end we normalize the number counts.

To correct for completeness in volume, we apply the classical V/V_{max} technique described in Schmidt, 1968 [11]. Errors are estimated assuming a Poissonian distribution for

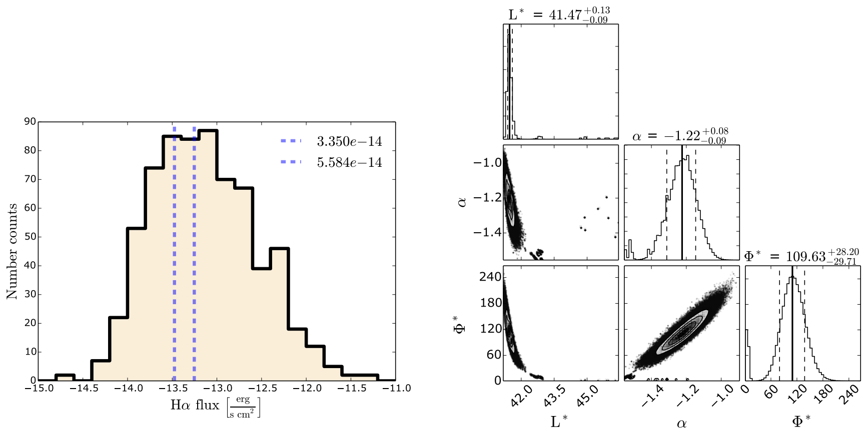

Figure 3: **Left panel:** Histogram of the Hα fluxes, and the flux cuts that we apply. **Right panel:** Probability distribution for each parameter of the fitting. Values in the titles represent the median, while errors correspond to the 16$^{\text{th}}$ and 84$^{\text{th}}$ percentiles of the stacked distributions.

the number counts. Finally, we fit the resulting distribution of number counts to a Schechter 1976 function:

$$n\left(L\right)\mathrm{d}L = \phi^{*}\left(\frac{L}{L^{*}}\right)^{\alpha} e^{\frac{L}{L^{*}}}\frac{\mathrm{d}L}{\mathrm{d}L^{*}}. \tag{2}$$

To perform the fitting and explore the parameter space, we use a MCMC approach. We use the code `emcee` [3]. We sample the 3-dimensional parameter space (i.e. L^{*}, α, and ϕ^{*}) for different 11 different values of limiting flux equally spaced between 3.35×10^{-14} and $5.58 \times 10^{-14}\,\mathrm{erg\,s^{-1}}$. These cuts can be found in Figure 3. We do this to include the uncertainty in the emission-line completeness in the final error of our parameters. We stack all the sampler chains and perform the statistical analysis in the resulting stacking. This is shown in Figure 4.

For each of the 11 values of limiting flux, we perform a fitting to a Schechter distribution (see [10]). We present the individual LFs, and the average one, in Figure 4

The values that we obtain for the fitting are: $\log_{10}\left(L^{*}\right) = 41.47 \pm^{0.13}_{0.09}$ $\left[\frac{\mathrm{erg}}{\mathrm{s}}\right]$, $\alpha = -1.22\pm^{0.08}_{0.09}$, $\log_{10}\left(\phi^{*}\right) = -2.55 \pm^{0.1}_{0.13}$ $\left[\mathrm{Mpc}^{-3}\right]$.

The integral of this distribution is analytical under the condition $\alpha \leq -2$,

$$\mathcal{L} = \int \phi^{*}\frac{L}{L^{*}}\exp\left(-\frac{L}{L^{*}}\right)\frac{\mathrm{dL}}{L^{*}} = \phi^{*}L^{*}\Gamma\left(\alpha+2\right). \tag{3}$$

4.2 The Star Formation Rate Density at $z = 0$

To estimate the Star Formation Rate Density ρ_{*} of the local volume (up to ~ 73 Mpc distance in radius) we use the the Kennicutt (1998) relation (see [5]). This relation assumes a Salpeter [9] Initial Mass Function, and case B recombination.

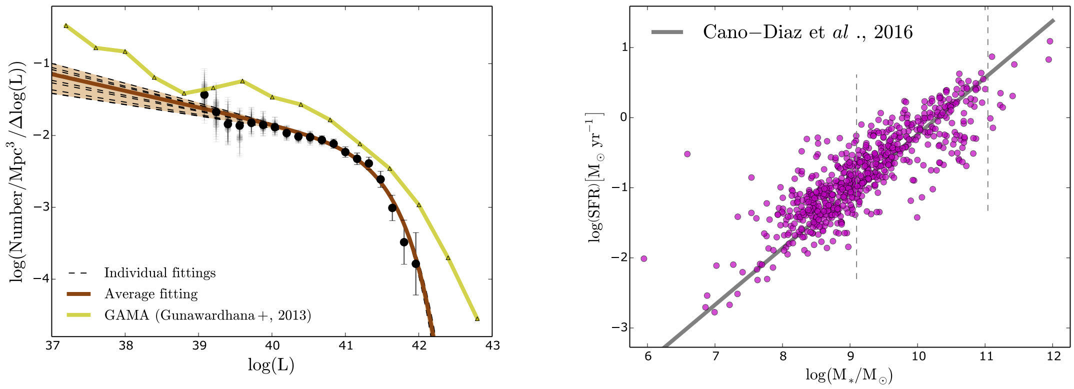

Figure 4: **Left panel**: Hα Luminosity Function. Grey dots represent the frequencies for each of the 11 realizations with different limiting flux. Black dashed lines are the individual fittings that are obtained with each limiting flux cut. Solid brown curve is the curve that has the median values for each of the three parameters. **Right panel:** Galaxy Star Formation Main Sequence obtained with J-PLUS DR1 data. Dashed vertical lines are 5$^{\rm th}$ and 95$^{\rm th}$ percentiles of the masses in the Cano-Díaz *et al.*, 2016, CALIFA sample

$$\mathrm{SFR} = 7.9 \times 10^{-42} \mathcal{L} \quad \frac{\mathrm{M}_\odot}{\mathrm{year}}, \tag{4}$$

where $\mathcal{L}$ is the total luminosity of Hα, as computed from Equation 3. If we divide by the total volume up to $z = 0.017$, we obtain a SFRD $\log(\rho_*) = -2.10\pm^{0.04}_{0.05}$. This is in good agreement with previous values in the literature (see, for instance [4]).

4.3 The Galaxy Star Formation Main Sequence

Finally, we plot the so called as Galaxy Star Formation Main Sequence [8], which relates the SFR of galaxies with their total stellar mass, M$_*$. This is shown in Figure 4. We overplot the fitting for the relation M$_*$ (SFR) obtained with spectroscopic data from the CALIFA Survey, as found in Cano-Díaz *et al.*, 2016.[1]. We find an excellent agreement between our measurements and CALIFA ones, giving us strong confidence in our findings.

5 Summary and conclusions

In this work we have presented three main results that are derived from the J-PLUS first Data Release, publicly available to the community in the J-PLUS website. These are the Hα Luminosity Function, the Star Formation Rate Density of the local Universe, and the Galaxy Main Sequence of Star Formation of a sample of 632 Hα emitters. To do that, we first selected all our sources from the catalogs, and to make sure that our sample was pure, we visually checked more than 1500 candidates.

After this visual inspection, our sample of emitters includes 632 galaxies, of which 166 had not been previously assigned a redshift. These galaxies present compact morphologies and blue colors, being an interesting population for further analysis.

The Hα LF shows consistency with previous values in the literature. It is in good agreement with a Schechter distribution, which allows us to perform an analytical integral to compute the total Hα luminosity and the star formation rate density. This value is also in agreement with previous studies.

Finally, we compute the Galaxy Star Formation Main Sequence, which relates the star formation rate of a galaxy with its mass, and shows a correlation that spans for 3 orders of magnitude. We compare our result with the one obtained using spectroscopic measurements from the CALIFA survey, showing not only an excellent agreement, but a wider mass range.

References

[1] Cano-Díaz, M., et al., 2016, ApJ, 821, 26

[2] Cenarro, A.J., et al. 2018, A&A submitted, arXiv:1804.02667

[3] Foreman-Mackey, D., et al., 2013, PASP, 125, 306

[4] Gunawardhana et al., 2013, 433, 2764

[5] Kennicutt, R. C. 1998, ARA&A, 36, 189

[6] Logroño-García, R. et al. 2018, A&A accepted, arXiv:1804.04039

[7] López-Sanjuan, C., et al. 2018, A&A accepted, arXiv:1804.02673

[8] Noeske, K., et al., 2007, ApJ, 660, 43

[9] Salpeter, EE. 1955, ApJ, 121, 161

[10] Schechter, P. 1976, ApJ, 203, 297

[11] Schmidt, M. 1968, ApJ, 151

[12] Vilella-Rojo, G. et al. 2015, A&A, 580, A47

Highlights on Spanish Astrophysics X, Proceedings of the XIII Scientific Meeting of the Spanish Astronomical Society held on July 16 – 20, 2018, in Salamanca, Spain. B. Montesinos, A. Asensio Ramos, F. Buitrago, R. Schödel, E. Villaver, S. Pérez-Hoyos, I. Ordóñez-Etxeberria (eds.), 2019

TRUE2: establishing a detectability limit on hidden broad line regions.

Agís González, B.[1,2], Hutsemékers, D. [1], Acosta Pulido, J.A.[3,4] and Ramos Almeida, C.[3,4]

[1] Space Sciences, Technologies and Astrophysics Research (STAR) Institute, Université de Liège, Allée du 6 Août 19c, B5c, 4000 Liège, Belgium
[2] Instituut voor Sterrenkunde, KU Leuven, Celestijnenlaan 200D, bus 2401 3001 Leuven, Belgium
[3] Instituto de Astrofísica de Canarias, Calle Vía Láctea, s/n, E-38205 La Laguna, Tenerife, Spain
[4] Departamento de Astrofísica, Universidad de La Laguna, E-38205 La Laguna, Tenerife, Spain

Abstract

True Seyfert 2 candidates are those Seyferts galaxies whose optical spectral do not show broad lines, nevertheless in the X-ray domain, they exhibit some characteristic behavior of Seyferts 1 such as lack of X-ray obscuration and/or short timescale variability. A true 2 candidate will be confirmed as a true Seyfert 2 if the lack of its broad line region (BLR) is not only observational but physical. These kind of objects are thought to accrete at low Eddington rates, in agreement with theoretical models that predict that the BLR disappears below a certain critical value of accretion rate and/or luminosity. In the last decade, a significant number of true Seyfert 2s with low accretion rates has been claimed in the literature. However, some exceptions as GNS 069 or 2XMM J1231+1106 show high accretion rates, which seem to contradict the generally accepted explanation.

A limit on the detection of hidden broad line regions (HBLRs) must be established in order to make sure that BLRs are not present intrinsically. Since true Seyfert 2 candidates are selected by the absence of X-ray obscuration, the most plausible explanation to cause the non-detection of a physically present HBLR would be the absence of an adequate scattering medium. Polarimetry can play a key role to answer this question. The presence of an efficient scattering region would imply a high continuum of polarization. We propose to assess what degrees of polarization are high enough to indicate the presence of a scattering medium able to act as a mirror and thus providing us with the indirect view of the HBLRs.

We got new imaging polarimetry data from ISIS@WHT of 10 true 2 candidates which had not been checked in polarized light. If scattering regions are present, undeniable degrees of polarization around 1?3% should be measured. Comparing the measured continuum of polarization with simulations we will be able to estimate a decidability limit on HBLRs. Specifically, we will apply STOKES, a Monte Carlo radiative transfer code which can be used to model, predict, fit and interpret the polarization of AGN. (See poster).

Highlights on Spanish Astrophysics X, Proceedings of the XIII Scientific Meeting of the Spanish Astronomical Society held on July 16 – 20, 2018, in Salamanca, Spain. B. Montesinos, A. Asensio Ramos, F. Buitrago, R. Schödel, E. Villaver, S. Pérez-Hoyos, I. Ordóñez-Etxeberria (eds.), 2019

Optical follow-up of galaxy cluster candidates detected by Planck satellite in the PSZ catalogue.

A. Aguado-Barahona[1,2], R. Barrena[1,2], A. Strebyanska[1,2], A. Ferragamo[1,2], and J.A. Rubino-Martin[1,2]

[1] Instituto de Astrofísica de Canarias, C/Via Lactea s/n, E-38205 La Laguna, Tenerife, Spain
e-mail: aaguado@iac.es

[2] Universidad de La Laguna, Departamento de Astrofísica, E-38206 La Laguna, Tenerife, Spain

Abstract

The Legacy PLANCK all-sky Sunyaev-Zeldovich (SZ) galaxy cluster catalogues PSZ1 and PSZ2 (Planck Collaboration XXIX 2013; Planck Collaboration XXVII 2015) provide for the first time the possibility to detect galaxy clusters using the SZ effect signature in a full sky survey. However, in order to constrain cosmological parameters from these catalogues, the clusters must be characterized in their physical properties, mainly redshift and mass. Here, we describe our optical follow-up programme, which has been developed with the aim of validating SZ Planck sources with no known optical counterparts. Thanks to a 4-year observational programme, using the 4.2m WHT and 2.5m INT telescopes at the Observatorio Roque de los Muchachos (La Palma), we identify the optical counterparts of the SZ candidates and estimate their photo-z's. After this, we study spectroscopically a significant sample of the confirmed clusters. We perform multi-object spectroscopy (MOS) with the 3.5m TNG and 10.4m GTC telescopes, in order to retrieve redshifts, velocity dispersions and dynamical masses. This allows us to compare SZ masses with dynamical ones and calibrate the uncertainties in this scaling laws understanding possible biases. This poster presents the status of the imaging observations (more than 400 objects observed), the spectroscopic observations (more than 120 MOS masks), and the first scientific results of this programme. (See poster).

Highlights on Spanish Astrophysics X, Proceedings of the XIII Scientific Meeting of the Spanish Astronomical Society held on July 16 – 20, 2018, in Salamanca, Spain. B. Montesinos, A. Asensio Ramos, F. Buitrago, R. Schödel, E. Villaver, S. Pérez-Hoyos, I. Ordóñez-Etxeberria (eds.), 2019

Phase-referencing measurements of positional frequency-dependent shifts in ultra-compact AGN cores.

R. Azulay[1,2], A. P. Lobanov[2], E. Ros[2], J. C. Guirado[1,3], and R. W. Porcas[2]

[1] Departamento de Astronomía y Astrofísica, Universidad de Valencia, Dr. Moliner 50, E-46100 Burjasot, Valencia, Spain
[2] Max-Planck-Institut für Radioastronomie, Auf dem Hügel 69, D-53121 Bonn, Germany
[3] Observatorio Astronómico, Universidad de Valencia, Parque Científico, Catedrático José Beltrán 2, E-46980 Paterna, Valencia, Spain

Abstract

Accurate alignment of the optical reference frame with the VLBI based International Celestial Reference Frame (ICRF) requires good understanding of the positional discrepancies of the reference objects used for the alignment. The compactness of the ICRF objects requires relative astrometry for measuring the frequency-dependent core shifts, however, there are no established methods and approaches for such measurements. We have designed a project aimed at testing several potential methods for core shift measurements using relative astrometry. For that purpose, we have used phase-referencing VLBA observations at 5 and 15 GHz in a sample of 10 compact, high declination radio sources. These observations will provide crucial input for devising an optimal approach for the radio-optical reference frame aligment. (See poster).

Acknowledgments

R.A. is supported for this research by the Generalitat Valenciana project APOSTD/2018/177 and has also been supported by the Max-Planck-Institut für Radioastronomie. This work has also been partially supported by the Spanish MINECO project AYA2015-63939-C2-2-P and by the Generalitat Valenciana project PROMETEO/2009/104 and PROMETEOII/2014/057. The VLBA is a facility of the National Science Foundation operated by the National Radio Astronomy Observatory under cooperative agreement with Associated Universities, Inc.

Highlights on Spanish Astrophysics X, Proceedings of the XIII Scientific Meeting of the Spanish Astronomical Society held on July 16 – 20, 2018, in Salamanca, Spain. B. Montesinos, A. Asensio Ramos, F. Buitrago, R. Schödel, E. Villaver, S. Pérez-Hoyos, I. Ordóñez-Etxeberria (eds.), 2019

Characterization of ionized outflows in optically obscured quasars (QSO2) at z $\sim 0.3 - 0.5$.

E. Bellocchi[1], M. Villar Martín[1], A. Cabrera Lavers[2,3]

[1] Centro de Astrobiología (CAB, CSIC–INTA), Departamento de Astrofísica, Cra. de Ajalvir Km. 4, 28850 - Torrejón de Ardoz, Madrid, Spain
[2] Instituto de Astrofísica de Canarias (IAC), Vía Láctea s/n, E–38200 La Laguna (Tenerife, Spain)
[3] GRANTECAN, Cuesta de San José s/n, E–38712 Breña Baja (La Palma, Spain)

Abstract

Feedback induced by the activity of supermassive black holes (SMBH) in massive galaxies is thought to play a critical role in their evolution. In particular, the most powerful outflows with the most extreme effects on the environment are expected in quasars (QSOs). Type 2 QSOs (QSO2) are the best objects to study the way feedback works since the active nucleus is obscured allowing one to better study the properties of the surrounding medium. Ionized outflow are ubiquitous in this kind of systems at different redshift (z), whose kinematics is identified by the presence of a broad component characterized by FWHM > 1000 km s^{-1} and velocity shift vs. $\sim$several $\times$ 100 km s^{-1} with respect to the narrow (systemic) one.
The 'radio–induced' mechanism is another way to feed the AGN, not been sufficiently explored in radio quiet QSOs: it is known that ionized outflows are also ubiquitous in non radio–loud QSO2s at different z. The actual size of the outflows and their efficiency for gas ejection and star formation truncation are controversial. We have recently proposed that large scale ($\geq$ several kpc) extended radio structures might be necessary to identify (even to trigger) outflow signatures across such large spatial scales (Villar-Martín, 2017). Based on this, we investigated the properties and sizes of the ionized outflows in a sample 6 SDSS QSO2 at z $\sim 0.3 - 0.5$ with known extended radio structures with the goal of searching for spatially extended outflow signatures. The study is based on long slit Osiris/GTC spectroscopy and complemented by FORS2/VLT data (Villar-Martín, 2011). (See poster).

Highlights on Spanish Astrophysics X, Proceedings of the XIII Scientific Meeting of the Spanish Astronomical Society held on July 16 – 20, 2018, in Salamanca, Spain. B. Montesinos, A. Asensio Ramos, F. Buitrago, R. Schödel, E. Villaver, S. Pérez-Hoyos, I. Ordóñez-Etxeberria (eds.), 2019

Accurate number densities and environment for compact and relic massive galaxies.

Fernando Buitrago[1,2], and Ignacio Ferreras[3,4]

[1] Instituto de Astrofísica e Ciências do Espaço, Universidade de Lisboa, OAL, Tapada da Ajuda, PT1349-018 Lisbon, Portugal
[2] Departamento de Física, Faculdade de Ciências, Universidade de Lisboa, Edifício C8, Campo Grande, PT1749-016 Lisbon, Portugal
[3] Instituto de Astrofísica de Canarias (IAC), La Laguna, E-38205, Spain
[4] Departamento de Astrofísica, Universidad de La Laguna (ULL), E-38200, La Laguna, Spain

Abstract

The quest to find relic galaxies is ongoing, i.e. galaxies that seem to remain untouched from the primeval Universe. These galaxies are usually massive ($> 8{\times}10^{10}$ $M_\odot$), with very small sizes (effective radius < 2 Kpc) and with old (> 10 Gyr) stellar populations. Observationally, it is not well tested whether these objects live in galaxy overdensities, as simulations predict. Additionally, their number densities in the nearby Universe ($z< 0.3$) are also under debate, due to the lack of large area spectroscopic surveys. To top it up, their sizes and structural parameters are not very reliable due to the shallow ancillary imaging of previous works, typically SDSS. I take advantage of the GAMA spectroscopic survey, in the KiDS and VIKING fiels ($\sim$150 deg^2, 2 mag deeper) to create a complete census of this elusive galaxy population. Each of the galaxies in my sample, surprisingly being many of them satellites of bigger objects, are a treasure trove to understand the properties of the high redshift Universe. (See poster).

Highlights on Spanish Astrophysics X, Proceedings of the XIII Scientific Meeting of the Spanish Astronomical Society held on July 16 – 20, 2018, in Salamanca, Spain. B. Montesinos, A. Asensio Ramos, F. Buitrago, R. Schödel, E. Villaver, S. Pérez-Hoyos, I. Ordóñez-Etxeberria (eds.), 2019

First results of an observational test of a double reionization scenario by searching for galaxies at high redshift.

C. Cabello[1], J. Gallego[1], N. Cardiel[1], R. Guzmán[2], J. M. Rodríguez-Espinosa[3], A. Herrero[3], M. Mas-Hesse[4], E. Salvador-Solé[5], A. Manrique[5], A. Marín-Franch[6] and S. Eikenberry[2]

[1] Departamento de Física de la Tierra y Astrofísica, Universidad Complutense de Madrid, E-28040 Madrid, Spain
[2] Department of Astronomy, University of Florida, 211 Bryant Space Science Center, Gainesville, FL 32611, USA
[3] Instituto de Astrofísica de Canarias y Depto. de Astrofísica. Universidad de La Laguna, E-38205 La Laguna, Spain
[4] Centro de Astrobiología, CSIC/INTA, km 4, Crtra de Ajalvir, 28850, Torrejon de Ardoz, Madrid, Spain
[5] Institut de Ciències del Cosmos. Universitat de Barcelona (UB-IEEC), E-08028 Barcelona, Spain
[6] Centro de Estudios de Física del Cosmos de Aragón, E-44001 Teruel, Spain

Abstract

The study of high redshift galaxies is crucial for understanding the reionization process, the formation and evolution of galaxies, and the large-scale structure in the Universe. The main goal of this project was to obtain an ultra-deep image taken with a narrow-band filter (FWHM = 11nm and central wavelength $\lambda_c = 1.254\ \mu$m), designed by the ALBA team, and installed in the CIRCE nIR camera for GTC, with the aim of detecting LAEs (Luminous Lyman-α Emitters) at z = 9.3 by the flux excess due to their Lyα emission. In this sense, this project would allow to support or reject the double reionization scenario predicted by the AMIGA model (Salvador-Solè 2015). The ultra-deep image has been obtained within the Extended Groth Strip (EGS) field, reaching a limiting AB magnitude ~ 22 in the ALBA narrow-band filter. With this depth we could not detect any candidate for LAE at high redshift. In addition, we have performed a scientific analysis of some properties of the identified galaxies, gathering the available ancillary information of these objects from the 3D-HST and CANDELS surveys. (See poster).

Highlights on Spanish Astrophysics X, Proceedings of the XIII Scientific Meeting of the Spanish Astronomical Society held on July 16 – 20, 2018, in Salamanca, Spain. B. Montesinos, A. Asensio Ramos, F. Buitrago, R. Schödel, E. Villaver, S. Pérez-Hoyos, I. Ordóñez-Etxeberria (eds.), 2019

Testing Cosmological Structure formation in Unified Dark Matter-Energy models.

Diogo Castelão[1,2], Alberto Rozas-Fernández[2], and Ismael Tereno[1,2]

[1] Departamento de Física, Faculdade de Ciências, Universidade de Lisboa, Edifício C8, Campo Grande, PT1749-016 Lisboa, Portugal
[2] Instituto de Astrofísica e Ciências do Espaço, Faculdade de Ciências, Universidade de Lisboa, Tapada da Ajuda, PT-1349-018 Lisboa, Portugal

Abstract

Unified Dark Matter-Energy models (UDM) are a class of models where dark matter and dark energy exist as a single essence and have been proposed as an alternative approach to ΛCDM. In this work we focus on a specific UDM model that contains a fast transition between dark matter-like and dark energy-like behaviours. The rapidity and redshift of the transition are important features of the model. We compute structure formation in this model, using a modified version of CLASS, and study its viability against a combination of SNe Ia, BAO, CMB and weak lensing data, performing MCMC and Nested Sampling analyses. We find that the inclusion of current weak lensing data, from the KiDS survey, allows us to strongly constrain the redshift of the transition and find a viable range of parameter values for which structure formation is similar to the one predicted by ΛCDM. (See poster).

Highlights on Spanish Astrophysics X, Proceedings of the XIII Scientific Meeting of the Spanish Astronomical Society held on July 16 – 20, 2018, in Salamanca, Spain. B. Montesinos, A. Asensio Ramos, F. Buitrago, R. Schödel, E. Villaver, S. Pérez-Hoyos, I. Ordóñez-Etxeberria (eds.), 2019

MEGARA Early-Science results: Stellar populations in nearby galaxies.

Á. Castillo-Morales[1], M. Chamorro-Cazorla[1], A. Gil de Paz[1], J. Gallego[1], E. Carrasco[2], J. Iglesias-Páramo[3], B. T. Dullo[1], C. Catalán-Torrecilla[1], S. Pascual[1], N. Cardiel[1], M. L. García-Vargas[4] and MEGARA Commissioning Team

[1] Departamento de Física de la Tierra y Astrofísica, Universidad Complutense de Madrid, E-28040 Madrid, Spain
[2] Instituto Nacional de Astrofísica, Óptica y Electrónica Luis Enrique Erro No.1, C.P. 72840, Tonantzintla, Puebla Mexico
[3] Instituto de Astrofísica de Andalucía-CSIC, Glorieta de la Astronomía s/n, 18008, Granada, Spain
[4] FRACTAL, S.L.N.E., Madrid, Spain

Abstract

Our objective is to target a well-defined sample of 150 nearby disks from the S4G survey to measure their light-weighted (1) stellar velocity ellipsoids, (2) stellar population ages and (3) abundances along the galaxies' major and minor axes using MEGARA spectroscopy in the CaT region at R=20000 and in multiple Low-resolution (R=6000) setups. In a first step we have obtained HR-I data on a subsample of S4G objects plus nearby galaxies (NGC7025, UGC10205, M32). In this poster different showcase examples are presented for the central (12.5 arcsec x 11.3 arcsec) stellar properties. MEGARA allows us to study the radial variation of the effective star formation history of the galactic disks and of its stellar abundances by means of comparing R=6k-20k data with the predictions of the galaxy evolution (backward) modeling of the effective (in-situ plus ex-situ) star formation history and chemical abundances. The deviations of our observations from the smooth inside-out growth predicted by the models would reflect the presence of ex-situ processes, such as radial migration and/or satellite accretion. (See poster).

Acknowledgments

MEGARA acknowledges financial support by GRANTECAN S.A. and contributing institutions, UCM, INAOE, IAA-CSIC, UPM, and companies, Fractal, AVS. Authors acknowledge financial support by the MINECO project AYA2016-75808-R.

Highlights on Spanish Astrophysics X, Proceedings of the XIII Scientific Meeting of the Spanish Astronomical Society held on July 16 – 20, 2018, in Salamanca, Spain. B. Montesinos, A. Asensio Ramos, F. Buitrago, R. Schödel, E. Villaver, S. Pérez-Hoyos, I. Ordóñez-Etxeberria (eds.), 2019

MEGARA Early-Science results: neutral and ionized galactic winds in the central parts of nearby galaxies.

Catalán-Torrecilla, C.[1,*]; Castillo-Morales, Á.[1]; Gil de Paz, A.[1]; Gallego, J.[1]; Carrasco, E.[2]; Iglesias-Páramo,J.[3]; Pascual, S.[1]; Chamorro-Cazorla, M.[1]; Dullo, B. T.[1]; García-Vargas, M. L.[4]; and MEGARA Commissioning team

[1] Departamento de Física de la Tierra y Astrofísica, Universidad Complutense de Madrid, Spain (*ccatalan@ucm.es); [2]Instituto Nacional de Astrofísica, Óptica y Electrónica, Mexico; [3]Instituto de Astrofísica de Andalucía−CSIC, Spain; [4] FRACTAL S.L.N.E, Spain.

Abstract

Galactic winds are widely recognized as essential components in the evolution of galaxies. In order to study the multi-phase structure of winds, we are analyzing high-quality IFS MEGARA IFU [1] data taken during the Commissioning Period (June 2017). We present the first results obtained from the mapping of the central regions of a small sample of nearby galaxies. On one hand, the neutral gas outflows are traced by the interstellar Na I $\lambda\lambda$ 5890,5896 doublet excess using a low-resolution set-up (5143−6164 Å at R=6K). On the other hand, the ionized gas phase and its connection to nuclear star formation is analyzed thanks to the high-resolution set-up (6445−6837 Å at R=20K). This study will shed light on the role that AGN activity [2] and galactic outflows [3] play on the evolution of galaxies and measure the balance between negative and positive feedback in the center of galaxies. Authors acknowledge financial support by the MINECO project AYA2016-75808-R. C.C.-T. gratefully acknowledges the support of the European Youth Employment Initiative (YEI) by means of the Postdoctoral Fellowship Program. (See poster).

References

[1] Gil de Paz, A. et al. 2018, Proceedings of the SPIE, Volume 10702, 1070217

[2] Catalán-Torrecilla, C. et al. 2017, ApJ, 848, 87

[3] Veilleux, S. et al. 2005, ARAA, 43, 769

Highlights on Spanish Astrophysics X, Proceedings of the XIII Scientific Meeting of the Spanish Astronomical Society held on July 16 – 20, 2018, in Salamanca, Spain. B. Montesinos, A. Asensio Ramos, F. Buitrago, R. Schödel, E. Villaver, S. Pérez-Hoyos, I. Ordóñez-Etxeberria (eds.), 2019

MEGARA Early-Science results: Stellar dynamics in external galaxies.

M. Chamorro-Cazorla[1], Á. Castillo-Morales[1], A. Gil de Paz[1], J. Gallego[1], E. Carrasco[2], J. Iglesias-Páramo[3], B. T. Dullo[1], C. Catalán-Torrecilla[1], S. Pascual[1], M. L. García-Vargas[4] and MEGARA Commissioning Team

[1] Departamento de Física de la Tierra y Astrofísica, Universidad Complutense de Madrid, E-28040 Madrid, Spain
[2] Instituto Nacional de Astrofísica, Óptica y Electrónica Luis Enrique Erro No.1, C.P. 72840, Tonantzintla, Puebla Mexico
[3] Instituto de Astrofísica de Andalucía-CSIC, Glorieta de la Astronomía s/n, 18008, Granada, Spain
[4] FRACTAL, S.L.N.E., Madrid, Spain

Abstract

We present the capabilities of the MEGARA instrument at GTC for studying stellar dynamics in external galaxies. The analysis carried out so far in this regard is based on data taken with MEGARA during the commissioning period with the LCB IFU between June and August 2017. We show results on stellar kinematics in the central regions of a number of nearby galaxies such as velocity, velocity dispersion, skewness (h3) and kurtosis (h4) maps, obtained with the pPXF code, including NGC 7025, M 32, etc. These results are helping to reveal the role of dynamical processes in the formation and evolution of galaxies, thanks to the unprecedented capabilities of MEGARA@GTC, mainly its combination of spaxel size (0.62 arcsec), FoV (12.5 arcsec x 11.3 arcsec), efficiency and spectral resolution (R=6,000-20,000). (See poster).

Acknowledgments

MEGARA acknowledges financial support by GRANTECAN S.A. and contributing institutions, UCM, INAOE, IAA-CSIC, UPM, and companies, Fractal, AVS. Authors acknowledge financial support by the MINECO project AYA2016-75808-R.

Highlights on Spanish Astrophysics X, Proceedings of the XIII Scientific Meeting of the Spanish Astronomical Society held on July 16 – 20, 2018, in Salamanca, Spain. B. Montesinos, A. Asensio Ramos, F. Buitrago, R. Schödel, E. Villaver, S. Pérez-Hoyos, I. Ordóñez-Etxeberria (eds.), 2019

Dynamical properties determination from stellar kinematics in local LIRGs:the case of ESO320-G030.

Crespo Gómez, Alejandro[1]; Piqueras López, Javier[1]; Arribas, Santiago[1]

[1] Centro de Astrobiología (CSIC-INTA), Crta. de Torrejón a Ajalvir, km 4, 28850, Torrejón de Ardoz, Madrid, Spain

Abstract

In recent years, integral field spectroscopy techniques (IFS) have become a powerful tool to observe Ultra/Luminous Infrared Galaxies (U/LIRGS), allowing us to carry out spatially and spectrally resolved studies. These studies are aim to wide or understanding of galaxy evolution since these systems are thought to be the dominant component to the energy density of the Universe beyond z$\sim$2. Most of the effort has been focused on a wide variety of physical processes by studying the different phases of the gas. However, stars are a key component that governs the dynamics of these complex systems, and is key to understand how U/LIRGs builds up their mass during their evolution.

In this work, we present a IFS near-IR stellar kinematic study of a local sample of 10 LIRGs observed with SINFONI at the VLT. We have extracted the line-of-sight velocity distribution (LOSVD) using the CO stellar absorption bands in the K-band and obtained the two-dimensional velocity and velocity dispersion maps of the stellar component. By combining our kinematic maps and light profiles with a Navarro-Frenk-White dark matter halo profile we have obtained the dynamical masses of these galaxies.Here we introduce this procedure as well as the main kinematic and dynamical results. (See poster).

Highlights on Spanish Astrophysics X, Proceedings of the XIII Scientific Meeting of the Spanish Astronomical Society held on July 16 – 20, 2018, in Salamanca, Spain. B. Montesinos, A. Asensio Ramos, F. Buitrago, R. Schödel, E. Villaver, S. Pérez-Hoyos, I. Ordóñez-Etxeberria (eds.), 2019

Discovery of a lensed ultrabright submillimeter galaxy at z=2.0439.

A. Díaz-Sánchez[1], S. Iglesias-Groth[2], R. Rebolo[2], and H. Dannerbauer[2]

[1] Departamento Física Aplicada, Universidad Politécnica de Cartagena, Campus Muralla del Mar, 30202 Cartagena, Murcia, Spain
[2] Instituto de Astrofísica de Canarias, Vía Láctea, La Laguna 38200, Spain

Abstract

We report an ultra-bright lensed submillimeter galaxy (SMG) at $z = 2.0439$, *WISE* J132934.18+224327.3, identified as a result of a full-sky cross-correlation of the *AllWISE* and *Planck* compact source catalogs aimed to search for bright analogs of the submillimeter galaxy SMMJ2135, the Cosmic Eyelash. Inspection of archival SCUBA-2 observations of the candidates revealed a source with fluxes ($S_{850\mu m}$= 130 mJy) consistent with the *Planck* measurements. The centroid of the SCUBA-2 source coincides within 1 arcsec with the position of the *AllWISE* mid-IR source, and, remarkably, with an arc shaped lensed galaxy in *HST* images at visible wavelengths. Low-resolution rest-frame UV-optical spectroscopy of this lensed galaxy obtained with 10.4 m GTC reveals the typical absorption lines of a starburst galaxy. Gemini-N near-IR spectroscopy provided a clear detection of H_α emission. The lensed source appears to be gravitationally magnified by a massive foreground galaxy cluster lens at $z = 0.44$, modeling with Lenstool indicates a lensing amplification factor of 11 ± 2. We determine an intrinsic rest-frame 8-1000-μm luminosity, $L_{\rm IR}$, of $(1.3 \pm 0.1) \times 10^{13}$ $L_\odot$, and a likely star-formation rate (SFR) of $\sim 500 - 2000$ $M_\odot yr^{-1}$. The SED shows a remarkable similarity with the Cosmic Eyelash from optical-mid/IR to sub-millimeter/radio, albeit at higher fluxes. (See poster).

Highlights on Spanish Astrophysics X, Proceedings of the XIII Scientific Meeting of the Spanish Astronomical Society held on July 16 – 20, 2018, in Salamanca, Spain. B. Montesinos, A. Asensio Ramos, F. Buitrago, R. Schödel, E. Villaver, S. Pérez-Hoyos, I. Ordóñez-Etxeberria (eds.), 2019

Molecular gas in/outflows in the nuclear regions of five Seyfert galaxies.

A. J. Domínguez-Fernández[1,2], A. Alonso-Herrero[3], S. García-Burillo[1], L. Colina[4,5], P. Esquej[6], M. Imanishi[7], N. Levenson[8], R. Mason[9], C. Packham[10], M. Pereira-Santaella[11], C. Ramos Almeida[12,13], D. Rigopoulou[11], P. Roche[11], J. M. Rodríguez-Espinosa[12,13], and E. Sani[14]

[1] Observatorio Astronómico National, Alfonso XII 3, 28014 Madrid, Spain
[2] Departamento de Física de la Tierra y Astrofísica, Facultad de Ciencias Físicas, Universidad Complutense de Madrid, E-28040 Madrid, Spain
[3] Centro de Astrobiología (CAB, CSIC-INTA), ESAC Campus, E-28692 Villanueva de la Cañada, Madrid, Spain
[4] Centro de Astrobiología (CAB, CSIC-INTA), Carretera de Ajalvir, 28850 Torrejón de Ardoz, Madrid, Spain [5] ASTRO-UAM, Universidad Autónoma de Madrid (UAM), Unidad Asociada CSIC, Madrid, Spain
[6] Herschel Science Centre, ESA, Villafranca del Castillo, Apartado 78, E-28691 Villanueva de la Cañada, Spain
[7] National Astronomical Observatory of Japan, National Institutes of Natural Sciences (NINS), 2-21-1 Osawa, Mitaka, Tokyo 181-8588,Japan
[8] Space Telescope Science Institute, 3700 San Martin Dr, Baltimore, MD 21218, USA
[9] Gemini Observatory, Hawaii, Northern Operations Center, 6 70 North A'ohoku Place, Hilo, HI 96720, USA
[10] Department of Physics and Astronomy, University of Texas at San Antonio, One UTSA Circle, San Antonio, TX 78249, USA
[11] Oxford Astrophysics, Department of Physics, University of Oxford, Denys Wilkinson Building, Keble Rd, Oxford OX1 3RH, UK
[12] Instituto de Astrofísica de Canarias, C/Vía Láctea, s/n, E-38205 La Laguna, Tenerife, Spain
[13] Departamento de Astrofísica, Universidad de La Laguna, E-38205 La Laguna, Tenerife, Spain
[14] European Southern Observatory, Alonso de Cordova 3107, Casilla 19, Santiago 19001, Chile

Abstract

One of the most challenging open questions in Astrophysics is how Active Galactic Nuclei (AGNs) are fueled. For this to happen, gas has to be driven from the outskirts of the galaxy to the nuclear regions. Different mechanisms such as bars (large-scale and nuclear), lopsided disks, m=1, 2 instabilities or warps have been suggested to remove the gas angular momentum at different spatial scales of galaxy disks. On the other hand, stellar and AGN feedback in the form of outflows prevents galaxies from becoming overmassive. In this work we present the results of interferometric observations of the cold CO(2-1) molecular gas and 1.3 mm continuum obtained with NOEMA of five nearby (mean luminosity distance of 34 Mpc) Seyfert galaxies. The superb angular resolution of the NOEMA data (∼0.6"∼100 pc) enables us to study the CO(2-1) morphology and kinematics as well as to measure the molecular gas content of the nuclear regions. Although all galaxies in our sample show evidence of non-circular motions in their nuclear regions, these are detected more clearly in the interacting systems. Our goal is to find out if these motions are related to molecular gas flows.

Highlights on Spanish Astrophysics X, Proceedings of the XIII Scientific Meeting of the Spanish Astronomical Society held on July 16 – 20, 2018, in Salamanca, Spain. B. Montesinos, A. Asensio Ramos, F. Buitrago, R. Schödel, E. Villaver, S. Pérez-Hoyos, I. Ordóñez-Etxeberria (eds.), 2019

Deep Learning for morphological classification of galaxies.

Helena Domínguez Sánchez [1], Marc Huertas Company[2,3,4,5], and Mariangela Bernardi[1]

[1] Department of Physics and Astronomy, University of Pennsylvania, Philadelphia, PA 19104, USA
[2] LERMA, Observatoire de Paris, PSL Research University, CNRS, Sorbonne Universités, UPMC Univ. Paris 06, F-75014 Paris, France
[3] University of Paris Denis Diderot, University of Paris Sorbonne Cité (PSC), F-75205 Paris, Cedex 13, France
[4] Instituto de Astrofísica de Canarias, E-38200 La Laguna, Tenerife, Spain
[5] Departamento de Astrofísica, Universidad de La Laguna, E-38206 La Laguna, Tenerife, Spain

Abstract

Galaxies exhibit a wide variety of morphologies which are strongly related to their star formation histories. Having large samples of morphologically classified galaxies is fundamental to understand their formation and evolution. Morphological classification of galaxies based on visual inspection is extremely time consuming: an impossible task when dealing with the immense number of galaxy images (billions!) that future Big Data surveys such as LSST or EUCLID will release. Deep Learning algorithms (DL), which automatically extract high-level features at the pixel level, have been proven very successful in the last years for many different image recognition purposes. Here we show the excellent performance of DL algorithms to reproduce (or even improve) visual classification of galaxies for SDSS-DR7 images.The main results of this poster and the morphological catalogue with classifications for 670,000 SDSS-DR7 galaxies are presented in Domínguez Sánchez et al. (2018a). (See poster).

Highlights on Spanish Astrophysics X, Proceedings of the XIII Scientific Meeting of the Spanish Astronomical Society held on July 16 – 20, 2018, in Salamanca, Spain. B. Montesinos, A. Asensio Ramos, F. Buitrago, R. Schödel, E. Villaver, S. Pérez-Hoyos, I. Ordóñez-Etxeberria (eds.), 2019

Environmental dependence of the IMF-sensitive features in intermediate-mass quiescent galaxies.

Elham Eftekhari[1,2], Alexandre Vazdekis[1,2], Moein Mosleh[3,4], and Saeed Tavasoli[5]

[1] Institute de Astrofisica de Canarias, E-38200 La Laguna, Tenerife, Spain
[2] Departamento de Astrofisica, Universidad de La Laguna, E-38205 La Laguna, Tenerife, Spain
[3] Biruni Observatory, Shiraz University, Shiraz 7145, Iran
[4] Physics Department, Shiraz University, Shiraz 7145, Iran
[5] Department of Astronomy and High Energy Physics, Faculty of Physics, Kharazmi University, Mofateh Ave., Tehran, Iran

Abstract

In this work, we investigate the impact of large-scale environment on the IMF in quiescent galaxies. For this purpose, we compare the trend of IMF-sensitive spectral features with respect to galaxy mass in three samples of intermediate-mass galaxies that reside in low, intermediate and high-density environments. Using SDSS DR7 spectra stacked by velocity dispersion and redshift, in a purely observational approach, we find that the IMF of intermediate-mass galaxies does not significantly depend on the galactic environment. (See poster).

Highlights on Spanish Astrophysics X, Proceedings of the XIII Scientific Meeting of the Spanish Astronomical Society held on July 16 – 20, 2018, in Salamanca, Spain. B. Montesinos, A. Asensio Ramos, F. Buitrago, R. Schödel, E. Villaver, S. Pérez-Hoyos, I. Ordóñez-Etxeberria (eds.), 2019

The MUSE Atlas of Disks (MAD): Ionized gas properties in local galaxies.

Santiago Erroz-Ferrer[1], and the MUSE collaboration

[1] Department of Physics, ETH Zurich, CH-8093 Zurich, Switzerland

Abstract

We study the physical properties of the ionized gas in local disks using the sample of 38 nearby $\sim 10^{8.5-11.2}$M$_\odot$ Star-Forming Main Sequence (SFMS) galaxies observed so far as part of the MUSE Atlas of Disks (MAD). Specifically, we use all strong emission lines in the MUSE wavelength range 4650-9300 Å to investigate the resolved ionized gas properties on $\sim$100 pc scales. This spatial resolution enables us to disentangle HII regions from the Diffuse Ionized Gas (DIG) in the computation of gas metallicities and Star Formation Rates (SFRs) of star forming regions. The gas metallicities generally decrease with radius. The metallicity of the HII regions is on average $\sim$0.1 dex higher than that of the DIG, but the metallicity radial gradient in both components is similar. The mean metallicities within the inner galaxy cores correlate with the total stellar mass of the galaxies. On our $<$100 pc scales, we find two correlations previously reported at kpc scales: a spatially resolved Mass-Metallicity Relation (RMZR) and a spatially resolved SFMS (RSFMS). We find no secondary dependency of the resolved RMZR with the SFR density. We find that both resolved relations have a local origin, as they do not depend on the total stellar mass. (See poster).

Highlights on Spanish Astrophysics X, Proceedings of the XIII Scientific Meeting of the Spanish Astronomical Society held on July 16 – 20, 2018, in Salamanca, Spain. B. Montesinos, A. Asensio Ramos, F. Buitrago, R. Schödel, E. Villaver, S. Pérez-Hoyos, I. Ordóñez-Etxeberria (eds.), 2019

What do we find when nothing is found? A deep search for planetary nebulae at the outskirts of M33.

R. Galera-Rosillo[1,2], R.L.M. Corradi[3] and A. Mampaso[1]

[1] Instituto de Astrofísica de Canarias, Calle Vía Láctea, s/n, E-38205, La Laguna, Tenerife, Spain
[2] Departamento de Astrofísica, Universidad de La Laguna, E-38206, La Laguna, Tenerife, Spain
[3] GRANTECAN, Cuesta de San José s/n, E-38712 , Breña Baja, La Palma, Spain

Abstract

Planetary nebulae (PNe) are excellent tracers of stellar populations with low surface brightness, and therefore provide a powerful method to detect and explore the rich system of substructures discovered around the main spiral galaxies of the Local Group.
A search of PNe at the outskirts of the spiral galaxy M33 has been performed over a set of wide-field images in the [OIII]λ5007Å and Hα + [NII] nebular lines and continuum broadband filters (g', r'), within a completeness limit of 26 mag in the narrowband filters. The images from the INT telescope cover a 4.5 square degree area and reach a projected distance of 40 Kpc from the center of the galaxy towards M31.
An exhaustive study of the photometric data, combined with a visual search, shows the absence of bright PNe outside the limits of the disc of the galaxy on the sampled region. Inside the bright optical disc of M33, eight new PN candidates were identified, three of which were spectroscopically confirmed. Fourteen additional sources, showing [OIII] excess, were also discovered.
The results set an upper limit of $\sim 1.6 \cdot 10^7 L_\odot$ to the luminosity of the underlying population in the region covered by this survey, suggesting the lack of a massive classical halo. This is in agreement with the results obtained using the RGB population and it questions the claimed interaction between M31 and M33. (See poster).

Highlights on Spanish Astrophysics X, Proceedings of the XIII Scientific Meeting of the Spanish Astronomical Society held on July 16 – 20, 2018, in Salamanca, Spain. B. Montesinos, A. Asensio Ramos, F. Buitrago, R. Schödel, E. Villaver, S. Pérez-Hoyos, I. Ordóñez-Etxeberria (eds.), 2019

JWST-MIRI Integral Field Spectroscopy of high-z galaxies.

A. Labiano[1], J. Álvarez-Márquez[1], L. Colina[1], A. Alonso-Herrero[1], R. Azzolini[2], T. Böker[3], K. Caputi[4], A. Eckart[5], M. García-Marín[3], S. Kendrew[3], O. Le Fèvre[6], H.U. Norgaard- Nielsen[7], G. Ostlin[8], P. Pérez-González[9], J. Pye[10], P. Van der Werf[11], F. Walter[12], M. Ward[13], and G. Wright[14]

[1] Centro de Astrobiología (CSIC-INTA), Madrid, Spain
[2] Mullard Space Science Laboratory, Surrey, UK
[3] European Space Agency, c/o STScI, Baltimore, MD, USA
[4] Kapteyn Astronomical Institute, Groningen, The Netherlands
[5] 1st Institute of Physics, Cologne, Germany
[6] Laboratoire d'Astrophysique de Marseille, Marseille, France
[7] National Space Institute, Lyngby, Denmark
[8] Stockholm University, Stockholm, Sweden
[9] Universidad Complutense de Madrid, Madrid, Spain
[10] University of Leicester, Leicester, UK
[11] Leiden University, Leiden, The Netherlands
[12] Max Planck Institut für Astronomie, Heidelberg, Germany
[13] Durham University, Durham United Kingdom
[14] The UK Astronomy Technology Centre, Edinburgh, UK

Abstract

Due to its sensitivity and spectral coverage, the James Webb Space Telescope (JWST) Mid-Infrared Instrument (MIRI) is optimum to detect the H_α emission line on sources at redshifts beyond 6.7. The European MIRI Guaranteed Time Observations (GTO, PI: G. Wright) will dedicate 65 hours to observe three Ly_α emitters (LAEs) and two quasars in the Epoch of Reionization (EoR), plus two dusty star-forming galaxies (DSFG) at z$\sim$4-7. We present the realistic simulations we created in preparation for the MRS data expected for the High- z GTO program.

Highlights on Spanish Astrophysics X, Proceedings of the XIII Scientific Meeting of the Spanish Astronomical Society held on July 16 – 20, 2018, in Salamanca, Spain. B. Montesinos, A. Asensio Ramos, F. Buitrago, R. Schödel, E. Villaver, S. Pérez-Hoyos, I. Ordóñez-Etxeberria (eds.), 2019

2D Star Formation Rate Properties of Nearby Galaxies with J-PLUS DR1.

R. Logroño-García[1], G. Vilella-Rojo[1], C. López-Sanjuan[1], J. Varela[1], K. Viironen and the J-PLUS team

[1] Centro de Estudios de Física del Cosmos de Aragón (CEFCA)

Abstract

The Javalambre Photometric Local Universe Survey (J-PLUS; Cenarro et al. 2018), is observing thousands of square degrees of the northern sky from the Observatorio Astrofísico de Javalambre (OAJ) in Teruel, Spain. The survey is being carried out with the 0.83 meter JAST/T80 telescope and the panoramic camera T80Cam with a 2 deg^2 FoV. A set of twelve broad, intermediate, and narrow band optical filters is used. The large FoV, the position of the filters, and the survey strategy; are suitable to perform science that will expand our knowledge in many fields of astrophysics. More concretely, the $J0660$ narrow-band filter covers the Hα emission-line flux of nearby galaxies up to $z \leq 0.017$, making J-PLUS a powerful tool to study the 2D star formation rate (SFR) properties of these galaxies. (See poster).

Highlights on Spanish Astrophysics X, Proceedings of the XIII Scientific Meeting of the Spanish Astronomical Society held on July 16 – 20, 2018, in Salamanca, Spain. B. Montesinos, A. Asensio Ramos, F. Buitrago, R. Schödel, E. Villaver, S. Pérez-Hoyos, I. Ordóñez-Etxeberria (eds.), 2019

AGN demography with JWST broad-band imaging to the rescue.

Hugo Messias[1], Mark Lacy[2], and CAST team[3]

[1] Joint ALMA Observatory, Alonso de Córdova 3107, Vitacura , Santiago, Chile
[2] National Radio Astronomy Observatory, 520 Edgemont Road, Charlottesville, VA 22903
[3] CAST stands for *Chasing dusty-AGN up to redShift Two* and is a team comprised by ∼40 members who contributed to the current status of the project.

Abstract

With a 5 to 10 year life-span and being a 6 m-class telescope in space, the *James Webb Space Telescope* (*JWST*) will be a highly competitive relatively short-lived tool toward knowledge revolution, with considerable operation overheads. As a result, it is both of interest to the community and facility to conduct observations as efficiently as possible. This abstract highlights a colour criterion prposed by Messias et al. 2014 to select active galactic nuclei (AGN) from the local Universe as far back as the end of the epoch of reionization ($0 < z < 6$). Depending on the targetted Universe cosmic time, one is able to conduct a demographic study of dusty AGN with only up to four broad-band filters required (F200W, F440W, F770W, F1800W), three of which can be observed at the same time. This allows MIRI surveys wider than the ones by JADES and CEERS teams. The fine spatial resolution enabled by JWST will allow one to deblend host and AGN light, hence selecting less-luminous AGN, a phase where AGN pass most of their life-cycle. Such observations will also allow for the community to assess stellar assembly in galaxies or to identify very high-redshift sources.

Highlights on Spanish Astrophysics X, Proceedings of the XIII Scientific Meeting of the Spanish Astronomical Society held on July 16 – 20, 2018, in Salamanca, Spain. B. Montesinos, A. Asensio Ramos, F. Buitrago, R. Schödel, E. Villaver, S. Pérez-Hoyos, I. Ordóñez-Etxeberria (eds.), 2019

Role of dust in galactic chemical evolution.

Iker Millan-Irigoyen[1], Yago Ascasibar[2], and Mercedes Mollá[1]

[1] Centro de Investigaciones Energéticas Medioambientales y Tecnológicas(CIEMAT), Madrid, Spain
[2] Universidad Autónoma de Madrid, Madrid, Spain

Abstract

Abstract : Even though dust grains contribution to the mass of a galaxy is tiny, they play a huge role in its chemical evolution because they are the main mechanism of molecular hydrogen formation. Furthermore, dust grains shield the H2 that constitutes star formation regions. Thus, its very critical to include the evolution of the dust in the models of chemical evolution. Therefore, we have created a one zone model of galactic chemical evolution of the Milky Way that includes the life cycle of the dust grains. In this life cycle we have included the creation in the AGB phase of low mass stars and SNe, their destruction via SN shock waves and their growth via accretion in the ISM. We have found that our model reproduces the observed dust to gas ratio, it overestimates it by just 0.08 dex. However, the model underestimates the metallicity of the ISM. We have found out that this underestimation occurs due to the high depletion of the metals inside the dust grains, the dust to metals ratio is 1 since early ages in the galaxy. This work has been partially supported by MINECO-FEDER-grants AYA2013-47742-C4-4-P, AYA2016-79724-C4-1-P and AYA2016-79724-C4-3-P. YA is supported by contract RyC-2011-09461 of the *Ramón y Cajal* programme.

Highlights on Spanish Astrophysics X, Proceedings of the XIII Scientific Meeting of the Spanish Astronomical Society held on July 16 – 20, 2018, in Salamanca, Spain. B. Montesinos, A. Asensio Ramos, F. Buitrago, R. Schödel, E. Villaver, S. Pérez-Hoyos, I. Ordóñez-Etxeberria (eds.), 2019

2D-Chemical Evolution Models: The spiral wave over-density role.

M. Mollá[1], S. Wekesa[2], D. S. Wamalwa[3], O. Cavichia[4], B. K. Gibson[5] Á. I. Díaz[6], Y. Ascasibar[6], F. F. Rosales-Ortega[7], S. F. Sánchez[8].

[1] CIEMAT, Avda. Complutense 40, 28040-Madrid, Spain
[2] University of Nairobi, Nairobi, Kenya
[3] Meru University of Science and Technology, Meru, Kenya
[4] Universidad de Itajubà, Itajubà, Brasil
[5] University of Hull, Hull, United Kingdom
[6] Universidad Autónoma de Madrid, Madrid, Spain
[7] INAOE, Puebla, México
[8] Universidad Nacional Autónoma de México, México

Abstract

Chemical evolution models are a powerful tool to interpret and explain the possible scenarios of galaxies formation and evolution. They infer how the chemical elements, formed inside the stars, are redistributed into the interstellar medium. Until recently, due to the lack of 2D information, these models assumed azimuthally symmetric abundances distributions, and the important issue of the possible dispersion of abundance values at a given galactocentric distance was not addressed. A spiral disk, however, requires a full 2D description so that arms, bars and other structures, as those produced by mergers or interactions, may be also included. Our objective is to develop the most comprehensive and sophisticated 2D chemical evolution models for spiral and irregular galaxies, constrained by observed abundance distributions using the state of the art IFS data of nearby galaxies, which have improved extraordinarily the spatial resolution. In the present preliminary work we start by including the spiral wave as a first step. The spiral wave produce an over-density in comparison with the average mass density on the disk (with its radial exponential decrease).We have modified our classical chemical evolution model in 1D and performed a first 2D-model applied to a Milky Way like galaxy. We analyze the resulting elemental abundances and star formation rate (SFR) 2D-distributions. (See poster).

Highlights on Spanish Astrophysics X, Proceedings of the XIII Scientific Meeting of the Spanish Astronomical Society held on July 16 – 20, 2018, in Salamanca, Spain. B. Montesinos, A. Asensio Ramos, F. Buitrago, R. Schödel, E. Villaver, S. Pérez-Hoyos, I. Ordóñez-Etxeberria (eds.), 2019

Dust-to-gas ratio in a complete sample of type-1 AGN.

I. Ordovás-Pascual[1], S. Mateos[1], F. J. Carrera[1], A. Caccianiga[2], R. Della Ceca[2], P. Severgnini[2], A. Moretti[2], L. Ballo[3] and A. Corral[1]

[1] Instituto de Física de Cantabria (CSIC-UC), E-39005, Santander, Spain
[2] INAF-Osservatorio Astronomico di Brera, Via Brera 28, I-20121, Milan, Italy
[3] XMM-Newton Science Operations Centre, ESAC/ESA, PO Box 78, E-28692 Villanueva de la Cañada, Madrid, Spain

Abstract

According to the Unified Model of Active Galactic Nuclei (AGN), unobscured AGN based on its optical spectrum (detection of rest-frame UV-optical broad emission lines, type-1 AGN) should appear as X-ray unabsorbed AGN. However, there is an important fraction (10-30%) of AGN whose optical and X-ray classifications do not match, and the origin of the discrepancy is not clear. To provide insight into this topic, we have conducted a statistical analysis of the optical obscuration and X-ray absorption properties of the optically type-1 AGN from the Bright Ultra-hard XMM-Newton Survey (BUXS) with $L_{2-10keV} > 10^{42}$ erg s^{-1} and z=0.05-1. We have high-quality spectra from XMM-Newton and either SDSS spectra or proprietary observations for the selected sample. In order to provide the most complete sample as possible, we have conducted a detailed analysis of the emission lines to provide a reliable classification of the AGNs. We derive the X-ray absorption by fitting their XMM-Newton spectra and the optical extinction using UV/optical spectral continuum fits. As BUXS is a flux limited X-ray selected sample at hard energies ($f_{4.510keV} \leq 6\times10^{-14}$ erg s^{-1} cm^{-2}), it is complete for N_H column densities up to the Compton-thick limit ($\sim10^{24}$ cm^{-2}). Our preliminary results show that most type-1 AGN in our sample show consistent optical and X-ray classification, but there is a large fraction (20%) of objects with large N_H column densities ($N_H > 4\times1021$ cm^{-2}). (See poster).

Highlights on Spanish Astrophysics X, Proceedings of the XIII Scientific Meeting of the Spanish Astronomical Society held on July 16 – 20, 2018, in Salamanca, Spain. B. Montesinos, A. Asensio Ramos, F. Buitrago, R. Schödel, E. Villaver, S. Pérez-Hoyos, I. Ordóñez-Etxeberria (eds.), 2019

Can we use the dust luminosity of galaxies to estimate their star formation rate?

Ciro Pappalardo[1], Maarten Baes[2], Sebastien Viaene[2,3], George J. Bendo[4], Simone Bianchi[5], Jacopo Fritz[6], and Mederic Boquien[7]

[1] Instituto de Astrofísica e Ciencias do Espaço, Universidade de Lisboa, OAL, Tapada da Ajuda, 1349-018 Lisboa, Portugal
[2] Sterrenkundig Observatorium, Universiteit Gent, Krijgslaan 281 S9, B-9000 Gent, Belgium
[3] Centre for Astrophysics Research, University of Hertfordshire, College Lane, Hatfield, AL10 9AB, UK
[4] UK ALMA Regional Centre Node, Jodrell Bank Centre for Astrophysics, School of Physics and Astronomy, The University of Manchester, Oxford Road, Manchester M13 9PL, United Kingdom [5] Osservatorio Astrofisico di Arcetri - Largo E. Fermi 5, I-50125, Florence, Italy
[6] Instituto de Radioastronomía y Astrofísica, IRyA, UNAM, Campus Morelia, A.P. 3-72, C.P. 58089, Mexico
[7] Centro de Astronomía (CITEVA), Universidad de Antofagasta, Avenida Angamos 601, Antofagasta, Chile

Abstract

The huge growth of data available for the scientific community in the last decade allowed, for the first time in astronomy, a truly panchromatic approach. These data shed light on fundamental correlations, linking the dust component of a galaxy with its star formation rate (SFR). However, the relation between the SFR and dust emission is complex, and still it is not clear what mechanism drives it, motivating a further investigation. This poster will re-examine these correlations considering the intrinsic properties of the galaxies dust, and relating them to the SFR. We selected a sample of ~800 normal star forming galaxies with photometric data between $0.15 < \lambda < 500$ μm, and analyzed them with different spectral energy distribution fitting methods.

The dust luminosities and the SFR show a strong correlation, but for low values of both parameters, the scatter in the correlation increases. We show that introducing a selection based on the fraction of ultraviolet emission absorbed by dust, we can reduce drastically the data scatter. Galaxies with similar absorption coefficients, despite a different SFR, have a similar balance between the fraction of dust heated by the star formation and the interstellar radiation field (IRF). Dust masses and SFR also show a correlation, but weaker with respect to the dust luminosities. Our results indicate that this scatter is due to a different intensity of the IRF produced by stars during late evolutionary stages, and this shifts the galaxies position in the dust mass-SFR plane. The differences in the intensity of the IRF is the origin of the observed scatter, and the correlation becomes stronger once selected galaxies following an IRF based selection criteria.

In the SFR versus stellar mass (M_*) plane these galaxies occupy a region included between local spirals and higher redshift star forming galaxies. These galaxies represent the population that at $z < 0.5$ quenches their star formation activity and reduces their contribution to the cosmic Star formation rate density. The galaxies subsample with the higher masses ($M_* > 3{\times}10^{10}$ $M_\odot$) does not lie on the main sequence, but shows a small offset, as a consequence of the decreased star formation. Low mass galaxies ($M_* < 1{\times}10^{10}$ $M_\odot$) settle in the main sequence with SFR and M_* consistent with local spirals. The multi-wavelength approach allows the identification of a mixed galaxy population, with galaxies still in an assembly phase, or galaxies at the beginning of their passive evolution. We show that if we include in the analysis the internal properties of the dust, the scatter between SFR and dust mass and/or luminosities can be removed. (See poster).

Highlights on Spanish Astrophysics X, Proceedings of the XIII Scientific Meeting of the Spanish Astronomical Society held on July 16 – 20, 2018, in Salamanca, Spain. B. Montesinos, A. Asensio Ramos, F. Buitrago, R. Schödel, E. Villaver, S. Pérez-Hoyos, I. Ordóñez-Etxeberria (eds.), 2019

The Portuguese Alma Center of Expertise: ALMA research in Portugal after 3 years.

Ciro Pappalardo[1], José Afonso[1], Israel Matute[1], Stergios Amarantidis[1], and Sandra Homem[1]

[1] Instituto de Astrofísica e Ciencias do Espaço, Universidade de Lisboa, OAL, Tapada da Ajuda, 1349-018 Lisboa, Portugal

Abstract

In the past years, the Institute of Astronomy and Space Sciences of Lisbon has seen its capabilities for ALMA research internationally recognized, being named by ESO as an ALMA Centre of Expertise. This is a result of an objective effort over the last few years to increase the national capability in the exploration of this revolutionary observatory. The Portuguese ALMA Centre of Expertise (PACE) provided along these years face-to-face support to the Portuguese community regarding all stages of ALMA observations: pre-Cycle ALMA promotion, proposal preparation and submission, data reduction and archival research. PACE is also already actively supporting the ALMA project by participating in the task of ALMA data validation and quality assurance. The Atacama Large (sub-)Millimetre Array consortium is composed by three partners (Europe, North-America, and East-Asia) and the host country (Chile). Each of the partners has an ALMA Regional Centre (ARC), which works as a means of closer contact between the local community and the facility. The European ARC is organized distinctively, where "nodes" and "Centres of Expertise" have been created in specific research centres in Europe in addition to the central ARC node, at ESO.

PACE will continue the task of organizing the ALMA National Community Days in preparation for upcoming ALMA Calls for Proposals and international meetings to promote ALMA and increase its use by the scientific community. As a support facility, it welcomes visitors at the Astronomical Observatory of Lisbon, where it is located, and where the community will find dedicated personnel and computer hardware. PACE plans to develop unique expertise among the EU ARC network, thus further improving the ALMA user support capability in Europe. (See poster).

Highlights on Spanish Astrophysics X, Proceedings of the XIII Scientific Meeting of the Spanish Astronomical Society held on July 16 – 20, 2018, in Salamanca, Spain. B. Montesinos, A. Asensio Ramos, F. Buitrago, R. Schödel, E. Villaver, S. Pérez-Hoyos, I. Ordóñez-Etxeberria (eds.), 2019

MEGARA Data Reduction Pipeline.

Sergio Pascual[1], Nicolás Cardiel[1], Armando Gil de Paz[1], Esperanza Carasco[2], Jesús Gallego[1], Jorge Iglesias-Páramo[3], and Raquel Cedazo[4]

[1] Universidad Complutense de Madrid, Spain
[2] Instituto Nacional de Astrofísica, Óptica y Electrónica, Mexico
[3] Instituto Astrofísica de Andalucía, Spain
[4] Universidad Politécnica de Madrid, Spain

Abstract

The data reduction software for MEGARA, **megaradrp**, is an open source (GPLv3) Python package.

- Devel: `https://github.com/guaix-ucm/megaradrp`
- Issues: `https://github.com/guaix-ucm/megaradrp/issues`
- Docs: `https://megara-drp.readthedocs.io/`
- PyPI: `https://pypi.org/project/megaradrp/`

The **megaradrp** package can be used both as a standalone program or as a component of the GTC control system. The same pipeline processes MEGARA images during the observation and offline, although using different reduction strategies.
megaradrp provides two methods for extraction:

- **TraceMap** is fast, well suited for online extraction at the telescope. The peak of the spectra are detected in halogen lamp images and then a fixed extraction window is applied to images with the same instrumental configuration. The window is half the distance between peaks.
- **ModelMap** is slow, as it models the PSF as a bivariate Gaussian along the spectral and spatial direction of halogen map images. At different positions along the dispersion axis, the algorithm fits iteratively the 600 peaks. Then, a spline is fitted to the parameters to recover the model for all the original image.

SP acknowledges financial support from the Spanish Ministry of Economy and Competitiveness (MINECO) under grant number AYA2016-75808-R, which is partly funded by the European Regional Development Fund (ERDF). (See poster).

Highlights on Spanish Astrophysics X, Proceedings of the XIII Scientific Meeting of the Spanish Astronomical Society held on July 16 – 20, 2018, in Salamanca, Spain. B. Montesinos, A. Asensio Ramos, F. Buitrago, R. Schödel, E. Villaver, S. Pérez-Hoyos, I. Ordóñez-Etxeberria (eds.), 2019

O VI in the CGM: Dependence on z and galaxy mass.

Roca-Fabrega, S.[1], and Dekel, A.[2]

[1] Departamento de Fisica de la Tierra y Astrofisica, Universidad Complutense de Madrid
[2] Racah Institute of Physics, The Hebrew University of Jerusalem

Abstract

We study the components of cool and warm/hot gas in the circumgalactic medium (CGM) of simulated galaxies and address the relative production of OVI by photoionization versus collisional ionization, as a function of halo mass, redshift, and distance from the galaxy halo center. We find that collisional ionization by thermal electrons dominates at high redshift, while photoionization of cool or warm gas by the metagalactic radiation takes over near z=2. In massive halos collisions become important again at low redshift while photoionization remains dominant for less massive halos down to z=0.

Highlights on Spanish Astrophysics X, Proceedings of the XIII Scientific Meeting of the Spanish Astronomical Society held on July 16 – 20, 2018, in Salamanca, Spain. B. Montesinos, A. Asensio Ramos, F. Buitrago, R. Schödel, E. Villaver, S. Pérez-Hoyos, I. Ordóñez-Etxeberria (eds.), 2019

Inner and outer HII regions over the discs of spiral galaxies. Physical properties and evolutionary stages.

M. Rodríguez-Baras[1], A. I. Díaz[1], F.F. Rosales-Ortega[2], and S.F. Sánchez[3]

[1] Departamento de Física Teórica, Universidad Autónoma de Madrid, 28049 Madrid, Spain.
[2] Instituto Nacional de Astrofísica, Óptica y Electrónica, Luis E. Erro 1, 72840 Tonantzintla, Puebla, México.
[3] Instituto de Astronomía, Universidad Nacional Autónoma de México, A.P. 70-264, 04510 México D.F., México.

Abstract

The knowledge of abundance distributions is central to understanding the formation and evolution of galaxies. So far most of the relations employed for the derivation of gas abundances have been derived from observations of intermediate disk HII regions and are assumed to be valid for all the ionized regions, despite the known differences betwen inner and outer regions. The objective of this work is exploring the existence of intrinsic differences in the star formation processes of inner and outer HII regions and their influence in derived properties of the regions, such as elemental abundances, ionization structure, evolutionary state, etc. Using integral field spectroscopy observations from the CALIFA survey and photoionization models, we perform a systematic study and comparison of two inner and outer HII regions samples, obtaining information about their physical properties and evolutionary stages. (See poster).

Highlights on Spanish Astrophysics X, Proceedings of the XIII Scientific Meeting of the Spanish Astronomical Society held on July 16 – 20, 2018, in Salamanca, Spain. B. Montesinos, A. Asensio Ramos, F. Buitrago, R. Schödel, E. Villaver, S. Pérez-Hoyos, I. Ordóñez-Etxeberria (eds.), 2019

Exploring Galaxy Clustering with the Dark Energy Survey Dataset.

Martin Rodriguez-Monroy[1], Jack Elvin-Poole[2], Ignacio Sevilla-Noarbe[1], Eusebio Sanchez[1], Aurelio Carnero[1], and Juan De Vicente[1], on behalf of the DES Collaboration.

[1] Centro de Investigaciones Energeneticas Medioambientales y Tecnologicas (CIEMAT), Madrid, Spain
[2] Jodrell Bank Center for Astrophysics, School of Physics and Astronomy, University of Manchester, Manchester, UK

Abstract

The Dark Energy Survey is an international collaboration whose main goal is to understand the nature of the dark energy. To achieve this, it is performing a 5-year photometric survey from Cerro Tololo (Chile), covering around 5000 square degrees of the southern sky up to magnitude i =23.7 or redshifts of about 1.2. One of the main cosmological probes used by DES is the angular galaxy clustering in photometric redshift shells.

When studying galaxy clustering, the impact of systematics and observing conditions must be taken into account, since they can introduce an artificial clustering. In order to mitigate the influence of these conditions, Survey Property maps (SPs) are created, allowing to characterize their magnitude. The aim of this contribution is to showcase how the influence of these SPs on the clustering is identified and to explain the procedure that is followed to reduce their impact. (See poster).

Highlights on Spanish Astrophysics X, Proceedings of the XIII Scientific Meeting of the Spanish Astronomical Society held on July 16 – 20, 2018, in Salamanca, Spain. B. Montesinos, A. Asensio Ramos, F. Buitrago, R. Schödel, E. Villaver, S. Pérez-Hoyos, I. Ordóñez-Etxeberria (eds.), 2019

Overview of the study of radio-AGN in the local Universe with LOFAR. The most massive galaxies are always switched on.

J. Sabater[1], P. N. Best[1], and the LOFAR collaboration

[1] SUPA, Institute for Astronomy, Royal Observatory, Blackford Hill, Edinburgh, EH9 3HJ, UK

Abstract

The LOFAR Two-metre Sky Survey (LoTSS) is an ongoing radio-continuum survey of the northern sky at 150 MHz. With a resolution of 6 arcseconds and a median sensitivity of 71 microJy per beam it provides a source density that is about 10 times higher than the most sensitive existing very wide-area radio-continuum surveys. The first public data release covering 20% of the final area is soon to be published (early 2019) in an special issue of Astronomy & Astrophysics.
We studied the radio-AGN sources of the Sloan Digital Sky Survey (SDSS) 7th Data Release covered by LoTSS. A method to separate radio-AGN is presented. Its robustnest was checked by producing and comparing the luminosity functions with previous studies. The prevalence of radio-AGN activity is confirmed to show a strong dependence on stellar mass and black hole masses. At the higher stellar masses ($> 10^{11}\mathrm{M}_{\odot}$) the rate of radio-AGN activity reaches a 100 %; thus, the most massive galaxies are always switched on at some level. The full Eddington-scaled accretion rate distribution (a proxy for the duty cycle) was probed for massive galaxies finding that more than 50 per cent of the energy is released during the ≤ 2 per cent of the time spent at the highest accretion rates, $L_{\mathrm{mech}}/L_{\mathrm{Edd}} > 10^{-2.5}$. These results will be also published in the special issue of Astronomy & Astrophysics.
Additional updated information can be found in `https://www.jsabater.info/sea2018/`

Highlights on Spanish Astrophysics X, Proceedings of the XIII Scientific Meeting of the Spanish Astronomical Society held on July 16 – 20, 2018, in Salamanca, Spain. B. Montesinos, A. Asensio Ramos, F. Buitrago, R. Schödel, E. Villaver, S. Pérez-Hoyos, I. Ordóñez-Etxeberria (eds.), 2019

The host galaxies of luminous type 2 AGN at z 0.3-0.4.

Juan José Urbano-Mayorgas[1], Montserrat Villar-Martín[1], and Fernando Buitrago[2]

[1] Centro de Astrobiología (CSIC-INTA), Carretera de Ajalvir, km 4, 28850 Torrejón de Ardoz, Madrid, Spain
[2] Instituto de Astrofísica e Ciências do Espaço, Universidade do Lisboa, Tapada da Ajuda - Edificio Leste 2 Piso, 1349-018, Lisboa, Portugal

Abstract

We study the morphological and structural properties of the host galaxies associated with 57 optically-selected luminous type 2 AGN at z ∼0.3-0.4: 16 high-luminosity Seyfert 2 (HLSy2, 8.0≤log($L_{[\mathrm{OIII}]}/L_\odot$) <8.3) and 41 obscured quasars (QSO2, log($L_{[\mathrm{OIII}]}/L_\odot$) ≥8.3). With this work, the total number of QSO2 at $z < 1$ with parametrized galaxies increases from ∼35 to 76. Our analysis is based on HST WFPC2 and ACS images that we fit with GALFIT. HLSy2 and QSO2 show a wide diversity of galaxy hosts. The main difference lies in the higher incidence of highly-disturbed systems among QSO2. This is consistent with a scenario in which galaxy interactions are the dominant mechanism triggering nuclear activity at the highest AGN power. There is a strong dependence of galaxy properties with AGN power (assuming $L_{[\mathrm{OIII}]}$ is an adequate proxy). The relative contribution of the spheroidal component to the total galaxy light (B/T) increases with $L_{[\mathrm{OIII}]}$. While systems dominated by the spheoridal component spread across the total range of $L_{[\mathrm{OIII}]}$, most disk-dominated galaxies concentrate at log($L_{[\mathrm{OIII}]}/L_\odot$) <8.6. This is expected if more powerful AGN are powered by more massive black holes which are hosted by more massive bulges or spheroids. The average galaxy sizes ($\langle r_\mathrm{e} \rangle$) are 5.0±1.5 kpc for HLSy2 and 3.9±0.6 kpc for HLSy2 and QSO2 respectively. These are significantly smaller than those found for QSO1 and narrow line radio galaxies at similar z. We put the results of our work in context of related studies of AGN with quasar-like luminosities. (See poster).

Highlights on Spanish Astrophysics X, Proceedings of the XIII Scientific Meeting of the Spanish Astronomical Society held on July 16 – 20, 2018, in Salamanca, Spain. B. Montesinos, A. Asensio Ramos, F. Buitrago, R. Schödel, E. Villaver, S. Pérez-Hoyos, I. Ordóñez-Etxeberria (eds.), 2019

High-resolution imaging of the multiphase AGN-driven outflow of NGC1068.

Héctor Vives-Arias[1,2], Santiago García-Burillo[3], and Cristina Ramos Almeida[1,2]

[1] Instituto de Astrofísica de Canarias, Vía Láctea, s/n, E-38205 La Laguna, Tenerife, Spain
[2] Departmento de Astrofísica, Universidad de La Laguna, E-38205, La Laguna, Tenerife, Spain
[3] Observatorio de Madrid, OAN-IGN, Alfonso XII, 3, E-28014, Madrid, Spain

Abstract

We analyze Atacama Large Millimeter Array (ALMA) observations of the CO(6–5) molecular line and the 432 μm continuum emission from the circumnuclear disk (CND) and the putative torus of the Seyfert 2 galaxy NGC 1068. The kinematics of both the CND and the torus show non-circular motions that are caused by outflows from the AGN. We compare the ALMA data with high-resolution near-infrared integral field spectroscopy of the molecular H_2 1–0S(1) line and some ionized species obtained with the VLT, and investigate the multiphase nature of the different ISM components of this prototypical AGN-driven outflow. (See poster).

Highlights on Spanish Astrophysics X, Proceedings of the XIII Scientific Meeting of the Spanish Astronomical Society held on July 16 – 20, 2018, in Salamanca, Spain. B. Montesinos, A. Asensio Ramos, F. Buitrago, R. Schödel, E. Villaver, S. Pérez-Hoyos, I. Ordóñez-Etxeberria (eds.), 2019

Fullerene and graphene molecular nanostructures in evolved stars.

D. A. García-Hernández[1,2]

[1] Instituto de Astrofísica de Canarias, C/ Via Láctea s/n, 38205 La Laguna, Spain
[2] Departamento de Astrofísica, Universidad de La Laguna, 38206 La Laguna, Spain

Abstract

The detections of fullerenes and (possibly) planar C_{24} (a small fragment of a graphene sheet) in the H-rich circumstellar environments of evolved stars show that formation of these complex species does not require an H-poor environment contrary to general expectation. This together with the very recent identification of the fullerene cation ${C_{60}}^+$ as a diffuse interstellar band (DIB) carrier (the only DIB carrier known to date) reinforce the idea that these molecular nanostructures are ubiquitous in space. The understanding of the formation route of these complex organic species requires an interdisciplinary research, crossing the boundaries between astronomers, chemists, and physicists, with potential applications in nanotechnology and industry. Here, I review the main results of the interdisciplinary approach carried out at the Instituto de Astrofísica de Canarias (IAC) in order to learn about complex molecular nanostructures in evolved stars. Finally, I underline the main open questions and future directions like the expected observations on these complex organics in evolved stars from future facilities such as the James Webb Space Telescope.

1 Fullerenes in space: a brief history

Fullerenes such as C_{60} and C_{70} are very stable molecules very important for interstellar and circumstellar chemistry because they may explain many astrophysical phenomena like the diffuse interstellar bands (DIBs) or the ultraviolet bump. Fullerenes were discovered in the laboratory by [31] and they are also found on Earth and meteorites. The fullerene cation ${C_{60}}^+$ was also tentatively detected in the interstellar medium in the nineties ([15]) and this has been recently confirmed ([2], [3]). At laboratory, fullerenes are efficiently produced under H-poor conditions ([31], [11]) and fullerenes were expected to be detected in the extremely H-poor and so-called R Cor Bor (RCB) stars (e.g., [28]).

All previous searches of fullerenes in space have not detected them. This included searches in RCB stars ([10], [34]), post-AGB stars ([33]), and reflection nebulae ([36], [40]).

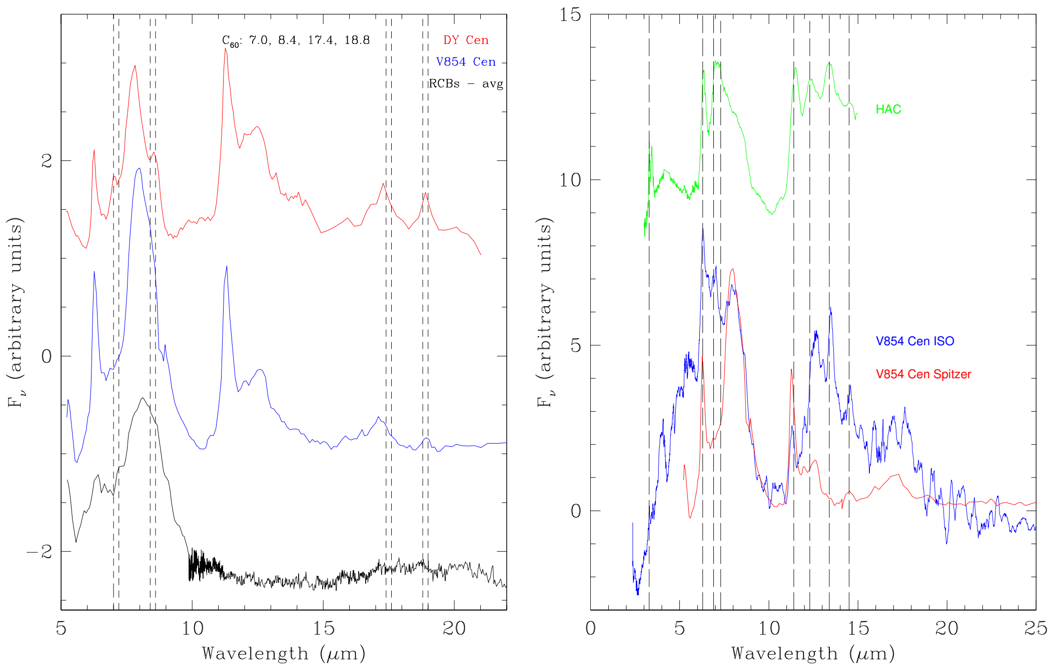

Figure 1: Left panel: *Spitzer/IRS* residual spectra in the wavelength range ∼5−20 μm of the RCB stars DY Cen (in red) and V854 Cen (in blue). The average residual spectrum of nine extremely H-deficient RCBs with little reddening (in black) is also shown. The expected temperature-dependent positions of the neutral C_{60} features are marked with black dashed vertical lines. Right panel: Residual *ISO* 1996 September 9 (in blue) and *Spitzer/IRS* 2007 September 7 (in red) spectra in the wavelength range ∼2-25 μm for the RCB star V854 Cen. A blackbody of ∼1000 K was subtracted from both spectra. The *ISO* spectrum (R∼1000) has been smoothed with a 13 box car in order to be compared with the *Spitzer* spectrum. The laboratory emission spectrum of HAC at 773 K (in green; [39]) is shown for comparison. The main laboratory HAC emission features ([39]) are marked with black dashed vertical lines (both figures adapted from [17]).

I started to be interested in fullerenes in space about ten years ago when I was doing a postdoc with Prof. David Lambert in Austin. He observed the three brightest RCB stars with the *"Infrared Space Observatory"* (*ISO*) ([34]) and I had experience with *Spitzer*, so we submitted a *Spitzer* proposal to get mid-IR spectra for a complete sample of 30 RCBs. One of the goals was to look for fullerenes in these fascinating stars. Once I was back to the Instituto de Astrofísica de Canarias (IAC) and after data reduction, we looked for C_{60} in the full sample of RCBs and we got the unexpected result that C_{60}-like features were detected only in the two least H-deficient stars ([17]). This is shown in Fig. 1 (left panel) where we compare the average RCB spectrum with those of the two C_{60}-detected stars. Interestingly, for one of these stars, the infrared spectrum dramatically changed in a timescale of about ten years (Fig.1, right panel). The spectrum evolved from hydrogenated amorphous carbon (HAC)-like (with *ISO*) to policyclic aromatic hydrocarbons (PAH)- and C_{60}-like features with *Spitzer*.

Due to the unexpected result in RCB stars, we then looked for fullerenes in about 240 Planetary Nebulae (PNe) and we got 5 clear fullerene detections. Meanwhile, [1] reported the first IR detection of C_{60} and C_{70} in the young PN Tc 1. In [16], we show that all PNe with fullerenes (including Tc 1) are low-mass C-rich sources with normal hydrogen abundances. The *Spitzer* spectra of some of these PNe dispaly both the C_{60} and C_{70} features and some of them also display PAH-like features in their spectra (see e.g., [18], [20]).

Thus, we now know that fullerenes can be detected together with PAHs and that they are efficiently formed in H-rich circumstellar envelopes only. Fullerenes are detected in PNe with normal H abundances ([16]). This is confirmed by the independent detection of C_{60} in only those RCB stars with some H ([17]) and mentioned above. Fullerene PNe display broad dust features at $\sim$9$-$13 and 25$-$35 μm, suggesting that both fullerenes and PAHs probably evolve from the photochemical processing of mixed aromatic/aliphatic nanoparticles similar to that of HAC-like dust ([16]), as suggested by some laboratory experiments ([39]). Fullerenes have also been detected in a proto-PN ([43]), reflection nebulae ([41]), and young stellar objects ([38]), and none of these space environments is H-poor.

Fullerenes have been detected in PNe of the Magellanic Clouds (MCPNe) and the first extragalactic detection of C_{70} was reported ([18]). The combination of the *Spitzer* information with laboratory data ([29]) permitted the determination of accurate abundances of C_{60} and C_{70}. The great variety of molecular species (HACs/PAHs clusters, fullerenes, etc.) observed in MCPNe seems to support the HACs scenario, where fullerenes may evolve from the UV-induced HACs decomposition ([20], [35]).

2 Fullerenes vs. metallicity and other C molecular nanostructures

Interestingly, the detection rate of fullerenes in C-rich PNe increases with decreasing metallicity, 5% of fullerene PNe are found in our Milky way, while it is 20% in the Large Magenallic Cloud and 44% in the Small Magellanic Cloud ([20]). This suggests a more limited dust processing (or the general presence of small dust grains) at low metallicity. Indeed, [37] have

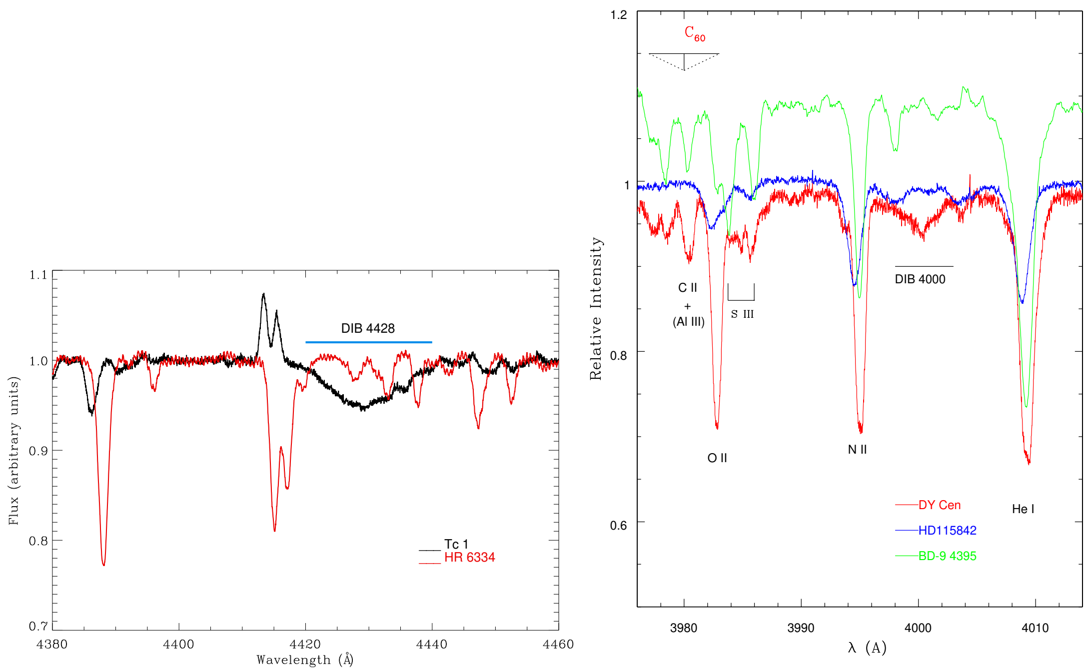

Figure 2: Left panel: Spectra of Tc 1 (in black) and HR 6334 (in red) around the 4428 Å DIB. This DIB is found to be unusually strong in Tc 1 while HR 6334 - with a higher E(B-V) of 0.42 - does not show evidence of its presence (adapted from [12]). Right panel: The spectra of DY Cen (in red) and HD 115842 (in blue) around and 4000 Å where the eHe star BD $-9°$ 4395 is also displayed (in green). The expected position and FWHM of the C_{60} feature at 3980 Å are marked on top of the spectra; there is no evidence (additional absorption) in DY Cen for the presence of this neutral C_{60} feature. However, there is an additional absorption band at 4000 Å in DY Cen, which is not present in HD 115842 neither in BD $-9°$ 4395 (adapted from [19]).

shown that all Galactic fullerene PNe are subsolar metallicity low-mass PNe, which demonstrate that low-metallicity environments favours fullerene production and detection. Also, it is curious that the still unidentified 21 μm feature is more common in the MCs than in the Galaxy ([42]) and the carrier could be related with the formation of fullerenes.

[42] reported an anti-correlation between the 30 μm feature and the unidentified infrared (UIR) features for the Magellanic Cloud 21 μm sources. Such an anti-correlation could result from radiation-induced decomposition of HAC-like grains into PAHs and fullerenes. Note that in the HACs scenario, the 21μm feature is also related with the formation of fullerenes and its carrier may be a fragile intermediate product from the decomposition of HACs or a similar material.

Unusual emission features at $\sim$6.6, 9.8, and 20 μm have been also detected in PNe ([18]). These features are coincident with the theoretical transitions of the planar C_{24} molecule (just a piece of graphene; [32]). However, a confirmation has to wait for laboratory spectroscopy, which is extremely difficult because of the high reactivity of C_{24}. The most interesting point here is that the possible detection of graphene precursors (C_{24}) opens the possibility of detecting other carbon molecular nanostructures such as nanotubes in space.

Sadjadi et al. (in preparation) have recently carried out density functional theory (DFT)-based couple-cluster calculations of the four C_{24} isomers (graphene, fullerene, ring, and bowl). They find the fullerene and graphene forms to be more stable but their simulated spectra show that only planar C_{24} displays features close to the astronomical bands. So, this new work also reinforces the idea of planar C_{24} being the most likely carrier of these IR features seen in space.

3 DIBs and fulleranes in fullerene environments

We have also done the first studies of DIBs in fullerene sources like PNe and RCB stars ([19], [21], [12]). The strongest electronic transitions of C_{60} are not detected in the optical and the DIBs are different for both types of stars (see Fig. 2). In particular, the 4428 Å DIB, shown in Fig.2 (left panel) for Tc 1, is found to be unusually strong in fullerene PNe, while a new DIB at 4000 Å was detected in the RCB star DY Cen (Fig. 2, right panel).

Regarding fulleranes (or hydrogenated fullerenes), the lab spectra of highly hydrogenated fullerenes like $C_{60}H_{18}$ and $C_{70}H_{38}$ show that the most intense transitions are found in the 3−4 μm range. We looked for these species in two fullerene PNe but no features were found ([13]), likely indicating that if present in these objects, then they are by far less abundant than C_{60} and C_{70}. However, [44] have reported a tentative detection of hydrogenated fullerenes in a proto-PN, that would be consistent with $C_{60}H_{18}$ and $C_{60}H_{36}$. Both works suggest that hydrogenated fullerenes may be formed in the post-AGB phase but they are quickly destroyed by the ultraviolet radiation from the central star.

More recently, [45] have done DFT simulations of 5 isomers for a full set of hydrogenated fullerenes with very different hydrogen content (see Fig. 3). Interestingly, they find that hydrogenated fullerenes with very low H-content do not display IR features at 3−4 μm but still contribute to longer wavelengths. Thus, we cannot discard the presence of hydrogenated fullerenes with low H-content in space and they indeed could contribute to the 17.4 and 18.9 μm features seen in fullerene sources.

4 Fullerenes with GranTeCan

For the study of fullerenes, we have also used the mid-IR instrument Canaricam at the Spanish ten meter telescope GranteCan on the island of La Palma. In particular, we got mid-IR images (in the N and Q bands, covering several spectral features and their adjacent continua) of the brightest fullerene PN IC 418 ([14]).

The mid-IR images covered the dust continuum at 9.8 microns, the broad ∼9−13 μm feature, the C_{60} feature at 17.4 μm, and the dust continuum around 20 μm. The emission

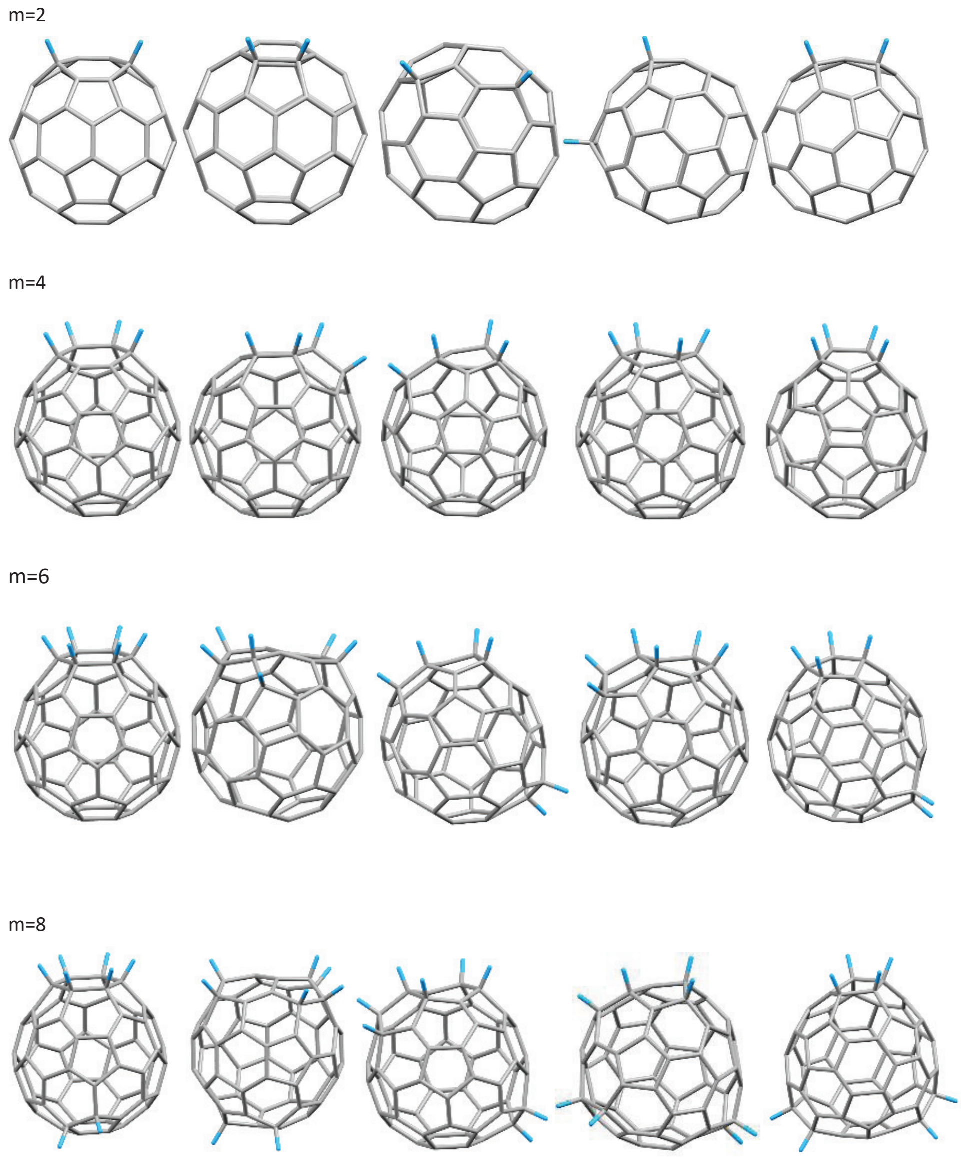

Figure 3: Local minimum geometries of $C_{60}H_m$ ($m = 2, 4, 6, 8$) isomers from model calculations. A total of 55 structures, 5 isomers for each of $C_{60}H_m$, $m = 2, 4, 6, 8, 10, 12, 14, 16, 18, 20, 36$, were included in [45]. The numbers of the isomers are assigned as 1 to 5 from left to right. The carbon cage is shown in grey and the C−H bonds are shown in blue. We can clearly see the geometric distortion of the C_{60} cage when hydrogen atoms are attached (adapted from [45]).

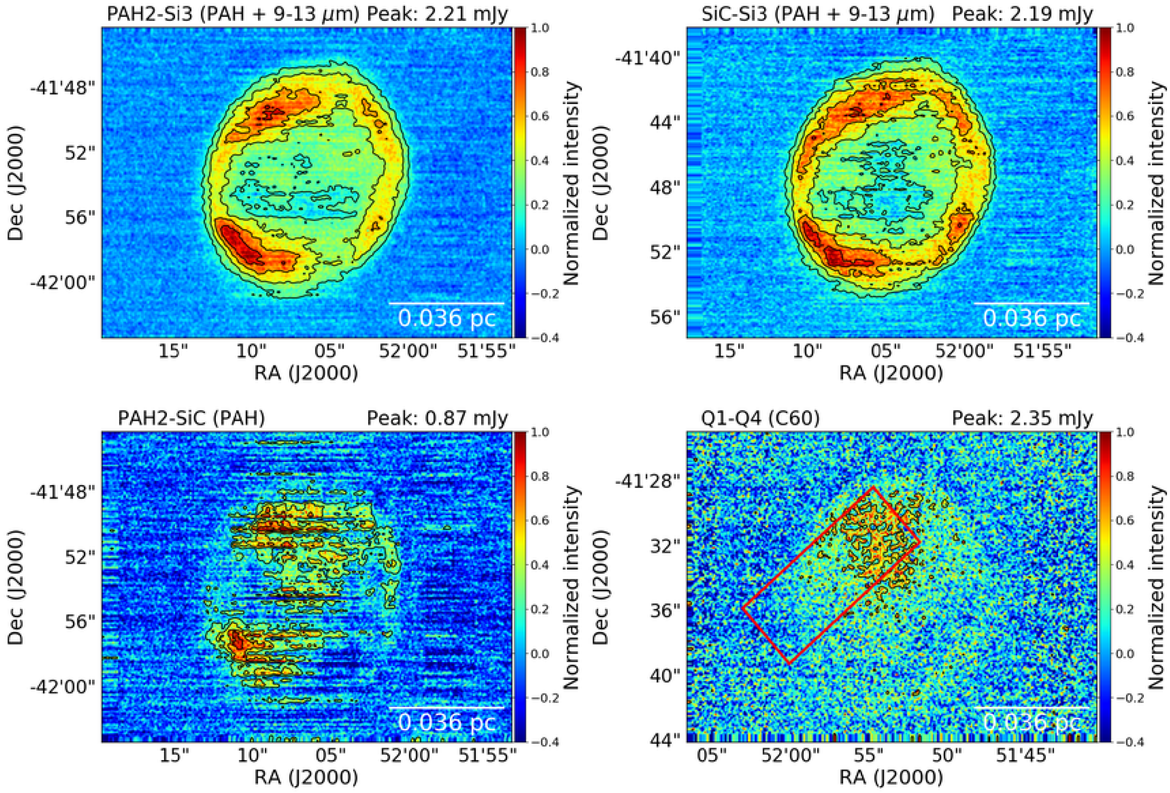

Figure 4: Contour maps of the mid-IR GTC/CanariCam PAH2−Si3, SiC−Si3, PAH2−SiC, and Q1−Q4 images of IC 418 when calibrating with the standard stars (case i in [14]). Note that only two contours at 0.4 and 0.6 are displayed in the Q1−Q4 image, which also displays the *Spitzer* slit in red (adapted from [14]).

seen in these images is mainly coming from a ring-like structure that is seen in all filters, with the exception of the dust continuum emission at 9.8 μm, which peaks near the central star (see [14]). The very similar spatial distribution seen in the Q1 and Q4 filters covering the C_{60} feature and the dust continuum already suggests that both filters are dominated by the dust continuum emission. This is not strange if we take into account that IC 418 has a very low C_{60} to continuum ratio.

We have subtracted the dust continuum emission from our images (see Fig. 4), recovering a nice ring-like structure for the broad ∼9−13 μm emission. We have tried to recover the spatial distribution of the weak PAH-like feature at 11.3 μm and it seems to be less well defined than for the broad ∼9−13 μm feature. However, only a residual C_{60} emission (at about 5-σ from the sky background) is seen when subtracting the dust continuum emission at 20 μm. If real, this could explain why *Spitzer* clearly detected fullerenes in this PN, because *Spitzer* just observed this region.

The observed spatial distribution of C_{60} may have several interpretations and the data

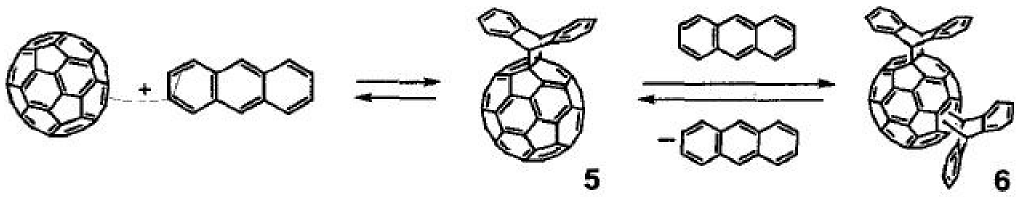

Figure 5: Scheme of the addition reaction of anthracene to C_{60} fullerene. It is schematized the fact that initially anthracene forms a mono-adduct (#5) but in an excess of anthracene, a bis-adduct (#6) is obtained ([30]) (adapted from [30], [22]).

are not conclusive about fullerene formation and excitation. So, higher sensitivity observations (especially in the Q-band where water vapour severely limits the ground-based observations) are needed; for example by using the future James Webb Telescope (see [14] for more details).

5 Other fullerene compounds in the lab

Independently of the relevance of the laboratory induced reactions (e.g., Diels-Alder, the Scholl reaction) in circumstellar environments, the organic chemistry techniques are useful to synthesize/characterize some specific molecular nanostructures of our interest.

For example, we know that fullerenes and PAHs may coexist in fullerene PNe. C_{60} can react with a small PAH like anthracene via Diels-Alder reactions to form fullerene/anthracene mono-adducts or bis-adducts (see Fig. 5). Such fullerene/PAHs adducts display the same mid-IR features of isolated C_{60} molecules and we could not distinguish them via mid-IR spectroscopy only ([22]). Indeed, as for the case of hydrogenated fullerenes with low H-content, such fullerene adducts may contribute to the observed fullerene-like features observed in space.

Until now, we have synthesized and characterized adducts of C_{60} and C_{70} with small PAHs like anthracene, tetracene, and pentacene as well as adducts of fullerenes with iron penta-carbonyl ([22], [23], [24], [4], [5],[6]).

More recently, we have studied charge-transfer interactions between fullerenes and a series of alkylnapthnalenes, pinenes, and dienes like those shown in Fig. 6 ([25], [26]). We basically found that these interactions are rather weak.

In addition, we have recently obtained IR laboratory spectroscopy of several carbonized PAHs ([27]). The scheme displays the carbonization pathway for napthalene. Interestingly, such carbonized PAHs display infrared features coincident with the set of unidentified infrared bands (UIRs). The PAHs, if present in space, could experience carbonization under the action of shock waves, which are know to be very common in circumstellar and interstellar media.

It is to be noted here that in the lab, we have studied a new route towards graphene

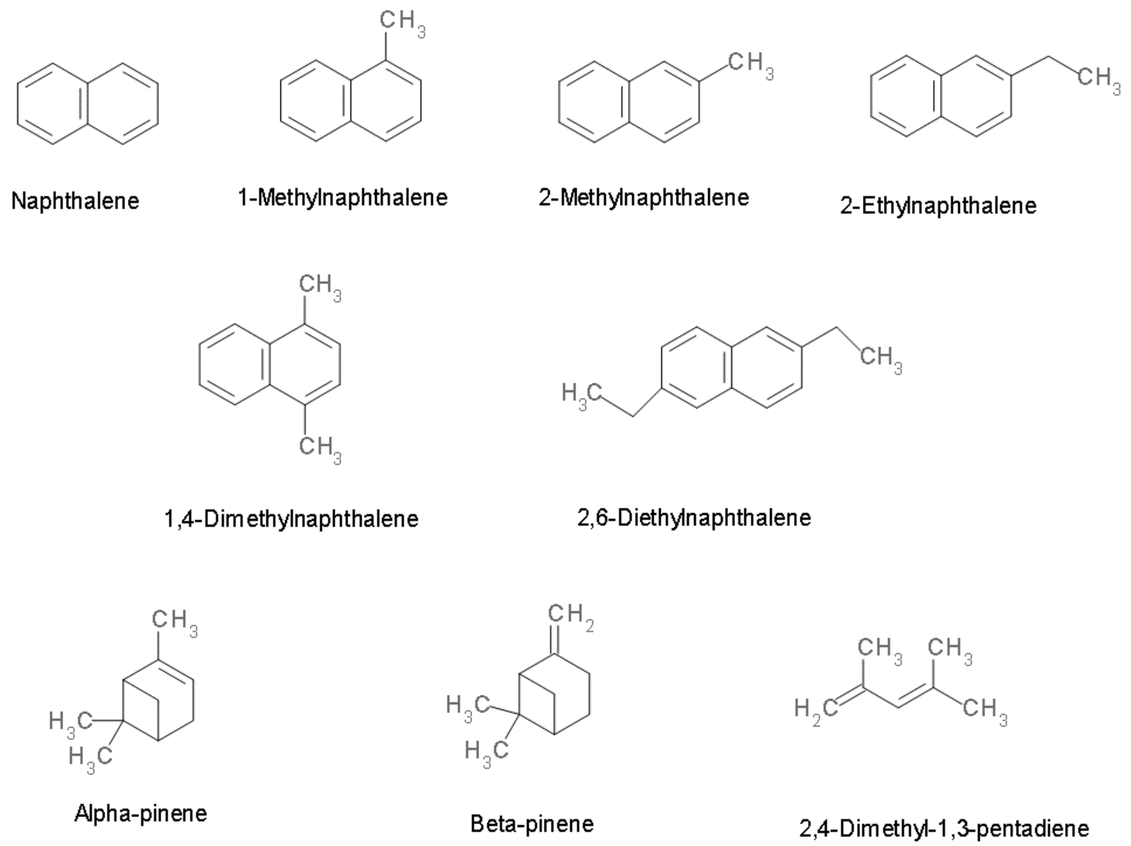

SCHEME 1

Figure 6: Chemical structures of a series of alkylnapthnalenes, pinenes, and dienes used to study the $C_{60,70}$ charge-transfer interactions (adapted from [26]).

starting from heavily ozonided fullerenes (or C_{60} and C_{70} ozopolymers; [7], [8], [9]). This approach is found to be easier and more consistent preparation than the one for graphene oxide (GO).

6 Fullerenes with the James Webb Space telescope

Finally, the future James Webb Space telescope will be much more sensitive than Spitzer, with access to the near-IR range. This mission will permit near- and mid-IR spectroscopic and imaging studies of individual fullerene-containing sources. The James Webb will permit us to know the relative sub-arcsecond spatial distribution of the fullerenes, and other dust features and much higher spectral resolution to cleanly resolve the fullerene-like features. With such observations we will learn about fullerene formation and excitation, and we could detect other fullerene-based compounds in space.

7 Summary - open questions

In short, the knowledge of the chemical route to form fullerenes in space remains as the main open question. The astronomical observations suggest a top-down fullerene formation. Two main chemical routes starting from the photochemical processing of PAHs or HAC-like nanoparticles have been proposed to explain the detection of fullerenes in the interstellar medium and in evolved stars, respectively.

Another open questions are the following: i) What is the excitation mechanism of the fullerene emission? Thermal or fluorescence emission? Can the photo-switching give an extra-stability to fullerene compounds ? ; ii) Why DIBs are so different in the fullerene-containing environments around RCB stars and PNe?

What it seems to be clear is that a complex family of fullerene- and graphene-based molecules is very likely to be present in space but more laboratory, theoretical, and observational efforts are needed.

Acknowledgments

DAGH was acknowledges support provided by the Spanish Ministry of Economy and Competitiveness (MINECO) under grant AYA−2017−88254-P.

References

[1] Cami, J. et al. 2010, Science, 329, 1180

[2] Campbell, E. K. et al. 2015, Nature, 523, 322

[3] Campbell, E. K. et al. 2016, ApJ, 822, 17

[4] Cataldo, F., García-Hernández, D. A., & Manchado, A. 2014, FNCN, 22, 565

[5] Cataldo, F., García-Hernández, D. A., & Manchado, A. 2015a, FNCN, 23, 760
[6] Cataldo, F., García-Hernández, D. A., & Manchado, A. 2015a, FNCN, 23, 818
[7] Cataldo, F. et al. 2016a, FNCN, 24, 52
[8] Cataldo, F. et al. 2016b, FNCN, 24, 62
[9] Cataldo, F. et al. 2016c, FNCN, 24, 195
[10] Clayton, G. C. et al. 1995, AJ, 109, 2096
[11] de Vries, M. S. et al. 1993, GeCoA, 57, 933
[12] Díaz-Luis, J. J. et al. 2015, A&A, 573, A97
[13] Díaz-Luis, J. J. et al. 2016, A&A, 589, A5
[14] Díaz-Luis, J. J. et al. 2018, AJ, 155, 105
[15] Foing, B. H., & Ehrenfreund, P. 1994, Nature, 369, 296
[16] García-Hernández, D. A. et al. 2010, ApJ, 724, L39
[17] García-Hernández, D. A., Rao, N. K., & Lambert, D. L. 2011, ApJ, 729 126
[18] García-Hernández, D. A. et al. 2011, ApJ, 737, L30
[19] García-Hernández, D. A., Rao, N. K., & Lambert, D. L. 2012, ApJ, 759, L21
[20] García-Hernández, D. A. et al. 2012, ApJ, 760, 107
[21] García-Hernández, D. A., & Díaz-Luis, J. J. 2013, A&A, 550, L6
[22] García-Hernández, D. A., Cataldo, F., & Manchado, A. 2013, MNRAS, 434, 415
[23] García-Hernández, D. A., Cataldo, F., & Manchado, A. 2016a, FNCN, 24, 225
[24] García-Hernández, D. A., Cataldo, F., & Manchado, A. 2016b, FNCN, 24, 679
[25] García-Hernández, D. A., Cataldo, F., & Manchado, A. 2017a, FNCN, 25, 223
[26] García-Hernández, D. A., Cataldo, F., & Manchado, A. 2017b, FNCN, 25, 505
[27] García-Hernández, D. A., Cataldo, F., & Manchado, A. 2018, FNCN (in press)
[28] Goeres, A., & Sedlmayr, E. 1992, A&A, 265, 216
[29] Iglesias-Groth, S., Cataldo, F., Manchado, A. 2011, MNRAS, 413, 213
[30] Komatsu, K. et al. 1999, FNCN, 7, 609
[31] Kroto, H. W. et al. 1985, Nature, 318, 162
[32] Kuzmin, S., & Duley, W. W. 2011, Arxiv:1103.2989
[33] Kwok, S. et al. 1999, A&A, 350 L35
[34] Lambert, D. L. et al. 2001, ApJ, 555 925
[35] Micelotta, E. et al. 2012, ApJ, 761 35
[36] Moutou, C. et al. 1999, A&A, 347, 949
[37] Otsuka, M. et al. 2014, MNRAS, 437, 2577
[38] Roberts, K. R. G., Smith, K. T., & Sarre, P. J. 2012, MNRAS, 421, 3277

[39] Scott, A. et al. 1997, ApJ, 489, L123

[40] Sellgren, K., Uchida, K. I., & Werner, M. W. 2007, ApJ, 659, 1338

[41] Sellgren, K. et al. 2010, ApJ, 722, L54

[42] Volk, K. et al. 2011, ApJ, 735, 127

[43] Zhang, Y., & Kwok, S. 2011, ApJ, 730, 126

[44] Zhang, Y., & Kwok, S. 2013, EP&S, 65, 1069

[45] Zhang, Y. et al. 2017, ApJ, 845, 76

Highlights on Spanish Astrophysics X, Proceedings of the XIII Scientific Meeting of the Spanish Astronomical Society held on July 16 – 20, 2018, in Salamanca, Spain. B. Montesinos, A. Asensio Ramos, F. Buitrago, R. Schödel, E. Villaver, S. Pérez-Hoyos, I. Ordóñez-Etxeberria (eds.), 2019

TROY – The Search for Exotrojan Planets.

Lillo-Box, J.

European Southern Observatory (ESO), Alonso de Cordova 3107, Vitacura, Santiago, Chile

Abstract

As the field of extrasolar planets evolves with numerous discoveries of new and diverse planets, we can start thinking in more challenging (observationally speaking) scientific cases that can bring up new, hidden pieces of the exoplanetary science puzzle. This is the case of the TROY project, a multi-technique effort to look for the first co-orbital planets and to provide estimates of the occurrence rate of these bodies down to the Earth-mass regime. Despite being missed in our Solar System, where only kilometer-size (or smaller) bodies co-rotate with most of the planets, theory allows even equal-mass planets to co-exist in the same orbit. In this invited talk I will present the news on the TROY project including the last ground-based observations, the results from the first radial velocity search involving 46 planetary systems and the first results from our Kepler/K2 search.

1 Introduction

After millennia of wondering, we now know that extrasolar planets abound [30, 27, 2, 25]. We have also proven several instances of exocomets (β Pic, [16]) and since 1984, with IRAS, we are also aware of Kuiper belt structures around other stars (see [29] and references therein). These discoveries imply that the non-planetary components of our Solar System are not an exception but instead the rule, being also present in extrasolar systems as a result of the planet formation process. Thus, it becomes clear that other existing bodies in our planetary system that have not yet been found abroad should (or at least can) also exist. Two examples are natural satellites (or moons) and trojans. Both types of objects abound in our Solar System, with the gas giants hosting tens of moons and Jupiter having thousands of trojans at both Lagrangian points. The hunt for exomoons is being carried out by several groups, including the HEK project (see [17] and the recent result of this project in [32]) and other different works (see, e.g., [33, 12]). In this project, we deal with the challenge of detecting and characterizing trojans co-orbiting to extrasolar planets (hereafter exotrojans).

The gravitational forces exerted by two massive bodies create a gravitational field with a distinct peculiarity: five locations of this field (called Lagrangian points) happen to be of

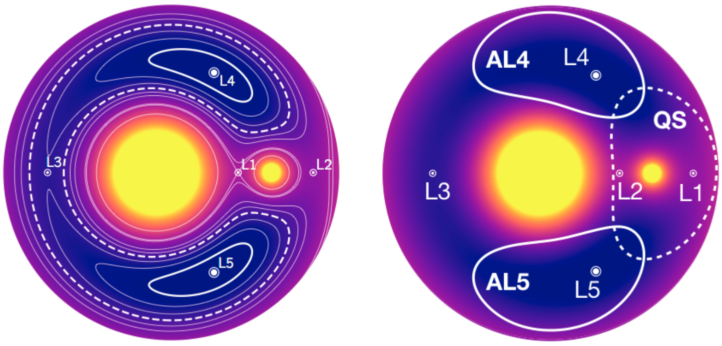

Figure 1: Stable co-orbital configurations. The left panel shows the tadpole (thick solid lines around L4 and L5) and horseshoe (thick dashed line) orbits. The right panel shows the location of the quasi-satellite stability point surrounding the planet (QS) and the two anti-Lagrangian stable points (AL) surrounding the Lagrangian points in the co-rotating frame.

equilibrium. Among them, three (L1, L2, and L3) are unstable to small perturbations (i.e., hills of gravitational potential) and two (L4 and L5) are stable to small perturbations (i.e., valleys of gravitational potential). The stable regions form an equilateral triangle with the planet and the star, being at $\pm 60°$ leading and trailing the planet on the exact same orbit (see Fig. 1, left). This implies that these are stability regions for wandering objects co-orbiting with the planet. Indeed, the analysis of orbital dynamics offers a whole buffet of co-orbital stable configurations: In tadpole orbits, the trojan inhabits one of the Lagrangian points, surrounding it with libration periods that scale with the mass ratio of the three objects. The Jupiter trojans describe this type of orbits. In horseshoe, the co-orbital moves from L4 to L5 describing a horseshoe-shape. The only example of this in the solar system are the Saturnian moons Epimetheus and Janus. In eccentric planets, new configurations become possible: in quasi-satellite orbits (QS, [28]) the co-orbital surrounds the planet in a very wide orbit in the co-rotation frame, like if it were a natural satellite (see Fig. 1, right); in anti-Lagrangian configurations (AL4 and AL5, [11]) the stability point (and hence the co-orbital) surrounds each of the Lagrangian points in the co-rotation frame. In total, in a star-planet system, there are six known islands of stability that allow other objects to co-orbit with the planet: L4, L5, horseshoe, QS, AL4, and AL5.

There are two main mechanisms for the formation of co-orbital planets. [5] presented the in situ scenario where these bodies are allowed to grow through accretion at the Lagrangian regions. [4] went a step further and demonstrated that in both gas-free and gas-rich evolutionary stages of the protoplanetary disk this accretion process is efficient in forming co-orbitals in situ of up to 6 $M_{\rm Mars}$ (0.6 $M_{\rm Earth}$) that will remain stable in tadpole orbits. This process is supported by different hydrodynamical simulations of planet formation showing that gas and dust accumulates already in the Lagrangian points of the forming planets (e.g., [18]; [10]). A second possible mechanism is the capture of the co-orbitals during the early stages of the planetary system through dynamical interactions. Indeed, co-orbital bodies are common outcomes of the planet formation and early evolution studies. [6] demonstrated that more than 30% of the simulated multi-planetary systems end up with long-lived co-orbital configurations of the proto-planets being formed. The conditions for capture strongly depend on the disk surface density profile and the number of planets in the system. Even more, the resonant capture of co-orbitals prevented the ejection or fate of the other planets in the system, thus acting as anchors of the multi-planetary system, with strong impact in the architecture of planetary systems. Regardless of their formation scenario, once trapped, the co-orbital configuration can remain stable during the inward migration of the planet, with the only caveat of an increase in the libration amplitude that eventually can lead to the co-orbital disruption. Very close-in co-orbital configurations are thus disfavored, although they can survive under certain conditions ([7])

The implications of their presence in a planetary system (or even of short-term co-orbital phases) has key implications in many aspects of the formation and evolution of planetary systems. For instance, [7] demonstrated that the capture of planet-size co-orbitals during the first stages strongly depends on the properties of the disk; and in particular on its surface density. Additionally, the dynamical properties of the co-orbital bodies strongly depend on the migration history of the system, with large librations indicating large journeys of the planet inward into the system. The Lagrangian regions are also a reservoir of bullets for the so-called giant-impacts that have been proposed as mechanisms to form moons of rocky planets and that strongly influence the atmospheric composition of planets. Indeed, this is one of the proposed mechanisms for the formation of our own Moon. [3] proposed a trojan origin for *Theia*, the Mars-size body that could have hit the proto-Earth to form the present (unique) Earth-Moon system.

Hence, co-orbital planets can be formed and remain stable in planetary systems under certain (very much relaxed) conditions. And their mere formation can have relevant implications for our understanding of the history of planetary systems. The past, current, and forthcoming instrumentation (Kepler, TESS, CHEOPS, PALTO, etc.) and the detection techniques developed over several decades allow us to start a homogeneous search and study of these bodies that might be one of the few missing pieces of planetary systems [23]. The TROY project is leading this effort through an exhaustive study and search of co-orbital planets.

2 The combined radial velocity - transit technique

In [8] the authors demostrate that if the radial velocity (RV) of a star is induced by a pair of co-orbital planets, the predicted time of transit from the RV data is shifted with respect to the actual time of transit of either of the two co-orbitals. Indeed, even though the Keplerian signal in the RV of the star is induced by the barycenter of the two co-orbitals, the time of transit predicted from the RV is hence the time of transit of that barycenter, while the actual planets transit before and after, if at all. This detection technique was applied by [8] to a handful number of known planets at the time, while assuming circular orbits, to set upper limits to the masses of possible trojan bodies in those systems. Also, [26] applied this technique to 25 known planets and found no evidence for a trojan up to their upper mass limits.

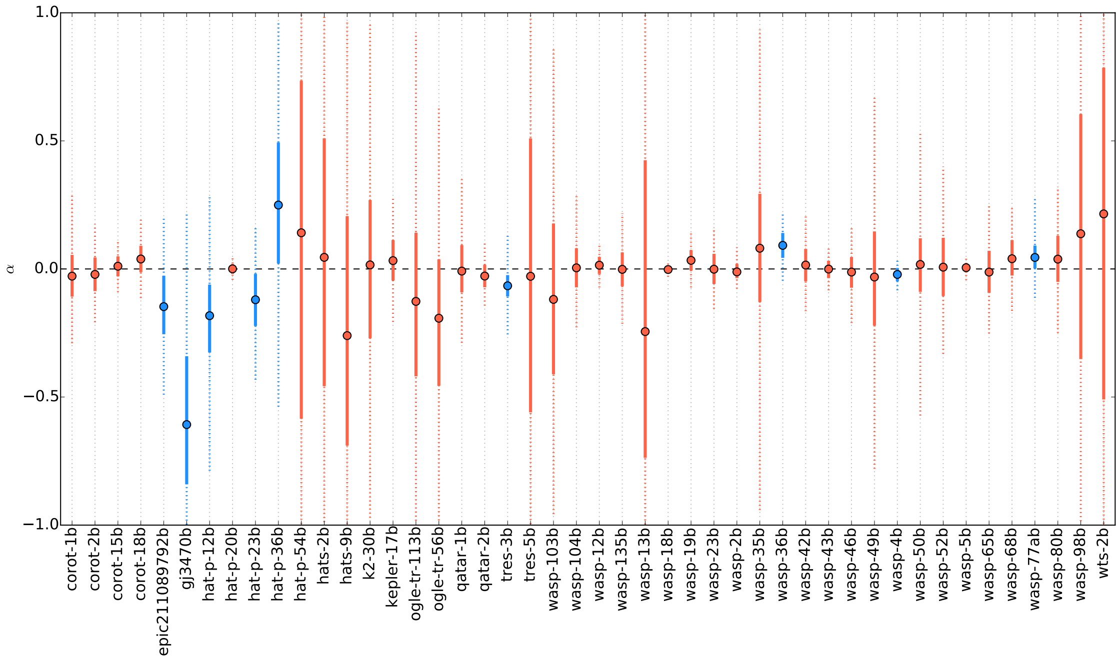

Figure 2: Results for the α parameter from the radial velocity analysis. Color error bars indicate the 68.7 confidence intervals (i.e., 1σ) while the dotted error bars indicate the 99.7% confidence intervals (3σ). We show in blue symbols the 9 systems where the null value for α ($\alpha = 0$) lies outside of the 1σ limits.

A downside of this method is that it is strongly dependent on the eccentricity of the transiting planet. Any error in the determination of the eccentricity would also produce a shift between the predicted transit time from the RV of a single planet and its actual time of transit. We tackled this problem in [19], where we generalized the equations presented in [8] for the case of eccentric orbits in order to extract as much information as possible from the RV signal. This is achieved through the determination of the α parameter, which is proportional to the trojan-to-planet mass ratio ($\alpha \approx m_t/m_p \sin\zeta$, with ζ being the deviation from the Lagrangian point). A value of α that deviates significantly from zero is thus a hint for the presence of a co-orbital planet, with $\alpha < 0$ indicating an L4 co-orbital and $\alpha > 0$ an L5 co-orbital. The constraint on the mass of the co-orbital companion to the transiting planet are in any case greatly improved if the secondary eclipse of the transiting planet can be observed, thanks to the precise determination of the parameter $e \cos\omega$.

In [21], we applied this technique to 46 planetary systems with only one (giant) planet known in the system and having an orbital period shorter than 5 days. We constrained the presence of co-orbital planets in both Lagrangian regions by just using public radial velocity data and determining the α parameter. In Fig. 2, we show the α values for the 46 systems. We found nine cases where α was at least 1σ away from the null value (in blue in this figure), although some of the posteriors are too broad to extract clear conclusions. Furthermore, in two cases (GJ 3470 and WASP-36), the median value for the α parameter is $> 2\sigma$ away from the null hypothesis.

Despite the low number statistics, these results allow us to start estimating occurrence rates of exotrojans in the particular sample studied here (i.e., short-period -$P < 5$ day- single planets). Since we only detect upper mass limits, we can estimate the upper limits for the occurrence rate of trojans up to a certain mass, which is defined as the 95.4% confidence level for the α parameter assuming that the trojan is located exactly at the Lagrangian point. We can say in general terms that at least 12% of planets with periods shorter than five days do not have co-orbital planets more massive than Neptune. Equivalently, at least 50% lack trojans more massive than Saturn. Also, we can discard Jupiter-mass trojans in this particular sample at a $\sim 90\%$ level. The reasons for this absence of massive trojans can be numerous (e.g., difficulties in forming such large bodies in situ at the Lagrangian points or keeping them stable during planetary lifetimes, difficulties in capturing such massive planets in stable orbits around the Lagrangian points, etc.). But in any case, the evidence presented for each individual system already provides empirical feedback to formation and migration theories.

3 The multi-technique approach

The above-described analysis (detailed in [21]) yielded nine potential candidates with values of the α parameters slightly different from zero (although not statistically significant), suggesting the possible presence of co-orbital planets. We used these systems for a more in-depth study using and combining the results from different observing techniques, presented in [22]. In particular, for the nine planetary systems we compiled observations from several observing techniques, including i) new radial velocity data obtained through dedicated observing programs with HARPS, HARPS-N, and CARMENES, ii) archive transit timing variations of the planet (TTVs), which might be explained by the libration of a co-orbital planet (see [9]), and iii) new high-precision photometric observations (with WiFSIP, CAFOS and FORS2) of the transit of the Lagrangian points of the nine systems where the co-orbitals were suspected to lie from the α parameter analysis.

We analyzed each dataset independently to constrain the existence of any co-orbital at the Lagrangian regions in the trojan mass versus libration amplitude parameter space. In particular, the new radial velocity data were used to update the α values; the TTVs were fitted to search for periodic variations and their scatter was used to constrain the trojan parameters (see Eq. 1 in [9] and [1] for a detailed analysis of Kepler data); and the serval photometric observation of the Lagrangian point passages were used to search for the trojan transit and to perform a dynamical analysis to also constrain the libration amplitude based on the non detections. All these allowed us to set important constraints on the presence of these bodies in the system by combining the independent analysis from the different techniques. In Fig. 3 (left panel), we show how the different techniques can constrain the relevant parameter space of trojan mass versus libration amplitude. As shown, each particular technique covers a different region of the parameter space, thus complementing each other. This makes clearer

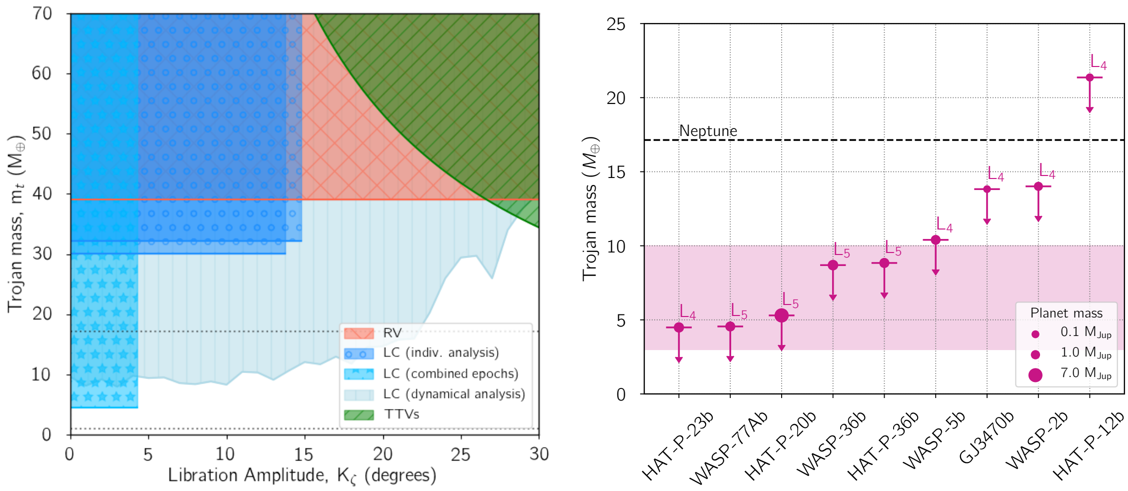

Figure 3: **Left:** Detailed example of the multi-technique constrain of the trojan mass versus libration amplitude parameter space for WASP-77A (see [22]). Only the white region is not explored by our data. **Right:** Upper mass limits for co-orbitals seating exactly at (or with very small librations around) the Lagrangian points for the nine systems studied in [22].

the need for a multi-technique approach to appropriately rule out (and search for) trojans of any kind.

4 Space-based long term photometric monitoring

The obvious question when discussing about the possible presence of planet-size co-orbital companions is: why have they not been detected by long-term high-precision photometric space-based missions like Kepler? The question is indeed very pertinent. The fact that no clear evidence of these bodies was found in the data from these missions (although note that some candidates have already been proposed, see [20, 31, 24]) already provides relevant information.

First of all, it is worth to mention that some works have already dug into these data looking for these bodies. In [15], the authors performed a dedicated search for small librating trojans around 2244 Kepler candidates with no success down to 1 R_{Earth}. The reasons for this unsuccessful search can be multiple but one main conclusion can be drawn: trojans larger than Earth seem to not exist lying exactly at the Lagrangian points of their planets. However, the search by [15] suffered from several limitations. First of all, they used KOIs instead of confirmed planets so a large part of their sample was contaminated by false positive planets (note that less than one third of Kepler KOIs have been confirmed/validated). Also, they used the first 12 quarters of the mission (among the 17 available at the end of the mission). Regarding the equations used to search for these bodies, they assumed very small librations around the Lagrangian points. We now know that inward migration excite the libration in

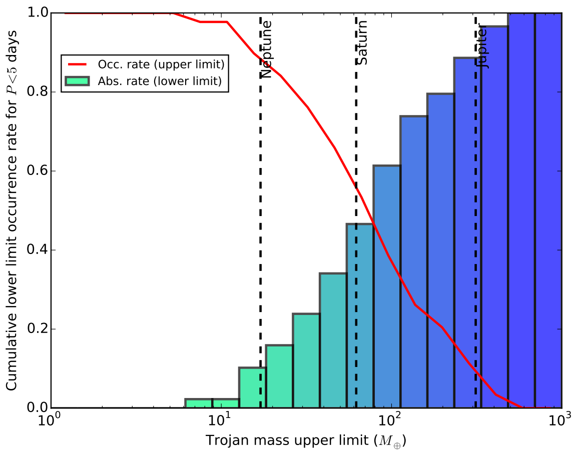

Figure 4: Occurrence rate of co-orbital planets to short-period ($P < 5$ days) giant planets ([21]). These occurrence rates were computed from a sample of 46 planetary systems with only one planet known.

the co-orbital regions and so we expect trojans to librate with relatively large amlpitudes for the kind of planets found by Kepler (i.e., in orbits inner to 1 au).

By contrast, [14] combined all light curves from Kepler candidates to get an average phase-folded light curve of all systems. The results showed dimmings at both L4 and L5 locations, suggesting the presence of an average population of trojans of 970 km in size (Pluto-like) in one third of the systems. This result demonstrates that co-orbital bodies exist with a high probability. Detecting individual co-orbitals is, hence, the challenge.

Consequently, a more dedicated and general search is needed. We have started this search by deriving new equations of motion for the trojan on its co-orbital configuration including several aspects missed by previous works. The preliminary results are promising and a paper is in preparation to describe the methodology and show the outcomes of this search.

5 Conclusions

During the last two years, the TROY project have started to pave the road towards a more comprehensive and homogeneous search and study of co-orbital planets in extrasolar systems. These bodies contain crucial information about the history of a planetary system, including clues on the planet formation and migration mechanisms, the shaping of the different components and architectures, and their potential habitability (see, e.g., [13]). The determination of the occurrence rate of co-orbital planets is thus a missing piece in the jigsaw puzzle of planetary systems that the community has been building up during the past few decades. Although theories of planet formation show that these configurations are common outcomes of the planet formation process, either in situ or captured, no planet-size trojan has yet been found. However, so far all efforts to detect these bodies, although very relevant and inspiring, have either focused on small samples and/or relied on simple assumptions that could have hidden the presence of these bodies. The new computational capabilities and the large amount of data from either space-based observatories or GTO programs from state-of-the-art ground-based instrumentation (like ESPRESSO or HARPS) offer a unique opportunity to push this field forward and provide and empirical feedback to theoretical works developed along decades.

TROY is a dedicated effort in this direction. We have started a search for co-orbital planets in known extrasolar systems by using different techniques and focusing on a main goal of constraining these co-orbitals at any possible configuration and down to the Earth-like domain. The first results presented in [21] and [22] proof that we digging into the correct direction. The use of multiple techniques was proven essential to really constrain the whole parameter space of possible co-orbital bodies. The future is bright for this flourishing field with the many planet-detection-driven facilities that are already working or that will be ready in the forthcoming years.

Acknowledgments

The TROY project is composed of a team of experts in different fields that is critically helping in the development of this project: A. Leleu, A.C.M. Correia, P. Robutel, P. Figueira, N.C. Santos, D. Barrado, J. Faria, M. Lendl, H. Parviainen, M. Mallonn, H.M.J. Boffin.

References

[1] Atienza J. & Lillo-Box J., 2018, Master Thesis Dissertation, Valencia International University

[2] Batalha, N. M. 2014, Proceedings of the NAS, 111, 12647

[3] Belbruno, E. & Gott, III, J. R. 2005, AJ, 129, 1724

[4] Beauge, C., Sándor, Z., Erdi, B., & Suli, A. 2007, A&A, 463, 359

[5] Chiang, E.I., & Lithwick, Y. 2005, ApJ, 628, 520

[6] Cresswell, P., & Nelson, R. P. 2008, A&A, 482, 677

[7] Cresswell, P. & Nelson, R. P. 2009, A&A, 493, 1141

[8] Ford, E. B. & Gaudi, B. S. 2006, The Astrophysical Journal, 652, L137

[9] Ford, E. B. & Holman, M. J. 2007, ApJ, 664, L51

[10] Fuente, A., Baruteau, C., Neri, R., et al. 2017, ApJ, 846, 3

[11] Giuppone, C.A., Beauge, C., Michtchenko T. A., Ferraz-Mello S. 2010, MNRAS, 470, 390

[12] Heller, R., Williams, D., Kipping, D., et al. 2014, Astrobiology, 14, 798

[13] Hill, M. L.; Kane, S. R.; Seperuelo Duarte, E., et al. 2018, ApJ, 860, 67

[14] Hippke, M. & Angerhausen, D. 2015, ApJ, 811, 1

[15] Janson. 2013, ApJ, 774, 156

[16] Kiefer, F., Lecavelier des Etangs, A., Boissier, J., et al. 2014, Nature, 514, 462

[17] Kipping, D. M., Bakos, G. A., Buchhave, L., Nesvorny, D., & Schmitt, A. 2012, ApJ, 750, 115

[18] Laughlin, G. & Chambers, J. E. 2002, Astronomical Journal, 124, 592

[19] Leleu, A., Robutel, P., Correia, A. C. M., & Lillo-Box, J. 2017, A&A, 599, L7

[20] Lillo-Box, J., Barrado, D., Moya, A., et al. 2014, A&A, 562, A109

[21] Lillo-Box, J., Barrado, D., Figueira, P., et al. 2018a, A&A, 609, 96

[22] Lillo-Box, J., Leleu, A., Parviainen, H., et al. 2018b, A&A, 618, 42

[23] Lillo-Box, J., Kipping, D., Rebollido, I., et al., 2018c, White Paper in response to the solicitation of feedback for the "Exoplanet Science Strategy" by the National Academy of Sciences, Engineering, and Medicine

[24] Lissauer, J.J., Ragozzine, D., Fabrycky, D.C., Steffen, J.H. 2011, ApJS, 197, 8

[25] Lissauer, J. J., Dawson, R. I., & Tremaine, S. 2014, Nature, 513, 336

[26] Madhusudhan, N. & Winn, J. N. 2009, ApJ, 693, 784

[27] Mayor, M., Lovis, C., & Santos, N. C. 2014, Nature, 513, 328

[28] Mikkola, S., Innanen, K., Wiegert, P., Connors, M., & Brasser, R. 2006, MNRAS, 369, 15

[29] Moro-Martin, A., Wyatt, M. C., Malhotra, R., & Trilling, D. E. 2008, Extrasolar Kuiper Belt Dust Disks, ed. M. A. Barucci, H. Boehnhardt, D. P. Cruikshank, A. Morbidelli, & R. Dotson, 465-480

[30] Pepe, F., Ehrenreich, D., & Meyer, M. R. 2014, Nature, 513, 358

[31] Placek, B., Knuth, K. H., Angerhausen, D., & Jenkins, J. M. 2015, ApJ, 814, 147

[32] Teachey & Kipping 2018, Science, 4, 10

[33] Weidner, C. & Horne, K. 2010, A&A, 521, A76

Highlights on Spanish Astrophysics X, Proceedings of the XIII Scientific Meeting of the Spanish Astronomical Society held on July 16 – 20, 2018, in Salamanca, Spain. B. Montesinos, A. Asensio Ramos, F. Buitrago, R. Schödel, E. Villaver, S. Pérez-Hoyos, I. Ordóñez-Etxeberria (eds.), 2019

Optical and X-ray observations of the microquasar V404 Cyg during its June 2015 outburst.

J. Alfonso-Garzón[1], C. Sánchez-Fernández [2], P.A. Charles[3], J.M. Mas-Hesse[1], P. Gandhi[3], M. Kimura[4], A. Domingo[1], J. Rodriguez[5], and J. Chenevez[6]

[1] Centro de Astrobiología – Departamento de Astrofísica (CSIC-INTA), Camino Bajo del Castillo s/n, E-28692 Villanueva de la Cañada, Spain
[2] European Space Astronomy Centre (ESAC), Camino Bajo del Castillo s/n, E-28692 Villanueva de la Cañada, Spain
[3] Department of Physics and Astronomy, University of Southampton, Southampton SO17 1BJ, UK
[4] Department of Astronomy, Graduate School of Science, Kyoto University, Oiwakecho, Kitashirakawa, Sakyo-ku, Kyoto 606-8502, Japan
[5] Laboratoire AIM (CEA/IRFU - CNRS/INSU - Université Paris Diderot), CEA DSM/IRFU/SAp, 91191, Gif-sur-Yvette, France
[6] DTU Space—National Space Institute, Technical University of Denmark, Elektrovej 327-328, DK-2800 Lyngby, Denmark

Abstract

We present a multiwavelength analysis of the simultaneous optical and X-ray light curves of the microquasar V404 Cyg during the June 2015 outburst. We have performed a comprehensive analysis of all the INTEGRAL/IBIS, JEM-X, and OMC observations during the brightest epoch of the outburst, along with complementary NuSTAR, AAVSO, and VSNET data, to examine the timing relationship between the simultaneous optical and X-ray light curves, in order to understand the emission mechanisms and physical locations. We identified all optical flares with simultaneous X-ray observations, and performed cross-correlation analysis to estimate the time delays between the optical and soft and hard X-ray emission. We have also compared the evolution of the optical and X-ray emission with the hardness-ratios. From this analysis, we identified several types of behaviour during the outburst, including simultaneous optical/X-ray flares, optical flares lagging the X-ray flares, and optical emission preceding the X-ray emission.

1 Introduction

V404 Cygni (hereafter V404 Cyg) is a transient low-mass X-ray binary (LMXB) consisting of a black hole (BH) that accretes mass from a low-mass optical companion. The distance to the system is 2.39±0.14 kpc (15). The orbital period is 6.47 d and the mass function is $f(M)$=6.08±0.04 $M_\odot$ (4). The inclination of the orbit is in the range 56–67° (17; 16; 10). The donor star is a K0 III–K2 IV (10; 7), and the mass of the black hole is M_{BH} = 9–12 $M_\odot$.

The X-ray counterpart GS 2023+338 was discovered in X-rays by the Ginga satellite during an X-ray outburst in May 1989 (13). On 15 June 2015 18:32 UTC (MJD 57188.772), after 26 years of quiescence, the Burst Alert Telescope (BAT, Barthelmy et al. 2) on board the *Swift* satellite (6) detected renewed X-ray activity from V404 Cyg (3). This outburst reached its peak on 26 June 2015 and then rapidly decayed, returning to quiescence in mid-August (18). The outburst was intensively observed by most of the available space telescopes and ground-based facilities worldwide.

In this work, we analyse all the available *INTEGRAL* data during the brightest period of the June 2015 outburst, that is, from 18 June 2015 to the fast decay of the optical and X-ray emission in 27 June 2015.

2 Observations

The INTErnational Gamma-Ray Astrophysics Laboratory (*INTEGRAL*, (21)) observed V404 Cyg in the period MJD 57191.5 to 57216. We analyse here the data obtained during the interval MJD 57191.75 to 57200.25, when intense flaring activity was detected from the system. We study the optical light curves in the V band provided by the Optical Monitoring Camera (OMC, (14)), and the X-ray light curves provided by the Joint European X-Ray Monitor (JEM-X, (12); 3–10 keV), and by the Imager on Board the *INTEGRAL* Satellite (IBIS, (19); 20–80 keV and 80–200 keV). We complemented our data with the X-ray light curves provided by the Nuclear Spectroscopic Telescope Array (*NuSTAR*, (8)) in the 3–10 and 10–79 keV band (see (20) for details on these observations), and with public optical observations provided by the American Association of Variable Star Observers (AAVSO, (9)) and with optical data from the Variable Star Network (VSNET) Collaboration (see (11) for a description of this dataset).

3 Data analysis

We have identified all the optical flares that have simultaneous X-ray observations in our data. These flares are flagged with identifying numbers in Fig. 1. For all of them, we performed a cross-correlation analysis with the X-ray light curves of the system in order to identify possible time lags between the optical and X-ray emission.

For this analysis, we used the discrete cross-correlation function (DCF, (5)), a method that avoids interpolating in the temporal domain when the temporal binning is not regular (this is the case for some of the optical observations in this work). In the results from the

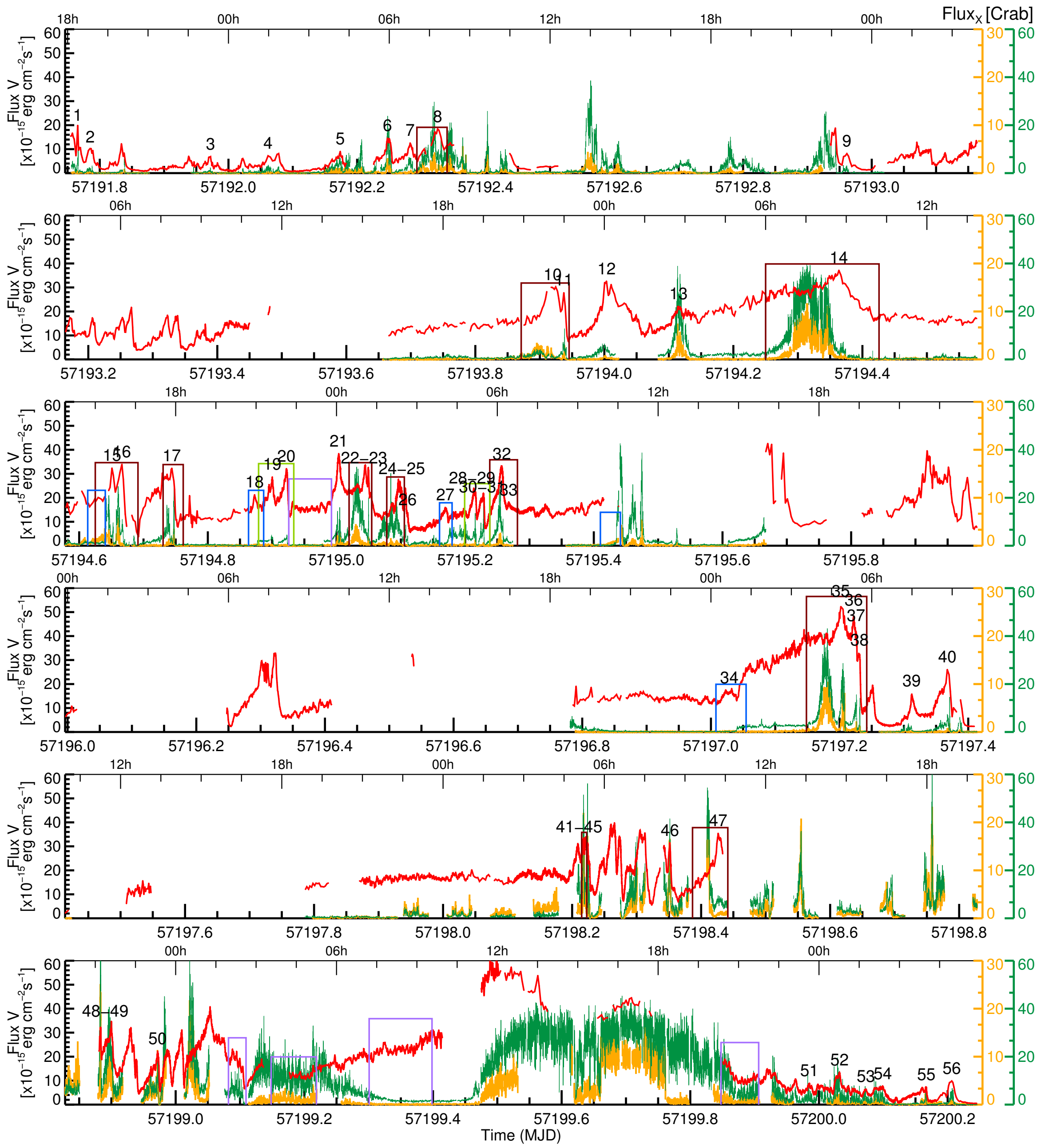

Figure 1: Optical and X-ray light curves of V404 Cyg during the June 2015 outburst from MJD 57191.75 to MJD 57200.25. The optical observations are plotted in red, the soft X-ray emission in the 3–10 keV band is plotted in orange, and the hard X-ray emission in the 20–80 keV band for *INTEGRAL*/IBIS and in the 10–79 keV band for the *NuSTAR* observations are plotted both in green. The numbers in black refer to the optical flare identifications. Brown and blue boxes mark flares with positive and negative lags, respectively. Light green boxes represent double symmetric optical flares with simultaneous X-ray emission. Purple boxes represent epochs where heartbeat-type oscillations are observed (see text).

DCF analysis, a positive lag means that the optical follows the X-rays, a negative lag means that the optical precedes the X-rays, and zero lag means that the optical and the X-rays are simultaneous. Some flares displaying the different observed behaviours are shown in Fig. 2. For each subplot, the optical and X-ray light curves (top), the hardness-ratios (middle), and the DCF (bottom) are shown.

4 Discussion

We studied the optical and X-ray light curves of V404 Cyg during the June 2015 outburst, and identified those flares observed in both energy ranges. We have used the DCF technique to search for time lags between the flare emission detected at both wavelengths.

For one third of the flares, we do not find any lags between the optical and X-ray flares (taking the uncertainties in the determination of the lags into account). In this case, we interpret that the optical and X-ray emission is coming from the same, or at least physically very close regions within the system, which can include emission from the inner hot flow and from the base of the jet.

In other cases, we measured short positive lags (<2 min). We have observed these lags in single flares and in intervals with flickering (heartbeat-type) oscillations. In this case, the optical lags could be due to reprocessing of the X-ray emission on the companion star, and/or the external parts of the accretion disc.

For other flares, we measured optical lags longer than 2 minutes, and the optical emission cannot be due to reprocessing inside the binary system. These long lags could be explained by irradiation of surrounding material around the system or by interaction of jet ejections blobs with this surrounding material or with other ejected blobs. We observed a large variety of measured lags, shape and brightness of the optical flares. It seems that in the case of long lags, different mechanisms should be taking place along the outburst, including interaction of ejections from the jet with the surrounding material or with previous ejected blobs, irradiation of distant surrounding material by the central source, or synchrotron emission from discrete ejections.

A complete analysis of all the flares identified during these observations, and a more detailed discussion can be found in (1).

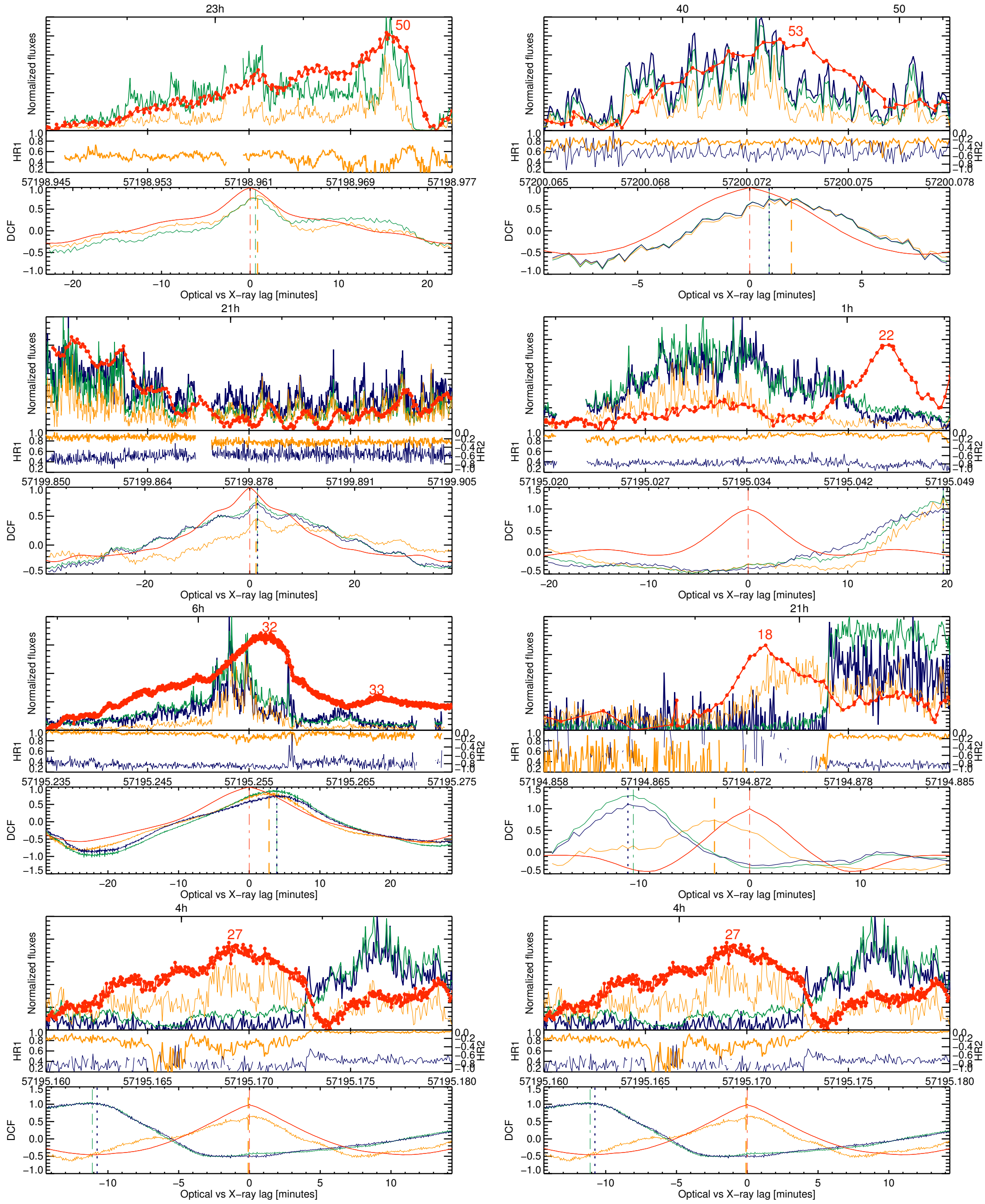

Figure 2: Zoomed-in optical and X-ray light curves where optical/X-ray flares lags display different behaviours: zero lags (top), short positive lags (second row), long positive lags (third row), negative lags (bottom). Optical observations are shown in red, soft X-ray (3-10keV) in orange, hard X-ray (20-80keV for ISGRI, or 10-79keV for *NuSTAR*) in green, and very hard X-ray (80-200keV) in dark blue. For each subplot, HR1 (the ratio between the soft and the hard X-ray bands) is plotted in orange; and HR2 (the ratio between the hard and very hard bands) is plotted in dark blue. The DCFs (optical autocorrelation function is shown in red, optical/soft X-ray DCF in orange, optical/hard X-ray DCF in green, and optical/very hard X-ray in dark blue) are shown below the light curves.

References

[1] Alfonso-Garzón, J., Sánchez-Fernández, C., Charles, P. A., et al. 2018, ArXiv e-prints, 1810, arXiv:1810.03870

[2] Barthelmy, S. D., Barbier, L. M., Cummings, J. R., et al. 2005, Space Science Reviews, 120, 143

[3] Barthelmy, S. D., D'Ai, A., D'Avanzo, P., et al. 2015, GRB Coordinates Network, Circular Service, No. 17929, #1 (2015), 17929

[4] Casares, J. & Charles, P. A. 1994, Monthly Notices of the Royal Astronomical Society, 271, L5

[5] Edelson, R. A. & Krolik, J. H. 1988, The Astrophysical Journal, 333, 646

[6] Gehrels, N., Chincarini, G., Giommi, P., et al. 2004, ApJ, 611, 1005

[7] González Hernández, J. I., Casares, J., Rebolo, R., et al. 2011, The Astrophysical Journal, 738, 95

[8] Harrison, F. A., Craig, W. W., Christensen, F. E., et al. 2013, The Astrophysical Journal, 770

[9] Kafka, S. 2018, Observations from the AAVSO International Database, https://www.aavso.org

[10] Khargharia, J., Froning, C. S., & Robinson, E. L. 2010, The Astrophysical Journal, 716, 1105

[11] Kimura, M., Isogai, K., Kato, T., et al. 2016, Nature, 529, 54

[12] Lund, N., Budtz-Jørgensen, C., Westergaard, N. J., et al. 2003, Astronomy and Astrophysics, 411, L231

[13] Makino, F., Wagner, R. M., Starrfield, S., et al. 1989, International Astronomical Union Circular, 4786

[14] Mas-Hesse, J. M., Giménez, A., Culhane, J. L., et al. 2003, Astronomy and Astrophysics, 411, L261

[15] Miller-Jones, J. C. A., Jonker, P. G., Dhawan, V., et al. 2009, The Astrophysical Journal, 706, L230

[16] Sanwal, D., Robinson, E. L., Zhang, E., et al. 1996, The Astrophysical Journal, 460, 437

[17] Shahbaz, T., Ringwald, F. A., Bunn, J. C., et al. 1994, Monthly Notices of the Royal Astronomical Society, 271, L10

[18] Sivakoff, G. R., Bahramian, A., Altamirano, D., et al. 2015, The Astronomer's Telegram, 7959

[19] Ubertini, P., Lebrun, F., Di Cocco, G., et al. 2003, Astronomy and Astrophysics, 411, L131

[20] Walton, D. J., Mooley, K., King, A. L., et al. 2017, The Astrophysical Journal, 839, 110

[21] Winkler, C., Courvoisier, T. J., Di Cocco, G., et al. 2003, Astronomy and Astrophysics, 411, L1

Highlights on Spanish Astrophysics X, Proceedings of the XIII Scientific Meeting of the Spanish Astronomical Society held on July 16 – 20, 2018, in Salamanca, Spain. B. Montesinos, A. Asensio Ramos, F. Buitrago, R. Schödel, E. Villaver, S. Pérez-Hoyos, I. Ordóñez-Etxeberria (eds.), 2019

Clusters with K-type (super)giants.

J. Alonso-Santiago, I. Negueruela, A. Marco, and H. M. Tabernero

Dpto de Física, Ingeniería de Sistemas y Teoría de la Señal. Escuela Politécnica Superior. Universidad de Alicante. Apdo.99 E-03080. Alicante (Spain).

Abstract

Young open clusters are the natural laboratories to constrain stellar evolution models. During my PhD thesis we studied the red (super)giants hosted in six open clusters with the aim of exploring the boundary between AGB stars and RSGs. These clusters (NGC 2345, NGC 3105, NGC 6067, NGC 6649, NGC 6664 and Trumpler 35) were selected taking into account that their evolved stars, K (super)giants, covered the mass transition (5.5–$9.5\,\mathrm{M}_{\odot}$) around the minimum mass which produces a supernova explosion.
By combining photometry and low/moderate-resolution spectroscopy, we studied the clusters in order to obtain accurate ages (and masses) for their evolved stars. From FEROS spectra of the FGK (super)giants contained in the clusters we derived their stellar atmospheric parameters as well as their chemical abundances.
Besides the characterization of each cluster, the most complete to date, two remarkable results are found: i) the over-abundance of Ba found in young clusters (30-90 Ma), which supports the enhanced s-process and the role of i-process and ii) the relationship between spectral type and evolutionary stage of stars in open clusters: the AGB/RSG boundary could be related to the presence or lack in the cluster of K/M supergiants at solar metallicity.

1 Introduction

The initial mass with which a star is born is the fundamental parameter that will determine the evolution and properties of the star. According to their mass, stars follow two different evolutionary branches: either the red giant or the red supergiant phase (RSG). In the first case, the red giant evolves into an AGB star and ends its life expelling its outer layers in the form of a planetary nebula, leaving as a remnant a white dwarf. In the second, the RSG suffers a core collapse which releases a large amount of energy, exploding as a supernova (SN); the residual object is very compact (a neutron star or a black hole). The boundary between both scenarios would be approximately around 8–$9\,\mathrm{M}_{\odot}$, depending on models.

In recent years, several programmes for the search of SNe progenitors have been carried out ([21]). Their results are questioning the classical paradigm which explains the origin of these objects. The minimum mass to produce a SN explosion might be up to two solar masses below the limit traditionally accepted: stars of only 6–7 $M_\odot$ could become a SN in low-metallicity environments and binary systems [20], [12], [19]).

With the aim of exploring the border between stars that explode as a SN and those that do not, we resorted to the best laboratories to study stellar evolution: stellar clusters. In this work our goal is to provide for the first time a series of observational evidences that may serve to constrain theoretical models ([17]). To do this, we have studied a sample of evolved stars contained in young open clusters.

2 Sample, observations and analysis

We performed a literature search ([15]) for young open clusters with ages between 30–100 Ma, which cover the AGB/RGB mass transition according to recent works (6–9 $M_\odot$). We found that clusters in this age range have on average only two red (super)giants. Nevertheless, for our sample we selected the clusters statistically more significant, those containing at least five evolved stars, listed in Table 1. In total, they host half a hundred of (super)giants, comprising blue (A-type), yellow (F to early-G, including some Cepheids) and red ones (late-G to M). Most of them have K spectral types.

Table 1: Sample of bright giants and supergiants, i.e. (super)giants, contained in the target clusters.

Cluster	Age (Ma)	(Super)giants		
		Blue	Yellow	Red
NGC 2345	60	2	0	6
NGC 3105	30	2	1	5
NGC 6067	90	2	2	12
NGC 6649	60	0	2	3
NGC 6664	50	0	1	5
Trumpler 35	40	0	1	4

On the one hand, we carried out a classical photometric analysis study of every cluster in a consistent way by strengthening the photometry (our own or archival) with low- or moderate-resolution spectroscopy. In this manner, besides the characterisation of the cluster itself, we obtain the age and mass of its evolved stars. On the other hand, from high-resolution spectroscopy (R = 48 000) taken with FEROS ([13]), an échelle spectrograph mounted on the 2.2-m telescope at the La Silla Observatory (Chile), we characterised these stars by calculating both their atmospheric stellar parameters and chemical abundances.

In every cluster we performed the spectral analysis, when possible, for both blue (i.e. B-type giants and A supergiants) and FGKM stars. In the first case we used the technique described by [5] with a grid of FASTWIND synthetic spectra for deriving the atmospheric stellar parameters and, only for the earliest stars, some chemical abundances (C, N, O, Si, and Mg). For the FGK stars, the bulk forming our sample, we employed a tailored version of the STEPAR code [22] based on equivalent widths with the iron linelist of [10] an a grid of MARCS synthetic spectra. For these stars we obtained the abundances for Li, O, Na, Mg, Si, Ca, Ti, Ni, Rb, Y, and Ba. Finally, for the M-type stars we only could roughly estimate their stellar parameters by using the method described by [8] with the same grid used for the FGK stars.

3 Results

In this work we have performed the most complete study to date of the clusters contained in our sample. The in-depth analysis of NGC 3105 (see [2]) and NGC 6067 ([3]) are already available. For the remaining clusters the studies are going on and final results will still take some time.

For the first time, a detailed spectroscopic analysis has been carried out on stars of NGC 3105, NGC 6649, NGC 6664 and Trumpler 35. For the other two clusters, NGC 2345 and NGC 6067, the number of objects studied here is higher than that reported in the only paper previously published in each case. In this age range, our sample represents half the clusters observed spectroscopically and 87% of the evolved stars analysed.

We have worked in a very consistent way and our results show a great reliability. Stars according to their $\log g$ and $\log T_{\text{eff}}$ (derived spectroscopically) occupy positions on HR diagrams in good agreement with their expected evolutionary stage for the cluster age, inferred photometrically from the best-fitting isochrone (see Fig. 1).

For all clusters, using iron abundance as a proxy, we obtained metallicities compatible with the Galactic gradient derived from Cepheids ([9]), although our values are systematically somewhat lower (see Fig. 2). Chemical abundances are also compatible with the Galactic trend observed in the thin disc ([6], [1]) as well as the theoretical scenario which describes the chemical evolution of the Milky Way ([14]). Particularly noteworthy is the overabundance of [Ba/Fe] found in our sample, which probably supports the enhanced *s*-process and the additional contribution of the *i*-process suggested to explain the enrichment of Ba in young open clusters (see e.g. [7] and [16]).

Some of our obsevations conflict with current stellar evolution models. By the one hand, PARSEC models ([4]) fail when predicting the existence of Cepheids at supersolar metallicity in the age range in which we have worked. At metallicity higher than the solar value the blue loop decreases rapidly and moves away from the instability strip, where Cepheids spend almost their entire life. By the other hand, the observed ratios of evolved supergiants do not agree with those predicted by Geneva models ([11]), in which stars of 7–9 $M_\odot$ pass a significant fraction of their lifetime as blue supergiants in the blue loop, whereas these objects are usually observed leaving the main sequence.

Finally, we have covered a range of masses between 5.5–9.5 $M_\odot$. We have not found any significant trend in the chemical composition from red luminous giants to supergiants. We have not spotted any super-AGB star either. From an observational point of view, the transition of the spectral types observed in our sample, from medium- or late-K II/Ib to

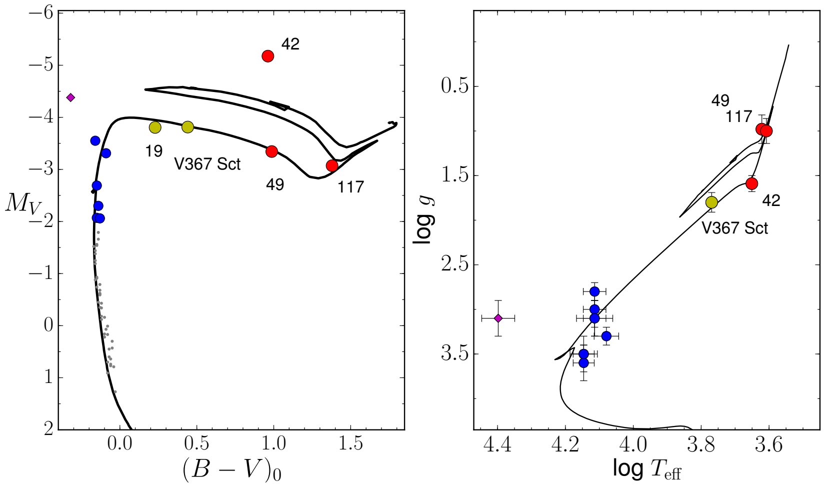

Figure 1: An example of the reliability of our results in the analysis of NGC 6649. Left: Dereddened $M_{\rm V}/(B-V)_0$ diagram. Right: $\log g\,/\log T_{\rm eff}$ Kiel diagram. Symbols are the same in both diagrams: the black line is the best-fitting isochrone (the same in both panels), the magenta diamond represents an extreme Be star, blue circles represent B stars (dwarfs and giants), whereas yellow and red circles are for F and K supergiants, respectively. Because of its binary nature star 42 occupies a wrong position on both diagrams. It has only been included in the figure to show all the cluster supergiants.

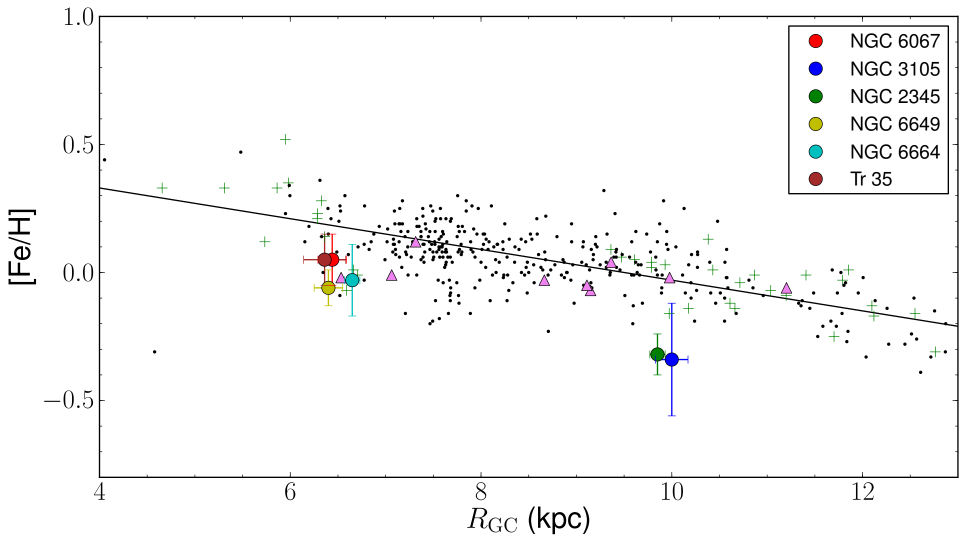

Figure 2: Iron abundance gradient in the Milky Way (black line) found by Genovali et al. 2014 ([9]) from Cepheids studied by them (green crosses) or taken from the literature (black dots). Pink triangles represent young open clusters (<500 Ma) compiled by [18]. Finally, coloured circles are the clusters studied by us.

early-M Ib, might be related to the AGB/RSG mass boundary at solar metallicity.

Acknowledgments

This research is partially supported by the Spanish Ministerio de Economía y Competitividad (MINECO) under grants BES-2013-065384 and AYA2015-68012-C2-2-P.

References

[1] Adibekyan, V. Th., Sousa, S. G., Santos, N. C., et al. 2012, A&A, 545, 32

[2] Alonso-Santiago, J., Negueruela, I., Marco, A., et al. 2018, A&A, 616, 124

[3] Alonso-Santiago, J., Marco, A., Negueruela, I., et al. 2017, MNRAS, 469, 1330

[4] Bressan, A., Marigo, P., Girardi, L., et al. 2012, MNRAS, 427, 127

[5] Castro, N., Urbaneja, M. A., Herrero, A., et al. 2012, A&A, 542, 79

[6] Delgado-Mena, E., Tsantaki, M., Adibekyan, V. Th., et al. 2017, A&A, 606, 94

[7] D'Orazi, V., Magrini, L., Randich, S., et al. 2009, ApJ, 693, 31

[8] García-Hernández, D. A., García-Lario, P., Plez, B., et al. 2007, A&A, 462, 711

[9] Genovali, K., Lemasle, B., Bono, G., et al. 2014, A&A, 566, 37

[10] Genovali, K., Lemasle, B., Bono, G., et al. 2013, A&A, 554, 132

[11] Georgy, C., Ekström, S., Eggenberger, P., et al. 2013, A&A, 558, 103

[12] Ibeling, D. & Heger, A. 2013, ApJ, 765, 43

[13] Kaufer, A., Stahl, O., Tubbesing, S., et al. 1999, The Messenger, 95, 8

[14] Magrini, L., Sestito, P., Randich, S., & Galli, D. 2009, A&A, 494, 95

[15] Mermilliod, J. C., Mayor, M., & Udry, S. 2008, A&A, 485, 303

[16] Mishenina, T., Pignatari, M., Carraro, G., et al. 2015, MNRAS, 454, 1585

[17] Negueruela, I., Alonso-Santiago, J., Tabenero, H. M., et al. 2017, MmSAI, 88, 368

[18] Netopil, M., Paunzen, E., Heiter, U., & Soubiran, C. 2016, A&A, 585, 150

[19] Podsiadlowski, Ph., Langer, N., Poelarends, A. J. T., et al. 2004, ApJ, 612, 1044

[20] Smartt, S. J. 2015, PASA, 32, 16

[21] Smartt, S. J. 2009, ARA&A, 47, 63

[22] Tabernero, H. M., Dorda, R., Negueruela, I., & González-Fernández, C. 2018, MNRAS, 476, 3106

Highlights on Spanish Astrophysics X, Proceedings of the XIII Scientific Meeting of the Spanish Astronomical Society held on July 16 – 20, 2018, in Salamanca, Spain. B. Montesinos, A. Asensio Ramos, F. Buitrago, R. Schödel, E. Villaver, S. Pérez-Hoyos, I. Ordóñez-Etxeberria (eds.), 2019

Do M dwarfs pulsate? The search with the Beating Red Dots project using HARPS.

Zaira M. Berdiñas [1], Eloy Rodríguez [2], Pedro J. Amado [2], Cristina Rodríguez-López[2], Guillem Anglada-Escudé [3], and James S. Jenkins[1]

[1] Departamento de Astronomía, Universidad de Chile, Camino el Observatorio 1515, Las Condes, Santiago, Chile.
[2] Instituto de Astrofísica de Andalucía–CSIC, Glorieta de la Astonomía S/N, E-18008 Granada, Spain
[3] School of Physics and Astronomy, Queen Mary University of London, 327 Mile End Rd., London, E1 4NS, UK.

Abstract

Only a few decades have been necessary to change our picture of a lonely Universe. Nowadays, red stars have become one of the most exciting hosts of exoplanets (e.g. Proxima Cen [1], Trappist-1 [8], Barnard's star [12]). However, the most popular techniques used to detect exoplanets, i.e. the radial velocities and transit methods, are indirect. As a consequence, the exoplanet parameters obtained are always relative to the stellar parameters. The study of stellar pulsations has demonstrated to be able to give some of the stellar parameters at an unprecedented level of accuracy, thus accordingly decreasing the uncertainties of the mass and radii parameters estimated for their exoplanets. Theoretical studies predict that M dwarfs can pulsate, i.e. they can drive and maintain stellar oscillations, however, no observational confirmation has been reported yet. The Beating Red Dots project uses the HARPS and HARPS-N high-resolution spectrographs with the aim of detecting pulsations in M dwarfs for the first time. Here, we summarise the project details as well as presenting the first results and future prospects.

1 Introduction

Stars are not static spheres of plasma in an immutable state. Magnetic cycles, granulation, or plasma ejections are just examples of their variable nature. These are mechanisms the stars undergo to come back to its equilibrium. Similarly, stars can also show oscillations on their stellar surfaces. These oscillations can be explained as periodic contractions and expansions of the star's outer layers driven by energetic processes that occur in the inner layers of the

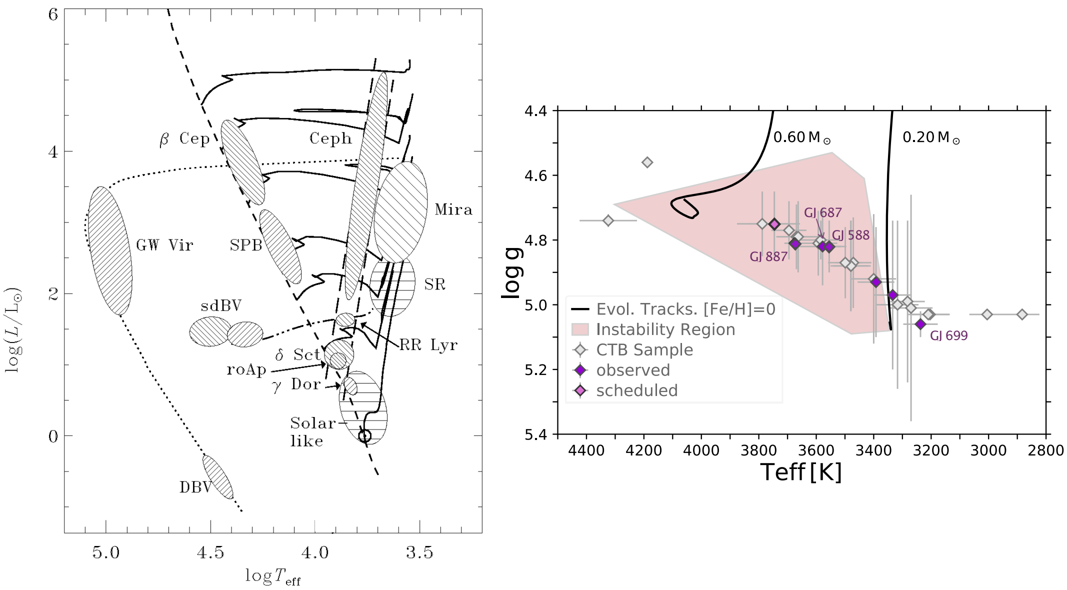

Figure 1: (Right) Pulsations HR diagram. Stripped areas highlight different pulsating regimes. Stars of different masses, radii, ages and spectral types can drive and maintain stellar pulsations. However, no pulsation areas appear for M dwarfs, located at the lower right part of the main-sequence. *Source: SOHO14/GONG workshop (2004).* (Left) Instability region (pink-shaded area) of main-sequence M dwarfs predicted by Rodríguez-López et al. [14] over the sample (grey diamonds). The dark and light pink diamonds correspond to targets observed with at least four consecutive nights at high-cadence and to scheduled targets, respectively. The dark lines are the evolutionary tracks at 0.6 and 0.2 M⊙ that delimit the instability region. *Adapted from Berdiñas et al. [6].*

star such as nuclear reactions or energy stacking at certain energy transitions layers (e.g. the radiative-to-convective transition zone). The theory of asteroseismology makes use of these stellar oscillations to permeate throughout the stellar atmosphere. This allows to measure the physical parameters of the star at an unprecedented level of accuracy. Characterising the star parameters very precisely not only has a great impact in stellar physics but also in the field of exoplanets. Most techniques used to detect exoplanets are indirect methods, meaning that exoplanet candidates are confirmed by the changes they induce in the starlight. As a consequence of that, the exoplanet parameters and their uncertainties are defined relative to the host star. The study of the stellar pulsations of the stars hosting exoplanets has demonstrated to provide parameters such as the planet mass and radius –essential to know if the planet density supports a rocky surface– with precisions down to 5% [9], and 2-4%[7], respectively. Among the roughly four thousand exoplanets discovered, only fourteen are considered as potentially habitable[1], twelve of them orbiting M-type red dwarf stars. Thus,

[1]Exoplanets are considered as potentially habitable if they are likely to have: i) a rocky composition, i.e. $R_{\rm p}[R_\oplus]\sim(0.5,1.5)$ and $M_{\rm p}[M_\oplus]\sim(0.1,5)$, and ii) surface liquid water, i.e. is they orbit in temperate orbits within the conservative habitable zone [10].

the use of the asteroseismology should in theory help in characterising some of most exciting exoplanetary systems. Stellar pulsations appear all across the HR diagram (Fig.1, left panel), where different oscillation mechanisms dominate the different instability regions. However, no stellar oscillations have been detected for this spectral type yet. Thus, the question is: do M dwarfs pulsate?

Theoretical studies carried out by our team indicate that M dwarfs should be able of driving and maintaining stellar pulsations. In particular, Rodríguez-López et al. [15, 14] predict two main instability regions for M dwarfs, one dominated by young stars and the other by partially-convective M dwarfs in the main-sequence. Our model predicts for the stars in the main-sequence region oscillations with periods ranging from 20 min up to 3 h. However, the detectability of these oscillations would directly depend on their amplitudes. However, the current existing linear oscillation codes cannot predict the amplitude of these oscillations. Previous observational attempts to detect these oscillations using photometric data from the the *Kepler* spacecraft have established upper limits for the amplitudes of a few μmag [13]. Although this is a very low photometric limit, it does not imply that stellar pulsations cannot be detected using other technique such as the radial velocity (RV) method. This statement is based on previous studies performed for other spectral types in which a combination of photometric and spectroscopic observations demonstrated that amplitudes can be up to 100 times larger in RVs (e.g. δ Scuti and γ Dor oscillators such as FG Vir, RZ Cas, HR 8799; [17; 11; 16]). This would mean that a 10 μmag signal could have a counterpart of 1 m/s in RVs; a signal that should be detectable with current most precise spectrographs. This is the main goal of our "Beating Red Dots" programme, that would open a new field of study for this spectral type.

2 Previous work on the field

"Beating Red Dots" (BRD) was born in 2013 under the name of "Cool Tiny Beats" (CTB). This precursor campaign joined efforts from several exoplanet and asteroseismology teams to detect, using a single observational strategy, close-in orbit exoplanets hosted by M dwarfs as well as the first observational confirmation of a stellar pulsation signal for this spectral type. CTB used the high-precision spectrographs HARPS and HARPS-N to observe a sample of main-sequence M dwarfs with a strategy based on getting short time spans between exposures (i.e. high-cadence). This should have ensured the monitoring of exoplanets in the innermost circumstellar regions, as well as the predicted 20 min to 3 h periods of the stellar pulsations. However, even when the observing cadence was adequate for the exoplanet science case (e.g. Proxima b [1], Kapteyn b and c [2], Luyten b and c [3; 4]), only a few targets were finally observed with the extremely high-cadence that is essential to monitor the predicted stellar pulsations of M dwarfs: GJ 725A and B as well as GJ 588 and GJ 699 (Barnard's star). The first two stars were monitored from HARPS-N, where we detected a source of sub-night instabilities in the RVs that made it difficult to study the stars behaviour in the same time regime. Nevertheless, the analysis of these high-cadence CTB observations gave us a large experience that resulted in a detailed characterisation study of the instrument [5]. On the contrary, GJ 588 and Barnard's star were observed from HARPS. In that case, even when

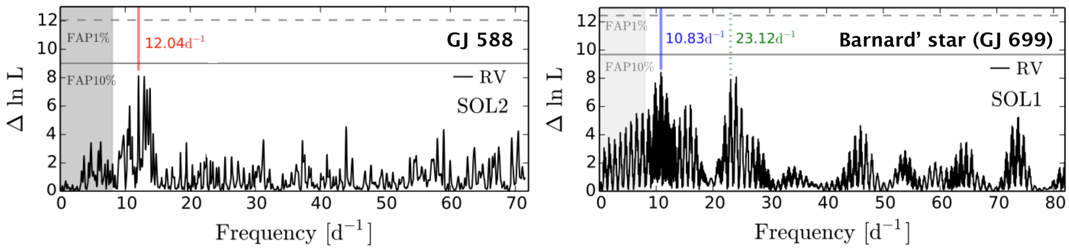

Figure 2: Likelihood periodogram of the GJ 588 (left) and Barnard's star (right) RV time-series observed with CTB during 2013. GJ 588 was modelled with two sinusoids ("SOL2"). The grey area highlights frequencies outside the predicted pulsation regime. Horizontal dashed and solid lines account for 10% and 1% FAPs. No significant signals compatible with pulsations were found above these thresholds, however, the noise seems not being purely white. The vertical red line highlights a putative signal at 12 c/d that resulted to be compatible with an exited pulsation mode in GJ 588.

no signals compatible with pulsations were detected above the classical confidence thresholds of periodograms (false-alarm probability, or FAP=1%), we detected some excess of power in the periodograms of both stars (see Fig.2). Such excess could correspond to real non-resolved, low-amplitude oscillation signals that cannot be detected with the precision of our observations. In fact, the highest peak of the periodogram of GJ 588, that corresponds to a sinusoid with a frequency of 12 c/d (P$\sim$2 h, A=0.36 m/s), was found to be compatible with excited low-radial, low degree l=1 and l=2 g-modes produced in stellar theoretical models with the physical parameters of GJ 588. However, higher precision data were needed to confirm/refute this putative 12 c/d signal.

3 The Beating Red Dots programme: First results

Motivated by the detection of a putative stellar pulsation signal on GJ 588, we decided to push the search with a new dedicated programme: "Beating Red Dots" (BRD). This programme is focused on gathering observations with the adequate cadence needed to detect stellar pulsations in M dwarfs (i.e. continuos monitoring of each target during at least four consecutive nights). Our observational strategy includes photometric campaigns from the ASH2 and LCOGT telescopes to help us distinguishing between actual stellar pulsations and ultra-short period planets.

Currently, eight nights have been allocated during P101 in HARPS to observe the BRD sample (see diamonds in Fig.1, right panel) and a second run is scheduled for P102. Besides, another four nights have been awarded in HARPS-N. The P101 observations from HARPS were performed between May and September this year. The targets selected were GJ 588 and GJ 887. Simulations perform based on previous observations indicated that four extra nights of GJ 588 data should be enough to detect the 12 c/d putative candidate. However, the four nights obtained in 2018, together with the previously data obtained in 2013, revealed no significant signals above the detection threshold within the predicted pulsation regime (see

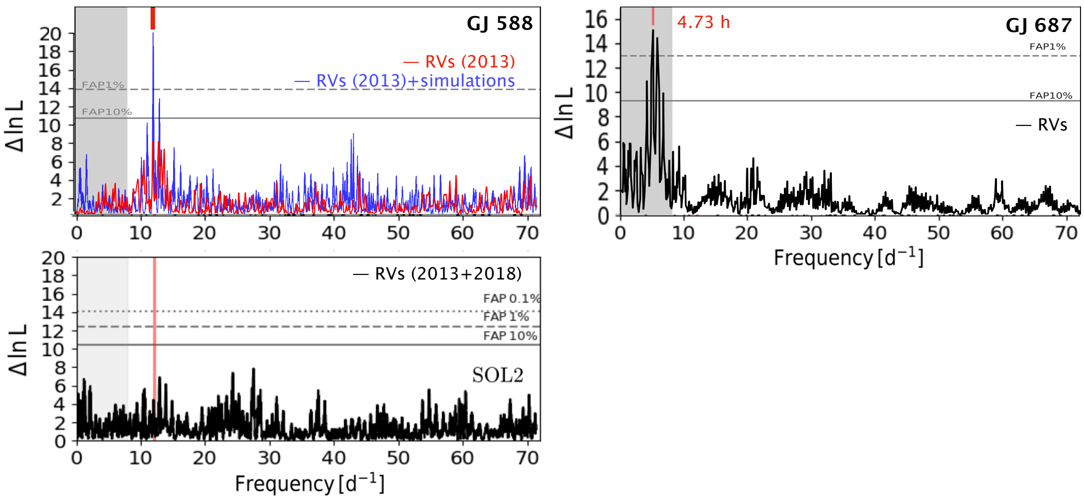

Figure 3: (Right) The top figure compares the 2013 periodogram of GJ588 (red line), with our predicted result after adding four extra nights of high-cadence observations in 2018 (blue line). The bottom panel corresponds to real 2013+2018 observations. The lack of detections ruled out the putative 12 c/d signal obtained in 2013. (Left) Periodogram of the first M dwarf observed from HARPS-N. A peak at 4.73 h was detected above the 1%-FAP. Its origin is under study.

Fig 3, left panels). A similar case occurred with GJ 887, observed during 4 nights in Sep 2018. However, the RV periodogram of GJ 687, the only target observed from HARPS-N, showed a 4.73 h periodic signal. Although this signal is outside the predicted pulsation period range, it is not very far away (see Fig 3, right panel). However, a more detailed analysis is required to rule out a spurious detection especially because this star is the host of an exoplanet.

4 Conclusions and future work

Consequently, the fact that no strong detections were made can be attributed to: i) the sample not being statistically significant (only a few targets have been analysed), ii) the instability strip is not pure and we analysed non-pulsators, iii) the detection limits reached were not enough and pulsating amplitudes were buried in the noise, iv) oscillations are not spectroscopically detectable, and/or v) shortcomings in the theoretical models lead us to wrongly predict the excitation of M-dwarf modes, although we do not think this is the case (see [13]). At least, points i) and ii), are very plausible and both can be addressed by increasing the size of the analysed sample and pushing down the detection thresholds. Regarding point iii), we plan to make use of the better sensitivity and radial velocity precision (goal of 10 cm/s) of ESPRESSO/VLT (0103.D-0005 proposal submitted, PI: Berdiñas). Additionally, we also plan to extend the search towards the near infrared using instruments such as CRIRES+/VLT, NIRPS/VLT or CARMENES/CAHA. This wavelength coverage extension is motivated by the fact that stellar pulsation signatures for other spectral types show amplitudes and phases varying systematically with wavelength.

In summary, regardless of the current negative results, the BRD survey is taking us one step closer to the observational detection of M star pulsations and illustrating the challenges of high precision experiments even with current state-of-the-art spectrographs.

Acknowledgments

Z.M.B. acknowledges funds from CONICYT/FONDECYT POSTDOCTORADO 3180405. P.J.A., C.R-L. and E.R. acknowledge funding from AYA2016-79425-C3-3-P by MICINN/Spain. This study is based on observations made with the 3.6 m ESO Telescope at la Silla and with the Italian Telescopio Nazionale Galileo (TNG) operated on the island of La Palma by the Fundación Galileo Galilei of the INAF (Istituto Nazionale di Astrofisica) at the Spanish Observatorio del Roque de los Muchachos of the Instituto de Astrofísica de Canarias under programmes ID 191.C-0505, 0101.D-0494 and CAT_83, CAT13B_136, CAT14A_43, and CAT17A_95, respectively.

References

[1] Anglada-Escudé, G., Amado, P. J., Barnes, J., et al. 2016, Nature, 536, 437

[2] Anglada-Escudé, G., Arriagada, P., Tuomi, M., et al. 2014, MNRAS, 443, L89

[3] Astudillo-Defru, N., Forveille, T., Bonfils, X., et al. 2017, A&A, 602, A88

[4] Berdiñas, Z. M. 2016, PhD thesis, Instituto de Astrofísica de Andalucía-CSIC; Universidad de Granada

[5] Berdiñas, Z. M., Amado, P. J., Anglada-Escudé, G., Rodríguez-López, C., & Barnes, J. 2016, MNRAS, 459, 3551

[6] Berdiñas, Z. M., Rodríguez-López, C., Amado, P. J., et al. 2017, MNRAS, 469, 4268

[7] Chaplin, W. J., Basu, S., Huber, D., et al. 2014, ApJS, 210, 1

[8] Gillon, M., Triaud, A. H. M. J., Demory, B.-O., et al. 2017, Nature, 542, 456

[9] Huber, D., Ireland, M. J., Bedding, T. R., et al. 2012, ApJ, 760, 32

[10] Kopparapu, R. K., Ramirez, R. M., SchottelKotte, J., et al. 2014, ApJ, 787, L29

[11] Lehmann, H. & Mkrtichian, D. E. 2004, A&A, 413, 293

[12] Ribas, I., Tuomi, M., Reiners, A., et al. 2018, Nature, 563, 365

[13] Rodríguez, E., Rodríguez-López, C., López-González, M. J., et al. 2016, MNRAS, 457, 1851

[14] Rodríguez-López, C., MacDonald, J., Amado, P. J., Moya, A., & Mullan, D. 2014, MNRAS, 438, 2371

[15] Rodríguez-López, C., MacDonald, J., & Moya, A. 2012, MNRAS, 419, L44

[16] Zerbi, F. M., Garrido, R., Rodriguez, E., et al. 1997, MNRAS, 290, 401

[17] Zima, W., Wright, D., Bentley, J., et al. 2006, A&A, 455, 235

Highlights on Spanish Astrophysics X, Proceedings of the XIII Scientific Meeting of the Spanish Astronomical Society held on July 16 – 20, 2018, in Salamanca, Spain. B. Montesinos, A. Asensio Ramos, F. Buitrago, R. Schödel, E. Villaver, S. Pérez-Hoyos, I. Ordóñez-Etxeberria (eds.), 2019

Evolved Open Clusters in the Gaia era: the case of the Hyades.

Casamiquela, L. [1], Soubiran, C.[1], Olivares, J.[1], Bouy, H.[1], Ikhenache, N.[1], Jofré, P.[2], Blanco-Cuaresma, S.[3], and Heiter, U.[4]

[1] Laboratoire d'Astrophysique de Bordeaux, Univ. Bordeaux, CNRS, France
[2] Núcleo de Astronomía, Facultad de Ingeniería y Ciencias, Universidad Diego Portales, Santiago De Chile, Chile
[3] Harvard-Smithsonian Center for Astrophysics, Cambridge, MA 02138, USA
[4] Department of Physics and Astronomy, Uppsala University, Uppsala, Sweden

Abstract

Evolved Open Clusters (OCs) are excellent tracers of the formation and evolution of the galaxy, as well as an ideal laboratory to test theories of star formation and evolution. In particular, nearby OCs are commonly used as benchmark objects to assess the determination of physical properties of field stars. We have designed a project to perform an in-depth study of the physical properties of a sample of benchmark evolved clusters inside a radius of 500 pc around the Sun. We aim to determine shape, radii, extinction, galactic velocity, age and chemical composition, using recent data from Gaia DR2, and complementary ground-based high resolution spectroscopic data. Here we present the first results of this project after the release of Gaia DR2 concerning the Hyades, the most nearby open cluster. We do a membership selection around a large region from the cluster center. And we perform a spectroscopic analysis of the cluster using HARPS spectra of main sequence stars and red giants. We obtain chemical abundances for 11 species with a typical precision of 0.01 dex.

1 Introduction

Open Clusters (OCs) are widely used to trace the history of the Galactic disk. Also, since their stellar populations cover a wide range of masses and evolutionary phases, their HR diagrams represent snapshot in stellar evolution. That is why they are ideal to test theories of stellar evolution. In particular, nearby OCs spanning different ages and chemical compositions are perfect targets to calibrate and validate astrometric, photometric and spectroscopic surveys.

The majority of them dissolve during the first 100 Myr of evolution. Internal interaction between members, encounters with giant molecular clouds and gravitational harrassment by the galactic potential are the processes which contribute to the disruption of an OC. For this reason, OCs which have survived these effects are valuable targets to understand them.

We have designed a project devoted to determine physical properties of the most nearby and evolved OCs in the light of Gaia data and combined with high precision spectroscopy. This will allow to investigate a handful of things: explore the outskirts of the clusters looking for tidal tails and escapees, which provide information about disruption processes, and relate this to the chemical signature; explore how do the kinematical properties correlate with age and environment; among others. We also aim to provide a comprehensive investigation of benchmark OCs to be used to validate and calibrate future studies and large surveys. So far, we are also in process of revisiting the old nearby OC Ruprecht 147 [9]

In the presented context the Hyades play a significant role being the nearest OC to the Sun, and among the best studied stellar groups. Recently, [1] used the *T*ycho-Gaia astrometric solution (TGAS) results from Gaia DR1 ([2]) to build a membership list in a large area up to 30 pc from the center of the cluster. This makes a good opportunity to test with good statistics the typical dispersion of abundances, or whether there are variation of abundances depending on the distance from the center of the cluster. We do a preliminary analysis with a membership selection using cartesian heliocentric velocities calculated from Gaia DR2 results ([3]). We retrieve several spectra of main sequence and giant stars to do a chemical abundance analysis and test the chemical homogeniety of this cluster.

2 Membership selection

After the Gaia DR2 ([3]) we have performed our own membership selection to recover members up to 30 pc from the center. We have queried the catalog 40° around the center of the cluster $(\mathrm{RA}, \mathrm{DEC}) = (67°, 16°)$, restricting to stars having v_r, and parallaxes $\varpi > 10$ mas. We have constrained the sample using stars with low errors in parallax and proper motions: $\delta\varpi < 0.3$ mas, $\delta\mathrm{pm} < 0.3\,\mathrm{mas\,yr^{-1}}$. Because of its large extension in the sky we have changed to cartesian heliocentric coordinates using the package *p*ygaia to avoid the projection effects in proper motions. After all thi, we obtain 8119 stars in the selected region.

We have used the most central stars ($60 < \mathrm{RA} < 75°$, $10 < \mathrm{DEC} < 25°$) to intially pinpoint the motion of the cluster. Then we do a selection of the whole sample of stars cutting at 2σ in the cartesian velocities. Finally we recalculate the center of the cluster with these stars and we restrict the final selection to 30 pc.

We obtain 167 members with median values of: (X, Y, Z)= $(-43\pm8, 1\pm7, -17\pm4)$ pc, (U, V, W)= $(-42.3\pm0.6, -19.2\pm0.3, -1.2\pm0.4)$ $\mathrm{km\,s^{-1}}$. Their distribution in the 6D space, and the resulting color-magnitude diagram (CMD) are shown in Figure 1. The resulting sample is incomplete because only the brighter stars with a RV in Gaia DR2 have been considered. This selection is well adapted for our study of chemical composition of the cluster but not to derive its physical parameters.We obtain a very consistent HR diagram, which ensures us that the recovered stars are true members. There are four known K giants in the cluster which we do not recover for being out of the bright limit of Gaia DR2.

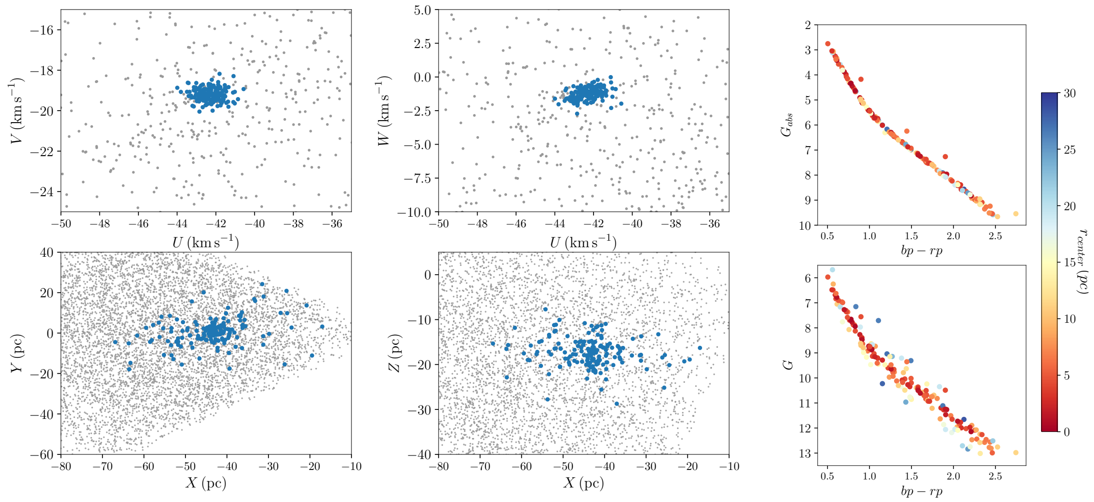

Figure 1: *L*eft: Distribution in velocity (top panels) and physical (bottom panels) space of the selected stars as members of the Hyades (blue), and the whole analyzed sample (grey). *R*ight: CMD diagram in apparent and absolute magnitudes from Gaia DR2 of the selected stars, they are colour-coded according to the distance to the center of the cluster.

3 Spectroscopic analysis

With this selection we have queried the HARPS (R=115,000) archive looking for high-resolution and high SNR (> 100) spectra. We have retrieved spectra for 21 main sequence (MS) stars and of the 2 giants[1] with 7 and 12 spectra each.

We have used iSpec [4] to derive atmospheric parameters and abundances from spectral synthesis fitting using a grid of precomputed synthetic spectra available in the new version of iSpec (Blanco-Cuaresma et al., in prep). The derived $T_{\rm eff} - \log g$ diagram is shown in Figure 2. In general, stars with $T_{\rm eff} > 6500$ K show wider correlation peak in the cross-correlation function. This has an impact in the derived abundances adding more line-by-line dispersion. So, for our purpose, we have focused in the range 6300-5300 K, which are solar-type stars, colored in blue in the left panel of Figure 2. This effect has direct consequences in the expected precision of Galactic archaeology surveys which usually tag giants or turnoff stars because of their brightness.

3.1 Chemical abundances

Chemical abundances are obtained from spectral synthesis fitting using iSpec. In brief, it compares regions of the observed spectrum with synthetic ones generated on-the-fly. The line selection was done based on the automatic detection of absorption lines in a solar spectrum from the Gaia Benchmark Stars library ([5]). Each line was cross-matched with the atomic

[1] In fact, we found spectra for 3 giants. However, one of them gave inconsistent results of abundances, probably because it is an spectroscopic binary. Therefore, we have not included its analysis.

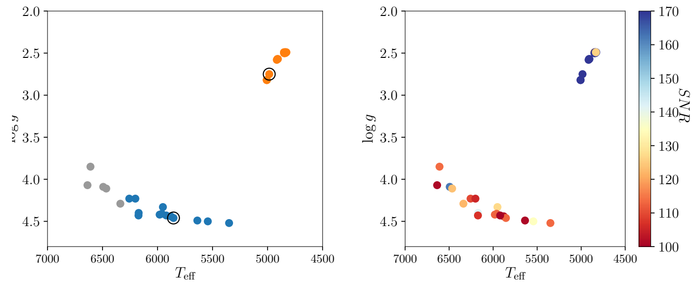

Figure 2: $T_{\rm eff} - \log g$ diagram of the stars in the Hyades observed with HARPS. In the right panel the stars are coloured SNR of the spectrum, and in the left panel we show the two groups of stars made to derive the differential abundances (orange-red giants, and blue-solar type) and the reference star chosen.

line list and we derived solar line-by-line chemical abundances using the reference atmospheric parameters for the Sun. Good lines lead to abundances similar to the solar ones ([7]), thus we selected all lines with an abundance that falls in the range ± 0.05 dex. Atomic data is taken from the v5 of the Gaia-ESO survey master line list ([8]).

We have used a strictly line-by-line differential abundance strategy to obtain abundances of 11 different species including Fe-peak and α elements. This technique consists in using a reference star within the cluster which is in the same evolutionary state as the other stars. This allows to reach a very high precision in abundances (~ 0.01 dex) because it erases the differences that arise from slightly wrong atomic parameters in the lines and other effects. The purpose is to show how different are the stars among them. We have made this in two groups: solar type stars using as reference HIP19793, and giants with reference HIP20885. References are indicated in Figure 2. Typical errors in the obtained abundances are of the order of 0.01 dex. This can be checked using the different spectra that we have for HIP20889, which are analysed as if they were different stars. As shown in Figure 3, indeed the 12 spectra of the star give dispersions of the order of 0.01 dex.

We have not found any significant trend of the derived abundances with $T_{\rm eff}$ or $\log g$. However, if we plot the abundance of each element with respect to all the others, very significant correlations show up (see Figure 4). Also, almost all elements show an amplitude in abundance of 0.1 dex, one order of magnitude larger than the typical error. It is improbable that these trends are caused by random errors. Furthermore, most of the stars are physically very similar and doing a differential analysis, the difference in abundance could not be explained by difference in diffusion. This leads to think that in the cluster some of the stars have different abundances, as already reported [6].

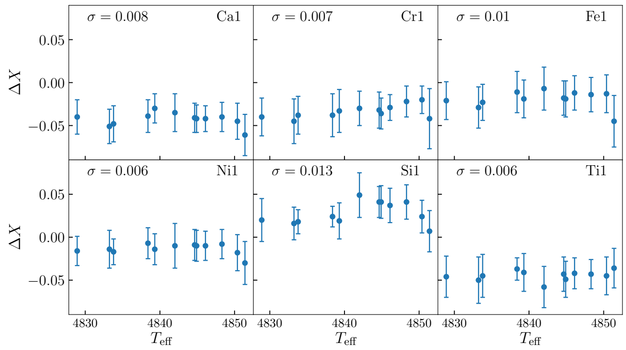

Figure 3: Differential abundances (based on lines of neutral Ca, Cr, Fe, Ni, Si, Ti) for the 12 spectra of the giant star HIP20889 as a function of the derived effective temperature. Abundance dispersion is indicated in each panel

Acknowledgments

This research made use of the SIMBAD database, operated at the CDS, Strasbourg, France, NASA Astrophysics Data System, and the TOPCAT tool version 4.5. This work has made use of the VALD database, operated at Uppsala University, the Institute of Astronomy RAS in Moscow, and the University of Vienna. We acknowledge financial support from the "Programme National Cosmologie et Galaxies" (PNCG) of CNRS/INSU. U.H. acknowledges support from the Swedish National Space Agency (SNSA/Rymdstyrelsen)

References

[1] Reino, S. et al. 2018, MNRAS, 477, 3197

[2] Gaia Collaboration et al. 2016, A&A, 595, A2

[3] Gaia Collaboration et al. 2018, A&A, 616, A1

[4] Blanco-Cuaresma, S. et al. 2014, A&A, 569, A111

[5] Blanco-Cuaresma, S. et al. 2014b, A&A, 566, A98

[6] Liu, F. et al. 2016, MNRAS, 457, 3934

[7] Grevesse, N. et al. 2007, SSRv, 130, 105

[8] Heiter, U. et al. 2015, Physica Scripta., 90, 054010

[9] Casamiquela, L. et al. 2018, "The 20th Cambridge Workshop of Cool Stars, Stellar Systems and the Sun (CS20)", Boston, MA, `https://doi.org/10.5281/zenodo.1452285`

Figure 4: Differential abundances of all elements with respect to all others. Solar-type stars plot in blue, giants in orange.

Highlights on Spanish Astrophysics X, Proceedings of the XIII Scientific Meeting of the Spanish Astronomical Society held on July 16 – 20, 2018, in Salamanca, Spain. B. Montesinos, A. Asensio Ramos, F. Buitrago, R. Schödel, E. Villaver, S. Pérez-Hoyos, I. Ordóñez-Etxeberria (eds.), 2019

Detection of new Open Clusters with *Gaia*.

A. Castro-Ginard[1], C. Jordi[1], X. Luri[1], L. Balaguer-Núñez[1], and T. Cantat-Gaudin[1]

[1] Dept. Física Quàntica i Astrofísica, Institut de Ciències del Cosmos (ICCUB), Universitat de Barcelona (IEEC-UB), Martí i Franquès 1, E08028 Barcelona, Spain.

Abstract

The publication of the *Gaia* Data Release 2 (*Gaia* DR2) includes precise astrometric data (positions, proper motions and parallaxes) for more than 1.3 bilion sources, mostly stars. This such a vast amount of new data requires the use of machine-learning and data-mining techniques to handle large scale analysis. In particular, the search for open clusters (OCs), groups of stars that were born and move together, located in the disc, is a great example for the application of these techniques.

We explore the performance of a density based clustering algorithm, DBSCAN, to find clusters in the data together with a supervised learning method such as an Artificial Neural Network (ANN) to automatically distinguish between real OCs and statistical clusters.

The development and implementation of this method in a five-dimensional space $(\alpha, \delta, \varpi, \mu_{\alpha^*}, \mu_\delta)$ of the *Tycho-Gaia* Astrometric Solution (TGAS) lead to the proposal of a list of new nearby OCs candidates. This contribution shows the validation of the candidates with *Gaia* DR2 data and a framework designed to be applied to the full *Gaia* DR2 archive.

1 Introduction

The analysis of astronomical catalogues is becoming more complex as the data volume of these catalogues is increasing. For instance, the *Gaia* mission [1] in its first data release (*Gaia* DR1 [2]) contains positions for more than one bilion sources. Even though this large amount of sources, full five-parameter astrometric data is available only for a small subset: the *Tycho-Gaia* Astrometric Solution (TGAS [3, 4]). The TGAS subset represents a perfect scenario to develop and test scientific applications, based on data-mining techniques and machine-learning algorithms, in preparation for larger releases. The use of these techniques is mandatory from the second *Gaia* data release (*Gaia* DR2 [5]) onwards, which contains precise five-parameter astrometric data for more than 1.3 bilion sources, together with three-band photometry.

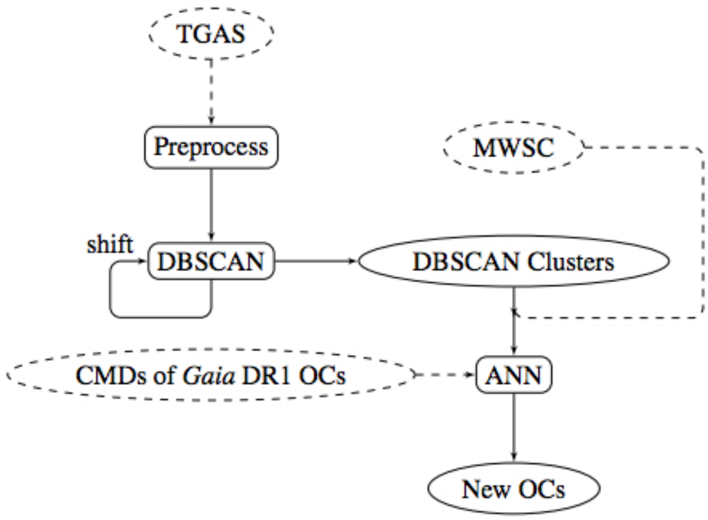

Figure 1: Application of the method represented by a flow chart diagram. Figure taken from Fig. 1 in [6].

We have developed a method [6] to automatically search for overdensities in the five-dimensional astrometric data, *i.e.* positions, parallax and proper motions $(\alpha, \delta, \varpi, \mu_{\alpha^*}, \mu_\delta)$, and decide if they are open clusters (OCs) based on the photometry (G, G_{BP}, G_{RP}). The method is developed and tested on the TGAS subset, with the final goal of its application to the full *Gaia* DR2 archive.

2 Method

Figure 1 shows a diagram of the methodology used to identify possible new OCs. Using TGAS as our initial database, we apply an unsupervised learning algorithm such as DBSCAN [7] to detect groups of stars showing an overdensity in the five-parameter space. Then, these overdensities are classified into statistical clusters or physical OCs using an Artificial Neural Network (ANN [8]), which identifies an isochrone on a Color Magnitude Diagram (CMD). In this case, because the TGAS subset is purely astrometrical data, the CMD is built using the photometric data from the *Two Micron All Sky Survey* catalogue (2MASS [9]).

2.1 Preprocessing

Before the application of the method, we select a region of the sky where we expect to find most of the clusters. According to existing OCs catalogues such as the DAML [10] and MWSC [11], most of the clusters are found at $|b| < 20$deg (96% and 94% respectively). In addition, we reject stars with high or negative parallaxes (selecting only stars with 0mas$\leq \varpi \leq$ 7mas) or with high proper motions ($|\mu_{\alpha^*}|, |\mu_\delta| > 30mas\cdot$yr^{-1}); this facilitates the determination of the DBSCAN parameters with no loss of generality since these conditions would make an OC easily detectable.

The region of study is further divided into smaller rectangles of size L deg. This second division is done to reduce the volume of data in each region in order to reduce computational time; and to define a more representative density of field stars, so the algorithm can search for a significant overdensity in that region. As a last step, because the algorithm computes the distance between pairs of stars in the five-dimensional parameter space, and decides if they are clustered or not based on these distances, we standarise the star parameters (to have mean zero and variance one) so their weights in the process are the same.

2.2 DBSCAN

DBSCAN is a density-based clustering algorithm that identifies overdensities in the parameter space as clusters. The definition of what DBSCAN considers a cluster depends on two parameters: ϵ and *minPts*. The parameter *minPts* refers to the minimum number of members of a cluster, while ϵ refers to the radius of the hypersphere (in the parameter space) centred in each star where this *minPts* members have to be located (see Fig. 2 of [6]).

The determination of the *minPts* parameter, together with L, is left to be optimised using simulations (see Sect. 3 of [6] for details). The values for these parameters found to be optimal in this case are: $L = \{12, 13, 14, 15, 16\}$ and *minPts*$= \{5, 6, 7, 8, 9\}$.

For the determination of ϵ, we take advantage of the fact that the distance from a star to its k_{th} nearest neighbour from stars belonging to the cluster is smaller than from stars belonging to the field. Figure 2 shows an example of the determination of ϵ in a region around a known cluster, the red line (ϵ) separates the stars belonging to the cluster (green) from the stars belonging to the field (orange).

2.3 Identification of OCs

DBSCAN finds clusters in an statistical sense, they can be real OCs or just statistical clusters. To distinguish between these two posibilities, we use an ANN with a multilayer perceptron arquitecture with one hidden layer. The ANN is able to recognise the isochrone pattern in the CMD, and therefore identify real OCs among all the candidates. This is achieved by training the ANN with examples of CMDs of real OCs. Since we work with TGAS data, the OCs examples are those from the *Gaia* DR1 [12]. The test CMDs are classified with a precision of a 97.05% to the right class, OC or statistical cluster.

Because the ANN is trained with clusters from [12], we expect to find clusters with the same characteristics. The OCs used to train the ANN are nearby clusters with ages from 40 to 850 Myr and no significant differential extinction.

3 Results

The whole method is applied to the TGAS data, and after the removal of coincident clusters with [11], we end with a list of 31 probable OC candidates (see Table 1 in [6], cluster candidates

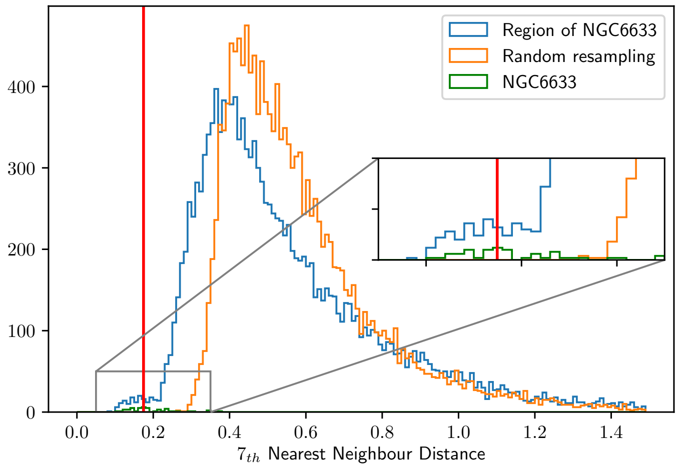

Figure 2: Histogram of 7_{th}-NN distances of a region around NGC6633 (in blue), stars belonging to NGC6633 (in green) and random realization of field stars in that region (in orange). Figure taken from Fig. 3 in [6].

are sorted by number of detections through the explored parameters). Each of the OC candidates is then analysed using *Gaia* DR2 data, which provides more precise astrometric data, photometry more precise than that of 2MASS catalogue and the availability of those parameters down to magnitude $G \sim 21$.

In order to confirm or discard each OC candidate, the DBSCAN algorithm is executed on a *Gaia* DR2 region around the expected centre of the candidate. With this last step, we are able to confirm 23 OC candidates with members down to magnitude $G \leq 17$. These 23 confirmed OCs represent a 70% of the proposed candidates; 100% of the initial OCs candidates found with $N_{\text{found}} \geq 5$ among the explored parameters are confirmed, while for $N_{\text{found}} < 5$ we are able to confirm 59% of the initial candidates. Mean values for position, parallax and proper motion, as well as for radial velocity when available, can be found in Table 2 of [6]. General comments and comments on individual proposed new OCs can be also found in [6].

4 Conclusions

We describe an automated data-mining method for the detection of OCs. The method is based on the use of machine learning techniques such as a clustering algorithm, DBSCAN, to detect overdensities in astrometric data; and a classification algorithm, an ANN, to distinguish between statistical clusters and real OCs.

The application of the method to TGAS data allows the proposal of 31 new OCs candidates, of which 23 (around 70%) are validated using *Gaia* DR2 data.

Looking forward to the application of the method to the all-sky *Gaia* DR2, we have to optimize the parameters L and $minPts$ to account for the larger stellar densities. As well, the better characterization of known OCs [13] with DR2, provides a wider training set for the ANN step.

Acknowledgments

This work was supported by the MINECO (Spanish Ministry of Economy) through grant ESP2016-80079-C2-1-R (MINECO/FEDER, UE) and MDM-2014-0369 of ICCUB (Unidad de Excelencia 'María de Maeztu'). This work has made use of the data from the European Space Agency (ESA) mission Gaia, processed by the Gaia Data Processing and Analysis Consortium (DPAC). Funding for the DPAC has been provided by national institutions, in particular the institutions participating in the Gaia Multilateral Agreement.

References

[1] Gaia Collaboration (Prusti, T. et al) 2016, A&A 595, A1

[2] Gaia Collaboration (Brown, A.G.A., et al.) 2016, A&A, 595, A2

[3] Lindegren, L., Lammers, U., Bastian, U., et al. 2016, A&A, 595, A4

[4] Michalik, D., Lindegren, L. & Hobbs, D. 2015, A&A, 574, A115

[5] Gaia Collaboration (Brown, A.G.A., et al.) 2018, A&A, 616, A1

[6] Castro-Ginard, A., Jordi, C., Luri, X., et al. 2018, A&A, 618, A59

[7] Ester, M., Kriegel, H.-P., Sander, J., & Xu, X. 1996, in Proc. of the Second International Conf. on Knowledge Discovery and Data Mining, KDD9́6 (AAAI Press), 226

[8] Bishop, C.M. 1995, Neural Networks for Pattern Recognition (New York, NY, USA: Oxford University Press, Inc.)

[9] Skrutskie, M.F., Cutri, R.M., Stiening, R., et al. 2006, The Astronomical Journal, Volume 131, Issue 2, pp. 1163-1183

[10] Dias, W.S., Alessi, B.S., Moitinho, A., & Lépine, J.R.D. 2002, A&A, 389, 871

[11] Kharchenko, N.V., Piskunov, A.E., Schilbach, E., Röser, S., & Scholz, R.-D. 2013, A&A, 558, A53

[12] Gaia Collaboration (can Leeuwen, F. et al.) 2017, A&A, 601, A19

[13] Cantat-Gaudin, T., Jordi, C., Vallenari, A., et al 2018, ArXiv e-prints [arXiv:1805.08726]

Highlights on Spanish Astrophysics X, Proceedings of the XIII Scientific Meeting of the Spanish Astronomical Society held on July 16 – 20, 2018, in Salamanca, Spain. B. Montesinos, A. Asensio Ramos, F. Buitrago, R. Schödel, E. Villaver, S. Pérez-Hoyos, I. Ordóñez-Etxeberria (eds.), 2019

Search for wide substellar companions to young nearby stars with the VISTA Hemisphere Survey.

P. Chinchilla[1,2], V.J.S. Béjar[1,2], N. Lodieu[1,2], M.R. Zapatero Osorio[3], B. Gauza[4], R. Rebolo[1,2,5], and A. Pérez Garrido[6]

[1] Instituto de Astrofísica de Canarias (IAC), c/Vía Láctea S/N, 38200 La Laguna, Tenerife, Spain
[2] Dpto. de Astrofísica, Universidad de La Laguna (ULL), 38206 La Laguna, Tenerife, Spain
[3] Centro de Astrobiología (CSIC-INTA), Ctra. de Ajalvir km 4, 28850 Torrejón de Ardoz, Madrid, Spain
[4] Dpto. de Astronomía, Universidad de Chile, Camino el Observatorio 1515, Casilla 36-D, Las Condes, Santiago, Chile
[5] Consejo Superior de Investigaciones Científicas (CSIC), Spain
[6] Dpto. de Física Aplicada, Universidad Politécnica de Cartagena, 30202 Cartagena, Murcia, Spain

Abstract

We have performed a search for substellar objects as common proper motion companions to young nearby stars (including members of the Young Moving Groups AB Doradus, TW Hydrae, Tucana-Horologium and Beta Pictoris, and the Upper Scorpius young association) up to separations of 50,000 AU, using the VISTA Hemisphere Survey and 2MASS astrometric and photometric data. We have found tens of candidates with spectral types from M to L, and estimated masses from low-mass stars to the deuterium-burning limit mass. For some of these candidates, we have also obtained optical and/or near-infrared spectroscopy confirming them as true companions. We present the preliminary results of our searches and discuss the most outstanding cases. Our studies show that the frequency of young companions is higher than of the field-age ones.

1 Introduction

Substellar objects (brown dwarfs and planetary-mass objects) have masses below the minimum mass required to stably burn hydrogen in their interiors. This limit is theoretically established around 0.072–0.080 solar masses [2], depending on factors such as metallicity.

Because of the lack of a stable hydrogen burning phase, substellar objects keep on cooling down with time, and their effective temperature and spectral type strongly depend on their age (see Fig. 10 in [8]). This makes it difficult to characterize the properties of substellar objects, such as the mass, when the age is unknown. Also, they become fainter with time, making it more difficult to find and observe them when they are old.

Searching for wide companions to young nearby stars have advantages to find, analyze and characterize new substellar objects. We can derive important properties, such as the age, the metallicity and the distance, from their brighter primaries. Moreover, substellar objects orbiting at very wide distances give us the opportunity to carry out a complete photometric and spectroscopic characterization, which is very challenging to obtain in the case of objects orbiting at very close distances from their primaries.

Theoretical evolutionary and atmospheric models in the substellar regime can be tested against these new benchmark objects. The known population of ultra-cool companions is still very limited, for example only a dozen of young planetary-mass objects have been found by direct imaging at distances higher than >100 AU (see [1] and references therein). Most of them have been found using adaptive optics, and are too close to their primaries to permit a thorough spectral characterization.

2 Looking for wide substellar companions: Search method

We have used direct imaging to search for common proper motion companions orbiting young nearby stars at separations up to 50,000 AU in the Upper Scorpius OB association (USco) and four Young Moving Groups (YMGs): AB Doradus, Beta Pictoris, Tucana-Horologium and TW Hydrae. To identify these companions, we have used proprietary data of the Vista Hemisphere Survey (VHS)[12] in combination with other public surveys.

VHS is a near infrared survey that will cover the whole southern celestial hemisphere to a depth around ∼4 magnitudes deeper than 2MASS and DENIS (up to $J < 20$, $Ks < 18$, Vega mag). It is carried out by the VISTA Telescope, a 4.1m modified Ritchey-Chrétien telescope operated by ESO in Cerro Paranal Observatory, Chile. This survey is almost complete at the moment.

To build the sample, we have made a compilation of ∼1,300 and ∼1,500 known members and candidates of USco and YMGs from the literature, respectively.

Then, we have cross-correlated the VHS catalog with near-infrared catalogs from public surveys to measure proper motions. For the YMGs search, we use the Two Micron All Sky Survey (2MASS) catalog [3], since the members of the YMGs are widely spread in the sky, and 2MASS covers the whole sky surface, although it is not as deep as VHS. For the search in USco, we use the UKIRT Infrared Deep Sky Survey Galactic Clusters Survey (UKIDSS GCS) [9], which covers the USco region in JHK to a similar depth as VHS.

We have also collected all the available photometric data from other catalogs such as 2MASS, DENIS, USNO, AllWise, PanSTARRS and SDSS to complete our study of the candidates. Gaia DR2 has also provided accurate proper motions and parallaxes for most of the primaries and the brightest candidate companions. This allowed us to discard casual

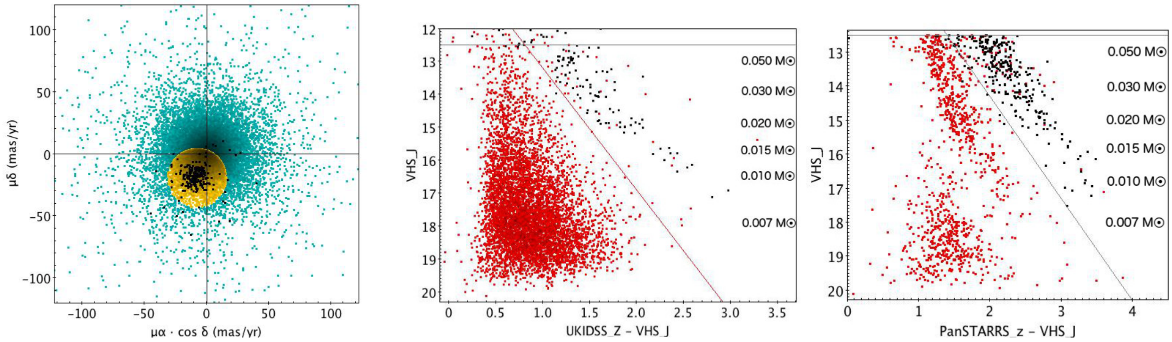

Figure 1: (Left panel) Proper motion selection of the USco candidates. Known members of USco are indicated as black dots, selected proper motion candidates within the circle as yellow dots, objects discarded as contaminants as green dots. (Middle and right panels) J vs Z-J color-magnitude diagrams with VHS+UKIDSS, and VHS+PanSTARRS photometry, in the middle and right panel respectively. USco known members are marked in black, objects selected by proper motion are marked in red. We used the lower envelope of the USco sequence in each diagram to select photometric candidates. We limit the selection to $J > 12.5$ mag to avoid saturated targets.

alignments and confirm the companionship of some of these systems.

3 Upper Scorpius

Upper Scorpius is a nearby young association, with an age of 5–10 Myr and placed at a distance of around ∼145 pc [13] [15].

For this search, we have cross-correlated VHS and UKIDSS GCS in a region of 60 arcsec around every known USco member or candidate member. This corresponds to separations up to ∼9,000 AU around each member at the mean distance of the association.

Figure 1 (left) shows the proper motion diagram for the selection of the candidates. Using VHS and UKIDSS GCS, we find a proper motion of $(-7.1, -18.3) \pm (6.9, 8.6)$ mas/yr for USco members. Candidates were selected with proper motions consistent with USco within a radius of 14.4 mas/yr, which is the RMS of the background objects with null motion. Since the proper motion is relatively low, and our selection criteria are generous, the results of this first selection step contain a high number of contaminants.

To filter out the contaminants, we have performed a photometric selection using J vs. J-Z color-magnitude diagrams. We determined the lower envelope of the distribution of known members in the color-magnitude diagram, and selected as good candidates those located above this envelope. We obtained Z-band photometry from UKIDSS GCS only for a fraction of the candidates, since this survey does not cover all the region in the Z-band, so for the candidates without Z-band information in GCS, we used PanSTARRS to perform a similar selection. Only targets with $J > 12.5$ mag were selected, as objects brighter than

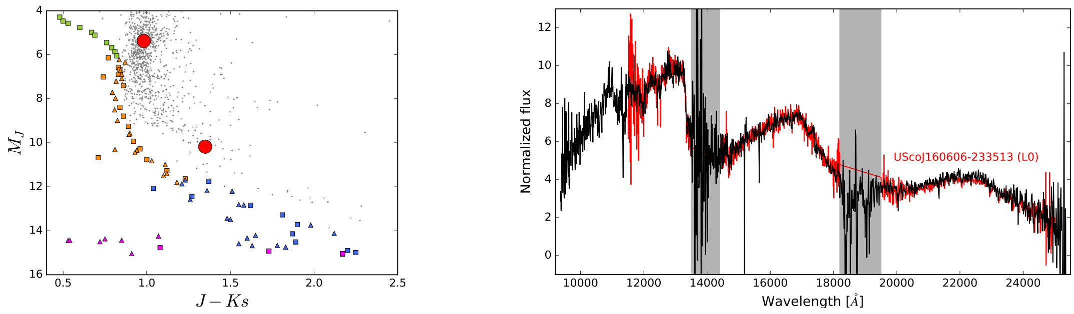

Figure 2: (Left panel) J vs J-Ks color-magnitude diagram for the USco M2.5+L0 system. USco known members are shown as gray dots. Field sequence from [14] (squares), [11] (orange triangles) and [4] (blue and pink triangles). Primary and companion are shown as red circles. (Right panel) Near Infrared spectrum of the wide L0 companion from NTT/SOFI (black). Spectrum of the USco known L0 member J160606-233513 from [10] (red) for comparison.

this may be affected by saturation in VHS. The middle and right panels of Figure 1 show the resulting color-magnitude diagrams.

We also used Gaia DR2 parallax and proper motion data for the brightest candidates, to discard foreground or background contaminants located at different distances than the association and distinguish true companions from chance alignments of USco members located at close positions in the sky but at different distances within the association. From Gaia DR2, we obtained a mean proper motion for Upper Scorpius of $(-11.7, -23.6) \pm (3.8, 3.3)$ mas/yr, which is more accurate than the previously reported value.

As a result of our searches, we found 35 wide companion candidates, 16 of which are new discoveries. Their expected spectral types range from M to L. The separation range explored for this search is 400–9,000 AU. These candidates have been already spectroscopically observed, and are under analysis and pending of confirmation at the moment. If confirmed, the rate of wide companions is $\sim$3%.

3.1 Example: A L0 companion to a M2.5 member of Upper Scorpius

One of the most interesting systems found in this search is a $J = 15.9$ mag brown dwarf companion, classified in the near-infrared as an L0 dwarf, orbiting at 3,000 AU of an M2.5 USco low-mass star. The estimated mass is around 15–20 Jupiter masses, which is slightly above the deuterium burning mass limit.

Fig 2 (left) shows the J vs J-Ks color-magnitude diagram for this system. Fig 2 (right) shows the infrared spectrum of the L0 companion obtained using SOFI spectrograph at NTT telescope in La Silla Observatory, in Chile.

4 Young Moving Groups: AB Doradus, Beta Pictoris, Tucana-Horologium and TW Hydrae.

For this search, we have cross-correlated VHS and 2MASS in the regions corresponding to physical separations up to 50,000 AU around each member, using their parallaxes from Gaia DR2, or their spectrophotometric distance for those primaries with no parallax.

We have included only YMG members belonging to the southern hemisphere (with available data from VHS), and proper motions higher than 60 mas/yr, to avoid contaminants. Around 650 primaries satisfied these criteria.

In this case, we have also performed a proper motion selection for the candidates, and we have used J vs. J-Ks color-magnitude diagrams to identify candidates compatible with being located at the same distance. For the brightest targets, we have also used Gaia DR2 parallaxes and proper motions to discard chance alignments or confirm companionship. For the candidates with no parallax, we have also used optical photometry from PanSTARRS, SDSS, DENIS and USNO when available to discard contaminants.

Table 1 shows the number of candidates found and expected companion rate. The results show a frequency of companion candidates higher than the frequency for field age [6], and also a possible tendence to a higher companion rate for the youngest moving groups. These results are preliminary and should be taken with caution since the newly identified candidates require spectroscopical confirmation and characterization.

Table 1: Companion candidates found

YMG	Age	Primaries searched	Systems found[a]	Comp. cand. rate	Comp. cand. rate (>M5)
AB Doradus	$\sim$150 Myr	197	12	6.1$\pm$1.8%	3.6$\pm$1.3%
Tuc-Hor	$\sim$45 Myr	320	19	5.9$\pm$1.4%	2.5$\pm$0.9%
β Pictoris	$\sim$25 Myr	159	13	8.2$\pm$2.3%	3.1$\pm$1.4%
TW Hydrae	$\sim$10 Myr	69	6	8.7$\pm$3.5%	7.2$\pm$3.2%

[a]Candidates need to be spectroscopically confirmed.

4.1 Example: An L-type companion to an M6 brown dwarf in Beta Pictoris

In these searches we have found a very interesting substellar object orbiting at 1,200 AU from the Beta Pictoris M6 brown dwarf 2MASS J0249-0557. The system is located at 30 pc from our Solar System. Using optical spectroscopy, we classified this object as a young L3 $\pm$ 1 dwarf. The estimated mass of the companion is around the deuterium burning mass limit.

The discovery of this companion has been recently reported by [5], who also find that the primary of the system is itself a binary.

Fig. 3 (left panel) shows the proper motion diagram for the 2MASS J0249-0557 system.

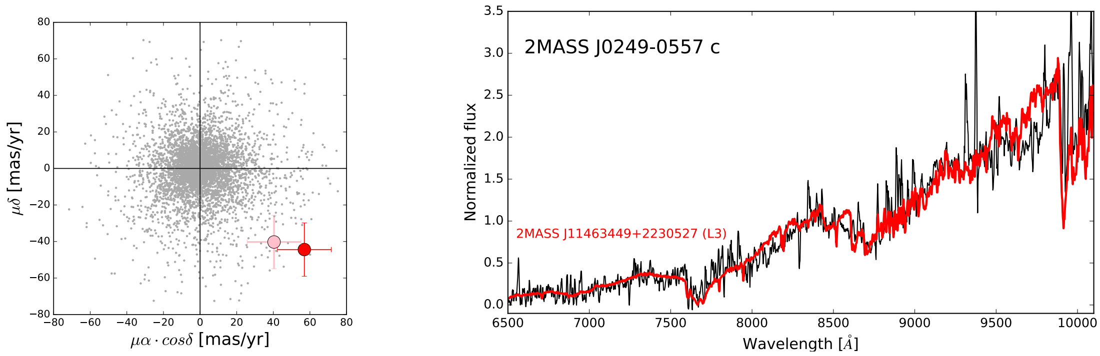

Figure 3: (Left) Proper motion diagram for the 2MASS J0249-0557 system. Primary is plotted in light pink, companion in red. (Right) Optical spectrum of 2MASS J0249-0557 c (black) from eBOSS, overplotted for comparison with an L3 standard (red) from [7].

Fig. 3 (right panel) shows the eBOSS optical spectrum of the L companion.

5 Summary and final remarks

- We have performed a search for common proper motion companions to young nearby stars in Upper Scorpius (∼5–10 Myr) and four Young Moving Groups: AB Doradus (∼150 Myr), Tucana-Horologium (∼45 Myr), Beta Pictoris (∼25 Myr) and TW Hydrae (∼10 Myr).

- We find an estimated companion rate for Upper Scorpius (mid-M to L) of around 3%.

- The preliminary companion rates for Young Moving Groups and USco are higher than the ones found for the field age and might depend on age.

- The candidate companions require spectroscopic confirmation.

Acknowledgments

The authors want to thank the XIII SEA Meeting organizers for a wonderful and enriching week of conferences. P.C. wants to thank E. Congiu for very helpful improvements of this manuscript. P.C., V.J.S.B. and N.L. are partially supported by grant AyA2015-69350-C3-2-P; A.P.G by program AyA2015-69350-C3-3-P; R.R. by program AyA2014-56359-P; and M.R.Z.O. by program AyA2016-79425-C3-2-P from the Spanish Ministry of Economy and Competitiveness (MINECO/FEDER). B.G. acknowledges support from the CONICYT through FONDECYT Fellowship grant No 3170513.

References

[1] Bowler, B.P. 2016, PASP, 128, 102001

[2] Chabrier, G., Baraffe, I. 2000, ARA&A, 38, 337C

[3] Cutri, R.M., Skrutskie, M.F., van Dyk, S. et al. 2003, The IRSA 2MASS All-Sky Point Source Catalog, NASA/IPAC Infrared Science Archive, tmc book

[4] Dupuy, T.J., Liu, M.C. 2012, ApJS, 201, 19D

[5] Dupuy, T.J., Liu, M.C., Allers, K.N. et al. 2018, AJ, 156, 57

[6] Gauza, B. 2016, A direct imaging search and characterization of brown dwarfs and massive planets around stars, PhD Thesis, IAC

[7] Kirkpatrick, J.D. 1999, ApJ, 519, 802K

[8] Kirkpatrick, J.D. 2005, ARA&A, 43, 195K

[9] Lawrence, A. 2007, MNRAS, 379, 1599

[10] Lodieu, N. 2013, MNRAS, 383, 1385

[11] Lodieu, N. 2013, MNRAS, 431, 3222

[12] McMahon, R.G., Banerji, M., Gonzalez, E., et al., 2013, Msngr, 154, 35M

[13] Pecaut, M.J., Mamajek, E.E., Bubar E.J., 2012, ApJ, 746, 154P

[14] Pecaut, M.J., Mamajek, E.E., 2013, ApJS, 208, 9P

[15] de Zeeuw, P.T., Hoogerwerf, R., de Bruijne, J.H.J., et al., 1999, ApJ, 117, 354D

Highlights on Spanish Astrophysics X, Proceedings of the XIII Scientific Meeting of the Spanish Astronomical Society held on July 16 – 20, 2018, in Salamanca, Spain. B. Montesinos, A. Asensio Ramos, F. Buitrago, R. Schödel, E. Villaver, S. Pérez-Hoyos, I. Ordóñez-Etxeberria (eds.), 2019

What can VLBI do for your research? The EVN and JIVE.

F. Colomer[1]

[1] Joint Institute for VLBI ERIC (JIVE)

Abstract

Very Long Baseline Interferometry (VLBI) is providing key information to the study of processes in the Universe, from star formation regions and circumstellar envelopes around evolved stars, to galactic structure and cosmology. The European VLBI Network (EVN) offers superb observational capabilities and, most importantly, expert support to users through the Joint Institute for VLBI ERIC (JIVE), ensuring that the EVN research infrastructure is fully accessible for the best science to emerge.

1 Introduction

Very Long Baseline Interferometry (VLBI) is a radio astronomy technique in which an array of telescopes, distributed many hundreds and thousands of kilometres apart, provide milliarcsecond resolution images of bright radio sources on the sky. VLBI is sensitive to special conditions in many astrophysical objects, from AGN to Galactic masers. Among other applications, this technique allows for kinematic studies of objects, even when they are at cosmological distances and astrometry delivering parallax distances. The sub-arcsecond resolution is also attractive for studying transient phenomena, which has become very relevant recently and is associated with the development of real-time VLBI.

The European VLBI Network (EVN, Fig. 1) is an interferometric array of up to 21 radio telescopes spread throughout Europe (and beyond) that conducts unique, high resolution, radio astronomical observations of cosmic radio sources. It is the most sensitive VLBI array in the world, thanks to the collection of extremely large telescopes that contribute to the network. The EVN is a large scale astronomical facility that is open to all astronomers. It operates for 3 periods per year, known as “VLBI sessions”, each of which are approximately 3-4 weeks long and typically involve 3-4 different observing frequencies. In addition, there are about ten 24-hour runs per year in real time (e-EVN), approximately once per month outside the main EVN sessions, and out-of-session (OoS) observations to accommodate special projects.

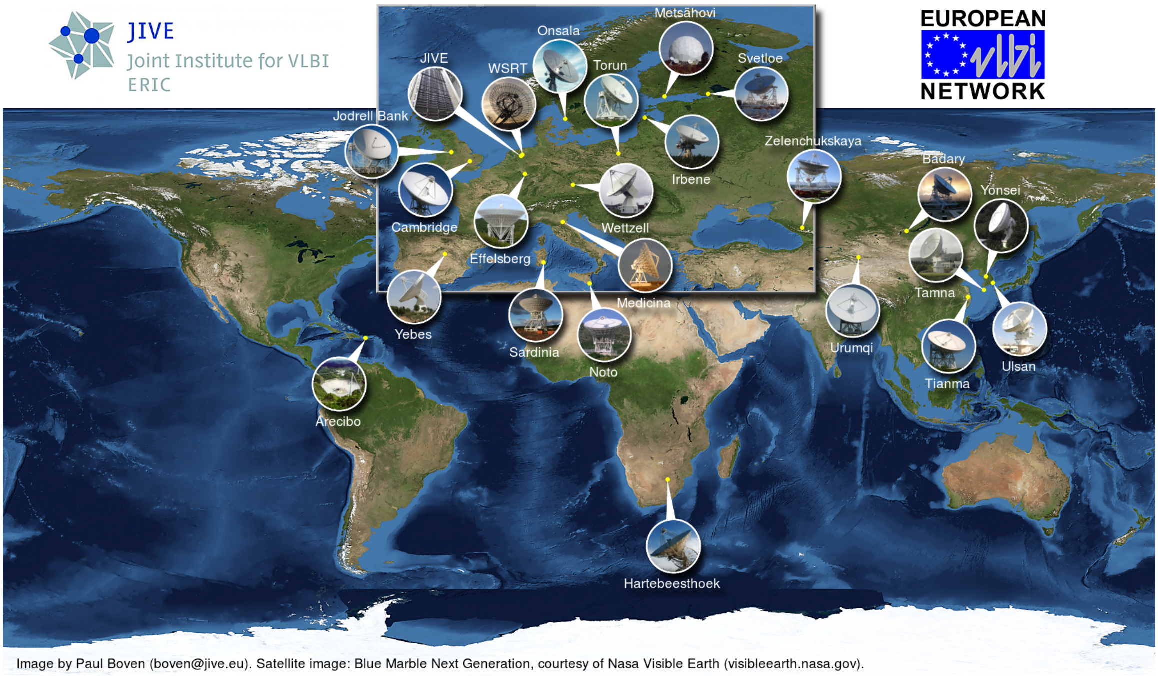

Figure 1: Map of the EVN telescopes and JIVE.

The central organisation of the EVN is the Joint Institute for VLBI – European Research Infrastructure Consortium (JIV-ERIC, JIVE), which at present unifies as its member-countries France, Latvia, The Netherlands (host), Spain, Sweden, United Kingdom as well as associated research organisations in China, Germany, Italy and South Africa.

As the EVN telescopes observe the same cosmic radio source simultaneously, the data are recorded and later combined at a special purpose data processor, often referred to as the "correlator". The EVN software correlator (SFXC) at JIVE processes since 2012 essentially all of the EVN observations.

In addition to these "EVN-only" observations, the EVN array often links-up with (e-)MERLIN, an interferometer network of telescopes distributed around the UK. In this extended mode, the coverage of the EVN-MERLIN array ranges from a few tens to many thousands of kilometers. The EVN-MERLIN array is thus sensitive to a wide range of radio structures from the arcsecond scale to the milliarcsecond scale. The EVN also observes simultaneously with other VLBI arrays such as the USA VLBA in a "global VLBI" configuration, obtaining sub-milliarcsecond resolution at frequencies higher than 5 GHz. The EVN also participates in Space VLBI observations as part of a ground array of radio telescopes observing simultaneously with the Russian RadioAstron satellite.

In Spain, the National Geographic Institute (IGN, Ministerio de Fomento) operates a 40m radio telescope at Yebes Observatory (Guadalajara) which is member of EVN. The NASA DSN MDSCC (Robledo de Chavela, near Madrid) are also associated EVN telescopes.

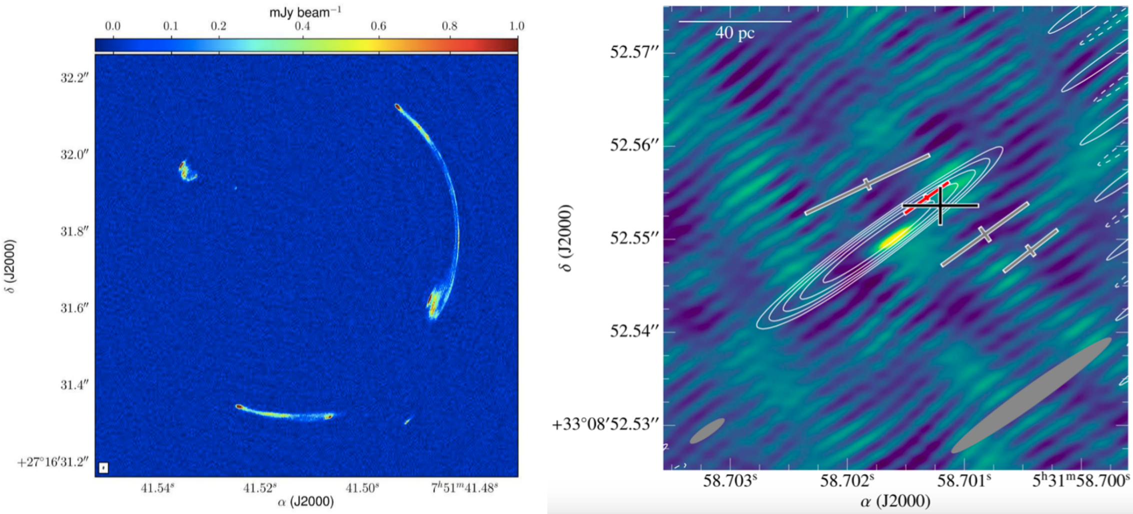

Figure 2: Recent examples of EVN science: (Left) Gravitational lens helps understanding dark matter [8]. (Right) The detected pulses related to FRB121102, near a persistent radio source as detected by the EVN. The location of the transient source was narrowed down to a star forming region within a dwarf galaxy at a redhsift of z=0.193 [4].

2 EVN recent science highlights

As recent examples, it is worth mentioning the production of one of the sharpest astronomical images ever [8], using a global VLBI array: a gravitational lens demonstrating that dark matter is distributed unevenly across a distant galaxy, which distorts the image of the background source (a black hole with radio jets) into extended arcs (Fig. 2).

Another outstanding result is in the field of fast transient research, and pioneering work in millisecond-duration transient signal detection with the VLBI technique has resulted in the detection of single pulses observed in Rotating Radio Transients (RRATS). The first known repeating fast radio burst, FRB121102, following the initial localization with the JVLA, was successfully detected with the EVN and its location refined. These observations provide the ultimate evidence that FRBs are indeed extragalactic [1] [4]. This work was the outcome of several years of research in the area of short transient localization, which itself was made possible by the advanced features added to the EVN Software Correlator (SFXC) at JIVE, and are now available to the whole astronomical community.

The first direct evidence for jet-induced AGN feedback has been obtained through spectral line global VLBI imaging of 4C12.50 [6]. The observations revealed a compact region of atomic hydrogen at high velocity at the terminating point (and its surroundings) of the jet, providing a direct connection to the large scale molecular outflow seen on larger scales. The result showcase the unique power of the EVN and global VLBI, thanks to the large collecting area needed to detect the weak spectral feature related to the high-velocity outflows.

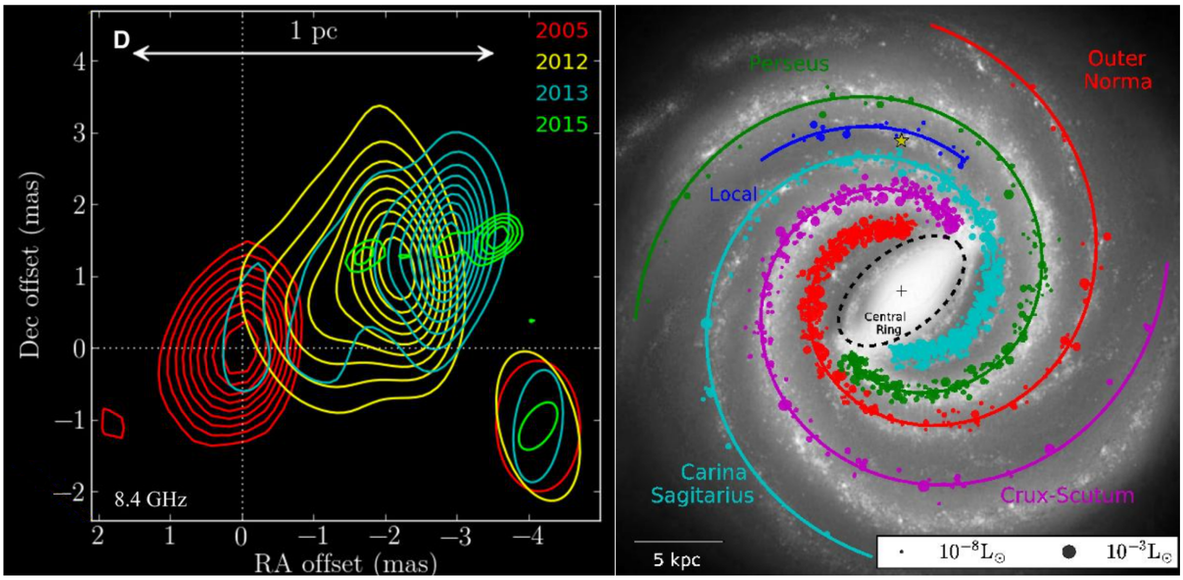

Figure 3: (Left) The powerful gravity of a SMBH rips apart a star that has wandered too close [5]. (Right) Simulation of how VLBI observations of methanol masers can identify spiral arms in our galaxy [7].

The discovery with the EVN of the double compact nature of the inner core of an already confirmed dual AGN identifies a system as an excellent candidate to represent a triple active supermassive black hole. While this result needs confirmation, similar systems have received a lot of attention because close pairs of binary supermassive black holes are the parent population for SMBH mergers to be discovered by the LISA mission in the future [3].

A tidal disruption event, or TDE, occurs when a star is being pulled apart by a supermassive black hole. Following the evolution of Arp299B during several years with the EVN and VLBA, it could track the radio emission of jets of material launched outwards from the poles of a rotating disk that had formed of material around the black hole [5] (Fig. 3).

There are also some very good examples of the application of VLBI to the study of astrophysical masers in the Universe, from star formation regions or circumstellar envelopes around evolved stars, to Galactic structure and cosmology, through precise astrometry (see [2] and references therein).

Late–type stars on the Asympthotic Giant Branch (AGB) have circumstellar envelopes (CSEs) rich in molecules, in different layers. VLBI maps the maser emission, which is compact and very intense, of SiO, H_2O and OH, providing extremely valuable information on the spatial structure and dynamics of the circumstellar shells around AGB stars. These masers can provide accurate distances to significant numbers of variable stars, and a critical check on Gaia parallaxes. Moreover, methanol class II masers at 6.7 GHz are well known tracers of high-mass star-forming regions, but their origin is still not clearly understood. Studies with the EVN have provided high sensitivity images with milliarcsecond angular resolution.

Figure 4: (Left) EVN SFXC correlator at JIVE. (Right) JIVE support scientists in action.

Hundreds of trigonometric parallaxes and proper motions for masers associated with young, high-mass stars have been measured with VLBI arrays, including the EVN, some with accuracies of ± 10 microarseconds. These measurements provide strong evidence for the existence of spiral arms in the Milky Way, accurately locating many arm segments, with the widths of spiral arms increasing with distance from the Galactic center (Fig. 3).

Water megamasers can be used to test the unified model for AGNs, the need for a torus, and the physics of the central engine; actually, they currently provide the only way to map the structure of circumnuclear accretion disks within a parsec of AGN supermassive black holes. Maser distance estimations can also be used to measure H0 accurately and constrain cosmological parameters.

Many astronomical areas of research benefit from complementary VLBI observations. An updated science vision for VLBI in the next decade is being produced by EC H2020 project JUMPING JIVE.

3 User access to the EVN and JIVE

The EVN is a research infrastructure open to all astronomers. Observing proposals will be assessed based exclusively on scientific merit and technical feasibility by the EVN Programme Committee.

A EVN User Guide can be consulted for help with proposing, scheduling, observing and reducing EVN data. Additionally, EVN users can obtain assistance and support from JIVE via its support scientists on many different aspects of EVN observations, including proposal preparation (to be submitted using the tool *NorthStar*) and best technical feasibility, scheduling, quality assurance for correlator data products, and/or data analysis. In this way, usage of the EVN becomes easier for astronomers not specialised in the VLBI technique.

Financial support may be available to EVN users who wish to visit JIVE in order to analyze correlated EVN data under the Trans-National Access program of EC H2020 project RadioNet.

Acknowledgments

This publication has received support from JUMPING JIVE (for "Joining up Users for Maximizing the Profile, the Innovation and Necessary Globalization of JIVE"), an H2020-INFRADEV-2016-1 project under contract grant agreement N^o 730884.

References

[1] Chatterjee, S. et al., 2017, Nature 541, 58

[2] Colomer, F. & van Langevelde, H.J., 2018, In: "Astrophysical Masers: Unlocking the Mysteries of the Universe", Proceedings of the IAU Symposium, Volume 336, pp. 411-416

[3] Deane, R. et al., 2014, Nature 511, 57

[4] Marcote, B., et al., 2017, ApJ 834, 8

[5] Mattila, S., Pérez-Torres, M., et al. 2018, Science, 361, 482

[6] Morganti, R. et al., 2013, Science 341, 1082

[7] Quiroga, L. et al., 2017, A&A 604, 72

[8] Spingola, C., et al. 2018, MNRAS, 478, 4816

Highlights on Spanish Astrophysics X, Proceedings of the XIII Scientific Meeting of the Spanish Astronomical Society held on July 16 – 20, 2018, in Salamanca, Spain. B. Montesinos, A. Asensio Ramos, F. Buitrago, R. Schödel, E. Villaver, S. Pérez-Hoyos, I. Ordóñez-Etxeberria (eds.), 2019

The tricky line of sight towards Cygnus-X: The [DB2001] CL05 embedded cluster as a pilot case.

D. de la Fuente[1], C. G. Román-Zúñiga[1], E. Jiménez-Bailón[1], J. Alves[2], and S. Venus[1]

[1] Instituto de Astronomía, Unidad Académica de Ensenada, Universidad Nacional Autónoma de México, Ensenada 22860, Mexico
[2] Institute for Astrophysics, University of Vienna, Türkenschanzstrasse 17, 1180 Vienna, Austria

Abstract

The nearest massive star-forming complex, Cygnus-X, is widely used as a laboratory for star cluster formation and feedback processes, under the implicit assumption that all its components are located roughly at the same distance. We present a multi-wavelength study of a $15' \times 15'$ field in southern Cygnus-X, where different components involving clustered star formation are overlapped. Preliminary results indicate that the Berkeley 87 and [DB2001] CL05 clusters are actually located at very different distances, invalidating previous claims of physical interaction between them. This shows the importance of a careful treatment of extinction and distance calculations for cluster formation studies, particularly in Cygnus-X.

1 Introduction

The Cygnus-X star-forming complex is usually regarded as an ideal workbench for understanding massive star formation as a whole, thanks to its proximity and richness in young star clusters and cluster-forming clouds ([11, 18]). This unique combination helps to connect the small- and large-scale processes that are involved in massive star formation, and allows to test the effects of feedback from recently formed massive clusters in detail. However, these studies have been often performed under the assumption that all the Cygnus-X components are located roughly at the same distance (e.g. [10, 15, 16]), despite multiple evidence against it (e.g. [17, 21, 13]). Furthermore, [21] claimed that interstellar clouds and OB associations are actually arranged in several layers at different distances, following the direction of the Local Galactic Arm, which is nearly perpendicular to the sky plane at Cygnus.

Unfortunately, distance estimation is particularly problematic for Cygnus-X. Due to the fact that the line of sight is roughly tangent to the Galactic rotation curve, kinematic

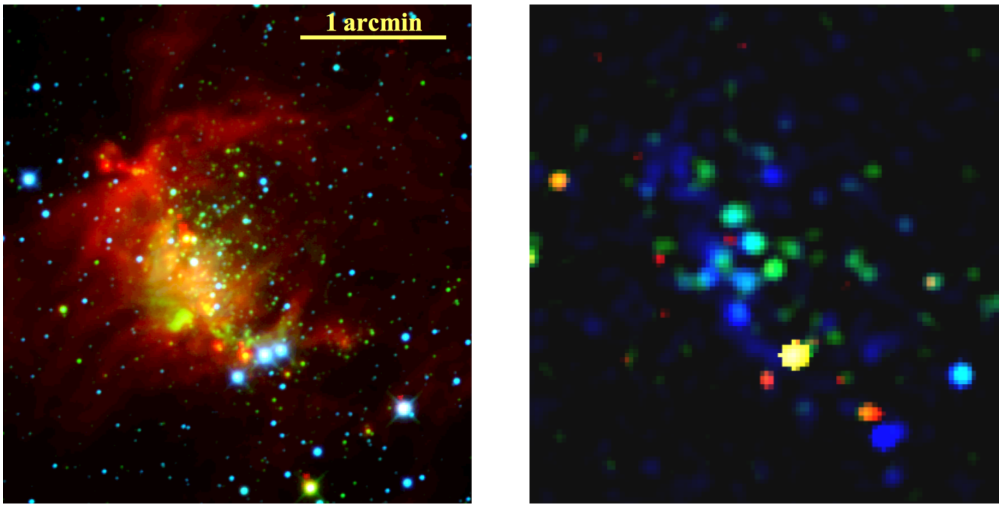

Figure 1: Infrared (left) and X-ray (right) RGB images covering the [DB2001] CL05 region and the overlapping part of Berkeley 87. Colors are R = [5.8], G = K, B = J for the infrared image, and R = $0.5 - 1.2$ keV, G = $1.2 - 2$ keV, B = $2 - 7$ keV for the X-rays. Both images cover the same coordinate ranges; north is up and east is left.

distances (as measured by either radial velocities or proper motions) are ill-defined at $l \sim 80°$, up to several kiloparsecs ([5]). Morever, *Gaia* [8] parallaxes are usable only to the extent that the target is unextinguished enough to be optically detected, which happens at $d \lesssim 2$ kpc in the Cygnus-X direction.

This work is focused on a small region at the southern tip of Cygnus-X, where distinct components related to recent or ongoing star formation are overlapped, namely: the well-studied young massive cluster Berkeley 87 ([19]); the ON2 star-forming cloud hosting several masers and compact HII regions ([3]); and an embedded cluster, [DB2001] CL05, discovered independently by [2] and [4]. The latter seems coincident with a clump of hard X-ray emitters that was detected by [16]. By assuming that all the components belong to a single star-forming complex, [16] interpreted these X-ray features in terms of interaction between winds from Berkeley 87 massive stars and the ON2 cloud. This scenario was subsequently challenged by the trigonometric parallax measurement of a ON2 water maser located at northern [DB2001] CL05, yielding $d = (3.83 \pm 0.13)$ kpc [1], three times farther than Berkeley 87 (Cf. [20]).

2 Multi-wavelength observations and extinction maps

A $15' \times 15'$ field covering Berkeley 87 and [DB2001] CL05 was observed through the 3.5-meter telescope of the Calar Alto Observatory, Spain. The resulting near-infrared images and photometry are merged with those from the Cygnus-X *Spitzer* Legacy Survey. We also make use of archival data from the *Chandra* X-ray Observatory. Fig. 1 displays the corresponding RGB compositions in a subfield covering [DB2001] CL05, where several spectroscopically confirmed massive members of Berkeley 87 show clearly distinct colors. Specifically, the

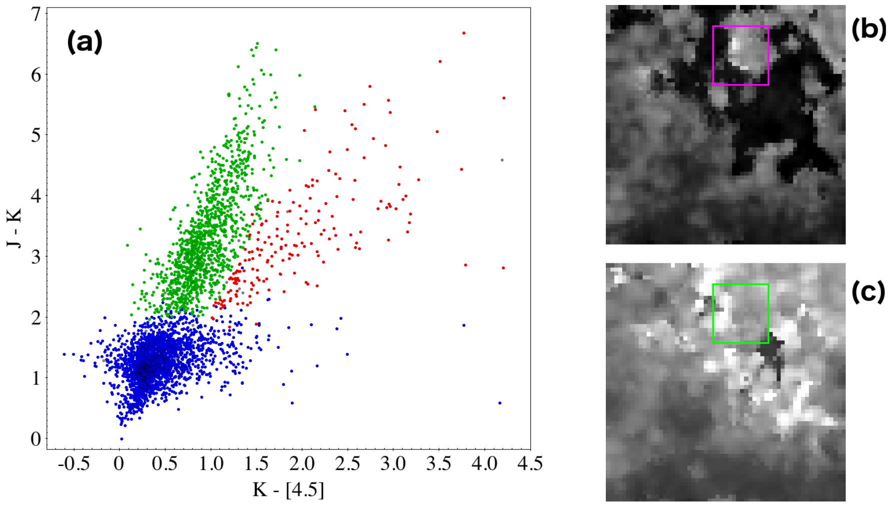

Figure 2: (a) Color-color diagram of point sources within the $15' \times 15'$ OMEGA2000 field, showing the low-reddening population in blue, highly extinguished stars with no intrinsic reddening in green, and highly extinguished objects with extra mid-infrared excess in red. (b) NICEST extinction map for all sources in the OMEGA2000 field. (c) Same as pannel b, but using only sources with high extinction and no intrinsic reddening (i.e. green dots in pannel a). These extinction maps are drawn in a common linear scale where black is set at $A_V = 3$, and white at $A_V = 25$. The colored squares enclose the region displayed in Fig. 1.

latter appear bluish in the infrared image, and orange/red (i.e. soft) in X-rays, in contrast to the souces that seem to be part of the [DB2001] CL05 overdensity. This color distinction, also seen as bimodal distributions in near-infrared colors (e.g. the two groups of data points above/below $J - K \approx 2.0$ in Fig. 2a), hints at a line-of-sight superposition of young stellar populations that are affected by very different amounts of foreground extinction.

Using color cuts that will be explained in detail in our forthcoming paper (de la Fuente et al., in prep.), we separate highly reddened sources with/without intrinsic reddening from the low-reddening population (Fig. 2a). Then, we use the NICEST method ([12]) to create an extinction map using the whole near-infrared dataset. The resulting map (Fig. 2b) shows an extinction "hole" whose position and size is consistent with the Berkeley 87 cluster, but clearly contradicts the existence of interstellar clouds. On the other hand, we create another NICEST map taking into account only sources from the high-reddening group that do not show extra mid-infrared excess. The new map (Fig. 2c) reveals a high-extinction clumpy structure whose geometry is consistent with the ON2 star-forming clouds.

Additionally, we employ parallaxes from *Gaia* DR2 [7] to calculate distances for optically detectable stars (which do not include the [DB2001] CL05 cluster). A new distance for Berkeley 87, (1669 ± 12) pc, is obtained as the median of spectroscopically confirmed cluster members (taking spectral types from the literature). Although somewhat higher than previous distance estimates (e.g. [19, 20]), this revised value is still much lower than the aforementioned water maser distance measured by [1].

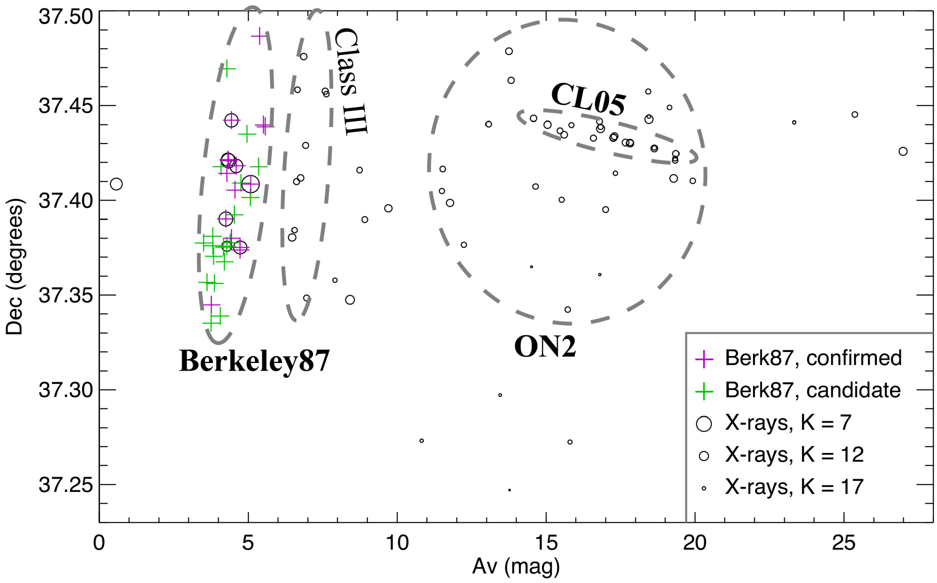

Figure 3: Declination vs. visual extinction for infrared counterparts of *Chandra* detections within the 15′ × 15′ OMEGA2000 field, shown as open circles whose radii are scaled with K-band magnitude. Pink and green crosses represent spectroscopically confirmed Berkeley 87 members, and further candidates listed by [19], respectively.

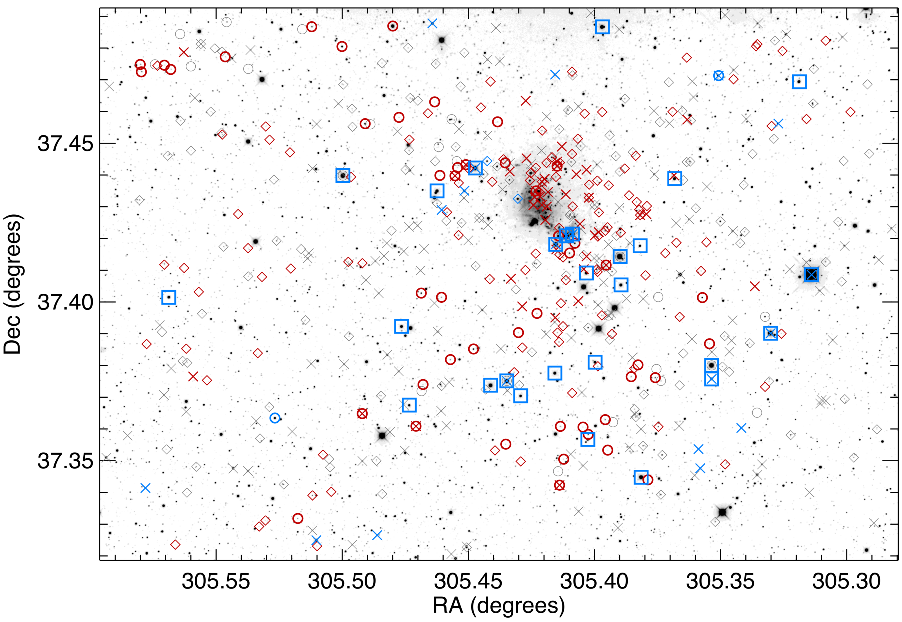

Figure 4: Berkeley 87 confirmed members (squares), primary (circles) and secondary (diamonds) YSO candidates, and X-ray sources (crosses) over the OMEGA2000 K-band image (excluding the less relevant southern part). Color symbols are objects assigned to the Berkeley 87 layer (blue) or the ON2 layer (red).

3 Layer separation

Observational evidence presented in previous sections may indicate that the overlapping young star clusters are part of at least two physically unrelated regions, being located at very different distances. Unfortunately, distances cannot be accurately determined beyond the Berkeley 87 layer, and evidence for [DB2001] CL05 and the 3.83 kpc maser belonging to the same star-forming complex is inconclusive. Consequently, we aim at separating the Berkeley 87 and ON2 populations through extinction estimates to individual objects displaying signs of young age – in a chronological sense. Such category includes Young Stellar Objects (YSOs) but also evolved massive stars whose ages are limited to a few Myr. In this regard, X-ray emission, which is expected to be displayed by both YSOs and hot massive stars ([6]), becomes an ideal diagnostic for inhomogeneous young populations.

Primary YSO candidates are found using the classical criteria from [9], and a larger amount of secondary candidates are selected through our own method for measuring intrinsic reddening (de la Fuente et al., in prep.). X-ray sources whose infrared counterparts show no intrinsic color excess are considered to be class III pre-main sequence stars, or Berkeley 87 members (note that these two options are not mutually excluding).

To provide optimal extinction estimates for as many sources as possible, several methods are combined. First, direct measurement of color excess is performed for stars of known spectral type. Second, the Rayleigh-Jeans Color Excess (RJCE) method ([14]) is used in the suitable cases. Finally, the extinction map of 2c (whose validity is checked against sources in common with the RJCE method) is applied for stars belonging to the high-reddening group (See Sect. 2), including those that show intrinsic color excess (red dots in Fig. 2a). The extinction results for X-ray emitters are shown in Fig. 3, where several components can be clearly distinguished, and a wide gap between the Berlekey 87 and [DB2001] CL05 layers is evident. The apparent extinction shift within Berkeley 87 is attributed to class III objects experiencing residual color excesses that affect RJCE results[1].

Based on Fig. 3, YSO candidates with extinction values $A_V > 11$ are assigned to the ON2 layer. Moreover, any objects with signs of young ages (including spectral types) whose parallaxes are compatible with the Berkeley 87 distance are allocated in the corresponding layer. The outcome is displayed in Fig. 4. A vast majority of YSO candidates are located in the ON2 layer, with a strong overdensity at the position of [DB2001] CL05, while Berkeley 87 hosts only a few, mainly class III sources in the outskirts. These results are consistent with two independent clusterings of different evolutionary stage.

4 Conclusions

In contrast to previous claims, our preliminary results prove that star formation and X-ray emission from [DB2001] CL05 cannot be physically related to Berkeley 87 by no means, since these clusters are separated by a long distance (despite the line of sight coincidence). This

[1]Note that intrinsically red YSOs in ON2 are not affected by this problem, since their extinction values are obtained through a NICEST map where such sources have been excluded from the map creation process.

case illustrates the importance of a careful treatment of extinction and distance for Galactic studies of clustered star formation, in order to avoid reaching wrong conclusions about feeback from fake neighbors.

Acknowledgments

D. dF acknowledges the UNAM-DGAPA postdoctoral grant. C.R.Z. and E.J.B. acknowledge support from Programa de Apoyo a Proyectos de Investigación e Innovación Tecnológica, UNAM-DGAPA, grants IN108117 and IN109217, respectively. The scientific results reported in this article are based in part on data obtained from the Chandra Data Archive. This research has made use of software provided by the Chandra X-ray Center (CXC) in the application package CIAO. This work has made use of data from the European Space Agency (ESA) mission *Gaia*, processed by the *Gaia* Data Processing and Analysis Consortium (DPAC).

References

[1] Ando, K., Nagayama, T., Omodaka, T., et al. 2011, PASJ, 63, 45

[2] Comerón, F., & Torra, J., 2001, A&A, 375, 539

[3] Dent, W. R. F., MacDonald, G. H., & Andersson, M., 1988, MNRAS, 235, 1397

[4] Dutra, C. M., & Bica, E. 2001, A&A, 376, 434

[5] Ellsworth-Bowers, T. P., Rosolowsky, E, Glenn, J., et al. 2015, ApJ, 799, 29

[6] Feigelson, E., Townsley, L., Güdel, M., & Stassun, K. 2007, Protostars and Planets V, 313

[7] Gaia Collaboration, Brown, A. G. A., Vallenari, A., et al. 2018, A&A, 616, 1

[8] Gaia Collaboration, Prusti, T., de Bruijne, J. H. J., et al., 2016, A&A, 595, 1

[9] Gutermuth, R.A., Megeath, S. T., Myers, P. C., et al. 2009, ApJS, 184, 18

[10] Knödlseder, J., Cerviño, M., Le Duigou, J. M., et al. 2002, A&A, 390, 945

[11] Le Duigou, J.-M., Knödlseder, J. 2002 A&A, 392, 869

[12] Lombardi, M. 2009, A&A, 493, 735

[13] Maia, F. F. S., Moraux, E., & Joncour, I., 2016, MNRAS, 458, 3027

[14] Majewski, S.R., Zasowski, G., & Nidever, D.L. 2011, ApJ, 739, 25

[15] Motte, F., Bontemps, S., Schilke, P., et al. 2007, A&A, 476, 1243

[16] Oskinova, L.M., Gruendl, R.A., Ignace, R., et al. 2010, ApJ, 712, 763

[17] Pipenbrink, A., & Wendker, H. J., 1988, A&A, 191, 313

[18] Reipurth, B., & Schneider, N. 2008, in Handbook of Star Forming Regions (ASP Monograph Publications), 4, 36

[19] Turner, D.G., & Forbes, D. 1982, PASP, 94. 789

[20] Turner, D. G., Rohanizadegan, M., Berdnikov, L. N., & Pastukhova, E. N. 2006, PASP, 118, 1533

[21] Uyanıker, B., Fürst, E., Reich, W., et al. 2001, A&A, 371, 675

Highlights on Spanish Astrophysics X, Proceedings of the XIII Scientific Meeting of the Spanish Astronomical Society held on July 16 – 20, 2018, in Salamanca, Spain. B. Montesinos, A. Asensio Ramos, F. Buitrago, R. Schödel, E. Villaver, S. Pérez-Hoyos, I. Ordóñez-Etxeberria (eds.), 2019

Investigating the true nature of the red hypergiants.

Ricardo Dorda[1], Hugo M. Tabernero[1], and Ignacio Negueruela[1]

[1] Universidad de Alicante, San Vicente del Raspeig - Alicante (Spain)

Abstract

Red hypergiants (RHGs) are evolved high-mass stars with very low temperatures and extreme mass-loss rates, whose luminosities are close to the empirical upper luminosity boundary. Classically, these stars have been considered as a peculiar group among red supergiants (RSGs), as they have supposedly evolved from very high initial masses (above $30\,M_{\odot}$), far above the 10 to 25 $M_{\odot}$ expected for most RSGs. However, evolutionary models do not offer a satisfactory explanation for the observations of RHGs, and a new scenario has been proposed to explain these stars, that they are regular RSGs which are in their last stage. In order to understand the true nature of these stars, we have performed a spectroscopic following of some well-known galactic RHGs along two years, covering approximatively one of their variability perdiods. Our results on the most remarkable star in our sample, VX Sgr, were unexpected and show that there is yet much to understand about these stars.

1 Introduction

Red supergiants (RSGs) are evolved stars with moderately-high initial masses, between 10 and $40\,M_{\odot}$ ([3, 7]). These are the largest stars known, with radios between 400 and $1\,700\,R_{\odot}$, and characterized by their low effective temperatures ($T_{\rm eff}$), which implies late spectral types (SpTs), mainly M in Galactic RSGs, and their very high luminosities, in the range of $\log(L/L_{\odot}) \sim 4.5-5.8$. Among these stars, there is a small subpopulation that present even more extreme characteristics (see Table 1), known as "OH/IR M-type supergiants", "extreme red supergiants", or "red hypergiants" (RHGs).

There are two scenarios for the origin of RHGs. The classical interpretation, based on the prediction of evolutionary models([7]), says that these stars come from the evolution of stars with initial masses between 30 and 40 $M_{\odot}$ ([17]). However this scenario has some problems. Evolutionary tracks in the range of 30 and $40\,M_{\odot}$ do not reach temperatures lower than those of lower masses [18]. Thus, it is not easy to explain why they present much later

Table 1: Comparative between "average" RSGs and red hypergiants.

Property	Average RSGs	Red hypergiants
Luminosity [$\log(L/\mathrm{L}_{\odot})$]	$\sim 4.7-5.1$	$\sim 5.3-5.8$
Mass-loss [$\log(M_{\mathrm{loss}}/\mathrm{M}_{\odot})$]	~ -6	~ -5 to -4[a]
Spectral type	Centred distribution around M2[b]	M4 or later[c]
Spectral variability	$\sim$ 1 subtype or less	From 2 subtypes up to 6[d]
Photometric variability	$\sim$ 1 mag in V	$2-3$ mag in V
	< 0.5 mag in I	> 0.5 mag in I

[a]In addition, RHGs also present H_2O masers while normal RSGs do not.
[b]Most RSGs between M0 and M4
[c]As late as M10
[d]From M4 to M10

SpTs. Moreover, according to the models, they stay only for such a short time at the coolest end of the tracks that it would be impossible to observe any of them ([6]). A new scenario was proposed a few years ago. It is based on observations of clusters rich in RSGs whose age correspond to stars with initial masses in the range 15 and 20 $\mathrm{M}_{\odot}$. Sometimes these clusters also host a few (one or two) RHGs, which are expected to be already dead according to the first scenario ([16, 2]). Therefore, this scenario proposes that evolutionary models are underestimating the luminosity of RSGs at the end of their lives, and that RHGs are the last and brief stage of RSGs.

Our approach to RHGs is motivated by the lack of modern studies about these stars, as the only recent works are about their envelopes. Thus, the information about their chemical composition and spectral variability is scarce. To understand better these stars, we observed a significant sample of them (8) with high resolution spectroscopy along one of their photometric periods (typically about two years). For this, we used the spectrograph mounted on the robotic telescope Stella (1.2 m, R$\sim$ 55 000 from 3 900 to 8 700 Å). We observed our targets with a frequency of one observation every $2-3$ months during two years. Now we have almost finished the analysis of the most extreme star in our sample, VX Sgr, and we have began the analysis of the other seven.

2 Analysing VX Sgr

2.1 Data

VX Sgr has been studied in many works. It is known to present the largest SpT variations found in a RSG ([11, 15]), from M4 up to M10, along a period of about 2 years (732 d according to [13], and 750 d [12]). VX Sgr also presents variable veiling (weakened atomic lines) and activity in H lines ([11]). Its photometric variation has an irregular amplitude, alternating quiescent periods (amplitudes of $\sim$ 2 mag) with active periods, when it varies up to 6 mag ([12]).

The distance to VX Sgr has been calculated through different methods, an it ranges from 1.1 to 1.8 kpc, but there is not a definitive value. Depending on the method, $T_{\rm eff}$ and the distance used, its bolometric magnitude vary from $M_{\rm bol} = -8.4$ ([4]) to $M_{\rm bol} = -9.1$ mag ([1, 14]).

We have observed VX Sgr at 8 different times during the last two years with the Stella Spectrograph. For each spectrum collected we obtained its $T_{\rm eff}$, SpT and radial velocity (RV). In addition, we observed it on three extra epochs with UVES (mounted on the Very Large Telescope), but from these spectra we could not obtain the $T_{\rm eff}$, due to the spectral range covered.

2.2 Which is the true nature of VX Sgr?

Examining the spectra we found present the Rb lines at 7 800.3 and 7 947.6 Å. In the subsequent revision of bibliography, this fact was already reported by [8], in a work about asymptotic giant branch (AGB) stars which has not been accounted in any work about VX Sgr. Rb is an s-element which is only present in the atmospheres of AGB stars, evolved stars with initial masses from ~ 1 to $10\,{\rm M}_\odot$. Moreover, their abundances are specially high in AGb with high masses ($> 4-5\,{\rm M}_\odot$; [8]) Thus, the presence of Rb is not compatible with the assumption that VX Sgr is a RSG.

Nonetheless, it is not straightforward that VX Sgr is an AGB star. The highest-luminosity AGB stars observed have $M_{\rm bol} \sim -8$ mag ([10, 9]). This is in agreement with the highest luminosities predicted for AGB stars, which are expected to be reached by those with highest masses and lower metallicities ($M_{\rm bol} \sim -8.2$mag for masses from $M \sim 8$ to $M \sim 9{\rm M}_\odot$; [5]). However, the range of $M_{\rm bol}$ obtained for VX Sgr goes from -8.4 to -9.1 mag and it is not a low-metallicity star. Thus, only one key point is clear: VX Sgr is not an usual RSG neither a typical AGB star. However, it is more likely that it is an extreme AGB star, than a high-mass RSGs, as it is easier to explain an extreme luminosity in an AGB star, than the presence of Rb in a RSG. Also, a new question arises from this: is VX Sgr an isolated anomaly among high-mass hypergiants or are all the others intermediate-mass stars?

2.3 Unexpected results

The presence of Rb lines is not the only unexpected result: they present two anomalies. The first one is that the both lines are shifted toward the blue. This shift has been detected before in a few other AGBs and has been explained assuming that the Rb lines have a circumstellar origin ([19]). The second anomaly has not been observed before. In one of our epochs, in addition to the the blue-shifted Rb lines, another pair of Rb lines appeared on the position expected for the phostospheric Rb lines. We think that the photospheric component in the Rb lines is usually hidden by the P-cygni emission of the circumstellar component. According to the models calculated by [19] such emission depends on the density of the envelope. Therefore, a reduction of the P-Cygni emission can be caused by a decrease of the envelope density, which probably is related to spectral and photometric variations.

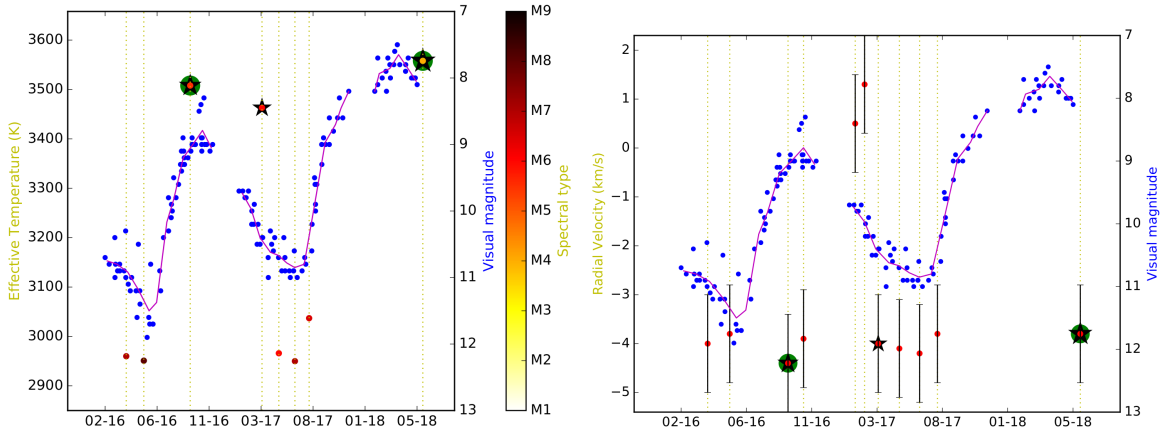

Figure 1: Light curve of VX Sgr. Blue dots are visual magnitude observations from AAVSO and the magenta line indicates the average value (magnitude scale is indicated in the right axis). Epochs with significant veiling are indicated by background black stars, while green halos indicate H emission. The Rb anomaly (see text) happened on 04/04/17. Reddish points are our spectral data and their corresponding values are given in left axis: Fig.1a (left): T_{eff} and point colors represent the SpT. Fig.1b (right): Radial velocity.

To study the variations of VX Sgr we used the data collected by AAVSO[1] for the visual band. We compare the light curve with our own data in Figure 1. The light curve of VX Sgr has been linked to the formation and evaporation of molecular layers, mainly TiO ([12]). This is coherent with the variation of the SpT, as later types, which have more intense TiO bands, happen at minimum light while earliest types happen at maximum light (see 1a). In Mira stars (which are also AGB stars), these variations are caused by the pulsation of the star. However, we found the RV of VX Sgr to be constant at -4 km/s (see Figure 1b). However, there is a sudden variation in the spectra obtained in January and February 2017. These spectra show very different velocities, and thus happens not long before the Rb anomaly (April 2017). This does not seem related to a periodic pulsation, but a sudden change in the star.

2.4 Period analysis

There are two more hints that point toward a sudden change in VX Sgr. Firstly, we used the 83 years of AAVSO data to calculate the period, obtaining 750 d (consistent with [12] results). However, this does not match with the last two years. Only 520 d passed between the two last maxima, and 450 d between last to minima. This anomaly supports the idea that something changed in VX Sgr that altered its usual periodic variation. Secondly, the last maximum light, at the beginning of 2018, has reached the lowest magnitudes since 1968, almost 1.5 mag brighter than the previous one in 2016.

[1]American Association of Variable Star Observers

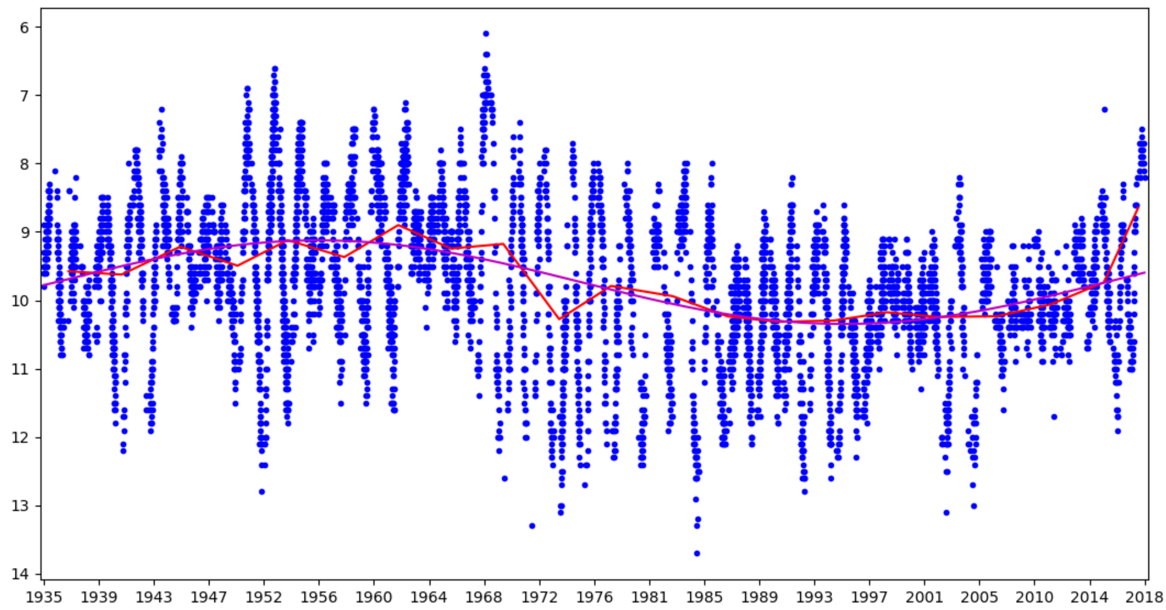

Figure 2: Light curve for VX SGr. Blue dots are visual magnitude observations from AAVSO. The red line indicate the average value, while the magenta line is a sinusoidal model with $P \sim 27\,600$ d.

When we analysed the light curve, we found a tentative secondary ultra-long period of $\sim 27\,600$ d (~ 75.5 a), never detected before. We think that it is an intrisic variation, as there are no signs of an unknown companion in the circumstellar envelope ([12]). When we examined the 83-year light curve, we found that the only maximum lights in the main period similar or brighter than the last one, are those happening around during the last maximum in the secondary period, as shown in Figure 2. According to our fit of a 75-year period, VX Sgr is about to reach (less than one decade away) the maximum in this secondary period. Thus, we speculate that whatever are the processes drive this secondary period, they are related to the violent change that we have observed.

3 Conclusions

The analysis of VX Sgr is almost finished, but we do not have definitive conclusions yet. The detailed analysis and our conclusions will be published in Tabernero et al. (in prep). However, this is only the beginning. Many new questions about this star have arisen from our observations. To answer them we are performing a spectroscopic follow up programme with much higher time resolution (one observation each ~ 10 d), that will allow us to examine in much higher detail any other sudden episode like the one happened in 2017. Also, we are still analysing the other RHGs. From that work we would be able to stablish whether VX Sgr is an isolated case among RHGs or not, and the nature of these mysterious stars.

Acknowledgments

This research is partially supported by the Spanish Government Ministerio de Economía y Competitividad under grant AYA2015-68012-C2-2-P (MINECO/FEDER).

References

[1] Arroyo-Torres B., Wittkowski M., Marcaide J. M., et al. 2013, A&A, 554, A76

[2] Beasor, E. R. & Davies, B. 2016, MNRAS, 463, 1269

[3] Brott, I., de Mink, S. E., Cantiello, M., et al. 2011, A&A, 530, A115

[4] Chiavassa A., Lacour, S., Millour, F., et al. 2010, A&A, 511, A51

[5] Doherty C. L., Gil-Pons P., Siess L., et al. 2015, MNRAS, 446, 2599

[6] Dorda, R., Negueruela, I., González-Fernández, C., et al. 2016, A&A, 592, 16

[7] Ekström, S., Georgy, C., Meynet, G., et al. 2013, EAS publication series, 60, 31

[8] García-Hernández, D. A.; García-Lario, P.; Plez, B., 2006 Science 314 1751

[9] García-Hernández D. A., Manchado, A., Lambert, D. L., et al. 2009, ApJ, 705, L31

[10] Groenewegen M. A. T., Sloan G. C., Soszyński I., et al. 2009, A&A, 506, 1277

[11] Humphreys R. M., Strecker D. W. & Ney E. P., 1972, ApJ, 172, 75

[12] Kamohara R., Deguchi S., Miyoshi M., et al. 2005, PASJ, 57, 341

[13] Kukarkin B. V., et al., 1969, General Catalogue of Variable Stars. Volume 1. Constellations Andromeda - Grus.

[14] Liu J., Jiang B. W., Li A., et al. 2017, MNRAS, 466, 1963

[15] Lockwood G. W. & Wing R. F., 1982, MNRAS, 198, 385

[16] Negueruela, I. 2015 IAUGA 2252230N

[17] Schuster M. T., Humphreys R. M., Marengo M., 2006, AJ, 131, 603

[18] Tabernero, H. M., Dorda, R., Negueruela, I. et al. 2018 MNRAS 476 3106

[19] Zamora, O.; García-Hernández, D. A.; Plez, B. et al. 2014 A&A 564 4

Highlights on Spanish Astrophysics X, Proceedings of the XIII Scientific Meeting of the Spanish Astronomical Society held on July 16 – 20, 2018, in Salamanca, Spain. B. Montesinos, A. Asensio Ramos, F. Buitrago, R. Schödel, E. Villaver, S. Pérez-Hoyos, I. Ordóñez-Etxeberria (eds.), 2019

The shape of the Galactic abundance gradient of oxygen from deep spectra of H II regions.

C. Esteban[1,2]

[1] Instituto de Astrofísica de Canarias, E-38200, La Laguna, Tenerife, Spain
[2] Departamento de Astrofísica, Universidad de La Laguna, E-38206, La Laguna, Tenerife, Spain

Abstract

We present results of an ongoing project dedicated to reassess the shape of the radial abundance gradient of O in the Milky Way based on deep spectroscopy of H II regions. Most of he data have been obtained with spectrographs attached to 8-10 m telescopes. The actual sample comprises 35 objects located at Galactocentric distances, $R_{\rm G}$, from 5.1 to 17 kpc, covering a substantial fraction of the Galactic disc. We determine $T_{\rm e}$ from the direct method for all of the objects, implying that the abundance determinations are very reliable. We confirm the absence of flattening of the O gradient in the outer Milky Way beyond R_{25}, at least up to $R_{\rm G} \sim 17$ kpc. We report the presence of a flattening or drop of the O abundance in the inner part of the Galactic disc, at $R_{\rm G} <$ 7-8 kpc. Finally, we find that the scatter of the O abundances of H II regions with respect to the gradient fitting is not substantially larger than the observational uncertainties, indicating that O is well mixed in the interstellar gas along the observed section of the Galactic disc.

1 Introduction

The determination of radial gradients of chemical abundances in galactic discs is a powerful observational constraint for chemical evolution models. These gradients reflect the distribution of star formation history and the effects of gas flows and other processes over the chemical composition of the galaxies. H II regions trace the present-day composition of the interstellar medium and are used to determine the abundance of several elements, especially of O, the proxy of metallicity in the analysis of ionised nebula. In these objects, the O abundance can be derived adding the ionic abundances of O^{+} and O^{2+}, that can be obtained from the intensity of bright optical collisionally excited lines (hereafter CELs).

Oxygen is produced mostly by massive, short-lived stars. There are numerous determinations of the radial abundance gradient of O of the Milky Way based on H II regions observations (e.g. [25], [5], [23] or [2], among others). Although the recent determinations agree on that the gradient slope is between -0.040 and -0.060 dex kpc^{-1}, its exact shape has been debated. Based on H II regions and planetary nebulae data, some authors have claimed that the gradients flatten out at the outer parts of the Galactic disc (e. g. [10], [26], [17]), while others do not find evidences of such flattening (e.g. [4], [14]). On the other hand, certain works on metallicity gradients based on Cepheids and red giants observations find indications of a flattening of the gradients in the inner Galactic disc, at $R_{\rm G}$ < 5-6 kpc ([12], [18], [1]). However, no evidences of a inner flatter slope has been reported from observations of ionized nebulae.

The paucity of accurate abundance determinations for H II regions in both extremes of the Galactic disc – central zones and anticentre – has been an enduring problem in the exploration of the shape of the Galactic O gradient. Those distant nebulae are usually faint, heavily reddened and the number of them with direct determinations of $T_{\rm e}$ – essential for determining reliable abundances – is rather limited (e.g. [19], [9]). Several of the most cited papers on the Galactic O abundance gradient (e.g. [25] or [5]) use optical spectra of H II regions and $T_{\rm e}$ determinations from radio observations. Optical and radio measurements are not cospatial and the aperture sizes of both kinds of data are very different. In addition, radial abundance gradient studies based on FIR observations (e.g. [23]) combine measurements of CELs from FIR spectra and $T_{\rm e}$ determined from radio observations with also different apertures.

We are carrying out a project to obtain very deep spectroscopy of a selected sample of H II regions covering the largest possible fraction of the Galactic disc. By now, the observed sample covers 35 objects located at Galactocentric distances, $R_{\rm G}$, between 5.1 and 17.0 kpc. The main preliminary results concerning the O and N gradients have been published in [7] and [8]. Thirteen objects of the sample are located beyond the isophotal radius of the Milky Way, R_{25} = 11.5 kpc [6] and have been selected to investigate the behavior of the radial abundance gradients at the Galactic anticentre. Almost all the spectra have been taken with high or intermediate-resolution spectrographs attached to 8 - 10 m telescopes. In all the H II regions the $T_{\rm e}$-sensitive auroral [O III] 4363 Å and/or [N II] 5755 Å lines have been measured, assuring a direct and precise determination of the ionic abundances and avoiding uncertainties due to the combination of non-coespatial data used in previous abundance determinations.

We have taken special care in selecting appropriate values of $R_{\rm G}$ for the sample objects. For each one, we have assumed the mean values of the kinematic and stellar distances given in different published references (see [7] and [8] for details). We have associated an uncertainty for each distance, which corresponds to the standard deviation of the values considered for calculating the mean. In contrast to what is customary in many previous works, we include the errors in $R_{\rm G}$ when calculating the linear fits of the gradients. We have assumed the Sun located at $R_{\rm G}$ = 8.0 kpc [21].

We have derived $n_{\rm e}$ and $T_{\rm e}$ using the density and temperature-sensitive emission line ratios of the CELs observed in each spectrum. Using the line intensities of available CELs, we have derived ionic and total abundances of several elements as N, O, S, Cl, Ne, Ar and Fe. We have used the same methodology and atomic dataset for the calculation of physical conditions and abundances in all the objects. In the case of O, we do not need to assume an ionising correction factor, so the total O abundance is simply the sum of the O^+/H^+ and

O^{2+}/H^+ ratios determined from the observed line ratios and physical conditions. Several of the objects included in [8] are of very low ionisation degree, for which the [O III] lines at 4959 and 5007 Å are not detected. In these cases, we applied the assumption $O/H \approx O^+/H^+$.

2 The shape of the Galactic abundance gradient of oxygen

The spatial distribution of the O abundances for the H II regions of our sample is shown in Fig. 1. The data represented in this figure were firstly published in [8]. The least-squares linear fit to the R_G and the O/H ratios, gives the following radial O abundance gradient (continuous line in Fig. 1):

$$12 + \log(\mathrm{O/H}) = 8.80(\pm 0.09) - 0.041(\pm 0.006) R_{\mathrm{G}}; \quad (1)$$

valid for R_G from 5.1 to 17.0 kpc. As it is evident in Fig. 1 and was reported by [7], the slope of the radial abundance gradient of O does not change for objects located beyond or inside R_{25} whereas $R_G > 8$ kpc. This fact demonstrate the absence of flattening of the O gradient in the outer Milky Way, at least up to $R_G \sim 17$ kpc.

Fig. 1 also shows that the O/H ratio of H II regions located at $R_G < 8$ kpc seem to break the general distribution of the rest of the objects. In fact, this zone shows an inner drop or flattening of the O gradient. As a simple exercise, we have made a double linear fit of the spatial distribution of the O abundances. Firstly, we made a least-squares linear fit to the R_G and the O/H ratios but only including objects with $R_G > 8$ kpc. In this case, the resulting radial O abundance gradient is:

$$12 + \log(\mathrm{O/H}) = 8.90(\pm 0.11) - 0.050(\pm 0.010) R_{\mathrm{G}}; \quad (2)$$

which is somewhat stepper than the fit we obtain for the whole sample (Eq. 1) but still consistent within the errors. The linear fit given in Eq. 2 is shown by a dashed line in Fig. 1. We have performed a final least-squares linear fit including the objects with $R_G < 8$ kpc, and we obtain a positive slope:

$$12 + \log(\mathrm{O/H}) = 8.35(\pm 0.13) + 0.023(\pm 0.019) R_{\mathrm{G}}. \quad (3)$$

The presence of a drop or flattening of the O/H ratio in the inner zones of the Galactic disc is a striking result that may have important implications for chemical evolution models of the Galaxy. There are indications of such a change in previous works on the abundance distribution of O, Fe and α-elements in Cepheids in the inner Galactic disc ([18], [1]). Metallicity gradients derived from SDSS-III/APOGEE observations of red giants by [12] also indicate an apparent flattening at $R_G < 6$ kpc, especially important for low-$[\alpha/Z]$ stars. The flattening found with Cepheids or red giants begins at somewhat smaller distances (at $R_G \sim$ 5-6 kpc) than suggested by H II region observations, but the results seem to be qualitatively consistent considering the uncertainties. [1] proposed that this change of slope could be due to a decrease or quenching of the star formation rate produced by gas flows towards the Galactic

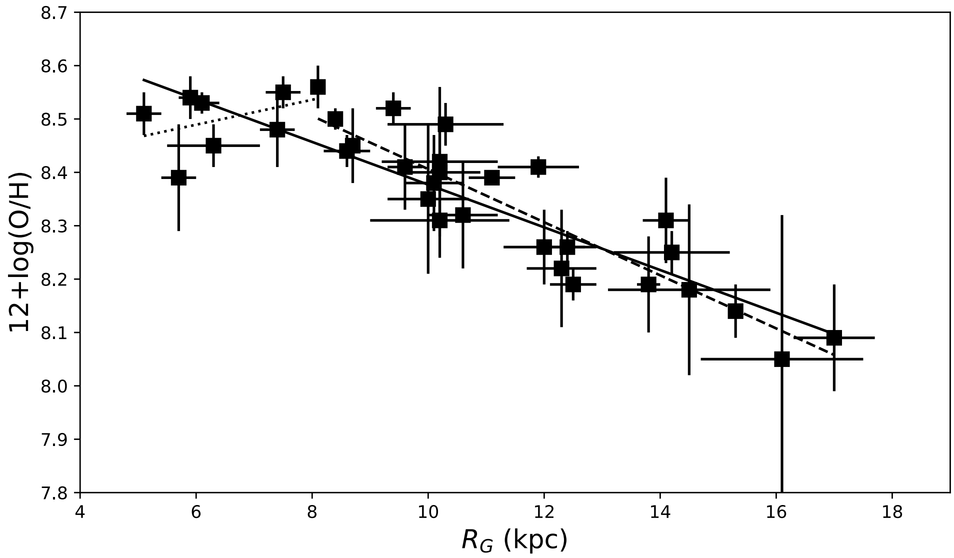

Figure 1: Radial distribution of the O abundance – in units of 12+log(O/H) – as a function of the Galactocentric distance, $R_{\rm G}$, for our sample of Galactic H II regions. The solid line represents the least-squares fit to all objects. The dashed line corresponds to the least-squares fit to the H II regions located at $R_{\rm G} > 8$ kpc and the dotted line to those with $R_{\rm G} < 8$ kpc.

Centre induced by the presence of the Galactic bar. On the other hand, [13] and [15] propose that the star formation quenching may be produced by the increasing of turbulence in the gas due to the stellar bar. The higher turbulence would prevent the gas from collapsing and producing a decrease of the star formation efficiency within the corotation radius of the bar.

The different estimations of the corotation radius of the Galactic bar go from 3.4 to 7 kpc [11]. Some dynamical models (e.g. [20], [16]) that reproduce recent density and kinematic data from red giants in the Galactic bulge/bar region require a corotation radius located at large distances for the Galactic Centre, $R_{\rm G} \sim$ 6-7 kpc. In this context, large a corotation radius is in reasonable agreement with our results for H II regions that suggest the inner drop or flattening at $R_{\rm G}$ of about 7-8 kpc.

Inner drops in the radial O abundance distributions have been already found in several spiral galaxies (e.g. [3], [22], [24]). In all the cases, these features have been obtained from abundance analysis based on strong-line methods and not on direct determinations of $T_{\rm e}$ of the H II regions. [24] have found that about 35% of the objects of their sample – about 100 – show an inner drop located about half of the effective radius, $R_{\rm e}$, of the galaxy. Considering that $R_{\rm e}$ is between 4-5 kpc in the Milky Way [6], the position of our change of slope is located at a considerably larger distance than expected if the behavior found by [24] is extrapolated to our Galaxy.

The mean difference of the O abundance of the H II regions represented in Fig. 1 and the abundance given by Eq. 1 at their corresponding distance is ± 0.05 dex, of the order of the typical uncertainties in the determination of individual abundances. This indicates that

O is well mixed in the interstellar gas along the observed section of the Galactic disc. This result contrast dramatically, for example, with the large scatter shown in figure 5 of [23]. The high quality of our data, the homogeneous analysis of a single set of observations and the cospatial direct determination of T_e for all the objects may be the reasons that explain these remarkably different results.

Acknowledgments

This work has been funded by the Spanish Ministerio de Ciencia, Innovación y Universidades under project AYA2015-65205-P. I thank the collaboration of J. García-Rojas, X. Fang and L. Toribio San Cipriano in different aspects of this project.

References

[1] Andrievsky, S. M., Martin, R. P., Kovtyukh, V. V., Korotin, S. A., & Lépine, J. R. D. 2016, MNRAS, 461, 4256

[2] Balser, D. S., Rood, R. T., Bania, T. M., & Anderson, L. D. 2011, ApJ, 738, 27

[3] Belley, J., & Roy, J.-R. 1992, ApJS, 78, 61

[4] Caplan, J., Deharveng, L., Peña, M., Costero, R., & Blondel, C., 2000, MNRAS, 311, 317

[5] Deharveng, L., Peña, M., Caplan, J., & Costero, R. 2000, MNRAS, 311, 329

[6] de Vaucouleurs, G., & Pence, W. D., 1978, AJ, 83, 1163

[7] Esteban, C., Fang, X., & García-Rojas, J. 2017, MNRAS, 471, 987

[8] Esteban, C., & García-Rojas, J. 2018, MNRAS, 478, 2315

[9] Esteban, C., García-Rojas, J., Peimbert, M., Peimbert, A., Ruiz, M. T., Rodríguez M., & Carigi, L. 2005, ApJ, 618, L95

[10] Fich, M., & Silkey, M. 1991, ApJ, 366, 107

[11] Gerhard, O. 2011, Mem. della Soc. Astron. Ital. Suppl., 18, 185

[12] Hayden, M. R. et al. 2014, AJ, 147, 116

[13] Haywood, M., Lehnert, M. D., Di Matteo, P., Snaith, O., Schultheis, M., Katz, D., & Gómez, A. 2016, A&A, 589, A66

[14] Henry, R. B. C., Kwitter, K. B., Jaskot, A. E., Balick, B., Morrison, M. A., & Milingo, J. B. 2010, ApJ, 724, 748

[15] Khoperskov, S., Haywood, M., Di Matteo, P., Lehnert, M. D., & Combes, F. 2018, A&A, 609, A60

[16] Li, Z., Gerhard, O., Shen, J., Portail, M., & Wegg, C. 2016, ApJ, 824, 13

[17] Maciel, W. J., Lago, L. G., & Costa, R. D. D. 2006, A&A, 453, 587

[18] Martin, R. P., Andrievsky, S. M., Kovtyukh, V. V., Korotin, S. A., Yegorova, I. A., & Saviane, I. 2015, MNRAS, 449, 4071

[19] Peimbert, M., Torres-Peimbert, S., & Rayo, J. F. 1978, ApJ, 220, 516

[20] Portail, M., Wegg C., Gerhard, O., & Martinez-Valpuesta, I. 2015, MNRAS, 448, 713

[21] Reid, M. J. 1993, ARA&A, 31, 345

[22] Rosales-Ortega, F. F., Díaz, A. I., Kennicutt, R. C., & Sánchez, S. F. 2011, MNRAS, 415, 2439

[23] Rudolph, A. L., Fich, M., Bell, G. R., Norsen, T., Simpson, J. P., Haas, M. R., & Erickson, E. F. 2006, ApJS, 162, 346

[24] Sánchez-Menguiano L., Sánchez, S. F., Pérez, I., Ruiz-Lara, T., et al. 2018, A&A, 609, A119

[25] Shaver, P. A., McGee, R. X., Newton, L. M., Danks, A. C., & Pottasch, S. R. 1983, MNRAS, 204, 53

[26] Vilchez, J. M., & Esteban, C. 1996, MNRAS, 280, 720

Highlights on Spanish Astrophysics X, Proceedings of the XIII Scientific Meeting of the Spanish Astronomical Society held on July 16 – 20, 2018, in Salamanca, Spain. B. Montesinos, A. Asensio Ramos, F. Buitrago, R. Schödel, E. Villaver, S. Pérez-Hoyos, I. Ordóñez-Etxeberria (eds.), 2019

The stellar cusp around the Milky Way's central black hole.

E. Gallego-Cano[1], R. Schödel[1], B. Shahzamanian[1], H. Dong[1], F. Nogueras-Lara[1], and A. T. Gallego-Calvente[1]

[1] Instituto de Astrofísica de Andalucía (CSIC), Glorieta de la Astronomía s/n, 18008 Granada, Spain

Abstract

The formation of a stellar cusp in a dense cluster around a massive black hole is a fundamental prediction of theoretical stellar dynamic, that has not been confirmed satisfactorily by observations so far. We address its study in the most suited laboratory: the inner parsecs at the Galactic centre. With improved methodologies, we find strong evidence of the existence of the stellar cusp around the Milky Ways's supermassive black hole, reaching finally an agreement between the theory and observation. The result is not only relevant for the Galactic centre but it has implications on other galactic nuclei and future observations, such as the frequency of observations of Extreme-Mass Ratio Inspirals with gravitational wave detectors.

1 Introduction

The majority of nearby galaxies have at their centres nuclear stellar clusters (NSCs), the densest and most massive stellar clusters (SCs) in the universe (see review by [28]). They are composed of multiple stellar populations, presenting a complex (even recent) star formation (SF) history, and they can coexist with massive black holes (BH). The study of NSCs can help us to make progress in many astrophysical fields (for example SF under extreme conditions) and study stellar dynamics, such as the formation of stellar cusps. Theoretical stellar dynamics predicts firmly the formation of a stellar cusp around a massive BH in a dense and dynamically relaxed SC (e.g., [24, 3, 15, 22]). They reach the same conclusion, by using analytical, Monte Carlo and N-body simulation: the stellar number density is described by a power law of the form $\rho \sim r^{-\gamma}$, where ρ is the stellar density and r is the distance from the black hole. For an SC composed of a single-mass stellar population, the cusp is developing with $\gamma = 1.75$ inside the radius of influence of the central BH. In general, if the SC consists of a range of stellar masses, we would expect a value of gamma between $1.5-2$, greater values for larger stellar masses.

Nevertheless, there are not observational confirmations supporting unambiguously the existence of stellar cusps up to now. Due to the great distance of the extragalactic systems, we only can study the light density averaged of hundreds to thousands (even millions) of stars, that in general are dominated by the brightest and youngest stars and therefore, not dynamically relaxed.

The Galactic centre (GC) is an ideal case for testing the existence of a stellar cusp. It is the closest nucleus of a galaxy, located at only ~ 8.12 kpc from Earth [21] and it has a $4\times 10^6\,\mathrm{M}_\odot$ [6, 20, 21] massive BH, Sagittarius A* (Sgr A*), surrounded by a $\sim 2.5\times 10^7\,\mathrm{M}_\odot$ NSC [31, 32, 13, 8, 14]. We can actually resolve the stars observationally on scales of about 2 milli-parsecs inside the radius of influence of the BH (~ 3 pc [1, 17, 33]). However, we can not find strong evidence for the existence (or not) of a stellar cusp at the GC so far. Many previous works have studied the surface of old stars. The first studies found a cusp-like structure [19, 30], but the successive ones, after removing properly young stars from the sample, determined that the distribution of stars around Sgr A* shows a core-like profile, resulting in the so-called *missing cusp* problem [4, 7, 11, 30]. Many theoretical papers have tried to explain this lack of cusp, mainly in two different research lines. On the one hand, some of them claim that the distribution that we observe is representative for the entire old population and there is no cusp, perhaps because the relaxation time is very long (>> 10 Gyr) [25] or because the cusp has been already destroyed [26]. On the other hand, other studies suggest that the distribution we observe is only representative for bright stars, and there is a hidden cusp. They explain the deficit of giants around Sgr A* by the destruction of their envelopes rendering them to invisible for observations, due to stellar collisions, that do not be able to fully explain the observed distribution [9], or fragmenting stellar discs, that [2] can.

The most important difficulty that we have to overcome to study this fundamental problem of theoretical stellar dynamics is the stellar classification. We have to select suited tracer populations, old enough to be dynamically relaxed. Due to the extreme interstellar extinction toward the GC and source crowding, observations studies are very challenging. The spectroscopic identification of stars is limited to brightest giants and massive, young stars ($\mathrm{K}\leq 16$). Moreover, the SF history of the NSC is complex: we find stellar population made up of multiple generations of stars: old (> 1 Gyr) population of stars, but also a young generation of stars (< 100 Myr). In order to study the cusp, we have to focus on stars with ages greater than the relaxation time at the GC (a few Gyr [1]). Only red clump (RC) stars fulfil that condition up to now and dominate the measurements. Moreover, the NSC is not isolated, so that when we measure stars number density and diffuse flux toward the GC, we find several superposed components: Galactic disc (GD), Galactic bulge (GB), nuclear stellar disc (NSD) and NSC. Therefore, our knowledge about the stellar population is limited to the brightest few percents of stars, either few million-year old hot post main sequence (MS) giants and MS O/B stars, or giants on the RC. In fact, the only study that analyzed fainter stars found a cusp within $5''/0.2$pc of Sgr,A* [34]. We present the latest works addressing the distribution of stars around Sgr A* with improved methodologies to reach the faintest stars studied so far and test other possibly tracer populations.

2 Data and methodology

In order to study the distribution of stars around Sgr A*, we use data obtained with NACO instrument at the ESO/Very Large Telescope (VLT) and we focus on two different methods to analyze three different stellar populations.

2.1 Star counts

We use S27 camera data with $0.027''$ pixel scale in H-band from 9 May/2010 and in K_s-band from 9 August/11-12 September 2012. All the data were acquired with similar four-point dither pattern centred on Sgr A*, that covers a field of view (FOV) of about $40'' \times 40''$ (deep mosaic in the left panel in Figure 1). Moreover, we use K_s-band data from 11 May 2012 in order to study larger distances. They cover a wider mosaic of about $1.5' \times 1.5'$ with a 4×4 dither pattern, centred on Sgr A*. The data are summarised in Table 1 from [17]. The standard data reduction (sky subtraction, bad pixel removal and flat fielding) was improved by rebbining the images a factor of two, via a quadratic interpolation, and removing of systematic horizontal noise from detector electronics. The final images were aligned, staked and combined in a simple mean. We also included the wider mosaic with a larger FOV, obtained the Figure 6 in [17]. We implemented the source detection, astrometry, and photometry with the point spread function (PSF) fitting program *StarFinder* [10]. We took into account the variability of the PSF across the FOV, and we divided the FOV into small sub-fields ($10'' \times 10''$), smaller than the isoplanatic angle. We enhanced the PSF extraction by considering the halo of the brightest star in the field GCIRS7 joined with the local PSF for each concrete sub-field. Moreover, we considered explicitly the systematic errors derived by the choice of the *StarFinder* parameters, by considering different sets of values to analyze the images. The methodology is described in detail in [17].

2.2 Diffuse light

We use the same data described in the previous Section but we add K_s-band VLT/NACO S13 camera data from 4 May/12 June/13 August 2011, 4 May/9 August/12 September 2012, and 29 March/14 May 2013. We also add the intermediate band (IB) filter imaging data at 2.27μm (details in Table 1 of [7]). We proceeded in the same way that we explained before, but we took care especially of the subtraction of stars close to the brightest stars (GCIRS7, IRS 16, IRS 1, IRS 33 and IRS 13) concentrated in the inner 0.5 pc, which is a critical step in the analysis of the diffuse light. Another crucial point is the correction of the so-called mini-spiral (see e.g.[18]). Therefore, we subtracted from our images the calibrated HST/NICMOS 3 image of the gas emission at 1.87μm from [12] (see left panel in Figure 2 of [33]). The details of the analysis are described meticulously in [33]. Figure 1 shows the different results obtained along with all the procedure. The middle and right panels show the same image with all detected stars subtracted by using a simple, constant PSF and by using a locally

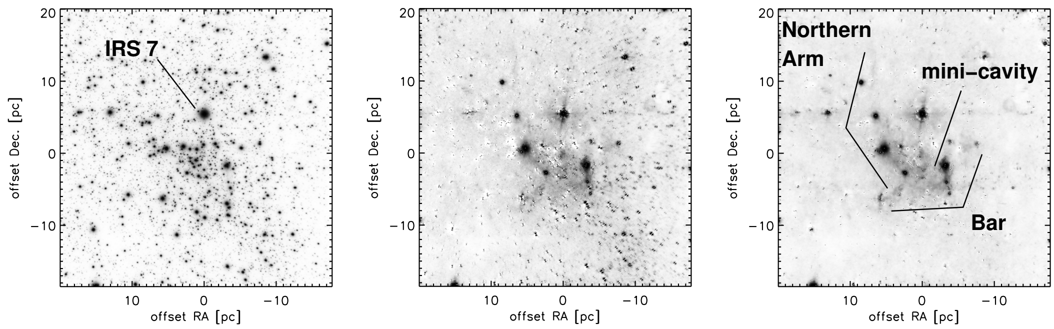

Figure 1: Images obtained along with all the procedure. *Left*: deep K_s-band mosaic centred on Sgr A*. *Middle*: the same image but with all the detected stars subtracted by using a single and constant PSF across the FOV. *Right*: Point source-subtracted K_s-band deep mosaic by using a local PSF kernel merged with a constant halo, determined from IRS 7. We can see the residuals due to consider the same PSF across the FOV. We use a logarithmic colour scale in all images. The middle and right panel have the same scale. North is up and East is to the left.

PSF kernel merged with a constant halo, respectively. We can see how we corrected the effect of the anisoplanatism that gives us an important source of residual in the image by using the variable core plus halo PSF.

3 Results

In order to study the existence of a relaxed cusp, we need to focus on stars that are at least several Gyr, similar to the relaxation time of the NSC at the GC (see [1]). The key point of our study is, on the one hand, pushing the completeness limit in stars counts about one magnitude deeper than in previous works and, on the other hand, study the surface brightness profile of the diffuse light, which traces even fainter stars. Figure 7 in [17] shows the K_s-Luminosity Function (KLF) determined from our deep mosaic. The new completeness limit from our work is $K_s \sim 18.5$, one magnitude deeper than in previous studies. Figure 16 of [30] shows the old star fraction, the mean stellar mass and the KLF as a function of theK_s magnitude based on a population synthesis model for the inner parsecs of the GC, assuming continuous star formation at a constant rate over the last 10 Gyr with a Miller-Scalo initial mass function [27]. We can see that the fraction of old stars reaches 80% at $K_s \sim 15.5$ magnitude, and again increases for $K_s > 17.5$. Whereas all the previous star density measurements were dominated by the RC and brighter giants ($K_s < 17.5$), now we can test two different new ranges of magnitude with a high fraction of old stars: faint stars with $17.5 \leq K_s \leq 18.5$ with masses of ~ 2.5 $M_\odot$ and even fainter, unresolved sources, with masses less than 1.5 $M_\odot$, probably sub-giants and MS stars.

The projected surface density of the old stars can be described by simple power laws

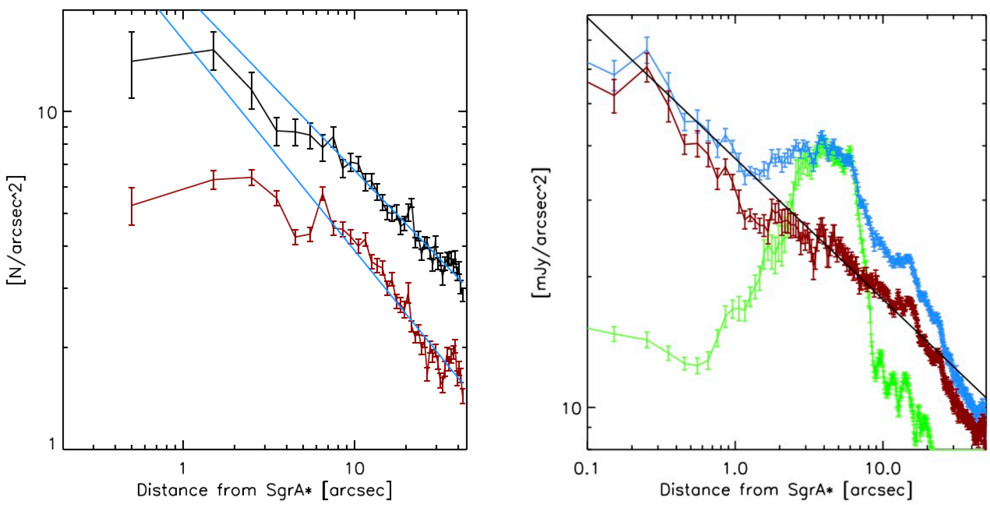

Figure 2: *Left*: Projected surface number density for giants (red) and faint stars (black). The blue lines are simple power-law fits to the data at 0.2 pc $\leq R \leq$ 1.0pc. *Right*: SB profile for the diffuse light for the wide-field K_s-image before (blue) and after (red) to the subtraction of the Paschen α emission (green). We multiply it by a adequate factor to optimise the plot. The black line is a simple power-law fit to the data at $R \leq 25''$(1 pc).

of the form $\Sigma(R) \propto R^{-\Gamma}$, where Σ is the surface number density, R the projected radius, and Γ the power-law index. We assume that the underlying spatial distribution of the stars in the central parsec is spherically symmetric, that is a good approximation for the central parsec. Table 2 in [17] show the different fits to the different distance ranges. The mean value and standard deviation for stars in the interval $17.5 \leq K_s \leq 18.5$ (faint stars) is $\Gamma_{faint} = 0.47 \pm 0.07$ (black line in right panel in Figure 2) and for stars in the magnitude interval $12.5 \leq K_s \leq 16$ (giants stars), $\Gamma_{giants} = 0.62 \pm 0.12$ (red line in right panel in Figure 2). For giants, only data at R $\geq 8''/0.24$pc gives us a good fit. The power law indices for the surface brightness (SB) profiles for the diffuse light are showns in Table 1 of [7]. The mean value is $\Gamma = 0.26 \pm 0.02_{stat} \pm 0.05_{sys}$.

To conclude, we aim to explore the 3D density structure of the stars near the massive black hole. Therefore, we need to convert the measure 2D profile into a 3D density law and deal with projection effects. For this reason, we have to add new data at projected radii R $\geq$ 2pc. We use the data from [16], that used extinction corrected near-infrared data from VLT/NACO, WFC/HST, and VISTA, and from [32], that used extinction-corrected Spitzer 4.5 μm. In order to isolate the star density of the NSC, we have to subtract from our sample the fore-/background contribution (NSD, GB, and GD). We used the Sérsic model for the non-NSC emission from Table 2 of [32]. Finally, in order to describe the 3D shape of the cluster, we use the *Nuker* model [23] as a generalization of a broken power law as given in equation 1 of [16]:

$$\rho(r) = \rho(r_b) 2^{(\beta-\gamma)/\alpha} \left(\frac{r}{r_b}\right)^{-\gamma} \left[1 + \left(\frac{r}{r_b}\right)^{\alpha}\right]^{(\gamma-\beta)/\alpha}, \tag{1}$$

where r is the 3D distance from the black hole, r_b is the break radius, ρ is the 3D density, γ is the exponent of the inner and β the one of the outer power-law, and α defines the sharpness of the transition. We projected it onto the sky via the following integral:

$$\rho(r) = \Sigma(R) = 2 \int_r^{\infty} \frac{r\rho(r)dr}{\sqrt{r^2 - R^2}}. \tag{2}$$

Table 4 from [17] and Table 2 from [33] show different Nuker fits for the data, exploring the effect of using different fore-/background emission models, fit ranges, integration boundaries and different values of the parameter α. We take the mean value of the best-fit parameters and the standard deviation. For the diffuse light we obtain: $r_b = 3.1 \pm 0.3$ pc, $\gamma = 1.13 \pm 0.03$, $\beta = 3.5 \pm 0.3$ and $\rho(r_b) = 0.028 \pm 0.005$ mJy arcsec^{-3}. For faint stars with $K_s \sim 18$, we consider explicitly the possible contamination by pre-MS stars in the star counts. We obtain a somehow larger value for the inner index $\gamma \approx 1.3$. For the RC and brighter giants, we have to exclude the inner data, obtaining a value of $\gamma \approx 1.53$. Like previous works, we do find a flat surface density inside around 0.3 pc of Sgr A*.

4 Discussion and conclusions

In order to clarify the controversial existence (or not) of the stellar cusp at the GC, we address the distribution of old stars around Sgr A* with improved methodologies. We push the completeness limit to reach the faintest stars studied so far and to test three different stellar populations, old enough to serve as tracers for the existence of a stellar cusp. We find that the stellar density decreases with a power-law index inside the range $\gamma = 1.1 - 1.4$ for distances smaller than the influence radius of Sgr A* (~ 3 pc). We can rule out a flat core with high confidence. The cusp is shallower than the predicted one by theory, but it can be explained if the star formation history of the NSC is taken into a count. In [5] a star cluster surrounding a central massive black hole is evolved over a Hubble time under the combined influence of two-body relaxation and continuous star formation. They compare their results with our observations, coming to an agreement between theory and observation for the first time. A caveat is a possible contamination by young stars in the distribution of faint stars. On the one hand, we explore explicitly the possible contamination by pre-MS stars, but on the other hand, we do not have data from stars that formed 100 Myr ago, although we know that the star formation rate in the central parsec was high in this epoch [29]. Like previous works, we find a lack of giants at projected distances of a few 0.1 pc of the supermassive black hole, that indicates some mechanism has altered their distribution. The number of missing giants estimated is on the order of 100.

Future works have to disentangle the intrinsic structure of the cusp, looking into the classification of the stars and rebuilding the 3D structure of the cluster by taking new faint and robust data to about 40 pc from the supermassive black hole. We are working on studing the different stellar populations across the NSC and improving the isolation of the NSC from the emission of the GB, GD, and NSD, taking into account more realistic models for them. The efforts made in clarifying our knowledge of the stellar cusp at the GC are fundamental for understanding not only the stellar dynamics at the GC but for the implications that have in other galactic nuclei and the observation of EMRIs with gravitational wave detectors in future observations.

Acknowledgments

The research leading to these results has received funding from the European Research Council under the European Union's Seventh Framework Programme (FP7/2007-2013) / ERC grant agreement n° [614922]. This work is based on observations made with ESO Telescopes at the La Silla Paranal Observatory under programmes IDs 183.B-0100 and 089.B-0162. We thank T. Fritz for detailed and valuable comments. This work has made use of the IAC-STAR Synthetic CMD computation code. IAC-STAR is suported and maintained by the computer division of the Instituto de Astrofísica de Canarias. PAS acknowledges support from the Ramón y Cajal Programme of the Ministry of Economy, Industry and Competitiveness of Spain. This work has been partially supported by the CAS President's International Fellowship Initiative.

References

[1] Alexander, T. 2005, physrep, 419, 65

[2] Amaro-Seoane, P., & Chen, X. 2014, apjl, 781, L18

[3] Bahcall, J. N., & Wolf, R. A. 1976, apj, 209, 214

[4] Bartko, H., Martins, F., Trippe, S., et al. 2010, apj, 708, 834

[5] Baumgardt, H., Amaro-Seoane, P., & Schödel, R. 2018, aap, 609, A28

[6] Boehle, A., Ghez, A. M., Schödel, R., et al. 2016, apj, 830, 17

[7] Buchholz, R. M., Schödel, R., & Eckart, A. 2009, aap, 499, 483

[8] Chatzopoulos, S., Fritz, T. K., Gerhard, O., et al. 2015, mnras, 447, 948

[9] Dale, J. E., Wünsch, R., Whitworth, A., & Palouš, J. 2009, mnras, 398, 1537

[10] Diolaiti, E., Bendinelli, O., Bonaccini, D., et al. 2000, aaps, 147, 335

[11] Do, T., Ghez, A. M., Morris, M. R., et al. 2009, apj, 703, 1323

[12] Dong, H., Wang, Q. D., Cotera, A., et al. 2011, mnras, 417, 114

[13] Feldmeier, A., Neumayer, N., Seth, A., et al. 2014, aap, 570, A2

[14] Feldmeier-Krause, A., Zhu, L., Neumayer, N., et al. 2017, mnras, 466, 4040

[15] Freitag, M., Amaro-Seoane, P., & Kalogera, V. 2006, apj, 649, 91

[16] Fritz, T. K., Chatzopoulos, S., Gerhard, O., et al. 2016, apj, 821, 44

[17] Gallego-Cano, E., Schödel, R., Dong, H., et al. 2018, aap, 609, A26

[18] Genzel, R., Eisenhauer, F., & Gillessen, S. 2010, Reviews of Modern Physics, 82, 3121

[19] Genzel, R., Schödel, R., Ott, T., et al. 2003, apj, 594, 812

[20] Gillessen, S., Plewa, P. M., Eisenhauer, F., et al. 2017, apj, 837, 30

[21] Gravity Collaboration, Abuter, R., Amorim, A., et al. 2018, aap, 615, L15

[22] Hopman, C., & Alexander, T. 2006, apjl, 645, L133

[23] Lauer, T. R., Ajhar, E. A., Byun, Y.-I., et al. 1995, aj, 110, 2622

[24] Lightman, A. P., & Shapiro, S. L. 1977, apj, 211, 244

[25] Merritt, D. 2010, apj, 718, 739

[26] Merritt, D., & Szell, A. 2006, apj, 648, 890

[27] Miller, G. E., & Scalo, J. M. 1979, apjs, 41, 513

[28] Neumayer, N. 2015, IAU General Assembly, 22, 2236674

[29] Pfuhl, O., Fritz, T. K., Zilka, M., et al. 2011, apj, 741, 108

[30] Schödel, R., Eckart, A., Alexander, T., et al. 2007, aap, 469, 125

[31] Schödel, R., Feldmeier, A., Kunneriath, D., et al. 2014, aap, 566, A47

[32] Schödel, R., Feldmeier, A., Neumayer, N., Meyer, L., & Yelda, S. 2014, Classical and Quantum Gravity, 31, 244007

[33] Schödel, R., Gallego-Cano, E., Dong, H., et al. 2018, aap, 609, A27

[34] Yusef-Zadeh, F., Bushouse, H., & Wardle, M. 2012, apj, 744, 24

Highlights on Spanish Astrophysics X, Proceedings of the XIII Scientific Meeting of the Spanish Astronomical Society held on July 16 – 20, 2018, in Salamanca, Spain. B. Montesinos, A. Asensio Ramos, F. Buitrago, R. Schödel, E. Villaver, S. Pérez-Hoyos, I. Ordóñez-Etxeberria (eds.), 2019

Precise surface gravitites of A-type stars from Asteroseismology.

Antonio García Hernández[1,2], Juan Carlos Suárez[1,3], Andrés Moya[1], Mário J. P. F. G. Monteiro[2,4], Zao Guo[5,6], Daniel R. Reese[7], Javier Pascual-Granado[3], Sebastià Barceló Forteza[8,9], Susana Martín-Ruiz[3], Rafael Garrido[3], and Jesús Nieto[10]

[1] Department ofTheoretical Physics and Cosmology, University ofGranada (UGR), E-18071 Granada, Spain
[2] Instituto de Astrofísica e Ciências do Espaço, Universidade do Porto, CAUP, Rua das Estrelas, PT4150-762 Porto, Portugal
[3] Instituto de Astrofísica de Andalucía (CSIC), Glorieta de la Astronomía S/N, 18008, Granada, Spain
[4] Departamento de Física e Astronomia, Faculdade de Ciências da Universidade do Porto, Rua do Campo Alegre, 4169-007 Porto, Portugal
[5] Copernicus Astronomical Center, PAN, Bartycka 18, 00-716 Warsaw, Poland
[6] Center for High Angular Resolution Astronomy and Department of Physics and Astronomy, Georgia State University, P. O. Box 5060, Atlanta, GA 30302-5060, USA
[7] LESIA, Observatoire de Paris, PSL Research University, CNRS, Sorbonne Universités, UPMC Univ. Paris 06, Univ. Paris Diderot, Sorbonne Paris Cité, 5 place Jules Janssen, 92195 Meudon, France
[8] Instituto de Astrofísica de Canarias, 38200 La Laguna, Tenerife, Spain
[9] Departamento de Astrofísica, Universidad de La Laguna, 38206 La Laguna, Tenerife, Spain
[10] Universidad Internacional de Valencia, Area de Ciencia y Tecnología, 46002, Valencia

Abstract

δ Sct are one of the most abundant pulsating stars in our Galaxy. In addition, they have moderate to fast rotations and periods of several hours. That makes them the suitable targets for studying the effects of rotation on stellar evolution. In this work, we show how to infer the mean density and the surface gravity of an A-type pulsanting star only from its oscillation frequencies. To do this, we used a separation between frequencies, known as large separation, which is proportional to the stellar mean density. This is the first step towards a reliable mode identification of their oscillation modes.

1 Introduction

Study of stars with solar-type pulsations has reached important milestones during the last decade [1] thanks to space missions dedicated to high-precision photometry, such as CoRoT [2] and Kepler [11]. This has been possible thanks to their relatively simple oscillation spectrum, characterized by a frequency spacing known as large separation ($\Delta\nu$). However, this advance has not been possible in any other kind of pulsators.

δ Sct are a group of well-known pulsating stars, very popular in the 90s. Their popularity is due to the fact that they are bright, very abundant and with periods that allow gathering data during one night. They have masses between M = 1.5-3 $M_\odot$, are in the main sequence or in the phase of burning of H in layer and locate in the classical instability strip. The mechanism that maintains its pulsations is the kappa mechanism (κ), related to the opacity change that takes place in the second He ionization zone (s.e., [14]). They present moderate to rapid rotations [15] and both pressure (p) and gravity (g) oscillation modes [8, 17].

The oscillation spectrum of δ Sct stars is difficult to interpret, due to phenomena such as avoided crossing, non-linear interactions between modes and, above all, the effect of rotation, which modifies the spectrum and multiplies the number of frequencies (see e.g. [7] for a review on the subject). The research presented in this article is a summary of the work published in [5] (from now on, GH2017), which advances in the interpretation of the oscillation spectrum by using $\Delta\nu$. This quantity was recently found for δ Sct (see e.g., [4]) and related to the stellar mean density ($\bar{\rho}$, [6]). In this work, we improved such relation and used $\Delta\nu$ to derive the surface gravity ($\log g$).

This article is divided into the following sections. In Sec. 2, we present the sample and its more relevant characteristics. Section 3 describes the properties of the large separation-mean relation, the methodology carried out to determine $\Delta\nu$ and to fit the data. In Sec. 4, we described the procedure we followed to determine $\log g$. And Sec. 5 details the conclusions of this work.

2 Data sample

Testing a relationship between $\Delta\nu$ and $\bar{\rho}$ requires obtaining a mean density that does not rely on any stellar evolution model. One of the few cases in which this quantity can be obtained is from the determination of masses and radii of eclipsing binary stars. Thus, we looked for such systems with at least one δ Sct component, observed by satellite and with measurements of masses and radii. We found 10 systems that fulfilled these conditions and the only δ Sct that harbour a planet to date (HD 15082).

Table 2 lists the main characteristics of the pulsating components of the systems studied. The stellar mean densities ($\bar{\rho}$) are derived from the masses and radii given by the different authors who studied the systems (see references in GH2017). The surface gravities correspond to the values that these same authors provide ($\log g_{\rm b}$). The surface gravity $\log g_{\hat{\pi}}$ in column 6 refers to the value calculated from large separations and parallaxes. The parallaxes were

Table 1: Characteristics of the systems taken from the literature (see GH2017) and calculated in this work. Columns 3 to 5 are values inferred from the binary analysis, whereas column 6 is calculated from the parallax. The information corresponds to the component showing the large frequency pattern (which is not necessarily the primary).

System	$\Delta\nu$ (μHz)	$\bar{\rho}$ ($\bar{\rho}_{\odot}$)	Ω ($\Omega_{\rm K}$)	$\log g_{\rm b}$ (cgs)	$\log g_{\hat{\pi}}$ (cgs)	$\hat{\pi}$ (mas)
KIC3858884	29.0 ± 1.0	0.0657 ± 0.0021	0.075	3.740 ± 0.012	3.76 ± 0.04	1.78 ± 0.22
KIC4544587	74.0 ± 1.0	0.414 ± 0.039	0.17	4.252 ± 0.033	4.27 ± 0.08	1.36 ± 0.41
KIC10661783	39.0 ± 1.0	0.1255 ± 0.0039	0.20	3.95 ± 0.011	3.95 ± 0.04	1.94 ± 0.26
HD172189	19.0 ± 1.0	0.0283 ± 0.0061	0.28	3.490 ± 0.082	3.53 ± 0.06	2.27 ± 0.34
CID100866999	56.0 ± 1.0	0.26 ± 0.11	–	4.14 ± 0.14	–	–
CID105906206	20.0 ± 2.0	0.02986 ± 0.00095	0.15	3.539 ± 0.012	3.52 ± 0.10	0.96 ± 0.25
HD159561	38.0 ± 1.0	0.124 ± 0.021	0.60	3.960 ± 0.072	3.93 ± 0.03	67.13 ± 1.06
KIC9851944	26.0 ± 1.0	0.0566 ± 0.0043	0.29	3.691 ± 0.028	3.75 ± 0.25	0.41 ± 0.38
KIC8262223	77.0 ± 1.0	0.423 ± 0.043	0.11	4.287 ± 0.034	4.23 ± 0.10	1.93 ± 0.59
KIC10080943	52.0 ± 1.0	0.205 ± 0.070	0.049	4.07 ± 0.11	4.06 ± 0.08	1.06 ± 0.28
HD15082	80.0 ± 2.0	0.507 ± 0.046	0.20	4.300 ± 0.030	4.31 ± 0.03	8.51 ± 0.24

obtained from the first Gaia data release, DR1 [3], or from Hipparcos [18].

3 The $\Delta\nu$-$\bar{\rho}$ relation

The mean densities were calculated from data of masses and radii obtained from the literature. To calculate the stellar volume, the flattening caused by the centrifugal forces were also taken into account. In this way, a more adequate value of the densities was achieved.

The large separations were obtained following the method described in [4]. First, we selected a group of frequencies with the highest amplitudes and then we applied a Fourier transform taking the amplitudes equal to 1 for all of them. In addition, the histogram of frequency differences was computed and compared to find the correct value of the periodicity. The uncertainty was determined by an échelle diagram, which allows us to measure the deviation for which the pattern disappears. It also allow us to differentiate if the periodicity corresponds to $\Delta\nu$, $\Delta\nu/2$ or another submultiple.

The results of this search are shown in Table 2. Clearly, a linear regression is obtained when these values are represented against the mean densities. This is shown in left panel of Fig. 1. We carried out a fit to the data by implementing a hierarchical Bayesian linear regression. The computation was carried out using the JAGS package (Just Another Gibbs Sampler, [12]). The resulting relationship was:

$$\bar{\rho}/\bar{\rho}_{\odot} = 1.50^{+0.09}_{-0.10}(\Delta\nu/\Delta\nu_{\odot})^{2.04^{+0.04}_{-0.04}}, \tag{1}$$

where $\Delta\nu_{\odot} = 134.8$ μHz [10]. This relation is an update of the one found in [6]. It closely follows the relations found using models without ([16]) and including rotation ([13]). Indeed, this relation is independent of the stellar rotation. That makes $\Delta\nu$ a very valuable observable.

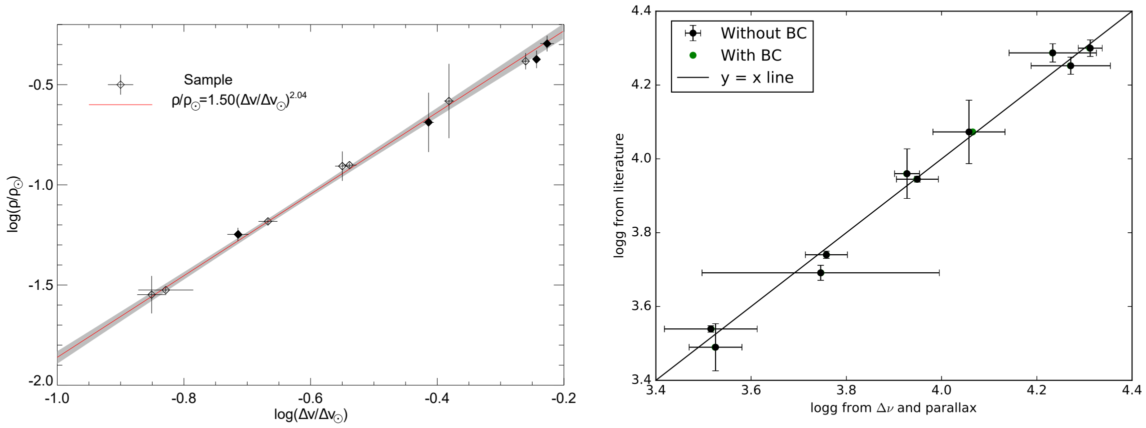

Figure 1: (Left) $\Delta\nu$-$\bar{\rho}$ relation for the 11 stars of our sample. The result of the fit is also shown. (Right) Plot showing the agreement between the $\log g$ from the literature (binary analysis) and that calculated with $\Delta\nu$ and the parallax.

4 Surfaces gravities from $\Delta\nu$ and parallaxes

In order to find if it was possible to determine the surface gravity of the δ Sct stars from $\Delta\nu$, it was necessary to have, at least, an estimation of the stellar mass. In the case of eclipsing binary stars, this is directly determined using Kepler's laws, but we wanted to test a valid method even for isolated stars. Therefore, we decided to take advantage of the recent Gaia data release (DR1) to obtain a measurement of the stellar parallax. This together with a mass-luminosity relation would allow us to find the masses of our objects.

The parallaxes found are shown in Table 2. We did not find parallaxes in the Gaia's DR1 for all the stars, so we completed the data with Hipparcos. Only for CID 100866999 we did not find any measure of parallax, so we did not include this star in our study.

We used the mass-luminosity relationship by [9], obtained from detached Algol binary systems. Although A-type stars have a small bolometric correction, we wanted to check its effect on our calculations. The results of calculating surface gravities with and without bolometric corrections are shown in the right panel of Fig. 1. In the plot, surface gravities obtained from the literature are shown versus values calculated with $\Delta\nu$ and the parallaxes. Line y = x is also plotted as a guide. It can be noticed that values determined by the method presented in this work coincide, within the uncertainties, with values from the literature. In addition, the $\log g$ calculated by applying the bolometric correction is represented in green. In most cases, these points are hidden by those considered without correction. And in the cases where a difference can be appreciated, the deviation is minimum.

In most cases, the uncertainties in $\log g$ from $\Delta\nu$ and parallaxes are of the order of those obtained from the literature. It can be clearly seen that the uncertainty depends directly on the errors coming form the parallax. It is noteworthy that the masses calculated from the mass-luminosity relation could not correspond to the masses obtained from the binary analysis. However, the weight of the calculation is in the radius obtained from the mean density, which has less dispersion than the mass. To check this case, we also made a simple calculation obtaining $\log g$ using random masses. We uses values in the range of M = [1,3] $M_{\odot}$, where the δ Sct starsare located. The result was that the uncertainties in $\log g$ for an incorrect determination of the mass was 0.1 dex, at most. This is below the typical errors obtained by spectroscopy.

5 Conclusions

In this work a methodology has been presented to determine mean densities and surface gravities from only the asteroseismological parameter known as large separation, $\Delta\nu$. For this, a sample of eclipsing binary stars with a δ Sct component was used. This allowed a determination of masses and radii independent of any modelling. The sample consisted of 10 binary systems and a star harbouring a planet.

We improved the relation $\Delta\nu$-$\bar{\rho}$ in [6], demonstrating that it is independent of the rotation of the star. In addition, from the mean densities it was possible to calculate the surface gravities. To do this, parallaxes and a mass-luminosity relation were used to estimate stellar masses. The values of $\log g$ thus obtained showed, in most cases, an uncertainty of the same order as the data obtained from the literature. The uncertainty is directly related to the errors in the parallaxes, so the measurement of $\log g$ could be improved thanks to the accuracy of Gaia.

In any case, the uncertainties in $\log g$ have a limiting value, as shown by its calculation using random masses. Calculating the gravities from these masses and $\Delta\nu$ only, the maximum dispersion of the values only reaches 0.1 dex. Therefore, this is the maximum uncertainty that must be considered when calculating $\log g$ from $\Delta\nu$.

Acknowledgments

AGH, JCS and AM acknowledge funding support from Spanish public funds for research under project ESP2015-65712-C5-5-R and ESP2017-87676-C5-2-R (MINECO/FEDER), and from project RYC-2012-09913 under the 'Ramón y Cajal' program of the Spanish MINECO. AGH also acknowledges support from Fundação para a Ciência e a Tecnologia (FCT, Portugal) through the fellowship SFRH/BPD/80619/2011. AGH, MJPFGM and JCS acknowledges support from the EC Project SPACEINN (FP7-SPACE-2012-312844). MJPFG also acknowledges partial support from FCT/Portugal through UID/FIS/04434/2013 and CMPETE/FEDER. JPG and RGH acknowledge support from the "Junta de Andalucía" local government under project 2012-P12-TIC-2469. SBF acknowledges support from IA (FCT-UID/FIS/04434/2013) to visit Porto, where part of this work was carried out.

References

[1] Víctor Silva Aguirre, Mikkel N. Lund, H. M. Antia, et al. *The Astrophysical Journal*, 835(2):173, jan 2017.

[2] A. Baglin, M. Auvergne, P. Barge, M. Deleuil, C. Catala, E. Michel, W. Weiss, and The COROT Team. Scientific Objectives for a Minisat: CoRoT. In M. Fridlund, A. Baglin, J. Lochard, and L. Conroy, editors, *ESA Special Publication*, volume 1306 of *ESA Special Publication*, page 33, 2006.

[3] Gaia Gaia Collaboration, A. G. A. Brown, A. Vallenari, T. Prusti, et al. *Astronomy & Astrophysics*, 595:A2, 9 2016.

[4] A. García Hernández, A. Moya, E. Michel, et al. *Astronomy & Astrophysics*, 506(1):79–83, 2009.

[5] A. García Hernández, J. C. Suárez, A. Moya, et al. *Monthly Notices of the Royal Astronomical Society: Letters*, 471(1):L140–L144, oct 2017.

[6] A. García Hernández, S. Martín-Ruiz, M. J. P. F. G. Monteiro, et al. *The Astrophysical Journal Letters*, 811(2):L29, 9 2015.

[7] M. J. Goupil, M. A. Dupret, R. Samadi, et al. *Journal of Astrophysics & Astronomy*, 26(2):249, 2005.

[8] A. Grigahcène, V. Antoci, L. Balona, et al. *The Astrophysical Journal*, 713(2):L192–L197, apr 2010.

[9] C. Ibanoglu, F. Soydugan, E. Soydugan, and A. Dervisoglu. *Monthly Notices of the Royal Astronomical Society*, 373(1):435–448, 11 2006.

[10] H. Kjeldsen, T. R. Bedding, and J. Christensen-Dalsgaard. *The Astrophysical Journal Letters*, 683(2):L175, 7 2008.

[11] D. G. Koch, W. J. Borucki, G. Basri, et al. *The Astrophysical Journal Letters*, 713(2):L79–L86, 1 2010.

[12] M. Plummer. JAGS: A Program for Analysis of Bayesian Graphical Models Using Gibbs Sampling. In Kurt Hornik, Friedrich Leisch, Achim Zeileis, and Martyn Plummer, editors, *Proceedings of the 3rd International Workshop on Distributed Statistical Computing*, 2003.

[13] D. Reese, F. Lignières, and M. Rieutord. *Astronomy & Astrophysics*, 481:449–452, 2008.

[14] E. Rodríguez and M. Breger. *Astronomy & Astrophysics*, 366(1):178–196, jan 2001. ISSN 0004-6361.

[15] F. Royer, J. Zorec, and A. E. Gómez. *Astronomy & Astrophysics*, 463:671–682, 2007.

[16] J. C. Suárez, A. García Hernández, A. Moya, et al. *Astronomy & Astrophysics*, 563(A7):11, 3 2014.

[17] K. Uytterhoeven, A. Moya, A. Grigahcène, et al. *Astronomy and Astrophysics*, 534:125, 10 2011.

[18] F. van Leeuwen and Floor. *Space Science Reviews*, 151(1-3):209–226, 3 2010.

Highlights on Spanish Astrophysics X, Proceedings of the XIII Scientific Meeting of the Spanish Astronomical Society held on July 16 – 20, 2018, in Salamanca, Spain. B. Montesinos, A. Asensio Ramos, F. Buitrago, R. Schödel, E. Villaver, S. Pérez-Hoyos, I. Ordóñez-Etxeberria (eds.), 2019

Progress in research on Fullerenes and PAHs in the interstellar and circumstellar medium.

Susana Iglesias-Groth[1]

[1] Instituto de Astrofisica de Canarias, E-38205 La Laguna, Tenerife, Spain

Abstract

Results on theoretical work, astronomical observations and laboratory measurements of the new form of carbon known as fullerenes and their hydrogenated forms (fulleranes) are reviewed. These molecules can be responsible for diffuse interstellar bands, for the UV *bump*, a prominent feature in the extinction curves observed in many lines of sight of our Galaxy and other galaxies, and the anomalous microwave emission discovered in several regions of star formation, in molecular clouds and HII regions. Recent detections of fullerene C_{60} and C_{70} in various astrophysical contexts from reflection nebulae to planetary nebulae and protoplanetary disks reinforce the hypothesis that fullerenes and fulleranes are common in the interstellar medium and could contribute significantly to extinction. Another potential agent of anomalous microwave emission processes and interstellar extinction bands are polycyclic aromatic hydrocarbons (PAHs). Identification of the simplest PAHs, naphthalene and anthracene, in the interstellar medium is also discussed.

1 Introduction

The experiments, carried out by Kroto and Smalley in 1985, aimed at reproducing the chemistry of giant red star atmospheres led to the discovery of a new form of carbon: the fullerenes, the third known allotropic form of carbon (the two others are graphite and diamonds). Laboratory experiments have shown that the most stable fullerene molecules are C_{60} and C_{70} and the most abundant is C_{60}, a hollow molecule with 60 carbon atoms distributed in 12 pentagons and 20 hexagons following the symmetry of truncated icosahedrons. The radius of this molecule is approximately 3.55 Å. The electronic structure of the C_{60} consists of 60 atomic 2pz orbitals and 180 sp^2 hybrid orbitals. The fullerenes with icosahedral symmetry I_h (C_{60}, C_{180}, C_{240}) have a high stability and are very stable against UV, gamma radiation and collisions. Fullerenes are efficiently formed in laboratory vaporization experiments of graphite [17] and could also be formed in asymptotic giant branch stars (AGB) where circumstellar molecular synthesis is very reach.

The fullerene family also includes the so-called buckyonions, conformed by several concentric fullerene shells with separations of order 3.4-3.5 Å. These molecules, which show an even greater stability than the individual icosahedral fullerenes, were first synthesized by electronic bombardment. Another very interesting form of fullerenes are fulleranes, hydrogenated fullerenes (C_nH_m), where the π electrons form a bond with hydrogen. The properties of fulleranes are not so well known as those of individual fullerenes, but on-going laboratory work is aimed to measure their optical and infrared spectra and molar absorptivity.

Polycyclic Aromatic Hydrocarbons (PAHs) are planar molecules consisting of carbon rings and hydrogen, these rings are similar to benzene. The most simple PAHs are naphthalene and anthracene with two and three benzene rings, respectively. PAHs have been proposed as carriers of the Unidentified Infrared Emission bands and of the diffuse interstellar bands which are ubiquitous in the interstellar medium and are also potential carriers of the anomalous microwave emission. Carbon ring based molecular forms are very stable against UV radiation. The stability of carbon ring structures, pentagons and hexagons, which conform fullerenes and PAHs is a remarkable property which may even have played a role in the development of life. The DNA bases are essentially conformed by combinations of such carbon rings and would also benefit from such stability properties.

2 PAHs

PAHs are widely distributed in the ISM and collectively detected in many galaxies, however, recognition of individual PAHs is difficult. The detection of discrete infrared emission bands near 3.3, 6.2, 7.7, 8.6, 11.3 and 12.7 μm in dusty environments excited by ultraviolet photons led to the suggestion that PAHs were present in the interstellar medium [15]. These infrared bands are due to C–C and C–H stretching and bending vibrations in an aromatic hydrocarbon material. Since these bands mostly probe specific chemical bonds and not any particular molecular structure, they cannot provide unambiguous identification of single PAHs. The naphthalene cation ($C_{10}H_8^+$) is the most simple PAH and one of the best characterized spectroscopically in low-temperature gas phase at laboratory [18]. The laboratory characterization, crucial for a potential identification in the interstellar medium, shows that the strongest optical band of the naphthalene cation is located at 6707.4 Åwith a full width at half-maximum (FWHM) of approximately 12 Å. Progressively weaker bands of similar width have been measured at 6488.9, 6125.2 and 5933.5 Å[2]. It has been reported the detection of weak absorption (less than 1.5 per cent of the continuum) broad optical bands in the spectrum of the star Cernis 52 (A3 V), a likely member of the very young star cluster IC 348, which appear to be consistent with the measured laboratory bands of the naphthalene cation [11]. Under the assumption that the bands are caused by naphthalene cations, a column density for Np^+ of order 1×10^{13} cm^{-2} was derived. A broad band at 7088.8 Å coincident to within the measurement uncertainties with the strongest band of the anthracene cation ($C_{14}H_{10}^+$) as measured in gas-phase laboratory spectroscopy at low temperatures is also detected in the line of sight of star Cernis 52 [12]. This is probably associated with cold absorbing material in an intervening molecular cloud of the Perseus star-forming region where various experiments have recently detected anomalous microwave emission. From the measured intensity and available oscillator strength it is implied that ∼0.008 per cent of the carbon in the cloud could be in the form of $C_{14}H_{10}^+$. A similar abundance was also claimed for the naphthalene cation in this cloud.

3 Fullerenes: theoretical and laboratory spectra, characterization and detection in space

Computation of the photoabsorption spectra of fullerenes using semiempirical models showed the potential role of these molecules to explain various interstellar absorption features [10]. The theoretical approach followed to compute photoabsorption cross sections was based in a Huckel and Pariser-Parr-Pople (PPP) models and took into account the strong electronic correlation and the screening effects associated to π electrons in these molecules. The spectral computations in the near UV and optical indicated strong absorption around 2175 Å and the formation of many weaker absorptions distributed through all the optical spectrum. Measurements of the extinction of radiation in the near UV/optical in different lines of vision of our Galaxy shows a main extinction feature in the range 2150-2190 Å, this so-called UV bump is very stable in wavelength. The calculated photoabsorption spectra of some individual fullerenes reproduce this feature of extinction curves remarkably well. If the abundance of fullerenes in the diffuse interstellar medium decreases as a function of size according to a power law, then it is possible to reproduce the UV bump with high precision for a power-law index in the range 3-4. From this comparison, it is possible to estimate the fraction of carbon locked in fullerenes and buckyonions in the ISM [10]. The numerical density of these molecules results in a range of 0.2-0.08 fullerenes per million hydrogen atoms. In the proposed scheme, small fullerenes would be the most abundant with abundances of order $n(C_{60})/n(H) \sim 10^{-6}$).

Laboratory studies have shown that hydrogenated fullerenes also reproduce well the peak and shape of the UV bump in the extinction curve. In particular, the electron absorption spectrum of $C_{60}H_{36}$, obtained in the laboratory using n-hexane (Fig. 1), shows maximum absorption precisely at 2175 Å with a molar absorption of 17140 L cm $^{-1}$ mol^{-1} corresponding to a cross section absorption of order 6500 Mbarn, approximately ten times higher than for C_{60}. It is very important to measure and characterize in the laboratory the transition bands of these molecules and carry out an extensive search in several phases of the interstellar medium.

Laboratory spectroscopy of the active IR bands of C_{60} and C_{70} at low temperatures is key to the search and identification of fullerenes in space. The main active bands of IR for the C_{60} are at 7.0, 8.5, 17.4 and 18.9 μm. These bands have been crucial in the search for fullerenes in space. Their detection led to the discovery of fullerenes C_{60} and C_{70} in the young planetary nebula Tc1 [3] with *Spitzer Space Telescope.* These molecules were subsequently identified in reflection nebulae [21], several planetary [8] and protoplanetary [22] nebulae, and in post-AGB stars [9].

Fullerenes are able to survive under the harsh conditions of the ISM as suggested by observations in several young stellar objects [20] and by the ubiquitous presence of the

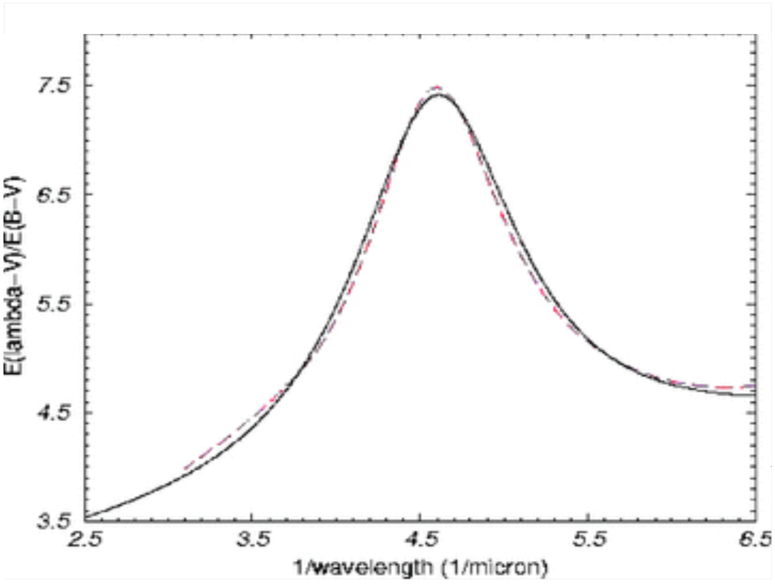

Figure 1: Comparison of the photoabsorption cross-section of fullerene $C_{60}H_{36}$ (continuous black line) with the interstellar extinction curve for a reddening factor RV= 3.1 (red dashed line) [6]. The vertical axis corresponds to normalized absorption at a certain wavelength, also known as reddening function.

diffuse interstellar bands at 957.7 and 963.2 nm which are associated to the cation C_{60}^{+} [7], [4]. These authors have inferred that a significant fraction of interstellar carbon is located in the C_{60} cation, although initial estimates of order 0.9% have been recently reduced to values of 0.1 % [1]. The cation bands were also detected in one protoplanetary nebula [13] deriving fullerene concentration values of order 0.05-0.1 ppm which are similar to values inferred from the UV bump at 217.5 nm under the assumption that this prominent feature of extinction is caused by fullerenes [10]. At such abundances, fullerenes can play an important role in interstellar chemistry [19], and given the stability of fullerenes against corpuscular and gamma radiation [5], it is likely that fullerenes originally formed in planetary nebulae later populate the interstellar medium and the clouds from which stars and planets form.

4 Fullerenes C_{60} and C_{70} in the circumstellar matter of stars with proto-planetary disks

I have carried out a systematic search of C_{60} and C_{70} in stars with protoplanetary disks in the young star cluster IC348 of the Perseus molecular complex. Here report results on a few selected stars (LRLL 1, LRLL 2 and LRLL 58)[16] with disk studies available in the literature. The spectra used in this work were obtained with the low resolution module-short wavelength (SL; 5-20 μm) and in one case with the high resolution short wavelength module (SH; 9.5-19.5 μm). The data processing is described elsewhere (see http://cassis.sirtf.com/).

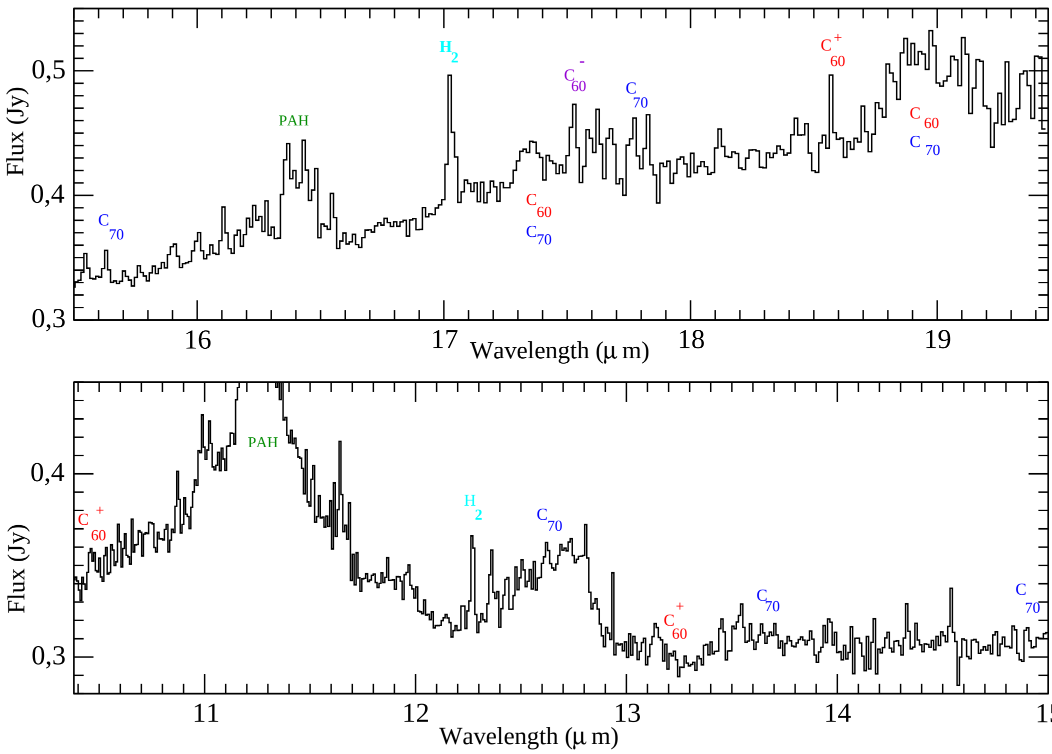

Figure 2: Mid-IR spectrum of star LRLL 2 obtained with Spitzer/IRS high resolution mode. Lines marked: C_{60} and C_{70} (17.4 and 18.9 μm), C_{70}(12.62, 13.83, 14.9,15.63 and 17.77 μm), C_{60}^{+} cation (10.47, 13.22,18.58 μm), C_{60}^{-} anion (17.51 μm), H2 (12.28, 17.03 μm)

The package CASSIS [14] was used to inspect and extract the spectra. The spatial scale of the IRS (approximately 5 arcsec per pixel) does not allow to disentangle emission lines originating in the disk from emission lines produced in the reflection nebulae surrounding the stars under consideration. It was adopted the integrated spectra as a suitable description of the emission line spectrum in the region around each star.

In the range 16-20 μm a prominent emission spectral band system is present in each star which has a well sampled band at 18.9 μm of C_{60} with contribution of C_{70} and a blended feature of PAHs at 16.4 μm, H_2 (17 μm) and fullerenes C_{60} and C_{70} at 17.4 μm.

In Fig. 2 we plot the IRS spectrum of the IC 348 LRLL 2 star obtained by Spitzer with the high spectral dispersion module (R=600) showing details of the bands and the continuum emission. The positions of known bands of C_{60} (17.4 and 18.9 μm) and C_{70} (17.4, 17.8 and 18.9 μm) are marked. Weak features of C_{70} appear to be present in the spectrum, remarkably at 17.8 and 21.8 μm (which is important in order to ascertain the relative contribution of this molecule to the strong bands at 17.4 and 18.9 μm. The spectrum also shows evidence for the C_{70} vibrational bands at 12.6, 14.9 and 15.6 μm and the C_{60}^{+} bands at 10.5, 13.2 and 18.6 μm.

The C_{60} features in the range 17-19 μm have a typical width of 0.3-0.4 μm, wider than the spectral resolution of the instrument and similar to the widths observed in planetary nebulae (like Tc 1). The contribution of C_{70} to the total emission of the bands observed at 18.9 μm and 17.4 μm has been established using the information provided by other bands of this molecule assuming a simple model to describe band ratios, and resulting C_{70} contributions are in the range 10-30% of the total band strengths.

The total flux of the band at 18.9 μm is rather stable among the observed circumstellar material ranging from 3×10^{-16} to 1×10^{-15} W m^{-2}, in spite of the very different luminosity and temperature of the studied disk host stars. Interestingly, I find the 16.4μm PAH emission in LRLL 58 is significantly enhanced with respect the 18.9 μm C_{60} band, contrary to what is observed in the other two targets of the sample where this PAH band appears weaker relative to fullerene emission. It is proposed that the relative enhancement of the PAH emission in this cooler object is a consequence of the higher sensitivity of PAHs to the physical conditions of the environment and in particular to the stellar radiation field. LRLL 58 has the lowest luminosity and the coolest effective temperature of the stars in the sample and this may favour the survival of PAHs. Fullerenes are expected to be more robust against radiation than PAHs.

5 Conclusions

- (i) Fullerenes and its hydrogenated forms could be responsible of the UV bump 2175 Å, a remarkable feature of interstellar absorption, and for several important diffuse interstellar bands.

- (ii) Fullerenes have been detected in planetary nebulae, 0.3-0.02 % of total carbon seems to be in the form of C_{60}.

- (iii) The cation C_{60} is detected in one protoplanetary nebulae and in the line of sight of many hot stars: 0.1-0.9% of total carbon appears to be in the form of ${C_{60}}^{+}$ in these environments.
- (iv) Fullerenes C_{60} and C_{70} are detected in the circumstellar matter of Perseus stars with protoplanetary disks where they coexist with PAHs. These fullerenes appear to lock 0.1-1 % of the carbon available in these regions. Cation and anions of C_{60} are also detected at 5-10 times lower abundances.
- (v) The cations of the most simple PAHs naphtalene and anthracene are present in the Perseus region with abundances 10-100 times lower than the neutral form of the most simple fullerene C_{60}.

References

[1] Berné, O., Cox, N. L. J., Mulas, G. & Joblin, C., 2017, A&A 605, L1

[2] Biennier L. Salama F. Allamandola L. J. Scherer J. J., 2003, J. Chemical Phys. , 118, 7863

[3] Cami, J., Bernard-Salas, J., Peeters, E., & Malek, S. E. 2010, Science 329, 1180

[4] Campbell, E. K., Holz, M. & Maier, J. P. 2016, ApJ Lett. 826, L4

[5] Cataldo, F., Strazzula, G. & Iglesias-Groth, S. 2009, MNRAS, 394,615

[6] Fitzpatrick,E. L., Massa, D. 1999, BAAS, 31, 1238

[7] Foing, B. H.& Ehrenfreund, P. 1994, Nature 369, 296

[8] García-Hernández, A.D. Iglesias-Groth, S., et al. 2011, ApJ Lett. 737, L30

[9] Gielen, C., Cami, J.,Bouwman,J., Peeters,E.& Min, 2011, A&A 536, A54

[10] Iglesias-Groth 2004, ApJ 608, 37

[11] Iglesias-Groth S., Manchado A., García-Hernández A., González-Hernández J. I., Lambert D., 2008, ApJ , 685, L5

[12] Iglesias-Groth S., Manchado A., Rebolo R. González Hernández J. I. García-Hernández D. A. Lambert D. L., 2010, MNRAS , 407, 2157

[13] Iglesias-Groth, S. & Esposito,M. 2013, ApJ Left. 776, L21

[14] Lebouteiller, V., Barry, D.J., Goes, C., Sloan, G.C., Spoon, H.W.W., Weedman, D.W., Bernard-Salas, J., Houck, J.R., 2015, ApJS, 218, 21

[15] Léger A. Puget J., 1984, A&A , 137, 5

[16] Luhman, K. L., Rieke, G.H., Lada C.J. & Lada E.A. 1998, ApJ, 508, 347

[17] Krätschmer, W., Lamb, L. D., Fostiropoulos, K., & Huffman, D. R. 1990, Nature 347, 354

[18] Pino T. Boudin N. Bréchignac P., 1999, J. Chemical Phys. 111, 7337

[19] Omont, A. 2016, A&A 590, A52

[20] Roberts, K.R.G., Smith, K.T. & Sarre, P.J. 2012, MNRAS, 421, 3277

[21] Sellgren, K. et al. 2010, ApJ Lett,722, L54

[22] Zhang, Y & Kwok, S. 2011, ApJ, 730, 126

Highlights on Spanish Astrophysics X, Proceedings of the XIII Scientific Meeting of the Spanish Astronomical Society held on July 16 – 20, 2018, in Salamanca, Spain. B. Montesinos, A. Asensio Ramos, F. Buitrago, R. Schödel, E. Villaver, S. Pérez-Hoyos, I. Ordóñez-Etxeberria (eds.), 2019

The first winged microquasar.

Josep Martí-Ribas[1], Pedro L. Luque-Escamilla[2], Valentí Bosch-Ramon[3], and Josep M. Paredes[3]

[1] Departamento de Física, Escuela Politécnica Superior de Jaén, Universidad de Jaén, Campus Las Lagunillas s/n, A3, E-23071 Jaén, Spain
[2] Departamento de Ingenieria Mecánica y Minera, Escuela Politécnica Superior de Jaén, Universidad de Jaén, Campus Las Lagunillas s/n, A3, E-23071 Jaén, Spain
[3] Departament de Física Quàntica i Astrofísica, Institut de Ciències del Cosmos (ICCUB), Universitat de Barcelona, IEEC-UB, Martí i Franquès 1, E-08028 Barcelona, Spain

Abstract

Microquasars are stellar binary systems that share strong physical and morphological analogies with extragalactic sources of relativistic jets. In this work, we report very deep radio images of the microquasar GRS 1758−258 . At sensitivities down to the few μJy level, GRS 1758−258 broadens these already known analogies by including the same 'wing' phenomenon observed in some radio galaxies. The so called winged radio galaxies display secondary radio lobes, with Z or X-shaped morphologies, whose physical interpretation often invokes the merger of super-massive black holes with spin-flip. GRS 1758−258 remarkably displays Z-type wings too, extending on parsec linear scales as long as the main jet flow. Owing to its stellar nature, the most physically conceivable explanation is based on hydrodynamic backflow when the relativistic ejecta interacts with a nearby cloud. Moreover, emission line surveys of the region do confirm the existence of such a cloud at a kinematic distance consistent with that of GRS 1758−258. By extrapolating these findings to the extragalactic case, we conclude that not all winged radio galaxies are secure sites of previous black hole coalescence since the alternative backflow scenario could also be at work in many cases.

1 Introduction

The realm of extragalactic radio sources hosts objects with a rich variety of morphologies in their large-scale collimated outflows. In particular, the so-called radio galaxies are often sorted into one of the two Fanaroff-Riley types (FRI or FRII) according to their radio lobe brightness aspect [1]. Yet, there is a significant fraction of distorted cases that challenge the simplicity of this historical classification scheme. Among them, the growing group of winged radio galaxies (WRGs) stands out as a remarkable sub-class whose radio lobe morphology, with X or Z-type appearances, is not apparently consistent with a single ejection axis [2, 3]. It is worth to mention here that a high fraction of X-type sources could actually be Z-types too distant to be recognized as such [4]. Different physical explanations have been proposed to account for the WRG existence with no consensus being reached within the astrophysical community. The strongest debate is between, but not limited to, the supporters of the hydrodynamic [5, 6, 7] versus the super-massive blackhole merger scenarios with spin-flip [8, 9, 10]. Solving this issue is nowadays relevant in the context of the new-born gravitational wave astronomy since WRGs could have implications for the gravitational wave background if a blackhole coalescence is indeed behind their origin [3].

In this contribution, we report about the remarkable winged features found in the microquasar known as GRS 1758−258 located in the close vicinity of the Galactic Center. This object was originally discovered in hard X-rays by the coded mask telescope *SIGMA* on board the satellite *GRANAT* back in the 90s of the past century [11]. Bipolar radio jets were detected soon after [12] and they have been intensively studied over the years [13, 14]. The similarity of the newly found wings with those seen in some WRGs reinforces the parallelism between stellar sources of relativistic jets and their extragalactic relatives, such as radio galaxies and quasars. Moreover, the maturity of nowadays stellar evolution knowledge also enables a new perspective when trying to discriminate among possible physical scenarios where wings can form. A fully detailed account of all our results can be found elsewhere [15].

2 Radio observations

To obtain a radio image of GRS 1758−258 as deep as possible, we carried out dedicated observations with the *Jansky* Very Large Array (VLA) at the 6 cm wavelength. In addition, historical VLA runs of the same source were retrieved from the NRAO Science Data Archive with the idea of trying to merge them with the modern data. To achieve good sensitivity at the arc-minute angular scales, typical of our target radio jets, the C configuration of the array was preferred. The log of observations used and their instrumental setup are listed in Table 1.

Table 1: Radio observations of GRS 1758−258

Run Id.	Date	Array Configuration	Bandwidth (MHz)
AM385	1992 Sep 10-11	D	50
AM345	1992 Sep 26-27	D	50
AM428	1993 Oct 03-04	CD	50
AM560	1997 Aug 03-24	C	50
AS930	2008 Apr 01-12	C	50
16A-005	2016 Mar 04-22	C	2048

The reader is referred to the Methods section in [15] for a comprenhensive account of how calibration was carried out using both the CASA and AIPS software packages. This was a painful process because combining modern and historical VLA data sets is by no means straightforward. The final result is presented in the map shown in Fig. 1 whose noise level is a low as 4.3 μJy beam^{-1} and noticeably improved over our previous works[14].

3 Discussion

In addition to the already known extended radio jets, the most interesting fact in Fig. 1 is that GRS 1758−258 exhibits the same characteristics of a Z-type WRG. Notably, the observed secondary lobes have an angular scale comparable to that of the main jet flow. This is the first time that such a morphology in observed in a microquasar system. Two consequences immediately follow from this discovery: i) The analogy between galactic and extragalactic sources of relativistic outflows is reinforced to include the terminal jet lobes; ii) The spin-flip scenario is ruled out in a downsized winged jet flow. This is because our current understanding of stellar evolution in binary systems precludes the merger of black holes during the past existence of this microquasar. Indeed, a non-degenerate star, acting as mass donor onto a single compact object, is presumed to exist in GRS 1758−258 [16].

In this context, what is the physical scenario that better fits the existence of a Z-type winged microquasar? In an attempt to answer this question, we inspected the environments of GRS 1758−258 using the Dame's carbon monoxide (CO) survey of the Galactic Plane[17]. As we report and discuss in [15], a conspicuous gas cloud appears to be hit by the microquasar jets and the backflow caused by this interaction with the interstellar medium (ISM) is very likely related to the formation of the wings. The CO cloud velocity with respect to the Local Standard of Rest (LSR) is centered at about 210 km s^{-1}, and the associated kinematic distance for this LSR velocity turns out to be $\sim$ 8.5 kpc. This is in good agreement with the value usually adopted for this microquasar as required for this interpretation to be correct. The brightness difference between the northern and southern ejecta is attributed to a ISM with an asymmetric density distribution. Recent hydrodynamic backflow scenarios, such as [7], are thus favored to be also at work in the particular case of this microquasar.

4 Conclusions

Secondary radio lobes similar to those observed in WRGs have been detected for the first time in a microquasar. This observational discovery provides a step forward towards a unified knowledge of relativistic outflows in the universe, to be pursued in future works. By extrapolating our GRS 1758−258 findings to the extragalactic domain, another important conclusion is that WRGs are no longer secure tracers of past black hole mergers in the universe. Therefore, estimates of the gravitational wave background based on their observed population can be lower than predicted and in likely need of revision.

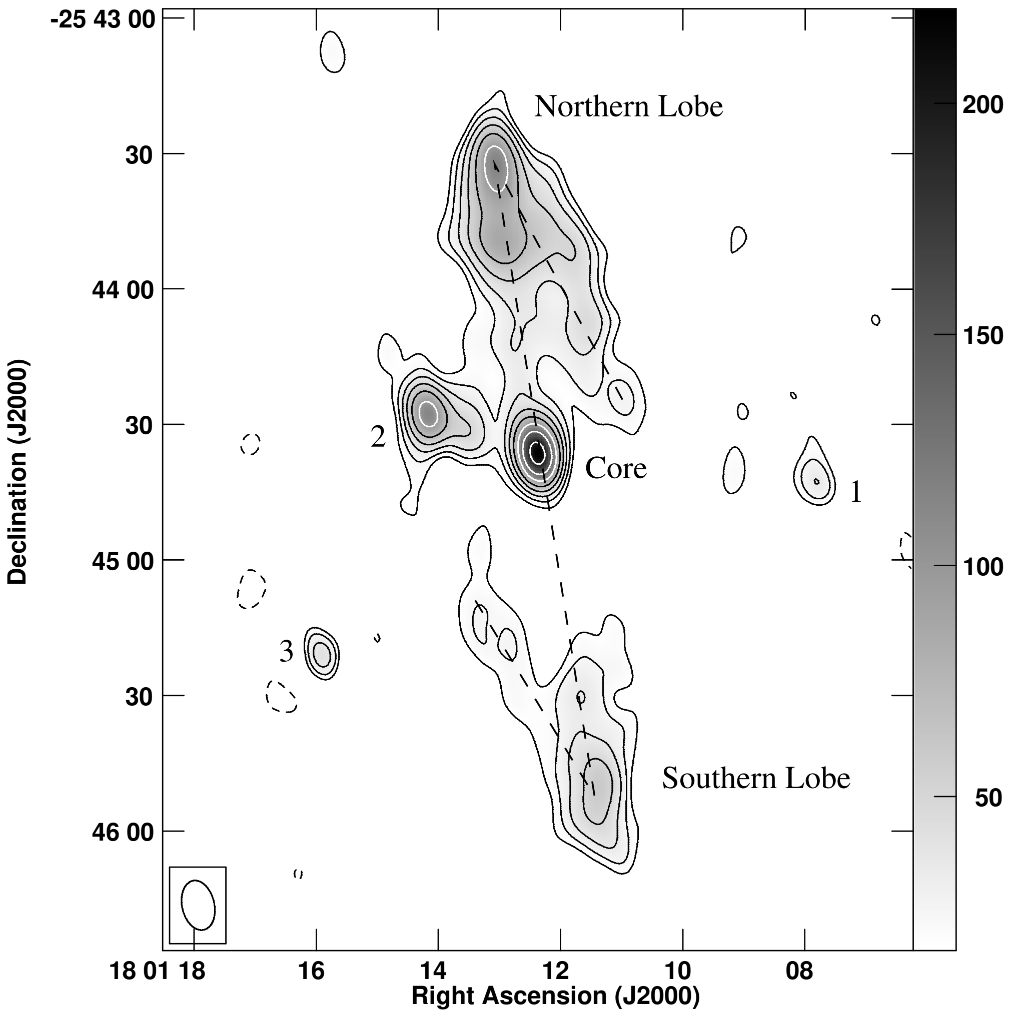

Figure 1: Deep radio image of the GRS 1758−258 radio jets and lobes at the 6 cm wavelength obtained as described in the text using the JVLA and the historical VLA data. The Z-shaped winged morphology is outlined by the dashed line. The bottom-left ellipse represent the half-power beam width of the restoring beam, measuring 11.13×7.12 arcsecond^2 with position angle of 12.7°. The positive contours shown start at the 4-σ level of 17.2 μJy beam^{-1}, and increase progressively by a factor of $\sqrt{2}$. The brightness scale is illustrated by the vertical bar in units of μJy beam^{-1}. Sources labelled 1, 2, and 3 are believed to be unrelated objects.

.

Acknowledgments

The National Radio Astronomy Observatory is a facility of the National Science Foundation operated under cooperative agreement by Associated Universities, Inc. This research was supported by the Agencia Estatal de Investigación grants AYA2016-76012-C3-1-P and AYA2016-76012-C3-3-P funded by the Spanish Ministerio de Economía y Competitividad (MINECO), by the Consejería de Economía, Innovación, Ciencia y Empleo of Junta de Andalucía under research group FQM-322, by grant MDM-2014-0369 of the ICCUB (Unidad de Excelencia 'María de Maeztu'), and by the Catalan DEC grant 2014 SGR 86, as well as FEDER funds. V.B.-R. also acknowledges financial support from MINECO and the European Social Funds through a Ramón y Cajal fellowship. This work was also supported by the Marie Curie Career Integration Grant 321520.

References

[1] Fanaroff, B. L., Riley, J. M. 1974, MNRAS, 167, 31P

[2] Cheung, C. C. 2007, AJ, 133, 2097

[3] Roberts, D. H., Saripalli, L., Subrahmanyan, R. 2015, ApJ, 810, L6

[4] Roberts, D. H., Cohen, J. P., Lu, et al. 2015, ApJSS 220, 7

[5] Capetti, A. et al. 2002, A&A, 394, 39

[6] Hodges-Kluck, E. J., Reynolds, C. S. 2011, ApJ, 733, 58

[7] Gopal-Krishna, B. P. L., Gergely, L. A., Wiita, P. J. 2012, A&A, 12, 127

[8] Merritt, D., Ekers, R. D. 2002, Science, 297, 1310

[9] Dennett-Thorpe, J. et al. 2002, MNRAS, 330, 609

[10] Gergely, L. A., Biermann, P. l. 2009, ApJ, 697, 1621

[11] Sunyaev, R. et al. 1991, A&A, 247, L29

[12] Rodríguez, L. F., Mirabel, I. F., Martí, J. 1992, ApJ, 401, L15

[13] Martí, J., Mirabel, I. F., Rodríguez, L. F., et al. 2002, A&A, 386, 571

[14] Martí, Luque-Escamilla, P. L., Romero, G. E. et al. 2015, A&A, 587, L11

[15] Martí, J., Luque-Escamilla, P. L., Bosch-Ramon, V., Paredes, J. M. 2017, Nature Communications 8:1757 open access available at `http://rdcu.be/zgX8`

[16] Martí, J., Luque-Escamilla, P. L., Muñoz-Arjonilla, A. J. 2016, A&A, 596, A46

[17] Dame, T. M., Hartmann, D., Thaddeus, P. 2001, ApJ, 547, 792

Highlights on Spanish Astrophysics X, Proceedings of the XIII Scientific Meeting of the Spanish Astronomical Society held on July 16 – 20, 2018, in Salamanca, Spain. B. Montesinos, A. Asensio Ramos, F. Buitrago, R. Schödel, E. Villaver, S. Pérez-Hoyos, I. Ordóñez-Etxeberria (eds.), 2019

The binary central stars of planetary nebulae.

David Jones[1,2]

[1] Instituto de Astrofísica de Canarias, E-38205 La Laguna, Tenerife, Spain
[2] Departamento de Astrofísica, Universidad de La Laguna, E-38206 La Laguna, Tenerife, Spain

Abstract

It is now clear that central star binarity plays a key role in the formation and evolution of planetary nebulae, with a significant fraction playing host to close-binary central stars which have survived one or more common envelope episodes. Recent studies of these systems have revealed many surprises which place important constraints on the common envelope - a critical phase in the formation of a wide variety of astrophysical phenomena, including the cosmologically important supernovae type Ia and other transient phenomena which will be detected by next-generation facilities, like the Large Synoptic Survey Telescope and the space-based gravitational wave detector the Laser Interferometer Space Antenna.

1 Introduction

It is now clear that binary interactions play a key role in the shaping of planetary nebulae (PNe; [12]) and that the binary fraction among PNe must be at least 20% [23] but perhaps as high as 80% [8, 9]. However, in spite of their importance in understanding the origins of PNe, only some ∼60 binary central stars are known[1] and, moreover, very little is known about these systems beyond their orbital periods. In an attempt to reach a statistically significant sample of binary central stars, the author and collaborators are undertaking an observational campaign to search for and characterise these systems. The search for new binary central stars has focussed primarily on targeted photometric and spectroscopic monitoring of the central stars of PNe which present morphological features believed to be characteristic of a binary evolution [24]. These searches have been extremely successful leading to a rapid increase in the rate of discovery [4, 2, 16, 17, 32, 20]. Detailed studies of these systems and those from the literature have revealed many interesting results with important implications for our understanding of close-binary evolution and the common envelope (CE) phase, in particular.

[1] A complete list is maintained at http://drdjones.net/bCSPN.

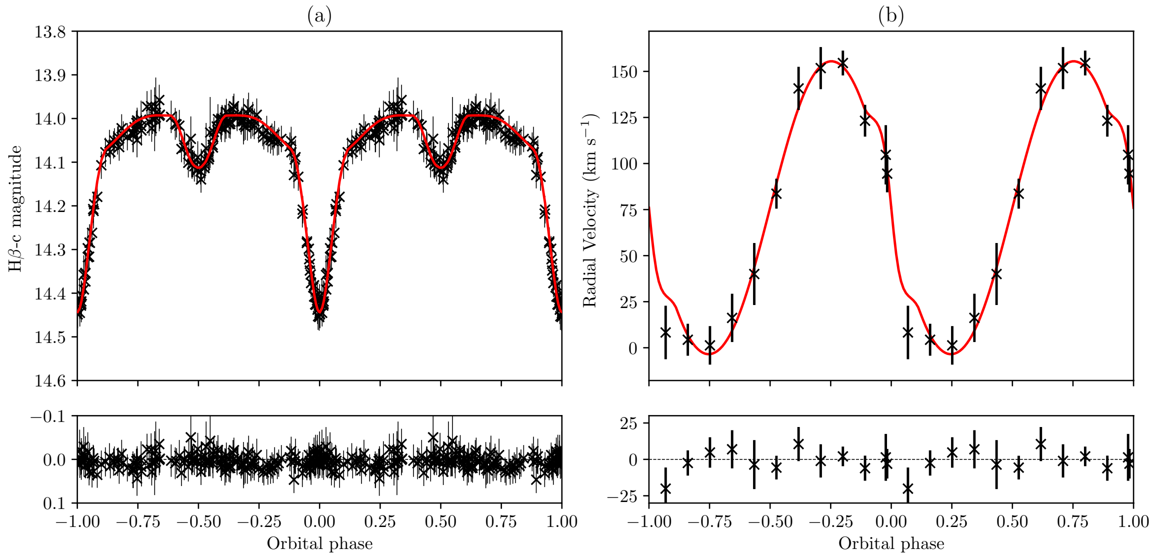

Figure 1: An example of the simultaneous modelling of light (a) and radial velocity (b) curves required to derive stellar (mass, temperature, radii) and binary (period, orbital inclination) parameters, in this case the central star of M 3-1 (reproduced from [20]).

2 Probes of common envelope evolution

The close-binary central stars of PNe are thought to have formed via a CE interaction, where the nebula itself is the remnant ejected envelope (see [18] for a review). The presence of the short-lived ($\tau \leq 30{,}000$ years) nebula makes these systems of particular interest for studying the CE, as they offer a unique opportunity to directly observe the properties of the ejected envelope (see, for example, Santander-García in these proceedings) as well as observe the stars themselves "fresh-out-of-the-oven", before the system has had time to adjust.

A key prediction of all CE models is that, due to the transfer of orbital angular momentum, the envelope should be preferentially ejected in the orbital plane of the binary such that the symmetry axis of the resulting nebula lies perpendicular to this plane [29]. In order to test this prediction, one must determine the morphology and orientation of the PN, via spatio-kinematical modelling [15, 35, 13], as well as the inclination of the central binary, via simultaneous modelling of light and radial velocity curves (see figure 1; [17, 20]). To date, only eight systems have been the subject of sufficiently detailed study in order to test the prediction, however all eight systems present with the expected correlation (see figure 2). The probability of chance alignment amongst all systems is less that one in a million, as such this constitutes a statistically significant demonstration of the direct link between the central binary and the ejected envelope/nebula [12].

Beyond the simple correlation between nebular symmetry axes and binary planes, close-

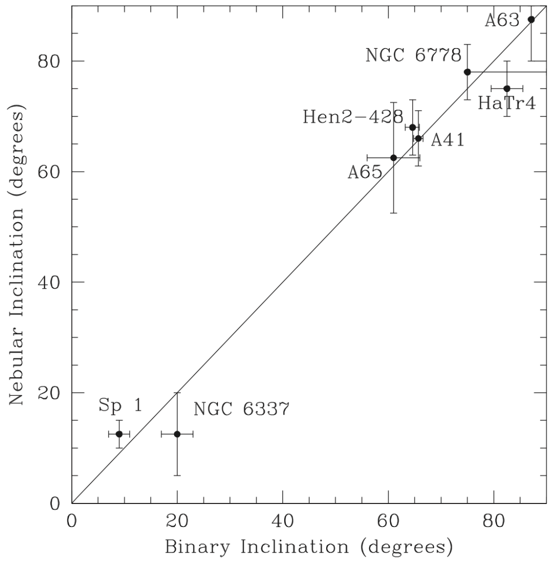

Figure 2: The observed correlation between binary and nebular inclinations in post-CE PNe, reproduced from [12].

binary PNe reveal much about the CE process. For example, detailed studies have revealed that main sequence companions are always found to be greatly inflated with respect to isolated stars of the same mass [17] - with one exception where the companion is found to present with a relatively normal radius, but at such a short period that it is filling its Roche lobe [20]. The observed inflation is believed to be a result of rapid mass transfer onto the companion knocking the star out of thermal equilibrium. Further evidence for such mass transfer is found in the central star of the Necklace, where the companion is found to be greatly enhanced in Carbon [27] - a third dredge-up product which can only have been deposited into the atmosphere of the main sequence star via mass transfer from the primary while it was on the AGB. In isolation, these results do not say much about when this episode of mass transfer must have occurred, other than that it must have been relatively recently. However, kinematical studies of several post-CE PNe presenting with extended polar structures, like jets, have shown that these features are kinematically older than the central regions of the nebulae - indeed, in the Necklace, the polar caps are found to be twice as old as the ringed, nebular waist [4]. Given that the nebular waists are thought to represent the ejected CE, these older polar ejections are likely the product of mass transfer immediately prior to entering into the CE. Further support for such pre-CE mass transfer is found in the PN Fleming 1, where the precession period of the jets is consistent with a much longer, pre-CE orbital period compared to the 1.2 day, post-CE period now observed [2].

Given that post-CE central stars have only recently left the CE phase, their stellar and orbital parameters can be used to constrain the efficiency of the process - the holy-grail of close-binary population synthesis. Of particular interest here are the mass and orbital period distributions, both of which can be altered in more evolved post-CE populations (by mass transfer, magnetic braking, etc.). The observed orbital period distribution shows a strong peak at periods less than one day, while CE models generally predict a significant number of longer period systems at longer periods [7]. This makes the recent spate of discoveries of longer period systems [25, 32, 28], all of which would not have been detected via photometric monitoring, particularly intriguing - perhaps indicative of a missing long-period population that has, thus far, evaded detection [6, 19]. Furthermore, in this longer period regime one finds the most massive companion post-CE companion known (not just in terms of central stars of PNe but of all post-CE systems, in general) - that of NGC 2346 weighing in at more than 3.5 $M_{\odot}$ [3] - making this an especially interesting system with which to probe the apparent connection between CE efficiency and binary parameters [5]

3 Double-degenerates and supernovae Ia progenitors

Based on the shapes of their discovery light curves a significant fraction of post-CE central stars of PNe are thought to be double-degenerate (DD) systems [11]. Given the intrinsic difficulty in their detection (DD central stars will not present photometric variability except at very high orbital inclinations and/or very short orbital periods [2, 18]), the true fraction of DD central stars is likely much higher. This has critical implications for our understanding of other astrophysical phenomena - in particular, the cosmologically important supernovae type Ia (SNe Ia), used to explore the expansion of the Universe at high redshifts (ultimately leading to the award of the 2011 Nobel Prize in Physics). The merger of two white dwarfs in a close-binary system may represent the main, or even sole, pathway by which SNe Ia occur [22], however to-date no bona-fide progenitor system has been discovered. Such a system has to meet two main criteria: the total mass of the system must be greater than the Chandrasekhar mass, and the orbital separation should be small enough that the system will merge in less than the age of the Universe.

Given the apparent over-abundance of DD central stars, as well as the observation that a significant fraction of SNe are found to explode in circumstellar environments consistent with a remnant PN [33], it is no surprise that the most promising candidate SN Ia progenitors have been found inside PNe. The central star system of TS 01 is a short-period DD system the total mass of which may be greater than the Chandrasekhar mass, however the uncertainties on the derived total mass encompass sub-Chandrasekhar values [34]. A second candidate is found in the central star of Hen 2-428, where the simultaneous light and radial velocity curve modelling by Santander-García et al. derived a total mass of 1.76±0.26 $M_{\odot}$ and a time to merger of approximately 700 millions years [31]. However, the modelled parameters lie far from evolutionary tracks, leading García-Berro et al. to question the DD nature of the system, instead proposing that the observed spectral line profiles could arise from a white dwarf and main sequence companion combined with variable nebular line emission [10]. Recent analyses rule out this hypothesis, clearly demonstrating conclusively that the system comprises two white dwarfs [14, 30]. However, Reindl et al. find that the measured radial velocity semi-amplitude of the stars (critical in determining their masses) differ depending on the line or lines used - repeating the analysis of Santander-García et al. the results agree to within uncertainties, but including other absorption lines of He II they derive lower semi-amplitudes and, therefore, a sub-Chandrasekhar total mass [30]. While there is no clear explanation for a dependence of the radial velocity on the choice of spectral line, the lower masses do bring the derived solution closer to evolutionary tracks. However, caution must still be exercised in adopting the lower total mass as fact given that, as highlighted by Miller-Bertolami [26], these evolutionary tracks do not and, thus far, cannot account for a CE evolution (the exact details of which are far from being understood) and, similarly, it is unclear to what extent the tracks are valid for over-contact systems [30]. As such, the central stars of TS 01 and Hen 2-428 still represent plausible and, to-date, the strongest candidates to be SN Ia progenitor systems.

4 Conclusions

Central star binarity plays a key role in the formation and evolution of PNe, with the clearest impact being found in post-CE systems. Post-CE PNe are important laboratories for constraining the CE process and, therefore, for understanding the formation of a wide-range of astrophysical phenomena. The continued presence of the PN ensures that the central star system has only recently exited the CE phase and has not yet had time to adjust, and furthermore as the PN is formed from the remnant envelope it offers a unique opportunity to study the ejection process. Recent studies of post-CE PNe and their central stars have revealed important information about the CE phase, including evidence of a period of intense mass transfer from the primary onto the companion immediately before entering the CE phase. Studies of the population as a whole will be key in constraining the CE efficiency and its dependencies - critical in all population synthesis studies, which will have a key role to play in interpreting the results of the next generation of variability surveys including those from the Large Synoptic Survey Telescope (LSST) and the space-based gravitational wave detector the Laser Interferometer Space Antenna (LISA) [1, 21].

Amongst the other phenomena the understanding of which is greatly impacted by studies of post-CE PNe are SNe Ia. Beyond simply constraining the CE, through which all models of SN Ia formation pass, PNe have much to reveal about individual models - in particular, for the DD merger scenario. DD central stars appear over-abundant amongst the total post-CE central star population. Given that the strongest candidate SN Ia progenitor systems are found in PNe, follow-up observations and modelling of other DD central stars may prove a happy hunting ground in the search for a bona-fide progenitor system. Even if they do not reveal a robust detection of a progenitor, these studies may prove crucial in constraining the importance or even viability of the DD merger scenario, greatly furthering our understanding the origin of SNe Ia and what makes them such astonishingly accurate standard candles.

Acknowledgments

This research has been supported by the Spanish Ministry of Economy and Competitiveness (MINECO) under the grant AYA2017-83383-P.

References

[1] Belczynski, K., et al. 2008, ApJS, 174, 223
[2] Boffin, H.M.J., et al. 2012, Science, 338, 773
[3] Brown, A.J., et al. 2018, MNRAS, in press arXiv:1810.09764
[4] Corradi, R.L.M., et al. 2011, MNRAS, 410, 1349
[5] Davis, P.J., Kolb, U., Knigge, C. 2012, MNRAS, 419, 287
[6] De Marco, O., et al. 2004, ApJ, 602, 93
[7] De Marco, O., Hillwig, T.C. & Smith, A.J. 2008, AJ, 136, 323
[8] De Marco, O., et al. 2015, MNRAS, 448, 3587
[9] Douchin, D., et al. 2015, MNRAS, 448, 3132
[10] García-Berro, E., et al. 2016, New Astronomy, 45, 7
[11] Hillwig, T.C., et al. 2010, AJ, 140, 319
[12] Hillwig, T.C., et al. 2016, ApJ, 832, 125
[13] Huckvale, L., et al. 2013, MNRAS, 434, 1505
[14] Finch, N.L., et al. 2018, Open Astronomy, 27, 57
[15] Jones, D., et al. 2012, MNRAS, 420, 2271
[16] Jones, D., et al. 2014, A&A, 562, 89
[17] Jones, D., et al. 2015, A&A, 580, 19
[18] Jones, D., & Boffin, H.M.J. 2017, Nature Astronomy, 1, 117
[19] Jones, D., et al. 2017, A&A, 600, 9
[20] Jones, D., et al. 2019, MNRAS, 482, L75
[21] Korol, V., et al. 2017, MNRAS, 470, 1894
[22] Maoz, D., Mannucci, F., Nelemans, G. 2014, ARA&A, 52, 107
[23] Miszalski, B., et al. 2009a, A&A, 496, 813
[24] Miszalski, B., et al. 2009b, A&A, 505, 249
[25] Manick, R., Miszalski, B. & McBride, V. 2015, MNRAS, 448, 1789
[26] Miller-Bertolami, M.M. 2017, IAUS, 323, 179
[27] Miszalski, B., Boffin, H.M.J. & Corradi, R.L.M. 2013, MNRAS, 428, 39
[28] Miszalski, B., et al. 2018, MNRAS, 473, 2275
[29] Nordhaus, J. & Blackman, E. G. 2006, MNRAS, 370, 2004
[30] Reindl, N., et al. 2018, Galaxies, 6, 88
[31] Santander-García, M. et al. 2015, Nature, 519, 63
[32] Sowicka, P., et al. 2017, MNRAS, 471, 3529
[33] Tsebrenko, D. & Soker, N. 2015, MNRAS, 447, 2568
[34] Tovmassian, G., et al. 2010, ApJ, 714, 178
[35] Tyndall, A.A., et al. 2012, MNRAS, 422, 1804

Highlights on Spanish Astrophysics X, Proceedings of the XIII Scientific Meeting of the Spanish Astronomical Society held on July 16 – 20, 2018, in Salamanca, Spain. B. Montesinos, A. Asensio Ramos, F. Buitrago, R. Schödel, E. Villaver, S. Pérez-Hoyos, I. Ordóñez-Etxeberria (eds.), 2019

GALANTE: finding all the optically accessible Galactic O+B+WR stars in the Galactic Plane.

J. Maíz Apellániz[1], E. J. Alfaro[2,3], R. H. Barbá[4], A. Lorenzo[2], A. Marín-Franch[3,5], A. Ederoclite[3,5], J. Varela[3,5], H. Vázquez Ramió[3,5], J. Cenarro[3,5], D. J. Lennon[6], and P. García-Lario[6]

[1] Centro de Astrobiología, CSIC-INTA, Madrid, Spain
[2] Instituto de Astrofísica de Andalucía, CSIC, Granada, Spain
[3] Unidad Asociada CEFCA-IAA, CSIC, Teruel, Spain
[4] Universidad de La Serena, La Serena, Chile
[5] Centro de Estudios de Física del Cosmos de Aragón, Teruel, Spain
[6] European Space Agency, ESAC, Madrid, Spain

Abstract

GALANTE is an optical photometric survey with seven intermediate/narrow filters that has been covering the Galactic Plane since 2016 using the Javalambre T80 and Cerro Tololo T80S telescopes. The P.I.s of the northern part (GALANTE NORTE) are Emilio J. Alfaro & Jesús Maíz Apellániz. and the P.I. of the southern part (GALANTE SUR) is Rodolfo H. Barbá. The detector has a continuous $1.^{\circ}4\times1.^{\circ}4$ field of view with a sampling of $0.''55$/pixel and the seven filters are optimized to detect obscured early-type stars. The survey includes long, intermediate, short, and ultrashort exposure times to reach a dynamical range close to 20 magnitudes, something never achieved for such an optical project before. The characteristics of GALANTE allow for a new type of calibration scheme using external Gaia, Tycho-2, and 2MASS data that has already led to a reanalysis of the sensitivity of the Gaia G filter. We describe the project and present some early results. GALANTE will identify the majority of the early-type massive stars within several kpc of the Sun and measure their amount and type of extinction. It will also map the Hα nebular emission, identify emission-line stars, and do other studies of low- and intermediate-mass stars.

1 Motivation

GALANTE is a project that is imaging the Galactic Plane (Fig. 1) using the Javalambre T80 and Cerro Tololo T80S twin telescopes [1, 10]. The detector, footprint, exposure times, magnitude range, survey dates, and filters are given in Table 1. The main goal of the project

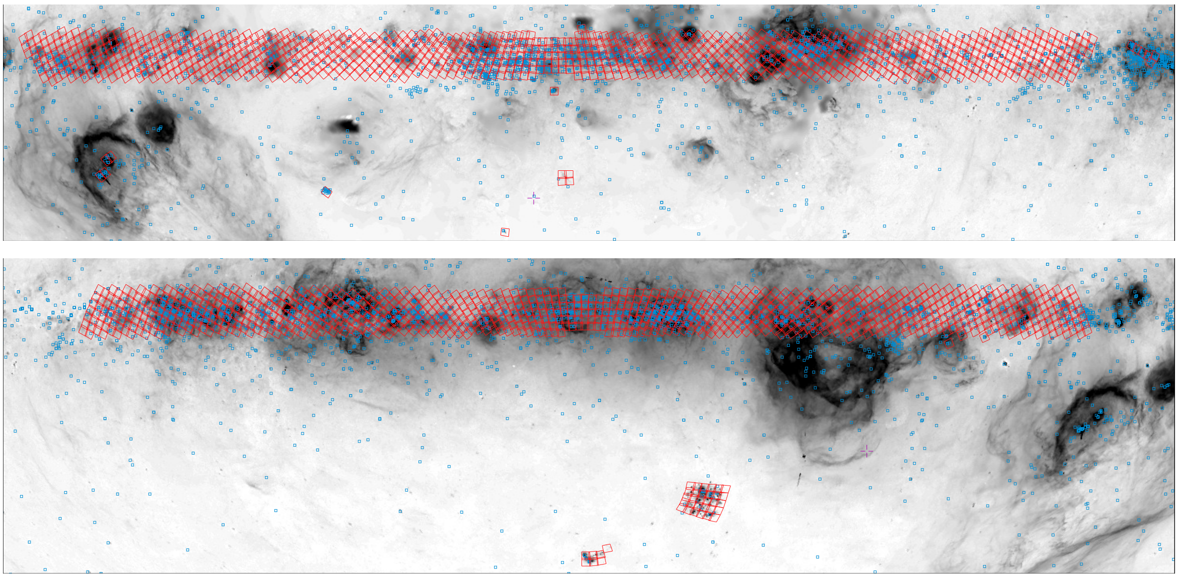

Figure 1: Footprint (red) of the 2009 GALANTE fields divided by hemisphere (top: north, bottom:south). Blue symbols are stars from the Galactic O-Star Catalog (GOSC, [15, 17, 20, 21], `http://gosc.cab.inta-csic.es`), which are mostly O+B+WR stars. The background is an Hα image [2] in a log scale aligned with Galactic coordinates using an Aitoff projection. The off-plane fields include the LMC, the SMC (bottom), M31, and M33 (top).

is to identify a near complete sample of Galactic obscured O+B+WR stars up to several kpc and measure their extinction but other objectives will be achieved with the survey. As there are a number of other large-area or whole-sky existing/ongoing photometric surveys (Tycho-2, 2MASS, SDSS, EGAPS, Gaia, Pan-STARRS, J-PLUS, S-PLUS, J-PAS, VVV...), the reader may ask him/herself: why one more? Because none has the GALANTE characteristics:

Region of the sky: Some surveys (e.g. SDSS) concentrate in areas away from the Galactic plane, which they do not cover (or do not do it completely). GALANTE covers the Galactic Plane, LMC, SMC, M31, M33, and a few off-plane Galactic clusters.

Magnitude range: Most ground-based surveys use 2-4 m telescopes with one or two exposure times. Hence, they saturate around magnitude 11-12 and cover a dynamic range of 10-12 magnitudes. GALANTE uses 80 cm telescopes with four exposure times to photometer all stars down to magnitude 19-20 (Fig. 2). This is important for obscured stars, which may be close to the detection limit in the blue and be brighter than magnitude 10 beyond 8000 Å.

Filter selection: Some surveys use filter sets not optimized for (e.g. SDSS *ugriz*) or incapable of (e.g. Tycho-2 *BV* or 2MASS *JHK*) measuring the Balmer jump, which is the only realistic method to determine $T_{\rm eff}$ for hot stars [11, 8, 18, 12]. Also, no similar survey includes two narrow filters (on-band and off-band) for Hα in order to photometer that line for stars (in absorption or emission) and to map the nebulosity with subarcsecond pixels.

Calibration accuracy: GALANTE uses narrow/intermediate band filters, which are less sensitive to photometric accuracy problems induced by atmospheric extinction.

Detector:	$1\overset{\circ}{.}4\times1\overset{\circ}{.}4$ continuous FOV with $0\overset{\prime\prime}{.}55$ pixels.
Footprint:	T80: $\lvert l\rvert < 3^{\circ} + \lvert\delta\rvert > 0^{\circ}$ plus selected regions, 1100 sq. dg., Fig. 2.
	T80S: $\lvert l\rvert < 3^{\circ} + \lvert\delta\rvert < 0^{\circ}$ plus selected regions, 1100 sq. dg., Fig. 2.
Exposure times:	2×0.1 s + 2×1 s + 2×10 s + 4×50/100 s (at two different airmasses).
Magnitude range:	Unsat. AB mag 3-17 with S/N > 100 in all filters, detect. to AB mag 19-20.
Survey dates:	GALANTE NORTE (T80): 2016-2021. GALANTE SUR (T80S): 2018-2023.
Filters:	F348M Strömgren u equivalent, T_{eff} + extinction determination.
	F420N Continuum between Hδ and Hγ, T_{eff} + extinction determination.
	F450N Continuum between Hγ and Hβ, T_{eff} + extinction determination.
	F515N Strömgren y equivalent, T_{eff} + extinction determination.
	F660N Hα line, pure nebular images + emission-line star detection.
	F665N Hα continuum, pure nebular images + emission-line star detection.
	F861M CaT, tie-in with Gaia-RVS and 2MASS, extinction typing.

Table 1: GALANTE in a nutshell

Confusion: The three-band (G+G_{BP}+G_{RP}) Gaia photometric survey will address most of the problems above, especially after the full spectrophotometry is available in DR3. However, it will suffer from confusion in crowded and/or nebular regions (common for O+B+WR stars), as the G_{BP}+G_{RP} instrument behaves as a slitless spectrograph.

2 Measuring temperature

Figure 3 shows the seven passbands used in the GALANTE survey, four of them in common with the J-PLUS survey [1] (F348M+F515N+F660N+F861M) and three specifically designed for the project (F420N+F450N+F665N). The four bluemost filters have been chosen to measure the Balmer jump: F348M measures the continuum to its left while F420N+F450N+F515N do it to the right avoiding the Balmer lines. GALANTE will be used to measure T_{eff} in two steps.

First, we build the two indices (analogous to m_1 and c_1 in the Strömgren system) $m' = \mathrm{F420N}-1.47\,\mathrm{F450N}+0.47\,\mathrm{F515N}$ and $c' = \mathrm{F348M}-3.44\,\mathrm{F420N}+2.44\,\mathrm{F450N}$, where the coefficients were determined empirically. As shown in the left panel of Fig. 4, those indices are nearly independent of gravity, metallicity, and type or amount of extinction for hot stars (T_{eff} > 10 kK) and depend almost only on T_{eff} with a large dynamic range in c' of more than one magnitude between 10 kK and 40 kK. For cooler stars, the position in the index-index diagram depends not only on T_{eff} but also on gravity, and to some extent on the other quantities. The validity of this method is shown on the right panel of Fig. 4, where a preliminary analysis (see below for calibration issues) of one of the GALANTE fields in Cygnus OB2 using aperture photometry correctly places the stellar locus and classifies the stars with known spectral types. Therefore, we will use these indices to give a preliminary estimate of stellar temperature.

As a second step, we will combine GALANTE with 2MASS and process the photometry with CHORIZOS [3], a Bayesian photometric code that allows the simultaneous calculation

Figure 2: GALANTE RGB (F665N+F450N+F420N) image of the Pleiades obtained with the Javalambre T80 telescope. The combination of four exposure times (from 0.1 s to 50 s) yields not a single saturated pixel (despite the presence of the 2[nd] magnitude Alcyone) while detecting faint objects with magnitudes 19-20. The field of view is $1^{\circ}\!.4\times1^{\circ}\!.4$ with N toward the top and E toward the left.

of $T_{\rm eff}$, luminosity class, $E(4405-5495)$ or amount of extinction, and R_{5495} or type of extinction from photometric data. The output will be combined with Gaia parallaxes to compare trigonometric and spectroscopic distances and build a 3-D extinction map of the solar vicinity more accurate than previous attempts, allowing for different types of extinction.

3 Photometric calibration

The primary photometric calibration of GALANTE uses the fact that a typical $1^{\circ}\!.4\times1^{\circ}\!.4$ Galactic Plane field contains $\sim$ 100 objects with good-quality Tycho-2 B_T+V_T + Gaia G+$G_{\rm BP}$+$G_{\rm RP}$ + 2MASS J+H+K (8 filters) and $\sim 10^4$ objects with their Gaia and 2MASS equivalents (6 filters). We process that input photometry with CHORIZOS [3] and the SED grid of [7] to generate synthetic predicted magnitudes (and their uncertainties) in each of the seven GALANTE filters allowing for arbitrary variations in $T_{\rm eff}$, luminosity class, $E(4405-5495)$, and R_{5495}. The resulting predicted uncertainties for a single star are in the range of one hundredth to a few tenths of magnitude, with lower values for objects with 8-filter photometry and lower input uncertainties and for redder filters. For each field and filter we first combine the information from the $\sim 10^4$ objects with 6-filter photometry to detect (and correct if necessary) possible low-order flat-field issues and we then use objects with 8-filter photometry to calculate the zero point, which has a typical uncertainty of one hundredth of a magnitude. The whole process is dependent on the accuracy of the calibration

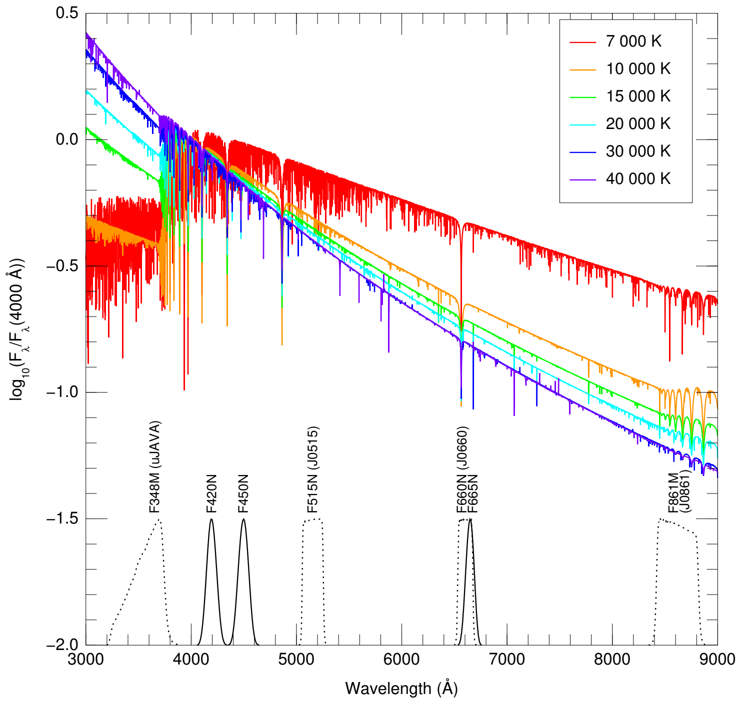

Figure 3: Normalized passbands for the seven GALANTE filters compared with model SEDs of stars with different $T_{\rm eff}$ [7]. The filter combination F438M+F420N+F450N+F515N has been chosen to accurately measure the Balmer jump using continuum regions that avoid the strong Balmer lines. J-PLUS filters are plotted with dotted lines and filters exclusive to GALANTE are plotted with solid lines.

of the input photometry (Tycho-2, Gaia, and 2MASS), to which we have devoted a strong effort until being satisfied [4, 5, 6, 9, 13, 14]. The right panel of Fig. 4 shows how well this works even with a preliminary version in which we used (a) aperture instead of PSF photometry and (b) the $\sim$ 100 object calibration sample and only six filters (it was done before Gaia DR2 so no $G_{\rm BP}$+$G_{\rm RP}$ photometry was available and we used the calibrations of [6] and [9] instead of those of [13] and [14]).

We also use several secondary calibration mechanisms:

- Comparison of results for the same field using different exposure times and air masses to check for anomalous detector effects or atmospheric extinction.
- Comparison between adjacent fields. The GALANTE strategy leaves a generous overlap ($\sim$ 12′) between fields to allow for the identification of possible zero point offsets.
- Use of spectrophotometric standards. Note that the GALANTE FOV is large enough that $\sim$ 10% of the fields have standards of one type or another. Also note that we have recently increased the sample of spectrophotometric standards [14].
- Use as CHORIZOS input the temperature and gravity of objects with accurate spectroscopic classifications, especially early-type stars for which the intrinsic SED is well known. This leads to reduced uncertainties for the predicted magnitudes. For this purpose we use the spectral classifications from the Galactic O-Star Spectroscopic Survey (GOSSS, [16, 19, 22, 23]).

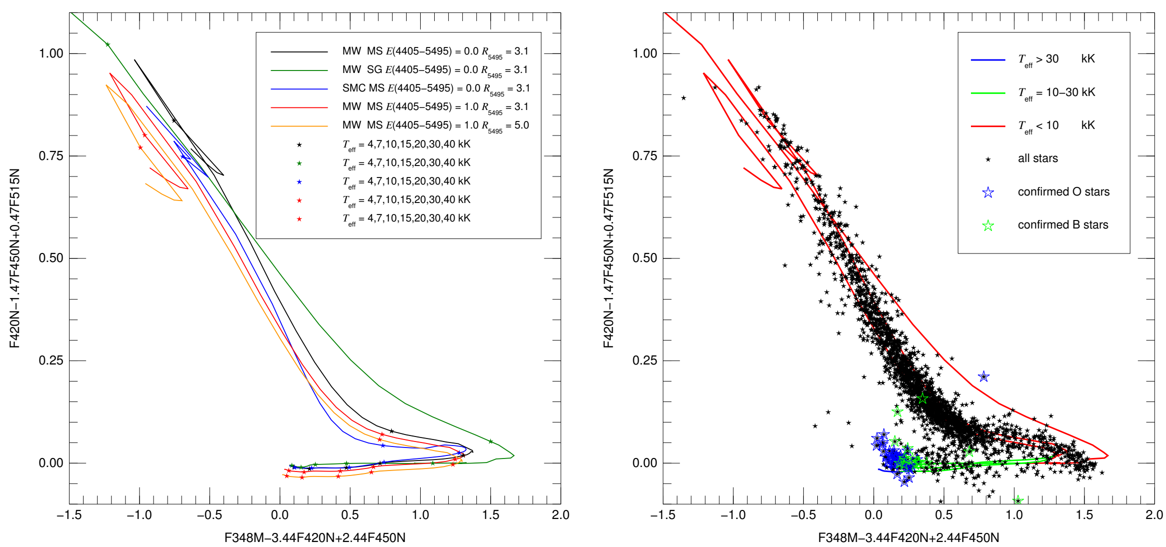

Figure 4: [left] A index-index diagram using model SEDs from [7]. Note how we can measure $T_{\rm eff}$ for hot stars (lower branch) independently of gravity, metallicity, and reddening. [right] Same diagram with only the first, second, and fourth synthetic photometry functions plus overplotted data from one of the GALANTE fields in Cygnus OB2 (using a preliminary calibration). Most of the stars in the diagram follow the main-sequence track between A and K stars, as expected. The field contains a very rich highly extinguished OB association. This results in few late-B stars present (they are too dim for GALANTE at the distance and extinction of the association) but also in 100+ O and early B stars detected. Despite their high extinction ($A_V \sim 6$ mag), they are at the expected location in the diagram and the existing spectral types confirm their nature, thus providing an indication of the excellent quality of the data and calibration.

4 Objectives and planning

The main objective of GALANTE is to identify all Galactic O+B+WR stars down to magnitude 17 and estimate their $T_{\rm eff}$. We will cross-match all OBA stars with 2MASS and measure their $E(4405-5495)$ and R_{5495}. We will coordinate our efforts with the Stellar, Circumstellar, and Interstellar Physics WEAVE survey and with GOSSS to acquire follow-up spectroscopy of the newly found O+B+WR stars.

Some additional objectives include (a) a magnitude-limited catalog of emission-line stars, (b) the IMF of large-area clusters and associations, (c) a continuum-subtracted Hα map with subarcsecond pixels, and (d) cross-calibration with Gaia.

GALANTE NORTE started taking data in 2016 and GALANTE SUR in 2018. If weather behaves, we should complete the northern survey in 2021 and the southern one in 2023. For the long-term future several extensions are possible: deep surveys of interesting regions, multiple epochs, and additional filters are some of the possibilities.

Acknowledgments

Based on observations made with the JAST/T80 telescope at the Observatorio Astrofísico de Javalambre, in Teruel, owned, managed and operated by the Centro de Estudios de Física del Cosmos de Aragón. J.M.A., E.J.A., and A.L. acknowledge support from the Spanish Government Ministerio de Ciencia, Innovación y Universidades through grant AYA2016-75 931-C2-1/2-P. R.H.B. acknowledges support from DIDULS project PR18143.

References

[1] Cenarro, A. J. et al. 2017, HSA IX, 11

[2] Finkbeiner, D. P. 2003, ApJS 146, 407

[3] Maíz Apellániz, J. 2004, PASP 116, 859

[4] Maíz Apellániz, J. 2005, PASP 117, 615

[5] Maíz Apellániz, J. 2006, AJ 131, 1184

[6] Maíz Apellániz, J. 2007, ASPC 364, 227

[7] Maíz Apellániz, J. 2013a, HSA VII, 657

[8] Maíz Apellániz, J. 2013b, HSA VII, 583

[9] Maíz Apellániz, J. 2017, A&A 608, L8

[10] Maíz Apellániz, J. 2017, Early Data Release + Scientific Exploitation of the J-PLUS Survey, 15

[11] Maíz Apellániz, J. & Sota, A. 2018, RMxAC 33, 44

[12] Maíz Apellániz, J. & Barbá, R. H. 2018, A&A 613, A9

[13] Maíz Apellániz, J. & Pantaleoni González, M. 2018, A&A 616, L7

[14] Maíz Apellániz, J. & Weiler, M. 2018, arXiv:1808.02820, A&A accepted

[15] Maíz Apellániz, J. et al. 2004, ApJS 151, 103

[16] Maíz Apellániz, J. et al. 2011, HSA VI, 467

[17] Maíz Apellániz, J. et al. 2012, ASPC 465, 484

[18] Maíz Apellániz, J. et al. 2014, A&A 564, A63

[19] Maíz Apellániz, J. et al. 2016, ApJS 224, 4

[20] Maíz Apellániz, J. et al. 2017b, HSA IX, 509

[21] Sota, A. et al. 2008, RMxAC 33, 56

[22] Sota, A. et al. 2011, ApJS 193, 24

[23] Sota, A. et al. 2014, ApJS 211, 10

Highlights on Spanish Astrophysics X, Proceedings of the XIII Scientific Meeting of the Spanish Astronomical Society held on July 16 – 20, 2018, in Salamanca, Spain. B. Montesinos, A. Asensio Ramos, F. Buitrago, R. Schödel, E. Villaver, S. Pérez-Hoyos, I. Ordóñez-Etxeberria (eds.), 2019

How do massive stars form? Finding targets for MIRADAS.

Amparo Marco[1], Ignacio Negueruela[2], Stephen S. Eikenberry[3] and Artemio Herrero[4]

[1] Departamento de Física, Ingeniería de Sistemas y Teoría de la Señal, University of Alicante, Spain
[2] Departamento de Física Aplicada, University of Alicante, Spain
[3] Department of Astronomy, University of Florida, USA
[4] Instituto de Astrofísica de Canarias ; Departamento de Astrofísica, University of La Laguna, Spain

Abstract

Observations from massive stars in H II regions can help to clarify theories of massive star formation because they show the degree of isolation under which massive stars can be formed. We present a new survey, called 'A-SMASHeR', consisting of massive stars associated to not yet characterized H II regions that are either more distant or more heavily embedded than the traditional samples. It will allow us to study in a homogeneus way many massive stars placed at different distances between l=30° and 180°, presenting different reddenings and metallicities. Besides, we will use it to constrain better the theories of stellar formation and design future observations with MIRADAS

1 Introduction

High mass stars ($M \geq 8\ M_{\odot}$) are crucial agents in the evolution of galaxies and have a disproportionate effect upon their environment. They provide most of the mechanical energy input into the interstellar medium through stellar winds and supernovae, and most of the UV ionizing radiation of galaxies. They also power the far-IR luminosities of galaxies through the heating of dust and are the primary source of CNO enrichment of the interstellar medium [1]. However, we still know very little about their formation, structure, evolution and death.

How do massive stars form? This is a fundamental question in astrophysics to clarify nowdays. At present, two main theories are invoked: (a) monolithic core accretion, basically a scaled-up version of classical low-mass formation theories, where very high opacities allow infalling material to overcome the radiation pressure ([2] and [3]) and (b) competitive accretion, where massive stars are formed in cluster cores, benefiting from the gravitational potential of the whole cluster to accrete more material ([4] and [5]). One of the key observations that may help to clarify theories of massive star formation is the degree of isolation under which massive stars can be formed [6].

H II regions are places of very recent massive star formation. They are made of plasma ionized by the far-ultraviolet radiation from the massive O-type and B-type stars living in their interior. They can be seen across the entire Galactic disk, because they are very bright at mid-infrared to radio wavelengths. We can use them to answer one of the main questions in the modern theory of star formation: to which degree OB stars can form in true isolation ([6] and [7]). Isolated OB stars are known to exist, but the present controversy is if they were formed in situ. OB stars within an H II region have recently formed within it, and are thus ideal targets to test this hypothesis. To characterize the whole population associated with the H II regions, we must use infrared detectors.

MIRADAS is a Mid-resolution InfRAreD Astronomical Spectrograph that will be installed on the GTC in 2019 [8]. It is a near-infrared multi-object echelle spectrograph operating at spectral resolution $R = 20\,000$ over the $(1 - 2.5)$ microns range that can obtain simultaneous spectra of up to 12 targets. *The massive stellar content of the Milky Way* is one of the MIRADAS science design reference cases because MIRADAS@GTC at $R = 20\,000$ is the ideal instrument to enable a proper abundance and radial velocity analysis of massive stars. Observing programmes with MIRADAS will provide insights on the details of the formation and stellar evolution of massive stars, the chemical composition of the inner Galaxy and the role of the different kinematical populations that populate the inner regions of the Milky Way.

2 Alicante Survey of MAssive Stars in H II Regions (A-SMASHeR)

Members of the MIRADAS science team are getting ready for the arrival of MIRADAS. We are looking for candidate massive stars to observe with MIRADAS by identifying the population of massive stars associated to the H II regions that have not been yet characterized [9]. This new survey of massive stars is formed by objects that are either more distant or more heavily embedded than the traditional samples. It will allow us to study in a homogeneus way many massive stars placed at different distances between l=30° and 180°, presenting different reddenings and metallicities. The more embedded population will signal the youngest sites of star formation. On the other hand, we are selecting a sample of H II regions with a wide variety of shapes and sizes. We want to study the formation of massive stars in small and isolated H II regions as well as in extended H II regions belonging to large areas of star formation. In some cases, we are choosing fields containing different small H II regions and we are very interested in studying if the massive populations of these regions are connected between them. We used LIRIS at the WHT to obtain images for a hundred different fields in the JHK_S bands and now we are getting spectra with EMIR at the GTC for those fields with apparently isolated stars.

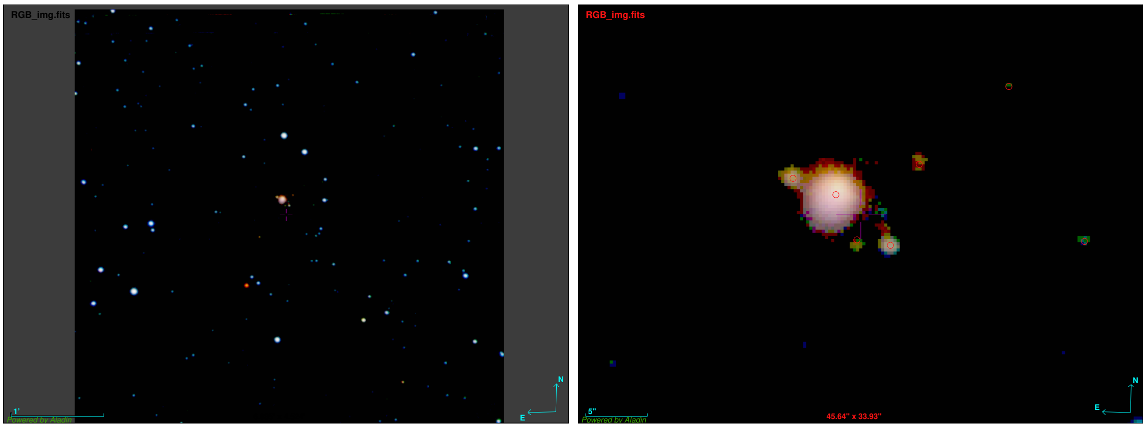

Figure 1: **Left:** Field observed with LIRIS for the H II region G124.640+02.536. The image is a 3 colour composite (JHK_S) and has asize $4.632' \times 4.369'$. We can see that the majority of the stars have blue colour. Only a few stars in the center are reddened stars. **Right:** Zoom for the center of the field where the reddened stars lie. It has a size $44.89'' \times 42.33''$.

We are building a new survey called "*Alicante Survey of MAssive Stars in H II Regions (A-SMASHeR)* " with a new sample of massive star forming regions that are either very distant, very reddened or both. It will represent a very significant contribution to the number of massive H II regions whose stellar population is characterized. Besides, it will allow us to constrain better the theories of stellar formation and will be very useful to design the future observations with MIRADAS

3 Results

From an initial study using images and JHK_S photometry, we could identify the massive star population associated to the H II regions. Initially, we have selected 18 candidate massive stars to be apparently isolated. Here, we present an example with the study of the H II region G124.640+02.536. In Fig. 1 we show the images in three colours taken with LIRIS. We can see the different colours of the stars in the field (Left). The redder stars are lying in the center (Right). We carry out the JHK_S photometry and build the $(J-K_S)$.vs.K_S diagram (see Figure 2). Stars located beyond $(J-K_S) \geq 2.5$ are clearly separated and correspond to the redder stars in Figure 1. In Fig. 3 we plot the position of these reddened stars in a WISE image and in a LIRIS image, respectively. We can observe that the brightest reddened star ($K_S = 11.82$; $(J-K_S) = 3.51$) is inside the H II region while the next in brightness but less reddened star ($K_S = 12.25$; $(J-K_S) = 2.92$) is outside the H II region at $1.5'$ in the SW direction. Therefore, we have a clear photometric candidate OB star ionizing the H II region whose nature will be confirmed using EMIR spectroscopy. With the spectral type we will estimate its intrinsic brightness and then we will use our LIRIS photometry to verify if any other massive stars could be present in the H II region by checking if they have the expected magnitude and colours.

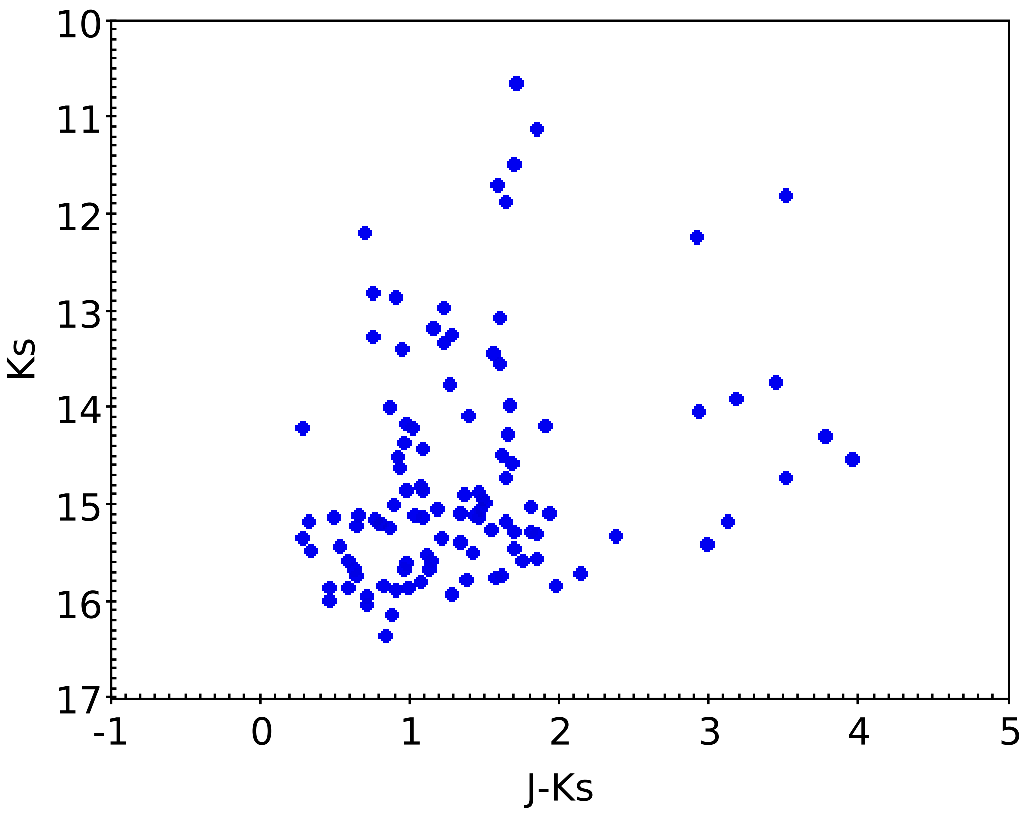

Figure 2: $(J - K_S)$.vs.K_S diagram for the stars in the field from our LIRIS photometry. The group of the stars lying beyond $(J - K_S) \geq 2.5$ correspond to the heavily reddened stars in the field.

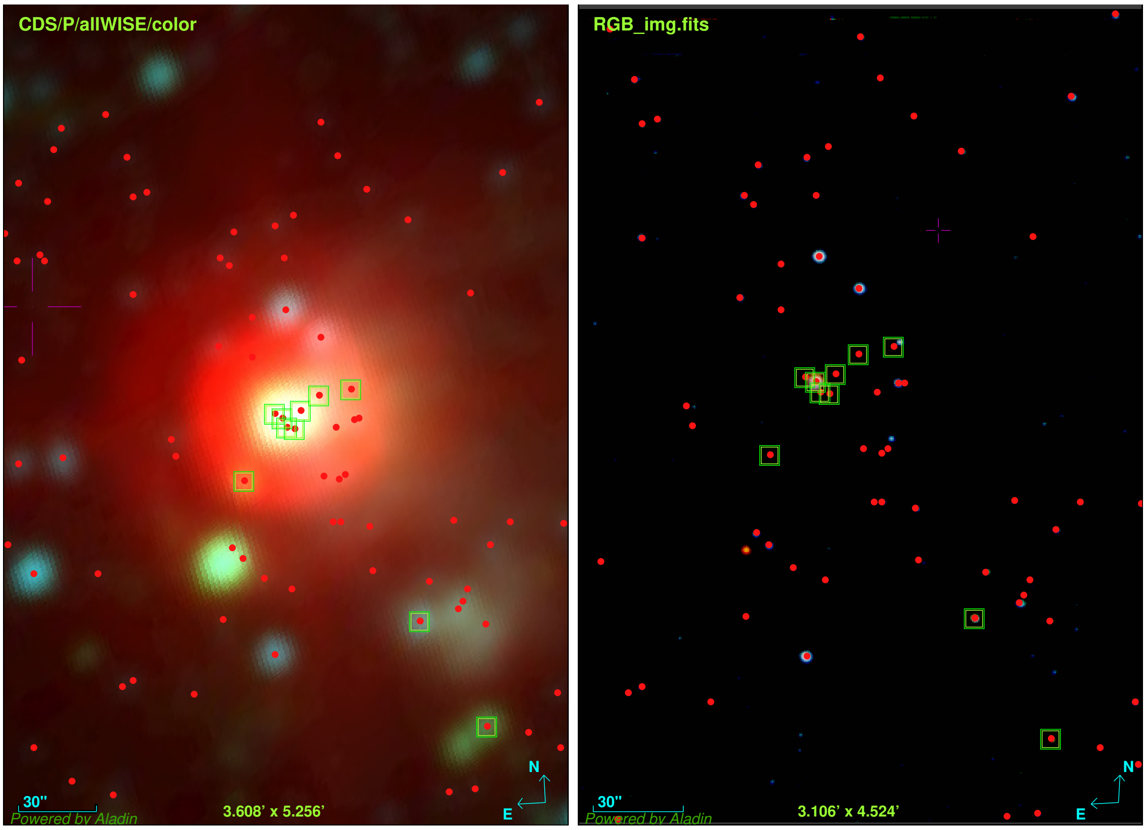

Figure 3: **Left:** WISE image for the H II region G124.640+02.536. Stars lying beyond $(J - K_S) \geq 2.5$ in Figure 2 are marked as green open squares **Right:** Zoom in of the LIRIS image for the H II region G124.640+02.536 shown before. Stars lying beyond $(J - K_S) \geq 2.5$ in Figure 2 are marked as green open squares

Acknowledgments

This research is partially supported by the Spanish Government Ministerio de Economía y Competitividad under grant AYA2015-68012-C2-2-P (MINECO/FEDER). The photometric observations were obtained with the WHT, which is operated on the island of La Palma by the Isaac Newton Group and installed in the Spanish Observatorio del Roque de Los Muchachos of the Instituto de Astrofísica de Canarias. This research has made use of Aladin, operated at CDS, Strasbourg (France).

References

[1] Massey, P. 2003, ARA&A, 41, 15

[2] Yorke, H.W. and Sonnhalter, C. 2002, ApJ, 569, 846

[3] Krumholz, M.R., Klein, R.I., McKee, C.F., Offner, S.S.R. and Cunningham, A.J. 2009, Science, 323, 754

[4] Bonnell, I.A. and Bate, M.R. 2006, MNRAS, 370, 488

[5] Smith, R.J.; Longmore, S. and Bonnell, I. 2009, MNRAS, 400, 1775

[6] Lamb, J.B., Oey, M.S., Werk, J.K, and Ingleby, L.D. 2010, ApJ, 725, 1886

[7] Oey, M.S., Lamb J.B., Kushner C.T., Pellegrini E.W. and Graus A.S. 2013, ApJ, 768, 66

[8] Eikenberry, S. S. 2013, RMxAA, 42, 93

[9] Anderson, L.D., Bania, T. M., Balser, Dana S. and Rood, Robert T. 2011, ApJ, 194, 32

Highlights on Spanish Astrophysics X, Proceedings of the XIII Scientific Meeting of the Spanish Astronomical Society held on July 16 – 20, 2018, in Salamanca, Spain. B. Montesinos, A. Asensio Ramos, F. Buitrago, R. Schödel, E. Villaver, S. Pérez-Hoyos, I. Ordóñez-Etxeberria (eds.), 2019

The potential of Hα spectro-astrometry to detect forming planets in disks around young stars.

I. Mendigutía[1]

[1] Centro de Astrobiología (CSIC-INTA), Departamento de Astrofísica, ESA-ESAC Campus, PO Box 78, 28691 Villanueva de la Cañada, Madrid, Spain

Abstract

This proceedings paper discusses how spectro-astrometry in Hα can be used as an alternative technique to detect planets in formation around young stars. The basic principles, methodology, and observational constraints in terms of brightness contrast, angular accuracy and signal to noise ratio are summarized, along with the specific capability of spectro-astrometry to eventually separate the individual spectra of a system formed by a young star plus an accreting planet. The case of LkCa 15 serves to illustrate the first use of spectro-astrometry to accurately test the presence of a forming planet in a protoplanetary disk.

1 Introduction

Thousands of exoplanets orbiting stars different than our Sun have been confirmed to date. However, the vast majority of them are found around relatively evolved stars, and only a few candidates have been proposed to be located in the places they form: the inner $\sim$ 100 au within the protoplanetary disks that surround the stars when these are young ($<$ 10 Myr).

Current detection methods of young planets in orbits between 1 and 100 au are mainly based on high-contrast, high-angular resolution techniques like interferometry, sparse aperture masking, or differential imaging [13, 18, 10]. However, these techniques rely on complex, state of the art instrumentation and data reduction processes, which is partially leading to a debate on the interpretation and real origin of the detections [19, 7, 15, 11, 9]. Moreover, among the few young candidate planets only two have been reported to be in the actual formation phase, based on the detection of Hα emission associated to active accretion of the circumplanetary material. The first one was reported around LkCa 15 [16], although the infrared (IR) brightness originally associated to planet emission is now attributed to persistent structures in the inner disk [19]. The second accreting planet has been reported very recently around PDS 70 [20].

Complementary observational methods are thus useful to test the presence of planets in formation and eventually provide new detections from alternative approaches. Sect. 2 shows the potential of Hα spectro-astrometry to detect such planets (for more general spectro-astrometric reviews see [1, 23, 6]), Sect. 3 provides an example of spectro-astrometry applied to LkCa 15, and Sect. 4 summarizes the main conclusions.

2 Hα spectro-astrometry and planet detection

The simplest instrumental requirement to carry out spectro-astrometry is a spectrograph with an orientable long-slit, providing 2D spectra with the dispersion axis perpendicular to the slit and the spatial axis in the parallel direction. The spectro-astrometric methodology is summarized in Fig. 1. The blue plane represents the CCD with the dispersion (λ) and the spatial (x) axes perpendicular to each other. The number of counts per second is represented by the I-axis perpendicular to the detector. The usual "intensity spectrum" is the representation of I vs λ. Spectro-astrometry also exploits the spatial information contained in the CCD by fitting the spatial profile at each wavelength, normally by means of a Gaussian characterized by its centre and full width half maximum (FWHM). Therefore, the spectro-astrometric observables include, apart from the intensity spectrum, a "position spectrum" (x_c vs λ) and a "full width half maximum spectrum" (FWHM vs λ). The position spectrum contains information about the wavelength-dependent photocentre of the emitting source in the direction of the slit, and the FWHM spectrum about the wavelength-dependent emitting size in such direction (apart from the seeing for Earth-based telescopes and the instrumental point spread function, both roughly constant for a small wavelength range). For a given target, the typical spectro-astrometric observing strategy requires two slit positions perpendicular to each other, plus two slit orientations per position (parallel and anti-parallel). The former serve to constrain the position and extent of the different sub-structures in the plane of the sky from photocentre displacements and FWHM signals, and the latter serve to address possible instrumental artifacts (real photocentre features from the sources will reverse, whereas instrumental effects remain the same, and can be removed; [1]).

Using this clever and relatively simple technique, it is possible to probe structures at angular scales of (sub-)mas [22], even with mid-size telescopes non-assisted by adaptive optics (Sect. 3). Particularly relevant for the scope of this paper is that spectro-astrometry has demonstrated to be a key technique to test the presence and find new stellar companions around young T-Tauri and Herbig Ae/Be stars, when the contrast between the corresponding Hα emission lines is different than in the continuum [2, 17, 4, 21]. The situation is similar for a system formed by a young star and a forming planet. Although these are faint and the optical continuum is clearly dominated by the central star, planets in formation are accreting their circumplanetary material and thus they probably show strong Hα emission that significantly reduces the contrast at these specific wavelengths [24].

By definition, the photocentre shift expected for a young star and a forming planet

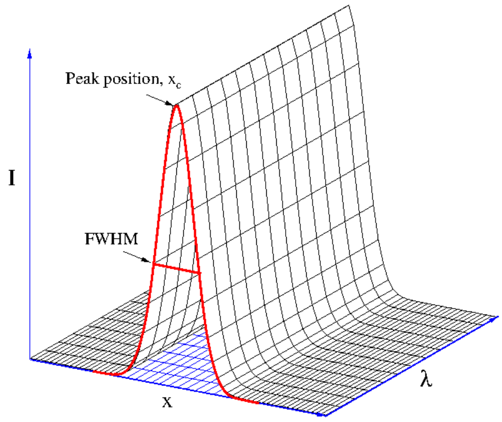

Figure 1: (Taken from [3]) The blue plane represents the CCD, with the spectral and spatial axis indicated by λ and x, respectively. The vertical, I-axis represents the intensity. For each wavelength λ, the spatial distribution in the x-axis is fitted to a Gaussian characterized its centre (x_c) and FWHM. The spectro-astrometric observables are the intensity (I vs λ), position (x_c vs λ) and FWHM (FWHM vs λ) spectra.

separated s mas in the plane of the sky and with an Hα contrast of $c_{H\alpha}$ magnitudes is:

$$\delta_{\rm phot} = \frac{I_p \times s}{I_* + I_p} = \frac{s}{10^{0.4c_{H\alpha}} + 1}, \tag{1}$$

where I_* and I_p are the Hα intensities of the central star and the planet, and the zero-point is the photocentre position of the adjacent continuum mainly coming from the star. In turn, the accuracy needed to detect such a photocentre shift is mainly determined by the atmospheric seeing and the signal to noise ratio (SNR) of the spectra [6]:

$$\delta_{\rm phot} \sim 0.4 \times \frac{\rm seeing}{\rm SNR}. \tag{2}$$

Based on the two previous equations, Fig. 2 shows the expected photocentre shifts (left) and the nominal SNRs (right) necessary to make spectro-astrometric detections for different Hα contrasts and a range of star-planet separations. A distance of 140 pc (the rough average to Taurus) has been adopted, as well as two limits representing good and bad seeing conditions (0.6” and 1.5”, respectively). These estimates show that (sub-)mas photocentre shifts are expected for accreting planets located between 1 and 100 au from the star with Hα contrasts between 4 and 9 magnitudes. Those shifts can be measured under good seeing conditions and maximum spectral SNRs arbitrarily set to 1500. For worse seeing conditions the sensitivity can decrease by up to 1 magnitude. Reaching high SNRs depends on the R-band brightness and can require co-adding individual spectra of faint stars, for which one can take advantage of the spectro-astrometric observing strategy previously mentioned.

The discussion above does not consider other aspects that are also important for spectro-astrometry. For instance, based on Hα spectra of wide-orbit sub-stellar mass ob-

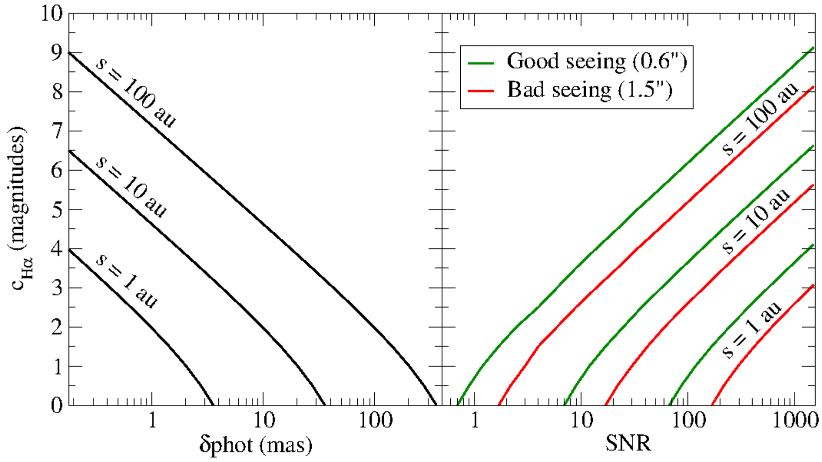

Figure 2: Star-planet Hα contrast reached as a funtion of the photocentre shift (left) and the corresponding spectral SNR (right) for different star-planet separations (at the Taurus distance of 140 pc) and seeing conditions, as indicated.

jects [5], a minimum spectral resolution of $\lambda/\delta\lambda > 1000$ is in principle necessary to resolve the spectral lines and detect planetary photocentre shifts. Indeed, higher resolution spectra are desirable to apply spectral binning and significantly improve the spectro-astrometric accuracy without losing the shape of the Hα emission. In addition, CCDs with small plate scales (in "/pixel) provide better accuracy when spectro-astrometric signals, measured in pixels, are converted into angular units.

Finally, the high angular resolution and brightness contrast that can be probed through spectro-astrometry are not the only advantages of this technique. Probably the most relevant characteristic is that spectro-astrometry is potentially capable of recovering the individual spectra of the star and the planet from the unresolved, total observed spectra $I(\lambda) = I_*(\lambda) + I_p(\lambda)$. In the simplest approach, Eq. 1 implies

$$I_p(\lambda) = I(\lambda) \times \frac{\delta_{\mathrm{phot}}(\lambda)}{s}; I_*(\lambda) = I(\lambda) \times (1 - \frac{\delta_{\mathrm{phot}}(\lambda)}{s}), \quad (3)$$

which requires knowing the star-planet separation from complementary methodologies [1, 8]. Moreover, the individual spectra in a binary system can also be deconvolved from the three spectro-astrometric observables, I(λ), δphot(λ), and FWHM(λ), without a priori knowledge of the position of the companion [14, 21]. The eventual extraction of the Hα emission spectrum of a planet from spectro-astrometry, combined with detailed accretion modelling [24], can be a unique tool to understand the accreting phase of planets in formation.

3 A pilot study: LkCa 15

The first Hα emission attributed to a forming planet was observed around the young T-Tauri star LkCa 15 [16]. This and two more candidate planets in orbits of ~ 15 au around the same

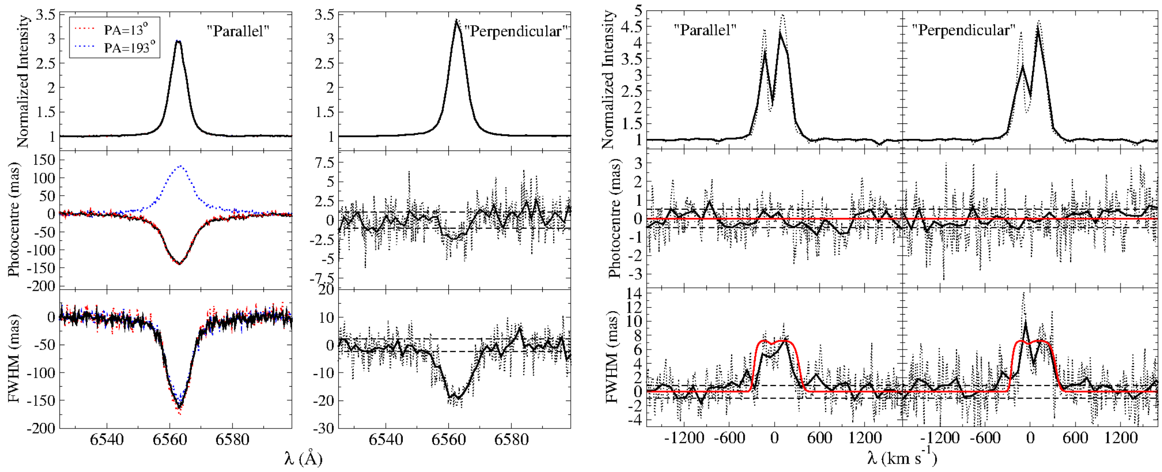

Figure 3: (Adapted from [12]) Spectro-astrometric spectra of GU CMa (left panels) and LkCa 15 (right panels). For GU CMa, the left sub-panels plot the individual spectra for the two slit orientations parallel to the position of the companion (red and blue) and the averaged spectra (black). For the perpendicular position of GU CMa, and for LkCa 15, only the averaged spectra are shown both with the original spectral resolution (dotted lines) and after rebinning (solid lines). The rebinned accuracies are indicated with the horizontal dashed lines, reaching less than 1 mas for LkCa 15. The red lines result from a model of symmetric Hα emission with extent similar to the orbit initially attributed to a planet.

star appeared bright also in the IR. A more recent work by [19] shows that the IR-bright sources could instead be part of the inner disk that extends up to $\sim$ 30 au, although the Hα emission would remain unexplained. We have recently applied Hα spectro-astrometry to LkCa 15 [12]. We first observed the well known young binary star GU CMa to test the spectro-astrometric performance of ISIS mounted on the 4.2m William Herschel Telescope. The main results are shown in Fig. 3, which serves to illustrate different topics mentioned in this work. The observed position and FWHM spectra of GU CMa are consistent with a binary system with similar continuum brightness and Hα emission dominated by the central star. In turn, the lack of photocentre shift and the similar FWHM signatures at both slit positions cannot be explained by an accreting planet around LkCa 15, but by a roughly symmetric Hα emission with size comparable to the orbit originally associated to that planet. The origin of such an extended emission is perhaps related to a variable disk wind [12].

Although our data are not consistent with the presence of an accreting planet in the case of LkCa 15, they show for the first time that spectro-astrometry can reach enough brightness contrast and spatial resolution to test the presence of forming planets in disks around young stars and look for new candidates.

4 Conclusions

Spectro-astrometry is capable of reaching an Hα brightness contrast of several magnitudes within the inner 100 au of protoplanetary disks by measuring (sub-)mas photocentre shifts. This property, along with the fact that spectro-astrometry is technically capable of extracting the Hα emission spectrum of a forming planet, makes it ideal for future surveys that allow us to increase the sample of such planets and understand their formation process.

Acknowledgments

The author acknowledges Deborah Baines for providing a high resolution version of Fig. 1 and reading the manuscript before this was submitted. The author also acknowledges the Government of Comunidad Autónoma de Madrid, Spain, which has funded this work through a "Talento" Fellowship (2016-T1/TIC-1890)

References

[1] Bailey, J. A. 1998, in Proc. SPIE, Vol. 3355, Optical Astronomical Instrumentation, ed. S. D'Odorico, 932-939

[2] Bailey, J. 1998, MNRAS, 301, 161

[3] Baines, D. 2004, PhD thesis, University of Leeds (UK). "Resolving binaries and the circumstellar environment of Herbig Ae/Be stars with spectro-astrometry."

[4] Baines, D., Oudmaijer, R. D., Porter, J. M., & Pozzo, M. 2006, MNRAS, 367, 737

[5] Bowler, B. P., Liu, M. C., Kraus, A. L., & Mann, A. W. 2014, ApJ, 784, 65

[6] Brittain, S. D., Najita, J. R., & Carr, J. S. 2015, Ap&SS, 357, 54

[7] Follette, K. B., Rameau, J., Dong, R., et al. 2017, AJ, 153, 264

[8] Garcia, P. J. V., Thiébaut, E. & Bacon, R. 1999, A&A, 346, 892

[9] Huélamo, N., Chauvin, G., Schmid, H. M., et al. 2018, A&A, 613, L5

[10] Keppler, M., Benisty, M., Müller, A., et al. 2018, A&A, 617, A44

[11] Mendigutía, I., Oudmaijer, R. D., Garufi, A., et al. 2017, A&A, 608, A104

[12] Mendigutía, I., Oudmaijer, R. D., Schneider, P.C. et al. 2018, A&A, 618, L9

[13] Pinte, C., Price, D. J., Ménard, F., et al. 2018, ApJ, 860, L13

[14] Porter, J. M., Oudmaijer, R. D., Baines, D. 2004, A&A 428, 327

[15] Rameau, J., Follette, K. B., Pueyo, L., et al. 2017, AJ, 153, 244

[16] Sallum, S., Follette, K. B., Eisner, J. A., et al. 2015, Nature, 527, 342

[17] Takami, M., Bailey, J., & Chrysostomou, A. 2003, A&A, 397, 675

[18] Teague, R., Bae, J., Bergin, E. A., Birnstiel, T., & Foreman-Mackey, D. 2018, ApJ, 860, L12

[19] Thalmann, C., Janson, M., Garufi, A., et al. 2016, ApJ, 828, L17

[20] Wagner, K., Follete, K. B., Close, L. M., et al. 2018, ApJ, 863, L8

[21] Wheelwright, H. E., Oudmaijer, R. D. & Goodwin, S. P. 2010, MNRAS, 401, 1199

[22] Wheelwright, H. E., Bjorkman, J. E., Oudmaijer, R. D. et al. 2012, MNRAS, 423, L11

[23] Whelan, E. & Garcia, P. 2008, in Lecture Notes in Physics, Berlin Springer Verlag, Vol. 742, Jets from Young Stars II, ed. F. Bacciotti, L. Testi, & E. Whelan, 123

[24] Zhu, Z. 2015, ApJ, 799, 16

Highlights on Spanish Astrophysics X, Proceedings of the XIII Scientific Meeting of the Spanish Astronomical Society held on July 16 – 20, 2018, in Salamanca, Spain. B. Montesinos, A. Asensio Ramos, F. Buitrago, R. Schödel, E. Villaver, S. Pérez-Hoyos, I. Ordóñez-Etxeberria (eds.), 2019

H_2S Formation in Dark Clouds.

D. G. Navarro[1], A. Fuente[1], P. Caselli[2], M. Gerin[3], C. Krammer[4], E. Roueff[5], V. Wakelam[6], T. Alonso-Albi[1], R. Bachiller[1], S. Cazaux[7], B. Commerçon[8], R. Friesen[9], S. García-Burillo[1], B. M. Giuliano[2], J. R. Goicoechea[10], P. Gratier[6], A. Hacar [11], I. Jiménez-Serra[12], J. Kirk[13], V. Lattanzi[2], J. C. Loison[14], P. J. Malinen[15], N. Marcelino[10], R. Martín-Doménech[16], G. Muñoz-Caro[12], J. Pineda[2], M. Tafalla[1], B. Tercero[1], D. Ward-Thompson[17], S. Treviño-Morales[18], P. Riviére-Marichalar[10], O. Roncero[10] and T. Vidal[6].

[1] Observatorio Astronómico Nacional (OAN), Alfonso XII, 3 28014, Madrid, Spain
[2] Centre for Astrochemical Studies, Max-Planck-Institute for Extraterrestrial Physics, Giessenbachstrasse 1, 85748, Garching, Germany
[3] Observatoire de Paris, PSL Research University, CNRS, École Normale Supérieure, Sorbonne Universités, UPMC Univ. Paris 06, 75005, Paris, France
[4] Instituto de Radioastronomía Milimétrica (IRAM), Av. Divina Pastora 7, Nucleo Central, 18012, Granada, Spain
[5] LERMA, Observatoire de Paris, PSL Research University, CNRS, UMR8112, Place Janssen, 92190, Meudon Cedex, France
[6] Laboratoire d'astrophysique de Bordeaux, Univ. Bordeaux, CNRS, B18N, allée Geoffroy Saint-Hilaire, 33615, Pessac, France
[7] Faculty of Aerospace Engineering, Delft University of Technology, Delft, The Netherlands ; University of Leiden, P.O. Box 9513, NL, 2300 RA, Leiden, The Netherlands
[8] École Normale Supérieure de Lyon, CRAL, UMR CNRS 5574, Université Lyon I, 46 Allée d'Italie, 69364, Lyon Cedex 07, France
[9] Dunlap Institute for Astronomy & Astrophysics, University of Toronto, 50 St. George Street, Toronto, ON M5S 3H4, Canada 0000-0001-7594-8128
[10] Instituto de Física Fundamental (CSIC), Calle Serrano 121, 28006, Madrid, Spain
[11] Laboratoire d'Astrophysique de Bordeaux, Univ. Bordeaux, CNRS, B18N, Allée Geoffroy Saint-Hilaire, 33615, Pessac, France
[12] Leiden Observatory, Leiden University, PO Box 9513, 2300-RA, Leiden, The Netherlands
[13] Centro de Astrobiología (CSIC-INTA), Ctra. de Ajalvir, km 4, Torrejón de Ardoz, 28850, Madrid, Spain
[14] Department of Physics, University of Warwick, Coventry CV4 7AL, UK
[15] Institut des Sciences Moléculaires (ISM), CNRS, Univ. Bordeaux, 351 cours de la Libération, F-33400, Talence, France
[16] Department of Physics, University of Helsinki, PO Box 64, 00014, Helsinki, Finland; Institute of Physics I, University of Cologne, Cologne, Germany
[17] Harvard-Smithsonian Center for Astrophysics, Cambridge, MA 02138, USA
[18] Jeremiah Horrocks Institute, University of Central Lancashire, Preston PR1 2HE, UK
[19] Chalmers University of Technology, Onsala Space Observatory, 439 92 Onsala, Sweden.

Abstract

Sulfur is of fundamental importance in a wide variety of phenomena such as life on Earth. This element is one of the most abundant elements in space S/H $\sim 1.3\times10^{-5}$, but sulfuratted molecules are not as abundant as expected, thus a better understanding of sulfur chemistry is needed. We study and model the abundance of H_2S in two prototypical dark clouds, TMC1 and Barnard 1, to shed light on the physical and chemical processes involved in H_2S creation and destruction. Our observations are consistent with a PDR model in which H_2S is formed in grain mantles and released to gas phase via photodesorption. We cannot discard the contribution of other desorption processes, such as chemical desorption and/or grain-grain collisions, to enhance the H_2S abundance.

1 Introduction

Astrochemistry is an important tool to characterize the evolution of molecular gas from diffuse clouds to dense cores. In this dynamical evolution, gas cooling and gas ionization degree regulate cloud collapse. Sulfur plays an important role in this collapse since it is one of the most abundant elements in the universe, with a relative abundance of S/H$\sim 1.3 \times 10^{-5}$ [1], and it is the main donor of electrons in the 3.7 - 7 magnitude range. Despite its high relative abundance, sulfuratted compounds are not as abundant as expected in molecular clouds. Sulfur is thought to be depleted by a factor of 10^3 inside dark clouds compared to its cosmic abundance. The missing sulfur might be locked into grain mantles (e.g. [18]), which would form H_2S preferentially due to the high hydrogen abundance and mobility in the ice matrix. Therefore, studying the abundance of the H_2S molecule, which cannot be explained solely by gas-phase chemical reactions [24], may shed light into the physical and chemical processes responsible for sulfur depletion. We investigate the H_2S gas-phase abundance in two prototypical dark clouds: TMC1 and Barnard 1.

2 TMC1 and Barnard 1

TMC1, part of the Taurus molecular cloud (TMC), is one prototypical filamentary dark cloud cold core with quiescent star forming regions, at 140 pc. One of the largest Planck Galactic Cold Clumps (PGCC) groups in TMC is the Heiles Cloud 2 [13][20][22]. Malinen et al [17] identified two long filaments in HCL 2 at the eastern edge of the Taurus Molecular Ring, based on near-IR (NIR) extinction and Herschel data; one of these filaments was TMC-1. There are three visual extinction peaks along the TMC-1 filament, the well-known positions TMC1-CP, TMC1-C2 and TMC1-NH3 (see Fig. 1).

Barnard 1, embedded in the western sector of the 30pc wide molecular cloud complex Perseus, is a close (230pc) and young, intermediate-mass star forming cloud. It is known to host class 0 protostars [11][12], providing a bridge between the low-mass star formation of Taurus, and the massive star forming regions such as the Orion molecular cloud. This core

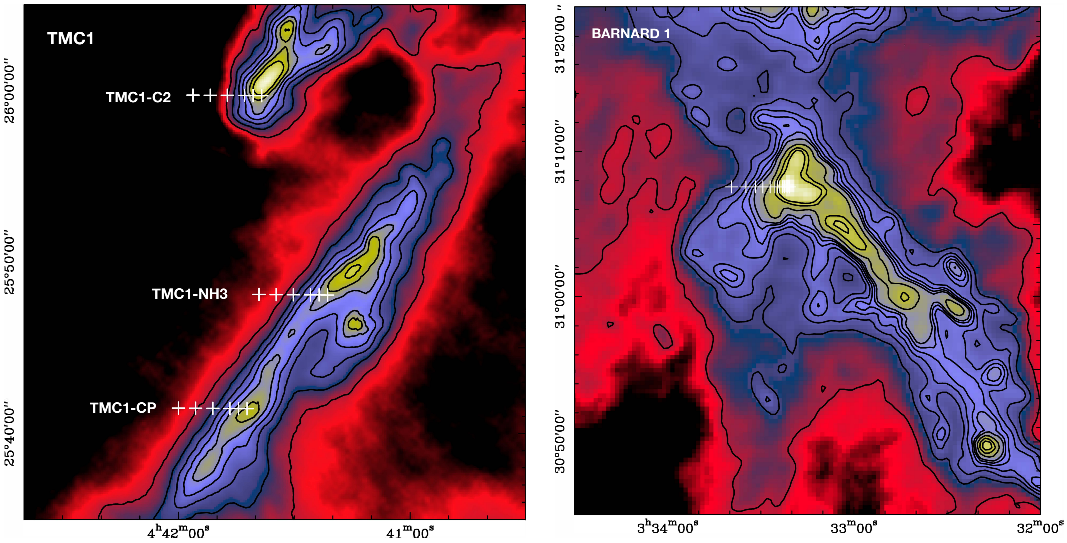

Figure 1: Visual extinction maps of TMC1 and Barnard 1 filaments, respectively (Kirk et al., in prep, Zari et al. 2015). White crosses mark the observed positions.

hosts two candidates for a first hydrostatic core [8], B1b-N and B1b-S, proving its young star formation. We observed through a cut associated with the extinction peak in B1b (see white marks in Fig. 1), which is the most prominent core in B1.

3 IRAM 30m and Yebes 40m telescopes

This work is based on data from the GEMS IRAM 30m Large Program (Gas phase Elemental abundances in Molecular CloudS, PI: A. Fuente) and complementary observations carried out with the Yebes 40m telescope. Using the wide bandwidth of the IRAM 30m receivers, we can observe the most intense 3mm and 2mm lines of these species with only 4 receiver setups. As backends we used the Fast Fourier Transform spectrometers (FFTS) correlators, which provide a frequency resolution of $\sim$ 49 kHz, enough to resolve the narrow lines expected in this dark cloud. The Yebes 40m telescope is equipped with HEMT receivers for the 2.2-50 GHz range, and a SIS receiver for the 85-116 GHz range. Single-dish observations in K-band (21-25 GHz) and Q-band (41-50 GHz) can be performed simultaneously. The intensity scale is T_{MB} and calibration errors are $\sim$ 20%.

4 H_2S abundances

The analysis of the $J = 1 \to 0$, $J = 2 \to 1$ and $J = 3 \to 2$ lines of CS and its isotopologues allows us to derive reliable values of line opacities and hydrogen densities towards the considered regions. We use Markov Chain Montecarlo sampling methods [5] as described in [7], and the radiative transfer code RADEX [23] to estimate the physical conditions of the gas. To estimate

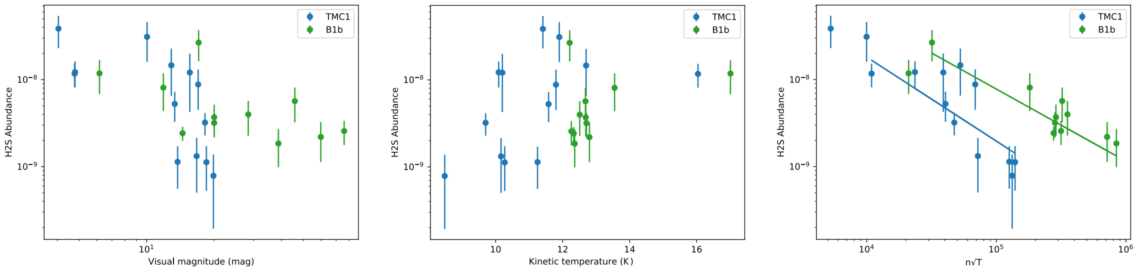

Figure 2: H_2S abundance against visual magnitude, kinetic temperature, and $n\sqrt{T}$ respectively, to show the dependence in eq. (1), for TMC1 (blue) and Barnard 1 (green).

the ortho-H_2S abundances we have used the code RADEX and the collisional coefficients for ortho-H_2O [4], assuming thermal ortho-para ratio for H_2 and scaled to ortho-H_2S. We hence fit the line intensities of the o-H_2S J = $1_{1.0}\rightarrow 1_{0,1}$ line assuming the physical conditions derived from CS observations. The H_2S abundance is calculated assuming an ortho-to-para ratio of 3. Fig. 2 shows the H_2S abundances as a function of the visual extinction in TMC 1 and Barnard 1b. The H_2S gas-phase abundance reaches its maximum value, X(H_2S) $\sim 1 - 3 \times 10^{-8}$, at the edges of the clouds. For visual extinctions larger than $\sim$ 10 mag, the abundance steeply decreases until values of $\sim$ a few 10^{-10} at $A_V \sim 20$ mag. For dust grain temperatures below the H_2S evaporation temperature, $\sim$ 50 K [16], the H_2S molecules are expected to stick on grains in every collision and the depletion time scale is given by

$$X(H_2S) \propto t_{\rm st} \equiv \frac{1}{n_{\rm gr}\sigma_{\rm gr}v_0} \propto \frac{1}{n\sqrt{T}}. \tag{1}$$

Fig. 2 shows the derived H_2S abundances abundances as a function of the gas kinetic temperature and the parameter, $n\sqrt{T}$. Towards both sources, the H_2S abundance decreases as $\sim \frac{1}{n\sqrt{T}}$, which corresponds to the slope of -1 seen in Fig. 2c, as expected when molecular freeze-out on grain surfaces is the main destruction mechanism. The scattering in the estimated values of the H_2S abundances is, however, large. Besides, the H_2S abundances estimated towards Barnard 1-b seems to be systematically higher than those towards TMC 1 by a factor of $\sim$ 3.

5 Chemical model

One interesting issue is to compare the sulfur and oxygen chemistry. Similarly to H_2O, H_2S cannot be efficiently formed in gas phase in dark clouds. The observed abundances of H_2S should be the consequence of the desorption of H_2S molecules from the grain surfaces. The physical conditions in dark clouds greatly constrain the possible desorption mechanisms: thermal desorption is only feasible for grain temperatures greater than 50 K [16], and sputtering is important in fast shocks ($v_s >$ 5 km s^{-1}), requiring our line profiles to be much wider. In a first approximation, we can consider that photodesorption by UV field and secondary photons are the main desorption agents. We have adapted the analytical model proposed for H_2O by

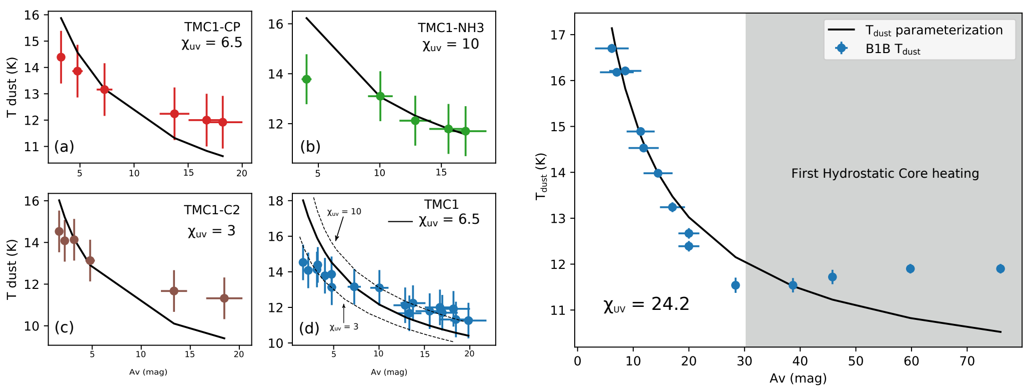

Figure 3: Fits of the dust temperature vs A_V for the three cuts in TMC 1 and the one in Barnard-1b, according to [14] parameterization. The best fit value of the incident UV field is $\chi_{UV} \sim 6.5$ for TMC 1 and $\chi_{UV} \sim 24$ for Barnard-1b, in units of the Draine field.

[15] to the case of H_2S molecule. In this model, the grains are supposed to be covered by an ice layer and photodesorption is the only H_2S formation path. On the other hand, freezing onto grain mantles and photodissociation are responsible for gas-phase H_2S destruction. We assume that secondary photons do not contribute to the photodissociation rate R_{H_2S}, and their extinction is similar to that of the FUV radiation. In the stationary state, creation (lhs of (2)) and destruction rates (rhs of (2)) are equal, and therefore:

$$(G_0 F_0 e^{-1.8A_V} + \Phi_{\rm SP}) Y_{\rm H_2S} f_{s,\rm H_2S} n_{\rm gr}\sigma_{\rm gr} = G_0 R_{\rm H_2S} e^{-1.7A_V} n({\rm H_2S}) + n({\rm H_2S}) v_0 n_{\rm gr}\sigma_{\rm gr}, \quad (2)$$

where $Y_{\rm H_2S}$=1.2×10^{-3} molecules per incident photon is the photo-desorption yield of H_2S [6], $f_{s,\rm H_2S}$ is the fraction of desorption sites occupied by H_2S ice, G_0 is the Habing field ($G_0 = 1.7\chi_{\rm UV}$), F_0 is the flux of UV photons, and $\Phi_{\rm SP}$ is the rate of secondary photons produced by cosmic rays interacting with H_2 [9]. Rearranging:

$$x({\rm H_2S}) = \frac{(G_0 F_0\; e^{-1.8A_V} + \Phi_{\rm SP})\, Y_{\rm H_2S}\, f_{s,\rm H_2S}\, \sigma_{\rm H}}{G_0 R_{\rm H_2S}\; e^{-1.7A_V} + v_0\, n_{\rm H}(A_V)\, \sigma_{\rm H}} \quad (3)$$

In addition, we equate the sticking rate of S atoms to the desorption rate of H_2S to get the analytic expression for the fraction of sites covered by H_2S:

$$f_{S,H_2S} = \frac{n(S) v_0}{Y(G_0 F_0 e^{-1.8A_V} + \Phi_{\rm SP})} \quad (4)$$

Equations (3) and (4) determine the H_2S abundance for given values of A_v and n. Now, we discuss the general properties of the model before going into detail on the selected sources. When the visual magnitude increases, f_{S,H_2S} in Eq. (4) increases as well, reaching a saturation value. The abundance relative to water found in comets is of the order of 2% [2], thus we take the saturation value as $f_{S,H_2S,\rm max} = 0.02$. In the low visual magnitude and density regime, both gas-phase H_2S formation and destruction processes are proportional to G_0. As a consequence, the gas-phase H_2S abundance should reach an equal value, independently of G_0.

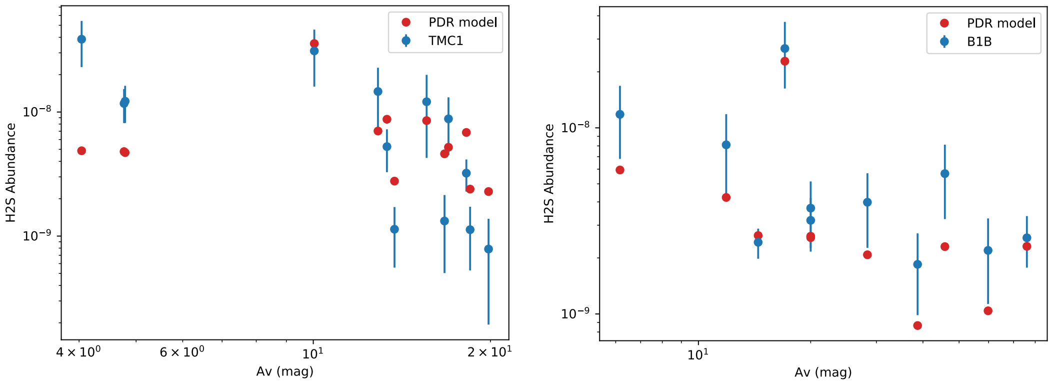

Figure 4: H_2S abundance (blue) and the model prediction (red) for TMC1 and Barnard 1, assuming a secondary photon flux of $\Phi_{SP} = 2 \times 10^4$ photons cm^{-2} s^{-1} and $\Phi_{SP} = 4 \times 10^4$ photons cm^{-2} s^{-1}, respectively.

Once saturation occurs, $X(H_2S)$ in Eq. (3) starts dropping due to the increasing density, and therefore depletion onto grains. In the shielded regime, the flux of secondary photons, Φ_{SP} and the gas density determine the H_2S abundance, Values of Φ_{SP} between 750 and a few 10^4 photon cm^{-2} s^{-1} have been reported in the literature [10][21]. We let Φ_{SP} to vary within this range.

6 Comparison with observations

In order to compare our model with the TMC 1 and Barnard 1b observations, the incident radiation field needs to be quantified. This is done using the parametric expression that relates dust temperature, visual magnitude, and Draine field reported by [14]. We obtain the best fit with incident UV field of $\chi_{UV} \sim 6.5$ for TMC 1 and $\chi_{UV} \sim 24$ for Barnard-1b, in units of the Draine field (see Fig. 3). We have introduced these numbers in equations (3) and (4) to fit the H_2S abundances and obtain a reasonable fitting of the observed H_2S abundances with $\Phi_{SP} = 2 \times 10^4$ photons cm^{-2} s^{-1} in TMC 1 and $\Phi_{SP} = 4 \times 10^4$ photons cm^{-2} s^{-1} in Barnard 1b (see Fig. 4). Within this scenario, the difference between the measured H_2S abundance between TMC 1 and Barnard 1b is due to a different cosmic ray ionization rate. A more detailed and complete chemical modeling of the two targets is required to confirm this hypothesis. First of all, we need to take into account the 3D physical structure of the cores in order to derive a precise H_2S abundance profile. Recent laboratory work suggests that chemical desorption might be important for H_2S [19]. To introduce chemical desorption in the model would allow to explain the H_2S abundance in the shielded cloud with a lower secondary photons flux. Our simple model considers adsorption and desorption processes but does not account for surface chemistry and thus neglects the influence that the grain temperature is expected to have in the H_2S formation rate. Moreover, although fast shocks are not occurring in these dense clouds, [3] suggests that sputtering by grain-grain collisions could be efficient to desorb molecules at low velocities, hence increasing the H_2S abundance.

7 Conclusions

Single-dish observations of two nearby dark clouds, TMC1 (140 pc) and Barnard 1 (235 pc) are used to investigate the chemistry of H_2S in starless cores. We have found that the H_2S abundance presents its maximum abundance at the cloud edge, X(H_2S) $\sim 1 - 3 \times 10^{-8}$ and decrease with density towards the visual extinction peaks. To explain this behavior we propose a simple chemical model which assumes that H_2S is formed on grain mantles, and released into gas via photodesorption. Even though this model is quite simple, we find a general agreement with the observations which supports that hydrogenation of S atoms on the grain surfaces is the main formation path for H_2S.

Acknowledgments

We thank the Spanish MINECO for funding support from AYA2016-75066-C2-1/2-P, and ERC under ERC-2013-SyG, G. A. 610256 NANOCOSMOS. JM acknowledges the support of ERC-2015-STG No. 679852 RADFEEDBACK. SPTM and JK acknowledges to the European Union's Horizon 2020 research and innovation program for funding support given under grant agreement No 639459 (PROMISE).

References

[1] M. Asplund, N. Grevesse, A.J. Sauval, P. Scott, Ann. Rev. Astron. Astrophys. 47, 481 (2009)

[2] D. Bockelée-Morvan, N. Biver, 2017 Phil. Trans. R. Soc. A 375: 20160252

[3] P. Caselli, T.W. Hartquist and O. Havnes, A&A 322, 296–301 (1997)

[4] M.L. Dubernet, F.Daniel, A. Grosjean and C.Y.Lin, A&A 497, 911–925 (2009)

[5] D. Foreman-Mackey, D. W. Hogg, D. Lang, J. Goodman, 2013 PASP 125, 306

[6] A. Fuente et al, 2017 ApJL 851 L49

[7] A. Fuente et al. arXiv:1809.04978 [astro-ph.GA]

[8] M. Gerin et al. A&A, 606 (2017) A35

[9] R. Gredel, S. Lepp and A. Dalgarno, ApJ 347:289-293, 1989

[10] T.W. Hartquist and D.A. Williams, 1990 MNRAS 247, 343

[11] J. Hatchell, J. S. Richer, G. A. Fuller et al. 2005, A&A, 440, 151

[12] J. Hatchell, G. A. Fuller, J. S. Richer, 2007, A&A, 472, 187

[13] E. C. Heiles , Astrophys. J. , 1968, vol. 151

[14] S. Hocuk, L. Szűcs, P. Caselli, S. Cazaux, M. Spaans and G. B. Esplugues, A&A 604, A58 (2017)

[15] D. Hollenbach, M. J. Kaufman , E. A. Bergin, and G. J. Melnick, ApJ 690 1497

[16] A. Jiménez-Escobar and G. M. Muñoz Caro, A&A 536, A91 (2011)

[17] J. Malinen et al. A&A, 544 (2012) A50

[18] T. J. Millar, E. Herbst, 1990, A&A, 231, 466

[19] Y. Oba, T. Tomaru, T. Lamberts, A. Kouchi and N. Watanabe, Nat. Astron. 2 (2018) 228

[20] T. Onishi, A. Mizuno, A. Kawamura, H. Ogawa & Y. Fukui, 1996, ApJ, 465,815

[21] C. J. Shen, J. M. Greenberg, W. A. Schutte and E. F. van Dishoeck, A&A 415, 203-215 (2004)

[22] L. V. Tóth, M. Haas, D. Lemke, K. Mattila and T. Onishi, A&A, 420 2 (2004) 533-546

[23] F.F.S. Van der Tak et al, 2007, A&A 468, 627-635

[24] V. Wakelam, P. Caselli, C. Ceccarelli, E. Herbst, & A. Castets, 2004a, A&A, 422, 159

Highlights on Spanish Astrophysics X, Proceedings of the XIII Scientific Meeting of the Spanish Astronomical Society held on July 16 – 20, 2018, in Salamanca, Spain. B. Montesinos, A. Asensio Ramos, F. Buitrago, R. Schödel, E. Villaver, S. Pérez-Hoyos, I. Ordóñez-Etxeberria (eds.), 2019

Star formation and ionized regions in the Inner Galactic Plane.

P. Palmeirim[1], A. Zavagno[2], and D. Elia[3]

[1] Instituto de Astrofísica e Ciências do Espaço, Universidade do Porto, CAUP, Rua das Estrelas, PT4150-762 Porto, Portugal
[2]Aix Marseille Univ, CNRS, LAM, Laboratoire d'Astrophysique de Marseille, Marseille, France
[3] Istituto di Astrofisica e Planetologia Spaziali INAF-IAPS, via Fosso del Cavaliere 100, I-00133 Roma, Italy

Abstract

We present a comprehensive statistical study to understand the impact of galactic bubble structures detected in the *Spitzer* observations throughout the galactic plane on the star formation process. We analysed 1 360 galactic bubbles and ∼70 000 star-forming sources, from both Hi-GAL and GLIMPSE surveys, located in their vicinity. The spatial distribution of the star-forming sources seen in surface density maps reveal a clear evolutionary gradient, were more evolved Young Stellar Objects (YSOs) are typically found in the center, while recent star-forming sources (prestellar and protostellar) can be seen at the edges of the bubbles.
Based on the dynamic ages derived for the bubbles and numerical simulations we find that the timescale for star-formation are better describe advocating for the pre-existence of density structures in the medium prior to the creation of the ionizing source(s).
Identical pattern of age distribution of star-forming sources has been found in a recent detailed study of the nearby λ Ori bubble using APOGEE-2 and GAIA DR2 observations, which provides compelling evidence of what we obtained in our statistical result. In light of these results we propose a scenario for the star formation process in expanding ionizing bubbles.

1 Introduction

Spitzer images at 8 μm and 24 μm reveal an almost ubiquitous presence of bubble structures throughout the entire Galactic Plane [4, 5]. These bubbles are associated to H II regions that are generated by massive stars that ionize the surrounding medium, causing it to expand isotropically. The expansion against the surrounding cold molecular medium may induce the triggering of star formation as shown in several observational studies [28, 29, 7, 21, 15].

This study aims to understand the relation between the presence of an H II region, its expansion and how star formation is progressing in its vicinity by combining information of Galactic Plane surveys in a large sample of Galactic bubbles.

2 Statistical Sample

We made use of the The Milky Way Project (MWP) catalog [22] of bubbles extracted from Spitzer-GLIMPSE 8 μm and 24 μm maps and selected 1 360 bubbles with radii larger than $72''$ to ensure that the bubbles were resolved in the *Herschel* maps. We searched for all star-forming sources that were found within four times the effective radius of a bubble.

The YSO candidates were selected from the GLIMPSE catalog by following the same approach as [10]. Subsequently, they were further classified into different evolutionary stages Class I and Class II according to both their infrared spectral index [13] and their position in the IRAC color-color diagram [2]. This led to a total sample of 10 694 Class I and 18 209 Class II sources. Class III YSOs were excluded due to the high level of contamination of asymptotic giant branch (AGB) stars in the Galactic Plane that harbour thin disks that can mimic the SED of class III YSOs [19].

To probe the most recent star formation activity we made use of the Hi-GAL source catalog [8] and found a total sample of 25 911 prestellar (gravitationally bound) and 14 918 protostellar (based on 70 μm detection) clumps at the vicinity of our sample of bubbles.

This lead to a final sample of $\sim$70 000 star-forming sources at different evolutionary stages located towards 1360 bubbles.

3 Results

3.1 Spatial distribution and evolutionary gradient of star-forming sources

The spatial information of all the star-forming sources located towards the 1 360 galactic bubbles was compiled into surface density maps (see Fig. 1). These maps are spatially normalized by the bubble radius and display the location of all star-forming source at a given evolutionary stage. The surface density maps reveal how star-forming sources follow a clear evolutionary trend, where more evolved star-forming objects are found spatially located near the center, while younger star-forming objects are found at the edge of the bubbles. Furthermore, considering all the star-forming sources we find $\sim$80% more star-forming objects per unit area toward the direction of bubbles compared with their surrounding outer fields.

3.2 Dynamic age estimates of the bubbles

Considering that the 1 360 bubbles are at different stages of their expansion we derived dynamic ages for a subsample of 182 HII regions, for which kinematic distances and radio continuum flux measurements were available, by following the approach presented in Tremblin et al. (2014)[23]. The analytical solutions and numerical simulations performed in their paper

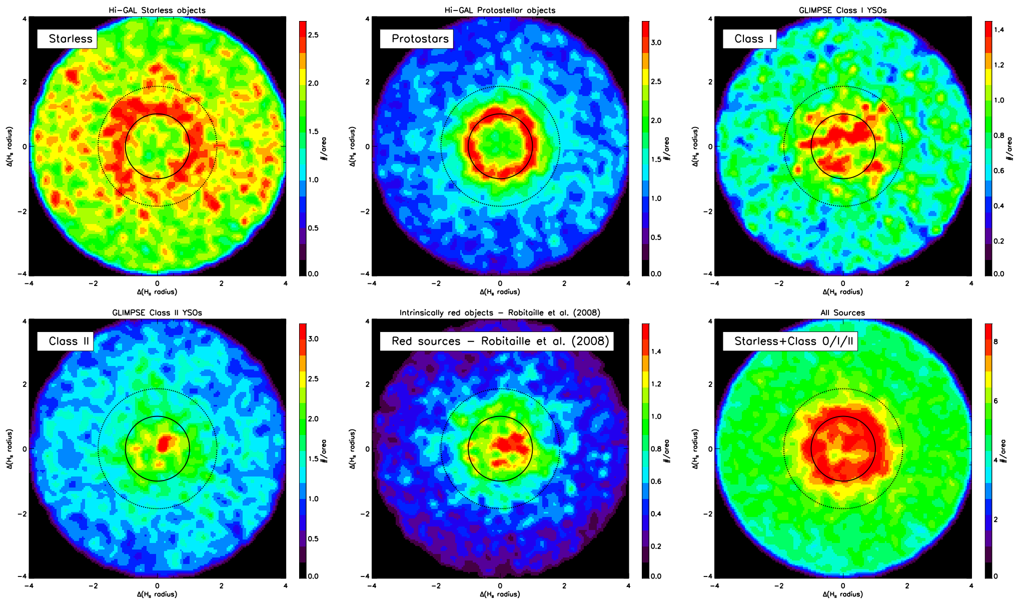

Figure 1: Surface density maps for all star-forming objects - Hi-GAL clumps, IRAC YSOs and intrinsically red sources from [19] - associated to the bubble sample. The spatial scale of the maps are normalized by the bubble radius (solid black circle). The dash black circle represents the average shell radius.

demonstrated that the expansion of H II regions is slowed down by turbulent ram pressure (P_{turb}) of the environment until it reaches quasi-static equilibrium with the pressure of the ionized gas (P_{II}). With the use of radio continuum flux measurements and by applying the Larson laws (see [14]) to infer P_{II} and P_{turb}, respectively, dynamic age estimates were obtained by comparing the results with the isochrones provided by the grid of 1D models of expanding H II regions. The derived dynamic ages are in good agreement with the photometric ages of the ionizing stars in well-known regions (e.g., Rosette, RCW 36, RCW 79, and M16)[23].

Following this approach we derived dynamic ages for the 182 bubbles with distance determination (obtain from the WISE catalog of Galactic H II regions [3]) and radio continuum flux measurements (1.4 GHz and 4.85 GHz from the NVSS [6] and PMNS [27], respectively). In Fig. 2a) we present a top view of the location of the 182 bubbles in the Galactic plane, with their respective dynamic ages and sizes. We find that the majority of the of the bubbles follow the Galactic spiral arms and have ages younger than 4 Myr ($\sim$80%), which can be related with the typical lifetime of high-mass stars (a main-sequence spectral type O5 star, for example, has an expected lifetime of $\sim$4 Myr [1].

3.3 Clump formation efficiency

To better comprehend the impact of H II regions on the star formation process we need to understand how efficient the conversion of cold neutral matter collected in their shells com-

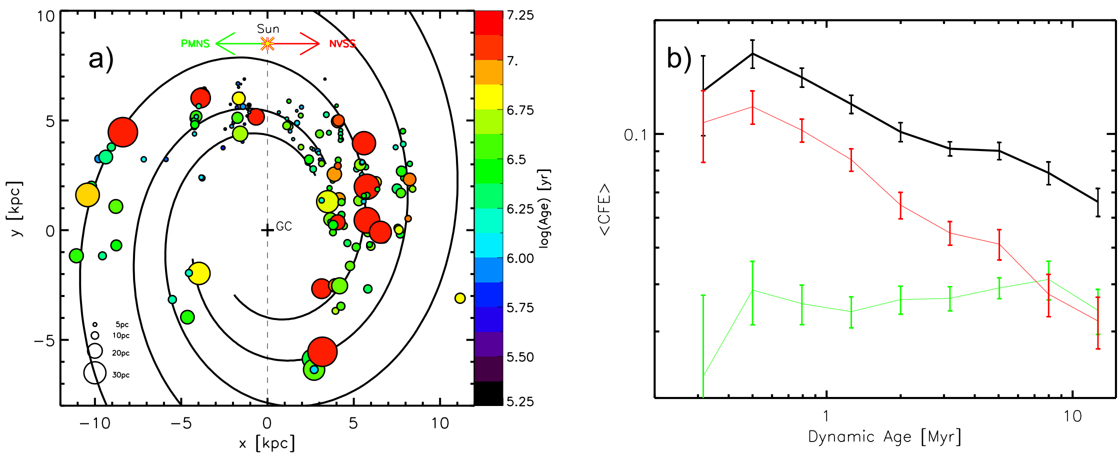

Figure 2: **a)** Bubble distribution in Galactocentric coordinates with their respective diameter and age. The black solid curves represent the position of the 4 Galactic spiral arms based on [20]. **b)** CFE of the Hi-GAL star-forming clumps as a function of the dynamic age of the bubbles (solid black), prestellar (solid green), and protostellar (solid red) sources.

pares with region that are not affected by feedback processes. The clump formation efficiency (CFE) was determined by calculating the ratio between the masses of the bubbles and the masses of the respective associated Hi-GAL sources (prestellar and protostellar clumps). We obtained a CFE ∼15% for the Hi-GAL star-forming sources, which means that typically ∼15% of the molecular gas around the bubbles are concentrated in the form of prestellar or protostellar clumps. This value is a factor of ∼2 higher than the CFE estimated outside the bubbles and compared with other well-known active star-forming regions (e.g., RCW106[17] and W43[16]).

In Fig. 2b) we can see how the CFE varies with the evolution of the bubbles. Interestingly, we find that CFE for protostellar clumps tends to decrease with the age of the bubble, while CFE of prestellar clumps seems to remain nearly constant. We interpret this trend as a possible increase in the formation rate from the prestellar to protostellar phase at the early stages of the bubble expansion, which would eventually decrease as the impact of the expansion and the ionization weakens.

4 Conclusions

The evolutionary gradient seen in the spatial distribution of star-forming sources sets strong constrains in the star formation mechanisms around ionizing sources. A large number of the Class II YSOs are found in the inner parts of bubbles that have younger dynamic ages than the typical lifetime of low- and intermediate-mass Class II objects $\sim 2 \pm 1$ Myr [9]. This suggests that these YSOs have probably undergone their formation process prior to the expansion of the bubble, possibly as part of the same star-forming complex that gave birth to the ionizing massive stars that are responsible for the expansion of the bubbles. This is consistent with the fact that in cluster-forming environments, massive stars are expected to form after low-mass stars have completed their accretion phase [12]. Furthermore, the shell fragmentation times estimated (following [26]) to understand if gravitational instability of the shells alone could be responsible for the triggering showed that a significant fraction of bubble shells would in fact not have had time to fragment. Thus, we advocate that dense structures existed in the medium prior to the bubble expansion to allow for a more comparable star-formation timescale, as shown in the simulations performed in [24, 25]. Furthermore, the fraction of clumps that is spatially associated with bubbles is ~23%, consistent with the fraction of ATLASGAL clumps in the vicinity of MWP bubbles (Kendrew et al. 2016). However, for the individual fraction of protostellar clumps we obtain 41%. Thus, we argue that the higher fraction of protostellar clumps may be related with the higher protostellar clump formation rate in bubbles, as discussed in Sect. 3.3.

A recent study [11] combining APOGEE-2 and GAIA observations of the λ Ori bubble located in the nearby Orion molecular cloud complex revealed, with a very high detail, how older YSOs are clustered in the center of the bubble while younger at scattered around the center. In particular, the YSOs are moving radially away from the center with the further away sources moving faster. This result is in completely consistent with what we found in our statistical analysis and interpretation of our galactic bubbles sample, which could indeed describe a more universal process of formation and evolution of star formation in ionizing bubbles.

Based on the results from Palmeirim et al. (2017)[18] here summarized, we propose a scenario for the process of star formation in ionizing expanding bubbles. 1) Formation of low- and intermediate-mass stars is undergoing prior to the formation of the massive ionizing star(s); 2) As the medium is expanding due to the ionizing pressure more evolved star-forming sources which are denser are less influenced than the more diffused cold neutral matter; 3) the cold molecular matter is accumulate in the shell of the bubbles and fragments into stars via gravitational instabilities as the bubble expands.

Acknowledgments

Pedro Palmeirim acknowledges support from the Fundação para a Ciência e a Tecnologia of Portugal (FCT) through national funds (UID/FIS/04434/2013) and by FEDER through COMPETE2020 (POCI-01-0145-FEDER-007672) and also by the fellowship SFRH/BPD/110176/2015 funded by FCT (Portugal) and POPH/FSE (EC).

References

[1] Allen, C. W. 1973, Astrophysical quantities

[2] Allen, L. E., Calvet, N., D'Alessio, P., et al. 2004, ApJS, 154, 363

[3] Anderson, L. D., Bania, T. M., Balser, D. S., et al. 2014, VizieR Online Data Catalog, 221

[4] Churchwell, E., Povich, M. S., Allen, D., et al. 2006, ApJ, 649, 759

[5] Churchwell, E., Watson, D. F., Povich, M. S., et al. 2007, ApJ, 670, 428

[6] Condon, J. J., Cotton, W. D., Greisen, E. W., et al. 1998, AJ, 115, 1693

[7] Deharveng, L., Schuller, F., Anderson, L. D., et al. 2010, A&A, 523, A6

[8] Elia, D., Molinari, S., Schisano, E., et al., 2017, MNRAS, 471, 100

[9] Evans, II, N. J., Dunham, M. M., Jørgensen, J. K., et al. 2009, ApJS, 181, 321

[10] Gutermuth, R. A., Megeath, S. T., Myers, P. C., et al. 2009, ApJS, 184, 18

[11] Kounkel, M., Covey, K., Suárez, G., et al. 2018, AJ, 156, 84

[12] Kumar, M. S. N., Keto, E., & Clerkin, E. 2006, A&A, 449, 1033

[13] Lada, C. J., Muench, A. A., Luhman, K. L., et al. 2006, AJ, 131, 1574

[14] Larson, R. B. 1981, MNRAS, 194, 809

[15] Liu, H.-L., Li, J.-Z., Wu, Y., et al. 2016, ApJ, 818, 95

[16] Nguyen Luong, Q., Motte, F., Schuller, F., et al. 2011, A&A, 529, A41

[17] Nguyen, H., Nguyen-Luong, Q., Martin, P. G., et al. 2015, ApJ, 812, 7

[18] Palmeirim, P., Zavagno, A., Elia, D. et al. 2017, A&A, 605, A35

[19] Robitaille, T. P., Meade, M. R., Babler, B. L., et al. 2008, AJ, 136, 2413

[20] Russeil, D. 2003, A&A, 397, 133

[21] Samal, M. R., Zavagno, A., Deharveng, L., et al. 2014, A&A, 566, A122

[22] Simpson, R. J., Povich, M. S., Kendrew, S., et al. 2012, MNRAS, 424, 2442

[23] Tremblin, P., Anderson, L. D., Didelon, P., et al. 2014, A&A, 568, A4

[24] Walch, S., Whitworth, A. P., & Girichidis, P. 2012, MNRAS, 419, 760

[25] Walch, S., Whitworth, A. P., Bisbas, T. G., Hubber, D. A., & Wünsch, R. 2015, MNRAS, 452, 2794

[26] Whitworth, A. P., Bhattal, A. S., Chapman, S. J., Disney, M. J., & Turner, J. A. 1994, MNRAS, 268, 291

[27] Wright, A. E., Griffith, M. R., Burke, B. F., & Ekers, R. D. 1994, ApJS, 91, 111

[28] Zavagno, A., Pomarès, M., Deharveng, L., et al. 2007, A&A, 472, 835

[29] Zavagno, A., Russeil, D., Motte, F., et al. 2010, A&A, 518, L81

Highlights on Spanish Astrophysics X, Proceedings of the XIII Scientific Meeting of the Spanish Astronomical Society held on July 16 – 20, 2018, in Salamanca, Spain. B. Montesinos, A. Asensio Ramos, F. Buitrago, R. Schödel, E. Villaver, S. Pérez-Hoyos, I. Ordóñez-Etxeberria (eds.), 2019

Kinematic structure in the Solar Neighbourhood and surroundings with *Gaia*: a vast richness to explore.

P. Ramos, T. Antoja, and F. Figueras

Dept. FQA, Institut de Ciències del Cosmos (ICCUB), Universitat de Barcelona (IEEC-UB), Martí Franquès 1, E08028 Barcelona, Spain

Abstract

Following from the recent second data release of the *Gaia* mission, we used the ~5 million stars with high-quality six-dimensional phase-space information in the catalogue to explore the kinematic substructure of different Galactic neighbourhoods, including our own. As a result, we obtain a precise characterisation of these structures in the solar neighbourhood and their evolution with Galactocentric distance. Some are seen to have nearly constant kinetic energy at a given volume (e.g. Sirius), while others evolve keeping their vertical angular momentum nearly unchanged (e.g. Hercules). This information yields valuable insight about their respective origins and thus on the dynamics of the Milky Way.

1 Introduction

One of the major goals of Galactic dynamics is to obtain a self-consistent model of the Milky Way (MW) that reproduces to high accuracy the distribution of observed stars both in position and velocity. This task, however, has proven to be utterly complex, in part due to the lack of information of our own galaxy and on the phase-space distribution. Now, with the *Gaia* mission [9], we have access to a wealth of data never seen before which opens new horizons for our understanding of the Milky Way.

In the past, some of the works in this field explored the phase-space by looking at the velocity distribution of stars in the solar neighbourhood (SN). Then, they tried to recreated the different kinematic structures it contains, like the moving groups (MG), by modelling the MW with a bar, spiral arms, or other non-axisymmetric components (see [1] and references therein). Nonetheless, the large degree of degeneracy between models at the SN demands a deeper exploration of phase-space by extending the study of the velocity plane to other Galactic neighbourhoods. This has only been possible just recently, being [2] the first to do so, followed by other authors (e.g., [20, 13]) that worked with increasingly better data.

The recent publication of the *Gaia* second data release (DR2) [8] entails an order of magnitude improvement over past surveys, both in quantity and quality. In this work, we present the results of using ~5 millions stars with full 6D information to study the changes in the velocity distribution with Galactocentric radius and azimuth by means of the wavelet transformation (WT).

This talk is organised as follows. In Section 2, we summarise the main properties of the sample and outline the methods used for its exploitation. Then, in Section 3 we characterise the structures found at the SN to, afterwards, follow their evolution with Galactocentric distance and azimuth in Section 4. Finally, Section 5 contains a short discussion and the conclusions.

2 Methodology

The study of phase-space requires full 6D data, three coordinates for position and three for velocity. Therefore, from the whole *Gaia* DR2 catalogue, we selected those stars with parallax, proper motion and radial velocity. Furthermore, in order to use the inverse of the parallax as distance, we restricted ourselves to stars with small relative error ($\varpi/\sigma_\varpi \geq 5$) which mitigates the bias [5]. The sample we are left with is composed of 5,136,533 stars.

We used the Galactocentric cylindrical coordinates with the following constants: Sun at (R, ϕ, Z)=(8.34 kpc, 0°, 14 pc) [17, 6], peculiar velocity of the Sun of ($U_\odot$, $V_\odot$, $W_\odot$) = (11.1, 12.24, 7.25) $\mathrm{km\,s^{-1}}$ [18], and circular velocity for the Local Standard of Rest (LSR) of 240 $\mathrm{km\,s^{-1}}$ [17]. Consequently, we studied the velocity distributions in the Galactic plane ($|Z| < 500$ pc) with the variables $\dot{R} = V_R$ and $R\dot{\phi} = V_\phi$. We presented the density map of the sample in Fig. 1 of [16] along with the spatial distribution of the sub-samples used for the kinematic exploration. Each of these volumes is a portion of a cylinder with a width of 200 pc in Galactocentric radius and 3 degrees in azimuth, layout along the Sun-Galactic centre (GC) line from 6.04 kpc to 11.04 kpc every 100 pc.

Each volume in the sample is then decomposed into layers of different spatial frequencies (or sizes) using the WT. In particular, the *à trous* algorithm [19], which preserves the size of the original 2D image, in our case the histogram of the velocity plane, at each layer (or scale). At every pixel of each scale, the wavelet coefficient measures the degree of overdensity (positive coefficient) or underdensity (negative coefficient) compared to its 2^j closest neighbours, with j=0,1,..,J being the scale. In this sense, the WT highlights the structures of sizes between roughly $\Delta 2^j$ and $\Delta 2^{j+1}$, where Δ is the size of the pixels in the underlying histogram (for this work, 0.5 $\mathrm{km\,s^{-1}pixel^{-1}}$). Here, we focused on structures with sizes ~4-8 $\mathrm{km\,s^{-1}}$ (j=3) and ~8-16 $\mathrm{km\,s^{-1}}$ (j=4).

After calculating the wavelet coefficients, we performed a peak search and detected the local maxima which signals the location of different structures within the velocity distribution. Since these peaks are found in the wavelet space, we then performed an statistical evaluation of their significance with two indicators: Poisson noise, measured with the level of confidence at which the structure is likely to be real (C.L.= {0,1,2,3}), and Bootstrap noise, which measures the probability of having observed the peak in the data ($P_{BS} \in [0, 1]$). We say a

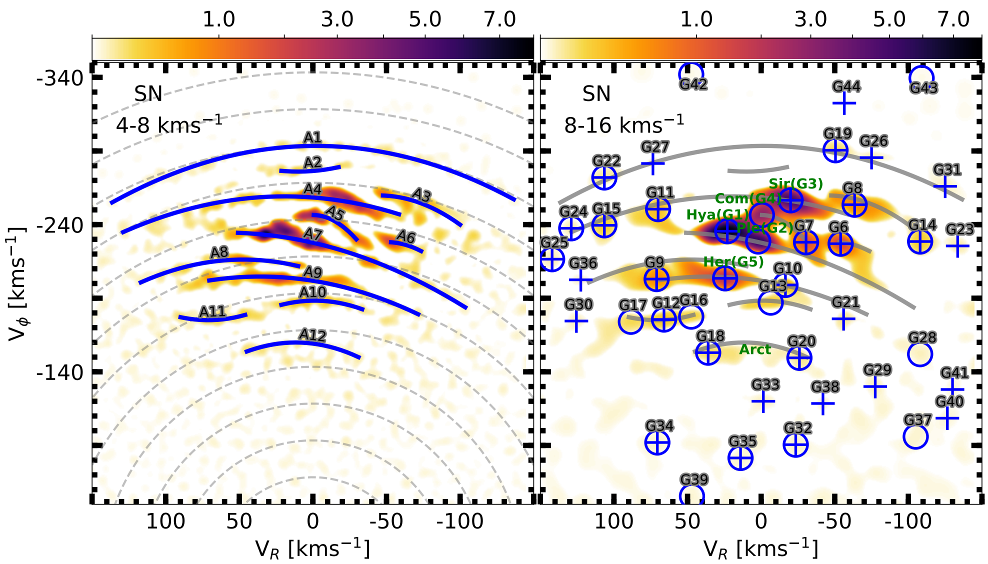

Figure 1: Wavelet coefficients of the velocity distribution at the SN. The structures found are shown for two different scales: arches at 4-8 km s^{-1} (left) and peaks at 8-16 km s^{-1} (right). For the former, dashed grey lines represent constant kinetic energy tracks. Circles on the right plot correspond to peaks that are significant according to Poisson noise (C.L.$\geq$2), while crosses correspond to those significant with respect to Bootstraps ($P_{BS} \geq 0.8$). Also, the arches found on the left panel are shown on the right panel as grey lines.

structure is significant if C.L.$\geq$2 or $P_{BS} \geq$0.8. For more details, see [16].

3 Solar neighbourhood

Figure 1 shows the result of applying the methodology described in the previous section to the sub-sample centred at the Sun's position (R$\in$[8.24, 8.44] kpc, $\phi \in$[-1.5,1.5] degrees). In particular, the wavelet scales corresponding to 4-8 km s^{-1} and 8-16 km s^{-1}. At the lower wavelet scale (left panel), we see that the coefficients are arranged in rather elongated structures and thus we chained the significant peaks found into arches (A1 to A12). The existence of such features in the velocity plane was already predicted based on alternative surveys by other authors (e.g., [1, 13]), yet with *Gaia* DR2 these can be seen simply by visual inspection of the histogram [11]. In fact, the prominent arch 1, which crosses the whole plane, was discovered for the first time in with this data [11]. [14, 12] showed that a disk out of equilibrium (e.g., by the close passage of a satellite galaxy) develops arch-like features of constant radial frequency due to phase mixing. Since the radial frequency mostly depends on the orbital energy [7], we plotted on the left panel of Fig.1 tracks of constant kinetic energy as dashed grey lines. In turn, this allows us to explain features such as A1 and A10. Other arches, like A4 (referred to as Sirius MG in the literature) can also be related to this dynamical mechanism knowing that the presence of a bar can cause some structures to deviate from symmetry [4].

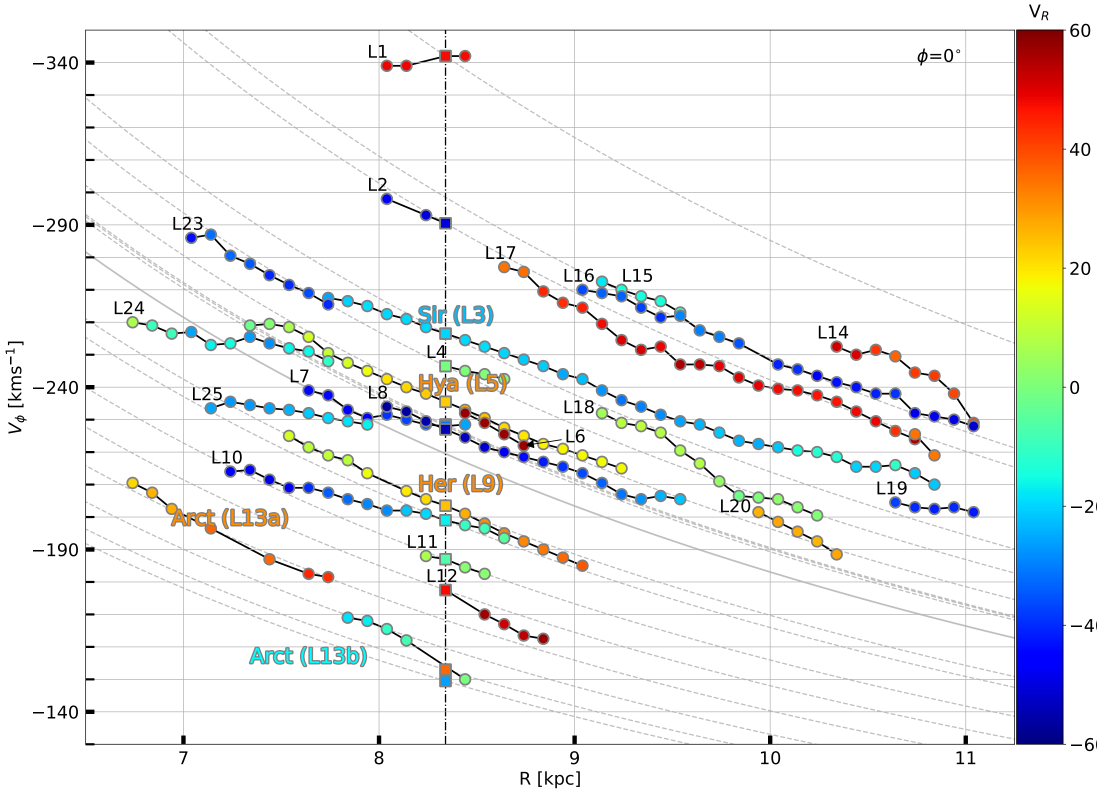

Figure 2: Evolution of the azimuthal velocity of the peaks with Galactocentric distance. The colour corresponds to the radial velocity, while the dashed grey lines are tracks of constant angular momentum. The dotted dashed line marks the position of the Sun. The names of relevant structures have been added for reference.

At the larger wavelet scale (8-16 km s^{-1}, right panel of Fig.1), the structures appear like rounded groups identified with circles (C.L.≥2) and/or crosses ($P_{BS} \geq 0.8$). The well-known structures from the literature (Table C.1 from [16]) are all among the most prominent peaks in the sample. Still, we found ∼30 new candidates to MG. Whereas some have few stars and are significant solely due to their isolation, most are in fact produced by an elongated structure. When plotting the arches in the left panel on the right panel, we can see that some of the MGs are related to those features, such as Hercules (G5), G9 and G10 sitting on top of A9. Similarly, G16 (Bobylev16-22 and Arifyanto05, see [16] for more details) is related to G12 and G17, or G18 and G20 to the MG known as Arcturus.

4 Other Galactic neighbourhoods

After having analysed the SN, we performed an exhaustive search of peaks in the wavelet layer j=4 at all the Galactic neighbourhoods in the Sun-GC line, from 6.04 kpc to 11.04 kpc. As a result, we obtained a table with the velocity coordinates (V_R - V_ϕ) of each significant overdensity in kinematic space and the corresponding Galactocentric distance (R) of the volume it was found in (see [16] for more figures and animations). After clustering together by eye the peaks according to their trend in R vs V_ϕ plane, and also taking into account V_R, we obtained a set of lines which are presented in Fig. 2. We observe that different structures follow distinct slopes but, on average, all of them fall at a rate of $\sim$23 $\mathrm{km\,s^{-1}kpc^{-1}}$, consistent with previous estimates [15].

Some structures, like Hercules (line 9), are most likely produced by a resonance. Such structures should evolve keeping the angular momentum roughly constant with radius, for small epicyclic amplitudes and to first order approximation [15]. Therefore, we plotted tracks of constant vertical angular momentum, L_z (dashed grey lines in Fig. 2). As a result, we noted how the Hercules and Hyades lines follow this trend quite closely, whereas Sirius does not. By taking the mean L_z of lines L5 and L9, we estimated the pattern speed of the bar using the Eq. 6 from [15], which yields $\Omega_b \sim 54\ \mathrm{km\,s^{-1}kpc^{-1}}$. This estimate is consistent with previous values [3, 15] and would correspond to a fast bar.

We also observe some lines that do not cross the SN, meaning that extra-solar MGs exist in other Galactic neighbourhoods. It is not the case of L14 to L17, which are the continuation of L2 and are related to the aforementioned arch 1 (A1, see Fig. 1).

5 Discussion and conclusions

With the study of the 6D *Gaia* DR2 data using the WT we have clearly seen that the classic MGs are part of elongated features, or arches, and have a continuity outside the SN. Some of the structures present a roughly constant energy at a given volume and are probably related with the phase-mixing mechanism, while others evolve with radius at a nearly constant angular momentum, which is to be expected in resonances. As a result, with this new and unprecedentedly accurate data we can now classify each structure and study their dynamical origin in detail. In particular, the characteristics and evolution of the Hercules MG is consistent with the outer Lindblad resonance (OLR) 2:1 models, in which case its pattern speed is $\sim 54\ \mathrm{km\,s^{-1}kpc^{-1}}$. Nonetheless, some of the arches observed in the SN above Sirius MG could be caused by the 4:1 OLR of a slow bar [10].

Future data releases will improve the quality and spatial extension of the data, allowing to further explore the kinematic substructure of our Galactic disk. Nonetheless, with this work we have shown that it is already possible to explore as never before both numerical and theoretical models and, thus, gain new insights into the dynamics of the MW.

Acknowledgments

This work has made use of data from the European Space Agency (ESA) mission Gaia, processed by the Gaia Data Processing and Analysis Consortium (DPAC). Funding for the DPAC has been provided by national institutions, in particular the institutions participating in the Gaia Multilateral Agreement. This project has received funding from the University of Barcelona's official doctoral program for the development of a R+D+i project under the APIF grant and from the European Union's Horizon 2020 research and innovation programme under the Marie Skłodowska-Curie grant agreement No. 745617. This work was supported by the MINECO (Spanish Ministry of Economy) through grants ESP2016-80079-C2-1-R (MINECO/FEDER, UE) and ESP2014-55996- C2-1-R (MINECO/FEDER, UE) and MDM-2014-0369 of ICCUB (Unidad de Excelencia 'María de Maeztu').

References

[1] Antoja, T., Figueras, F., Fernández, D., & Torra, J. 2008, A&A, 490, 135

[2] Antoja, T., Helmi, A., Bienayme, O., et al. 2012, MNRAS, 426, L1

[3] Antoja, T., Helmi, A., Dehnen, W., et al. 2014, A&A, 563, A60

[4] Antoja, T., Valenzuela, O., Pichardo, B., et al. 2009, ApJ, 700, L78

[5] Bailer-Jones, C. A. L. 2015, PASP, 127, 994

[6] Binney, J., Gerhard, O., & Spergel, D. 1997, MNRAS, 288, 365

[7] Dehnen, W. 1999, AJ, 118, 1190

[8] Gaia Collaboration, Brown, A. G. A., Vallenari, A., et al. 2018a, A&A, 616, A1

[9] Gaia Collaboration, Prusti, T., de Bruijne, J. H. J., et al. 2016b, A&A, 595, A1

[10] Hunt, J. A. S. & Bovy, J. 2018, MNRAS477, 3945

[11] Katz, D., Sartoretti, P., Cropper, M., et al. 2018, ArXiv e-prints, arXiv:1804.09372

[12] Gómez, F. A., Minchev, I., Villalobos, Á., O'Shea, B. W., & Williams, M. E. K. 2012, MNRAS, 419, 2163

[13] Kushniruk, I., Schirmer, T., & Bensby, T. 2017, A&A, 608, A73

[14] Minchev, I., Quillen, A. C., Williams, M., et al. 2009, MNRAS, 396, L56

[15] Quillen, A. C., De Silva, G., Sharma, S., et al. 2018, MNRAS

[16] Ramos, P., Antoja, T., Figueras, F., 2018, ArXiv e-prints, arXiv:1805.09790

[17] Reid, M. J., Menten, K. M., Brunthaler, A., et al. 2014, ApJ, 783, 130

[18] Schönrich, R., Binney, J., & Dehnen, W. 2010, MNRAS, 403, 1829

[19] Starck, J.-L. & Murtagh, F. 2002, Astronomical image and data analysis, ed. Starck, J.-L. and Murtagh, F. (Springer)

[20] Xia, Q., Liu, C., Xu, Y., et al. 2015, MNRAS, 447, 2367

Highlights on Spanish Astrophysics X, Proceedings of the XIII Scientific Meeting of the Spanish Astronomical Society held on July 16 – 20, 2018, in Salamanca, Spain. B. Montesinos, A. Asensio Ramos, F. Buitrago, R. Schödel, E. Villaver, S. Pérez-Hoyos, I. Ordóñez-Etxeberria (eds.), 2019

The complexity and richness of the Galactic disc velocity field unveiled by Gaia DR2.

Romero-Gómez, M.[1], Antoja, T.[1], Figueras, F.[1], Mateu, C.[2], Aguilar, L.A.[3] Castro-Ginard, A.[1], Carrasco, J.M.[1], and Masana, E.[1]

[1] Institut de Ciències del Cosmos, Universitat de Barcelona (IEEC-UB), Martí i Franquès 1, E-08028 Barcelona, Spain
[2] Departamento de Astronomía, Instituto de Física, Universidad de la República, Iguá 4225, CP 11400 Montevideo, Uruguay
[3] Instituto de Astronomía, Universidad Nacional Autonóma de México, Apdo. Postal 877, Ensenada, 22800 Baja California, Mexico

Abstract

In this talk, we summarise the main results from the Gaia data release (GDR2) science demonstration paper on the Milky Way disc kinematics. GDR2 provides the largest existing full 6D phase-space coordinates catalogue. We benefit for the first time from a sample of 4.9 million stars with full 6-D phase-space coordinates, precise parallaxes (with a relative error less than 20%) and precise Galactic cylindrical velocities (median uncertainties of 0.9-1.4 km/s and 36% of the stars with uncertainties smaller than 1 km/s on all 3 components). The 2.4 million giant stars from this sample map the velocity field of the galactic disc from about 5 to 13 kpc from the galactic centre. We also study the distribution of 0.3 million solar neighbourhood stars (r < 200 pc), with impressive median velocity uncertainties of 0.4 km/s. The maps show the complexity and richness of the velocity field of the galactic disc

1 Introduction

Gaia Data Release 2 was published in April 2018 providing the five-parametric astrometric solution for 1.3 billion sources up to magnitude G $\sim$ 21 mag (positions, parallaxes and proper motions). For a subset of 7.2 million sources brighter than $G_{RVS} = 12$ mag and with effective temperature in the range $\sim [3550, 6900]$ K, it also provides line-of-sight velocities. This allows for the first time to study kinematic maps for a large amount of stars that extend well beyond the immediate vicinity of the Sun. The precision of the line-of-sight velocities are at the $\mathrm{km\,s^{-1}}$level being, at the bright end, of the order of 0.2 $\mathrm{km\,s^{-1}}$and, at the faint end, of the order of 1.4 $\mathrm{km\,s^{-1}}$(for $\mathrm{T}_{eff} = 5000$ K) and of the order of 3.7 $\mathrm{km\,s^{-1}}$(for $\mathrm{T}_{eff} = 6500$ K).

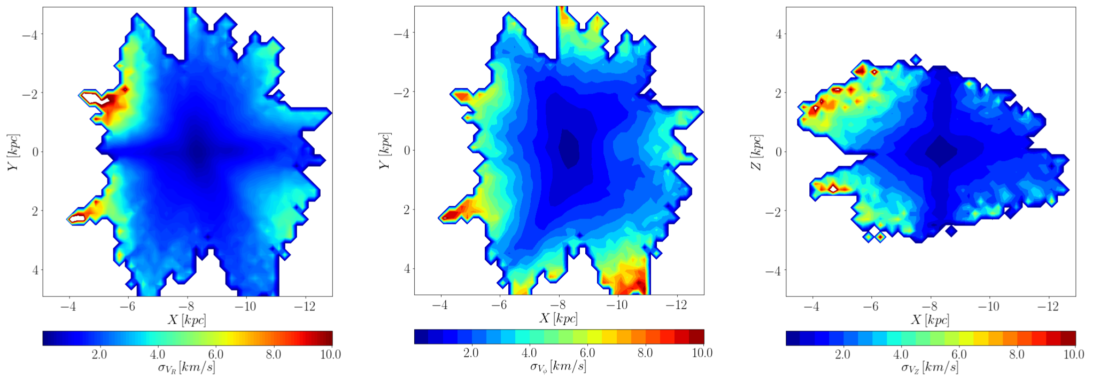

Figure 1: Median uncertainties in V_R, V_ϕ and V_Z (form left to right) for the giant sample. Note that for the uncertainties in V_R and V_ϕ, we use the (X,Y) galactocentric cartesian projection, while for the V_Z, we use the (X,Z) plane projection.

2 Mapping the Milky Way disc kinematics

Out of the 7.2 million sources with line-of-sight velocities, we select those with relative error in parallax smaller than 20 % and galactocentric cylindric distance between $5 < R < 13$ kpc, up to magnitude $G < 13$. This reduces the sample to 6.4 high quality sources, and we refer to it as the Main sample. From the Main sample, we select the giant stars by using a de-reddened HR diagram using 2MASS photometry (see [5] for details). We select the giants by requiring that the absolute magnitude in G band $M_G < 3.9$ and intrinsic colour $(G_{BP} - G_{RP})_0$ >0.95. The Giants sample contains ~ 3.1 million sources.

The kinematic maps shown below are represented in galactocentric cylindric coordinates, whose errors are obtained using the full covariance matrix and the inverse of the parallax as the distance estimator.

Figure 1 shows the median uncertainties in the radial, tangential and vertical directions for the giant sample in the (X,Y) projection (with $|Z| < 200\ pc$) for the radial and tangential components and in the (X,Z) projection (with $|Y| < 200\ pc$) for the vertical component. The median uncertainties are $(\epsilon_{V_R}, \epsilon_{V_phi}, \epsilon_{V_Z}) = (1.4, 1.4, 0.9)$ km s^{-1} and about 20% of the giant stars have all velocity components with a median uncertainty smaller than 1 km s^{-1}.

The high quality of the giants sample allows to compute kinematic maps in different cuts in Z, to make 3-dimensional views of the motion of the stars in a large sphere. In the top panels of Fig. 2 we show the face-on views of the kinematics in the mid plane $[-200, 200]$ pc. To make a comparison of what we should expect from an axisymmetric distribution in equilibrium, we show the same projection for an ensemble of test particles relaxed in an axisymmetric disc [7]. Note the large streaming motion in both velocity components, some of them already known (see [5] for details) and some new features, which depart from the equilibrium and axisymmetric conditions.

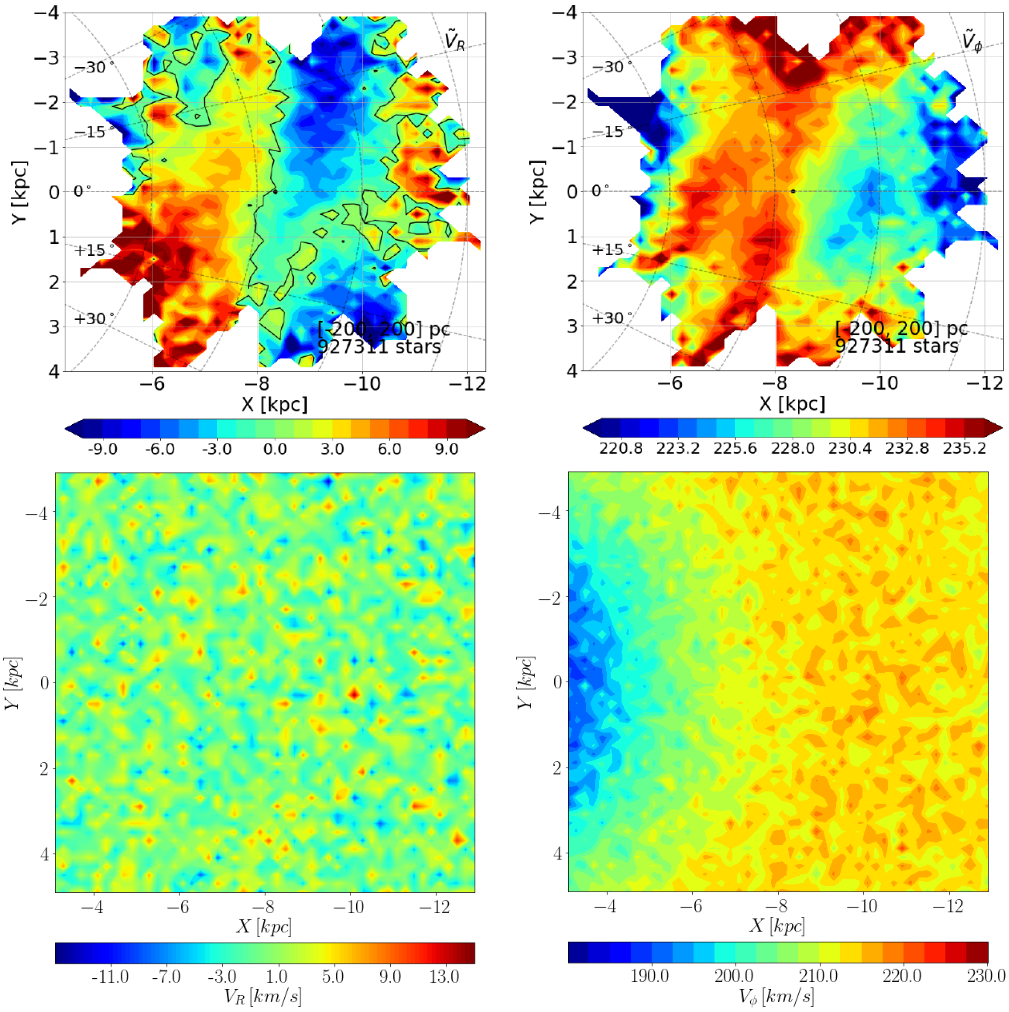

Figure 2: Face-on views of the kinematics in the mid plane $[-200, 200]$ pc, medians in radial and tangential velocities (left and right panels, respectively). Top row: for the giant sample. Bottom row: for an axisymmetric disc in equilibrium.

3 The Galactic warp signature using disc kinematics

In this section we focus on the vertical component and its applications to characterise the Galactic warp of the Milky Way. We use a different sample from that in Sect. 2. We develop the methods to study the warp in such a way they work as much as possible in the observable space, so, we only need the proper motions: μ_l^* and μ_b in the galactic longitude and latitude directions, respectively. Therefore, we select sources from the Gaia Data Release 2 with full 5-astrometric solution. From the 1.3 billion sources, we select stars with parallaxes up to magnitude G$\sim$ 20 and with absolute value of the relative error in parallax smaller than 50%. For these stars, we compute bayesian distances, d, with an exponentially decreasing space density prior with scale-length $L = 2$ kpc (see Romero-Gomez et al (2018, in preparation) for details). We then remove the cool main sequence stars by applying the cut: $M'_G < 1.95{*}(G_{BP} - G_{RP}){+}2.$, following the extinction line, where M'_G is the absolute G magnitude of the star uncorrected for extinction; M'_G is given by $M'_G = G - 5\log 10(d) + 5$; and $(G_{BP} - G_{RP})$ is the observed colour. We compute the absorption in V using Drimmel extinction model [3], and a fit to obtain the absorption in the G band and the colour excess (Carrasco, private communication). From the de-reddened HR diagram, we select two intrinsically bright populations with different ages: an OB-type sample if young stars: $M_G < 2.$ and $(G_{BP} - G_{RP})_0 < 0$; an the Red Giant Branch (RGB): $M_G < 3.9$ and $(G_{BP} - G_{RP})_0 > 0.95$.

The two methods developed in the research group are the LonKin method and the nGC3 PCM method. The former relies on selecting stars in cylindrical radial rings and plotting the median proper motion in latitude, with respect to the Local Standard of Rest, as a funcion of the galactic longitude. If the Galactic disc is flat, the median $\mu_{b,LSR}$ should be constant and equal to zero, but if it is warped, a particular variation will be introduced as a function of l. If the disc is symmetrically warped and the line-of-nodes is aligned with the Sun-Galactic Centre line, the LonKin method predicts a maximum in $\mu_{b,LSR}$ in the anticentre direction. The nGC3 method of the family of Great Circle Cell Counts (hereafter, GC3) methods [4, 6] searches for overdensities in great circle cells in the sky, by sweeping over the sky counting how many stars have position and velocities (nGC3 does not require line-of-sight velocities) lying in a great circle within a given tolerance, each great circle being defined uniquely by its normal vector or *pole*. The all-sky sweep over all possible great circle cells results in a Pole Count Map (hereafter, PCM). If the Galactic disc were flat, the peak in stellar density would be located in the North Galactic Pole of the PCM. If the disc is not flat, the peak of over-density moves in the PCM providing information on the amplitude and tilt angle of the warp, as well as the azimuth (twist) of the line-of-nodes as a function of radii (see [1] for detailed examples).

In Fig. 3, we show the result of applying the LonKin method to the OB (left) and RGB samples (right). We use a different color for each radial ring. Note that, the larger the radius, the larger the value of $\mu_{b,LSR}$, as expected. Note as well, that the trend is not smooth and that the $\mu_{b,LSR}$ does not peak in the anticentre direction, indicating that the Galactic warp is not symmetric. We also note a clear difference between the two populations. The amplitude of the warp is larger in the RGB sample, than in the OB, and we also detect that the warp onset radius is slightly larger for the OB than for the RGB, in agreement with

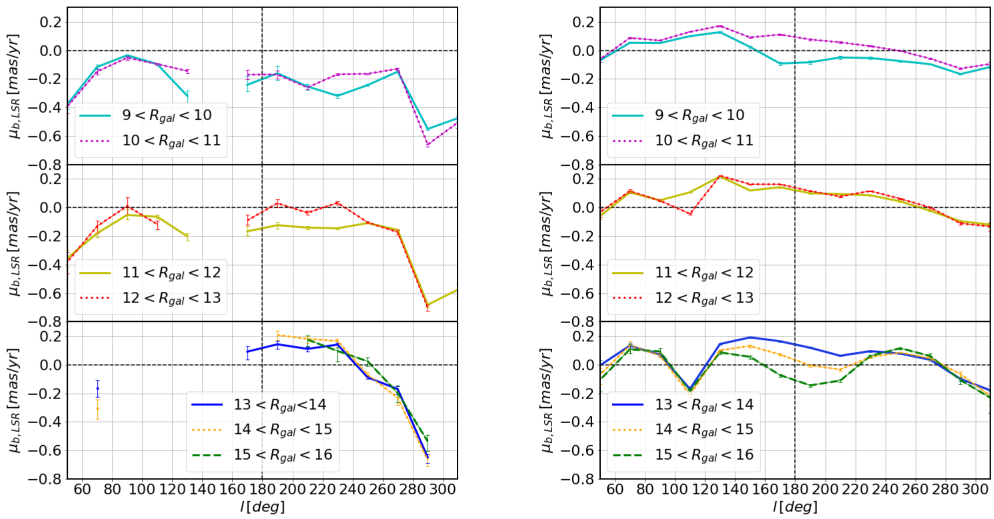

Figure 3: LonKin method applied to the OB and RGB samples (left and right panels, respectively). From top to bottom, different radial cylindrical galactocentric rings specified in the legend. Only bins in longitude with at least 300 stars are plotted. Horizontal dashed line shows the zero-axis while the vertical dashed line shows the anticenter direction at 180 deg, the error bars show the lower and upper 1σ uncertainty.

previous studies that estimate that the starting radius of the warp is anti-correlated with the age of the population [2].

In Fig. 4, we show the results of applying the nGC3 method to both samples (OB, top and RGB, bottom). We show the PCM per radial shell in each column, moving outwards from left to right. We observe how as a function of radius, a secondary peak appears detached from the one in the North Galactic Pole (corresponding to stars in the flat disc), indicating that, again, the Galactic warp is not symmetric. We also see that the secondary peak appears at a different radial bin depending on the population: in the panel $R \in [13, 14]$ kpc in the OB sample, while it is clear at the bin $R \in [12, 13]$ kpc in the RGB sample, in agreement with the LonKin method. The position of the secondary peak indicates a clear Lopsided warp.

4 Conclusions

So, in this talk, we show that Gaia Data Release 2 reveals a rich and complex kinematic structure in the disc. The sample with line-of-sight velocities points to the fact that the disc is not in equilibrium, and models need to be adapted to fit the complexity of the data. The study of the vertical velocities, without the need of line-of-sight velocities, to tackle the Galactic warp, reveal, again, the fact that the disc is not in equilibrium, that the data do reflex the expected motion of a warped disc, but this is not symmetric at both sides.

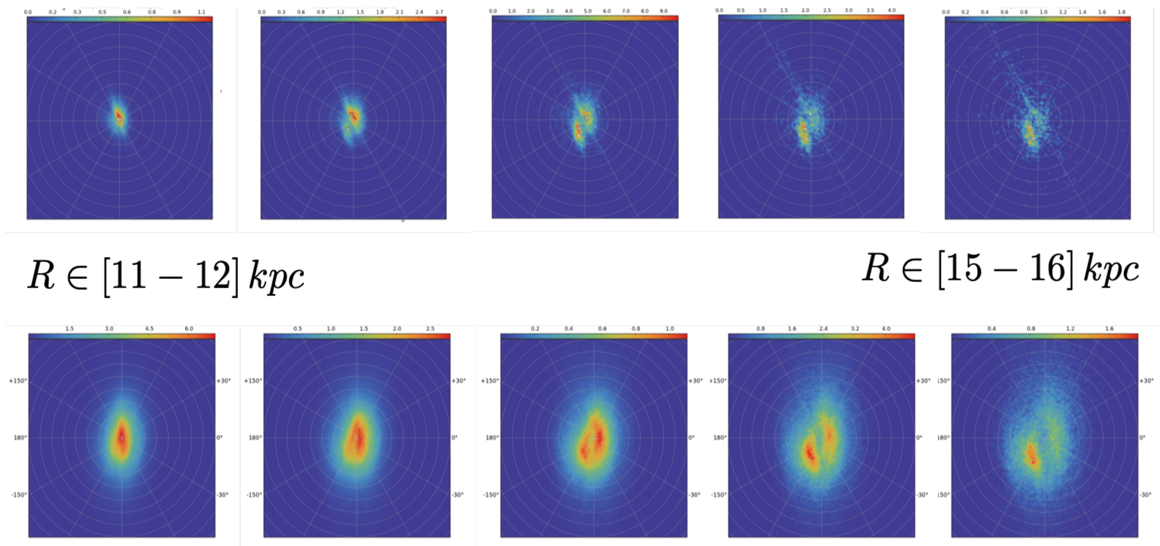

Figure 4: nGC3 PCM applied to OB and RGB samples (top and bottom rows, respectively), the radial shells increasing from left to right.

Acknowledgments

This work was supported by the MINECO (Spanish Ministry of Economy) - FEDER through grant ESP2014-55996-C2-1-R and MDM-2014-0369 of ICCUB (Unidad de Excelencia "María de Maeztu"), the European Community's Seventh Framework Programme (FP7/2007-2013) under grant agreement GENIUS FP7 - 606740. We also acknowledge the team of engineers (GaiaUB-ICCUB) in charge to set up and maintain the Big Data platform (GDAF) at University of Barcelona. CM is grateful for the hospitality and support from ICCUB and IA-UNAM, where part of this research was carried out. We thank the PAPIIT program of DGAPA/UNAM for their support through grant IG100319.

References

[1] Abedi, H. and Mateu, C. and Aguilar, L. A. and Figueras, F. and Romero-Gómez, M. 2014, MNRAS, 442, 3627

[2] Amôres, E. B. and Robin, A. C. and Reylé, C. 2017, A&A, 602, 67

[3] Drimmel, R.; Cabrera-Lavers, A.; López-Corredoira, M. 2003, A&A, 409, 205

[4] Johnston, K. V. and Hernquist, L. and Bolte, M. 1996, ApJ, 465, 278

[5] Katz, D., Antoja, T., Romero-Gomez, M. et al (Gaia Collaboration) 2018, A&A, 616, 11

[6] Mateu, C. and Bruzual, G. and Aguilar, L. and Brown, A. G. A. and Valenzuela, O. and Carigi, L. and Velázquez, H. and Hernández, F. 2011, MNRAS, 415, 214

[7] Romero-Gómez, M., Figueras, F., Antoja, T., Abedi, H., Aguilar, L. 2015, MNRAS, 447, 218

Highlights on Spanish Astrophysics X, Proceedings of the XIII Scientific Meeting of the Spanish Astronomical Society held on July 16 – 20, 2018, in Salamanca, Spain. B. Montesinos, A. Asensio Ramos, F. Buitrago, R. Schödel, E. Villaver, S. Pérez-Hoyos, I. Ordóñez-Etxeberria (eds.), 2019

The missing mass conundrum of post-common-envelope planetary nebulae.

Miguel Santander-García[1], David Jones[2,3], Javier Alcolea[1], Roger Wesson[4,5] and Valentín Bujarrabal[1]

[1] Observatorio Astronómico Nacional, Alfonso XII, 3, 28014, Madrid, Spain
[2] Instituto de Astrofísica de Canarias, E-38205 La Laguna, Spain
[3] Departamento de Astrofísica, Universidad de La Laguna, E-38206 La Laguna, Spain
[4] Department of Physics and Astronomy, University College London, Gower St, London, UK
[5] European Southern Observatory, Alonso de Córdova 3107, Casilla 19001, Santiago, Chile

Abstract

Most planetary nebulae (PNe) show beautiful, axisymmetric morphologies despite their progenitor stars being essentially spherical. Angular momentum provided by a close binary companion is widely invoked as the main agent that would help eject an axisymmetric nebula, after a brief phase of engulfment of the secondary within the envelope of the Asymptotic Giant Branch (AGB) star, known as a common envelope (CE). The evolution of the AGB would be thus interrupted abruptly, its (still quite) massive envelope fully ejected to form the PN, which should be more massive than a PN coming from the same star were it single. We test this hypothesis by deriving the ionised+molecular masses of a pilot sample of post-CE PNe and comparing them to a regular PNe sample. We find the mass of post-CE PNe to be actually lower, on average, than their regular counterparts, raising some doubts on our understanding of these intriguing objects.

1 Introduction

Most planetary nebulae (PNe) show beautiful, aspherical morphologies with high degrees of symmetry, despite their progenitor stars being essentially spherical. The mechanism behind their shaping, however, is still poorly understood (e.g. [2]). Angular momentum provided by a close binary companion has been widely invoked as the main shaping agent that would eject an axisymmetric nebula [14].

The mechanism in close binary systems is thought to be as follows: a star undergoing the Asymptotic Giant Branch (AGB) stage engulfs a companion via Roche-lobe overflow as it expands during the Asymptotic Giant Branch (AGB) phase. The system then undergoes a very brief ($\sim$1 year) common-envelope (CE) stage, where the evolution of the AGB star is abruptly interrupted. Spiraling-in of the secondary and drag forces would then lead to the ejection and shaping of this CE into a bipolar PN whose equator would be coincident with the orbital plane of the binary star, as happens to occur in every single case analysed so far [12].

On theoretical grounds, however, the physics of the CE "friction" and ejection processes remain very elusive. Simulations show most of the gas to be ejected along the equatorial plane, but are unable to gravitationally unbind the whole envelope of the AGB (e.g. [9],[7]). An exception would imply tapping energy from atomic recombination in the envelope (e.g. [16]), but then the achieved expansion velocities would likely be too large.

This draws a somewhat uncomfortable big picture: we simply do not understand the physics lying behind the death of a significant fraction of stars in the Universe.

Single star vs. CE evolution: the total nebular mass. It can be argued that CE evolution implies significant differences in the mass-loss history of the primary star.

Let us consider a single AGB star on its way to produce a PN. Most of its envelope's mass is slowly lost along the AGB evolution, and gets too diluted in the Interstellar Medium (ISM) to be detected. In contrast, the mass lost by the star during the superwind phase (last $\sim$500-3000 years), which amounts to $\sim$0.1-0.6 $M_\odot$ for a 1.5 $M_\odot$ star (see review in [13]), will form the nebula visible during the PN stage.

On the other hand, let us consider the same AGB star, but now as part of a binary system close enough to engulf its companion and undergo a CE stage. AGB engulfment will thus occur during the last few ($\sim$1-20) million years of the AGB stage (e.g. Fig. 1 in [15]), effectively interrupting the evolution of the star. All the mass the star did not lose into the ISM during these last million years will be present in the CE, and therefore will *also* be part of the PN as it is suddenly ejected.

In other words, despite the large uncertainties in the mass-loss history along the AGB, *PNe arising from CE events should, on average, be more massive than their single star counterparts.*

This additional mass should be detectable, as it will be close to the central stars during the lifetime of the PN, as opposed to the single star case, where it will be long gone, diluted into the ISM. Testing this hypothesis would lead to a better understanding of the ejection process. Nevertheless, complete mass determinations of post-CE PNe are virtually nonexistent, the only dedicated study so far being that by [6], which found that the ionised masses of a sample of post-CE PNe are indeed lower than those of regular PNe, but did not account for the potential presence of molecular mass. We hereby present the results of a pilot survey including both the ionised and molecular content of a different PNe sample.

2 Sample and Observations

Our pilot sample is composed of 10 post-CE PNe, which amount roughly to 1/6$^{\rm th}$ of the total currently known. It covers a broad range of kinematical ages, central star effective temperatures and luminosities, orbital periods and morphologies. These objects are PM 1-23, Abell 41, Hen 2-428, ETHOS 1, NGC 6778, Abell 63, the Necklace, V 458 Vul, Ou 5, and NGC 2346. They lacked any attempt at detecting their molecular content by means of radioastronomical observations, except for NGC 6778 (undetected in [10]), and NGC 2346, already known to host a massive molecular envelope (e.g. [1]). We therefore carried out spectral observations of the sample (except NGC 2346), in search for ^{12}CO and ^{13}CO J=1-0 and J=2-1 emission, using EMIR in the IRAM 30m radiotelescope. The angular size of the objects of the sample is generally well suited to the telescope Half Power Beam Width at the observed frequencies.

We complemented the mm-range data with archival Hα images and optical spectra of the sample, from various telescopes and instruments, to derive their ionised masses.

3 Results

Molecular content. No object was detected in ^{12}CO or ^{13}CO down to a *rms* sensitivity limit in the range 6-25 mK at 230 GHz, except for NGC 6778. This PN shows a simple, broad ^{12}CO J=1-0 emission profile, as well as double-peaked emission profiles in ^{12}CO and ^{13}CO J=2-1, whose kinematics correspond to the broken, equatorial ring investigated by [8]. The peak intensity relations lead us to conclude that the ^{12}CO J=1-0 is optically thin, and the excitation temperatures relatively low. Further analysis of these profiles and the excitation conditions in this nebula will be presented in Santander-García (in preparation).

The ^{12}CO J=1-0 profile of NGC 6778 allows us to derive a molecular mass of 5×10^{-4} $M_\odot$ (at 1 kpc) for this PNe by assuming a representative value of the ^{12}CO abundance of 3×10^{-4}. On the other hand, the sensitivities achieved in the rest of the observations allow us to derive conservative (3-σ) upper limits for the molecular masses of the other objects in the sample.

Ionised content. The ionised mass of NGC 6778, NGC 2346, Abell 41, ETHOS 1, Hen 2-428 and PM 1-23 were derived from their Hβ fluxes and apparent sizes extracted from archival data. Assumptions about the electronic temperatures were made where necessary, in order to produce conservative estimates of the ionised masses of these nebulae (i.e. largest $T_{\rm e}$ wherever more than one was available). Ionised masses of the Necklace, Abell 63, Ou 5, and V458 Vul were obtained from [4], [5], [5], and [20], respectively.

Total mass comparison at 1 kpc. Masses found in this work scale with the distance to the nebulae squared. Distances to PNe, however, are still poorly known. Hence, in order to do a proper comparison with PNe not undergoing CE, we must first remove this large dependance by examining the mass every PNe would have at the same distance. Figure 1 shows the ionised and molecular masses of our sample of post-CE PNe at 1kpc, together with the ionised and molecular masses of a large sample of 44 PNe selected in [11] in an attempt to approach a volume-limited sample, and another sample of 27 PNe in the galactic disk, whose ionised/molecular masses were determined in [3] and [10], respectively.

Strikingly, except for NGC 2346, the total masses of the post-CE sample seem similar, if not lower, than those of regular PNe. The median mass at 1 kpc of the combined comparison samples is 0.021 $M_{\odot}$, whereas for the post-CE sample it is $\leq$0.0081 $M_{\odot}$.

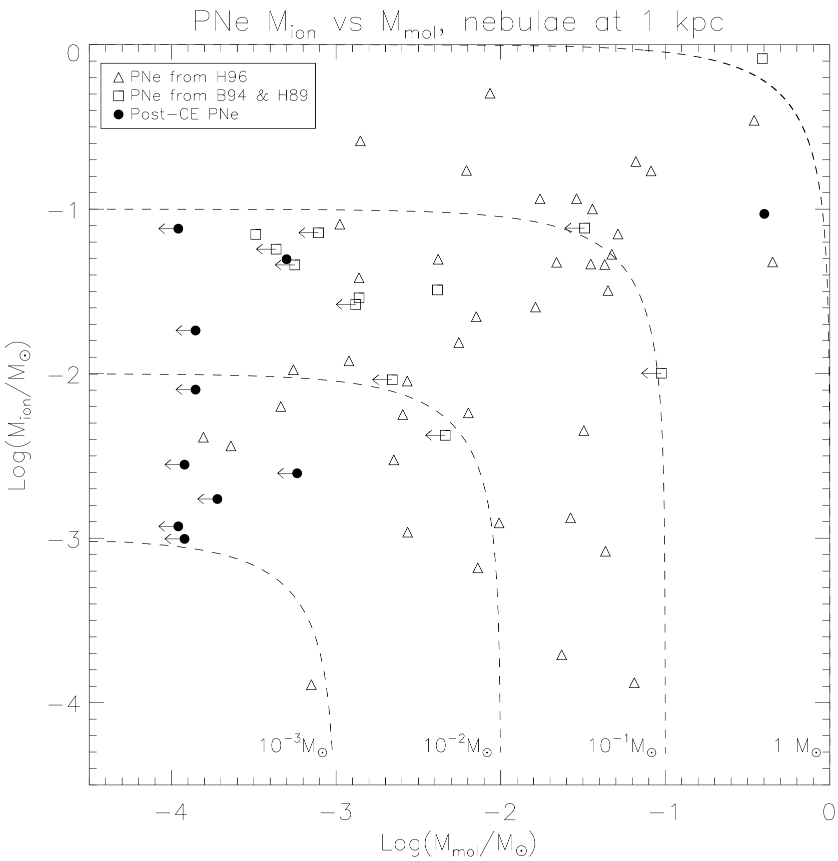

Figure 1: Logarithmic ionised mass vs. logarithmic molecular mass at 1 kpc of our post-CE PNe sample (filled circles), PNe from Huggins et al. (1996) (triangles), and a combined sample from Boffi et al. (1994) and Huggins et al. (1989) (squares). Dashed lines indicate equal total (ionised+molecular) mass; individual nebulae run along these lines as their gas content is progressively ionised.

4 Conclusions

This preliminary work provides an indication that, contrary to expectations, post-CE PNe seem to be slightly less massive, on average, than their single star counterparts. This discrepancy could however be removed if the molecular gas of these nebulae were too cold (or hot) to be detected, or the ionised gas too hot to emit Hα, but these possibilities seem rather unlikely. Some of the mass could also be in atomic, neutral form, which has not been investigated in this work, and will be part of a future study.

On the other hand, should these results be confirmed by further observations and careful analysis of the possible biases involved, they would present us with the following interesting (and so far speculative) implications. The problem of models unable to unbind such a large mass would be less severe. A fraction of the mass could fall back forming a circumbinary disk (as in [17]). If any of this material reaches the central stars, it could then be reprocessed perhaps offering an explanation for the correlation between large abundance discrepancy factors and post-CE central stars in PNe [21]. We can thus wonder whether the CE itself could be not a unique, only-once process, but an episodic, recurrent one. Grazing Envelope Evolution proposed by [18] and [19] could help explain such a phenomenon.

References

[1] Bachiller, R., Planesas, P., Martín-Pintado, J., et al., 1989, A&A, 210, 366

[2] Balick, B. & Frank, A., 2002, ARA&A, 40, 439

[3] Boffi, F. R., & Stanghellini, L., 1994, A&A, 284, 248

[4] Corradi, R. L. M., Sabin, L., Miszalski, B., et al., 2011, MNRAS, 410, 1349

[5] Corradi, R. L. M., García-Rojas, J., Jones, D., Rodríguez-Gil, P., 2015, ApJ, 803, 99

[6] Frew, D. J. & Parker, Q. A., 2007, Proceedings of the Asymmetrical Planetary Nebulae IV conference, R. L. M. Corradi, A. Manchado & N. Soker eds.

[7] García-Segura, G.; Ricker, P. M.; Taam, R. E., 2018, ApJ, 860, 19

[8] Guerrero, M. A., & Miranda, L. F., 2012, A&A, 539, 47

[9] Huarte-Espinosa, M., Frank, A., Balick, B., et al., 2012, MNRAS, 424, 2055

[10] Huggins, P. J., & Healy, A. P., 1989, ApJ, 346, 201

[11] Huggins, P. J., Bachiller, R., Cox, P., et al., 1996, A&A, 315, 284

[12] Hillwig, T. C., Jones, D., de Marco, O., et al., 2016, ApJ, 832, 125

[13] Höfner, S.; Olofsson, H., 2018, A&AR, 26, 1

[14] Jones, D., & Boffin, H. M. J., 2017, Nature Astronomy, 1, 117

[15] MacLeod, M., Guillochon, J., Ramirez-Ruiz, E., 2012, ApJ, 757, 134

[16] Ohlmann, S. T.; Röpke, F. K.; Pakmor, R.; Springel, V.; Müller, E., 2016, MNRAS, 462, L121

[17] Reichardt, T. A., De Marco, O., Iaconi, R., et al., 2018, MNRAS, submitted (*arXiv*:1809.02297)

[18] Soker, N., 2015, ApJ, 800, 114

[19] Shiber, Sagiv; Kashi, Amit; Soker, Noam, 2017, MNRAS, 465, L54

[20] Wesson, R., Barlow, M. J., Corradi, R. L. M., et al., 2008, ApJ, 688, L21

[21] Wesson, R., Jones, D., García-Rojas, J., et al., 2018, MNRAS, 480, 4589

Highlights on Spanish Astrophysics X, Proceedings of the XIII Scientific Meeting of the Spanish Astronomical Society held on July 16 – 20, 2018, in Salamanca, Spain. B. Montesinos, A. Asensio Ramos, F. Buitrago, R. Schödel, E. Villaver, S. Pérez-Hoyos, I. Ordóñez-Etxeberria (eds.), 2019

Planetary nebula LoTr5: hints of a possible third companion in a long-period binary central star.

A. Aller[1], J. Lillo-Box[2], M. Vučković[1], H. Van Winckel[3], D. Jones[4,5], B. Montesinos[6], M. Zorotovic[1], and L. F. Miranda[7]

[1] Instituto de Física y Astronomía, Facultad de Ciencias, Universidad de Valparaíso, Gran Bretaña 1111, Playa Ancha, Valparaíso, 2360102, Chile
[2] European Southern Observatory (ESO), Alonso de Cordova 3107, Vitacura, Casilla 19001, Santiago de Chile, Chile
[3] Instituut voor Sterrenkunde, KU Leuven, Celestijnenlaan 200D bus 2401, 3001, Leuven, Belgium
[4] Instituto de Astrofísica de Canarias, 38205 La Laguna, Tenerife, Spain
[5] Departamento de Astrofísica, Universidad de La Laguna, 38206 La Laguna, Tenerife, Spain
[6] Departamento de Astrofísica, Centro de Astrobiología (INTA-CSIC), PO Box 78, E-28691 Villanueva de la Cañada (Madrid), Spain
[7] Instituto de Astrofísica de Andalucía - CSIC, C/ Glorieta de la Astronomía s/n, E-18008 Granada, Spain

Abstract

LoTr 5 is a planetary nebula with an unusual long-period binary central star. The pair consists of a rapidly rotating G-type star and a hot star, which is responsible for the ionization of the nebula. Both components are in a wide orbit with a period of about 2700 days, one of the longest in central star of planetary nebulae. In this contribution, we present new radial velocity observations of the central star. These data provide evidence of a third component in the system at 129 days to the G star. This periodicity is also present in the photometry of this target from the superWASP survey, providing an additional hint for its presence. We also present a detailed analysis of the complex Halpha double-peaked profile, which varies with very short time scales, and whose origin is still unknown. We conclude that it does not present correlation with the rotation period ($\sim$5.95 days and detectable in all photometric time series from superWASP, OMC and ASAS) and that the presence of an accretion disk via Roche lobe overflow is unlikely. A.A. acknowledges support from FONDECYT through postdoctoral grant 3160364. Based on observations obtained with the HERMES, CAFOS and ELODIE spectrographs, and from OMC, SuperWASP and ASAS data. (See poster).

Highlights on Spanish Astrophysics X, Proceedings of the XIII Scientific Meeting of the Spanish Astronomical Society held on July 16 – 20, 2018, in Salamanca, Spain. B. Montesinos, A. Asensio Ramos, F. Buitrago, R. Schödel, E. Villaver, S. Pérez-Hoyos, I. Ordóñez-Etxeberria (eds.), 2019

Open Clusters Membership by Clusterix 2.0 for Gaia DR2 http://clusterix.cab.inta-csic.es.

L. Balaguer-Núñez[1], M. López del Fresno[2,3], E. Solano[2,3], D. Galadí-Enríquez [4], C. Jordi[1], E. Masana[1] and E. Paunzen[5]

[1] Dept. FQA, Institut de Ciències del Cosmos. Universitat de Barcelona IEEC-UB, Barcelona, Spain
[2] Centro de Astrobiología (INTA-CSIC), Departamento de Astrofísica. P.O. Box 78, E-28691, Villanueva de la Cañada, Madrid, Spain
[3] Spanish Virtual Observatory
[4] Centro Astronómico Hispano Alemán CAHA, Almería, Spain
[5] Masaryk University, Brno, Czech Republic

Abstract

We present an advanced version of Clusterix, a tool for the determination of membership probabilities in stellar clusters from proper motions adapted to the new wealth of Gaia data. Clusterix is a VO web-based, interactive application that allows the computation of membership probabilities from proper motions through a fully non-parametric method (Galadí-Enríquez et al. 1998). Clusterix 2.0 has been adapted to the exploitation of Gaia Data Release 2 and now features an improved user interface for a faster, easier and more accurate interactive definition of the cluster and field proper motion distributions. The system provides fast feedback between membership probability determinations and the distribution of the observables for the most probable members and field stars. We present the first results of Clusterix for the case of one area where two clusters (NGC 1750 and NGC1758) are found without a priory knowledge. (See poster).

Highlights on Spanish Astrophysics X, Proceedings of the XIII Scientific Meeting of the Spanish Astronomical Society held on July 16 – 20, 2018, in Salamanca, Spain. B. Montesinos, A. Asensio Ramos, F. Buitrago, R. Schödel, E. Villaver, S. Pérez-Hoyos, I. Ordóñez-Etxeberria (eds.), 2019

Taking advantage of Machine Learning to identify potential T-Tauri star candidates.

Leire Beitia-Antero[1], Javier Yáñez[1], and Ana Inés Gómez de Castro[1]

[1] AEGORA Research Group, Universidad Complutense de Madrid

Abstract

Over the last decades, the vast amount of data together with the easiest access to high-performance computers have favoured the development and application of powerful mathematical algorithms, the so-called machine learning algorithms. In astronomy, the classification of certain types of objects has been historically made through a detailed and supervised analysis of colour-colour diagrams or spectra of single sources, but handling with billions of sources is virtually impossible for any human being. Thus, Machine Learning techniques are really useful for solving astronomical problems, but it requires a balanced, representative qualification sample. Sometimes it is not possible to have it, as occurs when dealing with T-Tauri Stars. In this work, we have explored the usefulness of a particular machine learning method that has been scarcely applied in astronomy, Logistic Regression, that when combined with an appropiatedly tuned training sample, provides fairly good results. This work has been partly funded by the Ministry of Economy, Industry and Competitiveness of Spain through grants ESP2014-54243-R, ESP2015-68908-R and TIN2015-66471-P as well as by the local Government of Madrid through grant S2013/ICE2845. (See poster).

Highlights on Spanish Astrophysics X, Proceedings of the XIII Scientific Meeting of the Spanish Astronomical Society held on July 16 – 20, 2018, in Salamanca, Spain. B. Montesinos, A. Asensio Ramos, F. Buitrago, R. Schödel, E. Villaver, S. Pérez-Hoyos, I. Ordóñez-Etxeberria (eds.), 2019

Tracing back the mass loss history of MGE042.0787+00.5084.

Cristobal Bordiu[1], Jose Ricardo Rizzo[1], and Alessia Ritacco[2]

[1] Centro de Astrobiologia (INTA-CSIC), Ctra. M-108, km. 4, 28850 Torrejon de Ardoz, Madrid, Spain
[2] Institut de RadioAstronomie Millimetrique (IRAM), Granada, Spain

Abstract

The luminous blue variable (LBV) phase is a short period of high instability that some high mass stars experiment after leaving the main sequence. Through steady and dense winds and sporadic giant eruptions, LBV stars can lose several solar masses in very short timescales (10^4–10^5 years), producing large circumstellar nebulae. By the action of stellar winds, high UV fields and low velocity shocks, these nebulae may become a breeding ground for molecular gas. The study of the chemistry and kinematics of this molecular component has proven extremely useful to reconstruct the mass loss history of these objects and estimate their energetic output.

In this poster we report the detection of an expanding torus-like structure surrounding the LBV candidate MGE042.0787+00.5084, achieved by means of CO observations at 1 and 3 mm with IRAM's 30m telescope. We analyze the physical parameters derived from the detected lines, with a particular emphasis on the isotopic ratios and the estimated mass loss rate. A dynamical model of the structure is also presented. We discuss the implications of these findings in the context of LBV mass loss. (See poster).

Highlights on Spanish Astrophysics X, Proceedings of the XIII Scientific Meeting of the Spanish Astronomical Society held on July 16 – 20, 2018, in Salamanca, Spain. B. Montesinos, A. Asensio Ramos, F. Buitrago, R. Schödel, E. Villaver, S. Pérez-Hoyos, I. Ordóñez-Etxeberria (eds.), 2019

A Gaia DR2 view of the open cluster population in the Milky Way.

T. Cantat-Gaudin[1], C. Jordi[1], L. Balaguer-Núñez[1], and A. Castro-Ginard[1]

[1] Institut de Ciències del Cosmos, Universitat de Barcelona (IEEC-UB), Martí i Franquès 1, E-08028 Barcelona, Spain

Abstract

As simple stellar populations, made of a dozen to several thousand stars of the same age and chemical composition, open clusters are basic constituents of our Galactic disk. Their ages, ranging from a few million to several billion years, can be estimated relatively easily. Their distances can also be estimated more precisely than for individual stars. We take advantage of the exquisite astrometry of the second Gaia data release (Gaia DR2, Gaia collaboration et al. 2018) to establish a list of members in all clusters listed in the literature.
We queried the Gaia DR2 data in the field of view of over 3000 open clusters and candidates listed in the catalogues of Dias et al. (2002) and Kharchenko et al. (2013). We applied the unsupervised classification approach of UPMASK (Krone-Martins & Moitinho, 2014) to the Gaia positions, proper motions and parallaxes.
We derived a secure membership list for over 1200 open clusters. We also discovered 60 previously unreported objects. The distances we derive allow us to draw a portrait of the Milky Way disk out to distances of $\sim$4 kpc. The youngest clusters in our sample clearly trace the spiral structure of the disk. We observe that in the outer disk, clusters older than log t$\sim$8.5 stray away from the Galactic plane, while old clusters appear to be non-existent in the inner disk. The precision of the Gaia astrometry shows that a significant fraction of the clusters listed in the literature are coincidental asterisms. (See poster).

Highlights on Spanish Astrophysics X, Proceedings of the XIII Scientific Meeting of the Spanish Astronomical Society held on July 16 – 20, 2018, in Salamanca, Spain. B. Montesinos, A. Asensio Ramos, F. Buitrago, R. Schödel, E. Villaver, S. Pérez-Hoyos, I. Ordóñez-Etxeberria (eds.), 2019

Open clusters through the eyes of WEAVE.

R. Carrera[1], and GA-OC team

[1] INAF-Osservatorio Astronomico di Padova, vicolo dell'Osservatorio 5, 35122 Padova (Italy)

Abstract

WEAVE is a new multi-object survey spectrograph for the 4.2-m William Herschel Telescope (WHT) at the Observatorio del Roque de los Muchachos, on La Palma (Spain). WEAVE will have two observation modes. The multi-object spectra (MOS) will allow to take optical spectra for up to ∼1000 targets over a two degrees field of view. Moreover, it will be able to carry out integral-field spectroscopy using 20 deployable mini integral-field units (mIFUs) or one large fixed integral-field unit (LIFU). WEAVE have two optical arms which allow to observed at the same time blue and red wavelengths. Moreover, two possible resolutions are available, 5000 and 20000. The first light of WEAVE is scheduled by 2019.

WEAVE will cover a wide range of scientific cases from the Galactic archaeology to the clusters of galaxies. A large fraction of the WEAVE time will be devoted to the Galactic archaeology survey that will sample the main structures of the Milky Way. In particular, on of the GA sub-surveys will study the open clusters. They are key systems to investigate a variety of astrophysical topics from the stellar evolution itself to the evolution of the Galaxy. The targets to be observed within the Galactic Archaeology Open Cluster survey (GA-OC) cover a wide range of ages, including star forming regions together with young and old open clusters. This will allow to address a large variety of scientific topics such as: star formation, stellar evolution, cluster formation and disruption, or the structure of the Galactic disk. (See poster).

Highlights on Spanish Astrophysics X, Proceedings of the XIII Scientific Meeting of the Spanish Astronomical Society held on July 16 – 20, 2018, in Salamanca, Spain. B. Montesinos, A. Asensio Ramos, F. Buitrago, R. Schödel, E. Villaver, S. Pérez-Hoyos, I. Ordóñez-Etxeberria (eds.), 2019

A new OSIRIS/GTC and IDS/INT spectroscopic survey of young stars in the σ Orionis cluster.

A. de Burgos[1], J. A. Caballero[1], F. J. Alonso-Floriano[2,3], A. Cabrera-Lavers[4,5,6], D. García-Álvarez[4,5,6], and D. Montes[3]

[1] Centro de Astrobiología (CSIC-INTA), European Space Astronomy Centre, PO Box 78, 28691 Villanueva de la Cañada, Madrid, Spain
[2] Leiden Observatory, Leiden University, P.O. Box 9513, 2300 RA Leiden, The Netherlands2300 RA Leiden, The Netherlands
[3] Departamento de Astrofísica y Ciencias de la Atmósfera, Facultad de Física, Universidad Complutense de Madrid, 28040 Madrid, Spain
[4] Instituto de Astrofísica de Canarias, Avenida Vía Láctea, 38205 La Laguna, Tenerife, Spain
[5] Grantecan S. A., Centro de Astrofísica de La Palma, Cuesta de San José, 38712 Breña Baja, La Palma, Spain
[6] Departamento de Astrofísica, Universidad de La Laguna, 38205 La Laguna, Tenerife, Spain

Abstract

The young σ Orionis cluster in the Ori OB 1b association is one of the most important clusters for understanding the stellar and substellar formation and evolution. In this work, we used 197 low-resolution optical spectra of 167 stars. We determined spectral types and measured Li I and Hα equivalent widths (EWs). We used *Gaia* DR2 astrometry together with youth features indicators from literature to derive the true membership to the cluster. (See poster).

Highlights on Spanish Astrophysics X, Proceedings of the XIII Scientific Meeting of the Spanish Astronomical Society held on July 16 – 20, 2018, in Salamanca, Spain. B. Montesinos, A. Asensio Ramos, F. Buitrago, R. Schödel, E. Villaver, S. Pérez-Hoyos, I. Ordóñez-Etxeberria (eds.), 2019

15 years of *INTEGRAL*/OMC monitoring.

Albert Domingo[1], Julia Alfonso-Garzón[1], and J. Miguel Mas-Hesse[1]

[1] Centro de Astrobiología (CAB-CSIC/INTA), ESAC Campus, Camino Bajo del Castillo S/N, 28692 Villanueva de la Cañada, Spain

Abstract

OMC, the Optical Monitoring Camera onboard *INTEGRAL*, has been monitoring the optical emission of thousands of potentially variable astronomical objects during the latest 15 years. OMC takes one image of its $5^\circ \times 5^\circ$ field of view every 10, 50 or 200 seconds, downloading the photometric data for around 100 objects in each exposure. The OMC Archive, publicly available at http://sdc.cab.inta-csic.es/omc/, contains the light curves of around 90 000 scientific objects with more than at least 50 photometric points, including the optical emission of the high-energy targets being observed simultaneously by the other instruments on *INTEGRAL*: IBIS, SPI and JEM-X. The "First *INTEGRAL*-OMC catalogue of optically variable sources" contains already a complete analysis of more than 5000 variable sources. At the end of the *INTEGRAL* mission we will compile and publish the final catalogue containing the light curves and variability analysis of all the sources monitored by OMC during its lifetime. (See poster).

Highlights on Spanish Astrophysics X, Proceedings of the XIII Scientific Meeting of the Spanish Astronomical Society held on July 16 – 20, 2018, in Salamanca, Spain. B. Montesinos, A. Asensio Ramos, F. Buitrago, R. Schödel, E. Villaver, S. Pérez-Hoyos, I. Ordóñez-Etxeberria (eds.), 2019

The Spanish Network for Gaia Science Exploitation and GDR2.

F. Figueras[1], C. Jordi[1], X. Luri[1], J. Torra[1] on behalf of the REG Executive Committee and Gaia UB Team

[1] Dept. FQA, Institut de Ciències del Cosmos. Universitat de Barcelona IEEC-UB, Barcelona, Spain

Abstract

The "Red Española de Explotación Científica de Gaia" (REG) continues to intensify its activities after the second Gaia Data Release (April 25th, 2018). Some of the collective activities developed by its members have been, among others: 1) the presentation and discussion on the first science outcome from Gaia-DR2 data in the annual meeting (May 28th, 2018); 2) the preparation of the Spanish community for the use of the Gaia Data Archive and VO facilities; 3) the exchange of codes, tools and facilities for an optimum exploitation of Gaia-DR2; 4) the joint effort supporting the preparation of the WEAVE Operational Rehearsals (first light, 2019) and, last but not least, the engagement on new common projects for exploiting this huge and impressive new data. These activities are described together with the schedule of future national and international science meetings and the outreach activities being organized. (See poster).

Highlights on Spanish Astrophysics X, Proceedings of the XIII Scientific Meeting of the Spanish Astronomical Society held on July 16 – 20, 2018, in Salamanca, Spain. B. Montesinos, A. Asensio Ramos, F. Buitrago, R. Schödel, E. Villaver, S. Pérez-Hoyos, I. Ordóñez-Etxeberria (eds.), 2019

The origin of the most luminous planetary nebulae: M31.

R. Galera-Rosillo[1,2], R.L.M. Corradi[3,1], A. Mampaso[1], B. Balick[4], K. B. Kwitter[5], and J. García-Rojas[1,2]

[1] Instituto de Astrofísica de Canarias, Calle Vía Láctea, s/n, E-38205, La Laguna, Tenerife, Spain

[2] Departamento de Astrofísica, Universidad de La Laguna, E-38206, La Laguna, Tenerife, Spain

[3] GRANTECAN, Cuesta de San José s/n, E-38712 , Breña Baja, La Palma, Spain

[4] Astronomy Department, University of Washington, Seattle WA, 98195-1580, USA

[5] Williams College, Department of Astronomy, Williamstown, MA 01267, USA

Abstract

The Planetary Nebulae Luminosity Function (PNLF) is an important standard candle on the extragalactic distance ladder. Its use is based on the empirical evidence that the [OIII]5007Å luminosity of PNe reaches a maximum value, M*, invariant with galaxy type and with a small dependence on metallicity.

The PNLF method, applied to more than 50 galaxies with satisfactory results, is well established, but it lacks of a theoretical interpretation. Despite the relevance of the topic, thorough spectroscopic studies of PNe at the tip of the PNLF are still missing.

As part of our systematic effort to characterize the properties of the brightest PNe and their progenitors, we obtained deep optical spectra of a sample of PNe in two galaxies with different metallicities: 8 PNe in M31 ($Z/Z_{\odot}\sim 1$) using OSIRIS at the 10mGTC and 4 PNe in LMC ($Z/Z_{\odot}\sim 0.5$) withFORS2, at the VLT. The results of our analysis will be presented in Galera-Rosillo et al. I and II (in prep.). (See poster).

Highlights on Spanish Astrophysics X, Proceedings of the XIII Scientific Meeting of the Spanish Astronomical Society held on July 16 – 20, 2018, in Salamanca, Spain. B. Montesinos, A. Asensio Ramos, F. Buitrago, R. Schödel, E. Villaver, S. Pérez-Hoyos, I. Ordóñez-Etxeberria (eds.), 2019

Identification of very cool and ultracool dwarfs in ALHAMBRA and COSMOS fields using Virtual Observatory tools.

M.C. Gálvez-Ortiz[1,2], Enrique Solano[1,2], Inés M. Gómez Muñoz [3], and Eduardo L. Martín[4]

[1] Centro de Astrobiología (CSIC-INTA), E-2861, Villafranca del Castillo, Madrid, Spain.
[2] Spanish Virtual Observatory.
[3] Universidad Internacional de Valencia, C/ Pintor Sorolla 21, 46002, Valencia, Spain.
[4] Centro de Astrobiología (CSIC-INTA), E-28850,Torrejón de Ardoz, Madrid, Spain.

Abstract

Through Virtual Observatory (VO) tools we have searched for new ultracool dwarfs in the ALHAMBRA[a] (Advance Large Homogeneous Area Medium Band Redshift Astronomical) and COSMOS[b] (Cosmological Evolution Survey) extragalactic surveys. The photometric coverage and the magnitude limits of these surveys make them valuable resources to look for this type of objects. We made quality cuts in each survey to select stellar objects with good photometric information. We took advantage of a Virtual Observatory tool like VOSA to, first, add new data to the Spectral Energy Distribution by querying in VO archives and services and, then, to obtain effective temperatures from the SED fitting to the BT-Settl collection of theoretical models. Keeping objects with Teff<3000K, we used color-color diagrams and measured proper motions to clean the sample from possible contaminants (e.g., extragalactic objects or giant stars), leaving a list of more than a hundred ultracool dwarf candidates. This study validates the procedure and the performance of VO tools to make similar searches in other deep, small-area extragalactic as well as shallower, large-area galactic surveys, and to be ready for the scientific exploitation of the Euclid[c] survey for which we will have priority access in the framework of our ESA ultracool Independent Legacy Project. (See poster).

[a]http://svo2.cab.inta-csic.es/vocats/alhambra/
[b]http://cosmos.astro.caltech.edu/page/photom3
[c]http://sci.esa.int/euclid/

Highlights on Spanish Astrophysics X, Proceedings of the XIII Scientific Meeting of the Spanish Astronomical Society held on July 16 – 20, 2018, in Salamanca, Spain. B. Montesinos, A. Asensio Ramos, F. Buitrago, R. Schödel, E. Villaver, S. Pérez-Hoyos, I. Ordóñez-Etxeberria (eds.), 2019

Widespread FUV-irradiated warm and dense gas in Orion Molecular Cloud (OMC-1).

Miriam G. Santa-Maria[1], Javier R. Goicoechea[1], Emeric Bron[1], David Teyssier[2], Nuria Marcelino[1], Jose Cernicharo[1] and Sara Cuadrado[1]

[1] Instituto de Física Fundamental (CSIC). Calle Serrano 121, E-28006 Madrid, Spain.
[2] Telespazio Vega UK Ltd for ESA/ESAC. Urbanización Villafranca del Castillo, Villanueva de la Cañada, E-28692 Madrid, Spain.

Abstract

Young massive stars ($> 8\,M_\odot$, OB stars) regulate the evolution of their parental molecular cloud, dominating the injection of radiative energy, through far ultraviolet (FUV) photons; and mechanical energy, through stellar winds, supernovae and/or merger explosions, into the interstellar medium (ISM). It is important to find tracers that help to quantify the stellar feedback processes that take place at different spatial scales. In this contribution we report velocity-resolved maps of the central 0.85 arcmin^2 ($\sim$0.9 pc$\times$ $\sim$1.4 pc) of the Orion molecular cloud (OMC-1), the closest high-mass star-forming region, in several submillimeter lines that can hardly be observed from ground-based radiotelescopes: CH^+(J=1-0), CO (J=10-9), HCO^+ (J=6-5) and HCN (J=6-5). The maps reveal an extended but thin component of warm molecular gas associated with the FUV irradiated skin of OMC-1. We find that the CH^+ (J=1-0) emission spatially correlates with the strengh of the flux of FUV photons arising from the Trapezium cluster and impinging the cloud. The CH^+ (J=1-0) emission also correlates with the widespread infrarred emission from FUV-pumped, vibrationally excited, H_2 ($v \geq$1), and with that of [CII] 158 μm, both emerging from FUV-irradiated gas. The correlation of the extended CH^+ (J=1-0) and narrow-line mid-J CO emissions from OMC-1 implies that both emerge from gas in the photodissociation region (PDR), the skin of the molecular cloud, and not from shocked gas. These line tracers probe the radiative feedback from young massive stars at large cloud spatial scales.

Highlights on Spanish Astrophysics X, Proceedings of the XIII Scientific Meeting of the Spanish Astronomical Society held on July 16 – 20, 2018, in Salamanca, Spain. B. Montesinos, A. Asensio Ramos, F. Buitrago, R. Schödel, E. Villaver, S. Pérez-Hoyos, I. Ordóñez-Etxeberria (eds.), 2019

Stellar atmospheric parameters of FGK-type stars from high-resolution optical and near-infrared CARMENES spectra.

E. Marfil[1], D. Montes[1], H. M. Tabernero[1,2], J. A. Caballero[3], J. I. González Hernández[4], A. Kaminski[5], S. Simón-Díaz[4], S. V. Jeffers[6], A. Quirrenbach[5], P. J. Amado[7], I. Ribas[8], A. Reiners[6], W. Seifert[5], and the CARMENES Consortium[1,3,4,5,6,7,8,9,10,11,12]

[1] Departamento de Física de la Tierra y Astrofísica, Facultad de Ciencias Físicas, Universidad Complutense de Madrid, E-28040 Madrid, Spain
[2] Departamento de Física, Ingeniería de Sistemas y Teoría de la Señal, Universidad de Alicante, Carretera de San Vicente del Raspeig, E-03690 Alicante, Spain
[3] Departamento de Astrofísica, Centro de Astrobiología (CSIC-INTA), Camino Bajo del Castillo s/n, ESAC Campus, E-28691 Villanueva de la Cañada, Madrid, Spain
[4] Instituto de Astrofísica de Canarias, Vía Láctea s/n, E-38205 La Laguna, Tenerife, Spain, and Departamento de Astrofísica, Universidad de La Laguna, E-38206 La Laguna, Tenerife, Spain
[5] Zentrum für Astronomie der Universität Heidelberg, Landessternwarte, Königstuhl 12, D-69117 Heidelberg, Germany
[6] Institut für Astrophysik, Georg-August-Universität, Friedrich-Hund-Platz 1, D-37077 Göttingen, Germany
[7] Instituto de Astrofísica de Andalucía (IAA–CSIC), Glorieta de la Astronomía s/n, E-18008 Granada, Spain
[8] Institut de Ciències de l'Espai (CSIC-IEEC), Can Magrans s/n, Campus UAB, E-08193 Bellaterra, Barcelona, Spain
[9] Thüringer Landessternwarte Tautenburg, Sternwarte 5, D-07778 Tautenburg, Germany
[10] Hamburger Sternwarte, Gojenbergsweg 112, D-21029 Hamburg, Germany
[11] Max-Planck-Institut für Astronomie, Königstuhl 17, D-69117 Heidelberg, Germany
[12] Centro Astronómico Hispano-Alemán (CSIC-MPG), Observatorio Astronómico de Calar Alto, Sierra de los Filabres, E-04550 Gérgal, Almería, Spain

Abstract

With the aim of using classic spectroscopic methods with high resolution and high signal-to-noise ratio in the NIR spectral window, we made a selection of 66 FGK-type stars observed with CARMENES, the brand-new, ultra-stable, double-channel spectrograph at the Spanish-German 3.5m Calar Alto telescope. These spectra are part of a CARMENES stellar library. We applied the equivalent width method to derive the spectroscopic stellar parameters ($T_{\rm eff}$, $\log g$, $\xi_{\rm micro}$, and [Fe/H]) using the StePar code along with four new iron line lists covering the whole CARMENES spectral range (550 - 1700 nm). (See poster).

Acknowledgments

This work has been partly supported by Ministerio de Educación y Formación Profesional under fellowship FPU15/01476, and by Ministerio de Ciencia, Innovación y Universidades under grant FJCI-2014-23001, and projects AYA2015-68012-C2-2-P, AYA2016-79425-C3-1/2-P.

References

[1] Andreasen, D. T. et al. 2016, A&A, 585, A143

[2] Blanco-Cuaresma, S., Soubiran, C., Heiter, U. and Jofré, P. 2014, iSpec: Stellar atmospheric parameters and chemical abundances, Astrophysics Source Code Library

[3] Heiter, U. et al. 2015, A&A, 582, A49

[4] Jofré, P., Heiter, U., Soubiran, C., et al. 2014, A&A, 564, A133

[5] Jofré, P., Heiter, U., Soubiran, C., et al. 2015b, A&A, 582, A81

[6] Quirrenbach, A. et al. 2018, SPIE, 10702, 0W

[7] Ryabchikova, T. et al. 2015, Phys. Scr, 90, 054005

[8] Sneden, C. A. 1973, PhD thesis, The University of Texas at Austin

[9] Sousa, S. G., Santos, N. C., Mayor, M., et al. 2008, A&A, 487, 373

[10] Tabernero, H. M., Montes, D., and González Hernández, J. I. 2012, A&A, 547, A13

[11] Tabernero, H. M., 2014, PhD thesis, Departamento de Física de la Tierra y Astrofísica, Universidad Complutense de Madrid

[12] Tsantaki, M., Sousa, S. G., Adibekyan, V. Z., et al. 2013, A&A, 555, A150

Highlights on Spanish Astrophysics X, Proceedings of the XIII Scientific Meeting of the Spanish Astronomical Society held on July 16 – 20, 2018, in Salamanca, Spain. B. Montesinos, A. Asensio Ramos, F. Buitrago, R. Schödel, E. Villaver, S. Pérez-Hoyos, I. Ordóñez-Etxeberria (eds.), 2019

Physical parameters of the low-mass eclipsing binary NSVS 10653195.

Iglesias-Marzoa, R.[1,2], Arévalo, M. J.[1,3], López-Morales, M.[4], Torres, G.[4], Lázaro, C.[1,3], and Coughlin, J.[5]

[1] Dpto de Astrofísica, Universidad de La Laguna, Tenerife
[2] Centro de Estudios de Física del Cosmos de Aragón (CEFCA), Teruel
[3] Instituto de Astrofísica de Canarias, La Laguna, Tenerife
[4] Harvard-Smithsonian Center for Astrophysics, Cambridge, MA, USA
[5] SETI Institute, Mountain View, CA, USA

Abstract

NSVS 10653195 is a double-line detached eclipsing binary star found in 2007 by [1] among the NSVS periodic variable stars. The first analysis of the optical VRI light curves by [1] show that this binary could be composed by two low mass stars. Other authors ([2, 3]) analyzed new optical light curves for this system, obtaining some parameters, like the mass ratio (q) from the light curves, given the absence of radial velocity (RV) measurements.This procedure is unreliable in the case of detached eclipsing binaries, leading to large uncertainties in the physical parameters of the system.

We obtained new IR light curves and radial velocity measurements to characterize the physical properties of this system, in particular masses and radii. In addition, calibrated optical BVRI photometry was obtained to fully constrain the effective temperature of the two components of this system. The modelling of this system with the `rvfit` and Phoebe package show that the mass ratio q is very different of previously published values, showing that the secondary component, as defined by the light curve, is slightly more massive than the primary. We are currently finishing the modelling of this interesting eclipsing system. (See poster).

References

[1] Coughlin, J., & Shaw, J. S. 2007, JSARA, 1, 7

[2] Wolf, M., et al. 2010, ASP Conference Series, 435, 441

[3] Zhang, L.-Y., et al. 2014, MNRAS, 442, 2620

Highlights on Spanish Astrophysics X, Proceedings of the XIII Scientific Meeting of the Spanish Astronomical Society held on July 16 – 20, 2018, in Salamanca, Spain. B. Montesinos, A. Asensio Ramos, F. Buitrago, R. Schödel, E. Villaver, S. Pérez-Hoyos, I. Ordóñez-Etxeberria (eds.), 2019

The Pleiades as seen by TGAS and the Virtual Observatory.

F. Jiménez-Esteban[1,2], M. Cortés Contreras[1,2], M. López del Fresno[1,2], E. Solano[1,2], and J.A. Caballero[1]

[1] Departmento de Astrofísica, Centro de Astrobiología (CSIC-INTA), ESAC Campus, Camino Bajo del Castillo s/n, E-28692 Villanueva de la Cañada, Madrid, Spain
[2] panish Virtual Observatory, Spain

Abstract

Using the Tycho-Gaia Astrometric Solution (TGAS), we revisited the very well known Pleiades open cluster. With Clusterix, a Virtual Observatory (VO) tool developed by the Spanish Virtual Observatory (SVO) which is presented in this meeting, we were able to provide membership probabilities to the TGAS sources in the Pleiades region, separating cluster member candidates from field stars. In a second step, we refined the membership assignation fitting Gaussians to the astrometric solution. We identified 156 Pleiades members, and ruled out 173 sources which are classified as Pleiades members in SIMBAD. Finally, we used VOSA, VO SED Analyser, another VO tool also developed by the SVO, to derive the physical parameter of the Pleiades members with the goal of study the IMF of the open cluster. (See poster).

Highlights on Spanish Astrophysics X, Proceedings of the XIII Scientific Meeting of the Spanish Astronomical Society held on July 16 – 20, 2018, in Salamanca, Spain. B. Montesinos, A. Asensio Ramos, F. Buitrago, R. Schödel, E. Villaver, S. Pérez-Hoyos, I. Ordóñez-Etxeberria (eds.), 2019

The longest stellar dance inside a planetary nebula.

David Jones[1,2]

[1] Instituto de Astrofísica de Canarias, E-38205 La Laguna, Tenerife, Spain
[2] Departamento de Astrofísica, Universidad de La Laguna, E-38206 La Laguna, Tenerife, Spain

Abstract

The importance of long-period binaries for the formation and evolution of planetary nebulae is still rather poorly understood, which in part is due to the lack of central star systems that are known to comprise such long-period binaries. Here, we report on the latest results from the on-going Mercator-HERMES survey for variability in the central stars of planetary nebulae. We present a study of the central stars of NGC 1514, revealed to be a highly eccentric binary system with a period of more than nine years, making it the longest known period central star to date. The morphology of the nebula shows the clear shaping influence of the binary in spite of its long period, highlighting that even wide companions can have a very significant impact on mass loss evolution. This study demonstrates not only the importance of wide binaries in late stellar evolution but also the importance of long-term monitoring campaigns which are only now possible due to modern high-stability instruments and queue mode observing. (See poster).

Highlights on Spanish Astrophysics X, Proceedings of the XIII Scientific Meeting of the Spanish Astronomical Society held on July 16 – 20, 2018, in Salamanca, Spain. B. Montesinos, A. Asensio Ramos, F. Buitrago, R. Schödel, E. Villaver, S. Pérez-Hoyos, I. Ordóñez-Etxeberria (eds.), 2019

The OCCASO open clusters revisited with Gaia data.

C. Jordi[1], R. Carrera[2], L. Balaguer-Núñez[1], L. Casamiquela[3], J. Carbajo-Hijarrubia[1], M. Romero-Gómez[1], S. Blanco-Cuaresma[4] and E. Pancino[5]

[1] Dept. FQA, Institut de Ciències del Cosmos. Universitat de Barcelona IEEC-UB, Barcelona, Spain
[2] INAF-Osservatorio Astronomico di Padova
[3] Laboratoire d'Astrophysique de Bordeaux
[4] Harvard-Smithsonian Center for Astrophysics
[5] INAF-Osservatorio Astronomico di Arcetri

Abstract

Galactic Open Clusters (OCs) are crucial to investigate the formation and evolution of the Galactic disc. However, complete information is available for only 5% of the 2100 OCs in the Milky Way listed in the literature. Therefore, OCs are main targets in space missions (Gaia, Kepler), and in large ground-based spectroscopic surveys. However, these ground-based surveys are mainly sampling the Southern hemisphere OCs (Gaia-ESO survey, GALAH), or do not have an specific program for homogeneously sample OCs (APOGEE). The Open Clusters Chemical Abundance from Spanish Observatory survey (OCCASO) aims to complement these surveys obtaining detailed abundances for more than 20 chemical species in around 30 Northern OCs (Casamiquela et al, 2016 MNRAS 458, 3150). The advent of Gaia Data Release 2 (DR2, Gaia Collaboration 2018, arXiv:1804.09365) has allowed a redetermination of the membership and of the mean proper motions and parallaxes for all known clusters (Cantat-Gaudin et al, arXiv:1805.08726). Using these data, we have revisited the membership of our observed stars and obtained mean parameters for all our OCCASO OCs. Gaia DR2 mean parallaxes and proper motions and OCCASO radial velocities have been combined to obtain 3D spatial velocities and peculiar velocities with respect to the RSR. The results significantly differ from our previous calculations due to the differences with previous proper motions studies. The orbits of the OCs have been calculated using a gravitational potential of the Galaxy with two spirals arms and no central bar (Pichardo et al 2003, ApJ 582, 230). The assumed mass of the arms is 5% of the mass disc. The arms have a pitch angle of 12 deg and a pattern speed of 30 km/s/kpc. All OCs show velocities and orbits typical of the disc. (See poster).

Highlights on Spanish Astrophysics X, Proceedings of the XIII Scientific Meeting of the Spanish Astronomical Society held on July 16 – 20, 2018, in Salamanca, Spain. B. Montesinos, A. Asensio Ramos, F. Buitrago, R. Schödel, E. Villaver, S. Pérez-Hoyos, I. Ordóñez-Etxeberria (eds.), 2019

Direct Deconvolution: a method to minimize the effects of the observational window on power spectra.

Lares-Martiz,M.[1], Garrido,R.[1], Pascual-Granado,J.[1], and Scargle,J.[2]

[1] Institute of Astrophysics of Andalucía (IAA-CSIC)
[2] NASA Ames Research Center

Abstract

Fourier transforms of observed light curves, obtained by ground observations or by space photometers, exhibit interference effects that are consequence of the convolution of the true Fourier transform with a spectral window (Deeming, 1974).

These interferences in the power spectra makes the analysis of them very difficult in terms of the asteroseismology techniques, specifically to identify modes of non-radial oscillation of multiple periodic variable stars.

This identification has been made by heuristic methods such as the detection of periodicities or patterns that match the "large separation" or "small separation" as used in the sun itself and solar like stars. But these frequencies patterns are not easily observed for δ Scuti stars or other types of variable stars because of their denser power spectra. In order to identify potential patterns, it is necessary to obtain a reliable list of frequencies that really belong to the star and not due to the external causes given by spurious peaks in the power spectra.

For the moment, the reliable list has been obtained using algorithms such as Period04 or SigSpec that performs a prewhitening of the light curve in the same manner as the CLEAN algorithm (Roberts, 1986) do for radio observation. But in our case this is not a solution because the frequencies found must have a physical meaning and not be just a way to recover a CLEANed radio image.

The Direct Deconvolution method is aimed to fulfill the purpose of removal or minimizing the interference in power spectra due to the observational window. Its theoretical basis are explained in this poster, as well as some issues to be addressed before the full implementation of the method regarding numeric problems that arise when testing the algorithm. (See poster).

Highlights on Spanish Astrophysics X, Proceedings of the XIII Scientific Meeting of the Spanish Astronomical Society held on July 16 – 20, 2018, in Salamanca, Spain. B. Montesinos, A. Asensio Ramos, F. Buitrago, R. Schödel, E. Villaver, S. Pérez-Hoyos, I. Ordóñez-Etxeberria (eds.), 2019

Spectral synthesis of CARMENES M-type stars: stellar atmospheric parameters.

F.J. Lázaro[1], G. Montes[1], H.M. Tabernero[1,12], E. Marfil[1], J.A. Caballero[2], J. I. González Hernández[3] CARMENES Consortium[1,2,3,4,5,6,7,8,9,10,11]

[1] Universidad Complutense de Madrid
[2] Centro de Astrobiología
[3] Instituto de Astrofísica de Canarias
[4] Institut für Astrophysik Göttingen
[5] Institut de Ciòncies de l'Espai
[6] Thüringer Landessternwarte Tautenburg
[7] Max-Planck-Institut für Astronomie
[8] Hamburger Sternwarte
[9] Landessternwarte Königstuhl
[10] Instituto de Astrofísica de Andalucía
[11] Centro Astronómico Hispano-Alemán-Calar Alto Observatory
[12] Universidad de Alicante

Abstract

We show our very first results regarding the stellar atmospheric parameter determinations ($T_{\rm eff}$, log g, [Fe/H]) of M-type stars observed with CARMENES [3] by means of the spectral synthesis method. We have selected spectral ranges around iron and titanium lines and molecular bands in three reference M-type stars: GX And (M1.0 V), Luyten's star (M3.5 V),and Teegarden's star (M7.0 V). We employ PHOENIX stellar model atmospheres [2], the radiative transfer code TurboSpectrum [1] and line data from the VALD3 database [4] to obtain a grid of synthetic spectra, and a Markov Chain Monte Carlo process implemented in SteParSyn code [5] to derive the value of the stellar atmospheric parameters. (See poster).

Acknowledgments

FJCI-2014-23001, FPU15/01476, AYA2015-68012-C2-2-P, AYA2016-79425–C3–1/2–P

References

[1] Álvarez, R., Plez, B. 1998, A&A, 330

[2] Husser, T.O., Wende-von Berg, S., Dreizler, S., et al. 2013, A&A, 553, A6

[3] Quirrenbach, A., Amado, P. J., Caballero, J. A., et al. 2016, ProcSPIE, 9908, 990812

[4] Ryabchikova, T., & Pakhomov, Y. 2015, Baltic Astronomy, 24, 453

[5] Tabernero, H. M., Dorda R., Negueruela, I., & González-Fernández, C. 2018, MNRAS, 476, 3106

Highlights on Spanish Astrophysics X, Proceedings of the XIII Scientific Meeting of the Spanish Astronomical Society held on July 16 – 20, 2018, in Salamanca, Spain. B. Montesinos, A. Asensio Ramos, F. Buitrago, R. Schödel, E. Villaver, S. Pérez-Hoyos, I. Ordóñez-Etxeberria (eds.), 2019

TROY – The Search for Exotrojan Planets.

J. Lillo-Box

European Southern Observatory (ESO), Alonso de Cordova 3107, Vitacura, Santiago, Chile

Abstract

As the field of extrasolar planets evolves with numerous discoveries of new and diverse planets, we can start thinking in more challenging (observationally speaking) scientific cases that can bring up new, hidden pieces of the exoplanetary science puzzle. This is the case of the TROY project, a multi-technique effort to look for the first co-orbital planets and to provide estimates of the occurrence rate of these bodies down to the Earth-mass regime. Despite being missed in our Solar System, where only kilometer-size (or smaller) bodies co-rotate with most of the planets, theory allows even equal-mass planets to co-exist in the same orbit. In this poster I present the news on the TROY project including the last ground-based observations, the results from the first radial velocity search involving 46 planetary systems and the first results from our Kepler/K2 search. (See poster).

Acknowledgments

The TROY project is composed of a team of experts in different fields that is critically helping in the development of this project: A. Leleu, A.C.M. Correia, P. Robutel, P. Figueira, N.C. Santos, D. Barrado, J. Faria, M. Lendl, H. Parviainen, M. Mallonn, H.M.J. Boffin.

Highlights on Spanish Astrophysics X, Proceedings of the XIII Scientific Meeting of the Spanish Astronomical Society held on July 16 – 20, 2018, in Salamanca, Spain. B. Montesinos, A. Asensio Ramos, F. Buitrago, R. Schödel, E. Villaver, S. Pérez-Hoyos, I. Ordóñez-Etxeberria (eds.), 2019

Analysis of the physical properties of jets/outflows in T Tauri stars.

F. Lopez-Martinez[1] **and J.F. Gameiro**[1,2]

[1] Instituto de Astrofísica e Ciências do Espaço, Universidade do Porto, CAUP, Rua das Estrelas, PT4150-762 Porto, Portugal.
[2] Departamento de Física e Astronomia, Faculdade de Ciências, Universidade do Porto, Rua do Campo Alegre, 4150-762 Porto, Portugal.

Abstract

Jets and outflows from Young stellar objects are fundamental for the star formation process. Accretion has a significant impact on the evolution of low-mass stars by providing both mass and angular momentum. However, most of the actively accreting T Tauri stars rotate rather slowly. Outflows/jets are one of the mechanisms through which stars may lose angular momentum. The evolution and ultimate fate of jets/outflows and circumstellar accretion disks have become increasingly important issues since the discovery of extrasolar planetary systems. The optical forbidden [N II], [O I] and [S II] lines are good tracers of outflows and jets. They are optically thin providing us important information about the gas physics where they are formed. In many T Tauri stars these lines are characterized by two components: a high velocity component (HVC) and a low velocity component (LVC). In this work we derived the physical properties of the HVC and LVC emitting region where [N II], [O I] and [S II] lines are formed using their theoretical flux ratios. We analyzed these properties for DG Tau, SZ 102, CW Tau and RW Aur jets. We also studied the origin of the LVC, which is not yet fully understood. In addition, we calculated mass loss rates for all the observations. We found two well-defined ranges of temperatures and densities for the emitting region: one with $4.125 \leq \log T_{\rm e}({\rm K}) \leq 4.55$ and $2.25 \leq \log n_{\rm e}({\rm cm}^3) \leq 5.25$ and another one with $5.25 \leq \log T_{\rm e}({\rm K}) \leq 5.6$ and $5.25 \leq \log n_{\rm e}({\rm cm}^3) \leq 6.75$. For SZ 102 the LVC is formed in a region with low density and temperature, whereas for DG Tau and CW Tau the LVC is emitted in a hotter and denser region. Peak velocities and full width at half maximum of the LVC point out that its origin is from a MHD disk wind at 0.05-1.69 AU from the source and that the lines are broadened by Keplerian rotation. (See poster).

Highlights on Spanish Astrophysics X, Proceedings of the XIII Scientific Meeting of the Spanish Astronomical Society held on July 16 – 20, 2018, in Salamanca, Spain. B. Montesinos, A. Asensio Ramos, F. Buitrago, R. Schödel, E. Villaver, S. Pérez-Hoyos, I. Ordóñez-Etxeberria (eds.), 2019

LiLiMaRlin and applications to OWN, MONOS, and CollDIBs.

Jesús Maíz Apellániz[1], Emilio Trigueros Páez[1,2], Irene Jiménez Martínez[1,3], Rodolfo H. Barbá[4], Sergio Simón-Díaz[5], Anne Pellerin[6], Ignacio Negueruela[2], and João Rodrigo Souza Leão[7]

[1] Centro de Astrobiología, CSIC-INTA, Spain
[2] Universidad de Alicante, Spain
[3] Universidad Complutense de Madrid, Spain
[4] Universidad de La Serena, Chile
[5] Instituto de Astrofísica de Canarias and Universidad de La Laguna, Spain
[6] State University of New York at Geneseo, U.S.A.
[7] Universidade Federal do Rio Grande do Norte, Brazil

Abstract

LiLiMaRlin is a library of libraries of massive-star high-resolution optical spectra built by collecting data from [a] our spectroscopic surveys (OWN, IACOB. NoMaDS, and CAFÉ-BEANS) and programs and [b] searches in public archives. The current version has 18 077 spectra of 1665 stars obtained with seven different telescopes (HET 9.2 m, NOT 2.56 m, CAHA 2.2 m, MPG/ESO 2.2 m, OHP 1.93 m, Mercator 1.2 m, and Stella 1.2 m). All the spectra have been filtered to eliminate misidentifications and bad-quality ones, uniformly reprocessed, and placed on a common format. We present applications of this library of libraries to the analysis of spectroscopic binaries (OWN and MONOS, see poster by E. Trigueros Páez at this meeting) and the study of the interstellar medium (CollDIBs). We discuss our plans for the future. (See poster).

Highlights on Spanish Astrophysics X, Proceedings of the XIII Scientific Meeting of the Spanish Astronomical Society held on July 16 – 20, 2018, in Salamanca, Spain. B. Montesinos, A. Asensio Ramos, F. Buitrago, R. Schödel, E. Villaver, S. Pérez-Hoyos, I. Ordóñez-Etxeberria (eds.), 2019

The Gaia photometric calibration and results on Galactic runaways.

Jesús Maíz Apellániz[1], Michelangelo Pantaleoni González[1,2], Daniel J. Lennon[3], Rodolfo H. Barbá[4], and Michael Weiler[5]

[1] Centro de Astrobiología, CSIC-INTA, Spain
[2] Universidad Complutense de Madrid, Spain
[3] European Space Agency, ESAC, Spain
[4] Universidad de La Serena, Chile
[5] Universitat de Barcelona, Spain

Abstract

We present results on two different Gaia-related topics. First, we describe our efforts to calibrate the three Gaia photometric passbands G, $G_{\rm BP}$, and $G_{\rm RP}$. We have built a new spectrophotometric HST/STIS library and used it to derive new sensitivity curves and zero points for the three bands, including recipes on how to correct some cases. Second, we present our results on Galactic runaway stars using Gaia DR1 proper motions: we detect 76 runaway stars, 17 (possibly 19) of them not previously identified as such. (See poster).

Highlights on Spanish Astrophysics X, Proceedings of the XIII Scientific Meeting of the Spanish Astronomical Society held on July 16 – 20, 2018, in Salamanca, Spain. B. Montesinos, A. Asensio Ramos, F. Buitrago, R. Schödel, E. Villaver, S. Pérez-Hoyos, I. Ordóñez-Etxeberria (eds.), 2019

The 1989 and 2015 outbursts of V404 Cygni: a global study of optical features.

D. Mata Sánchez [1,2,3], T. Muñoz-Darias[2,3], and Jorge Casares[2,3]

[1] Jodrell Bank Centre for Astrophysics, School of Physics and Astronomy, The University of Manchester, Manchester M13 9PL, UK
[2] Instituto de Astrofísica de Canarias (IAC), E-38205 La Laguna, Tenerife, Spain
[3] Departamento de astrofísica, Univ. de La Laguna, E-38206 La Laguna, Tenerife, Spain

Abstract

The black hole transient V404 Cygni exhibited a bright outburst in June 2015 that was intensively followed over a wide range of wavelengths. Our team obtained high time resolution optical spectroscopy ($\sim$ 90 s), which included a detailed coverage of the most active phase of the event. We present a database consisting of 651 optical spectra obtained during this event, that we combine with 58 spectra gathered during the fainter December 2015 sequel outburst, as well as with 57 spectra from the 1989 event. We previously reported the discovery of wind-related features (P-Cygni and broad-wing line profiles) during both 2015 outbursts. Here, we build diagnostic diagrams that enable us to study the evolution of typical emission line parameters, such as line fluxes and equivalent widths, and develop a technique to systematically detect outflow signatures. We find that these are present throughout the outburst, even at very low optical fluxes, and that both types of outflow features are observed simultaneously in some spectra, confirming the idea of a common origin. We also show that the nebular phases depict loop patterns in many diagnostic diagrams, while P-Cygni profiles are highly variable on time-scales of minutes. The comparison between the three outbursts reveals that the spectra obtained during June and December 2015 share many similarities, while those from 1989 exhibit narrower emission lines and lower wind terminal velocities. The diagnostic diagrams presented in this work have been produced using standard measurement techniques and thus may be applied to other active low-mass X-ray binaries. (See poster).

Highlights on Spanish Astrophysics X, Proceedings of the XIII Scientific Meeting of the Spanish Astronomical Society held on July 16 – 20, 2018, in Salamanca, Spain. B. Montesinos, A. Asensio Ramos, F. Buitrago, R. Schödel, E. Villaver, S. Pérez-Hoyos, I. Ordóñez-Etxeberria (eds.), 2019

One correlation to rule them all (linking young stars, clouds, and galaxies).

I. Mendigutía[1], C. J. Lada[2], and R. D. Oudmaijer[3]

[1] Centro de Astrobiología (CSIC-INTA), Departamento de Astrofísica, ESA-ESAC Campus, PO Box 78, 28691 Villanueva de la Cañada, Madrid, Spain.
[2] Harvard-Smithsonian Center for Astrophysics, 60 Garden Street, Cambridge, MA 02138, USA.
[3] School of Physics and Astronomy, University of Leeds, Woodhouse Lane, Leeds LS2 9JT, UK.

Abstract

The star formation rate linearly correlates with the dense gas mass involved in the formation of stars both for distant galaxies and star-forming clouds in our Galaxy. Similarly, recent studies confirm that the mass accretion rate and the circumstellar gas disk mass of young, Class II stars are also linearly correlated. This poster shows that both relations can be unified. We find a statistically significant, roughly linear correlation between the rate of gas transformed into stars and the mass of gas directly involved on star formation, ranging 16 orders of magnitude and encompassing kpc-size galaxies, pc-size star forming clouds within our Galaxy, and young stars with au-size protoplanetary disks. In order to explain this finding we propose a bottom-up hypothesis suggesting that a relation between the stellar mass accretion rate and the total (disk+envelope in Class 0/I stars) circumstellar mass drives the correlation in clouds (hosting protostars) and galaxies (hosting clouds). Lines of evidence supporting this hypothesis and a future observational test are provided. If this scenario was confirmed, theories aiming to explain the correlations for stars, clouds, and galaxies should not remain isolated from each other. Instead, all scales and physical systems involved in one single, global correlation must be considered. Additional details can be found in Mendigutía, Lada, & Oudmaijer, 2018, A&A, 618, A119. (See poster).

Highlights on Spanish Astrophysics X, Proceedings of the XIII Scientific Meeting of the Spanish Astronomical Society held on July 16 – 20, 2018, in Salamanca, Spain. B. Montesinos, A. Asensio Ramos, F. Buitrago, R. Schödel, E. Villaver, S. Pérez-Hoyos, I. Ordóñez-Etxeberria (eds.), 2019

Decoding the local star formation scenario with the Besançon Galaxy Model.

R. Mor[1], A.C. Robin[2], and F. Figueras[1]

[1] Dept. Física Quàntica i Astrofísica, Institut de Ciències del Cosmos, Universitat de Barcelona (IEEC-UB), Martí Franquès 1, E08028 Barcelona, Spain.
[2] Institut Utinam, CNRS UMR6213, Université de Bourgogne Franche-Comté, OSU THETA , Observatoire de Besançon, BP 1615, 25010 Besançon Cedex, France.

Abstract

The recent full sky large data surveys (e.g. Gaia data release 2) represents a challenge for the Galaxy modelling and requires new frameworks and tools to deal with huge amounts of data. We developed a new strategy to infer, all at once, the parameters describing the local star formation history (SFH), the initial mass function (IMF) and the density laws of the Galactic thin disc component by comparing synthetic versus observed colour-magnitude diagrams. The developed framework combines both the generation of Besançon Galaxy Model fast approximate simulations (BGM FASt; [1]) and approximate Bayesian computation methods, to obtain a posterior probability distribution function of the inferred parameters. A robust mathematical development and the adequate codification, using Apache Spark and Apache Hadoop environments, make BGM FASt about 10^4 times faster than the standard Besançon Galaxy Model and specially suited to deal with huge data sets.
From the analysis of Tycho-2 colour-apparent magnitude diagrams we want to spotlight the resulting thin disc SFH with a decreasing trend and a present rate of star formation of $1.2{\pm}0.2 M_{\odot}/yr$. It is known that in the colour-apparent magnitude diagrams, as the distance of the star is not taken into account, the position of giants and main sequence stars are degenerated . Additionally we estimate, using the Besançon Galaxy Model, that the position of old stars (ages$> 8 Gyr$) is mixed with stars with masses larger than $1.53 M_{\odot}$. This lack of information of the intrinsic brightness of the stars is a clear handicap when aiming to derive the local IMF and SFH from the population synthesis side. Gaia parallaxes are very valuable to infer the intrinsic brightness of the stars and brake some of this degeneracies. Gaia parallaxes, colours and magnitudes represents an unprecedented opportunity to constrain the IMF and the SFH using BGM FASt. (See poster).

References

[1] Mor, R. and Robin, A. C. and Figueras, F. and Antoja, T., 2018, ArXiv e-prints, arXiv:1809.03511

Highlights on Spanish Astrophysics X, Proceedings of the XIII Scientific Meeting of the Spanish Astronomical Society held on July 16 – 20, 2018, in Salamanca, Spain. B. Montesinos, A. Asensio Ramos, F. Buitrago, R. Schödel, E. Villaver, S. Pérez-Hoyos, I. Ordóñez-Etxeberria (eds.), 2019

A new classification scheme for B-type stars.

Ignacio Negueruela[1], Sergio Simón[2], Ricardo Dorda[1], Carlos González-Fernández[3], Gonzalo Holgado2[2], Jesús Maíz Apellániz[4], Maria Monguió[5] and Sara R. Berlanas[2]

[1]Universidad de Alicante (Spain)
[2]Instituto de Astrofísica de Canarias (Spain)
[3]Institute of Astronomy, University of Cambridge (UK)
[4]Centro de Astrobiología (Spain)
[5]University of Hertfordshire (UK)

Abstract

The criteria for spectral classification of B-type stars were established almost 80 years ago from low-resolution spectra on photographic plates. Since *Hipparcos* measured accurate distances for nearby stars, it has been clear that, although sound in general terms, the current set of MK standard stars in the B range has many inconsistencies, with luminosity class not always reflecting the actual intrinsic brightness of an object. As part of the efforts to build the IACOB database of high-quality, high-resolution spectra of OB stars, we have gathered the largest existing collection of spectra of B-type MK standards. We have developed a new classification scheme, based on high-S/N spectra at resolving power $R = 4\,000$, that solves most of the inconsistencies of the original system. The result is a new list of standard stars that will be used for a catalogue in the *Gaia* RVS spectral range. (See poster).

Highlights on Spanish Astrophysics X, Proceedings of the XIII Scientific Meeting of the Spanish Astronomical Society held on July 16 – 20, 2018, in Salamanca, Spain. B. Montesinos, A. Asensio Ramos, F. Buitrago, R. Schödel, E. Villaver, S. Pérez-Hoyos, I. Ordóñez-Etxeberria (eds.), 2019

Observing stellar flares with Bayesian Blocks and Super-resolution techniques in A-type stars observed by Kepler.

J. Pascual-Granado[1], A. García Hernández[2], and J. J. Pérez Moreno[3]

[1] Instituto de Astrofísica de Andalucía - CSIC
[2] Universidad de Granada
[3] Universidad Internacional de Valencia

Abstract

Flares are a sudden release of energy in the stellar atmospheres that can be observed photometrically at all wavelengths across the spectrum, especially in UV and X rays. The origin is the reconnection of magnetic field lines. They are observed in solar-type stars since there is a dynamo mechanism and a convective envelope that can support the magnetic field lines. On the other side, theoretical models predict a very thin, if any, convective envelope in A-type stars but some observations point to a convective envelope that might be effective in producing granulation effects and even magnetic activity. In order to detect and characterize stellar flares we need a systematic and self-consistent detection algorithm. Nevertheless, to date all the results obtained by flares detection and their characterization that can be found in the literature are based on a set of ad-hoc criteria that are verified manually with no physical support. We are developing an automatic detection pipeline based on Bayesian Blocks detection and wavelet decomposition that will be capable to detect a flare candidate and reject false positives providing at the same time physical parameters that can be useful for the characterization of stellar activity in A-type and other stars. Here we will introduce the algorithm for flares detection using a sample of Kepler stars and the characterization of the candidates using superresolution techniques.

Highlights on Spanish Astrophysics X, Proceedings of the XIII Scientific Meeting of the Spanish Astronomical Society held on July 16 – 20, 2018, in Salamanca, Spain. B. Montesinos, A. Asensio Ramos, F. Buitrago, R. Schödel, E. Villaver, S. Pérez-Hoyos, I. Ordóñez-Etxeberria (eds.), 2019

Clustering properties of Herbig Ae/Be stars.

A. Pérez Blanco[1,2], R. Oudmaijer[1], R. Pérez-Martinez[2], and D. Baines[3]

[1] University of Leeds (Leeds - UK)
[2] ISDEFE (ESAC, Madrid - Spain)
[3] QUASAR (ESAC, Madrid - Spain)

Abstract

We study Herbig Ae/Be (HAeBe) stars which are optically visible pre-main sequence stars of intermediate-mass. They represent the most massive objects to experience an optically visible pre-main sequence phase, bridging the gap between low- and high-mass stars. Building on the ideas from Testi et al. (1997, 1998, 1999), we are investigating the presence of clusters around previously known and newly discovered intermediate-mass pre-main sequence HAeBe stars with the detailed astrometric data offered by Gaia. This will enable us to determine the position of the HAeBe stars in the HR diagram and allow us to detect and confirm the presence of the clusters around them. In the poster, we outline the preliminary results obtained with Gaia DR2 through the algorithm we developed for the detection and analysis of the clusters and clustering properties of the HAeBe stars. (See poster).

Highlights on Spanish Astrophysics X, Proceedings of the XIII Scientific Meeting of the Spanish Astronomical Society held on July 16 – 20, 2018, in Salamanca, Spain. B. Montesinos, A. Asensio Ramos, F. Buitrago, R. Schödel, E. Villaver, S. Pérez-Hoyos, I. Ordóñez-Etxeberria (eds.), 2019

Circumstellar effects on the Li and Ca abundances in massive Galactic O-rich AGB stars.

V. Pérez-Mesa[1,2], O. Zamora[1,2], D. A. García-Hernández[1,2], Y. Osorio[1,2], T. Masseron[1,2], B. Plez[3], A. Manchado[1,2,4], A. I. Karakas[5] and M. Lugaro[5,6]

[1] Instituto de Astrofísica de Canarias (IAC), E-38205 La Laguna, Tenerife, Spain
[2] Universidad de La Laguna (ULL), Departamento de Astrofísica, E-38206 La Laguna, Tenerife, Spain
[3] Laboratoire Univers et Particules de Montpellier, Université de Montpellier2, CNRS, 34095 Montpellier, France
[4] Consejo Superior de Investigaciones Científicas (CSIC), E-28006 Madrid, Spain
[5] Monash Centre for Astrophysics, School of Physics and Astronomy, Monash University, VIC3800, Australia
[6] Konkoly Observatory, Research Centre for Astronomy and Earth Sciences, Hungarian Academy of Sciences, 1121 Budapest, Hungary

Abstract

We explore the circumstellar effects on the Li and Ca abundances determination in a complete sample of massive Galactic AGB stars. The Li abundance is an indicator of the hot bottom burning (HBB) activation, while the total Ca abundance could be affected by overproduction of the short-lived radionuclide ^{41}Ca by the *s*-process. The Li abundances were previously studied with hydrostatic models, while the Ca abundances are determined here for the first time. The pseudo-dynamical abundances of Li and Ca are very similar to the hidrostatic ones, indicating that the circumstellar effects are almost negligible. The new Li abundances confirm the (super-)Li-rich character of the sample Li-detected stars, supporting the HBB activation in massive Galactic AGB stars. Most sample stars display nearly solar Ca abundances that are consistent with predictions from the *s*-process nucleosynthesis models. A minority of the sample stars show a significant Ca depletion. Possible reasons for their (unexpected) low Ca content are given. (See poster).

Highlights on Spanish Astrophysics X, Proceedings of the XIII Scientific Meeting of the Spanish Astronomical Society held on July 16 – 20, 2018, in Salamanca, Spain. B. Montesinos, A. Asensio Ramos, F. Buitrago, R. Schödel, E. Villaver, S. Pérez-Hoyos, I. Ordóñez-Etxeberria (eds.), 2019

Establishing the nature of X-ray binaries through infrared spectroscopy.

J. J. Rodes[1], G. Bernabeu[1], J. M. Torrejón[1], A. Magazzù[2], and E. Solano[3]

[1] University of Alicante
[2] Telescopio Nazionale Galileo
[3] Centro de Astrobiología

Abstract

European Space Agency's INTEGRAL (International Gamma-Ray Astrophysics Laboratory) satellite have discovered new X-ray sources due to its sensitivity above 20 keV. Most of these sources suffer from high absorption and the classical blue band spectral classification region is normally not accessible. This can be overcome, however, through infrared spectroscopy. The characterisation of these systems can influence the population synthesis models currently in use. In this work, we present the first H and K band spectra for three INTEGRAL sources using the $NICS$ instrument mounted on the *Telescopio Nazionale Galileo* (TNG) 3.5-m telescope. This study was complemented with infrared photometry from *UKIDSS*, *2MASS*, *WISE* and *NEOWISE* databases. Our spectra show all the significant features in emission and are, thus, consistent with a Be nature of the companions. Owing to their X-ray characteristics, these systems were classified as Be X-ray binaries. This allowed us to refine its distances to the sources using suitable calibrations that take into account the contamination by the circumstellar disk. (See poster).

Acknowledgments

This work was supported partially by the project **ESP2017-85691-P** AM acknowledges the support by the **VIDI de la UA** under visiting programme **INV17-26**.

Highlights on Spanish Astrophysics X, Proceedings of the XIII Scientific Meeting of the Spanish Astronomical Society held on July 16 – 20, 2018, in Salamanca, Spain. B. Montesinos, A. Asensio Ramos, F. Buitrago, R. Schödel, E. Villaver, S. Pérez-Hoyos, I. Ordóñez-Etxeberria (eds.), 2019

VOSA: SED building and analysis of thousands of stars in the framework of Gaia.

C. Rodrigo[1,2], E. Solano[1,2], A. Bayo[3,4], M. Cortés-Contreras[1,2] and F. Jiménez-Esteban[1,2]

[1] Centro de Astrobiología (INTA-CSIC)
[2] Spanish Virtual Observatory
[3] IFA, U. de Valparaíso, Chile
[4] Núcleo Milenio de Formación Planetaria, Valparaíso, Chile

Abstract

VOSA (Virtual Observatory Sed Analyzer, http://svo2.cab.inta-csic.es/theory/vosa/) is a public web-tool developed by the Spanish Virtual Observatory (http://svo.cab.inta-csic.es/) and designed to help users to (1) build Spectral Energy Distributions (SEDs) combining private photometric measurements with data available in VO services, (2) obtain relevant properties of these objects (distance, extinction, etc) from VO catalogues, (3) analyze them comparing observed photometry with synthetic photometry from different collections of theoretical models or observational templates, using different techniques (chi-square fit, Bayesian analysis) to estimate physical parameters of the observed objects (temperature, mass, luminosity, etc), and use these results to (4) estimate masses and ages using collections of isochrones and evolutionary tracks from the VO. In particular, VOSA offers the advantage of deriving physical parameters using all the available photometric information instead of a restricted subset of colors. The results can be downloaded in different formats or sent to other VO tools using SAMP. VOSA is in operation since 2008 (Bayo et al, 2008, A&A 492,277B), with more than 1600 active users ($\sim$5 million objects analysed), and $\sim$ 150 refereed papers published making use of this tool.

We have upgraded VOSA to provide access to Gaia DR2 photometry and parallaxes and give a reliable estimation of the physical parameters (effective temperatures, gravities, metallicities, masses and ages) of thousands of objects at a time. This upgrade has required the implementation of a new computation paradigm, including a distributed environment, the capability of submitting and processing jobs in an asynchronous way, the use of paralelized computing to speed up processes ($\sim$ ten times faster) and a new design of the web interface. (See poster).

Highlights on Spanish Astrophysics X, Proceedings of the XIII Scientific Meeting of the Spanish Astronomical Society held on July 16 – 20, 2018, in Salamanca, Spain. B. Montesinos, A. Asensio Ramos, F. Buitrago, R. Schödel, E. Villaver, S. Pérez-Hoyos, I. Ordóñez-Etxeberria (eds.), 2019

The spatial distribution of Cyg OB2 from *Gaia* DR2.

S. R. Berlanas[1,2], N. Wright[3] and A. Herrero[1,2]

[1] Instituto de Astrofísica de Canarias, 38200 La Laguna, Tenerife, Spain
[2] Departamento de Astrofísica, Universidad de La Laguna, 38205 La Laguna, Tenerife, Spain
[3] Astrophysics Group, Keele University, Keele, ST5 5BG, UK

Abstract

A key difficulty in the study of Milky Way massive stars and OB associations has been the large uncertainty in their distances, hindering the comparison with theories of stellar and cluster evolution. The recent second release of data from the *Gaia* satellite has provided unprecedented high quality astrometry for more than 1.3 billion of objects, all of them with measured parallaxes. For the first time ever, we have explored the spatial substructure of the Cygnus OB2 association using parallaxes from the recent second *Gaia* data release. We used a Bayesian inference procedure to model the observed parallax distribution. Our analysis reveals a foreground group separated from the main Cygnus OB2 population. This result could unravel the internal kinematics and evolution of this massive star-forming region. (See poster).

Highlights on Spanish Astrophysics X, Proceedings of the XIII Scientific Meeting of the Spanish Astronomical Society held on July 16 – 20, 2018, in Salamanca, Spain. B. Montesinos, A. Asensio Ramos, F. Buitrago, R. Schödel, E. Villaver, S. Pérez-Hoyos, I. Ordóñez-Etxeberria (eds.), 2019

The intricate nebular architecture of The Rotten Egg disclosed by ALMA.

C. Sánchez Contreras[1], J. Alcolea[2], V. Bujarrabal[3], A. Castro-Carrizo[4], L. Velilla Prieto[5], M. Santander-García[2], G. Quintana-Lacaci[5], and J. Cernicharo[5]

[1] Centro de Astrobiología (CSIC-INTA). Postal address: ESAC, Camino Bajo del Castillo s/n, Urb. Villafranca del Castillo, E-28691 Villanueva de la Cañada, Madrid, Spain
[2] Observatorio Astronómico Nacional (IGN), Alfonso XII No 3, 28014 Madrid, Spain
[3] Observatorio Astronómico Nacional (IGN), Ap 112, 28803 Alcalá de Henares, Madrid, Spain
[4] Institut de Radioastronomie Millimetrique, 300 rue de la Piscine, 38406 Saint Martin d'Heres, France
[5] Instituto de Fisica Fundamental (CSIC), C/ Serrano, 123, E-28006, Madrid, Spain

Abstract

In only a few years of operations, ALMA is revolutionising the field of AGB-to-PN research by providing unprecedented detailed information on the complex nebular architecture, dynamics and chemistry of the envelopes of low-to-intermediate mass stars in their late stages of the evolution. We report continuum and molecular line mapping studies with ALMA of OH 231.8+4.2 (also known as *The Rotten Egg*), a pre-Planetary Nebula (pPN) candidate that is key to understand the complex PN-shaping process. The high angular resolution (0.2-0.3 arcsec) and sensitivity of our ALMA maps provide the most detailed and accurate description of the overall nebular structure and kinematics of this object to date. We have identified a number of outflow components previously unknown. Species studied in this work include ^{12}CO, ^{13}CO, CS, SO, SO_2, OCS, SiO, SiS, H_3O^+, Na^{37}Cl and CH_3OH. The molecules Na^{37}Cl and CH_3OH are first detections in OH 231.8+4.2, with CH_3OH being also a first detection in an AGB star. Our ALMA maps bring to light the totally unexpected position of the mass-lossing AGB star relative to the large-scale outflow and disclose a compact bipolar outflow that emerges from QXPup's vicinity (amongst other puzzling discoveries). The presence of bipolar ejections less than $\sim$80 yr old indicate that the collimated fast wind engine is still active at the core of this outstanding object. (See poster).

Highlights on Spanish Astrophysics X, Proceedings of the XIII Scientific Meeting of the Spanish Astronomical Society held on July 16 – 20, 2018, in Salamanca, Spain. B. Montesinos, A. Asensio Ramos, F. Buitrago, R. Schödel, E. Villaver, S. Pérez-Hoyos, I. Ordóñez-Etxeberria (eds.), 2019

Determining the radius of an open cluster from stellar proper motions.

Nestor Sanchez[1,2], Emilio Alfaro[3], and Fatima Lopez-Martinez[4]

[1] Departamento de Física, Universidad de Murcia, E-30100 Murcia, Spain.
[2] Universidad Internacional de Valencia, Calle Pintor Sorolla 21, 46002, Valencia, Spain.
[3] Instituto de Astrofísica de Andalucía, CSIC, Glorieta de la Astronomía s/n, 18008, Granada, Spain.
[4] Centro de Astrofísica da Universidade do Porto, Rua das Estrelas, P-4150-762 Porto, Portugal.

Abstract

We propose a new method for calculating the radius of an open cluster in an objective way from an astrometric catalogue containing, at least, positions and proper motions. It uses the minimum spanning tree in the proper motion space to discriminate cluster stars from field stars and it quantifies the strength of the cluster-field separation. This is done for a range of different sampling radii from where the cluster radius is obtained as the size at which the best cluster-field separation is achieved. The novelty of this strategy is that the cluster radius is obtained independently of how its stars are spatially distributed. We test the reliability and robustness of the method with both simulated and real data from a well-studied open cluster (NGC 188), and apply it to UCAC4 data for five other open clusters with different catalogued radius values. NGC 188, NGC 1647, NGC 6603, and Ruprecht 155 yielded unambiguous radius values. However, ASCC 19 and Collinder 471 showed more than one possible solution, but it is not possible to know whether this is due to the involved uncertainties or due to the presence of complex patterns in their proper motion distributions. (See poster).

Highlights on Spanish Astrophysics X, Proceedings of the XIII Scientific Meeting of the Spanish Astronomical Society held on July 16 – 20, 2018, in Salamanca, Spain. B. Montesinos, A. Asensio Ramos, F. Buitrago, R. Schödel, E. Villaver, S. Pérez-Hoyos, I. Ordóñez-Etxeberria (eds.), 2019

The entropy of stellar oscilations.

J.C. Suárez[1,4], A. Moya[2,1], L.M. Sarro[3], A. García Hernández[1] and M. A. Mendoza[1]

[1] University of Granada (UGR). Dept. Theoretical Physics and Cosmology. 18071. Granada. Spain
[2] School of Physics and Astronomy. University of Birmingham.Edgbaston, Birmingham B15 2TT. England, UK.
[3] Dpto. de Inteligencia Artificial, UNED, c/ Juan del Rosal, 16, Madrid E-28040, Spain
[4] Instituto de Astrofísica de Andalucía (IAA-CSIC). Glorieta de Astronomía s\n, 18008, Grana

Abstract

This work presents a simple yet powerful method based on Shannon's entropy to detect frequency patterns in the stellar oscillation spectra. In particular we seek for the so-called "large separation", which is proportional to the stellar mean density. This method relies only on the observed power spectra. We show here how large separation of the Sun, solar-like stars and even A-F, main-sequence stars are accurately detected with this method. Likewise, an estimate of the mean densities for A-F stars is provided. Due to its simplicity, this method can easily be implemented in automated pipelines, like those providing precise values of the mass, radius, and age of stars hosting planets in space missions like TESS or PLATO.(See poster).

Highlights on Spanish Astrophysics X, Proceedings of the XIII Scientific Meeting of the Spanish Astronomical Society held on July 16 – 20, 2018, in Salamanca, Spain. B. Montesinos, A. Asensio Ramos, F. Buitrago, R. Schödel, E. Villaver, S. Pérez-Hoyos, I. Ordóñez-Etxeberria (eds.), 2019

O-Star binaries in the Northen Hemisphere. Explotation of the LiLiMaRlin data.

E. Trigueros Páez[1,2], I. Negueruela[1], and J. Maíz Apellániz [2]

[1] Departamento de Física Aplicada. Universidad de Alicante. Carretera San Vicente del Raspeig s/n. E-03 690 San Vicente del Raspeig, Spain.
[2] Centro de Astrobiología, CSIC-INTA. Campus ESAC. Camino bajo del castillo s/n. E-28 692 Villanueva de la Cañada, Madrid, Spain.

Abstract

We present the first stages of the MONOS: Multiplicity Of Northern O-type Spectroscopic systems, PhD Thesis of the PI of the poster, a description of the work done and to be done in the future. MONOS is an ambitious project designed to collect information about O-type spectroscopic multiple systems in the northern hemisphere, including an extensive bibliographic search, new orbital solutions, spectral classification both from the literature and from the Galactic O-Star Spectroscopic Survey (GOSSS). The MONOS project aim is therefore to exploit the data from LiLiMaRLin. LiLiMaRlin is a library of libraries of high-resolution spectroscopy of massive stars obtained from four different surveys (CAFÉ-BEANS, OWN, IACOB, and NoMaDS) and additional data from our own observing programs and public archives. (See poster).

Highlights on Spanish Astrophysics X, Proceedings of the XIII Scientific Meeting of the Spanish Astronomical Society held on July 16 – 20, 2018, in Salamanca, Spain. B. Montesinos, A. Asensio Ramos, F. Buitrago, R. Schödel, E. Villaver, S. Pérez-Hoyos, I. Ordóñez-Etxeberria (eds.), 2019

Identification of RR Lyrae stars in the Javalambre Photometric Local Universe Survey.

Héctor Vázquez Ramió[1], David Cristóbal-Hornillos[1], Alessandro Ederoclite[1,2], Devin Whitten[3], Vinicius Placco[3] and the J-PLUS Team

[1] Centro de Estudios de Física del Cosmos de Aragón, Teruel, Spain - Unidad Asociada CEFCA-IAA, CSIC, Spain
[2] Instituto de Astronomia, Geofísica e Ciências Atmosféricas, Universidade de São Paulo, Brazil
[3] Department of Physics and JINA Center for the Evolution of the Elements, University of Notre Dame, Notre Dame, IN 46556, USA

Abstract

The large and indiscriminate area Javalambre Photometric Local Universe Survey (J-PLUS) will observe, together with the survey's depth, $\mathrm{mag_{AB}}$=22 in the broad bands, makes it very convenient for deriving properties of the Galactic halo structure. Among the stars than can be used for that purpose, RR Lyrae pulsating stars are of outstanding importance for several reasons (see e.g. Sarajedini 2011): i) they are ubiquitous species in our Galaxy, so they can be found distributed virtually everywhere without being linked to any particular Galactic component; ii) they are relatively bright ($\mathrm{M_V}$ ∼0.6 for mean halo metallicity), so they are easily detectable up to a few hundred kpc from us; iii) their pulsation periods obey a period-luminosity-metallicity relation that makes them standard candles, becoming very useful to constraint distances; iv) they are stars older than 10 Gyr, so they are fair tracers of the Milky Way old component. J-PLUS will provide the SED of a unprecedented amount of RR Lyrae stars.

Here, the first preliminary mandatory step towards the achievement of those goals is addressed: the development of a method allowing the identification of RR Lyrae star candidates. The stellar locus of the RR Lyraes at different color-color spaces is inspected in order to isolate highly pure and complete candidate samples. A machine-learning technique is applyied, employing *Gaia* DR2 identifications (which are complete for *Gaia*'s $G \lesssim 17$) for building the training and test sets. The resulting completeness is 85% with a purity of 77%, obtaining $\sim 5,000$ RR Lyrae stars candidates with $17.0 \leq r \leq 19$ in J-PLUS DR1.

That result is using J-PLUS colors only. A significant improvement is expected when including variability information, e.g. from the comparison of J-PLUS photometry with other archives. This methodology will be applied to the whole survey data. (See poster).

Highlights on Spanish Astrophysics X, Proceedings of the XIII Scientific Meeting of the Spanish Astronomical Society held on July 16 – 20, 2018, in Salamanca, Spain. B. Montesinos, A. Asensio Ramos, F. Buitrago, R. Schödel, E. Villaver, S. Pérez-Hoyos, I. Ordóñez-Etxeberria (eds.), 2019

Gaia study on the formation of intermediate mass stars.

M. Vioque[1,2], R. D. Oudmaijer[1], D. Baines[3], I. Mendigutía[4] and R. Pérez-Martínez[2]

[1] School of Physics and Astronomy, University of Leeds, Leeds LS2 9JT, UK
[2] Ingeniería de Sistemas para la Defensa de España (Isdefe), XMM/Newton Science Operations Centre, ESA-ESAC Campus, PO Box 78, 28691 Villanueva de la Cañada, Madrid, Spain
[3] Quasar Science Resources for ESA-ESAC, ESAC Science Data Center, PO Box 78, 28691 Villanueva de la Cañada, Madrid, Spain
[4] Centro de Astrobiología (CSIC-INTA), Departamento de Astrofísica, ESA-ESAC Campus, PO Box 78, 28691 Villanueva de la Cañada, Madrid, Spain

Abstract

Herbig Ae/Be stars are intermediate mass Pre-Main Sequence objects, thus constituting a bridge between the low mass T-Tauris and the non-optical Massive Young Stellar Objects. Therefore they are a key subset for understanding the differences in formation mechanisms between the low and high-mass regimes. We have derived luminosities, optical variabilities and infrared excesses for most known Herbig Ae/Be stars (Vioque et al. 2018). In addition, by using *Gaia* parallaxes, we placed 218 of these objects in an HR diagram, which allowed us to homogeneously estimate masses and ages for the most complete sample of Herbig Ae/Be stars to date. Our main conclusions after analysing the sample are that high-mass stars mostly do barely display an infrared excess and show little optical variability. We do note that the break is around $\sim 7M_{\odot}$. This may be related to dusty disks which signpost a different or more efficient disk dispersal mechanism for high mass objects. We also found that $\sim 25\%$ of all Herbig Ae/Be stars are strongly variable. These variable sources mostly present doubly peaked $H\alpha$ line profiles, which trace edge-on disks. This project has received funding from the European Union's Horizon 2020 research and innovation programme under MSCA ITN-EID grant agreement No 676036. (See poster).

Highlights on Spanish Astrophysics X, Proceedings of the XIII Scientific Meeting of the Spanish Astronomical Society held on July 16 – 20, 2018, in Salamanca, Spain. B. Montesinos, A. Asensio Ramos, F. Buitrago, R. Schödel, E. Villaver, S. Pérez-Hoyos, I. Ordóñez-Etxeberria (eds.), 2019

Low-mass planets around low-mass stars: Highlights from the HADES survey.

J. Maldonado[1]

[1] INAF - Osservatorio Astronomico di Palermo, Piazza del Parlamento 1, 90134 Palermo, Italy, e-mail:jesus.maldonado@inaf.it

Abstract

While most of the planets discovered so far have been found orbiting around solar-type stars, low-mass stars have recently been recognised as a "shortcut" to glance into an exo-life laboratory. The HArps-N red Dwarf Exoplanet Survey (HADES) program is a long-term project at the Telescopio Nazionale Galileo aimed to the monitoring of nearby, early-type, M dwarfs, using the HARPS-N spectrograph to search for small, rocky planets. In this contribution we present a summary of the project status, our methodology to determine accurate stellar parameters for these stars, as well as our efforts to understand magnetic activity in M dwarfs taking advantage of the high-quality HARPS-N spectra.

1 Introduction

Low-mass stars (M dwarfs) are nowadays recognised as promising targets in the search for rocky, small planets with the potential capabilities of supporting life [8, 24]. The HArps-N red Dwarf Exoplanet Survey (HADES) [2] is an radial velocity survey for low-mass planets around a sample of northern-hemisphere early-M dwarfs. HADES constitutes a collaborative effort between the Italian Global Architecture of Planetary Systems project (GAPS)[1] [7], the Institut de Ciències de l'Espai (ICE/CSIC), and the Instituto de Astrofísica de Canarias (IAC).

Up to date, seventy-one nearby, bright (V $<$ 12 mag) stars have been observed. They have effective temperatures ranging from 3400 to 3900 K, with spectral types between K7.5 and M3V. Our targets were selected from the Palomar-Michigan State University (PMSU) catalogue [22], from [12], and are targets observed with the APACHE transit survey [24] and with an expected high number of *Gaia* mission scans.

High-resolution échelle spectra of the stars were obtained at La Palma observatory (Canary Islands, Spain) during several observing runs (from September 2012) using the HARPS-

[1]http://www.oact.inaf.it/exoit/EXO-IT/Projects/Entries/2011/12/27_GAPS.html

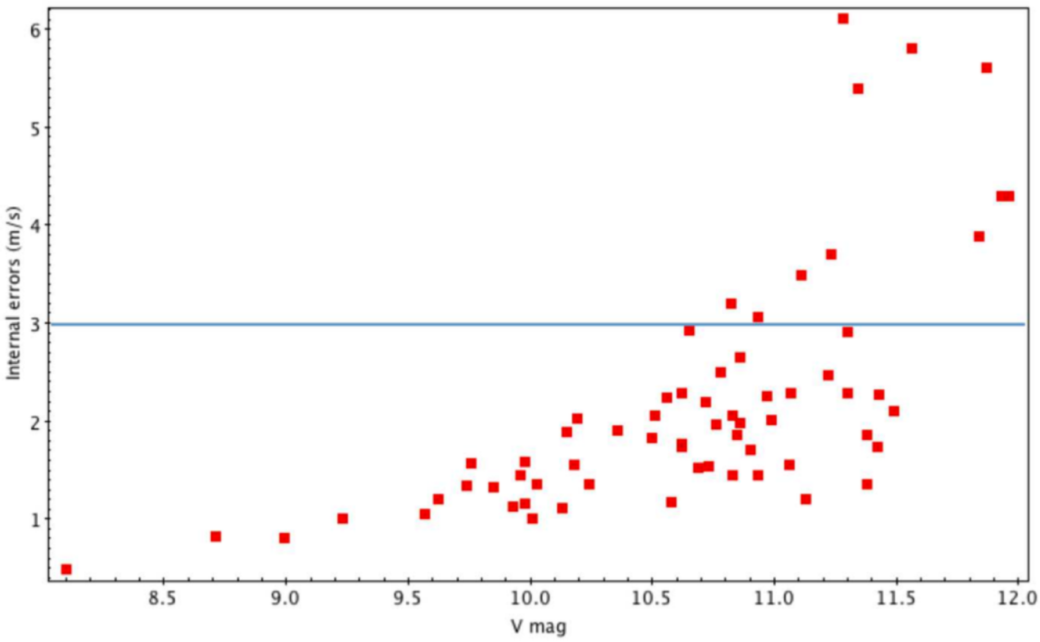

Figure 1: Radial velocity precision vs V magnitude for series of 15 min HARPS-N spectra of M dwarfs.

N instrument [6] at the Telescopio Nazionale Galileo (TNG). HARPS-N spectra cover the wavelength range 383-693 nm with a resolving power of R $\sim$ 115000. Spectra were automatically reduced using the Data Reduction Software (DRS) [13]. The DRS calculates the cross-correlation function, which is the correlation of the spectrum with an M2-type template mask in velocity space. However, we decided not to use the radial velocities determined by the DRS, but to use the Java-based Template-Enhanced Radial velocity Re-analysis Application (TERRA) [3] as we found it to deliver more accurate radial velocities in the case of M-type stars [18]. Figure 1 shows the achieved radial velocity precision as a function of the V magnitude of the stars for series of 15 minutes of exposure time. It can be seen that a radial velocity precision of the order of 1 ms^{-1} is achieved for stars with V $\sim$ 10.

2 The survey results

At the time of written, five new planets have been discovered within the HADES survey while one previously known planet has been confirmed.

GJ 3998b,c [2]. The radial velocity analysis of the M1 star GJ 3998 showed four significant signals at 30.7, 13.7, 42.5, and 2.65 days. We used state of the art techniques to disentangle keplerian from stellar signals including the analysis of optical activity indicators (Ca II H & K lines, Hα), photometry (APACHE [24], and EXORAP at INAF-Catania Astrophysical Observatory), and gaussian process analysis. An example is shown in Fig. 2 where

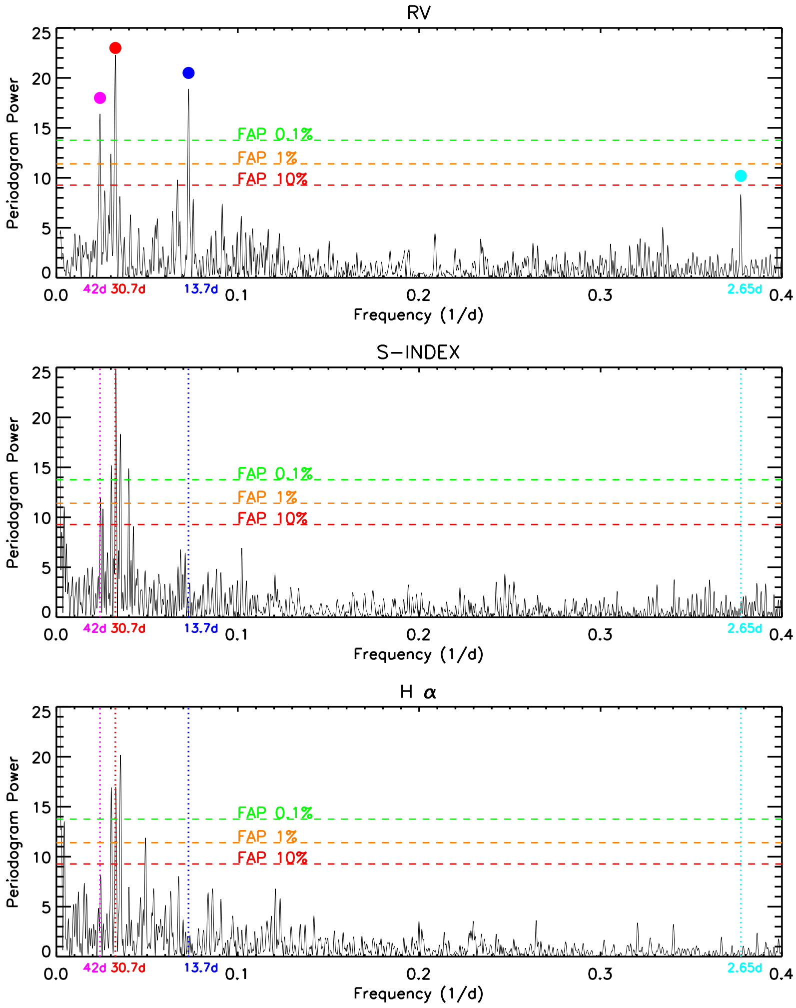

Figure 2: From top to bottom: Generalised Lomb-Scargle periodogram of radial velocities, Ca II H & K index, and Hα index for the star GJ 3998, zoomed around the frequencies of interest. The dotted blue and cyan lines indicate the frequencies corresponding to orbital periods of the candidate planets at 13.7 and 2.65 days, respectively, while the dotted red and magenta lines show the frequencies corresponding to the activity periods at 30.7 and 42.5 days, respectively. Figure taken from [2].

we show the use of activity indicators. We identified the periods of 30.7 and 42.5 days as the result of chromospheric inhomogeneities modulated by stellar and differential rotation, respectively. The shorter periods are well explained with the presence of two super-Earth like planets (GJ 3998b: P=13.74 ± 0.02 days, $m_C \sin i = 6.26 \pm 0.79\ M_\oplus$, a = 0.089 au; GJ 3998c: P=2.6498 ± 0.0008 days, $m_C \sin i = 2.47 \pm 0.27\ M_\oplus$, a = 0.029 au).

GJ 625b [26]. A super-Earth orbiting at the inner edge of the habitable zone of the star GJ 625 was discovered from the analysis of our HARPS-N radial-velocity time series. The characteristics of GJ 625b are $m_C \sin i = 2.82 \pm 0.51\ M_\oplus$ with an orbital period of 14.628 ± 0.013 days at a distance of 0.078 au. A second radial-velocity signal in the range 74-85 days was related to stellar rotation after the analysis of optical activity indicators, cross-correlation function asymmetry diagnostics and photometry light curves.

GJ 3942b [17]. By analysing five years of observations of this star we identified the rotation period of GJ 3942 at 16.3 days and discovered a new super-Earth, GJ 3942b, with an orbital period of 6.9 days and a minimum mass of 7.1 $M_\oplus$. An additional signal in the periodogram of the residuals was found. If confirmed, this planet candidate would have a minimum mass of 6.3 $M_\oplus$ and a period of 10.4 days.

GJ 15Ab,c [19]. Twenty years of radial velocity measurements of the M1 dwarf GJ 15A were analysed by combining our HARPS-N data with 15 years of archival HIRES/Keck data. We confirmed the keplerian nature of the 11.44 days period super Earth GJ 15Ab ($m_C \sin i = 3.03\ ^{+0.27}_{-0.44}\ M_\oplus$) and discovered a second long-period (76000 days) super-Neptune mass planet ($m_C \sin i = 36\ ^{+25}_{-18}\ M_\oplus$). Our best fits to the radial velocity data of GJ 15A are shown in Fig. 3.

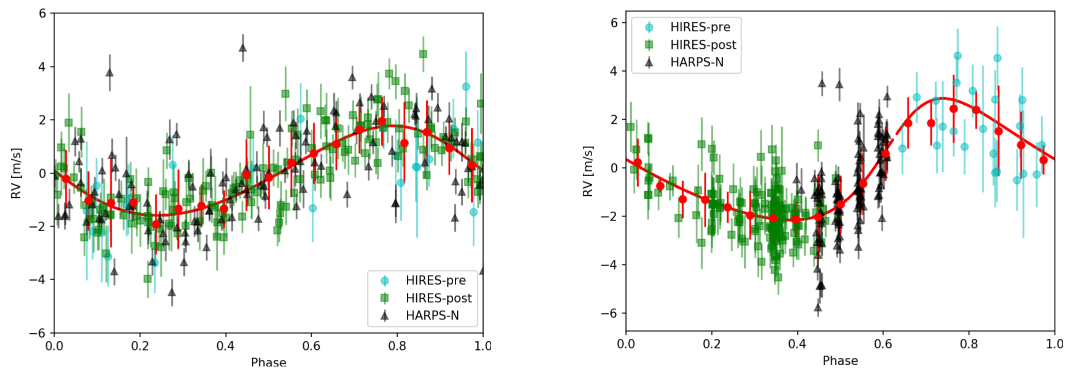

Figure 3: Phase folded radial velocity curves for GJ 15Ab (left) and GJ 15Ac (right). Each curve shows the residuals after the subtraction of the other planet and the stellar correlated signal. The red curve represents the best-fit keplerian orbit, while the red dots and error bars represent the binned averages and standard deviations of the radial velocities. Figure taken from [19].

Figure 4 summarises the HADES discoveries up to now. It can be seen that our discoveries are located in the lower part of the (minimum) mass vs period diagram of known planets around M-dwarfs. The HADES planets are mainly super-Earth like planets with minimum masses in the range 2-7 $M_\oplus$ and typical periods around 10 days. Figure 4 points

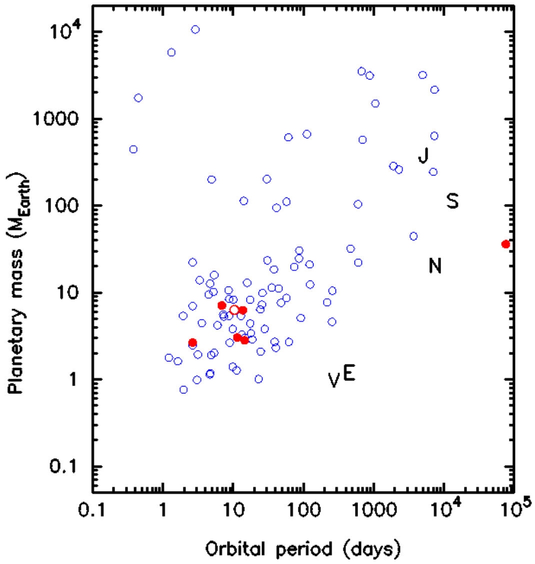

Figure 4: Known planets around M dwarfs. Data is from http://exoplanet.eu. Filled red circles indicate the HADES discoveries while candidates are shown in open circles. For comparison, the position of several Solar System planets, namely Venus, Earth, Jupiter, Saturn, and Neptune is indicated with the labels V, E, J, S, and N, respectively.

out that most planets orbiting around M dwarfs are super-Earth planets while there seems to be a lack of massive planets in close-in orbits orbiting M dwarfs.

3 Characterising the nearby early-M dwarf population

In contrast to solar type stars, the stellar parameters of M dwarfs are in general not well understood. Few M dwarfs are bright enough for a direct measurement of their radii and, in addition, there are disagreements between observations and theoretical models: observations show that M dwarfs are cooler and larger than expected.

Within HADES we have developed a technique to calibrate empirical relationships in order to determine the stellar parameters of early M-dwarfs [15]. Our methodology is based on the use of pseudo-equivalent widths of features measured in the optical spectra. A feature can be a line or a blend of lines. Pseudo-equivalent widths are defined as "traditional" equivalent-widths but measured with respect to the value of the flux between the peaks of the feature at each wavelength.

We have identified and calibrated 112 temperature sensitive ratios of features using as calibrators a sample of early M-dwarfs with angular sizes obtained with long-baseline interferometry. Typical uncertainties in our derived T_{eff} are about 70 K. Figure 5 shows same examples of ratios of features found to be sensitive to T_{eff}. In a similar way, 82 spectral-type sensitive ratios with a standard deviation lower than 0.5 spectral subtypes were identified. For metallicity, we searched for empirical relationships as a function of individual features

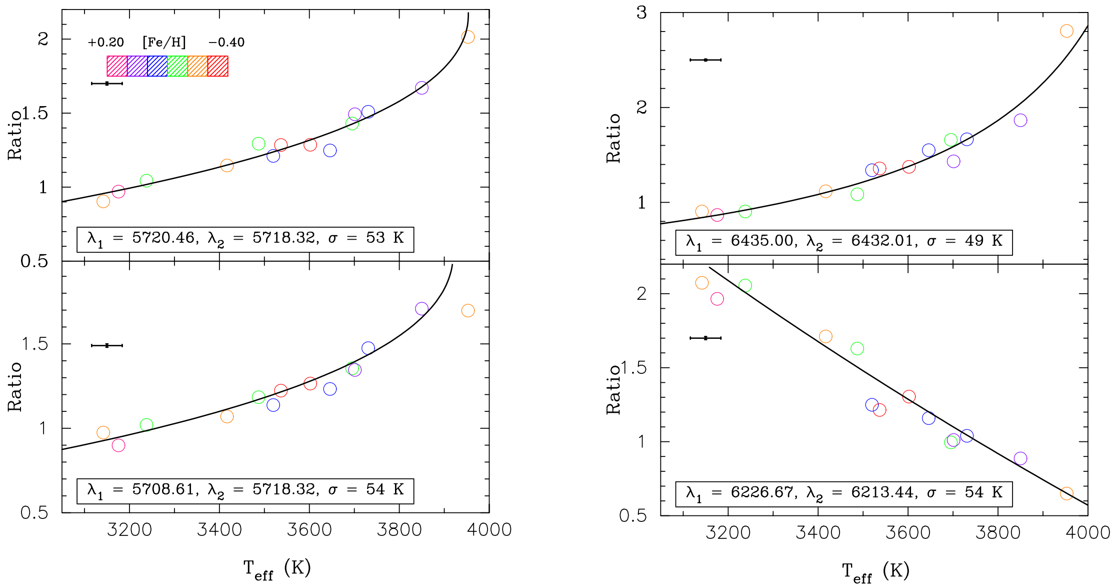

Figure 5: Examples of ratios of some features identified to be sensitive to T_{eff} in early-M dwarfs. Stars are plotted using different colours according to their metallicity. The corresponding fits are shown. The features' central wavelengths as well as the rms standard deviation of the residuals are given in each plot. Figure taken from [15].

and T_{eff}-sensitive ratios. A total of 696 calibrations with standard deviation values between 0.07 and 0.10 dex were identified. Finally, we made use of our temperature and metallicity values to search for empirical relationships with the stellar evolutionary parameters (mass, radii, $\log g$, luminosity). Our codes are public available for the community[2].

Other HADES studies have focused on understanding the chromospheres of M dwarfs. This is crucial for the HADES objectives. Stellar activity, including stellar spots, oscillations, and granulation are challenging the detection of low-mass planets via radial velocity. Further, the high-levels of activity (strong flares and high UV emission in quiescence) of M dwarfs may constitute a potential hazard for habitability.

In [14] the stellar parameters-activity relationships for early-M dwarfs were revisited. To do that, we first determine the emission excess in the different chromospheric indicators (Ca II H & K, Balmer's lines) by applying the spectral subtraction technique which allow us to subtract the underlying photospheric contribution from the stellar spectrum. We also computed rotational velocities by using the cross-correlation function and estimate the age of the stars by analysing their spatial Galactic velocity components and possible membership to stellar kinematic groups. Our results are summarised as follows: i) the strength of the chromospheric emission is constant in the M0-M3 spectral range; ii) we find lower rotation levels in cooler stars; iii) a tendency of higher rotation values with increasing activity is found; and iv) young stars tend to show higher levels of activity.

[2]https://github.com/jesusmaldonadoprado/mdslines

Figure 6 shows some examples of the comparison between pairs of fluxes of different chromospheric lines and coronal X-ray emission for the stars in our sample. The analysis of the flux-flux relationships shows that our M dwarfs sample is complementary to other literature samples, extending the analysis of the flux-flux relationships to the low-chromospheric fluxes domain. Our results confirm that field stars deviating from the "general" flux-flux relationships are likely to be young. We conclude that our sample represents a benchmark for the characterisation of magnetic activity at low levels.

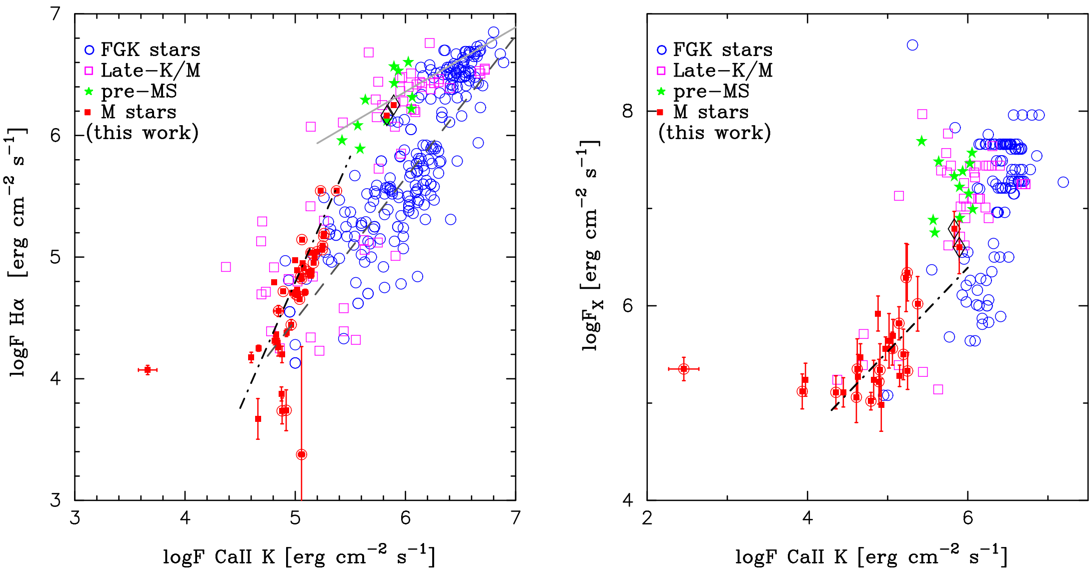

Figure 6: Flux-flux relationships between between Hα and Ca II K (left panel) and between X-ray and the calcium line Ca II K (right panel). M dwarfs from the HADES survey are plotted with red filled squares; FGK stars from the literature with open circles, late-K and M stars from the literature are shown by purple open squares; green stars denote M0-M3 pre-MS M stars. Possible young disc stars in our M star sample are shown by circles. The black dash-dotted line represents our best fit; the relations for the "active" and "inactive" branches by [16] are shown in light grey solid and dashed dark grey lines, respectively. Two "deviating" stars are indicated by diamonds. Figure taken from [14].

The short term variability of our targets is analysed in detail in [23]. The time variability of the emission fluxes is analysed by using the pooled variance technique. We derive a tentative estimate of the rotation period (on the order of a few tens of days) for some HADES targets, while we found the typical lifetime of chromospheric active regions to be of the order of a few stellar rotations. A couple of examples are shown in Fig. 7. We also find that the variance of the flux excess is an increasing function of stellar activity, and that even the quietest stars show some degree of variability.

We also find that the Hα emission does not increase monotonically with the Ca II H & K line flux, showing some absorption before being filled in by chromospheric emission when Ca II H & K activity increases, in agreement with chromospheric models.

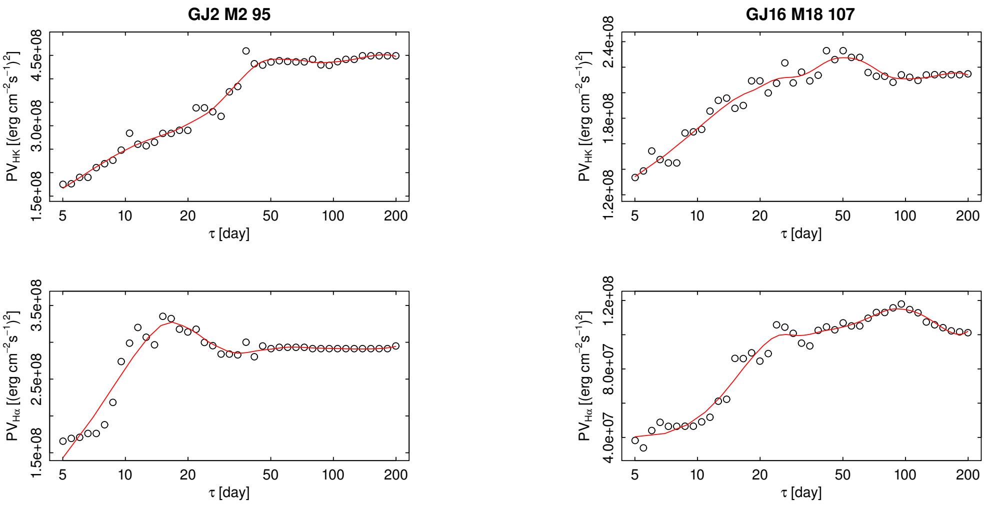

Figure 7: Pooled variance diagrams of the star GJ 2 (left) and GJ 16 (right). Top: Ca II H & K. Bottom: Hα. The red line is a smoothing function for ease of reading the graphs. Figure taken from [23].

We finally revisited the activity-rotation relationship, previously poorly constrained for M dwarfs (specially in the non-saturated regime). In [25] $\log R'_{\rm HK}$ values and rotational periods are derived from time series spectroscopy of the Ca II H & K and Hα activity indicators. Complementary ASAS photometry light-curves are also used. The typical level of activity in our sample is $\log R'_{\rm HK} \sim$ -5 while the mean rotation period of our stars is $\sim$ 40 days. The rotation-activity diagram is shown in the left panel of Fig. 8. The data is fitted to a relationship with the functional form $\log(P_{\rm rot}) = A + B \times \log R'_{\rm HK}$ being A = -2.15 and B = -0.731 for our early-M dwarfs.

The coronal activity-rotation relationship is analysed in [10]. It is important to note that all our targets except one are in the non-saturated regime where only one data point (that, in addition, corresponds to an upper limit) was reported in previous works [20]. Therefore, we are able to determine in a more accurate way than in previous works the value of the rotation period at which the saturation occurs ($P_{\rm sat}$) for M dwarfs. Figure 8, right, shows the fractional X-ray luminosity of the stars a function as a function of the period. From our analysis we derive $P_{\rm sat} \sim$ 9.6 days for stars in the 3400-3600 K range, while for stars with effective temperatures between 3700 and 3900 K the derived $P_{\rm sat}$ value is of the order of 4.4 days.

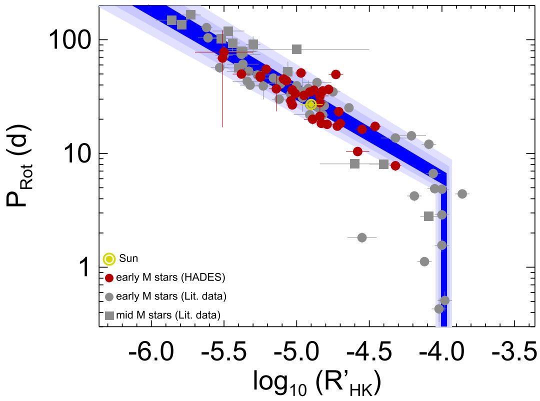

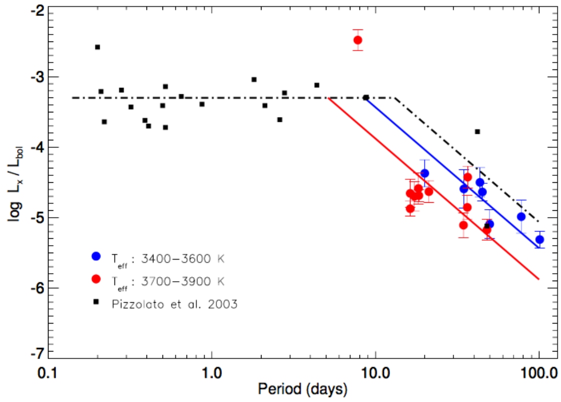

Figure 8: Left: Rotation period vs. chromospheric activity level, $\log R'_{\rm HK}$. The shaded region shows our best fit. HADES targets are shown in red, while literature data is plotted in grey. The Sun's value is included as a reference point. Figure taken from [25]. Right: $\rm L_X/L_{Bol}$ vs. rotation period. The black squares correspond to the upper limits from [20]. Blue and red dots correspond to the M dwarfs from this work in the two different range of temperatures indicated in the text. The black dashed line represents the broken power law obtained by the fitting procedure from [20]. The blue and red dash line represent our best fit for 3400-3600 K and 3700-3800 K $\rm T_{eff}$ range, respectively. Figure taken from [10].

4 Statistical analysis

While detailed statistical analysis are still on preparation, not far after the beginning of our survey we performed a series of simulations using state of the art planet occurrence statistics in order to define the "optimal" strategy (number of targets, number of observations, exposure time, etc.) for our survey [18]. In particular, we estimated a jitter of 2.3 $\rm ms^{-1}$ for our targets and compared the radial velocities as derived from the DRS with those provided by the TERRA pipeline (see Sect. 1). Our analysis showed that the TERRA radial velocities give lower rms values and should be preferred.

We analysed how the number of detected planets depends on the number of observations per star and the number of observed targets. The results can be seen in Fig. 9. Based on our analysis we expected (underestimated) the discovery of 2.4 $\pm$ 1.5 planets which is half the number of planets detected so far. We found that planets with $\rm m_C > 2\ M_\oplus$, $K > 2\ \rm ms^{-1}$ and orbital periods between 10 and 25 days should be easily detected. We conclude that optimal results are obtained for approximately 50 observations per star with exposure times of 900 s and precision of approximately 1 $\rm ms^{-1}$.

5 Summary

The HADES survey has been successful in the discovery of five new super-Earth like planets with periods around 10 days. These discoveries have been possible thanks to the development

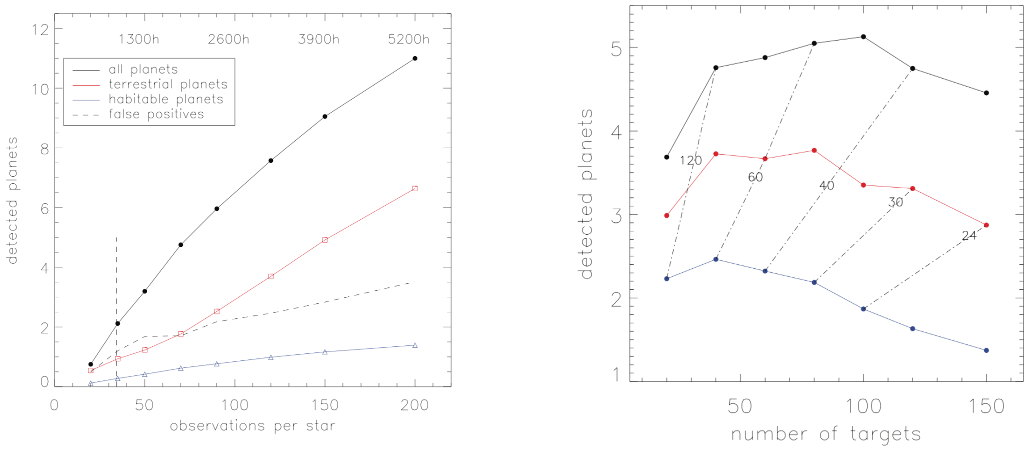

Figure 9: Left: Relationship between the amount of all detected planets and the number of observations per star (black dots), of the terrestrial planets (red squares), the habitable planets (blue triangles) and the false positives (black dashed line). The vertical black dashed line indicates the total observation time of our survey. Right: Relationship between the number of detected planets of our simulations and the number of stars used for the survey for a given total observation time of 800 (blue), 1200 (red) and 1600 h (black). Points with the same number of observations per star are connected using dash-dotted lines. Figure taken from [18].

of new and imaginative approaches to deal with the stellar noise problem. The survey is already ongoing and the analysis of the data has revealed several planetary candidates that will be the subject of further studies [1, 9].

Within HADES we have conducted several studies in order to characterise the nearby, early-M dwarf population. In particular we have analysed their stellar parameters, the relationship between them an stellar activity, the flux-flux relationships and the rotation-activity connection. In addition, several statistical analysis has been performed (regarding the survey strategy and expectations) or are in progress (including the survey sensitivity and frequency of planets, possible correlations with stellar properties, activity and binaries studies, etc.).

We finally mention the possible synergies with other projects, in particular with the development of near infrared high-resolution spectrographs like GIARPS [5] or CARMENES [21]. We note that the capabilities of combined optical/near infrared spectroscopy to confirm or reject planetary candidates have already been demonstrated [11, 4] offering an unique procedure to disentangle stellar from keplerian signals. Near infrared spectroscopy also opens for the first time the possibility of search for planets around late-type M dwarfs (spectral type later than M3-M4) for which the velocity amplitude of a terrestrial planet in the habitable zone is highest [8].

Acknowledgments

This research was supported by the Italian Ministry of Education, University, and Research through the *PREMIALE WOW 2013* research project under grant *Ricerca di pianeti intorno a stelle di piccola massa*. Additional support from the Ariel ASI-INAF agreement N. 2015-038-R.0 is also acknowledged.

References

[1] Affer L., et al., 2018, A&A, in prep.

[2] Affer L., et al., 2016, A&A, 593, A117

[3] Anglada-Escudé G., Butler R. P., 2012, ApJS, 200, 15

[4] Carleo I., et al., 2018, A&A, 613, A50

[5] Claudi R., et al., 2017, EPJP, 132, 364

[6] Cosentino R., et al., 2012, SPIE, 8446, 84461V

[7] Covino E., et al., 2013, A&A, 554, A28

[8] Dressing C. D., Charbonneau D., 2013, ApJ, 767, 95

[9] Garrido Rubio, A., et al., 2018, A&A, in prep.

[10] González-Álvarez E., et al., 2018, A&A, in prep.

[11] González-Álvarez E., et al., 2017, A&A, 606, A51

[12] Lépine S., Gaidos E., 2011, AJ, 142, 138

[13] Lovis C., Pepe F., 2007, A&A, 468, 1115

[14] Maldonado J., et al., 2017, A&A, 598, A27

[15] Maldonado J., et al., 2015, A&A, 577, A132

[16] Martínez-Arnáiz R., López-Santiago J., Crespo-Chacón I., Montes D., 2011, MNRAS, 414, 2629

[17] Perger M., et al., 2017, A&A, 608, A63

[18] Perger M., et al., 2017, A&A, 598, A26

[19] Pinamonti M., et al., 2018, arXiv, arXiv:1804.03476

[20] Pizzolato N., Maggio A., Micela G., Sciortino S., Ventura P., 2003, A&A, 397, 147

[21] Quirrenbach A., et al., 2014, SPIE, 9147, 91471F

[22] Reid I. N., Hawley S. L., Gizis J. E., 1995, AJ, 110, 1838

[23] Scandariato G., et al., 2017, A&A, 598, A28

[24] Sozzetti A., et al., 2013, EPJWC, 47, 03006

[25] Suárez Mascareño A., et al., 2018, A&A, 612, A89

[26] Suárez Mascareño A., et al., 2017, A&A, 605, A92

Highlights on Spanish Astrophysics X, Proceedings of the XIII Scientific Meeting of the Spanish Astronomical Society held on July 16 – 20, 2018, in Salamanca, Spain. B. Montesinos, A. Asensio Ramos, F. Buitrago, R. Schödel, E. Villaver, S. Pérez-Hoyos, I. Ordóñez-Etxeberria (eds.), 2019

From Mars Express to ExoMars: Two missions working together around Mars.

Alejandro Cardesín-Moinelo[1], Miguel Ángel López-Valverde[2] and the Mars Express and ExoMars Science Operations Centres[1]

[1] European Space Astronomy Centre, Villanueva de la Cañada, Madrid, Spain
[2] Intituto de Astrofísica de Andalucía, Granada, Spain

Abstract

This year 2018 is very important for the Mars scientific community in Europe since for the first time two missions of the European Space Agency coincide around the orbit of Mars, opening a great opportunity for collaboration to improve our understanding of our neighbour planet.
The Mars Express mission is fully operational and has been providing great amounts of data since its arrival at Mars in Christmas 2003, covering a wide range of science objectives from the surface and sub-surface geology, atmosphere dynamics and composition, up to the interaction with the magnetosphere and the characterization of the Martian system including Phobos and Deimos.
The ExoMars 2016 Trace Gas Orbiter mission arrived successfully at Mars in October 2016 and after the first calibration observations in the initial capture orbit and the long aerobraking phase of more than 12 months, the mission started its operational science phase in April 2018 aiming to fulfill the scientific goals of the mission: atmospheric trace gases, climatology, surface geology and subsurface ice detection.
In this contribution we provide a short summary of each mission and their mission profiles, with the characteristics of each orbit and their differences that drive the observation capabilities. We will then focus on the synergistic capabilities between all the instruments and the observations that can be combined to improve the scientific outcome of both missions. In particular we will show the preparations done by the science operations centers at ESAC and the work within the Science Ground Segments for the long term analysis of the geometrical conditions of both missions to perform coordinated science operations. We will provide details on the science opportunity analysis process, using various operational tools inherited from previous planetary missions to perform geometrical and operational simulations of both spacecraft, taking into account the observation requirements of all the instruments and the operational requirements for feasibility checks.

1 Mars Express Mission

Launched in June 2003, the Mars Express spacecraft has been steadily returning enormous volumes of science data since its arrival in Mars orbit in December 2003. While the mission was originally conceived to last 687 Earth days (one full Martian year), it has now been operating continuously for almost 15 years, covering a wide range of science objectives from the surface and sub-surface geology, atmosphere dynamics and composition, up to the interaction with the magnetosphere and the characterization of the Martian system including Phobos and Deimos.

The Mars Express spacecraft is in a highly elliptical polar orbit, with an inclination of 86 degrees from the equator and a period of nearly 7.5 hours, producing about three orbit passes per day. The pericentre height is approximately 350 Km, while the apocentre is at approximately 10,000 Km. The orbit is not synchronized in any way with Mars, Earth or the Sun, and so it is drifting freely by celestial mechanics with a slow precession movement that changes the orbit latitude and the illumination conditions, defining the long term seasons with a long period of nearly 20 months.

This high eccentricity of the orbit provides a very wide range of distances that allow for the observation of the planet with very different resolutions and observing conditions. However the long term evolution of the orbit precession causes very stable and slow changing seasons, with very slow variations of the latitude and illumination at pericenter where we can identify long observation campaigns (3 6 months).

2 ExoMars 2016 Trace Gas Orbiter Mission

ExoMars 2016 is the first of the ExoMars Programme developed jointly by ESA and Roscosmos. The key goal of this mission is to gain a better understanding of atmospheric trace gases that are present in small concentrations (less than 1% of the atmosphere) which are key in the understanding of the atmospheric climate evolution and potential evidence for biological or geological activity in the past.

The Trace Gas Orbiter (TGO) carries a scientific payload capable of addressing this scientific question, namely the detection and characterisation of trace gases in the Martian atmosphere. The spectrometers ACS and NOMAD will make use of the solar occultation observations to obtain the maximum sensitivity in the vertical profiles, and will use also nadir pointing to map the atmospheric conditions of the whole planet to detect a wide range of atmospheric trace gases, with an improved accuracy two or even of three orders of magnitude compared to previous measurements. The instrument CASSIS will also observe in nadir geometry to obtain super high resolution colour and stereo images of selected targets on the surface. The FREND instrument will analyse the subsurface hydrogen to a depth of a metre, to reveal any deposits of water-ice hidden just below the surface, which, along with locations identified as sources of the trace gases, and stereo colour imaging, could influence the choice of landing sites of future missions.

The nominal science orbit of TGO around Mars is circular at an altitude of 400km, with a high inclination of 74 deg and a characteristic node regression that makes the orbit plane rotate around the planet with a typical cycle of 7 weeks. The evolution of the beta angle (the angle between the orbit plane and the sun) drives the main seasons of the mission and defines the long term planning campaigns for solar occultation and nadir observations.

3 Sinergies and Areas for Collaboration

In general the ExoMars long term evolution is very dynamic compared to the evolution of Mars Express, and has short observing seasons that vary regularly on a weekly basis, based on the orbital node regression. That allows for a full surface and local time coverage on a monthly basis, except for the polar regions that the spacecraft is not able to reach.

The main advantage of ExoMars TGO compared to Mars Express is the capability to have almost continuous science observations. Thanks to a simplified mission profile the spacecraft is basically pointing Nadir by default and pointing the solar occultation channels to the Sun whenever needed for occultation measurements. Mars Express does not operate continuously, as most observations need to be stopped during ground communications but at least on the other side it provides a lot of pointing flexibility thanks to the maturity of the mission.

Here we list a few of the common scientific research areas for collaboration between both missions:

- Geology and subsurface: photometric properties, including temporal and spatial variations, evolution of the polar caps, sub-surface ice, surface water abundance and their correlation with surface geology and mineralogy.

- Meteorology and climate: extending record of climatological parameters (temperature, minor species, dust, clouds), improving the coverage (spatial, temporal, local time), study of couplings between the atmospheric layers and dependence of atmospheric parameters on dust loading

- Ionosphere and escape: structure of the ionosphere and upper atmosphere, dependence of escape on the state of the lower atmosphere, characterisation of water escape and its dependence on the state of the lower atmosphere and study of couplings between the atmospheric layers

In order to take advantage of these sinergies there is a common effort to promote the collaboration lines between both missions, not only in the data analysis, but also in the sharing and discussion of results, the comparison of retrieval tools and radiative transfer codes, climatological parameters, and the joint use of TGO and MEX data in Global Climate Models.

4 Analysis of coordinated science observations

This work focuses in the analysis of coordinated science observations and combined observation opportunities (surface, sun occultations, ...), which would then be used for the cross-calibration of different instruments that may contribute to complementary science objectives (surface, temperatures, clouds, context,...) and will be used in the preparation of a joint long-term science activity plan between both missions.

In order to study the various possibilities of coordinated science operations, we define here various types of combined observations:

- Simultaneous observations: these are observations of both missions that observe the same exact position, latitude and longitude coordinates, and occur exactly at the same time, therefore having the same illumination and local time conditions. These kinds of observations are the most interesting and would be extremely useful for cross-comparison and cross-calibration between the different instruments, however they are limited by the geometrical evolution of the orbit and may not be possible in all cases.

- Quasi-simultaneous observations: these are observations that are almost simultaneous but have one or more requirements relaxed, in terms of position, time or conditions. These may cover a wide range of options depending on the flexibility of the scientific requirements of each type of observation, and are still very useful for comparison and can provide very important information for wide scientific objectives both at the surface and atmosphere. We can distinguish here two main type of quasi-simultaneous observations:

  - Surface driven: these are observations of the same latitude and longitude coordinates, but performed at different times. This kind of observations may be useful for some scientific objectives, in particular for surface features and in general for the imaging cameras where the comparison of the results can still be relevant even if observations are taken at very different times, as long as the illumination conditions at the surface are similar.

  - Sun illumination driven: these are observations taken at the same latitude region and with the same illumination conditions, but the longitude coordinates may be different. In other words, these are two observations of the same geometry on Mars with respect to the sun, but where the actual point in the surface is different.

- Non-simultaneous seasonal observations: these are observations that do not occur close in time, but are at least performed in the same season with similar conditions and therefore they can still be used to infer useful information. This is in particular applicable to surface geology or mineralogy observations that are not expected to change within short time scales. In general the overall scientific requirement for both missions is to reach as much as possible a full coverage of the planet, not only in terms of surface latitude and longitude, but also in terms of season (Solar Longitude) and illumination conditions (Solar Elevation angle and Local Time) so that all the data can be ingested into the climate models for comparison.

4.1 Solar Occultations

The main scientific goal of ExoMars TGO is the analysis of trace gas species and the most important observation that will cover the sensitivity requirements are the solar occultations that will use the signal of the sun as it gets occulted by the atmosphere, providing very important information of the vertical profile of various gas molecules and their densities with the NOMAD and ACS spectrometers. Mars Express also has the SPICAM instrument that is able to perform solar occultation measurements in the infrared range and their results are very important for comparison of the measurements of the vertical profiles and the retrieval methods for various gases.

For this we have performed an analysis of all the occultation points MEX-Mars-Sun and TGO-Mars-Sun both for the in-gress and e-gress points (that is dusk and dawn). In order to identify all the quasi-simultaneous opportunities we have computed all occultations from both missions for the year 2018 and compared all times and geometrical conditions. This analysis has shown that MEX-TGO combined occultations are geometrically possible and occur every few weeks. We have found at least three optimal opportunities in 2018 (23-May, 16-August and 29-August) where the time difference is less than one minute, and we have identified many other quasi-simultaneous occultations that can be observed at the similar times in the same region of the planet within a few minutes difference. In particular we can observe that the periods May-June and August-September have quite a few combined occultation events that occur within 15min difference in the same region of the planet (0 30deg difference in latitude).

4.2 Nadir Observations

Both the Mars Express and Trace Gas Orbiter mission are also observing in Nadir geometry, not only performing high resolution imaging of the surface with MEX/HRSC, TGO/CASSIS, and characterizing the surface composition with MEX/OMEGA but also complementing the atmospheric analysis of various gases of the previously mentioned solar occultations, providing temperature profiles and various gas abundance maps with MEX/PFS and MEX/SPICAM, cloud monitoring and overall contextual information with MEX/HRSC, MEX/OMEGA and MEX/VMC. The nadir observations are also used by other instruments like TGO/FREND and MEX/MARSIS to provide mapping information of the subsurface that is of great importance to the analysis of ice content below the surface and other contextual interpretation of the data.

When looking at the orbits of both spacecrafts, it is easy to identify that there are orbit “alignment” seasons every few months, where both spacecrafts can fly “quasi-parallel” to each other, with elongated similar tracks on the surface. Also at any point in time there are always two crossing points between the orbits, although the distances may be very different due to the eccentricity of the MEX orbit, affecting the chances of having a simultaneous observation between the two spacecrafts.

5 Summary and Conclusions

In this contribution we have shown some of the potential science opportunities for combined observations between Mars Express and Trace Gas Orbiter that are an important input for the science operations planning of both missions. Our analysis shows that there are regular opportunities for combined observations between the missions for both the most important observation types, solar occultation and nadir.

MEX-TGO combined occultations are geometrically possible and occur every few weeks. Although we may not have many exact simultaneous observations of the same spot in time, we have identified many quasi-simultaneous occultations that can be observed at similar times in the same region of the planet within a few minutes difference. In particular the periods May-June and August-September have combined occultation events within 15min difference in the same region of the planet.

For nadir observations, simultaneous cross-calibrations are possible regularly at different distances, and all latitudes/longitudes can be covered by both spacecrafts, with the exception of the polar regions due to the TGO orbit inclination (74deg). Quasi-simultaneous observations are very common as there are always two TGO-MEX crossing points, which can be seen within one 1h difference thanks to TGO shorter orbital period. This 1 hour difference may be important or not depending on the scientific objective, or the proximity to terminator. The main driving factor is the distance of Mars Express, but depending on the type of observation it may be interesting to observe at pericenter (for high resolution) or at the apocenter for contextual information.

The results of this work are based on the lessons learned from Mars Express and other planetary missions and are intended to identify as soon as possible the feasible coordinated science campaigns so they can be allocated during the Long Term Planning process (LTP, 6-month cycles) for the definition of high level priorities between the two missions and all their instruments. This science campaigns can then be iterated, confirmed and implemented during the Medium Term Planning process (MTP, 4-week cycles), where all the observations are frozen and expanded for the final commanding of the instruments at Short term Planning (STP, 1-week cycles).

Acknowledgements

The authors acknowledge the contributions of the European Space Agency, Roscomos, all National Agencies, research institutions and teams involved in the success of the Mars Express and ExoMars 2016 mission.

Highlights on Spanish Astrophysics X, Proceedings of the XIII Scientific Meeting of the Spanish Astronomical Society held on July 16 – 20, 2018, in Salamanca, Spain. B. Montesinos, A. Asensio Ramos, F. Buitrago, R. Schödel, E. Villaver, S. Pérez-Hoyos, I. Ordóñez-Etxeberria (eds.), 2019

Can we really detect planets around evolved massive stars?

E. Delgado Mena[1]

[1] Instituto de Astrofísica e Ciências do Espaço, Universidade do Porto, CAUP, Rua das Estrelas, 4150-762 Porto, Portugal

Abstract

The discovery of planets around massive stars is important for understanding how planet formation and evolution is conditioned by different stellar environments. However, current planetary search surveys have failed to detect planets around massive evolved stars. This lack of planets might be a consequence of the specifities of planet formation around such objects. Alternatively, the detection of planets around evolved massive stars might be hindered by the increasing stellar jitter as the stars evolve. In this project we target planets around evolved stars in open clusters, most of them with masses above $2\,M_{\odot}$. We present the cases of three objects where long term (i.e. years) and high amplitude RV signals of probably stellar origin are mimicking the presence of planets.

1 Introduction

The last two decades have represented a strong success in the quest for exoplanets, mainly around late F and GKM stars. However, the search for planets around more massive stars (early F or A spectral types) is more difficult with the currently most used methods. For example, the Radial Velocity (RV) technique, cannot be used in stars hotter than $\sim 6500\,\mathrm{K}$ due to the increase in rotational velocities of those more massive stars and the lack of a sufficient number of spectral lines. Similarly, the larger radius of such stars hampers the discovery of planets with the transit method. Nevertheless, searching for planets around K giants, the evolved counterparts of those massive stars, has been a way to sort this problem out. The lower rotation rates and more crowded spectra of evolved stars facilitates the use of the RV technique [5, 22, 18].

Still, current planetary search surveys have failed to detect close-in planets around massive evolved stars [16]. In Fig. 1 we can see stars with $\log g < 3\,\mathrm{dex}$ do not have planets with periods shorter than 100 days. Whether this lack of short period planets around massive

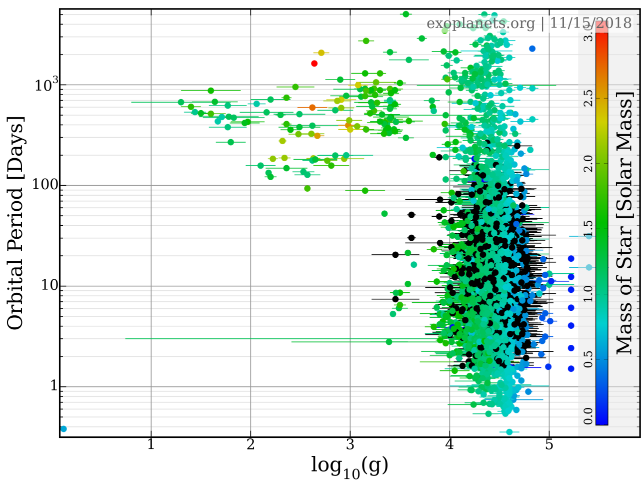

Figure 1: Orbital period of all planets discovered to date as a function of stellar surface gravity. Data and plot taken from exoplanets.org.

stars has a primordial origin or is produced by planet engulfment is still debated [24, 12]. Moreover, several works have found that the frequency of massive planets is higher around more massive stars [10, 20] but with a maximum around $2\,M_{\odot}$ and a sharp decrease for stars more massive than 2.5-3 $M_{\odot}$. Indeed, long-term surveys of giant stars such as the Lick Observatory survey [20] or the EXPRESS survey [11] have not found any planet in stars more massive than $\sim$2.7 $M_{\odot}$. Certainly, an important concern when interpreting *RV* variations in red giants is the presence of intrinsic stellar jitter (caused by p-mode oscillations) which shows a typical level of 10-20 $\mathrm{m\,s^{-1}}$ for stars at the base of the Red Giant Branch (RGB) [23] and increases as the stars further evolve [9]. The modulation of active regions in red giants can produce large amplitude *RV* variations as well. Therefore, analysing the stability of the *RV* signals over several orbits (and for a time span larger than the stellar rotational period) is needed before claiming the presence of a planet. In this work we present new results for a survey around evolved stars in open clusters started by [17], hereafter LM07. For more details about the present work we refer the reader to [4].

2 NGC2423No3 and NGC4349No127

In LM07, showing the first results of this survey, a planet in the cluster NGC2423 was announced after collecting 46 *RV* points (28 with CORALIE and 18 with HARPS) during 1529 days. Additionally, a brown dwarf was discovered around NGC4349No127, by using 20 *RV* measurements with HARPS along 784 days. In order to probe the planetary nature of the *RV* signals, the Ca II H&K lines and the Bisector Inverse Slope BIS [19] of the cross correlation function (CCF) were analyzed, but none of them showed a periodic variability. In the next two years after the publication of the results these two stars were followed up and additional data has been taken in 2017 and 2018. In the left panel of Fig. 2 we show the

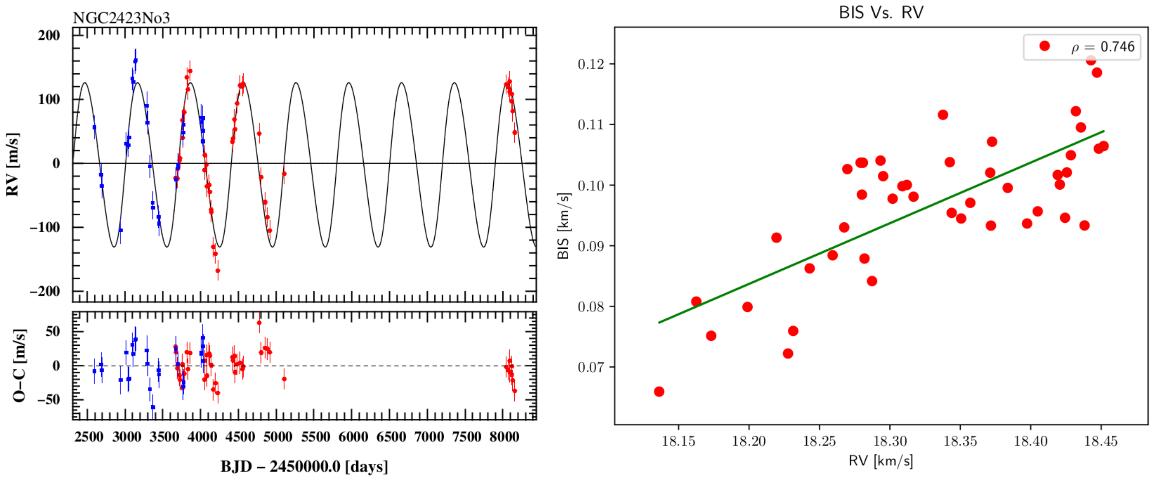

Figure 2: *Left:* RV curve as a function of time and as a function of orbital phase for NGC2423No3. *Right:* BIS vs RV for NGC2423No3.

RV variations of NGC2423No3 spanning 15 years of observations (although with a big gap in between 2009 and 2017) that can be fitted with a Keplerian fit with a period of 698 days. Considering the stellar mass ($2.26 \pm 0.07\,\mathrm{M}_\odot$) of this object [3], this signal would correspond to a planet with $m_2 \sin i = 9.6\,\mathrm{M}_J$ in a circular orbit with $a = 2.02$ AU. We note however, that the phase of the signal seems to slightly change along the time. The periodograms of the full-width-at-half-maximum (FWHM) of the cross-correlation function (CCF), the BIS and the Hα line do not show a significant variation with the period of the RV, however, we find that the BIS is strongly correlated with the RV (see the right panel of Fig. 2). This fact warns us about the possibility that the signals we are observing are related to inhomogeneities in the stellar surface and not with an orbiting body.

In the right panel of Fig. 3 we show the RV variations of NGC4349No127 for which 46 measurements were collected during 1587 days. The data can be fitted with a Keplerian orbit of 672 days, corresponding to a brown dwarf of $m_2 \sin i = 24.1\,\mathrm{M}_J$ (the stellar mass is $3.81 \pm 0.23\,\mathrm{M}_\odot$) in a near circular orbit. However, the periodogram of the FWHM has a strong peak at $\sim$666 days, the same period as observed in the RV periodogram (see left panel of Fig. 3). This fact indicates that there are variations in the star's atmosphere with the exact same period as the RV. Moreover, the Hα periodogram also shows a signal at a similar period, with $P \sim 689$ days (however just below the FAP = 1% level). Therefore, the strong RV signal is probably due to rotationally modulated active regions or long-period oscillations, and not as a result of an orbiting body.

3 IC4651No9122

In Fig. 4 we present the data for IC4651No9122, a star with a mass of $2.06 \pm 0.09\,\mathrm{M}_\odot$. The first set of data collected till 2009 (47 RV points during $\sim$4.5 years) shows a very clear and

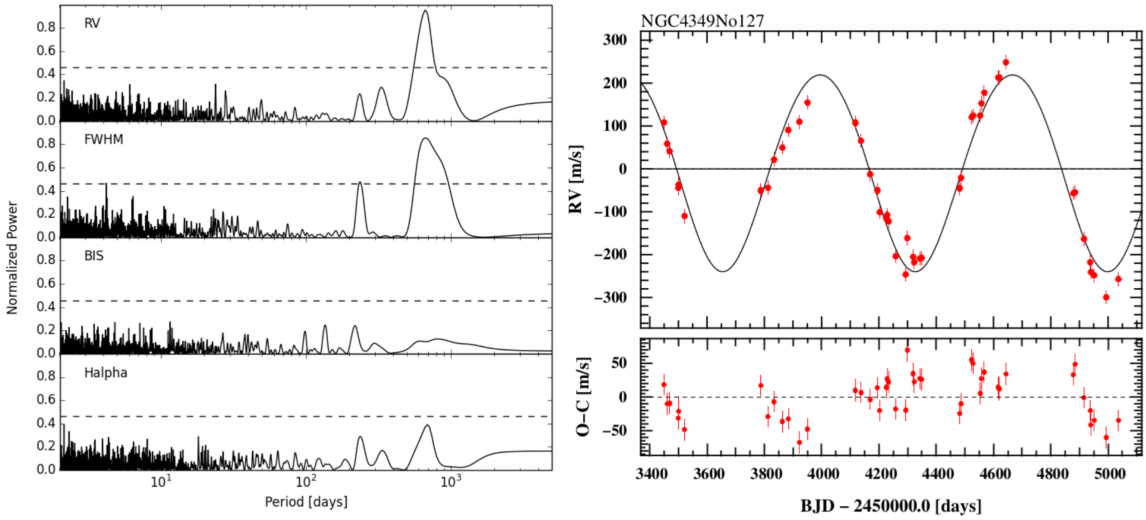

Figure 3: *Left:* Generalized Lomb-Scargle periodograms of *RV*, FWHM, BIS and Hα index for NGC4349No127. The dashed line indicates the FAP at 1% level. *Right:* *RV* curve as a function of time and as a function of orbital phase for NGC4349No127.

significant peak at 771 days (see left panel in Fig. 4). This *RV* variation can be explained by the presence of a planet with m_2 sin $i = 6.9\,\mathrm{M}_J$ in a 2.09 AU semi-major orbit. The Hα periodogram shows a statistically significant signal at 1052 days and a peak below the FAP = 1% line at 689.8 days. Moreover, the FWHM periodogram also shows a long-period signal at ∼689.8 days, close to the FAP = 1% line. This signal is probably due to rotational modulation of active regions in the atmosphere. Although the most plausible explanation for the *RV* variability is the presence of a planet, we considered a bit suspicious the fact that the period of the FWHM lies so close to the period of the planet candidate which in turn matches one of the peaks of the Hα index periodogram. Therefore, we decided to re-observe this star during 2017 and 2018 and we also collected 6 additional points from the ESO archive. The periodogram of the complete dataset is shown in the middle panel of Fig. 4. The *RV* has now a peak at 741 days whereas the FWHM presents a significant peak, just above the FAP level, at 714 days, closer to the *RV* period than with the initial set of data. The Hα index also shows two peaks at 952 and 714 days but they are not statistically significant. The *RV* curve with a Keplerian fit is shown in the right panel of Fig. 4. Although with the current data we cannot rule out the presence of a planet around IC4651No9122, these results cast doubts on the planetary nature of the signal and more data will be needed to confirm the presence of a planet.

4 Conclusions

Long-period *RV* variations with hundreds of days have been known to exist in several giant stars [25, 14, 7] with *RV* amplitudes in the order of ∼50-400 $\mathrm{m\,s^{-1}}$ which were attributed to

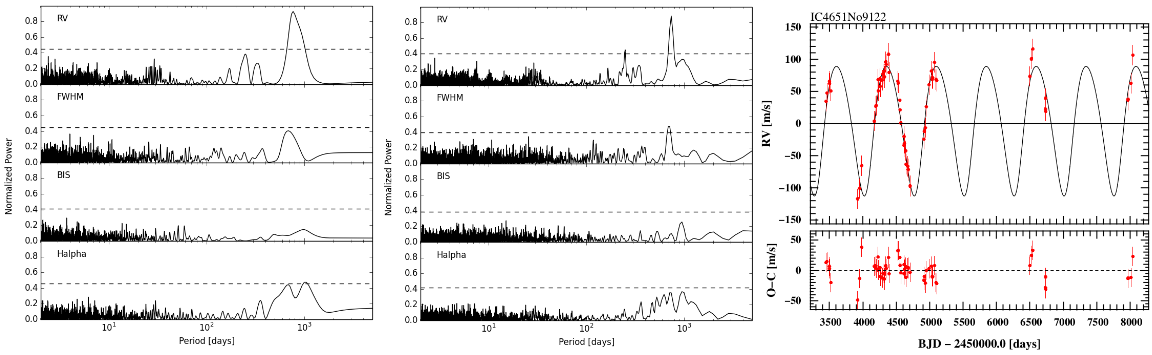

Figure 4: *Left:* Generalized Lomb-Scargle periodograms of RV, FWHM and Hα index for IC4651No9122 with data taken until 2009. The dashed line indicates the FAP at 1% level. *Middle:* The same for the full dataset. *Right:* *RV* curve as a function of time and as a function of orbital phase for IC4651No9122.

rotationally modulated active regions [14, 13] or radial and non-radial pulsations [6]. Moreover, a new kind of pulsations with period of hundreds of days have been recently proposed to be manifestations of oscillatory convective modes [21]. Although these pulsations are expected to be only present in high luminosity stars ($\log(\mathrm{L}/\mathrm{L}_\odot) > 3$ dex for a $2\,\mathrm{M}_\odot$ star) they might be an explanation for the variability found in NGC4349No127, the most evolved of our targets [4]. Recently, this kind of pulsations have also been considered as a possible explanation for the *RV* variations found in γ Draconis with a semi-amplitude of $148\,\mathrm{m\ s}^{-1}$ and a period of 702 days that changes in phase and amplitude [8]. Curiously, the suspicious *RV* variations of our targets also have a period close to 700 days. Furthermore, there are other cases in the literature with long-period *RV* variations in M giants that correlate with stellar activity indicators such as BIS or Hα [15, 2].

The three examples presented here clearly expose the difficulty of detecting planets around evolved stars, especially the most massive ones. Therefore, it is important to carry out long-term observations covering more than one period of the planet candidates (and for a time span larger than the stellar rotational period), to evaluate the stability of the hypothetical planetary signal and its possible relation with the rotational period of the star.

Acknowledgements

E.D.M. acknowledges the support from Fundação para a Ciência e a Tecnologia (FCT) through national funds and from FEDER through COMPETE2020 by the following grants: UID/FIS/04434/2013 & POCI–01–0145-FEDER–007672, PTDC/FIS-AST/1526/2014 & POCI–01–0145-FEDER–016886, PTDC/FIS-AST/7073/2014 & POCI-01-0145-FEDER-016880 and POCI-01-0145-FEDER-028953. E.D.M. acknowledges the support from FCT through Investigador FCT contract IF/00849/2015/CP1273/CT0003 and in the form of an exploratory project with the same reference.

References

[1] Aurière M., et al., 2015, A&A, 574, A90

[2] Bang T.-Y., Lee B.-C., Jeong G.-h., Han I., Park M.-G., 2018, JKAS, 51, 17

[3] Delgado Mena E., Tsantaki M., Sousa S. G., et al., 2016, A&A, 587, A66

[4] Delgado Mena, E. et al., 2018, A&A, 619, A2

[5] Frink S., Mitchell D. S., Quirrenbach A., Fischer D. A., Marcy G. W., Butler R. P., 2002, ApJ, 576, 478

[6] Hatzes A. P., Cochran W. D., 1999, MNRAS, 304, 109

[7] Hatzes A. P., Cochran W. D., 1993, ApJ, 413, 339

[8] Hatzes A. P. et al., 2018, AJ, 155, 120

[9] Hekker S., Snellen I. A. G., Aerts C., Quirrenbach A., Reffert S., Mitchell D. S., 2008, A&A, 480, 215

[10] Johnson J. A., Aller K. M., Howard A. W., Crepp J. R., 2010, PASP, 122, 905

[11] Jones M. I., Jenkins J. S., Brahm R., et al., 2016, A&A, 590, A38

[12] Kunitomo, M., Ikoma, M., Sato, B., Katsuta, Y., Ida, S., 2011, ApJ, 737, 66

[13] Lambert D. L., 1987, ApJS, 65, 255

[14] Larson A. M., Irwin A. W., Yang S. L. S., Goodenough C., Walker G. A. H., Walker A. R., Bohlender D. A., 1993, PASP, 105, 825

[15] Lee B.-C., Han I., Park M.-G., Mkrtichian D. E., Hatzes A. P., Jeong G., Kim K.-M., 2016, AJ, 151, 106

[16] Lillo-Box, J., Barrado, D., Correia, A. C. M, 2016, A&A, 589, A124

[17] Lovis C., Mayor M., 2007, A&A, 472, 657

[18] Niedzielski A., Villaver E., Wolszczan A., et al., 2015, A&A, 573, A36

[19] Queloz D., Henry G. W., Sivan J. P., et al., 2001, A&A, 379, 279

[20] Reffert S., Bergmann C., Quirrenbach A., Trifonov T., Künstler A., 2015, A&A, 574, A116

[21] Saio H., Wood P. R., Takayama M., Ita Y., 2015, MNRAS, 452, 3863

[22] Sato B., Ando H., Kambe E., Takeda Y., Izumiura H., Masuda S., 2003, ASPC, 294, 51

[23] Setiawan J., Pasquini L., da Silva L., Hatzes A. P., von der Lühe O., Girardi L., de Medeiros J. R., Guenther E., 2004, A&A, 421, 241

[24] Villaver, E., Livio, M., Mustill, A. J., Siess, L., 2014, ApJ, 794, 3

[25] Walker G. A. H., Yang S., Campbell B., Irwin A. W., 1989, ApJ, 343, L21

Highlights on Spanish Astrophysics X, Proceedings of the XIII Scientific Meeting of the Spanish Astronomical Society held on July 16 – 20, 2018, in Salamanca, Spain. B. Montesinos, A. Asensio Ramos, F. Buitrago, R. Schödel, E. Villaver, S. Pérez-Hoyos, I. Ordóñez-Etxeberria (eds.), 2019

Observations and numerical modelling of the 2018 Jupiter's South Temperate Belt Disturbance.

Peio Iñurrigarro[1], Ricardo Hueso[1], Agustín Sánchez-Lavega[1], Jon Legarreta[1] and Josep María Gómez-Forrellad[2]

[1] Escuela de Ingeniería de Bilbao, UPV/EHU
[2] Fundacio Observatorio Esteve Duran

Abstract

Moist convective storms can trigger atmospheric activity of different scales in Jupiter's atmosphere: From localized storms to planetary-scale disturbances including "contained" activity over a given region. In February 2018 a convective storm erupted in Jupiter's South Temperate Belt. This occurred inside an elongated cyclonic region informally known as the STB Ghost, close to the large anticyclone BA. The initial storm lasted only a few days but it broke the elongated Ghost into two structures, one of them interacting with oval BA and the other being expelled to the West. After the rupture both features continued to evolve over time-scales of several months. Here we present a study of this perturbation based on the long-term analysis of amateur, JunoCam and HST observations and we perform numerical simulations aimed to reproduce the phenomenology observed. The simulations are run using the General Circulation Model EPIC and require a complex interplay between the Ghost, the convective eruption and oval BA. We constrain the strength of the convective storm to levels that are only compatible with water powered moist convection.

1 Introduction

Convective storms are an important mechanism for triggering changes in Jupiter. These storms usually develop at various latitudes and can have different intensities, going from small-scale storms, such as at the west of the Great Red Spot, to storms that trigger full planetary scale disturbances, such as the North Temperate Belt Disturbance (see [9] and [11]) or the South Equatorial Belt Disturbance (see [8] and [2]). Since October 2016 several phenomena have been observed in Jupiter related with a convective nature. In October 2016 four convective storms in Jupiter's North Temperate Belt (NTB) ended up developing a planetary scale disturbance that lasted several months [11]. In December 2016 a convective storm in the South Equatorial Belt (SEB) developed also a large-scale disturbance in this region with large-scale turbulence extending over several months. In October 2017 another disturbance was observed by several telescopes and the JunoCam instrument aboard Juno spacecraft, this time in the South Tropical Zone. This disturbance developed a South Tropical Zone Disturbance ([7]) with a recirculation of the zonal winds followed by its interaction with the Great Red Spot over 2018.

The so called South Temperate Belt (STB) Ghost is an elongated low-contrast cyclonic region located at the South Temperate Belt, at a planetocentric latitude around 27°S, that has been observed in every Jupiter apparition since 2011-2012. In February 2018 a series of convective storms erupted in a matter of 3 days inside the STB Ghost developing strong turbulence initially confined to this cyclonic region developing a South Temperate Belt Disturbance (STBD). This has been the first time in which a confined convective disturbance has been observed in all its phases and high-spatial resolution.

2 Evolution of the disturbance

In order to study this phenomenon we have used observations from several datasets: Amateur observations, our own observations made with the PlanetCam UPV/EHU instrument in the 2.2 m telescope at Calar Alto observatory on May and June 2018, publicly released Hubble Space Telescope observations at different dates over 2017 and February and April 2018 and JunoCam observations on December 2017. High quality amateur observations have been indispensable to study this event due to their capability of providing high temporal coverage and the quick evolving nature of this phenomenon. We have separated the evolution in three stages: Fist the situation before the convective activity, second the start of the convective activity and third the long-term evolution of the disturbance.

2.1 The STB Ghost prior to the convective eruption:

We studied the dynamical context of the STB Ghost before the beginning of the perturbation using HST and JunoCam data. We obtained wind measurements that characterize the STB Ghost circulation on HST images on February and April 2017. These images showed that the cyclone is an elongated feature with a size of $24,000 \, \mathrm{x} \, 4,500$ km with an external cyclonic circulation (clockwise) of 60 ± 10 m/s. The JunoCam images on December 2017 showed the structure of the Ghost but the small time separation between the images resulted in an estimation of the Ghost circulation of 80 ± 20 m/s. Over 2017 the Ghost has been slowly approaching to the long-lived anticyclone BA and it has been elongating until reaching a size of $28,000 \, \mathrm{x} \, 5,500$ km when the disturbance started. By the date of the convective eruption the Ghost was at a distance of 17° from the large anticyclone BA. The interaction of the East side of the Ghost with BA modified their longitudinal drift.

2.2 Characterization of the convective eruption:

The onset of the convective outbreak that triggered the disturbance was reported on amateur observations obtained on 4 February 2018. In those observations a bright spot of size

$1,800 \times 1,400$ km was observed inside the STB Ghost, with its convective nature demonstrated with observations in the strong methane absorption band. Two days later a second convective nucleus, with a size of $3,400 \times 1,700$ km, was observed to the west of the first one. The first convective outbreak was active during 5 days, while the second one was active only during 1 day. These storms triggered a local disturbance which was contained inside the STB Ghost.

On observations made by Hubble Space Telescope on 7 February 2018 (see Fig. 1) the first stage of the evolution of the disturbance can be seen. These images were taken 3 days after the onset of the convective outbreak and show how the storm acquires it's characteristic shape due to the shear of the tangential velocity within the cyclone and how it recirculates at the west border of the STB Ghost.

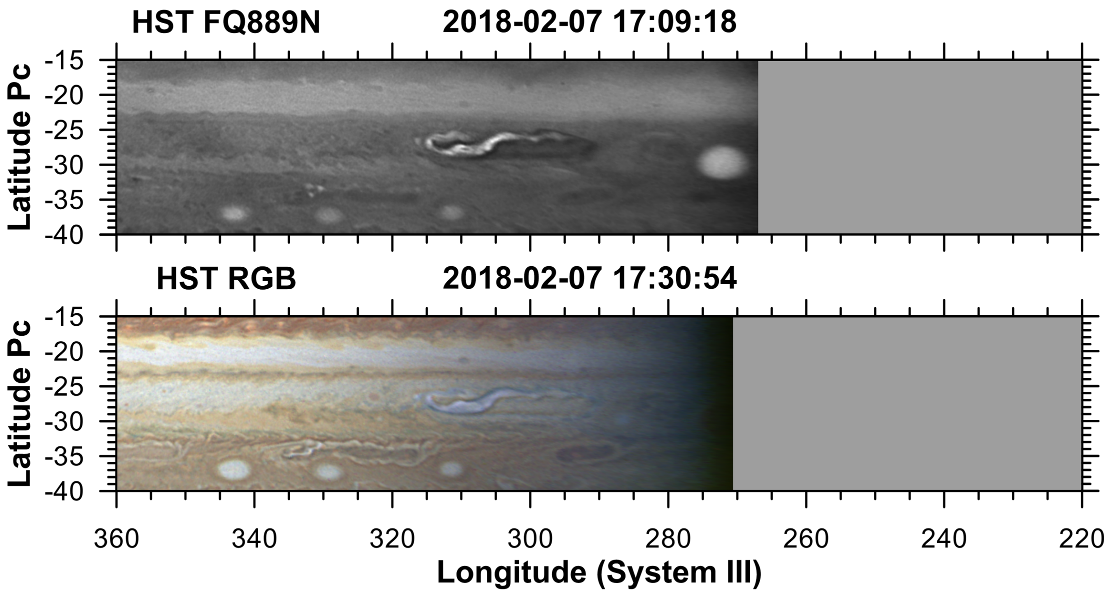

Figure 1: Observations of the South Temperate Belt Disturbance made with the HST the 7$^{\text{th}}$ of February 2018. The upper image is an image in the strong methane absorption band at 889 nm and the bottom image is a RGB colour composition.

2.3 Evolution of the STB Disturbance after the eruption:

We studied the long-term evolution of the disturbance through frequent observations obtained by amateur observers and available in the PVOL database (see [5]) and ALPO-Japan. The convection left the whole region perturbed with bright and dark filaments circulating the Ghost. As a result of this activity the Ghost was fully perturbed generating strong turbulence confined to the Ghost area. During the evolution of the disturbance different ovals were formed and some of them merged. The merger of two of those ovals at the beginning stages of the disturbance generated an oval that has been present for months, since its formation on March until the last analysed observations on September. Also, many small anticyclones moving westward were expelled from the active region. As the disturbance evolved the Ghost expanded slowly and its East side strongly interacted with the cyclonic region to the west of oval BA. It was observed that the outer ring of BA changed in color. On 1 April 2018 the Ghost broke-up creating a large dark structure on its southwest. On this epoch also the East side of the Ghost merged with the small cyclonic region that had always been present to the west of the anticyclone BA. Over May 2018 it seemed that the visible features were evolving to a more stable configuration, being the southwest structure clearly separated from the Ghost and drifting Eastwards and expanding zonally. The remains of the Ghost were retained West of BA and seemed to interact with an anticyclone on its South side. Observations made on 22 May 2018 with the PlanetCam UPV/EHU instrument at Calar Alto Observatory in the methane absorption band showed how some bright structures were still inside the Ghost, implying that vertical motions might be present even at that late date. By the end of May 2018 a large structure separated from the southwest structure and on July other two structures more. Over July and August 2018 the southwest structure slowly elongated in longitude simply following the differential drift of the winds and finally on September 2018 a large section of the East side of the southwest structure tore apart creating some small dark features.

3 Numerical modelling

We have used the General Circulation Model EPIC (Explicit Planetary Isentropic-Coordinate, [1]) to simulate the complex phenomenology observed. We tried to simulate the complex interaction between these three main elements: the STB Ghost, the anticyclone BA and the convective outbreaks. The EPIC model introduces vortices (for example the cyclonic Ghost and the anticyclone BA) by perturbing a stable atmosphere. As an initial stable atmosphere we have used a standard reference atmosphere (see [6]) with the zonal winds that characterize the domain of the simulatuon based on measurements over HST images of Jupiter obtained in 2016 ([4]). The storms are simulated introducing heat pulses with Gaussian shape with prescribed onset and offset times as it has been done in previous studies of other convective events in Jupiter (see [3], [9] and [11]) and Saturn (see [10]). The different elements in the simulation are introduced one by one letting the atmosphere to stabilize before introducing new perturbations. This is done because the perturbations used to introduce the Ghost and the oval BA in the atmosphere are relatively strong producing unrealistic turbulent patterns for the first tens of days. We started introducing the STB Ghost, after that the anticyclone BA and finally the convective storms.

The STB Ghost is well reproduced by an elongated vortex at planetographic latitude $-30.6\,^\circ$ with a semi-major and minor axes size of $10.5\,^\circ$ x $2.3\,^\circ$, vertically placed on a pressure level of 680 mbar with an upper vertical size of 3 scale heights and lower vertical size of 2 scale heights, tangential velocity of 80 m/s and shape parameter of 2. It has been allowed to evolve freely during 68 days to let the atmosphere stabilize.

The anticyclone BA has been introduced at planetographic latitude $-33.3\,^\circ$ with a semi-major and minor axes size of $3.5\,^\circ$ x $3.5\,^\circ$, vertically placed on a pressure level of 680 mbar with an upper vertical size of 3 scale heights and lower vertical size of 3 scale heights, tangential velocity of 100 m/s and shape parameter of 2. It has been allowed to evolve freely during 22 days. After a few days both the simulated Ghost and oval BA are located at the same relative distance as the Ghost and oval BA at the time of the onset of the convective storm.

We then perform an exploration of the space of parameters that define the convective perturbation. The best results are produced by introducing two pulses:

- First storm: It is injected at planetographic latitude $-30.8\,^\circ$ with a semi-major and minor axes size of $0.8\,^\circ$ x $0.5\,^\circ$. The convective pulse is introduced drifting at a velocity of 10.3 m/s with a pulse amplitude of 0.55 W/kg. The pulse is active during 5 days.
- Second storm: It is injected 2.5 days later than the first storm at planetographic latitude $-30.1\,^\circ$ and $2.5\,^\circ$ more to the west than the injection point of the first storm. The semi-major and minor axes of this storm are $0.4\,^\circ$ x $0.25\,^\circ$, the drift velocity is -3.5 m/s and the pulse amplitude is 0.4 W/kg. The pulse is active during 1 day.

After the injection of the second pulse the system is left to evolve freely. The result of the best simulation can be seen on Fig. 2. From the comparison between Fig. 1 and the second frame of Fig. 2 we can see that the first stages of the phenomenon are well simulated in the model.

4 Conclusions

From the analysis of the simulations we have constrained the vertical structure of the STB Ghost to be 4-5 scale heights, 2 of them below the visible clouds. We have also constrained the intensity of the first storm in the range $0.45 - 0.8$ W/kg and the intensity of the second storm in the range $0.3-0.6$ W/kg. Scale analysis shows that this energy can only be supplied by water condensation. We have also noted that the observations are best fitted when using a wind profile derived from HST 2016 observations. Using wind profiles from previous years only slightly different to the 2016 wind profile did not result in good results. Observations show that the storm drifts differently to the initial circulation at the STB Ghost with "own motions" with an intensity of 10m/s for the first storm that could be representative of a deep root of the convective storm also favouring water as the source of energy.

Acknowledgments

We are very grateful to the amateur astronomers community for posting their observations in image databases like PVOL and ALPO-Japan. We are also thankful to A. Simon and the rest of the HST/OPAL program (HST proposals 14334, 14756 and 15262) for running Jupiter observations. Further HST observations from proposals 14661 with M. Wong and 14839 and 14936 with I. de Pater have been used for this research. We are particularly grateful to the JunoCam team and the community of citizen scientists collaborating in the processing of Junocam images. This work has been supported by the Spanish MINECO project AYA2015-65041-P with FEDER, UE support and Grupos Gobierno Vasco IT-765-13. P. I. also acknowledges a PhD scholarship from Gobierno Vasco and Aula EspaZio for support in the observation campaign of Jupiter at Calar Alto Observatory.

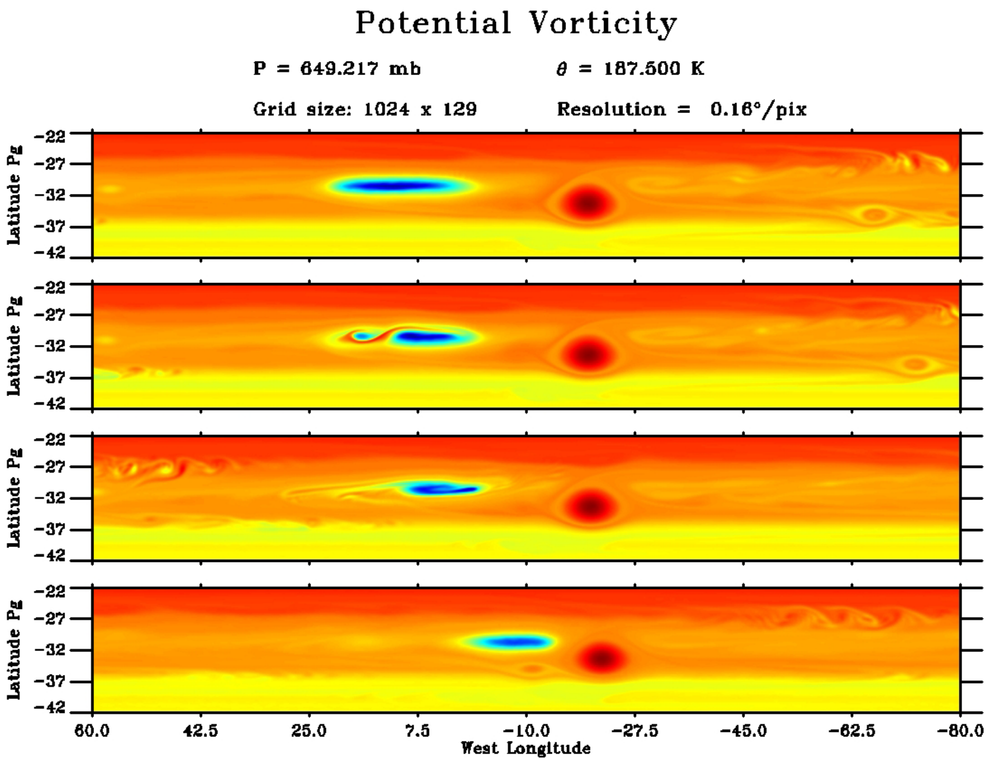

Figure 2: Some frames showing the potential vorticity of the best simulation obtained with the EPIC model. The days are corresponding to the simulation days 90.0, 93.54, 103.54, and 146.67 from the upper frame to the lower one.

References

[1] Dowling, T. E., Fischer, A. S., Gierasch, P. J., et al. 1998, Icarus, 132, 221-238

[2] Fletcher, L. N., Orton, G. S., Rogers, J. H., et al. 2017, Icarus,286, 94-117

[3] García-Melendo, E., Sánchez-Lavega, A., & Dowling, T. E. 2005, Icarus, 176, 272-282

[4] Hueso, R., Sánchez-Lavega, A., Iñurrigarro, P., et al. 2017, GRL, 44, 4669-4678

[5] Hueso, R., Juaristi, J., Legarreta, J., et al. 2018, Planetary and Space Science, 150, 22-35

[6] Legarreta, J., & Sánchez-Lavega, A. 2008, Icarus, 196, 184-201

[7] Sánchez-Lavega & A., Gómez 1996, Icarus, 121, 1-17

[8] Sánchez-Lavega, A., Gómez, J. M., Lecacheux, J., et al. 1996, Icarus, 121, 18-29

[9] Sánchez-Lavega, A., Orton, G. S., Hueso, R., et al. 2008, Nature, 451, 437-440

[10] Sánchez-Lavega, A., del Río-Gaztelurrutia, T., Hueso, R., et al. 2011, Nature, 475, 71-74

[11] Sánchez-Lavega, A., Rogers, J. H., Orton, G. S., et al. 2017, GRL, 44, 4679-4686

Highlights on Spanish Astrophysics X, Proceedings of the XIII Scientific Meeting of the Spanish Astronomical Society held on July 16 – 20, 2018, in Salamanca, Spain. B. Montesinos, A. Asensio Ramos, F. Buitrago, R. Schödel, E. Villaver, S. Pérez-Hoyos, I. Ordóñez-Etxeberria (eds.), 2019

Ground-based characterization of transiting exoplanets using the GTC.

D.Nespral[1,2], R.Alonso[1,2], and H.J.Deeg[1,2]

[1] Instituto de Astrofísica de Canarias, Tenerife, Spain
[2] Dpto. Astrofísica Universidad de La Laguna, Tenerife, Spain

Abstract

We observed the transits of six hot Jupiters with the Gran Telescopio de Canarias (GTC). The planets cover a large range of physical parameters such as planetary temperature, surface gravity, mass, radii and scale height (Table 1). This broad range of physical parameters allowed us to characterize different hot-Jupiter atmospheres. The transits were observed in the optical wavelength range, covering between 518 to 918 nm using the Optical System for Imaging and low Intermediate-Resolution Integrated Spectroscopy (OSIRIS) instrument. We present the different transmission spectra with different spectral absorption, depending on the atmospheric scale height.

1 Observations

The observations were carried out using long slit spectroscopy (to see Fig. 1), in which the target and one or more reference stars are placed inside one long slit. We used the R1000R grism to disperse the light over the total range from 500 to 1000 nm, with a pixel scale of 0.262 nm/pixel and a resolution of 1122. The time-series data were collected by two red-optimized 2048x4096 Marconi CCDs in the 200 or 500 kHz (according to the transit duration) and 2x2 binning readout mode. The full transits events along with one hour before the ingress and after egress were acquired. Depending on the seeing of the night, a slit of 12" or 40" was used.

2 Analysis

The transit light curves across the total range in wavelengths were fit simultaneously with instrument/weather systematics against the transit data to determine the physical planet parameters, which were then fixed for the analysis of the transmission spectra. For the

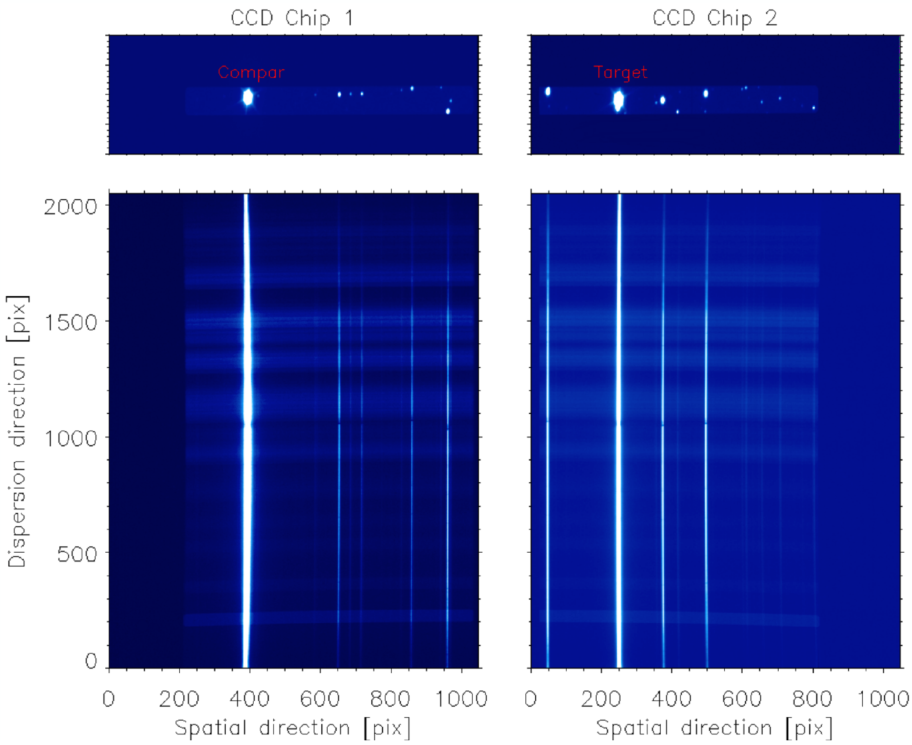

Figure 1: Example of long slit spectroscopy data. Through-slit images (top panels) and corresponding dispersed two-dimensional spectra images (bottom panels).

treatment of stellar limb darkening we employed the quadratic limb darkening law. We implement the same conditions as proposed by [4], using the parameters q1 and q2, which are related to the quadratic coefficients, u1 and u2. They were fixed using the Python package written by [2] given the effective temperature and surface gravity of the star. To create the transmission spectra, we extracted 10 nm bins in wavelength in the GTC/OSIRIS spectra and separately fit each bin for the planet-to-star radius ratio Rp/Rs and for instrument/ weather systematics. The analysis were carried out using MCMC methods, more specifically the MC3 code written by [1].

3 Results

The resulting transmission spectra are shown in Figure 2. They exhibit a variety of spectral absorption features as well as optical scattering slopes according to their scale height. We compared our transmission spectra to theoretical cloud-free models of [3]. Our results show several hot Jupiters that exhibit from clear to cloudy atmospheres. We found that only on planet with large scale height can their atmospheres be detected. But it not only depends on that feature, the hot Jupiters show strong pressure-temperature pro?iles due to the strong incident flux from their host star that hea3ng their upper atmospheric layers. Therefore

Table 1: Physical parameters of the planets studied in this work. H is the scale height.

Planet	T_{eq}(K)	g (ms^{-2})	$R_p(R_J)$	$M_p(M_J)$	P (days)	H (Km)
WASP-36b	1724	32.13	1.28	2.30	1.53	193
QATAR-1b	1500	26.65	1.18	1.33	1.42	210
TrES-3b	1620	27.54	1.29	1.92	1.30	211
HAT-P-33b	1782	6.91	1.68	0.72	3.47	926
HAT-P-41b	1941	6.91	1.68	0.80	2.69	1008
KEPLER-12b	1447	3.71	1.69	0.43	4.43	1426

a small shi9 on its temperature could move the cloud base and to change from clear to cloudy atmosphere or viceverse. Furthermore hot Jupiters have a wide variety of values of gravi3es and metallici3es , which affect the atmospheric temperatures. More ground-based observa3ons are needed to able to dis3nguish between clear and cloudy exoplanetary atmospheres.

References

[1] Cubillos, P., Harrington, J., Loredo, T. J., et al. 2017, AJ, 153, 3.

[2] Espinoza, N. & Jordan, A. 2015, MNRAS, 450, 1879.

[3] Fortney, J. J., Shabram, M., Showman, A. P., et al. 2010, ApJ, 709, 1396.

[4] Kipping, D. M. 2013, MNRAS, 435, 2152.

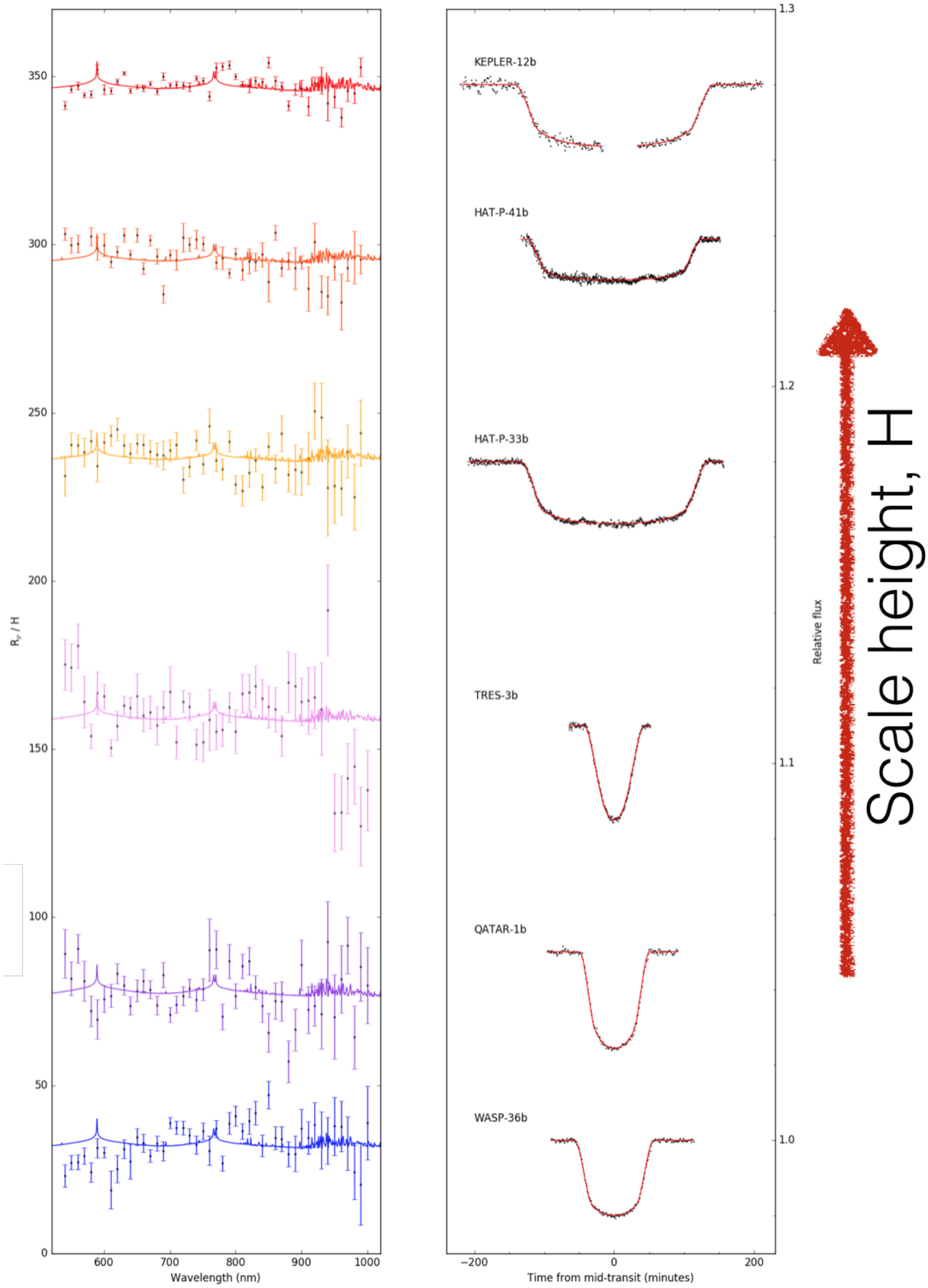

Figure 2: Left panel: GTC/OSIRIS transmission spectra, which are the difference between on-transit and offtransit spectra. Solid coloured lines show fitted atmospheric models corresponding to cloud-free models. The spectra have been offset and are ordered by values Rp/H. Right panel: Transit white light curves after removing the systematics, overlaid with the best fitting transit model.

Highlights on Spanish Astrophysics X, Proceedings of the XIII Scientific Meeting of the Spanish Astronomical Society held on July 16 – 20, 2018, in Salamanca, Spain. B. Montesinos, A. Asensio Ramos, F. Buitrago, R. Schödel, E. Villaver, S. Pérez-Hoyos, I. Ordóñez-Etxeberria (eds.), 2019

The search for exocomets. Gas around main-sequence stars.

Isabel Rebollido[1], Carlos Eiroa[1], Eva Villaver[1] and Benjamín Montesinos[2]

[1] Departamento. Física Teórica, Universidad Autónoma de Madrid, Cantoblanco, 28049 Madrid, Spain
[2] Centro de Astrobiología (CAB, CSIC-INTA), ESAC Campus, Camino Bajo del Castillo s/n, Villanueva de la Cañada, 28692 Madrid,Spain

Abstract

The environment of main sequence stars is expected to be depleted of gas once they have left the protoplanetary disc phase. Thus, a replenishment mechanism, such as grain-grain collisions or evaporation of solid bodies, is required to explain the presence of gas recently reported to be present around some MS stars. Here, we present a high resolution spectroscopic survey of over 100 A to G stars, searching for gas in the form of stable and variable non-photospheric absorptions in metallic lines (mainly Ca II and Na I). The observations were carried out in both hemispheres at La Palma (Spain), La Luz (México) and La Silla (Chile) observatories. The over 2000 spectra obtained allow us to construct time-series for most of the stars in the sample. So far, we have found gas compatible with circumstellar origin in almost half of the sample, and variable absorptions which can be interpreted as the evaporation of solid bodies, i.e. exocomets, in several objects, some of them being new detections.

1 Introduction

While exoplanets are routinely detected, we still have little information about the small components of planetary systems, such as asteroids and comets, which are key in the understanding of planet formation process. This lack of knowledge can be attributed to the challenging nature of direct detection, since given their small surface they have very marginal emission in thermal or scattered light. Infrared and (sub-)mm excesses due to the thermal emission of dust grains surrounding main sequence (MS) stars are indirect hints of the presence of planetesimals. Detection of molecular and atomic circumstellar (CS) gas emission has also been proposed to be at least partially originated by the outgassing of solid comet-like bodies. In the optical range, variable red-(and less frequently blue-)shifted absorptions of Ca

II H & K and Na I D have been attributed to the evaporation or sublimation of exocometary bodies when falling onto the star (Falling Evaporating Bodies or FEBs) [2]. Since the discovery of this phenomenon in the spectra of β Pic [4], around ~ 20 A-type stars have been reported to show these variable comet-like absorption features. A large body is often invoked as a perturber, driving the exocomets into the vicinity of the star. That appears to be the case of β-Pic, where a planet has been located in the system [5] in a position compatible with the observed dynamics of its exocometary events.

In order to further study this phenomenon, we have conducted a high-resolution spectroscopic survey, aiming at detecting and monitoring variable features in Ca II and Na I metallic lines of A to G stars.

2 Sample and observations

We have built a biased, non-homogeneous sample of 117 stars following different criteria with the aim of optimizing the detection of CS gas. The criteria are: stars with previously detected FEBs; debris disc stars; stars belonging to young associations; stars with near infrared (NIR) excesses (exozodii); stars with hot CS gas as revealed by the presence of Ti II; stars surrounded by cold molecular gas; and λ Böo stars. This sample allows us to monitor previously detected FEBs, and eventually to detect new stars with non-photospheric gas related to exocomets.

We have performed observations from September 2015 until September 2017 along 22 observing campaings in four different telescopes in both hemispheres: Mercator and NOT (La Palma, Spain); 2.2 MPG (La Silla, Chile) and TIGRE (La Luz, México). All these facilities are equiped with fibre-fed echelle spectrographs. We have obtained 2046 high resolution spectra, which will allow us to construct time series for most of the stars. Fig. 1 shows an example of time-series for one of the stars in the sample in four consecutive nights, where a variable event is detected.

3 Results

Gas detection

A median spectra was constructed for each star in order to maximize the signal to noise ratio and optimize the detection of stable components. The first results of our analysis of the Ca II K line show that a stable absorption is present in 59 stars. Out of those, we identify with a high level of confidence in 36 objects the absorption arising from CS gas in the inner regions of the system, as the radial velocity (RV) of the absorption matches that of the star. In 12 other cases the absorption's RV is closer to that of the interstellar medium (ISM) and so the origin of the gas is most likely interstellar. We can not discern whether the origin is CS or ISM in 8 cases so further investigation is needed. Among the 36 objects with CS gas, 12 of them show as well variable absorption features, detected when comparing every individual spectra, and in some cases daily or campaing medians, as shown in Figure 1. We also find 3 objects with variability and without any stable absorption in Ca II K line. The origin of the

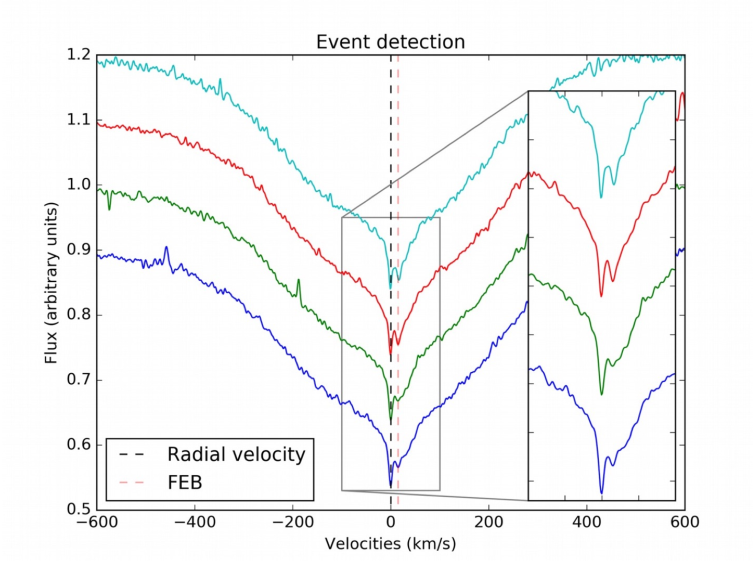

Figure 1: Ca II K line for four consecutive days of the same star. Each colour represents a different date. The vertical black dashed line shows the RV of the star, where a stable component is present. The red dashed line marks the position of the variable event.

variations could be attributed to multiple scenarios, including stellar winds or photospheric variability, so we will investigate other lines in the spectra in order to clarify this issue. Out of the 15 stars showing variability, 10 were already known in the literature to host FEB-like events, and therefore 5 are new additions. We also have 10 more stars in the sample with variability reported in the past, where we do not detect any variations in the line inspected so far. This could be due to the non-periodic nature of these events, rather than to false positives. The other 58 stars in the sample do not show any evidence of non-photospheric absorptions.

ϕ Leo

The A7 star ϕ Leo stood up in the survey sample, as it clearly shows variability in the Ca II K line [3]. This is particularly interesting, as it lacks a massive debris disc, and is much older that the rest of stars with detected exocometary activity: 500-900 Myr, against, for example, $\sim$ 20 Myr of β Pic. Since the strongest evidence of CS material found so far was the presence of Ti II [1], we investigated possible origins for the variations, but given the short time scales of the events (hourly, in some cases, as shown in Fig. 2), and the fact that they were only detected in Ca II K, we suggested exocometary activity in the inner regions of the system as the most likely explanation. We keep monitoring this object, aiming at better characterizing the absorptions, and looking for evidence of a possible massive perturber.

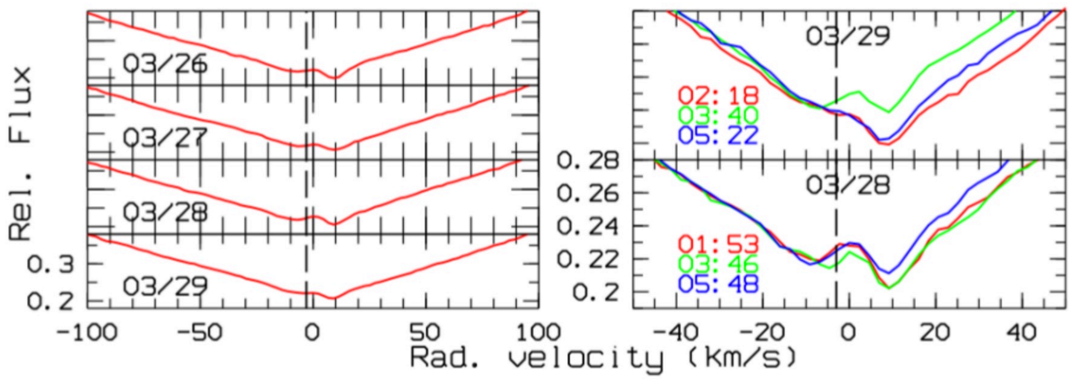

Figure 2: Detail of the Ca II K line of ϕ Leo. Left panel: Median spectra of four consecutive nights in March 2016. Right panel: Three consecutive spectra for two different nights where the hourly variations are detectable (Times are UT). Figure from [3].

Gas in debris discs

Gas-to-dust ratio is expected to decrease as planetary systems evolve their protoplanetary phase into debris discs. Nevertheless, there is a growing sample of debris discs with detected cold molecular and atomic gas in far-infrared and (sub-)mm wavelengths. To our knowledge, 17 objects show both a photometric excess related to the presence of a dusty debris disc and evidences of cold gas, located in the outskirts of the system. When analyzing the optical spectra of those 17 objects [6], we find stable non-photospheric absorptions in 10 of them, likely 7 being of CS origin (plus one of unclear origin). The narrow absorptions in the other two objects have most likely an interstellar origin. Interestingly, when considering the inclination angle of the discs, we find 7 out of 9 discs with edge-on inclination ($> 45^o$) to show non-photospheric absorption of CS origin and 7 out of 8 discs with face-on inclination ($< 45^o$) without any non-photospheric absorption, or with absorptions of ISM origin. This points towards the possibility of a geometrical effect being responsible for the detection or non-detection of the inner hot gas, revealed as stable non-photospheric absorptions when transiting the star.

4 Summary and conclusions

We have performed a non-homogeneous survey towards detecting CS gas in 117 stars, during two years in 22 observing campaings. We have found CS stable gas in at least 36 stars (plus 8 with non-clear origin) and variable gas features in 15 stars, out of which 5 are new detections. While we are still inspecting the data searching for gas evidence in other metallic lines, the results of the analysis of the Ca II K line have lead us to the discovery of highly variable absorptions in the star ϕ Leo, likely due to exocomets; and the possible geometrical effect in the detection of hot gas in cold gas bearing debris discs stars.

The available data collected on exocomets is still insufficient to fully understand how these bodies take part in planetary forming processes, therefore further time series studies are needed to better (chemically and dynamically) characterize these events.

Acknowledgments

Have also participated in this project: O. Absil; A. Bayo; H. Cánovas; A. Carmona; Ch. Chen; S. Ertel; A. Garufi; Th. Henning; D. P. Iglesias; R. Launhardt; R. Liseau; J. Maldonado; G. Meeus; A. Moór; A. Mora; J. Olofsson; G. Rauw; A. Roberge; P. Rivière-Marichalar. Based on observations made with the Mercator Telescope, operated on the island of La Palma by the Flemmish Community, and the Nordic Optical Telescope, operated by the Nordic Optical Telescope Scientific Association, at the Spanish Observatorio del Roque de los Muchachos of the Instituto de Astrofísica de Canarias. Based on observations made with ESO Telescopes at the La Silla Observatory under programmes 099.A-9004(A) and 099.A-9029(A). Also based on observations made with the TIGRE telescope funded and operated by the universities of Hamburg, Guanajuato and Liège. C.E., G.M., B.M., I.R., and E.V. are supported by Spanish grant AYA 2014-55840-P.

References

[1] Abt, H.A. 2008, ApJS 174, 499

[2] Beust, H. et al. 1998, A& A, 338, 1015

[3] Eiroa, C. et al. 2016, A&A, 594, L1

[4] Ferlet,R. et al. 1987 A&A, 185, 267

[5] Lagrange,A.M., et al. 2009, A&A 493, L21

[6] Rebollido, I., et al. 2018, A&A 614, A3

Highlights on Spanish Astrophysics X, Proceedings of the XIII Scientific Meeting of the Spanish Astronomical Society held on July 16 – 20, 2018, in Salamanca, Spain. B. Montesinos, A. Asensio Ramos, F. Buitrago, R. Schödel, E. Villaver, S. Pérez-Hoyos, I. Ordóñez-Etxeberria (eds.), 2019

Disentangling the albedo of the exoplanets from the stellar activity.

Luisa Maria Serrano[1,2],

[1] Instituto de Astrofísica e Ciências do Espaço, Universidade do Porto, CAUP, Rua das Estrelas, PT4150-762 Porto, Portugal
[2] Departamento de Física e Astronomia, Faculdade de Ciências, Universidade do Porto, Rua de Campo Alegre, 4169-007 Porto, Portugal

Abstract

The stellar phase curves of stars orbited by one planet include, in realistic conditions, the primary and secondary transit, three secondary effects, which are the beaming effect, the ellipsoidal modulation and the reflected light component of the planet, plus two sources of noise, the stellar activity and the instrumental noise. In our paper 'Distinguishing the albedo of the exoplanets from the stellar activity' we aimed at analyzing whether it was possible to detect the reflected light component of a planet in the case of an active bright star and supposing the instrumental noise to be on the same level of the predicted one for CHEOPS mission. The results of our work are important for planning observations of phase curves with CHEOPS and also with other future fotometric missions.

1 Introduction

The study of planetary atmospheres is an up-rising field of planetary characterization and it includes different techniques. One of them consists of analyzing the photometric emission of a star to retrieve the planetary albedo [3, 1].

A phase light curve is the flux emitted by the planetary system as a function of time. For a quiet star, it includes the primary transit, which happens when the planet crosses the stellar disc, the secondary eclipse, when the planet passes behind the star, and three weaker modulations. The first one is the doppler beaming effect, which consists of a change in the stellar brightness, proportional to the radial velocity amplitude of the planet. The second phenomenon is the ellipsoidal modulation, a shape modification of the star, which is deformed due to the gravitational attraction of the orbiting planet. The last component is the planetary flux, which includes the thermal proper emission of the planetary atmosphere and the reflected light component (the stellar light reflected by the planetary atmosphere). The thermal flux is stronger in the infrared observations, while the reflection dominates in the optical.

The future mission CHEOPS [5], which will be launched at the end of this year, among its secondary objectives, has the aim of analyzing the phase curves of exoplanets. Since CHEOPS observations will be performed in the optical domain, they will slightly be affected by the planetary thermal emission. The planetary flux will be dominated by the reflected component, which is proportional to the atmospheric albedo. Measuring the albedo is possible, but hampered by the two main sources of noise, the instrumental noise and the stellar activity, in the form of spots and plages [7]. Past works were capable to measure the albedo of hot Jupiters and some Neptunes, especially if observed with Kepler, because they had at disposition long observational periods [1, 3, 6]. Thus, by phase-folding the light curves, the instrumental error decreases and the albedo can be estimated with a high precision. CHEOPS will have a lower instrumental noise than Kepler, but, being an in-space telescope, it will have a limited time of observation for each target, maximum 20 days. Thus, applying the phase folding technique for determining the albedo of the planets observed with CHEOPS will not be possible. Serrano et al. 2018 [11] analyzed synthetic light curves adopting an MCMC which describes the stellar activity with a Gaussian Process. They demonstrated that with CHEOPS predicted level of noise and considering a maximum period of observation of 20 days (as programmed for each target observed with CHEOPS), it is possible to measure the albedo, distinguishing the reflected light component of the planet from the stellar activity, if the star is bright and the observations cover at least one entire stellar period of rotation.

2 Synthetic light curves and fitting method

Serrano et al. 2018 [11] produced simulations of phase light curves which included three main components: the reflected light component of the planet, the instrumental error and the stellar activity. They did not include the primary transit to focus the entire analysis on the reflected light component and how much the stellar activity can absorb it, hampering its detection. The secondary eclipse was also not included in the model because it is not always identified due to the stellar activity (see [6]). Moreover, not accounting for the two eclipses, they also tested the opportunity to detect non-transiting planets through their reflected light component, as suggested by Crossfield et al. 2010 [2]. For example, some planets, discovered through the radial velocity technique, do not transit their parent star because of the high orbital inclination. For this specific cases, the only way to study the atmosphere is through the reflected light component.

For modelling the reflected light component they adopted the lambertian model, which describes the planet as an isotropically reflecting sphere. The expression is:

$$\frac{F_p}{F_*} = A_g \left(\frac{R_p}{a}\right)^2 \frac{\sin z - (\pi - z)\cos z}{\pi} \tag{1}$$

with F_p the planetary flux, F_* the stellar flux, A_g the geometric albedo, R_p the radius of the planet, a the semi-major axis and z depends on the orbital inclination i and on the orbital phase.

For the stellar activity, the tool SOAP-T [8] was adopted to produce an activity pattern with an amplitude similar to those of moderately active stars. The instrumental noise was modelled as a white noise, with standard deviation equal to the predicted level of noise for CHEOPS. The produced simulations are characterized by 2 hours of timing. The reason of this choice is that, even if CHEOPS will have a timing of one point per minute, for data with shorter time periods than 2 hours, other stellar surface phenomena become significant (granulation for instance). Binning should help to reduce these extra noise sources. This said, CHEOPS predicted level of noise in 2 hours is 14 *ppm* for a 6.5 magnitude star, 17 *ppm* for an 8 magnitude star and 29 *ppm* if the magnitude is 10.

The final simulations are obtained by summing the three components:

$$\frac{F_{total}}{F_*} = \frac{F_p}{F_*} + \frac{F_{*,spotted}}{F_*} + \frac{F_{noise}}{F_*} \tag{2}$$

with $F_{*,spotted}$ the activity pattern and F_{noise} the instrumental noise.

Serrano et al. 2018 [11] adopted a Markov Chain Montecarlo (MCMC) as a fitting analysis method to recover the albedo, distinguishing it from the stellar activity. Modeling the stellar activity with an analytical model is not recommendable, given the high degeneracy of the problem. For this reason, the best approach so far developed consists of applying a Gaussian Process (GP), which treats the stellar activity as a correlated noise. As covariance function, the usual choice was the quasi periodic [4]. Since *SOAP-T* does not account for spot evolution, the chosen covariance function was totally periodic. Thus, the MCMC used the GP with periodic kernel to model the stellar activity and it adopted as fitting model the reflected light component of the exoplanet.

To sample from the posterior distributions the authors ran the tool *emcee*, which performs the MCMC. The estimated parameters were 5: the geometric albedo A_g, the stellar rotation P_*, the amplitude of the correlation p_1, the timescale decay of the periodic modulation p_2 , and an offset to fit the average value of the light curve. All the other planetary and stellar parameters were supposed to be known (for example with a transit or other detection methods), and thus fixed in the tests. For the albedo A_g and the offset the authors chose uniform priors, for the hyperparameters of the periodic kernel log-uniform priors, while for P_* a gaussian prior, centered on a previously estimated value. The stellar rotation is not always known, but some estimations can always be performed maybe with lomb-scargle periodogram or even an MCMC without imputing the reflected light component.

Each run of the MCMC required 30 chains from the prior distribution. A 500-step burn-in was performed, followed by a 1000 steps chains sampling. Thus, for each simulation the authors could obtain 30000 effective samples from the posterior distribution functions. The medians of the posterior distributions represented the best fit values of the free parameters. The 1σ uncertainties were the differences between the best-fit value and the 16^{th} and 84^{th} percentiles, respectively.

Table 1: Stellar and planetary properties adopted as starting parameters for the tests.

Stellar radius	R_*	1 $R_\odot$
Stellar inclination	I	90°
Stellar temperature	T_*	5778 K
Linear limb-darkening coefficient	c_1	0.29
Quadratic limb-darkening coefficient	c_2	0.34
Planet radius	R_p	0.1 R_*
Time of mid-transit	t_0	0.2 days
Eccentricity	e	0
Argument of periastron	w	0°
Inclination of the orbital plane	i	90°
Projected spin-orbit misalignment angle	λ	0°
Albedo	A_g	0.3

3 Minimum observation length for a target

Serrano et al. 2018 [11] produced simulations of stars with one orbiting planets, with the properties listed in table 1 for the planetary characteristics. For the spots properties refer to table 6 in [11]. The simulations had increasing durations, starting with one covering an entire orbital period and then augmenting by 3 days each time. The maximum observation length was 60 *days*. They performed this test for five different stellar rotational periods, 7, 11, 19, 23 and 26 *days*. The results are reported in the left side of figure 1, which shows the albedo as a function of the number of stellar rotations. For observation lengths shorter than the rotational period of the star, the *MCMC* cannot recover the albedo. After 1 stellar rotation, the errorbars significantly decrease and the albedo becomes closer to the inputed one. For more than 2 P_* the values are compatible to the real ones within 1σ. The main reason for this is that the albedo cannot be estimated without knowing well the stellar period of rotation, P_*. The Gaussian Process uses a periodic kernel for the activity and thus it needs observations longer than P_* itself, to predict it. There is also a duality between fast and slow rotators, with the $7-$ and $11 - days$ cases which converge to the inputed values well after 2 rotational periods. The other cases, instead, show a faster convergence, probably because for longer period of rotation, the rotation covers a longer time span and is described by more data points.

We can conclude that accounting for 20 *days* maximum period of observation with CHEOPS it is possible to measure the albedo for stars with a maximum period of rotation of 19 *days*. For fast rotators it would be better to cover all the 20 *days* of observations, or also decreasing the binning could be a solution. Serrano et al. 2018 [11] showed that for the $11 - days$ case, binning to 30 minutes the data instead of 2 hours, helps to get better albedo parameter after one stellar rotation, because the number of data points increases. It is important, anyway, to be careful with this smaller binning, because other activity features might rise, like the granulation.

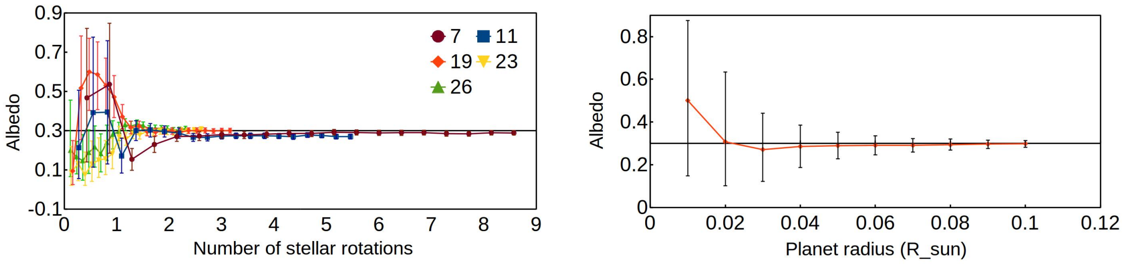

Figure 1: In the left, plot of the albedo and relative errors for the simulations obtained with $P_* = 7$, 11, 19, 23, and 26 *days* and increasing observational lengths. In the right, plot of the recovered albedo as a function of the planetary radius. These plots are taken from Serrano et al. 2018 [11].

4 Other results

Serrano et al. 2018 [11] also tested how the precision of the albedo estimation changes by varying other parameters. To do this, they fixed the length of the simulations to 39 *days* and the stellar period of rotation to 19 *days*.

Increasing the stellar magnitude, thus the amplitude of the instrumental noise, the convergence to the inputed albedo happens later than the 2 rotations boundary. For example, with 29 *ppm* of noise the stabilization is reached after 2.5 *days*.

Then, they varied the orbital period, increasing it of 1 *day* from 3 *days* until 15 *days*. As the period of the planet increases, the error of the identified albedo also increases. Increasing the period, indeed, lowers the signal of the planet and a longer time of observation is necessary to measure it.

Serrano et al. 2018 [11] also varied the planet radius from 0.1 R_* to 0.01 R_* and found that the albedo can still be measured until the regime of small neptunes, with $R_p = 0.04\ R_*$ (see the right side of figure 1). They additionally fixed R_p to 0.1 R_* and 0.05 R_* and varied the albedo from 0.6 to 0. Fitting them with the MCMC, they got the correct albedo and did not observe strong error variations between the different values, both for Jupiter size planets and Neptun size planets.

Finally, they varied the activity pattern by multiplying it by 100, 10, 5 and 0.1 and adding -99, -9, -4, and 0.9 respectively. Applying their *MCMC*, they demonstrated that once the activity pattern is well described by the kernel of the GP, the albedo is always retrieved. Thus, with this technique even if the star is very active, determining the planetary albedo is always possible. The main issue remains the instrumental noise.

5 Applying to real data

Serrano et al. 2018 [11] performed two different types of tests on real data. In the first one, they chose a periodic star from the McQuillan database of periodic stars, KIC 3643000, and they selected a portion of the light curve of the star in which the stellar activity does not significantly change. They added a planetary phase curve to this star, with the same properties as in table 1. They binned the data to have the same sampling as before and they obtained as level of noise 39 *ppm*, higher than the predicted one for CHEOPS. They applied the fitting tool on the phase curve and they got $A_g = 0.26 \pm 0.11$. The errorbar is twice the one obtained in the simulations. Apart from the instrumental noise, the main reason is connected to the kernel of the GP, which is periodic, while the stellar activity in the analyzed data is not exactly periodic. So, an aperiodic kernel would have probably helped to get a more precise result.

This is confirmed by the test performed on the star Kepler-7, which has a hot Jupiter orbiting aroun, Kepler-7b. This target was first analyzed by Angerhausen et al. 2015 [1], who retrieved an albedo of 0.35. Serrano et al. 2018 [11] extracted the entire 10th quarter of Kepler observations and binned the data to two hours. They applied their fitting tool and retrieved $A_g = 0.36$, close to the value found by Angerhausen et al. 2015 [1]. Anyway, the rotation period of the star results to be lower than the measured one (15.7 *days* instead of 16.7) and the hyper-parameters p_1 and p_2 are also physically poorly constrained. The fitted activity is not as periodic as it should be, given the adopted kernel, because Kepler-7 activity is not strictly periodic and shows evidence of spot evolution.

We can conclude that the fitting tool right now does not work for real data, because it requires the aperiodic component in the kernel of the GP. Nonetheless, once improved the tool with CHEOPS we will have the opportunity to measure the albedo of several Jupiter size planets and some small Neptunes. Much better results are instead expected with the launch of future photometric missions, like TESS [10] and PLATO [9], because their instrumental noise is lower and they will offer long periods of observations, thus allowing for data covering many stellar rotations. Using the GP for modelling the activity will allow to get rid of the extra noise which did not permit so far to measure the albedo of planets orbiting active stars.

Acknowledgments

This work was supported by Fundação para a Ciência e Tecnologia (FCT) through national fundsand by FEDER through COMPETE2020-Programa Operacional Competitividade e Internacionalização by these grants UID/FIS/04434/2013 & POCI-01-0145-FEDER-007672; PTDC/FIS-AST/28953/2017 & POCI-01-0145-FEDER-028953 and PTDC/FIS-AST/32113/2017 & POCI-01-0145-FEDER-032113.

L.M.S. also acknowledges support by the fellowship SFRH/BD/120518/2016 funded by FCT (Portugal) and POPH/FSE (EC).

References

[1] Angerhausen, D., DeLarme, E., & Morse, J. A. 2015, PASP, 127, 1113

[2] Crossfield, I. J. M., Hansen, B. M. S., Harrington, J., et al. 2010, ApJ, 723, 1436

[3] Esteves, L. J., De Mooij, E. J. W., & Jayawardhana, R. 2013, ApJ, 772, 51

[4] Faria, J. P., Haywood, R. D., Brewer, B. J., et al. 2016, A&A, 588, A31

[5] Fortier, A., Beck, T., Benz, W., et al. 2014, in Proc. SPIE, Vol. 9143, Space Tele- scopes and Instrumentation 2014: Optical, Infrared, and Millimeter Wave, 91432J

[6] Lillo-Box, J., Barrado, D., Moya, A., et al. 2014, A&A, 562, A109

[7] Oshagh, M., Santos, N. C., Ehrenreich, D., et al. 2014, A&A, 568, A99

[8] Oshagh, M., Boisse, I., Boué, G., et al. 2013a, A&A, 549, A35

[9] Rauer, H., Aerts, C., Cabrera, J., & PLATO Team. 2016, Astronomische Nachrichten, 337, 961

[10] Ricker, G. R., Winn, J. N., Vanderspek, R., et al. 2015, Journal of Astronomical Telescopes, Instruments, and Systems, 1, 014003

[11] Serrano, L. M., Barros, S. C. C., Oshagh, M., et al. 2018, A&A, 611, A8

Highlights on Spanish Astrophysics X, Proceedings of the XIII Scientific Meeting of the Spanish Astronomical Society held on July 16 – 20, 2018, in Salamanca, Spain. B. Montesinos, A. Asensio Ramos, F. Buitrago, R. Schödel, E. Villaver, S. Pérez-Hoyos, I. Ordóñez-Etxeberria (eds.), 2019

UV to far-IR reflectance spectra of carbonaceous chondrites- II. The Cg asteroid spectral class and the plausible link among CV and CK chondrites.

S. Tanbakouei[1,2], J. M. Trigo-Rodríguez [1,2], C.E. Moyano-Cambero[1,2], J. Llorca[3]

[1] Institute of Space Sciences (CSIC), Meteorites, Minor Bodies and Planetary Sciences Group, Campus UAB, c/Can Magrans s/n, 08193 Cerdanyola del Vallès (Barcelona), Catalonia, Spain.
[2] Institut d'Estudis Espacials de Catalunya, C/ Gran Capità, 2-4, despatx 201, 08034 Barcelona, Catalonia, Spain.
[3] Institute of Energy Technologies, Department of Chemical Engineering and Barcelona Research Center in Multiscale Science and Engineering, Universitat Politècnica de Catalunya, EEBE, 08019 Barcelona, Catalonia, Spain.

Abstract

Primitive carbonaceous asteroids are among the darkest objects in our solar system, being the target of future sample-return missions like e.g. Hayabusa 2 and OSIRIS-REx. So far the carbonaceous chondrites arrived to our planet are the only available samples representing these asteroids. The identification of the parent body of each chondrite group is a complex puzzle that requires gain insight into the mineralogy, and physico-chemical processes occurred in space to these undifferentiated bodies. Among the carbonaceous chondrites we concentrate here in the reflective properties of two groups that are chemically related and form the so-called CV-CK clan. We present CK reflectance data that is consistent with a separated evolutionary pathway from CV chondrites. Current data supports a scenario in which the CV and CK chondrites formed in a common parent asteroid that was disrupted by collisions at an early stage of its evolution. Then, at least two asteroid fragments evolved separately and ended with dinstinctive grades of metamorphism.

1 Introduction

Most meteorites arrived to Earth are samples of asteroids that can be studied in our laboratories at zero delivery cost. Despite the different size scales between an asteroid and a meteorite, the latter share compositional and reflectance properties with their parent bodies because they were part of them. In consequence, the undifferentiated chondritic meteorites have proven to be good proxies to understand the properties of chondritic asteroids. While we can study meteorites on the ground with laboratory experiments, the properties of an asteroid are often inferred from remote sensing. Significant differences arise, not only because of the different scale, but also due to the space weathering processes that alter asteroids in the interplanetary medium. After 4.5 Ga of asteroidal evolution, a meteoroid released from a parent body can attain a favorable orbit to produce surviving meteorites.

Recovered specimens show the diversity and heterogeneity of chondritic asteroids, and provide key information about the physical processes they experienced during the history of the solar system. Laboratory reflectance spectra of differentiated meteorites can be used to identify the rock-forming materials of asteroids ([4] and [12]).

The CK group defined by [8] has close compositional and textural relationship with the CV chondrites, but they are distinguishable from one another by their refractory lithophile abundances and other compositional features [14], e.g. the refractory inclusions abundances and the presence of igneous rims around chondrules. CKs are the most oxidized extra-terrestrial rocks found so far, owing to their low abundance in Ni and Fe and their high content of fayalite and magnetite [5]. There is a hypothesis that the CKs were formed from CVs after impacts and high temperatures, and these processes made them aqueously altered and annealed [14]. Such a working scenario implies an evolutionary processing of CKs and suggests that each specimen available in meteorite collections should exhibit gradational differences with significant consequences for their reflectance spectra. In order to test that collisional scenario, a significant number of CKs and CVs samples are needed. Fortunately, the last decades have seen the recovery of a significant number of CKs discovered in Antarctica, and with scarce terrestrial weathering that make them good to test spectroscopically probable links with their parent asteroids.

Consequently, as the goal of this paper, we use CK meteorite reflectance spectra to describe specified spectral features that can be used to identify the parent bodies of this chondrite groups in remote observations. On the other hand, as CK chondrites have experienced different degrees of metamorphism, we think that their reflective behavior might help to establish asteroidal evolutionary patterns.

2 Instrumental Procedure

We have obtained the reflectance spectra of several CK carbonaceous chondrites from the NASA Antarctic collection (Table 1) by using the experimental setup described by [13]. A Shimadzu UV3600 UV–Vis–NIR spectrometer is used to obtain reflectance spectra of thick and thin meteorite sections as in our previous work. The standard setting for the spectrometer is an integrating sphere (ISR) with a working range 0.18–2.6 μm, but working in laboratory conditions the signal is too noisy beyond about 2 μm.

The spectrometer light originates from one of two lamps and passes through a variable slit, then is filtered with a diffraction grating to select the desired wavelength and afterwards is split into two alternating but identical beams with a chopper. Next the beam interacts with the sample and is routed to the detector. The reference beam interacts with the material and then goes to the same detector. Inside of the ISR is coated with a duraflect reflecting polymer [13].

Table 1: Meteorite specimens from which reflectance spectra were obtained here.

CK samples
CK4 ALH 85002
CK4 LAR 04318
CK4/5 PCA 82500
CK5 LAR 12265 thin
CK5 LAR 12265 thick

3 Results and Discussion

The reflectance spectra obtained in this work for CK4 and CK5 were averaged in Fig. 1. We have compared our mean reflectance spectra for Cg asteroidal reflectance class by using the Bus-DeMeo Taxonomy Classification. We used the average data of CK spectral reflectance and normalized them at 0.65 μm. The spectra obtained with this spectrometer always show two instrumental peaks (one from 1.4 to 1.6 μm and the other from 1.9 to 2.2 μm) and noises between $\sim$0.8 and 0.9 μm. We used thin ($\sim$30 μm) and thick (mm) meteorite sections to obtain the spectra. The spectra presented here cover a wide range (0.4 to 1.9 μm) to be compared with asteroids spectra taken from ground or space-based telescopes. In the following discussion we compare our CK data with those published by [3].

The most common mineral in CK chondrites is olivine. It exhibits an absorption feature centered near 1.06 μm that can be seen in Fig.1 [3]. With increasing Fe^{2+} content, the center of this absorption band moves to longer wavelengths, becomes deeper and darker by increasing the overall reflectance (see e.g. [9]). In our data the olivine band extends between 0.95 and 1.15 μm (see Fig. 1). Plagioclase feldspar is a minority phase in CK silicates that may exhibit a weak Fe absorption band near 1.20 μm ([1]), which appears weakly in our spectra.

Table 2: Comparison between the CK spectral properties of the data in [3], NASA Relab Spectrum and our data. Wavelenghts (μm)

Wavelengths	Wavelengths ([3])	Wavelengths Relab	Minerals
0.6,0.90 - 1.10, 1.95-2.15	0.65,0.95,2.0 – 2.10	-	FeO and Fe_2O_3 contents
0.6,0.9 - 1.1,1.27-1.3	0.6 - 0.7,1.06,1.25	0.7,1.05	Olivine
0.6 - 0.7,0.8 - 0.9,1.25	0.65, 0.9, 1.25	1.35	Plagioclase Feldspar
0.98 - 1.05	1.0	1.03	Magnetite
2.05 - 2.15	2.1	-	Fassaite

The presence of pyroxene may be located at 2 μm band, varies from 1.80 to 2.08 μm for low -Ca pyroxenes, and 1.90–2.38 μm for high–Ca Pyroxenes [3]. Our CK spectral data shows an unusual increase, but still shows this band around 1.85 μm. Basically, the pyroxene has a minimal effect on the olivine band positions in CKs than other CCs [2].

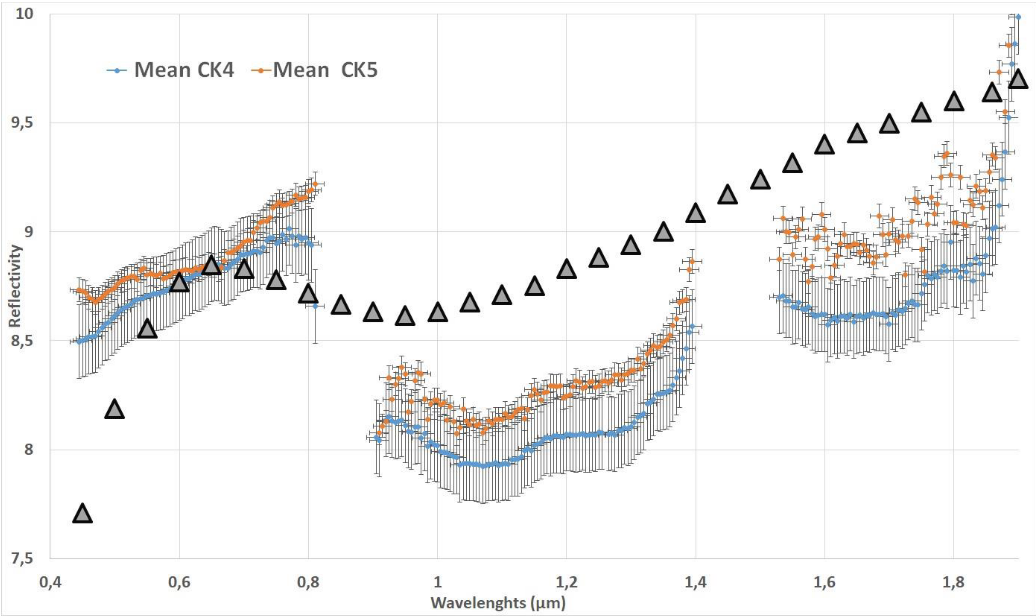

Figure 1: Reflectance averaged spectra of CK carbonaceous chondrites. The gaps are regions in which the spectrometer data show noises artifacts or were removed.

The spectral shape of the magnetite is a function of grain size and location [10] which can be seen near 1 μm. In our CK spectra, the location of this band vary from 0.98 to 1.05 μm depending on the specimen analyzed. We also noticed that other minor phases associated with refractory inclusions can be weakly featured as well, being fassaite, the most common mineral forming Ca- and Al- rich Inclusions (CAIs), the best example.

To discuss the main features observed in these spectra we focus on the main minerals forming CK chondrites. These are olivine, magnetite, Fe-sulfide, pyroxene (both low and high Ca), plagioclase feldspar, refractory oxides forming CAIs and minor amounts of carbonaceous phases [3]. As previously noted, the CKs and CVs are the only CC groups that have undergone thermal metamorphis to a significant extent [7]. Their petrologic type is suggestive of them experiencing impacts that promoted recrystallization, crushing, and aqueous alteration. Most of the CK chondrites experienced metamorphism and aqueous alteration, so these processes altered the rock-forming minerals and their reflectance properties.

Some authors have measured isotopic compositions in specimens of CV and CK chondrites precisely and found that many petrographic properties of these meteorites are nearly similar [6]. They suggested that CV and CKs come from the same reservoir but can be distinguishable by the level of experienced thermal metamorphism [14]. Fig. 1 compares the average reflectance spectra of two petrological types of CKs with increasing metamorphism. It shows that high-metamorphosed specimens have higher reflectances.

We have noticed in the CK spectra that the center of the absorption bands does not change with the metamorphic grades, but correlate with the olivine composition. The depth of bands also increases as the thermal metamorphism does and the deepest band depth is

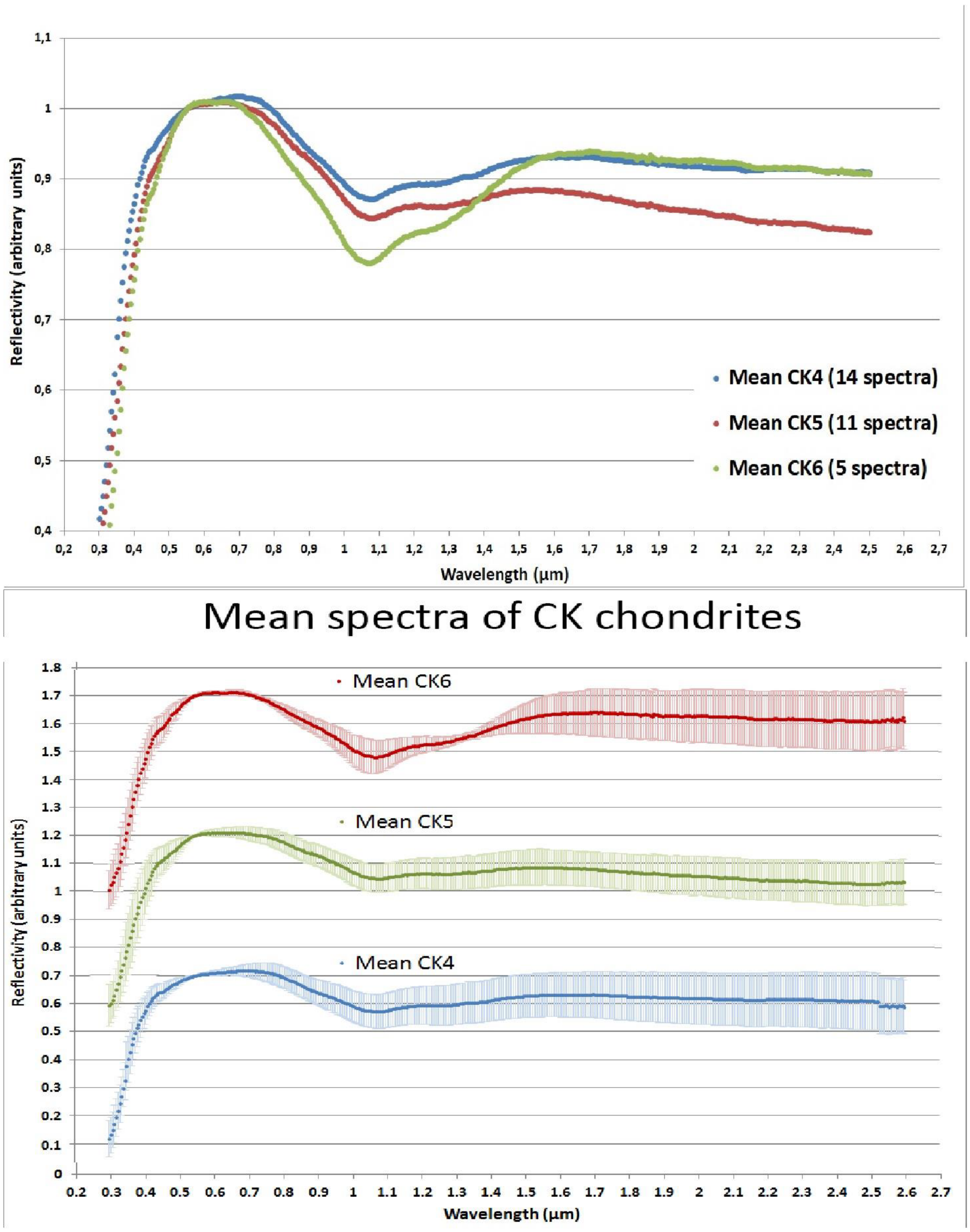

Figure 2: The mean spectral reflectance for CK4, CK5 and CK6 petrological types including the dispertion band. A total of 14, 11 and 5 spectra were plotted respectively [11].

shown in CK6 spectra Fig. 2.

We have compared our mean reflectance spectra in the range of 0.4–1.9 μm with Cg asteroidal reflectance class by using the Bus-DeMeo Taxonomy Classification. We noticed that a higher degree of metamorphism in CV-CK chondrites decreases the reflectance in the NIR that differs from Cg asteroid class. As metamorphism and aqueous alteration were followed by the formation of secondary minerals, their effect on the impact darkening in CV-CK chondrites in one of the main interest of Hayabusa 2 mission, which will return samples from the rare Cg-type asteroid (162173) Ryugu. Indeed, Cg-type asteroids, could be considered a good match for CK meteorites but differs in the NIR.

4 Conclusions

The plausible correlation between CV and CK reflectance spectra and their similar chemical compositions indicate that they could have a common parent body that was broke apart long time ago. Different parts and fragments were taken apart by non-gravitational forces and led to asteroids with different degree of space weathering, aqueous alteration and thermal metamorphism. Then, our study of the reflectance spectra of CK chondrites brought us to reach the following conclusions:

- We have found a common behavior in CK chondrite reflectance spectra. With increasing metamorphic grade, the reflectance decreases in a deeper 1 μm region absorption feature. In fact, higher petrographic degree is consistent with higher reflectivity.

- The band depth of olivine in CKs increases while the thermal metamorphism increases: the CK4–5.5 petrographic grades of meteorites display shallower band depths, while the CK6 spectra exhibit the deepest band depths.

- The best strategy to explain the mentioned differences between CV and CK chondrites is invoking a common parent body, that experienced fragmentation in an early stage of its evolution. Then at least two asteroid fragments evolved separately so they ended with distinctive grades of metamorphism.

- The parent body of CK chondrites has experienced significant collisional processing that ended in distinctive mineralogy and buck chemistry because of thermal annealing.

Acknowledgments

This work has been funded by AYA 2015-67175-P (PI: J.M. Trigo-Rodríguez). This study was done in the frame of a PhD. on Physics at the Autonomous University of Barcelona (UAB). JL is a Serra Húnter Fellow and is grateful to ICREA Academia program and GC 2017 SGR 128.

References

[1] Adams J.B., Goullaud, 1978. Proc. Lunar Planet. Sci. Conf. 9, 2901–2909.

[2] Cloutis E.A., Gaffey M.J., et al., 1986. Geophys. Res. 91, 11641–11653.

[3] Cloutis E.A. Hudon P., Hiroi T., et al., 2012a. Icarus 221. 911

[4] Gaffey M.J., 1976, JGR, 81, 905

[5] Geiger T. & Bischoff A., 1995. Planet. Space Sci. 43, 485

[6] Greenwood R. Franchi I.A., Kearsley A.T., et al., 2010, Geochim. Cosmochim, Acta 74, 1684.

[7] Huss G.R., Rubin A.E., Grossman J.N., 2006, Meteorites and the Early Solar System II.

[8] Kalleman G. W., Rubin, A. E., et al., 1991. Geochim. Cosmochim. Acta 55, 881

[9] King T.V.V., Ridley I.W., 1987. J. Geophys. Res. 92, 11457–11469.

[10] Morris R.V., Lawson C.A., Gibson E.K. Jr., et al., 1985. J. Geophys. Res. 90, 3126.

[11] Moyano- Cambero C.E., Trigo-Rodríguez J.M., et al., 2016. Meteorit. Planet. Sci. 51, 1795.

[12] Trigo-Rodríguez J.M., 2015, In Planetary Mineralogy, M.R. pp. 67-87

[13] Trigo-Rodríguez J. M., Moyano-Cambero C.E., et al., 2014, MNRAS 437, 227

[14] Wasson J. T., Isa J. and Rubin A.E., 2013, GCA 108, 45

Highlights on Spanish Astrophysics X, Proceedings of the XIII Scientific Meeting of the Spanish Astronomical Society held on July 16 – 20, 2018, in Salamanca, Spain. B. Montesinos, A. Asensio Ramos, F. Buitrago, R. Schödel, E. Villaver, S. Pérez-Hoyos, I. Ordóñez-Etxeberria (eds.), 2019

The catalytic role of chondrites in the prebiotic enrichment of Earth.

Josep M. Trigo-Rodriguez[1,2], and Raffaele Saladino[3]

[1] Institute of Space Sciences (CSIC), Campus UAB, c/Can Magrans s/n (Bellaterra), 08193 Cerdanyola del Vallès (Barcelona), Catalonia, Spain
[2] Institut d'Estudis Espacials de Catalunya (IEEC), C/ Gran Capità, 2-4, desp 201, 08034 Barcelona, Catalonia, Spain
[3] Biological and Ecological Department (DEB), University of Tuscia, 01100 Viterbo, Italy.

Abstract

The carbonaceous chondrites are among the most primitive materials arrived to the Earth's surface, and they are associated with undifferentiated bodies. Their chemical and mineralogical content reveal that they probably accreted far from the Sun and formed part of transitional asteroids and comets, both C and water-rich. Formed by fine-grained aggregates at relatively low-encounter velocities, they ended as porous bodies that retained significant amounts of water, organics and volatile compounds that were available in the outer protoplanetary disk. These bodies participated actively in the delivery of volatiles to the planets, particularly during the so-called Late Heavy Bombardment, but we should take into account that also preserved and transported highly reactive minerals to planetary bodies at different moments of their evolution. The catalytic properties found of these meteorites suggest that the arrival of these minerals to planetary surfaces with abundant water and N-bearing species could have promoted organic complexity. .

1 Introduction

The scientific interest of understanding the physico-chemical properties of the accretionary materials available in the protoplanetary disk is out of doubt. Meteoritica give us an amazing opportunity because mother nature offers in every meteorite fall rocks arrived from remote, but typically unknown, bodies. Then, it is not surprising that the currently ongoing sample return missions, Hayabusa 2 and OSIRIS REx, have primitive carbonaceous asteroids as targets, respectively named 162173 Ryugu and 101955 Bennu.

The growing interest of the scientific community can be understood given that the carbonaceous chondrite meteorites (hereafter CCs) have being identified as pristine materials with a primordial chemical content and specific unique properties [12] and [1]. The key role of these materials in the origin of life was envisioned many decades ago [14], but it is now reinforced by new discoveries about aqueous alteration ago [9], and [25]. CCs formed in the outer regions of the protoplanetary disk and accreted crystalline and amorphous minerals, plus organics, ices and hydrated minerals. Being formed so far away as part of relatively small asteroids that never melted, the CCs available in meteorite collections are fine-grained rocks that we could consider a kind of fossil sediments of creation. Being highly porous and fragile, these fascinating meteorites share unusual properties with their undifferentiated parent bodies: low conductivity and thermal inertia, weak magnetism and low tensile strength. CCs can be considered good proxies of the materials forming C-rich asteroids, but still can be considered rocks biased by the nature, as they have arrived to the Earth's surface after many destructive processes. Then, not only similar properties, but also spectral signatures point that small asteroids and comets are formed by CCs. Being small and fragile [22] remnants of creation, at the very beginning were scattered all over the solar system and subjected to collisions, and fragmentations [2]. In particular, close approaches experienced to planets could have induced the fragmentation of these fragile objects. As a natural consequence of being weakly compacted and collisionally fragmented objects, I envision that they were easily disrupted and arrived to different planetary bodies as a rain of meteoroids [22]. Such processes could have being necessarily intense during the Late Heavy Bombardment. By comparing with the measured projectile Lunar flux over time, we estimated that the early Earth was subjected to a meteoritic flux that could have been at least about 5-6 orders of magnitude larger than the current one [20]. It obviously traduces in huge amounts of chondritic materials reaching the Earth's surface about 4 Ga ago, at an annual rate of thousands of billions of metric tons [20]. Consequently the amount of volatiles delivered under such high-flux circumstances are also very significant, playing a key role in fertilizing the Earth's surface [5]. Then, the reactive minerals forming CCs reached the surface of Earth and other planetary bodies, being exposed to a warm, and water-rich environment that was probably promoting the first steps towards the origin of life [20]. To support the previously outlined hypothesis we have recently made a significant progress in understanding the role of chondrites in prebiotic evolution. In a previous paper we analyzed the catalytic effect of six CCs. Here we will focus in the main implications of our previous discovery [16] concerning the catalytic properties of the rock-forming chondritic minerals.

2 Technical procedure

We developed an experiment to know the reactivity of CCs that was previously described [16]. The procedure started with ∼50 mg of each selected stone that were ground in an agate mortar. Then, the extraction of the meteorite powder to remove endogenous organics is carried out in two steps as previously reportedmarty12. Mass spectrometry was performed by the following program: injection temperature 280°C, detector temperature 280°C, gradient 100°C×2min, 10°C/min for 60 min. To identify the structure of the products, two strategies were followed. First, the spectra were compared with commercially available electron mass spectrum libraries such as NIST (Fison, Manchester, UK). Secondly, GC-MS analysis was repeated with standard compounds. The results clearly indicate that carbonaceous chondrites catalyze the synthesis of natural nucleobases, carboxylic acids, and amino acids from mixtures of NH2CHO and water at 140°C. Two general scenarios were analyzed: thermal water (TW) and seawater (SW), both tested in the presence of formamide for six CCs that are listed in Table 1.

Table 1: Antarctic carbonaceous chondrites used in the experiments described

Meteorite name	Group and petrologic type	Discovery year
Allan Hills 84028	CV3	1984
Elephant Moraine 92042	CR2	1992
Miller Range 05024	CO3	2005
Larkman Nunatak 04318	CK4	2003
Grosvenor Mountains 95551	C-ung	1995
Grosvenor Mountains 95551	C2-ung	1995

3 Discussion

The results of our experiments were presented in [16]. They confirm that carbonaceous chondrites in presence of warm water and formamide catalyze the synthesis of natural nucleobases, carboxylic acids, and amino acids from mixtures of NH2CHO and water at 140°C (see Fig. 1). This experimental evidence supports a parent body origin for the complex organic compounds found in CCs, probably coming from hydrated asteroids as previously suggested [25]. Secondary minerals being the product of such primordial aqueous alteration were originated in a first stage of water release due to radiogenic heating [1], and show evidence of static aqueous alteration with limited water availability producing complex organic chemistry [17];[11]. Still in such restrictive conditions the reactive minerals could act as catalyzers and promote increasing organic complexity in chemical evolution, tens of millions of years before to be completed the formation of Earth [16]. These results shape a prebiotic scenario consisting of CCs debris reaching the Earth's surface and acting as catalysts, particularly in a volcanic-like environment. Such scenario could be favoured by the fact that the the flux of chondritic materials was probably very high in the remote past. We have suggested that chondritic materials reaching the Earth's surface about 3.8 Ga ago during the so-called Late Heavy Bombardment, may have reached an annual rate of thousands of billions of metric tons [20]. Such amounts could have increased as consequence of the disruption of fragile C-rich transitional objects scattered by the inwards migration of the giant planets probably occurred 3.8 Ga ago [3].

In view of our results, we think that new experimental and theoretical approaches are needed to understand the role of certain reactive minerals in promoting the catalytic reactions. For example, the interaction of organic compounds with water and chondritic silicate surfaces has been recently explored using quantum chemical periodic simulations [15]. Often we get clues on the required experiments when we study the nature of aqueous alteration minerals

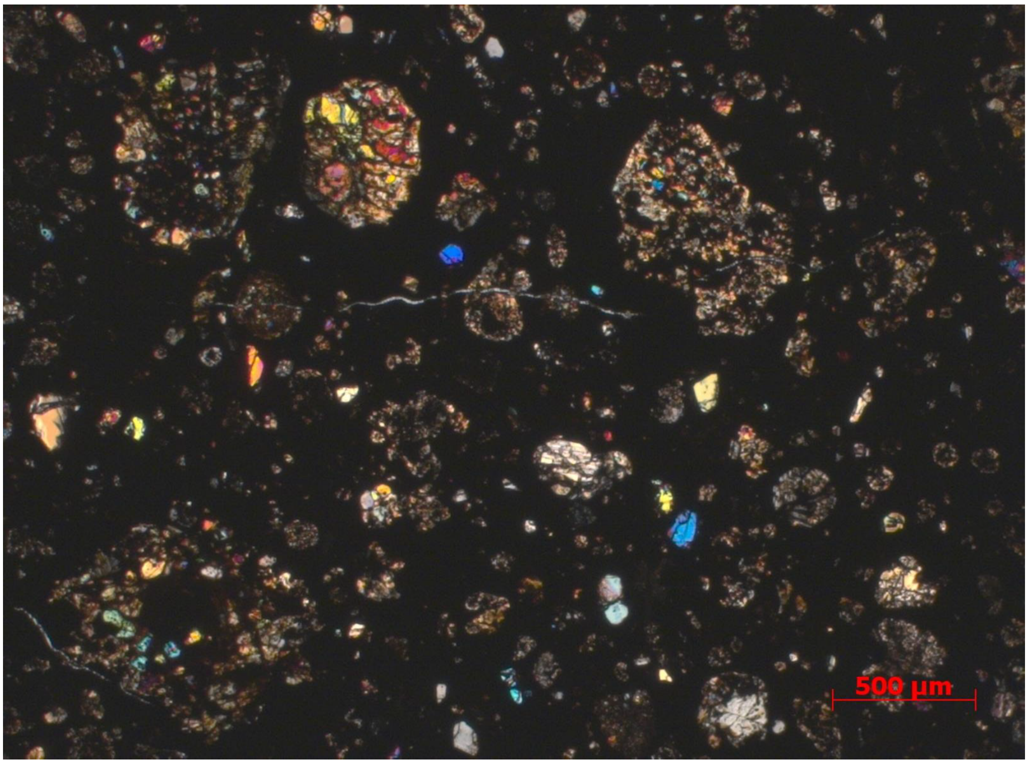

Figure 1: Prebiotic synthesis of biomolecules from the selected meteorites and water in the presence of formamide. Experimental conditions: 1% meteorite, 59% NH2CHO, 40% water, 140 °C, 24 h. The meteorite shown as example is GRO95551 in a NASA image containing a cubic cm as scale.

in the matrices of carbonaceous chondrites (see Fig.2). We notice that water played a major role in mobilizing certain elements initially present in the interiors of the chondrules, sulphide and metal grains of carbonaceous chondrites [18]. In some groups, like e.g. CM and CR chondrites, the action of water was pervasive, and participated in the partial or complete replacement of mineral grains located in the matrix. Minerals preferentially grew in the pores available in the matrix of carbonaceous chondrites [21]. In general, we can say that liquid water availability was very limited, and dependent of the primordial heat produced by the decay of short-lived nuclides. This is consistent with the dated aqueous alteration minerals, formed during the first 10 Ma after parent body accretion, see e.g. [8]. Then, we can conclude that aqueous alteration was localized and static [24]. Consequently, even when we found that chondritic minerals are extremely reactive, we think that planetary bodies are far better candidates to catalyze complex organics over long time scales. That point is not a big issue given the continuous delivery of chondritic minerals to the surface of Earth and other solar system planetary bodies [4].

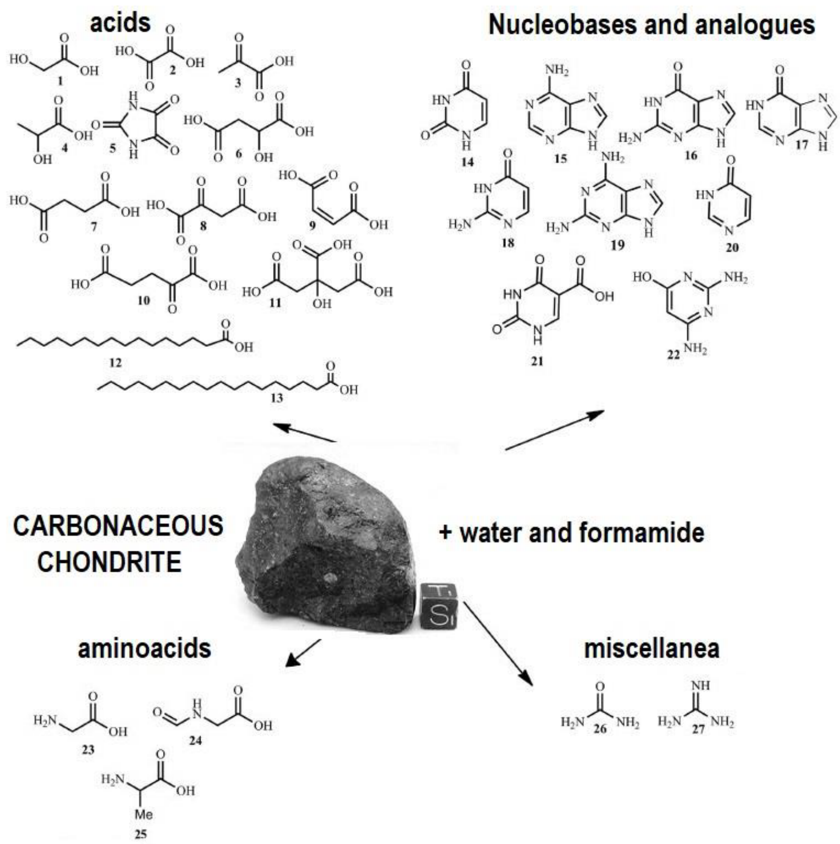

Figure 2: Transmitted image of the pristine CO3 chondrite Allan Hills 77307. The fine-grained organic-rich matrix of carbonaceous chondrites was a perfect place to retained hydrated minerals, and ices during parent body accretion. Crystalline silicate chondrules share their boundaries with the matrix and participate in the elemental mobilization.

Table 2: The products listed in Fig. 1 of the thermal condensation from NH2CHO/water mixtures in the presence of the powders of selected carbonaceous chondrites. For more details see: [16].

Product #	Compound
1	Glycolic acid
2	Oxalic acid
3	Pyruvic acid
4	Lactic acid
5	Parabanic acid
6	Malic acid
7	Succinic acid
8	Oxaloacetic acid
9	Fumaric acid
10	Ketoglutaric acid
11	Citric acid
12	Palmitic acid
13	Stearic acid
14	Uracil
15	Adenine
16	Guanine
17	Hypoxanthine
18	Isocytosine
19	2,6-Diaminopurine
20	4 (3H)-pyrimidinone
21	Uracil 5-carboxylic acid
22	2,4-diamino-6-hydroxypyrimidine
23	Glycine
24	Formyl glycine
25	Alanine
26	Urea
27	Guanidine

4 Conclusions

We have performed a series of laboratory experiments with carbonaceous chondrites that demonstrate that these meteorites can actively and selectively catalyze the formation of biomolecules from formamide in aqueous media and under presence of formamide. The presence of a N-bearing specie like formamide was found to be an important premise to catalyse organics [19]. In our new experiment we found specific catalytic behaviours, depending on the origin and composition of the chondrites and on the type of water present in the system (activity: thermal > seawater > pure). In any case, we reported in the one-pot synthesis of all the natural nucleobases, of aminoacids and of eight carboxylic acids (forming, from pyruvic acid to citric acid, a continuous series encompassing a large part of the extant Krebs cycle). See Figure 1, and Table 2 for a short list of the main products found in our experiments.

As it was previously explained in discussion, having into account the intense meteoritic flux extracted from the study of the Moon surface [20], we envision a general prebiotic scenario consisting of carbonaceous meteorite debris reaching the Earth's surface and acting as catalysts in a volcanic-like environment providing heat, thermal waters and formamide. Obviously that scenario can be extended to other planetary bodies, particularly those who had water- and N-rich environments. Consequently, other potential planetary bodies could have experienced a significant delivery of carbonaceous chondrite materials, like e.g.: Mars, Europe or Titan [20]. Our scenario is particularly favourable for Mars, which has been exposed to the continuous infall of chondritic materials over the eons, and with a extremely thin atmosphere. It is also remarkable that atmospheric changes in Mars were regional or even global, involved in brine evolution and the formation of evaporites during the Amazonian era [7]. The interaction of water with the Mars surface is demonstrated by the presence of aqueous alteration minerals found in old Martian meteorites, like e.g. the carbonates formed in the fractures of Allan Hills 84001 orthopyroxenite about 4 Ga ago [13]. Over time, varying rock/soil compositions could have produced water fluids with different PH levels, so some specific environments could have being more favourable to organic catalysis. In fact, recent discoveries of organic matter preserved at Gale crater and other Martian environments are particularly promising [6], and could be used to encourage the search of older sediments not exposed to the extreme surface environment.

Consequently, we think that our discovery of the unique catalytic properties of the minerals forming chondritic meteorites could open a debate about the ability that these rocks have to produce favourable prebiotic scenarios in other worlds different to our own. Future exploratory missions of solar system planetary bodies should try to identify old terrains, carrying instrumentation to dig, collect and characterize the organic compounds present in sequential layers, and also including specific experiments to study the reactivity of the sampled minerals under the presence of hot water and formamide.

We have performed a series of laboratory experiments with carbonaceous chondrites that demonstrate that these meteorites can actively and selectively catalyze the formation of biomolecules from formamide in aqueous media and under presence of formamide. The presence of a N-bearing specie like formamide was found to be an important premise to catalyse organics [19]. In our new experiment we found specific catalytic behaviours, depending on

the origin and composition of the chondrites and on the type of water present in the system (activity: thermal > seawater > pure). In any case, we reported in the one-pot synthesis of all the natural nucleobases, of aminoacids and of eight carboxylic acids (forming, from pyruvic acid to citric acid, a continuous series encompassing a large part of the extant Krebs cycle).

Acknowledgments

We thank the NASA Meteorite Working Group for providing the samples that were studied in the framework of two Spanish research projects (AYA2011-26522 and AYA2015-67175-P, PI: JMTR) to identify pristine meteorites, and study their properties. Chemical analyses were supported by the Italian Space Agency (ASI) project "Esobiologia e Ambienti estremi: dalla chimica delle Molecola allaBiologia degli estremofili" Number 2014-026-R.0 (CUP: F 92I14000030005).

References

[1] Alexander, C.M.O'D., McKeegan, K.D. and Altwegg, K. (2016) Space Sci. Rev. 214, 36.

[2] Beitz E., Blum J., Parisi M.G., and Trigo-Rodríguez J.M. (2016) Ap.J. 824, art.id.12, 29 pp.

[3] Bottke W.F., Vokrouhlicky D., Minton D., Nesvorny D., Morbidelli A., Brasser R., Simonson B., and Levison H.F. (2012) Nature 485, 78-81.

[4] Brownlee, The origin and properties of dust impacting the Earth, in: Accretion of extraterrestrial matter throughout Earth's history, B. Peucker-Ehrenbrink and B. Schmitz Eds. Kluwer Academic/Plenum Publishers, New York, USA, 2001, pp. 1–12.

[5] Court R.W. and Sephton M. A. (2014) Geoch. Cosmoch. Acta, 145, 175.

[6] Eigenbrode J. L. et al. (2018) Science 360, 1096-1101.

[7] Fairén A.G., Schulze-Makuch D., Rodríguez A.P., Fink W., Davila A.F., Uceda E.R., Furfaro R., Amils R., McKay C.P. (2009) Plan. Space Sci., 57, 276-287.

[8] Fujiya W., Sugiura N., Sano Y., and Hiyagon H. (2013) Earth Planet. Sci. Lett. 362, 130-142.

[9] Glavin D. P. and Dworkin J. P. (2009) PNAS 106, 5487-5492.

[10] Martins, Z., Alexander, C. M. O'D., Orzechowska, G. E., Fogel, M. L., and Ehrenfreund P. (2007) Meteoritics & Planetary Science 42, 2125.

[11] Martins, Z., Price M.C., Goldman N., Sephton M.A., and Burchell M.J. (2013) Nature Geoscience volume 6, pages 1045–1049.

[12] Marty B. (2012) Earth Planet. Sci. Lett. 313-314, 56-66.

[13] Moyano-Cambero C.E., Trigo-Rodríguez J.M., Benito M.I., Alonso-Azcárate J., Lee M. R., Mestres N., Martínez-Jiménez M.; Martín-Torres F.J., and Fraxedas J. (2017) Meteorit. Planet. Sci. 52, 1030-1047.

[14] Oró J. (1961) Nature 190, 389-390.

[15] Rimola, Trigo-Rodríguez J.M., and Martins Z. (2017) Phys. Chem. Chem. Phys., 2017, 19, 18217

[16] Rotelli L., Trigo-Rodríguez J.M., Moyano-Cambero C.E., Carota E., Botta L., Di Mauro E. and Saladino R. (2016) Scientif. Rep. 6, doi:10.1038/srep38888

[17] Pizzarello S. and Cronin, J.R. (2000) Geoch. Cosmoch. Acta 64, 329-338.

[18] Rubin A.E., Trigo-Rodríguez J.M., Huber H., and Wasson J.T. (2007) Geoch. Cosmoch. Acta 71, 2361-2382.

[19] Saladino, R., Crestini, C., Cossetti, C., di Mauro, E., Deamer, D. (2011) Origins of Life and Evolution of Biospheres 41, 437-451.

[20] Trigo-Rodríguez J.M., Llorca, J. and Oró, J. (2004) In Life in the Universe: from the Miller experiment to the search for life in other worlds. Seckbach J., Chela-Flores J., Owen T. y Raulin F. (eds), Kluwer Publishers, Dordrecht, Holland, pp. 201-204

[21] Trigo-Rodríguez J.M., Wasson J.T., and Rubin A.E. (2006) Geoch. Cosmoch. Acta 70, 1271-1290.

[22] Trigo-Rodríguez J.M., and J. Blum (2008) Plan. Space Sci., 57, 243.

[23] Trigo-Rodríguez J.M., and J. Martín-Torres (2012) Plan. Space Sci., 60, 3-9.

[24] Trigo-Rodríguez J.M. (2015) In Planetary Mineralogy, EMU Notes in Mineralogy 15 pp. 67-87.

[25] Zolensky, M.E., Krot, A.N., Benedix, G. (2008) In: Oxygen in the Solar System (G.J. MacPherson, D.W. Mittlefehldt, J.H. Jones & S.B. Simon, editors). Reviews in Mineralogy & Geochemistry, 68. Mineralogical Society of America, Washington, D.C., pp.429-462.

Highlights on Spanish Astrophysics X, Proceedings of the XIII Scientific Meeting of the Spanish Astronomical Society held on July 16 – 20, 2018, in Salamanca, Spain. B. Montesinos, A. Asensio Ramos, F. Buitrago, R. Schödel, E. Villaver, S. Pérez-Hoyos, I. Ordóñez-Etxeberria (eds.), 2019

The role of viscosity and EUV/RX radiation in the dispersal of protoplanetary discs.

Juan C. Vallejo[1,2] **and Ana I. Gómez de Castro**[1,2]

[1] JCUVA, Joint Center for UV Astronomy, AEGORA research group,
Universidad Complutense de Madrid, 28040, Madrid, Spain
[2] Dpto. Física de la Tierra y Astrofísica, Fac. de CC. Físicas, Universidad Complutense de Madrid, 28040, Madrid, Spain.

Abstract

The EUV and X-ray radiation of host stars in protoplanetary discs produce photoevaporative processes that seem to play an important role in their evolutionary time-scales. The viscosity of the discs is a fundamental parameter when modeling these discs using the α-prescription. Unfortunately, there is no single accepted value for this viscosity, and the results are very dependant on that value. Our work has implemented a grid of simple $1D$ models in which the value of the viscosity is systematically changed. This allows to analyse how different diagnostic diagrams of observable quantities evolve as the α value changes.

1 Introduction

The protoplanetary discs are the natural scenario for planet formation processes. They provide the material from which planets form in between the accretion and post-accretion phases of the disc. Understanding their evolution and the mechanisms and time-scales by which the disc is eventually dispersed is a key issue in planet formation and life emergence theories.

Hence, the importance of analysing the mechanisms leading to changes in the accretion processes that may modify the disc's chemistry, the dust-to-gas ratio and can starve the gas reservoir available for planet formation. As the mass accretes onto star, the conservation of momentum implies that the disc spreads out, the accretion decreases with time and the radius increases with time. Internal viscous transport and magnetised winds are main candidates to explain this transport. There are other mechanisms, such as planet formation, dust growth and encounters with other stars. However, it is not clear how these mechanisms can produce global changes from 0.1au to 100au in the disc properties [5].

2 The viscous discs and the α prescription

The circumstellar optically thick discs are typically observed at ages of 1Myr, but such discs seem to have disappeared at ages around 10Myr. Therefore, transitional discs must be relatively short-lived, with transition times from primordial to discsless of roughly 10 per cent of the disc total lifetime [2]. The standard explanation to the observed spectral characteristics and the so-called "two-timescale behaviour" relies in a mass depletion mechanism, that produces a hole in the dust of the inner regions of the disc, and clearing processes quickly proceeding from the inside out once this gap opens.

The viscous evolution is a widely used model for explaining the transition from disc-possessing to discless status. The molecular viscosity of the gas is too small to produce significant evolution, but the viscous approach is quite common when ones interprets the viscosity as the outcome of a turbulent process. The so-called standard model, or α-model, for viscous accretion discs, was first formulated by Shakura and Sunyaev [11]. The original work relied on an optically thick accretion disc and a turbulent fluid described by a viscous stress tensor proportional to the total pressure. It can be shown that the kinematical viscosity can be written in this case as,

$$\nu(r) = \alpha c_s H(r), \tag{1}$$

where the $H(r)$ profile models the disc thickness, and the α parameter is a scaling factor of the friction between adjacent rings. Later on, this parameter turned into a "standard" dimensionless measure of viscosity, that conveniently hides the real viscosity mechanism, but somehow characterises its effectiveness. However, one must note that even within the same disc, the α value can have different values at different locations of the same disc, and even it can evolve with time.

There is a variety of mechanisms that can create these turbulent processes. The magnetorotational instability (MRI) has been a leading candidate for turbulence and angular momentum transport. However, the MRI can nonetheless be suppressed in non-ideal MHD [10], and there are other mechanisms to consider, such as outflows, hydrodynamical processes and gravitational instability, see [1] and references therein. Magnetic fields can be also of importance in momentum transport mechanisms and disc accretion may be primarily wind-driven with magnetised disc winds [3]. But, independently of the viscous mechanism, the α-parametrisation is still widely used as a way for hiding the details of the viscous transport mechanism. A value of $\alpha = 0.01$ was initially used because it provided evolutionary timescales in line with known properties of discs [7]. Later on, values ranging from 0.1 to 0.001 were in use (for instance, [8]). Nowadays, even lower values like 10^{-4} can be found [6].

3 Internal photoevaporation winds and viscosity

The observed two-timescale behavior in α-discs implies an efficient mass removal mechanism. The photoevaporation processes were firstly described in [4] as a convenient way to shutdown the mass accretion and trigger the disc dispersion. We briefly describe this model here. When

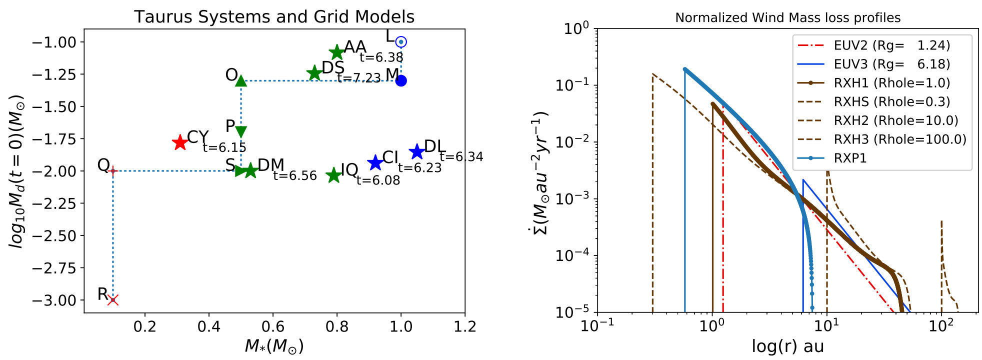

Figure 1: (Left) Some representative systems in the Taurus star forming region and the selected grid of discs models in the $M_* - M_d$ plane. The disc masses are the initial values. Hence, as the age of the discs increases, the initial points will move downwards in the diagram. In a very rough fashion, bluer Taurus stars means larger values for the mass of the host star. (Right) Normalised photoevaporative wind mass losses for diferent EUV and XEUV cases. The EUV winds have more localised wind losses, and the disc is hardly depleted at large radii. Conversely, XEUV winds are stronger and more extended. However, the X-ray winds strongly depend on the evolving geometry of the disc, mainly depending on the absence (RXP1 curve) or presence and size of a hole inside it (RXH1-3 curves).

the thermal velocity exceeds the local escape velocity, the surface layer gets unbound and evaporates, and a thermal wind with a speed comparable to the speed of sound (slow wind) takes away the disc gas. The calculation of the accreted mass can be done by computing the surface density $\Sigma(r,t)$ based on basic laws of mass and momentum conservation, as follows,

$$\frac{\partial \Sigma}{\partial t} = \frac{3}{r}\frac{\partial}{\partial r}[r^{1/2}\frac{\partial}{\partial r}(\nu \Sigma r^{1/2})] - \dot{\Sigma}_w, \tag{2}$$

where Σ_w denotes the mass loss by a given photoevaporative wind, functionally equivalent to have a sink for the mass.

We aim to analyse the interplay of the viscosity and photoevaporation processes, exploring the impact of the α values in the evolutionary time scales of different disc systems. For doing so, we have created a grid of models covering a variety of star masses and disc masses, for systematically changing the viscosity value. This grid is seen in the left panel of Fig. 1. The simple 1D model described by Eq. 2 allows to add different sink terms, corresponding to different thermal winds, to every modeled viscosity value. Therefore, we can solve the viscous evolution equation and compare the results got using EUV pure winds or EUV plus X-ray (XEUV) winds, with some real reference Taurus discs. The normalised winds mass profiles we have used are seen in the right panel of Fig. 1.

The final goal of our work is to crosscheck the results from our simulations with real systems, aiming to see how different viscosities affect typical diagnostic diagrams based on observable quantities. As a first approach, we have selected systems in the Taurus star-forming region because this is one of the nearest ($\approx$ 140 pc) and best-studied regions. Here,

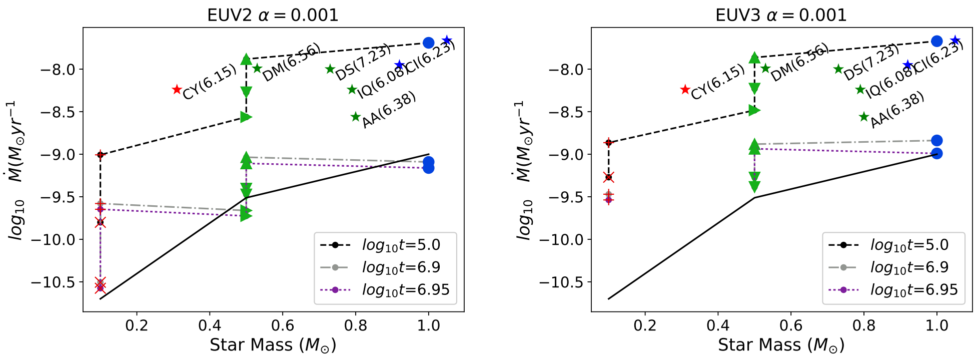

Figure 2: The role of the EUV strength in the evolution of the isochrones $\dot{M} - M_*$. (Left) The weakest EUV2 wind. (Right) The strongest EUV3 wind. As the age increases, the index of the power law relationship decreases. This decrease is faster as the viscosity and the strength of the EUV winds is larger. The Taurus systems and their ages are plotted for reference.

one can find loosely associated but rather isolated molecular cores. Hence, the influence of outflows, jets, or gravitational effects is minimised in this region.

3.1 EUV photoevaporation

The first photoevaporative process being added to the viscous evolution of a disc was the EUV photoevaporation [4]. The EUV computations are not quite complex, because the temperature of photoionised gas can be considered nearly constant $T \approx 10^4$K and one can compute mass losses based on a Stromgen criterion. However, when modelling these winds, we have seen the huge impact of some parameters in the results. Mainly, the gravitational radius, or distance at which the thermal energy is equal to the mechanical energy of a parcel of gas in keplerian rotation around the star. The strength of the wind heavily depends on both this radius and the EUV flux of the host star, and both values must be considered [12].

We have plotted diagnostic diagrams, such as the isochrones $\dot{M} - M_*$. The Figure 2 shows their evolution for two values of the viscosity. In a viscous-only disc, as the age increases, the power law relationship index decreases, faster as the viscosity is larger. When an EUV wind is added, this evolution is faster, but its very dependant on the gravitational radius. For the largest viscosities and stellar masses, the slope is made negative very quickly. For smaller viscosities, the change is no so fast, but still very noticeably. When comparing the rate of evolution of systems with the same stellar mass, the role played by the disc mass becomes very relevant, because the differences between these models grow with time faster than when the wind was not present.

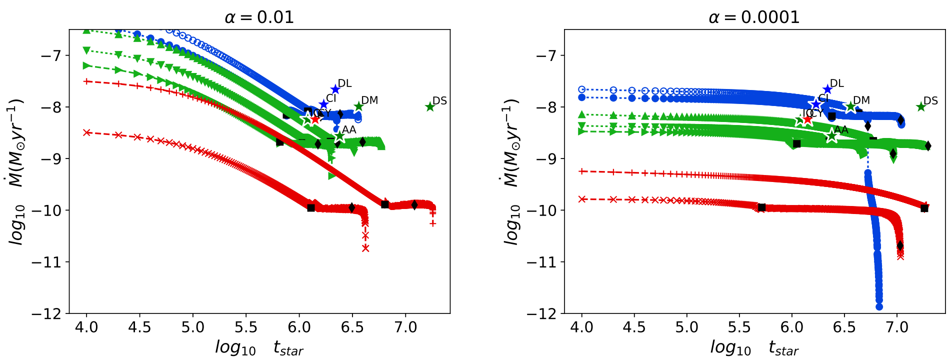

Figure 3: The role of the viscosity in the evolution of the mass accretion rate in the XEUV winds case. Same color and marker shape means same stellar mass. The bluer the color, the larger the mass. With the larger viscosities, the rate of accreted mass decreases faster. Black squares mark the hole opening time, black diamonds mark when the hole size is 100a.u.

3.2 XEUV photoevaporation

The physics of X-ray heating is by far more complex than the EUV processes described before. They rely in the X-ray photons in the $0.1 - 10$ KeV range that can tear off the electrons from the internal shells of metals. To treat the photoevaporative X-wind in the simple $1D$ viscous evolution model described by Eq. 2, we will follow the same approach taken in [6]. We will write a mass sink term $\dot{\Sigma}_{wind}$ based on the numerical fit to the simulations done by [9], where both EUV and X-ray contributions were introduced (noteworthy, the EUV contribution can be neglected when the X-ray radiation is present, even for the strongest UEV fields and the weakest X-ray fields). This model has two different epochs, hence two wind profiles delimited by the presence or not of a hole in the disc. There is an initial, primordial phase, that lasts until a gap opens. Once this gap is present, the wind fully clears the disc at given distances as gap grows and the inner edge of the outer disc is exposed directly to stellar irradiation.

The mass loss rate $\dot{M}$ is a fundamental observational parameter in the analyses of protoplanetary discs. This quantity is obtained by integrating the surface density $\dot{\Sigma}(r)$ at every instant during the numerical integration of the model. In general, as the viscosity decreases, the transport of mass, thus the evolution towards final state, is slower.

The Figure 3 shows this evolution for two values of the viscosity. We have also overlaid the representative Taurus systems. Obviously, Taurus ages, are subject ot experimental uncertainties. However, the main goal is to check the impact of the viscosity on the evolution of the disc, and these figures already show how one can match the theoretical and observational points by increasing the initial accretion rates $\dot{M}(t = 0)$. But the required increase seems to be huge. Therefore, a better alternative seems to consider lower values for the viscosities.

4 Conclusions and on going work

Simple 1D models based on the α-disc prescription, with α hiding a specific viscosity mechanism, can complement complex hydrodynamical simulations due to their simplicity in interpreting results. However, one should fully understand the limitations when handling this simplicity and modeling the discs with a single unique value. More work is needed for constraining the photoevaporative models with different observational parameters. The age of the systems and the disc masses must be improved for making these diagnostic diagrams more useful when comparing the results from simulations with real data. Future UV missions are required for providing further data in this area, and will help for improving these comparisons.

Acknowledgments

Juan C. Vallejo and Ana I. Gómez de Castro thank the Spanish Ministry of Economy, Industry and Competitiveness for grants ESP2014-54243-R and ESP2015-68908-R.

References

[1] Armitage, P.J. 2015, arXiv:1509.06382

[2] Anderson, K.R., Adams, F.C. and Calvet, N. 2013, ApJ, 774, 9

[3] Bai., X. 2016, ApJ, 821, 80

[4] Clarke, C.J., Gendrin, A. and Sotomayor, M. 2001, MNRAS, 328, 485

[5] Dullemond C. P., Dominik C. 2005, A&A, 434, 971

[6] Ercolano, B., Jennings, J., Rosotti, G., Birnstiel, T. 2017, MNRAS, 472, 411

[7] Hartmann L., Calvet, N., Gullbring, E., D'Alessio, P. 1998, ApJ, 495, 385

[8] Jones, M.G., Pringle, J.E., Alexander, R.D. 2012, MNRAS, 419, 925

[9] Owen, J.E., Clarke, C.J. and Ercolano, B., 2012, MNRAS, 422, 1880

[10] Riols, A., Lesur, G. 2018, A&A, 617, A117

[11] Shakura, N.I., Sundayev, R.A. 1973, A&A, 24, 337

[12] Vallejo, J.C., Gómez de Castro, A.I. 2018, APSS, 363, 246

Highlights on Spanish Astrophysics X, Proceedings of the XIII Scientific Meeting of the Spanish Astronomical Society held on July 16 – 20, 2018, in Salamanca, Spain. B. Montesinos, A. Asensio Ramos, F. Buitrago, R. Schödel, E. Villaver, S. Pérez-Hoyos, I. Ordóñez-Etxeberria (eds.), 2019

Numerical simulation of the interaction between planetary exospheres and the stellar wind.

Ada Canet[1] **and Ana I. Gómez de Castro**[1]

[1] AEGORA Research Group, Universidad Complutense de Madrid, Plaza de Ciencias 3, E-28040 Madrid, Spain

Abstract

Bow shock formation, magnetic reconnection and plasmoid ejection are thought to be present in most planetary environments. The aim of this work is to show that the presence of this kind of structures in the vicinity of planets is not restrictive to magnetized bodies. The presence of a interplanetary magnetic field carried with the stellar wind is responsible of the formation of a planetary magnetotail, ejection of plasmoids and magnetic reconnection events, even though the planet-obstacle is completely unmagnetized. We study the interaction of this magnetized winds coming from cool MS stars, solar analogues, with non-magnetized terrestrial planets provided of an extended earth-like exosphere thought 2.5D numerical simulations carried out with PLUTO. In this work, we show a preliminary study of the impact of stellar winds on the evolution and stability of Earth-like atmospheres/exospheres, in order to determine the position of the bow shock and its properties, and the position of the X point of magnetic reconnection in the case of non-magnetized rocky planets, in order to determine their emission and possible detection through these structures in the stellar winds. (See poster).

Highlights on Spanish Astrophysics X, Proceedings of the XIII Scientific Meeting of the Spanish Astronomical Society held on July 16 – 20, 2018, in Salamanca, Spain. B. Montesinos, A. Asensio Ramos, F. Buitrago, R. Schödel, E. Villaver, S. Pérez-Hoyos, I. Ordóñez-Etxeberria (eds.), 2019

Martian dust size and shape from MSL Engineering Cameras.

Hao Chen-Chen[1], Santiago Pérez-Hoyos[1], and Agustín Sánchez-Lavega[1]

[1] Dpt. Física Aplicada I, Escuela Ingeniería de Bilbao, University of the Basque Country (UPV/EHU). Bilbao, Spain.

Abstract

Although not designed for this specific purpose, images taken by the Mars Science Laboratory (MSL) rover Engineering Cameras (Navcam and Hazcam) can be used for retrieving the dust aerosol physical properties at Gale Crater by evaluating the sky brightness as a function of the scattering angle. A retrieval scheme based on a radiative transfer model using discrete ordinates is proposed in this poster. Results obtained for dust particle size distribution effective radius values (mostly within 1.0 and 1.9 microns range region) and particle shape (cylindrical, aspect ratios around 1.5) agree with previous studies (McConnochie, T., et al., 2017; Vicente-Retortillo, A., et al., 2017; Tomasko, M., et al., 1999; Smith, M. D., & Wolff, M. J. 2014). This work was supported by the Spanish project AYA2015-65041-P with FEDER support, Grupos Gobierno Vasco IT-765-13, Universidad del País Vasco UPV/EHU programme UFI11/55, and Diputación Foral de Bizkaia-Aula EspaZio Gela. Thanks to Dr Mark Lemmon for the MSL Mastcam optical depth data. (See poster).

Highlights on Spanish Astrophysics X, Proceedings of the XIII Scientific Meeting of the Spanish Astronomical Society held on July 16 – 20, 2018, in Salamanca, Spain. B. Montesinos, A. Asensio Ramos, F. Buitrago, R. Schödel, E. Villaver, S. Pérez-Hoyos, I. Ordóñez-Etxeberria (eds.), 2019

Spectral energy distributions and luminosities of M dwarfs in the CARMENES search for exoplanets.

C. Cifuentes[1,2], J.A. Caballero[1], M. Cortés-Contreras[1,3], D. Montes[2], A. Schweitzer[4], I. Ribas[5], P. J. Amado[6] and the CARMENES Consortium[1,2,3,4,5,6,7,8,9,10,11,12].

[1] Centro de Astrobiología
[2] Universidad Complutense de Madrid
[3] Spanish Virtual Observatory
[4] Hamburger Sternwarte
[5] Institut de Ciències de l'Espai
[6] Instituto de Astrofísica de Andalucía
[7] Max-Planck-Institut für Astronomie
[8] Landessternwarte Königstuhl
[9] Institut für Astrophysik Göttingen
[10] Instituto de Astrofísica de Canarias
[11] Thüringer Landessternwarte Tautenburg
[12] Centro Astronómico Hispano-Alemán – Calar Alto Observatory

Abstract

In the quest for Earth-sized exoplanets, M dwarfs are stars of increasing interest during the last two decades. Their small sizes and masses as compared to our Sun make them specially suitable targets to look for the signatures of planetary companions, as their habitable zones fall closer to their host star. Despite being the most abundant stars in our Galaxy, it still exists large uncertainty about basic physical properties of M dwarfs. In particular, determining properties such as luminosities and effective temperatures is essential to characterize their planetary companions, since their properties are derived from those of their host stars. This means that the larger the uncertainties in these fundamental stellar properties, the broader is the span of compatible planetary compositions and parameters. CARMENES is a next-generation spectrograph, built and operated by the homonymous German-Spanish consortium of eleven institutions, which monitorizes bright nearby M dwarfs using the radial velocity method. Carmencita, its input catalog, contains dozens of parameters for about 2200 M dwarfs, from M0.0 to M7.0, including photometric data in a broad range, from UV to mid-infrared. These photometric date, compiled and updated for 18 broadband filters, *FUV*, *NUV*, *u'*, B_T, *B*, *g'*, V_T, *G*, *V*, *r'*, *i'*, *J*, *H*, *Ks*, *W1*, *W2*, *W3*, *W4*, have made possible the determination of important stellar properties using the Virtual Observatory SED Analyzer (VOSA). (See poster).

Highlights on Spanish Astrophysics X, Proceedings of the XIII Scientific Meeting of the Spanish Astronomical Society held on July 16 – 20, 2018, in Salamanca, Spain. B. Montesinos, A. Asensio Ramos, F. Buitrago, R. Schödel, E. Villaver, S. Pérez-Hoyos, I. Ordóñez-Etxeberria (eds.), 2019

VLBI / VLTI exploration of the multiple system ABDorA/C.

J. B. Climent[1], J. C. Guirado[1,2], R. Azulay[1], J. M. Marcaide[1], and I. Martí-Vidal[3]

[1] Departament d'Astronomia i Astrofísica, Universitat de València, C. Dr. Moliner 50, 46100 Burjassot, València, Spain
[2] Observatori Astronòmic, Universitat de València, Parc Científic, C. Catedrático José Beltrán 2, 46980 Paterna, València, Spain
[3] Onsala Space Observatory, Space Earth and Environment, Chalmers University of Technology, 43992 Onsala, Sweden

Abstract

We report on radio and infrared interferometric observations of the ABDorA/C mutiple system addressed to study the radiation mechanism of its components, and the possible binarity of the low-mass companion C. Our results indicate 1) the presence of large coronal structures in ABDorA produced likely by magnetically confined plasma; 2) the possible binarity of ABDorC, as concluded by the infrared VLTI visibilities; and 3) the detection for the first time of (compact) radio emission from ABDorC. With only 0.09 $M_{\odot}$, ABDorC is one of the lowest mass objects detected by VLBI arrays. (See poster).

Highlights on Spanish Astrophysics X, Proceedings of the XIII Scientific Meeting of the Spanish Astronomical Society held on July 16 – 20, 2018, in Salamanca, Spain. B. Montesinos, A. Asensio Ramos, F. Buitrago, R. Schödel, E. Villaver, S. Pérez-Hoyos, I. Ordóñez-Etxeberria (eds.), 2019

Identification and characterization of asteroids using the WFCAM Transit Survey and the Virtual Observatory.

M. Cortés-Contreras[1,2], **F. Jiménez-Esteban**[1,2,3], **E. Solano**[1,2], **B. Carry**[4] **and C. Rodrigo**[1,2]

[1] Centro de Astrobiología (CSIC-INTA)
[2] Spanish Virtual Observatory
[3] Suffolk University
[4] Observatoire de la Côte d'Azur

Abstract

Small Solar System bodies are objects that are neither planets nor dwarf planets, nor satellites of a planet or dwarf planet. More than 750,000 small Solar System bodies are known today, most of them asteroids, occupying a variety of orbits ranging from near-Earth to the Kuiper belt. Their study is motivated by their intrinsic importance as remnants of the early stages of the solar system formation process as well as by practical reasons concerning space exploration or the impact frequency with Earth.

We describe here a methodology to identify asteroids serendipitously observed in the WFCAM Transit Survey using Virtual Observatory tools like SkyBoT, Miriade, TOPCAT, STILTS and Aladin. We provide near 15,000 accurate positions and J-band magnitudes for over 1,600 asteroids. We build light curves and plan to use them to determine their fundamental physical parameters, such as the asteroid's shape, rotational period or the binary nature. (See poster).

Highlights on Spanish Astrophysics X, Proceedings of the XIII Scientific Meeting of the Spanish Astronomical Society held on July 16 – 20, 2018, in Salamanca, Spain. B. Montesinos, A. Asensio Ramos, F. Buitrago, R. Schödel, E. Villaver, S. Pérez-Hoyos, I. Ordóñez-Etxeberria (eds.), 2019

TFAW: signal detection, reconstruction and de-noising for time-domain surveys using wavelets.

D. del Ser[1,2,3], O. Fors[1,2,3], and J. Núñez[1,3]

[1] Dept. de Física Quàntica i Astrofísica, Institut de Ciències del Cosmos (ICCUB), Universitat de Barcelona, IEEC-UB, Martí i Franquès 1, E08028 Barcelona, Spain
[2] University of North Carolina at Chapel Hill, Department of Physics and Astronomy, Chapel Hill, NC 27599-3255, USA
[3] Observatori Fabra, Reial Acadèmia de Ciències i Arts de Barcelona, Rambla dels Estudis, 115, E-08002 Barcelona, Spain

Abstract

There have been many efforts to correct systematic effects in astronomical light curves to improve the detection and characterization of planetary transits and astrophysical variability. Algorithms like the Trend Filtering Algorithm (TFA) use simultaneously-observed stars to measure and remove these systematic effects. We present TFAW, a modified version of TFA which reduces the high-and-low-frequency noise in variable-star light curves without changing their intrinsic characteristics. We modified TFA's signal detection by adding a Stationary Wavelet Transform filter that allows to do a preliminary noise and outlier removal to increase the signal-to-noise ratio of any variable signal within the data. An additional wavelet-based filter is added to TFA's iterative signal reconstruction to characterize the noise- and trend-free signal and the underlying noise contribution at each iteration. This adaptive noise estimation reduces correlated and uncorrelated noise while preserving signals typical of astrophysical changes. We carried out a series of tests over simulated sinusoidal and transit-like signals to assess the effectiveness of the method, and applied TFAW to real light curves from the TFRM and K2 datasets. TFAW is a generic algorithm applicable to any kind of ground- or space-based time-domain survey and stellar variability type. TFAW improves the signal detection rate by increasing the signal detection efficiency (SDE) up to a factor $\sim$2.5$\times$ for low S/R light curves. The simulated transit detection rate improves by a factor $\sim$2-5$\times$ in the low-S/R regime compared to TFA. The standard deviations of simulated and real TFAW light curves are $\sim$40% better compared to TFA. TFAW yields better MCMC posterior distributions and returns lower uncertainties, less biased transit parameters and narrower credibility intervals for simulated transits. We applied TFAW to multiperiodic light curves to show its capabilities to separate the different signal contributions. (See poster).

Highlights on Spanish Astrophysics X, Proceedings of the XIII Scientific Meeting of the Spanish Astronomical Society held on July 16 – 20, 2018, in Salamanca, Spain. B. Montesinos, A. Asensio Ramos, F. Buitrago, R. Schödel, E. Villaver, S. Pérez-Hoyos, I. Ordóñez-Etxeberria (eds.), 2019

Towards a comprehensive view of planet formation: The role of the host star's metallicity.

J. Maldonado[1], E. Villaver[2], C. Eiroa[2], and G. Micela[1]

[1] INAF - Osservatorio Astronomico di Palermo, Piazza del Parlamento 1, 90134 Palermo, Italy, email:jesus.maldonado@inaf.it
[2] Universidad Autónoma de Madrid, Dpto. Física Teórica, Facultad de Ciencias, Campus de Cantoblanco, 28049 Madrid, Spain

Abstract

The role of the host star's metallicity in planet formation has been largely discussed in the framework of the so-called gas-giant/planet metallicity correlation. However, previous works are mainly focused on particular kinds of stars or planets. In this contribution we aim to put together all the pieces of the planet formation puzzle by analysing in the most homogeneous possible way a large sample of stars (without any restriction on spectral type or evolutionary status) showing all the possible outcomes of the planet formation process (from debris discs to massive brown dwarfs). (See poster).

Highlights on Spanish Astrophysics X, Proceedings of the XIII Scientific Meeting of the Spanish Astronomical Society held on July 16 – 20, 2018, in Salamanca, Spain. B. Montesinos, A. Asensio Ramos, F. Buitrago, R. Schödel, E. Villaver, S. Pérez-Hoyos, I. Ordóñez-Etxeberria (eds.), 2019

Characterization of a dust storm on Mars with REMS measurements and MARCI / MRO images

Iñaki Ordóñez-Etxeberria[1], Ricardo Hueso[1], and Agustín Sánchez-Lavega[1]

[1] Dpto. de Física Aplicada I, Universidad del País Vasco / Euskal Herriko Unibertsitatea.

Abstract

The REMS instrument (Gómez-Elvira et al., 2012) on board the Curiosity rover, has been collecting meteorological data from Gale crater on Mars since August 2012 (Ordóñez-Etxeberria et al., 2018). Although it is possible to observe frequent dust storms on Mars atmosphere, during these years only one local dust storm has passed directly above the rover. This storm was visible for a few days at the end of December 2014 on imagery data acquired by the MARCI instrument on the Mars Reconnaissance Orbiter (MRO). The storm initiated on the 852 sol of the MSL mission northwest of Gale crater and spread over Gale during sols 852-856 (Ls 263°, late spring in the southern hemisphere). MARCI images show that the storm raised up material to altitudes of 19 km. The storm evolved very quickly depositing most of its material in 2 sols. However, UV measurements obtained by REMS from the ground show increased optical depth of the atmosphere well after the storm ceased to be observable from orbit. REMS measurements show that the amplitude of the daily pressure tides at Gale increased by about a 15% the sol the dust arrived and then returned to usual values during that season over the next three sols. The air temperature in the surface at noon also increased by about 15K (although previous studies (Guzewich, S. D. et al., 2016; Zurek, R. W., 1981) suggest that air should cool down by the reduced solar flux at the surface). Our interpretation is that the dust raised by the storm had descended to low altitudes when it arrived to Gale heating the lower part of the atmosphere. The atmospheric response to this small storm can be used to understand better the atmospheric response to large-scale storms as the global one that covered nearly the full planet over July 2018. (See poster).

Highlights on Spanish Astrophysics X, Proceedings of the XIII Scientific Meeting of the Spanish Astronomical Society held on July 16 – 20, 2018, in Salamanca, Spain. B. Montesinos, A. Asensio Ramos, F. Buitrago, R. Schödel, E. Villaver, S. Pérez-Hoyos, I. Ordóñez-Etxeberria (eds.), 2019

GJ 273: Formation, dynamical evolution and habitability of one of the most interesting planetary systems.

Francisco J. Pozuelos[1], Juan C. Suárez[2,3], Gonzalo C. de Elía[4,5] and Agustín Dugaro[4,5]

[1] Space sciences, Technologies and Astrophysics Research (STAR) Insitute. Institut d'Astrophysique et Géophysique. Université de Liège. Belgium.
[2] Departamento de Física Teórica y del Cosmos, Universidad de Granada, Granada, Spain.
[3] Instituto de Astrofísica de Andalucía (IAA - CSIC), Granada, Spain.
[4] Instituto de Astrofísica de La Plata, La Plata, Argetina.
[5] Facultad de Ciencias Astronómicas y Geofísicas, Universidad Nacional de La Plata. La Plata, Argentina.

Abstract

The planetary system GJ 273 is one of the closest multi-planetary systems known so far at only 3.8 pc away. Recent studies showed that it harbours two Earth-like planets, one of them being in the habitable zone. In this work, still in progress, we show our latest results regarding the planetary formation and the water delivery in early times; the dynamical stability of the system as well as the dynamical environment, where we study the regions where the system may harbour minor bodies in stable orbits, i.e., Main Asteroids Belt analogues; and the effects of tides on the planets, i.e., spin-orbit alignment, pseudo-synchronization and tidal heating. All these parameters have important influence on the potential habitability of the planet located on the habitable zone, GJ 273-c. (See poster).

Highlights on Spanish Astrophysics X, Proceedings of the XIII Scientific Meeting of the Spanish Astronomical Society held on July 16 – 20, 2018, in Salamanca, Spain. B. Montesinos, A. Asensio Ramos, F. Buitrago, R. Schödel, E. Villaver, S. Pérez-Hoyos, I. Ordóñez-Etxeberria (eds.), 2019

Inference of physical parameters in solar prominence threads.

M. Montes-Solís[1,2], **I. Arregui**[1,2]

[1] Instituto de Astrofísica de Canarias, E-38205 La Laguna, Tenerife, Spain
[2] Departamento de Astrofísica, Universidad de La Laguna, E-38206 La Laguna, Tenerife, Spain

Abstract

We consider magnetohydrodynamics models and observations of transverse oscillations in prominence threads to obtain information on their physical properties such as the magnetic field strength, the plasma density, or the length. We further compare between short and long thread limits in period ratio models and compute the relative plausibility of alternative mechanisms in explaining the observed damping of transverse oscillations. Bayesian techniques are used for both analyses. The results show that the physical parameters of interest can be inferred. Values of period ratio around 1 are more likely in the long thread limit while shorter and larger values are more likely in the short thread limit. The mechanism known as resonant absorption in the Alfvén continuum is the most plausible damping mechanism.

1 Introduction

High-resolution observations have permitted to resolve fine-structure of prominences as threads that support transverse oscillations and flows [4, 5, 6]. In the last years, coronal seismology has been used to infer properties of the solar corona and structures therein, such as prominence threads [2]. In this work, we apply Bayesian techniques to the study of transverse kink oscillations in prominence threads to infer some of their physical features. In particular, if we take a model M with n parameters θ and some data d, these techniques enable us to infer the posterior distribution of each parameter or marginal posterior as

$$p(\theta_i|M,d) = \int p(\theta|M,d)d\theta_1...d\theta_{i-1}d\theta_{i+1}...d\theta_n, \tag{1}$$

where $p(\theta|M,d)$ is given by the Bayes' Rule in the form

$$p(\theta|M,d) = \frac{p(\theta)p(d|M,\theta)}{p(d|M)}. \tag{2}$$

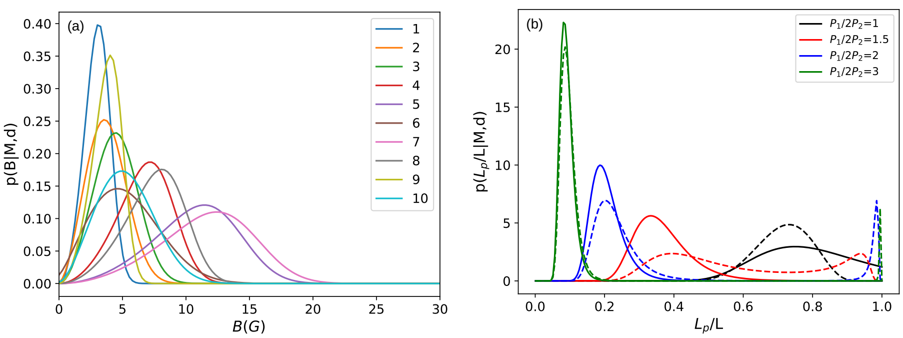

Figure 1: (a) Posterior distributions of magnetic field strength corresponding to the threads observed by [4]. Parameters are considered in plausible ranges of $B \in [0.01, 50]$ G and $\rho_p \in [10^{-12}, 10^{-9}]$ kg m^{-3}. (b) Posterior distributions of L_p/L for different $P_1/2P_2$ values with an uncertainty of 10% in the long thread limit. $L_p/L \in (0, 1)$ has been selected as plausible range. The continuous lines correspond to results using the first equation in (5) and dashed lines to the second one.

Including then the prior information, $p(\theta)$, the likelihood of the data, $p(d|M, \theta)$, and the normalization constant or marginal likelihood, $p(d|M)$, we can extract the probability of each parameter taking on certain values. On the other hand, Bayesian statistics allows us to compare plausibilities between alternatives mechanisms M_i and M_j with the computation of the Bayes' factors defined by

$$B_{ij} = \frac{p(d|M_i)}{p(d|M_j)}. \tag{3}$$

This relation of marginal likelihoods indicates which model better explains the observations.

2 Parameter inference

2.1 Magnetic field strength

Our first analysis is focused on the inference of the magnetic field strength in prominence threads. Assuming threads as totally filled thin tubes, theory predicts a phase velocity of transverse waves, v_{ph}, as a function of the magnetic field strength, B, and the density of the thread, ρ_p, in the form

$$v_{ph} = \sqrt{\frac{2}{\mu_0 \rho_p}} B, \tag{4}$$

if the density contrast between the thread and the background corona is sufficiently large.

Applying Bayesian techniques, marginal posteriors of the two unknowns $\theta = \{B, \rho_p\}$ can be computed, conditional on the observed phase velocity, $d = v_{ph}$ and the theoretical model. Figure 1a shows posterior distributions of the magnetic field strength associated to different threads whose phase velocities were measured by [4].

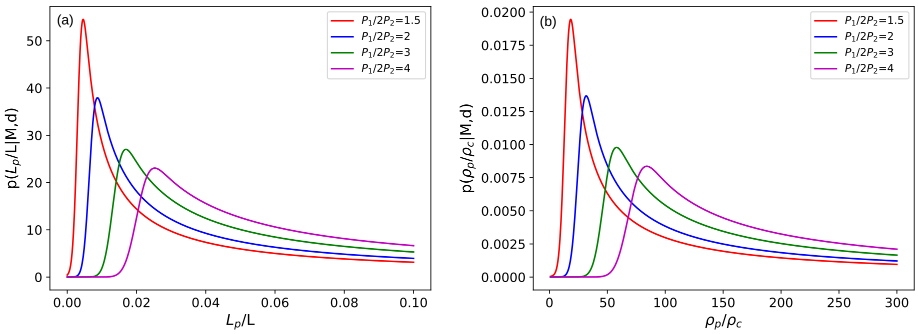

Figure 2: Posterior distributions of (a) L_p/L and (b) ρ_p/ρ_c for different $P_1/2P_2$ values with an uncertainty of 10% in the short thread limit.$L_p/L \in [0, 0.1]$ and $\rho_p/\rho_c \in [1.01, 300]$ has been selected as plausible ranges of parameters.

All 10 distributions can be properly inferred. They spread over a range of values although threads are in the same quiescent prominence and a very small probability of magnetic field strengths larger than 20 G is appreciable.

2.2 Lengths and densities in a partially filled tube

Our second analysis considers the relation between the periods of the fundamental and first overtone of transverse waves, $d = P_1/2P_2$, as a seismological tool. Assuming threads as partially filled thin tubes, theory [3] offers analytical expressions of the period ratio as a function of the thread length under two different approximations. In the long thread approximation, it can be approximated as

$$\frac{P_1}{2P_2} \approx \sqrt{\frac{3}{4L_p/L}} \text{ or } \frac{P_1}{2P_2} \approx \sqrt{\frac{3}{4L_p/L}} \sqrt{\frac{1+\sqrt{(1+L_p/3L)/(1-L_p/L)}}{1+\sqrt{(9/5-L_p/L)/(1-L_p/L)}}}, \tag{5}$$

both depending on only one parameter, the ratio of the length of the thread to the length of the tube, $\theta = \{L_p/L\}$. Marginal posteriors computed for different values of the period ratio are plotted in Figure 1b. The distributions are centred around smaller values of the parameter for longer values of the period ratio. The largest discrepancies between both equations in (5), are obtained for the longest threads. If we now focus on the short thread limit, the theoretical periods ratio can be expressed in the following manner

$$\frac{P_1}{2P_2} \approx 1 + (f^2 - 2)\frac{L}{L_p} - (f^2 + 1)\left(\frac{L}{L_p}\right)^2. \tag{6}$$

The equation depends on two parameters, the previous one and the density contrast between the thread and the corona through $f = \sqrt{(\rho_p/\rho_c + 1)/2}$, hence $\theta = \{L_p/L, \rho_p/\rho_c\}$. Repeating the process, we obtain their marginal posteriors plotted in Figure 2. In contrast to the previous result, the posteriors for L_p/L are centred around larger values of the parameter for

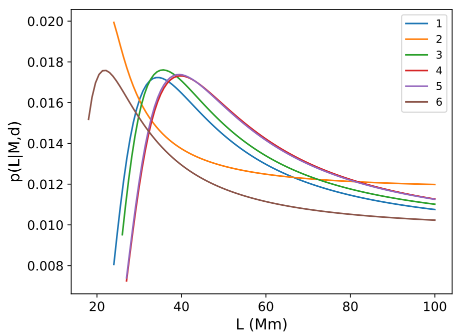

Figure 3: Posterior distributions of L for oscillating and flowing threads observed by [5]. An observation time of 180 s and a ratio $P(t)/P(0) = 0.9$ with an uncertainty of 10% have been considered.

larger values of the period ratio. The same trend is observed for ρ_p/ρ_c, with a very small probability for values larger than 200.

2.3 Lengths in a partially filled tube with flow

Observations show that threads are not steady, they flow through prominence. This plasma flow introduces the necessity of considering the temporal dependence of wave periods. Theory [10] predicts an analytical expression for the change in period of the form

$$\frac{P(t)}{P(0)} = \sqrt{1 - \frac{4v_0^2t^2}{(L+\frac{1}{3}L_p)(L-L_p)}}. \tag{7}$$

The observable, $d = P(t)/P(0)$, is a function of three parameters, the flow velocity, v_0, the length of the thread, L_p, and the total length of the flux tube, L, $\theta = \{v_0, L_p, L\}$. In this particular case, Gaussian priors for v_0 and L_p are assumed using measurements by [5] for the computation of marginal posteriors of L in Figure 3. Posteriors are not properly inferred since they show long and high tails. However, they show a common tendency to peak at around 20 to 40 Mm, with the shortest threads supporting the smallest flow velocities.

3 Model Comparison

3.1 Period ratios in the short and long thread limits

In section 2.2, we made parameter inference using period ratios under the long and short thread approximations. To compare the two approximations, we compute marginal likelihoods and Bayes' factors in Figure 5. Period ratios smaller than 0.5 and larger than 2 are more likely for the short thread limit, while period ratios around 1 are better explained by the long thread limit.

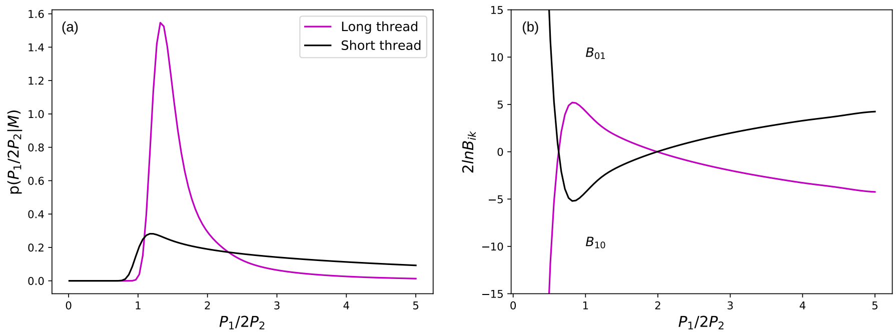

Figure 4: Marginal likelihoods (a) and Bayes' factors (b) for long and short thread approximations. $P_1/2P_2 \in [0.01, 5]$ with an uncertainty of 10%.

3.2 Damping mechanisms

Damping of transverse waves is a common observed phenomenon in prominence threads but the causative mechanism is not well known. We consider as plausible mechanisms resonant absorption in the Alfvén continuum, resonant absorption in the slow continuum, and Cowling's diffusion to derive which one is more plausible in explaining observed damping ratios, $d = \tau_d/P$. Theoretical damping ratios [1, 7, 8, 9] for these three cases are

$$\left(\frac{\tau_d}{P}\right)_{RAAC} = \frac{2}{\pi}\frac{R}{l}; \quad \left(\frac{\tau_d}{P}\right)_{RASC} = \frac{2}{\pi}\frac{R}{l}\left(\frac{k_z R}{1+\frac{2}{\gamma\beta}}\right)^{-2}; \quad \left(\frac{\tau_d}{P}\right)_{CD} = \frac{\sqrt{2}}{\pi k_z R \tilde{\eta}_c}, \tag{8}$$

respectively. Computed marginal likelihoods for each damping mechanism are presented in Figure 5a-c. Each marginal likelihood peaks around well differentiated damping ratio values, so that resonant absorption in the slow continuum can be directly discarded.

The remaining mechanisms are compared using Bayes' factors in Figure 5d. Damping ratios smaller than 10 are more plausible for resonant absorption in the Alfvén continuum and the rest for the Cowling's diffusion.

4 Conclusions

Applying Bayesian techniques to the study of prominence threads, magnetic field strengths of units to few tens of Gauss are obtained in quiescent prominences. When we use period ratios to infer the length of the threads, different tendencies in long and short approximations are observed. Introducing flows, the inferred total length of flux tubes in an active prominence region indicate they are shorter than expected.

Model comparison shows differences of periods ratio values in short and long thread limits and resonant absorption in the Alfvén continuum as the most plausible mechanism for explaining damping of transverse waves.

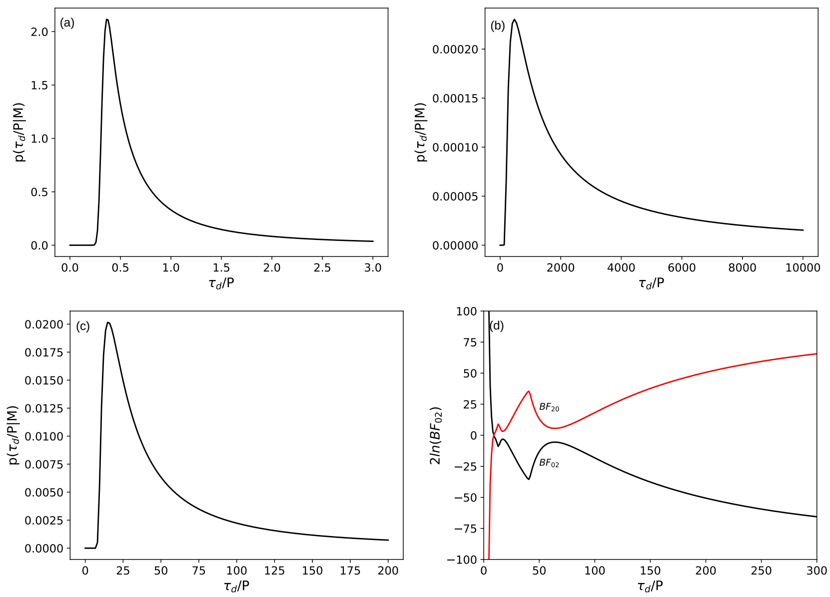

Figure 5: (a)-(c) Marginal likelihoods associated to each damping mechanism. Ranges of damping ratios are displayed in x-axis. (d) Bayes' factors associated to resonant absorption in the Alfvén continuum and Cowling's diffusion comparison for $\tau_d/P \in [0.01, 300]$ with an uncertainty of 10%.

Acknowledgments

We acknowledge financial support from the Spanish Ministry of Economy and Competitiveness (MINECO) through projects AYA2014-55456-P (Bayesian Analysis of the Solar Corona), AYA2014-60476-P (Solar Magnetometry in the Era of Large Telescopes), and from FEDER funds. M.M-S. acknowledges financial support through a Severo Ochoa FPI Fellowship under the project SEV-2011-0187-03.

References

[1] Arregui, I., Terradas, J., Oliver, R., et al. 2008, ApJ, 682, L141

[2] Arregui, I., Oliver, R., & Ballester, J. L. 2018, Living Reviews in Solar Physics, 15, 3.

[3] Díaz, A. J., Oliver, R. & Ballester, J. L. 2010, ApJ, 725, 1742

[4] Lin, Y., Soler, R., Engvold, O., et al. 2009, ApJ, 704, 870

[5] Okamoto, T. J., Tsuneta, S., Berger, T. E., et al. 2007, Science, 318, 1577

[6] Okamoto, T. J., Antolin, P., De Pontieu, B., et al. 2015, ApJ, 809, 71

[7] Soler, R., Oliver, R., Ballester, J. L., et al. 2009, ApJ, 695, L166

[8] Soler, R., Oliver, R. & Ballester, J. L. 2009, ApJ, 693, 1601

[9] Soler, R., Oliver, R. & Ballester, J. L. 2009, ApJ, 707, 662

[10] Soler, R. & Goossens, M. 2011, aap, 531, A167

Highlights on Spanish Astrophysics X, Proceedings of the XIII Scientific Meeting of the Spanish Astronomical Society held on July 16 – 20, 2018, in Salamanca, Spain. B. Montesinos, A. Asensio Ramos, F. Buitrago, R. Schödel, E. Villaver, S. Pérez-Hoyos, I. Ordóñez-Etxeberria (eds.), 2019

Solar wind - magnetosphere coupling via magnetic reconnection and the effects of ionospheric plasma.

Sergio Toledo-Redondo[1]

[1] European Space Agency, ESAC, Spain (sergiotr@ugr.es)

Abstract

Magnetic reconnection is a key plasma process that couples the solar wind to the Earth's magnetosphere, permitting the exchange of energy and mass between these two plasmas, and converting large amounts of energy stored in the magnetic fields into kinetic energy of the particles. The magnetospheric side of the subsolar magnetopause is often populated by cold (10 eV) plasma of ionospheric origin, in addition to the hot (10 keV) magnetospheric plasma coming from the ring current. The presence of this cold plasma can mass-load the magnetospheric interface with the solar wind by 2-3 orders of magnitude, reducing the rate at which magnetic reconnection operates. In addition, the ion gyroradius of the cold plasma is much smaller than the hot ion gyroradius and introduces a new length-scale into reconnection and its associated processes. Finally, the cold plasma is heated inside the separatrix region of magnetic reconnection, although this mechanism is not always present.

1 Introduction

Our Sun is continuously expelling magnetized charged particles from its corona, the so-called solar wind. It expands along the Heliosphere, and interacts with the planets of the Solar system. Magnetic reconnection is a key plasma process which permits that magnetized planets like Earth, which are surrounded by a magnetosphere, exchange mass and energy with the solar wind. Magnetic reconnection enables breaking and merging antiparallel magnetic field lines locally, and therefore reconfigure the magnetic field topology at large scales, converting large amounts of energy stored in the magnetic field lines into kinetic energy of the charged particles during the process [1].

Magnetic reconnection initiates at electron scales of the plasma, in the so-called Electron Diffusion Region (EDR), a narrow region where electrons are not frozen-in to the magnetic field, and the magnetic field diffuses and reconnects. However, the mechanism that permits the magnetic field to diffuse in the required short time scale is a subject of debate, since in the collisionless regime of space plasmas the magnetic diffusion time is typically much larger than the required for reconnection to occur. The Magnetospheric MultiScale (MMS) mission [3] was launched in 2015 with the purpose of providing a better understanding of the processes that occur in the EDR and which mechanisms are responsible for the anomalous resistivity.

Magnetic reconnection occurs in many regions of the heliosphere, including the Solar corona, the turbulent solar wind, at the Earth's dayside magnetosphere, the Earth's magnetotail, or in Kelvin-Helholmtz vortices, to name a few. Here we focus in magnetic reconnection occurring at the dayside interface between the solar wind and the Earth's magnetosphere, the so-called magnetopause. This reconfiguration of the magnetic field lines occurs at large time- and space-scales, lasting tens of minutes to few hours, and producing X lines of several Earth Radii (R_E). It is responsible for magnetospheric convection and transport of magnetic flux towards the tail, where reconnection also occurs in order to keep the magnetic field divergence-free. This transport of magnetic field lines from the dayside to the tail and back to the dayside is known as the Dungey cycle.

The interface between the solar wind and the magnetosphere is largely asymmetric. The solar wind side is composed of solar wind plasma that has undergone through the bow shock, owing to the supersonic nature of the solar wind. The magnetospheric side is typically composed of hot plasma that comes from the ring current. Typical parameters of the solar wind near the magnetopause, i.e., at $\sim$12 R_E, are B = 15 nT, n = 20 cm^{-3}, T_i = 400 eV, while the typical parameters of magnetospheric plasma at $\sim$12 R_E are B = 40 nT, n = 0.1 cm^{-3}, T_i = 4 keV, where B stands for magnetic field magnitude, n stands for plasma density and T_i for ion temperature. But in the magnetospheric side, in addition to the (hot) ring current plasma component there is often a cold, and therefore difficult to measure, plasma component that originates in the Earth's ionosphere, see Figure 1. In this work we summarize some of the implications of this cold ionospheric plasma component for solar wind - magnetosphere coupling.

2 Cold ion length-scale and its implications for magnetic reconnection

In plasmas such as the Earth's magnetosphere, the density is so low (usually below 1 cm^{-3}) that Coulomb collisions between particles can often be neglected. Interaction between the particles occur indirectly via the electric and magnetic fields, such as wave - particle interactions. In this regime, the particle distribution function does not easily relax into a Maxwellian distribution, as classic statistical mechanics predict, and the phase-space density can remain far from equilibrium for very large time-scales. Under such situation, the definition of temperature itself is not well defined.

In the dayside magnetosphere, often a hot (several keV) ion population that originates in the ring current, and a cold (tens of eV) ion population that originates at the ionosphere can be observed together, although the cold plasma component is more difficult to detect and characterize with spacecraft detectors. The ion gyroradius of each of these populations

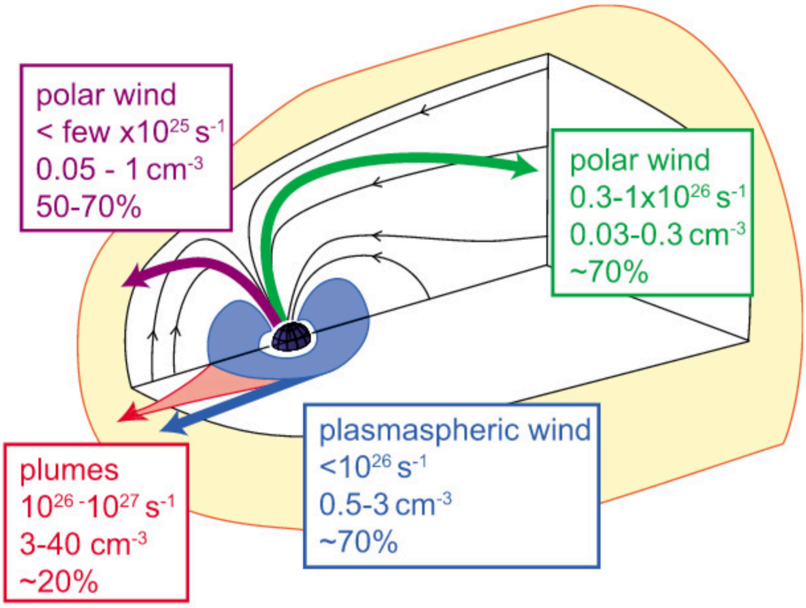

Figure 1: Extracted from [2]. Statistics of cold ionospheric ions at different regions of the Earth's magnetosphere using ten years of Cluster spacecraft mission observations. Cold ions dominate the magnetospheric mass density most of the time.

differs by roughly one order of magnitude, and therefore the cold ion population can remain frozen-in to the magnetic field lines inside small regions where the hot ions cannot, see Figure 2. Inside these small regions, the frozen-in term of the generalized Ohm's law must be split into two terms, one for the hot and one for the cold ion components. The generalized Ohm's law can be then written as follows, after neglecting the electron inertial term and assuming steady-state:

$$\mathbf{E} = \frac{1}{en}\mathbf{j} \times \mathbf{B} - \frac{1}{en}\nabla \cdot \mathbf{P_e} - \frac{n_{ih}}{n}\mathbf{v_{ih}} \times \mathbf{B} - \frac{n_{ic}}{n}\mathbf{v_{ic}} \times \mathbf{B}, \tag{1}$$

where $\mathbf{E}$ and $\mathbf{B}$ correspond to the electric and magnetic fields, $\mathbf{j}$ corresponds to the current density, $\mathbf{P_e}$ corresponds to the electron pressure tensor, n corresponds to the number density and subscripts ih and ic indicate hot and cold ions, respectively. The ability of the cold ionospheric ions to remain frozen-in at smaller length-scales has various implications for the microphysics of magnetic reconnection.

When magnetic reconnection between the Earth's magnetosphere and the solar wind occurs, a thin structure of enhanced normal electric field is created along the magnetospheric side of the separatrix region. The width of this narrow region is of the order of the hot ion gyroradius. Inside this region, hot ions are demagnetized and the Hall term (-$\mathbf{j}\times\mathbf{B}$/en) balances the electric field [5]. However, when cold ions are present, they $\mathbf{E}\times\mathbf{B}$ together with electrons, reduce the perpendicular currents and therefore the Hall term, see Figure 2. The ions are partially frozen-in, and the last term of equation 1 also contributes to the electric field. This has been shown using in-situ spacecraft observations [4, 6] and numerical

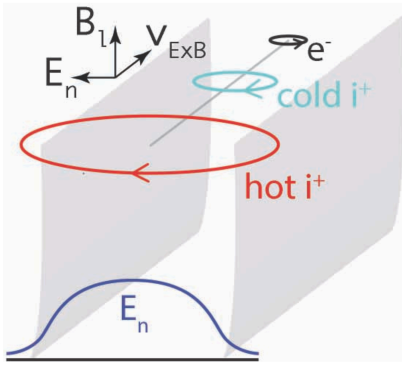

Figure 2: Extracted from [4]. Sketch of a narrow region, such as the Hall region in the magnetospheric separatrix region, where electron and cold ions can remain magnetized while hot ions do not. The cold ions $\mathbf{E}\times\mathbf{B}$ drift together with electrons and partially cancel the perpendicular current that electrons carry.

Particle-In-Cell (PIC) simulations [7, 8].

Figure 3 shows two examples of MMS in-situ observations of magnetic reconnection at the Earth's magnetopause. The left hand-side panels correspond to a magnetopause crossing without the cold ionospheric plasma component, while in the right hand-side panels the mass density of the magnetospheric side is dominated by cold ionospheric ions. In panels a1 and a3 the magnetic field gradient of the magnetopause can be observed. Panels b1 and b3 show the ion density. Panel b1 shows a density asymmetry between the solar wind (before 07:32:30 UT) and the magnetosphere (after 07:32:40 UT) of more than one order of magnitude. On the other hand, panel b3 shows roughly the same ion density in the solar wind (before 11:42:25 UT) and the magnetosphere (after 11:42:40 UT), owing to the cold ion density in the magnetosphere. Panels c1 and c3 show the ion velocity, where reconnection jets can be observed in the magnetopause. Panels d1 and d3 correspond to ion differential energy flux, and three ion populations can be distinguished: (hot) solar wind ions, (hot) magnetospheric ions, and (cold) magnetospheric ions of ionospheric origin (marked using a white box). Panels e1 and e3 correspond to measurements of the Ohm's law terms. In the crossing without cold ions, the electric field is roughly balanced by the Hall term, while in the crossing with cold ions the electric field is roughly balanced by the frozen-in cold ion term, with a small contribution of the Hall term.

Another consequence of cold ions in magnetic reconnection is that the Ion Diffusion Region (IDR) that surrounds the EDR is split into two subregions: a hot IDR (hIDR) and a cold IDR (cIDR). Again, this has been recently shown using in-situ MMS observations [9] and PIC simulations [10]. The cold ions remain frozen-in inside the hIDR, and are demagnetized only inside the much narrower cIDR region, where they are accelerated parallel to the electric field. Understanding the IDR is key for studying the EDR, the main goal of the MMS spacecraft mission.

The cold ions can in turn be accelerated and heated by magnetic reconnection, and their associated length-scale is therefore dynamically modified. The heating mechanisms are

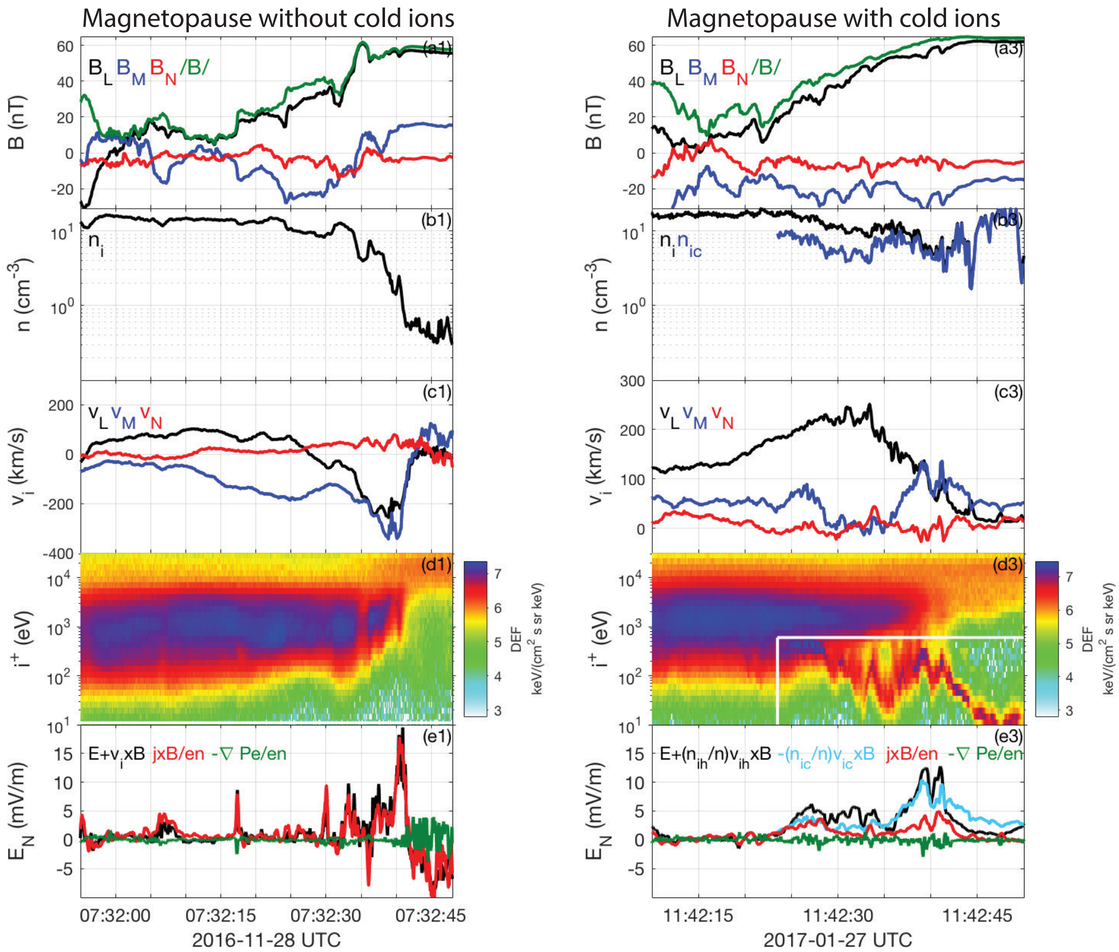

Figure 3: Extracted from [8]. MMS observations of magnetic reconnection at the Earth's magnetopause, without (left) and with (right) the presence of cold ions of ionospheric origin. (a) Magnetic field in LMN coordinates (magnetopause boundary coordinates). (b) Total (black) and cold (blue) ion densities. (c) Total ion velocity in LMN coordinates. (d) Ion differential energy flux. (e) Various terms of the Ohm's law, see equation 1.

associated to large electric field gradients and wave-particle interactions [11, 12]. Heating cold ions takes a non-negligible portion (25% of heating that goes into cold ions has been reported) of the energy budget of magnetic reconnection, and can have implications at large scales [13]. However, cold ion heating is not always observed in association with magnetic reconnection [14].

3 Conclusions

The main conclusions of this work can be summarized as follows:

- Cold ions of ionospheric origin dominate the mass density of the Earth's magnetosphere most of the time, introducing a smaller length-scale into magnetic reconnection owing to their smaller gyroradius.
- They reduce the perpendicular currents associated to the Hall term in the separatrix.
- They form a cIDR embedded in the wider hIDR that surrounds the EDR.
- Cold ions are heated by reconnection and take a significant part of the energy budget.

Acknowledgments

We acknowledge support from the ISSI international team *Cold plasma of ionospheric origin at the Earth's magnetosphere*. We thank the Cluster and MMS teams for the high-quality data provided.

References

[1] Biskamp, D. 2005, Magnetic reconnection in plasmas No. 3 (Cambridge University Press)

[2] André, M. & Cully, C. M. 2012, GRL, 39, L03101

[3] Burch, J. L., Moore, T. E., Torbert, R. B., & Giles, B. L. 2016, Spa. Sci. Rev., 199(5), 21

[4] Toledo-Redondo, S., Vaivads, A., André, M., & Khotyaintsev, Y. V. 2015, GRL, 42, 6146

[5] Khotyaintsev, Y. V., Vaivads, A., Retinò, A., A., et al. 2006, PRL, 97, 205003

[6] André, M., Li, W., Toledo-Redondo, S., et al. 2016, GRL, 43, 6705

[7] Dargent, J., Aunai, N., Lavraud, B., et al. 2017, JGR, 122, 5290

[8] Toledo-Redondo, S., Dargent, J., Aunai, N., et al. 2018, GRL, In press

[9] Toledo-Redondo, S., André, M., Khotyaintsev, Y. V., et al. 2016a, GRL, 43, 6759

[10] Divin, A., Khotyaintsev, Y. V., Vaivads, A., et al. 2016, JGR 121, 12001

[11] Toledo-Redondo, S., André, M., Vaivads, A., et al. 2016b, GRL, 43, 58

[12] Graham, D. B., Khotyaintsev, Y. V., Norgren, C., et al. 2017, JGR, 122, 517

[13] Toledo-Redondo, S., André, M., Khotyaintsev, Y. V., et al. 2017, JGR, 122, 9396

[14] Li, W. Y., André, M., Khotyaintsev, Y. V., et al. 2017, JGR, 122, 10194

Highlights on Spanish Astrophysics X, Proceedings of the XIII Scientific Meeting of the Spanish Astronomical Society held on July 16 – 20, 2018, in Salamanca, Spain. B. Montesinos, A. Asensio Ramos, F. Buitrago, R. Schödel, E. Villaver, S. Pérez-Hoyos, I. Ordóñez-Etxeberria (eds.), 2019

First results of EMIR at the GTC. Status and Short Term Plan.

F. Garzón[1,2], L. Patrick[1], P. Hammersley[3], A. Streblyanska[1], M. Insausti[1], M. Barreto[1], P. Fernández[1], E. Joven[1], P. López[1], A. Mato[1], H. Moreno[1], M. Núñez[1], J. Patrón[1], S. Pascual[4], and N. Cardiel[4]

[1]Instituto de Astrofísica de Canarias, La Laguna, Spain
[2]Departamento de Astrofísica, Universidad de La Laguna, Spain
[3]European Southern Observatory, Garching bei Müchen, Germany
[4]Universidad Complutense, Madrid, Spain

Abstract

We report the results on the EMIR (Espectrógrafo Multiobjeto Infra-Rojo) performances after two semesters of scientific operations at the Gran Telescopio Canarias (GTC). EMIR is one of the first common user instruments for the GTC, the 10 meter telescope operating at the Roque de los Muchachos Observatory (La Palma, Canary Islands, Spain). EMIR have been built by a Consortium of Spanish and French institutes led by the Instituto de Astrofísica de Canarias. EMIR is primarily designed to operated as a multi-object spectrograph in the K band, but offers a wide range of observing modes, including imaging and spectroscopy, both long slit and multi-object, in the wavelength range 0.9 to 2.5 μm. The development and fabrication of EMIR is funded by GRANTECAN and the Plan Nacional de Astronomía y Astrofísica.

EMIR was shipped to the GTC on May 2016 for its integration at the Nasmyth platform. From June till November 2016 several commissioning periods were conducted. Then a short Science Verification phase was launched on which EMIR was offered to the community to test its capabilities on sky in image and long-slit observing modes. In March 2017, EMIR was included in the call for observing time in semester 17B and started routine scientific operations at the GTC from July 2017. In November 2017, EMIR was lifted off the Nasmyth platform for the first maintenance period and resume operations at the end of February 2018. Multi-object spectroscopy (MOS) commissioning has taken place, in two periods, starting at the beginning of March 18. At the time of this writing, the MOS commissioning and internal verification phases have been completed and the open science verification is underway. The MOS mode has been offered in the CAT19A.

This contribution summarises the results and performances of the EMIR operation at the GTC since the beginning of its routine operation at the GTC.

1 Introduction

EMIR (Espectrógrafo Multi-objeto InfraRrojo – Infrared Multiobject Spectrograph, [2] and [3]), is a common-user, wide-field camera-spectrograph operating in the near-infrared (NIR) wavelengths 0.9-2.5 μm, using cryogenic multi-slit masks as field selectors. EMIR provides GTC with imaging, long-slit and multi-object spectroscopic capabilities. The EMIR consortium is formed by the IAC, Universidad Complutense de Madrid (UCM, Spain), the Laboratoire d'Astrophysique de Toulouse-Tarbes (LATT, France) and the Laboratoire d'Astrophysique de Marseille (LAM, France). EMIR was shipped to the GTC on May 19th, 2016; it was integrated on the Nasmyth A platform on June, 3rd, 2016; and the commissioning periods took place from June to November 2016. A short Science verification phase was run shortly after the commissioning, in the first semester of 2017 and then the instrument was offered to the community, beginning in 2017B. The results of the commissioning have been presented in [4] and [5], among other publications.

Due to the high complexity of the instrument, the tuning EMIR at the GTC has run in parallel to the scientific operations, with the participation of the scientific and technical staff of EMIR at the IAC and the UCM and the corresponding groups at GRANTECAN. Only recently, EMIR has reached a decent degree of maturity at the GTC and can be operated smoothly and efficiently. The last observing mode of the three mains, the MOS, has completed its first runs at the GTC in the last months. With this achievements, the status of EMIR at the GTC can be considered stable enough as as the team can concentrated from now on of the monitoring and improvements of its capabilities. The next sections will summarise what EMIR has already achieved at the GTC and what are the plans for the short term.

2 Calibrations and corrective actions on EMIR subsystems

2.1 Detector

From the beginning at the GTC, EMIR has suffered of two problems associated with the detector. The first one consisted in a poor orientation of the detector array with respect to the instrument focal plane which resulted in a marked loss of image quality. During the maintenance period of November 16 - February 17 on which EMIR was removed from the Nasmyth platform, this tilt was largely corrected with a residual inclination of around 4 and 2 mrad with respect to the detector X and Y axes respectively, to be compared with the previous value of 12 and 8 mrad, and currently in 0.8 arcsec seeing the increase in FWHM is at most 20% at the edge of the field as can be seen in Fig. 1. Figure 1, a composite image made using many Ks images in good seeing condition, show an alternative representation to the image quality after the correction, where the colour and circle size indicates the measured FWHM for each source in a star field. Again it is clear that there is only a slight loss if image quality in the corners of the field.

The EMIR detector also showed an irregular and somewhat erratic behaviour under low illumination conditions. This is particularly important in spectroscopy, where in between the sky lines the background is really low hence permitting a proper detection of faint signals.

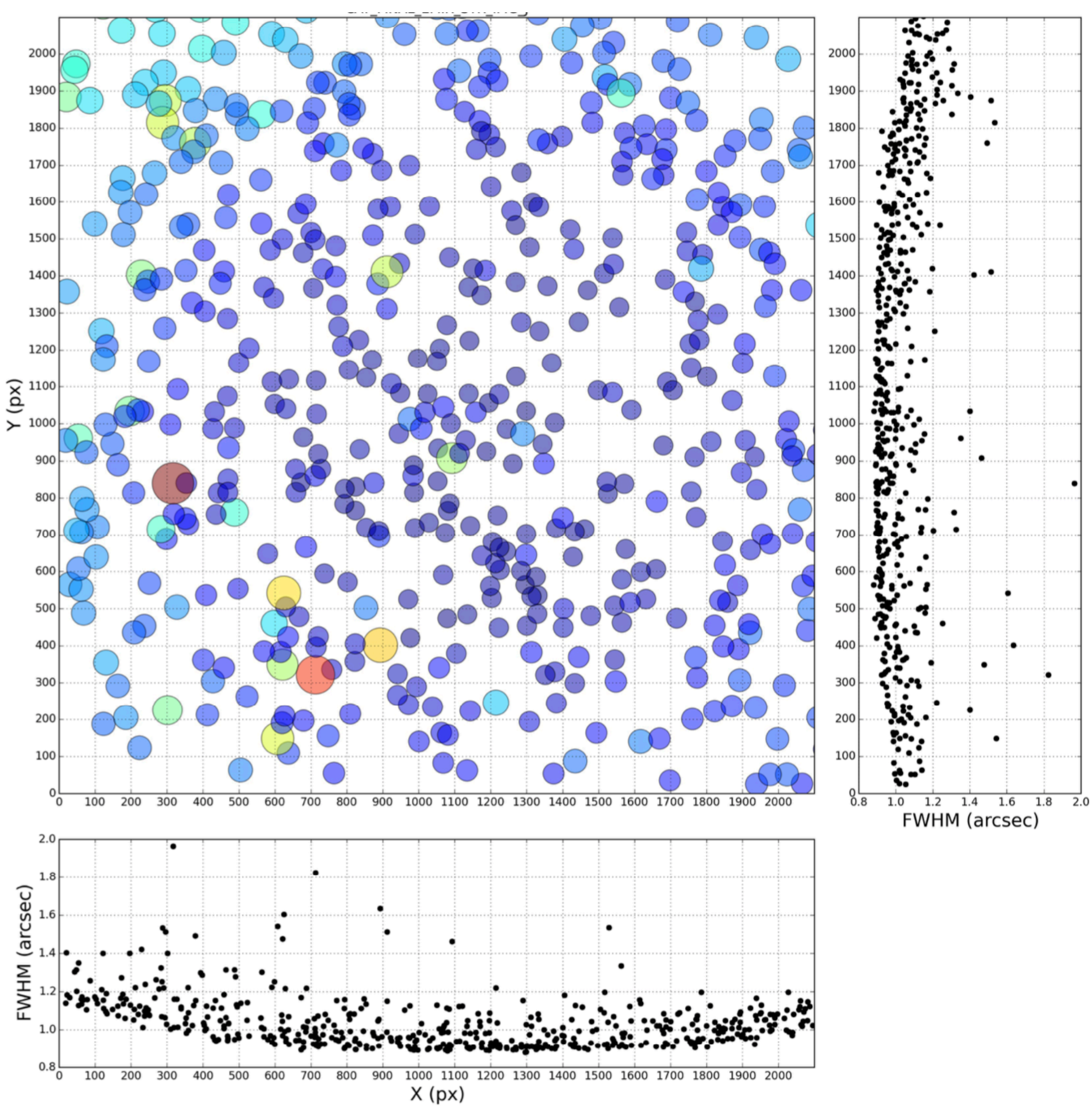

Figure 1: PSF sizes of the images on the detector. The sizes of the circles are proportional to the PSF size. The two small panels show the variation of the PSF with respect to the X and Y pixels at the detector.

We have undertaken an intensive campaign for exploring different ways of configuring the detector readout modes using dark current measurements as a proxy for this purpose. The objective has been to achieve a more regular pattern of the detector reads that permit the calibration and on-line removal of this effect. Figure 2 shows the results of this campaign. A single panel on Fig. 2 represents the average of a section of 5k pixels on the centre of each of the 32 detector channels. Only four of these segments are shown. It can be seen how the trend of the detector reads in 10 consecutive ramps is markedly more regular on the right side

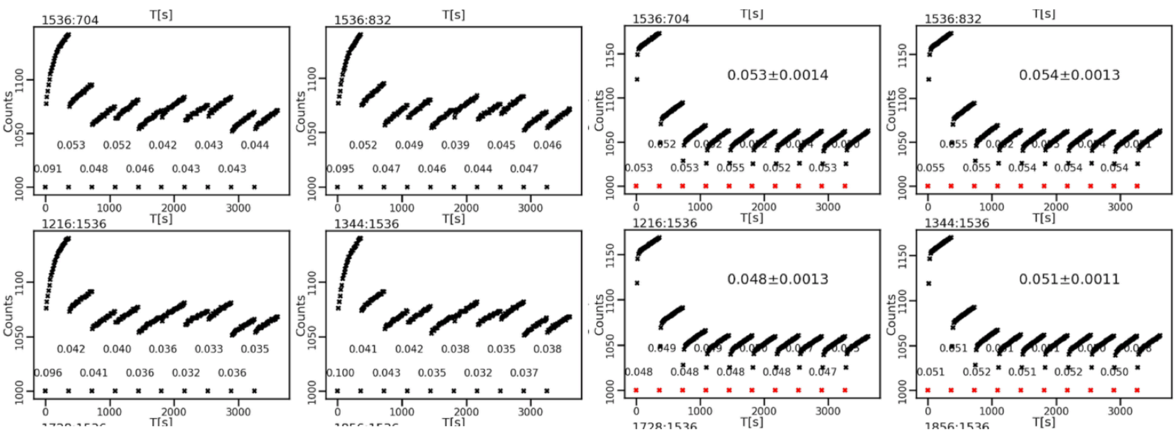

Figure 2: DC level in 10 consecutive ramps, 360s of integration time each. The 4 panels on the left correspond to the old read modes and the ones in the right, to the new modes. See text.

panels compared to the left ones. These calibrated DC measurements, a sequence of 10 series for each of the permitted single integration times, are loaded by the Emir Control System (ECS) at the GTC and removed from the detector reads before saving the data to disk. Hence, a large fraction of the non-uniformities in the detector frame series are not present in the final data. A point to be taken into account for those users interested in reaching the very faint limit of EMIR, is the fact that this removal has the unavoidable effect of adding the noise of the DC calibration, which is a small fraction of that in the object frames, but might be not negligible. It is always possible to revert the effect of the DC and detector drift calibration using simple scripts that can be made available to the interested users.

2.2 Cold Slit Unit (CSU)

The CSU is a system that lies in the heart of EMIR as its spectroscopic capabilities, both in long slit and in MOS, relies on its proper functioning. During the maintenance period mentioned before, we replaced a significant fraction of the cryogenic piezo set, which are the motors of the actuators that control the the bar motion, that have shown signs of degradation, by new ones with better specs in cryogenic conditions. After this, a long calibration campaign took place, again during day time, which have resulted in a control of the position of each sliding bar with accuracy better than 0.15 px in the worst cases. Figure 3 shows the accuracy over the whole length of a long slit 0.6 arcsec wide measured in terms of the flux variation over the slit under uniform illumination conditions.

2.3 On-line and off-line Data Reduction Pipeline

Since day one of EMIR at the GTC, much efforts have been devoted to, first tune an operative pipeline at the telescope that permits a real time monitoring of the observations, and then

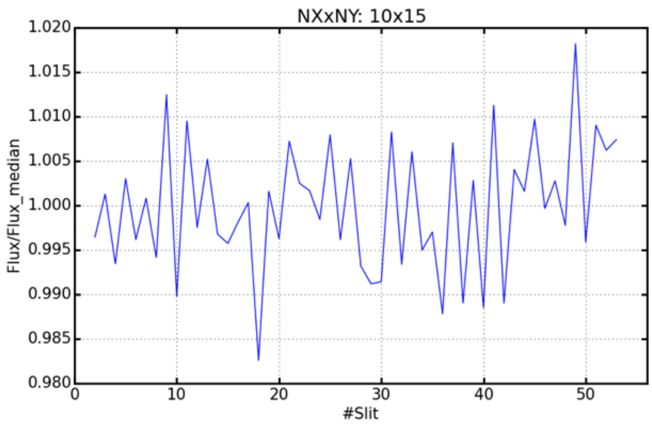

Figure 3: Ratio of the flux measured in a box of NX×NY pixels centred on each slitlet with respect to the median flux over the whole long slit.

to build a stand-alone system which will do the full reduction of the EMIR data till the level on which the scientific analysis can start. The first of these task is of outmost importance to make it possible the EMIR observations at the GTC, as the on-line DRP is providing a quick look of the data taken for initial configuration of the instrument and telescope, in one hand, and then of the observation products as they are being taken. The EMIR group at the UCM, together with software engineers of the teams at the IAC and and GRANTECAN, is coping with this task, that has to develop in the framework of the GTC Control System (GCS) which is updated frequently to accommodate new features and/or remove bugs and inefficiencies in the performances. After many interventions, the EMIR on-line DRP is now capable to deal with the run of the observations in an efficient way and it can be considered on its final status except, maybe, for minor adjustments dictated by upgrades in the GCS. The current version of the on-line pipeline includes the automatic wavelength calibration of data taken in spectroscopic modes, as described in [1] and in Cardiel et al. (*Reducing EMIR spectroscopic data with Python*, these proceedings).

Many of the capabilities of the on-line pipeline can be found also in the off-line version (*pyemir*), which can be downloaded from (https://github.com/guaix-ucm/pyemir). There are still some features which are missing in the current version of *pyemir*, for example the spectral flat fielding correction, but the team is working to be able to accommodate the needed capabilities in the short term.

3 Science observations with EMIR

In this section a brief sketch of some results obtained from observations with EMIR will be given. Some are not yet published but all together can provide a picture of the present day capabilities of the instrument. During the last observing campaign of the commissioning of the MOS mode, several scientific programmes were used as test beds to verify the performances of EMIR in MOS mode, and some preliminary results from them will also be shown here.

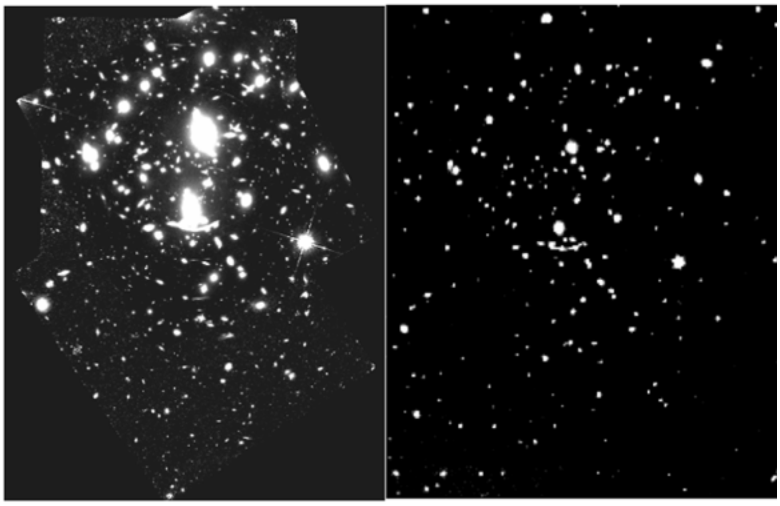

Figure 4: A370 images from HST in FW160 filter, left, and from EMIR in K_s.

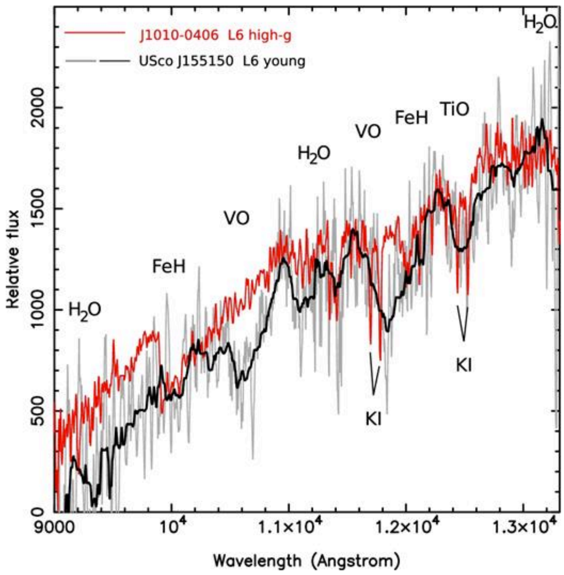

Figure 5: EMIR spectra of 2MASS 10101480-0406499 (red) and USco J155150.2-213457.

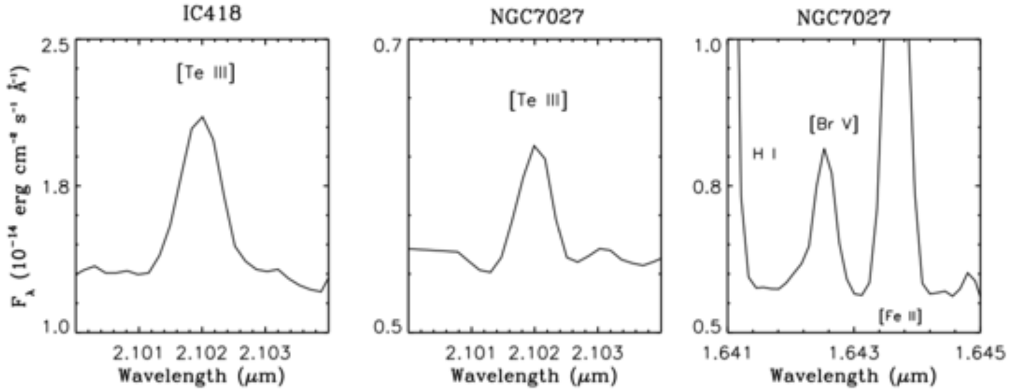

Figure 6: EMIR spectra of the newly detected PNe emission lines.

During the initial science verification after the first commissioning runs, a deep image of the Abell 370 galaxy cluster in K_s was taken and is shown in Fig. 4, together with the corresponding HST image of the same field.The image is the result of the co-adding of many individual frames of 3s exposure time each, totalling 1470s, with average PSF FWHM of 0.8 arcsec. The limiting magnitude at SNR=3 is 20.17. The HST image of A370, covering roughly the same area, is shown in Fig. 4 for comparison. That has a total integration time of 75788s with pixels size of 60 mas after drizzling.

[6] was the first in publishing an infrared spectrum taken with EMIR, which is shown in Fig. 5. These are a couple of L6 dwarfs of young planetary-mass in the Upper Scorpius association.

In [7] two new near-infrared emission lines, [Te III] 2.1019 μm and [Br V]] 1.6429 μm, in the spectra of planetary nebulae (PNe) arising from heavy elements produced by neutron capture reactions were identified in two PNe, NGC 7027 and IC 418. [Te III] was detected in both PNe, while [Br V] was seen in NGC 7027 only. The emission lines are shown in Fig. 6.

To end with this short review of EMIR results, some fresh observations of two programmes in MOS mode are presented. The first one correspond to a MOS mask of the GALEP project. GALEP aims at using EMIR to obtain near IR spectroscopy of many thousands sources, the vast majority of which are located in the inner Galaxy. Its main aim is to accurately classify the sources to tackle ambiguities in the interpretation of structures in the inner Galaxy. Figure 7 depicts several spectra of GALEP sources in the K band taken in a single shot with a MOS mask designed for the field, using the mask designer tool (OSP) developed at LATT. The spectra in Fig. 7 will be analysed by the Ferre code used in the APOGEE, for which it is necessary to develop a sort of *interface* to conform to the APOGEE prescriptions. This work is underway.

A second programme, with obvious areas in common with GALEP, deals with the search and characterisation of red supergiants in the Galaxy. In Fig. 8 the spectra in the J band are of 9 RSG candidates in the Young Massive Cluster RSGC01, which contains a very rich population of RSG stars. The goal is to provide metallicity estimates, for the first

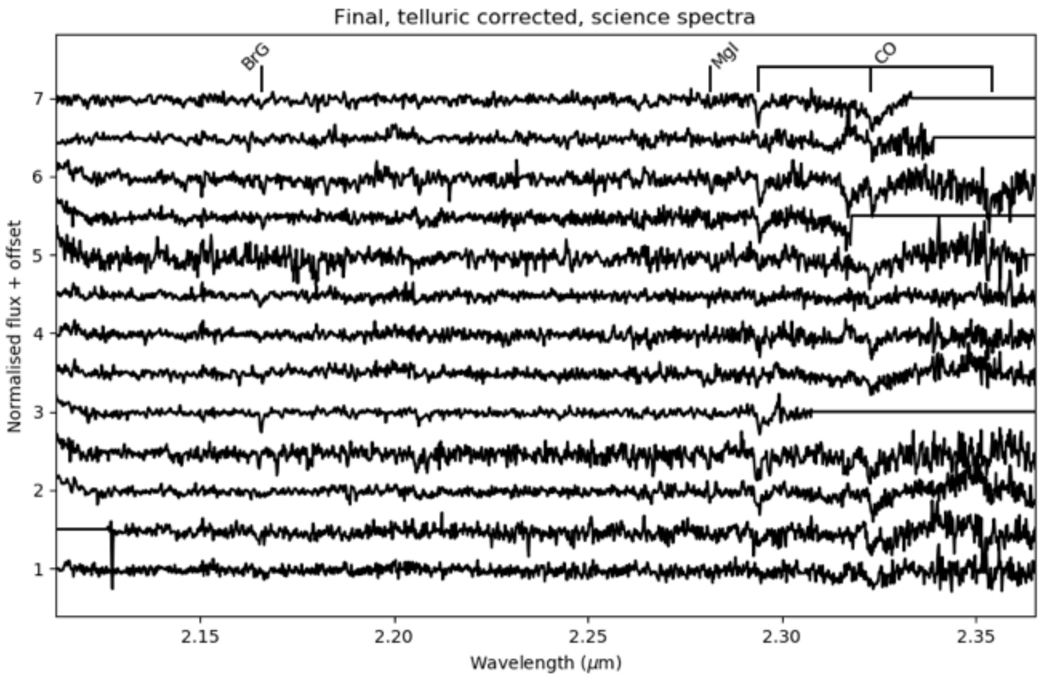

Figure 7: EMIR spectra of GALEP sources in the K band taken with a single MOS mask.

time, for this cluster. This will be done using a narrow spectral window in the J-band where elemental features arising from Fe, Mg, Si, Ti dominate the spectral appearance.

4 Plans for the short term

As mentioned before, at the time of this writing the MOS commissioning and internal verification phases have been completed and the open science verification is underway, and the MOS mode has been offered in the CAT19A. The plan for further actions on EMIR includes several tasks to maintain and improve whenever possible the performances of the instrument. The foreseen actions act in three main areas of the instrument: the ECS and software in general, including both on-line and off-line pipelines; the EMIR hardware subsystems; and the EMIR observing modes.

The plan for the ECS aims at a complete refactoring of the software, once the desired capabilities of the control system have been achieved. The ever changing environment of the GCS is imposing this action. That will include the interfaces between the ECS and the on-line DRP, which has to be modified accordingly. This upgrade will have very little, if any, influence in the observation results but will make the EMIR operations at the GTC more efficient, reliable and robust. An important aspect of the EMIR general software upgrades, and with a high impact in the user community, is the evolution of the off-line DRP to include the missing capabilities and permit a more complete data treatment.

As per the actions in the EMIR hardware, the current plan includes a maintenance stop during 2019 or 2020, yet to be decided, to remove the residual tilt of the EMIR detector,

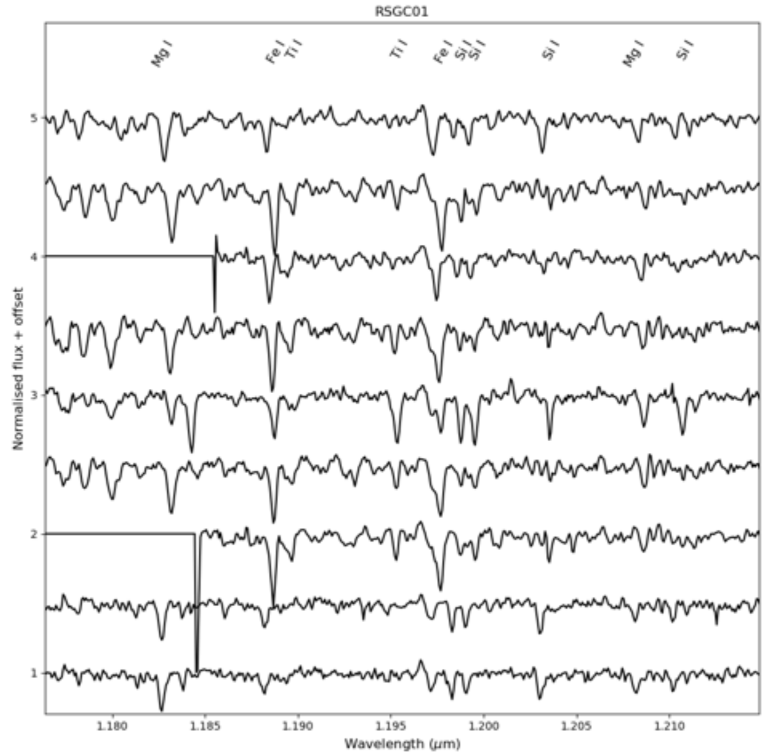

Figure 8: EMIR spectra of RSG in the J band taken with a single MOS mask.

commented in section 2.1. During this stop, the remaining set of old model CSU piezos will be replaced by the new ones.

Finally, the plans to improve the EMIR performances also contemplates the tuning of the detector read modes design to get rid of as many artefacts as possible. That will need a close monitoring of the data taken in different modes by the user community to first identify the spurious effects and then design and test ways of treating them.

Acknowledgments

EMIR is being operated at the GTC by a dedicated team composed by scientist engineers and technicians of the IAC, in close collaboration with the GTC astronomical and technical staff. All of them deserves special thanks for an extremely professional job executed under pressing conditions and with excellent results. EMIR is supported by the Spanish Ministry of Economy and Competitiveness (MINECO) under the grant AYA2015-66506-P; the Canarian Agency for Research, Innovation and Society of Information (ACIISI) under the grant ProID2017010117; GRANTECAN, S.A., via a development contract, and the EMIR partnership institutions, in alphabetical order, IAC, LAM, LATT and UCM.

References

[1] Cardiel, N., Pascual, S., Picazo, P., Gallego, J., Garzón, F., Castro-Rodríguez, N., González-Fernández, C., Hammersley, P., Insausti, M., Manjavacas, E., and Miluzio, M. 2017, Highlights on Spanish Astrophysics IX 702-702

[2] Garzón, F., Abreu, D., Barrera, S., Becerril, S., Cairós, L. M., Díaz, J. J., Fragoso, A. B., Gago, F., Grange, R., González, C., López, P., Patrón, J., Pérez, J., Rasilla, J. L., Redondo, P., Restrepo, R., Saavedra, P., Sánchez, V., Tenegi, F., Vallbé, M. 2006, Proc. of SPIE 6269, 18-7

[3] Garzón, F., Castro-Rodríguez, N., Insausti, M., López-Martín, L., Hammersley, Peter, Barreto, M., Fernández, P., Joven, E., López, P., Mato, A., Moreno, H., Núñez, M., Patrón, J., Rasilla, J. L., Redondo, P., Rosich, J., Pascual, S., Grange, R. 2014, Proc. of SPIE 9147

[4] Garzón, F., Castro, N., Insausti, M., Manjavacas, E., Miluzio, M., Hammersley, P., Cardiel, N., Pascual, S., González-Fernández, C., Molgó, J., Barreto, M., Fernández, P., Joven, E., López, P., Mato, A., Moreno, H., Núñez, M., Patrón, J., Rosich, J., and Vega, N. 2016, Proc. of SPIE 9908, 99081J-

[5] Garzón, F., Castro, N., Insausti, M., Manjavacas, E., Miluzzio, M., Hammersley, P., Cardiel, N., Pascual, S., González-Fernández, C., Molgó, J., Barreto, M., Fernández, P., Joven, E., López, P., Mato, A., Moreno, H., Númez, M., Patrón, J., Rosich, J., and Vega, N. 2017, Highlights on Spanish Astrophysics IX 652-659

[6] Lodieu, N., Zapatero Osorio, M. R., Béjar, V. J. S., and Peña Ramírez, K., MNRAS 2018, 473, 2020-2059

[7] Madonna, S., Bautista, M., Dinerstein, H. L., Sterling, N. C., García-Rojas, J., Kaplan, K. F., del Mar Rubio-Díez, M., Castro-Rodríguez, N., and Garzón, F. 2018, ApJL 861, L8-

Highlights on Spanish Astrophysics X, Proceedings of the XIII Scientific Meeting of the Spanish Astronomical Society held on July 16 – 20, 2018, in Salamanca, Spain. B. Montesinos, A. Asensio Ramos, F. Buitrago, R. Schödel, E. Villaver, S. Pérez-Hoyos, I. Ordóñez-Etxeberria (eds.), 2019

The GTC Adaptive Optics system: the high spatial resolution Adaptive Optics facility at GTC.

Béjar, V. J. S.[1,2], García-Talavera, M. R.[1], Patrón, J.[1], Hernández, E.[1], López, R.[1], Marco de la Rosa, J.[1], Montilla, I.[1], Nuñez Cagigal, M.[1], Puga Antolín, M.[1], Rodríguez-Ramos, L. F.[1], Rosich, J.[1], Sánchez-Capuchino, J.[1], Simoes, R.[1], Tubio, O.[1], Acosta-Pulido, J. A.[1,2], Prieto, A.[1,2], Watson, A. M.[3], and Zapatero Osorio, M. R.[4],

[1] Instituto de Astrofísica de Canarias, E-38205, La Laguna, Tenerife, Spain
[2] Universidad de La Laguna, Departamento de Astrofísica, La Laguna, Tenerife, E-38206, Spain
[3] Instituto de Astronomía, Universidad Autónoma de Mexico (UNAM), México
[4] Centro de Astrobiología (CSIC-INTA). E-28850, Torrejón de Ardoz, Madrid, Spain

Abstract

The GTC Adaptive Optics (GTCAO) system is the general Adaptive Optics facility that will provide diffraction limited images in the near-infrared to the GTC telescope. At Day 1 it will consist of a single deformable mirror with 21×21 actuators (373 useful actuators), conjugated to the telescope pupil and a Shack-Hartmann wavefront sensor with 20×20 sub-apertures using a Natural Guide Star (NGS) as a reference source. The GTCAO system is expected to provide a Strehl ratio of 0.65 in the K-band with a bright NGS, and it will be later upgraded to a Sodium Laser Guide Star (LGS) to significantly increase the sky coverage. In this proceeding, we describe the GTCAO and the LGS system, we summarize some of the scientific cases that can be carried out with the GTCAO LGS system and the FRIDA instrument, and we review the planned schedule for the GTCAO system first with the NGS and later with the LGS system.

1 Introduction

The Adaptive Optics (AO) systems allow to correct the atmospheric turbulence and produce images near the diffraction limit [1]. This is fundamental for large diameter telescopes (8–10 m), where the diffraction limit (~ 40 mas in the K-band for a 10 m telescope) is ten times smaller than typical good seeing conditions (~ 0.6"). The AO systems have two major components: a wavefront corrector, usually based on deformable mirror, and a wavefront sensor,

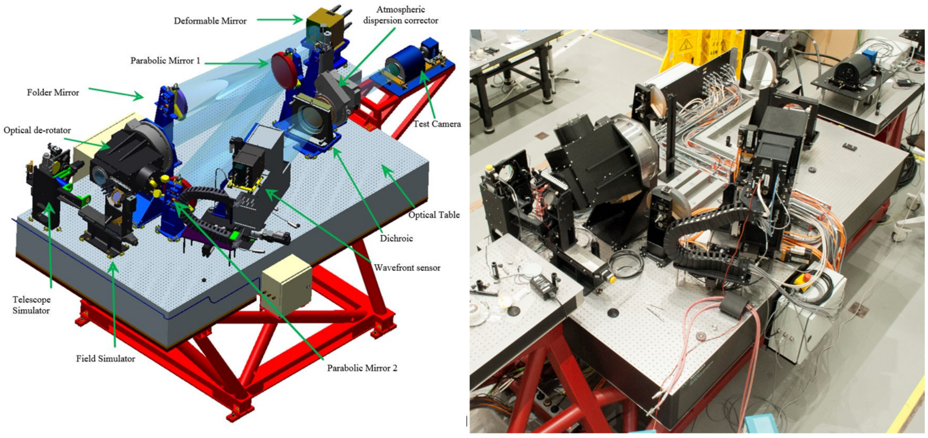

Figure 1: (left) Opto-mechanical design of the GTCAO system. (right) A picture of the fully integrated GTCAO system, currently at the IAC laboratory.

in most cases based on a Shack-Hartmann. A real time control system is also necessary to compute and correct the optical aberrations thousand of times per second.

2 The GTCAO system

The GTC Adaptive Optics (GTCAO) is a post focal AO system that will be installed on the GTC Nasmyth platform B, which corrects the optical beam to feed the scientific instrument placed after it. GTCAO follows the classical collimator-camera design of an AO system with the use of two identical off-axis parabolas (one acting as the collimator and the other as the camera), maintaining the effective focal distance of the telescope (see left panel of Fig 1). On Day 1, the system will provide a single deformable mirror conjugated to the telescope pupil and will use natural stars (NGS) for wavefront sensing. The GTCAO system is expected to provide a corrected beam that will achieve a Strehl Ratio (SR) of 0.65 in K-band with bright guide stars. The size of the transmitted field of view is 1.5 arcmin diameter and the optical layout of the system has been designed to be able to work up to 60 deg of zenithal distance. For the wavefront sensing, the GTCAO has a Shack-Hartmann wavefront sensor with 20x20 subapertures (FOV of 3.5"/subaperture) and an OCAM2 camera with a low noise EMCCD detector CCD220 (240×240 pix, 0.35"/pix). For the wavefront correction, the GTCAO has a CILAS deformable mirror with 21×21 actuators (373 useful actuators), and for tip-tilt correction it uses the GTC secondary mirror (see main characteristics of the system in Fig 2). A more detailed description of the different GTCAO sub-systems can be found in [2]. The GTCAO system is planned to be upgraded in the future by the use of a sodium laser guide star (LGS) for wavefront sensing to significantly increase the sky coverage (see section 4). The first scientific instrument to use GTCAO will be FRIDA (inFRared Imager and Dissector for Adaptive optics), an integral field spectrograph in the near infrared with imaging capability.

Mode	Single conjugate correction, NGS (first light)
Wavelength range	1.0-2.5μm (goal 0.8-5.0μm)
Strehl ratio	Bright NGS on axis, SR≥0.65 @ 2.2μm
	NGS m_R=14.5, SR≥0.1 @ 2.2μm
Wave-Front Sensor	Shack-Hartmann 20x20 (FOV 3.5”), EMCCD (240 x 240pix)
Wave-Front Corrector	Deformable Mirror (21x21, 373 actuators, Fried Geometry)
Throughput	at least 70% in the range 1.0-2.5 μm
Emissivity	less than 20% at 3.8 μm
Seeing	Up to 1.5 arcsec
Science FOV	Up to 1.5 arcmin
Zenith distance	0-60º
Exposure time	at least one hour
Ghost images	Defocused ghosts <1e^{-5} (except dichroic 1e^{-4}) Focused ghosts: <1e^{-3} and located within 0.2 arcsecs)
Tracking	Non-sidereal targets used as NGS
Dithering	offsets of 0.25 arcsecs (goal 1.0 arcsec) with closed-loop

Figure 2: Main characteristics of the GTCAO system.

3 The GTCAO AIV tests

The GTCAO system is currently fully aligned and integrated at the IAC laboratory. The first tests at the system level have been carried out, but possible adjustments are still required during this stage. For this reason, the general enclosure of GTCAO has not been mounted, and the air conditioning system of the clean room introduces a small and slow local turbulence in the optical bench. For these tests, we used TestCam, a near-infrared camera for the characterization of GTCAO performances, and the H-band filter. Two values were used for the OCAM2 camera frame rate, 1000 Hz and 2000 Hz. The telescope and turbulence simulator (GTCsim) of the Calibration System was set to the standard scenario, with r_0=20 cm and wind speed=10 m/s. Under these standard turbulence conditions, we compared the the Point Spread Function (PSF), obtained with the TesCam after closing the loop, with the simulated PSF in H-band, and measured a Strehl Ratio (SR) of 0.66, which has to be compared to the SR of 0.72, as expected from the simulations (see Fig 3).

4 The GTCAO LGS system

AO systems using bright NGS provide wavefront corrections in a limited region of the sky. The AO system using LGS provides a better correction and SR than NGS for natural tip-tilts stars of R>14–15 mag, and a sky coverage of nearly the 100% [3]. The GTCAO LGS system will be based in the commercially available Na laser, built by the company TOPTICA, which delivers a total output power of 20 W. The laser is sent to the atmosphere through a laser launch telescope (LLT), and focused on the mesosphere, at $\sim$90 km distance pointing at zenith, where the Na atoms are stimulated generating the LGS. For the installation of the LLT, the

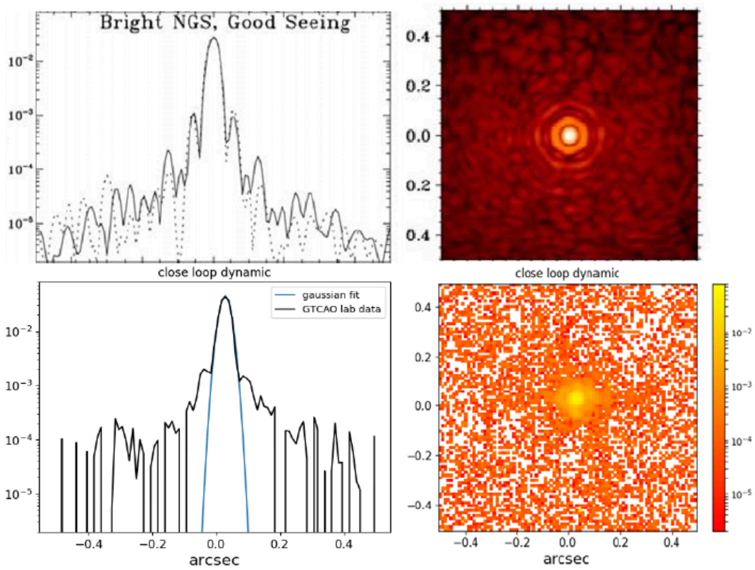

Figure 3: Simulated PSF (top) and real PSF measured with the TestCam (bottom) in the H-band. Left panels show an horizontal cut of the PSF and right panels show the 2-D images of the PSF. A Streh Ratio of 0.72 is predicted from simulations, while 0.66 is measured.

side (off-axis) laser launch configuration from the GTC elevation ring has been chosen as the concept baseline. The GTCAO LGS system will provide single-conjugate correction in the near-infrared using a LGS to perform high-order wavefront corrections and a tip-tilt NGS to provide tip-tilt and defocus corrections. The LGS system will be able to operate under similar conditions as the GTCAO system using a tip-tilt guide star of magnitude R<18 mag located at an angular separation up to 60 arcsec from the center. The main characteristics and the top level requirements of the LGS are indicated in Fig 4.

5 Science with the GTCAO LGS system

Most of the science cases proposed for NGS can also be done with the GTCAO LGS facility. In these cases the advantage of the use of LGS and a relatively faint tip-tilt guide star is that the sky coverage increases from about 10% with GTCAO NGS to about 60-100% with GTCAO LGS for average and good seeing conditions, and hence the number of accessible targets increase substantially.

The upgrade of the GTCAO system to the LGS facility will also allow GTC community to carry out some science cases that are not feasible with NGS, because there is no star bright enough in the FOV to perform the AO corrections. Some references science cases are mentioned here:

Mode	Single conjugate correction, 1 LGS (HOWFS) + NGS tip-tilt
Science focus Wavelength range	1.0-2.5μm
Strehl ratio	Bright tip-tilt NGS on axis, SR≧0.5 @ 2.2μm
	NGS m_R<18, SR≧0.1 @ 2.2μm
NGS Wave-Front Sensor	Shack-Hartmann 2x2 subap, EMCCD (240 x 240pix) (0.47-0.9 μm)
LGS Wave-Front Sensor	Shack-Hartmann 20x20 (FOV 5"), EMCCD (240 x 240pix)
Wave-Front Corrector	Deformable Mirror (21x21, 373 actuators, Fried Geometry)
Seeing	Up to 1.5 arcsec
Science FOV	Up to 1.5 arcmin
Zenith distance	0-60º
Exposure time	maximum one hour

Figure 4: Main characteristics of the GTCAO LGS system.

- AO observations of the nearest galaxies: The GTCAO with LGS will allow us mapping the full body of the nearest galaxies at unprecedented sub parsec scales, almost twice the resolution achievable with JWST. Because of the brightness and extension of nearby galaxies, very often the nucleus itself is the only suitable source for NGS AO correction. Subsequently, AO studies of galaxies are mostly restricted to the active galactic nuclei class. GTCAO with LGS is thus a must if we are to extend current studies to representative members of different galaxy types, across the Hubble sequence.

- AO observations of high-redshift galaxies: The Laser capability of GTCAO will be instrumental to sample z>4 at kpc scales. Dynamical studies at z>2 with the IFU will yield first determinations of galaxy virial masses at those z. The angular resolution and sensitivity of FRIDA in imaging mode will represent a step further in our quest to unveil the morphology of galaxies at higher z: mergers, discs and/or spheroids.

- Dynamical masses of very-low mass stars and brown dwarfs: Brown dwarf binaries offer a unique opportunity to determine their physical properties and test theoretical evolutionary models. The GTCAO LGS system will allow us to investigate the multiplicity and to determine the dynamical masses of the least massive brown dwarfs and planetary-mass objects.

- Multiplicity and dynamical masses of young brown dwarfs: Since the physical properties of substellar objects evolve with time, it is fundamental to find brown dwarfs and planets at different ages to investigate their evolution and test theoretical models. The GTCAO LGS system will allow us to study the multiplicity and to determine dynamical masses of brown dwarf binaries belonging to Young Moving Groups of the solar vicinity.

6 The GTCAO and LGS system schedule

The GTCAO sytem is fully integrated and we are currently performing tests at the system level at the IAC laboratory. The LGS system is in the Preliminary Design Phase, which is based on the side launch baseline. The expected schedule of the GTCAO and LGS systems are:

- GTCAO Acceptance Tests at IAC laboratory: September 2019.
- Preliminary Design of LGS: March 2019.
- Laser Acceptance at the IAC: September 2019.
- Detailed Design of LGS: end of 2019.
- AIV of the LGS subsystems: mid 2021.
- LGS Acceptance Tests at IAC laboratory: early/mid 2022.

Acknowledgments

The GTCAO system is co-funded by the Canary Islands Local Government, within the program for Regional Development of the European Union, program 2014–2020. This work is partially financed by the Spanish Ministry of Science through grant AYA2015-69350-C3-2-P.

References

[1] Babcock, H. W. 1953, PASP, 65, 386

[2] Garcia-Talavera, M. R. et al. 2018, Proceedings of the SPIE,

[3] Wizinovich, P. 2013, PASP, 125, 798

Highlights on Spanish Astrophysics X, Proceedings of the XIII Scientific Meeting of the Spanish Astronomical Society held on July 16 – 20, 2018, in Salamanca, Spain. B. Montesinos, A. Asensio Ramos, F. Buitrago, R. Schödel, E. Villaver, S. Pérez-Hoyos, I. Ordóñez-Etxeberria (eds.), 2019

10 years of GTC - GTC Science Operations Status.

A. Cabrera-Lavers[1,2]

[1] GRANTECAN, Cuesta de San José s/n, E-38712, Breña Baja, La Palma, Spain
[2] Instituto de Astrofísica de Canarias (IAC), E-38205 La Laguna, Tenerife, Spain

Abstract

10 years after Gran Telescopio Canarias' First Light, GTC is producing science in a routinely manner but at the same time enhancing its capabilities with the continuous advent of new instruments at the facility. This contribution summarizes the current status of the night operation of the 10.4 m Gran Telescopio CANARIAS (GTC) and describe GTC short- and medium- term instrumentation plan, that will make possible to provide access up to six different instruments to the GTC-users community from middle 2018, largely enhancing the scientific return from the telescope.

1 GTC telescope operation

The GTC was conceived as a general-purpose facility with a capability to host several instruments simultaneously. In this sense, the GTC can work from the UV atmospheric cutoff to the mid-IR with a wide instruments suite. In its original design, GTC allows the possibility to use two Nasmyth, a main Cassegrain, a Prime, a Coudé, and four Folded Cassegrain (these latter ones for lighter instruments) focal stations. Presently, the two Nasmyth and the two Folded Cassegrain foci are in use, but additional focal stations are being equipped at the same time as new instruments are developed. During night operations, it is possible to switch from one instrument to any other in the order of few minutes.

GTC is operated mainly in queue-scheduled mode (>90% of the time is used in this mode), where programs are selected in a dynamic fashion based on their ranking by the Time Allocation Committees from Spain, Mexico and University of Florida, matching their requirements to the prevailing observing conditions. This produces that GTC staff might play an extraordinary role in exploiting the full capabilities of the telescope and its instruments, as the night operation rely completely on their shoulders: they have to operate the full system with all its complexity, and resolve faults that might occur; there is no night-time engineering support. Data handling activities such as quality control, data packaging and time accounting take place during normal week days, as is the overall planning of observing priorities. GRANTECAN has opted for a relatively low-cost support model, and hence the service that can be offered to the community is rather restricted.

2 GTC observing time distribution

The overall demand for the telescope from the user community has seen large fluctuations from one semester to others. Despite of the overall oversubscription factor has peaked at 6, in the last six years has reduced to a constant value of about 3. Of the science time, in round figures about 5% of the available time has been lost due to technical problems, while some 30% of the time the weather was too poor to observe (in agreement with the predictions for the observing site at ORM).

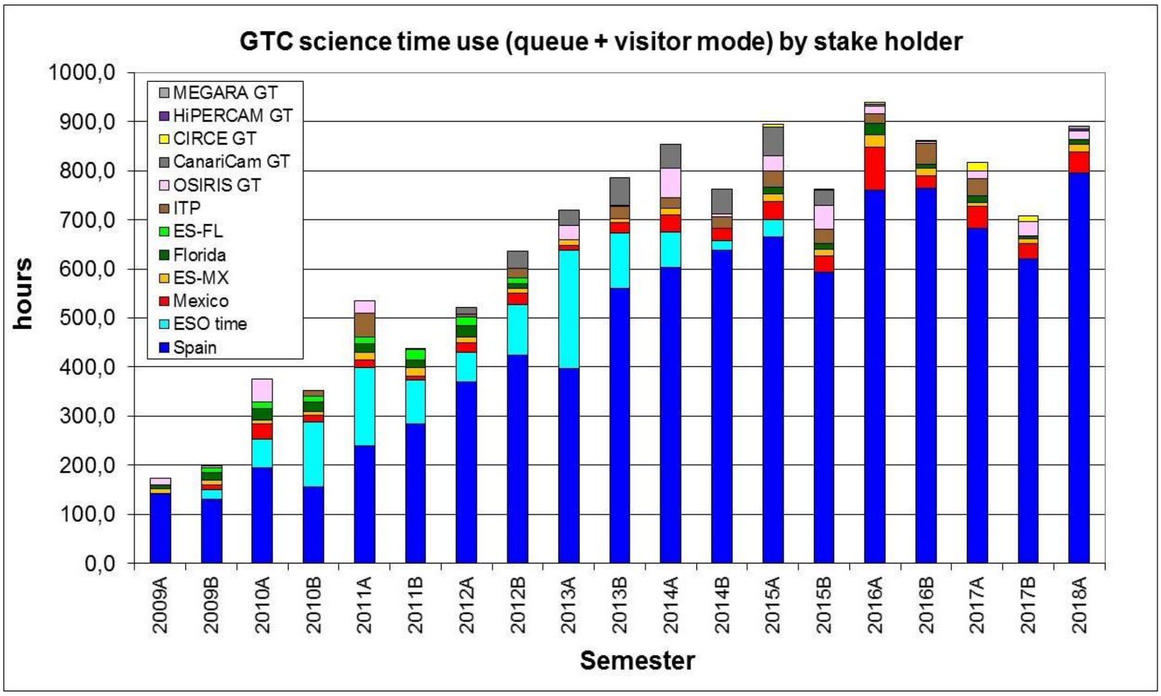

Figure 1: Evolution in the number of hours of scientific data provided by GTC with time.

Despite every semester a certain fraction of time is reserved for commissioning of new functionalities and forthcoming instruments (about a 20% of the total available time), the amount of scientific data provided by GTC has been progressively increasing with time (Fig. 1) simultaneously with a notable progress on the nightly queue efficiency with a value as high as 95%. This means that every night assigned for scientific observations, from the total amount of available time (once discounted technical and weather losses) we are able to produce useful science 95% of the time, that gives an idea of the current high-efficiently exploitation of the telescope time. These numbers translate in more than 630 observing programs completed to date and more than 12000 hours worth of data delivered to the GTC community.

Note also that in queue mode all the time delivered must fulfill the observing conditions initially required by the user (following the aim of this operational mode), hence each observing hour delivered to the user might be useful for retrieving the expected scientific return. All those data (mostly raw data, but also some reduced datasets) are freely available once the proprietary (1 year) is over via the GTC public archive at http://gtc.sdc.cab.inta-csic.es/gtc/.

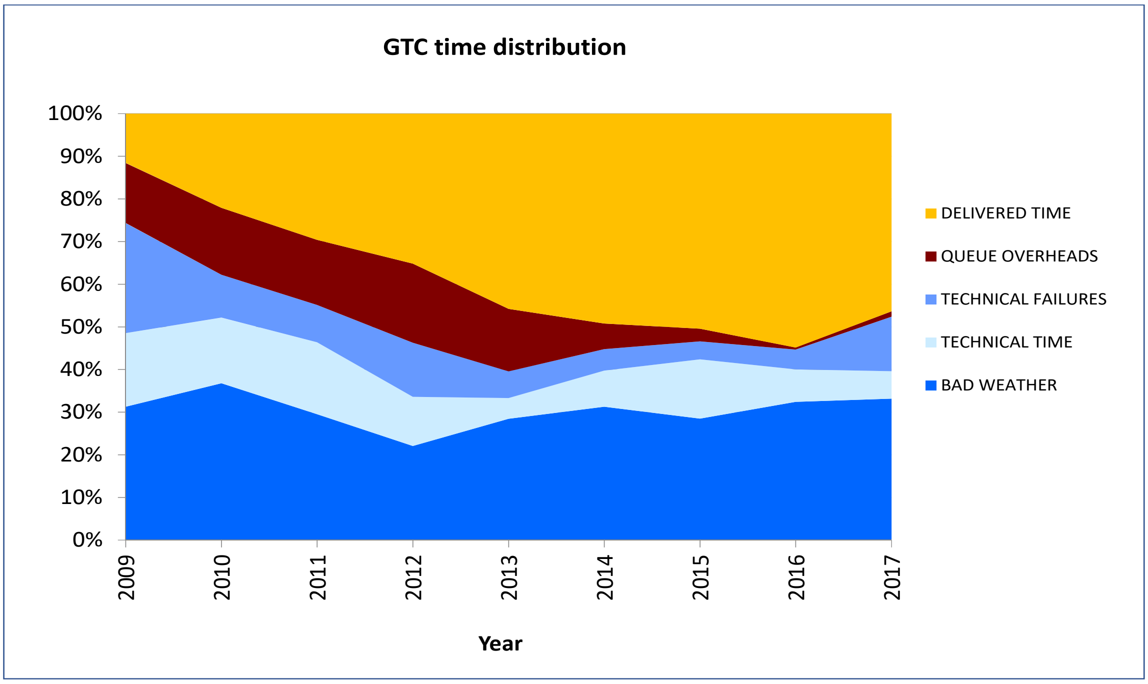

Figure 2: Evolution in the GTC time distribution with time.

3 GTC telescope instrumentation plan

Regarding telescope instrumentation, GTC currently operates with three major facility instruments: **OSIRIS** ([1]), an optical imager - intermediate resolution spectrograph with narrow band imaging (via Tunable Filters), fast imaging and Multi-object spectroscopy capabilites, **EMIR** ([4]), a near-infrared (0.9 - 2.5 μm) wide-field imager and medium-resolution multi-object spectrograph and **MEGARA** ([5]), an optical integral-field Unit (IFU) and multi-object spectrograph (MOS); as well as with **HiPERCAM** ([2]), a visitor intrument able to image simultaneously in 5 channels (ugriz), at (windowed) rates of over 1 kHz. An additional fourth facility instrument, **Canaricam** ([8]), the Mid-Infrared imager, spectrograph and polarimeter provided by the University of Florida (that has been in use from 2012 to 2016, when it was decommissioned to let its place to EMIR in the Nasmyth-A focus of the telescope) will be available again by the end of 2018, but now located in a new focal station (Fig. 3). Finally, at early 2019 GTC will incorporate **HORS** ([7]), a visitor instrument that provide point source fiber spectroscopy at R 23000 in the blue optical band (377-691 nm).

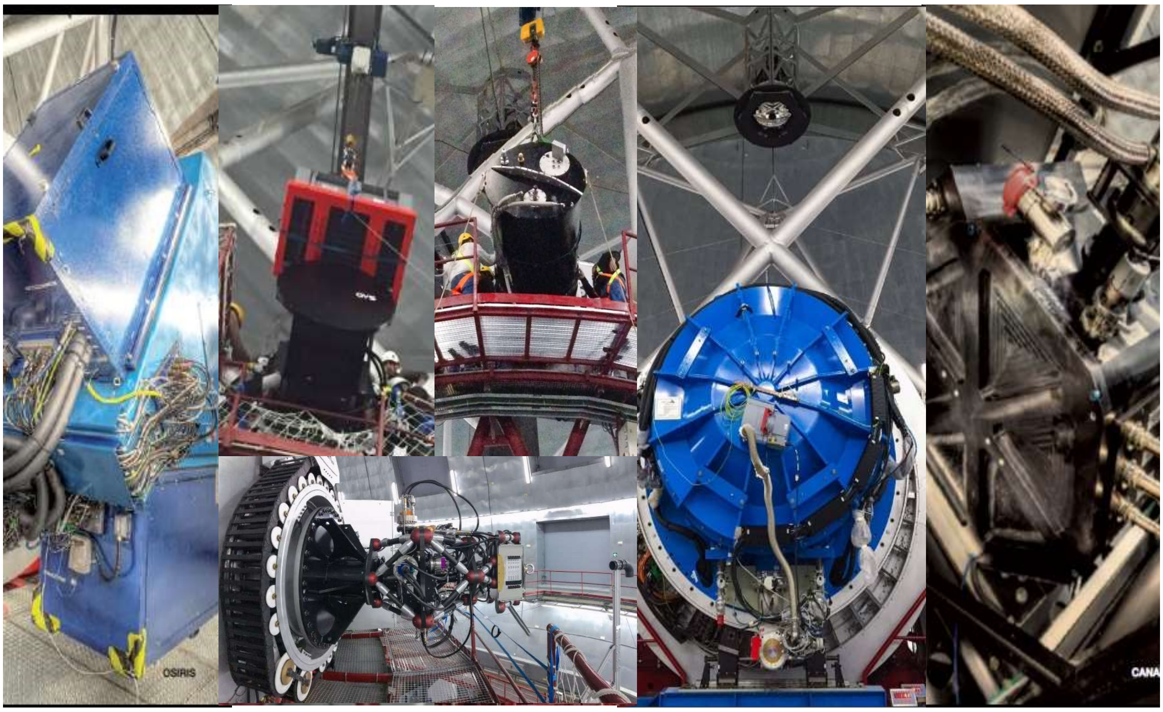

Figure 3: Detailed view of OSIRIS, MEGARA, HiPERCAM, CIRCE, EMIR and Canaricam (from left to right), the different instruments available at the currently operational foci of GTC.

In a short-term, period 2019-2020, the instrument suite for GTC will be enhanced with **MIRADAS** ([3]), a near-infrared multi-object echelle spectrograph under development at the University of Florida, operating at spectral resolution R 20000 over the 1-2.5 micron bandpass. MIRADAS selects targets from a 5 arcmin field using up to 12 deployable probe arms with pickoff mirror optics, each feeding a 3.7 arcsec x 1.2 arcsec field of view to the spectrograph. GTC will also incorporate Adaptive Optics (GTCAO) by 2019. Currently, the integration is being done at the Instituto de Astrofísica de Canarias (IAC) in collaboration with the GTC. GTCAO is planned to work in the NIR (0.9-2.5 micron) with the corrections made in visible light with a Shack-Hartmann wavefront sensor. The system will operate initially with a Natural Guide Star (NGSAO), and with a Laser Guide Star (LGSAO) probably one or two years later. The GTCAO will be placed at the Nasmyth-B platform, displacing OSIRIS instrument to the Main Cassegrain Station whose equipment is under development. The GTCAO system will feed **FRIDA** ([6]). This is a near infrared, diffraction limited imager and integral field spectrograph that has been designed and is being built as a collaborative project between GTC partner institutions from Mexico, Spain and USA. FRIDA will operate with GTCAO in imaging mode at three different scales, namely 0.010, 0.020 and 0.040 arcsec/pix. The integral field unit is based on a monolithic image slicer that will slice the field of view into 30 slices. Spaxels have a 2:1 pixel aspect ratio (2 pixels along the spectral axis and 1 along the spatial axis) and it will offer three different spectral resolutions, R=1000, 5000 and 30000, the latter over selectable regions in the HK bands.

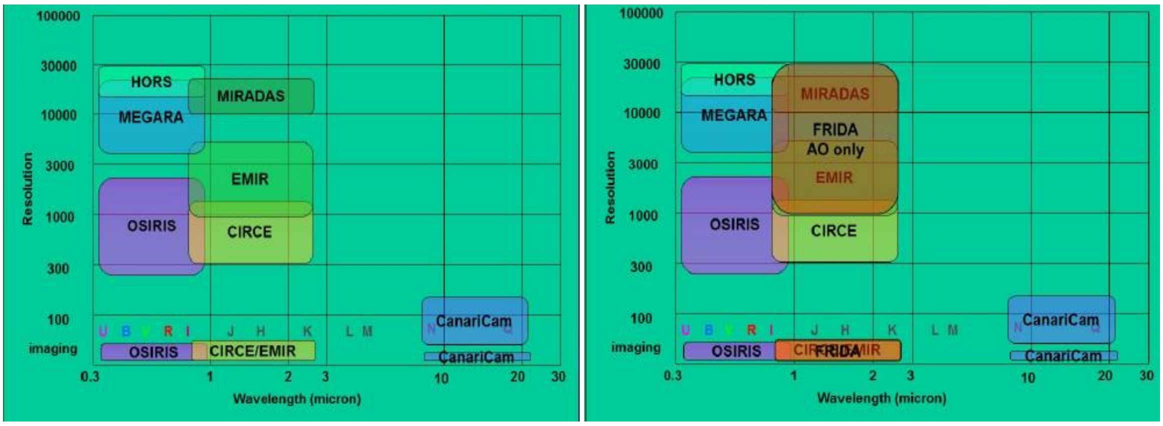

Figure 4: Global scheme of the GTC instrumentation available by 2019-2020.

4 Next Generation of Instruments for the GTC

Current GTC instrumentation plan will be completed around 2022. At that time, six or seven science instruments will fill the large suite of focal stations of the GTC. They should guarantee the scientific competitiveness of the telescope for several years to come, also considering that the GTC will continue to be the largest optical telescope in operation. Even so, it is time to think about the future. Defining and building new instruments is a complex process that takes a minimum of five years. This puts us to around 2025, when the new generation of extremely large telescopes will presumably start operation.

For this reason, GRANTECAN has opened a process to define the next generation of GTC instruments, with science as the main driver in this process. In this sense, the input of the whole GTC community is vital to address the process from a wide perspective, taking advantage of the expertise that our community has gained with its participation in many front-end astronomical projects and facilities. Young and mid-career astronomers should have a pivot role in the process, not only because of its timescale, but also to provide innovative and visionary ideas anticipating the future trends of observational astrophysics.

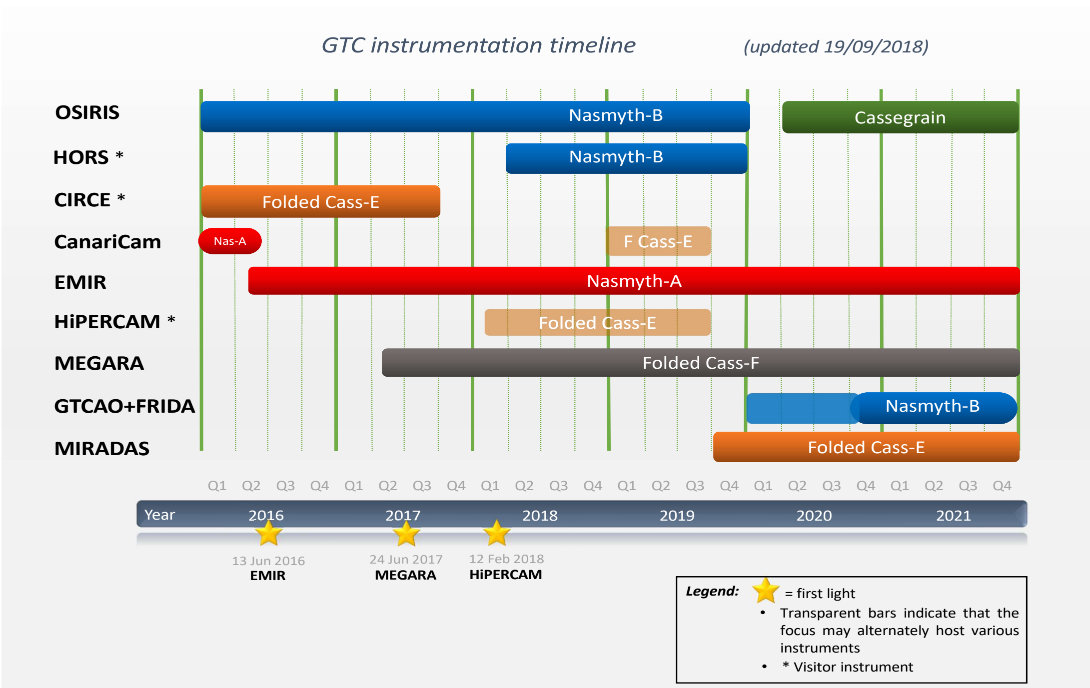

Figure 5: Current timeline for GTC instruments in the period 2016-2021.

References

[1] Cepa, J., Aguiar, M., Escalera, V. G., et al., 2000, SPIE, 4008, 623

[2] Dhillon, V. S., Marsh, T. R., Bezawada, N., et al., 2016, SPIE, 9908, 99080Y

[3] Eikenberry, S. S., Raines, S. N., Stelter, R. D., et al. 2016, SPIE, 9908, 99081L

[4] Garzón, F., Abreu, D., Barrera, S., et al., 2006, SPIE, 6269, 18

[5] Gil de Paz, A., Gallego, J., Carrasco, E., et al., 2014, SPIE, 9147, 91470O

[6] López, J.A., Acosta, J., Alvarez, L.C., et al. 2014, SPIE, 9147, 91471P

[7] Peñate, J., Gracia, F., Allende, C., et al. 2014, SPIE, 9147, 91478J

[8] Telesco, C. M., Ciardi, D., French, J., et al., 2003, SPIE, 4841, 913

Highlights on Spanish Astrophysics X, Proceedings of the XIII Scientific Meeting of the Spanish Astronomical Society held on July 16 – 20, 2018, in Salamanca, Spain. B. Montesinos, A. Asensio Ramos, F. Buitrago, R. Schödel, E. Villaver, S. Pérez-Hoyos, I. Ordóñez-Etxeberria (eds.), 2019

Stellar astrophysical parameters combining JPLUS and *Gaia* surveys.

Carrasco, J. M., Jordi, C. and Masana, E.

Institut de Ciències del Cosmos, Universitat de Barcelona (IEEC-UB), Martí i Franquès 1, E-08028 Barcelona, Spain, carrasco@fqa.ub.edu

Abstract

The first JPLUS Data Release (July 2018) provided data in 12 filters, covering a total area of 1022 deg^2, collected from November 2015 to January 2018 by the JAST/T80 telescope. The JPLUS Consortium aims to include the astrophysical parameters of the sources in the JPLUS DR1 added value catalogue. As a first step temperatures are derived for a small set of stars (Gold sample) with the best photometric precision in all filters. This work derives temperatures from JPLUS colours of this Gold sample. The addition of *Gaia* mission second release (*Gaia*-DR2, April 2018) information, with magnitudes, parallaxes and colours for more than one billion sources is very useful to determine the astrophysical parameters of the stellar content in JPLUS data. In particular, the use of *Gaia* parallaxes are used to improve the characterisation of the observed sources.

1 Introduction

During the "XIII Reunión Científica de la Sociedad Española de Astronomía" (July 2018, this meeting), the first data release of JPLUS (Javalambre Photometric Local Universe Survey, [3]) project was made public. This first release consists on 511 fields observed in 12 optical bands covering a total sky surface of 1022 deg^2 observed from November 2015 to January 2018 by the JAST/T80 telescope. Besides this data some value added catalogues (VAC) are also published (photometric redshifts, star-galaxy separation, crossmatch with other surveys and stellar astrophysical parameters). This work belongs to the VAC working group in charge of the stellar parameters determination. In the first estimations included here, only temperature determination for a small set of well-behaved sources were explored, although in the future this temperature determination will be expanded to all other sources in JPLUS DR1.

Several approaches were explored in VAC working group to determine the astrophysical parameters: Spectral Energy Distribution (SED) fitting, machine learning [15] and colour based relationships. This work uses the third approach deriving stellar parameters from calibrated colour dependencies. For this purpose we try to avoid the use of external information

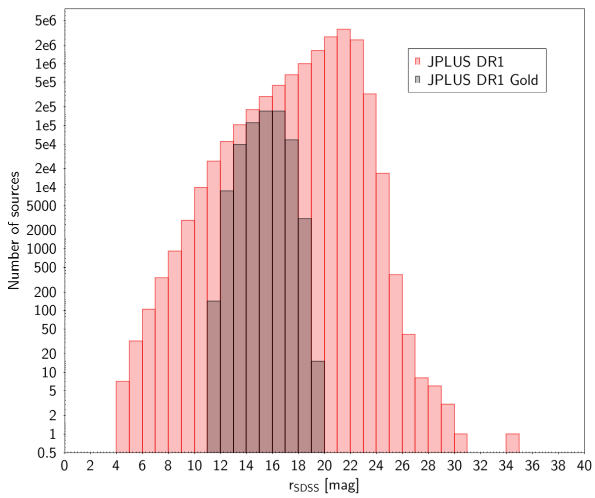

Figure 1: r JPLUS magnitude histogram of the total sample published in DR1 (red) and the gold sample used to derive their temperatures (black).

as much as possible, and only use JPLUS observables. Nevertheless, we also crossmatched JPLUS data with *Gaia* data release 2 (*Gaia*-DR2, April 2018, [6]) to refine our initial estimations by using *Gaia* parallaxes and photometry and also to derive photometric transformations between both surveys. In the first phase of stellar parameters determination by the VAC team, we have concentrated our efforts to determine effective temperatures for a set of stellar sources (morph_prob_star$>$ 0.9) with photometric uncertainties better than 0.1 mag in all JPLUS passbands. This dataset (named as *Gold sample*) consists on 563 367 sources (see Fig. 1). All methods proposed in the VAC team have to provide effective temperatures and their uncertainties for this Gold sample.

2 Photometric transformations

This section crossmatch JPLUS DR1 dataset with *Gaia*-DR2 [6] and provide photometric transformations between them. From the initial amount of about 13.5 million sources published in JPLUS DR1, 5.5 million are also present in *Gaia*-DR2. Among them, 4.9 million have *Gaia* parallaxes available (1.4 million with parallax uncertainties better than 20%).

Among these common sources with *Gaia*-DR2 we filtered out those observations with $\sigma_{Gaia} < 0.003$ mag and $\sigma_{\rm JPLUS} < 0.03$ mag. The recommended *Gaia* excess flux factor filtering recommended by [5] was also applied $\left(\frac{F_{BP}+F_{RP}}{F_G} < 1.3 + 0.06(G_{\rm BP} - G_{\rm RP})^2\right)$. The fitted transformations are shown in Fig. 2 and Table 1.

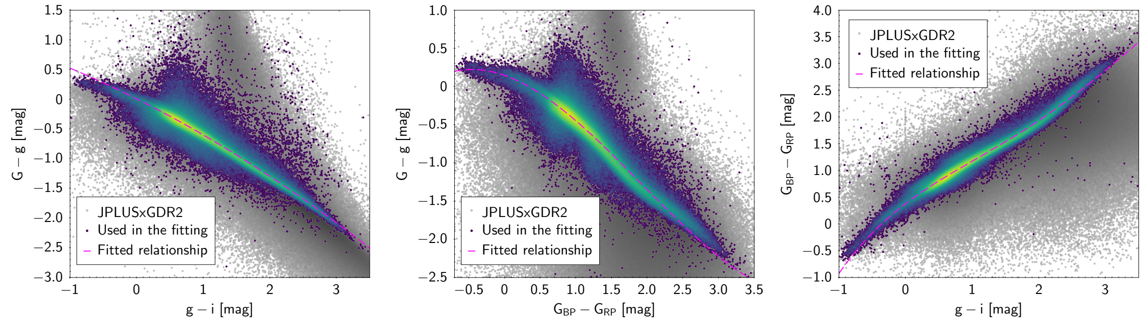

Figure 2: Photometric transformations between JPLUS and *Gaia*-DR2 surveys.

Table 1: Polynomial transformations between *Gaia*-DR2 and JPLUS colours. These transformations fit one colour (C_1) as a function of another colour (C_2) as a polynomial: $C_1 = a_0 + a_1C_2 + a_2C_2^2 + a_3C_2^3 + a_4C_2^4$.

C_1	a_0	a_1	a_2	a_3	a_4	σ	N
			$\mathbf{C_2 = G_{BP} - G_{BP}}^a$				
$G - g_{\rm SDSS}$	0.147	-0.327	-0.323	0.056	-	0.089	1513781
			$\mathbf{C_2 = g_{SDSS} - i_{SDSS}}^b$				
$G - g_{\rm SDSS}$	0.0075	-0.562	-0.045	-	-	0.078	1387830
$G_{\rm BP} - G_{\rm BP}$	0.386	0.947	-0.244	0.102	-0.011	0.054	1387830

[a]Applicability: $-0.7 < G_{\rm BP} - G_{\rm BP} < 3.5$
[b]Applicability: $-1.0 < g_{\rm SDSS} - i_{\rm SDSS} < 3.2$

3 Colour index and χ^2 method

Crossmatch between JPLUS DR1 sources and other catalogues in the literature including temperature values (see Table 2) was done. Among these literature catalogues, LAMOST DR2 [11] and Kepler Input Catalogue (KIC) [8] for the central range of temperatures were used. In order to expand this calibration also to high and low temperatures, white dwarfs (WDs, [9],[13]) and hot subdwarfs ([7]) and also late type stars ([12]) libraries were added.

Table 2: Range of JPLUS sources with effective temperatures works covered by the different literature used to calibrate our relationships in Fig. 3.

Reference	$T_{\rm eff}$ range [K]	$N_{\rm sources}$	Reference	$T_{\rm eff}$ range [K]	$N_{\rm sources}$
LAMOST DR2 [11]	3735–8454	90550	KIC [8]	2661–11076	3332
WDs [13]	6530–126360	237	WDs [9]	6127–87641	456
Hot subdwarfs [7]	23290–99999	208	Late type [12]	2490–3289	1206

After testing several JPLUS colours ($g_{\rm SDSS} - J861$, $g_{\rm SDSS} - z_{\rm SDSS}$, $J410 - J660$, $J410 - J861$, $J430 - z_{\rm SDSS}$, $J515 - i_{\rm SDSS}$, $J515 - J861$ and $J515 - z_{\rm SDSS}$) we concluded that $g_{\rm SDSS} -$

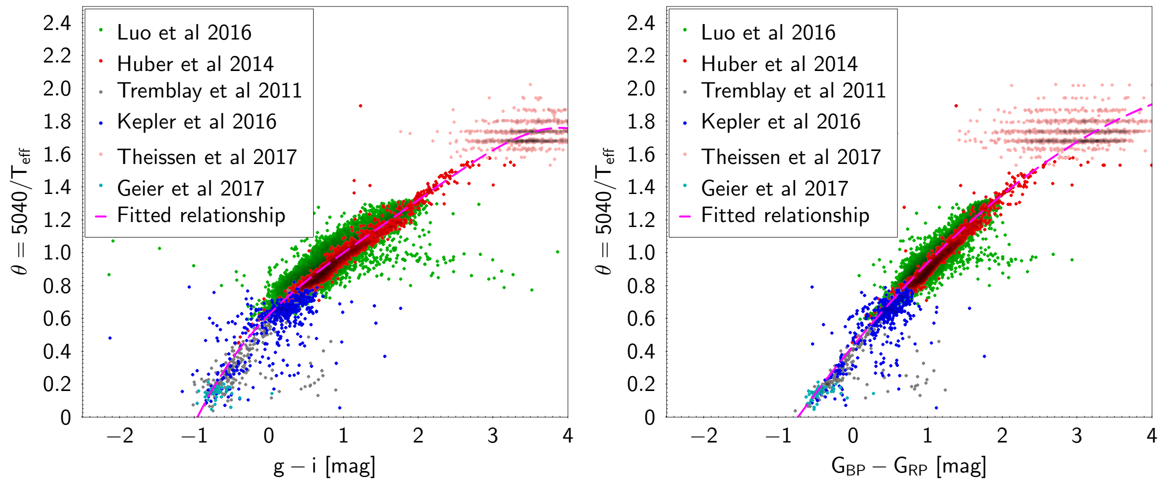

Figure 3: Effective temperature, represented in inverse using $\theta = \frac{5040}{T_{\rm eff}}$, calibrated from JPLUS $g_{\rm SDSS} - i_{\rm SDSS}$ colour (left) and from *Gaia*-DR2 $G_{\rm BP}-G_{\rm RP}$ colour using different temperature estimations from the bibliography.

$i_{\rm SDSS}$ provides the best correlation with effective temperature and we fitted a polynomial law (black line in left panel in Fig. 3). We also derived an analogous relationship using *Gaia*-DR2 colour (right panel in Fig. 3). The fitted relationships (Table 3) are applied to all other sources in JPLUS (red and orange points in Fig. 4).

Grey points in Fig. 4 show the temperature of the star with closest JPLUS photometry to our target source. The criterion to choose which photometry is closer to our source is a simple χ^2 weighted by the magnitude uncertainties (Eq. 1),

$$\chi^2 = \frac{\sum_{i=1}^{N_{\rm passb}} \omega_i \cdot (m_{\rm obs} - m_{\rm templ})^2}{N_{\rm passb} \cdot \sum_{i=1}^{N_{\rm passb}} \omega_i} \tag{1}$$

where $N_{\rm passb} = 12$ is the number of JPLUS passbands, $\omega_i = 1/\sigma_i$ is the weight of every observation, derived from its uncertainty σ_i. $m_{\rm obs}$ and $m_{\rm templ}$ are the JPLUS observed and template magnitudes, respectively. The template magnitudes used here are the ones observed by JPLUS for the sources included in the bibliography mentioned above. Then their magnitudes and temperatures associated to these sources are not coming from SED libraries but from preexisting determinations of real sources with photometry observed with JPLUS as our target star.

The application of the $T_{\rm eff}$-colour relationships derived results in reliable temperature estimations provided that the target sources have similar extinction that the literature sources from which the relationships have been determined. Being the stars in the halo, this is likely true.

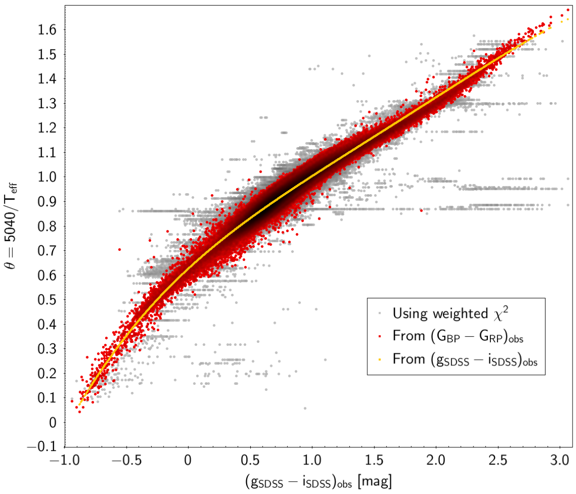

Figure 4: θ derived for all sources in the Gold sample using fitted polynomials represented in Fig. 3.

Table 3: Polynomial expressions $\theta = 5040/T_{\rm eff} = b_0 + b_1C + b_2C^2 + b_3C^3 + b_4C^4$ from JPLUS ($C = g_{\rm SDSS} - i_{\rm SDSS}$) or *Gaia*-DR2 ($C = G_{\rm BP} - G_{\rm BP}$) colours.

C	b_0	b_1	b_2	b_3	b_4	σ	N
$g_{\rm SDSS} - i_{\rm SDSS}$	0.625	0.465	-0.134	0.0539	-0.0079	0.036	94875
$G_{\rm BP} - G_{\rm BP}$	0.43547	0.553	-0.0464	-	-	0.037	95709

4 Conclusions and future work

This work shows the preliminary derivation of temperatures for JPLUS DR1. In the near future, these methods will be improved and also expanded to derive abundances and surface gravities (using colour-colour diagrams or improving the χ^2 method). Once the methods are finally settled, we aim to apply the astrophysical parameters estimations to all content in JPLUS DR1. The temperatures derived using our method will also be compared with other methods being tested in the JPLUS collaboration in order to determine the best temperature estimations for each star and their reliability.

Acknowledgments

This work was supported by the MINECO (Spanish Ministry of Economy) through grant ESP2016-80079-C2-1-R (MINECO/FEDER, UE) and MDM-2014-0369 of ICCUB (Unidad de Excelencia 'María de Maeztu').

References

[1] Bailer-Jones, C. A. L., Rybizki, J., Fouesneau, M., Mantelet, G., Andrae, R. 2018. Estimating Distance from Parallaxes. IV. Distances to 1.33 Billion Stars in Gaia Data Release 2. The Astronomical Journal 156, 58.

[2] Cardelli, J. A., Clayton, G. C., Mathis, J. S. 1989. The Relationship between Infrared, Optical, and Ultraviolet Extinction. The Astrophysical Journal 345, 245.

[3] Cenarro et al 2018, A&A in press, arXiv:1804.02667

[4] Drimmel, R., Cabrera-Lavers, A., & López-Corredoira, M. 2003, A&A, 409, 205

[5] Evans, D. W., Riello, M., De Angeli, F., et al. 2018, A&A, 616, A4

[6] Brown, A. G. A., and 452 colleagues 2018. Gaia Data Release 2. Summary of the contents and survey properties. Astronomy and Astrophysics 616, A1.

[7] Geier, S., and 7 colleagues 2017. The population of hot subdwarf stars studied with Gaia. I. The catalog of known hot subdwarf stars. Astronomy and Astrophysics 600, A50.

[8] Huber, D., et al., 2014. VizieR Online Data Catalog: Revised stellar properties of Q1-16 Kepler targets (Huber+, 2014). VizieR Online Data Catalog J/ApJS/211/2.

[9] Kepler, S. O., et al., 2016. VizieR Online Data Catalog: New white dwarf and subdwarf stars in SDSS DR12 (Kepler+, 2016). VizieR Online Data Catalog J/MNRAS/455/3413.

[10] Lallement, R., and 8 colleagues 2018. 3D maps of interstellar dust in the Local Arm: using $Gaia$, 2MASS and APOGEE-DR14. ArXiv e-prints arXiv:1804.06060.

[11] Luo, A.-L., et al., 2016. VizieR Online Data Catalog: LAMOST DR2 catalogs (Luo+, 2016). VizieR Online Data Catalog V/149.

[12] Theissen, C. A., West, A. A., Shippee, G., Burgasser, A. J., Schmidt, S. J. 2017. The Late-Type Extension to MoVeRS (LaTE-MoVeRS): Proper Motion Verified Low-mass Stars and Brown Dwarfs from SDSS, 2MASS, and WISE. The Astronomical Journal 153, 92.

[13] Tremblay, P.-E., Bergeron, P., Gianninas, A. 2011. An Improved Spectroscopic Analysis of DA White Dwarfs from the Sloan Digital Sky Survey Data Release 4. The Astrophysical Journal 730, 128.

[14] Westera, P., Lejeune, T., Buser, R., Cuisinier, F., & Bruzual, G. 2002, A&A, 381, 524

[15] Whitten et al 2018, J-PLUS: Identification of low-metallicity stars with artificial neural networks using SPHINX. ArXiv eprint arXiv:1811.02279.

Highlights on Spanish Astrophysics X, Proceedings of the XIII Scientific Meeting of the Spanish Astronomical Society held on July 16 – 20, 2018, in Salamanca, Spain. B. Montesinos, A. Asensio Ramos, F. Buitrago, R. Schödel, E. Villaver, S. Pérez-Hoyos, I. Ordóñez-Etxeberria (eds.), 2019

Gaia source list evolution: Data Release 2 and beyond.

J. Castañeda[1], F. Torra[1], M. Clotet[1], J.J. González-Vidal[1], and C. Fabricius[1]

[1] Institut de Ciències del Cosmos, Universitat de Barcelona (IEEC-UB), C/Martí Franquès 1, E08028 Barcelona, Spain.

Abstract

The working catalogue of sources in *Gaia* evolves as new observational data is received from the spacecraft and it enters the iterative processing loop. The precision and accuracy of source parameters will improve with the addition of the new measurements but at the same time a change in source character and source identification can always occur as observations are added and linked to the already known sources. The source list is expected to stabilize in future *Gaia* data releases, specially once the spacecraft stops its operations, but some evolution of a substantial fraction of sources will take place up to the final data release (e.g., a stable source can turn into a variable from one data release to the next). In this paper, we describe the main causes that lead to the *Gaia* Data Release identification and major parameters updates, the nature of the updates and the best approach that the user can take to match the data of the current and subsequent data releases.

1 Introduction

The determination of the catalogue of sources from the processing of the observational data is an inherently complex issue in astronomy. For *Gaia* this issue is even more complex as new observations are received every day which must be linked to the sources so that further data reduction can take place. The process in charge of this task is the Cross Matching [6] which is executed at least once over all the accumulated observations for each scheduled *Gaia* Data Release (DR).

This work is organized as follows. In Section 2 we describe how the *Gaia* source list is determined, describing the main processes and techniques used and the source identification scheme adopted. In Section 3 we present some of the most common scenarios which trigger the updates on the source list and on the derived source attributes. Finally, Section 4 is devoted to summarize the major updates in the last published catalogue with respect the previous

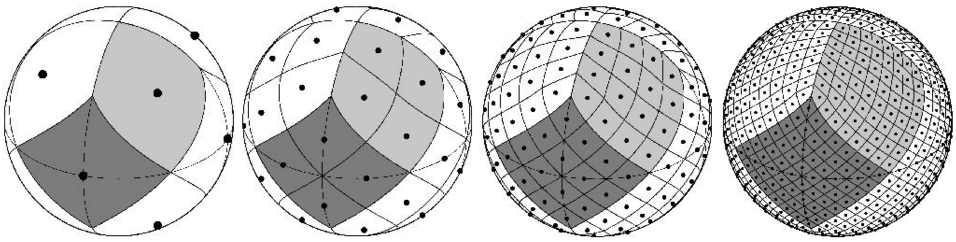

Figure 1: Orthographic view of *HealPix* partition of the sphere. From left to right the grid is hierarchically subdivided in subsequent level starting from 0 (Credit: [1]).

release, the expectations for the third release and the most important remarks regarding the tracing of sources across the published and future data releases.

2 Gaia Source list determination

The *Gaia* source list is determined just from the spacecraft detections, spacecraft attitude and orbit by means of classification and clustering techniques:

- Classification; mainly to censor the spurious detections [7].
- Clustering; to group all the detections from each individual object [6] [8].

The identified clusters of observations are then linked to the existing entries in the working source list. This working source list was initialized from on ground catalogues before *Gaia* launch and it has been updated progressively as new data has been processed. These changes are not limited to the source parameter updates - position, motion, parallax and magnitude among others - but also implies the addition of new entries and the removal of superseded or no longer matched entries.

To be able to track properly all these operations over the source list, all *Gaia* sources have been given unique source identifiers. This identifier is basically a numeric field assigned to each source to allow its unique identification and support its spatial arrangement. This numeric field basically codes a spatial *HealPix* index [1], the producer system and a sequence number. More specifically, the source identifiers have a level 12 *HealPix* index which is determined from the detections used in its creation time and it is encoded in the upper bits of the identifier.

The *HealPix* tessellation was adopted because of its mathematical properties and computation efficiency and its hierarchical numbering scheme is quite useful to speed up spatial queries or for massive job processing distribution. Fig. 1 shows the orthographic view of *HealPix* partition of the sphere.

Finally, it is worth pointing out that the *HealPix* index coded for a given source is never updated and discrepancies may appear when source position is updated. These discrepancies are more frequent in sources close to the the *HealPix* pixel boundaries.

3 Gaia Source list evolution

The Cross Matching task is executed periodically using the improved source parameters, spacecraft attitude, instrument calibrations and the updated censoring of spurious detections. Additionally, each new run starts from scratch ignoring any previous match solution so an independent new solution is obtained. Consequently, the new match solution may bring major updates in the observation assignations and the actual list of sources.

In this section, we describe some of the most common scenarios triggering updates of the source list by means of:

- New source creation: Fig. 2.
- Source list updates: Fig. 3 and 4.
- Source parameters updates: Fig. 5 and 6.

In the figures, we show the scenario and resolution in first *Gaia* Data Release (DR1) followed by the updated scenario and resolution in the second release (DR2). The symbols shown in the figures have the following meaning:

- Numbered circles represent observations from different scans; painted in blue the observations used in DR1, in yellow the DR1 observations affected by the updates on attitude and calibrations and in gray the observations classified as spurious detections and thus discarded in DR2.
- The stars represent source entries in the catalogue; in red the sources from DR1, in green the new sources in DR2 and in gray the superseded/deleted sources. Green stars with a red outline represents DR1 sources suffering major attributes updates.
- The black lines represent links between observation and sources.

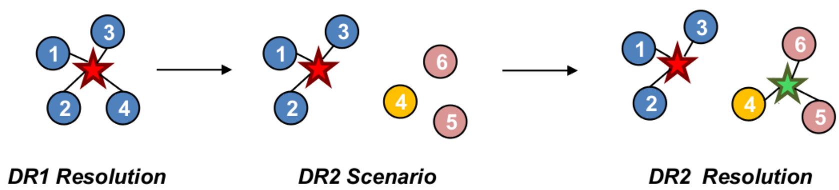

Figure 2: Example of new source creation. In this case the sky position of the observation belong to the fourth scan (4) used in DR1 has been updated and two new observations have entered the process. Due to the update of its position, the old observation (4) is no longer matched to the DR1 source and instead a new source is created together with the two new observations. As a consequence, the parameters of the source in DR1 will be slightly updated and a new source entry will appear in DR2. Legend in Sec. 3.

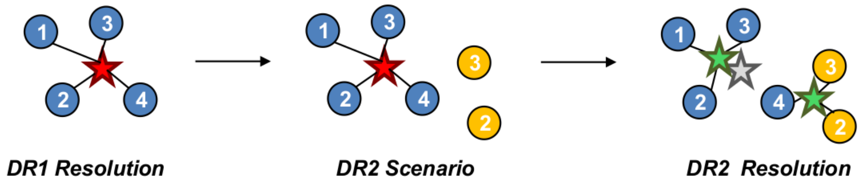

Figure 3: Example of new source creation by a split operation. In this case two observations from the same DR1 time period have been recovered i.e. reclassified as good detections. Consequently, for DR2 we have two scans with two nearby observations which is in general a clear indication of the presence of more than one source. In this situation, instead of creating just a new source and rearranging the observations, the policy in *Gaia* is to supersede the previous source and create two new entries so the evolution of all affected sources can be tracked across the different solutions. This split operation is only applied for observations and sources within a configured distance limit of ∼1-2 arcseconds. Legend in Sec. 3.

Figure 4: Example of new source creation by a merge operation. This case is basically the inverse operation of the split shown in Fig. 3. In DR1 we have two close observations in the same scan that triggered the creation of two sources. However, in DR2 one of those observations is no longer present i.e. discarded as spurious detections or suffering a large sky position update. In this situation, the policy in *Gaia* is to create a new source and supersede the previous sources with the same idea to be able to track the source list evolution across the different solutions. As in Fig. 3 case, this operation is limited to observations and sources within a configured distance limit of ∼1-2 arcseconds. Legend in Sec. 3.

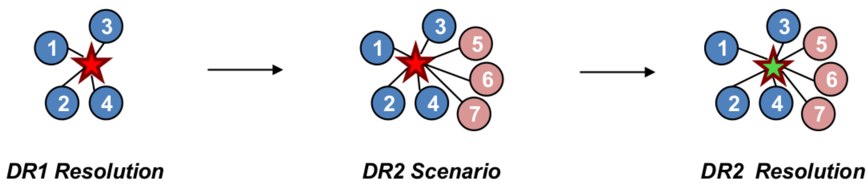

Figure 5: Example of source parameter updates. This example represents the most common scenario responsible of the source parameters updates across *Gaia* data releases. Each data release includes new observational data and/or new algorithms that revise and update previous solutions and the same source identifier can be present in DR1 and DR2 but the actual source features may be quite different. Legend in Sec. 3.

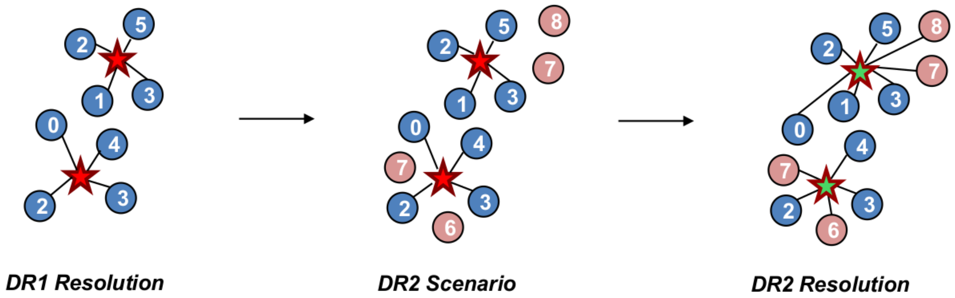

Figure 6: A more complex example of source parameters updates as the one shown in Fig. 5 with two sources involved. In this case we have new observations in DR2 that help the cross matching algorithm to resolve a source with a high proper motion (the one on the top right corner) which cause a rearrangement of the observation between the two existing sources. With this new match solution, the astrometry and photometry solution will be updated introducing a major revision on the source features. Legend in Sec. 3.

4 Conclusion

The working catalogue of sources in *Gaia* evolves as new observational data is received from the spacecraft and it enters the iterative processing loop. At the same time, the algorithms in charge of deriving the source parameters are also evolving taking advantage of a better knowledge of the instrument and the updates of the calibrations. Consequently, the source character and even the source identification are subject to change as observations are added and linked to the already known and published sources.

In 2016, the first *Gaia* catalogue (DR1 [3]) was published and the second release (DR2 [5]) has been recently made public this year. In DR2, ∼25% of the DR1 source identifiers have been deleted and as a result ∼75% have persisted. However, it must be mentioned that the attributes of ∼70-80% of the sources brighter than 16^{th} magnitude that have persisted (whose source identifiers are still present in DR2) have been largely updated. These changes come from the updated censor of spurious detections and the rearrangement of the source matches procured by the clustering techniques implemented for DR2.

To provide support for the comparison of both releases, a table to trace sources from DR1 to DR2 has been provided in the *Gaia* Archive. This table can be used to identify which source identifiers from DR1 have changed or disappeared in the new release but also to identify possible replacements for the superseded or deleted sources.

In future releases, the source list is expected to become progressively more stable. In fact, source list changes between DR2 and DR3 are expected to be much less in terms of deleted/superseded sources:

- Just ∼2-3% of DR2 source identifiers may be deleted in DR3.
- Less than ∼4-5% of DR2 source identifiers may be superseded due to merge or split operations.

On the other hand, the source parameters may still show major updates and therefore the following remarks should be taken into account:

- Identifiers are not unique/maintained across different data releases.
- Never rely on a direct source identifier match or, even better, just treat the source identifiers in each release as being from completely different catalogues.

Acknowledgments

This work was supported by the MINECO (Spanish Ministry of Economy) - FEDER through grant ESP2016-80079-C2-1-R and MDM-2014-0369 of ICCUB (Unidad de Excelencia *María de Maeztu*)

References

[1] Górski,K. M., Hivon,E., Banday,A. J., et al. 2005, ApJ, 622, pp.759-771.

[2] Gaia Collaboration (Prusti et al.) 2016, A&A, 595, A1.

[3] Gaia Collaboration (Brown et al.) 2016, A&A, 595, A2.

[4] Fabricius, C., Bastian, U. Portell, J., et al. 2016, A&A, 595, A3.

[5] Gaia Collaboration (Prusti et al.) 2018, A&A, 616, A1.

[6] Clotet, M., González-Vidal, J.J., Castañeda, J., et al. 2016, in Highlights of Spanish Astrophysics IX, pp.634-639.

[7] Garralda, N., Fabricius, C., Castañeda, et al. 2016, in Highlights of Spanish Astrophysics IX, pp.646-651.

[8] Torra, F., Clotet, M., González-Vidal, J.J. et al. 2018, in Highlights of Spanish Astrophysics X (this volume).

Highlights on Spanish Astrophysics X, Proceedings of the XIII Scientific Meeting of the Spanish Astronomical Society held on July 16 – 20, 2018, in Salamanca, Spain. B. Montesinos, A. Asensio Ramos, F. Buitrago, R. Schödel, E. Villaver, S. Pérez-Hoyos, I. Ordóñez-Etxeberria (eds.), 2019

A Wide Field Monitor (WFM) for the new generation X-ray missions eXTP (China) and STROBE-X (NASA).

J. L. Gálvez, M. Hernanz, C. Mansanet on behalf of the LOFT-WFM collaboration

Instituto de Ciencias del Espacio (ICE, CSIC) & IEEC

Abstract

We present the recent development of a Wide Field Monitor (WFM) in the X-ray range from 2 to 50 keV, with about 4 sr field of view capability. Such instrument based on European technology meets the challenge to be part of future X-ray spectral timing space missions currently under study, such as the Chinese enhanced X-ray Timing and Polarimetry mission (eXTP) and the NASA Probe mission "Spectroscopic Time-Resolving Observatory for Broadband Energy X-rays" (STROBE-X). The WFM design is inherited from the Large Observatory For X-ray Timing (LOFT) mission concept which was proposed and selected by ESA in 2011 as an M3 mission candidate.

The WFM is a set of coded mask cameras with solid state-class energy resolution, thanks to the use of Silicon Drift Detectors (SDDs). Since SDDs provide accurate event position measurements in one direction and only coarse positional information along the other direction, pairs of two orthogonal cameras are used to obtain precise 2D source positions. The useful effective field of view of one camera pair is about 28° x 28° (90° x 90° at zero response). A set of 3 or 4 camera pairs can be implemented to provide fully sky coverage. The working principle of the WFM is the classical sky encoding by coded masks, that has been widely used in space borne instruments (e.g. INTEGRAL, RXTE/ASM, Swift/BAT). The coded mask imaging is the most effective technique to observe simultaneously steradian-wide sky regions with arc min angular resolution.

1 WFM heritage from LOFT ESA (M3 call)

The Large Observatory For X-ray Timing (LOFT) was selected by ESA as one of the four M3 space missions concepts of the Cosmic Vision programme 2015 - 2025 for a feasibility study [1], [2] and [3]. Two instruments were included in the scientific payload of LOFT: the

Large Area Detector (LAD) and the Wide Field Monitor (WFM). The WFM is a coded mask instrument, based on the principle of sky encoding by a coded mask; the mask shadow is recorded by the position sensitive detectors and can be deconvolved to recover the image of the sky. Silicon drift detectors (SDDs) are used for both the LAD and WFM instruments.

The main goal of WFM is to detect transient X-ray sources at outburst to be pointed with LAD; therefore, the field of view is designed to have a maximum overlap with the sky accessible to LAD pointing. These sources are new transients, as well as known sources undergoing spectral state changes, e.g., neutron stars and black holes.

1.1 WFM X-ray detector

The WFM detector is based on the large area SDD technology [4] which allows very small weight, low power consumption and low fabrication cost, in addition to enable excellent timing capabilities and energy resolution. One of the four SDD tiles of the WFM detector plane is shown in Fig. 1 left. The SDD detector is divided into identical parts as illustrated in Fig. 1 left. When a X-ray photon interacts with the detector, an electron cloud is generated and drifted towards the read-out anodes driven by a constant electric field sustained by a progressively decreasing negative voltage applied to a series of cathodes, down to the anodes at 0V . While drifting, the electron cloud size increases due to diffusion. The charge distribution over the collecting anodes depends on the absorption point in the detector.
We measure for each photon its deposited energy, proportional to the collected charge, the so called X-position, the center of the charge cloud (< 60 μm), the Y-position proportional to the width of the charge cloud (< 8 mm), and the time of the event. The analysis of the charge distribution over the anodes is performed on-board by the FPGA-based BEE on each event and therefore results in the determination of the amplitude, the anode position and the drift position of the event.

1.2 WFM imaging design

As commented in subsection 1.1, the SDD provides accurate position in the anodes side but only coarse positional information in the other one; when combined with a 1D coded mask in each WFM camera (Fig. 2 left), they provide "1.5D" positions of celestial sources. Pairs of two orthogonally oriented co-aligned cameras (Fig. 2 right) will give precise 2D source positions. The FoV of each camera (and camera pair) is 90° x 90° FoV, at zero response (FWZR), and the fully illuminated FoV is approximately 30° x 30°. The detector-mask distance is 202.9 mm (Fig. 1 right). The angular resolution (FWHM) for the on-axis viewing direction is the ratio of the mask pitch and the detector-mask distance, 4.24 arcmin in the fine resolution direction and 4.6° in the coarse resolution direction.

1.3 Elements of the WFM camera

The mechanical design of the WFM camera is described in Fig. 3 left. The elements under our responsibility are highlighted with a red circle. A brief description of each element is

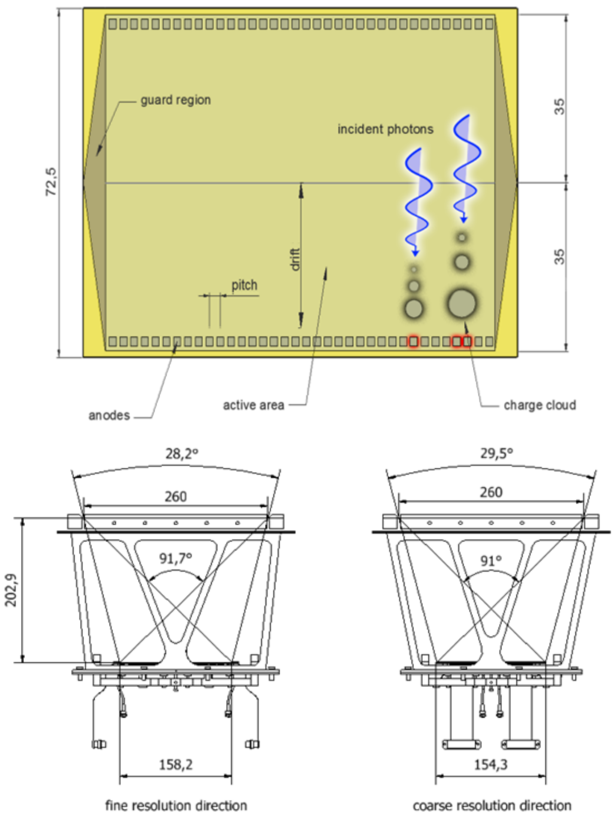

Figure 1: Left: Working principle of the SDD detector and dimensions, in mm, of the SDD tile. Right: Optical configuration of a WFM camera showing the fine and coarse resolution

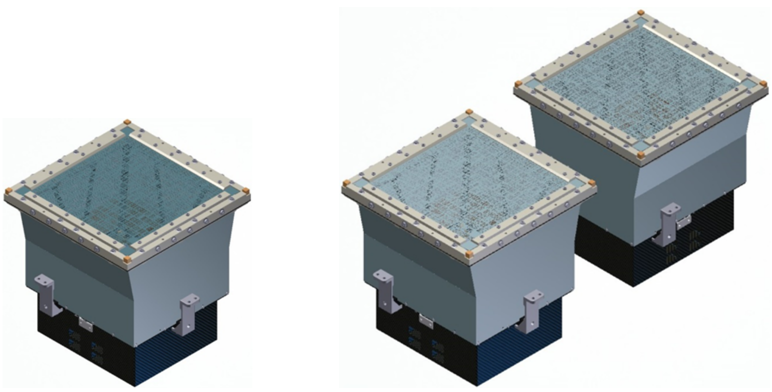

Figure 2: Left: One camera providing "1.5D" positions. Right: One camera pair results from the combination of two orthogonal cameras; it provides accurate 2D positions

given below:

- The **Coded mask** is manufactured from a 150 μm thick Tungsten foil and has a coded area of 260 mm x 260 mm (Fig. 3 centre).
- The **Collimator** is made of an open CFRP structure (Fig. 3 right) 3 mm thick. It holds the mask assembly and shields the detector plane from photons coming from outside of the field of view and cosmic rays since it is outer covered by a 150 μm thick Tungsten sheet.
- A 25 μm thick **Beryllium filter** above SDDs prevents impacts of micro-meteorites and small orbital debris particles.
- The **Detector tray** hosts the four SDD tiles and their corresponding read-out electronics.
- The **Detector Tray Support Structure** holds the detector tray and facilitates the mounting of the collimator and the Back-End Electronics (BEE) box.
- The **BEE** (including the Power Supply Unit of the camera) determines positions, energy and time of the recorded photons.

2 The WFM in the enhanced X-ray Timing and Polarimetry (eXTP) mission

The eXTP (enhanced X-ray Timing and Polarimetry) mission [5] is a major project of the Chinese Academy of Sciences (CAS) and China National Space Administration (CNSA) currently performing an extended phase A study and proposed for a launch by 2025 in a low-earth orbit. The eXTP scientific payload (Fig. 4 left) envisages a suite of instruments: Spectroscopy Focusing Array (SFA), Polarimetry Focusing Array (PFA), Large Area Detector (LAD) and Wide Field Monitor (WFM) offering unprecedented simultaneous wide-band X-ray timing and polarimetry sensitivity. A large European consortium is contributing to the eXTP study and it is expected to provide key hardware elements, including a Wide Field Monitor (WFM). Our institute is deeply involved as explained with more detail in section 4.

3 The WFM in the Spectroscopic Time-Resolving Observatory for Broadband Energy X-rays (STROBE-X) satellite

The Spectroscopic Time-Resolving Observatory for Broadband Energy X-rays (STROBE-X) is a probe-class mission concept that will provide an unprecedented view of the X-ray sky, performing timing and spectroscopy over both a broad energy band (0.2 - 30 keV) and a wide range of timescales from microseconds to years [6]. STROBE-X includes two narrow-field instruments, i.e. X-ray Concentrator Array (XRCA) and the Large Area Detector (LAD),

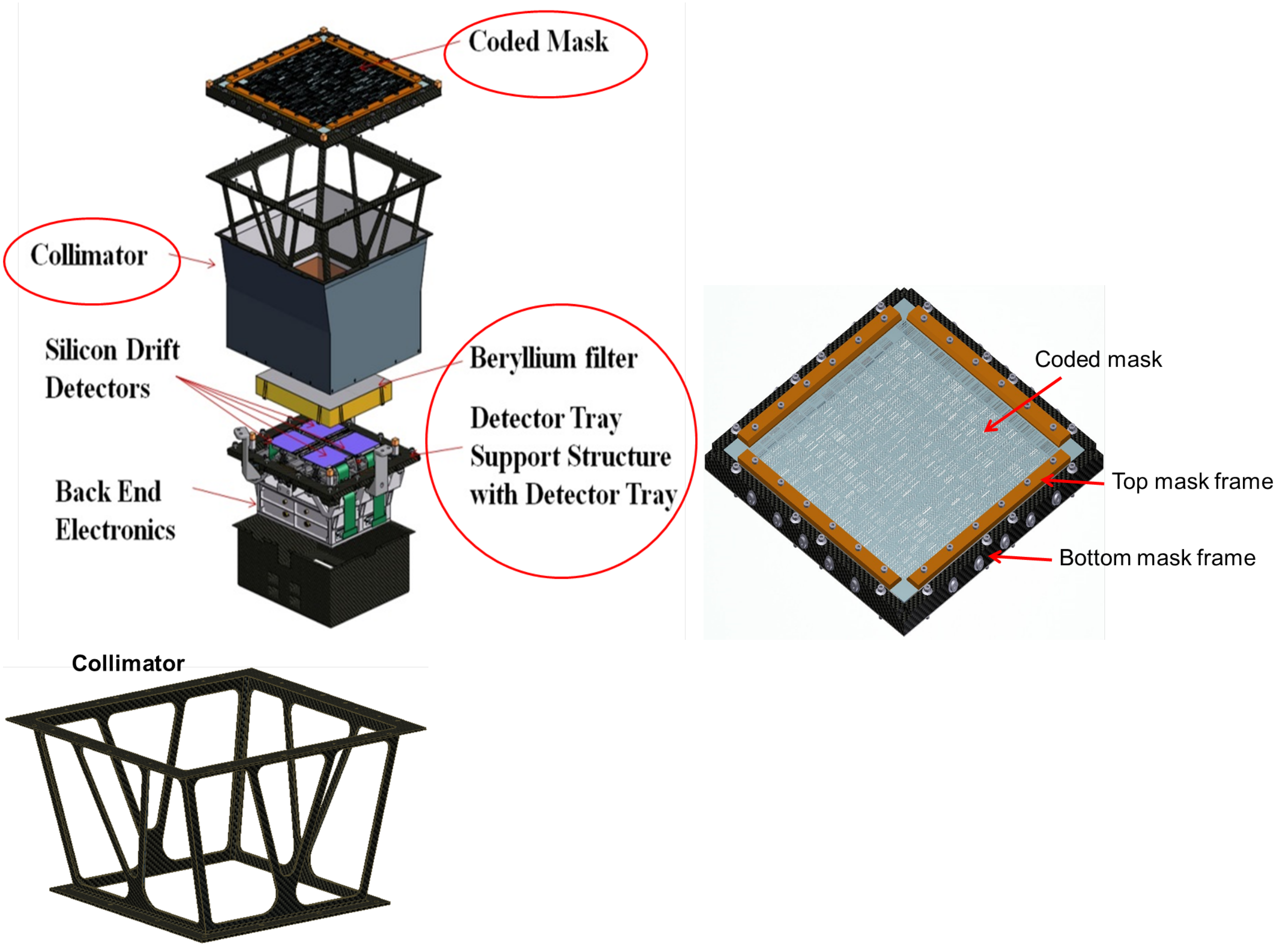

Figure 3: Left: Exploded view of the WFM camera elements. Centre: Coded mask assembly. Right: Collimator structure

and a Wide Field Monitor (WFM) as shown in Fig. 4 right. Our institute has taken part in the update of the WFM design led by the NASA Instrument Design Lab. STROBE-X mission concept will be presented to the 2020 Decadal Survey.

4 Spanish contribution to the WFM - eXTP

The WFM of eXTP mission [7] comprises six identical cameras grouped in three camera pairs as shown in Fig. 4 left. The WFM has an unprecedented combination of simultaneous FoV, i.e. covering 180° x 90° of the accessible sky to the LAD and the other pointed instruments, and imaging capability. It achieves the required 1 arcmin source localization accuracy in 2D. The eXTP mission is currently performing an extended phase A study which will finish in December 2018. The Institute of Space Sciences (ICE, CSIC & IEEC) plays an important

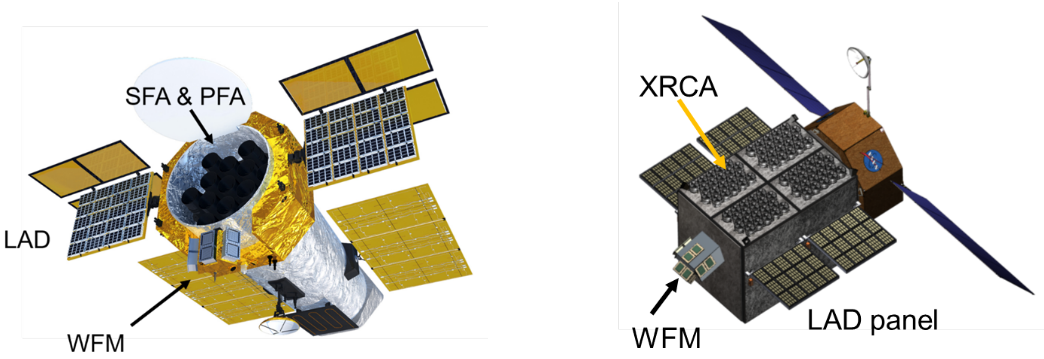

Figure 4: Artist's impression of: Left: e-XTP spacecraft with its science payload. Right: STROBE-X satellite with its scientific instruments

role in the coordination of the WFM instrument at PI level. We are also responsible of the mechanical design, manufacturing and test of the coded mask, collimator, Beryllium filter and detector tray of the WFM camera. In addition, we are also in charge of thermal control of the WFM instrument.

During the LOFT feasibility study, a finite element method (FEM) analysis of the mask design was performed to validate its operation during launch and orbit conditions. In addition, two pieces of $\frac{1}{4}$ of coded mask were built as shown in Fig. 5 left. The samples dimension was 100 mm x 100 mm x 0.1 mm and the pattern consisted on random slits of 14 mm x 0.250 mm with a separation of 2.4 mm between slits. The samples were manufactured by means of the chemical etching technique. Other techniques such as micro-milling and electrodischarge wire cutting were tested but finally both discarded because on one hand Tungsten is a highly abrasive material and this fact increased the fabrication cost and on the other, it was also difficult to achieve slits dimensions and chamfer requirements. A dimension control, i.e. slits position, dimensions, parallelism and chamfer, was performed for ten specific slits in both mask pieces by means of a vision machine. The general result of the dimension control showed that chemical etching is a valid technique, but there is still room to improve the procedure in order to fulfill slit requirements. Currently, we are working on more detailed mechanical and thermal analysis. On the mechanical side, we are performing a non lineal analysis in the temperature operation range in order to check displacements of the mask. And, on the thermal side, we have updated the WFM camera thermal model (Fig. 5 right) to the new ESATAN-TMS software version in order to improve the simulations.

Acknowledgments

We acknowledge the support from the MINECO grant ESP2017-82674-R and FEDER funds.

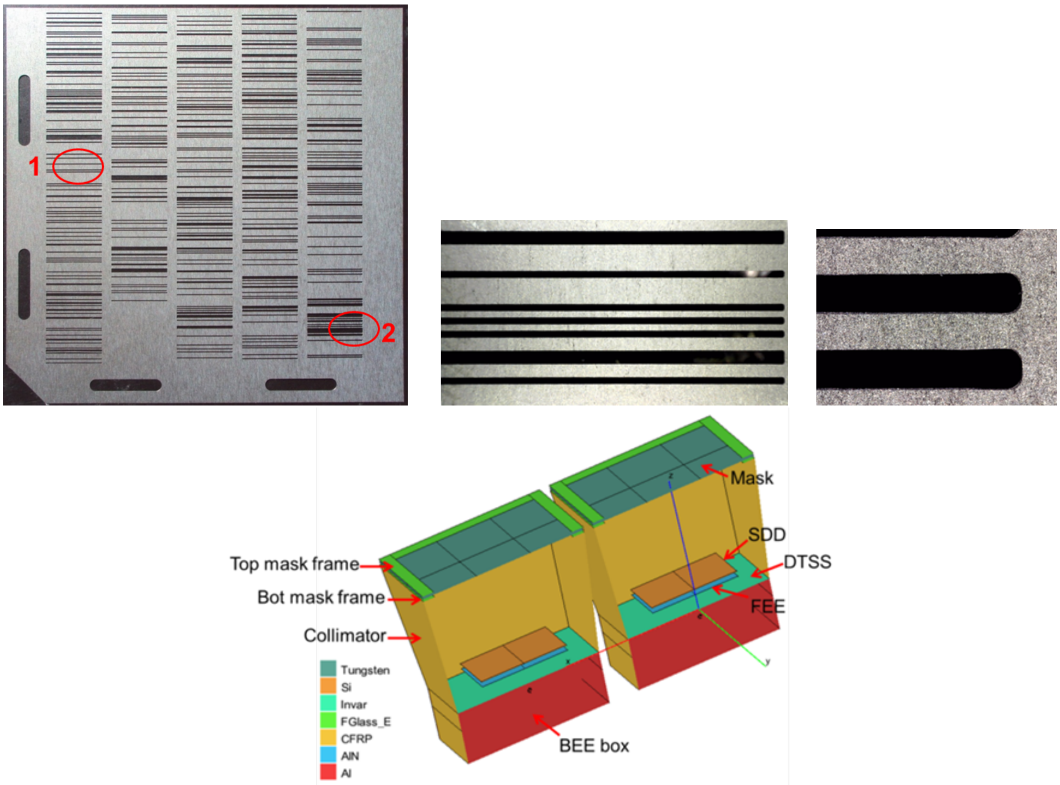

Figure 5: Left: View of the manufacturing of $\frac{1}{4}$ size of the coded mask. Centre: Zoom 1 shows a group of slits in a column. Zoom 2 illustrates the detail of the slit chamfer. Right: WFM camera thermal model

References

[1] ESA, "LOFT: The Large Observatory for X-ray Timing," ESA Assessment Study Report (Yellow Book), ESA/SRE(2013)3 (2013). http://sci.esa.int/loft/53447-loft-yellow-book/

[2] Feroci, M., et al., "The Large Observatory for X-ray Timing (LOFT)," Experimental Astronomy, 34, 415-444 (2012)

[3] Feroci, M., den Herder, J.W., Bozzo, E., Barret, D., Brandt, S, Hernanz, M., van der Klis, M. et al., "The Large Observatory For x-ray Timing," Proc. SPIE 9144, 91442T (2014)

[4] Rashevsky, A., et al., "Large area silicon drift detector for the ALICE experiment," Nuclear Instruments and Methods in Physics Research A 485, 54-60 (2002)

[5] Zhang S., Feroci M., et al., "The enhanced x-ray timing and polarimetry mission (Conference Presentation)," Proc. SPIE 10699, Space Telescopes and Instrumentation 2018: Ultraviolet to Gamma Ray, 106991A (2018)

[6] Ray P. S., Arzoumanian Z., et al., "STROBE-X: a probe-class mission for x-ray spectroscopy and timing on timescales from microseconds to years," Proc. SPIE 10699, Space Telescopes and Instrumentation 2018: Ultraviolet to Gamma Ray, 1069919 (2018)

[7] Hernanz M., Brandt S., et al., "The wide field monitor onboard the eXTP mission," Proc. SPIE 10699, Space Telescopes and Instrumentation 2018: Ultraviolet to Gamma Ray, 1069948 (2018)

Highlights on Spanish Astrophysics X, Proceedings of the XIII Scientific Meeting of the Spanish Astronomical Society held on July 16 – 20, 2018, in Salamanca, Spain. B. Montesinos, A. Asensio Ramos, F. Buitrago, R. Schödel, E. Villaver, S. Pérez-Hoyos, I. Ordóñez-Etxeberria (eds.), 2019

Release of the WSO–UV Software tools to attend the call for the Core Scientific Program.

Pablo Marcos-Arenal[1], Juan Carlos Vallejo Chavarino[1], Ignacio Bustamante Bengoechea[1], and Ana I. Gómez de Castro[1]

[1] AEGORA Research Group, Universidad Complutense de Madrid, Spain

Abstract

In October 2018 there will be a fist call for the Core Scientific Program to the WSO–UV observatory. In order to attend the needs of the appliers to that call, we present a set of tools including a simulator for the instrumentation of the mission (WSO–UV Simulator) and an Exposure Time Calculator (ETC). The WSO–UV space observatory, to be launched in 2023, will provide with slitless, long-slit and echelle spectroscopy with the WSO–UV Spectrographs (WUVS) and high resolution images and low resolution spectra with the Field Camera Unit (FCU). The Core Scientific Program of the WSO–UV observatory will include the key scientific research projects driving the development of the mission. In order to guarantee that possible preparatory observations are carried out on due time before launch, the first call to the core program will be open 4 years before the launch. We developed a set of tools to support the astronomers attending this call and made them available through the Remote Proposal System (RPS) web site.

1 Introduction

The World Space Observatory – Ultraviolet (WSO–UV) [4] scientific payload consists of a 170 cm primary space telescope, equipped with instrumentation for imaging and ultraviolet spectroscopy in the 115 to 315 nm range. The WSO–UV will be placed in geosynchronous orbit in 2023 by a Proton launcher becoming the first 2-m class ultraviolet observatory flown into High Earth Orbit (HEO). The telescope feeds two main instruments: WUVS for long-slit and echelle spectroscopy and the FCU for imaging and slitless spectroscopy. WUVS includes two high resolution echelle spectrographs to observe point sources in far UV (VUVES, working in the range 115-175 nm, $R \approx 50,000$) and near UV (UVES, working in the range 175-310 nm, $R \approx 50,000$) and the Long-Slit Spectrograph (LSS, $R \approx 1,000$; range 115-310 nm). FCU includes a far UV channel (115-176 nm) based on CsI Micro Channel Plate (MCP) detector with a Complementary Metal-Oxide-Semiconductor (CMOS) readout and a near UV channel (115-1,000 nm) with a cooled Charge Coupled Device (CCD).

In October 8th, 2018 will be opened the Call for Proposals for the WSO–UV Core Program; This is a special call for scientific projects requiring preparatory observations. In order to support the users attending this call, we have developed a set of tools to ease the preparation of proposals to the Call. This tools, accesible via the Remote Proposal System web site (https://wsorps.ucm.es), include the WSO Simulator and the Exposure Time Calculator.

2 WSO–UV Software tools

In the following sections 2.1, 2.2 and 2.3 it is briefly described the available tools for any user willing to submit a proposal to the WSO–UV Scientific Core Program requiring preparatory observations.

2.1 Remote Proposal System

The web interface to the Remote Proposal System (see Fig. 1) provides access to proposals submission, but also provides with some tools to generate these proposals. The RPS requires login to the system in order to add a proposal, including information of the Principal Investigator (PI) and co-investigators (CoIs). Once the abstract, list of observations and justification files have been submitted, a PDF file is generated with the information of the proposal, and sent to PI, CoIs and WSO–UV Time Allocation Committee (TAC).

2.2 WSO–UV Simulator

This section provides a brief summary of the information on the overall characteristics of the simulator built to pre-evaluate the performance of WSO–UV instruments. The WSO Simulator allows to evaluate the instrumental performance of the instruments in terms of noise source response, data quality, and number of counts detected for different types of configurations and observing parameters. Although the WSO Simulator provides with the scientific data outcome of each of the channels of WUVS and FCU, the LITE version of the simulator accessible via RPS web site only generates images for the FCU instrument. The full version of the simulator will be made available for the WSO–UV Spectrographs (WUVS) in a near future.

The WSO–UV Simulator (WSOSim) has been implemented as a further development of the PLATO Simulator (PLATOSim) [1]. PLATO is a medium-class space mission approved by the European Space Agency, aimed to find and study extrasolar planetary systems with emphasis on the properties of Earth-like planets in the habitable zone around solar-like stars [3]. PLATOSim is an end-to-end software tool developed at the Institute for Astronomy at KU Leuven for the validation of the noise level requirements of the PLATO mission. This software tool has been designed to be easily adaptable to similar types of missions [2],

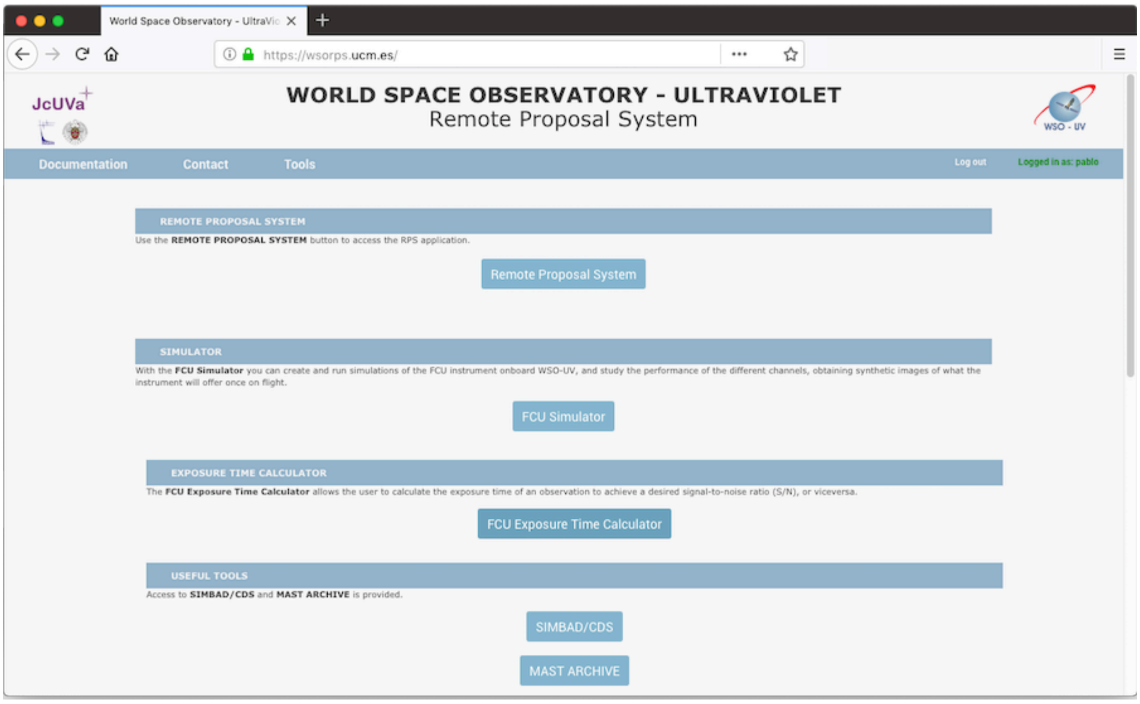

Figure 1: Caption of the WSO–UV Remote Proposal System and its available tools.

and probe of this is that has been employed in both PLATO and WSO–UV Simulators. PLATOSim is open source and available at the PLATO Simulator web site.

The WSO–UV Simulator is open source and have been developed in C++ programming language to be used under Linux platforms. WSOSim generates sets of realistic images of the foreseen observations by including models of the detector and its electronics, the telescope optics, the stellar field, the jitter movements of the spacecraft, exposure time, number of images and all important natural noise sources. Inputs to WSOSim are the equatorial coordinates of the astronomical sources in the field of view, their magnitudes, and the characteristics of the optics and detection chain. WSOSim output includes time-series of the instrument observation and the photometric analysis of the sources in the generated images, their magnitude, and an estimate of the noise level.

The full version of the simulator is accessible via command line, although there is a work in progress to develop a web interface devoted to ease the modification of the input parameters. The complete functionality of the simulator is mainly intended to be used by the WSO–UV Science Control Center and Instrument Team.

2.3 Exposure Time Calculator

For a certain observation, the ETC web interface provides with estimations of the signal to noise ratio or exposure time (in seconds) for the two channels of the FCU. This software tool takes as input the available filters for each channel and the spectral energy distribution

(SED) of the selected source. The SED can be given as a flat continuum, a black body, a spectral line, a Kurucz model or an uploaded spectral file. Further details on the usage of the ETC can be found on the documentation available in the dedicated page at the RPS web site. The ETC for the WUVS instrument in under development.

Acknowledgments

This publication is produced on the frame of the development of the WSO–UV Ground Segment, as part of the Spanish Contribution to the WSO–UV mission, under contract of the Ministerio de Economía y Competitividad (MINECO).

References

[1] Marcos-Arenal, P., Zima, W., De Ridder, J., Aerts, C., Huygen, R., Samadi, R., Green, J., Piotto, G., Salmon, S., Catala, C. & Rauer, H. 2014, Astronomy & Astrophysics, 566, A92

[2] Marcos-Arenal, P., Zima, W., De Ridder, J., Huygen, R., Aerts, C. 2014, Space Research Review, 2, 19

[3] Rauer, H., Catala, C., Aerts, C., et al. 2014, Experimental Astronomy, 38, 249

[4] Shustov, B., de Castro, A. I. Gómez, Sachkov, M., Vallejo, J. C., Marcos-Arenal, P., Kanev, E., Savanov, I., Shugarov, A., Sichevskii, S. 2018, Astrophys Space Sci, 363, 62

Highlights on Spanish Astrophysics X, Proceedings of the XIII Scientific Meeting of the Spanish Astronomical Society held on July 16 – 20, 2018, in Salamanca, Spain. B. Montesinos, A. Asensio Ramos, F. Buitrago, R. Schödel, E. Villaver, S. Pérez-Hoyos, I. Ordóñez-Etxeberria (eds.), 2019

Space developments at IACTec.

A. Oscoz[1,2], C. Colodro-Conde[1,2], J. Cózar[1,2], J. J. Díaz-García[1,2], R. López[1,2], P. Redondo[1,2], J. C. Sanluís[1,2], S. Sordo[1,2], L. Suárez-Andrés[1,2], S. Velasco[1,2], and A. Ynigo[1,2]

[1] Instituto de Astrofísica de Canarias, c/Vía Láctea s/n, La Laguna, E-38205, Spain
[2] Departamento de Astrofísica, Universidad de La Laguna, La Laguna, E-38200, Spain

Abstract

IACTec is a technological and business space created by the Instituto de Astrofísica de Canarias (IAC) to promote collaboration between the public and private sectors. Our objective is to foster the creation of quality employment and the generation of value-added technological products with high marketing potential, both nationally and internationally. In the growing field of innovation related to the payload of microsatellites and nanosatellites, our initial focus is on Earth Observations. In this paper we present IACTec Space, our plans for the future, including the design of cameras based on the heritage of the knowledge acquired in the IAC on detectors and optics or the use of new techniques such as superresolution.

1 Introduction

The Instituto de Astrofísica de Canarias (IAC) is a public research consortium located in the Canary Islands. The main headquarters of the IAC is located in La Laguna with a secondary office in La Palma, the CALP. In addition to this, we have two astronomical observatories: the Observatorio del Teide in Tenerife and the Observatorio del Roque de los Muchachos in La Palma. In total, we are approximately 400 people in the IAC alone, apart from those who work for foreign institutions.

One of the most important assets of the IAC is its astronomical observatories, with almost 60 different facilities from 27 countries. This is the largest multinational collection of professional telescopes in the world. There are both solar and night time telescopes, including the world's largest telescope, GTC, and other telescopes to observe the cosmic microwave background, Cherenkov telescopes, etc.

The presence of these observatories for more than 50 years has made a crucial contribution to the development of research in the IAC, turning it into a center with a recognized

Figure 1: Image of the future IACTec headquarters.

research prestige at this time. We currently cover virtually all branches of astrophysics: solar physics, solar system and exoplanets, stellar and interstellar physics, galactic formation and evolution and cosmology.

2 IACTec

This same presence of observatories, telescopes and instruments has also meant that the IAC has had to make a huge effort in the instrumental area. We have been doing instrumentation applied to astrophysics for 40 years and we have acquired a great experience and knowledge. We are currently involved in more than 20 instrumental projects and we have really outsanding capabilities, characteristics and laboratories. And these are precisely the foundations of the new IAC project: IACTec. IACTec is a space for collaboration with companies to take advantage of the experience acquired in instrumentation, technology and engineering with a social base. The main motivation of IACTec is to create a business and employment network in the Canary Islands that generates alternatives to absolute dependence on tourism. A network evidently related to science and technology and with the purpose of being self-sufficient within 4-5 years. Our idea is to prioritize and promote the regional economy, but having behind the support, experience and knowledge of the IAC, which will also seek the return of all this.

There are three niches that will work within IACTec. The most obvious is that of large

Figure 2: GTC (left) and EMIR (right), two examples of our experience with telescopes and instruments.

telescopes, including, for example, the Cherenkov Telescope Array, CTA-N, the European Solar Telescope, EST, or the New Robotic Telescope, NRT. Other important niche is medical technology, something that the IAC has been working on for several decades. And, finally, the small satellites.

These developments will be carried out in a new building located 2 km from the IAC, within a new technological park that is being built and will be ready in less than a year. In this park will be located the buildings of IACTec, Nanosciences, Parque Científico-Tecnológicos de Tenerife, the companies that want to accompany us, etc. And, to carry out the projects, we have an excellent team of engineers financed mainly by training programs of the Cabildo de Tenerife.

3 IACTec Space

In recent years, a kind of democracy has come to space with cheaper components and the use of commercial off-the-shelf (cots) and this has led to more and more companies or institutions have embarked on the design and manufacture of satellites of much lower-size than the big monsters that were traditionally the only projects that were sent to space. This means that there are great opportunities when it comes to small satellites, but it also makes the competition very big and wild. Therefore, before embarking on a project like this we did a very important exercise to see the niches in which the IAC could be competitive, given our previous experience.

- First of all, we are telescope manufacturers, and we do it quite well. From the IAC80, the first telescope of this type designed and built in the Canary Islands, to GTC, the largest telescope in the world, through QUIJOTE and other projects. We are used to making new and better optical and opto-mechanical designs and testing them.
- We are also experts in detectors, their use, characterization and improvements, reducing their noise and improving their efficiency and reliability.
- In addition, as astronomers, our tool is light and we are used to getting as much

Figure 3: IACTec Space logo.

information as possible about it and improving the data obtained. We have been improving data acquisition with our instruments for years, making algorithms for image processing and using other improvement algorithms, such as compression or super-resolution

- In the Observatorios de Canarias we are also used to transmit information, mainly from Earth to satellites or with ground-ground links, making use of optical communications.
- And, finally, the presence of the atmosphere has led us to develop instruments and techniques to compensate it and greatly improve the quality of our images: adaptive optics, cophasing, lucky imaging, etc.

The analysis of all these points led us to decide that where we could really be competitive was in the design and manufacture of payloads for Earth Observation at small satellites, combining our experience in the five points above.

To accomplish this, we have marked three different stages and two main objectives. On the one hand, DRAGO (Demonstrator for the Remote Analysis of Ground Observations) a SWIR instrument on board the ALISIO (Advanced Land-Imaging Satellite for Infrared Observations) project. ALISIO will be a 3U nanosat in LEO orbit that will help us position ourselves in the market, learn what a project of this style entails and carry out the first launch of a Canarian satellite at the end of 2019, early 2020. ALISIO will have as first objective observations in the SWIR range and as a secondary objective to test a magnetic measurement card useful for LISA. On the Other hand, IACSat-1, a long-term and more ambitious project for an optical and infrared microsatellite with a resolution close to the meter.

The first stage (2017) consisted of the creation and training of a well prepared team for the space and the first steps of the two projects. In addition, there was an important didactic and outreach activity, and the analysis and solutions for the RFI of a sub-meter resolution camera for a private collaborator. This stage ended with the conceptual design of DRAGO at ALISIO.

In a second period (2018 - 2020) we will seek to consolidate the IACTec team with the launch of ALISIO. This involves several phases: Preliminary Design Review (PDR), Critical Design Review (CDR) and manufacturing, Assembly-Integration-Verification (AIV), launch and follow-up. In parallel, there will be important advances in the sub-meter resolution line with its PDR and detailed design along with new projects in collaboration with companies related to small satellites payloads.

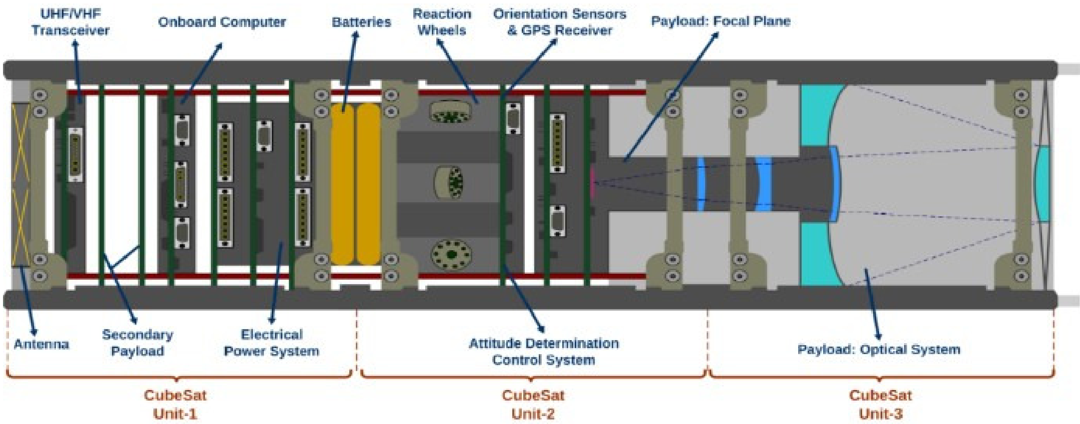

Figure 4: Scheme of ALISIO.

Finally, the third stage (2021-2022) will contemplate the stabilization of the team, with the launch of this microsatellite and with the independence and self-sufficiency of IACTec Space.

Our goals and motivation for the following five years can be summarized as:

- Create and train a multidisciplinary team in space engineering.
- Consolidate new projects to design and manufacture payloads that allow remote imaging the Earth from space with nano-satellites.
- Placement of IAC and the Canary Islands within the world map of small satellites.
- Generation of a business network in Tenerife / Canary Islands linked to space.
- Promotion of public-private collaboration in the space sector in the Canary Islands.
- Launch of the first Earth observation satellite with a sub-meter resolution with charge designed and manufactured in the Canary Islands.
- Open new windows for research.

Acknowledgments

IACTec and IACTec Space are a reality thanks to the following institutions: MINECO, Gobierno de Canarias, FEDER funds, Horizonte 2020, Fondo de Desarrollo de Canarias, MEDI and Tenerife 2030.

Highlights on Spanish Astrophysics X, Proceedings of the XIII Scientific Meeting of the Spanish Astronomical Society held on July 16 – 20, 2018, in Salamanca, Spain. B. Montesinos, A. Asensio Ramos, F. Buitrago, R. Schödel, E. Villaver, S. Pérez-Hoyos, I. Ordóñez-Etxeberria (eds.), 2019

The Gran Telescopio Canarias Archive.

Enrique Solano[1], José Manuel Alacid[2]

[1] Departmento de Astrofísica, Centro de Astrobiología (INTA-CSIC), ESAC Campus, Camino Bajo del Castillo s/n, E-28692 Villanueva de la Cañada, Spain.
[2] Spanish Virtual Observatory.

Abstract

The Gran Telescopio Canarias (GTC) archive is operational since November 2011. The archive, developed and maintained at Centro de Astrobiología (INTA-CSIC) in the framework of the Spanish Virtual Observatory project, provides access to raw, calibration and science ready data and has been designed in compliance with the standards defined by the International Virtual Observatory Alliance (IVOA) to guarantee a high level of data accessibility and handling.
In this presentation I will describe the main capabilities the GTC archive offers to the community, in terms of functionalities and data collections, to carry out an efficient scientific exploitation of GTC data.

1 Introduction

The GTC archive is not something new but there is a long history behind it. In fact, the first GTC archive meeting took place in 2003, fifteen years ago. Already at that time, the need of a Virtual Observatory (VO) compliant archive to ensure the long term preservation as well as the optimum scientific exploitation of GTC data was clearly identified.

Eight years later, in November 2011, the first operational version of the archive was released[1]. The GTC archive has always been managed in the framework of the Spanish Virtual Observatory[2] and is part of the CAB Scientific Data Centre. In this context it is important to remark that the GTC archive is the only entry point for the national and international astronomical community to access GTC data.

At the time of writing the GTC archive contains more than 160 000 science files of five instruments (OSIRIS, CanariCam, CIRCE, EMIR and HIPERCAM) and is intensively used

[1]http://agencias.abc.es/agencias/noticia.asp?noticia=1002094
[2]http://svo.cab.inta-csic.es

by the community as demonstrated by the fact that users from the five continents have made hundreds of queries to download thousands of files.

2 The GTC archive. Characteristics and functionalities

2.1 Data transfer and ingestion

GTC data are periodically transferred through a secure connection from the telescope in La Palma to the archive in Madrid. At their arrival, a number of quality control tests are carried out to ensure data integrity and metadata coherence. Problematic files are inspected and remedial actions are taken in agreement with GTC staff. After passing the tests, metadata information is extracted from the FITS header and stored in a database while FITS files are moved into the data storage system. Once data and metadata have been successfully ingested, they are automatically available to the general public through the web a VO interfaces.

In order to guarantee a safe long-term preservation of GTC data, a well-defined backup and data safekeeping policy have been established.

As of January 2018 the GTC archive also provides access to private data, identified according to their observing date. Principal Investigators are provided with a login/password to access their private data. They are also emailed whenever new data of their programmes arrive. At present (October 2018) the archive contains 93 private programmes with more than 9 000 science files.

2.2 Web interface. Data query

The GTC archive is friendly enough to be potentially used by a wide variety of users. From the home page, the user can get information on the archive through three different channels: Reading the system overview section, checking the FAQ system or directly asking GTC archive staff using the available HelpDesk.

The input query form is very simple and allows typical queries by list of objects names and/or coordinates, observing date, type of instrumentation, and programme. Special programmes like the ESO-GTC or the GTC Large Programmes have their specific entry access.

In addition to basic metadata, the table of results obtained after a query also includes links to the paper where the observations have been published as well as to NED and the CDS portal. These are powerful functionalities to easily get additional information on a GTC object. The output fields can be ordered by date, instrument, program or product identifier and the number of results shown per page can also be customized.

As said in the abstract, one of the main requirements of the GTC archive is its compliance with the Virtual Observatory, with the objecting of taking advantage of the VO standards and protocols. The Multi-Object Coverage (MOC[3]) is one of these standards. It helps users in the identification of the sky regions covered by GTC observations. MOC not only facilitates the visualisation of the footprint of a given survey but also, making use of a

[3]http://www.ivoa.net/documents/MOC/20140602/REC-MOC-1.0-20140602.pdf

VO tool like Aladin, permits operations to know, for instance, the region in common between two surveys or the part of the sky that contains observations of only one of the surveys.

A remarkable strength of the VO protocols is their ability to discover information using VO tools. By providing seamless access to thousands of archives and services, VO-compliance facilitates research projects that, otherwise, would be extremely difficult to perform outside the Virtual Observatory. In this sense, SIAP (Simple Image Access Protocol) has been implemented to access GTC images from VO tools.

Figure 1: GTC archive query form

2.3 Reduced data

Reduced data are of fundamental importance for archives as they enhance their use by the community and provide a higher visibility of the project results. The bad news is that there is no official reduction pipeline for the GTC instruments. To overcome this problem three channels have been defined to feed the GTC archive with science-ready data products.

- Reduced data provided by the community: On a monthly basis, GTC archive staff query ADS looking for papers containing GTC observations. Once identified, we contact the first author inviting him to send us their reduced data using a system similar to ESO-Phase 3 but much simpler. In short, the users have to submit a single FITS file or a zip file with their data in FITS format in the case of multiple products. As soon as reduced data are ingested in the archive, they are linked to the associated raw products and are available for downloading.

At the time of writing (October 2018), we have identified 355 publications containing GTC data and have ingested reduced data for 103 ($\sim 30\%$).

- Use of existing pipelines: In collaboration with GTC staff, we are working in the use of existing pipelines to reduce in a systematic and homogeneous way data from an observing mode or instrument. This is, for instance, the case of CanariCam and EMIR.
- Provision of high level data products: The goal of this line of work is to generate high level products (astrometrically and photometrically corrected images and the associated source catalogues) of the broad-band images obtained with the instrument OSIRIS. We have used 2MASS-PSC as the reference catalogue for astrometry while Pan-STARRS (PS1) was used for the photometric calibration. Corrected images and the associated catalogues will be publicly available soon.

3 Conclusions

The main ideas described in this paper are briefly summarized here:

- The GTC archive is a research resource in operation since 2011. A lot of science can already be done with the current archive contents and functonalities.
- It contains raw, calibration as well as reduced data provided by the community.
- New high level data products (i.e. source catalogues, images processes in a standard and automated way) will be available soon.

Highlights on Spanish Astrophysics X, Proceedings of the XIII Scientific Meeting of the Spanish Astronomical Society held on July 16 – 20, 2018, in Salamanca, Spain. B. Montesinos, A. Asensio Ramos, F. Buitrago, R. Schödel, E. Villaver, S. Pérez-Hoyos, I. Ordóñez-Etxeberria (eds.), 2019

Proper motion and other challenges in cross-matching *Gaia* observations.

F. Torra[1], M. Clotet[1], J. J. González-Vidal[1], C. Fabricius[1] and J. Castañeda[1]

[1] Institut de Ciències del Cosmos, Universitat de Barcelona (IEEC-UB), Martí i Franquès 1, E08028 Barcelona, Spain.

Abstract

The cross-matching (XM) in *Gaia* is a sophisticated process that provides a consistent match between observations and sources in the working catalogue for subsequent data reduction processes

Although the fraction of high proper motion stars that *Gaia* observes is small, their absolute number is not, and therefore the proper motion as well as other parameters have to be taken into account in the cross-matching of *Gaia* observations. In consequence, we describe the improvements and the identification of new proper motion sources thanks to a generalized algorithm based on clustering analysis, and a post-processing algorithm which identifies variable stars.

These improvements with respect the *Gaia* DR2 catalogue will imply a better identification of the observations of these kinds of stars and more precise astrometric and photometric parameters for subsequent data releases.

1 Introduction

Gaia [5] is a mission of the European Space Agency (ESA) which aims to measure the positions, motions and distances of more than 1 billion stars producing the most precise three-dimensional map of our Galaxy. Before the astrometric and photometric reductions, a pre-processing and source list creation (presented in [3]) is necessary to determine the parameters of each of the celestial objects (sources) that *Gaia* observes and, more specifically, the observation-to-source cross-matching (XM) of *Gaia* objects which provides the link between the *Gaia* detections and the sources.

The XM process has two preparatory stages in order to isolate groups of observations and sources of a specific sky region which are matched in the final XM resolution stage (see [2]). Furthermore, the resolution stage is divided into two substages, a first clustering stage and a final conflict resolution stage to solve all conflict scenarios, as described previously in [2].

We describe a generalization of the clustering algorithm used for *Gaia* DR2 [4] and we focus on interesting cases such as the high proper motion sources not found in DR2 and the variable stars, providing significant improvements of the algorithms for *Gaia* DR3.

2 Cluster analysis

Cluster analysis aims to divide data into groups (the so-called clusters), where the objects in each cluster are similar between them and different from objects within other clusters.

The model pretends to be independent from other catalogues, so the input only consists of a set of observations and, therefore, the positions and motions have to be determined as the number of observations in the cluster increases. Following a proposal by Lindegren [6], we consider here a hierarchical agglomerative algorithm because it presupposes very little in the way of data characteristics (i.e. in our case it does not require previous knowledge of the number of clusters to be created).

In order to decide which clusters should be agglomerated a measure of dissimilarity between sets of observations is required, which is a positive semi-definite symmetric mapping of pairs of observations and/or clusters of observations onto the reals (i.e. $\Delta(C_i, C_j) \geq 0$ and $\Delta(C_i.C_j) = \Delta(C_j, C_i)$ for clusters $C_i,\ C_j$). Note that, the triangular inequality is not necessarily satisfied for our type of problem.

Moreover, we have to consider an efficient algorithm to agglomerate the observations according to the corresponding definition of the dissimilarity.

2.1 The minimum variance criterion

The dissimilarity measure chosen is the Ward's dissimilarity which is defined as the increase of the sum of squared residuals when using a common coordinates compared to the value obtained when the two terms are separately minimized,

$$\Delta(C_i, C_j) = R(C_i \cup C_j) - R(C_i) - R(C_j), \tag{1}$$

where $C_i,\ C_j$ are two disjoint clusters and $R(C)$ is the sum of squared residuals in the corresponding cluster C.

If we consider the simple model where the coordinates of the observations do not depend on time, the dissimilarity between the clusters C_i and C_j can be written as

$$\Delta(C_i, C_j) = \frac{n_i n_j}{n_i + n_j} \left\| \boldsymbol{x}(C_i) - \boldsymbol{x}(C_j) \right\|^2, \tag{2}$$

where n_i (n_j) is the number of observations in the cluster C_i (C_j), and the vector $\boldsymbol{x}(C) = \frac{1}{n} \sum_{O \in C} \boldsymbol{x}(O)$ is the cluster center given by the center of gravity of the observations in the cluster.

This dissimilarity allows to agglomerate with the minimum increase in information loss and can be generalized to a linear model such as the inclusion the proper motion.

Note that the norm used in (2) may contain weight factors if required to include more parameters such as the magnitude.

2.2 Nearest Neighbor Chain

An efficient algorithm for hierarchical clustering is the nearest neighbor chain [7] based on the construction of nearest neighbor chains and reciprocal nearest neighbors. More specifically, the algorithm builds a chain of nearest neighbors, starting from an arbitrary (agglomerable) cluster, until a pair of mutual nearest neighbours has been found and agglomerated.

In this algorithm the agglomeration is carried all the way to the point where all observations are in a single cluster but for the XM process this makes little sense.

Therefore we consider that the agglomeration only makes sense while the dispersion of residuals within the clusters is below a given limit. This dispersion is measured by the variance $\sigma^2(C) = R(C)/n$ and the limit depends on *Gaia* observation error and the model error caused by not including the parallax.

3 Inclusion of proper motion

In Section 2.1 we have supposed that the coordinates do not depend on time, but for the inclusion of the proper motion we have to consider a linear model for each direction u,

$$u(t) = u_0 + u_1 t \tag{3}$$

where u_0 is the mean position and u_1 is the proper motion.

The linear system in matricial form is

$$\boldsymbol{b} = \boldsymbol{A}\boldsymbol{u} + \boldsymbol{e} \tag{4}$$

where $\boldsymbol{u} = (u_0, u_1)$, $\boldsymbol{b}$ is a $n-$vector of observations, $\boldsymbol{e}$ is a $n-$vector of observation errors, and $\boldsymbol{A}$ is a $2 \times n-$matrix with the time functions.

Therefore, applying the definition of (1) and using some equations, the dissimilarity in u-direction can be expressed

$$\Delta_u(C_i, C_j) = (\widehat{\boldsymbol{u}}_i - \widehat{\boldsymbol{u}}_j)^T \boldsymbol{N}_i(\boldsymbol{N}_i + \boldsymbol{N}_j)^{-1}\boldsymbol{N}_j(\widehat{\boldsymbol{u}}_i - \widehat{\boldsymbol{u}}_j), \tag{5}$$

where $\boldsymbol{N}_i = \boldsymbol{A}^T\boldsymbol{A}$ is the normal matrix and $\widehat{\boldsymbol{u}} = \boldsymbol{N}^{-1}(\boldsymbol{A}^{-1}\boldsymbol{b})$ minimizes the sum of squared residuals.

Note that the above equation reduces to (2) when the normal matrices are of dimension 1×1, i.e., without applying the linear model.

In the example shown in Figure 1, the XM created more than one source in DR2 because the proper motion model was not used in the clustering stage. Moreover, the observations which are processed for first time are unmatched in the input of the final stage because they are so far to be matched in the preparatory stages. However, the generalized XM algorithm including the proper motion merges the sources of the previous cycle (and therefore calculate the proper motion) thanks to the new implementation and the major number of observations.

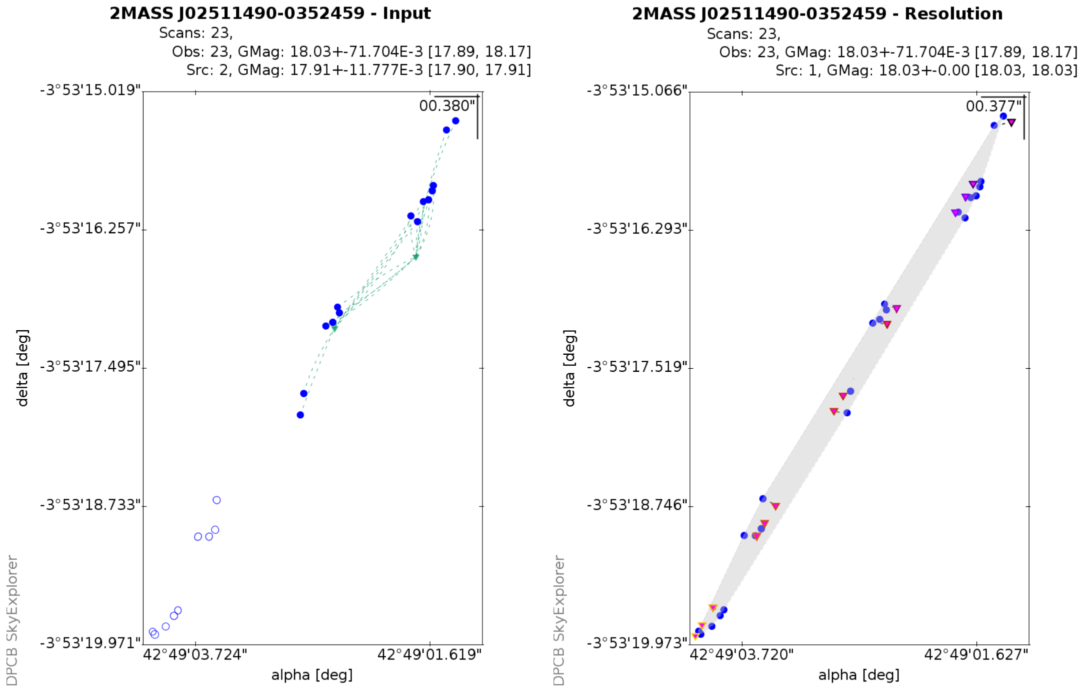

Figure 1: XM resolution around 2MASS J02511490-0352459. Left: XM resolver input including observations (blue dots, empty for unmatches in the input of final resolver), input sources (green triangles) and input resolver links (dashed green lines); right: resolution including the observations, the New Source propagated to the observation epoch (triangles) and the grey area is the cluster region.

4 Post-processing analysis

As mentioned in Section 2.1, a magnitude criterion can be included in the clustering algorithm with a scale factor which makes a magnitude error comparable with an error in position. This criterion leads to separate valid and spurious detections into different clusters, and improves the resolution in crowded areas significantly. However, it creates problems for variable stars creating several clusters at the same position (and different scans) but with different magnitude.

In this post-processing procedure, we detect these clusters with very close centres (about 120 mas) and without any common scan (i.e. compatible in time). After that, they are agglomerated into a single one without using any magnitude criterion. Therefore, this post-process avoids the creation of several sources corresponding to a variable source.

Gaia17aru is a confirmed cataclysmic variable star detected by the Gaia Science Alerts system (http://gsaweb.ast.cam.ac.uk/alerts) which runs at the Cambridge Institute of Astronomy to look for sources that suddenly change dramatically in brightness. This Alert is split into 2 clusters without the post-processing analysis, the brighter transits (outbursts) being grouped in one cluster, and the fainter with the other, whereas applying the post-processing all the transits are grouped together with one of the input sources (see Figure 2).

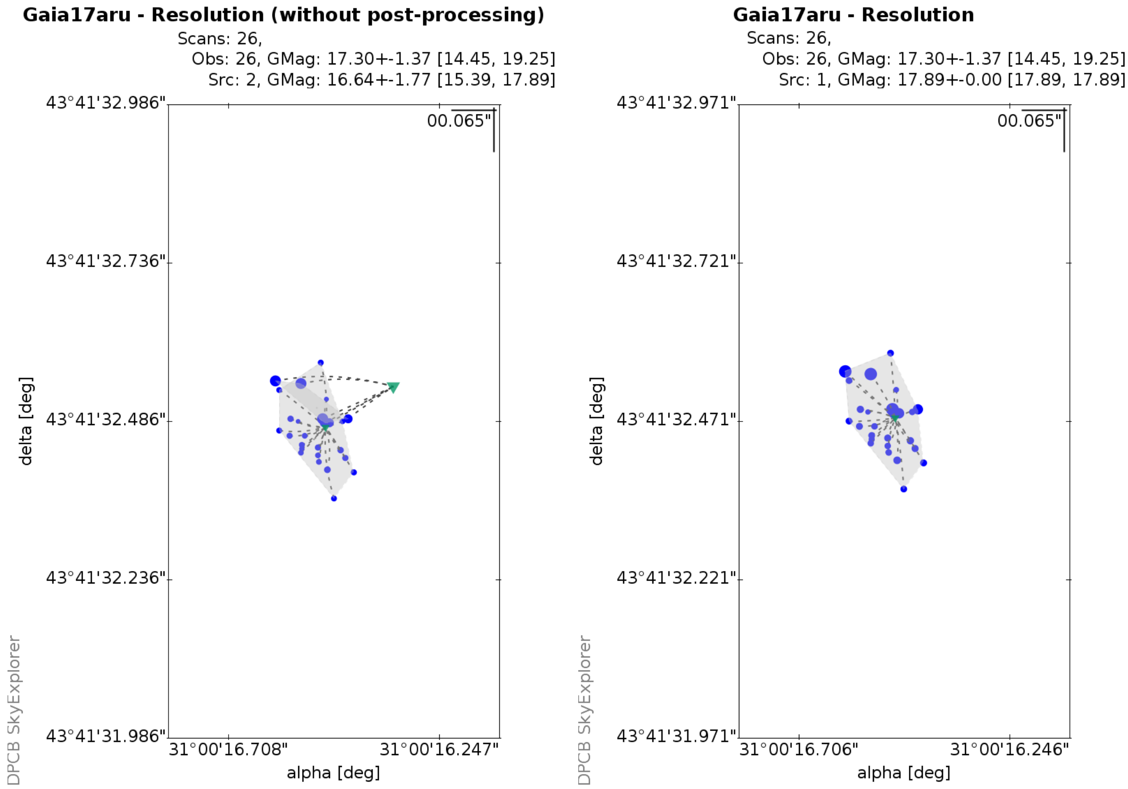

Figure 2: XM resolution around Gaia17aru. Left: XM resolver without post-processing including observations (blue dots), input sources (green triangles) and resolver links (dashed black lines); right: resolution with post-processing including the observations and the persisting source (green triangle). Grey areas are the cluster regions.

5 Conclusion

We have shown that the cross-matching algorithm for *Gaia* can include parameters such as the proper motion and the magnitude which are necessary to identify some kinds of stars and provide precise parameters of them, applying a generalization of the Ward's dissimilarity and defining suitable post-processing algorithms. Therefore, the number of high proper motion stars and variable stars will increase in *Gaia* DR3 respect to *Gaia* DR2 and in addition their parameters will be more precise because of the creation of new sources and the increasing number of matched observations.

These improvements on the clustering algorithm may imply an update of the *Gaia* DR2 identification and the astrometric and photometric parameters because some of the observations will be matched to other sources (see details on the source evolution in [1]).

Acknowledgments

This work was supported by the MINECO (Spanish Ministry of Economy) through grant ESP2016-80079-C2-1-R (MINECO/FEDER, UE) and MDM-2014-0369 of ICCUB (Unidad de Excelencia 'María de Maeztu').

References

[1] Castañeda, J., Torra, F., Clotet, M., et al. 2018, Highlights of Spanish Astrophysics X (this volume).

[2] Clotet, M., González-Vidal, J. J., Castañeda, J., et al. 2017, Highlights on Spanish Astrophysics IX, pp.634-639.

[3] Fabricius, C., Bastian, U., Portell, J., et al. 2016, A&A, 595, A3.

[4] Gaia Collaboration (Brown et al.) 2018, A&A, 616, A1.

[5] Gaia Collaboration (Prusti et al.) 2016, A&A, 595, A1.

[6] Lindegren, L. 2005, Gaia Data Processing and Analysis Consortium (DPAC) technical note GAIA-LL-060.

[7] Murtagh, F. 1983, The Computer Journal, 26(4), pp.354-359.

Highlights on Spanish Astrophysics X, Proceedings of the XIII Scientific Meeting of the Spanish Astronomical Society held on July 16 – 20, 2018, in Salamanca, Spain. B. Montesinos, A. Asensio Ramos, F. Buitrago, R. Schödel, E. Villaver, S. Pérez-Hoyos, I. Ordóñez-Etxeberria (eds.), 2019

Status of the commissioning of the JPAS-Pathfinder camera at JST/T250 at the Observatorio Astrofísico de Javalambre.

H. Vázquez Ramió[1,2], J. Varela[1,2], C. López-Sanjuan[1,2], A. Ederoclite[1,2,3], D. Cristóbal-Hornillos[1,2], C. Íñiguez[1], A. Marín-Franch[1,2], S. Chueca[1], N. M. Lasso-Cabrera[1], M. C. Díaz-Martín[1], R. Iglesias-Marzoa[1], A. Moreno-Signes[1], J. Hernández-Fuertes[1], T. Civera[1], D. Muniesa-Gallardo[1], A. Yanes-Díaz[1], S. Rueda-Teruel[1], F. Rueda-Teruel[1], G. López-Alegre[1], R. Bello[1], J. L. Antón-Bravo[1], S. Bielsa de Toledo[1], M. Domínguez-Martínez[1], J. Castillo[1], Á. López-Sáinz[1], A. J. Cenarro[1,2], M. Moles[1] & the J-PAS Collaboration

[1] Centro de Estudios de Física del Cosmos de Aragón (CEFCA), Teruel, Spain
[2] Unidad Asociada CEFCA-IAA, CSIC, Teruel, Spain
[3] Instituto de Astronomia, Geofísica e Ciências Atmosféricas, Universidade de São Paulo

Abstract

The Javalambre Physics of the Accelerating Universe Astrophysical Survey (J-PAS) is an unprecedented photometric sky survey of $8,500\,\mathrm{deg}^2$ visible from the Observatorio Astrofísico de Javalambre (OAJ) in 59 colors, using a set of broad, intermediate and narrow band filters. J-PAS is going to provide the first complete 3D map of a large volume of the Universe and will contribute on many astrophysical science cases, from Solar System minor bodies to Cosmology. The survey will be conducted by the Javalambre Survey Telescope, JST/T250, with Javalambre Panoramic Camera (JPCam), which is currently in its engineering phase. Until then, the interim JPAS-Pathfinder camera, mounting a single CCD covering the center of the FoV, is installed at the telescope. Its filter wheel is ready to host the J-PAS filters already available for use on sky. This is permitting the commissioning of the equipment and is providing the first scientific data: the mini J-PAS. The up-to-date JPAS-Pathfinder commissioning and the results of the science operation is summarized here.

1 Introduction

The science case motivating the J-PAS survey is the study of the nature of the dark energy causing the accelerating expansion of the universe through the measurement of the Baryon Acoustic Oscillations (BAO). In order to tackle this topic, large volumes of the universe have to be probed, sampling regions much larger than the typical spatial scales associated to the

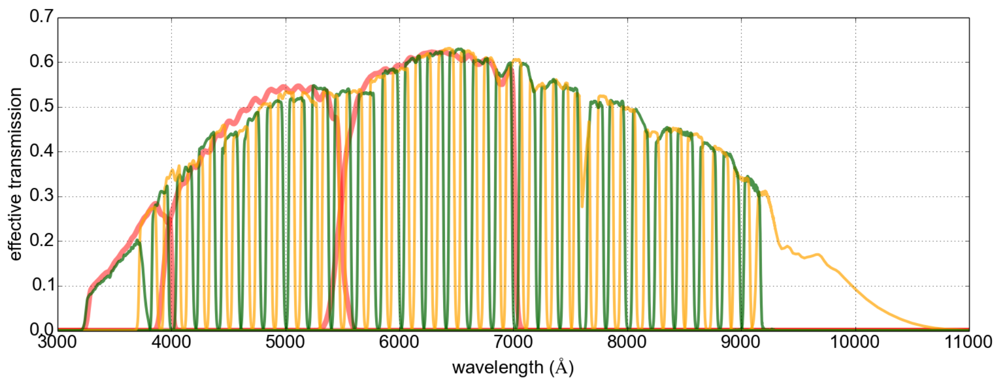

Figure 1: The J-PAS bandpass system. Overall expected efficiency for JPCam at JST/T250, filters system and assuming a particular atmosphere model.

BAO peak. Given the very weak nature of this signal, the positions and distances of millions of galaxies have to be measured with high enough accuracy, in particular, a precision in the redshift determinations of $\sigma_z/(1+z) < 0.003$ is required [1].

In practice this implies carrying out a survey of large areas of the sky at an adequate depth, and for that, a telescope combining a large field of view (FoV) with a relatively large collecting area is needed; i.e. a telescope with a large étendue. This motivated the building of the OAJ, at the Sierra de Javalambre in Teruel, Spain, and the settling of a survey-oriented 2.55m-class telescope, the JST/T250, with a large FoV ($4.2\,\mathrm{deg}^2$ with JPCam, the camera that is going to be devoted to carry out the J-PAS survey). This configuration yields an étendue of $26.5\,\mathrm{m}^2\mathrm{deg}^2$. On the other hand, to obtain the 0.3% accuracy in the photometric redshifts, photo-z, a set of 54 narrow band filters, plus one mid-band one at the blue end and a high-pass one at the red end have been specifically designed for this purpose. Those are centred at the visible region of the spectrum (see Fig. 1). Their width, FWHM$\sim 145\,$Å, and separation of their central wavelengths $\Delta\lambda \sim 100\,$Å will allow the achievement of the degree of precision mentioned. The set is completed with three broad-band filters: u_{J-PAS} and two Sloan-like g_{J-PAS} and r_{J-PAS}. The goal of J-PAS is to observe $8,500\,\mathrm{deg}^2$ of the observable sky at the OAJ, avoiding the Galactic plane. J-PAS will provide a huge amount of pseudo-spectra with enormous potential not only for Cosmology and Galactic Evolution, but for many different science cases from high-z studies to Solar System minor bodies.

2 JPCam: the survey camera

The J-PAS survey will be carried out by JPCam, a mosaic of 14 CCDs covering an area on the sky of $4.2\,\mathrm{deg}^2$ once attached to the JST/T250. Details on the different subsystems of the camera and its main features can be found in [2]. JPCam is currently at the OAJ in the engineering phase. In the forthcoming months a dedicated team of scientists and engineers will work with the final goal of getting the camera ready for attaching it to the JST/T250, so allowing the starting of the commissioning of the main camera.

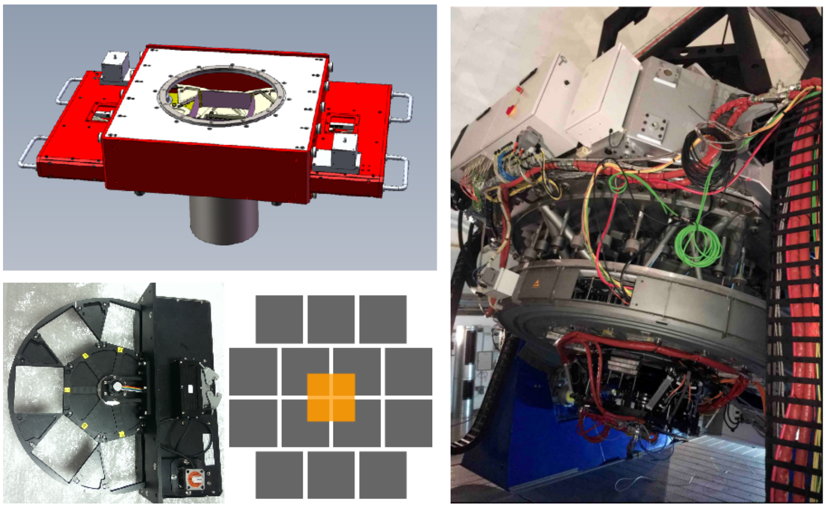

Figure 2: JPAS-Pathfinder. Sketch of JPAS-Pathfinder, a picture of the filter wheel and another of the camera attached to JST/T250, holded by the actuator system. The diagram illustrates the FoV of the camera (at the center in orange) compared to the whole JPCam FoV provided by the 14 CCDs.

3 JPAS-Pathfinder: the interim camera

Since February 2017 the interim JPAS-Pathfinder camera is attached to the JST/T250. In short, it is a replica of the T80Cam carrying out the Javalambre-Photometric Local Universe Survey (J-PLUS), also at the the OAJ with a 80cm-class telescope, whose first data release, DR1[1], has been presented during this meeting [3]. The JPAS-Pathfinder consists of a single CCD of 9.2k×9.2k pixels[2] and it mounts a filter wheel that can host up to 7 filters. From there it provides an unvignetted FoV of 0.34 $\deg^2$ covering the central part of the FoV that JPCam will offer (see Fig. 2). The resulting spatial resolution is 0.227 arcsec/pixel. In the nominal read-out mode it offers a read-out noise below 3.4e^-, being the read-out time around 12 s. The goals with this camera are two-fold: i) carrying out a technical commissioning and ii) starting the scientific operation.

3.1 Technical commissioning

The goal of the commissioning is to advance in as many aspects as possible while JPCam is not ready to be installed to the telescope and, at the same time, to minimize the risks when that happens. This phase allows the identification of issues, needs and implementation of solutions at different levels: on the technical side, concerning the optics, the observation procedures and the image reduction and data processing.

JPAS-Pathfinder is mainly aimed to perform the commissioning of the actuators system (AS) that supports the camera and permits the its postitioning to compensate for mechanical

[1] http://archive.cefca.es/catalogues/jplus-dr1

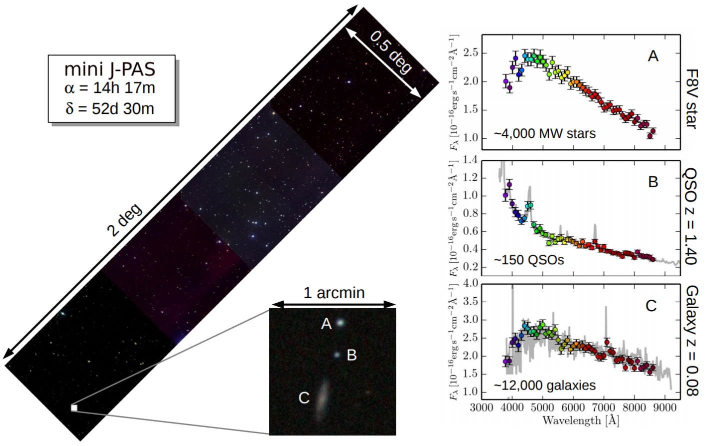

Figure 3: The area covered by the mini J-PAS. The zoom-in shows 3 objects, a star, a quasar and a galaxy, whose J-spectra are shown on the right together with a smoothed spectrum taken from SDSS-DR14 (when available). The number of each type of objects with J-spectra in the mini J-PAS is also shown. Classification and z also taken from SDSS-DR14.

flexures caused by gravity so the alignment of the optics, in conjunction with an hexapod at the level of the secondary mirror, M2, is optimized in every pointing of the telescope. The exact optimal positions of both the AS and M2 hexapod (amounting 10 degrees of freedom) depend on the pointing of the telescope, the angle of the de-rotator and the temperature. The analysis of a pair of intra- and extra-focal images taken on each new pointing allows the study of the main aberration components through the fitting of 3D Zernike polinomials, that yields a best solution for AS and M2 hexapod position to get the best image quality.

So far, the performance of the active optics system as a whole (hardware, control and analysis software) is satisfactory within the FoV of JPAS-Pathfinder. The statistics of the first few thousands images (both scientific and technical) has yielded a mode of the PSF of 0.7 arcsec with a mode in the homogeneity of the same parameter of 2.5% across the image. Further details on this and other commissioning tasks can be found here [4].

3.2 First scientific operation: mini J-PAS

In parallel to the commissioning, the first scientific operation with JPAS-Pathfinder has started. Given the complete set of J-PAS filters are already available for use, the J-PAS Collaboration decided to observe a patch on the sky with all of them to get the first J-PAS-like data. That field was carefully selected favouring those with lots of ancillary data to compare with ours. The choice was the All-wavelength Extended Groth strip International Survey[2] (AEGIS) with around 20 thousand spectroscopic redshift determinations up to $R_{\mathrm{AB}} = 24$ and also overlaping with other surveys, like Sloan Digital Sky Survey (SDSS)[5] and one of the Advance Large Homogeneous Area Medium-Band Redshift Astronomical (ALHAMBRA)[6]

[2] `http://aegis.ucolick.org`

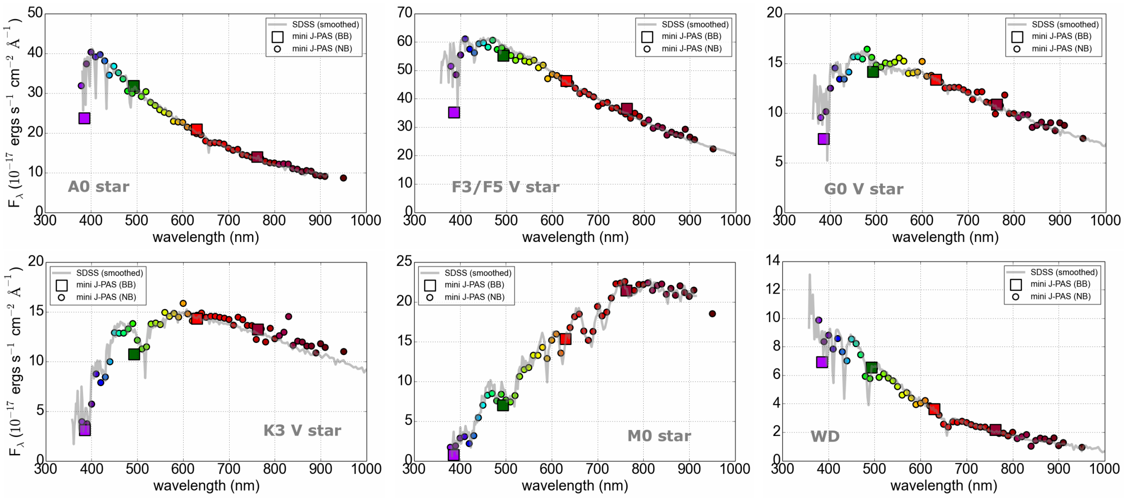

Figure 4: mini J-PAS: Galactic J-spectra samples. Classification taken from SDSS-DR14.

fields, among some others. The area eventually observed with the whole set of filters is a stripe of $\sim 1\,\mathrm{deg}^2$ ($1.9\,\mathrm{deg} \times 0.5\,\mathrm{deg}$) and it is shown in Fig. 3.

An initial reduction, source extraction and photometry was made by the Processing and Data Archival Unit (UPAD) at CEFCA using the same pipeline employed for J-PLUS, `jype`[7], with a few modifications required to fit the JPAS-Pathfinder setup. An initial photometric calibration has been performed as well using the synthetic photometry computed from the available SDSS-DR14[3] stellar spectra on each of the fields associated with J-PAS bandpasses. The pseudo-spectra, *J-spectra* presented here are preliminary since the image acquisition was very recent and there's still, in some cases, a few steps missing on the processing (like the fringing in the reddest filters and the illumination correction) or several of them could be improved, so the figures have to be considered a frozen result of a work in progress. At present, the catalogs are only available for internal use of the J-PAS Collaboration.

Some examples of normalized J-spectra of Galactic Fig. 4 and extra-Galactic sources Fig. 5 are shown together with the J-PLUS DR1 pseudo-spectra and the smoothed spectra of the same objects taken from SDSS-DR14. Despite the preliminary state of the whole data processing, these first results are really encouraging and show the enormous potential of the J-PAS data, tracing with detail many of the spectral features of the objects. It is worth highlighting the ability of the J-PAS data to trace broad features such as the molecular absorption bands of cool stars and the broad emission lines of the QSOs. As mentioned, those data must allow the determination of the photo-z with an accuracy of 0.3%; this is currently under assessment for confirmation.

Fig. 3 shows the count of gathered J-spectra: 4,000 Milky Way stars, around 150 quasars and about 12,000 galaxies. Extrapolating this numbers to the expected total area it would yield obtaining $\sim$ 60 million stars, 1.3 million QSOs and $\sim$ 100 million galaxies at the completion of the survey. Each of these pseudo-spectra is similar to a low-resolution

[3] `https://skyserver.sdss.org/dr14`

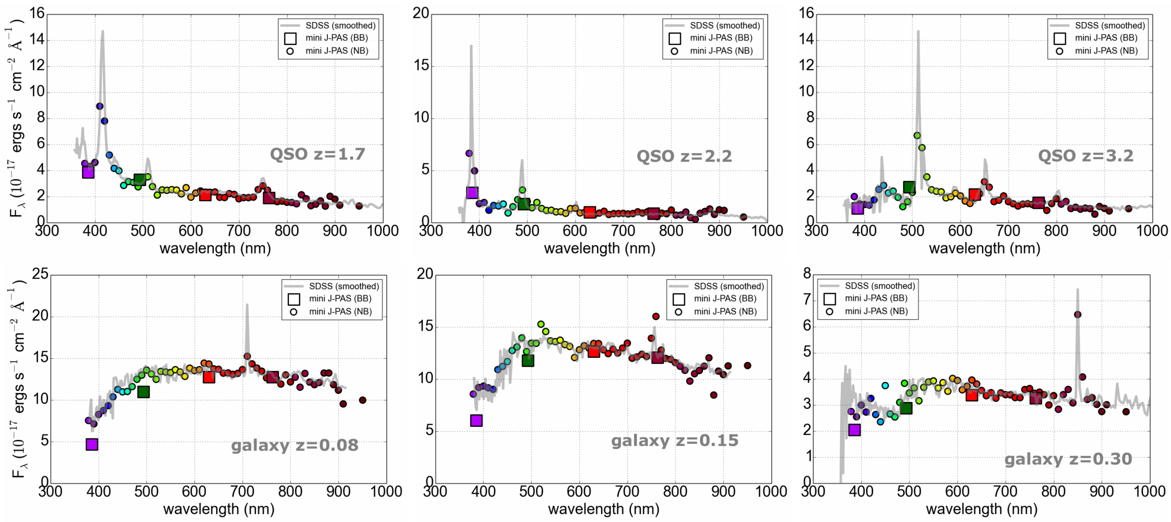

Figure 5: mini J-PAS: extra-Galactic J-spectra samples. Classification and z taken from SDSS-DR14.

one with $R \sim 50$, comparable to that of the low-resolution spectra Gaia will provide[8], but J-PAS is going to be ~ 2 magnitudes deeper. It is worth mentioning that in many cases, these currently represent the highest quality data for those objects. At the end of J-PAS, based on the mini J-PAS numbers, ~ 150 million J-spectra are going to be obtained.

Acknowledgments

The OAJ has been funded by the Governments of Spain and Aragón through the Fondo de Inversiones de Teruel, the Spanish Ministry of Economy and Competitiveness (MINECO; under grants AYA2015-66211-C2-1-P, AYA2015-66211-C2-2, AYA2012-30789, and ICTS-2009-14), and European FEDER funding (FCDD10-4E-867, FCDD13-4E-2685). The Brazilian agencies FAPESP and the National Observatory of Brazil have also contributed to the development of instrumentation for the OAJ.

References

[1] Benítez, N., Dupke, R., Moles, M., et al. 2014, `arXiv:1403.5237`

[2] Marín-Franch, A., Taylor, K., Santoro, F., et al. 2017, Highlights on Spanish Astrophysics IX, 670

[3] López-Sanjuan, C., et al. 2019, Highlights on Spanish Astrophysics XIII (these proceedings)

[4] Cenarro, A. J., Ederoclite, A., Íñiguez, C., et al. 2018, SPIE Conference Series, 10700, 107000D

[5] Abolfathi, B., Aguado, D. S., Aguilar, G., et al. 2018, ApJS, 235, 42

[6] Molino, A., Benítez, N., Moles, M., et al. 2014, MNRAS, 441, 2891

[7] Cristóbal-Hornillos, D., Varela, J., Ederoclite, A. & Vázquez Ramió, H. 2017, RIA J-PLUS EDR

[8] Carrasco, J. M., Evans, D. W., Montegriffo, P., et al. 2016, A&A, 595, A7

Highlights on Spanish Astrophysics X, Proceedings of the XIII Scientific Meeting of the Spanish Astronomical Society held on July 16 – 20, 2018, in Salamanca, Spain. B. Montesinos, A. Asensio Ramos, F. Buitrago, R. Schödel, E. Villaver, S. Pérez-Hoyos, I. Ordóñez-Etxeberria (eds.), 2019

The Legacy Herschel Science Archive.

Eva Verdugo

European Space Astronomy Centre (ESAC). E-28692 Madrid. Spain

Abstract

On 22 May 2018, a new version (v9.0) of the Herschel Science Archive (HSA) was publicly available. Together with some other minor implementation changes, this version constitutes the 'legacy' version of the Herschel Science Archive, this is, no more development is foreseen at the user interface level, although it is expected that its contents will still continue growing with the ingestion of new products provided by the community and by the mission experts in the Herschel ground segment. The main functionalities of this version are presented here.

1 Introduction

The Legacy Herschel Science Archive (HSA) offers access to all public Herschel data and offers a host of features:

- Access to all Herschel science data products at various (user selected) levels of processing.
- Access to interactively reduced data provided by the community (User Provided Data Products; UPDPs).
- Access to interactively reduced data produced by ground segment experts (Highly Processed Products; HPDPs)
- Visualization of accurate footprints projected onto the Digitized Sky Survey (DSS) image of the field
- Search on publications, providing links to the Herschel data used for these publications and to the corresponding publication registry in ADS, including the possibility to search for observations in the archive without known associated publications
- Preview images and connectivity to common astronomical tools over Virtual Observatory (VO) protocols
- Search on Herschel Catalogues through the VO Table Access Protocol (TAP)

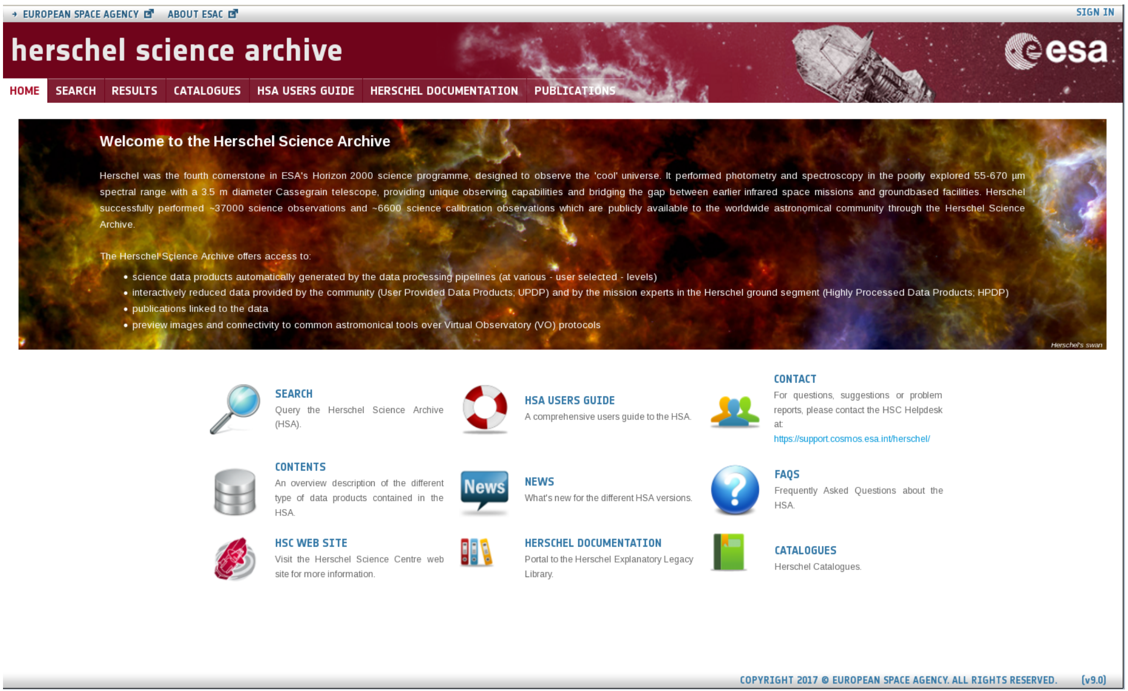

Figure 1: Web-based User Interface of the Herschel Science Archive.

2 Search capabilities

On the top of the interface there are three different tabs for searching:

The SEARCH tab with three main panels to search by Target Name, NAIF ID or Coordinates. It is also possible to submit a list of targets, NAIF IDs or coordinates. Observation Constraints which are contained in different tab filters per observation ID, instrument and refined queries by instrument settings, proposal information, pipeline processing constraints, date and publications. And for Product Selection: The query can be restricted to those observations which are contained in an UPDP or an HPDP. Also, a set of Ancillary Data Products (ADPs) can be retrieved directly from this panel.

The CATALOGUES tab. The User Interface also allows to query the contents of the main Herschel catalogues: The Photometric Catalogues and the Spectral Line Catalogues. The selection of the catalogue can be combined with geometrical searches by target name or coordinates. Also after selection of one catalogue, extra conditions for the query can be added and the columns displayed as output can be selected. The result can be saved as VOTable, CVS, FITS...

Users can also perform more complex queries through a TAP/ADQL Form.

The PUBLICATIONS tab. This functionality allows to make all kind of queries on the database of refereed publications linked to Herschel observations. Different filters (and combinations of them) for making queries are possible. In the results table, column "BIB

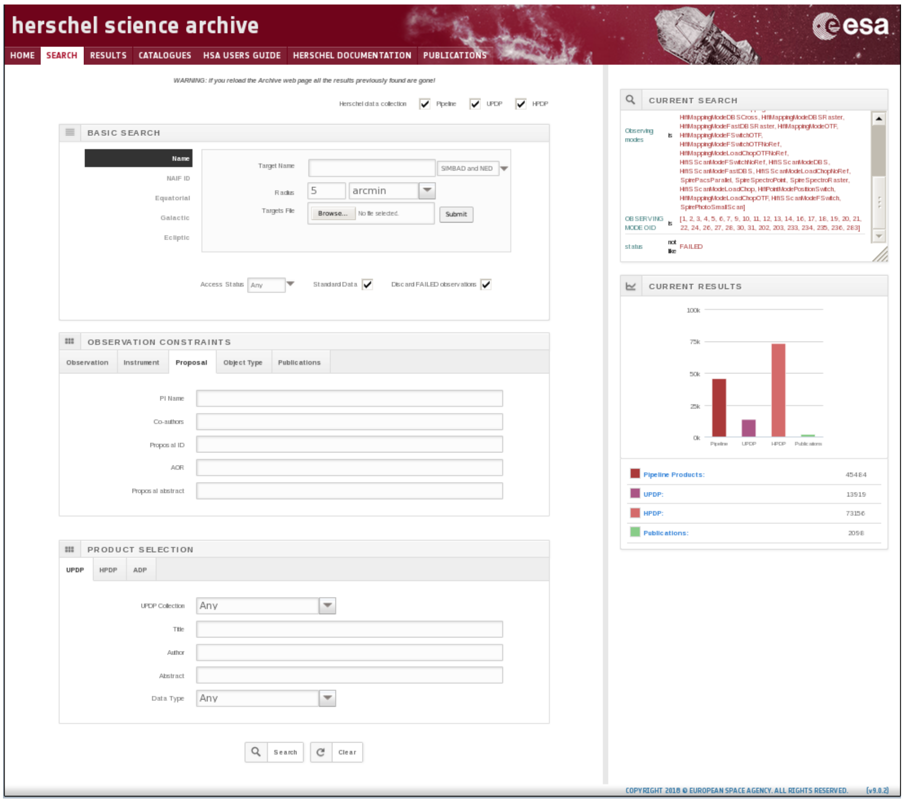

Figure 2: The SEARCH tab of the HSA User Interface

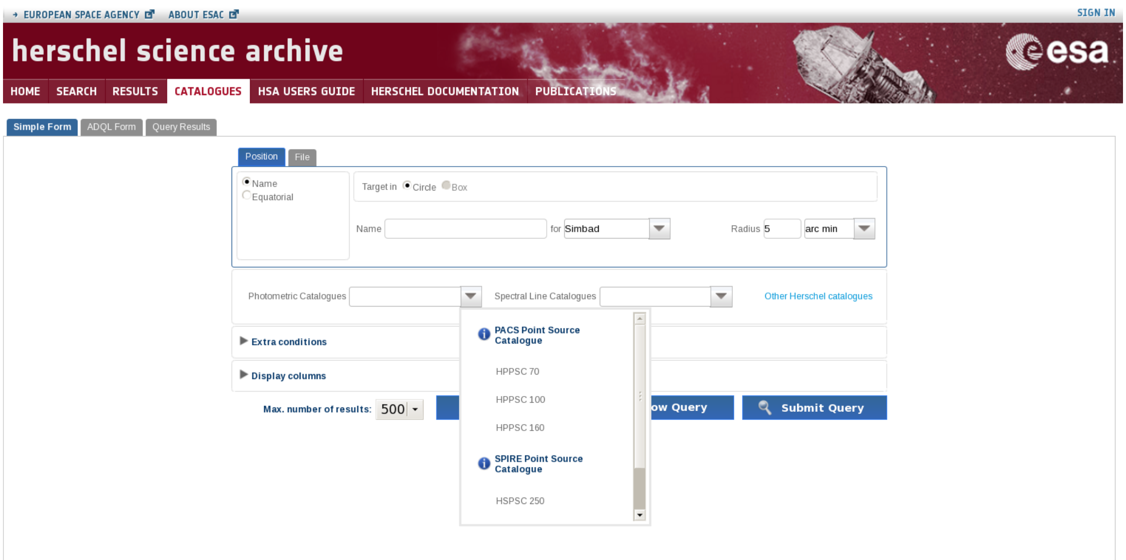

Figure 3: The CATALOGUES tab of the HSA User Interface

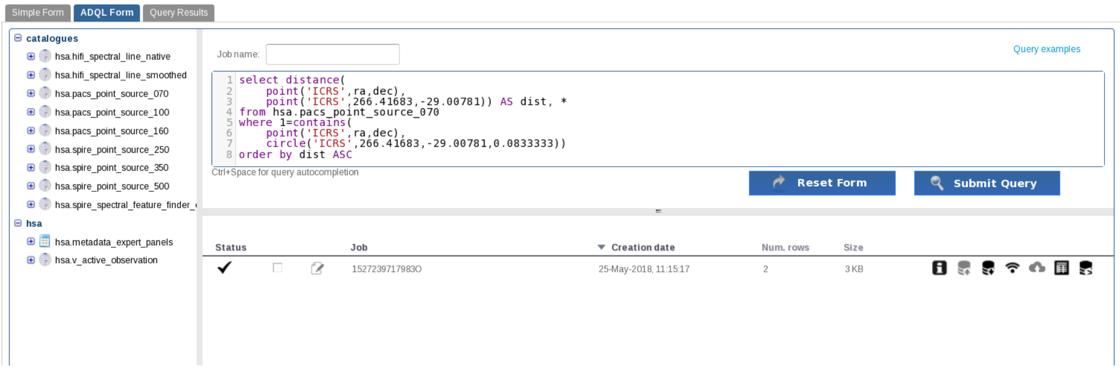

Figure 4: Searching catalogues and the HSA database through TAP/ADQL

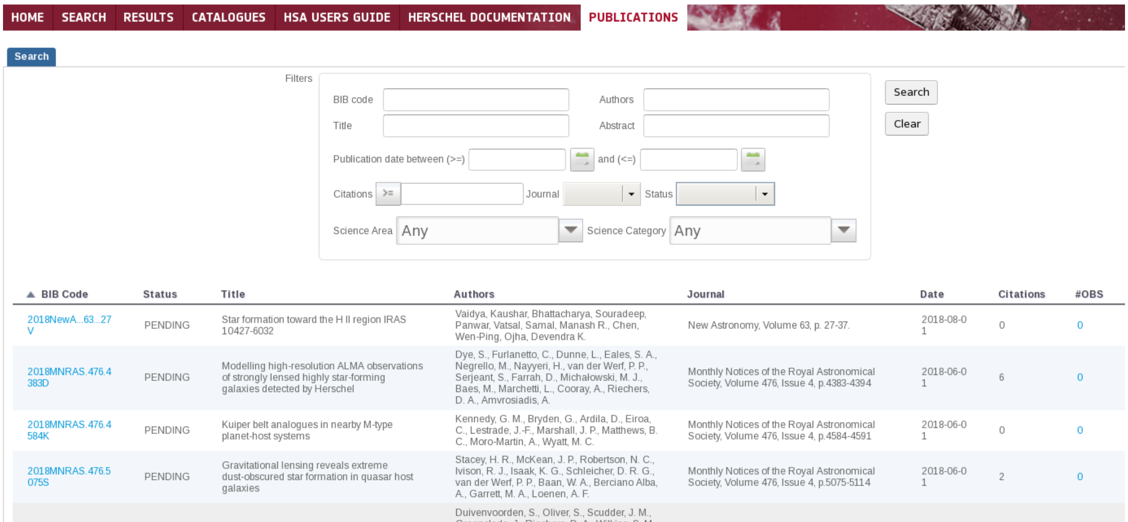

Figure 5: The PUBLICATIONS tab of the HSA User Interface

Code" is a link to ADS and "OBS" gives the number of observations linked to this paper. Clicking on this number, the list of observations is given.

3 The Result of a query

The result of a query is always a list of observations which match the conditions given by the parameters used for searching the Herschel archive.

The Interface provides 4 different result tabs per query. The Pipeline tab gives the list of observations matching the query and information related to every observation and the associated Pipeline products. The UPDP tab gives the list of observations which are contained in one or more user provided datasets. It provides information on the UPDP (through the UPDP Keyword column) which is also illustrated when available through a

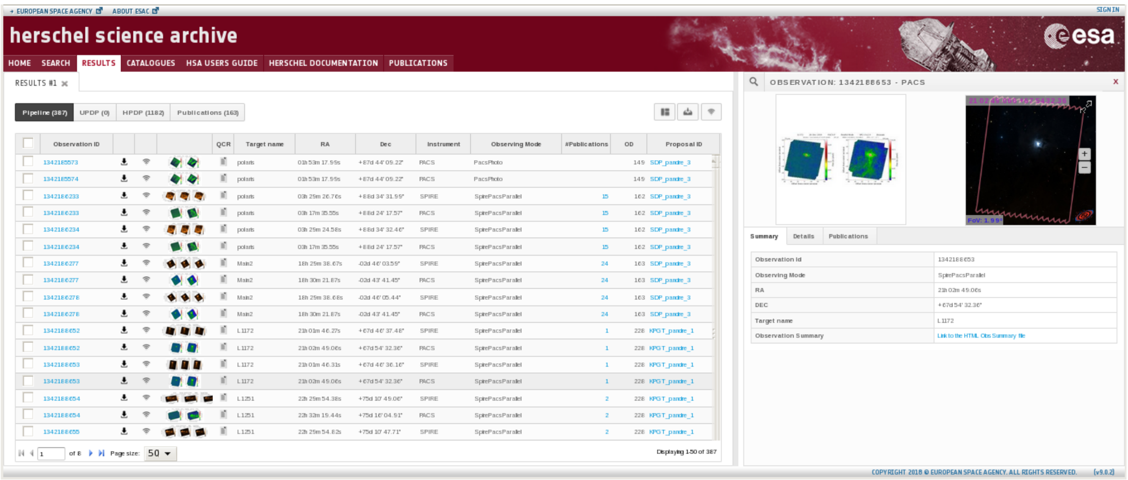

Figure 6: The RESULT of a query

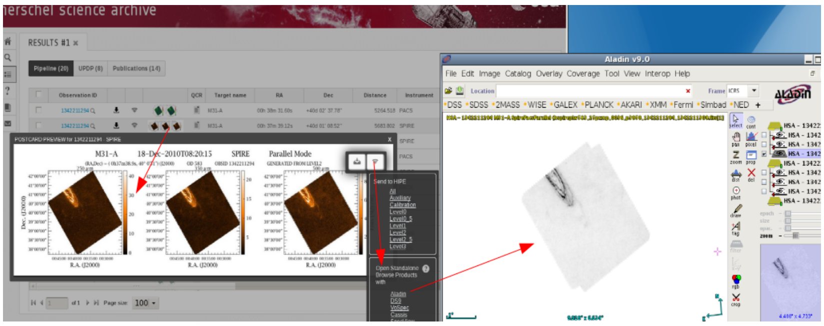

Figure 7: Sending Herschel products to Aladin via SAMP

Postcard per observation. Like the UPDP tab, the HPDP tab gives the list of observations matching the query which are contained in one or more expert reduced dataset and gives similar information about it. And the Publications tab which gives the total list of papers in which any of the observations resulting from the query is included and a link to the corresponding publication registry in the ADS. Also, the number of observations included in every paper is given.

4 How to retrieve/visualize Herschel Data

The Herschel Science Archive makes use of the SAMP Web Profile (Javascript library) to interoperate with other astronomy tools via SAMP (Simple Application Messaging Protocol). This allows visualization and inspection of the Herschel data before the actual data download. Herschel products can be sent to the Herschel Interactive Processing Environment (HIPE) for their visualization and analysis and to VO tools like Aladin, DS9, VOSpec, CASSIS...

There are several methods to retrieve Herschel data: Pipeline products are retrieved

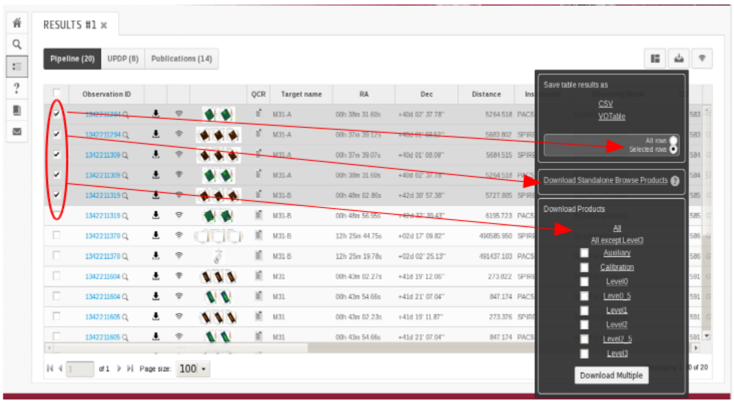

Figure 8: Retrieving pipeline products and table of results from the Search tab

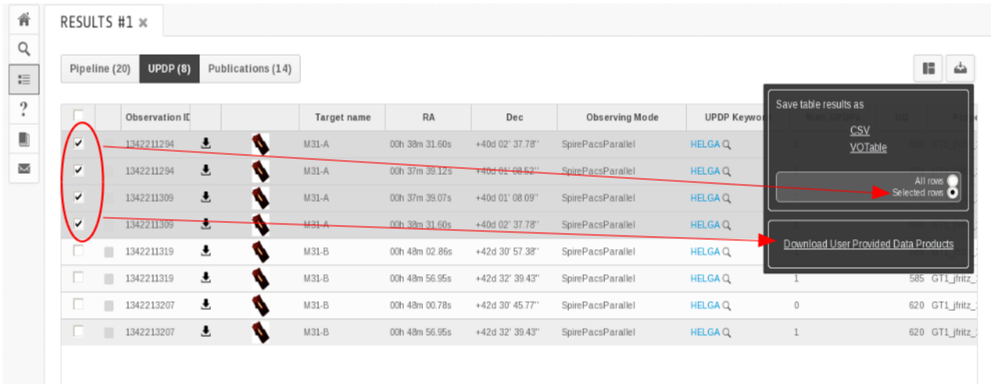

Figure 9: Retrieving UPDPs from the Search tab

from the results tab while UPDP/HPDP can be also retrieved from the dedicated panel in the Search tab. The table of results (metadata) can also be saved as CVS or VOTable.

The complete guide on the usage of the Herschel Science Archive User Interface is provided inside the own interface and also as a document at:

https://www.cosmos.esa.int/web/herschel/legacy-documentation-observatory[1]

References

[1] Verdugo, E. 2018, HERSCHEL-HSC-DOC-2172

Highlights on Spanish Astrophysics X, Proceedings of the XIII Scientific Meeting of the Spanish Astronomical Society held on July 16 – 20, 2018, in Salamanca, Spain. B. Montesinos, A. Asensio Ramos, F. Buitrago, R. Schödel, E. Villaver, S. Pérez-Hoyos, I. Ordóñez-Etxeberria (eds.), 2019

Night Sky Brightness monitoring in Spain.

Jaime Zamorano[1], Carlos Tapia[1], Sergio Pascual[1], Cristóbal García[2], Rafael González[2], Esteban González[3], Oscar Corcho[3], Lucía García[1], Jesús Gallego[1], Alejandro Sánchez de Miguel[4], Enrique Solano[5], and J. Manuel Alacid[5]

[1] Departamento de Física de la Tierra y Astrofísica, Universidad Complutense de Madrid
[2] Asociación Astronómica Astro Henares
[3] Ontology Engineering Group, Facultad de Informática, Universidad Politécnica de Madrid
[4] Environment and Sustainability Institute, Cornwall, TR10 9FE University Exeter
[5] Spanish Virtual Observatory (SVO), Centro de Astrobiología (INTA-CSIC) ESA - ESAC

Abstract

The estimation of the light pollution and the study of its eventual evolution can be established by monitoring the night sky brightness. We present the monitoring stations of the Spanish Light Pollution Research Network (REECL) and some results. The advantages of the new TESS-W photometer developed for the STARS4ALL project are described, along with the incipient global network of monitoring stations using TESS-W.

1 Introduction

One of the unwanted effects of the light pollution is the brightening of the sky at night. The dark natural brightness of unpolluted skies is only found in remote locations far from big cities. The sky brightness depends on the number, nature and location of the light emitting sources and can be predicted using models of the dispersion of the light by the atmosphere. We are interested in measuring the sky brightness in dark protected places (national parks, astronomical observatories, etc.) and also in places with medium and heavy contamination at different distances from the main urban areas. The spatial and temporal variation of the sky brightness is used to test and improve the models (see for instance [3] & [6]).

The sky brightness at night can be used as a proxy of the light pollution. Besides the natural component, introduced by the moon for instance, the variations in the artificial light input and the conditions of the atmosphere are reflected in the brightness. A monitoring station with a fixed photometer measuring the sky brightness in the zenith should be used to record these changes. After a long term series of measurements it is possible to perform statistics to determine the characteristics of the sky brightness at this location and one can determine the eventual evolution of the light pollution.

The change of artificial light technologies in our cities, mainly from high pressure sodium (HPS) to LED lamps, is changing the sky in brightness and also in color [4]. It is important to measure these changes over time (before, during and after the retrofit) to establish whether we are really reducing the impact of light pollution in our skies.

2 The Spanish REECL monitoring network

Most of the Spanish researchers that study the light pollution effects from different aspects (astronomy, biology, human health, etc) are collaborating under the framework of the Spanish Light Pollution Network (REECL). One of the results of these collaborations is the network of monitoring stations that was originally created by the Universidad Complutense de Madrid which is in charge of its maintenance.

The SQM (Sky Quality Meter, Unihedron) photometer are being used in most of the stations. The photometer should be protected with an enclosure and linked to a computer. To record, plot and share the data we are using the PySQM free software developed at the Universidad Complutense de Madrid [2]. The data is plotted in realtime at the SQM-REECL network webpage and it is stored for free access at the Spanish Virtual Observatory [1]. The description of the network and some results were presented at XXIX IAU meeting [5].

Figure 1 shows the locations of the SQM stations that are linked to the REECL network. Note the one in Porto (Portugal). There are other monitoring networks in Spain. The Galician NSB monitoring network which is a collaboration of Universidade de Santiago and Meteogalicia [1] and the Catalan network which depends of the Parc Astronomic Montsec and the Generalitat de Catalunya, and also some institutions or individuals with photometers that are not sharing the data.

A comparison of the results for the heavily polluted city of Madrid and a rural village (Villaverde del Ducado) is presented in Fig. 2. The upper panel shows the evolution of the brightness recorded at the astronomical observatory of the UCM located on top of the Physics building. The vertical axis represents the time along the night while the x-axis runs along the days during several years. The brightness of the sky is color coded; most of the data is around 18 magnitudes/arcsec^2 in the SQM magnitude system. The sinusoidal shape of the graph is due to the variation of the length of the night along the year. It is interesting to note the effect of ornamental lights, traffic and other human activity that yield a brighter sky at the beginning of the night. The same plot for a rural area shows darker skies reaching 21.5 mag/arcsec^2 in the SQM system. In this case the brightening due to the presence of the moon over the horizon is apparent in every lunation. Figure 3 presents an histogram for the values obtained from Villaverde del Ducado during long series of measures. Even at this rural area the sky brightness is affected by Madrid at 130 km in linear distance.

There are 47 monitor stations sending data at the time of writing this contribution. Most of the persons in charge of the photometers are individuals. The PySQM software

[1] http://sdc.cab.inta-csic.es/pdd/jsp/busSQM.jsp

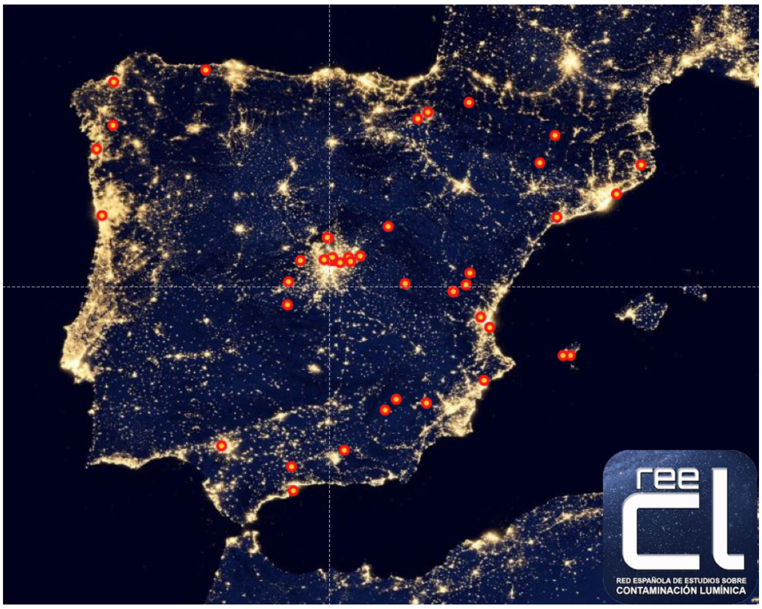

Figure 1: Distribution of SQM monitor stations on the Iberian Peninsula and Balearic islands that are linked to the network.

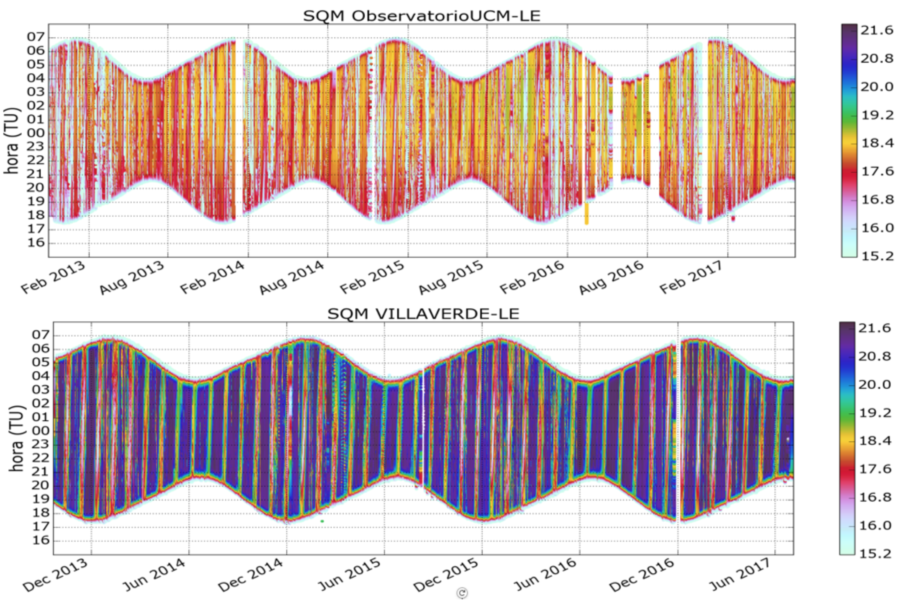

Figure 2: Record of observations from the Observatorio UCM station inside Madrid (upper panel) and a rural village (Villaverde del Ducado) (lower panel).

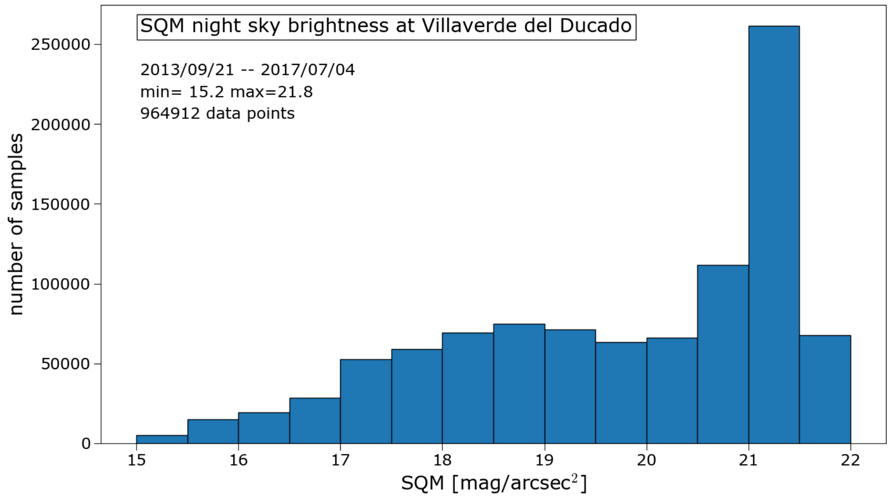

Figure 3: Histogram with the observations obtained with one of the SQM photometers at a rural location. The sky brightness is affected by Madrid at 130 km in linear distance.

creates the plot for each night and stores the data following the IDA-IAU standard format. Besides a monthly data file is also stored. The data is shared via dropbox or google drive.

3 The European Photometer Network

3.1 The TESS-W photometer

Mounting a SQM monitor station implies the purchase of the photometer and the enclosure, and the connection of the photometer to a personal computer linked to internet. The computer should be connected to the electrical power all the time waiting to the twilight for storing the measures of the whole night and it is idle during the day.

One of the goals of the STARS4ALL European project is to extend this network to an European night sky brightness network and also to include the other smaller or local existing networks in Europe. Our plan is to grow the number of monitor stations with the help of interested citizens. We have designed a low-budget photometer (TESS-W) which is open hardware and software and have some interesting features. The photometer works unattended without the need of a dedicated computer. It only needs a quick setup to communicate with a local wifi that is used to send the data using the internet of things (IoT) protocols. The photometer has also an infrared sensor to estimate the cloud coverage by comparing the ambient temperature with that of the sky. More information on the photometer at [7].

The data obtained by each TESS-W unit is sent in real time to the repositories and is inmediately ready for the public (open data) and also from the Spanish Virtual Observatory[2]. The researchers and interested citizens can browse the plots, compare the readings from

[2]http://sdc.cab.inta-csic.es/pdd/jsp/tessindex.jsp

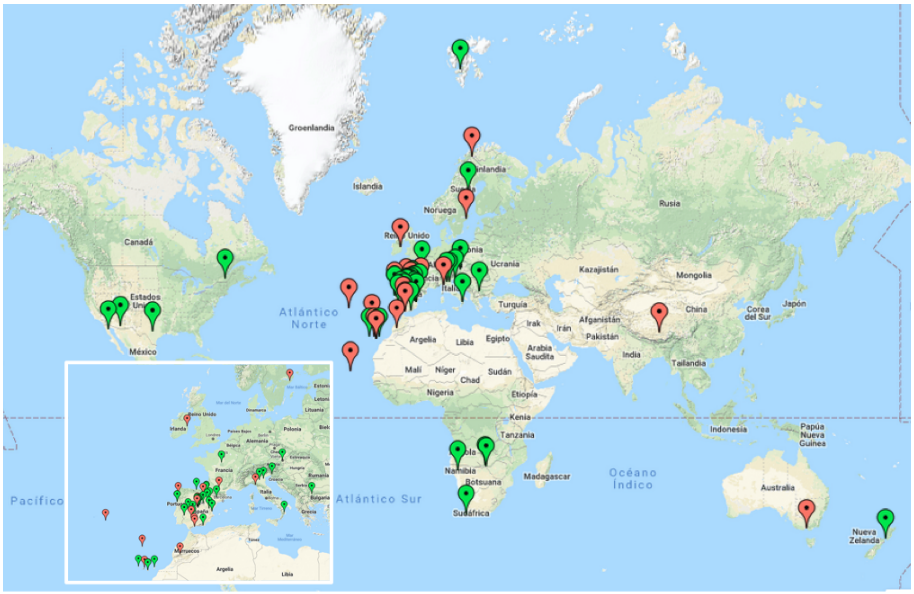

Figure 4: Map with the location of the TESS-W photometers sending data. The inset shows a better view of the photometers in Europe.

different stations and also to download the data[3].

3.2 The TESS-W photometer network

The first units produced were tested and calibrated, before sending to the beta testers. They perform as expected and only some minor changes were made to the second series. There are 180 TESS-W photometers built, 50 of them in the process of calibration at *Laboratorio de Instrumentación Científica Avanzada* (LICA-UCM).

Although the network was originally designed to cover Europe, the first 60 photometers that are sending data from several places along the globe (see Fig.4). This reflects the location of the citizen science volunteers and that of the interested researchers working in the field of light pollution. Most of the first series of photometers (37) are located in Spain.

The data gathered with the photometers is already available for the interested scientist to research. In Figure 5 we present example of the measures for one night in four locations of different geographical coordinates. We are waiting for a long series of observations to determine eventual evolution and other interesting statistical results.

Acknowledgments

The devices were tested LICA, a facility of UCM-UPM Campus de Excelencia Internacional. The support of the Spanish Network for Light Pollution Studies (REECL) (Ministerio de Economía y

[3]http://tess.stars4all.eu/plots/

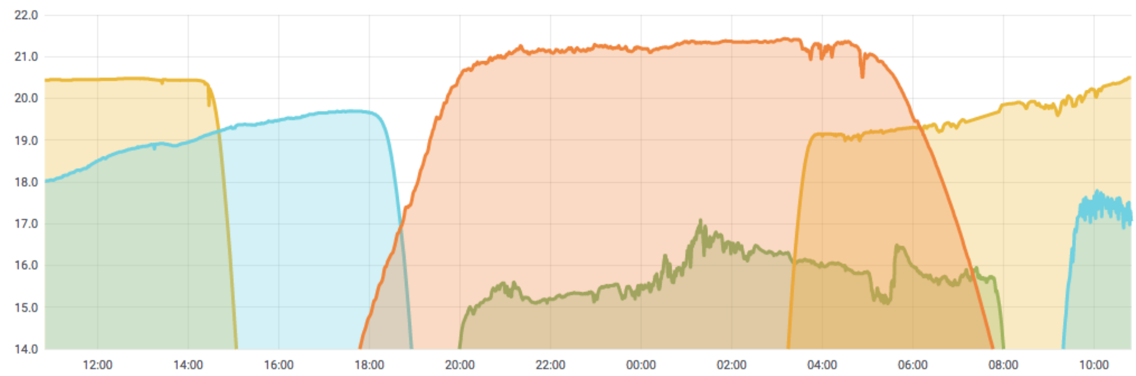

Figure 5: Variation of the night sky brightness measured in four locations of the network during the night (2018/10/18-19). Wellington (New Zealand) in yellow; Coslada near Madrid in green; Tucson (Arizona) in blue and Svalbard (Norway) in orange.

Competitividad, Red de Excelencia AYA2015-71542-REDT) is acknowledged. The TESS-W photometer has been developed with the support of STARS4ALL, a project funded by the European Union H2020-ICT-2015-688135. This work has been partially funded by the Spanish MICINN (AYA2016-75808-R) and by the Madrid Regional Government through the SpaceTec Project (S2013/ICE-2822). This research has made use of the Spanish Virtual Observatory (http://svo.cab.inta-csic.es) supported from the Spanish MINECO/FEDER through grant AyA2014-55216

References

[1] Bará S, 2016, Royal Society Open Science 3:160541. (doi: 10.1098/rsos.160541).

[2] Nievas, M. & Zamorano, J. 2014 "PySQM the UCM open source software to read, plot and store data from SQM photometers" UCM eprint 25900

[3] Sánchez de Miguel, A. 2015, PhD thesis Universidad Complutense de Madrid https://zenodo.org/record/1422725

[4] Sánchez de Miguel, A., Aubé, M., Zamorano, J., Kocifaj, M., Roby, J., & Tapia, C. (2017) Monthly Notices of the Royal Astronomical Society, 467(3), 2966-2979.

[5] Zamorano, J., Sánchez de Miguel, A., Nievas, M., Tapia, C., Ocaña, F., Izquierdo, J., Gallego, J., Pascual, S., Colomer, F., Bará, S., Ribas, S. , Morales-Rubio, A., Marco, E., Baixeras, J., Muñoz-Tuñón, C., Díaz Castro, J., Solano, E., Alacid, J.M., Naves, R., Salto, J.L., Luque, S., García, F., Quejigo, R., Ribas, J., Díez, R.,García, C., Jáuregui, F. 2015 XXIX IAU FM 21: Mitigating Threats of Light Pollution & Radio Frequency Interference, Honolulu (Hawaii)

[6] Zamorano J., Sánchez de Miguel A, Ocaña F, Pila-Díez B, Gómez Castaño J, Pascual S, Tapia C, Gallego J, Fernández A, Nievas M., 2016, Journal of Quantitative Spectroscopy and Radiative Transfer 181:52,66. (doi: 10.1016/j.jqsrt.2016.02.029)

[7] J. Zamorano, C. García, R. González, C. Tapia, A. Sánchez de Miguel, S. Pascual,, J. Gallego, E. González, P. Picazo, J. Izquierdo, M. Nievas, L. García, O. Corcho, and The STARS4ALL consortium, 2016, "STARS4ALL night sky brightness photometer" The International Journal of Sustainable Lighting 35, 49-54

Highlights on Spanish Astrophysics X, Proceedings of the XIII Scientific Meeting of the Spanish Astronomical Society held on July 16 – 20, 2018, in Salamanca, Spain. B. Montesinos, A. Asensio Ramos, F. Buitrago, R. Schödel, E. Villaver, S. Pérez-Hoyos, I. Ordóñez-Etxeberria (eds.), 2019

Reducing EMIR spectroscopic data with Python.

Nicolás Cardiel[1], Sergio Pascual[1], Jesús Gallego[1], Cristina Cabello[1], Francisco Garzón[2,3], Marc Balcells[4], Nieves Castro-Rodríguez[5], Lilian Domínguez-Palmero[4,2], Peter Hammersley[6], Nicolas Laporte[7], Lee R. Patrick[2], Roser Pelló[7], Mercedes Prieto[2], and Alina Streblyanska[2]

[1] Departamento de Física de la Tierra y Astrofísica, Universidad Complutense de Madrid, Spain
[2] Instituto de Astrofísica de Canarias, Tenerife, Spain
[3] Departamento de Astrofísica, Universidad de La Laguna, Spain
[4] Isaac Newton Group of Telescopes, La Palma, Spain
[5] Gran Telescopio Canarias, La Palma, Spain
[6] European Southern Observatory, Garching bei München, Germany
[7] Observatoire Midi-Pyrénées, Toulouse, France

Abstract

EMIR, the near-infrared camera and multi-object spectrograph operating in the spectral region from 0.9 to 2.5 μm, has been commissioned at the Nasmyth focus of the Gran Telescopio CANARIAS. One of the most outstanding capabilities of EMIR is its multi-object spectroscopic mode which, with the help of a robotic reconfigurable slit system, allows to take around 53 spectra simultaneously. A data reduction pipeline, `pyemir`, based on Python, is being developed in order to facilitate the automatic reduction of EMIR data taken in both imaging and spectroscopy mode. This package, as well as the auxiliary package `numina`, are both available at GitHub (`https://github.com/guaix-ucm`). The user's guide is being currently written after the experience gained analysing the commissioning data, and will be soon available in the documentation hosting platform Read the Docs. Focusing on the reduction of spectroscopic data, some critical manipulations are the geometric distortion correction and the wavelength calibration. Using a large set of tungsten and arc calibration exposures, both calibrations have been modelled for any arbitrary configuration of the multi-object slit system. This model can be easily employed to obtain a preliminary rectified and wavelength calibrated EMIR spectroscopic image without additional calibration images. This facilitates both the on-line quick reduction of the data at the telescope and the off-line detailed reduction of the data by the astronomer.This work was funded by the Spanish Programa Nacional de Astronomía y Astrofísica under grant AYA2016–75808–R.(See poster).

Highlights on Spanish Astrophysics X, Proceedings of the XIII Scientific Meeting of the Spanish Astronomical Society held on July 16 – 20, 2018, in Salamanca, Spain. B. Montesinos, A. Asensio Ramos, F. Buitrago, R. Schödel, E. Villaver, S. Pérez-Hoyos, I. Ordóñez-Etxeberria (eds.), 2019

The WEAVE Core Processing System at CASU.

J. Lewis[1], M. J. Irwin[1], C. Worley[1], D. N. A. Murphy[1], L. Peralta de Arriba[1], N. A. Walton[1] and the WEAVE Instrument Consortium

[1] Institute of Astronomy, University of Cambridge, Madingley Road, Cambridge CB3 0HA, UK

Abstract

WEAVE is the spectrograph for the new 2-degree field of view on the William Herschel Telescope. First light on WEAVE (expected for mid-2019) will permit either multi-object observations (MOS) using ∼1000 fibres or observations using Integral Field Units (either one large IFU, or 20 mini-IFUs). Another relevant feature of this instrument are the two resolution modes: $R \sim 5000$ in the range $370 - 1000$ nm, and $R \sim 20000$ in the ranges $405 - 465$ nm or $475 - 545$ nm, and $595 - 685$ nm.

The processing and analysis of WEAVE observations will be carried out by a collaboration between the Cambridge Astronomical Survey Unit (CASU) from the Institute of Astronomy, the Instituto de Astrofísica de Canarias and the Telescopio Nazionale Galileo.

In this poster, we describe the contribution from CASU: the WEAVE Core Processing System, which includes a platform for preparing the observations, a real-time analysis utility for checking the data, quality control checks from the images and data reduction including spectral extraction and calibration. (See poster).

Highlights on Spanish Astrophysics X, Proceedings of the XIII Scientific Meeting of the Spanish Astronomical Society held on July 16 – 20, 2018, in Salamanca, Spain. B. Montesinos, A. Asensio Ramos, F. Buitrago, R. Schödel, E. Villaver, S. Pérez-Hoyos, I. Ordóñez-Etxeberria (eds.), 2019

Object classification in Big Astronomical surveys by Self Organizing Maps (SOM). Application to the Alhambra survey.

Minia Manteiga[1], Marco A. Álvarez González[1], Daniel Garabato[1], Carlos Dafonte[1], Ángel Gómez[1], Ana Ulla[2], and Ruth Carballo[3]

[1] CITIC. Universidade da Coruña, Spain
[2] Depto. de Física Aplicada. Área de Astonomía e Astrofísica. Universidade de Vigo, Spain
[3] Departamento de Matemática Aplicada y Ciencias de la Computación. Universidad de Cantabria, Spain

Abstract

Self-Organizing Maps can effectively assist researchers in the process of the analysing information presented in extended and complex databases by reducing the dimensionality of the sample to a number of prototypes in an unsupervised fashion. We have used the available information on the spatial size of photometric images available in Alhambra archive to label the objects between point-like (stars and qso) and extended objects. We also crossmatched the astrometry with Simbad database and found coincidences for about 15% of the objects. By comparing results, we are able to constrain the physical nature of the prototypes in each of the neurons clustered by our SOM. (See poster).

Acknowledgments

This work is supported by MINECO grant ESP-2016-80079-C2-2-R

References

[1] Fustes et al. 2013, Astronomy and Astrophysics 559, A7

[2] Garabato et al. 2017, in Early Data Release and Sc. Exploitation of the J-PLUS Survey, id. 16

Highlights on Spanish Astrophysics X, Proceedings of the XIII Scientific Meeting of the Spanish Astronomical Society held on July 16 – 20, 2018, in Salamanca, Spain. B. Montesinos, A. Asensio Ramos, F. Buitrago, R. Schödel, E. Villaver, S. Pérez-Hoyos, I. Ordóñez-Etxeberria (eds.), 2019

The WEAVE Quick-Look GUI.

L. Peralta de Arriba[1], J. Lewis[1], D. N. A. Murphy[1], M. J. Irwin[1] and the WEAVE Instrument Consortium

[1] Institute of Astronomy, University of Cambridge, Madingley Road, Cambridge CB3 0HA, UK

Abstract

The Cambridge Astronomical Survey Unit (CASU) is commissioning a Quick-Look (QL) system for WEAVE, the upcoming spectroscopic facility of the William Herschel Telescope. The aim of the QL processing is to analyse data from WEAVE in real time, allowing the On-Island Survey Management Team to monitor the quality of each observation.

In this poster, we show the interface of the interactive display program which is currently available in the telescope control room. (See poster).

Highlights on Spanish Astrophysics X, Proceedings of the XIII Scientific Meeting of the Spanish Astronomical Society held on July 16 – 20, 2018, in Salamanca, Spain. B. Montesinos, A. Asensio Ramos, F. Buitrago, R. Schödel, E. Villaver, S. Pérez-Hoyos, I. Ordóñez-Etxeberria (eds.), 2019

GRAVITY – Reaching out to SgrA* with VLTI.

GRAVITY Collaboration - R. Abuter[8], A. Amorim[6,14], N. Anugu[7], M. Bauböck[1], M. Benisty[5], J. P. Berger[5,8], N. Blind[10], H. Bonnet[8], W. Brandner[3], A. Buron[1], C. Collin[2], F. Chapron[2], Y. Clénet[2], V. Coudé du Foresto[2], P. T. de Zeeuw[12,1], C. Deen[1], F. Delplancke-Ströbele[8], R. Dembet[8,2], J. Dexter[1], G. Duvert[5], A. Eckart[4,11], F. Eisenhauer[1], G. Finger[8], N. M. Förster Schreiber[1], P. Fédou[2], P. Garcia[7,14], R. Garcia Lopez[15,3], F. Gao[1], E. Gendron[2], R. Genzel[1,13], S. Gillessen[1], P. Gordo[6,14], M. Habibi[1], X. Haubois[9], M. Haug[8], F. Haußmann[1], Th. Henning[3], S. Hippler[3], M. Horrobin[4], Z. Hubert[2,3], N. Hubin[8], A. Jimenez Rosales[1], L. Jochum[8], L. Jocou[5], A. Kaufer[9], S. Kellner[11], S. Kendrew[16,3], P. Kervella[2], Y. Kok[1], M. Kulas[3], S. Lacour[2], V. Lapeyrère[2], B. Lazareff[5], J.-B. Le Bouquin[5], P. Léna[2], M. Lippa[1], R. Lenzen[3], A. Mérand[8], E. Müler[8,3], U. Neumann[3], T. Ott[1], L. Palanca[9], T. Paumard[2], L. Pasquini[8], K. Perraut[5], G. Perrin[2], O. Pfuhl[1], P. M. Plewa[1], S. Rabien[1], A. Ramírez[9], J. Ramos[3], C. Rau[1], G. Rodríguez-Coira[2], R.-R. Rohloff[3], G. Rousset[2], J. Sanchez-Bermudez[9,3], S. Scheithauer[3], M. Schöller[8], N. Schuler[9], J. Spyromilio[8], O. Straub[2], C. Straubmeier[4], E. Sturm[1], L. J. Tacconi[1], K. R. W. Tristram[9], F. Vincent[2], S. von Fellenberg[1], I. Wank[4], I. Waisberg[1], F. Widmann[1], E. Wieprecht[1], M. Wiest[4], E. Wiezorrek[1], J. Woillez[8], S. Yazici[1,4], D. Ziegler[2] and G. Zins[9]

[1] Max Planck Institute for extraterrestrial Physics, Giessenbachstraße 1, 85748 Garching, Germany
[2] LESIA, Observatoire de Paris, Université PSL, CNRS, Sorbonne Université, Univ. Paris Diderot, Sorbonne Paris Cité, 5 place Jules Janssen, 92195 Meudon, France
[3] Max Planck Institute for Astronomy, Königstuhl 17, 69117 Heidelberg, Germany
[4] 1 st Institute of Physics, University of Cologne, Zülpicher Straße 77, 50937 Cologne, Germany
[5] Univ. Grenoble Alpes, CNRS, IPAG, 38000 Grenoble, France
[6] Universidade de Lisboa – Faculdade de Ciências, Campo Grande, 1749-016 Lisboa, Portugal
[7] Faculdade de Engenharia, Universidade do Porto, rua Dr. Roberto Frias, 4200-465 Porto, Portugal
[8] European Southern Observatory, Karl-Schwarzschild-Straße 2, 85748 Garching, Germany
[9] European Southern Observatory, Casilla, 19001 Santiago 19, Chile
[10] Observatoire de Genève, Université de Genève, 51 Ch. des Maillettes, 1290 Versoix, Switzerland
[11] Max Planck Institute for Radio Astronomy, Auf dem Hügel 69, 53121 Bonn, Germany

[12] Sterrewacht Leiden, Leiden University, Postbus 9513, 2300 RA Leiden, The Netherlands
[13] Departments of Physics and Astronomy, Le Conte Hall, University of California, Berkeley, CA, 94720 USA
[14] CENTRA – Centro de Astrofísica e Gravitação, IST, Universidade de Lisboa, 1049-001 Lisboa, Portugal
[15] Dublin Institute for Advanced Studies, 31 Fitzwilliam Place, Dublin 2, Ireland
[16] European Space Agency, Space Telescope Science Institute, 3700 San Martin Drive, Baltimore, MD 21218, USA

Abstract

As one of the 2nd generation of interferometric instruments in VLTI, GRAVITY was installed at the end of 2015 and has been observing the Galactic Center since May 2016. With the goal to reach an accuracy of tens of micro arcseconds, it is able to perform the most precise astrometric measurement of SgrA* to date. For that purpose, GRAVITY combines the light collected (coherently) from of all the 8 m UTs or the four 1.8 m ATs providing infrared wavefront sensing to control the telescope adaptive optics, two interferometric beam combiners (one for fringe-tracking and one for the science object), an acquisition camera and various laser guiding systems for beam stabilization, as well as a dedicated laser metrology to trace the optical path length differences for narrow angle astrometry. Operating in K band with an active stabilization of the science channel, GRAVITY is able to increase the typical integration time from a few milliseconds (the typical atmospheric coherence time) to minutes, which implies a big leap in sensitivity allowing to observe fainter objects (K=19 in science detector) with the power of a 130m baseline interferometer, as it is the close environment of the supermassive black hole located in the center of our Galaxy. (See poster).

Highlights on Spanish Astrophysics X, Proceedings of the XIII Scientific Meeting of the Spanish Astronomical Society held on July 16 – 20, 2018, in Salamanca, Spain. B. Montesinos, A. Asensio Ramos, F. Buitrago, R. Schödel, E. Villaver, S. Pérez-Hoyos, I. Ordóñez-Etxeberria (eds.), 2019

SVO Discovery Tool: A Science booster; let machines do the routine work.

A. Velasco[1,2], E. Solano[1,2], and C. Rodrigo[1,2]

[1] Centro de Astrobiología (CSIC-INTA)
[2] Spanish Virtual Observatory

Abstract

SVODiscoveryTool (https://sdc.cab.inta-csic.es/SVODiscoveryTool) is a tool that has been developed in the framework of the Spanish Virtual Observatory for the discovery of archive information about astronomical targets. Given a list of objects, this tool allows the access to information such as physical paramenters, images, spectra and photometry. In addition to be a service available for the whole astronomical community, our aim is that SVODiscoveryTool becomes part of the 'Gaia Alerts' project, http://gsaweb.ast.cam.ac.uk/alerts/home, complementing with archive data the information obtained through 'follow up' campaigns. (See poster).

Highlights on Spanish Astrophysics X, Proceedings of the XIII Scientific Meeting of the Spanish Astronomical Society held on July 16 – 20, 2018, in Salamanca, Spain. B. Montesinos, A. Asensio Ramos, F. Buitrago, R. Schödel, E. Villaver, S. Pérez-Hoyos, I. Ordóñez-Etxeberria (eds.), 2019

From the school to the space: outreach experience in Astronomy at IFCA.

M.T. Ceballos[1]

[1] Instituto de Física de Cantabria (CSIC-UC)

Abstract

For the last 5 years, the Instituto de Física de Cantabria (CSIC-UC) has developed a titanic effort in disseminating the Astronomy in spite of a scarce funding. The activities supported by a tenacious group of enthusiastic astronomers have been mainly focused (but not only) in the youngest students, visiting their schools or receiving them in the institute. The Athena mission outreach group, managed by the Athena Community Office, has also added its own resources to support the scholar activities to take advantage of the synergy when resources are limited.

1 Introduction

The Instituto de Física de Cantabria (IFCA) [1]is a small institute with a staff of about 80 people dedicated to different lines of research in Physics (Galaxies and AGNs, Cosmology and observational instrumentation, Particle Physics, Non-linear Physics, Advanced computing and Climate and data mining). Under the administrative tree, there is a Vice-directorate of Outreach, that in spite of the difficulty of assigning funds or human resources to its activities in a small centre like this one, it shows the commitment of the institute management to the science dissemination. With the help of the Sociedad Española de Astronomía (SEA)[2] and the other outreach unit at the institute (Athena Community Office (ACO)'s [3] outreach unit) and the sound compromise of the researchers, IFCA's dissemination activities have been numerous along the last 5 years, becoming a solid reference for the educational centers in the region.

2 Motivation

Among all the activities performed by the scientists during the development of their profession, unfortunately outreach is not one that could be considered as highly recognized or appreciated by the evaluation panels. When done, it always takes part of the personal time of the researchers usually buried under loads of administrative tasks. It cannot be considered an easy job to do, since being able to explain latest scientific developments to a non-professional audience requires an extraordinary effort to talk about complex things with a simple language. And it does not make scientists rich, either! Then, why are there enthusiastic disseminators that still keep the commitment with science dissemination?

As Carl Sagan said "We live in a society absolutely dependent on science and technology and yet have cleverly arranged things so that almost no one understands science and technology. That's a clear prescription for disaster". We believe that is also our responsibility, not only to give society the latest developments but also to educate citizens in science to help them to make funded decisions in their everyday life. And, from our point of view, science dissemination at schools, from the very first years is the most powerful tool.

We consider that not only education in science is essential, but education in equality in science is fundamental. That is why the second pillar of our outreach activities is the compromise with the visualization of the female role in science to contribute to a more egalitarian and fair society. For this purpose it is vital to incorporate women to the scientific careers and to create the conditions for them to stay. From our positions we can at least highlight female scientists work and try to change stereotypes.

3 Activities

The objectives outlined in previous section have been shaped in four different outreach activities at IFCA during the term 2017-2018:

- *Expanding Science: researchers at schools*: bring science closer to children and teenagers in their own environment
- *Visits to IFCA*: introduce scientist' activities in their work places
- *European Researcher Night*: bring science to the streets to involve local society
- *11 February*: highlight female scientists role and change stereotypes

3.1 Expanding science: researchers at schools

With the financial help of the SEA to cover the travel expenses of the staff, schools along the region receive astronomers in their classes, having the opportunity to listen to a talk about a selected subject in Astronomy (Solar System, Exoplanets, Scales of the Universe, Life in the Universe, Black Holes, Big Bang, Dark matter) and after that to chat with them and raise their questions. The audiences are scholars from Preschool to Secondary levels (3 to 17 years old). In addition to the talks about Astronomy, scientists make with them different types of workshops according to their ages, being the Virtual Reality views one of the most successful.

According to the school teachers these are very motivating experiences in class and students are willing to dedicate research time to the Astronomy subject before and after

Figure 1: S. Martínez-Núñez (left) and X. Barcons (right) giving talks at primary and secondary schools in Cantabria.

Figure 2: M.T. Ceballos in school workshops with VR glasses.

the astronomer's visit. Very frequently the groups reflect the activity in their webs, blogs or periodic paper publications. Last term, this activity reached more than 80 talks in 35 different scholar centers and more than 2000 students.

3.2 Visits to IFCA

For the first time in the scholar term 2017-2018 and as a pilot experience, IFCA opened its doors during the whole term (one visit per month) to the secondary classes willing to know how scientific work is done in a research center. They had the opportunity to be in contact with different research groups and visit the IFCA facilities, where special emphasis is put on the multidisciplinary scientific collaboration.

They are also offered different workshops that include a demonstration of the space curvature in a gravitational table, kahoot[4] games for smartphones or VR movies with VR glasses.

3.3 European Researchers Night

Every year IFCA joins the European Researcher's Night (ERN)[5] to bring science to the streets of Santander and get a close contact with the local general public. The astronomy group is always very active and organizes several activities related to Solar System, Cosmology (cosmic microwave background and gravity) and X-ray astronomy, this last one led by the outreach group of the Athena Community Office. This group is dedicated to the dissemination of the Athena [3] project and its news and activities not only among the scientific community but also for the general public. They are also members of IFCA, since the ACO is based at the institute and they actively participate in all the outreach events. Many activities are focused on the children (like the multiwavelength drawings of emblematic astronomical objects) or the photo-call with the satellite but there are also opportunities for the adult people which can have a look to the X-ray sky in 360 deg or with the VR glasses.

Figure 3: Summary of activities organized by the ACO for the ERN2017.

3.4 International Day of Women and Girls in Science

Another initiative in which IFCA is involved every year is the celebration of the *International Day of Women and Girls in Science*[6], declared by the UN "in order to achieve full and equal access to and participation in science for women and girls, and further achieve gender equality and the empowerment of women and girls". Considering this endeavor fundamental in the every day life of our institute, the staff took part in 2017 in four different activities:

- talks in educational centers to highlight science (past and present) done by female scientists
- outreach videos: IFCA female staff participated in a collaboration with Javier Santaolalla ("Date un Vlog") to produce a video[7] about pulsars and in the elaboration of another one about two of the scientific projects in the institute where these female scientist participate (CMS[8] and Athena[9]).
- female scientists mosaic: in a joint effort and both for the Athena project and SEA, we created two mosaics with the face photos of female scientists in each community. In addition, the Athena outreach group elaborated a video-clip with Athena community female scientists sharing motivating sentences about science [10].
- Science for Her: some of the female scientists at IFCA participated in a mentorship initiative to foster scientific vocation in young girls by sharing with them part of their workday[11].

4 Conclusions

It is indisputable that giving back to society its inversion in Science is a duty of the scientists. However the evaluation panels that judge the scientists performance in their careers do not assign a great value to this dedication, leaving the outreach work to the will of the researchers. All the activities presented here have been done with the dedicated effort of a group of selfless people that truly believe in the importance of outreach, with a little funding and a great commitment. A lot can be done under these conditions, but in spite of being a rewarding experience it is clear that public outreach in science has to be organizationally supported with adequate material and human resources to fulfill its mission of educating society in science.

Acknowledgments

This work has been funded by the Spanish Ministry MINECO under project ESP2016-76683, co-funded by FEDER funds. Special thanks are giving to Javier Santaolalla for the fruitful collaboration in the pulsar's video. This work would have been impossible without the selfless implication of IFCA astronomy staff (15 people) and IFCA's management and their real commitment with science dissemination and female scientists visibility.

References

[1] IFCA website

[2] SEA website

[3] Athena website

[4] Kahoot

[5] ERN website

[6] 11 February website

[7] Qué son las estrellas de neutrones (Date un Vlog)

[8] Mujeres IFCA-CMS

[9] Mujeres IFCA-Athena

[10] 11 February - ACO clips

[11] Stem Talent Girl

Highlights on Spanish Astrophysics X, Proceedings of the XIII Scientific Meeting of the Spanish Astronomical Society held on July 16 – 20, 2018, in Salamanca, Spain. B. Montesinos, A. Asensio Ramos, F. Buitrago, R. Schödel, E. Villaver, S. Pérez-Hoyos, I. Ordóñez-Etxeberria (eds.), 2019

Chat with a Woman Astronomer. A pioneery activity organised by SEA's Comisión Mujer y Astronomía to commemorate 11F.

Adriana de Lorenzo-Cáceres[1,2], and Comisión Mujer y Astronomía

[1]Instituto de Astrofísica de Canarias (IAC), E-38205 La Laguna, Tenerife, Spain
[2]Universidad de La Laguna (ULL), Departamento de Astrofísica, E-38206 La Laguna, Tenerife, Spain
[3]Spanish Astronomical Society

Abstract

Since 2015, February 11th commemorates the *International Day of Women and Girls in Science*, as set up by the United Nations. Such vindication is fully supported by the Spanish Astronomical community, represented by the Spanish Astronomical Society (SEA) and, particularly, by its *Woman and Astronomy Unit* (Comisión Mujer y Astronomía, CMyA). *Chat with a woman astronomer* was organised by CMyA on February 7th, 2018 with the aim at approaching the role of women in Astronomical research to the general public. During almost the full day, women astronomers were constantly available through an online platform to chat about their job as professional astronomers or their experience as women working in science.

1 11F: International Day of Women and Girls in Science

In 2015, the United Nations established that the *International Day of Women and Girls in Science* will be celebrated on February 11th (11F) every year. Since September 2016, focused activities are organised in Spain under the umbrella of 11defebrero.org, in order to approach the reality of women working in science and promote scientific vocation among young girls. This initiative is supported and spread out by a non-profit-group of researchers and science communicators.

The Spanish Astronomical Society (SEA), represented by its Woman and Astronomy Unit (Comisión Mujer y Astronomía, CMyA), shares the worrisome behind 11F and supports the organisation of activities helping to 1) recognise the role of women astronomers; and ii) disseminate the message that Astronomy is a career suitable for women as well as for men.

In February 2017, CMyA organised two activitites within the framework of 11F: 1) the publication of a panel including pictures of women astronomers, either Spanish or working in Spain; and 2) *Chat with a Woman Astronomer*, a full-day activity carried out on February 7th, consisting of an online platform through which anyone, regardless of gender or age, could connect and talk to a professional woman astronomer.

2 Chat with a Woman Astronomer: the activity

Chat wit a Woman Astronomer was organised through the online chatting platform PureChat in its free version. PureChat allows to set up a group of *chatters* with access to all possible chats requested through an external link, which was disseminated by the SEA through its usual channels and mailing list. An automatic message is received by the external user, asking for patience while a woman astronomer is connecting to his/her/their chat. As soon as one chatter accepts the chat, the header of the chatting window changes to show the name and photo of the woman astronomers. Chats may last for as much as time as desired by both chatter and external user. We note that no information from the user is previously requested; while it is possible to create an input form through PureChat, we decided to minimise barriers between the user and chatter.

CMyA made a call looking for volunteer woman astronomers to participate in this activity, which was very well accepted by the astronomical community. The final calendar shown in Figure 1 includes 32 women astronomers, spread in 30-minutes slots covering the full February 7th day from 8am to 12pm (time of Mainland Spain).

3 Some statistics and results

Chat with a Woman Astronomer proved as a huge success: 513 chats were answered during the day. The chat was definitively closed at 12:30pm, thus the activity lasted for 16.5 hours in total. We must note that the pioneery nature of the activity prevented us from disseminating it as much as we could: such high demand despite of the limited advertising indicates the great interest of the Spanish people in Astronomy.

Figure 2 shows the amount of chats requested along the day: the red histogram corresponds to answered chats, while the remaining represent missed chats. The grey histogram indicates chats that were closed in $<$1 minute of waiting time; the majority of these cases correspond to disconnections or non-desired chats, i.e., users that were curious but did not have true intention of chatting. The yellow histogram therefore represents the actual distribution of unanswered chats, which amounts to 44.

We received chat requests from a variety of people of all ages and gender. The morning hours were mostly occupied by students between 10 and 17 years old at school. Teachers from science and computing lessons allowed the students to connect, both in groups or individually. Individual cases caused some saturation as they implied many simultaneous chat requests. For this reason, many women astronomers connected for longer times than their planned 30-minutes slots, and they even reconnected several times during the day to help answering chats. Each chatter answered between 5 and 68 chats, with a maximum of 20 simultaneous chats.

Charla con una Astrónoma

Actividad organizada por la Comisión Mujer y Astronomía de la Sociedad Española de Astronomía

El 7 de febrero ¡anímate a charlar con una astrónoma a través de este link: https://app.purechat.com/w/11FMujerYAstro!

8:00 - 8:30	Asunción Fuente	Observatorio Astronómico Nacional (Madrid)	Formación estelar, discos protoplanetarios
8:30 - 9:00	Olga Suárez	Observatorio de la Costa Azul (Francia)	Física Estelar
9:00 - 9:30	Consuelo Cid	Universidad de Alcalá (Madrid)	Heliofísica y Meteorología Espacial
9:30 - 10:00	Minia Manteiga	Universidad de La Coruña (Galicia)	Física Estelar, Inteligencia Artificial
10:00 - 10:30	Almudena Zurita	Universidad de Granada (Granada)	Regiones HII, galaxias espirales
10:30 - 11:00	Julia de León	Instituto de Astrofísica de Canarias (La Palma)	Cuerpos menores del Sistema Solar
11:00 - 11:30	Beatriz Ruiz	Instituto de Astrofísica de Canarias (Tenerife)	Cosmología
11:30 - 12:00	María Santos-Lleó	ESAC (Madrid)	Núcleos activos de galaxias, rayos-X
12:00 - 12:30	Amelia Ortiz	Observatorio de Valencia (Valencia)	Divulgación a público con diversidad funcional
12:30 - 13:00	Lourdes Verdes-Montenegro	Instituto de Astrofísica de Andalucía (Granada)	Medio interestelar, radiotelescopios
13:00 - 13:30	Naiara Barrado-Izagirre	Universidad del País Vasco (País Vasco)	Atmósferas planetarias, Júpiter
13:30 - 14:00	Sara Cazzoli	Instituto de Astrofísica de Andalucía (Granada)	Núcleos activos de galaxias
14:00 - 14:30	Montserrat Villar	Centro de Astrobiología (Madrid)	Súpervientos galácticos
14:30 - 15:00	Mar Mezcua	Instituto de Ciencias del Espacio (Barcelona)	Núcleos activos de galaxias, rayos-X
15:00 - 15:30	Pepa Masegosa	Instituto de Astrofísica de Andalucía (Granada)	Núcleos activos de galaxias
15:30 - 16:00	Cesca Figueras	Universidad de Barcelona (Barcelona)	Astrometría, Vía Láctea
16:00 - 16:30	Judith Palacios	Universidad de Alcalá (Madrid)	Física Solar
16:30 - 17:00	Maite Ceballos	Instituto de Física de Cantabria (Cantabria)	Instrumentación de rayos-X
17:00 - 17:30	Mercedes Mollá	CIEMAT (Madrid)	Evolución química de galaxias
17:30 - 18:00	Luisa Lara	Instituto de Astrofísica de Andalucía (Granada)	Sistema Solar, cometas
18:00 - 18:30	Celia Sánchez	ESAC (Madrid)	Rayos-X, estrellas de neutrones
18:30 - 19:00	Isabel Márquez	Instituto de Astrofísica de Andalucía (Granada)	Núcleos activos de galaxias
19:00 - 19:30	Miriam García	Centro de Astrobiología (Madrid)	Estrellas masivas
19:30 - 20:00	Josefina F. Ling	Observatorio Ramón María Aller (Galicia)	Sistemas estelares dobles y múltiples
20:00 - 20:30	Amelia Bayo	Universidad de Valparaíso (Chile)	Formación estelar y planetaria
20:30 - 21:00	Helena Domínguez-Sánchez	Universidad de Pennsylvania (Estados Unidos)	Formación y evolución de galaxias
21:00 - 21:30	Nuria Álvarez Crespo	Universidad de Turín (Italia)	Galaxias con núcleos activos
21:30 - 22:00	Isabel Rebollido	Universidad Autónoma de Madrid (Madrid)	Sistemas planetarios
22:00 - 22:30	Mayra Osorio	Instituto de Astrofísica de Andalucía (Granada)	Formación estelar y planetaria
22:30 - 23:00	Marina Rodríguez	Universidad Autónoma de Madrid (Madrid)	Regiones HII, formación estelar
23:00 - 23:30	Patricia Chinchilla	Instituto de Astrofísica de Canarias (Tenerife)	Enanas marrones y exoplanetas
23:30 - 24:00	Adriana de Lorenzo-Cáceres Rodríguez	Instituto de Astrofísica de Canarias (Tenerife)	Galaxias con barras, poblaciones estelares

Horario de la Península
(este calendario está sujeto a ligeras modificaciones)

Figure 1: Calendar of the Chat with a Woman Astronomer activity, which took place on February 7th, 2018 from 8am to 12pm. 32 Spanish or Spanish-based women astronomers volunteered to be available to chat online about their research or their experience as women working in science.

The great success of the activity is hugely due to the friendly willingness of the volunteers.

We should also note that most people expressed their interest in having activities like Chat with a Woman Astronomer more often, which they found very positive and useful.

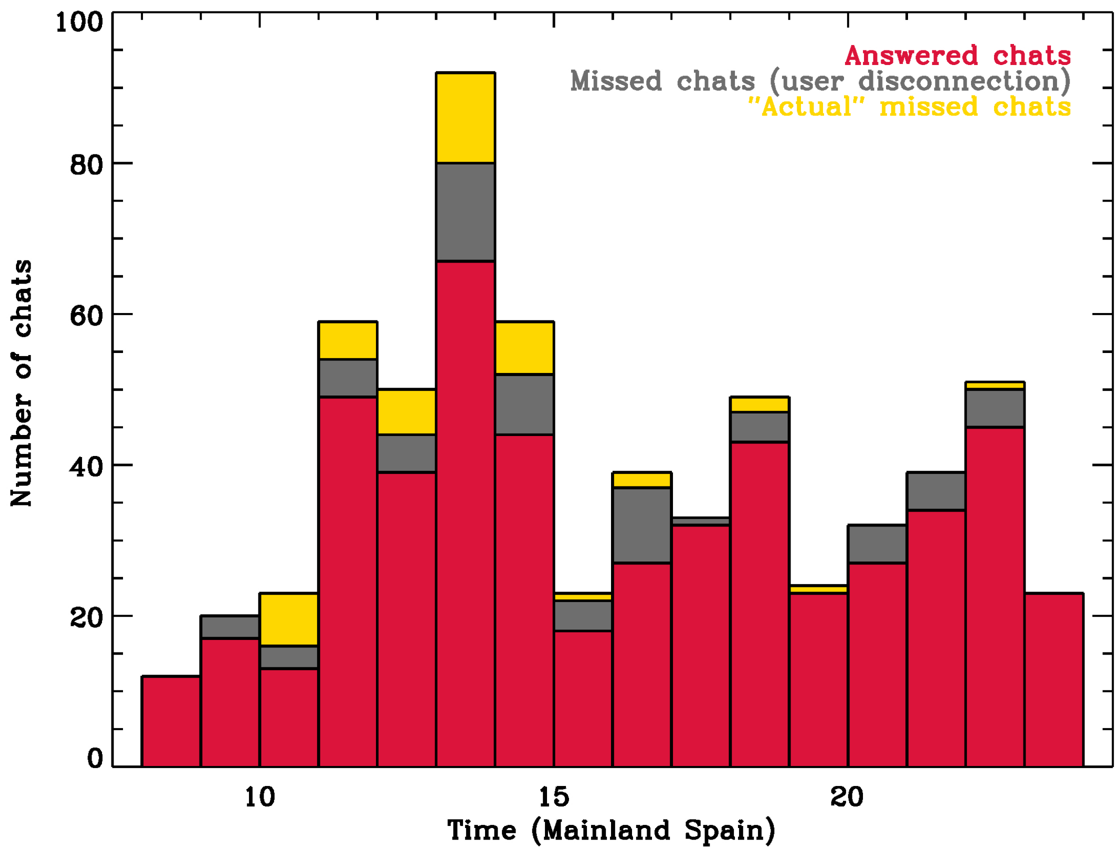

Figure 2: Answered and missed chats along the day. The 513 answered chats are shown in red, while yellow and grey histograms account for actually missed and not-true chats, respectively. Not-true chats correspond to premature disconnections by the users.

4 Some comments from the chatters

While we cannot keep record of the conversations due to legal protection of personal data, the Chat with a Woman Astronomer was a rewarding activity not only for the public but also for the chatters; here we transcribe some comments from the volunteers.

I was surprised by the fact that many questions came from very young girls and boys in high school. They were very keen in learning how to become professional astronomers. They showed passion and happiness of being able to talk to us and ask questions. Very beautiful experience!

It has been amazing, I think since Univerisity I had not written down so much!

It has been great, funny and a huge success! I was chatting with a 10-years-old boy!

It was such an experience. I hope to participate again next year... many people asked me whether we were going to organise this again!

It was a challenge and an adrenaline rush to try to answer all kind of questions. Beautiful experience!

It reminded me of when I was a child and they set up a phone to talk to an astronaut.

Parents connected to help their young children and at the end they told me how excited the kids were. They even made me a drawing! Very gratifying for both sides.

I was happy, inspired, excited by this experience. I want to repeat now!

Goal accomplished! It is such a proud that we were so many in this first experience.

I met a 18-years-old girl who wanted to become a professional astrophysicist, but people around her used to tell her that it is a men's career. She said that talking to me helped her decide to go for it!

Highlights on Spanish Astrophysics X, Proceedings of the XIII Scientific Meeting of the Spanish Astronomical Society held on July 16 – 20, 2018, in Salamanca, Spain. B. Montesinos, A. Asensio Ramos, F. Buitrago, R. Schödel, E. Villaver, S. Pérez-Hoyos, I. Ordóñez-Etxeberria (eds.), 2019

Astronomy and its application to the study of the religion of ancient Iberians.

C. Esteban[1,2]

[1] Instituto de Astrofísica de Canarias, E-38200, La Laguna, Tenerife, Spain
[2] Departamento de Astrofísica, Universidad de La Laguna, E-38206, La Laguna, Tenerife, Spain

Abstract

This paper reviews some of the main results of archaeoastronomical fieldworks carried out in sanctuaries and temples belonging to the Iron Age Iberian culture. Most of this work has been done in close collaboration with archaeologists. The orientation pattern of the Iberian sacred buildings seems to be related to the rising sun. A significant fraction of the sanctuaries show astronomical markers over topographic elements of the local horizon, most of them indicate the rising sun at the equinoxes or the temporal midpoint between the solstices. Iberian cave-sanctuaries – that tend to be oriented to the west – show illumination phenomena in their interior at sunset in singular moments of the solar calendar.

1 Introducion

Without any doubt, astronomy and archaeology are among the scientific disciplines that attract the most attention of the general public. Since astronomy is devoted to the study of things distant in space, archaeology is dedicated to the recovery of the images and memories of the human past, distant in time. On the other hand, knowledge of the origins and history of human collectivities is of paramount social and political interest. Therefore, archaeoastronomy is an interdisciplinary activity that can play a significant role in science outreach. Archaeoastronomy has still a short history, although raised some controversies in its beginnings, has now an increasing academic recognition in the field of humanities. Since the 1990s this discipline has had an increasing presence in Spanish sicence. In fact, the papers published in Spanish refereed archaeological journals are each year more numerous and it is becoming customary to see astronomers presenting works in meetings on archaeological topics. However, as an interdisciplinary activity, the best possible archaeoastronomy is that made in collaboration of both, astronomers and archaeologists, the first ones scrutinizing the sky and the second ones excavating the ground.

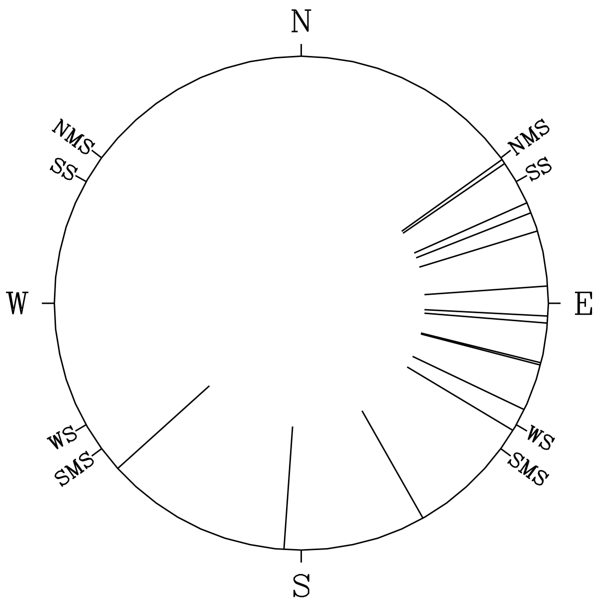

Figure 1: Orientation diagram of a sample of Iberian temples with direct orientation measurements and where the position of the entrance has been well established. SS: summer solstice; WS: winter solstice; NMS: northern major standstill limit of the moon; SMS: southern major standstill limit of the moon.

2 Archaeoastronomical fieldwork in Iberian sanctuaries

The Iberian culture developed in the east and south of the Iberian Peninsula from the sixth century BC up to the Roman conquest of the territory in 206 BC, during the so-called Late Iron Age. The Iberians were the product of the acculturation of Bronze Age indigenous populations due to the presence of Phoenician, Punic, and Greek colonies in their coasts since the beginning of the first millennium [11]. The main Iberian deity was apparently a fertility goddess. Its image is influenced by exogenous models and sometimes represented with attributes of Eastern goddesses such as Astarte, Tanit, Artemis or Demeter [9]. Iberian sanctuaries were usually located in open-air deposits on the top of mountains, within caves or in proximity to springs. Their temples were usually of small size, containing a statue of the divinity and a large number of offerings [1].

Since the end of the 1990s and in collaboration of archaeologists, I have surveyed several tens of Iberian sanctuaries across the territory once occupied by the Iberian culture. The measurements are taken with a theodolite and a precision compass. The fieldwork at each site is based in the measurement of the orientation of the standing constructions, the entrances and main axes of the temples or caves and – in all the cases – the astronomical analysis of the horizon surrounding the sites. The technical description of the measurements can be found in [5].

3 Orientation pattern of Iberian temples

Analyses of the orientation pattern of the entrances of Iberian sacred buildings have been presented in [2] and [3]. In Fig. 1, we show a compilation of data for temples with direct orientation measurements and where the position of the entrances has been well established. From the figure, it can be seen that Iberian temples are orientated in a non-random manner. In fact, most of them are facing the zone of the horizon where the sun (or moon) rises along the year. As it was discussed by [3], the orientation pattern of the Iberian sanctuaries is different from that shown by Roman and Etruscan temples but similar to that of Greek ones of Magna Graecia and Sicily and of Punic sanctuaries.

4 Equinoctial markers in Iberian sanctuaries

The most remarkable archaeoastronomical result in Iberian sanctuaries is the discovery of equinoctial markers in an important fraction – about 40% – of the sites studied, from Aragon to Andalusia. This clearly indicates that equinoxes – or dates close to them – were important moments of the Iberian ritual. The markers are produced on the horizon surrounding the sanctuaries, i.e. the sunrise at the equinoxes occurs over conspicuous topographical elements, usually mountain peaks (El Amarejo, La Serreta, La Carraposa, Sant Miquel de Llíria, Mazaleón) or even nearby islands (La Malladeta). Several of these sanctuaries also contain a temple oriented to the equinox, increasing the likelihood that the astronomical relation was deliberate.

Although we generically call them "equinoctial markers", most of the evidences indicate that the target of the orientations should be the temporal midpoint between solstices (hereinafter TMPS) also known as "megalitic equinox", introduced by [12]. This corresponds to the day just in the middle between the exact dates of summer and winter solstices and occurs between one or two days after spring equinox or before the autumn equinox. The declination of the sun at that moment is between $+0.3°$ and $+1.0°$ in the moment of the sunrise closer to the TMPS. Therefore, the TMPS permits to divide the year in four equal parts in coincidence with our seasons at intermediate latitudes, and seems to be an intuitive concept with more practical utility than the equinox. In some places, the equinoctial markers are spectacular, as in El Amarejo [2] or La Malladeta ([4], see Fig. 2) but most of them lack of spectacularity, indicating that it should be better used as a practical tool for pinpointing the calendar and not for a public ritual.

Archaeological findings at the sanctuaries showing equinoctial markers indicate that they were dedicated to a fertility goddess. Festivities related to agricultural fertility were common in the ancient Mediterranean, such as those dedicated to the "resurrection" of Melqart (Heracles) or the Great Mysteries at Eleusis related to the Greek goddess Demeter. These mysteries represented the annual growth cycle through the myth of the descent and return of Kore from the underworld. A similar mythic narrative, where the protagonist is a possible hero-god of vegetation, is shown in the reliefs of the Iberian funerary monument of Pozo Moro, that have been interpreted as a representation of the Labours of Heracles [9]. The symbol of the natural cycle of death and resurrection might be inspired in the annual

Figure 2: Left: Image taken at sunrise on March 22nd, 2017 – date corresponding to the temporal midpoint between solstices – from the Iberian coastal sanctuary of La Malladeta (Vila Joiosa, Alicante). The solar disc appears just over the southern slope of the islet of Benidorm. A surviving wall of the ancient temple is pointing toward the island. Photo taken by A. Espinosa Ruiz (Vilamuseu). Right: Sunset at the winter solstice as seen from the innermost area of the north gallery of the Iberian cave-sanctuary of Umbría de Salchite (Cueva de la Nariz, Moratalla Murcia). Photo taken by J. A. Ocharan Ibarra.

solar motion on the celestial sphere. The moments of death and descent of the divinity to the underworld and her subsequent rebirth or return to earth might be related to the autumnal and spring equinox, respectively.

The sanctuaries with equinoctial markers show a chronology in the interval from about mid IV until II century BC (see [3] for references). The absence of sanctuaries of this kind with earlier dating indicates a date *post quem* such rituals related to the equinox appeared in the Iberian world. According to different authors, the beginning of the IV century BC was a moment of consolidation of the aristocratic system and territorial expansion of the Iberian urban settlements, as well as the emergence of an ideological model based on the figure of a heroized ancestor (e.g. [10]). The relation between these changes in the social organization and astronomical aspects of the ritual is a promising field of future interdisciplinary investigation.

5 Iberian cave-sanctuaries and the sunset

The few archaeoastronomical studies carried out in Iberian cave-sanctuaries have provided striking results. In the cave-sanctuary of La Lobera, [7] found that the innermost part of the cavity, a kind of natural niche, is illuminated at sunset around the equinoxes through an opening located at the west end of the cave. The shapes of the niche and the sunlight spot fit better at the precise date of the TMPS. There are indications that the western opening was retouched at some point in the past. Another suggestive feature of the phenomenon is that the shape of the sunlight spot recalls the profile of some of the ex-votos found at the site and other Iberian sanctuaries that represent the typical schematic female figure that has been interpreted as an Iberian goddess. [7] propose that, in La Lobera, the Iberians were able to carry out a dramatization of a perceptive experience of the divinity as part of the ritual.

In the Iberian cave-sanctuary of Umbría de Salchite (also known as Cueva de la Nariz), [6] report another remarkable illumination phenomenon. This cave has a striking symmetrical morphology, with two parallel galleries of very similar dimensions. It is located on the western slope of a mountain, in an area of difficult access. Both cavities contain water springs and carved basins to collect the water in their innermost areas. By direct observations at the site, [6] found that, at the northern cavity, just during few minutes just before winter solstice sunset (see Fig. 2), sunlight illuminates the basin. Moreover, at the last moments of sunset, the reddish sunlight spot fits the shape of the basin and the canals carved in the rock. Especially suggestive is the tangential illumination of the water contained in the basin by last sun rays of the day.

A last example of astronomically oriented cave-sanctuary is Cueva Santa del Cabriel, an isolated contemporary place of popular Catholic cult to the Virgin Mary that was a sacred place in Iberian times or even earlier. The cave contains a water spring that is considered to have health properties. [8] has found that the narrow 12 m-long corridor that connects the entrance and the main gallery of the cave is very precisely oriented towards the sunset at the summer solstice sunset. This is the only moment of the year when the sun rays touch the cave interior.

Most of the caves considered as Iberian cave-sanctuaries show a westerly orientation. This contrasts with the orientation pattern of the Iberian temples or open-air sanctuaries, which face predominantly to the east. This dichotomy between cave and open-air sanctuaries should be associated with different characteristics of the cult carried out in both kinds of sites. The westerly orientation of cave-sanctuaries might be related to the chthonic character of the rites carried out in them or perhaps rites of passage. However, in Iberian temples or open-air sanctuaries we would have an emphasis on cosmic aspects of the worship.

Acknowledgments

Part of this study is based on the results of fieldworks funded by the research project *Arqueoastronomía* (P/308614) of the Instituto de Astrofísica de Canarias.

References

[1] Blázquez, J. M. 1975, Diccionario de las religiones prerromanas de Hispania. (Ediciones Istmo, Madrid)

[2] Esteban, C. 2002, Trabajos de Prehistoria, 59, 81

[3] Esteban, C. 2017, Entre el cielo y la tierra: arqueoastronomía del mundo fenicio-púnico, ed. B. Costa & A. C. González García (Museo Arqueológico de Ibiza, Ibiza), 81

[4] Esteban, C., & Espinosa Ruiz, A. 2018, Archivo Español de Arqueología, 91, 265

[5] Esteban, C., & Moret, S. 2006, Trabajos de Prehistoria, 63, 167

[6] Esteban, C., & Ocharan Ibarra, J. A. 2016, The Materiality of the Sky, ed. F. Silva, K. Malville, T. Lomsdalen and F. Ventura (Sophia Centre Press, Ceredigion), 189

[7] Esteban, C., Rísquez, C., & Rueda, C. 2014, Archivo Español de Arqueología, 87, 91

[8] Machause López, S., Esteban, C., & Moya, F. 2018, Journal of Skyscape Archaeology, in press

[9] Moneo, T. 2003, Religio Iberica. Santuarios, ritos y divinidades (siglos VII-I A.C.). (Real Academia de la Historia, Madrid)

[10] Rueda, C. 2011, Territorio, culto e iconografía en los santuarios iberos del Alto Guadalquivir (ss. IV a.n.e.-I d.n.e.). (Universidad de Jaén, Jaén)

[11] Ruiz, A., & Molinos, M. 1993, Los Iberos. Análisis arqueológico de un proceso histórico. (Crítica, Barcelona)

[12] Thom, A. 1967, Megalithic Sites in Britain. (Oxford University Press, Oxford)

Highlights on Spanish Astrophysics X, Proceedings of the XIII Scientific Meeting of the Spanish Astronomical Society held on July 16 – 20, 2018, in Salamanca, Spain. B. Montesinos, A. Asensio Ramos, F. Buitrago, R. Schödel, E. Villaver, S. Pérez-Hoyos, I. Ordóñez-Etxeberria (eds.), 2019

The CESAR Initiative.

Beatriz María González García[1], Michel Breitfellner[2] on behalf of the CESAR Team

[1] ISDEFE at the European Space Astronomy Centre (ESAC), PO Box 78, 28691 Villanueva de la Cañada, Madrid, Spain
[2] SERCO at the European Space Astronomy Centre (ESAC), PO Box 78, 28691 Villanueva de la Cañada, Madrid, Spain

Abstract

The CESAR Initiative, which stands for 'Cooperation through Education in Science and Astronomy Research', is an educational project whose main objective is to engage school students with the wonders of Astronomy and, more generally, Science and Technology. The main areas covered by the project are presented here as well as our new projects.

1 Introduction

CESAR is a joint Educational and Scientific Initiative developed in 2012 by the European Space Agency (ESA), the Spanish National Institute for Aerospace Technology (INTA) and the company ISDEFE, aimed at students from European secondary schools as well as Universities. The agreement, signed in 2015 for five years, aim for bridging the gap between Research and the Education Community, by

- using Astronomy as a motivational element to learn about our planet, the Universe, science and technology;
- contributing to improve knowledge of Astronomy and science in general and understand scientific and technological concepts from the simplest to the most advanced ones;
- making Astronomy fun and interesting to stimulate the active participation and interaction of the students,
- disseminating to society the lastest astronomy developments.

2 The CESAR educational activities

The CESAR Initiative provides to students access to astronomical data, tools and expertise of the European Space Agency scientists, to help them in the analysis of their scientific results and understanding their impact in the current state-of-the-art scientific panorama. The CESAR Team offers teachers resources to prepare and support their students, as well as dedicated workshops, organised in collaboration between ESA and CTIF, to inspire them to use space as a context when teaching STEM subjects (Science, Technology, Engineering and Mathematics) at school.

2.1 The Space Science Experiences

Primary and secondary school teachers from ESA's Member States can register their class for a unique 2-hour session of real hands-on astronomy at ESAC. The students will be guided by ESA scientists through a group activity during which they will be assigned a 'mission' within a space science subjects that the teachers can choose at the time of registration (based on the students' age and curriculum). To accomplish their mission, the students will have to answer questions, use imagery taken by the CESAR telescopes and other ESA space missions, analyse the data, and communicate their results to their classmates (the Scientific Community). The teachers will be provided in advance with some explanations and resources to prepare their students to the experience itself, including a videoconference with a scientist (if technically feasible at the school). The main goal of these activities is to *learn-by-doing* and get used to work within teams. See some examples of these sessions are shown in Figure 1.

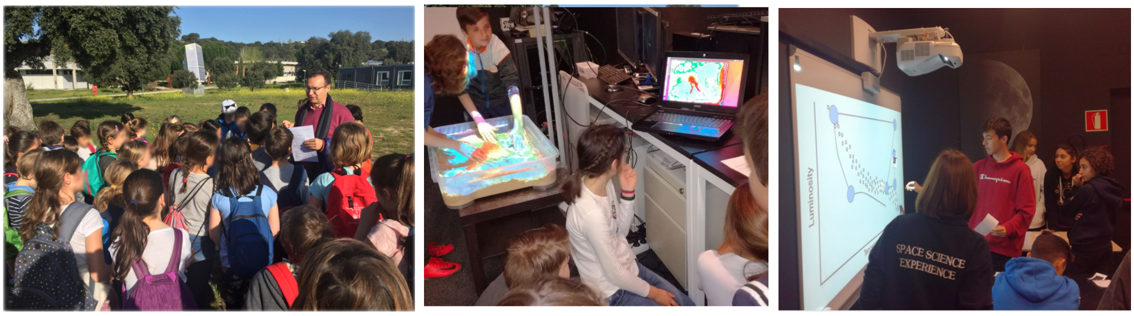

Figure 1: Pictures taken during Space Science Experiences organized by the CESAR Team.*(Credit: CESAR)*

2.2 Teacher Workshops

Every year, the CESAR Team makes a selection of special topics related to the state-of-the-art science, together with ESA scientists, and organise conferences and lectures to introduce Astronomy and Space Science to teacher. This should provide hints and inspiration to use space related subjects in their lessons, and make them interact with real space experts. Figure 2 shows the dynamics followed at them.

Figure 2: Pictures taken during some of the XII Teachers Workshops held by the CESAR Team.*(Credit: CESAR)*

3 The CESAR science cases

This is a series of classroom resources, containing teacher and student guides, real astronomical data and the astronomical tools, on astronomical topics ranging from the Sun to the Deep universe. These resources can be used by the teachers as a basis for their STEM lessons in the classroom. In Figure 4 it is indicated where in the CESAR website this material is available.

Figure 3: Location of the on-line science cases in the CESAR website.*Credit: CESAR*

4 CESAR observatories

The CESAR programme provides students with access to several ground-based observatories:

- Two solar telescopes (visible light), one mobile unit which is used to observe special astronomical events (see Section 5) and one permantly installed unit to observe the Sun every day, weather conditions permitting.]
- Two night telescopes (visible light)

These telescopes are all based at, or in the vicinity of, ESA's European Space Astronomy Centre (ESAC) near Madrid, Spain, where the control centre is located.

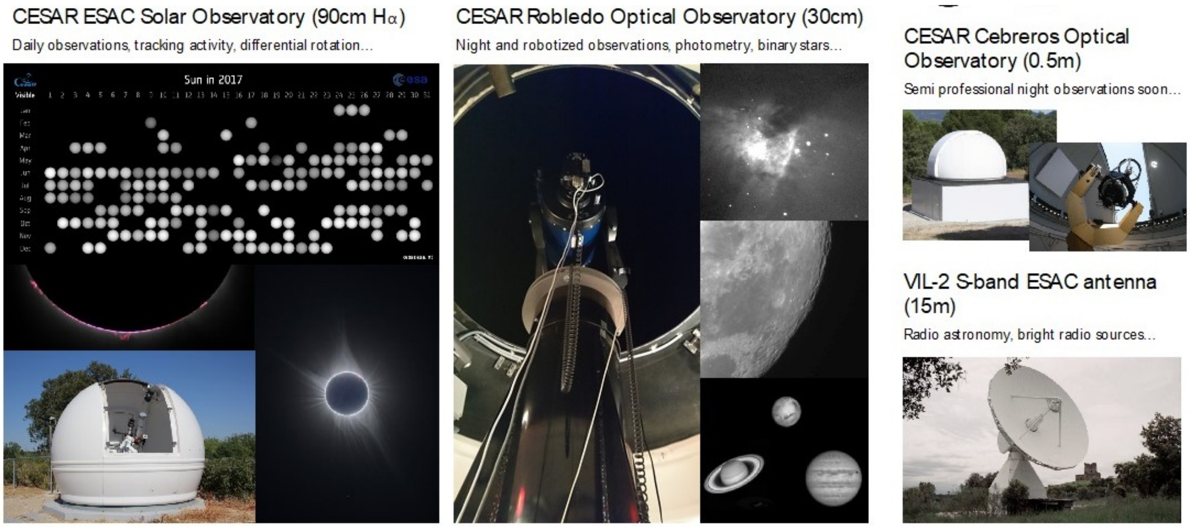

Figure 4: Summary of CESAR telescopes. *(Credit: Abel de Burgos).*

5 CESAR special events

The CESAR Team participates in Astronomical Events, such as the August 2017 Solar Eclipse, the 2016 Mercury transit and the 2012 Venus transit. Part of the team travels to locations from where the event is well visible while another part of the team is in charge of streaming the event to the internet providing also background lectures to the general public and answering questions.

Acknowledgments

Acknowledgments to all the CESAR Team members, Javier Ventura, Manuel Castillo, Miguel Perez Ayucar, David Cabezas, Rebecca Barnes, Abel de Burgos, Angel del Pino, Santa Martinez, ESASky Team among others. Most of the known and unknown contributors are listed here

Highlights on Spanish Astrophysics X, Proceedings of the XIII Scientific Meeting of the Spanish Astronomical Society held on July 16 – 20, 2018, in Salamanca, Spain. B. Montesinos, A. Asensio Ramos, F. Buitrago, R. Schödel, E. Villaver, S. Pérez-Hoyos, I. Ordóñez-Etxeberria (eds.), 2019

The Astronomy & Astrophysics Master Degree at Universidad Internacional de Valencia: the experience of a pioneer model.

Vicent Martinez-Badenes[1], Nestor Sanchez[1], Lorena Nieves-Seoane[1], and Pere Blay[1]

[1] Universidad Internacional de Valencia - VIU, C/Pintor Sorolla 21, 46002, Valencia, Spain.

Abstract

Founded in 2008, the Valencia International University (VIU) started its Master Degree in Astronomy & Astrophysics in 2011, becoming *Master Universitario Oficial* in 2013. This is the first completely online Master Degree in Astronomy in Spain. After having completed 6 editions as *Master Oficial*, it is mandatory to take a look back and compile the most relevant experiences of this challenging model.

1 Introduction

VIU is a young university, with barely 10 years of life. Founded as a public, on-line teaching institution, it became private during 2013. From its very beginning, the Master Degree in Astronomy & Astrophysics has been one of its key programs, being the only one in the Science & Technology area until 2016, when the Computer Engineering Degree started. The Sci & Tech area is now rapidly growing at VIU, with 1 Degree, and 8 Master Degrees (2 of them recognized as Master Universitario Oficial).

During these years, the Master Degree itself has undergone an evolution from its original model to the current one, with an increasing number of students and a higher ratio of international demand.

2 Organisation and methodology

As part of VIU, the Master Degree in Astronomy & Astrophysics is organised as a completely online learning process. The student is not required to be in Valencia (or any other place) at any moment, for all the learning steps (classes, exams, telescope observations, Master Thesis tutoring and defense) are done remotely.

With the aim of avoiding the coldness derived from the lack of a physical contact with professors and colleagues, online lessons are programmed in the so-called *e-presencial* way. In this method, lessons are planned to be live followed by the students, so discussion and interaction are feasable in real time in the digital platform. Anyway, lessons are recorded, allowing students not only to watch them as many times as required, but also to skip a live session when their schedules do not permit them to be connected at the time lessons are scheduled (tipically 8:00 PM CET/CEST). The feedback provided by the students shows them to have a high degree of satisfaction with this *e-presencial* mode.

The theoretical contents in the Master Degree are organised into 12 subjects (3 ECTS each), covering a wide sample of astronomical topics, and paying attention to both purely astrophysical and technical contents. Subjects are organised within the academic year in 3 periods of approximately 2 months and a half each, according to the following distribution:

Table 1: Distribution of theoretical subjects during the year

1st quarter	2nd quarter	3rd quarter
Classical Astronomy and Astronomical Instrumentation	Analysis of Astronomical Images	Optical and IR Astronomy
Solar System	Stellar Astrophysics	Radioastronomy
Exoplanets & Astrobiology	Extragalactic Astrophysics	High Energy Astrophysics
Databases: the Virtual Observatory	Cosmology	Communication of Astronomy

For each subject, 7 videoconferences are scheduled, each of them expected to last for 2 hours. Within these 7 sessions, there are an opening and closing session (used to present and synthesize the contents of the subject), 2 theoretical lessons, 2 sessions dedicated to guided activities and a Seminar generally used to introduce the frontier science currently going on each field. The final grade is calculated from the synchronous exam mark and the score of the activities asked by the professor.

As part of the formation, the students must undergo the complete process of an astronomical observation. Organised by themselves in groups with up to 6 students, they are expected to follow the same steps a professional astronomer would perform during a scientific research, here summarized as follows:

1. The students choose a workgroup based on the interest on working with a certain instrument or their schedules. Before that, they already know the telescopes and instrumentation available. A professor with observational experience is assigned to each group.

2. Once the group is formed, the students must look for at least one scientific case (choosing at least two is explicitly recommended). The students may ask their professor for advice

at any moment. The professor will, as well, help to fit the original idea to the technical capabilities of the telescope and the instrument. The final proposal (written using a professional template) is sent to the telescope operator 10 days before the observations. The proposal represents 30% of the final mark.

3. The observations are performed remotely for three consecutive nights.

4. Once the observations are done, the students must download the data to reduce and analyze them, following the professor instructions.

5. Finally, the results are presented and discussed in a memo, to be graded by the professor. The memo has a weight of 70% in the final mark.

During the last editions of the degree, the observations have been performed using the Observatorio de Aras de los Olmos (Observatori Astronòmic de la Universitat de València), the T150 telescope at Observatorio de Sierra Nevada (IAA-CSIC) and the IAC80 at Observatorio del Teide (IAC).

The year is completed with the Master Degree Thesis or *Trabajo Fin de Master* (TFM), with an academic load of 18 ECTS. The TFMs are supervised by professional astronomers, either related to the University or not, who send their proposals. Students are also encouraged to suggest a specific project if they contact an advisor by themselves. The TFM is finally presented to a panel of 3 astronomers, who grade them. The ratio of TFMs that, with some extra work, become published in peer-reviewed journals is increasing year after year.

Since 2017, there are two editions of the Master per year, starting in April and October, with the number of students rising up to 90 during 2018.

3 Staff and student profile

The subjects in the 2 editions of the Master Degree are taught by 4 full-time professors and 9 professors which are developing their scientific careers out of VIU. The staff is completed by the advisors and operators associated to the observations and the TFM advisors (42 during 2017-18 academic year), most of them collaborators from other institutions. All but one professor have a PhD in astronomy, and so the TFM advisors have.

The student profile is slightly different from the on-site alumni. Apart from showing a higher average age, the ratio of them aiming to start a research career with a PhD is generally low, with only 3 to 5 students per edition. Apart from this, there are two main reasons that lead the students to start the Master Degree. One is purely professional, with technic, high-profile workers, from fields related to astronomy such as aerospace industry, willing for an upgrade in their capabilities and professional prospects. The other is the mere passion for astronomy. Even considering that PhD candidates are a low fraction of the students, we already have some TFM advisors that got their PhD after completing the Master Degree on its first editions. The ratio of students from Latin America is increasing, being around 1/3 of the total number.

4 Conclusions

The increasing number of students in the VIU Master Degree in Astronomy & Astrophysics shows that there was a need of an online option in this field of education, with the feedback from the students being usually very good. It becomes clear that this Master Degree does not collide or compete with the already existing, but just complete the scene, offering an option for those students who cannot follow an onsite course for any reason. The response of the Spanish astronomy community is being very positive, making the Master Degree possible.

Highlights on Spanish Astrophysics X, Proceedings of the XIII Scientific Meeting of the Spanish Astronomical Society held on July 16 – 20, 2018, in Salamanca, Spain. B. Montesinos, A. Asensio Ramos, F. Buitrago, R. Schödel, E. Villaver, S. Pérez-Hoyos, I. Ordóñez-Etxeberria (eds.), 2019

Gaia mission outreach activities.

Eduard Masana[1],

[1] Institut de Ciències del Cosmos (ICCUB), Universitat de Barcelona (IEEC-UB). C/ Martí i Franquès, 1. E08028 Barcelona, Spain

Abstract

Gaia is an European Space Agency (ESA) mission in charge of charting a three-dimensional map of the Milky Way. In addition to its huge impact on all fields of Astrophysics that is already taken place, Gaia is a very good opportunity to do astronomical outreach activities for the general public. In this sense, we have prepared, together with other people from the Gaia community, different materials and activities to bring Gaia to a wide audience, from schools to amateur astronomers. In this paper we present some of these materials.

1 Introduction

Gaia is an European Space Agency (ESA) mission in charge of charting a three-dimensional map of our Galaxy, the Milky Way. In doing so, it provides a census of about one and a half billion stars, which amounts to about 1.5 per cent of the Galactic stellar population. The second Gaia Data Release (Gaia DR2) was published on April 2018.

From the beginning of Gaia, outreach and educational activities around the mission has been considered as key activities. Gaia is a great opportunity to bring science in general and Astronomy in particular to the students and general public. The wide range of topics covered by the mission allows to explain to the public not only the technical aspects of the mission, but also such diverse topics as the Solar System history, the concept of parallax, the distance ladder or the General Relativity Theory. In the next sections we show some of the outreach material and activities developed to this aim.

2 *Gaiaverse*

The *Gaiaverse* portal (`http://gaiverse.eu`) is devoted to the outreach of Gaia in the framework of the GENIUS project, an European project (finished in 2018) whose aim was to contribute to the design, implementation and operation of the Gaia archive system. GENIUS

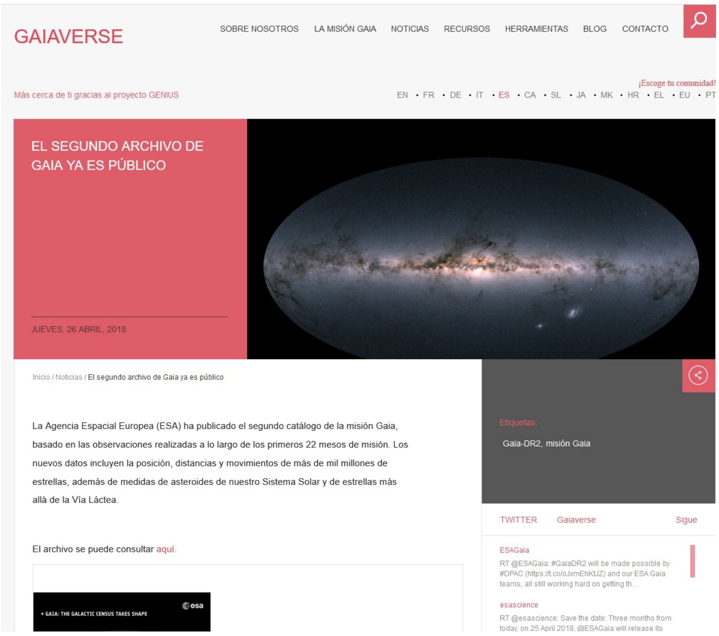

Figure 1: The *Gaiaverse* portal.

aims at becoming a hub of Gaia's spreading knowledge by collecting all kind of outreach materials such as presentations, videos, posters, brochures, tools, news... which are all available through this portal, *Gaiaverse*.

The portal is translated to eleven languages (English, French, German, Italian, Spanish, Catalan, Slovak, Japanese, Macedonian, Croatian and Greek). A version in Euskara is currently under development. The contents in each languages could not be exactly the same. For instance, some local news could be present in only one version of the portal. In this sense, we prefer to speak of "eleven communities" more than "eleven languages".

Gaiaverse is addressed to the general public. It is complementary to the official ESA's portal (`http://www.esa.int/Our_Activities/Space_Science/Gaia`). It has several sections, from the latest news of the mission, to a repository of outreach material. The portal is administrated by the Universitat de Barcelona (UB) and the Consorci de Serveis Universitaris de Catalunya (CSUC).

3 One billion eyes for a one billion stars

The exhibition *One billion eyes for a one billion stars* was originally designed and created in 2013 at the Universitat de Barcelona. At the beginning it was composed by 14 posters, covering both the scientific and the technical aspects of the Gaia mission. With the release of the first (September 2016) and second (April 2018) Gaia catalogs, new posters were added to explain the contents of the catalogs and the first scientific results of the mission.

Currently the exhibition is composed of 20 posters. Apart from the whole exhibition,

Figure 2: One of the posters of the *One billion eyes for a one billion stars* exhibition.

two possibles itineraries with less posters are available, one of them focused in the technical aspects behind the mission and other focused in its scientific aspects. The exhibition is translated to English, Spanish, Catalan and German. A on-line version is available at `http://www.am.ub.edu/twiki/bin/view/ServiAstro/ExpoGaia`.

4 Gaia Data Release 2: A guide for scientists

This set of 15 videos has been created by Stefan Jordan, from the Astronomisches Rechen-Institut (ZAH, Universität Heidelberg) and Klaus Jäger. Each video covers a different topic of the mission, explained by an specialist in the field, all of them directly related to Gaia consortium. The videos are addressed to people interested on the contents of the Gaia DR2 and how to use it. They are available at `https://www.cosmos.esa.int/web/gaia/guide-to-scientists`.

5 Gaia Sky

Gaia Sky is a real-time, 3D, astronomy visualisation software that runs on Windows, Linux and macOS. It is developed in the Gaia group of the Astronomisches Rechen-Institut (ZAH, Universität Heidelberg). Gaia Sky is an open source project. It offers the possibility to generate videos for outreach, showing for instance the proper motion of the stars or allowing to travel across the Milky Way. The current version uses the Gaia-DR2 data. For more information, visit `https://zah.uni-heidelberg.de/institutes/ari/gaia/outreach/gaiasky`.

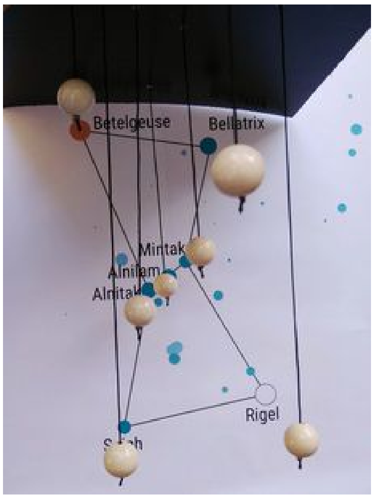

Figure 3: 3D model of the Orion constellation.

6 Other material and activities

- Bookmark - rule with the distance scale of the Universe.
- Memory game with 20 pairs of images related to the Gaia mission.
- 3D constellations. This activity for the schools allows to built a 3D model of the Orion constellation to emphatize the different distances of the stars of the constellation. Also allows to change the point of view of the observer. See figure 3.

Acknowledgments

This work was supported by the MINECO (Spanish Ministry of Economy) through grant ESP2016-80079-C2-1-R (MINECO/FEDER, UE) and MDM-2014-0369 of ICCUB (Unidad de Excelencia 'María de Maeztu').

Highlights on Spanish Astrophysics X, Proceedings of the XIII Scientific Meeting of the Spanish Astronomical Society held on July 16 – 20, 2018, in Salamanca, Spain. B. Montesinos, A. Asensio Ramos, F. Buitrago, R. Schödel, E. Villaver, S. Pérez-Hoyos, I. Ordóñez-Etxeberria (eds.), 2019

A Tactile Voyage Through the Solar System: Venus.

Amelia Ortiz-Gil[1], Jordi Burguet-Castell[1], Enrique Pérez-Montero[2], Fernando Ballesteros[1], Lina Canas[3], Alberto Fernández-Soto[4], Andrés Gálvez[5], Thilina Heenatigala[6], Mariana Lanzara[1], M. Jesús Moya,[1], Mónica Pallardó[1], and João Retrê[7]

[1] University of Valencia Astronomical Observatory
[2] Instituto de Astrofísica de Andalucía-CSIC
[3] National Astronomical Observatory of Japan
[4] Instituto de Física de Cantabria - CSIC - UC
[5] European Space Agency, ESA-HQ
[6] NUCLIO
[7] Instituto de Astrofísica e Ciências do Espaco

Abstract

"A Touch of Venus" is a project funded by the International Astronomical Union's Office of Astronomy for Development (OAD) with the goal of developing educational tactile resources focused on the planet Venus. The project has developed a three-dimensional (3D) tactile model of Venus and a series of related educational activities for the general public, including people with low vision and blind. The model was created from the topographic map obtained by NASA's Magellan spacecraft by using a novel software specifically developed for this project (Mapelia). The educational activities to use the tactile globe will be freely downloadable from the project's website and from IAU's online peer review educational repository AstroEDU. The funding allowed the project to print 20 globes and activity books that will be sent to educators/science communicators around the world that work with groups of blind persons mainly in developing countries or underserved communities. Social media will be used to reach to a wider community and will allow for the exchange of ideas and experiences among all those who wish to be involved in this project of tactile astronomy.

1 Introduction

The project "A Touch of the Universe" ([4]) was funded in 2013 by the IAU's Office of Astronomy for Development (OAD) with the goal of developing a kit of educational tactile astronomy materials that educators/science communicators could use with the general public, including blind or visually impaired persons. A total of 30 kits were distributed among educators and teachers in underdeveloped countries in the Americas, Asia and Africa. Among the materials included in the kit there was a tactile globe of the Moon ([7]) and a half-sphere with some relevant constellations of the northern sky engraved on it that was part of the planetarium show for the blind "The sky in your hands" ([2], [8]). The project was very successful and we have received many requests for the kit materials. We could only provide them in digital formats to be downloaded, though, as we lacked any further funds to print more kits.

The resources in the kit of "A Touch of the Universe" were developed according to the Universal Design for Learning (UDL, see [9] for example), a learning framework which allows to reach to the general public as well as to audiences which might be regarded as "special" because they have some disability. It has been shown that everybody has a preferred style of learning (some remember better what they see, others what they hear or what they touch) and therefore, everybody is more or less able under the different styles of learning. We believe that these principles of the UDL should be applied in the teaching and communication of astronomy ([10]), and therefore we implemented them in the project "A Touch of the Universe" ([5]).

In 2017 we applied again for funding to the OAD for the project "A Touch of Venus" which intends to be an addition to the materials that were part of the initial kit of "A Touch of the Universe". In this case we intended to build a 3D tactile model of the planet Venus supporting the users with a related activity book and some video tutorials. A first 3D test model was produced with the financial support of ESA ([3])and tested at the SpaceIn event in ESA/ESAC in June 2017 ([11]).

2 From the 2D map to the 3D globe

We started with the topographical map that was created from radar data obtained by NASA's Magellan space probe during its exploration from orbit of the planet Venus between 1990 and 1994 (Fig. 1). Magellan employed a radar technique to create topographical maps of the surface below the thick atmosphere that makes it impossible to probe the surface in optical wavelengths from orbit.

The next step was to enhance the contrast of the most relevant features and to smooth out the smallest structures to simplify the model and get rid of details that could lead to confusion when touching the globe without seeing it.

When the image was ready for our purposes we processed it with Mapelia[6], a software which produces digital 3D tactile globes from 2D maps in an easy and fast way. It works with many different map projections and the output is a ready-to-print 3D file in several

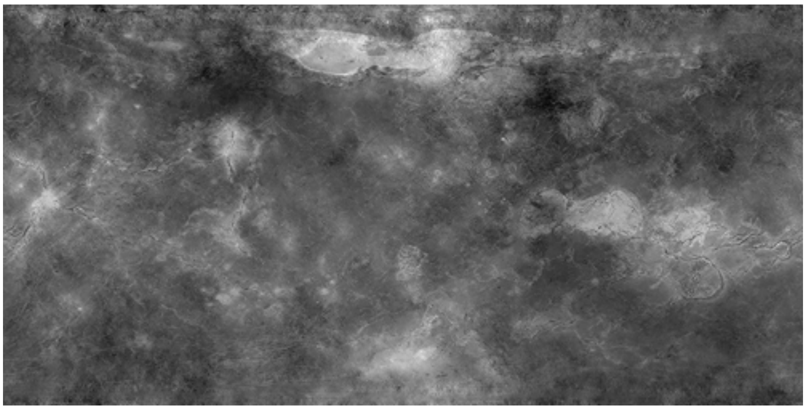

Figure 1: Radar map of Venus surface in grayscale. Source: NASA.

digital formats. Examples of the 3D files created by Mapelia are shown in Fig. 2, and can be downloaded from the "A Touch of the Universe" website.

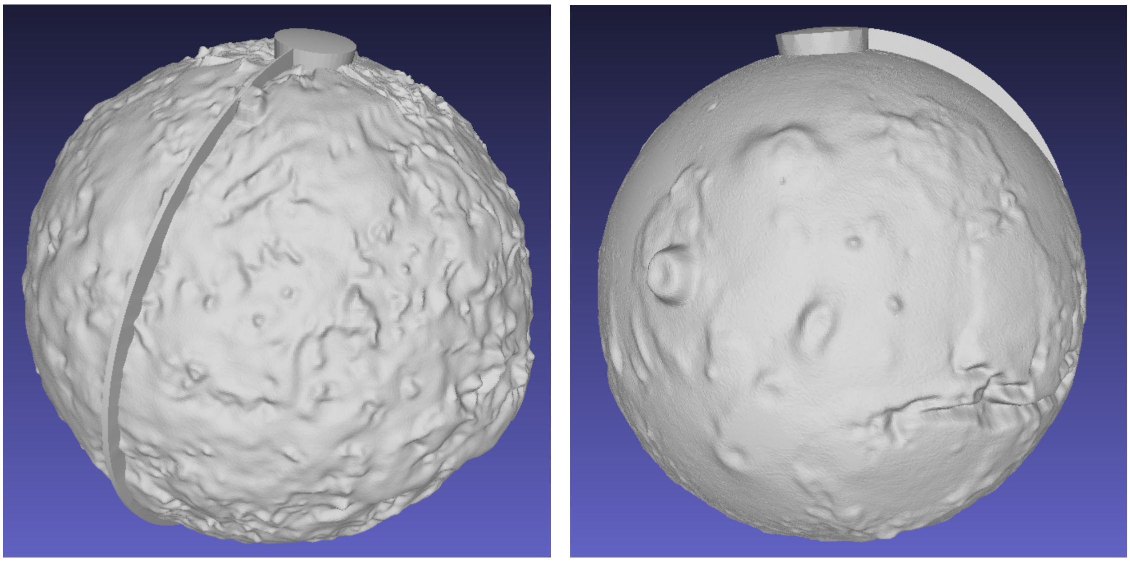

Figure 2: 3D rendered tactile models of Venus (left) and Mars (right) obtained with Mapelia. Credit: A. Ortiz-Gil & J. Burguet-Castell.

3 Activity book

A series of educational activities to be carried out with the Venus globe have been developed teaching the user how to identify craters, volcanos, mountains, plains and highlands by touching the model. Other activities reflect on Venus retrograde motion, phases and global warming. Finally one activity has been devoted to the nomenclature of Venus features, which are mostly named after female characters, both real and fictional or legendary. In the activity we highlight the particular achievements of some of them.

The activity book has been printed in Braille and large fonts to make it readable for blind, low-vision and non-blind users.

These activities will be expanded to fit the format of the IAU's educational repository AstroEDU ([1]). Once submitted they will be peer-reviewed and the final approved versions will be published at the AstroEDU as well as at the "A Touch of the Universe" website.

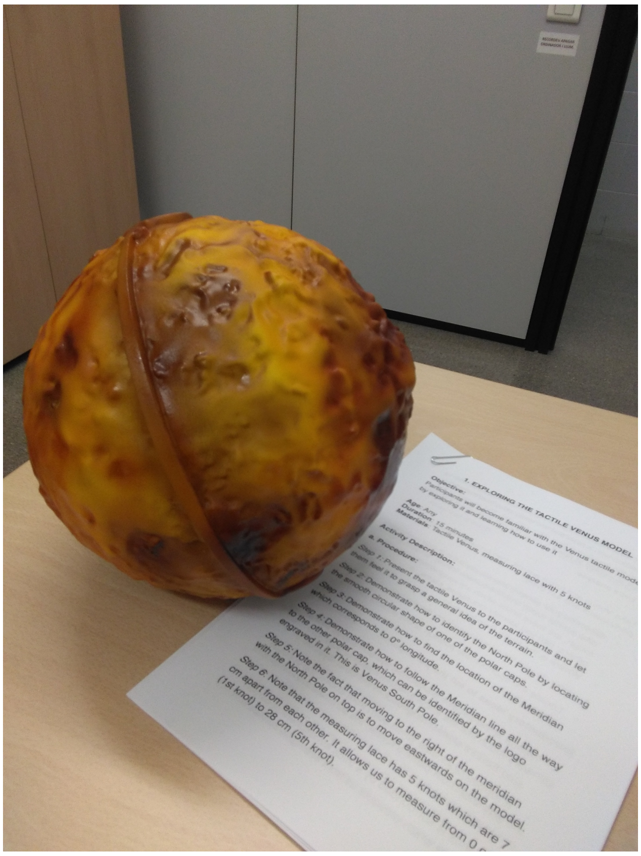

Figure 3: Venus 3D printed globe with the plain text version of the activity book. Credit: A. Ortiz-Gil.

4 Reaching out to the community

As we did with the "A Touch of the Universe" kits, we now intend to print 20 Venus globes and activity books that will be sent to educators/science communicators around the world who work with visually impaired or blind persons mainly in developing countries or underserved communities.

In order to reach a larger community than only those 20 teachers, we will publish the 3D model of Venus (already available) and the final peer-reviewed activity book on the project's website ([4]). Social media (e.g. Facebook group) will allow the exchange of ideas and experiences among all those who would like to be part of the project. A video tutorial will explain how to use the resources, give some hints and ideas about the activities and serve as the basis for online training sessions that will be offered to the recipients of the materials.

Acknowledgments

This project has been possible thanks to the grant scheme of the IAU's Office of Astronomy for Development (OAD). Amelia Ortiz-Gil, Fernando Ballesteros and Alberto Fernández-Soto were supported by the Spanish Ministry of Science project AYA2016-81065-C2-2.

References

[1] AstroEDU, Peer-reviewed Astronomy Education Activities `http://astroedu.iau.org/`

[2] Canas, L., Borges, I., & Ortiz-Gil, A. 2013. Proceedings of the European Planetary Science Congress 2013, 2013EPSC....8..716C

[3] Gálvez, A., Ballesteros, F., García-Frank, A., Gil, S., Ortiz-Gil, A., Gómez-Heras, M., Martínez-Frías, J., Parro, L. M., Parro, V., Pérez-Montero, E., Raposo, V. & Vaquerizo, J. A. 2017. EPSC 2017 - 905-2, Vol. 11.

[4] Project "A Touch of the Universe" website, Ortiz-Gil, A. 2013, `https://astrokit.uv.es`

[5] Ortiz-Gil, A., Ballesteros, F., Espinós, H., Fernández-Soto, A., Lanzara, M., Moya, M. J., & Navarro, J. 2015, Highlights of Spanish Astrophysics VIII, ISBN 978-84-606-8760-3. A. J. Cenarro, F. Figueras, C. Hernández-Monteagudo, J. Trujillo Bueno, and L. Valdivielso (eds.), p. 880-888

[6] Ortiz-Gil, A., & Burguet-Castell, J. 2018, Journal of Open Source Software, 3(25),660

[7] Ortiz-Gil, A. 2018. Proceedings of the European Planetary Science Congress 2018, in press

[8] Pérez-Montero, E.; García Gómez-Caro, E.; Sánchez Molina, Y.; Ortiz-Gil, A.; López de Lacalle, S.; Tamayo, A. 2017, Highlights on Spanish Astrophysics IX, ISBN 978-84-617-8931-3. S. Arribas, A. Alonso-Herrero, F. Figueras, C. Hernández-Monteagudo, A. Sánchez-Lavega, S. Pérez-Hoyos (eds.), p. 742-747

[9] Rose, DH, & Meyer, A. 2002. "Teaching Every Student in the Digital Age: Universal Design for Learning", Alexandria, VA: ASCD

[10] "Space Science Is for Everyone: Lessons from the Filed", 2008. Runyon, C., Hall, C., Heitger, C., Gonzales, L. (eds.), `https://www.nasa.gov/pdf/259240main_Space_Science_Is_for_Everyone.pdf`

[11] SpaceIn meeting, 2017. `http://www.esa.int/esl/ESA_in_your_country/Spain/SpaceIN_en_ESAC`

Highlights on Spanish Astrophysics X, Proceedings of the XIII Scientific Meeting of the Spanish Astronomical Society held on July 16 – 20, 2018, in Salamanca, Spain. B. Montesinos, A. Asensio Ramos, F. Buitrago, R. Schödel, E. Villaver, S. Pérez-Hoyos, I. Ordóñez-Etxeberria (eds.), 2019

"May infinity be left without stars". Dissemination of Astronomy from planetariums and science museums.

Inés Rodríguez Hidalgo

Museo de la Ciencia de Valladolid, Avda. de Salamanca, 59, 47014, Valladolid (Spain)
(irh@museocienciavalladolid.es)

Abstract

The title (borrowed from a famous *bolero*) is not so exaggerated when we remember that more than twenty five planetariums, scattered about the Spanish territory, do "ex officio" the magic of making the stars accessible to the public. They are unique spaces that simulate, in a very realistic way, the celestial vault as seen from different places and dates, giving back to their visitors the emotion of gazing at a night sky free of light pollution. They can also project fulldome programs of astronomical content. Therefore, planetariums turn into valuable tools for the teaching and dissemination of Astronomy.
At the same time, more than twenty Spanish science museums, with or without planetarium, bring Astronomy closer to the public of all ages and backgrounds through numerous and varied activities.
This paper aims to be a meeting between the Spanish professional astronomers and those essential allies in the dissemination of Astronomy. The last ones offer intelligent fun and unforgettable experiences, transmitting basic knowledge and showcasing the latest advances. They definitely contribute to promote vocations and to educate society in positive attitudes towards Astronomy and Science in general.

1 Introduction

The history of modern planetariums starts in 1919, when Walther Bauersfeld, chief design engineer and later director of Carl Zeiss, had the idea of projecting the celestial vault in a dark room. The first shows of the optical star projector Model I took place in a dome set up on the roof of the Zeiss factory in Jena. In 1925, the Deutsches Museum in Munich was the venue for the world premiere of the so-called "Wonder of Jena".

The physicist Frank Oppenheimer (brother of the Project Manhattan director) created in 1969 the *Exploratorium* of San Francisco, the first interactive science musem. It is a center for non-formal learning, considered as the prototype for participatory museums.

Following the example of these pioneering centers, the planetariums and science museums proliferated all over the world and turned into modals of the astronomical and scientific outreach, addressed to the great public. Let's meet these invaluable resources.

2 Essential allies in the dissemination of Astronomy

2.1 Planetariums: The stars within reach of the public

Spanish planetariums have a wide variety of sizes (domes from 5 to 20 m), setups (from 1 eyefish projector to several ones, in different settings), capacities (from about 25 to 245 seats), and ownerships (private or public). There are veteran planetariums (since the 70's of the last century) or very recent (the last one of 2014). Some of them are within science museums, observatories or schools, while some others are isolated. In addition to the fixed installations, there are portable planetariums, which can easily be moved to other centers, star partys, villages or cities, etc. From the technical point of view, the first planetariums had opto-mechanical projection systems. They have later been replaced or complemented by digital systems, and some planetariums currently benefit from the best of each option, with hybrid setups.

All planetariums possess the technical resources to simulate in a very realistic way the celestial vault as seen from different places and dates. On the starry night, free of light pollution, it is possible to superimpose circles, axes, coordinates, orbits, lines, drawings, images, texts, animations, videos... They finally allow to project spectacular fulldome shows of astronomical content, thus bringing the stars within reach of the public.

2.2 Science museums: Non-formal learning, educating in attitudes

According to the European Commission, non-formal learning is embedded in planned activities not always explicitly designated as learning (in terms of objectives, time or support), but which contains an important learning element. It is intentional from the learner's point of view, and can take place in museums, science camps/clubs, etc. Besides their vocation as centers de information, formation, and education in scientific contents, the interactive museums of science especially aim to educate the public in positive attitudes towards the science.

Activities of astronomical outreach organized by the science museums are very numerous and varied: popular talks and cycles of talks, courses, meetings, workshops, etc.; permanent or temporary exhibitions, some of them interactive; workshops, astronomical camps, contests, shows...; astronomical observations, often in collaboration with amateur astronomers' associations. Moreover, these centers participate in the IYA2009, World Space Week, anniversaries, astronomical ephemerides...

3 Census, geographical distribution, and overview

The census of planetariums and science museums engaged in activities of dissemination of Astronomy is:

- ≥ 6 fixed and isolated (not in science museums or observatories) planetariums
- ≥ 3 portable planetariums
- ≥ 4 planetariums integrated in astronomical observatories
- 8 science museums without planetarium
- 14 science museums with planetarium

Some numbers are approximate, provided there are other less known planetariums whose public activity and information I have not confirmed. (See the list in the Appendix, and further information in this link).

Figure 1: Location of the above mentioned centers, according to the following code: **P**: Fixed and isolated (not in science museums or observatories) planetarium; **pP**: Portable Planetarium; **OP**: Planetarium in Astronomical Observatory; **M**: Science Museum without planetarium; **MP**: Planetarium in Science Museum

All the centers appearing in Table 1 organize activities of dissemination of Astronomy for general public. The information has been provided by their own staffs.

In this link a table with information of all Spanish planetariums ans science museums engaged in astronomical activities can be found.

Every center in this list carries out in its environment an irreplaceable activity, and thus deserves institutional and economic support, and the appreciation of the public. Though not intended to be exhaustive, let me remark some of them:

The first planetariums in Spain were those associated with naval schools and naval museums, but the first one for astronomical outreach was the Planetari Municipal of Barcelona (1973), which still continues offering educational activities for public from 2 years on. In 1981, there was the opening of the planetarium of the Science Museum of Barcelona, transformed into CosmoCaixa in 2004. It is the only one in Europe offering the "accessibility pack": audio-description, subtitles, video in sign language, and system of inductive loop. The planetarium of the Casa de las Ciencias (Coruña), the first Spanish interactive science museum of public ownership, was opened in 1985. It offers daily live shows, produces numerous planetarium programs, has created the exhibition "Astronomy as they're telling you", and much more.

The Planetarium of Pamplona (1993) is the biggest one in Spain, and has gained a well-deserved prestige due to its live sessions for students, and own production shows. They also organize exhibitions, courses, popular talks, workshops, educational activities, meetings, astronomical observations, etc. The second one in size is the Planetarium of Madrid, widely renowned and popular. Opened in 1986, and re-opend in 2017 after a deep technical upgrading, it has produced numerous shows for all kinds of public, in which careful attention has been paid to the scripts and music.

In the 90's, the planetariums of Castellón, La Laguna, Santander, Barcelona (Museu Maritím), Granada, Murcia, Valencia, Las Palmas de Gran Canaria, Cuenca and Málaga were created. Among them, it stands out the Science and Cosmos Museum by its close link to the Instituto de Astrofísica de Canarias. Besides live and own production shows, it organizes popular talks, Astronomy courses for general public, university students and teachers, astronomical camps, astronomical contemporary dance, Cosmos-cinema, etc. The Parque de las Ciencias de Granada is an enormous complex with nothing less than 5 planetariums, observatory and other facilities dedicated to the Astronomy.

The first 15 years of the 21st century have seen the birth of new planetariums and science museums. The one of Valladolid (2003) was of the first ones in Europe with digital system, and of the first ones in the world in using LED's projectors after its technical updating in 2015.

Among the centers without planetarium, San Pedro Cultural, a restored Romanesque church, mainly aimed to the dissemination of Astronomy, stands out by its originality. The planetariums within astronomical observatories offer singular facilities as opening ceilings or projections of images observed through the telescopes.

4 Milestones, *the name of which we will have desire to call to mind*

In 2016, the fourth centenary of Miguel de Cervantes' death was celebrated. The beginning of El Quijote, *"In a village of La Mancha, the name of which I have no desire to call to mind"...*, serves us to introduce some milestones of the dissemination of Astronomy driven by Spanish planetariums and science museums.

Estrella Cervantes, the project of the Planetarium of Pamplona, SEA and the Cervantes Institute, winned the IAU contest "NameExoWorlds" with a 69% of all the registered votes. As a consequence, the system mu Arae received the names of Cervantes for the star and Quijote, Sancho, Dulcinea and Rocinante for its four planets. In addition, the Science Museum of Castilla-La Mancha, the Planetarium of Pamplona and the Impulsa CLM Foundation have produced a fulldome planetarium show offered to all the interested centers under CC license of free culture.

Several years before, the planetariums of Pamplona, Coruña and Cuenca created the fulldome show *Evolution* to commemorate the Darwin Year and the International Year of Astronomy 2009. It was the first great production in digital format, projected in practically all the Spanish planetariums. The Science Museum of Valladolid made a subtitled and audio-described version, accessible to visually and hearing impaired persons. Examples of other spectacular fulldome shows, produced with the collaboration of different planetariums, are *Starry night at the museum*, *Energy for life* or the recent *Night is necessary.*

Most of planetariums and science museums has celebrated relevant anniversaries such as 20 and 25 years of HST, 10 years of GTC, 50 years of ESO, 50 years of the Moon landing, IYA2009, World Space Week... and astronomical events such as solar or lunar eclipses (10000! persons attended the Planetarium of Madrid to observe the 2005 solar eclipse), Mercury or Venus transits, meteor showers, etc., with a rich variety of activities. Astronomical observations are carried out in observatories, planetariums and museums, often with the collaboration of amateur astronomers' associations.

Let us emphasize the training courses addressed to general public, students, and teachers, who thus turn into new transmitters of astronomical information and knowledge. Some examples are the 20 editions of the Introduction to Astronomy course organized by the Planetarium of Castellón, the "astro-tourism" course of the Centro Astronḿico Aragonés or the starting of the ESERO Spain office of ESA, aimed to the training and elaboration of didactic material for teachers, by the Parque de las Ciencias.

Last, but not least, here is a brief list of other original initiatives:

- *Meteorite, a rock of the space*, the first planetarium show with puppets (Science and Cosmos Museum)
- Evenings of remote observation with the IAC80 telescope (several museums)
- *All-night planetarium*, 24 hours of projections (Science Museum of Valladolid)
- Dinners or concerts under the stars (Madrid, Montsec, Tiedra, San Sebastián...)

- Popular talks given by astronauts Pedro Duque and Scott Kelly (Madrid), cosmonauts Valentina Tereshkova or Aleksandr Lazutkin (Valladolid), the Discovery's crew or astronaut André Cuiper in the ISS (Granada), etc.

- Exhibition *Mars, the conquest of a dream* (Valencia, with Fundación Telefónica, INTA, ESA, INAF)

- *The Galaxy Garden*, by the artist Jon Lomberg, consists of an outdoor scale model of the Milky Way, mapped in living plants and flowers and based on current astrophysical data. In Spain, it is located in the Yamaguchi park around the Planetarium of Pamplona. Hopefully, it will soon be replicated in other places.

5 Conclusions

Let us remark the main strengths of planetariums and science museums as powerful actors for the dissemination of Astronomy:

- They are spaces valued and estimated by the citizenship

- satisfy a social demand

- offer information and non-formal education in Astronomy for publics of all ages and trainings

- are excellent showcases of the astronomical advances

- return to the public the enjoyment of the starry night

- educate in the respect and defense of the dark sky, in the appreciation and support to the astronomical research

- have staffs full of professionalism and enthusiasm that master the technical, explanatory, didactic and communicative resources

- bring together a variety of collaborations: with universities, research centers, observatories, associations of amateur astronomers, researchers, etc.

- are real crowd-pullers, offering their platforms of dissemination and advertising, especially trough social networks

I hope that this rendezvous of professional astronomers with the Spanish planetariums and science museums will lead to an increasing and more fruitful collaboration.

Appendix

Links of interest:

- Sociedad Española de Astronomía (SEA): Outreach
- Liga Iberoamericana de Astronomía (LIADA)
- World Planetariums Database

As mentioned in Sect. 3, other planetariums are itemized below:

- Parque Aldea Nova (San Estevo de Sedes, Narón, Coruña)
- Planetario - Centro Cultural Jose María Gutiérrez Romero (El Limonar, Málaga)
- Escuela Superior de la Marina Civil (Portugalete, Vizcaya)
- Planetario de Úbeda (Úbeda, Jaén)
- Museu de Ciencies Naturals de Granollers (Granollers, Barcelona)
- Facultad de Naútica de Barcelona (Barcelona)
- Instituto Politécnico Marítimo Pesquero del Mediterráneo (Alicante)
- Planetario de la Base Aérea de Matacán (Salamanca)
- IES Náutico Pesquero de Pasaia (Pasaia, San Sebastián)
- Kosmos Lanzarote (Arrecife, Lanzarote)
- Universidad de Oviedo (Gijón, Oviedo)
- Instituto Marítimo Pesqueiro do Atlántico (Vigo, Pontevedra)
- Universidad de Cádiz (Puerto Real, Cádiz)
- Castillo de Hornos de Segura (Hornos de Segura, Jaén)
- Universidad de la Laguna (La Laguna, Tenerife)
- El Parque de la Vida (La Mata, Valdés, Asturias)

Finally, there are in Spain around 30 astronomical observatories not listed before. Some of them are professional, while other are of public or private ownership, or managed by amateur astronomers' associations. Many of them organize astronomical activities open to the public, and frequently collaborate with science museums and planetariums. References can be found in the links of interest.

Acknowledgments

I wish to make public acknowledgement of the excellent work of all the planetariums and science museums' teams that I have the honor and the responsibility of representing.

Highlights on Spanish Astrophysics X, Proceedings of the XIII Scientific Meeting of the Spanish Astronomical Society held on July 16 – 20, 2018, in Salamanca, Spain. B. Montesinos, A. Asensio Ramos, F. Buitrago, R. Schödel, E. Villaver, S. Pérez-Hoyos, I. Ordóñez-Etxeberria (eds.), 2019

When Astrochemistry is a Journey.

Natalia Ruiz Zelmanovitch[1], and Marcelo Castellanos[1]

[1] Grupo de Astrofísica Molecular, Departamento de procesos atómicos, moleculares y en superficies del Instituto de Física Fundamental (IFF), Consejo Superior de Investigaciones Científicas (CSIC), c/Serrano, 123, 28006, Madrid (Spain)
natalia.r.zelmanovitch@iff.csic.es; marcelo.castellanos@iff.csic.es

Abstract

The project "NANOCOSMOS, Gas and dust from the Stars to the Laboratory: Exploring the Nanocosmos", funded by the European Research Council (ERC) with a Synergy Grant, obtained, in the call for 2016, funds of the Spanish Foundation for Science and technology (FECYT) in order to produce a documentary about the project, entitled "Nanocosmos: a journey to the small". In this presentation we will talk about the experience that resulted in this audio-visual project.

1 Introduction

"Gas and dust, from the Stars to the Laboratory: Exploring the Nanocosmos" is the name of a project funded by the European Research Council (ERC) through a Synergy Grant with 15 million Euros. The group comprises three teams (two in Spain and one in France)[1]. The main goal of the project is to go in-depth on the understanding of how dust grains form in the envelopes of evolved sun-like stars. In order to do so, and besides observations, models and other developments, this Astrochemistry project has successfully developed an experimental set-up, called the Stardust machine, in the ICMM-CSIC (Madrid, Spain) whose goal is to reproduce those processes in an ultra-high vacuum environment. The importance of publishing scientific results based on NANOCOSMOS in the scientific literature goes without saying, but it is also important and a stated NANOCOSMOS objective to disseminate the achievements of the team and its scientific and technological results to a wider audience. In this presentation we will discuss the tools we are using to spread them to the society, from the

[1] In Spain, the main groups are at the Instituto de Ciencia de Materiales de Madrid (CSIC) and Instituto de Física Fundamental (CSIC), and in France at the Institut de Recherche en Astrophysique et Planetologie (IRAP).

traditional webpages to an ERC_Comic, going deep in the elaboration of the documentary "NANOCOSMOS: Un viaje a lo pequeño."

2 Outreach in NANOCOSMOS

NANOCOSMOS has a "Communication team", composed by the Manager and the Public Information Officer (PIO). They are the contact points for the NANOCOSMOS community to spread all the information created by the project teams. Once the scientist/engineer has a result (accepted paper) or considers any advance interesting to a wider audience, the team, through the Principal Investigator (PI), should bring this to the "Communication team" attention that will be in charge of developing the information.

NANOCOSMOS has a web page to publish and disseminate news and releases based on scientific results. This is a key tool to raise the image of the project and improve dissemination to specialists, potential users of the technologies being developed, politicians and public funding authorities, as well as the general public. Also social media accounts facebook and twitter are very useful to spread all the news and information generated in the website.

The process begins with the accepted paper: from that scientific result we can obtain several products as press releases (for the mass media), outreach articles (to be published in the NANOCOSMOS website or in the Naukas web page, the main site for science outreach in Spanish), notes for the blog, social media posts (twitter and/or facebook), interviews (written or in video for the youtube NANOCOSMOS channel), videos and animations explaining those results, visits to the different machines where the experiments take place, talks, etc. We have also collaborated in radio programs talking about science.

Figure 1: Promotion of the "NANOCOSMOS: Un viaje a lo pequeño" road movie. Credit: LuzLux.

3 "NANOCOSMOS: Un viaje a lo pequeño", the documentary

"NANOCOSMOS: Un viaje a lo pequeño" is a 40-minute road movie about laboratory astrophysics supported by FECYT, the Spanish Foundation for Science and Technology from the Spanish Ministry for Economy, Industry and Competitiveness and CSIC, the Spanish Council for Scientific Research, through the European Research Council (ERC). This documentary is a journey to the origins of dust grains through Laboratory Astrophysics.

The story unfolds in three levels: the journey of the recording team from Madrid (Spain) to Toulouse (France), the laboratory experiments explained by its principal investigators and the journey of the cosmic dust grains since they are born in the envelope of an evolved star until they become part of something bigger (a star, a planet or, why not, a living being). This work wants to transmit the expectations of the teams struggling to understand this process, the technological and human challenge involved in building complex machines whith a goal: to reproduce in a laboratory what happens in space.

The documentary will circulate along circuits of scientific movies and specific science channels for a year, and after that it will be available on the NANOCOSMOS website. The movie is available in Spanish with subtitles in English and French.

4 How to make a science documentary funded by FECYT

In 2016 the outreach team of Nanocosmos ERC, in CSIC, participated in an open call for funds made by the Spanish Foundation for Science and technology (FECYT) in order to produce a documentary about the project, entitled "Nanocosmos: a journey to the small". Writing such a proposal is, in itself, a hard and demanding work, as the templates are full of details that must be fulfilled.

The answer (positive) came in January 2017, but it was a provisional answer, so in order to initiate the process of making an open call for allocating a public contract, we had to wait for the definitive acceptance, given in May 2017. We were granted with 30,000 € (we asked for 33,000 €) for a project valued in 64.000 €. In the Spanish Public Administration, when the cost of a work is higher than 18,000 € it is compelling to do a public open contract process. As the institution awarded with the FECYT money (a public institution) was the ICMM-CSIC (also public), the contract had to be elaborated in the Public Procurement Department of CSIC. So, together with them, we began the redaction and elaboration of the documents needed to open a call for the enterprises specialized in science outreach documentaries. There was no precedent in the CSIC institution, so we had to begin from scratch. Once elaborated and approved by the Public Procurement Department of CSIC, we initiated the open process that usually requires three months to be completed.

In our case, August was just in the middle of that period of time, so we had to wait one more month to know which enterprise was selected. Finally, from the four enterprises that participated in the open call, the selected one was LuzLux S.L. It was announced in middle September. The team had barely six months to familiarize with the issue (laboratory astrophysics and astrochemistry), document, write, record, edit and promote a 40-minute documentary... We were already running out of time -as FECYT gives extension of deadlines if you do it in time, we asked for it, so our deadline was extended for three months (officially, from December 2017 to March 2018).

The initial agenda had to change, as we had to record travelling from Madrid to Toulouse and we could not risk the winter time to avoid us to do the recordings outdoors. The recordings and interviews were made during several weeks in November, December and January. The final script was finished at the end of January. The spot was ready the 20th of March 2018. The director, Fernando Rey, the promoter and Principal Investigator of the documentary FECYT project, Natalia Ruiz Zelmanovitch, the Scientific Adviser and Principal Investigator of NANOCOSMOS ERC, José Cernicharo, and the rest of the team [2], presented the documentary, together with Ana M. Correas, Coordinator of the Museo Nacional de Ciencia y Tecnología (MUNCYT) at the Coruña Headquarters. It was the 13th of April of 2018, as FECYT allows one more month to do administrative activities (mainly, paying bills).

Once presented, the documentary is participating in circuits of scientific movies and specific science channels (until March 2019), and after that it will be available on the NANOCOSMOS website. The movie is available in 4 HD and 4k, and has four different versions: Spanish without subtitles, Spanish with subtitles in Spanish, Spanish with subtitles in English and Spanish with subtitles in French.

5 Last steps: justification, promotion and distribution

The period established for the justification process was one month (April 2018). In our case, we had just three bills to present, as everything was included in two packs: LuzLux (producer of the whole movie) and Scixel (3D design). FECYT also requested the whole contracting dossier (400 pages) and other documents. The final answer accepting all the documents required arrived the 2nd of July 2018.

Concerning the promotion and distribution, as the money granted by FECYT has to be spent in the period stablished by the deadlines (in our case, all the bills had to be paid before the 30th of April), we couldn't hire a distribution company to take care of those tasks. We are now using online platforms to promote and distribute the movie, also participating in contests as the Premios Prismas de la Casa de las Ciencias a la Divulgación and the Bienal Internacional de Cine Científico and offering it to schools, associations, science platforms and all kind of people previously interested in science.

[2]Original idea: Natalia Ruiz Zelmanovitch; Realization: LUZLUX S.L.; Direction: Fernando Rey Daluz; Scientific Advisor: José Cernicharo Quintanilla; Script: Luis Rodríguez Cao, Natalia Ruiz Zelmanovitch, Sara Fernández; Production: Gonzalo Corral, Patricia Fernández, QUADRADO VERDE, Natalia Ruiz Zelmanovitch, Miguel Rey; Recordings: Santiago Blanco, Fernando Rey Daluz; Sound: Santiago Blanco, Gonzalo Corral; Postproduction: LUZLUX S.L.; 3D Design: Enrique Sahagún, SCIXEL; Voiceover: Ana Lemos.

Figure 2: Poster of the "NANOCOSMOS: Un viaje a lo pequeño" road movie premiere, and institutions participating in the documentary. Credit: LuzLux.

6 Summary

Increasing resources invested to create knowledge and improving the mechanisms used to transfer such knowledge so that it benefits society as a whole must be top priorities of all governments. This is why our project pulls for science and science outreach as some of the best ways to make a better society.

In short, we have a documentary talking about laboratory astrophysics that defends basic science, team work, the relevance of instrumentation in astrochemistry, the science internationalization, and the gender focus, telling a story as a road movie, in an adventure seeking for knowledge.

Our motto is:

Figure 3: "#NoScience, no future" motto campaign.

Acknowledgments

NANOCOSMOS ERC has received funding from the European Research Council (ERC) under the European Union's Seventh Framework Programme (FP7/2007-2013) / ERC-2013-SyG Grant Agreement no. 610256.

"NANOCOSMOS: Un viaje a lo pequeño" is funded by the Fundación Española para la Ciencia y la Tecnología (FECYT) from the Ministerio de Ciencia, Innovación y Universidades (Spain) through the Project FCT-2016-10779.

People in the movie "NANOCOSMOS: Un viaje a lo pequeño": GEM: José Luis Alonso, Santiago Mata, Lucie Kolesniková, Elena Rita Alonso, Iker León. CRESU: Elena Jiménez, Bernabé Ballesteros, Antonio José Ocaña Fernández, Sergio Blázquez González. TOULOUSE: Christine Joblin, Richard Clergereaux, Hassan Sabbah, Anthony Bonnamy, Karine Demyk, Shubhadip Chakraborty, Rémi Bérard, Ming-Chao Ji, Olivier Berné, Kremena Makasheva, Mathias Rojo, Simon Dap, Xavier Glad, Pavel Yuryev. MADRID ICMM (CSIC): José Ángel Martín Gago, Lidia Martínez, Gonzalo Santoro, Pablo Merino, Mª Francisca López, Koen Lauwaet, Javier Méndez, Carlos Sánchez. MADRID IFF (CSIC): José Cernicharo, Nuria Marcelino, Marcelino Agúndez, Javier Rodríguez Goicoechea, Sara Cuadrado, Marcelo Castellanos, Juan Ramón Pardo, José Pablo Fonfría, Luis Velilla, Emeric Bron, Sarah Massalkhi, Guillermo Quintana, Elena Moreno, Jason Champion, Octavio Roncero. MADRID IEM (CSIC): Isabel Tanarro, Victor José Herrero, Ramón Javier Peláez. YEBES: Juan Daniel Gallego, Belén Tercero, Miguel Santander, Javier Alcolea, Ricardo Ignacio Amils, Rafael Bachiller, Valentín Bujarrabal, Francisco Colomer, Pablo de Vicente Abad, Mª Carmen Díaz, Asunción Fuente, Miguel Gómez, Isaac López Fernández, Antonio José Ocaña Fernández.

Highlights on Spanish Astrophysics X, Proceedings of the XIII Scientific Meeting of the Spanish Astronomical Society held on July 16 – 20, 2018, in Salamanca, Spain. B. Montesinos, A. Asensio Ramos, F. Buitrago, R. Schödel, E. Villaver, S. Pérez-Hoyos, I. Ordóñez-Etxeberria (eds.), 2019

Studying Astronomy in Portugal and the IA, the best choice for your future career.

Fernando Buitrago[1,2], **and Jose Afonso**[1,2]

[1] Instituto de Astrofísica e Ciências do Espaço, Universidade de Lisboa, OAL, Tapada da Ajuda, PT1349-018 Lisbon, Portugal
[2] Departamento de Física, Faculdade de Ciências, Universidade de Lisboa, Edifício C8, Campo Grande, PT1749-016 Lisbon, Portugal

Abstract

When Spanish students (and not only those) consider possible places where to study Astronomy in the Iberian peninsula, many of them overlook Portugal as an interesting destination. Both the University of Lisbon and the University of Porto offer high quality university degrees in Astronomy. Moreover, the Institute of Astrophysics and Space Sciences (IA) links in a single institute researchers from both institutions, making it one of the best places for interacting and learning from top astronomers in many different areas (Solar System and Exoplanets, Stars, Galaxies and Cosmology, Instrumentation). Additionally, a number of PhD positions are offered every year. With so many good things going on... why don't you join us? (See poster).

Highlights on Spanish Astrophysics X, Proceedings of the XIII Scientific Meeting of the Spanish Astronomical Society held on July 16 – 20, 2018, in Salamanca, Spain. B. Montesinos, A. Asensio Ramos, F. Buitrago, R. Schödel, E. Villaver, S. Pérez-Hoyos, I. Ordóñez-Etxeberria (eds.), 2019

The telescopes of the CESAR initiative of the European Space Agency.

A. de Burgos[1,2], M. G. Breitfellner[1], M. P. Ayúcar[1], E. Fini[3], and M. Castillo[1]

[1] European Space Astronomy Centre (ESAC), PO Box 78, 28691 Villanueva de la Cañada, Madrid, Spain
[2] Departamento de Astrofísica y Ciencias de la Atmósfera, Facultad de Física, Universidad Complutense de Madrid, 28040 Madrid, Spain
[3] Politecnico di Milano, Piazza Leonardo da Vinci, 32, 20133 Milano, Italy

Abstract

CESAR (Cooperation through Education in Science and Astronomy Research) is an educational program from the European Space Agency (ESA), which aims to provide European students with practical experience in astronomical research, in particular in the fields of space science, optical astronomy and radioastronomy. To do so, it makes use of an infrastructure based on semi-automatized observatories and antennas which observe during day and night. (See poster).

Highlights on Spanish Astrophysics X, Proceedings of the XIII Scientific Meeting of the Spanish Astronomical Society held on July 16 – 20, 2018, in Salamanca, Spain. B. Montesinos, A. Asensio Ramos, F. Buitrago, R. Schödel, E. Villaver, S. Pérez-Hoyos, I. Ordóñez-Etxeberria (eds.), 2019

Un tros de Cel (A piece of sky).

Cristina Negro[1], Mónica Pallardó[1], M. Jesús Moya[1], and Amelia Ortiz-Gil[1]

[1] University of Valencia Astronomical Observatory (Spain)

Abstract

Exhibition that aims to help students learn more about our Solar System and see it as something closer and familiar. The students will be able to see in each cube a piece of each planet or moon, feeling that they have in their hands "un tros de cel" - "a piece of sky". Likewise, students can perform different activities with the exhibition, such as identifying cubes with planets and moons, discussing the possibility of life, inferring the corresponding temperatures... (See poster).

Highlights on Spanish Astrophysics X, Proceedings of the XIII Scientific Meeting of the Spanish Astronomical Society held on July 16 – 20, 2018, in Salamanca, Spain. B. Montesinos, A. Asensio Ramos, F. Buitrago, R. Schödel, E. Villaver, S. Pérez-Hoyos, I. Ordóñez-Etxeberria (eds.), 2019

Radio-astronomy projects for university students.

J. Sabater[1], **and S. Johnston**[1]

[1] SUPA, Institute for Astronomy, Royal Observatory, Blackford Hill, Edinburgh, EH9 3HJ, UK

Abstract

The recent availability of cheap Software Defined Radio (SDR) receivers makes possible the exploration of new aspects of radio-astronomy in a practical and inexpensive way. The SDR is one of the base technologies of upcoming data intensive radio-telescopes, like the Square Kilometre Array (SKA). We are currently building a radio station based on general use SDR receivers at the Royal Observatory of Edinburgh. Our main aim is to develop innovative projects for the training of students in the new radio data intensive techniques. The projects range from the measurement of Milky Way atomic gas to the detection of pulsars. In this poster we present an overview of the observatory and the projects under development and show how it can be used to train students in the new aspects of astronomical research.

Additional updated information can be found in `https://www.jsabater.info/sea2018/`.

This project was supported by alumni and friends of the University of Edinburgh through an Innovation Initiative Grant. (See poster).

Highlights on Spanish Astrophysics X, Proceedings of the XIII Scientific Meeting of the Spanish Astronomical Society held on July 16 – 20, 2018, in Salamanca, Spain. B. Montesinos, A. Asensio Ramos, F. Buitrago, R. Schödel, E. Villaver, S. Pérez-Hoyos, I. Ordóñez-Etxeberria (eds.), 2019

Inclusion of teaching aspects of astronomy in scientific-technical degrees. Case studies and examples.

Ana Ulla[1], Minia Manteiga[2,3], Pablo López Varela[2], Alsira Salgado Don[2], and Carlos Dafonte[3,4]

[1] Depto. de Física Aplicada. Área de Astonomía e Astrofísica. Universidade de Vigo
[2] Depto. Ciencias de la Navegación e Ingeniería Marina. Universidade da Coruña
[3] CITIC, Universidade da Coruña
[4] Departamento de Computación. Universidade da Coruña

Abstract

Astronomy is a powerful teaching tool, as it provides a realistic and very illustrative vision of how the universe works. Complemented by the use of the laws of physics and mathematics, it helps to understand from a scientific-technical point of view many situations, processes and phenomena of daily life or others at all scales, from subatomic to cosmological. In this contribution we will present several representative cases of the inclusion of astronomical knowledge as part of the daily teaching methodology in degree studies whose main subject is not astronomy itself.(See poster).

Highlights on Spanish Astrophysics X, Proceedings of the XIII Scientific Meeting of the Spanish Astronomical Society held on July 16 – 20, 2018, in Salamanca, Spain. B. Montesinos, A. Asensio Ramos, F. Buitrago, R. Schödel, E. Villaver, S. Pérez-Hoyos, I. Ordóñez-Etxeberria (eds.), 2019

NixNox project: places to stargaze.

Jaime Zamorano[1], Lucía García[1], Francisco Ocañal[1], Alejandro Sánchez de Miguel[2], Carlos Tapia[1], Mireia Nievas[3], Jesús Gallego[1], Emilio Alfaro[4]

[1] Departamento de Física de la Tierra y Astrofísica, Universidad Complutense de Madrid
[2] Environment and Sustainability Institute, University Exeter (UK)
[3] Deutches Elektronen-Synchrotron (DESY), Zeuthen (Germany)
[4] Instituto de Astrofísica de Andalucía (CSIC), Granada

Abstract

The places where you can enjoy the celestial vault in its greatest splendour are disappearing with the increase of light pollution. The NixNox project promotes a collaborative effort of amateur and professional astronomers to locate y characterize the night sky of spots of easy access where star gazing under unpolluted skies.
To obtain the night sky background it is necessary to observe and measure standard stars using a telescope and CCD camera. This is a technical task that demands time and data analysis. We designed a simple method that relies in measures with a hand-held device, as the Sky Quality Meter (SQM) or the TESS photometer, during clear and moonless nights. Besides the usual measure at zenith, the NixNox method demands observations at 20, 40, 60 y 80 degrees over the horizon at 12 orientations in all cardinal directions. The resulting all-sky map representing the night sky brightness of the complete vault provides visual information of the location of the sources of light pollution and their relative contribution to the brightness.
We have more that 130 characterized places with information of the location, how to arrive, facilities, and panoramic pictures (day and night) that allow the interested citizen to get an idea of horizon of the open-air observatory. The information is displayed in a webpage and our goal is to encourage the society to enjoy these places and the public administration to appreciate and to preserve them. (See poster).